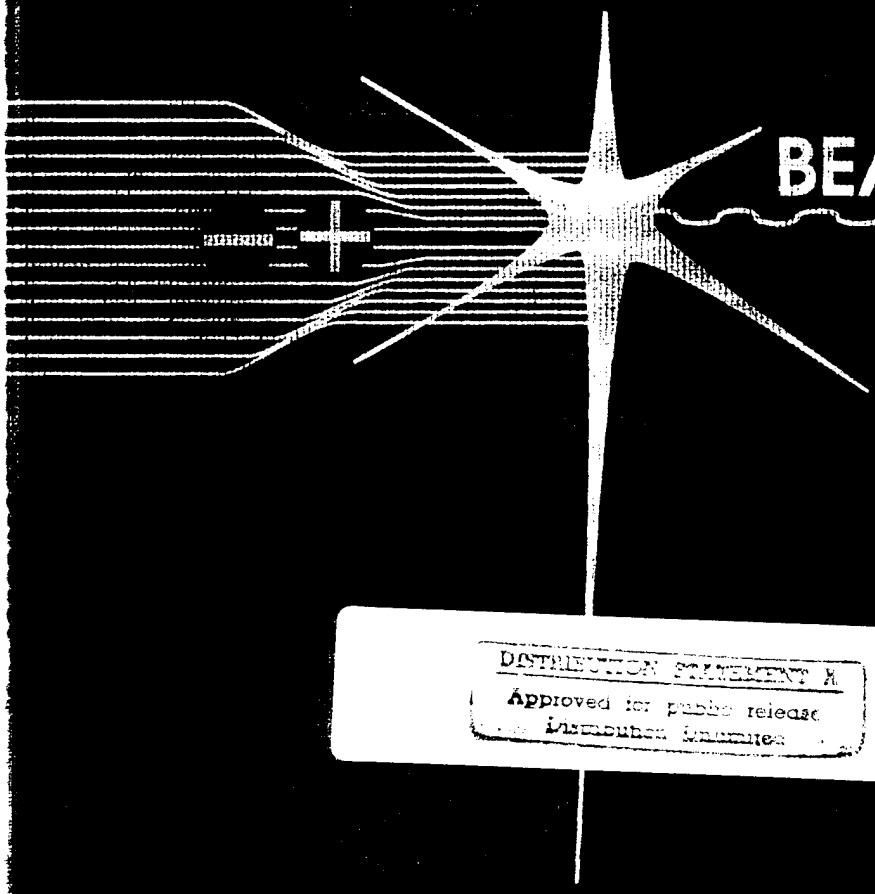
10th International Conference on High Power Particle Beams

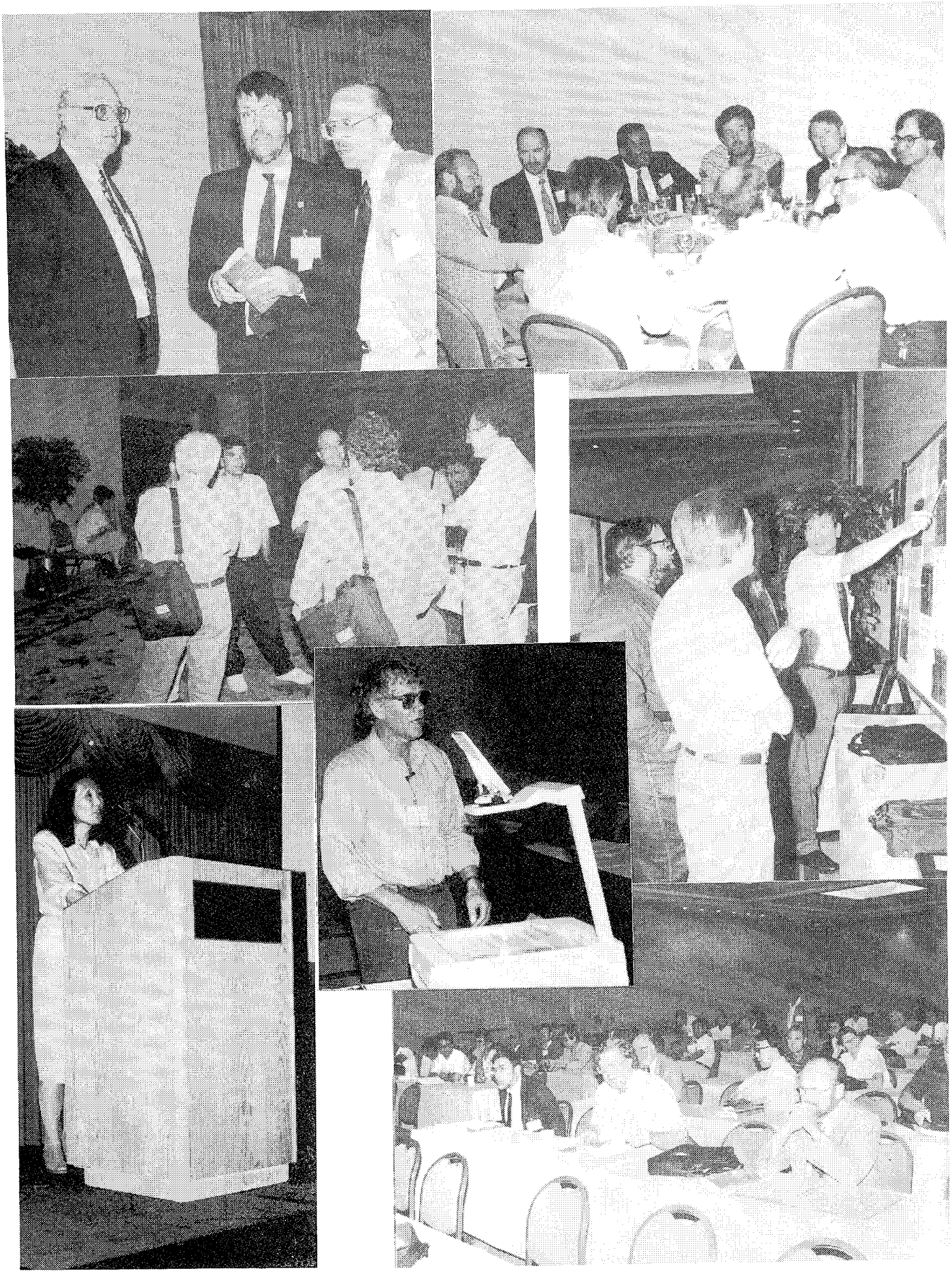


BEAMS '94

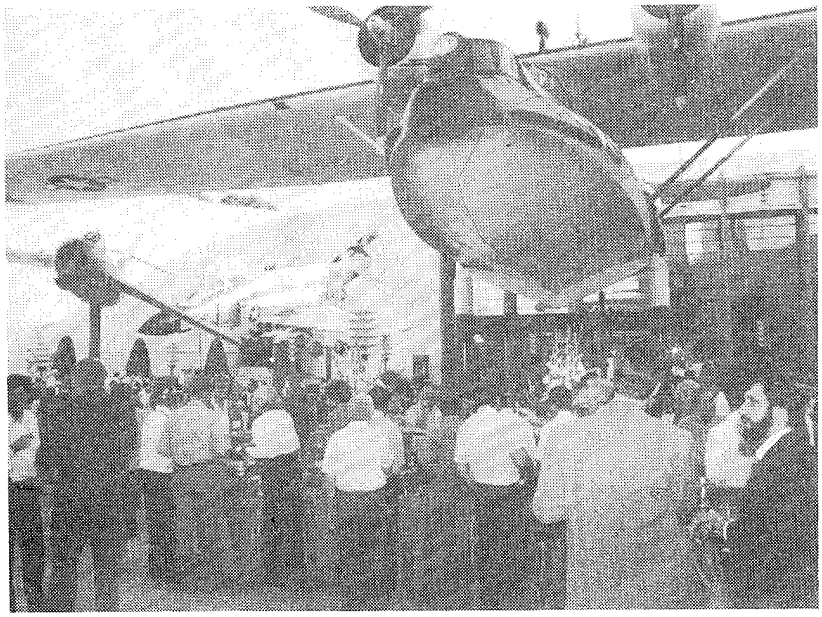
DISTRIBUTION STATEMENT A
Approved for public release
Distribution Unlimited

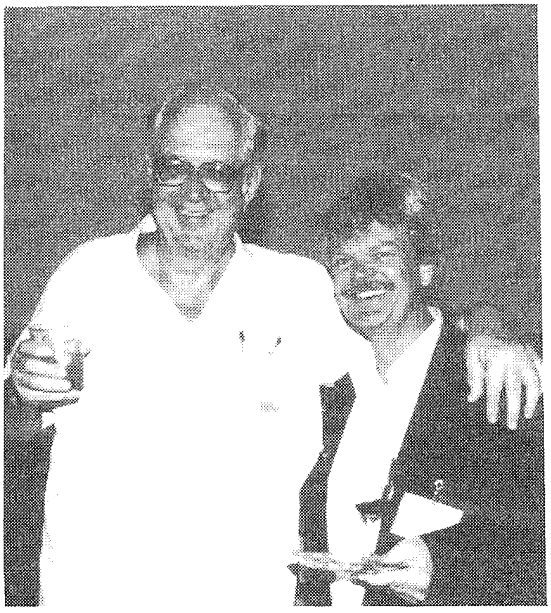
June 20-24, 1994
San Diego, CA

19950711 015

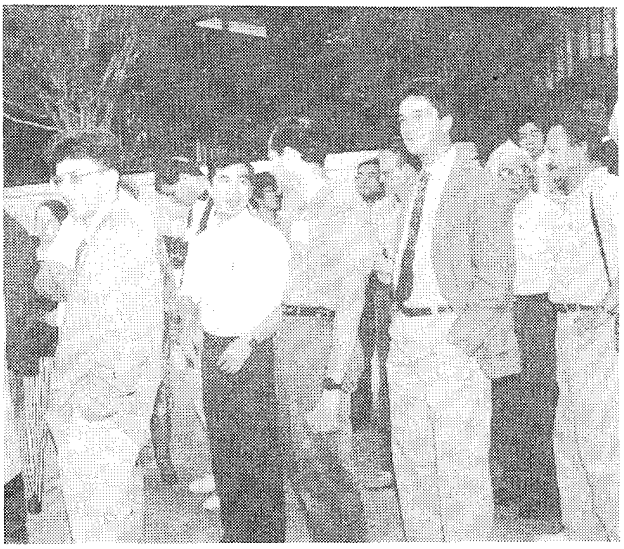


DTIC QUALITY INSPECTED 5

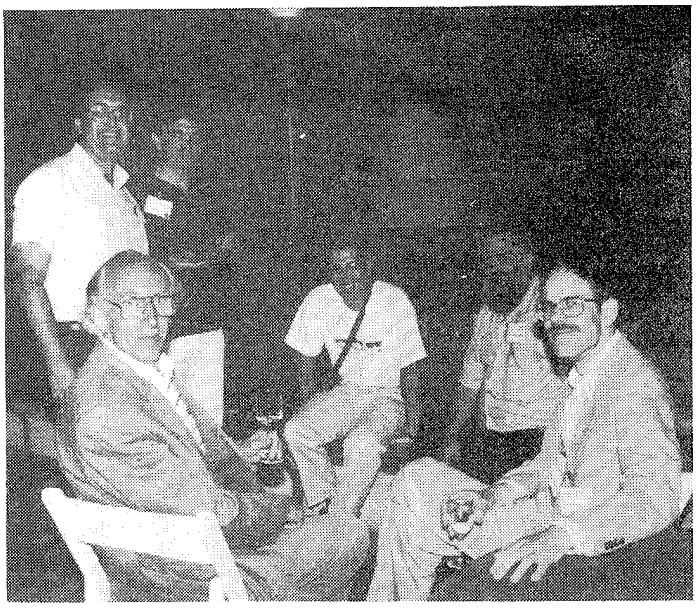












10th International Conference

on

High Power Particle Beams

June 20-24, 1994
San Diego, California

CONFERENCE HOST
Maxwell Laboratories, Inc.

Conference Chairman
Alan C. Kolb

Conference Co-Chairman
Roger White

Technical Chairman
William Rix

Conference Coordinator
Amanda Ness

Accesion For
NTIS CRA&I
DTIC TAB
Unannounced
Justification
By
Distribution /
Availability Codes
Dist | Avail and / or Special
A-1

INTERNATIONAL COMMITTEE

A. Blaugrund, Weizmann Inst. of Science, Israel

T. Coffey, Naval Research Laboratory, USA

D. Cook, Sandia National Laboratories, USA

G. Cooperstein, Naval Research Laboratory, USA

H. Doucet, C.E.A. Ecole Polytechnique, France

K. Jungwirth, Czech Academy of Sciences, Czech

G. Kessler, Kernforschungszentrum Karlsruhe, Germany

A. Kolb, Maxwell Laboratories, Inc., USA

G. Mesyats, Academy of Sciences, Russia

S. Nakai, Osaka University, Japan

W. Rix, Maxwell Laboratories, Inc., USA

D. Ryutov, Inst. of Nuclear Physics, Russia

V. Smirnov, TRINITI, Troitsk, Russia

C. Stallings, Physics International Co., USA

R. Sudan, Cornell University, USA

R. White, Maxwell Laboratories, Inc., USA

K.Yatsui, Nagaoka University of Technology, Japan

NATIONAL STEERING COMMITTEE

F. Agee, Phillips Laboratory

R. Barker, Bolling Air Force Base

J. Benford, Physics International Company

C. Fenstermacher, Los Alamos National Lab.

B. Godfrey, Phillips Laboratory

V. Granatstein, University of Maryland

D. Hammer, Cornell University

D. Hinshelwood, Jaycor

S. Humphries, Acceleration Associates

A. Hyder, University of Notre Dame

N. Luhmann, UCLA

J. Ma Piere, Defense Nuclear Agency

D. Mosher, Naval Research Laboratory

N. Pereira, Berkeley Research Associates

D. Prosnitz, Lawrence Livermore National Lab.

M. Reiser, University of Maryland

C. Roberson, Office of Naval Research

N. Rostoker, UC Irvine

P. Rustan, BMO

M. Sluyter, U.S. Department of Energy

I. Smith, Pulse Sciences, Inc.

I. Vitkovitsky, Logicon/RDA

A. Wilson, Energy Compression Res. Corp.

G. Yonas, Sandia National Laboratories

TECHNICAL COMMITTEE

C. Deeney, Physics International

E. Garate, UC Irvine

D. Hinshelwood, Jaycor

S. Humphries, Acceleration Associates

I. Maron, Weizmann Institute

D. Mosher, Naval Research Laboratory

W. Rix, Maxwell Laboratories, Inc.

N. Rostoker, UC Irvine

R. Stinnett, Sandia National Lab.

E. Waisman, Maxwell Laboratories, Inc.

F. Wessel, UC Irvine

The 10th International Conference on High Power Particle Beams was held in San Diego, California on 20-24 June 1994 and was hosted by Maxwell Laboratories, Inc. These conferences began in 1974 and have been held at various locations throughout the world in the intervening years. BEAMS 94 drew on this rich heritage but was different from previous meetings in two aspects

The Political/Economic Climate

For the entire history of the conference, the purpose of the BEAMS meetings has been to provide a forum to discuss technical developments and increased understanding in the field of high power beams. The BEAMS 94 meeting was unique because of dramatic changes in the international political climate. One of the primary application for beams technology has been in the military realm. Consequently the information exchange had been previously limited to issues relating to the physics of beams. In the new political climate of 1994, military budgets are shrinking and military requirements are no longer the primary driver for technology development. Economics is emerging as a more important consideration than military applications. BEAMS 94 was characterized by increased openness of information exchange and by a universal emphasis on identifying commercial applications for beams technology.

The Structure of the Technical Program

The BEAMS meetings have traditionally avoided parallel sessions as a manifestation of the International Committee's belief in the integrated nature of this field. BEAMS 94 maintained this tradition. However at the advice of the International Committee, the program placed a relatively stronger emphasis on poster sessions. The meeting included four, two hour long poster sessions and authors were urged to display their papers for the entire day. Posters accounted for about 75 percent of the papers presented at the meeting. Also at the suggestion of Professor Ryutov, this year's meeting concluded with a panel discussion on the future of beams as an area.

Program Highlights

Some trends emerged from technical papers presented at the meeting. In the area of power conditioning and accelerator technology for large, single-shot machines, inductive energy storage techniques using vacuum opening switches have moved beyond the conceptual stage and into design and construction. By BEAMS 96, in Prague, Czech Republic, we should hear a number of reports on the initial operating performance of this type of driver. Smaller rep-rated machines are also being built and tested. Considerable progress has been made in the areas of ion beam generation and propagation through an intense collaboration of modeling and experiment. Many new applications for high power beams are under active investigation throughout the world.

The Panel Discussion served to summarize the goals and future directions envisioned for the field of high power beams by a group of international leaders. Members of the panel included Alan Kolb, Forrest J. Agee, Don Cook, and Ravi Sudan from the United States, Hans Bluhm from Germany, Henri Doucet from France, Leonid Rudakov from Russia, and Yoshi Yatsui from Japan. During the first hour of the discussion, each panelist presented a brief overview of his perspective on state of the high power beams field. Most members agreed that traditional applications of beams technology for military purposes or for inertial confinement fusion using ions will continue but will not be growth areas. Several speakers mentioned collaborations between government laboratories, universities, and industry for commercial usage of the technology as being the key to future growth in this field. After the initial statements, questions and comments from the audience were invited. During this discussion a number of concerns about keeping this field viable and attractive to younger scientists were expressed. Dr. Kolb concluded the session and the meeting by thanking the participants for their contributions and inviting everyone to continue these types of discussions at BEAMS 96 in Prague.

Proceedings Organization

The organization of these Proceedings parallels the organization of the technical sessions. The same topics were used for both the oral sessions and the poster sessions with the oral papers generally presenting more of an overview of the topic with more detailed discussions being covered in the posters. The sessions of the meeting were:

Oral Session 1: Power Conditioning and Accelerator Technology
Oral Session 2: Beam Generation
Oral Session 3: Beam Propagation
Oral Session 4: Applications of Beam Technology involving Plasmas
Oral Session 5: Beam-Matter Applications
Oral Session 6: Beams for FEL's, KrF Lasers, and High Power Microwaves

Poster Session 1: Power Conditioning, Accelerator Technology, and Ion Beam Generation
Poster Session 2: Electron Beam Generation and Beam Propagation
Poster Session 3: Applications of Beam Technology involving Plasmas and Beam-Matter Applications
Poster Session 4: Beams for FEL's, KrF Lasers, and High Power Microwaves

Acknowledgments

The papers in this Proceedings reflect the state of the field as of the Beams 94 meeting. We greatly appreciate the energy, support, and technical contributions of all the participants in BEAMS 94. The conference's success is due to their efforts.

A special thanks is extended to the sponsors of the BEAMS 94 Conference for their continued support of this meeting:

Army Research Laboratory
Defense Nuclear Agency
Department of Energy
Lawrence Livermore National Laboratory
Los Alamos National Laboratory
Maxwell Laboratories, Inc.
Naval Research Laboratory
Office of Naval Research
Phillips Laboratory
Physics International Company
Sandia National Laboratories
University of Maryland
University of Notre Dame

We look forward to the continued success of this meeting at BEAMS 96 in Prague.

TABLE OF CONTENTS

ORAL - POWER CONDITIONING AND ACCELERATOR TECHNOLOGY

Invited - Opening Switch Research and Development for DECADE, Goyer, J.R., Kortbawi, D., Childers, F.K., Dempsey, J.A., Roth, I.S., Sincerny, P.S. 1

Microsecond Conduction Time Plasma Opening Switch Research at NRL, Weber, B.V., Commisso, R.J., Cooperstein, G., Grossmann, J.M., Ottinger, P.F., Goodrich, P.J., Hinshelwood, D.D., Riley Jr., R.A., Swanekamp, S.B. 8

ACE 4 Inductive Energy Storage Power Conditioning Performance, Thompson, J., Coleman, P., Gilbert, C., Husovsky, D., Miller, A.R., Rauch, J., Rix, W., Robertson, K., Waisman, E. 12

Experiments with Microsecond Magnetically Controlled Plasma Opening Switch, Lisitsyn, I.V., Bystritskii, V.M., Sinebryukhov, A.A., Sinebryukhov, V.A., Kim, A.A., Kokshenev, V.A., Koval'chuk, B.M., Loginov, S.V., McDaniel, D.H., Mendel, C.W., Savage, M.E., Zagar, D.M., Simpson, W.W. 17

Repetitive Generators with Plasma Opening Switch, Ushakov, A.G., Barinov, N.U., Belenki, G.S., Dolgachev, G.I., Kovalev, Yu.I., Zakatov, L.P. 21

2D Simulations of Cascade Magnetocumulative Generators in Euler-LaGrange Variables, Zoubov, A.D., Simonenko, V.A. 25

Comparison of DC and Pulsed Beams for Commercial Applications, Adler, R. 29

Invited - Pulsed Power Accelerator Technology Based on Solid-State Semiconductor Opening Switches (SOS), Rukin, S.N., Kotov, Y.A., Mesyats, G.A., Filatov, A.L., Lyubutin, S.K., Alichkin, Y.A., Darznek, S.A., Telnov, V.A., Sloviskowvskii, B.G., Timoshenkov, S.P., Bushlyakov, A.I., Turov, A.M. 33

Novel, Compact Two-Beam Accelerator, Lau, Y.Y., Derbenev, Y.S., Gilgenbachk, R.M., Hochman, J., Luginsland, J., Walter, M., Ching, C.H. 37

Plasma Opening Switch Experiments at Sandia National Laboratories, Savage, M.E., Hong, E.R., Simpson, W.W., Usher, M.A. 41

Theory of Ion Beam Generation for Ripple Anode Surface, Fedorov, V.M. 45

ORAL - BEAM GENERATION

Invited - Progress in Lithium Beam Power, Divergence, and Intensity at Sandia National Laboratories, Mehlhorn, T.A., Bailey, J.E., Chandler, G.A., Coats, R.S., Cuneo, M.E., Derzon, M.S., Desjarlais, M.P., Dukart, R.J., Filuk, A.B., Haill, T.A., Ives, H.C., Johnson, D.J., Leeper, R.J., Lockner, T.R., Mendel, C.W., Menge, P.R., Mix, L.P., Moats, A.R., Moore, W.B., Pointon, T.D., Poukey, J.W., Quintenz, J.P., Rosenthal, S.E., Rovang, D., Ruiz, C.L., Slutz, S.A., Stygar, W.A., Wenger, D.F. 53

Charged Particle Dynamics in the Acceleration Gap of the PBFA II Ion Diode, Bailey, J.E., Carlson, A.L., Filuk, A.B, Johnson, D.J., Lake, P., McGuire, E.J., Mehlhorn, T.A., Pointon, T.D., Renk, T.J., Maron. Y. 57

TABLE OF CONTENTS

Results of the First 2-Stage Diode Experiments on PBFA II, Lockner, T.R., Slutz, S.A., Johnson, D.J., Desjarlais, M.P., Poukey, J.W. 61

Complete Mode-Set Stability Analysis of Magnetically Insulated Ion Diode Equilibria, Slutz, S.A., Lemke, R.W. 65

Energetic Ions and Electrons Produced in a Hollow Cathode Vacuum Spark, Skowronek, M., Ikhlef, A., Louvet, G., Romeas, P., Mittal, K.C. 69

Stability and Operating Characteristics of the Applied B Proton Extraction Diode on KALIF, Bluhm, H., Hoppe, P., Bachmann, H., Bauer, W., Baumung, K., Buth, L., Laqua, H., Ludmirski, A., Rusch, D., Stoltz, O., Yoo, S. 77

A Contribution to the Magnetic Focusing in an Applied B-Extractor Ion Diode by a Laser Pulse Driven Solenoid, Bauer, W.H., Hobel, W., E. Stein, Ludmirsky, A., Westermann, T., ...83

Intense Proton Beam Source for ITER Neutral-Beam Spectroscopy Diagnostics, Bartsch, R.R., Davis, H.A., Henins, I., Greenly, J.B. 87

Physics of the Electron Emission from Metal-Dielectric Cathodes, Mesyats, G.A. 93

The Dynamics of the Generation of High Current Relativistic Electron Beams in Coaxial Magnetically-Insulated Vacuum Diodes, Pegel, I.V., Korovin, S.D. 100

ORAL - BEAM PROPAGATION

Invited - LIF Standoff Research, Olson., C.L., Cuneo, M.E., Desjarlais, M.P., Filuk, A.B., Hanson, D.L., Lockner, T.R., Maenchen, J.E., Mazarakis, M.G., Mendel, C.W., Menge, P. R., Nash, T.J., Olson., R.E., Pointon, T.D., Poukey, J.W., Quintenz, J.P., Sanford, T.W.L., Slutz, S.A., Hinshelwood, D.D., Rose., D.V., Hubbard, R.F., Lampe. M., Mosher, D., Neri, J.M., Ottinger, P.F., Slinker, S.P., Stephanakis, S.J., Young, F.C., Welch, D.R., Greenly, J.B., Oliver, B.V., Olson, J.C., Smith, J.R., Peterson, R.R. 104

Light-Ion-Beam Transport Research at NRL, Ottinger, P.F., Hubbard, R.F., Lampe, M., Mosher, D., Neri, J.M., Slinker, S.P., Stephanakis, S.J., Young, F.C., Hinshelwood, D.D., Rose, D.V., Olson, C.L., Welch, D.R., Noonan, W. 112

Development of a Plasma Lens as a Fine Focusing Lens for Heavy-Ion Beams, Stetter, M., Christiansen, J., Kumpf, C., Neuner, U., Stowe, S., Tkotz, R., Tauschwitz, A., Hoffmann, D.H.H., Spiller, P. 116

Invited - Resonant and Chaotic Phenomena in a Periodically Focused Intense Charge-Particle Beam, Chen, C., Davidson, R.C., Qian, Q., Jameson, R.A. 120

High-Current Electron Beam Transport and Acceleration in LIA-30, Gordeev, V.S., Bossamykin V.S., Veresov, V.P., Gerasimov, A.I., Gritsina, V.P., Grishin, A.V., Gornostay-Pol'skii, S.A., Averchenkov, V. Ya., Lazarev, V.P., Syutin, O.N., Tarasov, A.D., Fedotkin, A.S. 128

High Current Beam Propagation Studies at the Naval Research Laboratory, Meger, R.A., Murphy, D.P., Myers, M.C., Weidman, D.J., Fernsler, R.F., Hubbard, R.F., Slinker, S. 132

TABLE OF CONTENTS

New Results of the Full Scale Ribbon Beam Experiments on U-2 Device, Arzhannikov, A. V., Bobylev, V.B., Nikolaev, V.S., Sinitsky, S.L., Tarasov, A.V. 136

Intense Electron-Beam Transport in the Ion-Focused Regime through the Collision-Dominated Regime, Sanford, T. W.L., Poukey, J. W., Welch, D.R., Mock, R.C. 140

Quasicontinuous Model for Electron Flow in Magnetically Insulated Multigap Inductive Accelerator, Ryutov, D., Sudan, R.N. 144

ORAL - BEAM TECHNOLOGY FOR PLASMA INTERACTIONS

Invited - Acceleration and Compression of Compact Toroid Plasmas, Kiuttu, G.F., Degnan, J.H., Peterkin, R.E., Ruden, E.L., Lehr, F.M., Outten, C.A., Holmberg, C.D., Baca, G.P., Bell, D.E., Chesley, A.L., Dearborn, M.E., Douglas, M.R., Englert, S.E., Englert, T.J., Havranek, J., Hussey, T.W., Marklin, G., Mullins, B.W., Price, D.W., Shumlak, U., Bird, G., Coffey, S.K., Seiler, S.W., Eddleman, J.L., Hammer, J.H., Hartman, C.W., McLean, H.S., Movlik, A.W., Chen, Y.G., Gale, D., Graham, J.D., Roderick, N.F., Turchi, P.J. 150

Plasma Radiation Source Implosion Limits Due to Azimuthal Asymmetries, Mosher, D. 159

Two-Dimensional Numerical Simulation of Imploding Plasma Liners, Zoubov, A.D., Adamkevich, G.A., Glazyrin, I.V. 163

Intermediate Density Z-Pinches Compression Dynamics Investigation, Gordeev, E.M., Dan'ko, S.A., Kalinin, Yu.G., Kopchikov, A.V., Korolev, B.D., Kuksov, P.V., Smirnova, E.A., Shashkov, A.Yu., Yan'kov, V.V. 167

Ka Spectral Diagnostics for Mg and A1 Plasmas Irradiated by Intense Li Beams, MacFarlane, J.J., Wang, P., Bailey, J.E., Mehlhorn, T.A., Dukart, R.J. 175

Numerical Simulation for a Practical Large-Size Pellet Implosion , Kawata, S., Saitoh, T. 179

Spectroscopic Investigations of the Plasma Behaviour in a Plasma Opening Switch Experiment, Maron, Y., Arad, R., Davara, G., Fruchtman, L., Krasik, Y.E., Shpitalnik, R., Weingarten, A., Sarfaty, M. 183

Self-Colliding Beams as an Alternative Fusion System, Rostoker, N., Binderbauer, M. 195

ORAL - BEAM-MATTER APPLICATIONS

Use of Pulsed E-Beams for the Initiation of Spectral Luminescence in Solids, Mesyats, G.A., Mikhaylov, S.G., Osipov, V.V., Solomonov, V.I. 202

Freon Destruction in Atmosphere by Relativistic Electron Beam, Kulbeda, V.E., Popov, N.A., Sopin, P.I., Sorokin, G.A. 205

Pulsed Electron Beams for the Irradiation of Flue Gases, Novoselov, Y.N., Mesyats, G.A. 207

TABLE OF CONTENTS

Invited - Hydrodynamic Beam-Target Interaction Experiments on the Karlsruhe Light Ion Facility KALIF, Baumung, K., Bluhm, H.J., Hoppe, P., Karow, H.U., Rusch, D., Stoltz, O., Singer, J., Kanel, G.I., Utkin, A.V., Razorenov, S.V. 211

Ion Beam Surface Treatment: A New Capability for Surface Enhancement, Stinnett, R.W., McIntyre, D.C., Buchheit, R.G., Neau, E.L., Greenly, J.B., Thompson, M.O. 215

Plasma and Particle Beam Processing at Los Alamos, Rej, D.J., Davis, H.A., Faehl, R.J., Henins, I., Reass, W.A., Scheuer, J.T., Tobin, J.A., Tuszewski, M., Waganaar, W.J., Wood, B.P., Contrad, J.R., Horswekk, N., Sridharan, K., Simpson, R.L., Tallant, D.R., Thompson, M.O. 222

Intense Ion Beam Characterization and Thermal Modeling for Beam Materials Processing, Davis., G.P., Rej, D.J., Ruiz, C.L., Waganaar W.J., H.A., Johston, Ruiz, C.L., Schmidlapp, F.A. 226

Utilization of High Power Ion Beams and High Current Electron Beams for Modification of Metalline Materials, Pogrebnjak, A.D. 232

Dynamics of the High-Power Ion Beam Interaction with Targets, Kanel, G.I., Utkin, A.V., Inst. of Chemical Physics-Russia - Baumung, K., Karow, H.U., Rusch, D. 236

E-Beam Heated Plasma as a Tool for ITER Disruption Simulations, Koidan, V.S., Astrelin, V.T., Burdakov, A.V., Filippov, V.V., Lebedev, S.V., Mekler, K.I., Melnikov, P.I., Postupaev, V.V., Rovenskikh, A.F., Sheheglov, M.A., Tsigutkin, K.V., Voropaev, S.G., Wuerz, H. ..240

Evaluation of Temperature and Pressure of Ablation Plasma in an Intense, Pulsed, Ion-Beam Evaporation, Yatsui, K., Kang, X., Masugata, K. 244

ORAL - FELs, KrF LASERS, AND HIGH POWER MICROWAVES

The Use of 2-D Distributed Feedback For Synchronization of Radiation in FEL's Driven by Intense Sheet and Tubular Relativistic Electron Beams, Peskov, N., Ginzburg, N.S., Sergev, A.S. 248

Increasing Useful FEL Undulator Aperture, Beam Current and Power of an Electron Beam Propagating in a Longitudinal Magnetic Field, Papadichev, V.A. 252

The NIKE Electron Beam-Pumped KrF Amplifiers, Sethian, J.D., Pawley, C.J., Obenschain, S.P., Gerber, K.A., Lehecka, T., McGeoch, M.W. 256

To the Electrodynamics of the Hybrid Plasma-Waveguide Structures (Theory and Experiment), Onishchenko, I.N., Antonov, A.N., Berezin, A.K., Bliokh, Y.P., Degtar, Y.A., Fainberg, Y.B., Egorov, A.M., Kovpik, OT., Kornilov, E.A., Lodygin, A.V., Lubarskij, M.G., Markov, P.I., Mitin, L.A., Miroshnichenko, V.I., Sotnikov, G.V., Svichensky, V.G. 260

Experimental Studies of High-Power Harmonic Gyroklystrons, Lawson, W., Calame, J.P., Cheng, I., Flaherty, M.K.E., Granatstein, V.L., Hogan, B., Irwin, V., Latham, P.E., Matthews, H., Nusinovich, G.S., Reiser, M. 264

The Long-Pulse, High-Current Relativistic Klystron at 500 MW and Beyond, Fazio, M.V., Carlsten, B.E., Haynes, W.B., Stringfield, R.M. 268

TABLE OF CONTENTS

Relativistic Magnetrons and Klystrons at Long Pulse Durations, Benford, J., Harteneck, B.D., Lam, S.K., Levine, J.S., Willey, M.J. 272

POSTER - POWER CONDITIONING, ACCELERATOR TECHNOLOGY, AND ION BEAM GENERATION

Modeling Magnetically Insulated Transmission Line Systems Using Flow Impedance, Mendel, C.W., Rosenthal, S.E. 276

Conduction Phase to Opening Phase Transition in the Plasma Opening Switch, Grossmann, J.M., Huba, J.D., Ottinger, P.F., Commisso, R.J., Weber, B.V., Swanekamp, S.B., Goodrich, P.J., Hinshelwood, D.D. 280

Magnetodynamics of Multicomponent Plasma, Rudakov, L.I. 284

Circuit Characterization of Magnetically Insulated Electron Flow, Parks, D.E., Steen, P. 291

Chordal Line-Integrals and the 2-D Snowplow Model of the Microsecond Plasma Opening Switch, Ingermanson, R., Parks, D., Waisman, E., Hinshelwood, D., Weber, B. 295

High Power Plasma Opening Switch Operation on HAWK, Goodrich, P.J., Hinshelwood, D.D., Commisso, R.J., Grossmann, J.M., Weber, B.V., P.F., Riley, Swanekamp, S.B. 299

Simulations of Vacuum Electron Flow in Inductive-Energy-Store Pulsed-Power Systems, Swanekamp, S.B., Commisso, R.J., Grossmann, J.M., Ottigner, P.F., Weber, B.V., Goodrich, P.J. 303

Experimental Research of Electron Magneto-Hydrodynamics Effects in the Microsecond POS, Belenki, G.S., Dolgachev, G.I., Kalinin, Yu.G., Nitishinski, M.S., Ushakov, A.G., Zakatov, L.P. 307

Experiments with Gas Puff Plasma Guns at GIT-4 Generator, Sinebryukhov, A.A., Sinebruyukhov, V.A., Ananjin, P.S., Karpov, V.B, Koval'chuk, B.M., Kokshenev, V.A., Fursov, F.I., Yakovlev, V.P. 311

First Experimental Observation of Switching the Microsecond Electron Beam by Reconnection of the Magnetic Field Lines, Sinitsky, S.L., Arzhannikov, A.V., Tarasov, A.V. 315

Switching Characteristics of Aluminum Foils Used in Small Inductively Energy Storage System, Sato, M., Nakamura, T., Nobuhara, S. 319

High Power Electron Generators Based on Charging of a Pulse-Forming Line by Means of Electrically Exploded Wire, Ratakhin, N.A., Kablambaev, B.A., Luchinsky, A.V., Makhrin, V.M., Sedio, V.S., Sergeenko, V.P. 323

High-Efficiency Pulsed Charging of Capacitors by Exploding Wires, Sedoi, V.S., Korostelev, A.F., Luchinsky, A.V. 327

Simulation of Flashover Generated by Strong TEM-Wave in MITL with Inner Coaxial Dielectric Insert, Galstjan, E. A. 331

TABLE OF CONTENTS

Outgassing and Plasma Development in the Early Phase of Dielectric Surface Flashover in Vacuum, Masten, G., Mueller, T., Krompholz, H., Hegler, F., Hatfield, L.L., Kristiansen, M. 335

Control of a Large Vacuum Wave Precursor on the SABRE Voltage Adder MITL and Extraction Ion Diode, Cuneo, M.E., Hanson, D.L., Poukey, J.W., Menge, P.R., Savage, M.E., Smith, J.R., Bernard, M.A. 339

Accelerating Voltage Increase in High-Power Accelerator, Kazanskiy, L.N., Korenev, I.L., Oreshin, A.A. 343

PBFA-II Modification for High-Power High-Convergence Implosion Experiments, Mazarakis, M.G., Smith, D.L., Bennett, L., Olson., R.E., Lockner, T.R., Poukey, J.W., Ramirez, J.J. 347

Power Electron Beam Front Shortening in MITL with Inner Coaxial Dielectric Insert, Kazanskiy, L.N., Galstjan, E.A. 351

MRTI Activity in the Field of Accelerators 1946-1992, Seleznev, V.D., Batskikh, G.I. 355

Status of AIRIX, Launspach, J., Anthouard, P., Bardy, J., Bonnafond, C., Delsart, P., Devin, A., Eyharts, P., Eyl, P., Labrouche, J., le Taillandier, P., de Mascureau, J., Merle, E., Ployart, G., Roques, A., Thevenot, M., Villate, D. 359

First Operation of New Inductive Accelerating Module at JAERI, Kawasaki, S., Shiho, M., Sakamoto, K., Maeda, H., Musyaki, S., Ishizuka, H., Watanabe, Y., Tokuchi, A., Yamashita, Y., Nakajima, S. 363

Multipole Field Calculations for DARHT, Hughes, T., Clark R., Allison, P., Moir, D.C. ...367

Device EMIR-M Generator of Impulse Electron Beams, Bremsstrahlung, and Electromagnetic Fields, Diyankov, V.S., Lavrent'ev, B.N., Munasypov, R.N., Prosolenki, I.V., Filatov, V.A. 371

Experimental Study of a High-Power Electron Beam Generator PIRIT-120, Pavalovskii, A.I., Popkov, N.F., Kargin, V.I., Pikar, A.S., Ryaslov, E.A. 375

Experimental Studies of Electron Beam Explosive Generators, Pavalovskii, A.I., Popkov, N.F., Kargin, V.I., Pikar, A.S., Ryaslov, E.A. 379

Electron Accelerators with Inductive Storages for Vircator Load, Tarakanov, V.P., Ivanov., A.B., Gorbachov, K.V., Didenko, A.N., Nesterov, E.V., Fortov, V.E., Chernikh, E.V., Shumilin, V.P., Stroganov, V.A. 383

Acceleration of Intense Ion Beam by Z-Pinch, Rahman, H.U., Ney, P., Wessel, F.J., Rostoker, N., Bystritskii, V.M. 387

Recent TWOQUICK Particle Simulations of One- and Two-Stage Transmission Lines and Diodes on PBFA and SABRE, Poukey, J.W., Cuneo, M.E., Lockner, T.R. 394

Extraction Ion Diode Studies for Optimized Performance: Divergence, Ion Species, and Parasitic Load, Greenly, J.B., Appartaim, R.K., Olson, J.C., Brissette, L. 398

TABLE OF CONTENTS

Impedance Characteristics of Multistage Ion Diodes, Desjarlais, M. P. 402

Properties of Multi-Stage Magnetically Insulated Ion Diode: Experimental Results and Scaling for Light Ion Fusion System, Miyamoto, S., Yasuike, K., Shirai, N., Takahashi, G., Shomoto, N., Yamamoto, K., Nakai, S., Imasaki, K., Yamanaka, C., Horioka, K., Aoki, T., Kawata, S. 406

Characterization of a High-Resolution Framing-Camera Diagnostic for SABRE Ion Beam Measurements, Smith, J.R., Sanford, T.W.L., Cuneo, M.E., Hanson, D.L., Bernard, M.A., Mock, R.C. 410

VUV Spectroscopic Observations on the SABRE Applied-B Ion Diode, Filuk, A.B., Nash, T.J., Noack, D.D. 414

Improved Field Geometries for SABRE Extraction Ion Diode Operation with Passive Ion Sources, Hanson, D.L., Cuneo, M.E., Rosenthal, S.E., Coats, R.S., Menge, P.R., Maenchen, J.E., Smith, J.R., Bernard, M.A. 418

LEVIS Ion Source and Beam Characterization on PBFA-II, Renk, T.J., Tisone, G.C., Adams, R.G., Bailey, J.E., Filuk, A.B., Johnson, D.J., Pointon, T.D. 422

Energy Resolved Measurement of the Characteristics of Br Ion Diode, Masugata, K., Chisiro, E., Matsuyama, A., Nakajima, H., Yatsui, K. 427

Extraction, Applied-B Ion Diode with Externally-Driven Active Anode Plasma Source, Neri, J., Boller, J.R., Ottinger, P.F., Stephanakis, S.J., Young, F.C., Fisher, R., Hinshelwood, D.D., Greenly, J., Noonan, W. 431

A Technological Ion Source with Hollow Cathode in Magnetic Field, Nikulin, M., Gavrilov, N.V., Mizgulin, V.N., Ponomarev, A.V. 435

Focusing Powerful Beams of Negative Ions and Neutrals, Papadichev, V.A., Mozgovoy, A.G. 439

Negative Ions from Magnetically Insulated Diodes, Prohaska, R., Garate, E., Rostoker, N., Fisher, A. 443

Pulsed Ion Beams Extracted From Vacuum Arc Ion Source with Double Accelerator Gap, Horioka, K., Hasegawa, J., Nakajima, M. 447

Catalytic Resonance Ionization - A Novel Universal Technique for the Formation of a Two-Component Anode-Plasma, Knyazev, B.A., Melnikov, P.I., Bluhm, H. 451

Results of the Reacceleration Experiment: Experimental Study of the Relativistic Klystron Two-Beam Accelerator Concept, Westenskow, G.A., Houck, T.L. 455

High Power Light Ion Beams at AEA Technology, Culham, Surrey, E. 459

Obtaining Negative-Ion Beams of Microsecond Duration in a Magnetically-Insulated Diode, Papadichev, V.A., Pashentsev, V.N. 463

TABLE OF CONTENTS

POSTER - ELECTRON BEAM GENERATION AND BEAM PROPAGATION

Investigation of Beam Acceleration and Extraction on a Stellatron, Song, Y., Rostoker, N., Fisher, A. 467

High Current Generation From Field Emission Tip Cathodes, Song, Y., Garate, E., Rostoker, N. 473

High Current Beam Emissions from Spacecraft, Lai, S.T. 479

Compact High-Current Ribbon E-Beam Diode, Yalandin, M.I., Shpak, V.G., Shunailov, S.A. 483

Ferroelectric Electron Beam Sources, Kerslick, G.S., Flechtner, D., Ivers, J.D., Nation, J.A., L. Schachter, L. 487

Model of the Vacuum Diode with Adsorbate Anode Operation, Engelko, V., Schultheiss, C. 491

A Large-Area X-ray Diode for the SNOP Accelerator, Bugaev, S.P., Buryak, I.A., Luchinsky, A.V., Ratakhin, N.A., Petin, V.K., Ferdushchak, V.F., Smirnov, N.A. 495

A Two-Beam Virtual Cathode Device, Peter, W., Krasik, Ya. E. 499

Numerical Study of Relativistic Electron Beam Pumping by Virtual Cathode, Kostov, K.G., Nikolov, N.A., Yovchev, I.G. 503

Powerful Plasma Cathode Electron Source Based on a Glow Discharge in Magnetic Field, Nikulin, S.P., Gavrilov, N.V., Ponomarev, A.V. 507

Equilibria and Waves in High-Current Electron Beams Emitted from Shielded and Immersed Cathodes, Agafonov, A. 511

Recent Results on the DARHT and AIRIX 4 MV ± 1%, 3.5 kA Electron Beam Injectors, Launspach, J., Bonnafond, C., de Mascureau, J., Villate, D., Allison, P., Builta, L., Kauppila, T., Moir, D., Taylor, B., Fockler, J., Bowen, B., Kishi, J., Morton, D. 515

An Electron Gun with Large Compression of a Thin Annular Beam, Krastelev, E.G., Agafonov, A.V., Bishaev, A.M., Voronin, V.S., Krasnopolsky, V.A., Lebedev., A.N. 522

High-Current Injectors of Long-Duration Pulse (Quasi-Stationary) Mode Electron Beams, Zavjalov, M.A., Perevodchikov, V.I. 526

Generation of Sheet Electron Beam for Experiments on a Wiggler-Focused Small Period Free Electron Laser Amplifier, Cheng, S.J., Destler, W.W., Granatstein, V.L., Rodgers, J. 532

Generation of a Microsecond Electron Beam in a Plasma-Filled Diode, Shcheglov, M.A., Lebedev, S.V., Voropaev., S.G. 536

Optimal Control of Low Energy Particle Beams, Allen, C., Guharay, S.K., Reiser, M. 540

TABLE OF CONTENTS

On Emittance Growth in High Intensity RF Linac with Solenoid Focusing, Batygin, Y. 544

Effects of Beam and Channel Parameters on Energy Spread in Periodically Focused Electron Beams, Brown, N., Reiser, M., Suk, H., Wang, J.G. 548

Three-Dimensional Thermal Distributions for Bunched Beams, Brown, N. 552

Transverse Oscillations of Intense Long-Pulsed Electron Beam in Extended Drift Channel, Bublik, N.P., Isaenkov, Yu.I., Kuleshov, G.D., Lisichkin, A.L., Mikhailov, V.M., Plaksina, S.D., Semenov, Yu.V. 556

The Method of an Intense Electron Beam Modulation, Astrelin, V., Lebedev, S.V. 560

A Study of Stochastic Oscillations Generated in the Beam-Plasma Discharge, Berezin, A.K., Fainberg, Y.B., Artamoshkin, A.M., Bez'yazychny, I.A., Kurilko, V.I., Lyapkalo, Y.M., Us, V.S. 564

Integrated Software System for High-Power Beam Design, Humphries, S. 568

Optimization of High-Current Ion Beam Acceleration and Charge Compensation in Two Cusps of Induction Linac, Karas, V.I., Kharkov, Ukraine- Belova, N.G. 576

Beam-Plasma Discharge in the Ionosphere During Active Experiments, Klumov, B.A., Rukhadze, A.A., Tarakanov, V.P. 580

Observation of Nonlinear Energy Flow in REB-Plasma System in a Magnetic Field, Kruglyakov, E.P., Burmasov, V.S., Kandaurov, I.V., Meshkov, O.I., Sanin, A.L., Tislenko, I.V., Vyacheslavov, L.N. 584

Studies of Electron Beam Interaction with Gas, Kulbeda, V.E., Mkrtchjan, A., Sopin P.I., Sorokin, G.A. 588

Correlation Between Spectroscopic and Laser Scattering Techniques in Investigation of REB-Driven Turbulence, Meshkov, O.I., Burmasov, V.S., Gorbatch, L.M., Kandaurov, I.V., Kruglyakov, E.P., Sanin, A.L., Vyacheslavov, L.N. 590

Ectons in High Power Charged Particle Accelerators, Mesyats, G.A. 594

The Quasistationary Nonlinear Waves on a Magnetized Hollow thin Electron Beam, Yudin, L.A., Korenev, I.L. 601

Anomalous Braking of Scanning REB and High-Power EMP Excitation Near a Conductive Surface, Rukhadze, A.A., Rybak, P.V., Kazanskiy, L.M. 605

Focusing of Intense Electron Beams for the 10 MeV LIA, Shi, J., Liu, C., Ding, B., Deng, J., Ma, Ya., Dai, G., Yao, L., He, Y., Li, Q., Zhang, S., Tao, Z. 608

Formation of an Electron Beam in its Squeezed State, Tarakanov, V.P., Ignatov, A.M., ... 612

Resonances of Electron Beam Focused by Helical Quadrupole Magnetic Field, Yudin, L.A., Efimov, S.P., Korenev, I.L 615

TABLE OF CONTENTS

Virtual Cathode In Magnetic Self Insulated Transmission Line, Structure, and Theory, Pashchenko, A.V., Tkach, Y.V., Novikov, V.E., Gorban, A.M., Latinsky, S.M. 618

Theoretical Analysis of Beam Conditioning on SUPERIBEX, Fernsler, R.F., Hubbard, R.F., Slinker, S.P., Meger, R.A., Murphy, D.P., Myers, M.C., Antoniades, J.A., Weidman, D.P. 622

Making PARMILA Easy to Use - Really Easy to Use!, Gillespie, G.H., Hill, B.W., Gillespie, J.S. 626

Slipping-Instability of a Relativistic Electron Beam, Nikulin, M., Shatalov, A. 634

Beam-Plasma Discharge During the Long-Pulse REB Injection in Rarefied Gas, Nikulin, M., Gladyshev, M.V. 637

The Expansion of the Plasma Channel Generated in Low Pressure Gas, Rudjak, Y.V., Vladyko, V.B. 641

The Transition from the Magnetic Focusing of the Relativistic Electron Beam to the Ion-Focused Regime, Rudjak, Y.V., Vladyko, V.B. 644

The REB Erosion Due to an External Transverse Field in the Ion Focused Regime, Vladyko, V.B., Rudjak, Y.V. 646

Ion-Hose Instability of the Relativistic Electron Beam in a Rarefied Gas, Vinogradov, S.V., Nikulin, M.G., Zakharova, S.S. 649

The Energy Lost by a Low-Energy, High-Current Electron Beam in its Transportation Through Rarefied Plasma, Ozur, G.E., Nazarov, D.S., Proskurovsky, D.I. 653

Resistive and Ion-Focused Electron Beam Transport in Capillaries, Hubbard, R.F., Fernsler, R.F., Slinker, S.P., Lampe, M., Fisher, A., Tang, C.M., Myers, M.C. 656

High-Quality Electron Beam with Non Adiabatic Pumping, Spassovsky, I.P., Correa, R.A., Barroso, J.J., Nikolov, N.A. 660

Time Resolved Multi-Dimensional Diagnostics for Intense Ion Beams, Yasuike, K., Shirai, N., Takahashi, G., Shoumoto, N., Yamamoto, K., Miyamoto, S., Nakai, S., Imasaki, K., Yamashita, T., Ochi, T. 664

Intense Ion Beam Optimization and Characterization with Thermal Imaging, Davis., H.A., Bartsch, R.R., Rej, D.J., Waganaar, W. J. 668

Transport of an Ion Beam with an Annular Plasma Channel, Welch, D.R. 674

Self-Field Generation in Solenoidal Focusing of Light Ion Beams, Oliver, B.V., Sudan, R.N. 678

Two Lens Focusing Systems for Intense Ion Beams, Olson, J.C., Kusse, B.R. 683

The Nonlinear Autosynchronization in Beam-Plasma Interaction, Onishchenko, I.N., Sotnikov, G.V., Balakirev, V.A. 687

TABLE OF CONTENTS

Compression of Intense Proton Beams, Engelko, V., Kuznezov, V., Vjazmenova, G., Wuerz, H. 691

Plasma Lens Focusing of Heavy Ion Beams Utilizing a Wall - Stabilized Discharge, Tauschwitz, A., Boggasch, E., Wetzler, H., Hoffmann, D.H.H., Seelig, W., Neuner, U., Stetter, M., Stowe, S., Tkotz, R., de Magistris, M. 695

Simulations of Proton Beam For ICF Propagating in Reactor, Niu, K. 699

Charge and Current Neutralization in the Formation of Ion Rings in a Background Plasma, Oliver, B.V., Sudan, R.N., Ryutov, D.D. 703

Formation of Ion Rings in a Magnetized Background Plasma, Omelchenko, Y.A., Sudan, R.N. 708

High-Impedance Nanosecond Megavolt-Range Diodes, Filatov, A.L., Kotov, Yu.A. 712

POSTER - BEAM TECHNOLOGY FOR PLASMA APPLICATIONS, BEAM-MATTER APPLICATIONS

The Hall Effect Influence on the Beam Plasma Interaction, Rudjak, Y.V., Vladyko, V.B. 717

REB Energy Transfer in Modified REBEX Experiment, Piffl, V., Raus, J., Vrba, P. 719

Calculations for Ka - Spectroscopy of Hot Dense Plasmas Produced by the KALIF Ion Beam, Ludmirsky, A., Baumung, K., Bluhm, H., Buth, L., Goel, B., Meisel, G., Rusch, G., Stoltz, O., MacFarlane, J.J., Wang, P. 723

Computational Modeling of Magnetized Target Fusion Experiments, Sheehey, P., Kirkpatrick R.C., Lindemuth, I.R., Eddleman, J.L., Hartmand, C.W. 727

Large-Scale I.C.F. Targets Driven by Particle Beams to Maximize Energy Gains, Piera, M., Martinez-Val, J.M. 731

Fast Ion Heating Due to REB-Induced Plasma Turbulence, Ullschmied, J., Kolacek, K., Clupek, M., Jungwirth, K., Ripa, M. 735

Low-Energy Beam Experiment and Beam-Particle Simulation for Beam Confinement Fusion, Ogawa, M., Yamazaki, H., Aoki, T., Fujii, K., Suto, O., Nakajima, M., Seki, H., Iwata, T., Naganuma, M., Oosaki, Y., Gono, Y., Koomoto, S., Suto, O. 739

Magnetic Field Distribution and Shell Structure in a Gas-Puff Z-Pinch Plasma, Gregorian, L., Davara, G., Kroupp, E., Markus, Y., Maron, Y. 743

Gas-Puff Implosion Experiments on the Inductive Storage Generator GIT-4, Baksht, R.B., Datsko, I.M., Kim. A.A., Kovalchuk, B.M., Kokshenev, V.A., Loginov, S.V., Oreshkin, V.I., Russkich, A.G., Fedunin, A.V., Shishlov, A.V. 748

Gas-Puff Z-Pinch Driven by Inductive Pulsed Power Generator, Akiyama, H., Imasaka, K., Hasegawa, K. Katsuki, S., Maeda, S., Imasaka, K., Hara, M. 752

TABLE OF CONTENTS

The MAGPIE Project: Full System Tests and Preliminary Plasma Experiments, Chittenden, J., Bayley, J.M., Mitchell, I.H., Wilson, K., Worley, J.F., Choi, P., Dangor, A.E., Haines, M.G. 756

Driver Coupling to Quasistatic Z-Pinches, Decker, G., Kies, W., Stein, S. 760

Spectroscopic Investigations of the X-ray Spectra From X-Pinch Plasmas, Pikuz, S.A., Romanova, V.M., Shelkovenko, T.A., Faenov, A.Y., Hammer, D.A. 764

Initial Characterization of Z-Pinch Load Discharges on the ACE 4 Pulse Generator, Loter, N., Coleman, P., Rauch, J., Rix, W., Thompson, J., Ingermanson, R., Murphy, H., Waisman, E., Apruzese, J.P., Maron, Y. 768

Spin Control of the Rayleigh-Taylor Instability in a High Density Pinch, Rostoker, N., Peterson, G.G., Tahsiri, H. 773

Plasma Liner Implosion With Microturbulence Effects Consideration, Glazyring, I.V., Karlykhanov, N.G., Timakova, M.S., Zoubov, A.D. 781

Pulsed Intense Proton Beam Facility for ITER Disruptions Simulation, Engelko, V., Schultheiss, C., Wuerz, H., Schalk, S. 785

Construction and Test-Operation of Apparatus for Interaction Between Pulsed Ion Beam and Gaseous Target, Kasuya, K., Kitabatake, N., Kamiya, T., Nishigori, K., Watanabe, M., Kawakita, Y., Kawamura, Y., Shioda, K. 789

Electron Beam Injection Schemes for Stack Gas Clean-Up, Ryzhov, V.V., Shemyakina, S.B., Turchanovsky, I.Y., Mesyats, G.A., Novoselov, Y.N. 793

Using a Radially Divergent E-Beam Accelerator to Irradiate Flue Gases, Novoselov, Y.N., Kuznetsov, D.L. 796

Personnel Protection in a High Average Power Electron Beam Scrubber Installation, Golub, T.A., Gondarenko, N.A., Pereira, N.R. 799

Flexural Waves Induced by a High Current Electron Beam in Thin Plate, Bardenstein, A.L., Bykov, V.I., Vaisburd, D.I. 803

High Power Optoelectronics Based on Synchronized High-Current Accelerators and Lasers: Applications for the Nonlinear Physics of Dielectric Instabilities and for Higher Education, Vaisburd, D. 807

Dislocation Structure of Copper After Exposure to High Power Pulsed Microwaves, Didenko, A.N., Sulakshin, A.S., Vernigorov, N.S., Kozlov, E.V., Sharkeev, Y.P., Paul, A.V. 813

Surface Sterilization Using Low-Energy Nanosecond Pulsed Electron Beam, Korovin, S.D., Bugaev, S.P., Kutenkov, O.P., Land, V.F., Mesyats, G.A., Sakharov, E.S. 817

The Short-Pulse Implanter, Remnev, G.E., Matvienko, V.M., Opekunov, M.S., Luconin, E.I., Vasilyev, V.V., Furman, E.F. 821

Application of Intense Ion Beams for Investigation of Matter Properties Under High Pressures and Temperatures, Vorobiev, O.Y., Goel, B. 825

TABLE OF CONTENTS

Investigation of Strong Shock Waves Generated in Condensed Targets by Soft X-rays, Vorobiev, O.Y., Lebedev, M.E., Fortov, V.E, Dyabilin, K., Grabovski, E., Smirnov, V. 829

Deposition by Means of Pulsed Electron Beam Ablation, Müller, G., Schultheiss, C. ..833

Promotion of Nitriding in Surface Layers of Metals by Preparative Irradiation of REB, Matsushita, H., Sato, M., Iwasaki, H., Nobuhara., S., Ando, R., Masuzaki, M., Nuogaki, M., Okada, T. 837

High-Rate Deposition of Thin Films by High-Power Ion Beam Target Evaporation, Remnev, G.E., Isakov, I.V., Zakoutayev, A.N. 840

Changes of Physical and Mechanical Properties of Alloys on the Base of Tungsten Carbides Exposed by High Power Ion Beams, Remnev, G.E., Isakov, I.V., Struts, V.K., Sergeev, A.N., Rudnev, S.V., Kutuzov, V.L., Kulikov, Y.Y., Ovsyannikov, M.N. 844

Flue Gas Cleaning using High Power Pulsed Discharge in the Heterogeneous Water-Air Mixture, Lisitsyn, I.V., Bystritskii, V. M., Sinebryukhov, A.A., Sinebryukhov, V.A., Yankelevich, E.B., Ryasanov, N.D., Ryshov, V.V., Suslov, A.I. 849

Effects of Weibel-type Instabilities in Laser-produced Plasmas, Okada, T., Satoh, K. 853

Surface Hardening of Steels by High-Energy Electron Beams of Microsecond Duration, Markov, A.B., Ivanov, Yu.F., Lykov, S.V., Rotshtein, V.P., Kashinskaja, I.S., Oks, E.M. 857

Description of Charged Particles Beam Interaction with Electrodynamical Structures By Means of Macroscopical Electrodynamics, Kapchinsky, M.I., Yudin, L.A. 861

Generation of High-Power Microwave Pulses of Ultrashort Duration, Magda, I.I., Chumakov, V.I., Gadestski, N.P., Kravtsov, K.A., Neisteter, S.I., Prokopenko, Y.V. 865

Electron Beam Dynamics in an Axially-Extracted Virtual Cathode Oscillator, Yatsuzuka, M., Nagakawa, K., Hashimoto, Y., Aoki, K., Nobuhara, S., Ishihara, O. 869

Comparisons between Simulation and Experiment on a Coaxial Vircator High-Power Microwave System, Crawford, M., Kristiansen, M., Hatfield, L.L. 873

High Power X-band Microwave TWT Amplifiers, Kerslick, G.S., Kuang, E., Naqvi, S.A., Nation, J.A., Schachter, L., Zhang, G. Davis, T. 877

New Developments in the Relativistic Klystron Amplifier Technology, Serlin, V., Friedman, M., Lampe, M., Hubbard, R. 881

Advanced Concepts for High-Power High-Frequency Klystrons, Uhm, H.S. 885

Gyrotwistrons as a Source for Future Particle Accelerators, Latham, P.E., Lawson, W., Irwin, V., Hogan, B., Nusinovich, G.S., Matthews, H.W., Flaherty, M.K.E. 889

Generation of UHF-Oscillations in Magnetic Insulated Slow-Wave Lines, Balakirev, V.A., Sidorenko, D.Y., Sotnikov, G.V., Tkach, Y.V. 892

TABLE OF CONTENTS

Research on S-Band Injector of 1+1/2 Cavity with Thermionic Cathode, Sunren, H., Xisan, L., Jiangjun, S., Kesong, H., Zucong, T., ...896

Accelerating Voltage Modulation as a Method for High-Power MW-Pulse Duration Control, Kazanskiy, L.N., Sinelshikov, A.V., Khomenko, A.I....901

Applications of Large-Scale Electromagnetic and Particle-in-Cell Simulation Models to RF Devices and Components, Mondelli, A., Petillo, J., Krueger, W., Mankofsky, A., Kostas, C., Ho, Y., Chang, C., Riyopoulos, S., Dialetis, D., Tsang, K., Chernin, D., Drobot, A. 905

A New Configuration of Vircator for Efficient, Narrow-Bandwidth Microwave Generation, Yatsui, K., Jiang, W., Masugata, K. 909

R&D of Pulsed-Power Technology and Its Applications at LBT, Yatsui, K., Jiang, W., Kang, X.D., Imada, G., Sonegawa, T., Chishiro, E., Kubo, H., Masugata, K., Masuda, S. 913

Relativistic Peniotron Experiment at JAERI, Ishizuka, H., Musyoki, S., Sakamoto, K., Watanabe, A., Shiho, M., Yokoo, K., Sato, N., Ono, S., Kawasaki, S. 917

Experiments on a Gyrotron Backward-Wave Oscillator with an Intense Relativistic Electron Beam, Kamada, K., Nawashior, K., Tamagawa, F., Ando, R., Masuzaki, M., Kawasaki, S. 921

Investigation of Plasma Producing by an Electron Beam in a Gas Filled Set of Coupled Cavities, Lisitsyn, A.I., Karbushev, N.I. 925

Interaction of Power Electron Beam with Plasma in Hybrid Slow-Wave Structures and Creation on this Base of Microwave Generators for Industrial Applications, Perevodchicov, V.I., Zavjalov, M.A., Mitin, L.A., S hapiro, A.L., Tskhai, V.N. 929

Experimental Study of the High Power Broadband Microwave Emission From Beam-Plasma Interaction, Ando, R., Masuzaki, M., Kobayashi, K. Yoshikawa, M., Morita, H. Koguchi, H., Yamada, D., Kamada, K. 933

Studies of High-Power Plasma-Filled Backward-Wave Oscillators, Ostrovsky, A.O., Markov, P.I., Onishchenko, I.N., Stonikov, G.V. 937

High-Current Electron Beam Microwave Excitation in Plasma-Filled Corrugated Coaxial Waveguide, Sotnikov, G.V., Onishchenko, I.N., Sideorenko, D.Y. 941

Correlation Between High-Power Microwave Radiation and High Frequency Electric Fields in a Strong Beam-Plasma Turbulence, Yoshikawa, M., Masuzaki, M., Ando, R., Kobayashi, K., Kamada, K. 945

Cyclotron-Cherenkov Instability in Dielectric-Loaded Circular Waveguides, Masuzaki, M., Lee, C.Y., Yamashita, R., Ando, R., Kamada, K. 949

The Dynamics of Stochastization of Microwave Oscillations in Powerful Beam-Plasma Amplifier with Inertial Back Coupling, Mitin, L.A., Perevodchicov, V.I., Blioh, Y.P., Fainberg, Y.B. 953

TABLE OF CONTENTS

High-Power Microwave Oscillator of Microsecond Pulse Duration Driven by Relativistic Electron Beam, Loza, O.T., Strelkov, P.S. 958

Applications of High-Power Microwave for Technological Purposes, Didenko, A.N. 962

Transverse Mode of KrF Laser Beam Under High Repetition Rate Operation: Preparatory Experiments, Kasuya, T., Watanabe, M., Kawakita, Y., Shioda, K., Kuwahara, T., Suzuki, T., Matsuno, S., Kanazawa, H., Okuda, H. 966

Interaction of Electron Beams with EM Waves in Conditions of Cherenkov and Cyclotron Resonance , Gerasimov, S.V., Karbushev, N.I. 970

An Electron Beam Formation and Cyclotron Radiation in Magnetic Cusp, Tarakanov, V.P., Ivantov, A.B., Michailov, V.M., Nestrov, E.V. 974

36 GHz, 10% Efficiency, High-Order Mode CARM Oscillator, Samsonov, S.V., Bratman, V.L., Denisov, G.G., B.D. Kol'chugin, Volkov, A.B. 978

A 94 GHz Free-Electron Laser (FEL) Driven by the NSWC THOR Generator, Pasour, J.A., Smutek, L., Nguyen, K., Woods, C., Schneider, R., Hudson, D., Miller, J., Freeman, W. 982

Dynamics of Electron Beam in Ion Undulator , Rozanov, N.E., Golub, Y.Y. 986

Opening Switch Research and Development for DECADE

J.R. Goyer, D. Kortbawi, F.K. Childers, J.A. Dempsey, I.S. Roth,
and P.S. Sincerny

Physics International Company
2700 Merced St.
San Leandro, CA 94577-0599

Abstract

DECADE is a very high peak power generator designed to drive both large area bremsstrahlung diode arrays and imploding plasma loads. The realization of this facility required significant improvement in the operation of the critical component, the plasma opening switch (POS). This presentation will address these improvements which were made in operation of the switch, and also discuss trends in opening switch performance that have not been reported previously, and which may be due to the use of relatively long magnetically insulated transmission lines (MITL) upstream of the POS. The performance of a plasma opening switch (POS), as measured by the peak opening voltage developed, has been improved from ≈ 1.2 to ≈ 2.7 MV through reductions in the size of the cathode used, and details of the anode configuration in and downstream of the switch region. This modification was motivated by observation of electron damage to the anode in the POS region, and consisted of the removal of any metallic surfaces that exhibited significant damage and were not essential to the integrity of the switch.

In this paper, recent developments in opening switch technology, specifically related to the DECADE simulator, will be presented and discussed. We will begin with a brief description of the DECADE facility along with one of the 16 modules that will be used to realize it. Following the description of the module and the diagnostics fielded, the opening switch will be discussed and data showing improved operation through modifications of the standard geometry, along with degradation of operation with increasing conduction times, will be presented.

DECADE is a very high peak power generator that has been designed to drive large area bremsstrahlung diodes and imploding plasma loads. Up to 2 MJ of electrons with a peak voltage of 1.5 MV, or current in excess of 20 MA may be produced by the machine in its two modes of operation. To reduce risk in scaling to such a high power machine, DECADE is composed of 16 modules, one of which has been used for development efforts and will be used to demonstrate predictable performance expectations for the full simulator. This module, referred to as DM1 (DECADE Module 1),[1] along with a lower energy scaled module, DPM1 (DECADE Prototype Module)[2], was also used for initial development efforts.

Because the architectures of both the DPM1 and DM1 pulsed power facilities are very similar, this section will begin by discussing the features common to both. Following that, the items specific to each machine will be briefly mentioned and a summary of the current waveforms driving the opening switches for the various configurations under discussion will be presented.

Both machines use a water transfer capacitor to drive current into vacuum to flux the circuit including the opening switch. The capacitor is pulse charged by an oil-insulated Marx bank (storing 280 kJ and 500 kJ in the case of DPM1 and DM1, respectively), which has a discharge time of ≈1.5 μs. This capacitor has two purposes: first, to provide a

low inductance driver for the POS, thus increasing the efficiency of energy extraction of the overall system, and second, decreasing the output pulse quarter period and therefore the conduction time the opening switch needs to obtain. Following the transfer capacitor, a set of triggered output switches couples the energy through a vacuum interface to a magnetically insulated transmission line (MITL), which drives the opening switch. There is an additional element in DM1, a water compensating capacitor, located between the output switches and the vacuum interface, that is used to further compress in time the pulse that drives the POS. The time to peak current for DPM1 is ≈700 ns, while this time is reduced for DM1 through a lower inductance output circuit and the addition of the compensating capacitor to ≈350 ns. After the opening switch, a short section of output line is used to couple to a bremsstrahlung diode load.

The diagnostics used for both facilities are virtually identical. The currents in the system are measured by B-dot monitors located on the anode electrode at the beginning of the vacuum section, just upstream of the POS, and at the load: a typical set of voltage and current waveforms is shown in Figure 1. Voltage at the POS is determined by using a resistive monitor at the vacuum interface that is inductively corrected using the current signals. This inductive correction is an increasing function of the switch voltage and reaches a maximum value of about 1.2 MV at a peak POS voltage of 2.4 MV. The diagnostics are calibrated prior to installation, and the calibration is then verified *in situ* by using a detailed circuit model to match such characteristics as the temporal history of the currents and voltages in the system.

Plasma anode results

Having briefly discussed the DECADE facility and requirements, we turn now to summarize the primary development effort that was necessary to make an inductive energy store machine viable: improving the operating voltage of the POS from nominally 1.2 MV to greater than 2 MV. This was done through modifications to the standard POS configuration, and the experiments were performed using the DPM1 generator.

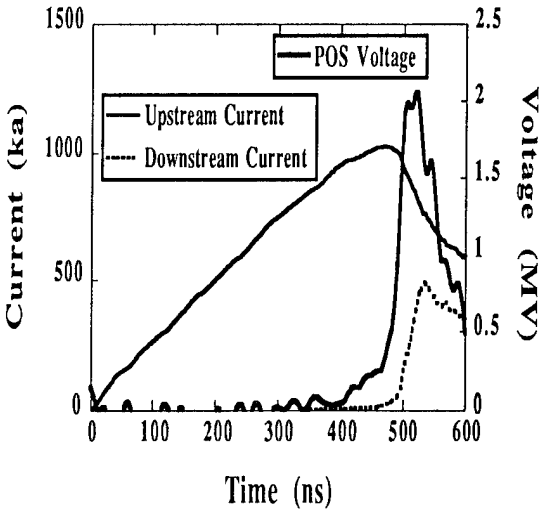


Figure 1. Typical waveforms in the DPM1 experiments.

The standard POS, shown in Figure 2(a), is coaxial, approximately 4 cm long. It consists of a 13-cm-diameter cathode and a 22-cm-diameter anode, and is driven by a current waveform that can be approximated as a linear ramp with a rise of ≈ 2.5 kA/ns during the conduction phase. The anode remains at the same nominal radius upstream and downstream of the switch, and in the switch region is constructed of rods. These allow high transparency to the plasma, which is injected radially inward from eight equally spaced azimuthally, discrete plasma sources. These sources are cable guns,[3] and are each driven by a 0.6 μF capacitor charged to 20 kV and discharged with ≈400 ns quarter period. In both POS configurations the sources were located 13 cm from the cathode surface. The conduction time of the switch is varied by changing the delay time between firing the plasma source banks and firing the DPM1 Marx and output switch trigger generators. Typical delays are 3 to 5 μs, which allows time for the plasma to transit from the cable gun to the surface of the cathode. A set of adjustable baffles was used to define the length of the switch, which was fixed at

2.5 cm for the results discussed here, and a nominal 7 Ω bremsstrahlung diode located 50 cm downstream of the POS was used for the load.

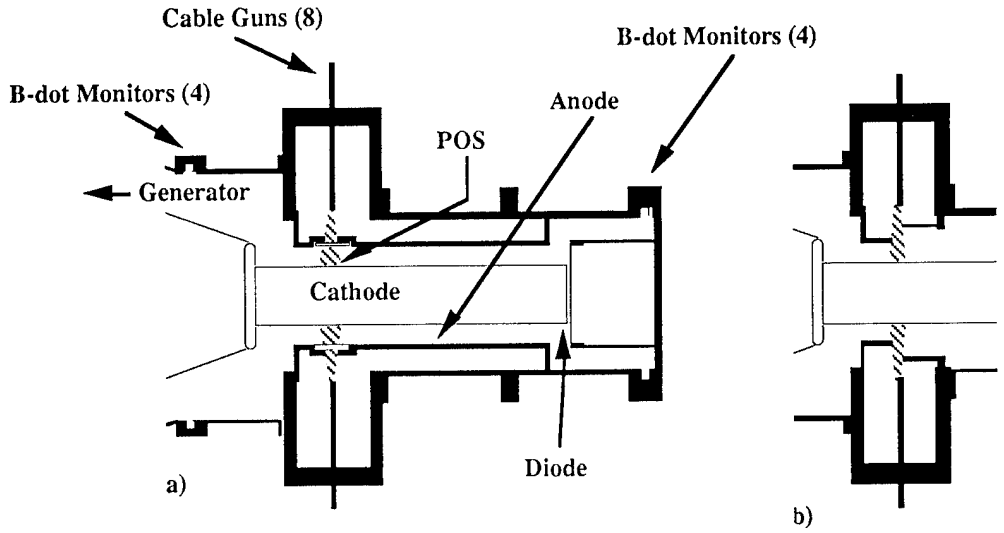


Figure 2. Cross-sections of a standard POS (a), and the plasma anode configuration (b).

With regards to the load, it should be pointed out that all the data to be presented were obtained in what has been referred to as switch limited operation.[4] That is, the impedance of the downstream load is sufficiently high that the POS voltage has reached a maximum value which no longer depends upon the precise value of the load impedance or the inductance that couples the switch to the load, and a direct comparison of data with changes in the downstream power flow region can validly be made. In the discussions that follow, we will take this maximum value of the POS voltage as a figure of merit, and examine how it varies as the anode structure of the switch is modified.

The data we will be comparing are shown in Figure 3, where the peak POS voltage is plotted as a function of the conduction time of the switch. This is a convenient format for presenting the data as both the peak operational voltage and the conduction time limitations of a switch are easily discerned. In the case of the standard POS design, the voltage reaches a maximum value of ≈ 1.2 MV over a rather broad range of 200- to 400-ns conduction times.

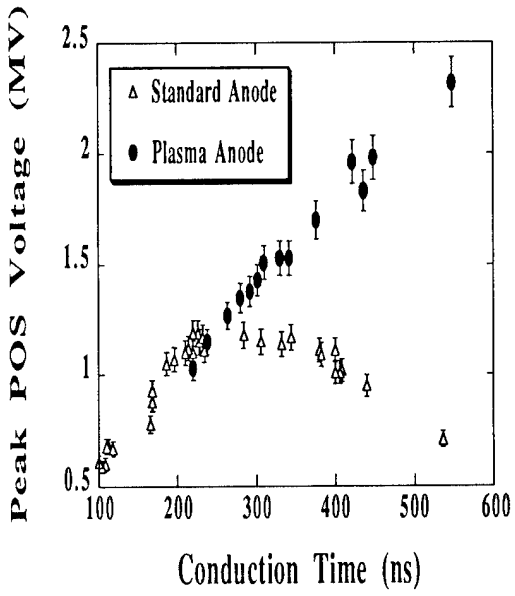


Figure 3. POS data in the standard and plasma anode configurations.

It had been previously conjectured that the observed limitation on this voltage could be due to excessive injected ion flux.[5]

However, examination of the anode structure of the POS showed signs of wear and roughening of the metal surfaces consistent with significant electron losses in that area. Time-integrated x-ray photographs of this area also confirm losses of electrons during the high voltage pulse from the POS.

Based on this evidence, and similar results observed at the Naval Research Laboratory,[6] the hardware of Figure 2(b) was designed and fabricated to minimize the losses of electron within and downstream of the switch. The anode rods which had been impacted by high energy electrons were removed, their role of providing a current path being transferred to the upstream and downstream baffles and to the injected plasma. To further minimize losses, the downstream anode was moved radially outward to a diameter of 32 cm. The downstream anode stays at this diameter for about 7 cm before obtaining a final diameter of 34 cm. If the assumption is made that the electron losses to the anode were the cause of the previous voltage limitations, the voltage would be expected to increase with the new design until it was high enough to resume having losses to the more distant anode, or until another limiting process became dominant.

Referring once again to Figure 3, it is seen that the voltages achieved with this new hardware, the "plasma anode" configuration, are indeed significantly higher than those achieved with the conventional design. At the maximum conduction time investigated, 550 ns, the peak POS voltage was ≈ 2.3 MV, or about twice that achieved in the standard configuration. After several shots at this voltage level, the downstream baffle in the POS, which was made of 2 mil stainless steel, experienced no noticeable damage due to electron impact. Based on this information, and the absence of emitted bremsstrahlung radiation from this area, it is concluded that the loss of electrons to the metallic anode no longer limits the voltage achieved by the POS. We conjecture that this voltage is now limited by the size of the gap opened in the injected plasma in the switch, either through electron-plasma interactions that cause loss currents, or through large ion currents drawn to the cathode by the high potential across the gap.

Degradation of POS voltage with conduction time

During the developmental effort described above, information on the change in performance of opening switches as conduction time is varied was obtained. The trends observed indicate limitations on performance that are very important in the context of future inductive store generators, and will be discussed in this section. The four datasets that will be presented use the peak voltage developed by the opening switch as a figure of merit, and were acquired using combinations of two MITL impedances, the two pulsed power drivers DPM1 and DM1, and the two different POS configurations discussed above. Leaving the POS variations for the moment, we will next discuss the different driving waveforms under consideration.

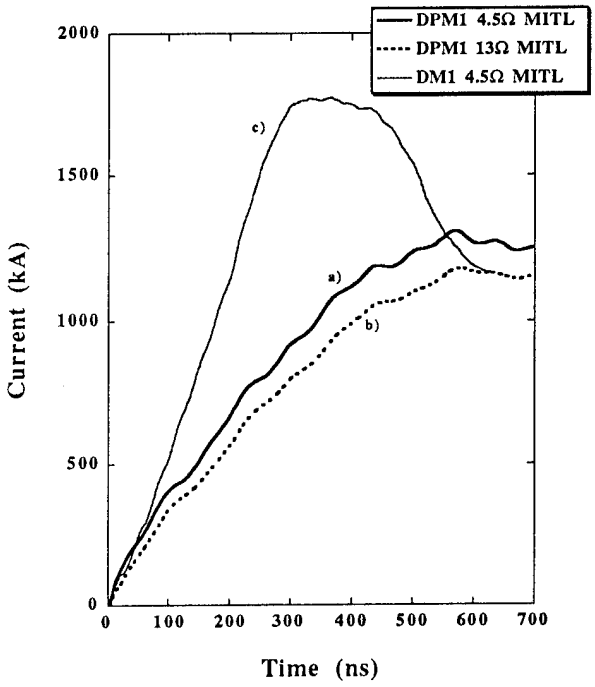


Figure 4 Current waveforms on DPM1 and DM1.

First, DPM1 was used with both a 4.5Ω and a 13Ω MITL upstream of the POS. The difference in inductance between these two cases made about a 10% difference in the peak current delivered to the opening switch, and correspondingly increased the time required to deliver it. The driving current waveforms for these two cases are shown in Figure 4 as traces (a) and (b). A 4.5Ω MITL was also used upstream of the POS in the DM1 experiments. The resulting waveform, which is noticeably non-sinusoidal due to the compensating capacitor prior to the vacuum line, is shown as trace (c) in the same figure.

The opening switch configurations used were the two types shown previously in Figure 2, and represented schematically in Figure 5. Table I summarizes the relevant parameters for the four configurations for which data will be presented.

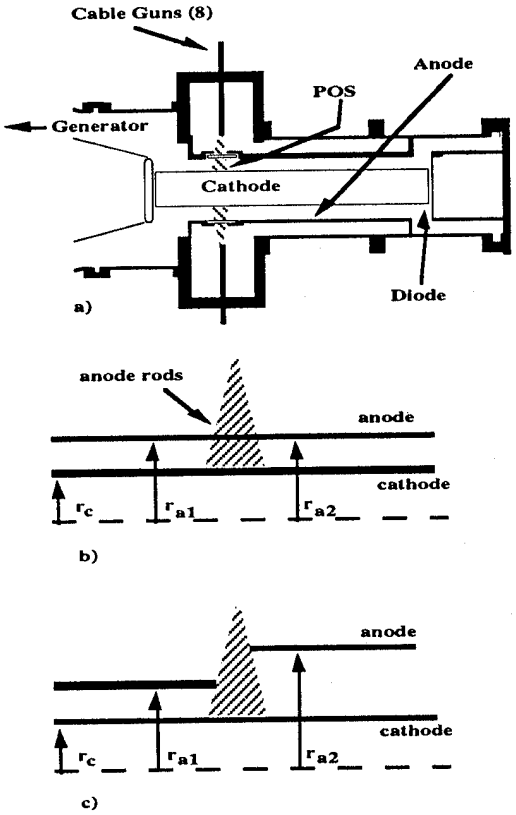


Figure 5. POS configurations used on DPM1 and DM1.

Table I

Configuration	Facility	Z_{MITL}	r_c (cm)	r_{a1} (cm)	r_{a2} (cm)	anode rods
1	DPM1	4.5Ω	12.5	17.1	17.1	yes
2	DPM1	13Ω	12.5	17.1	17.1	yes
3	DPM1	13Ω	4.44	7.62	10.2	no
4	DM1	4.5Ω	6.35	11.4	14.0	no

For the purposes of this discussion, the switch parameters of interest are the conduction time and peak voltage achieved by the POS, and the current flowing in it at the time of peak voltage. With the latter two quantities, the gap of the switch can be calculated using the critical current relationship:[7]

$$d = 8500\left(\gamma^2 - 1\right)^{\frac{1}{2}} \frac{r_c}{I}, \qquad (1)$$

where d is the gap at the upstream edge of the switch, r_c is the cathode radius, I is the total current entering the switch, and

$$\gamma = 1 + \frac{V_{POS}}{510\ \text{kV}}. \qquad (2)$$

If the calculated gap is plotted as a function of the conduction time of the switch, as is done in Figure 6 for the four configurations discussed above, the apparent linear decrease of gap with conduction time is clear. The gap has been normalized to the cathode radius in

this figure to point out the interesting but not understood fact that the normalized collapse velocities for all the cases presented are the same within about ±10%. The initial POS gaps (d_0) and collapse velocities (v_d) are summarized in Table II.

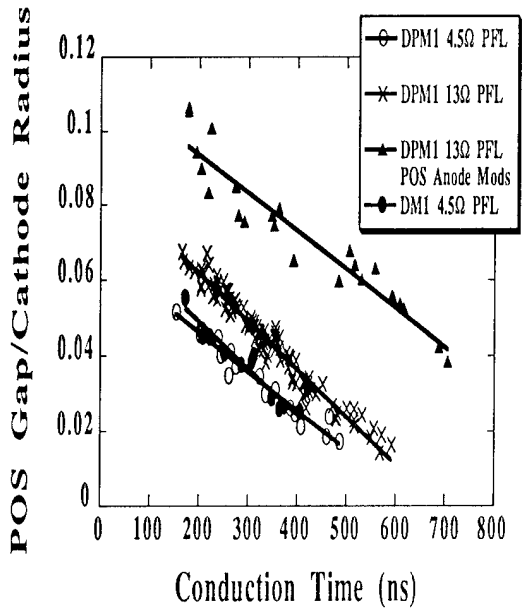


Figure 6. Data from DPM1 and DM1 inferring linear decrease in POS gap that can be opened as a function of conduction time.

Table II

Configuration	d_0 (cm)	v_d (cm/μs)	v_d/r_c (μs^{-1})
1	0.84	1.29	0.10
2	1.06	1.49	0.12
3	0.51	0.46	0.10
4	0.47	0.78	0.12

The data may be partially understood in terms of the hydromagnetic model of the conduction phase of the POS.[8] In this model, the magnetic pressure due to the conducted current pushes a channel through the injected plasma, opening a gap and increasing the current density at the load end of the switch. It is postulated that eventually the current density becomes sufficient to open the switch through ion erosion. Since the conduction time of the switch is varied by increasing the density, or mass, of the injected plasma, for a given configuration the radial gap opened should be independent of conduction time. That is, the shape and size of the gap at the time of opening should be invariant based on the hydromagnetic model without diffusion of plasma across magnetic field lines.

If, however, diffusion is allowed, one would expect the radial gap to close down as conduction time is increased because plasma has more time to diffuse across the magnetic field. This would be similar to the so-called "leaky piston" conduction phase model, in which not all of the plasma mass is removed from the gap by JxB forces, but some is postulated to leak or diffuse through the magnetic field.[9] To see this diffusion in a simulation it may be necessary, as in the case of broadening conduction current channels to agree with experiment, to add collisional effects.[10] Alternately, the highly dense plasma produced at the cathode surface may be closing the gap down over time, although it is difficult to see why this plasma expansion would result in a nearly constant normalized closure rate.

Regardless of the mechanism, the effect is obviously present in the data and in fact dominates switch behavior at the longer conduction times. This is an area that requires further investigation and may have large impact on future high-efficiency, long conduction time systems.

Summary

Results from a number of POS configurations have been presented to show improved operation of the switch with modifications to the anode electrode. The cause of this improvement is at present based on empirical arguments, and is in the process of being studied more carefully through the use of computer simulations. Also observed was a degradation of POS gap with conduction time. The linear relationship of these quantities is present in the data obtained from long MITL experiments, and may point to processes that are critical to control for future inductive store applications that may

require physically long MITLs and conduction times close to 1 μs.

---

1 P. Sincerny, S. Ashby, K. Childers, C. Deeney, D. Drury, J. Goyer, D. Kortbawi, I. Roth, C. Stallings, and L. Schlitt, "The DECADE high Power Generator," to be published.

2 C. McDonald, P. Sincerny, and L. Schlitt, Proc. 8th IEEE Pulsed Power Conf., San Diego, CA, p. 675, IEEE 91CH3052-8, 1991.

3 J.R. Goyer, D. Kortbawi, F.K. Childers, and P.S. Sincerny, "Low jitter operation of a plasma opening switch," J. Appl. Phys., 74 (6), pp. 4236-4238, 199.

4 R.J. Commisso, P.J. Goodrich, J.M. Grossmann, D.D. Hinshelwood, P.F. Ottinger, and B.V. Weber, "Characterization of a microsecond-conduction-time plasma opening switch," Phys. Fluids B 4 (7), pp. 2368-2376, July 1992.

5 J.R. Goyer, D. Kortbawi, I.S. Roth, F.K. Childers, and P.S. Sincerny, "Residual ion current as a limiting factor in plasma opening switch performance," J. Appl. Phys., Vol. 72 (4), p. 1277, 1992.

6 P.J. Goodrich, R.C. Fisher, D.D. Hinshelwood, J.R. Boller, R.J. Commisso, and B.V. Weber, "Microsecond plasma opening switch experiments on Hawk with an e-beam load," Proc. 9th International Conference on High-Power Particle Beams, D. Mosher and G. Cooperstein, eds., Washington, D.C., p. 609, 1992.

7 J.M. Creedon, "Relativistic brillouin flow in the high υ/γ diode," J. Appl. Phys., 46 (7), July 1975.

8 W. Rix, D. Parks, J. Shannon, J. Thompson, and E. Waisman, "Operation and empirical modeling of the plasma opening switch", IEEE Trans. Plasma Science, vol. 19, no. 2, pp., 400-407, 1991.

9 J.M. Grossmann, P.F. Ottinger, J.M. Neri, and A.T. Drobot, "Numerical simulation of a low-density plasma erosion switch," Phys. Fluids 29 (8), pp. 2724-2735, August 1986.

10 J.M. Grossmann, R. Kulsrud, J.M. Neri, and P.F. Ottinger, "Investigation of collisional effects in the plasma erosion opening switch," J. Appl. Phys. 64 (12), pp. 6646-6653, 1988.

MICROSECOND CONDUCTION TIME PLASMA OPENING SWITCH RESEARCH AT NRL

B. V. Weber, R. J. Commisso, G. Cooperstein, P. J. Goodrich,* J. M. Grossmann,
D. D. Hinshelwood,* P. F. Ottinger, R. A. Riley,** and S. B. Swanekamp,***
Pulsed Power Physics Branch, Plasma Physics Division
Naval Research Laboratory, Washington, DC 20375-5346

Abstract

Microsecond conduction time plasma opening switch (POS) research is being pursued to improve the understanding of the physical mechanisms responsible for conduction and opening with the goal of improved switching for pulsed power applications. Experiments on Hawk show the dominant effect of MHD distortion during conduction for a large range of experimental parameters. Electron and neutral densities are measured in the switch and load regions for comparison with theory. The dependence of the power flow on the load impedance time history is investigated using plasma-filled and vacuum diode loads.

The goals of microsecond conduction time plasma opening switch (POS) research at the Naval Research Laboratory (NRL) include improved understanding of physical mechanisms and limitations, and improved switching for pulsed power applications. This paper reviews research in several areas of POS physics based on experiments on the Hawk generator[1] and related theory work during the past two years.

Typical POS configurations on Hawk are illustrated in Fig. 1. Three different plasma sources have been investigated, including flashboards, cable guns, and gas guns. On Hawk, POS operation (voltage, switching time) is essentially independent of the choice of plasma source.

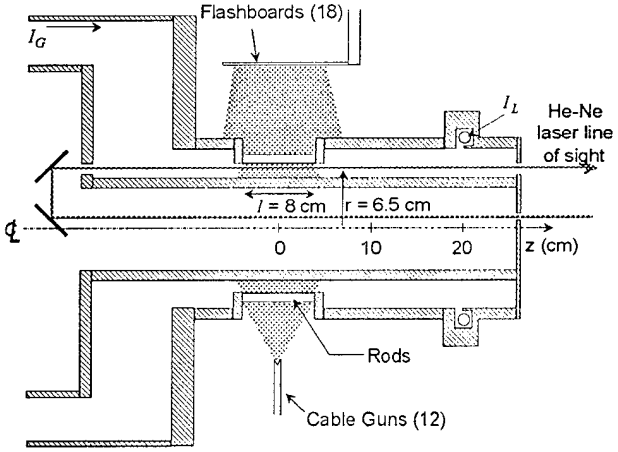


Figure 1. POS configuration on Hawk

POS conduction physics is investigated with interferometry.[2] Fig. 1 shows a line-of-sight for an axially-integrating He-Ne laser interferometer.[3] Typical results of this measurement at different radial locations are shown in Fig. 2a for flashboard plasma sources and in Fig. 2b for cable gun plasma sources. The time t = 900 ns in Figs. 2a and b corresponds to the time of opening, when the upstream (generator) current is about 600 kA. In the flashboard case, a minimum in the line-integrated density (denoted "Shot, 900 ns" in Fig. 2a) occurs at r = 6.5 cm, while in the cable gun case, the density minimum is closer to r = 5 cm, near the cathode surface. The localized density decrease in both cases is the result of MHD displacement and distortion of the plasma.

The traces labeled "FBs" and "CGs" are the densities measured by firing the plasma

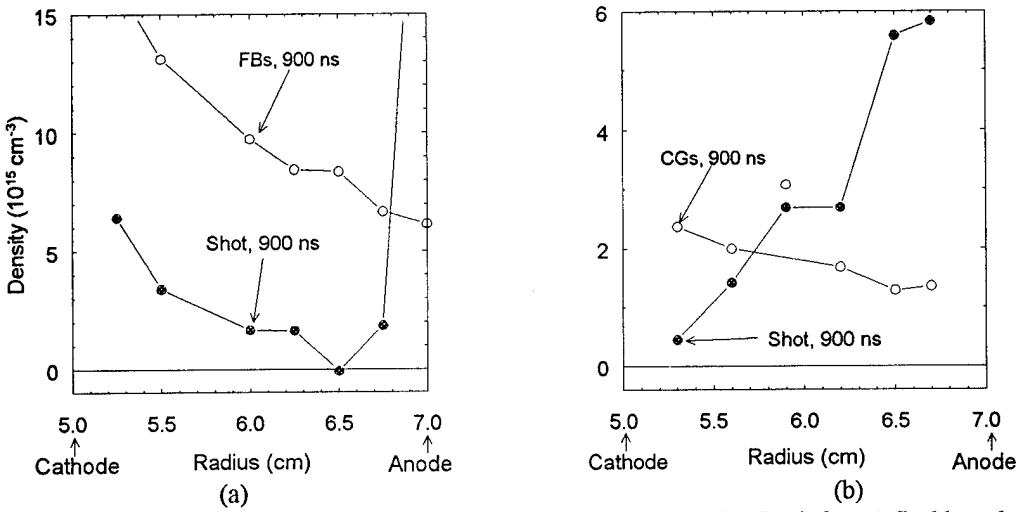


Figure 2. Axially-integrated electron density measurements in Hawk for (a) flashboard plasma sources and (b) cable gun plasma sources.

sources alone, without firing Hawk. The data taken during shots show how these densities are redistributed. The data in Fig. 2 give the impression that the cable gun plasma conducts more current for a given density than does the flashboard plasma, but this is not the case. Plasma redistribution limits the flashboard density to about 5 x 10^{15} cm^{-3} during conduction, while for the cable gun case the electron density inventory approximately doubles during conduction, probably by ionization, resulting in a similar density during conduction for the two cases. The conduction limit in Hawk can be calculated using a simple MHD-based model[4] using the measured plasma distribution.

A sophisticated two-color (1.06 and 0.53 μ) laser interferometer[5] was installed on Hawk to measure neutral and electron densities simultaneously, with a line-integrated electron density noise limit of only 2 × 10^{12} cm^{-2} (10^{-5} wavelengths for the IR beam). Data from this new diagnostic on Hawk are shown in Fig 3. The line of sight for the data in Fig 3a is a chord through the axial center of the plasma injection region (z = 0 in Fig. 1), approximately 1.5 cm from the center conductor, with a 3.5 cm separation between the inner and outer conductors. Metal tubes shield the laser beams from the flashboard plasma outside the anode rods. The electron density, n_{shot}, increases and decreases, evidence

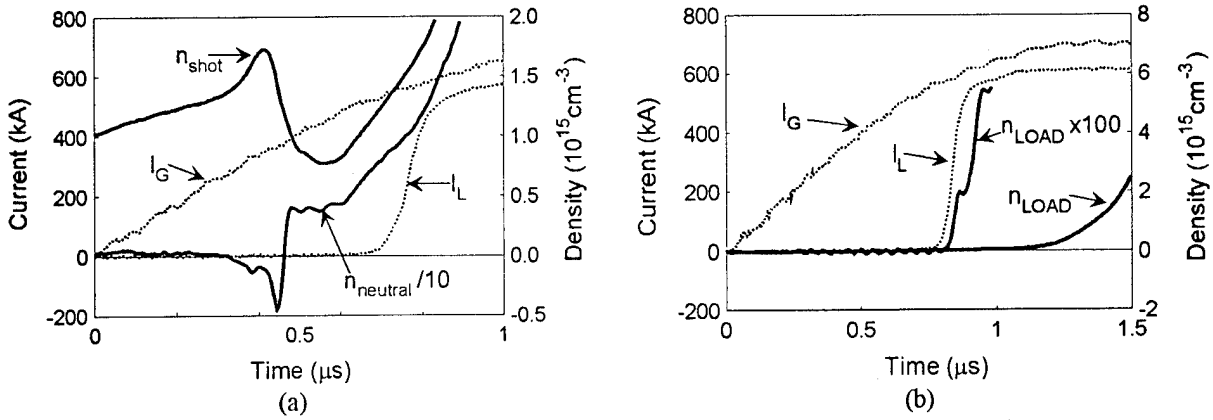


Figure 3. Two-color interferometry of (a) the POS region and (b) the load region.

of a 2D snowplow with finite axial extent moving through the POS during conduction. At a similar time, the inferred neutral density increases rapidly and is about five times greater than the electron density at the time of opening. This neutral density can be deleterious to switch opening, depending on its location. Attempts to reduce the neutral density generated during conduction can be diagnosed and evaluated in the future using this two-color technique.

The superior phase sensitivity of the two-color interferometer relative to the He-Ne interferometer was exploited for measuring the density near the load. The data in Fig. 3b were taken with the chordal line-of-sight located at z = 23 cm in Fig. 1, about 1.5 cm from the center conductor. The electron density measured with coarse (±1°) phase resolution, n_{LOAD}, implies that the high (10^{15} cm^{-3}) densities in the POS do not reach the load region until 100's of ns after switching.[4] With high phase resolution (±.01°), densities in the 10^{13} cm^{-3} range are measured in the load region beginning < 100 ns after the onset of the load current. This low density can affect power flow between the switch and load, and will be the subject of further investigations.

The Hawk conduction data have been modeled[2,6,7,8] with several fluid codes, including Hall effects. These simulations show good agreement with the measured plasma dynamics in Hawk, and their outputs may be used as inputs to particle codes to determine the physics of gap opening.[9] Understanding the gap formation mechanism and its relation to the conduction phase is the critical area of research for POS improvement.

An important new area of research on Hawk is the investigation of power flow between the POS and an e-beam diode load. The diagnostic setup in the load region is shown in Fig. 4, where a cable gun POS is used. The diagnostics include anode and cathode current monitors located between the

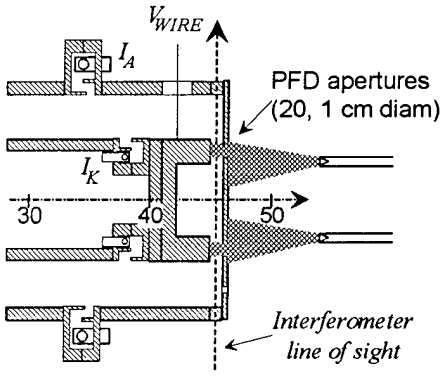


Figure 4. Hawk power flow experiment.

POS and the load, and a resistive divider to directly measure the load voltage. A plasma filled diode (PFD) is used to lower the initial impedance of the diode to investigate its effect on power flow. The two-color interferometer is used to diagnose the density in the PFD.

An example of the data obtained in this experiment is shown in Fig 5. I_A and I_K are the anode and cathode currents measured in the vicinity of the load, V is the directly-measured load voltage. Time t = 0 corresponds to the start of the POS conduction current. Density is injected into the 11 mm A-K gap of the diode as illustrated in Fig. 4 using three cable guns.

The electrical diagnostics indicate that the PFD is initially a short circuit, with $I_A = I_K$ and V = 0. When the PFD "opens," V increases, and $I_K < I_A$ indicating current flow in vacuum. Analogous shots with vacuum diodes show

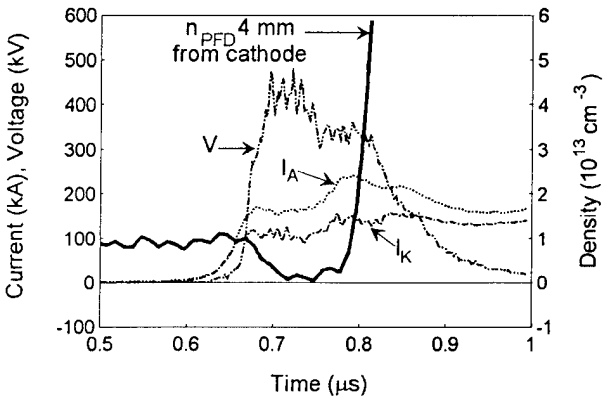


Figure 5. Power flow data with PFD load.

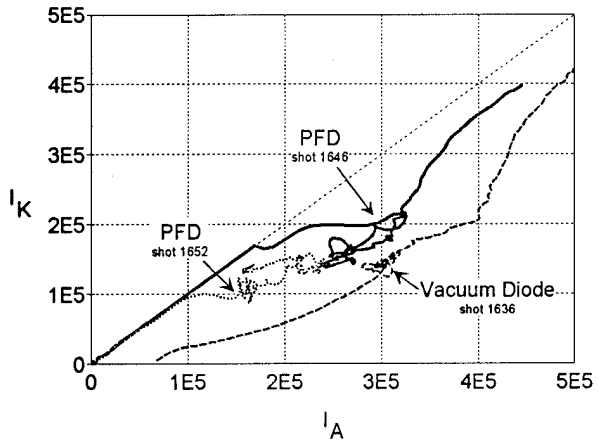


Figure 6. Comparison of PFD and vacuum diode loads.

different electrical behavior. V and I_A rise simultaneously, with a delayed and smaller I_K. This indicates the diode is initially an open circuit and all current flows in vacuum until the diode turns on. After diode turn-on there is more vacuum current than in the PFD case.

The initial PFD density in Fig. 5 is about 1 $\times$ 10^{13} cm^{-3}. (This phase shift corresponds to 10^{-4} wavelengths!) The density decreases to zero when the PFD opens, 4 mm from the cathode. Similar measurements 8 mm from the cathode show no density decrease. The evolution of the PFD density can be measured with this technique, and compared with PFD theory and PIC simulations.

A comparison of the power flow with and without PFD loads on Hawk is shown in Fig. 6. Data from two PFD shots and one vacuum diode shot are compared, plotting I_K versus I_A. These shots were chosen for comparison because they all had similar load impedance at peak power (defined as V/I_A, the impedance "seen" by the POS). The ratio I_K/I_A is higher for the PFD shots, a potentially important result for coupling useful power to loads.

The power flow in the Hawk experiments will be compared with PIC simulations.[10] Preliminary comparisons of experiments and simulations indicate the vacuum current in Hawk, I_A - I_K, is far greater than expected for pure electron flow. A low density plasma (of order 10^{12} cm^{-3}) would support the observed vacuum current.

In summary, MHD-limited conduction holds for a variety of plasma sources and plasma distributions on Hawk. Two-color interferometry shows high density neutrals in the switch region during conduction and low density plasma in the load region after opening. Power flow experiments indicate increased load cathode current using PFD loads. Simulations of power flow in Hawk are in progress.

Future POS research at NRL will emphasize modeling, combining fluid simulations of conduction with particle simulations of opening. These models will be benchmarked with well-diagnosed experiments, including a parallel plate POS on Hawk to take advantage of the two-color interferometer. This work will help to determine the ultimate limitations of POS systems for pulsed power applications.

* JAYCOR, Vienna, VA
** NRC Research Associate
*** SAIC, McLean, VA

---

[1]R. J. Commisso, *et al.*, Phys. Fluids B **4**, 2368 (1992).
[2]D. Hinshelwood, *et al.*, Phys. Rev. Lett. **68**, 3567 (1992).
[3]B. V. Weber and D. D. Hinshelwood, Rev. Sci. Instrum. **63**, 5199 (1992).
[4]B. V. Weber, *et al.*, in *Proc. 9th Int. Conf. on High-Power Particle Beams*, 375 (1992).
[5]The two-color interferometer was designed and built by S. F. Fulghum of Science Research Laboratory.
[6]R. Ingermanson, *et al.*, these *Proceedings*.
[7]J. J. Watrous and M. H. Frese, in *IEEE Conf. Record-Abstracts*, 139 (1994).
[8]J. D. Huba, *et al.*, to be published in Phys. of Plasmas.
[9]J. M. Grossmann, *et al.*, these *Proceedings*.
[10]S. B. Swanekamp, *et al.*, these *Proceedings*.

ACE 4 INDUCTIVE ENERGY STORAGE POWER CONDITIONING PERFORMANCE

J. Thompson, P. Coleman, C. Gilbert, D. Husovsky, A. R. Miller,
J. Rauch, W. Rix, K. Robertson, and E. Waisman
Maxwell Laboratories, Inc.
Balboa Division
9244 Balboa Avenue
San Diego, CA 92123

I. INTRODUCTION

ACE 4 is a 4 MJ compact pulsed power generator based on inductive energy storage technology utilizing Plasma Opening Switches (POS) for power conditioning. The prime power consists of 24 sub-Marxes, organized in four oil tanks, which drive multiple parallel plate transmission lines to a load coupler utilizing two parallel oil-vacuum interfaces. Each oil-vacuum interface drives power to one of two back-to-back large area POS. The POS couple to either separate short circuit loads as shown in Figure 1, or to a common e-beam load as shown in Figure 2. ACE 4 is capable of delivering up to 10 MA in 1.6 μs to the radial POS.

Most of the research performed on ACE 4 to date has concentrated on large area microsecond conduction time, radial geometry POS development and characterization. This paper describes results of an ongoing POS optimization and development program on ACE 4. The goal of this program is to develop both an optimized POS for ACE 4 and a methodology that can be used to design POS for future applications. Much of the theoretical and experimental basis for the approach comes from work originated by S-Cubed and the Naval Research Laboratory.[1,2]

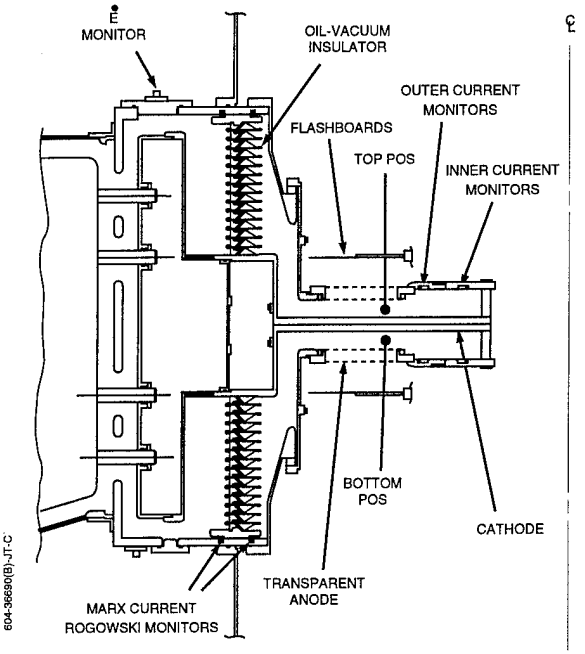


Figure 1. ACE 4 radial POS driving a short circuit load

II. EXPERIMENTAL DESIGN CONSIDERATIONS

The optimization and design approaches are based on the idea that the physics of high plasma density POS operation during the conduction phase is dominated by hydrodynamic effects. This view is able to explain how a long conduction time, high density POS can open rapidly. Rapid opening requires that low plasma densities be present at the time of opening. If the initial plasma density distribution has the right profile across the gap, the current front develops a bow which pushes much of the

plasma off to the sides, thinning the plasma in the region where a gap can be opened. How this can come about is shown in Figure 3, which gives the results of a simple two-dimensional snowplow calculation from an actual plasma source tested on ACE 4. In the case of the radial ACE 4 geometry where there is no magnetic field gradient across the gap, a minimum in the initial intergap density profile, as seen in Figure 3a, is required. Because of the intergap density minimum, the current front develops a bow, as shown in Figure 3b. Figure 3c shows the thinning effect in terms of the modeled line integrated density along the direction of power flow. According to the model the integrated line density is reduced by an order of magnitude by the time the current front reaches the end of the POS. The actual density at the point of opening is a function of the physical length of the plasma front. This length has not been determined by either our simple snowplow models or our experimental measurements.

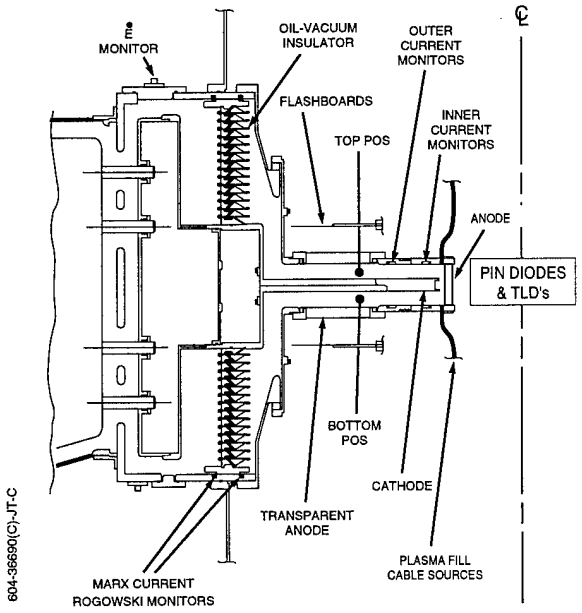


Figure 2. ACE 4 radial POS driving an e-beam dode load

Previously tested fast plasma flashboard sources were unable to provide a plasma density distribution across the gap with a sufficiently

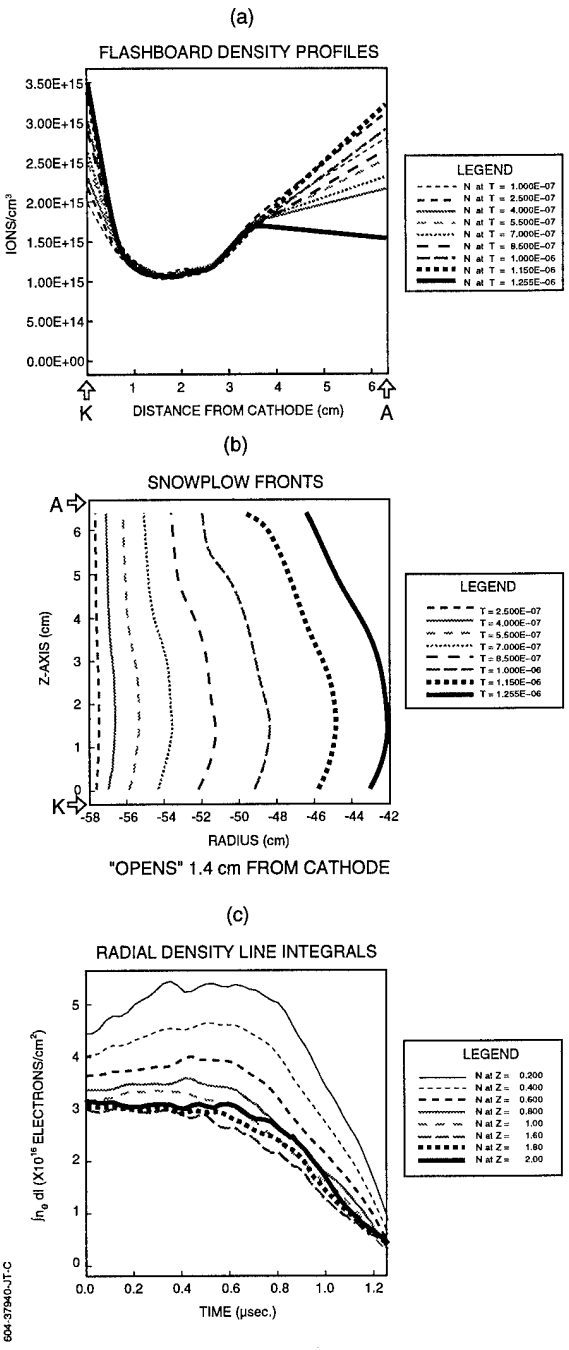


Figure 3. Application of snowplow model to ACE 4 SHOT 821

deep minimum. An additional requirement is that the rejected plasma reach the desired density in the switch region before the plasma drifts into the transmission line between the switch and the load. In the compact ACE 4 radial geometry, with a load located typically 25 cm downstream, this is an important constraint. To obtain the

required plasma distribution, a large area, slow plasma flashboard source was developed which had the following characteristics:[4]

1) An anode-cathode gap plasma density profile with a well defined minimum
2) A peak plasma density of 2-5 x 10^{15} cm^{-3}
3) A plasma velocity of 5 cm/μs
4) Density reproducibility to within 10%.

III. EXPERIMENTAL DATA AND INTERPRETATION

Figure 4 shows three of the 80 flashboards used on ACE 4. The flashboards are operated in both a low and high current drive configuration. Peak flashboard currents for these configurations were 8 kA and 11 kA per gap-chain, respectively. Good plasma uniformity, as evidenced by POS performance in terms of both azimuthal and top-to-bottom POS opening symmetry, is shown in Figure 5. Figure 5 shows the local current measurements about the azimuth just downstream of the physical POS for both the top and bottom POS.

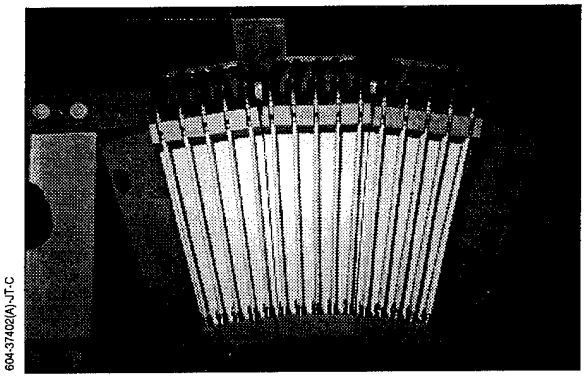


Figure 4. ACE 4 slow plasma flashboards

Figures 6a and b show the results of ACE 4 shots using the slow plasma flashboard plasma source in the high current configuration for both short circuit and e-beam loads. Conduction times approaching the ACE 4 quarter period were achieved with good top-to-bottom POS synchronization and opening times of about 150 ns. Figure 6b, however, shows that the ability of the POS to drive a nominally 0.25 Ω e-beam diode was poor. The calculated POS impedance for these shots was about half that previously reported using fast plasma flashboards.[4] Interferometry measurements of the high current drive configuration indicated that the desired density profile was not achieved in the relatively short injection times required to keep the POS conduction time under the ACE 4 quarter period.

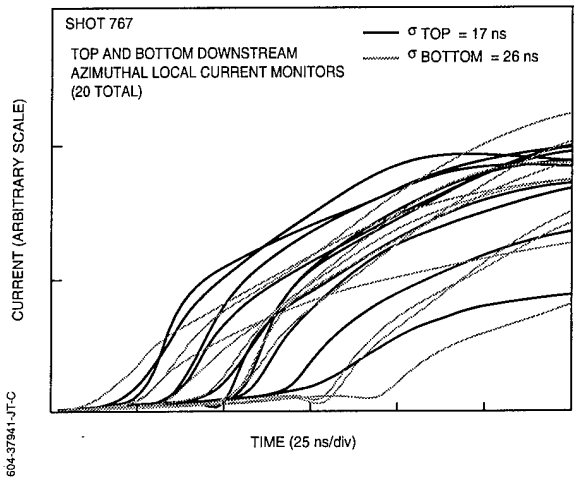


Figure 5. ACE 4 POS opening symmetry

The top POS flashboard plasma source was reconfigured to the low current configuration, which allowed the desired gap plasma distribution to be established with conduction times under the ACE 4 quarter period. Figure 7 shows the results for a short circuit shot in the plasma source configuration. In this case opening was not as good as predicted. The reason may be related to plasma moving past the end of the switch. A significant time delay was observed between the outer current monitors just downstream of the POS region and the inner current monitors farthest downstream. Also, the current monitors farthest downstream did not show current transfer consistent with the inductively corrected POS voltage. The calculated relative inductance downstream of E-dot monitor as a function of time overlaid in

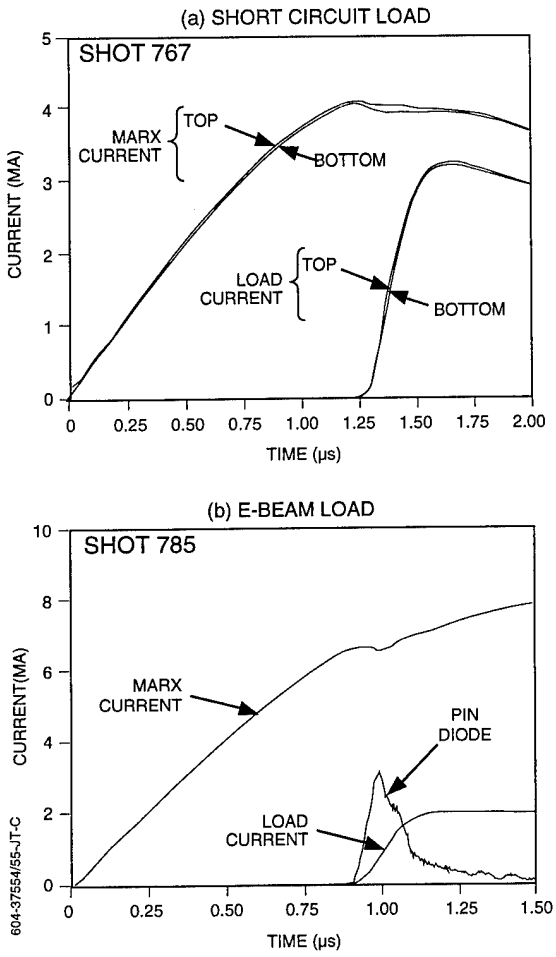


Figure 6. ACE 4 POS performance with unoptimized switch plasma distribution

Figure 7. During most of the conduction phase the inductance changes by approximately 6 nH, a value consistent with the POS region vacuum inductance. At the time that the outer cavity probes begin to come up, the inductance begins to increase more rapidly, and then plateaus shortly after the farthest downstream current monitor indicates current. The observed 10 nH change corresponds to 90 percent of the vacuum inductance downstream of the POS. This suggests that some portion of the POS plasma carrying the current across the anode-cathode gap was pushed beyond the end of the physical POS to the short 25 cm downstream. The observed POS voltage can be completely accounted for by plasma motion (IdL/dt) downstream of the physical POS.

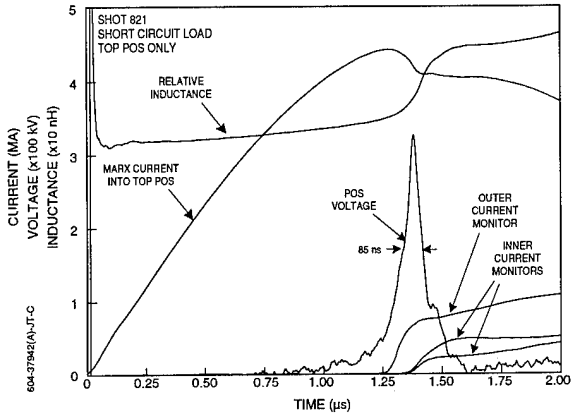


Figure 7. ACE 4 POS performance with optimized switch plasma distribution

Our modeling does not include the plasma profile or motion "downstream" of the POS, which may be a serious problem in the compact radial geometry of ACE 4. If sufficient thinning is not obtained by the end of the physical POS, switch opening may be affected by downstream geometry with the possibility of plasma motion for extended distances downstream.

IV. SUMMARY

A slow plasma flashboard source was designed and tested on ACE 4. While the optimized slow plasma flashboard source was capable of providing a intergap density profile which exhibited thinning during the conduction phase based on the snowplow model, it did not sufficiently localize the POS opening in the compact radial ACE 4 geometry to allow coupling to a load.

REFERENCES

1. R. Ingermanson, et. al., "Effects of Space-Time Density Variations on Microsecond Plasma Opening Switches," Proceedings of the 9th IEEE International Pulsed Power Conference, pg. 799-801 (1993).

2. D. D. Hinshelwood, et. al., "Density Measurements of Microsecond-Conduction Time POS," Beams 92 paper, PI-35.

3. J. Thompson, et al., "Flashboard Plasma Source Characterization for Microsecond Plasma Opening Switches," Proceedings of the 9th IEEE International Pulsed Power Conference, pg. 524-527 (1993).

4. J. Thompson, et. al., "ACE 4 Microsecond Plasma Opening Switch and Plasma Filled Diode Load Characterization," Proceedings of the 9th IEEE International Pulsed Power Conference, pg. 119-122 (1993).

Experiments with Microsecond Magnetically Controlled Plasma Opening Switch

I.V.Lisitsyn, V.M.Bystritskii, A.A.Sinebryukhov, V.A.Sinebryukhov
Institute of Electrophysics, Ekaterinburg;
A.A.Kim, V.A.Kokshenev, B.M.Koval'chuk, S.V.Loginov
Institute of High Current Electronics, Tomsk;
D.H.McDaniel,C.W.Mendel, M.E.Savage, D.M.Zagar, W.W.Simpson
Sandia National Laboratories, Albuquerque.

Presented are the results obtained in recent Magnetically Controlled Plasma Opening Switch experiments in submicrosecond conduction time range on the terawatt GIT–4 pulser at Institute of High Current Electronics. The opening time control was provided by variation of both slow magnetic field and fast magnetic field amplitudes in switch region. The additional trigger Plasma Opening Switch placed in fast coil circuit allowed to vary the fast coil "turn-on" and risetime of fast magnetic field. We investigated switch performance for both plasma injection directions: along slow magnetic field lines and across them. The coaxial inductance or electron beam diode served for a load in the experiments. The switching characteristics were studied as functions of plasma parameters.

Introduction

The worldwide effort to apply Inductive Energy Store (IES)— Plasma Opening Switch (POS) technology to pulsed power generators lead to appearance of a number of compact powerful drivers of particle beams diodes, Z-pinches etc. Nevertheless the fundamental POS limitation — the effect of partial opening on vacuum electron flow is not completely solved. The most practical measure of opening process uses POS flow impedance concept displaying the physical gap spacing [1]. The value of the flow impedance compared to vacuum line impedance shows what part of line gap is free of plasma during POS opening. Flow impedance of a plasma opening switch is calculated as follows:

$$Z_{flow} = U_{switch}/(I_{ua}^2 - I_{dc}^2)^{1/2}$$

where U_{switch} is POS voltage, I_{ua} is anode current upstream the switch, I_{dc} is cathode current downstream the switch.

The promising results with high flow impedance are obtained in MITE experiments at Sandia [1,2]. The usage of Magnetically Controlled POS (MCPOS) results in efficient and fast switching due to less required plasma mass in the switch region with slow magnetic field and due to plasma pushing away from the POS cathode as a result of fast field action.

Experimental Setup

GIT-4 is a terawatt pulsed power generator with pulsed capacity of a set of Marxes with

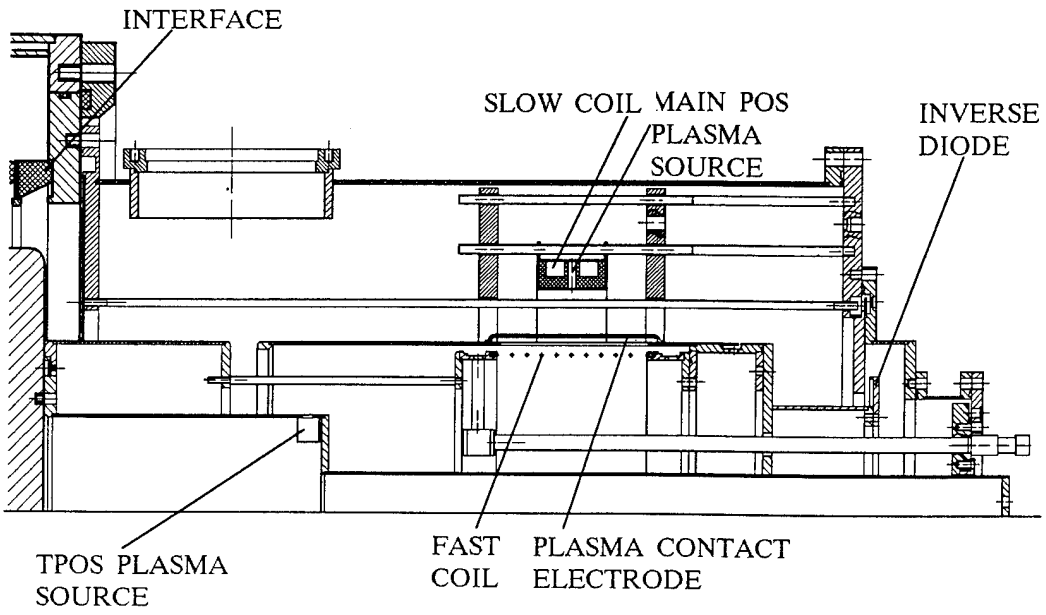


Fig. 1. MCPOS hardware scheme.

capacity of 4.7 μF and peak voltage up to 720 kV. In our MCPOS experiments we charged Marxes usually up to 40 kV (output voltage 480 kV of negative polarity) providing about 800 kA POS current in studied conduction time range within 400–500 ns. The MCPOS hardware scheme is shown in Fig. 1.

The vacuum line impedance in the switch region is 12 Ohm; the inner conductor diameter is 45 cm and the outer conductor diameter is 55 cm. A 20 mF, 5 kV capacitor bank energizes a total of 16 turn slow coil with inductance of 200 μH. The cable plasma guns serve for a plasma source. They display a reproducible plasma flow and no cable destruction occurs during a pulse. Guns can be located in two positions injecting plasma either in radial (across slow field) or in axial (along field lines) directions. Plasma sources are fed directly from 6 μF capacitor bank charged to 38 kV.

The generator pulse current energizes the fast coil, forcing an axial magnetic field in POS gap. This fast field is in the same direction as slow magnetic field. Hence a separatrix is formed between the slow applied field and the fast self generated field. The vacuum inductance of fast coil is about 30 nH; it consists of 0.5 turn with 36 spiral vanes. A trigger POS (TPOS) provides fast coil "turn-on" during its opening. Axial straight vanes located over the fast coil connect downstream side of coil with MCPOS cathode. These vanes, called plasma contact electrode, prevent plasma penetration inside fast coil cavity due to their "two-level" structure, being nevertheless transparent for fast axial field. The TPOS plasma is created by cable guns. On the generator side of the switch this plasma initially connects the vanes to the cathode upstream the MCPOS. When TPOS opens current is forced through the fast field coil. Plasma fill time variation allows to change fast coil "turn-on" time during current pulse.

Diagnostics used in the experiments consist of voltage monitor, placed at the oil-vacuum interface, and dI/dt monitors placed at anode and at cathode upstream and downstream the switch. In order to measure fast coil current we used similar monitors located in coil circuit.

The Experiment

MCPOS with plasma injection along slow field lines. A separate experimental run was dedicated to characterization of the

trigger POS. The variation of the conduction phase duration of the TPOS was provided by the controlling of the time delay within 2-8 μs. The highest current switching rate to the fast coil $(6-8)10^{12}$ A/s was measured for TPOS conduction time up to 500 ns with respective current front duration of 150 ns. The measurements showed that fast coil inductance remains almost the same as in the case of TPOS absence, this indicates that no plasma from the TPOS is in the fast coil region.

In the experimental run with high slow field magnitude (over 3 kGs), the opening of the TPOS produces distinct effect on the operation of the MCPOS in general. The substantial increase of the main POS conduction phase duration follows the increase of that of the TPOS. This fact proves the effectiveness of control of POS opening moment, using fast axial magnetic field, which pushes off the plasma from the cathode.

The maximum dI_{load}/dt is registered if fast field reaches its maximum at MCPOS opening. The switch voltage in this experimental run reached 500 kV, load current rise rate made up 5 kA/ns.

Plasma opening switch in a low impedance transmission line. In order to explain moderate switch parameters we performed an additional experimental run with conventional POS scheme with lower diameters of switch electrodes keeping low line vacuum impedance to examine self field magnitude influence.

Two pairs of electrode diameters in the switch region were tested. Plasma was injected radially through transparent anode in both cases. An inductive load about 50 nH was used. Besides that we performed experiment with MCPOS hardware having changed plasma flow direction to radial. The spiral entrance was shorted. The experimental conditions are collected in Table 1.

Table 1.

N exp. exp.	D_{an}, mm	D_{cat}, mm	Z_{wave}, Ohm	Gap, mm
1	140	102	19	19
2	360	280	15.1	40
3	540	440	12.3	50

The results obtained were a little bit unexpected because switch characteristics were similar and did not depend on switch electrode diameters. In all three cases POS voltage reached 700 kV, shunt impedance 1-1.5 Ohm for conduction time of 400-500 ns and switch current — 700-800 kA.

This fact shows that there are some other reasons playing the role in switch performance together with self magnetic field magnitude.

Noteworthy, that in experimental run with MCPOS hardware (radial injection), the switch voltage and impedance were higher that in previous experiments with the same inductive load and plasma injection along slow magnetic field. Twofold voltage rise leads to corresponding increase of load current rise rate. POS flow impedance reached 1 Ohm in case of zero axial magnetic field in switch region. This correspond to the shunt impedance of 1.5 Ohm.

Performance of the MCPOS with radial plasma injection and inductive load. Zero slow B-field case. Studying the main POS opening time versus fast coil turn on dependence, we found that the earlier the trigger POS opens the later main POS switching occurs (Fig. 2). The opening quality also sufficiently deteriorates: load current rise rate falls down, voltage decreases. The boundary case, when the fast coil was open since current start (no plasma in the trigger POS) we obtain very late and bad switching or absolutely no MCPOS opening. Varying

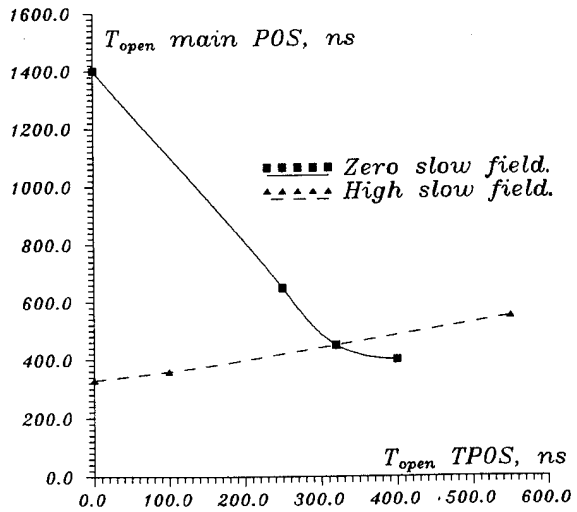


Fig. 2. Main switch opening time vs trigger POS opening time.

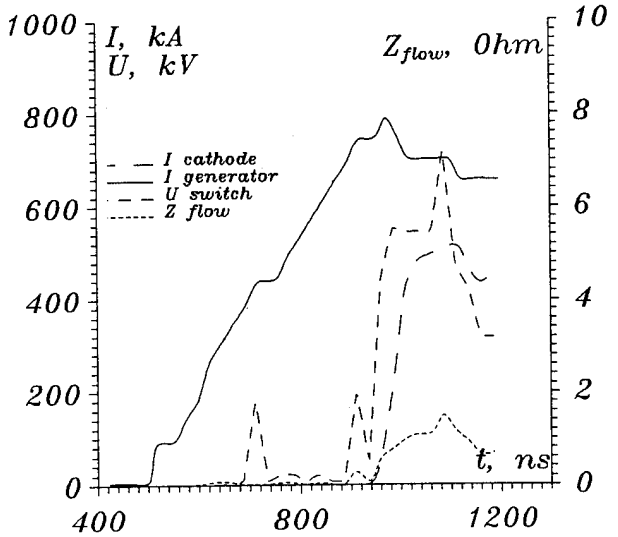


Fig. 3. Waveforms of generator and load currents, switch voltage and flow impedance.

(decreasing) the time delay and corresponding switch plasma density we obtain sharp transition from shorted to completely open switch state. These results prove the fact that axial field presence either applied slow of self generated fast, in the switch region leads to lower required plasma mass providing a certain switch current.

High slow B-field case. In this case the dependence of main POS opening time versus fast coil turn on time was similar to MITE experiments. This effect is shown in figure 2. Such a switch behavior starts if slow field magnitude exceeds 3 kGs. The minimum conduction time was obtained as well as we expected if there was no plasma in trigger POS. Therefore, only in case of high magnitude of slow B-field one can say about magnetically controlled plasma opening switch.

The plasma density needed to conduct a certain current in the case of high slow B-field was evidently lower than in zero B-field case. The time delay between plasma injection start and generator firing was shorter despite of transverse field presence, limiting plasma flow.

MCPOS performance with inverse pinch diode load. In our experiments an inverse pinch e-beam diode was used. The drawing of the MCPOS hardware is shown in Fig. 1.

Current from cathode downstream monitor reached 70-80% of generator current at optimum A-C gap. We tested a number of gaps to reach the highest e-beam power. The optimum gap was found to be 6 mm. The switch voltage made up in the optimum case 700-800 kV, diode current 600-650 kA. The respective waveforms are given in Fig. 3. The highest POS flow impedance was obtained in this run - 2 Ohm. Load current rise rate reached 10-12 kA/ns. The energy transfer efficiency into diode from inductor reached 50 %.

References

1. C.W.Mendel, M.E.Savage, D.M.Zagar, W.W.Simpson, T.W. Grasser, J.P.Quintenz. J. Appl. Phys.,**71**, 3731, (1992).

2.M.E.Savage, W.W.Simpson, G.W.Cooper, M.A.Usher, Proc. of BEAMS'92 Conference, Washington, 1992, p.621.

REPETITIVE GENERATORS WITH PLASMA OPENING SWITCH

N.U.Barinov, G.S.Belenki, G.I.Dolgachev,
Yu.I.Kovalev, A.G.Ushakov, L.P.Zakatov,

RRC Kurchatov Institute, 123182, Moscow, Russia

ABSTRACT

The peculiarities of repetitive generator using Plasma Opening Switch (POS) are considered. They are: limited drive current value, gas-generation, pulsed thermal loads on units etc. The voltage sharpening with relatively low (< 100 kA) current values is obtained. Design solutions of repetitive generator RS-20 main units (Marx generator, POS, X-ray target) are represented allowing to increase their resources up to 10^7 pulses and more.

The main appropriates of POS performance obtained experimentally allow to create on their basis a row of accelerators with parameters ranged widely[1].

Major perspective applications of these accelerators, for example, sterilizing, waste water decontamination, potable water desinfection[2] require repetitive performance with high average power. The parameters of pulse which determine the frequency **f=P/IUt** (**P**-average power, **I**- drive current, **U**-voltage. **t**-pulse width), are partially determined by POS properties. Effective POS operation is allowed when electrons are magnetically insulated and it requires the corresponding drive current value **I**>100 kA, when **U**<10 MV, **t**≈100 ns. In a range of average power **P**=10^5-10^7 W, **U**=10^6-10^7 V, so **I**=10^5-10^6 A and **f**≈10 Hz. What limits POS frequency if consider all technical problems on electric supply, heat-output etc. to be solved? The only one limit is the time of vacuum recovering down to <10^{-4} torr. To reduce this time it is necessary to exclude an electron (or ion) bombardment of the dielectric surface of plasma guns giving rise an uncontrolled gas emission. The time of the vacuum recover is determined by a rate of metal vapors and plasma flying away from POS electrode surfaces under bombardment. An estimation shows that POS characteristic frequency of 10 Hz is real.

Repetitive capacitors comparing with those single pulsed have lower energy density stored. This does not allow obtaining substantial current value in POS with reasonable dimensions of the storage system (Marx generator). In these conditions a practical assimilating of high average power range requires finding ways how to reduce the drive current value required for effective POS operation.

In 1991 a first repetitive generator RS-20 using POS was created for experiments on medical instruments and preparatory sterilizing with Bremsstrahlung radiation[3]. Maximum parameters of the accelerator are: electron energy 2-3 MeV, average beam power 10-20 kW, repetition frequency 2-

4 Hz. A two year period of generator exploitation allowed to elicit a row of problems stipulated by a repetitive regime.

RS-20 contains a vacuum chamber with an insulator placed vertically with 4 air-insulated Marx generators placed around closely to its surface. This scheme allows to reduce an inductance of the main circuit from Marx to POS.

The insulator is manufactured from polyethylene rings. The height of each ring is equal to that of one Marx generator section. Gradient rings are connected with corresponding sections of Marx generators that allows to make a potential division along the insulator length to be reliable.

Marx generators contain one capacitor 0.2 μF 50 kV in each of 20 stages. To reduce both internal inductance and Marx height the capacitors are placed into two "book-stands" which are shifted 10 cm (one stage height) in vertical direction. Spark air triggering switches are placed between the "book-stands"[4]. Three-electrode switches are assembled in the common dielectric body and work at atmospheric pressure with an air blow-out. The ultra-violet light and resistive connection between intermediate electrodes of spark switches allow to vary the work frequency without additional adjusting within limits 0.01-4 Hz when the electric strength of the switch gap is changed substantially. Instead of charging resistors TVO-20 used before the inductive coils were used in the final assembly as charging elements.

The coils are made as planar spirals mounted in pairs between dielectric plates. Packages from two coils are placed into gaps between adjacent capacitors. When charging capacitor magnetic flows of coils are deducted and when discharging (when switches are toggled on) they are added. This allowed to reduce the losses in the charging elements from 7% with resistors down to the part of percent with the magnetic coils. Three stages of the Marx generator were tested with an active load for 3 hours with repetition frequency 30 Hz (10^5 pulses). All elements kept their efficiency. The power density transformed by the Marx reached up to 150 kW/m^3. Parameters of Marx-POS circuit are as follows: T=2.4 μs, ρ=10 Ω. Major experiments were made with charging voltage of capacitors 40-42 kV making the corresponding value of Marx voltage 800 kV.

POS performance effectiveness is described by two main values: voltage increase coefficient: $k=U_{POS}/U_O$ and POS performance efficiency η, i.e. ratio of energy picked out in the load W_{load} to the initial value stored in the Marx $W_g=CU^2/2$ $\eta=W_{load}/W_g$. η could be written as a production of three factors $\eta=\eta_1\eta_2\eta_3$, where η_1- is efficiency of electric energy transformation W_g into the energy of the magnetic field of the inductive storage W_s, - in experiments $\eta_1<0/7$. η_2- efficiency of energy transformation stored in the inductive storage W_s into the energy of high-voltage pulse W_{pulse} when current interrupts $\eta_2=0.35\text{-}0.75$ limited by POS reclosure. η_3 - efficiency of energy transfer to the load within the time of interruption. The energy is picked out in the POS and in the load simultaneously, $\eta_3<0.5$. As a result it is possible to reach an efficiency up to 30%.

The effectiveness of microsecond POS performance depends on parameters of the generator, current value I_0, voltage of the Marx generator U_0, POS geometry and presence of the external

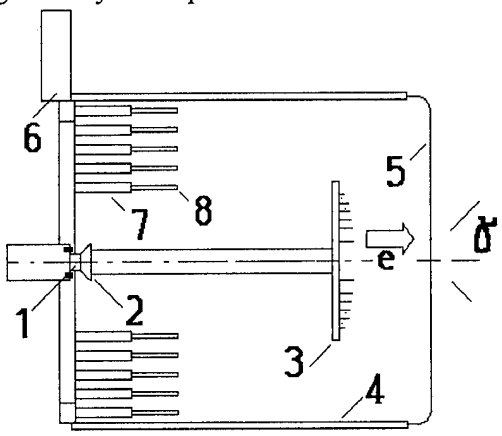


Fig.1 POS scheme 1-plasma guns, 2-deflector, 3-diode cathode, 4-target holder, 5-target, 6-high-voltage current drive, 7-brass rods, 8-tungsten anode rods.

magnetic field[1]. With moderate current values I_0<100 kA and substantial (>400 kV) voltages one can obtain a sufficient voltage increase ($k\approx3$) only owing to the external magnetic field application[5]. In these conditions a practically full current interruption takes place, i.e. $\eta_2\approx1$. But a scheme with an external magnetic field is rather complicated and requires additional energy supply for feeding a magnetic field solenoid.

Thus RS-20 uses reflecting system to suppress an electron component of the drive current containing a cylindrical anode having a variable transparency along its axis[6]. The anode is made as a "squirrel's cage" (**Fig.1**) from rods with a diameter changed along their length. The rods butt-ends having a grated diameter are mounted at the high-voltage drive using a ring made from stainless steel. When moving plasma crosspiece under the action of the self magnetic field or when magnetic field penetrates into the plasma along the axis) the anode transparency increases resulting in reducing of the electron component of the drive current as well as to the more sharp switching of the current. Voltage increase coefficient reaches up to k=(2,5-3) that is (1.2-1.5) times greater than having cylindrical entire anode.

Plasma guns are placed on the grounded butt-end of POS[7]. When plasma guns dielectric surface flashing over the gun plasma moves along z-axis toward the deflector filling the radial POS gap. This design allows to protect a dielectric surface of plasma guns from ion bombardment preventing gas emission and increasing the resource up to 10^7 pulses.

A new plasma gun for repetitive POS is proposed and made using dielectric surface with porous ceramics filled with oil to increase gun resource.

A new scheme of POS ***"anti-pinch"*** is proposed (**Fig.2**), with plasma volume placed in the break of the outer electrode of the coaxial line. In this scheme a self-magnetic field of the current going through POS pushes plasma in a radial direction from the central electrode resulting in plasma concentration reducing and sharper current switching. Moreover it is not necessary to use an electron diode as a load. The source of x-ray radiation is a POS anode itself (that results in η_3 .

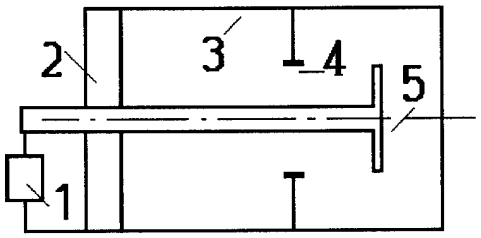


Fig.2, "Anti-pinch" POS scheme: 1- Marx generator, 2-insulator, 3-vacuum chamber, 4-plasma guns, 5 - anode.

increase). Recently this scheme is mounted and prepared for the experiment at RS-20.

An electron diode which is used in a usual scheme (**Fig.1**) performs parallel to POS with an anode converting the electron beam into x-ray radiation. For RS-20 machine an optimum mass thickness of the tungsten (or tantalum) target is 1.2 g/cm^2. A high pulsed beam power results in the fast (only 10^3-10^4 pulses) disruption of the target when average beam density is less than 20 W/cm^2. The tantalum target is alloyed while a tungsten one - is crumble (**Fig.3**).

The most steady material to pulsed power flow is a graphite. Graphite target is failed under power densities more than 100 W/cm^2.

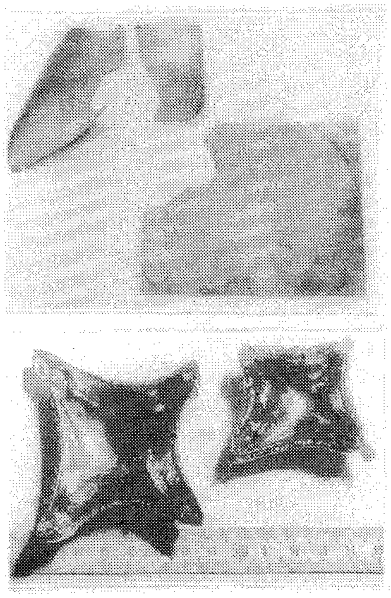


Fig.3 Photos of tantalum and tungsten targets after 10^3-10^4 pulses.

And so a combined target is proposed[8] to improve the resource which has a layer of small-grained tungsten (or tantalum) placed between two layers of the graphite (**Fig.4**), highly transparent to both electron beam and x-ray radiation. The target has its resource more than 10^7 pulses under power

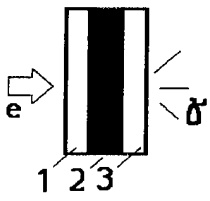


Fig.4 A scheme of combined target: 1-protective layer, 2 -converter, 3-supporting layer.

density 50 W/cm^2.

An experience coming from the repetitive generator based on POS creation and exploitation shows a perspective for this branch of accelerator technology. The relative simplicity and low cost of such a generator makes it competitive in a range of energies above 1 MeV[2]. Up to recently there is more than 10^7 shots obtained with all elements efficiency being retained. New ways of further resource increase are determined. The first experiments on sterilizing show that high pulse power rates allow to reduce a dose required for the effect of full sterilizing 2-5 times as low (depending on the type of microorganisms or spores) comparing with continuos action x-ray sources.

REFERENCES

1. G.I.Dolgachev et al. Sov. J.Plasma Phys., 17,10,1991,1171.

2. E.L.Neau IEEE Transactions on Plasma Science, 22,1,1994,2.

3. G.I.Dolgachev et al. Proc. of 9th Int. Conf. on High-Power Particle Beams BEAMS'92, Washington DC, 1992, v.1,p.512.

4. V.M.Babykin, G.I.Dolgachev, L.P.Zakatov, A.G.Ushakov Patent of the Russian Federation N5040386.

5. G.I.Dolgachev et al. Sov.J.Plasma Phys., 13,6,1987,760,

6. V.M.Babykin, G.I.Dolgachev, L.P.Zakatov, A.G.Ushakov Patent of the Russian Federation N5040387.

7. V.M.Babykin, G.I.Dolgachev, L.P.Zakatov, A.G.Ushakov Patent of the Russian Federation N5040385.

8. V.M.Babykin, G.I.Dolgachev, L.P.Zakatov, A.G.Ushakov Patent of the Russian Federation N014288.

2D SIMULATIONS OF CASCADE MAGNETOCUMULATIVE GENERATORS IN EULER-LAGRANGE VARIABLES

A.D.Zubov, V.A.Simonenko
Federal Nuclear Center - Research Institute of Technical Physics
P.O.Box 245, 456770, Chelyabinsk Region, Snezhinsk, RUSSIA

Abstract

The A.I.Pavlovskii's cascade magnetocumulative generator (MC-1) has been studied with the aid of the TIGR-M implicit simulational technique which is designed for computation of 2D MHD flows of heat-conducting gas in complex systems. The TIGR-M computations of 2D axially asymmetric perturbations development in 1-cascade MC generator show that in the process of magnetocumulative motion the curvature of the inside liner boundary reverses (even twice) in the points of internal shell boundary: concavity becomes convexity and alternatively.

Introduction

Cascade generator MC-1 of superhigh magnetic fields, designed by A.I.Pavlovskii's with colleges [1-4], allows to reproducibly generate up to 10-20 MG fields in a cavity volume of $2cm^3$ having diameter of 0.5 cm.

One of considerable problems to receive magnetic fields of high intensity is to explain the reason of magnetic flux compression stability destruction. It was noted in [3] that available experimental results did not give the reason of such destruction.

In this work we consider one of the possible reason leading to the compression symmetry destruction - the instability of the imploding liner due to non-simultaneous initiation of the explosion burst.

The TIGR-M computations of 2D axially asymmetric perturbations development in A.I.Pavlovskii's single-cascade MC generator show that in the process of magnetocumulative motion, curvature reverses in the points of internal shell boundary. This "inversion" effect is substantiated by experimental data. Thus, time scales of surface phase change, obtained in computations, agree with the experimental data.

Model

Set of equations describing the model include:

$$\frac{d\rho}{dt} + \rho \cdot div\mathbf{u} = 0, \tag{1}$$

$$\frac{d\mathbf{u}}{dt} + \frac{1}{\rho} \cdot \nabla P = -\frac{1}{4\pi\rho} \cdot [\mathbf{H} \times rot\mathbf{H}] \tag{2}$$

$$\frac{\partial H}{\partial t} = rot[\mathbf{u} \times \mathbf{H}] - rot(\chi \cdot rot\mathbf{H}) \tag{3}$$

$$div\mathbf{H} = 0, \tag{4}$$

$$\frac{dE}{dt} + \frac{P}{\rho} \cdot \nabla\mathbf{u} =$$

$$= \frac{1}{\rho} \cdot div(\kappa \cdot \nabla T) + \frac{\chi}{4\pi\rho} \cdot (rot\mathbf{H})^2, \quad (5)$$

where equations of states for matter and kinetic coefficients have been determined by relations: $P = P(\rho, T)$, $E = E(\rho, T)$, $\kappa = \kappa(\rho, T)$, $\sigma = \sigma(\rho, T)$, $\chi = c^2/4\pi\sigma$, and ρ - density of matter, E - specific internal energy, P - pressure, $\mathbf{u}$ - velocity, T - temperature, κ - coefficient of heat conduction, σ - electrical conductivity, $\mathbf{H}$ - magnetic field strength.

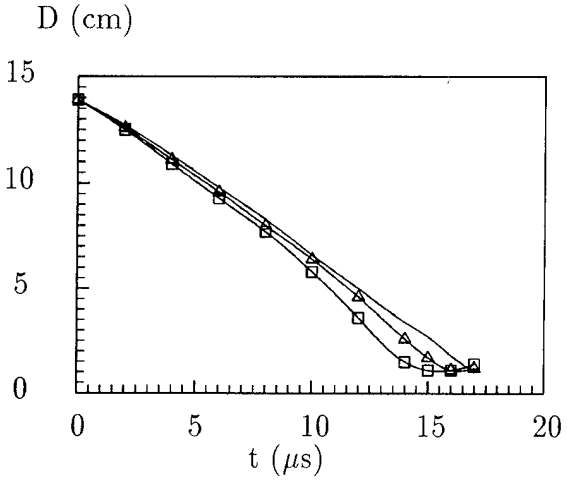


Figure 1. Diameters vs. time. Line - Pavlovskii [1]; Squares - TIGR-M with P=P(t) using VOLNA; Triangles - TIGR-M + VOLNA with P=0.9P(t).

The technique is designed on the basis of complex of TIGR codes [5] which is developed for simulation of non-viscosity heat-conducting compressible fluids by implicit algorothms. The equations are solved by the method of splitting according to corresponding physical processes and the directions. A mixed Euler-Lagrange way of gas motion description with special velocity vector decompositions applied. One coordinate lines family coinciding, in particular, with interfaces is Lagrange's one, the other is Euler's one and represents a set of straight lines . This way allows to follow interfaces and to compute overflowing of matter in layers.

Mixtures of two or three matters are computed by concentration method.

For testing of the MHD code some model tasks have been carried with theoretical studies of approximation and stability for using difference schemes.

Another calculations were conserned with 1D Kidder's problem [6] about compression of magnetic field by cupper cylindrical liner where different physical processes took into account such as liner compressibility, diffusion of magnetic field. Different approximations to the equation of state and conductivity have been considered too.

In addition some comparative calculations of the RT instability development in analogical liner system have been studied by Somon [7] theoretically and numerically. In this system initial harmonic disturbation was set on inside liner boundary.

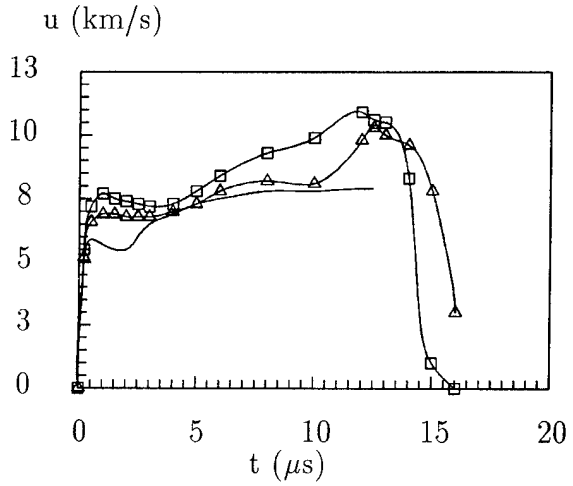


Figure 2. Velocity vs. time. Marks are the same as in Fig.1.

Results

The initiation of explosive is performed on the upper boundary. Because of the magnetic field begin to brake the compression on the later stage the first series of calculations has been carried out by 1D VOLNA code [8].

VOLNA is designed for simulation of gasdynamics calculation using specific algorithm of shock wave front distinguish. It takes into account phase transition and detonation processes. By the aid of VOLNA the pressure $P_0(t)$ has been tabulated for the upper bound of mixtures consist of copper and epoxy compound. This table of pressure vs. time was used for 1D and 2D TIGR-M calculations as a boundary condition for the cascade system. Thus we didn't consider the explosive layer and upper epoxy shell of first cascade.

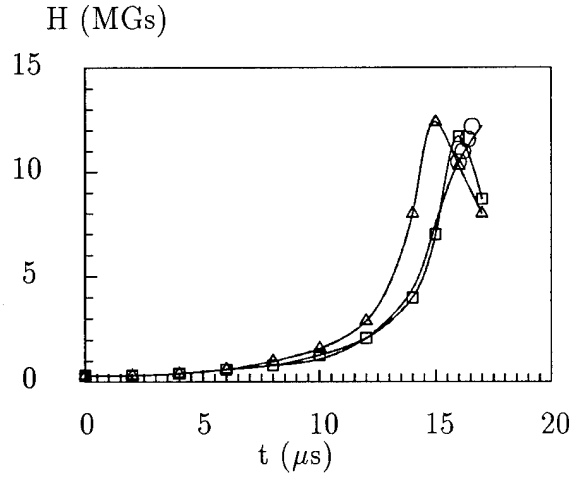


Figure 3. Magnetic field vs. time. Circules - experiment. Other marks are the same as in Fig.1.

At the time when detonation wave reaches first cascade initial magnetic field appears in the system. When the wave approaches the region consisting of copper thin wires and epoxide the matter becames conductor. At the moment the total set of MHD equations is started. During implosion the matter stays conducting.

The way of initial perturbation selection is the difficult question to answer. It has been suggested that the perturbation takes place due to nonuniformity of initiation on the upper bound. In 2D calculations by TIGR-M asymmetry in Θ - direction accounts using the boundary condition on first cascade top $P(t,\Theta) = P(t+\tau(\Theta))$, where the delay time

$$\tau(\Theta) = A_0 \cdot [cos(n\Theta) - 1], \quad 0 < \Theta < \pi/n. \quad (6)$$

According to experimental data, presented by A.A.Karpikov, we took $n = 5, A_0 = 0.3$ μsec.

The equations of state for copper and epoxy compound, electrical conduction of a mixture of copper wires and epoxide were determined according to [2].

Fig.1-3 show plots of time dependencies of inside diameter $D(t)$ of outer shell, rate of its change $u(t)$ and magnetic field on generator axis $H(t)$. All these dependencis are derived for MC-1 generator parameters with initial magnetic field of H_0=150 kGs.

Note that the run (2) was carried out with reducing boundary pressure $P_2(t) = 0.9 \cdot P_0(t)$.

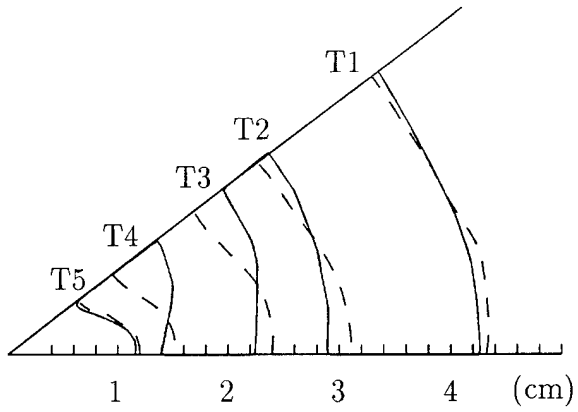


Figure 4. Upper boundary for $n = 5$: lines - with magnetic field; dashes - without magnetic field; T1=18.76μs; T2=21.96μs; T3=23.42μs; T4=25.42μs; T5=26.10μs.

The TIGR-M computations of 2D axially asymmetric perturbations development in 1-cascade MC generator show (see Fig.4) that in the process of magnetocumulative motion, curvature reverses (even twice) in the points of internal shell boundary: concavity becomes convexity and alternatively. This "in-

version" effect is substantiated by experimental data. Thus, time scales of surface phase change, obtained in computations, agree with the experiment.

Conclusion

In a short run in TIGR-M technique the 2D detonation accounting will be added. It will allow to simulate more accurately and to carry out the modeling from the beginning without 1D code using. In addition the more detailed physical model is needed for thermodynamical and electrophysical matter properties in a wide range of densities and temperatures variation (one need to account metal fusion, vaporization and model for conductivity taking into account phase transition).

Acknowledgments

The authors would like to thank A.A. Karpikov, V.I. Mamyshev, V.F. Kuropatenko and I.V. Glazyrin for setting up the problem and stimulating discussions.

References

[1] A.I.Pavlovskii, R.Z.Lyudaev, in *Voprosy Sovr. Eksper. i Teor. Fiz.,* (Mir, 1984), p.206 (in Russian).

[2] A.I. Pavlovskii, A.A. Karpikov, M.I. Dolotenko, V.I. Mamyshev, in *Megagauss Fields and Pulsed Power Systems*, ed. by V.M.Titov and G.A.Shvetsov (Nova Sci. Publs, New York, 1990) p.21.

[3] A.I.Pavlovskii et.al., in *Megagauss Physics and Technology*, ed. by P.J.Turchi (Plenum Press, New York, 1980), p.627.

[4] A.I.Pavlovskii, in *Ultrahigh Magnetic Field Cumulation*, ibidem, p.1.

[5] A.Yu.Bisyarin, V.M.Gribov, A.D.Zoubov, etc. VANT, Ser.: Metodiki i Programmy Chisl. Resheniya Zadach Matem. Fisiki, **3**(17), 34(1984) (In Russian).

[6] H.Knoepfel, *Pulsed high magnetic fields*, (North-Holland Publishing Company, Amsterdam – London, 1970).

[7] J.P.Somon, J.Fluid Mech., **38**(4), 769(1969).

[8] V.F.Kuropatenko, T.B.Es'kova, G.V. Kovalenko, et al., VANT, Ser.: Metodiki i Programmy Chisl. Resheniya Zadach Matem. Fisiki, **1**, 17(1984) (In Russian).

Comparison of DC and Pulsed Beams for Commercial Applications

R.J. Adler,
North Star Research Corporation
9931 Lomas, NE, Ste. A
Albuquerque, NM, 87112

Abstract

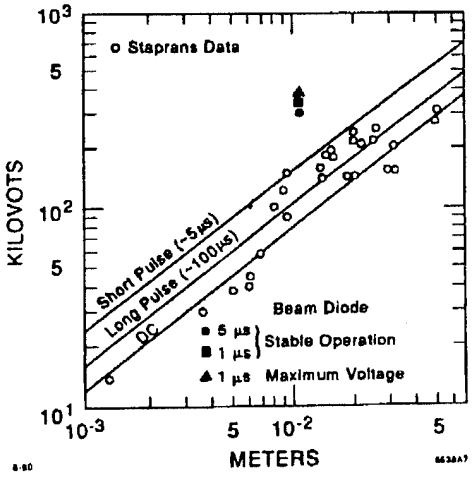
There has been increasing interest in the intense beam community in the applications of pulsed power and intense beam technologies. In this paper we attempt to compare the properties of pulsed, DC, and RF beams from the standpoint of understanding where intense beams can play a natural role, and where DC beams or RF accelerator beams are a more natural choice for application. This work is partly motivated by the availability of the pulsed/DC Nested High Voltage Generator (NHVG) which offers the possibility of producing a range of beam intensities and duty cycles in a single accelerator. In order to understand how to make these assessments, the economics of accelerators are also briefly reviewed.

DC and RF accelerators have been available at high energies since the 1940s and have achieved a degree of commercial acceptance since the 1960s. Pulsed electron and ion beam accelerators at > 1 MeV have been available as single pulse devices since the 1960s as high average power devices since the mid-1980s[1].

The comparative advantages and disadvantages of pulsed, RF, and DC beam technologies are determined primarily by the properties of high voltage generation systems and high voltage insulation. We outline these advantages and disadvantages in the sections below. Unless otherwise noted, we consider the Linear Induction Accelerator driven by Magnetic Compression as the prototypical pulsed machine. We are partly motivated in this work by the availability of a technology - the pulsed Nested High Voltage Generator (NHVG)[2] which can provide beams from 100 J at 1 microsecond pulse duration to 50 mA DC.

1.0 Vacuum Insulation

One of the primary advantages of pulsed beams derives from the fact that higher insulation gradients are possible when shorter pulses are used. In Figure 1 we show the dependence of vacuum breakdown on pulse duration in high repetition rate systems (microwave tubes)[3]. The trend clearly favors operation at short pulse duration. Surface Flashover of insulators has approximately the same dependence with allowable gradients a factor of about 2 - 3 lower than for the pure vacuum breakdown outlined in Figure 1.



DC accelerators operate at linear gradients between 30 and 50 kV/inch with the total accelerator length about 2-3 times the insulator length (15 - 25 kV/inch). Pulsed accelerators such as linear induction accelerators operate with actual vacuum insulator gradients which are considerably

higher (up to 100 kV/inch or higher) but the length of (for example) induction accelerators is dominated by core material rather than vacuum insulation. Induction accelerators have a maximum average gradient of about 1 MV/m (25 kV/inch) which leads to a slight advantage in length over DC machines. RF machines are limited in the trade-off between RF power and gradient. Medical therapy machines, for example, have gradients which exceed 20 MV/m, but the power system size in those machines far exceeds the size of the accelerating structure itself.

2.0 Gas and Liquid Insulation

The dependence of gas insulation on pulse duration is much weaker than the dependence of vacuum or liquid insulation on pulse duration. In general, short pulse gas breakdown electric fields are no more than 30 % higher than DC breakdown thresholds. Above DC voltages of 300 - 500 kV, the use of oil and other liquid insulations becomes problematic. The ability of pulsed machines to effectively and conveniently use transformer oil for insulation is an advantage since it reduced system diameter and avoids the use of pressure vessels and gas recovery systems.

3.0 System Electrical Efficiency

System electrical efficiency is a factor which influences overall system cost, and sometimes operating cost. For a pulsed system the factors which control this variable are the prime power efficiency, the power factor (as important as efficiency in most cases), the stray capacitance, leakage current (for transformer or magnetic compression systems), and number of energy compression stages. For DC accelerator systems such as Dynamitrons and Cockroft-Waltons, and for RF systems there is generally a minimum power required in order to keep the voltage at the specified level, and the power used for the beam is generally an added amount above the power required to maintain voltage. The DC systems tend to have efficiencies from 70 - 90 % excluding power factor when operated at full power. Pulsed systems tend to have efficiencies of 80 % or less. The energy in the pulse rise and fall time tends to be of minimal use in applications, and it has deleterious effects on such things as scanned beams. Pulsed generators must also provide energy to charge all stray capacitances on each pulse.

Pulsed power systems operate more efficiently at reduced power than DC because the power can be reduced by reducing the repetition rate and no "idling" power is required.

When all effects are included, pulsed generators tend to have efficiencies of 50 % (to as high as 80 % in some special cases) compared to DC generator efficiencies of 70 - 90 % and RF accelerator efficiencies of 5 - 25 %.

4.0 Maximum Power Limits

The maximum power limits of DC generators are limited by the series capacitance for Dynamitrons and Cockroft-Waltons, and by the series inductance in an Insulated Core Transformer. Dynamitron and Cockroft-Walton power levels can be increased by increasing the operating frequencies. Pulsed power systems, which tend to be designed in the range of 10 - 1000 ohms (and closer to 1000 ohms for rep rate systems) are designed to produce a fixed energy per pulse. The repetition rate limits therefore translate into power limits. Typical systems have >500 J/pulse, and modern thyratrons can reliably operate for long periods at 1 - 2 kHz (or higher in some cases). These specifications lead to a natural power level of order 1 MW for present pulsed power systems.

5.0 Beam Sources and Beam Optics

Beam sources for DC machines are extremely simple - for a 200 kW, 5 MeV accelerator, the required beam source is a 40 mA thoriated tungsten cathode wire. A similar RF accelerator at 1 % duty cycle would require a 4 A dispenser cathode while a similar induction accelerator with a 1 kHz., 100 ns. spec(10^{-4} duty cycle)requires a 400 ampere dispenser cathode. An induction accelerator in this parameter regime requires beam optical components such as DC or pulsed magnets while the DC and RF machines do not have space charge expansion concerns and so operate with modest lenses for beam confinement.

Pulsed ion sources are more problematic than electron sources. Adequate DC ion sources exist up to the 100s of milliampere level. Pulsed ion sources have always been problematic and subject to contamination.

In one parameter regime - single gap high voltage - pulsed beams have a significant advantage. A "shank" which holds a large area single gap electron gun can be operated pulsed up to at least 2.5 MeV. Single gap electron guns have not operated reliably above 300 kV in DC situations. In situations where large area irradiation is superior to scanning the ability of pulsed beams to provide a large area irradiation capability is significant. For a typical 1 cm diameter pulsed beam on a 1 m^2 area target the dwell "duty cycle" time on a given spot is 7.5 X 10^{-5} By comparison the induction accelerator example we used had a dwell time duty cycle of 10^{-4}. This characteristic of pulsed beams has been exploited to advantage in the DNA/SAIC e-SCRUB program where a large gun on the end of a shank is used for large area flue gas irradiation.

6.0 Ancillary Equipment

The diagnostic equipment required for pulsed measurements (fast scopes, pulse transformers fast scintillators, streak cameras, etc.) is relatively expensive and difficult to use. RF accelerator diagnosis is equally difficult, while DC measurements are significantly easier. For example measurement of an X-ray energy spectrum from a DC machine is straightforward with a Multichannel analyzer and Sodium Iodide scintillator. The measurement of a pulsed beam X-ray spectrum is much more difficult. DC machines have a significant advantage in the ease with which process variables may be measured. Since the beam output variables are a significant part of the interface with the customer their ease of measurement will bear on the selection of equipment for an application.

Beam manipulations such as bends, scanning etc. are often problematic with pulsed beams due to space charge and emittance driven expansion. Emittance generally increases with current. Even in the absence of those effects the variation of voltage over the "flat-top" may be as large as a few percent which leads to a requirement for expensive, difficult to design achromatic lenses.

7.0 Reliability

Reliability is the most important concern for the commercial users of accelerators. DC accelerators such as Dynamitrons and Pelletrons have millions of demonstrated reliable operating hours. Pulsed systems inherently store and release larger amounts of energy than DC systems, and as such, they must be able to tolerate larger fault mode energies. Pulsed systems also intrinsically charge and discharge components which leads to shorter life for a given insulator size (this is epitomized by the limitations on capacitor life). Fault problems can be partially mitigated by good design but the reliability of pulsed systems must still be demonstrated in a factory environment.

8.0 Cost

Relative and absolute cost comparisons are difficult and depend on both the actual manufacturing costs and on the cost structure of the manufacturing organization. In general, large DC accelerators cost about $15-20/watt at 200 kW while induction accelerators cost about $3/watt at 1 MW, but they probably cost about $12/watt at 200 kW since the cost is primarily the cost per pulsed joule. The cost of induction accelerators is primarily dependent on beam energy, with a cost of order $.50 - $1.50/volt. DC accelerators at low power (for example surface analysis machines) cost about $.20/volt while machines for high power production tend to cost about $.70/volt. In general, DC accelerators are less expensive than induction accelerators in terms of $/volt. RF accelerator costs depend primarily on power output at about $75-120/watt. In terms of cost per volt, RF accelerators cost in the range of $.10 - $.30/volt (but the power characterization is more accurate).

9.0 Conclusions

An examination of the merits of pulsed and DC accelerators show that pulsed accelerators have advantages at high powers (above 200 kW)

and for situations where the superior vacuum insulation properties of pulsed systems are important. The various parameter regimes of interest are shown in Figure 2. A summary of the comparisons in this paper are shown in the table below.

Applications which intrinsically require pulsing are of greatest interest for pulsed systems. Examples of these applications include Plasma Source Ion Implantation (PSII) where the natural current level of the pulse is 100s of amperes as determined by Child-Langmuir current emission, annealing, powder consolidation, and metal vapor arc ion implantation. The application of pulsed accelerators to free electron lasers and other high power radiation sources is also advantageous due to collective effects often observed at high current. There is little likelihood, or economic incentive for the use of pulsed systems in applications such as plastic cross-linking or electron beam sterilization where demonstrated reliability is the most important consideration.

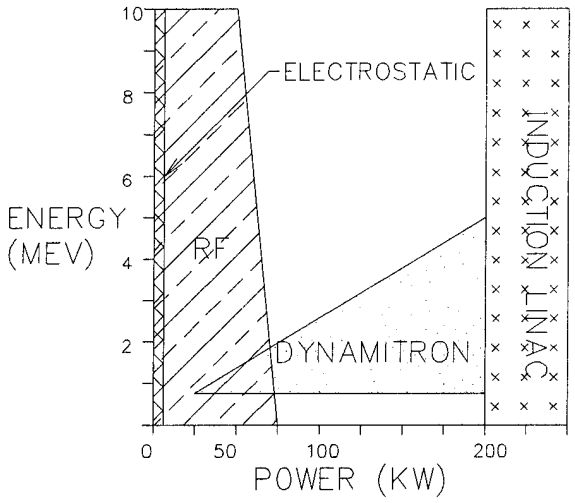


Figure 2 Parameter regimes of accelerator technologies.

Quantity	DC	RF	Pulsed
Length	>40 - 60"/MV	2" - 40"/MV	40"/MV (LIA)
Diameter	2 ft/MV	<2'	<3'
Elect. Eff.	70 - 90 %	<25%	<50 - 80 %
Beam Sources	Simple	Simple - Med	Complex
Scanning	Simple	Simple - Med	Simple - Complex
Beam Manipulation	Simple	Simple	Complex
Cost (per volt)	$0.20 - $.75/Volt	$.05 - $ .40/Volt	$.50 - $1.00/Volt
Cost (per Watt)	$10 - 20/Watt	$80 - 200/Watt	$4 - $20/Watt

References

1. See for example D.L. Birx, Procedings of the 1981 Pulsed Power Conference, Albuquerque,NM, p. 262, IEEE Cat. # 81CH1662-6

2. R.J. Adler, US Patent #5,124,658

3. K.S. Fant, G.Caryotakis,R.F.Koontz, And A.E. Vlieks, SLAC-PUB-5325, 1990, Stanford Linear Accelerator Center.

PULSED POWER ACCELERATOR TECHNOLOGY BASED ON SOLID-STATE SEMICONDUCTOR OPENING SWITCHES (SOS)

S.N.Rukin, Yu.A.Kotov, G.A.Mesyats, A.L.Filatov,
S.K.Lyubutin, Ye.A.Alichkin, S.A.Darznek, V.A.Telnov,
B.G.Slovikovskii, S.P.Timoshenkov, A.I.Bushlyakov,
and A.M.Turov

Institute of Electrophysics
Ural Division Russian Academy of Sciences
34, Komsomolskaya Str., Ekaterinburg 620219, Russia

Abstract

In 1991 we discovered a semiconductor opening switch (SOS) effect that occurs at a current density of up to 60 kA/cm^2 . The discovery of the effect provided a basis for the development of an opening switch with a gigawatt level of pulsed power, with an interrupted current of scores of kiloamperes, with a voltage of up to 0.5 MV, and with a current interruption time of 10 to 50 ns. Subsequent to those experiments, we developed a new circuitry ideology of constructing repetitive megavolt generators and accelerators with an all-solid-state switching system. In this approach, the SOS performs the function of a terminal power amplifier, by transforming the microsecond pumping pulse into a nanosecond output pulse. Significantly, the thyristor transformer delivers power to the SOS via an intermediate magnetic compressor. We present results of theoretical and experimental investigations of the SOS effect and describe the circuits and design of accelerators developed on the basis of it.

1.Introduction

To develop qualitatively novel high-power pulsed facilities capable of finding technological applications, the search is continued for new principles of accumulating and switching high-density energy. The most promise of success in this direction is shown by circuits with inductive energy storages and solid-state opening switches on the basis of which high-power pulsed devices can be developed that possess high specific energy characteristics and a virtually unlimited service life. The main problem here is to develop a high-power repetitive solid-state opening switch capable of switching off kiloampere currents within a few and dozens of nanoseconds and withstanding voltages of several hundred kilovolts.

The physical principles of fast current interruption in a solid that are known rest either on (1) producing high conductivity in an intrinsic semiconductor by laser radiation or an electron beam and then swiftly disconnecting the ionization source [1,2] or on (2) the current injection of a charge into the base of the p^+-n-n^+ structure within a time span much shorter than the nonequilibrium carrier lifetime and on subsequently extracting the accumulated charge by the reverse current [3]. Technical complexities of the first method along with low parameters of currents switched off and voltages endured virtually preclude the use of it in high-power pulsed technology. The second method employs the drift mechanism of conduction, which has a restriction in current-through-structure density. To realize the high-voltage mode of operation of a silicon switch with a voltage of 1000 to 1500 V per p-n junction, the donor impurity level N_d should not exceed 10^{14} cm^{-3}, a value which at the stage of current interruption corresponds to maximum current density j=100-160 A/cm^2 when equilibrium carriers are drift-transported from the base at saturated velocity V$\sim 10^7$ cm/s. Such drift step recovery diodes (DSRD) in the nanosecond time range are capable of switching a pulsed power on the order of several megawatts [3].

2. SOS effect: nanosecond interruption of superdense currents in semiconductors

In Ref.4 we observed nanosecond current interruptions in p^+-n-n^+ silicon structures at the current density j=1-60 kA/cm^2, which was two orders of magnitude higher than the density of the current interrupted in DSRDs. This semiconductor opening switch (SOS) effect was used to develop high-power semiconductor opening switches in intermediate-inductive-storage circuits [5-7]. The breaking power of opening switches was as high as 5 GW with the interrupted current up to 45 kA, with reverse voltage up to 450 kV and with the current interrupt-

ion time between 10 and 60 ns. The interrupters were assembled from silicon diodes containing p^+-n-n^+ structures with characteristic size of the n-base of up to 0.35mm, with the level doping of the initial material $\sim 10^{14}$ cm^{-3} and with an area of 0.02 to 0.2 cm^2. With the parallel-series connection of diodes into the interrupter the number of such structures totaled twelve thousand. In Fig.1 we show typical experimental time dependencies of voltage and current across the p^+-n-n^+ structure that demonstrate the SOS effect in a two-circuit pumping regime with reverse-current amplification.

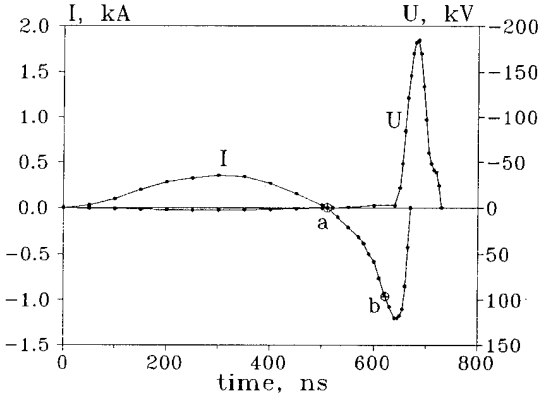


Fig.1. Typical experimental time dependencies of voltage and current across the SOS made up of 196 series-connected p^+-n-n^+ structures with an area of 0.2 cm^2 and with a width of 0.35 mm

To account for the SOS effect a theoretical model was developed [8]. Dynamics of the processes that occur in the structure was calculated with allowance for both a diffusive and a drift mechanism of carrier transport. Apart from this, two recombination types, viz., recombination via impurities and impact Auger recombination, were laid at the foundation of the model. Account was also taken of the influence that the structure exerts on pumping-circuit current and voltage. The real distribution of impurity doping in p^+-n-n^+ structure was also taken into consideration.

In the course of forward pumping the holes are electric-field-transported through the n-base from the high-doped p^+-region to the high-doped n^+-region, whereas from the n^+-region the electrons penetrate into the p^+-region. At current densities characteristic of the SOS effect the time needed for the holes to pass through the diode base is several nanoseconds. As these processes occur, injected carriers are accumulated mostly in the high-doped regions of the structure. In Fig.2a we show the calculated concentration distribution of accumulated carriers in the p^+-n-n^+ structure; this distribution corresponds to the moment "a" (see Fig.1), when the accumulated charge has the highest value.

When reverse pumping is effected, the accumulated carriers are carried out of the p^+- and n^+-regions. By the moment of time corresponding to point "b" in Fig.1 space charge regions arise in the high-doped regions of the structure, which are depleted of free carriers. The calculated plasma concentration distribution for this point is given in Fig.2b. Current interruption sets in 20 to 40 ns after the point "b". Within this delay time the residual plasma is in all likelihood removed from the base of the structure, because the reverse voltage that arises across the structure when the current is interrupted can be endured only by a base free from injected carriers. Before being interrupted the current flowing through the region poor in carriers may be associated with the multiplication of carriers in a strong electric field.

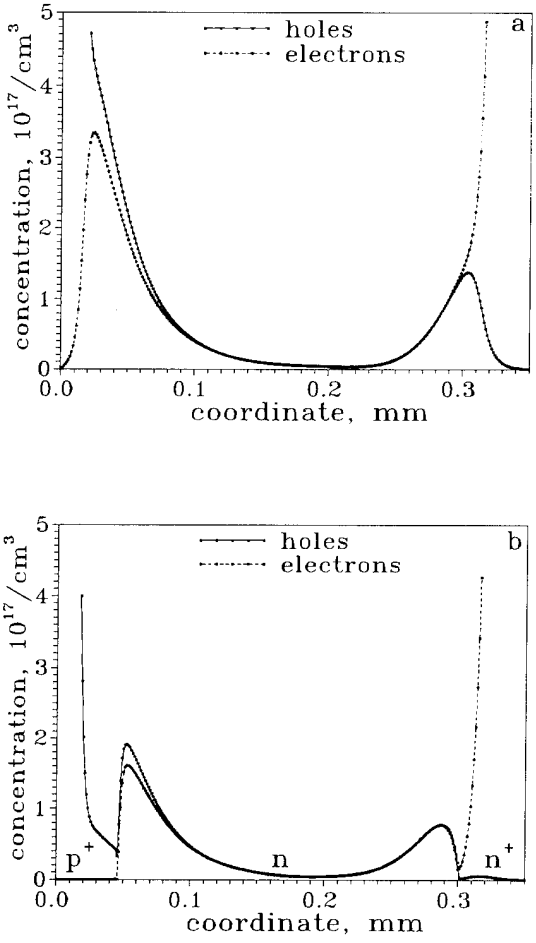


Fig.2. Calculated distribution of electron-hole plasma concentration in the p^+-n-n^+ srtucture

3. Ideology of constructing all-solid-state switching sytem generators

Subsequent to conducting experiments with the use of generators furnished with spark gaps [6], the possibility became apparent of constructing megavolt-range nanosecond pulsed generators with an all-solid-state switching system [7]. The circuitry ideology can be represented as follows (Fig.3).

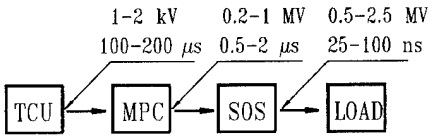


Fig.3. Block-diagram of nanosecond generators with an all-solid-state switching system

The thyristor charging unit, TCU, takes off a dosed amount of energy from the supply line. From the TCU the energy comes to a magnetic pulsed compressor, MPC, at a voltage of 1 to 2 kV within $\sim 10^{-4}$ s. The MPC compresses the energy in time to a value of the order of 10^{-6} s and increases the voltage to several hundred kilovolts. The SOS acts as a terminal power amplifier as it transfers the energy from microsecond to the nanosecond time range and increases the voltage by a factor of 2 or 3 and current by a factor of 5 or 6.

4. Facility with an all-solid-state switching system

To test the circuitry concepts outlined above, we have developed a number of units with an all-solid-state switching system.

One of the generators has an output voltage of 200 kV at a load of 200 Ohm, a half-height pulse duration of ~30 ns, and a pulse repetition rate of 50 pps. The generator is a 650 x 350 x 240 mm^3 unit weighing 40 kg.

Another unit was developed to check the possibility of raising the pulse repetition rate with a view to increasing the specific average power of the facilities. At a 150 Ohm load pulses of amplitude 140 kV and duration 80-100 ns were obtained, which recurred with a frequency of 1000 pps. The supply circuit elements (thyristors, inductance coils, capacitors, and magnetic switches) had forced air cooling, while the SOS and load were cooled with running water. The average power consumed by the facility was 17 kW, the power released in the load as high-voltage nanosecond pulses was 11-12 kW. The overall efficiency of the facility depends on under-load operation and ranges between 50 and 70%. Experiments have shown that the maximum pulse repetition rate has no fundamental restrictions due to the SOS and is determined only by the thermal operating conditions of the circuit elements and the recovery time of the thyristors in the power supply unit, i.e., by the same causes as those arising in ordinary electrical-engineering converters.

In 1993 we started developing a SIBERIA accelerator with an all-solid-state switching system for an output voltage of 1 MV, a current of 8 kA, a pulse duration of 50 to 60 ns, and a pulse repetition rate of 150 pps. The watt consumption is 107 kW, the power delivered to the SOS is ~ 75 kW, and the design value of output power is ~ 50 kW. For the diagram of the facility refer to Fig.4.

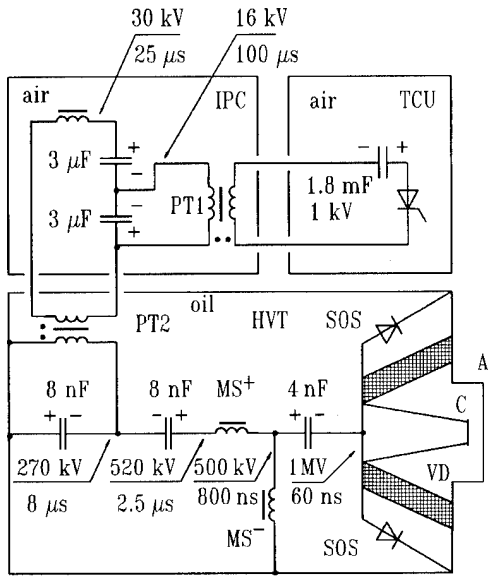


Fig.4. Circuitry of a 1-MV SIBERIA accelerator with an all-solid-state switching system

The accelerator consist of three modules, viz., thyristor charging unit TCU, an intermediate magnetic compressor IPC, and a high-voltage module HVT accomodated in a tank filled with transformer oil. The dimensions of the HVT, which weighs ~7 t, are 3700 x 1400 x 1200 mm^3.

The TCU forms a pulse of amplitude 15 kV and duration 10^{-4} s which is applied to the input of the IPC. Subsequent to double compression in the IPC, the energy is transmitted to the high-voltage compressor via the pulsed transformer PT2 to a voltage level of 270 kV within $8 \cdot 10^{-6}$ s. The subsequent double compression of the energy by the transformer PT2 and forward-pumping switch MS^+ leads to the pumping capacitor being charged to 500 kV within 800 ns. The design value of interrupter forward-pumping current is 3.8 kA, that of reverse-pumping current 11 kA. The value of the current switched over into the diode is 8 kA. The impedance of the vacuum diode with the explosion emission cathode should range between100 and 150 Ohm.

The SOS is composed of 12 parallel panels surrounding the vacuum diode insulator. Each panel is made up of 1088 series-connected p^+-n-n^+ structures with an area of 0.2 cm^2 and with a base thickness

of 0.3 mm each. The puncture voltage of a single structure with a direct current is ~1.5 kV for the initial level of n-base doping $N_d \sim 10^{14}$ cm^{-3}. The highest forward-pumping and reverse-pumping current densities are 1.6 and 4.6 kA/cm^2, respectively.

5. Goal of further investigations

An elementary analysis of a circuit with an intermediate inductive storage and a SOS shows that major parameters specifying the performance of opening switches include the reverse pumping time to current interruption time ratio t^-/t_0 and current interruption time t_0. The current interruption time t_0 determines the smallest length of a pulse being formed and the energy losses in the SOS when the current is interrupted, while the t^-/t_0 ratio the maximum possible overvoltage coefficient.

In this connection, the basic task is to search for ways of increasing the reverse pumping time t^-. An understanding of the physical picture of the processes that occur when p^+-n-n^+ structures are pumped permits a number of conclusions to be drawn. The restriction of the pumping time comes from the finite lifetime of nonequilibrium carriers in the n-base. Two recombination mechanisms are essential here: recombination on impurities and impact Auger recombination. The latter recombination mechanism is not decisive, for the carrier lifetime here can be controlled over a wide range by varying the level of injection and current density. The major restriction of the carrier lifetime is associated with deep-level impurity recombination. The point is that in the experiments we employed p^+-n-n^+ structures used for the making of high-voltage rectifier diodes. Accordingly, the lifetime of injected carriers into the diode base did not exceed some microseconds.

Computer-aided model experiments have shown that by using a semiconductor with a low level of lifetime killing impurity and selecting the level of injection and the width of the base, it is possible to obtain a structure pumping time over a range of some tens of microseconds while preserving the highly nonuniform base carrier concentration distribution needed for the diffusive carrier withdrawal mechanism.

Thus further investigations of the high-conductivity phase should include pumping regime optimization and computer-aided structure parameter selection followed by the fabrication and testing of prototype structures.

6. Conclusion

Today's level of understanding of the physics of the SOS effect as gained in the course of experimental and theoretical investigations permits the hope that the characteristics of semiconductor opening switches can be substantially improved owing to the conduct of further research. Specifically, going over to pumping duration of tens of microseconds while preserving the attained current interruption time at the level of some tens of nanoseconds will permit, on the one hand, increasing the overvoltage coefficient by several times and lowering the voltage of the primary storage and, on the other, simplifying the design of the generator as a whole, since the interrupter can be pumped directly from a low-voltage thyristor supply source without intermediate cells for the magnetic compression of energy in time. Such generators will be distinguished by simplicity in design, low cost, and long service life - features that will enable them to be extensively introduced in various industrial technologies.

References

[1]. M.S.Mazzola,K.H.Schoenbach, V.K. Lakdawala, S.T.Ko. Appl. Phys. Lett., 1989, v.55, p.2102.

[2]. K.H.Schoenbach, V.K.Lakdawala, D.C.Stoudt, et al. IEEE Trans. Electron Devices, 1989, v.36, p.1793.

[3]. V.M.Tuchkevich, I.V.Grekhov. "New principles of switching high-power by semiconductor devices". Leningrad: Nauka, 1988 (in Russian).

[4]. S.K.Lyubutin, S.N.Rukin, S.P.Timoshenkov. Proc. 9th Simp. on High-current Electronics, Russia, p.218-219, 1992 (in Russian).

[5]. Yu.A.Kotov, S.N.Rukin, A.L.Filatov. Ibid., p.220 -221.

[6] Yu.A.Kotov, G.A.Mesyats, S.N.Rukin, A.L.Filatov. Doklady AN, 1993, v.330, No3, p.315-317 (in Russian).

[7]. Yu.A.Kotov, G.A.Mesyats, S.N.Rukin et al. " A novel nanosecond semiconductor opening switch for megavolt repetitive pulsed technology: experiment and applications", Proc. of the 9th Pulsed Power Conf. (awaiting publication), Albuquerque, NM, June 21-23, 1993.

[8]. S.A.Darznek, Yu.A.Kotov, G.A.Mesyats, S.N.Rukin. Doklady AN, 1994, v.334, No3, p. 304-306 (in Russian).

Novel, Compact Two-Beam Accelerator

Y. Y. Lau, Ya. S. Derbenev, R. M. Gilgenbach,
J. Hochman, J. Luginsland, M. Walter, C. H. Ching
Intense Energy Beam Interaction Laboratory
Nuclear Engineering Department
University of Michigan
Ann Arbor, MI 48109-2104

Abstract

We present results of theoretical design studies of a novel, compact two-beam electron accelerator.[1] The primary electron beam is an annular, high-current (1-10 kA), moderate voltage (0.7-0.8 MV), long- pulse (0.5-1 μs) electron beam from the Michigan Electron Long Beam Accelerator, (MELBA). The design goal of the secondary electron beam is 4-10 MeV in a length of 1-2 meters. The primary electron beam is to be modulated in a manner similar to the relativistic klystron.[2] The on-axis secondary e-beam is accelerated by the wake-field on-axis in an array of TM_{020} mode cavities. A new phase-focusing technique has been developed by means of radius modulation of the primary e-beam. Design parameters for a proof-of-principal experiment will be presented.

Introduction

Many applications exist for electron beams with energy in the range from 1-10 MeV and currents of amperes, including: radiation-sterilization, X-ray radiography, and cross-linking polymers. During the past 20 years, a large number of Marx-generator, electron beam accelerators have been developed in the U.S. and elsewhere; thus, a means of upgrading these machines by multiplying the electron beam energy by a factor of 5-15 is an extremely attractive new technology. The two-beam accelerator[1] provides a means of accomplishing this goal of an electromagnetic transformer, with a transformer ratio of 5-15.

Several other researchers have investigated related two-beam accelerators. Friedman and Serlin utilized a modulated e-beam from a relativisitic klystron to drive a secondary electron beam from an accelerating gap.[2] Voss and Weiland utilized the wake-field from a train of short e-beam

micropulses passing near the outer wall of a series of cavities to accelerate an on-axis e-beam.[3] Humphries invented the Scantron, in which an array of 6-pencil beams are deflected transversely in a TM_{020} mode cavity to accelerate an on-axis e-beam.[4]

The present paper discusses a novel, new two-beam accelerator (Twobetron) in which an annular, high current, primary electron beam (500-700 kV) is axially-modulated by a relativistic-klystron; the energy transfer to an on-axis, high energy (4-10 MeV) secondary e-beam is coupled by the TM_{020} cavity mode in an array of cavities. The problem of phase-focusing between the primary and secondary electron beams is accomplished by a periodic modulation of the primary e-beam's radius.

Theory

A schematic drawing of the Twobetron is depicted in Fig. 1. The driver beam is an annular beam of radius r_o, carrying an AC current I_d at frequency ω. It passes through an accelerator structure, consisting of N cylindrical pillbox cavities. Each cavity has a radius $b = 5.52\ c/\omega$ so that ω is also the resonant frequency of the TM_{020} mode of the pillbox cavity. The secondary beam is an on-axis pencil beam, carrying an AC current I_s ($I_s << I_d$), also at frequency ω. Since the rf electric fields of the TM_{020} mode have opposite signs in the outer region and in the inner region, the mode retards the annular driver beam but accelerates the on-axis secondary beam. If the driver beam radius is modulated axially, phase focusing and tunability in the output energy of the secondary beam can be achieved. Specifically, if we write $r_o = a + D\cos(y)$, where $a = 2.405\ c/\omega$ is the radius of the rf electric field-null of the TM_{020} mode, D is the amplitude and y is the phase of the modulation in r_o, the general phase focusing condition reads $dy/dz = d\phi/dz$ where ϕ is the phase difference between the primary beam bunch and the secondary beam bunch at axial position z.

Shown in Fig. 2 is the evolution of the relativistic mass factors of the primary beam and the secondary beam when the above mentioned phase focusing technique is employed. The parameters used in the computation are: initial energy = 700 keV for both beams, $\omega/2\pi$ = 3.65 GHz, b = 7.221 cm, a = 3.146 cm, D = 0.176 cm, Q (TM_{020})= 100, I_d = 0.5 kA, and $\phi = 0$ when z = 0. These parameters may be used in a proof-of-principle experiment

using MELBA. With the cavity length L = 1 cm, the cavity number n is also the axial distance (z) in cm in Fig. 2, which shows that the secondary beam may be accelerated to 10 MeV over a distance of 2 m. This yields R = 14, where R is the "transformer ratio", the ratio of energy gain by the secondary beam to the energy loss by the primary beam. If we write d = 1.25 D/a, we find R=1/d, secondary beam energy gain per cavity=(17 keV)(ωL/c)Qd(I_d/1kA), and $I_s < I_d/2R$ under optimal conditions.

There are many issues which may affect the eventual usefulness of the two-beam accelerator concept outlined above. Chief among them is the modification of the rf characteristic that always accompanies an intense driver beam, which includes a detune of the structure frequency and modification of the gap transit-time factor. Also of concern is the beam breakup instability (BBU) on the driver beam. However, we have recently found that BBU in an annular beam may be far less serious than a pencil beam[5]. We have also examined the effects of the transverse wake and of the longitudinal instabilities and found that they are not serious, at least for the parameters used in the above numerical example, assuming a solenoidal field of 10 kG in the accelerating structure.

Acknowledgement

This research was supported by BMD/SDI-IST through an ONR contract.

References

1) Ya. S. Derbenev, Y. Y. Lau, and R. M. Gilgenbach, Phys. Rev. Lett. 72 3025 (1994)

2) M. Friedman, J. Krall, Y. Y. Lau, and V. Serlin, Rev. Sci. Instrum. 61 171 (1990)

3) G. Voss and T. Weiland, DESY Reports #M82-10 (1982); M82-079; (1982).
also T. Weiland, N. Holtkamp, P. Shutt, R. Wanzenberg, W. Bialowons, M. Bieler, F. -J. Decker, and H. -C. Lewin, Proc. 2nd Europ. Accel. Conf. , Nice, France, (1990)

4. S. Humphries, Nucl. Instrum. Meth. A258, 548 (1987).

5. Y. Y. Lau and J. W. Luginsland, J. Appl. Phys. 74, 5877 (1993). In the line above Eq. (7) of this paper, the factor (I/1 kA) should read (I/17 kA).

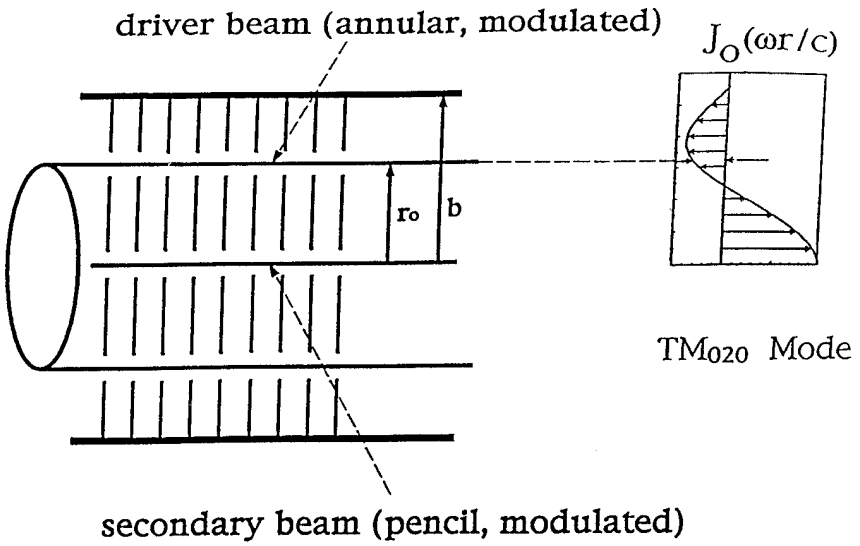


Figure 1. Schematic illustration of UM Twobetron concept.

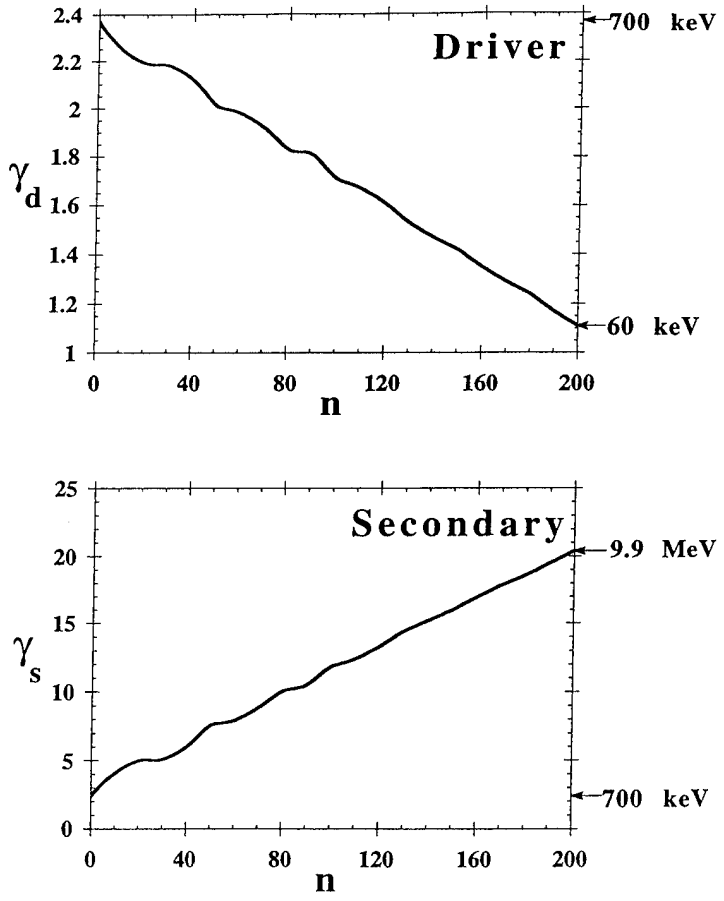


Figure 2. Energy of primary and secondary e-beams vs. cavity number.

Plasma Opening Switch Experiments at Sandia National Laboratories[a]

M.E. Savage, E. R. Hong, W.W. Simpson, M.A. Usher[b]
High Energy Plasma Physics Department

Sandia National Laboratories, Albuquerque, NM 87185-1194

With the present state of Plasma Opening Switch (POS) development, the POS itself is the limitation in inductive driver performance. There is a large payoff in improving the opening switch. Sandia is pursuing a POS that can use the advantages of inductive energy storage, namely, very high energy density and reduced driver size. This is a challenging goal.

The Sandia Magnetically Controlled Plasma Opening Switch is an attempt to overcome some of the problems found in earlier POS systems. The Sandia switch is unique because it holds plasma in place during the closed phase. Very large drivers have a large magnetic impulse. This can force plasma downstream into the load region, so it is an advantage to hold the plasma in place. Further, the Sandia switch operates in a low impedance coaxial geometry, so driver polarity is a minor issue. Lastly, the Sandia switch can be command-triggered (though with a large trigger pulser).

A vacuum opening switch is desirable because the output pulse does not have to flow through a vacuum interface. Operating in vacuum means it is not accurate to model the opening switch as a time-changing linear resistance; this does not consider axial-flowing electrons. A POS model that does consider vacuum electron flow is called *flow impedance*. Flow impedance relates voltage and currents in the opening switch region to a physical gap cleared of plasma. Clearing a physical gap is what a vacuum opening switch must do. This gap is the most important measure of a vacuum opening switch. We will present data on how we measure this gap in our experiments.

Introduction

Using inductively stored energy has advantages in terms of energy density. The vacuum interface is the weakest point in the power flow chain.[1] Compressing power in vacuum eases the stress on the vacuum interface and reduces the size of the system. The Plasma Opening Switch (POS) operates in vacuum, and therefore can use the high energy density of Magnetically Insulated Transmission Lines (MITLs).[2] Magnetically insulated transmission lines can withstand 100 MV/meter and tens of MA/meter. The POS in vacuum also behaves like a short section of MITL, but the plasma in the switch region is also a zero work-function source of ions. This is our conceptual view of the POS- a short section of magnetically insulated transmission line with one conductor moving. The gap in this transmission line goes from zero when the switch is closed, to some gap typically much less than the vacuum electrode spacing.

The plasma opening switch, as invented almost 20 years ago[3], consisted of plasma sources injecting through holes in the MITL. The plasma is an excellent conductor and acts as a short circuit in the transmission line. Plasma is also very low mass, so a gap can be opened in a nanosecond time scale without requiring a huge amount of energy. This first POS reduced the pre-pulse from the water switches to a level that allowed much improved load behavior. Later experiments[4] extended the opening switch to act as a pulse-compression element. As this development work continues, the ratio of conduction time to opening time should increase, as should the ratio of load power to driver power. A practical goal of opening switch research is to supply load power in excess of power flowing through the vacuum interface.

With the increased demands on the POS as a pulse compressor, we have refined the opening switch to better perform its two increasingly disparate tasks: staying closed and opening. The opening switch described here is the latest in the evolution of the POS at Sandia.

The Magnetically Controlled Plasma Opening Switch is an evolution of the Current Toggled POS[5] used on SuperMITE, a short-pulse 1.5 TW driver. We used the Magnetically Controlled POS on SuperMITE at 35 ns conduction time, then installed the same switch on MITE[6] for experiments at 220 ns conduction time. The MITE experiments showed that the Magnetically

---

[a] This work supported by the U.S. Department of Energy under Contract Number DE-AC04-94AL85000.

[b] General Technology Corporation

Controlled POS would work at 220 ns conduction time. Recently, MITE was re-configured to Tesla, a driver on which 500 ns conduction time experiments were performed. The Tesla experiments showed that the Magnetically Controlled POS would also work as well at 500 ns conduction time. Future experiments will raise the drive current to about 1 MA in 350 ns.

The Hardware

Figure 1 shows the Magnetically Controlled POS hardware as used on SuperMITE, MITE, and Tesla. Not shown is the 5.5 meter vacuum energy storage MITL upstream of the POS, nor the electron beam load downstream. Diagnostics consist of both anode and cathode currents, upstream and downstream of the switch, and various voltage monitors in the water and vacuum.[7]

In this switch, there are two separate plasma opening switches and two magnetic field coils. The applied magnetic field coil is energized by a 10 kV parallel bank with a time to peak flux of about 550 microseconds. This flux is essentially unchanging over the current pulse. The second magnetic field coil is energized by the storage inductor current and controlled by the Trigger POS. The fast magnetic field coil inductance is less than 10 percent of the inductance of the storage inductor. Storage inductor current flows through the Trigger POS; after the Trigger POS opens storage inductor current flows in the fast field coil. The Trigger POS opening time is set by its plasma fill time and is independent of the main switch. Energizing the fast magnetic field coil begins pushing the main switch open. This control of the fast magnetic field coil current from zero to full storage inductor current is the improvement of the Magnetically Controlled POS over the Current Toggle POS.

For the MITE experiments at 220 ns conduction time, the storage inductor was driven by an intermediate store water capacitor charged by a single Marx. The low impedance of the water capacitor allows high current in a short time; MITE supplied up to 800 kA in 250 ns. A single gas switch transferred the capacitor energy into the storage MITL. The vacuum interface voltage peaked at 1.5 MV with a sinusoidal shape and 250 ns base. The load voltage depends on the opening switch performance and the load impedance. For a moderate impedance load (7 Ω), load voltage could be about 2.5 to 3 MV for high current experiments. Raising the load impedance will raise the switch voltage until the cathode current downstream of the switch becomes very small. When the cathode current downstream of the switch is essentially zero, then the gap in the switch region is the voltage determinant. We are interested in coupling

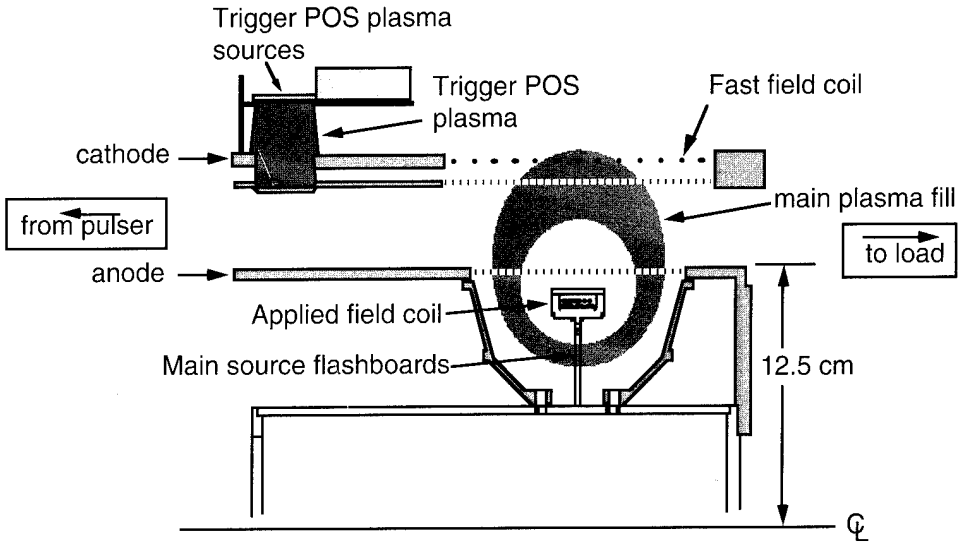


Figure 1. The Magnetically Controlled Plasma Opening Switch as used on MITE. The vacuum impedance in this region is 20Ω.

power to loads, so we do not operate with extremely high load impedance. The flow impedance of the opening switch determines the highest load impedance that can be tolerated. Higher switch flow impedance allows higher load impedance and therefore higher load power.

Flow impedance of the opening switch is

$$Z_{flow} = \frac{V_{POS}}{\left(I_a^2 - I_c^2\right)^{\frac{1}{2}}}$$

where I_a is anode current upstream of the switch, I_c is the cathode current downstream of the switch, and V_{POS} is voltage at the opening switch. This comes from a very general electron flow theory.[5] Flow impedance essentially measures electron flow and then solves electron flow equations for a consistent MITL gap. This gives opening switch gap as a function of time for every experiment, largely independent of the load impedance. The ratio of flow impedance to vacuum impedance is a figure of merit for a plasma opening switch. Flow impedance is zero while the switch is closed, and rises in a time much less than the input current rise time. Figure 2 shows flow impedance and percent gap (the ratio of flow impedance to vacuum impedance) as a function of time for a MITE experiment. The data in Figure 2 assumes that gap is a linear function of flow impedance; this is a close approximation for the relatively low (20Ω) vacuum impedance coaxial transmission line.

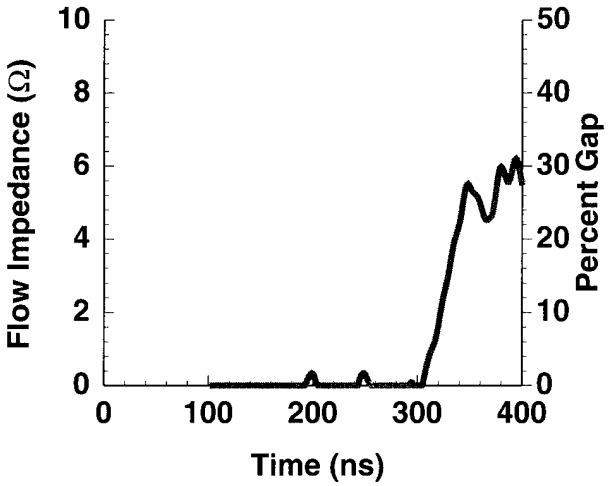


Figure 2. The measured flow impedance and equivalent opened gap for a MITE experiment. The load was an electron beam diode, but flow impedance is independent of load impedance. The vacuum gap in the switch region is 5.1 cm.

Given that the MITE experiments (at 220 ns) performed about as well as did the SuperMITE series (at 35 ns), we decided to extend the conduction time beyond 220 ns to study the opening at slower input times. This is because the cost of the driver is reduced if the POS can perform the pulse compression normally done in water. To perform this test, we simply shorted out the closing switch between the water intermediate store and the vacuum storage inductor. We also divided the Marx into 3 parallel sub-Marxes to reduce the inductance of the Marx. Power flows through the water capacitor; the water section inductance reduces peak current . The new configuration is called Tesla. Tesla can provide about 400 kA in 500 ns at a conservative 70 kV Marx charge. The peak current occurs at 1.6 microseconds, but our plasma sources could not supply enough plasma to conduct to peak current. The main switch plasma source uses 125 Joules of DC charged energy. Inadequate pulse-charged capacitance and excessive inductance between the pulse-charged capacitors and the plasma flash boards limits the amount of plasma created.

Figure 3 shows currents on a Tesla experiment into an electron beam load of about 10Ω.

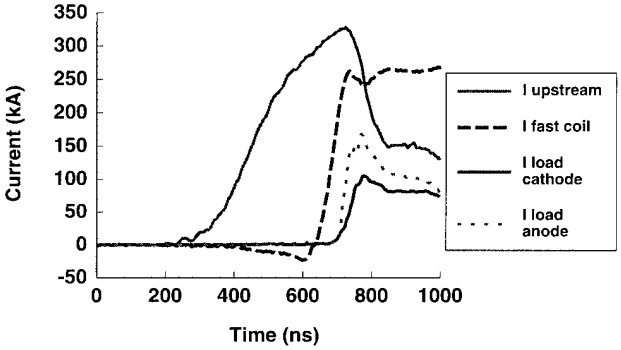


Figure 3. Currents for a Tesla experiment into a high impedance (10Ω) load. Peak Load voltage was about 2.5 times the peak interface voltage.

Figure 4 shows measured flow impedance for both a MITE experiment at 220 ns conduction time, and a Tesla experiment, at 500 ns conduction time. The peak current in the MITE experiment was 650 kA. The Tesla experiment was only 350 kA peak current. (The current is lower for the Tesla because we used a higher voltage Marx (higher inductance) to get the highest current at 500 ns.) Flow impedance rise time determines the voltage rise time into high impedance loads. For resistive loads, a fast switch opening is desirable, both for load rise time, and for switch losses. If the switch opens very slowly, more energy is deposited in the switch. This energy is deposited by electrons that are flowing nearly radially in the switch region. Inductive loads have losses determined by circuit inductance, but fast switch opening may move the losses downstream of the POS hardware.

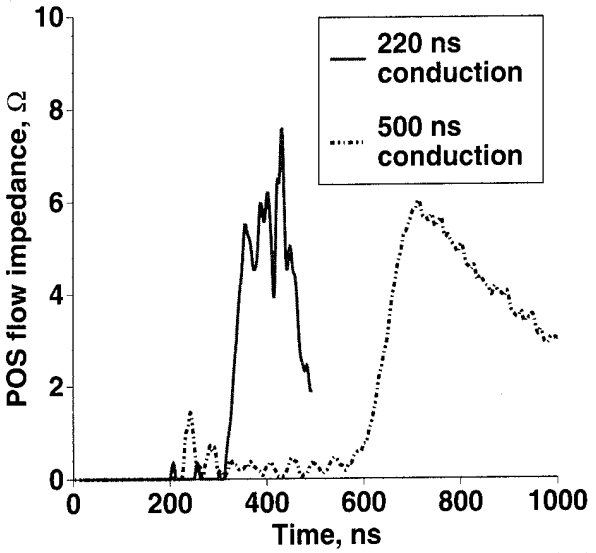


Figure 4. Measured flow impedance for 220 ns conduction time and 500 ns conduction time. The peak upstream current for 220 ns conduction was about twice that for the 500 ns conduction.

Upstream current starts at 90 ns in both cases. Note that the ultimate flow impedance is about the same in both cases, but that the rise time is slightly slower for the 500 ns conduction time. This is to be expected; the ultimate gap is largely determined by the magnetic fields but the opening rate is slowed by the increased plasma mass required for longer conduction time.

Figure 5 shows power measured at the vacuum interface and at the load for a 500 ns conduction time experiment. The load power is higher because the peak load voltage is about three times the peak interface voltage.

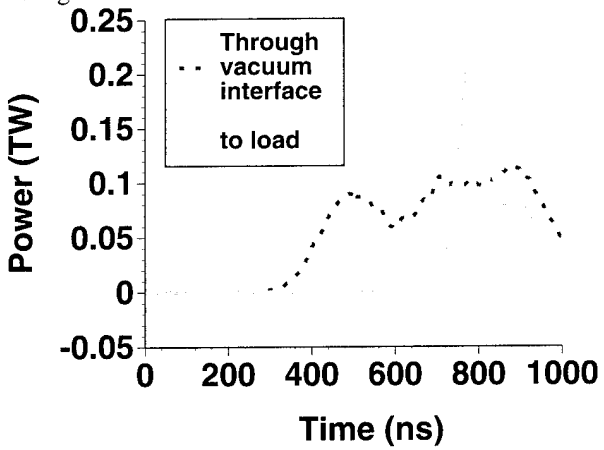


Figure 5. Interface power and load power for a Tesla experiment at 500 ns conduction time. The load is a 10Ω electron beam diode with no plasma fill.

The applied magnetic field is designed to hold the plasma in place during the time the POS is closed. We wish to both keep the POS closed and keep plasma out of the load region. This is increasingly important for longer conduction time switches because the impulse to force plasma downstream grows larger with conduction time. We observed plasma motion out of the switch region for very low applied magnetic fields and 500 ns conduction time. An applied magnetic field 0f 0.07 Tesla at the cathode allowed plasma motion with 350 kA, 500 ns conduction; twice that applied field held the plasma. The self-field of the drive current is 0.39 Tesla at 350 kA. Thus, for this particular magnetic topology, a cathode applied field of one-third the drive current field holds the plasma in place. This fraction will rise with increasing conduction time.

Summary

We presented data from recent Magnetically Controlled Plasma Opening Switch experiments at Sandia. We found that the switch scales to 500 ns conduction time and 400 kA currents without difficulty. The key feature to this POS is the magnetic fields and there is no shorting of the field coil windings in this regime. As always, we strive to increase the opened gap in the switch region to increase the usable load power out of the switch. Experiments with an improved applied field topology will begin shortly, as will testing at over 1 MA in 350 ns. Understanding the scaling to longer conduction time and higher current is an important part of studying the Magnetically Controlled Plasma Opening Switch. A switch that can conduct high currents for a long time, then deliver compressed power to a load is the goal.

---

[1]J.P. VanDevender, D.H. McDaniel, E.L. Neau, R.E. Mattis, K.D. Bergeron; J. Appl. Phys. **53**,4441(1982).

[2]C.W. Mendel, D.B. Seidel, S.E. Rosenthal; Laser Part. Beams **1**,311(1983).

[3] C.W. Mendel, Jr.,S.A. Goldstein; J. Appl. Phys. **48**,1004(1977).

[4] B.V. Weber, R.J. Commisso, G. Cooperstein, J.M. Grossmann, D.D. Hinshelwood, D. Mosher, J.M. Neri, P.F. Ottinger, S.J. Stephanakis; *IEEE Trans. Plasma Sci.*, **PS-15**, Dec. 1987, p. 635.

[5]C.W. Mendel, Jr., M.E. Savage, D.M. Zagar, W.W. Simpson, T.W. Grasser, J.P. Quintenz, J. Appl. Phys., **71**, 3731 (1992).

[6]M.E. Savage, G.W. Cooper, W.W. Simpson, M. A. Usher; Proc. of the 9th International Conf. on High-Power Particle Beams,**NTIS PB92-206168**,621,(1992).

[7]M.E. Savage, C.W. Mendel, Jr., T.W. Grasser, W.W. Simpson, D.M. Zagar, Rev. Sci. Instrum. **61,** 3812 (1990).

To be published in Proc. Beams'94 Conference, San Diego, June 1994

THEORY OF ION BEAM GENERATION FOR RIPPLE ANODE SURFACE

Vladimir M.Fedorov

Moscow Radiotechnical Institute of RAN, II35I9, Moscow, Russia

Abstract. Theoretical analysis of ion beam formation provided for the space charge-limit cold particle emission from slightly ripple anode. It can be applyed also for electron guns. The steady-state solution is obtained for a quasi-planar diode with the ripple anode by a sinusoidal profile. It is type of $X_A = \theta_A / k \cdot \sin ky$, where $\theta_A \lesssim 0.1$ ($\sim 6^\circ$) -angle small parameter, $\lambda = 2\pi/k$ -ripple wavelength, $\lambda \lesssim 0.5 d$, d - diode gap. The weak ripple emitter in the diode provides visible space variations of a current density of accelerated ion beam $\delta J/J_0 \sim 20\%$ for $\theta_A \sim 0.1$ ($|X_A/d| \lesssim 0.01$). Meanwhile the ion beam divergence is small $\bar{\theta}_i < 0.5^\circ$. The results agree with experimental dates. The theory model of the ripple emission charge flow may be used in computer codes.

A sharp roughness ($\theta_A \sim 1$) of the emitter may provide a non-stationary charge-limit emission with time-space fluctuations and high effective temperature $T_{ef} \gg T_E$ (T_E -emitter temperature). It is very complicated physics problem. For towards progress it will be needed systematic experimental dates concerning of a non-uniformity charge-limit emission.

I. Introduction

This paper is next step of previous work in ref.[1]. I wish it to dedicate to the memory of Professor Winfried Schmidt (1932 - 1992, Germany, Kernforschungzentrum).

The problem of a ripple emitter is arised owing to both experimental successes of late years to produce the high power proton beams with small divergence $\bar{\theta}_i \lesssim 20$mrad ($\sim 1^\circ$) and a necessity to achive more well focused ion beams for inertial confinement fusion. Ripples of the plasma emission surface are main factor of the ion beam divergence. Alredly in early works (see ref.[2])of high power ion beam generation physicistes have done attempts to use computer codes for a modeling of the ion beam divergence in a diode with a ripple anode. In ref.[2] the anode non-uniformity plasma was created by a flashover of the periodical ($\lambda < 0.5d$) metal-dielectric surface. But no significant results by the calculation were achived. Also late ten years it wasn't proposed sufficient codes for the ripple emitter modeling. The problem was showed difficalt (only space cell number $\sim 10^5$) and complicated in essence. Because it was poor convergence of an iterative solution and poor truth of results for a current density profile.

It is known special interactive software systems are widely used for the design of electron or ion guns of high intensity beams. Meanwhile this codes, for instance [3], use well known the Child-Langmuire solution which is correctly for the uniformity charge-limit emission [4]. A competent of this approach may be excused usually because they calculated enjectors [5,6] like the electron Pierce guns [4]. In 1940 J.Pierce has showed on possibility to realize straight electron trajectores (the Child-Langmuire charge flow) over the belt or disk cathode, if one connected a focusing electrode to the cathode edge with

an angle between they equals exactly the $\theta_{fp}=90+\theta_p \simeq 157.5^0$ ($\theta_p = 67.5^0$ is the Pierce angle) .In ref. [5] it was remarked some difference of the computer and experiment results.In particular,the distances of a beam high compression had a discrepancy of $(l_{cal}- l_{exp})/l_{exp}\sim 10\%$ for the electron gun with the focusing angle θ_f which was slightly differed from the Pierce gun angle θ_{fp} ($\delta\theta_f=\theta_f-\theta_{fp}=5^\circ$) .The authors proposed two main reasons of the discrepancy.The first is connected with a sharp dependence of the current density profile by the angle inclination $\delta\theta_f$ as it is predicted by the R.Lomax solution [7] . The second is non-thermal beam divergence (effective beam temperature $T_{ef}\simeq 10\cdot T_s$, T_s - thermal cathode temperature) which was provided a micro -roughness on the cathode surface.

In 1981 R.Sudan (Cornell Univer.,USA) during his lecture session in the Karlsruhe Kernforschungzentrum (FRG) proposed to solve analytically the problem of ion divergency by a sinusoidal ripple plasma anode in the Applied-B ion diode.But no a self-consistent solution has been given at that time.Apparent towards progress was done in[1]. The basic guiding line was used experimental dates on the Applied-B ion diodes [8,9] with the anode surface like in ref.[2].The experiments[8] were measured a time-space variation of the ion current density (~20%) .Authors of ref[9] measured small total divergence $\theta_i \simeq 1^\circ$ for proton beams.A phenomenological model proposed in ref.[1] has explained this results.Meanwhile the model had'nt provide self-consistent fields in the close range ripple anode in $(X-X_A)<0.1\cdot\lambda$ .In this paper I develop forward ideas given in [1].

2. General Description

For simplicity the sinusoidal profile of the ripple anode is used

$$X_A=\theta_A/K\cdot\sin Ky \quad , \quad \theta_A \lesssim 0.1 \quad , \quad \lambda=2\pi/K \lesssim 0.5\cdot d \qquad (1)$$

where θ_A is small perturbation parameter, λ is the ripple space wavelength, d is the basis diode gap(planar diode), $\lambda\lesssim 0.5d$ is the condition of small scale ripple, $|X_A|$ is the ripple height ($|X_A|/d\lesssim 0.01$), y is the axis of periodic perturbation.The X -axis is main direction of the diode gap in Fig.1 .The anode surface of Eq(1) has then

$$\theta_s=-\frac{dX_A}{dy}=-\theta_A\cdot\cos Ky \quad , \quad and \quad \varkappa_s=\frac{d\theta_s}{dy}=\theta_A\cdot K\cdot\sin Ky \qquad (2)$$

where θ_s is the angle of anode normal, $\varkappa_s$ is the anode surface curvature.Boundary conditions on the anode with the charge-limit cold ion emission enclude both ordinary relations and angle ratios :

$$E_x(X_A)=0 \quad , \quad E_y(X_A)=0 \quad , \quad U(X_A)=0 \quad , \quad v_x(X_A)=0 \quad , \quad v_y(X_A)=0 \qquad (3)$$

$$E_y/E=\theta_E(X\to X_A)=\theta_s \quad , \quad v_y/v=\theta_i(X\to X_A)=\theta_s \quad , \quad \theta_s=-\theta_A\cdot\cos Ky \qquad (4)$$

where E -electrical field, U -potential, v -ion velocity, θ_s -from Eq(2) .The θ_A is small value and so terms $\sim\theta_A^2$ ($\theta_A^2\lesssim 0.01$) will be neglected below.It means $\theta\simeq\sin\theta\simeq tg\,\theta$ and $E\simeq E_x$, $v\simeq v_x$ etc. The ratios of Eq(4) refer to the $\theta_E(x,y)$ and $\theta_i(x,y)$ functions of angle description should be included the first space harmonic as main term. It can be described by

$$\theta_E=E_y/E\simeq E_y/E_x=-\xi_E(x)\cdot\theta_A\cdot\cos Ky+\theta_{2E} \quad , \quad \xi_E(X_A)=1 \quad , \quad \theta_{2E}(X_A)=0 \qquad (5)$$

$$\theta_i = v_y/v \simeq v_y/v_x = -\xi_i(x)\cdot\theta_A\cdot\cos Ky + \theta_{2i}\,,\quad \xi_i(X_A)=1\,,\quad \theta_{2i}(X_A)=0 \qquad (6)$$

In this paper I will neglect the second space harmonic terms in three functions: $\theta_E(x,y)$-angle of electrical field line, $\theta_i(x,y)$-angle of ion trajectory, $J(x,y)$ -ion current density. The transverse particle motion of Eq(6) produce visible compression-decompression effects of the ion flow in the diode gap (see in Fig.I) .It may be essential in a case of small scale ripple ($\lambda \ll d$ and $\xi_i(x)\cdot\theta_A\cdot Kd \sim 1$).

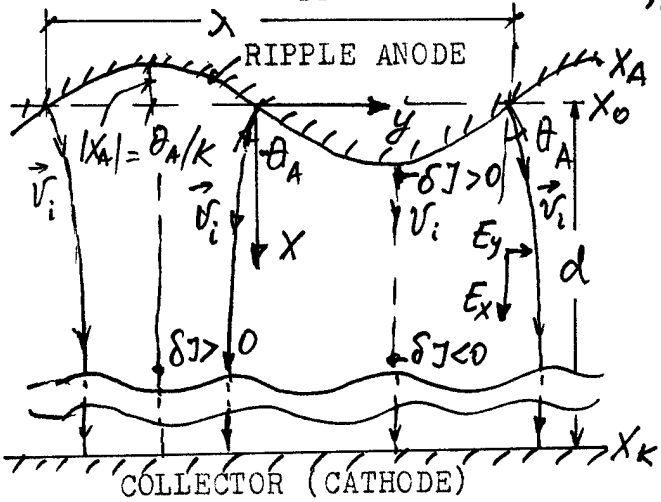


Fig.I. Quasiplanar ion diode schematic, and x,y -coordinate system and ion trajectory schematic are shown. A weak ripple anode is $X_A = \theta_A/K\cdot\sin Ky$, $\theta_A \le 0.1$, $Kd = 2\pi/\lambda\cdot d \ge 10$, $|X_A|/d \le 10^{-2}$. E_x-main accelerated electric field, E_y -deflection electric field, $E_A = V_A/d$ -average field. $\delta V_A \simeq V_A\cdot(2\theta/Kd)^{4/3}$ -groove-hill voltage drop.

Note that below normalized quantities will be used: $x/d \to x$, $y/d \to y$, $Kd \to K$, $V/V_A \to V$, E/E_A, $v/\sqrt{eV_A/M}$, J/J_{cl} . For simplicity it will be neglected a magnetic field influence to ions ($E \gg B\cdot v/c$). A set of two-dimention steady-state equations for the Poisson, and the particle motion, and the charge flow continuity are presented

$$-\frac{\partial^2 V}{\partial x^2} - \frac{\partial^2 V}{\partial y^2} = \frac{8}{\sqrt{2}\cdot 9}\cdot\rho(x,y) = \frac{8}{\sqrt{2}\cdot 9}\cdot J/v = \frac{4}{9}J/\sqrt{-V} \qquad (7)$$

$$E_x = -\frac{\partial V}{\partial x}\,,\quad E_y = -\frac{\partial V}{\partial y}\,,\quad \frac{\partial E_x}{\partial y} = \frac{\partial E_y}{\partial x}\,,\quad \theta_E \simeq E_y/E_x = -\xi_E\cdot\theta_A\cdot\cos Ky \qquad (8)$$

$$v_x \simeq v = \sqrt{-2V}\,,\quad v_y = \int_{X_A}^{x} E_y\,dx/v\,,\quad \theta_i = v_y/v = -\xi_i\cdot\theta_A\cdot\cos Ky \qquad (9)$$

$$J_x \simeq J = \rho v \simeq X_0\,(1 + X_1(x)\cdot\sin Ky) \qquad (10)$$

$$J_y = \rho\cdot v_y = J\cdot v_y/v \simeq -X_0\cdot\xi_i(x)\cdot\theta_A\cdot\cos Ky \qquad (11)$$

$$\operatorname{div}\vec{J} = \frac{\partial J_x}{\partial x} + \frac{\partial J_y}{\partial y} = 0\,,\quad \frac{dX_1(x)}{dx} + \theta_A\cdot K\cdot\xi_i(x) = 0 \qquad (12)$$

$$X_1(x) = X_1(X_A) - \theta_A\cdot K\cdot\int_{X_A}^{x}\xi_i(x)\,dx \qquad (13)$$

$$J_{cl} = \frac{1}{9\pi}\cdot\sqrt{\frac{2e}{M}}\cdot V_A^{3/2}/d^2\,,\quad J_A(r_A/r) = \frac{1}{9\pi}\cdot\sqrt{\frac{2e}{M}}\cdot E_{VA}^{5/3}/(V_A\cdot d^2)^{1/6} \qquad (14)$$

where J_{cl} is the Child-Langmuire current density for planar diode; $J_A(r_A/r)$ is the emission current density for a cylindrical or spherical diode, J_A is presented by my approach (accuracy ~ 2%) of the Langmuire-Blodgett current (see in ref.[4]) for a ratio of $0.6 \le r_A/r \le 1.6$; E_{VA} is the electrical field on the anode without ion emission.

The basis diode of $\theta_A = 0$ is described well known the Child-Langmuire solution of Eq(3-I0) as following

$$U_0(x) = -\chi_0^{2/3} \cdot (x - x_0)^{4/3} \quad , \quad v_0(x) = \sqrt{2} \cdot \chi_0^{1/3} \cdot (x - x_0)^{2/3} \quad , \quad J_0 = \rho_0 \cdot v_0 = \chi_0 \qquad (I5)$$

$$E_0(x) = \frac{4}{3} \chi_0^{2/3} \cdot (x - x_0)^{1/3} \quad , \quad \rho_0(x) = \frac{1}{\sqrt{2}} \chi_0^{2/3} \cdot (x - x_0)^{-2/3} \qquad (I6)$$

where χ_0 is the ion current enhancement by an electron cloud, $\chi_0 = 1$ in pure ion diode. Clear idea about the non-uniformity emission solution is to apply formally the Eq(I5) to the ripple anode by replacing χ_0 to $\chi_A(y)$ and χ_0 to $\chi_0 + \delta\chi(x,y)$ (see in ref.[I]). As a result of the boundary conditions of Eq(3) should be satisfied. Difficalt problem remains how to obtain a self-consistent solution for the $\delta\chi(x,y)$. In ref.[I] this problem was solved not enough. A basis of this difficalties is the non-linear singular solution of Eq(I6) with respect to $\delta x = (x - x_0)$. A known method of a singular removal is to use non-zero an emission temperature ($T_s \neq 0 \quad , \overline{v^2(x_A)} \neq 0$). But it provides other complicated problem namely the virtual emitter[4]. In this paper I research a case of the cold particle of $T_s = 0$ which conductes the simple boundary conditons by Eqs(3,4). A correctness of the $T_s = 0$ approach for the ripple emission problem is satisfied in a case of

$$e \cdot \delta U_A = e \cdot \chi_0^{2/3} \cdot (\theta_A / kd)^{4/3} \cdot U_A \gg T_s \text{, for } \theta_A \sim 0.1,\ kd \sim 30,\ eU_A/T_s \gg 2 \cdot 10^3 \qquad (I7)$$

So in high power beam experiments (see e.g.[5,6,8,9]) the eU_A/T_s ratio was in a range $eU_A/T_s = I0^4 - I0^6$. These are tipical values and it is satisfied Eq(I7). For my opinion in a case of a sharp roughness ($\theta_A \sim 1$) the ratio eU_A/T_s should be played a role in a fluctuation emission like the Reynolds number in a turbulent fluid flow of a boundary layer.

2. Known Solutions for Two-Dimention Gap

Simple solutions of Eq(3-9) for a small emitting anode of so-called the "vacuum" fields case are given by

$$-U_v = x - \theta_A / k \cdot \sin ky \cdot e^{-z} \quad , \quad U_v(x_A) = 0 \quad , \quad z = kx - \theta_A \cdot \sin ky \qquad (I8)$$

$$E_v = 1 + \theta_A \cdot \sin ky \cdot e^{-z} \quad , \quad \theta_{vE} = E_{vy}/E_v = -\theta_A \cdot \cos ky \cdot e^{-z} \qquad (I9)$$

$$\theta_{vi} = v_y/v = -\xi_{vi} \cdot \theta_A \cdot \cos ky \quad , \quad \xi_{vi}(z \leq 1) = 1 - z/3 + 0.1 z^2 \qquad (20)$$

where $\theta_{vi} = v_y/v$ is one-particle trajectory function. Thus electro-static perturbations by the ripple electrode are decreasing exponentially to the power $z = k(x - x_A)$. They may be neglected at a distance from the anode of $x > 3/k$ ($x \gtrsim 0.5\lambda$). In the charge space gap with the boundary of Eq(3) the electro-static perturbations will be prevailed at "middle" distances from the emission anode approximatly $0.5/k \leq x - x_A \leq 2/k$.

In order to define the $\chi_1(x_A)$ in Eq(I3) one can trying to apply formally the $E_v(x_A)$ of Eq(I9) into the $J_A(r_A/r)$ of Eq(I4) and it produces

$$J_v(x_A)/J_0 = (E_{vA}/E_{A0})^{5/3} \quad , \quad \chi_{1v}(x_A) = \frac{5}{3} \cdot \theta_A \qquad (2I)$$

The approach of Eq(2I) would be good if it is correctly. The result of ref.[7] das'nt support it. As noticed in the Intraduction, the cathode current density profile in the quasi Pierce electron gun (a focusing electrode is connected with the cathode in an angle $\theta_f \neq \theta_{fp} = I57,5°$)

was estimated in ref.[7] and is given by

$$J_s(y) = J_s(a)\cdot(a/y)^{K_f}, \quad K_f \simeq 0.011\cdot\delta\theta_f^{\circ}, \quad \delta\theta_f^{\circ} = \theta_f^{\circ} - 157.5 \qquad (22)$$

where $y=(a-r)$ is a distance from the cathode margin, $K_f(\theta_f)$ is presented my approximate formula, I used dates in [7]) for $|\delta\theta_f| \leq 20^{\circ}$. The $J_s(y=0)$ on the cathode margin changes dramaticaly in a respect to plus or minus sign of the $\delta\theta_f$, as following from Eq(22): $J_s(y=0, \delta\theta_f<0)=0$ and $J_s(y=0, \delta\theta_f>0)=\infty$. Meanwhile the "vacuum" electric field E_{vs} (without electron emission) in the same geometry has'nt change rapidly :

$$E_{vs}(y) \simeq E(a)\cdot(y/a)^{2/7(1-0.05\cdot\delta\theta_f^{\circ})}, \quad E_{vs}(y=0)=0 \text{ for } |\delta\theta_f| \leq 20^{\circ} \qquad (23)$$

In ref.[7] R.Lomax has used a non-linear equation of ref.[10] instead a set of Eqs(7-12). It is given

$$div\,\vec{J} = \nabla(\nabla\varphi\cdot(\nabla^2(\nabla\varphi)^2)) = 0 \qquad (24)$$

where φ is a velocity potential, $\nabla\varphi = \vec{v}$. In ref.[4] authors used the same approach and defined a variation $J_s(y)$ over the emitter throgh a curvature $\varkappa_i(X_A)$ of the particle trajectory :

$$\frac{\partial}{\partial y}\ln J(X_A, y) = -5\frac{\partial\theta_i(x\to X_A)}{\partial x} = 5\varkappa_i(X_A), \quad 5\theta_A\cdot\frac{d\xi_i(x\to X_A)}{K\cdot dx} = \chi_1(X_A) \qquad (25)$$

where I use also Eqs(9-10). Note that the charge-limit laminar (see Eq(24)) non-uniformity flow asymtotic solutions of ref.[4] are like the forms of Eqs(15,16) where the x - coordinat axes is replaced to the $X_i = X_i(x,y)$ -particle trajectory.
Using Eqs(7-13) I prepared other version of Eq(25) :

$$\frac{\partial}{\partial y}\ln J(X_A, y) = -2\frac{\partial\theta_E(x\to X_A)}{\partial x} = 2\varkappa_E(X_A), \quad 2\theta_A\cdot\frac{d\xi_E(x\to X_A)}{K dx} = \chi_1(X_A) \qquad (26)$$

where $\varkappa_E(X_A)$ is a curvature of an electric field line over the emitter (not the "vacuum" field). Using both Eqs(25,26) and the "vacuum" field results of Eqs(19,20) we can obtain approximate values for the $\chi_1^{*}(X_A)$ in an addition to the χ_{1v} of Eq(21), namely

$$\chi_{1vE}(X_A) = 2\theta_A\frac{d\xi_{Ev}(X_A)}{dx} = 2\theta_A, \quad \chi_{1vi}(X_A) = 5\theta_A\frac{d\xi_{vi}(X_A)}{dx} = \frac{5}{3}\theta_A \qquad (27)$$

3. Charge-limit Solution for Weak Ripple Emitter

One result of the provided analysis is the estimate by Eq(27) of a possible value range for the $\chi_1^{*}(X_A) = (1.6 \div 2)\theta_A$ in Eq(13). The other is the form of the potential asymtotic function over the ripple emitter:

$$U = X_0^{2/3}\cdot X_1^{4/3}, \quad X_1 = -U_v - X_A K U_v\cdot\left(1-\frac{0.5}{\theta_A}\cdot\chi_1(X_A)\right)(1+\alpha_1 z+\alpha_2 z^2+\dots) \qquad (28)$$

where $U_v(X,y)$ is the "vacuum" field potential of Eq(18) ($U_v(X_A)=0$, $U_v(X\gg 1/K)=X$) it will provide a small space charge disturbance by the Poisson Eq(7) at "middle" distance from the ripple emitter $X \sim 1/K$.

An iterative self-consistent solution for the charge-limit emission diode in Fig.1 was obtained during sequent approaches by reducing a discrepance between the $\chi_1(x)=\chi_{1i}$ of Eq(13) and the $\chi_1(x)=\chi_{1v}$ of Eqs(7,10). The iterative process was encluded to change free parameters of Eq(28) namely the $\chi_1(X_A)$ and small factors of α_1 and α_2 etc.
At last, the weak ripple charge-limit solutions are given

$$U(x,y) = X_0^{2/3}\cdot X_1^{4/3}, \quad X_1 = X - \frac{1}{K}\theta_A\cdot\sin Ky\cdot\left(e^{-z}(1+0.08z) - \frac{0.008\cdot z^2}{1+0.015z+0.029\cdot z^{2.6}}\right)$$
$$z = KX - \theta_A\cdot\sin Ky, \quad z(X_A)=0, \quad 0 \leq z \leq 20. \qquad (29)$$

$$E_x = \frac{4}{3}\chi_0^{2/3}\cdot X_1^{1/2}\cdot X_{1x}', \quad E_y = \frac{4}{3}\chi_0^{2/3}\cdot X_1^{1/3}\cdot X_{1y}', \quad \theta_E = \frac{X_{1y}'}{X_{1x}'} = -\xi_E\cdot\theta_A\cdot\cos ky \quad (30)$$

$$\xi_E(x) = e^{-z}(1+0.08z) - 0.008z^2/(1+0.15z+0.029\cdot z^{2.6}) \quad (31)$$

$$v = \sqrt{2}\cdot\chi_0^{1/3}\cdot X_1^{1/3}, \quad \theta_i = v_y/v = -\xi_i\cdot\theta_A\cdot\cos ky, \quad \xi_i = \frac{2}{3}z^{-2/3}\int_0^z \xi_E z^{-1/3}\,dz \quad (32)$$

$$J = \rho\cdot v = \chi_0 + \delta J = \chi_0\left(\left(X_{1x}'\right)^2 + \left(X_{1y}'\right)^2 + 3X_1\left(X_{1xx}'' + X_{1yy}''\right)\right) = \chi_0\left(1+\chi_{1i}\sin ky\right) \quad (33)$$

$$\chi_{1i} = \left(1.82 - \int_0^z \xi_i(z)\,dz\right)\cdot\theta_A, \quad \chi_1(\chi_A) = 1.82, \quad \left|\chi_{1i}(z) - \chi_{1v}(z)\right| \le 0.1\,\theta_A \quad (34)$$

The last term in Eq(29) is directly connected with transverse particle motions. At large distance $\chi \gg \lambda$ ($z \gg 6$) the asymtotics of the term $X_1 = \chi + \delta X_1$ can be defined using Eq(33), namely: for $z \gg 6$, $|\delta J|/\chi_0 \approx 3z\cdot K\cdot|\delta X_1|$ and $K\cdot|\delta X_1| \sim 1/z$. In Eq(29) this term is defined in a region $0 \le z \le 20$. The potential $U(X,y)$ of Eq(29) provides for a small discrepance between the current density perturbations of the $\chi_{1v}(z)$ by Eq(33) and the $\chi_{1i}(z)$ by Eq(34) and it is $|\chi_{1v} - \chi_{1i}|/\chi_1(\chi_A) \le 5\%$. A value of the $\chi_1(\chi_A)$ is occured equal to an average value between the χ_{1vE} and the χ_{1vi} which were defined by the "vacuum" field case of Eq(27). Some calculation results of Eqs(29-34) for relative values are given in Tab.I

$z = K(X-X_A)$	0.	0.35	I.	I.5	2.	2.7	3.4	5.	8.	I0.	I5.	20.
$E_{1y} = -\frac{4}{3}z^{1/3}\cdot\xi_E$	0	-0.68 (Max)	-0.51	-0.35	-0.23	-0.1	0.	0.1	0.15	0.16	0.16	0.15
$X_1(X)/\theta_A$	1.82	1.5	0.98	0.65	0.36	0	-0.28	-0.8	-1.5	-1.8	-2.3	-2.5
$\xi_i = \bar\theta_i(x)/\bar\theta_A$	1.	0.89	0.72	0.61	0.54	0.45	0.39	0.29	0.2	0.14	1/15	1/25
$\xi_{vi} = \bar\theta_{vi}(x)/\bar\theta_A$	1.	0.9	0.76	0.66	0.58	0.5	0.46	0.38	0.31	0.28	0.23	0.2

Transverse particle motions (see in Fig.I) lead to compression flow facing the groovs and a decompression flow facing the hills of the ripple anode. As a result, disturbans of the $\delta J \sim \chi_1(x)$ and $-\delta U \sim E_{1y}(x)$ are occured approximately zero at a distance $X \approx 3/K$. At a far distance $X > 3/K$ it is taken place a reverce for both the $\chi_1(X)$ and the $E_{1y}(x)$. This process is being provided by a momentum of particle transverse motions. The inverce electric field $E_y(x)$ at a distance $KX > 3.4$ is making more dicrease to an angle spread $\bar\theta_i = \xi_i\cdot\theta_A$ of accelerated ions (to compare $\xi_i(z)$ and $\xi_{vi}(z)$ in Tab.I).

At far distance from the ripple anode the ion angle spread is occured smaller, namely: $\bar\theta_i(Kd=15, \lambda\approx 0.4d) = \bar\theta_A/15$ and $\bar\theta_i(Kd=20) = \bar\theta_A/25$. Note about an account of a electron cloud influence in a case of the ion diode with the magnetic insulation of electrons (so-called the Applied-B ion diode). In tipical cases, electron orbit sizes along a transverse direction of y-axis (see in Fig.I) equal about two times a diode gap[I]. Clearly, the electron charge in main gap (excepting pre-cathode region) shouldn't provide a small space scale charge disturbance. In a case of the ion enhacement $\chi_0 = 2$-3 one can use the effective dicreased diode gap $d \approx 0.7 d_0$ for estimations of the $\bar\theta_i(Kd)$ and $\delta J(Kd)$ by Tab.I.

4. Limits of the $T_s \neq 0$ and $\theta_A \neq 0$

We should take into account the limit thermal ion transverse velocities $\bar{v}_y \sim (T_s/M)^{0.5}$ which produce in the diode gap as a beam divergence $\bar{\theta}_{iT} = \bar{v}_y/v(x) = \bar{\theta}_T \cdot (d/x)^{2/3}$ and as a weak smooth process to dicrease the distortion of Eqs(33,34). The letter can be estimated by

$$\frac{\partial}{\partial x}\delta J_T + \bar{v}_y \cdot \frac{\partial \rho}{\partial y} = 0 \quad , \quad \delta J_T = -\bar{\theta}_T \cos ky \int_{z_1}^{z} \chi_{1i}(z) \cdot \left(\frac{kd}{z}\right)^{2/3} dz \quad , \quad \bar{\theta}_T = \left(T_s/eU_A\right)^{1/2} \qquad (35)$$

Some results by Eq(35) for $\bar{\theta}_T = 0.01$ and $kd = 20$ are in $0 < z \leq 3$, $|\delta J_T| \simeq 0.2\theta_A$ and in $3 \leq z \leq 20$, $|\delta J_T| \simeq 0.4 \cdot \theta_A$. So one can see the thermal smooth effect does not exseed $|\delta J_T/\chi_1| \leq 15\%$. It means a component of the ion beam divergence by the weak ripple anode can be estimated by Eqs(29-34) or Tab.I and it is $\bar{\theta}_i \simeq \bar{\theta}_A/20 \leq 5$ mrad for $\lambda \simeq 0.3d$, $\bar{\theta}_A \leq 0.1$.

Other thermal effect connectes with so-called the "virtual cathode" (emitter) phenomenon [4,11] which is created by reflecting ions in a thin boundary emission layer δX_T ($X_{AV} - X_A = \delta X_T \simeq d \cdot (T_s/eU_A)^{0.75} \ll |X_A| \leq 10^{-2}$). General condition of the charge-limit emission is an emission charge flux J_T more than the diode current density J_0 : $J_T = \varkappa_T \cdot \varkappa_0 \cdot J_0$ typicaly $\varkappa_T \cdot \varkappa_0 \sim 10$. The emission layer δX_T creates a voltage drop $\delta U_T \sim T_s/e$ (electric mirror) and an electric field $E_T(X_A)$ on the anode surface X_A and the virtual emitter surface with the boundary condition $E_s(X_{AV}) = 0$. Becase a thickness of the layer δX_T is smaller $\delta X_T \ll |X_A|$ that is possible to neglect it and to use the "zero" boundary condition by Eq(3) in the solution of Eqs(29,30).

The approach $T_s \simeq 0$ of Eq(3) lets to use the laminar charge flow approximation which is presented as by Eqs(7-12) as by Eq(24). It suppouses than the Eq(29) is sufficiently only for the $\theta_A \simeq 0$. What is happend in a case of the $\theta_A \sim 0.1 \neq 0$ (limit small angle). I assume the limit smaller temperature ($T_s/eU_A \sim 10^{-5} \neq 0$) of the emitter provides two types of a smooth process. The first in the diode gap is the same of Eq(35) and it dicreases a discrepance of a second order approach $\sim \theta_A^2$. The second in the emission layer δX_T is connected with the boundary electric field $E_T(X_A)$. It can be estimated using the emission flux $J_T \sim 10 \cdot J_{CL}$ and a pressure balance equation, namely

$$E_T^2/8\pi \simeq 2J_T \cdot M\bar{v}_{xT}/e \quad , \quad E_T(X_A)/E_A \simeq 2 \cdot (T_s/eU_A)^{1/4} \quad , \quad E_A = U_A/d \qquad (36)$$

In typical high power experiments it was $E_T(X_A)/E_A \sim 0.1$. Small variations of the $E_T(X_A)$ should provide a smooth process to neglect some disorder of the "zero" boundary condition $\delta E_s(X_A) \sim \theta_A^2 \neq 0$. As a result, the solution of Eq(29) should be remained quite exactly for $\theta_A \sim 0.1$.

Note that a case of a sharp ripple $\theta_A \sim 1$ or a sharp emission margin (non-Pierce optics) is'nt described in frame a work of the steady-state laminar solutions. A main effect in this case is a crossing of particle trajectories at near region of the emission surface. For the sinusoudal profile with $\theta_A \sim 1$ it is occured at a distance $X \sim 1/k$. Many experiments with microwave devices refer on a presence of a high noise level in a case of the non-Pierce optics beam enjectors. Other experiments of ion and electron intence beams [8,12] with a plasma layer emitter indicate to time-space (small scale) fluctuations of the current density beam. It is unsolved at present very complicated physics problem concerning of a turbulent emission layer creation.

5. Conclusions

I.The charge-limit emission solution for a weak ripple anode is obtained.It is primal model of the self-consistent charge-limit flow solution for the variable curvature emitting surface.

A necessity of the analitical solutions is more evidently stood at present.Many physicistes are trying to apply modern computer codes for an accurate modeling of intence electron or ion beams of the non -Pierce optics enjectors.But this results are often unreliable.

2.It is provided more accurate estimations for both an angle spread $\bar{\theta}_i$ and a current space variation $\delta J/J_0$ of accelerating ions. Some discrepance with results in ref.[I] does not exceed a factor I.5.

In a case of the ion diode with weak ripple anode ($\bar{\theta}_A \leq 0.1$, $\lambda \leq 0.4d$) the ion beam divergence is occured smoller $\bar{\theta}_i \leq$ 5- I0 mrad.Meanwhile the ion current density spatial distortion is occured visible magnitude $\delta\bar{J}/J_0 \sim$ 20% .This results agree with known experimental data.

3.In a case of a rough ripple ($\theta_A \sim$ I) emission surface or a sharp emission margin (non-Pierce optics) that is possible created a turbulent emission layer which provides visible levels as a current density fluctuation as a beam divergence.

References

[I] V.Fedorov,W.Schmidt and Th.Westermann.-Proc.9th Conf.on High Power Particle Beams.v.II,Washington (I992),747.

[2] D.J.Johnson et al. -J.Appl.Phys.(I98I),v.52,NI,I68.

[3] M.A.Tiunov,B.M.Fomel and V.P.Yakovlev.-Preprins INP 87-35(I987) and 89-I59(I989),Novosibirsk (in Russian).

[4] P.T.Kirstein,G.S.Kino and W.E.Waters. -Space-Charge Flow, (McGraw-Hill,N.Y.,I967).

[5] G.I.Kuznetsov,M.A.Tiunov and V.P.Yakovlev. -Preprint INP 89-I6I, Novosibirsk (I989),(in Russian).

[6] Y.V.Baryshev et al. -Nucl.Instr.and Meth.A 340 (I994),24I.

[7] R.J.Lomax. -J.Electronics and Control .6(I) (I959),39.

[8] V.M.Fedorov and P.P.Deichuli. -Proc.8th Conf.on High Power Particle Beams.v.I,Novosibirsk (I990),p.p.2I5,469.

[9] D.J.Johnson et al. -Proc.7th IEE Pulsed Conf.,Monteray(I989),944.

[I0] B.Meltzer. -Proc.Phys.Soc. B 62,(I949),8I3.

[II] M.V.Nezlin. -Dynamics of Beams in Plasma.Energoizdat (in Russian) Moscow (I982).

[I2] S.G.Voropaev et al.Proc.of USSR Acad.Sci. ,v.276 (I984),III (in Russian).

Progress in Lithium Beam Power, Divergence, and Intensity at Sandia National Laboratories

T.A. Mehlhorn, J.E. Bailey, G.A. Chandler, R.S. Coats, M.E. Cuneo, M.S. Derzon, M.P. Desjarlais, R.J. Dukart, A. B. Filuk, T.A. Haill, H.C. Ives, D.J. Johnson, R.J. Leeper, T.R. Lockner, C.W. Mendel, P.R. Menge, L.P. Mix, A.R. Moats, W.B. Moore, T.D. Pointon, J.W. Poukey, J.P. Quintenz, S.E. Rosenthal, D. Rovang, C.L. Ruiz, S.A. Slutz, W.A. Stygar, D.F. Wenger
Sandia National Laboratories
P. O. Box 5800
Albuquerque, NM 87185-1187

Abstract

We have achieved lithium intensities of 1.4±0.4 TW/cm^2 and have performed target experiments at the ~1000 TW/g level on PBFA II achieving 58±6 eV radiation temperatures. Our near-term milestone of achieving a 100 eV radiation temperature in an ion-driven hohlraum will require an increase in lithium beam intensity to ~5±1 TW/cm^2. Our lithium beam intensity is presently limited by a parasitic load that restricts ion power and by the total beam divergence. Recent experiments indicate that the parasitic load is carried by ions and that the beam divergence is predominately caused by LiF source divergence and possibly by electric field non-uniformities. Visible spectroscopy shows both significant anode and cathode plasmas within the ion diode that could be the source of these parasitic ions and also contribute to the electric field non-uniformities. Diode impedance collapse may also be caused by the parasitic load. Cleaning the electrodes in the ion diode could eliminate the source of these parasitic ions. We plan to combine heating, RF-discharge cleaning, and Ti-gettering to clean the diode and improve the local vacuum. Simulations predict a 2-3 times increase in coupled ion power without the parasitic load. Beam divergence and diode impedance may also be improved as a result of diode cleaning.

BACKGROUND

We have achieved lithium beam intensities 1.4±.4 TW/cm^2 and have performed lithium-driven target experiments at the ~1000 TW/g level on the Particle Beam Fusion Accelerator II (PBFA II) at Sandia National Laboratories. We measured hohlraum radiation temperatures of 58±6 eV in these experiments. Our near-term milestone of achieving a 100 eV radiation temperature in an ion-driven hohlraum will require an increase in lithium beam intensity to 5±1 TW/cm^2 through an increase in coupled lithium power and a decrease in total beam divergence. Our lithium beam intensity is presently limited by a parasitic load that restricts ion power and by the total beam divergence. Recent experiments indicate that the parasitic load is carried by ions and that the beam divergence is predominately caused by LiF source divergence and possibly by electric field non-uniformities. Visible spectroscopy shows both significant anode and cathode plasmas within the ion diode that could be the source of these parasitic ions and also contribute to the electric field non-uniformities.

DEFINING THE PARASITIC LOAD

A diagram illustrating the transfer of power through the PBFA-II accelerator to the diode is shown in Fig. 1. We see the expected modest losses in the accelerator and insulator stack and in electron flow current losses in the magnetically-insu-

lated transmission lines (MITLs). It is evident that the greatest loss in power occurs in the ion diode and the adjacent feeds. Some of these losses are MITL flow electrons that are lost in the feed and to the anode within the ion diode. However, there is a large amount of current loss within the diode for which we cannot account. We have termed this loss, which presently limits our coupled lithium ion power to about 6-9 TW, a "parasitic load".

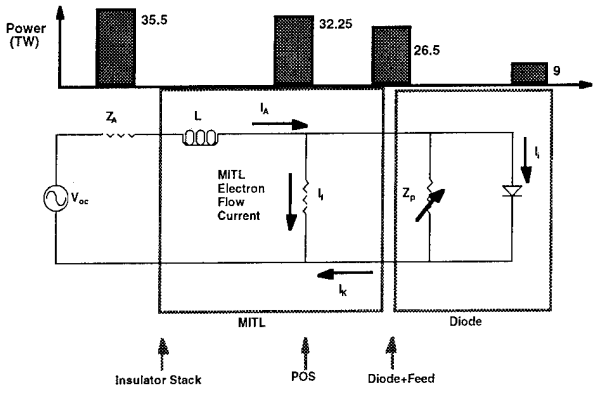


Fig. 1 PBFA-II accelerator schematic showing power transfer efficiency to lithium beam.

We define the parasitic load to be the difference between the total ion current that is seen by our gas cell B-dot (current) monitors and the lithium ions measured by filtered Faraday cups and on-axis diagnostics (e.g. the magnetic spectrometer). This difference between the B-dots and Faraday cup currents grows with time (Fig. 2). The parasitic load limits the coupled lithium current and may also contribute to the impedance decay of the diode. The peak lithium current is presently limited by the onset of the parasitic load.

DIVERGENCE LIMITATIONS

LiF divergence at the source presently appears to dominate our total beam divergence. Our best total lithium beam divergence of 22 mrad at peak power was obtained with a source divergence of ~18-20 mrad. The beam divergence at the source is inferred spectroscopically from Doppler-broadened lithium neutral emission that arises when lithium ions charge exchange in a thin contaminant layer near the anode surface. [1] This indicates that all other components of the divergence (e.g., electromagnetic instability, multiple scattering, canonical angular momentum variations, etc.) only contribute ~9-13 mrad. Decreasing the LiF source divergence to 8-10 mrad should decrease the total beam divergence to ~15 mrad and increase the focal power by a factor-of-two. Alternatively, recent spectroscopic measurements appear to show substantial azimuthal electric field asymmetries and evidence of nonuniform anode and cathode plasmas within the diode which could also contribute significantly to the beam divergence [2].

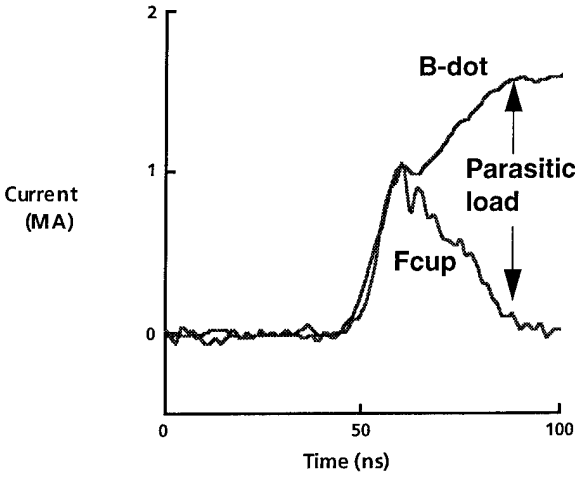


Fig. 2 Comparison of Faraday cup and gas cell B-dot current measurements showing parasitic load.

IDENTIFYING THE PARASITIC LOAD

There is a growing body of evidence from PBFA-II and SABRE experiments that the parasitic load is carried by ions. PBFA-II experiments have shown that these ions are stripped to a higher charge state when they pass through 1.5 μ of Mylar and are stopped by 22 μ of Mylar. The stripping indicates that a significant portion of the current is carried by high-Z (e.g. C,N,O,F) or molecular ions with energies ≥2 MeV; the remaining current is carried by protons or is electron loss. Recent evidence from Faraday cups with apertures large enough to avoid hole closure support these conclusions. Filters and collimators on these cups should allow us to better determine the energy and divergence of these parasitic ions.

DIODE CHARACTERISTICS

Analysis of spectroscopic data from several PBFA-II experiments has clearly indicated the presence of a large electric field at the LiF anode of our diodes during ion emission. This implies that

the LiF is not acting as a space-charge-limited (SCL) ion source [3]. Ion diode characteristics that take into account the 8-10 MV/cm electric field at the anode have been developed [4]. A consequence of the non-zero field threshold for the primary lithium beam is that it is at a great disadvantage compared to any SCL parasitic components such as would arise from regions where plasma forms on the anode or in the gap. As seen in Fig. 3, the parasitic component limits the voltage to values below V* [5] where the lithium beam is not highly enhanced, but the parasitic load can be. The result is a clamping of the lithium beam current. This may explain our experience on PBFA II where we have been unable to get more than ~1 MA of lithium beam from LiF. Note that development of a SCL source for the primary lithium beam would help this problem and may be a priority issue even if the parasitic load can be eliminated.

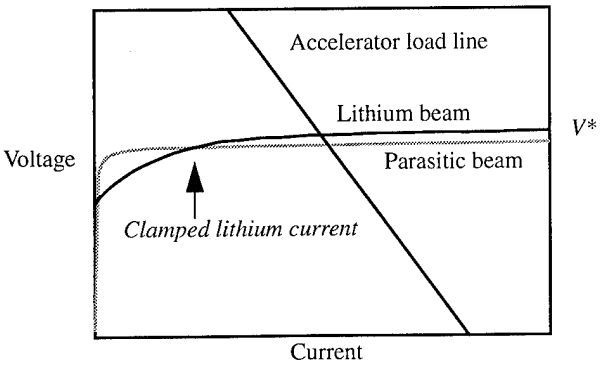


Fig. 3 Diode characteristics for a field-threshold lithium beam and a SCL parasitic beam.

PARASITIC LOAD MODEL

The diode vacuum is $\leq 10^{-4}$ torr prior to PBFA diode shots. This corresponds to less than 6×10^{12} particles within the accelerating gap which is not enough to account for the parasitic current. Therefore, these ions must come from the electrode surfaces. At a pressure of 2×10^{-5} torr, 10 monolayers of material will hit the electrodes each second and therefore we expect an equilibrium of several adsorbed monolayers on all diode surfaces. X-ray photoelectric spectroscopy (XPS) measurements indicate the LiF anodes have significant carbon contamination after exposure to the PBFA-II environment. There is also likely to be significant hydrogen on the anode which can not be measured using XPS. If fully ionized, one monolayer is enough to supply the charge for the entire ion beam. This adsorbed material could be desorbed when the magnetic field coils fire, when the machine prepulse arrives, or when the main power pulse arrives at the diode. Both analytic [6] and novel E-M PIC modeling including ionization physics [7] suggest that ion impact by the primary lithium beam is the initial ionization mechanism for a desorbed neutral layer; secondary electron ionization may become important. As shown in the previous section, once a SCL emitter is formed within the diode it will dominate the LiF field emission source and the increased ion current will drop the diode impedance.

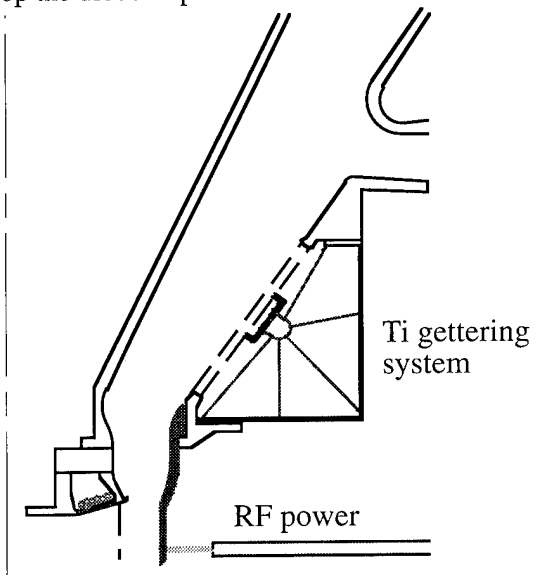


Fig. 4 Quadrant view of PBFA-II ion diode showing location of Ti gettering system, and RF power feed for discharge cleaning in A-K gap.

MITIGATION OF THE PARASITIC LOAD.

Removing the monolayer contaminations that can ionize and form a SCL source from the electrode surfaces, and improving the vacuum so that these surfaces stay clean until shot time, should reduce the parasitic load. Indeed, similar efforts have dramatically improved Tokamak performance [8]. A schematic of the new diode hardware to implement RF discharge cleaning, Ti gettering, and DC heating to 450°C on PBFA II is seen in Fig. 4. We plan to use a 1 mtorr Ar/O_2 13.5 MHz RF discharge to clean the diode electrode surfaces, a Ti

gettering system to differentially pump the liberated contaminants, and heating to minimize the sticking probability for recontaminating the anode surface. We are presently performing light lab tests of these concepts. Heating, cleaning and vacuum improvements (cryo-pumping) will be tested on our extraction diode accelerator, SABRE this summer. The first PBFA-II experiments, including Ti gettering, should begin this fall.

PREDICTED INCREASE IN POWER

Burns [9] and Struckman [10] have previously discharge cleaned lithium diodes and have found that contamination levels were lowered and diode impedance increased. Circuit model calculations indicate that we can double our coupled ion power by eliminating the parasitic current as shown in Fig. 5. Note the limited lithium power and rapid impedance collapse of the present diode. Elimination of the parasitic load roughly doubles the lithium beam power; going to full Marx charge in this configuration almost triples the lithium beam power and increases the ion beam energy from the present < 200 KJ to ~1 MJ.

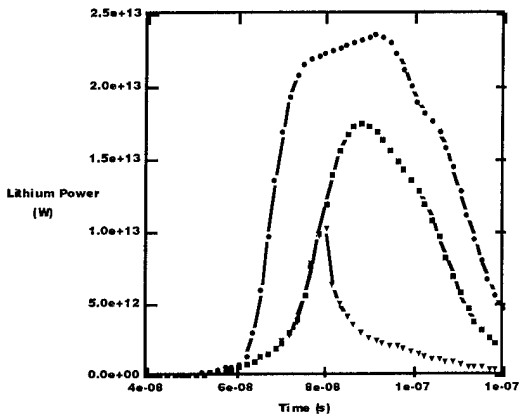


Fig. 5 Lithium beam power modeling with parasitic load ▼, without parasitic load ■, and without parasitic load and full-power operation ●.

ELECTRODE PLASMAS REVISITED

It appears that plasmas play an important limiting role in the behavior of applied-B ion diodes. Plasmas probably contribute to both the parasitic load and impedance collapse. Spectroscopy shows intense continuum emission during the pulse from the cathode side of the diode A-K gap. This emission is consistent with a 10^{16}-10^{18} cm^{-3} plasma that extends 4-5 mm from the cathode tip toward the anode. A correlation between midgap continuum intensity and impedance lifetime is also seen. Finally, the onset of near-anode continuum light is correlated with the onset of the parasitic load [11]. We still need to clarify the sources, ionizing mechanisms, and relative role of anode and cathode plasmas in high-power ion diode physics.

SUMMARY

We require a 2-3 times increase in lithium beam intensity to reach our 100 eV temperature milestone. Our lithium beam intensity is limited by a parasitic load which robs us of lithium power. A major component of this parasitic current has been identified as protons and higher-Z ions. These surface contaminants can be desorbed, ionized, and form a SCL source. Removing them by discharge cleaning may eliminate the parasitic load and increase lithium power. Reduction of LiF source divergence or elimination of electric field asymmetries from nonuniform plasmas should reduce the total lithium divergence. A combination of these two improvements should provide the desired increase in focused lithium intensity.

ACKNOWLEDGEMENTS

This work has been funded by the U. S. Department of Energy under Contract DE-AC04-94-AL85000. Thanks to Y. Maron of the Weizmann Institute and G. Jackson of General Atomics for useful discussions.

REFERENCES

[1] A.B. Filuk, et al, Proc. IEEE Conf on Plasma Science, (1993), p201.

[2] S.A. Slutz, Phys Fl. **B4**, (1992) p 2645.

[3] c.f. "LiF Ion Source Model", R.W. Stinnet, et al, Proceedings of Beams 92, (1992), p 788.

[4] M.P. Desjarlais, private communication.

[5] M.P. Desjarlais, Phs. Fluids **B1** (8) (1989) p1709.

[6] N. Krall, Krall Associates, KA-93-19R, (11/93).

[7] D. Welch, MRC, private communication.

[8] G.L. Jackson, T.S. Taylor, P.L. Taylor, Nuc Fusion **30**, (1990) p2305.

[9] E. Burns, et al., J. Appl. Phys. **63**, (1988) p11.

[10] C.K. Struckman & B.R. Kusse, J. Appl. Phys. **74** (1993) p3658.

[11] A.B. Filuk, private communication.

CHARGED PARTICLE DYNAMICS IN THE ACCELERATION GAP OF THE PBFA II ION DIODE

J. E. Bailey, A. L. Carlson, A. B. Filuk, D. J. Johnson, P. Lake,
E. J. McGuire, T. A. Mehlhorn, T. D. Pointon, and T. J. Renk
Sandia National Laboratories, P.O. Box 5800, Albuquerque NM, 87185-1187
and
Y. Maron
Weizmann Institute of Science, Rehovot 76100, Israel

Abstract

We are improving the understanding of pulsed-power-driven ion diodes using measurements of the charged particle distributions in the diode anode-cathode (AK) gap. We measure the time- and space-resolved electric field in the AK gap using Stark-shifted Li I 2s-2p emission. The ion density in the gap is determined from the electric field profile and the ion current density. The electron density is inferred by subtracting the net charge density, obtained from the derivative of the electric field profile, from the ion density. The measured electric field and charged particle distributions are compared with results from QUICKSILVER, a 3D particle-in-cell computer code. The comparison validates the fundamental concept of electron build-up in the AK gap. However, the PBFA II diode exhibits considerably richer physics than presently contained in the simulation, suggesting improvements both to the experiments and to our understanding of ion diode physics.

The ion current accelerated using an applied-B ion diode is primarily determined by the voltage and the charged particle distribution in the anode-cathode (AK) gap. We are improving the understanding of ion diode physics by measuring the charged particle distributions in the AK gap of the cylindrically-symmetric Applied-B ion diode on the PBFA II accelerator [1]. This diode generates a 15-25 nsec, ~10 MeV, 6-9 TW lithium ion beam, accelerated across a typically 18 mm AK gap [2]. A schematic of the diode is shown in Figure 1 and typical voltage and current waveforms are shown in Figure 2. The gap is insulated against electron current by the application of a 2-3 T magnetic field along the symmetry axis. During the pulse, electrons accumulate in the AK gap both by injection from the transmission line feeding the diode and from the cathode tips. The enhancement of the ion current above the Child-Langmuir space-charge limit is controlled by the number and radial distribution of these electrons across the AK gap. The charged particle distribution also affects the beam divergence, since non-radial electric fields can be generated either by instabilities or non-uniformities in the charged particle cloud. Our goal is to achieve an experimentally-validated understanding of the charged particle distributions that will lead to improved ion beam power.

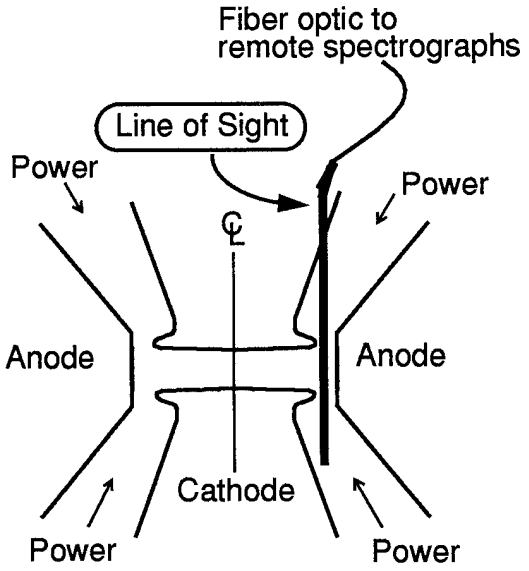


Figure 1. Schematic of PBFA II diode.

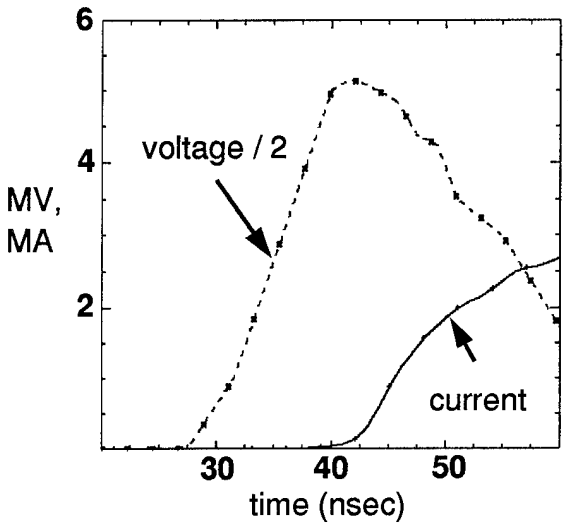


Figure 2. Voltage and current waveforms measured on PBFA II shot 6408.

Time- and space-resolved visible spectroscopy of emission from lithium neutrals in the AK gap is the primary diagnostic in this effort [3]. Fiber optics transport light collected from the diode to a remote screen room, where it is recorded using a novel streak camera/spectrograph configuration [4]. The diagnostic system simultaneously provides ~1 nsec time resolution, ~1 Å spectral resolution, and 2 mm spatial resolution, with 11 independently-aimed lines of sight presently available. The spatial resolution can be increased at the cost of lower collected light. A typical configuration is five lines of sight located at different radii in one azimuth and six lines of sight located at different radii in another azimuth 180° away. This enables us to measure both radial and azimuthal variations as a function of time in a single shot.

We investigate the AK gap dynamics using the Stark-shifted Li I 2s-2p line to measure the evolution of the electric field profile. Two independent calculations of the Stark pattern under crossed electric and magnetic fields were performed to ensure reliability. The field near the anode is typically ~10 MV/cm, the highest ever directly measured with the Stark effect. Measurements of the electric field E enable us to determine the charged particle distribution [5] from $\nabla \cdot E = 4\pi\rho = e(Zn_i - n_e)$, where ρ is the net charge density, e is the electron charge, and n_e, n_i are the electron and ion densities, respectively. Assuming that the electric field is predominantly radial, the ion velocity is given by integrating the field radially-inward from the anode, using $v_i^2 = 2\,Ze/m_i \int E_r\,dr$. Knowing the local ion velocity, we can determine the ion density from $n_i = J_i/(Zev_i)$, where J_i is the ion current density measured with Faraday cups or a magnetic spectrograph. The electron density n_e is obtained by subtracting the net charge density from the ion density times the ion charge. The result is a time- and space-resolved determination of n_e and n_i in the AK gap.

We evaluate our present understanding of ion diode physics by comparing the measured PBFA II electric field distribution and charged particle densities with results from QUICKSILVER [6], a three-dimensional fully-electromagnetic particle-in-cell computer code. This code uses the applied accelerator power pulse and realistic magnetic field geometries to calculate the ion and electron distributions self-consistently, including the effects of field fluctuations due to instabilities.

The electric field profile evolution on PBFA II shot #6408 with corresponding simulation results is shown in Figure 3. This shot used a 10 cm tall flat anode, an 18 mm AK gap, and a 17.5 MV V_{crit}, where V_{crit} quantifies the insulating magnetic flux in the AK gap as the electron

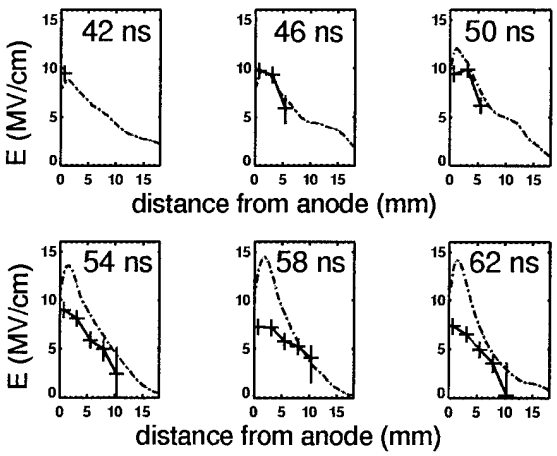


Figure 3. Electric field evolution on PBFA II shot 6408 compared to simulation. Crosses are data and solid line is simulation.

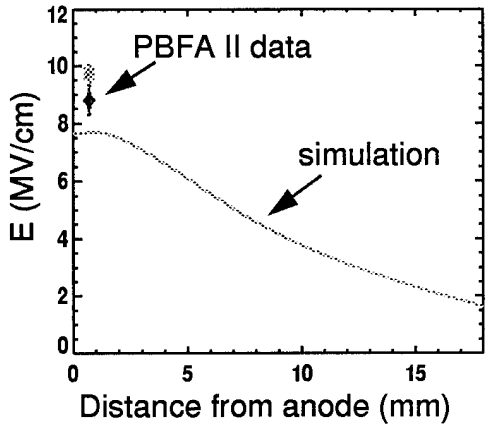


Figure 4. Data from PBFA II shot 6408 and simulation result, both corresponding to the onset of ion current (38 ns, see Figure 2).

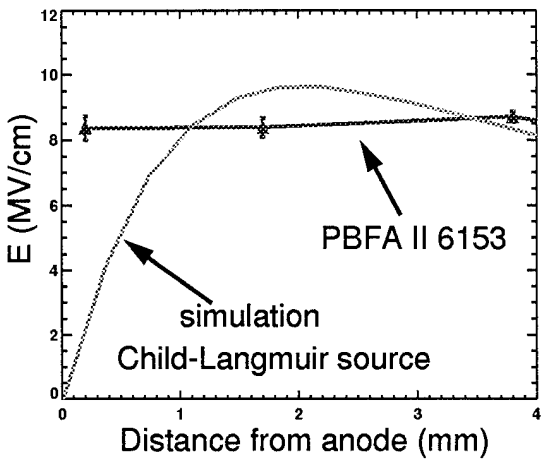


Figure 5. Electric field near the anode from PBFA II shot 6153, and a corresponding simulation that assumed a space-charge-limited source.

energy needed to cross the gap. Each plot represents an average over 4 nsec with an inter-plot spacing of 4 nsec. The error bars on this and subsequent plots represent one standard deviation. Qualitatively, the simulation fidelity is very reasonable early in the pulse, especially considering the complexity of the physics. However, there are clear discrepancies later in time, affecting predictions of divergence and power coupling. These discrepancies arise at the onset of non-uniform ion emission and a parasitic loss current in the experiments, which are not currently modeled in the simulations.

Typical data and simulation results corresponding to the onset of ion current are shown in Figure 4. The ~10 MV diode voltage across the 1.8 cm physical AK gap with ~9 MV/cm electric field near the anode at the onset of the ion current implies that the electron density in the diode is high enough to modify the field profile even at this early time. The initial field profile is also modified by electrons in the simulation, but the field value is somewhat lower, indicating fewer electrons in the gap. The simulations suggest that the high electron density in the gap early in time is primarily due to injection of electrons from the MITL.

The electric field measured near the anode surface remains high throughout most of the pulse (Figure 3). This observation is contrary to the expectation that the electric field for a space-charge-limited source should vanish at the anode. Figure 5 shows a comparison of the PBFA II electric field in the vicinity of the anode with a simulation that assumed a space-charge-limited source (all other simulations shown here assumed a field threshold of 7 or 9 MV/cm for ion emission). The data are consistent with a recent theory [7] that suggests the LiF ion source operates as an electron-deposition-assisted, field-limited ion emitter. The 7-9 MV/cm ion emission field we observe is also consistent with some electron filling of the diode prior to ion current initiation, in order to increase the ~5 MV/cm vacuum-gap field. Work is in progress to evaluate the impact of this field-limited emission effect on the diode power coupling.

Three other new diode phenomena have been observed in these experiments. First, over much of the pulse the net charge density is approximately zero near the PBFA II anode (Figure 6), implying that the electron density increases near the anode. This is in contrast to the simulations, which have a well-defined separation between the anode and the electrons. It should be noted that in the simulations there is no source of electrons at or near the anode. Second, strong azimuthal non-uniformities in electric field, and thus also in the charged particle densities, exist in the experiment (Figure 7). These non-uniformities persist over 10-30 nsec time-scales, despite the expectation that azimuthally drifting electrons should cancel such asymmetries in ~ 5 nsec. Third, the sign of dE/dr changes from negative to positive near the middle of the PBFA II gap (Figure 8), signifying that the

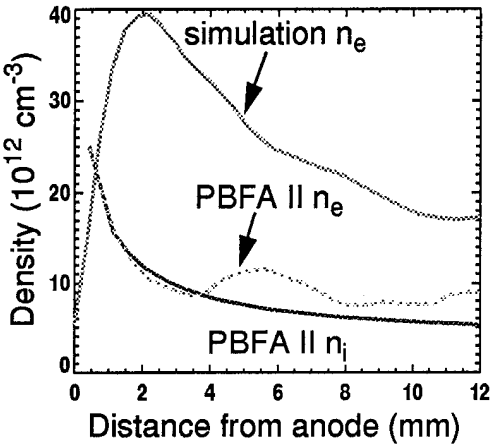


Figure 6. Electron and ion densities corresponding to the PBFA II electric field profile shown in Figure 5. Simulation assumed a 7 MV/cm threshold field for ion emission. Note simulation n_e is much larger than PBFA II n_e overall because of larger simulation ion current at this time.

local ion density exceeds the electron density. This indicates either a sudden loss of electrons or local surplus of ions.

The spectroscopic measurements in the diode acceleration gap provide information with a level of detail that was previously unattainable in high-power diodes, since only measurements of the accelerated ion beam properties were available. Some of the newly-discovered diode phenomena,

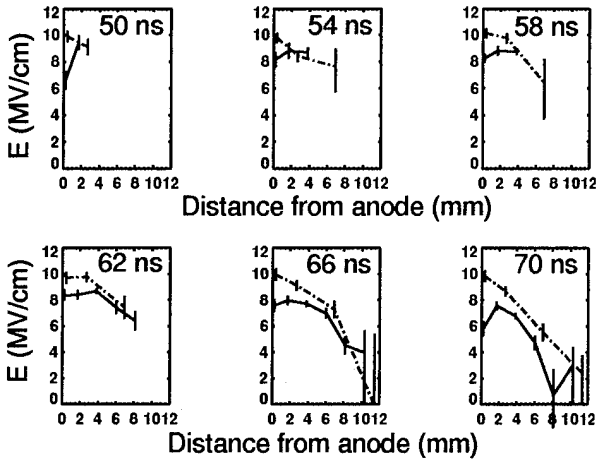


Figure 7. Electric field evolution on PBFA II shot 6153, measured in two azimuths separated by 180°. Ion current onset is at 46 nsec. The solid line is for one azimuth, the dashed line is for the other.

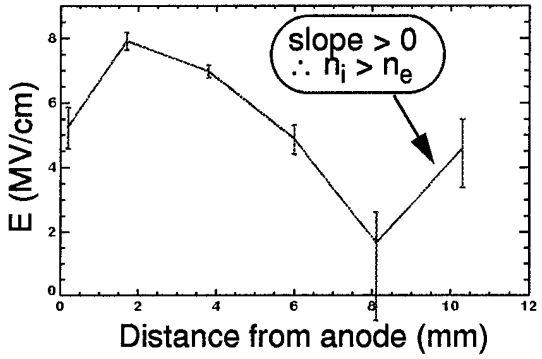


Figure 8. Electric field from PBFA II 6153 at t = 70 nsec.

such as azimuthal asymmetries, are probably best addressed by seeking to eliminate them from the experiments. This alone could be highly beneficial, since eliminating asymmetries may improve the diode impedance and beam divergence. However, our understanding of diode behavior must also be revised and expanded to incorporate this new information. The differences between the idealized diode simulated by QUICKSILVER and the actual PBFA II diode reflect this need. The results show that although the actual diode behavior is more complex than in our diode simulations, we now have a method for improving and experimentally validating our understanding of diode physics.

This work performed by Sandia National Laboratories, supported by the U.S. Department of Energy under contract DE-AC04-94AL85000.

[1] D.J. Johnson et. al., *Proc. 7th IEEE Pulsed Power Conf., Monterey, CA.*, ed. by R. White and B.H. Bernstein, p. 944 (1989).

[2] T.A. Mehlhorn et. al., these proceedings.

[3] J.E. Bailey, A.L. Carlson, R.L. Morrison, and Y. Maron, *Rev. Sci. Instr.* **61**, 3075 (1990).

[4] J.E. Bailey, A.L. Carlson, and P. Lake, *1994 IEEE Int. Conf. on Plasma Science, Santa Fe, N.M.* (Catalog #94CH3465-2), p. 133.

[5] Y. Maron, M.D. Coleman, D.A. Hammer, and H.S. Peng, *Phys. Rev. Lett.* **57**, 699 (1986) and *Phys. Rev.* **A36**, 2818 (1987).

[6] D.B. Seidel, M.L. Kiefer, R.S. Coats, T.D. Pointon, J.P. Quintenz, and W.A. Johnson, in *Computational Physics*, ed. by A. Tenner (World Scientific, Singapore, 1991), p. 475.

[7] T. Green, private communication, 1993.

Results of the First 2-Stage Diode Experiments on PBFA II

T. Lockner, S. Slutz, D.J. Johnson, M. Desjarlais, and J. Poukey

Abstract

A series of experiments have been performed on the PBFA II accelerator in a 2-Stage diode configuration. These experiments have demonstrated the generation and post acceleration of both proton and lithium beams. The second stage was also used to measure the ion current injected from the first stage. The ion current was found to be larger than the inferred current from Faraday cup measurements as is seen in single stage experiments. This result suggests that the current difference (known as the parasitic load) is carried by ions. A straightforward modification to the poor magnetic field geometry in the second stage is shown to improve transport to the axis.

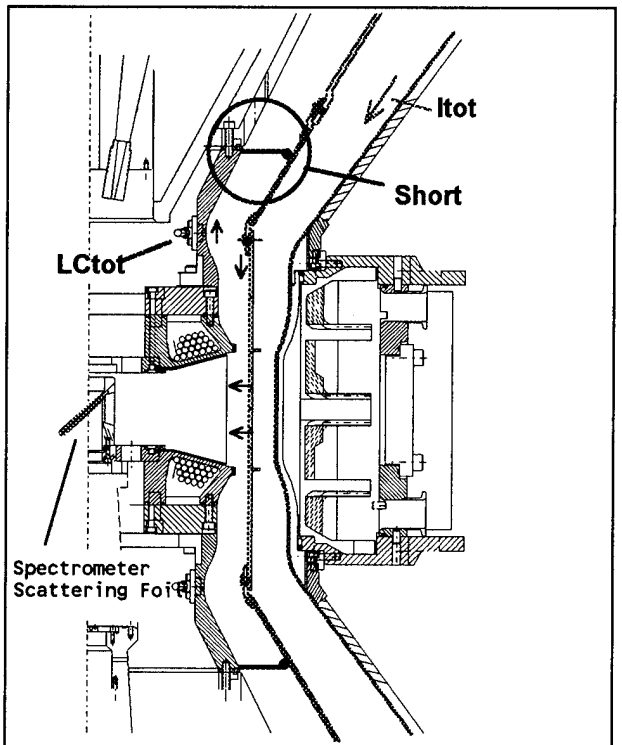


Figure 1. Layout of the radially focusing 2-Stage ion diode on PBFAII. The diode is shown in the geometry for single stage operation with the second stage shorted outside of the diode. The LCtot monitor measures the ion current injected from the first stage into the second stage.

Introduction

The 2-Stage diode is a variation of the magnetically insulated ion diode (MID) in which the A-K gap is divided into two gaps by the introduction of a mid-gap electrode [1]. The diode configuration can be designed in either extraction or radial focusing geometry. The diode design for the radial focusing diode on PBFA II is shown in figure 1. Benefits of this geometry include divergence reduction, independent voltage and current control, and improved power coupling. The drawbacks are a more complicated diode geometry, potential ion emission from the intermediate electrode into gap 2, stripping of the incident beam from plasma produced on the intermediate electrode, and possible electrostatic defocusing from this electrode.

A 2-Stage diode in radial focusing geometry has been fielded on the PBFA II accelerator to determine the potential of the configuration. The first experiments were designed to determine the operating parameters of the first stage and to perform preliminary post acceleration experiments. Two experimental configurations were used, single and normal 2-Stage configuration. Both proton and lithium beams were studied in order to obtain

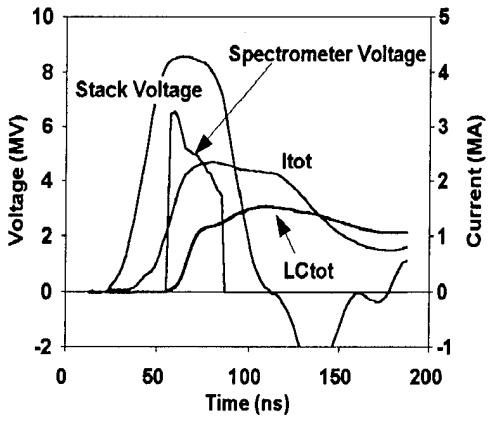


Figure 2. Single stage energized in 2-Stage geometry. The spectrometer voltage is obtained from lithium ions scattered on the axis. Note the length of the measured ion current (LCtot)

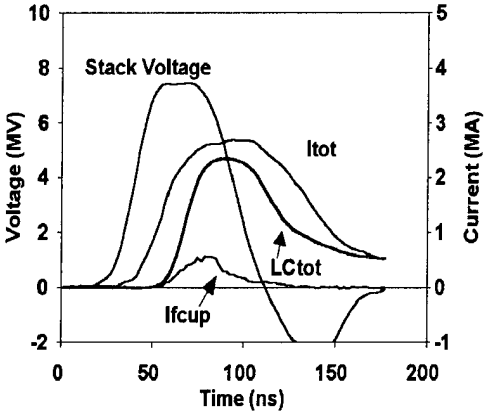


Figure 3. Single stage energized with stripping foil between first and second stage. Note that the ion current (LCtot) has increased dramatically indicating stripping of the first stage ions. The ion current is notably longer and larger than the current derived from the Fcups (Ifcup)

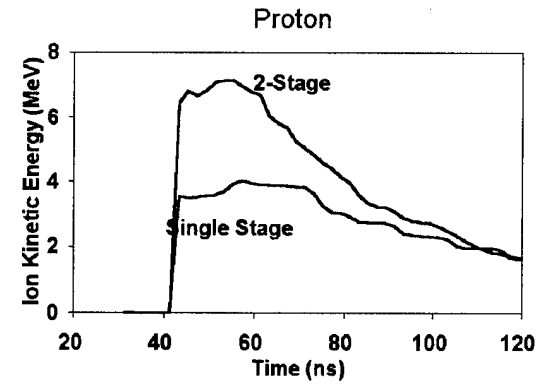
comparisons with previous single stage experiments. The single 2-Stage experiments demonstrated the production of both proton and lithium beams using 1/2 of the PBFAII accelerator. They also supplied valuable information on the character of the parasitic load observed in single stage experiments. The normal 2-Stage experiments demonstrated the post acceleration of the ion beam generated in the first stage, and the necessity of improving the field profile in the second stage from the initial design.

Single 2-Stage experiments

The diode configuration for the single 2-Stage experiments is shown in figure 1. The first stage was driven by the center half of the PBFA II accelerator and the second stage power was turned off. The second stage was shorted just upstream of the current monitors labeled LCtot. This minimized the inductance of the current path in the second stage while allowing both the ion current monitors and LCtot monitors to measure the ion current injected into the second stage. A voltage across the second stage A-K gap is generated by the LIdot from the injected current and the gap and feed inductance (~10 nH). Note that this voltage is in the opposite direction as the normal applied voltage during the current rise and would tend to decrease the measured current if there is electron flow across the magnetic field. This voltage is normally below 1 MV and since the Vcrit in the second gap is above 4 MV we expect no significant leakage current across the 2nd A-K gap.

The results of a single 2-stage full energy lithium shot are shown in figure 2. The magnetic spectrometer data is consistent with a >6 MV peak ion kinetic energy lithium beam. The ion current measurement in the second gap (LCtot) indicates that the diode is ~50% efficient with the current pulse continuing for over 150 ns. The Faraday cups for these shots have a FWHM of ~22 ns indicating that the ion current measured by the Bdots in the second gap continues far longer than the Fcups.

This is seen in more detail in figure 3 where a stripping foil has been installed on the outside surface of the electrode separating the two gaps. The measured ion current is larger and has a different temporal character than the non stripper case. We believe this is a result of a large fraction of the incident beam stripping to a higher charge state than was accelerated in the first stage. This current is also larger and



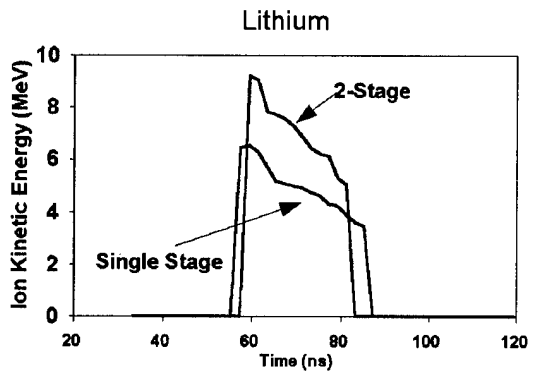


Figure 4. On axis magnetic spectrometer measurements of ion kinetic energy for proton and lithium post acceleration shots. The increase in ion energy is consistent with simulations of the second stage voltage.

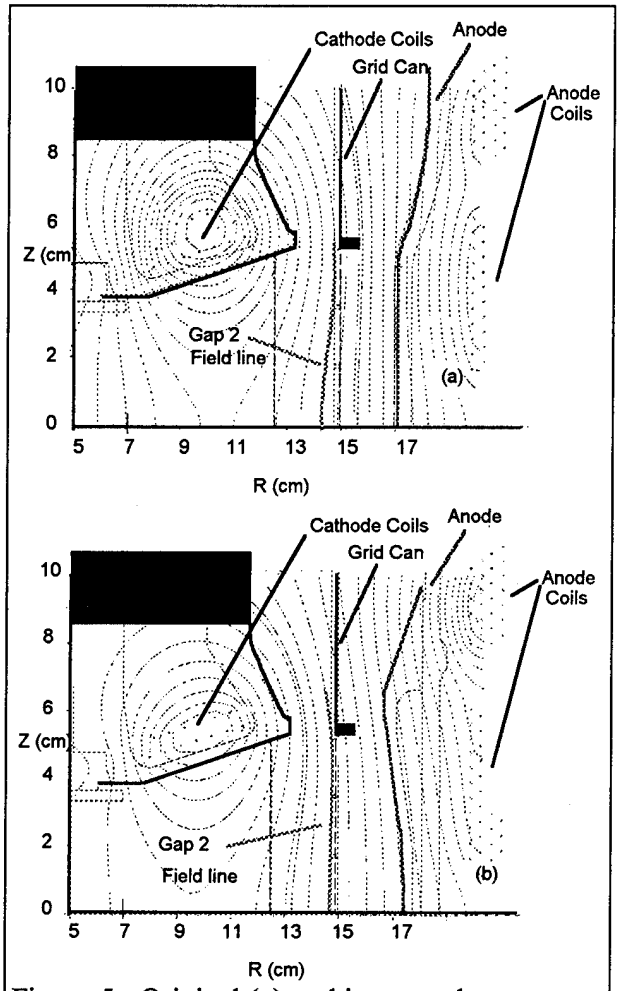


Figure 5. Original (a) and improved (b)magnetic field geometry plots. Note that the over insulation in the center of the second stage has been corrected in (b) by curving the anode and using 13 instead of 22 turn cathode coils. This reduces both the electrostatic defocusing and the space charge effects in the second stage.

wider than the ion current calculated from the Fcup signals. This is an indication that the excess ion current measured in figure 2 (the parasitic load current) is carried by energetic ions.

Post Acceleration results

Post acceleration of both proton and lithium beams was also demonstrated in the 2-Stage geometry. The short circuit shown in figure 1 was removed and power applied to the second stage for the post acceleration experiments. Figure 4 shows a comparison between magnetic spectrometer ion kinetic energy history of shots with and without the second stage energized. The increase in energy is consistent with the voltages inferred in the two stages based on simulations using the measured gap 1 current injected into the second stage. Although the ion energy increased, the intensity on axis was not large enough to determine the beam divergence. This was due to the non focusing anode used (flat) and the defocusing of the second stage described in the next section.

Post acceleration experiments in which a stripper foil was inserted between the two stages yielded no spectrometer data on axis.

This may be due to the large space charge forces on the beam and the severe voltage drop in the second stage due to the inductive voltage generated by the injected beam. The inductive effect is compounded by the stripping of the non lithium component of the incident beam.

Improvements in second stage field profile

The design of the field structure for the 2-stage diode experiments on PBFAII was initially driven by our desire to assure operation of the first stage, and allow quick and cheap installation of the anode. The resulting field geometry in the second stage was over-insulated in the center as seen in figure 5a. Not only is this geometry defocusing for an accelerating voltage applied to the second stage, but 2-D PIC simulations indicated that a virtual anode would be generated which would further defocus the beam. These predictions are consistent with the low ion intensity measured on axis for the post acceleration experiments and the absence of measurable ion flux in the stripper geometry (fig. 3).

The problem can be corrected by changing the cathode coils from the 22 turn coils used in the 2-stage experiment to the standard 13 turn coils for LiF shots and going from a flat to a curved anode geometry (Fig. 5b). This change reduces the calculated over-insulation in the second gap from >37% to 8%.

Conclusion

A 2-Stage radial focusing ion diode has been successfully fielded on the PBFAII accelerator. Both lithium and proton beams have been produced using half of the accelerator. Post acceleration of both lithium and proton beams has been observed from an increase in the ion kinetic energy on axis. Single 2-Stage experiments have also indicated that the excess current observed in standard single stage diodes may be carried by ions in the acceleration gap. This current presents a significant load to second stage in the present configuration.

The poor transport to the axis observed in the experiments is likely due to the defocusing and space charge effects in the second gap. A modified magnetic field geometry has been developed which promises to correct this problem in future experiments

This work has been funded by the U.S. Department of Energy under contract DEAC04-94-AL85000.

References

1. Proceedings of the 9th IEEE International Pulsed Power Conference, June 1993, Albuquerque, NM 'Theoretical and Experimental Studies of the 2-Stage Diode' T. Lockner, J.W. Poukey, S. Slutz and W. Stygar (to be published)

Complete Mode-Set Stability Analysis of Magnetically Insulated Ion Diode Equilibria

S.A. Slutz and R. W. Lemke
Sandia National Laboratories
P. O. Box 5800
Albuquerque, NM 87185-1187

Abstract

We present the first analysis of the stability of magnetically insulated ion diodes that is fully relativistic and includes electromagnetic perturbations both parallel and perpendicular to the applied magnetic field. Applying this formalism to a simple diode equilibrium model that neglects velocity shear and density gradients, we find a fast growing mode that has all of the important attributes of the low frequency mode observed in numerical simulations of magnetically insulated ion diodes, which may be a major cause of ion divergence. We identify this mode as a modified two-stream instability. Previous stability analyses indicate a variety of unstable modes, but none of these exhibit the same behavior as the low frequency mode observed in the simulations. In addition, we analyze a realistic diode equilibrium model that includes velocity shear and an electron density profile consistent with that observed in the numerical simulations. We find that the diocotron instability is reduced, but not fully quenched by the extension of the electron sheath to the anode. However, the inclusion of perturbations parallel to the applied magnetic field with a wavelength smaller than the diode height does eliminate growth of this instability. This may explain why the diocotron mode has been observed experimentally with proton sources, but not with LiF, since the turn-on of LiF is not uniform.

Background

High intensity light ion beams are being developed to drive inertial confinement fusion (ICF)[1]. Propagation and focussing requires these beams to have low ion divergence, ~ 6 mrad, as compared to ~20 mrad that has been experimentally achieved. Therefore understanding the mechanisms that generate ion divergence is critically important.

Three dimensional particle-in-cell simulations (3-D PIC) have been used to study the divergence generated in magnetically insulated diodes[3-4]. In these simulations, electrons stream into the diode along the magnetic field lines and form an electron sheath. Initially this sheath is quite thin with electrons flowing primarily in the **ExB** direction. There is considerable shear to this flow due to the large variation in the **E** field across the sheath and surface waves can flow at the edges of the sheath, see Fig. 1. The interaction of these surface waves leads to a fluid instability called the

"diocotron", which has a very fast growth rate and saturates in a few nanoseconds.

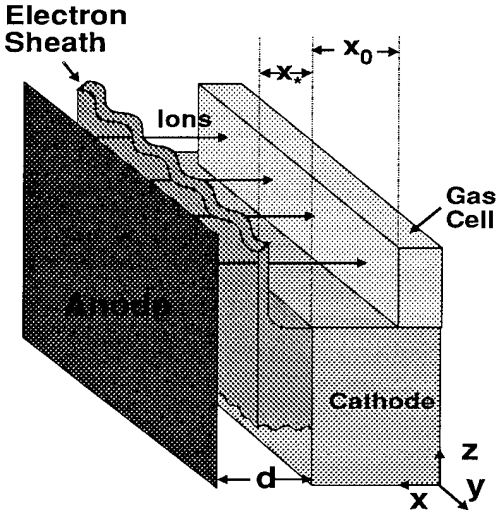


Fig. 1. A schematic of a magnetically insulated ion diode. The applied field is in the z direction.

The growth and saturation of the diocotron instability is fairly well understood. Linear stability theory gives a good estimate of the initial growth rates[4,5] and a simple trapping model[3] yields a saturated amplitude for the mode that is in good agreement with the simulations. The period of this instability is small compared to the ion crossing time and consequently it generates a relatively small ion divergence (<10 mrad). More importantly it allows electrons to cross the gap by breaking symmetry in the **ExB** direction. As the electron sheath broadens (x_* goes to d), the ion current density increases and simulations indicate that a transition to a low frequency instability occurs. This instability generates considerable divergence (>30 mrad), because the period is roughly equal to the ion transit time.

The physics of the low frequency mode is not well understood. Linear analyses[6], using a Brillouin model of the electron sheath, exhibit unstable modes, but not with the correct wavelength and frequency when realistic diode parameters are used. However, these analyses did not include perturbations in the direction of the applied magnetic field. It is known[7] that the frequency of the two-stream instability in the presence of a magnetic field depends strongly on the direction of propagation with respect to the magnetic field. Recently, Sudan and Longcope[8] have presented a stability analysis including mode structure in the direction of the applied magnetic field. They found instability at low phase velocities, (V_{ph}~c/15) which is characteristic of the low frequency mode observed in the numerical simulations, but in the opposite direction. In the simulations the waves travelled parallel to the electron drift velocity. The authors suggest that this may be due to their approximate treatment. In particular, their analysis was electrostatic and not fully relativistic. In this paper we remove these approximations and find an unstable mode that is low frequency, low phase velocity, and propagates in the same direction as the low frequency mode observed in the simulations. Furthermore, the growth rate of the mode increases with ion current density consistent with the simulation result that the transition to the low frequency mode depends on the ion current enhancement, defined as the ratio of the ion current density over the Child-Langmuir ion current density.

Stability formalism

The dynamics of a magnetically insulated ion diode can be described by Maxwell's equations and the equations governing the conservation of mass and momentum for the ions and the electrons. We treat both the ions and the electrons as laminar fluids. The ions propagating across the gap (-x direction) while the electrons drift parallel to ExB (y-direction), see Fig. 1. It is appropriate to treat the ions nonrelativistically since the ion velocity is about c/30. However, the electron velocities approach the speed of light so we have used the relativistic form of the momentum equation for the electrons. From these equations we have derived a system of linear equations that describe the stability of an arbitrary planar laminar fluid ion diode equilibrium[9]. The anal-

ysis is fully electromagnetic and accounts for wave propagation in a general direction relative to the applied magnetic field. This represents a generalization of previous work.

The constant parameter model

The constant parameter model, CPM, is an idealization of an ion diode equilibrium in which all electron and ion parameters are constant. Sudan and Longcope[8] used this model in their electrostatic stability analysis. In our relativistic electromagnetic analysis of this model, we find an unstable mode which travels in the proper direction, see Fig. 2.

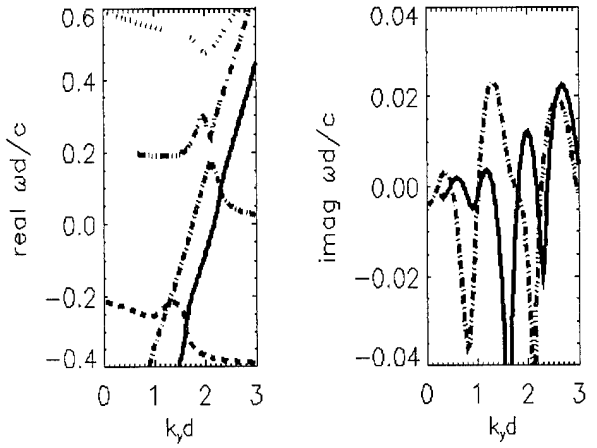


Fig. 2. The dispersion results for the CPM with $k_z d=1.9$, a Li^+ velocity of 0.05c, an electron drift velocity of $v_0=0.5c$, $B_{app}d=2.5$ T-cm, $\omega_p d/c=4.7$, and $\Omega_c=12.8$. Note the solid curve has maximum growth at a phase velocity of roughly c/9.

To understand this difference, we derived a relativistic electromagnetic dispersion relation for the electron fluid. In the limit of infinite applied magnetic field and phase velocities much less than the speed of light, the result is

$$\omega = v_0 k_y \pm \frac{(\omega_p/\gamma)\, k_z}{\sqrt{\frac{\omega_p^2}{c^2} + (m\pi/d)^2 + k_y^2 + k_z^2}}, \qquad (1)$$

where m is a nonzero integer and ω_p is the plasma frequency. This equation shows that there are an infinite number of discrete electron space charge waves, all of which originate on the beam line in k_y space for $k_z = 0$. This is due to the large applied magnetic field in combination with relativistic electron velocities, which hinder the electron response to transverse perturbations. However, electrons can easily respond to perturbations in the direction of the applied field and thus the degeneracy is removed for finite k_z. Equations similar to Eq. (1) were derived by Krall and Liewer[7], and Sudan and Longcope[8] using the electrostatic approximation. Their results did not have the plasma frequency term in the denominator which slows the rate that the y-phase velocity is reduced as k_z is increased. Instability results when the real part of the electron and ion space-charge waves are approximately equal. Therefore, the relativistic terms have an important effect on the phase velocity of the unstable waves. Furthermore, it is clear from the form of Eq. (1) that the instability of Fig. 2 is fundamentally the same as the modified two-stream instability studied by Krall and Liewer[7]. This identification is consistent with the increase in the growth rate that we obtain as the ion and electron densities are increased.

A realistic diode equilibrium

The 3-D numerical simulations show that electron density and velocity vary smoothly across the accelerating gap. These profiles are well approximated by letting the electron density be the simple function of the electric potential, $N(\phi) = n_0 + n_1\phi^\alpha + n_2\phi^\beta$. Values of $\alpha < 1$ and $\beta > 1$ insure that Poisson's equation and Amperes law can be satisfied along with the boundary conditions, E=0 at the virtual cathode and at the anode, $N(0)=N_i$, and $N(\phi_*)=0$. It is interesting to note that even when the electron distribution extends completely to the anode the diocotron instability still has a significant growth rate. However, the next figure shows that the growth rate of the

diocotron goes to zero as the value of k_z is increased.

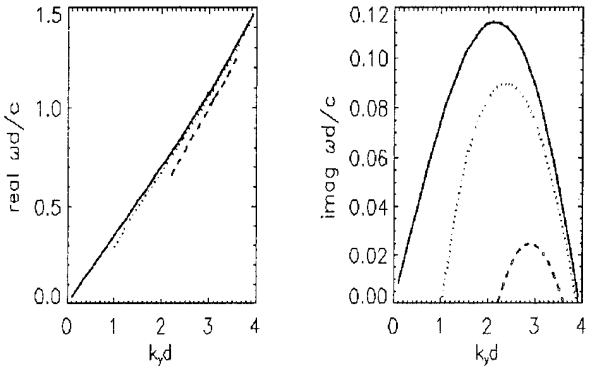


Fig. 3. The dispersion for ϕ_*=1 and only electron perturbations, k_z=0 (solid), k_z=0.3 (dotted), k_z=0.6 (dashed).

This behavior may explain why the diocotron phase has not been observed when a LiF anode source is used, since it is known that the uniformity of ion current density from these sources is poor.

Figure 4 shows the behavior of the dispersion relation when ion perturbations are included.

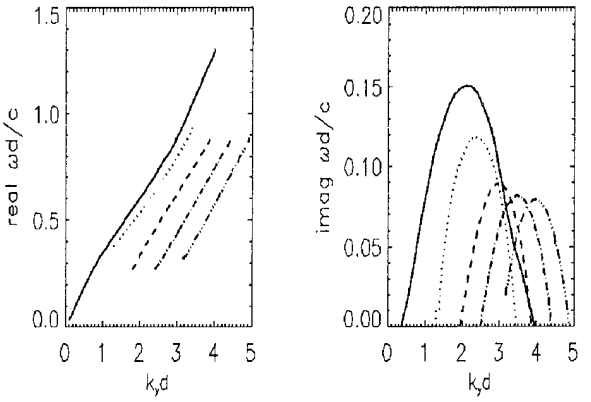


Fig. 4. The dispersion for ϕ_*=1 with both electron and ion (proton) perturbations, k_z=0 (solid), k_z=0.5 (dotted), k_z=1.0 (dashed), k_z=1.5 (dash-dotted), and k_z=2.0 (dash-dot-dot).

Notice that the phase-velocity decreases as k_z is increased in the same manner as observed from the constant parameter model. Further studies of this instability revealed the following behaviors that are consistent with the numerical simulations. The growth rate increases with the ion current density as determined by the equilibrium parameters α,β, and ϕ_*. The period of the instability is roughly equal to the ion transit time. Thus heavier ions result in a lower frequency. A space-charge limited ion source has the largest growth rate, i.e. a finite electric field at the anode lowers the growth rate. Finally, we found that injecting the ions with an initial velocity reduced the growth rate, which may explain the divergence reduction that has been observed both experimentally and numerically in two-stage diodes.

Acknowledgements

We gratefully acknowledge many helpful discussions and encouragement from M. P. Desjarlais. This work has been funded by the U. S. Department of Energy under Contract DE-AC04-94-AL85000.

REFERENCES

[1] J. P. VanDevender and D. L. Cook, Science **232,** 831 (1986).

[2] M. P. Desjarlais, T. D. Pointon, D. B. Seidel, R. S. Coats, M. L. Kiefer, J. P. Quintenz, and S. A. Slutz, Phys. Rev. Lett. **67**, 3094 (1991).

[3] T. D. Pointon, M. P. Desjarlais, D. B. Seidel, S. A. Slutz, R. S. Coats, M. L. Kiefer, and J. P. Quintenz, Phys. Plasmas 1, 429 (1994).

[4] S. A. Slutz, and W. A. Johnson, Phys, Fluids B **4**, 1349 (1992).

[5] C. L Chang, D. P. Chernin, A. T. Drobot, E. Ott, and T. M Antonsen, Jr., Phys. Fluids **29**, 1258 (1986)

[6] N. A. Krall and P. C. Liewer, Phys. Rev. A **4**, 2094, (1971).

[7] R. N. Sudan and D. W. Longcope, Phys. Fluids B, **5**, 1614 (1993).

[8] S. A. Slutz, T. A. Mehlhorn, J. E. Maenchen, C. Ruiz, and J. R. Woodworth, J. Appl. Phys. **62,** 16 1987.

[9] R. W. Lemke and S. A. Slutz, submitted to Phys. Plasmas.

[10] T M. Antonsen, Jr. E. Ott, Phys. Fluids **19**, 52 (1976).

[11] S. A. Slutz, J. W. Poukey, and T. D. Pointon, Phys. Plasmas 1, 2072 (1994).

Energetic ions and electrons produced in a hollow cathode vacuum spark.

M. Skowronek, A. Ikhlef, G. Louvet, P. Roméas
Laboratoire des Plasmas Denses, Univ.P&M.Curie, Tour 12 E5,
4, place Jussieu. F-75252 Paris cedex 05 (France).

K. C. Mittal
Accelerator and Pulse Power Division, Bhabha Atomic Research Center,
Trombay, Bombay 400 085 (India)

Abstract

A vacuum spark having a tungsten pointed anode and a hollow cathode is feeded by a small Marx generator (1J). It produces energetic beams of tungsten ions (E = 0.5 to 70 keV) and electrons beams in the first ignition phase. The electrons produce, an X-ray emission through Bremsstrahlung in the Teflon insulator and by Auger cascade in relation with particle emission. In the second phase, when the applied electric field is low and the current intensity is high, the electrons give rise to W (L_α and L_β) X-ray emission. The mechanism of this last part is ascribed to interactions either with the massive anode or a plasma surrounding the anode. In the case of dense plasma interaction, the emission is of the same type as observed in laser-plasma interaction. Spots of X-rays are also observed which may originate from pinching or interaction with drops or dust particles in the interelectrode spacing. Experimental results obtained using X-ray imaging are discussed.

1. Introduction.

Vacuum sparks are applied in many devices : spark gaps, commutation of high intensity and high frequency currents, etc... In conditions, defined by high values of the ratio E/N, secondary ionisation processes take place primarily on the electrodes[1]. In the presence of a suitable hollow cathode region the ionisation growth has been found to be significantly enhanced[2]. Ions and electrons may be accelerated by different fields ; some are related to the applied electric field, other are due to insulator volume (or surface) charge accumulation[3]. Electrons and ions acquire a high energy and produce X-ray with a relatively high efficiency by interaction with different materials. The presence of a hollow cathode is shown to produce electron beams more or less focused. We describe first in the following the experimental set-up, the main results of the oscillographic measurements are then

exposed ; a special chapter is devoted to the study of the expansion of thre anode vapor and plasma, this is followed by the description of some time integrated image followed by the results of time resolved imaging of the X-ray emission sites. A general conclusion is given in the last chapter.

2. Experimental set-up.

The vacuum discharge chamber is roughly a stainless steel cylinder 4-5 (ϕ = 50 mm ; l = 100 mm) on the axis of which are placed the pointed tungsten anode and the hollow cathode ; the hollow cathode is a steel cylinder with an axial hole through which the radiation is measured.

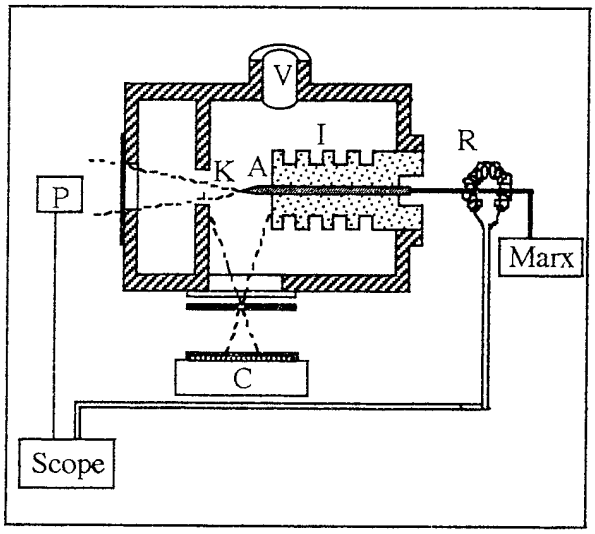


Figure 1. Experimental set-up. A : anode, K : cathode, P : PIN diode, C : camera, R : Rogowski coil, I : Insulator, V : Vacuum pump.

The anode-cathode distance AK = d can be varied by steps of 0.1 mm. The cathode and all the source vessel are grounded. The anode is insulated from the vessel by a Teflon insulator. The high voltage pulse, is characterized by its voltage V = 70 kV, and duration τ = 50 ns ; it is produced by a small 4-stage Marx generator and delivered through a 50 Ω cable.Three types of cathodes have been used :

I) the cathode is a massive cone,

II) a cylindrical hollow cathode,

III) a conical hollow cathode (figure 2).

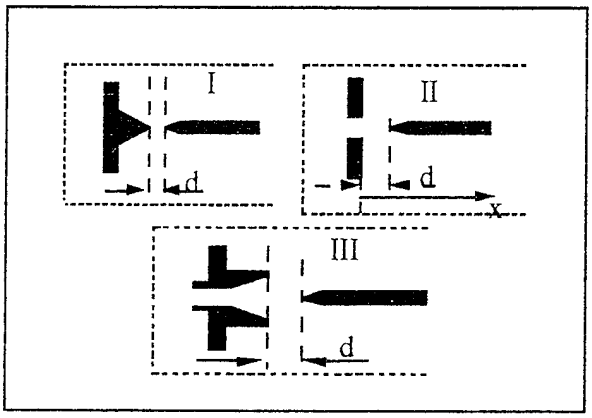


Figure 2. Different types of cathodes used

Several windows are placed around the gap, symmetrically, allowing the observation and the measurement side-on and end-on of the emitted X-rays. A mylar window of thickness 70 μm covers each aperture and limits the detection of the low energy part of the X-rays to 5 kev after 10 mm path in the air. The total X-ray output is measured by means of a calibrated PIN diode looking axially end-on into the discharge gap. The broadband emission of the X-rays is then measured in absolute value, if we know the range of energy of this emission. This has been evaluated, using different metal absorbers to be about 10 keV. A Rogowski coil is used to measure the di/dt evolution. All signals are displayed on a 4-channels 400 Mhz digital memory oscilloscope .

The image of the X-ray emitting sites is obtained using a pinhole of about 0,1 mm diameter drilled in a lead screen having a thickness of 1 mm and a scintillator in front of a sensitive intensified camera.

Ion and electron beams are studied, together with the electrical and X-ray signals versus the anode-cathode distance d. The relation between these beams and the X-ray image is determined.

3. Results of the oscillographic measurements.

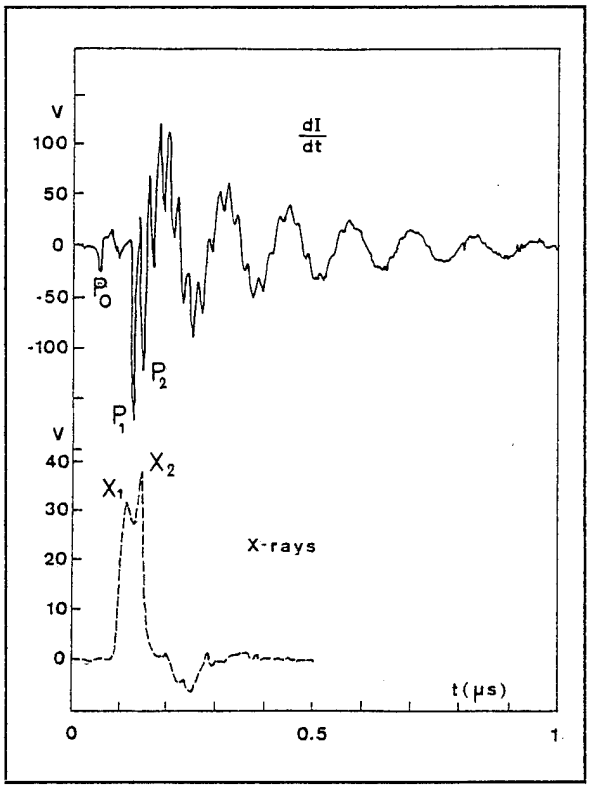


Figure 3: Oscillograms of di/dt and X-ray intensity .

Three successive pulses have been observed on each di/dt curve given by the Rogowski coil (figure 3) :

a) the pulse P_0 in coincidence with the voltage application ;

b) the pulse P1 corresponding to the breakdown ; the time delay between P_0 and P_1 is called Δt ;

c) another pulse P2 after a certain delay time δt.

The variation of Δt has been measured versus the anode-cathode distance d, which has been varied from 0 to 8 mm. Three curves have been obtained, each corresponding to a different cathode geometry (figure 4).

If we assume that the origin is different for each case, then it is possible to recover an unique curve IV by putting : $d_{II}' = d_{II} + 1$ mm ; $d_{III}' = d_{III} + 2$ mm. This allows the determination of the tungsten plasma cloud velocity.

Two X-ray pulses X_1 and X_2 are registered by the PIN diode, corresponding to the different phases of the spark :

a) X_1 is emitted during the high electric field phase ;

b) X_2 is emitted during the high intensity breakdown.

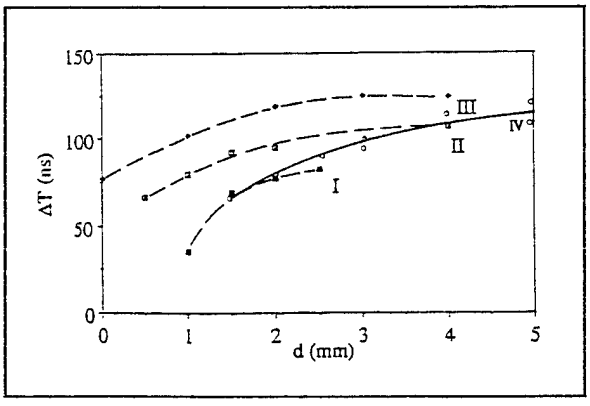


Figure 4: Variation of ΔT with d.

4. Expansion of the anode vapor.

In the vacuum spark model known as Explosive Electron Emission (EEE)[1], the

first step is connected to the field emission on a small protusion existing at the cathode. The 70 keV electron beam reaches the anode and the insulator teflon around it, in less than $5x10^{-11}$ s. No X-ray emission has been observed, in relation with this beam, due to its very low intensity. It produces a return emission of tungsten vapor (and ions) travelling to the cathode. The breakdown seems to occur at the moment when this cloud reaches the cathode. The mean velocity calculated from the slope of the curve IV is 25 km/s. This corresponds to a mean energy of 0.5 keV/particle for the tungsten. This cloud accelerate with the distance AK reaching 140 km/s (18 keV/particle). The effect of the cloud expansion has been pointed out in the case I, using the result of the X-ray chemical analysis of the surface, with an electron microscope. An uniform layer of tungsten is observed in the crater of the cathode (figure 5).

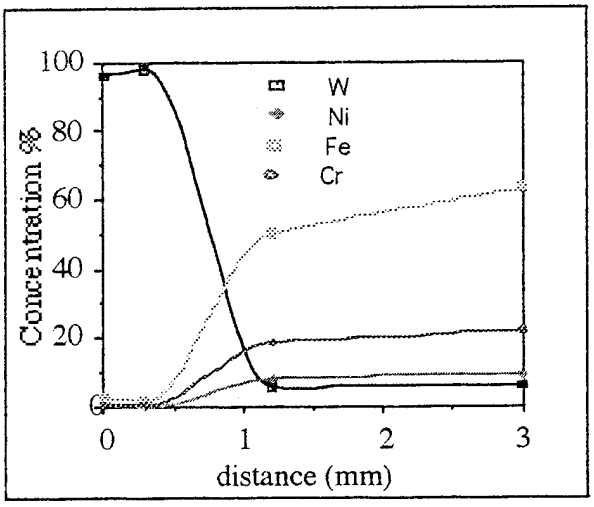


Figure 5: Surface analysis of the cathode (in the case I of a massive pointed cathode).

A first X-ray peak (X_1) is observed before the breakdown, at a time when the voltage is high and the current intensity very low. The second X-ray peak (X_2) occurs after the breakdown, when the current intensity is high and the voltage low.

The intensities of both emission peaks X_1 and X_2, as given by the PIN diode, are of the same order of magnitude, although their energy may be slightly different. Their relative intensity vary with the distance d.

When the anode tip, is introduced into the hollow cathode space, the oscillogram is modified mainly on its X_2 part because the PIN diode does not see the masked tip. Then X_2 seems to originate mainly from the tungsten anode tip and this will be confirmed by the pictures taken by the camera. These pictures shows also that X_1 originates mainly from the Teflon insulator region (figure 6). The X_2 peak is due to the interaction of an intense electron beam extracted from the plasma cloud near the cathode with the anode itself or a dense plasma surrrounding the anode. Its duration is of the order of 25 ns corresponding to the lifetime of this beam and it increases with the distance AK. The time delay between X_1 and X_2 increases with the distance AK : d from 15 ns to 30 ns. This corresponds to the rise time of the main intensity, i.e. to δt the delay between P_1 to P_2. The curve $\delta t = f(t)$ for the case I is situated between that of the case II (the longer) and that of the case III.

5. Time integrated imaging of the X-rays[6].

A sensitive camera preceded by an intensifier with the entrance covered by a phosphor which converts the X-ray into light takes the image of the X-ray emission site. In

takes the image of the X-ray emission site. In this case, the phosphor decay time is rather long : about $1\mu s$. To obtain the integrated image (figure 6) the camera was open during all discharge. The image is stored in the computer and may be processed and analyzed, using an imaging file.

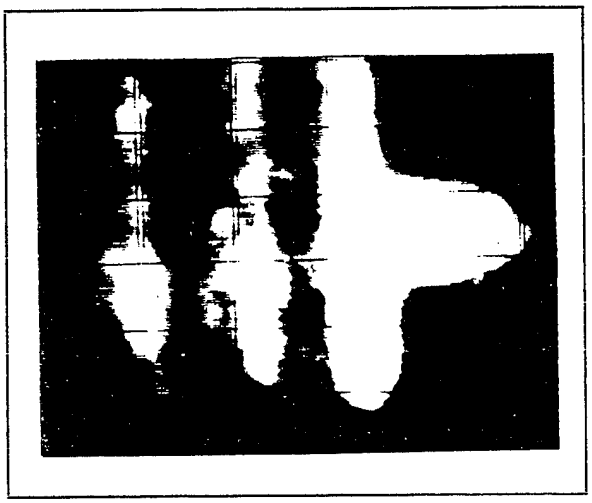


Figure 6: Time integrated image of the X-ray emission sites.

The grooves of the teflon insulator are clearly seen on the image (they correspond to the X-ray pulse X_1). This emission follows very closely the insulator surface.

The image corresponding to the X-ray pulse X_2, is near the anode surface, but also in its vicinity and is more likely due to the interaction of the electron beam with a dense vapor or a dense plasma.

In several cases, some spots completely separated from anode are seen. It may be due to the interaction of the electron beam either :

a) with some dust particle in suspension in the gap,

b) to a plasma emission,

c) to the radiative collapse due to the pinching of a plasma.

6. Time resolved imaging.

In order to obtain a time resolved image, we have used a plastic scintillator with a decay time of 1-2 ns and a camera upgraded with a more efficient intensifier, having an exposure time of 5 ns (figures 7a and 7b).
The figure 7a reproduces the image of the emission sites at the beginning of the discharge when the X-ray emission is of very low power. The sites are few points on the teflon surface and on the pointed anode (the insulator shape and that of the anode are shown in dotted line). The spatial resolution is limited by the pinhole, so we may conclude that each site has a diameter less than 0.1 mm. Moreover from shot to shot, the place of emission is different.

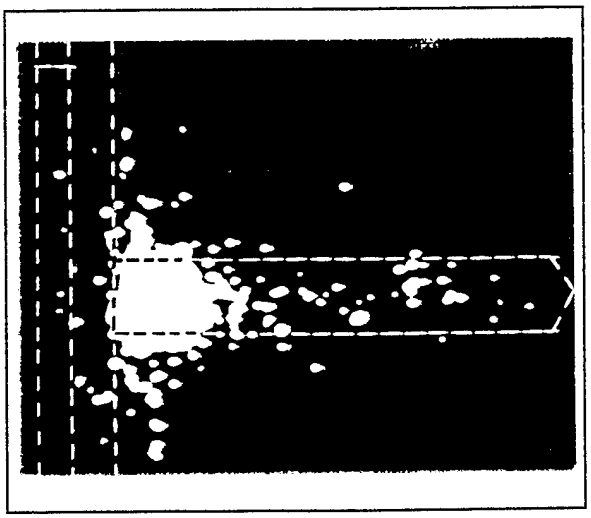


Figure 7a: Picture taken with an exposure time of 5 ns at the beginning of the X-ray flash.

In the case of an intense X-ray flash, single individual spots are also visible.

The teflon emission is difficult to ascribe to a discharge track. This is in general agreement with the observations reported earlier[7]. In analyzing cathode spots, the authors have shown that these spots are

dense plasma spheres having a time life of about 3 ns and a very small diameter (few μm). The difference is that, in our case, this plasma may be emitted by the insulator and the anode and is partly dependent of the initial electron beam.

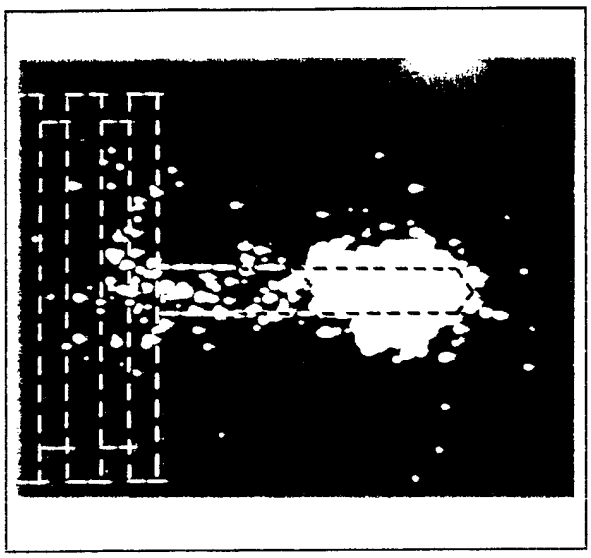


Figure 7b: Image of an intense X-ray emission near its maximum. Exposure time : 5 ns.

7. Mechanism of the different emissions.

In this part, we calculate the order of magnitude of the emission intensity during the high current intensity phase of the discharge i.e. corresponding to X_2.

As measured using the calibrated PIN diode, the total emitted energy is about 1 mJ, assuming that the mean photon energy is about 10 keV [6]. The number of emitted photons N is then $N = 10^{12}$. As the maximum current intensity is about 1 kA, during 10 ns, the number of accelerated electrons is about 10^{14} electrons. If the plasma (or the vapor) has a density of 10^{20} cm^{-3}, the emitting surface being about 10^{-2} cm^2 and its thickness 10^{-2} cm, then assuming a realistic cross section of $Q = 10^{-18}$ cm^2, we can deduce that 1% of the impiging particles give rise to a photon X. This is in agreement with the measured X-ray signal. If we assume that the radiation is produced by a plasma having 10^{16} particles heated at a temperature about 1 keV, the energy needed is 1 J. This corresponds approximately to the available electrical energy. But the Bremsstrahlung of such a plasma will be of the order of 10 mJ. This is a bit too high compared to the measured emission.

Evidently, we cannot explain the teflon emission by the same mechanism, as the intensity, during this period of time is divided by a factor 10^3. It is known that the yield of desorption may be as high as 7 to 12 molecules per incident electron. As the current intensity is about 1 A during about 10 ns, this corresponds to the emission of 10^{12} molecules/shot. Some holes have been seen on the teflon surface, then we may assume that the first electrons hitting the charged insulator produces a violent ejection of ions and even macro-particles and that the subsequent rearrangement may produce, through Auger cascade, an X-ray emission[3]. Under the high electrical field stress, this may explain the observed level of X-ray emitted due to rearrangement by an Auger mechanism.

If we assume that the emission is due to a sliding surface discharge, the emission track must follow very narrow lines. It is then difficult to obtain a surface emission. Moreover, the time resolved analysis prove

that the emission is changing very rapidly in few nanoseconds under the aspect of minus points.

Some regularities are observed in a series of points which are distributed, in some cases following lines. These points are situated outside the anode The separation between the points is of the order of 0.2-0.3 mm. This is similar to the figure observed in exploding fibers and wires. This suggests that a pinching instability is propagating in the plasma, having a wave mechanism . This wave is at the origin of the emission sites which are not situated on the electrodes or the insulator. As the period of this oscillation is about 1 ns (5 points in 5 ns), its propagation velocity should be on the order of 300 km/s.

8. Conclusion.

A low energy vacuum spark is shown to produce energetic ion and electron beams. In the spark gap, ions are accelerated by the electric field to the 70 keV level. Beams of tungsten ions having energies in the range 0.5 keV to 70 keV are produced. The Teflon vaporisation products has a strong influence on the X-ray intensity and on the ion current and also on the instant of breakdown. The effect of the ion displacement has been pointed out in the triggering of the high intensity breakdown which takes place only when the cloud of ions reaches the cathode producing a plasma which is an efficient source of electrons. The emission of the X-rays takes place in two different phases :

a) at the beginning of the breakdown during the rise of the intensity, the emission site is mainly on the insulator (and also partly on the anode). As the current intensity, at this time, is rising, the mechanism cannot be ascribed to the electron Bremsstrahlung in the insulator material. Another mechanism is needed.The ion emission may explain the appearance of these isolated emission sites. During the intense current phase, single anode spots are seen to emit X-rays, but also, spots are seen in the vicinity of the anode and even at great distances from it. This suggests that a plasma is created at the vicinity of the anode and that the radiation may come from a direct radiation of this plasma or from electron interaction with this plasma.

It must be noted that these phenomena have been observed at a energy scale of 1 J.

Acknowledgments

This work has been initiated under DRET contract 86/038. We thank P. Charles, professor at the University P. et M. Curie for his cooperation ; thanks are due to M. Bourdinaud, for useful discussions and material help ; we thank the Optectron Company for the supply of scintillators ; our camera has been supplied by the LHESA Company. This work is supported by the CNRS (URA-1096)

References

[1] G.A. Mesyats and D.I. Proskurovsky, *Pulsed Electrical Discharge in Vacuum*, Springer-Verlag, **1989**.

[2] H. Chuaqui, M. Favre, L. Soto and E.S. Wyndham, *IEEE Trans. on Plasma Science*, **21**(1993) 778.

[3] C. Le Gressus, F. Valin, M. Henriot, M. Gautier, J-P. Duraud, T.S. Sudarshan, R. B. Bommakanti and G. Blaise, J. Appl. Phys., **69** (1991) 6325.

[4] M. Skowronek and P. Roméas, *IEEE Trans. on Plasma Science*, **15** (1987) 589.

[5] M. Skowronek, P. Roméas and P. Choi, *IEEE Trans. on Plasma Science*, **17** (1989) 744.

[6] A. Ikhlef and M. Skowronek, *IEEE Trans. on Plasma Science*, **21** (1993) 669.

[7] A. Anders, S. Anders, B. Jüttner, W. Bötticher, H. Lück and G. Schröder,*IEEE Trans. on Plasma Science*, **20** (1992) 466.

Stability and operating characteristics of the applied B proton extraction diode on KALIF

H. Bluhm, P. Hoppé, H. Bachmann, W. Bauer,
K. Baumung, L. Buth, H. Laqua, A. Ludmirski,
D. Rusch, O. Stoltz, S. Yoo

Kernforschungszentrum Karlsruhe GmbH
Institut für Neutronenphysik und Reaktortechnik
Postfach 36 40, D-76021 Karlsruhe

In this paper we describe detailed investigations of the stability and operating characteristics of a magnetically insulated proton beam diode in extraction geometry developed for the 1 TW, 1.7 MV pulsed power generator KALIF. From an analysis of ion current density fluctuations the frequency spectrum of predominant instabilities has been determined. Although late in the pulse the main frequencies (1.2 GHz) are higher than expected they are compatible with an ion transit time mode. Combining the results from various detectors we suggest that the parallel load observed in our diode is probably due to a loss of low energy electrons into the expanding anode plasma.

Introduction

The magnetically insulated proton beam diode in extraction geometry developed for the 1 TW, 1.7 MV pulsed power generator KALIF has produced proton beams with greater than 0.65 TW power. The quality of these beams was sufficient to focus them to power densities around 1 TW/cm^2. These results were achieved by using an actively generated proton source and by applying rather strong magnetic insulation fields ($V_{crit}/V \geq 3$). This resulted in a good diode coupling to the generator, a high ion beam production efficiency and a high beam purity. Both, the ion diode and the anode plasma source have been described extensively in the literature /1, 2/.

Presently, the focusability of our beams is mainly limited by three factors: an ion beam divergence of about 17 mrad, an ion energy spread of about $\pm$ 15 %, and a nonzero canonical angular momentum of the ions due to a 2 mm anode plasma expansion across magnetic field lines. In addition a parasitic load occurring in the diode after peak power has been limiting the beam

energy content. These properties are the result of instabilities developing during diode operation. Therefore, to further improve the quality of our beams we must gain a better understanding of the nature and the dependability of the diode operating stability, which is mainly determined by the evolution of the anode plasma and of the electron sheath.

Our present understanding of electron sheath instabilities and their influence on beam divergence and ion energy spread is largely based on the three-dimensional particle-in-cell code simulations with QUICKSILVER /3/. These calculations require enormous computing resources. Therefore, only very simplified diode models can be treated. Especially, the diode geometry must be idealized and only a limited section along the symmetry coordinate of the diode can be modeled. Also the interaction between the gap instabilities and the expanding electrode plasmas have not been treated.

Therefore, we need some experimental checks of the simulation results to confirm that the features found are the dominating ones. In this paper we report on measurements that are pertinent to this comparison. In addition we describe recent results on the parallel load problem and on other diode operating features.

Diagnostic tools

Not all quantities which can be obtained from numerical simulations are also easily accessible to measurements. Among those which are both specific and measurable are the frequency spectrum and the phase velocity of the dominating electron sheath instabilities as a function of time. When these instabilities develop the ion current density should be strongly modulated with the electron density fluctuations close to the anode which occur with the frequency of the predominant mode and travel around the azimuthal direction with the phase velocity. Therefore, localized measurements of ion current density fluctuations should give information on the frequency spectrum, and correlating the results from measurements at different azimuthal positions should allow us to determine the phase velocity.

For that purpose we have used a set of six magnetically insulated Faraday cups located in the strong magnetic field ($\sim$ 3 T) of our diode coils, about 8 mm behind the initial position of the virtual cathode. They were distributed over three radial and six azimuthal positions covering 180° of the diode circumference. All Faraday cup signals were recorded on a 500 MHz analog bandwidth 16 channel digital scope (Tektronix TLS 216). In addition one signal was recorded in parallel on a 5 GHz transient digitizer

(Tektronix SCD 5000). This channel was used to explore the frequency spectrum and it was made sure that the Faraday cup itself and the signal cables did not introduce any further bandwidth limitations. Entrance holes with 0.3 to 1.1 mm diameter drilled into 0.1 mm thick plates of stainless steel or Mo were applied.

Another main diagnostic consisted of a Rutherford scattering foil placed in the beam focus in combination with a pinhole camera and a cross of 13 Si-pin-diodes. The ions scattered from a 3000 Å Au layer deposited on a 1.5 µm mylar foil were imaged with the help of a pinhole camera onto the pin-diode cross. Each pin diode had a sensitive area of 1 mm^2 and was covered with a 6 µm thick Al foil.

Finally, we used an array of 15 x 40 quartz fibers to locally resolve the light emitted from the diode gap in different spectral regions. Each of the 15 columns collected light from a 0.5 mm thick slice parallel to the anode surface. A fast photomultiplier connected to each of the columns was used to record the light intensity as a function of time. The spectral range was selected with the help of 10 nm wide interference filters.

Results

A typical Faraday cup signal recorded with the 5 GHz transient digitizer is shown in Fig. 1. A period of high frequency oscillations early in the pulse if followed by a period of lower frequency

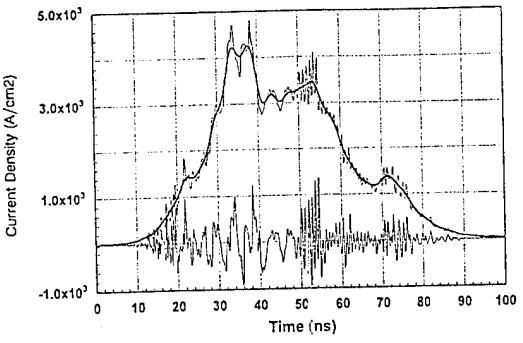


Fig. 1: Faraday cup signal recorded on a 5 GHz transient digitizer, together with smoothed signal and the difference between both (lower trace x 2).

oscillations and another period of high frequency oscillations. Before analyzing the frequency spectrum the signal was smoothed with the help of a Hanning window. Then, the smoothed signal was subtracted from the untreated one and the difference spectrum was subjected to a Fourier transformation. To make the time dependent structure of the spectrum apparent we restricted the analysis to certain time intervals.

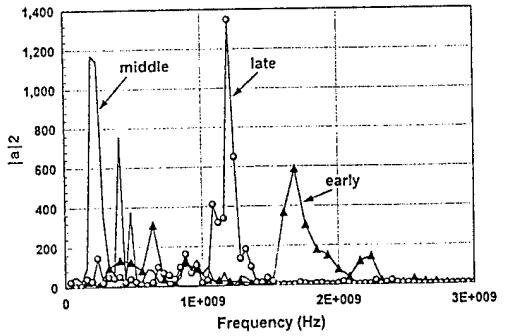


Fig. 2: Current density fluctuation spectrum at different times in the pulse.

As shown in Fig. 2 early in the pulse we observe two dominating frequencies at 1.67 GHz and at 2.20 GHz. This is followed by a lower frequency mode of 0.96 GHz superimposed on a few cycles with 4 - 5 ns period. This phase lasts for about 25 ns. Later in the pulse there is only one frequency at 1.2 GHz left. The general character of this spectrum is quite reproducible. Especially, the frequencies around 1.2 GHz and 1.7 GHz that have strong power appeared regularly with a variability of ± 150 MHz. However, an effective electron limiter distinctly shifts the spectrum to lower frequencies: Early in the pulse two frequencies at 0.5 and 1.0 GHz dominate. Later a frequency distribution centered around 0.86 GHz prevails.

Since we had only 1 channel with 5 GHz bandwidth available and since the predominant frequencies were distinctly above the 500 MHz limit of our other recording channels it was not possible to carry out a real correlation analysis to determine the frequency dependent phase velocities. However, we were able to look for prominent patterns in the Faraday cup signals surviving during the travel around the diode. From the times at which these pattern arrive at different locations it is possible to determine their propagation velocity. It turned out that this was possible only during the second half of the pulse. For Faraday cups aiming at the central part of the emission zone we obtained velocities of between 1/9 and 1/12 c. However these values need further verification using two 5 GHz channels.

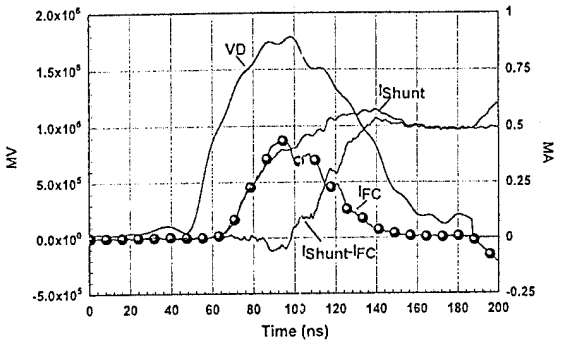


Fig. 3: Comparison of F.C. ion current with shunt ion current. VD is the diode voltage.

The effect of a parallel load growing during diode operation becomes evident from a comparison of the ion current measured with electrical monitors with that derived from Faraday cup signals. Such a comparison is shown in Fig. 3. The F.C. ion current has been obtained by averaging the signals from 6 cups and multiplying the result by the anode emission area. While excellent agreement is observed during the rising part of the pulse a rapidly growing discrepancy develops at peak diode voltage. It is remarkable that this coincides with a transition in the frequency spectrum.

If we use the electrical ion current and the diode voltage to predict the shape of a pin-diode signal at the position of the pin-diode cross we find that this shape is much wider than that actually measured. This is shown in

Fig. 4. Much better agreement is achieved if a current derived from F.C.s is taken for this comparison. Therefore, we can conclude that as long as the diode voltage remains above 0.6 MV a blockage of protons in the plasma created by ion beam bombardment of the F.C. aperture can be excluded.

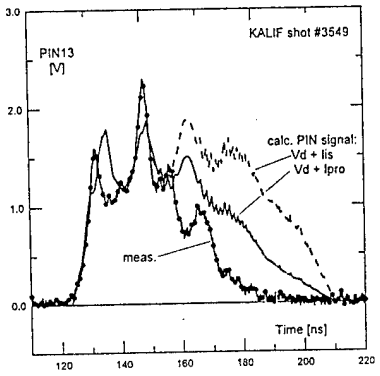


Fig. 4: Signal from the central pin-diode of the focus diagnostic compared to signals predicted from the diode voltage and the shunt or F.C. ion current respectively.

The main purpose of the pin-diode cross was to determine the time history of our beam focus which is sensitive to diode stability and operating characteristics. It was found that the duration of the power pulse was 40 ns fwhm. During this period of time the shape of the focus remained nearly unchanged with a diameter of 6.2 mm fwhm.

As expected the photomultiplier-fiber array showed that early in the pulse light was only emitted from a small zone in front of the anode and from the cathode tip. About 20 ns after anode plasma formation the light emitting zone had expanded roughly 1.5 mm into the diode gap. However, at the same time a 4 mm wide domain extending from the cathode into the gap began to emit light with growing intensity in a wavelength range around the hydrogen H_α-line. Late in the pulse the luminosity of this zone became even brighter than the anode plasma.

Conclusions

The high frequency fluctuations of the ion current density observed early in the pulse in shots without limiter can probably be identified with the diocotron instability of the electron sheath observed in numerical simulations /3/. At maximum diode operating voltage the current density reaches 4 kA/cm^2. This suggests that the effective diode gap is probably small at that time. Assuming a "saturated" enhancement of 5.5 an anode cathode gap of about 4 mm is predicted. This leads to an ion-transit time of about 0.7 ns. Therefore, also the predominant frequency of 1.2 GHz prevailing in the second half of the pulse is compatible with the predicted ion transit time mode. The very low frequency oscillations with periods of 4 - 5 ns occurring before that have also been observed in simulations of diodes with strong magnetic insulation ($V_{crit}/V > 2$) /3/. They have been attributed to cyclic electron losses resulting from an electron density peaked towards the anode.

Combining the results of F.C. and pin-diode focus measurements demonstrates that the parallel load can not be explained by a plasma blocking effect acting on protons accelerated with the full voltage present in the diode. Also a shortage of protons promoting the acceleration of heavier ion species (which then could be blocked off from the F.C.) is unlikely because this would increase the diode impedance at first. In addition we observe that the F.C. current signal very often follows the same $V^{3/2}$ law during the descending part of the voltage as it was during the rising part. Since both, the ion current monitor and the total current monitor far outside the diode show only very small differences it is also obvious that the parallel load develops inside the diode. There remain three possible explanations: low energy protons or neutrals created by various processes inside the diode or in the noncurrent neutralized zone, low energy electrons diffusing across the magnetic field lines, or negative ions from the cathode. Our present observations favour low energy electrons as the most likely origin of the parallel load. This statement is suggested by the results from the photomultiplier array which show expanding plasmas from the anode and the cathode side deeply into the gap which can reduce the magnetic insulation and suck up electrons from the gap. This process is probably especially effective if the electron density distribution is peaked towards the anode. However, further investigations are necessary to verify this conjecture.

Acknowledgement

The authors thank G. Keßler for his continued support of this work. They also thank the operational staff of KALIF as well as H. Lotz and G. Westenfelder for their technical assistance.

References

/1/ H. Bluhm, P. Hoppé, H. Laqua, D. Rusch; Proc. of the IEEE, Vol. 80, 995 (1992)

/2/ H. Bluhm, H. Laqua, L. Buth, P. Hoppé, D. Rusch; IEEE Trans. of Plasma Science, Vol. 21, 560 (1993).

/3/ T.D. Pointon, M.P. Desjarlais, D.B. Seidel, S.A. Slutz, R.S. Coats, M.L. Kiefer, and J.P. Quintenz; Phys. Plasmas 1, 429 (1994).

A CONTRIBUTION TO THE MAGNETIC FOCUSING IN AN APPLIED-B-EXTRACTOR ION DIODE BY A LASER PULSE DRIVEN SOLENOID

W. Bauer, W. Höbel, A. Ludmirsky*, E. Stein, T. Westermann**

Kernforschungszentrum Karlsruhe mbH, Postfach 3640, 76021 Karlsruhe, Germany

*Permanent address: SOREQ NRC, Yavne 7600, Israel
**Fachhochschule, Moltkestraße 4, 76133 Karlsruhe, Germany

Abstract

To obtain well focused beams is one of the key problems in light ion beam driven inertial confinement fusion. Extractor diodes with externally applied magnetic field show at present divergences of about 17 mrad. This work investigates the possibility of improving the focusing by applying a magnetic field in the vicinity of the focus which is generated by an intense laser beam. The focusing properties of the diode are simulated using a quasi-stationary 2.5-dimensional particle-in-cell code. The applied magnetic field which is needed as input to the PIC-code is computed by PROFI. The simulations show that the effect of the suggested solenoid is indeed an improvement of the focusing both for beams with a Gaussian distribution of divergence angles and for beams with an energy distribution taken from an actual experiment.

I. Introduction.

Ideally the ion beam generated in an applied B extractor ion diode is focused by proper shaping the geometry and the fields in the diode. For many reasons this ideal cannot be fully accomplished. Influences which are difficult to control are for instance the effect of non ideal shapes of the anode and cathode plasmas, the applied magnetic field, and the unknown self-fields generated by beam instabilities.

There are schemes described in the literature, see for instance [1], where the final focusing of an ion beam is accomplished by a solenoidal lens situated a few meters in front of the focus, some way downstream from the diode. In the present work we investigate the application of such a focusing magnet in close vicinity of the focus of the applied B-proton extraction diode presently under investigation at KALIF [2].

Particle-in-cell - calculations using the 2.5-dimensional quasi stationary code "BFCPIC2H" [3] suggest a positive effect of such a magnetic field on ion beam focusing.

The magnetic field can be generated by using an intense laser beam as described in [4, 5]: (see Fig. 1.) By interaction of a laser pulse of 100 J and $1.3 \cdot 10^{14}$ W/cm^2 with a target, a voltage of 220kV and an electric current of 100kA are generated. This current pulse of 1 ns duration drives a one-turn coil and generates magnetic fields of up to 600 kG [5].

There are many technical problems to solve, like how to produce a laser pulse of the appropriate time duration of at least 50 ns or how the vacuum system of the laser can be separated from the gas filled drift space. Assuming that these problems can be solved, we emphasize in this paper on the the improvements of the beam optics that could be achieved using such an additional magnetic field.

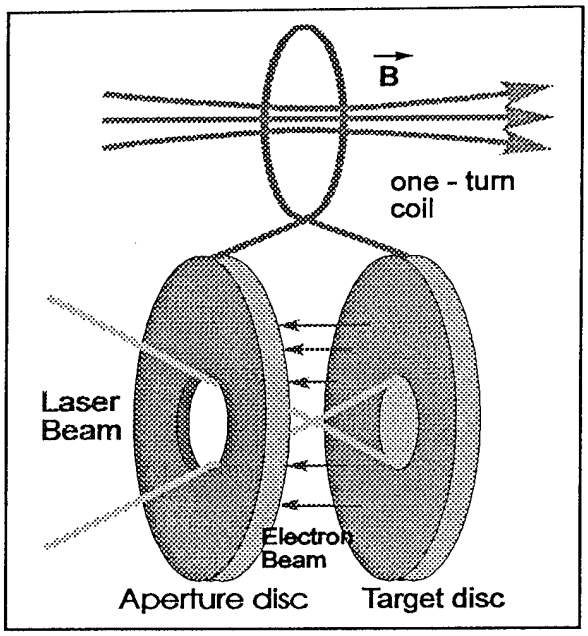


Fig. 1: Generation of a strong magnetic field using electrons released from the target disc by an intense laser beam. Target and aperture disc are connected by an one-turn coil.

II. Codes used for Particle-in-Cell Simulations.

We use a combination of codes to simulate the particle motion in and outside our diodes. They are based on "BFCPIC2H" that, using a boundary-fitted grid, calculates the electric fields of the empty diode, emits particles at the surfaces, follows them on their way through the diode and calculates self-consistently electric and magnetic fields generated by the particle flux. The code uses as input the static external magnetic field computed by the program "PROFI" [6]. Since PROFI uses its own (rectangular) grid, the magnetic field inside the diode is interpolated to the boundary-fitted grid inside the diode.

To follow the particles through the drift-space outside the diode up to the focus, the program "DRIFTPIC" [7] is applied. It self-consistently computes the magnetic fields in the drift-space. Again the magnetic field calculated by "PROFI" is used. DRIFTPIC assumes total space charge neutralization and current neutralization with a percentage that can be specified. Moreover, it takes into account that the neutralization is reduced in the vicinity of strong magnetic fields.

III. Results.

The following figures show the main contours of the diode together with trajectories outside the diode in the drift-space, using either some of the particles generated by the PIC-code or particles with special hand-selected starting conditions at the entrance of the drift-space. The figures have to be considered as rotationally symmetric around the Z-axis.

In fig. 2, ions as they are generated by the PIC-code in the diode are shown. They produce a rather broad focus around Z = 150 mm. Switching on the one-turn coil situated at Z = 140 mm as shown in fig. 3. the focusing behaviour is considerably improved. In fig. 4. three of the previous trajectories are given an artificially introduced divergence of ± 1°. The additional magnetic field apparently results in an improved focus also in this case.

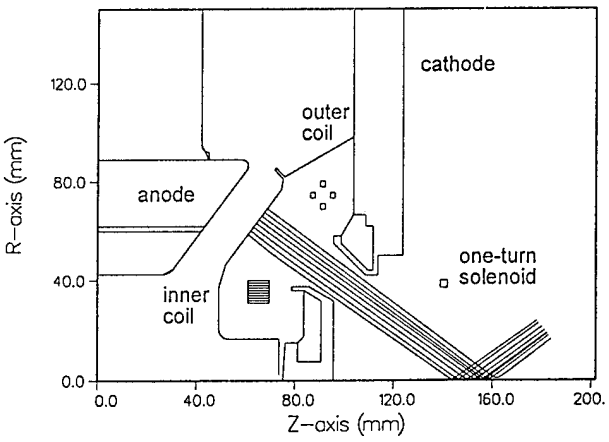


Fig. 2: 8 typical proton beams in the applied B proton diode [5] simulated by BFCPIC2H [3] showing a rather broad focus at about 150 mm.

The results discussed so far suggest, that in the case of a non ideally focusing diode the additional magnetic field indeed improves the focus. In fig. 5 the initial conditions have been changed in such a way, that all beamlets leaving the diode arrive at exactly one focus point, if the additional magnet is switched off. This perfect focus is made *worse* by the additional magnet, as fig. 6 shows.

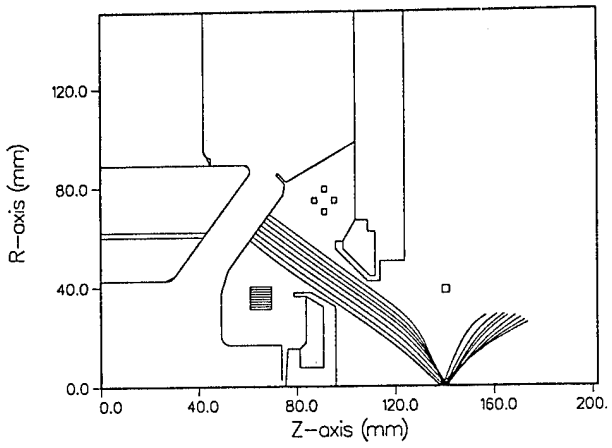


Fig. 3: A one-turn coil carrying a current of about 100 kA concentrates the beams at a somewhat smaller focus length of 140 mm with a considerably reduced focus diameter.

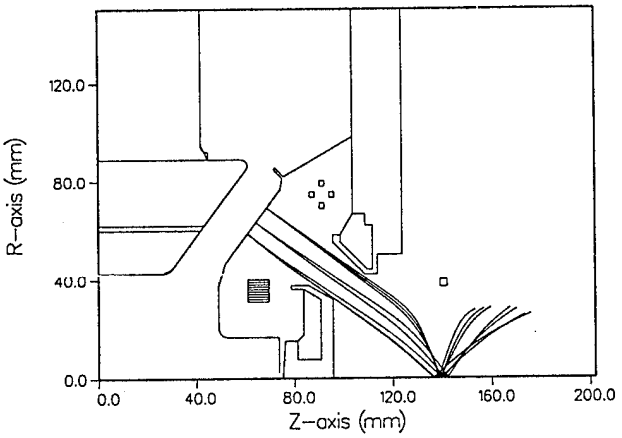


Fig. 4: Three of the above beams are shown with a 1° initial divergence at the diode exit, showing that the improvement of the focus by the magnet is maintained.

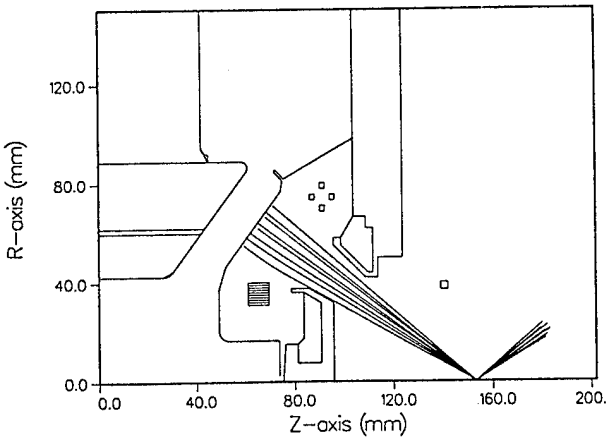


Fig. 5: Artificially changed initial conditions leading to an ideal focus.

To study more thoroughly the influence of the additional magnet in the presence of a beam divergence and for different beam energies, the following procedure was chosen: The beams leaving the diode and entering the drift region were given a Gaussian distribution of divergence angles with a half angle of

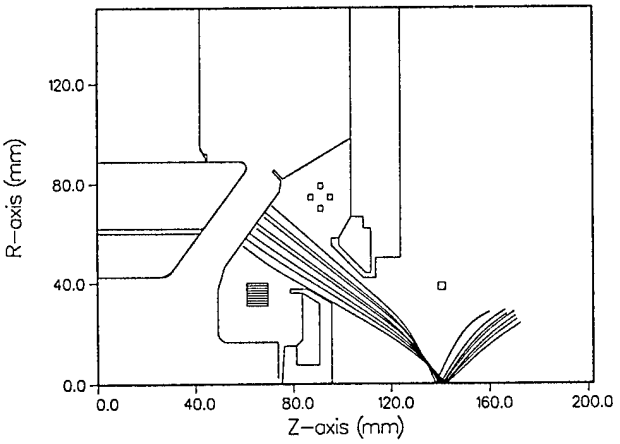


Fig. 6: The additional magnet disturbs the ideal focus of fig. 5.

1°. For each of these beamlets the radius R was recorded, at which they arrive at the distance Z of the smallest beam radius. This count was plotted versus the radius in fig. 7 for both cases when the the additional magnet is switched on and off. The corresponding curves demonstrate clearly an improvement of the focus by the magnet.

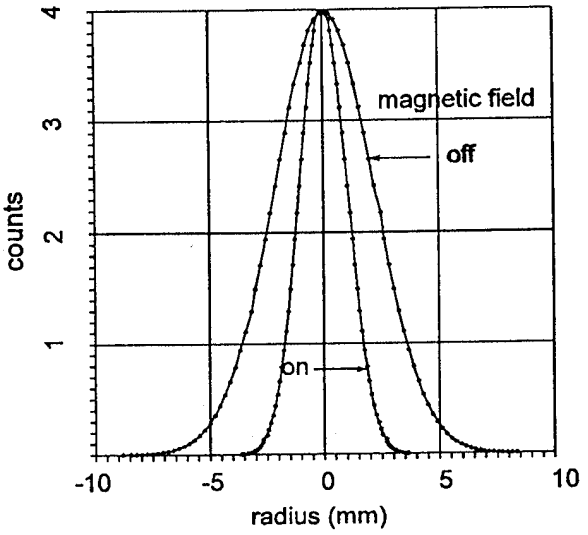


Fig. 7: Beam profile at the focus for a Gaussian-shaped divergence distribution. FWHM = 2.5 and 5.2 mm for magnetic field switched on and off, respectively.

In a similar way the influence of different beam energies was investigated in fig. 8. Here the particle distribution measured by a Thomson-parabola-spectrometer [8] was considered *in addition* to the Gaussian distribution of divergence. The improvement by the additional magnet can still be recognized, but is less pronounced than in fig. 7.

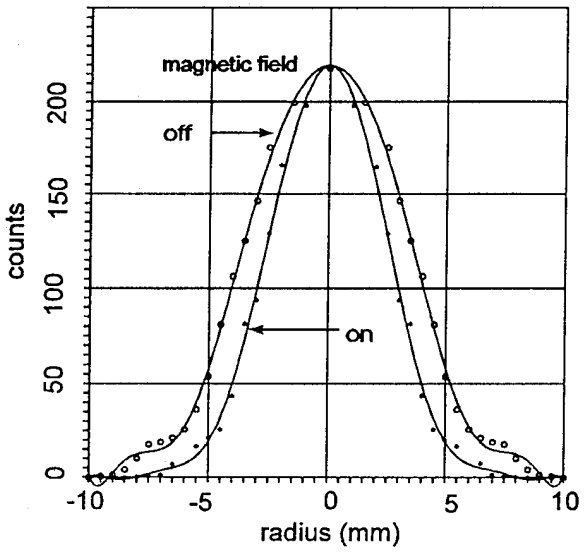


Fig. 8. Beam profile at the focus for a Gaussian-shaped divergence distribution and for an experimental energy distribution of the protons. FWHM = 5.6 mm with magnetic field and 7.7 mm without it.

IV. Conclusion.

The simulations have shown, that in the case of a non-ideally focusing diode an additional magnet in the vicinity of the focus can improve the focus considerably. The influence of beam divergence on the focal size can be reduced by a factor of about two for mono-energetic beams and by about 30 % for beams with a realistic energy distribution. If the technical task to design a laser driven solenoid in the vicinity of the focus can be solved it would be an interesting contribution to an improved focusing. Without the laser-scheme one could even think of a one-turn-coil sacrificed for each shot, that is driven from a condenser bank.

Apart from the question of a possible realization the investigation can be considered as an interesting example for the application of our PIC-code.

References:

[1] F. Ottinger, D. Mosher, J.M. Neri, D. V. Rose, C. L. Olson, "Transport and Focusing Considerations for Light Ion ICF Systems", 9th International Conf. on High-Power Particle Beams, Wahington, DC, 1992, p. 60

[2] H. Bluhm, P. Hoppé, H. Bachmann, W. Bauer, K. Baumung, L. Buth, H. Laqua, A. Ludmirski, D. Rusch, O. Stoltz, "Stability and operating characteristics of the applied B proton extraction diode on KALIF", this conference

[3] T. Westermann, "A Particle-in-Cell Method as a Tool for Diode Simulations", Nucl. Instr. Meth. **A 263**, (1988), p. 271, or more recently: "Numerical Modelling of the Stationary Maxwell-Lorentz System in Technical Devices, Int. J. Num. Modelling: Electronic Networks, Devices and Fields **7**, (1994), p. 43 - 67

[4] J. L. Borowitz, S. Eliezer, Y. Gazit, M Givon, S. Jackel, A. Ludmirski, D. Salzmann, E. Yarkoni, A. Zigler, B. Arad, "Temporally Resolved Target Potential Measurements in Laser-Target-Interactions", Journal of Applied Physics **20**, 1987, p. 210

[5] H. Daido, F. Miki, K. Mima, M. Fujita, K. Sawai, H. Fujita, Y. Kitagawa, S. Nakai, C. Yamanaka, "Generation of a Strong Magnetic Field by an Intense CO_2 Laser Pulse", Phys. Rev. Lett. **56 (8)** (1986) p. 846-849

[6] PROFI, Program Documentation Version 7.4, PROFI-Engineering, Otto-Röhm-Straße 26, 64293 Darmstadt, Germany

[7] L. Feher, W. Schmidt, T. Westermann, "DRIFTPIC, a Computer Program for the Calculation of Ion Trajectories in the Drift Section of Externally Applied-B Diodes", KfK-report 5207 (July 1993)

[8] H. Bluhm, P. Hoppé, H. Laqua, D. Rusch, "Production and Investigation of TW Proton Beams from an Annular Diode Using Strong Radial Magnetic Insulation Fields and a preformed Anode Plasma Source", Proc. IEEE, **80, NO. 6** (1992), p. 995 - 1009

INTENSE PROTON BEAM SOURCE FOR ITER NEUTRAL-BEAM SPECTROSCOPY DIAGNOSTICS.

R. R. Bartsch, H. A. Davis, and I. Henins
Los Alamos National Laboratory
Los Alamos, NM 87545

J. B. Greenly
Cornell University
Ithaca, NY 14853

An intense proton beam has been developed to evaluate a gas-cell neutralizer for use in an intense-neutral beam source for Tokomak Spectroscopy diagnostics. The allowed energy range of the proton stream is determined to be 50 to 70 keV from neutralization and reionization cross-sections and from the alpha particle charge exchange recombination intensity as a function of energy (baseline diagnostic). The neutralization evaluation source uses a flashover anode, magnetized, ion-diode. Neutral probes sensitive to energetic atomic and molecular hydrogen, developed to evaluate neutralizer performance, show neutral fluence from the ion-diode during the beam pulse. An array of Rogowski current probes, used to study the evolution of the current path, suggests that expansion of the anode plasma along the radial insulating magnetic field leads to impedance collapse.

I. INTRODUCTION

A flashover-anode, magnetized ion-diode has been developed for use in the evaluation of a gas-cell neutralizer. Impedance collapse in this ion-diode is observed when a parallel current path developes from expansion of anode plasma along the radial insulating field. Neutral hydrogen flux at energies up to the ion-beam energy, as well as a flux of energetic heavier ions, are seen at the output of the ion-diode. The gas-cell neutralizer will be part of an intense diagnostic neutral beam (IDNB) source for use as a probe beam with tokamak spectroscopy diagnostics.[1] For this application the flashover anode will be replaced with a plasma anode.[2]

Cross-sections for creation of the neutral beam as well as the intensity vs. probe-beam energy for the base line spectroscopy diagnostic--alpha particle charge exchange recombination-- require operation of the ion-beam source at 50 to 70 keV.[3,4] The intense probe beam operating at a current of ~10 kA has the potential of supplying a spectroscopy signal ~ 10^4 greater amplitude than with conventional heating-beam technology. This enables tokamak spectroscopy measurements with a signal to background ratio of greater than one on a single probe-beam pulse. The calculated spectroscopy signal intensity is shown in figure 1 as a function of hydrogen beam energy for both a steady-state and an intense beam. The signal is observed to fall off rapidly below ~50 keV neutral (Hydrogen) beam energy.

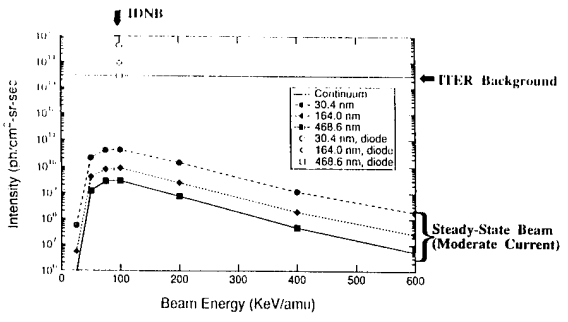


Figure 1: Calculated HeII line intensities at r/a=0 in ITER ignition scenario. Steady state beam assumes a one MW H° beam, 10 cm height in plasma. (Figure supplied by R. Fonck and E. DenHartog, University of Wisconsin.)

The neutralization process for protons passing through the hydrogen cloud of a neutralizer cell competes with reionization of the neutral H stream. At proton beam energies less than ~ 70 keV, the cross-section for neutralization dominates the reionization cross-section, as shown in figure 2. At energies above 70 keV, the reverse is true. At the crossover energy, the output of the neutralizer cell is one half protons and one half neutral hydrogen. Child-Langmuir scaling of ion-diode beam current with voltage can slightly shift the voltage for maximum neutral beam intensity.

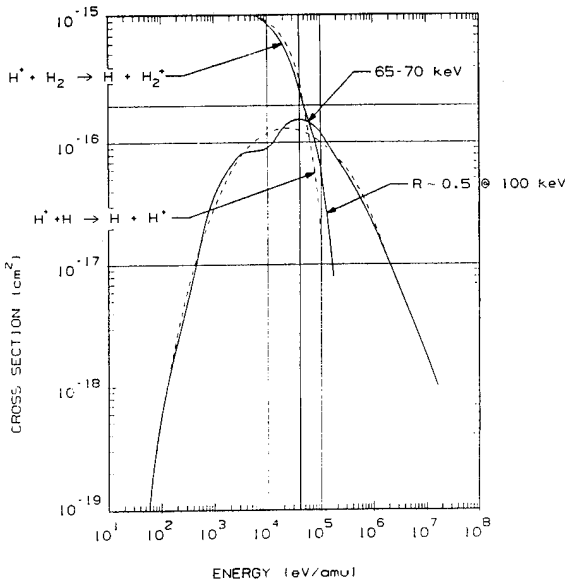


Figure 2: Charge exchange recombination cross section and reionization-by-neutral-impact cross section versus energy.[3]

II. EXPERIMENTAL CONFIGURATION

The driver for the magnetized ion diode is a 3.6 μF, rail-gap-switched, 120 kV capacitor bank in a configuration modeled on the SHIVA star modules used at Phillips Laboratory.[5] Slow coils, which provide the insulating field of the ion-diode, are powered by an ignitron-switched low voltage (10 kV) module.[6] The neutralizer section is an annular channel ~ 0.4 m long with a cross-section which matches the beam exiting the ion-diode. Gas (H_2) is injected at the mid-plane of the neutralizer ~ .25 milliseconds prior to the generation of an ion-beam. Small-cross-section probes, which discriminate against streaming ionized hydrogen but are sensitive to streaming neutral hydrogen, are located in the neutralizer channel. The neutralizer section, neutral probes and measurements of the neutral flow from the ion-diode are described in Section III. Tests of the neutralizer section are reported elsewhere.[7]The neutral probe array used to evaluate the neutralizer section has a probe located upstream of the neutralizer at the exit of the ion diode. Data from this probe and the downstream probes is used below to interpret the neutral flow from the ion-diode.

The magnetized ion-diode used for evaluation of the neutralization process utilizes a flashover anode. The current emission for the dielectric anode, at the low operating voltages of the IDNB, has been optimized by the use of metal field enhancement pins embedded in the anode material[8] and by field emission points installed on the edges of the cathode annuli which face the anode-cathode gap. An array of Rogowski current probes has been integrated into the ion-diode structure to investigate the current path evolution and the impedance collapse that terminates the ion-beam pulse. The ion-diode design and measurements of diode performance are given in Section IV.

III. NEUTRALIZER SECTION

The ion beam (H^+) from the magnetized ion-diode is passed through a gas-cell (H_2) in which the integral of the gas density along the cell is such that the cell length is approximately one mean free path for the neutralizing process. A puff of gas is injected at the mid plane of the 40 cm annular channel. The ion beam is generated when the gas cloud is 5 to 10 cm long and the maximum pressure at the center is ~ 10 mTorr. The timing delay is set to avoid gas in the anode-cathode region of the ion diode when the ion beam is generated. An array of 3 neutral probes is used to evaluate the neutralizer performance. One of these probes is located just downstream of the ion diode at the input to the neutralizer section. Another is located in a shield pipe to sample

the un-neutralized beam after it has transited the 40 cm neutralizer cell. The third probe measures the neutral (H) content of the beam after it has transited the gas cell and is located at the same axial location (near the downstream end of the neutralizer) as the shielded neutral particle probe.

The neutral probes use a 3 kilogauss transverse field to discriminate between H^+ and H at streaming energies less than 100 keV. A second, downstream aperture, internal to the probe, blocks deflected ions.[7] Neutrals passing through the second aperture impact on a beveled, negatively biased collector. The resulting secondary electron current is detected with a ratio of 1 to 1.5 electrons per incident hydrogen atom.

The neutral probes have been developed to evaluate performance of the neutralizer section, however the array of probes also provides information about the fluence of neutral hydrogen from the ion diode. Data for a typical shot is shown in figure 3. The voltage rings near 60kV and an ion beam is drawn out just before impedance collapse at 2 μsec. The total diode current is seen as a feature on the leading edge of the system current (as shown in the cathode-structure current). The large current excursion for t>2 μsec is due to a low-impedance arc which commences as the diode impedance collapses. Current downstream of the diode is shown in figure 3. The energetic ion flow is observed as the step on the leading edge of the neutralizer input current. Three neutral probe traces are also shown in figure 3. The top trace is the neutral (H) fluence at the input to the neutralizer cell, just downstream of the ion diode (z ~ 10 cm). Energetic, heavier ions such as C^+ contribute to this signal. The middle trace is a shielded probe to look at a sample of the un-neutralized beam at the downstream end of the neutralizer cell (z ~ 50 cm). At this location transit time broadening permits the observation of a burst of current at a transit time corresponding to energetic heavier ions. This is also seen in the bottom probe trace which shows the signal from the neutral probe downstream of the neutralizing gas cloud. Also visible is the probe-current peak caused by the neutral (H) flow at the transit time delay corresponding to energetic flow from the ion diode (immediately proceeding current collapse).

Probe-to-probe amplitude variations are due to azimuthal non-uniformity of the ion beam. Transit time and the identifiable downstream neutralized hydrogen flow permit qualitative interpretation of the neutral fluence from the diode. Since the neutral probe sensitivity for heavier ions, such as carbon, is ~ 2x the sensitivity for neutral hydrogen, and the neutralizer is ~ 50% efficient in converting the H^+ flow into H, the probe data suggest that the ion flow from the Lucite flashover anode is roughly equally divided between H^+ and heavier ions. Moreover, transit time broadening suggests that the hydrogen energy spectrum extends down to as low as a few kilovolts. The neutral hydrogen fluence observed at the downstream probe with and without neutralizing gas indicates that the ion-diode, may have a significant (≤ 50%) energetic neutral hydrogen content along with the extracted ion beam.

Section IV. ION-DIODE CURRENT INVENTORY

An array of Rogowski current probes has been used to investigate the ion-diode current inventory during impedance collapse. The probes are located in the annular ion-diode at positions that allow measurement of the net current to the inner cathode, net ion flow in the beam channel, net current to the outer cathode and total machine current. Probe locations are shown in figure 4 except for the machine-current probe.

Data for two representative shots is shown in figure 5. For shot no. 4239, a complete impedance collapse begins at 2.0 μsec as seen on the diode voltage. Prior to this time, the current monitors outside the beam channel and the total machine current are approximately the same as seen in the middle graph in figure 5. At this point the current to the outer cathode starts to rise rapidly along with the current to the inner cathode--both currents roughly double between 2.0 and 2.2 μsec. The lower left hand graph shows the current in the ion beam channel which rises to ~ 10 kA at the time of impedance and voltage collapse.

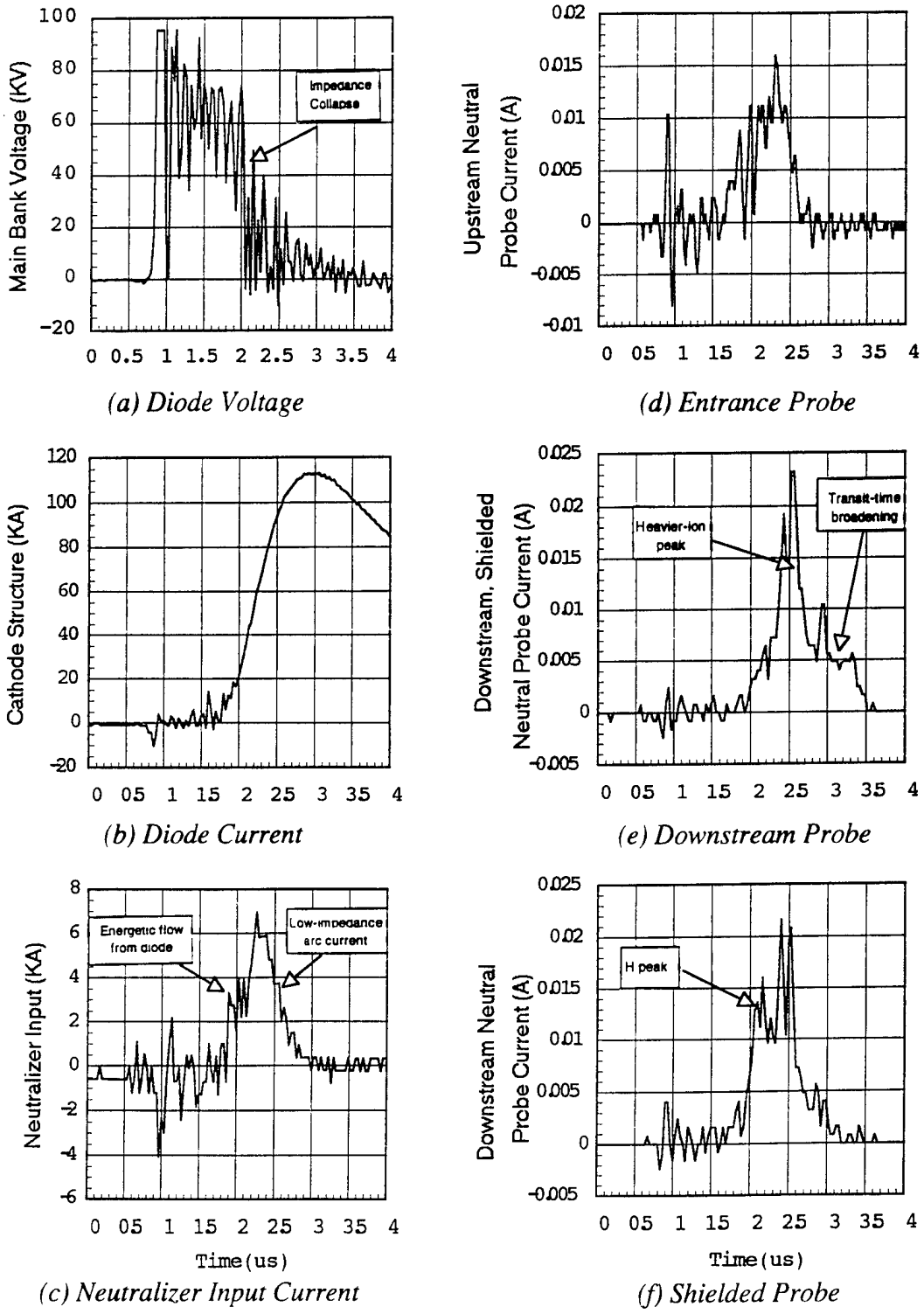


Figure 3: Beam diagnostics: (a) diode voltage, (b) diode current, (c) neutralizer input current. Currents of neutral probes: (d) entrance to neutralizer (e) downstream of neutralizer and (f) shielded (un-neutralized) downstream probe.

The increase in axial current to the electrodes located radially inside and outside of the Lucite anode indicates that the anode plasma expands radially along the insulating magnetic field allowing current to flow directly to the cathode cylinders. The radial distance traveled is ~ 0.5 cm in a time of ~ 0.5 μsec.

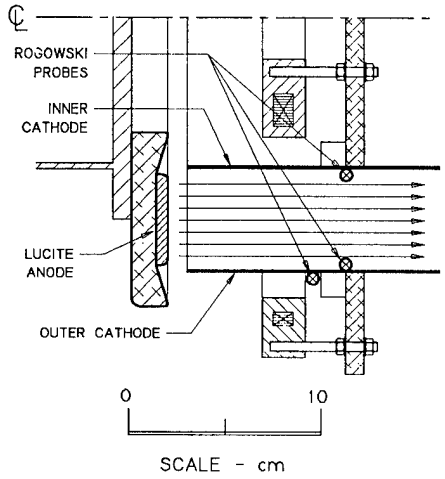


Figure 4: Cutaway view of flashover-anode, magnetized ion-diode showing locations of Rogowski current probes. Diode is axisymmetric with center line as shown.

The ion-diode has an insulating field of ~ 1.6 kilogauss with a 1.0 cm anode-cathode gap. The applied field is 1.6 times $B_{critical}$ and the anode area is ~ 200 cm^2. At 60 kV and 10 kA (just prior to impedance collapse) the ion-diode current density is 50 A/cm^2. This is 61 times the Child-Langmuir current density for an equivalent planar diode. The effective diode gap is ~ .13 cm at impedance collapse. Electron orbits from the cathode pass within 0.4 cm of the anode at the start of emission. A gap-closure rate can be estimated from the difference between the initial and final effective diode gap and the pulse width of the energetic part of the beam current. The rate is ~.54 cm/μsec which is similar to closure rates seen on other magnetically-insulated ion-diodes.[9]

A partial impedance collapse is observed on data from shot no. 4257 shown in the right hand column of figure 5. The initial portion of energetic ion flow is at a diode voltage of ~ 68 kV at 1.9 μsec. The impedance collapses partially and the diode voltage drops to ~ 40 kV. The initial ion current in the beam channel peaks at 6.5 kA and the second current pulse, during the partial collapse, peaks at 12.5 kA. Total impedance collapse occurs at 2.3 μsec as seen on the current to the inner cathode as well as on the ion current in the annular beam channel. During the time of the partial impedance collapse to 40 kV the flow in the beam channel rises to ~ 140 times the calculated Child-Langmuir value.

V. CONCLUSIONS

Measurements of the neutral (H) flow associated with a flashover-anode, magnetized ion-diode have indicated a flux of neutral hydrogen at transit times consistent with the 60 kV diode voltage as well as a tail down to an energy of several keV. Pronounced neutral probe signals are also observed at a transit time consistent with heavier ions such as carbon. Current inventory measurements indicate that the anode plasma expands radially along the insulating magnetic field at ~ 1 cm/μsec. The resulting increase in effective area of the diode leads to ion-flow directly to the cathode structure and the impedance collapse which terminates ion-flow in the beam channel.

The authors would like to express appreciation for the assistance of Robert J. Kasik and William B. Hinkley in the construction and operation of the IDNB facility. This work is supported by the USDOE on Contract W-7405-ENG-36.

---

[1]D.J. Rej, I. Henins, R.J.Fonck and Y.J. Kim, Rev. Sci. Instrum. 63, 4934 (1992)
[2]M. Ueda, et al, Rev. Sci. Instrum. 64(10), 2737 (1993).
[3]Atomic Data for Fusion Research, ORNL 5206.
[4]R.J. Fonck and E. DenHartog, private comm.
[5]R. Kasik, et al, 1993 IEEE Pulsed Power Meeting, paper 18-6, Albuquerque, NM.
[6]D.J. Rej and W. Waganaar, et al, 1991 IEEE Pulsed Power Meeting, Paper 8-1, San Diego, CA.
[7]R.R. Bartsch, H.A. Davis, J.B. Greenly and I. Henins, Proc. 10th Topical Conference on High Temperature Plasma Diagnostics, 1994, Rocherster, NY, (to be published, Rev. Sci. Instrum.).
[8]W. Schimassek, et al, Rev. Sci. Instr. **62**, 168 (1991).
[9]M. Tuszewski, M.P. Desjarlais, and W. Waganaar, submitted for publication.

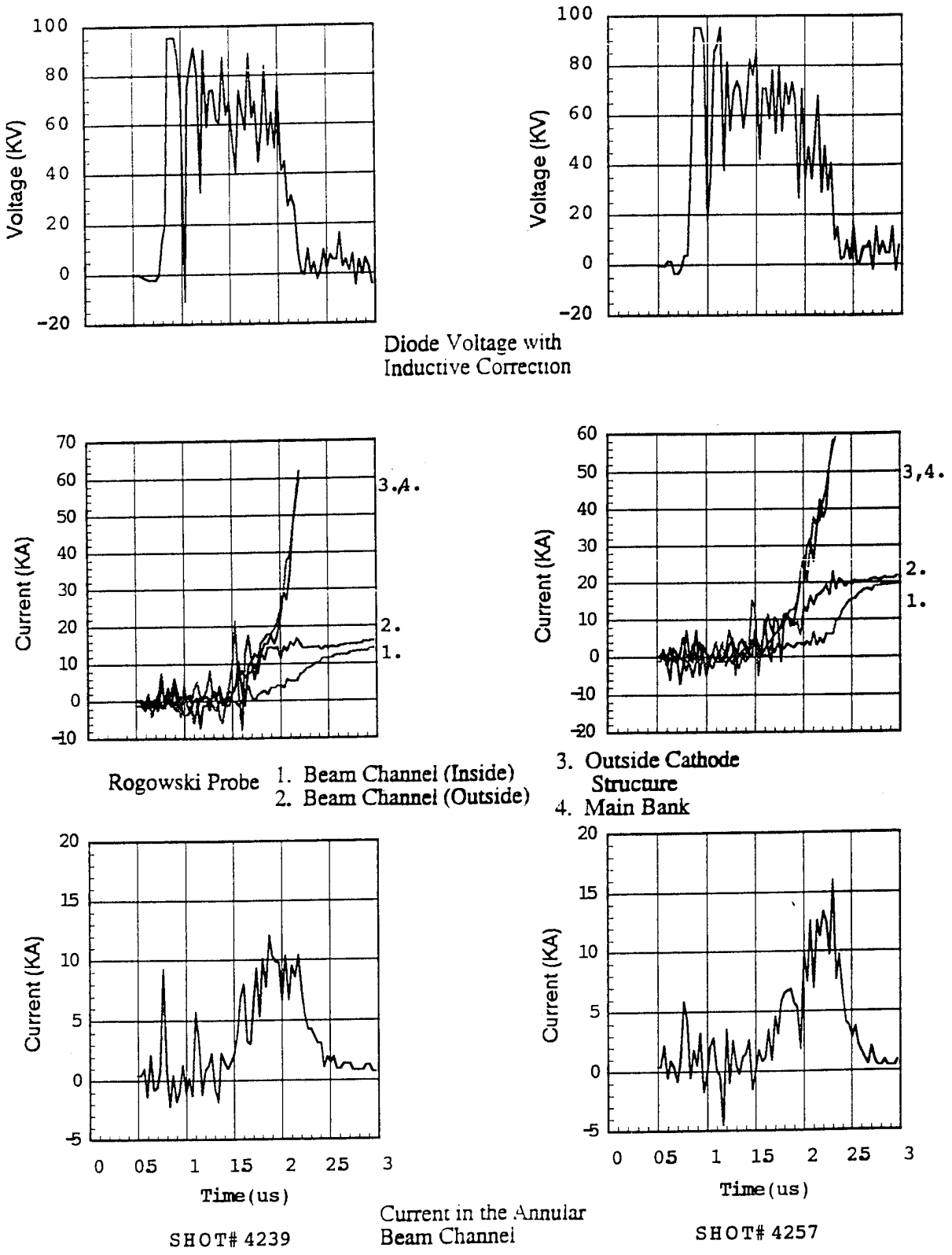


Figure 5: Diode voltage, diode currents and current downstream at the entrance to the annular beam channel of the neutralizer. Shot 4239 (left)--full impedance collapse; Shot 4257 (right)--partial impedance collapse.

PHYSICS OF ELECTRON EMISSION FROM METAL-DIELECTRIC CATHODES

Gennady A. Mesyats
The Electrophysics Institute
of the Russian Academy of Sciences,
Ural Division, 620219, Ekaterinburg, Russia

Abstract

The present paper gives a description of the metal-dielectric cathode operation. There is an explosive electron emission on the cathodes, that occurs through explosions of the metal microprotrusions at so-called triple points (metal-dielectric-vacuum). The current of a vacuum discharge over dielectric surface plays its initiating part. Such a mechanism of emission is operating in low-voltage ferroelectric cathodes, in cathodes of long service in high-power pulse repetitive accelerators as well as in the cathodes used in focusing high power electron beams.

1. Introduction

Metal-dielectric cathodes (MDC) have long been used as electron sources in pulsed high-current nanosecond electron accelerators.[1,2] They were used in the first Russian electron accelerators.[3] Unlike simplest metallic cathodes (MC) based on the explosive electron emission (EEE), the MDC, when used, provide a considerable increase in service life. They also make it possible to achieve currents much greater than the Child-Langmuir characteristic and to operate both with high-resistance (~100 Ohm and greater) and low-resistance (1 Ohm and lower) diodes. Besides, they enable diodes to be constructed for a very low voltage (down to hundreds of volts). MDC are divided into two groups: controllable and uncontrollable. The controllable MDC have a special trigger electrode to which a start pulse is applied to initiate the emission of electrons. In our opinion such an electron emission from MDC is dictated by microexplosive processes, an ecton initiation and, eventually, the explosive emission. However, in contrast to MC in that EEE is

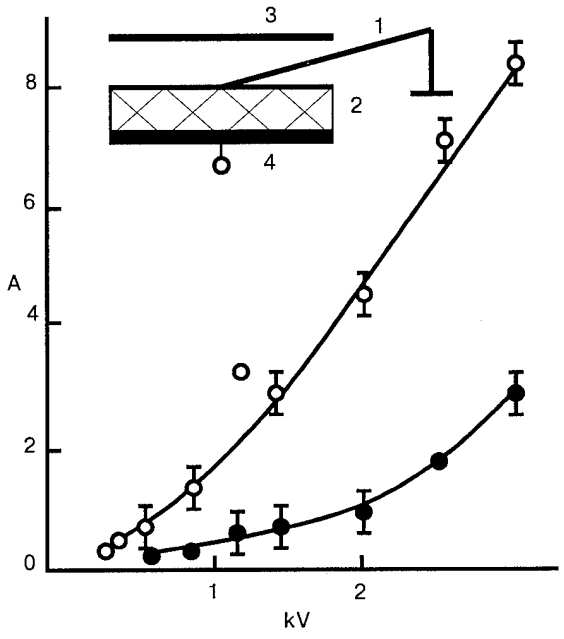


Fig. 1
Schematic of the experiment with a triple point: 1 - cathode; 2 - dielectric; 3 - anode; 4 - triggering electrode (a silver strip fused into the ceramics).
The discharge current over the surface of dielectric plate (BaTiO3) of 2 mm in thickness as a function of voltage: the upper curve corresponds to the negative electrode 1 relative to the electrode 4; the lower curve corresponds to the positive electrode 1.

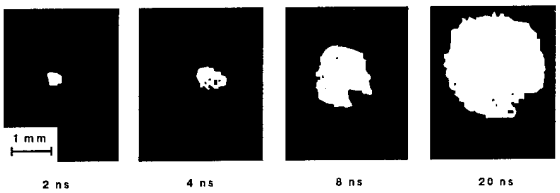


Fig. 2
Discharge glow in the region of a triple point at different instants of time.

initiated by the field emission current, in the MDC the EEE is initiated in so called triple points (TP - metal-dielectric-vacuum) through the current of a discharge over the dielectric surface.

2. Investigation into the role of triple points.

To explore the part played by TPs a special experiment was carried out. On one side of a $BaTiO_3$ (BT ceramic) disk of thickness $\delta = 2$ mm, a silver layer was applied, while against the other side a tungsten needle was retained. The needle served as a diode cathode, the anode being placed at a distance $d \sim 1$cm from the cathode (Fig.1). Voltage pulses of amplitude $U_0 = 0.4$ to 4 kV and duration 2, 4, 20 and 50 ns were applied between the silver layer and the needle. The voltage, the current through the ceramics and the electron emission current from the needle tip were measured simultaneously and the discharge glow was photographed. A voltage pulse of amplitude U up to 30 kV and duration 25 ns was applied to the anode. A discharge near the needle occurred once the voltage exceeded some threshold value. Some time later an electron current appeared in the diode. The discharge glow had the shape of a sphere and expended with a velocity $v_d = AU_0$, where $A = 5 \times 10^2$ and 2×10^3 cm/sV for positive and negative polarity of the needle, respectively (Fig.2).

Figure 3 shows the electron current as a function of diode voltage U depending

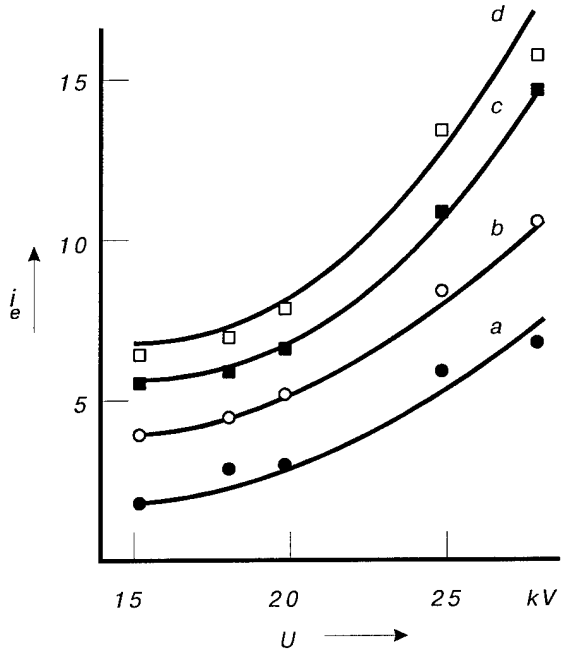


Fig. 3
Emission current from the discharge plasma into vacuum as a function of the voltage at the extractor, with point 3 being in positive polarity with respect to electrode 2. U_0=1.8 kV (a), 2.3 kV (b), 2.75 kV (c), and 3.1 kV (d).

on the dielectric voltage U_0. The increase in electron current is associated with a build-up of the emission area with speeding up the expansion of the discharge plasma.[4]

3. Ferroelectric cathodes.

In the recent years a number of publications on the electron emission from ferroelectric cathodes have appeared.[5,6] Ferrodielectrics are ceramics containing the compounds $PbZrO_3$, La_2O_3, and $PbTiO_3$. These ceramics are designated PLZT by the initial letters symbolising the metals involved. A cathode of this type is simple in construction. This is a PLZT ceramic plate of several milimeters in thickness with a solid silver layer fused into the plate from one side (a trigger electrode, TE). From the other side the plate is covered with a large number of silver strips parallel each other (a grid). The silver layer thickness is ≈ 1 μm on

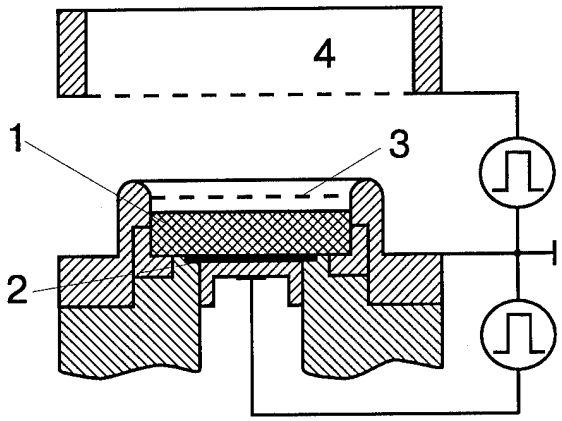


Fig. 4
Circuit diagram showing the connection of the electron source. 1 - dielectric, 2 - silver, 3 - grid, 4 - anode.

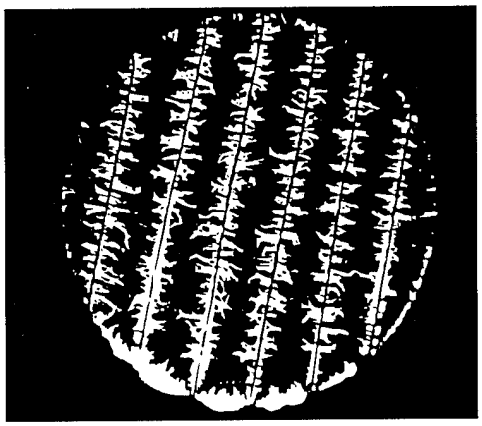


Fig. 5
The metal-dielectric cathode for electron production. Seen are the discharges on the surface of the dielectric.

both sides. The anode to which an acceleration voltage is applied is placed parallel to the grid. The grid is grounded. An up to 2 kV trigger pulse of duration $\approx 10^{-7}$ s is applied to the TE. In the cathode-anode vacuum gap of the diode an electron current appears; the current is a hundred or more times higher than the Child-Langmuir current and shows a pronounced threshold depending on the voltage applied to the ceramics. Early in the pulse the electron current increases almost linearly with time; An investigation into the current structure has shown that it consists of individual bursts that merge into a single flow.[6]

The PLZT ceramics possesses non-linear properties. The dependence of the charge on applied voltage has a hysteretic character.[5] The dielectric constant of the ceramics under normal conditions ranges[7] within $(1-5)\times 10^{-3}$. The authors of the available publications do not propose a convincing theory of the emission observed, relating it, however, to special properties of the PLZT ceramics. It is even stated that the case in point is an essentially new type of electron emission that they call "ferroelectric electron emission". The ferrodielectric cathodes are absolutely identical in design to those described in Ref. 5 and 6, except that it was barium titanate ($BaTiO_3$ with $\varepsilon \geq 10^3$) that was used as a ceramics component. (Bellow it will be referred to as BT ceramics.) The trigger electrode was made of fused silver, with the grid consisting of thin wires scratched (Fig. 4). The height of the T ceramic plate was several millimeters, and the trigger pulse had an amplitude up to 3 kV and duration of 100 ns. Thus, our BT cathode had the same design as the PLZT cathodes and the parameters close to the ones of the trigger circuit.

Studies of the BT cathodes[1-4] have demonstrated that a fundamental part is played by the triple points (TPs), metal-dielectric-vacuum, formed at the sites where the grid is in contact with the dielectric. At these sites a discharge over the dielectric surface occurs, whose current, when passing through the metal-dielectric contact, results in microexplosions of the grid microregions. This, in turn, causes the well-studied explosive electron emission (EEE).[3] These discharges over the surface of BTT ceramics are illustrated in Fig. 5. Used as a grid were thin copper wires tightly applied on the ceramics. The electron current from such a

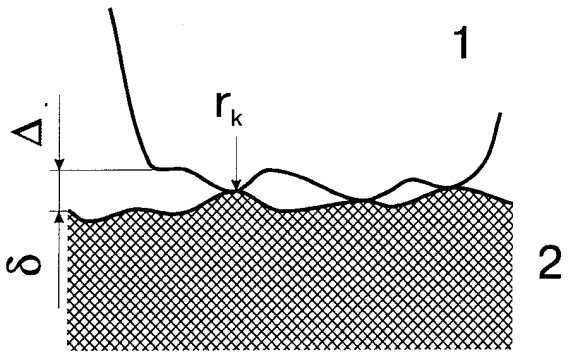


Fig. 6
Configuration of a metal-dielectric contact. 1- metal, 2 - dielectric.

cathode was more than an order of magnitude higher than the Child-Langmuir current.[2]

4. Mechanism of electron emission from MDC.

The above results furnish insight into the mechanism of the electron emission from MDC. The grid applied on the ceramics surface has numerous TPs on the silver strips. However, in order that these TPs be capable of initiating a discharge, there should be at least unit charged particles in the neighbourhood of TP. They may appear when the electric field E_m is rather high at the metal. With the uneven edges of the grid and the pores in the surface layer of the ceramics this field is defined as $E_m \approx U_0\, \varepsilon / d$ for $\delta << \varepsilon\, \Delta$, where Δ is an effective gap at a metal-dielectric contact (Fig. 6). Since $U_0 / \delta \approx 10^4$ V/cm and $\varepsilon > 10^3$, then we have $E_m > 10^7$ V/cm. Depending on the grid polarity this field causes an emission of positively or negatively charged particles which may initiate a surface discharge.

The current in the region of a TP will be determined from the relationship $i = U_0\, dc/dt$, where C is the dynamic capacitance created by the plasma and the TE. If $tv_d << d$, then we have $C = 4\varepsilon_o \varepsilon\, v_d t$, where v_d is the velocity of expansion of the discharge plasma over the dielectric. Hence, the current is defined as $i = 4\varepsilon_o \varepsilon\, AU_0^2$. Such a current will flow in the metal-dielectric contact through an area $S_k = \pi\, r_k^2$ (see Fig. 6). The current density through this contact will then be $j_k = 4\varepsilon_o \varepsilon\, AU_0^2 / \pi\, r_k^2$. The metal in contact will explode in a time $t_e = \bar{h} / j_k^2$, where $\bar{h}$ is a specific action which, to a first approximation, may be considered as a characteristic of the metal. The time t_e will then be found from the relationship:

$$t_e = \bar{h}\, \pi^2 r_k^4 / 16\varepsilon_o \varepsilon\, A^2 U_o^4. \qquad (1)$$

To produce a uniform electron beam it is essentially that for a large number of TPs the time t_e be much shorter than the trigger pulse duration t_p, $t_e << t_p$.

$$r_k << \left(\frac{16\varepsilon_o^2 \varepsilon^2 A^2 t_p U_o^4}{\pi^2 \bar{h}} \right)^{1/4}. \qquad (2)$$

For a silver contact we have $\bar{h} = 0.8 \times 10^9$ $A^2 cm^{-4} s$. For $t_p = 10^{-7}$ s, $\varepsilon \approx 10^3$, $U_0 = 10^3$ V, and $A = 5 \times 10^2$ cm $s^{-1} V^{-1}$ we obtain from the relationship (2) $r_k << 2 \times 10^{-5}$ cm. This means that for the time t_p microexplosions of the metal will occur at all the triple points where the contact radius is less than 10^{-5} cm. From the explosion sites electrons will be emitted by the EEE mechanism.

Reasoning from the above considerations we shall offer an explanation for some observations on PLZT cathodes.[5,6]

For instance, their high sensitivity to the voltage at the ceramics follows from Eq. (1), since the time to a microexplosion t_e is proportional to U_0^{-4}. The short time current bursts are closely related to the mechanism of EEE.[3] Once EEE has occurred, the cathode plasma starts propagating toward the anode with a velocity $v \approx 10^6$ cm/s. For a plane electrode the electron current will be written as follows:[3]

$$I = aU^{3/2}s / (d - vt)^2, \qquad (3)$$

where $a = 2.33 \times 10^{-6}$ $AV^{-3/2}$, U is the voltage across the diode, S - the cathode area and d - the cathode-anode separation. From Eq. (3) it follows that for $t << d / v$ the electron current will be given by

$$I \approx aU^{3/2} \frac{s}{d^2}\left(1 + \frac{2vt}{d}\right), \qquad (4)$$

i.e. the current will increase linearly with time, which was just observed in experiment by Gundel.[6] Formally, Eq. (3) suggests that it is possible to produce an electron current considerably greater than the Child-Langmuir current $I_{ChL} = aU_0^{3/2}s/d^2$, and this was actually observed both by Schachter et al.[5] and by Gundel.[6] Moreover, this should be the case for both PLZT ceramics and BT ceramics. The diode may be preliminary filled with plasma so that the current would then flow in the plasma-filled diode.

The delay in the appearance of an electron current concerning the application of a voltage to the ceramics is, on the one hand, due to the delay in the appearance of the EEE and, on the other hand, because, according to the Eq. (3), the current increases as the cathode plasma propagates deeper in the cathode-anode gap. This is why the current is initially small and it is exactly this fact that is taken for the delay of electron emission. Finally, Gundel[6] noted that as the temperature of the PLZT ceramics was elevated to 150°C, the charge of the electrons emitted by the cathode increases more than twice. Taken into account that the capacitance of the ceramics, and hence ε, increased almost three-fold,[6] we obtain that according to Eqs. (1) and (2) this causes an increase in both the number of microexplosions and the electron current from the cathode.

5. Different types of MDC.

There are a variety of MDC types performing different functions. For example, some MDC are capable of focusing a beam. One can find in Ref.8 a description of the cathode of half-cone shape. There is a bore in the cathode with a dielectric cylinder fixed in. The cylinder has a metallic pin inserted. As a voltage is applied to the diode, there is a discharge beginning with the pin. The dielectric is charged and a discharge is initiated over its surface. A plasma resulting from the discharge is instrumental in focusing the beam.

For the beam to be uniform in cross-section, the surface craters are filled with a plastic pressed in.[9] At the expense of the high electric field there are electrons emitted at the sharp edges of a crater. When hitting the dielectric, the electrons cause the discharge over the surface, which provides for the cathode to be filled uniformly with plasma.

For the purpose of having a large cross-sectional beam in pumping lasers one can refer to G.K. Loda[10] who offers a MDC with a dielectric plate covered with silver foil on both sides. One side of the foil is drilled with a great number of holes. Then the dielectric is put on with round pieces made of the same foil. Such pieces are fixed

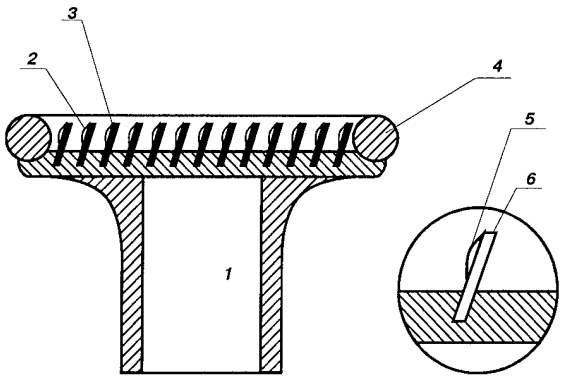


Fig. 7
Schematic of a metal-dielectric cathode: 1 - cathode holder; 2(5) - cathode made of bronze foil; 3(6) - dielectric; 4 - screen.

at the center of the holes. As a voltage is applied, at the edges of the pieces a strong electric field arises due to capacitive links between the pieces and the upper and lower foils. This field results in the discharge over the dielectric surface and thus in filling the cathode with plasma.

Recent trends are toward increased efforts in creating long-living MDC to serve in pulsed electron accelerators of technological purposes. One can find one of the first cathodes for "Sinus" accelerator described in Ref.11. The cathode has a ceramic cylinder to which two bronze foil plates are firmly attached. To fix the triple points more definitely there are dents made at the edges of the foil. One foil is connected with a negative electrode of the accelerator; the second foil is under the floating potential to provide capacitive link with the ground. To increase service life of the MDC the cylinder is rotated slowly. Such cathodes, at an average power of the electron accelerators of 10 - 15 kW, experienced more than 10^8 shoots with no destruction observed.

Fig.7 shows the MDC developed in Tomsk by S.D.Korovin et.al. The cathode is long-lived. The cathode has a plane metallic plate in the surface of which a number of slots are made. Many ceramic plates are inserted in these slots. A springy bronze foil in the form of arcs is pressed against these plates. One edge of the foil is fixed in the slot with the dielectric; another edge is pressed down to the tip of the ceramics. When a voltage pulse is applied, such a ceramic tip undergoes a surface discharge that results in initiation an ecton and the explosive electron emission.

References

1. S.P. Bugaev, F.Ya. Zagulov, B.M. Kovalchuk, G.A. Mesyats. A Pulsed Source of Great Electron Currents. - Izv. Vyssh. Uchebn. Zaved. Fizika, 1968, No 1, p.45.

2. G.A. Mesyats. Controllable Electron Sources. - In: Cold Cathodes, Moscow: Sov. Radio, 1974.

3. G.A. Mesyats. Generation of High-Power Nanosecond Pulses. - Moscow, Sov. Radio, 1974.

4. S.P. Bugaev, G.A. Mesyats. Electron Emission from the Plasma of an Uncompleted Discharge over a Dielectric in Vacuum. - Dokl. AN SSSR, 1971, v.196, p.324.

5. L. Schachter, J.D. Ivers, J.A. Nation, Kerslick. Analysis of Diode with a Ferroelectric Cathode. - J. Appl. Phys., 1993, 73(12), p.8097.

6. H. Gundel. Electron Emission by Nanosecond Switching in PLZT. - Integrated Ferroelectric, 1992, v.2, p.202.

7. L.L. Hench, J.K. West. Principles of Electronic Ceramics. - John Wiley & Sons, 1991.

8. A.L. Filatov, Yu.A. Kotov, V.A. Motovilov, V.A. Scotnikov. Electron Beam Focusing and Unfocusing Experiment. - Proc.XVIth Intern. Symp. on Discharges and

Electrical Insulation in Vacuum, 1994, Moscow-St. Petersburg, 23-30 May, SPIE Press, pp. 403-408.

9. H. Clark, M. Ury, M. Andrews, D.A. Hammer, S. Link. High Current Relativistic Electron Beam Accelerators at Cornell University. - Proc.Xth Symp. on Electron, Ion and Laser Beam Technology, Geitensburg, May 1969, San Francisco Press.

10. G.K. Loda. Recent Advances in Cold Cathode Technology as Applied to High Power Lasers. - Proc.IInd Intern. Topical Conf. on High Power Electron and beam Research and Technology, 1977, v.2, pp.879-890.

11. G.A. Mesyats. Vacuum Discharge Effects in the Diodes of High-Current Accelerators. - Plasma Science, 1991, v.19, No 5, pp.683-689.

THE DYNAMICS OF GENERATION OF HIGH CURRENT RELATIVISTIC ELECTRON BEAMS IN COAXIAL MAGNETICALLY-INSULATED VACUUM DIODES

S.D. Korovin, I.V. Pegel

High Current Electronics Institute, Russian Academy of Sciences, Siberian Branch

4 Akademichesky Ave., Tomsk, 634055 Russia

Abstract

The paper presents the results of both experimental and numerical (2D steady-state and 2D, 3D time-dependent PIC-codes) investigation of generation of high current moderately relativistic electron beams (500 keV, 5 kA, 20 ns) in a vacuum coaxial MID's within the full space charge regime. Explosive emission edge cathodes have been used in the experiment.

Conclusions are drawn how the beam generation is effected by:

- both the explosive emission expansion and the cathode plasma flying apart;
- vibrations of the electron flow self space charge within the crossed fields near the cathode surface.

High current hollow relativistic electron beams (REB's) are widely used to drive powerful microwave devices of different types. In this applications, the knowledge of both the spatial and temporal beam parameters is important.

For the generation of such beams, vacuum coaxial magnetically-insulated diodes (MID's) [1] with explosive emission edge cathodes are usually used. In this work, foilless MID's are investigated. To avoid the influence of drift instabilities onto the beam structure, the length of the drift tube was chosen small in the experiments. Attention was focused basically on the near-cathode region.

The full information about the experiment and computer simulations is contained in [4,5]. Below, the facts are mentioned relating only to nonsteady-state features of the beam behavior.

Experimental investigation was fulfilled on the high current electron accelerator SINUS-6 [2]. The beam energy was about 500 keV and the current was 5 kA, with the pulse duration of 20 ns. Explosive-emission graphite cathodes of 3 cm in diameter have been used with the edge as thick as 0.8 mm.

To measure the radial current density distribution of the beam, it was passed through small holes within a thin transversal diaphragm.

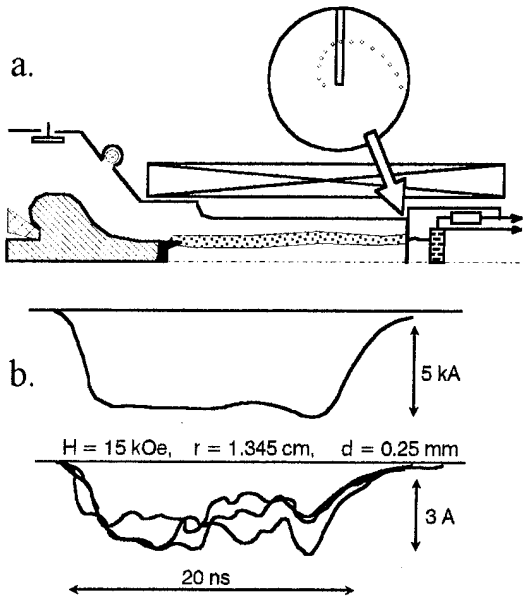


Fig. 1. Measurement of the beam radial current density distribution (a), and the traces of total beam current and the small hole current (b)

The pulses of the total beam current were smoothly shaped and repeated with the accuracy of 2-3%. In this connection, the instability of the small holes current came as a surprise (Fig. 1b). At each pulse, these currents oscillated with typical times of several nanoseconds.

The beam radial current distribution depends strongly on the value of guiding magnetic field. At low fields, it varies significantly with the length.

In strong magnetic fields (> 10 kOe) the distribution takes a typical two-maxima shape (Fig. 2b), with low current stability within the "valley". The latter is caused probably by electrostatic suppression of the central part of the cathode edge by electron flows from its periphery.

In both cases, the time-integrated beam cross-section pictures possessed good azimuthal uniformity.

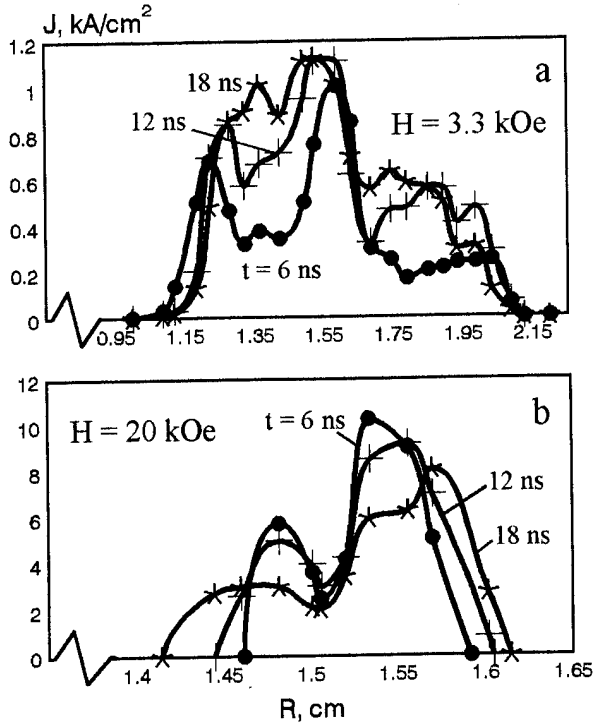


Fig. 2. The beam current density distribution in low (a) and high (b) magnetic field

At low magnetic field, regular growth in the total current was observed during the beam pulse but the increase in current density was observed only at specific radii (Fig. 2a). This phenomenon is caused, indubitably, by the cathode emission area evolution. It is interesting that the effective thickness of the beam increases in time, while the "formal" thickness even decreases.

In strong magnetic fields, conversely, the beam gets thicker during the time of a pulse duration, but its total current remains constant (Fig. 2b). In this case the values of electron cyclotron radii are small, and the effect was explained by transversal expansion of the cathode plasma. An estimation of the plasma velocity gave $2 \cdot 10^6$ cm/sec, which is in agreement with the known results [3].

It is obvious that the growth of current in small magnetic fields is a direct consequence of the increasing beam thickness. At constant diode voltage, the beam current is determined only by the electric charge distribution within the diode, and the decrease of distance between the beam and the anode wall should reduce the diode impedance. The emission surface evolution, which leads to the thickening of the beam, may be caused by gradual expansion of the explosive emission region onto the side cylindrical surface of the cathode, where the electric field is lower than on the edge and the explosive emission delay time is, consequently, larger [3]. Thus, the current is gradually redistributed to the electron fraction with largest cyclotron radii, and this effect causes the beam thickening and the current increase. This phenomenon takes place in strong magnetic fields as well, but it is not effective because of the small cyclotron radii of electrons. Thus, the leading role in the beam thickening is played by the transversal expansion of the plasma. However, at nanosecond pulse duration, it doesn't cause any significant growth of current because the related beam thickening is small compared to the diode gap.

When making measurements of cyclotron rotation radii of the beam electrons, the beam was passed through a collimator having long longitudinal leafs. As mentioned above, the pulses of the total beam current were smooth and well-reproducible. At the same time, however, for small collimator opening angles, the passed current was unstable from pulse to pulse, as well as during each pulse. The character of instability closely resembled the situation when using the small holes.

The scale of the beam "instant" azimuthal nonuniformity has been measured with the use of this collimator. It was found that the dependence of this scale on the magnetic field strength correlates with the dependence of maximum cyclotron radii of electrons.

The analysis of experimental facts suggests that the current oscillations measured within small beam cross-sections are not caused by either the beam drift instabilities or the collector plasma effects. As for the cathode processes, two possibilities remain:

1. Fast oscillating changes of the cathode emitting area, connected with the dynamics of explosive electron emission.
2. Electrodynamic phenomena within the electron flow near the cathode.

Below, the emphasis is placed on the phenomena of the second group.

Numerical Simulations. The Steady-State modeling of the diode has been performed with the use of 2D axisymmetric code SUPERSAM, developed at the Budker Institute of Nuclear Physics (Novosibirsk, Russia).

Agreement with the experiment was achieved only if the emission was coincident with the cathode edge. In the case of the emitting outer cylindrical surface, the convergence of the iteration procedure disappeared. The reason of the absence of a steady-state solution should be connected with an electron flow instability within the crossed fields near the cylindrical cathode surface. The instabilities of this sort are known in magnetron diodes.

PIC-simulations. The experiments testify the MID-generated beams to possess significant "instant" azimuthal nonuniformity. The consideration of a MID as a magnetron diode was useful to understand devices of azimuthal beam structure formation.

The process of an electron flow establishment within a 2D (infinitely long) magnetron diode has been simulated using the potential field approximation. Both the diode voltage and the emission current have been turned on instantly fast.

Pronounced oscillatory behavior and the azimuthal stratification of the electron flow have been demonstrated. The waves of total electrostatic screening have been observed propagating along the cathode surface. In the non relativistic case, the obtained dispersion relations agreed with the analytic expressions derived on the assumption that the evolution of the electron cloud starts within a two-flow regime with the following transition into a single-flow regime.

In order to account the effects of finite length of the diode, a simple 3D potential PIC-simulation has been fulfilled (Fig. 3). Two charge-carrying zones were included to form a longitudinal

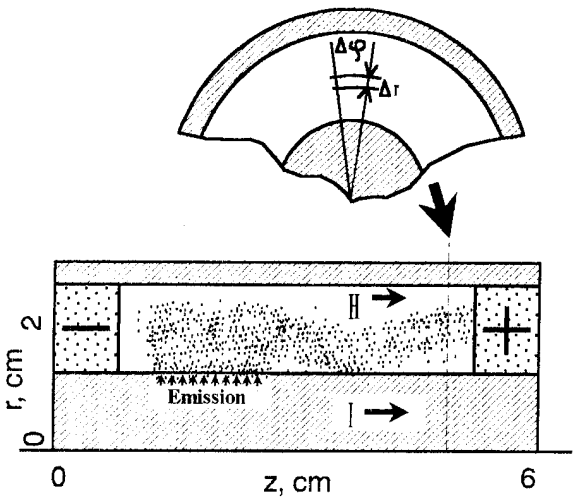


Fig. 3. The 3D PIC simulation region

electron flow, and a direct current flowing along the inner conductor to substitute the electron current from the cathode edge. The diode voltage was 500 kV.

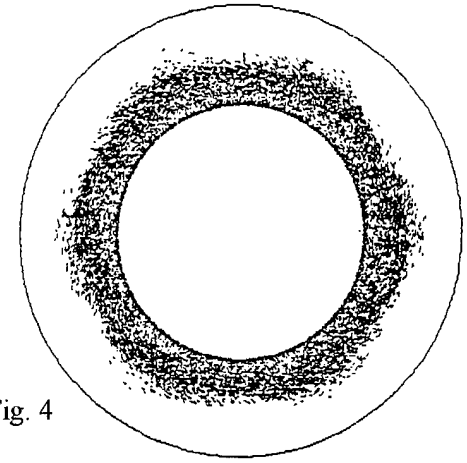


Fig. 4

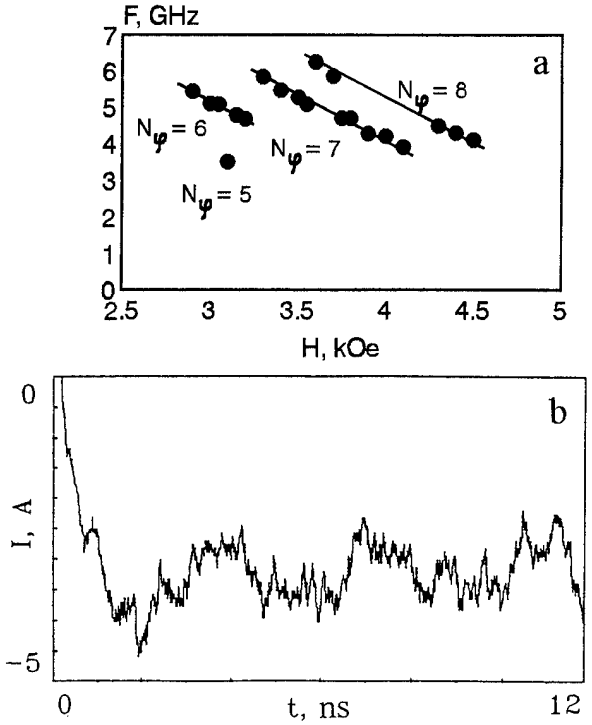


Fig. 5. Frequency of space charge oscillations and the number of azimuthal variations (a) and a trace of the small beam cross-section current after HF filtration (b). 3D simulation.

Fast "magnetron" oscillations have been observed within the electron cloud formed above the emitting zone, escorted with its azimuthal stratification (Fig. 4). The dependencies of the oscillation frequency and the number of azimuthal variations on the magnetic field are given on Fig. 5a.

The cloud oscillations cause the vibrations of current density within the beam produced. The scale of nonuniformity is determined by the value N_φ, and the depth of modulation is about 10%. Therefore, the beam possesses a multi-set helical modulation in current density.

The current oscillation spectra contain intensive chaotic background as well, especially, at the boundaries between different values N_φ. After a filtration of high frequencies, it appears as slow irregular oscillations within the current traces with typical times of several nanoseconds (Fig. 5b). Evidently, namely these oscillations have been observed in the experiment, while the fast "magnetron" vibrations could not be registered because of insufficient frequency bandwidth of the current measuring system.

Conclusions. At short pulse duration, the structure of the electron beam formed in a coaxial MID with an explosive-emission cathode is effected by nonsteady-state processes of the explosive emission expansion and the cathode plasma flying apart. Also, if the diode geometry allows the existence of strongly crossed fields near the electron emitting areas, oscillations of the space charge occur near the cathode. As a result, the electron beam possesses azimuthal nonuniformity. The current density oscillations appear within the small beam cross-sections.

References

1. Bugaev S.P., *et al.*, in Relativistic High Frequency Electronics. IPF USSR Acad. Sci., 1981, p. 37.

2. Elchaninov A.S., *et al.*, in Relativistic High Freq. Electronics. IPF USSR Acad. Sci., 1981, p. 5.

3. Mesyats G.A., Proskurovski D.I. Pulsed Electrical Discharge in Vacuum. Springer-Verlag, 1989.

4. Korovin S.D., Pegel I.V. Journal of Technical Physics (Russian), 1992, 62, N 4, p. 139.

5. Korovin S.D., Pegel I.V., to be published in Journal of Technical Physics (Russian).

LIF Standoff Research*

C.L. Olson,[1] M.E. Cuneo,[1] M.P. Desjarlais,[1] A. B. Filuk,[1] J. B. Greenly,[6] D.L. Hanson,[1] D.D. Hinshelwood,[2] R.F. Hubbard,[3] M. Lampe,[3] T.R. Lockner,[1] J.E. Maenchen,[1] M.G. Mazarakis,[1] C. W. Mendel, Jr.,[1] P. R. Menge,[1] D. Mosher,[3] T. J. Nash,[1] J.M. Neri,[3] W. Noonan,[3] B.V. Oliver,[6] J.C. Olson,[6] R.E. Olson,[1] P.F. Ottinger,[3] R.R. Peterson,[7] T.D. Pointon,[1] J.W. Poukey,[1] J. P. Quintenz,[1] D.V. Rose,[2] T.W.L. Sanford,[1] S.P. Slinker,[3] S.A. Slutz,[1] J. R. Smith,[5] S.J. Stephankis,[3] D.R. Welch,[4] and F.C. Young[3]

[1]Sandia National Laboratories, Albuquerque, NM 87185
[2]JAYCOR, Inc., Vienna, VA 22182
[3]Naval Research Laboratory, Washington, DC 20375
[4]Mission Research Corporation, Albuquerque, NM 87106
[5]Titan Corporation, Albuquerque, NM 87106
[6]Cornell University, Ithica, NY 14853
[7]University of Wisconsin, Madison, WI 53706

Abstract

Present LIF target experiments on PBFA II use a barrel diode in which the total transport length from the anode to the target is $\lesssim$15 cm. Future LIF development includes high yield applications (LMF) and energy production (ETF and LIBRA power plants) that require standoff - the generation of extracted ion beams and transport of these beams over distances of several meters. Standoff research includes the development of high efficiency extraction diodes (single stage and two-stage), improvements in beam quality (divergence, purity, uniformity, etc.), and the efficient transport and focusing of these beams over distances of several meters to a fusion target. Progress in all of these areas is discussed, as well as a strategy to reduce the divergence from the present 17 mrad for 5 MeV protons on SABRE to the required 6 mrad for 35 MeV Li ions for LMF. The status of experiments is summarized, and future directions are indicated.

Introduction

The Light Ion Fusion (LIF) program at Sandia National Laboratories (SNL) is developing light ion drivers for the long range goals of high-yield applications and energy production. The high yield applications require development of a laboratory microfusion facility (LMF) with a fusion yield of 200-1000 MJ for an input beam energy of the order of 10 MJ, on a single shot basis. Energy production requires fusion yields of the order of 200-600 MJ for an input beam energy of several MJ and a repetition rate of several Hz. Present LIF target experiments on PBFA II use a barrel diode in which the total transport length from the barrel-shaped anode to the centrally-located target is $\lesssim$15 cm. Future LIF development will require standoff - the generation of extracted beams and the transport of these beams over distances of several meters from the diode to the target. In this paper, recent results and the status of research on standoff are summarized, including future development options.

Generation of Extracted Beams

Extraction diodes are required for all high yield and energy applications. Barrel diodes and extraction diodes are compared in Fig. 1. Barrel diodes are used on PBFA II and have been the foundation of the LIF program. Extraction diodes have been used on

many smaller machines, including ALIAS (SNL), LION (Cornell), SABRE (SNL), KALIF (KfK), REIDEN IV (ILE, Osaka), and GAMBLE II (NRL). Both types of diodes have an applied B field to magnetically prevent the electrons from crossing the anode-cathode gap, cathode tips to generate the electron flow, an anode ion source, and a ballistic aiming geometry. Because of the placement of the applied B field coils, beams from extraction diodes are typically annular. Research on extraction diodes parallels that for barrel diodes, and is directed toward optimizing coupling to magnetically insulated transmission lines (MITLs), suppressing any parasitic load (as defined in the following), reducing beam divergence, and improving ion source characteristics.

Power flow and MITL coupling have been studied in SABRE experiments,[1,2] and with computer simulations.[3,4] TWOQUICK simulations of SABRE have been used to model the voltage adder, MITL extension and applied B extraction diode.[3] Voltage precursor effects were shown to dominate both the MITL operation and the diode impedance history. The precursor can be eliminated by (i) using a plasma opening switch, as has already been demonstrated on SABRE,[1] or by (ii) using field enhancing inserts on the cathode. SABRE experiments[2] iterated with TWOQUICK simulations,[4] including diffusive electron losses, have substantially improved the ion beam uniformity.

The parasitic load problem refers to the diode losses following the initial pulse of desired ions. The source(s) of the parasitic load apparently involves formation of ions from electron thermal and stimulated desorption of neutrals with subsequent avalanche ionization. Detailed experiments with extraction diodes on SABRE,[5] LION,[6] and GAMBLE II[7] are underway to diagnose, understand, and remedy this parasitic load loss. The formation of neutrals may be controllable by proper diode cleaning techniques which are presently under investigation (RF discharge cleaning, inductive heating, titanium gettering, etc.).

Ion source research is concentrating on development of EMFAPS (exploding metallic film active anode plasma source). EMFAPS is a separately-driven anode ion source that should provide better source turn-on, a more uniform beam, and a better diode impedance history than passive sources. Results on LION[6] and GAMBLE II[7] show these advantages. In addition, a new beam uniformity diagnostic has been developed at SNL that will be used to measure beam uniformity on both a macroscale (cm's) and microscale (~ 1 mm).[8]

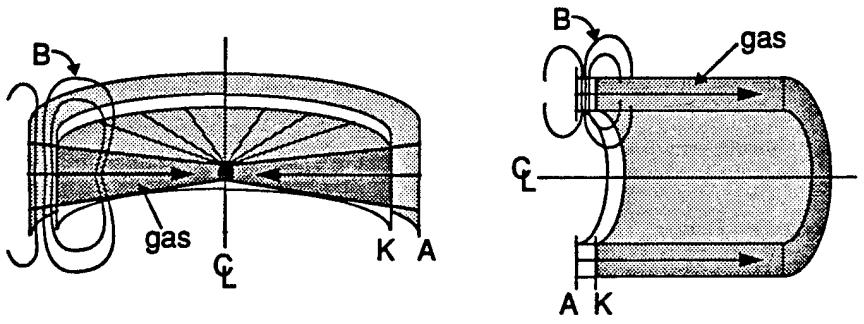


Fig. 1 Barrel diode and extraction diode compared.

The ion beam microdivergence θ_μ is being examined in 3D QUICKSILVER simulations of the SABRE diode[9]. Earlier work indicated divergences in extraction diodes were typically lower than in barrel diodes. The present simulations use a geometry closer to the SABRE diode, and actual values of experimental applied B fields and driver voltages. The instability evolution[10] still shows a diocotron instability (with $\theta_\mu \sim 10$ mrad) followed by a transition to the ion mode (with $\theta_\mu \gtrsim 30$ mrad).[9] VUV and visible spectroscopy diagnostics are now used to view the SABRE A-K gap and should help lead to a detailed understanding of $\theta_\mu(t)$.[11]

A divergence reduction strategy has been developed to reach the goal of $\theta_\mu \sim 6$ mrad for 35 MeV Li for LMF, which is required for all transport modes. In Table 1, a summary of achieved and proposed divergence values is given. For each case, the accelerator, ion species, diode type, ion energy, and θ_μ are shown. Also shown is the equivalent θ_μ for LMF. This is defined by assuming the ion transverse temperature is fixed and the ion axial velocity, v_i, is increased to $\beta = v_i/c = 0.1$. This concept of divergence reduction has already been demonstrated in two-stage diode experiments on ALIAS.[12] Note that a 5 MeV proton and a 35 MeV Li ion have the same value of β. Most importantly, note that LMF equivalent values of $\theta_\mu < 9$ mrad have already been achieved on ALIAS, KALIF, PBFA II, LION, and GAMBLE II.

The last three lines in Table 1 outline our strategy for achieving 6 mrad for LMF. The first goal is to achieve 12 mrad for 5 MeV protons in a single-stage diode on SABRE. This represents a substantial improvement

Table I. Microdivergence (θ_μ): Achieved and Proposed.

Accelerator	Ion	Diode	ε_i(MeV)	θ_μ(mrad)	Status	Equivalent θ_μ(mrad) for LMF ($\beta = 0.1$; 5 MeV p or 35 MeV Li)
ALIAS	p	1-stage	< 0.6	19	achieved	< 6.6
ALIAS	p	2-stage	> 1	10	achieved	> 4.5
KALIF	p	1-stage	1.7	15	achieved	8.7
PBFA II	Li	1-stage*	9	17	achieved	8.6
SABRE	p	1-stage	5	17	achieved	17
LION	p	1-stage	1	19	achieved	8.5
GAMBLE II	p	1-stage	1	17	achieved	7.6
SABRE	p	1-stage	5	12	proposed	12
Hermes III	Li	2-stage	14	9	proposed	6
LMF	Li	2-stage	35	6	proposed	6

*barrel diode; all other cases are extraction diodes.

over the current value of 17 mrad. The second goal is to achieve 9 mrad Li ions at 14 MeV in a two-stage diode on Hermes III. Note that in terms of LMF equivalent values of θ_μ, this requires only a reduction from the PBFA II equivalent LMF value of 8.6 mrad to 6 mrad. The third goal is to achieve 6 mrad for LMF. Having achieved 9 mrad on HERMES III at 14 MeV means that by simply increasing the diode voltage to the full LMF value will produce 35 MeV Li ions at the desired 6 mrad.

Beam Transport

High yield applications (LMF) and energy production have similar multiple-beam transport requirements.[13-15] For LMF, beams will be produced in extraction diodes which are voltage-ramped (26-35 MeV Li) to produce axial time-of-flight bunching by about a factor of two. The diode-to-target transport length will be 400 cm, and any final focusing shielding element must be at least 100 cm from the target to avoid excessive erosion. The transport method must accommodate the energy spread produced by the ramped voltage, the diode must be protected from the blast, and minimal transport apparatus is allowed inside the containment chamber.

The baseline LMF transport method, which satisfies all of the above LMF requirements, is an achromatic lens system.[16-18] This system consists of the high current extraction diode (which acts as a self-field lens) and a solenoidal lens. As shown in Fig. 2, the beam is transported ballistically in gas from the diode to the lens over a distance L, is focused by the lens, and then is transported ballistically in gas from the lens to the target over a distance F. For LMF, L = 300 cm and F = 100 cm. The gas is assumed to provide complete charge and current neutralization. The diode lens and solenoidal lens act together to form a system that is achromatic to lowest order in the diode voltage ramp variation. The main features are that the spot size is determined by $\theta_\mu F$ [and not $\theta_\mu(F + L)$], there is no apparatus inside the chamber, and the diode is shielded from debris by a center plug which fits inside the annular beam. The basic elements of this system (diode lens effect, gas neutralization, and solenoidal lens effect) are all routinely observed on PBFA II, although a complete extracted-beam, achromatic system has not been demonstrated.

Backup transport methods for LMF include wall-confined channel transport,[15,19,20] wire-guided transport,[15,21] and self-pinched transport.[22-24] For each of these "channel-like" schemes, the beam from the diode is first focused down to a small radius (< 1 cm) and then transported at small radius over several meters to the target. For LMF parameters (26-35 MeV Li, microdivergence $\theta_\mu \sim 6$ mrad), all channel-like

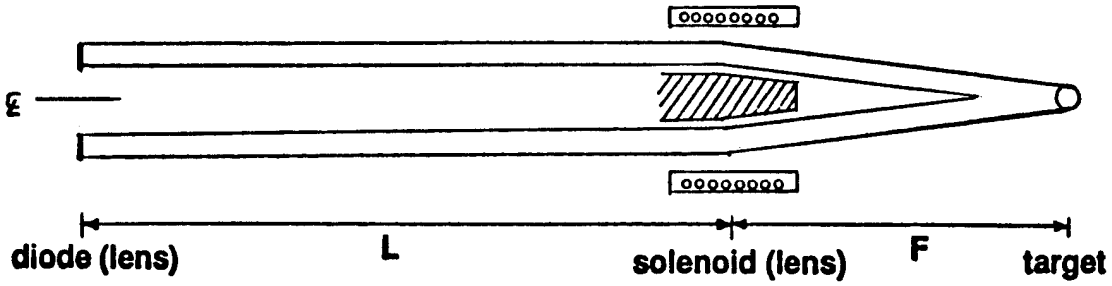


Fig. 2 Achromatic lens system for high yield and energy.

schemes require a channel current $I_c \sim 50$ kA. The current I_c can be from a preformed discharge (wall-confined transport), a wire (wire-guided transport), or from the net current resulting from gas breakdown (self-pinched transport).

Self-pinched transport, as shown in Fig. 3, should be particularly attractive for high yield and energy; here it is proposed to first transport the beam in the self-pinched mode in a guide tube over a sizeable distance ($\gtrsim$ 1 meter) to establish a propagation axis and a quasi-equilibrium radial distribution function. The aimed beam then continues directly into the chamber in the pinched mode. Self-pinched transport is attractive because it requires only small holes in the chamber wall, needs no apparatus inside the chamber, permits gas in the chamber, and allows the diode to be shielded from x-rays and debris. Self-pinched transport has not been demonstrated yet.

Both channel transport and wire-guided transport have been thoroughly demonstrated at low energy (1 MeV p) and are expected to work at LMF energies (35 MeV Li), but require some transport apparatus (low mass tubes or wires) inside the containment chamber; these schemes could be used for LMF. The achromatic lens system and self-pinched transport are attractive because no apparatus is required inside the containment chamber; these schemes can be used for LMF and LIBRA.

All light ion transport schemes involve ion beam interactions with neutral gas, plasma, or electrons to provide charge neutralization and some current neutralization. Present transport research is developing a thorough physics understanding of gas breakdown, which is needed for both the achromatic lens system and self-pinched transport, as well as the ballistic transport input section of all channel-like schemes. Specifically, very high current neutralization ($\gtrsim$ 99.9%) is needed for the achromatic lens system, and moderate current neutralization (~ 90-98%) is needed for self-pinched transport.

Detailed gas breakdown experiments[25,26] are being performed on GAMBLE II at NRL at the 10 kA proton level; the results are in good agreement with IPROP computer code[27] results (see following paper).[28] A unique result is that fast electrons can create a halo conductivity region outside the beam. IPROP treats fast electrons (> 100 eV) as particles, and is thus able to predict non-local breakdown effects.

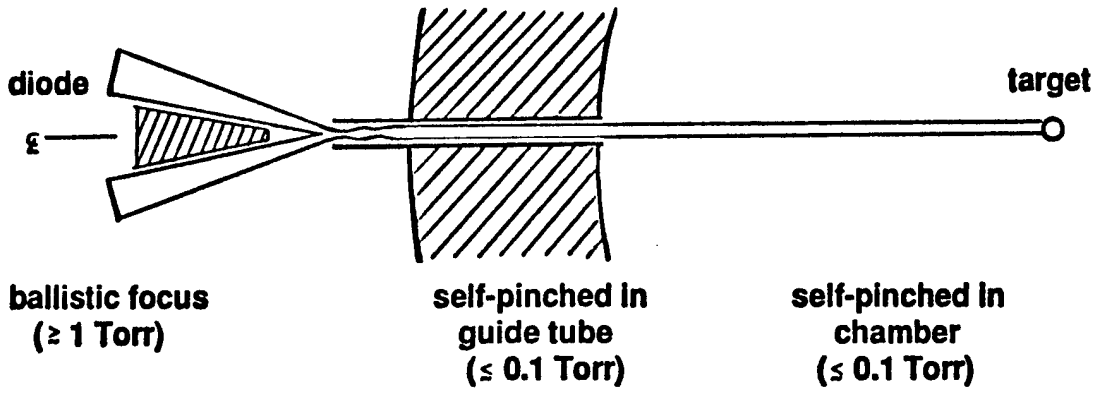


Fig. 3 Self-pinched transport for high yield and energy.

IPROP has also been used to compare with net current measurements for the barrel diode geometry of PBFA II, including applied magnetic field effects. IPROP predicts > 99.8% neutralization for 6 MeV Li ions in 4 Torr argon on PBFA II for ~ 1 MA Li particle current. These results suggest that the high current neutralization needed for the achromatic lens system should be achievable. IPROP simulations of self-pinched transport show that with appropriate parameters, net currents large enough for self-pinched transport should also be achievable.[22-24]

Transport experiments on SABRE and/or GAMBLE II should begin within the next year. The goals will be to continue the current neutralization study, analyze two-stream and filamentation instabilities, demonstrate the solenoidal lens system, and demonstrate self-pinched transport.

Towards High Yield and Energy

LIF is developing towards high yield (LMF) and energy (ETF and LIBRA power plants). Here, LMF, ETF, and LIBRA are briefly summarized, as well as possible LIF development options at SNL.

The light ion LMF consists of twelve A modules (19-24 MeV, 440 kA)[29] and twelve B modules (28-35 MeV, 0.85-1.0 MA) that provide a peak on-target power of ~ 700 TW and a total on-target Li ion energy of ~ 14 MJ on a single shot basis. Target yields will be in the range of 200-1000 MJ, and the standoff distance from the extraction diodes to the target will be 400 cm. This LMF is based on the Hermes III inductive voltage adder technology developed at SNL over the last decade. The mainline transport method is the achromatic lens system, with several back-up methods as discussed above.

The light ion ETF[30] will utilize Repetitive High Energy Pulsed Power (RHEPP) technology developed at SNL,[31] together with Hermes III technology. This ETF will consist of twelve A modules (4.2 MeV, 286 kA) and twelve B modules (37 MeV, 294 kA) that supply a peak on-target power of ~250 TW and a total on-target ion energy of ~ 2 MJ, with a repetition rate of 6 Hz. The pulsed power technology for an ETF test bed module is currently available. Repetitive ion diodes are being developed at Cornell and SNL presently at the ~ 0.1 TW, 1 MeV proton, 40 ns level. Ion diode operation at up to 100 Hz in a burst mode has been demonstrated. Self-pinched transport is the preferred transport mode for ETF.

There are presently three different LIBRA light ion power plant designs.[32,33] The original LIBRA used laser-created, free-standing, Z-discharge channels for transport. The more recent LIBRA-LiTE design uses the achromatic magnetic lens system. A new version, LIBRA-S, is currently being designed to use self-pinched transport. All three LIBRA designs deliver 4-6 MJ on target with a repetition rate of ~ 4 Hz.

In Table 2, the development of pulsed power, extraction diodes, and transport for high yield and energy is summarized. Shown are parameters for current facilities (discussed earlier), current options at SNL, and future directions (discussed above). Current options at SNL include (1) converting Hermes III to positive polarity with a two-stage extraction diode, (2) modifying PBFA II to a linear inductive voltage adder system with two ring-shaped two-stage extraction diodes,[34] and (3) converting PBFA II to a single central stalk to drive a single extraction diode.[35] Option (3) requires minimal changes to PBFA II, and presently appears to be the most attractive, cost-effective, near-term option.

Table II. Development of pulsed power/extraction diodes/transport for high yield and energy.

	ion	ε_i(MeV)	I_i (kA)	τ(ns)	θ_μ(mrad)
Present Facilities					
SABRE (SNL)	p	5	75	~40	17
GAMBLE II (NRL)	p	1	150	~50	17
LION (Cornell)	p	1	150	~40	19
Current Options at SNL					
Hermes III	Li	14	400	~25	9
PBFA II Voltage Adder	Li	20	2,500	~50	9
PBFA II Extractor	Li	17	800	~50	12
Future Directions					
LMF (B module)	Li	26-35	850-1,062	40	6
ETF (B module)	Li	37	294	40	6
LIBRA-LiTE	Li	25-35	313	40	4

References

*This research was supported by Martin Marietta/U.S. Dept. of Energy under contract DE-AC04-94AL85000.

1. M. E. Cuneo et al., this Conference; also see M. E. Cuneo et al., Proc. 9th Int. Pulsed Power Conf., 1993, p. 423.
2. D. L. Hanson et al., this Conference.
3. J. W. Poukey et al., this Conference.
4. R. E. Rosenthal et al., private communication (1994).
5. M. E. Cuneo, private communication (1994).
6. J. B. Greenly et al., this Conference.
7. J. M. Neri et al., this Conference.
8. J. R. Smith et al., this Conference.
9. T. D. Pointon and M. P. Desjarlais, private communication (1994).
10. S. A. Slutz et al., this Conference.
11. A. B. Filuk et al., this Conference.
12. T. R. Lockner, private communication (1993); also see M. P. Desjarlais, this Conference, and T. R. Lockner et al., this Conference.
13. C. L. Olson, J. Fusion Energy 1, 309 (1982).
14. D. Mosher et al., Proc. Eighth Int. Conf. High Power Beams (World Scientific, Singapore, 1991), p. 26.
15. P. F. Ottinger et al., Proc. IEEE 80, 1010 (1992).
16. C. L. Olson, Proc. 1988 LINAC Conf., CEBAF-89-001, p. 34 (1989).
17. P. F. Ottinger et al., J. Appl. Phys. 72, 395 (1992).
18. P. F. Ottinger et al., J. Appl. Phys. 75, 4402 (1994).

19. P. F. Ottinger et al., J. Appl. Phys. 70, 5292 (1991).
20. J. M Neri et al., Phys. Fluids B 5, 176 (1993).
21. J. J. Watrous et al., J. Appl. Phys. 69, 639 (1991).
22. D. R. Welch, Bull. Am. Phys. Soc. 38, 2046 (1993).
23. C. L. Olson et al., Il Nuovo Cimento 106A, 1705 (1993).
24. D. R. Welch, this Conference.
25. F. C. Young et al., Phys. Rev. Lett. 70, 2573 (1993).
26. F. C. Young et al., Phys. Plasmas 1, 1700 (1994).
27. D. R. Welch et al., Phys. Plasmas 1, 764 (1994).
28. P. F. Ottinger et al., this Conference (following paper).
29. R. E. Olson et al., Proc. 15th IEEE Symp. Fusion Eng., Hyannis, MA, Oct. 11-15, 1993.
30. R. E. Olson et al., Proc. ANS 11th Topical Mtg. Tech. Fusion Energy, New Orleans, LA, June 19-23, 1994.
31. D. L. Johnson et al., this Conference.
32. R. R. Peterson et al., U. Wisconsin, UWFDM-918, August 1993.
33. G. Kulcinski et al., Proc. ANS 11th Topical Mtg. Tech. Fusion Energy, New Orleans, LA, June 19-23, 1994.
34. M. G. Mazarakis et al., this Conference.
35. T. R. Lockner, private communication (1994).

Light-Ion-Beam Transport Research at NRL*

P.F. Ottinger[1], D.D. Hinshelwood[2], R.F. Hubbard[1], M. Lampe[1], D. Mosher[1], J.M. Neri[1], W. Noonan[+], C.L. Olson[3], D.V. Rose[2], S.P. Slinker[1], S.J. Stephanakis[1], D.R. Welch[4], and F.C. Young[1]

[1] Plasma Physics Division, Naval Research Laboratory, Washington, DC 20375
[2] JAYCOR, Inc., Vienna, VA 22182
[3] Sandia National Laboratories, Albuquerque, New Mexico 87185
[4] Mission Research Corporation, Albuquerque, New Mexico 87106

Abstract

Ion-driven inertial confinement fusion requires transport of intense beams over several meters to isolate the ion source from the target explosion and allow for focusing and time-of-flight bunching. Transport in a low pressure background gas is possible only if rapid beam-induced gas ionization leads to formation of a plasma with electrical conductivity sufficient to charge- and current-neutralize the beam. In order to minimize collisional energy loss and scattering of the beam, helium at 1-Torr pressure is proposed for the background gas. Transport in the 1-Torr regime is not well understood because this pressure falls between the high-density regime treated by resistive models, and the low-density regime treated by collisionless models. Experiments and theoretical analyses are being carried out to study beam-induced gas ionization in this pressure regime in order to evaluate its impact on the various transport schemes including ballistic transport with solenoidal lens focusing, self-pinched transport, z-discharge transport, and wire-guided transport. Work in this area is reviewed along with other transport considerations including beam transport efficiency, beam-driven instabilities, and beam energy losses.

I. Introduction

The Laboratory Microfusion Facility (LMF) has been proposed for the study of high-gain, high-yield ICF targets.[1] A number of transport and focusing schemes are being considered for LMF.[2] The baseline approach is ballistic transport with solenoidal lens focusing[3,4] (BTSF), and back-up approaches include z-discharge transport[5] (ZDT), wire-guided transport[6] (WGT), and self-pinched transport[7] (SPT). Work at the Naval Research Laboratory (NRL) is concentrating on the important physics issues associated with beam transport and on evaluating these transport schemes for LMF.

II. Beam-Induced Gas Ionization

Experiments and theoretical analyses are being carried out to study beam-induced ionization of gases in the 1-Torr pressure regime in order to evaluate its impact on the various transport schemes. This pressure regime falls between the high-density collisional regime and the low-density collisionless regime. Fast electrons, produced by beam-ion impact, knock-on collisions, and runaway processes, can have mean-free-paths on the order of the beam radius leading to nonlocal secondary ionization. In initial experiments to study this physics, 1-MeV, 1-kA/cm^2 proton beams were produced on Gamble II by collimating the beam from a pinch-reflex ion

Table I - Comparisons of Data with Theory for Helium

Pressure (Torr)	Net Currents (kA)				Electron Densities (10^{15} cm^{-3})			
	Measured (r = 4 cm)	IPROP (r = 4 cm)	IPROP (r = 1.5 cm)	DYNAPROP (r ≈ 1.5 cm)	Measured (line average)	IPROP (r = 0)	IPROP (r = 1.5 cm)	DYNAPROP (r = 0)
0.25	0.31	0.31	0.9	1.3	-	0.2	0.2	0.2
1.0	0.32	0.39	1.0	1.5	0.7	1.0	0.6	0.7
4.0	0.47	0.63	1.6	2.1	1.5	3.2	1.8	1.9

diode. The beam from the collimator was 1.5 cm in radius and limited to a divergence of about 50 mrad. Beams were transported through helium, neon, argon, and air at pressures in the range of 0.25 to 4 Torr. Details of this experiment are described in Ref. 8. Small net currents (2%-8%) were measured outside the beam channel with a dB/dt monitor located at a radius of 4 cm. Net current fractions are smaller for neon and air and larger for helium and argon. They also tend to increase with pressure. Interferometric measurements across the channel indicated that these gases are only weakly ionized (0.6%-5%) and that the ionization is confined predominantly to the beam channel. Measured net currents and electron densities for helium are shown in Table I. Transported beam currents for these shots were about 6 kA.

The DYNAPROP[9] and IPROP[10] codes were used to analyze these experiments. DYNAPROP is a 1-D code which uses a resistive model to treat plasmas created by beam interactions with high-density, collisional gases. Fast electrons are not treated. IPROP is a 3-D hybrid code which treats beam ions and fast electrons (>100 eV) as particles. The remaining electrons are treated as a resistive medium, and plasma ions form a stationary background. Results from the simulations are compared with the measurements for 1-Torr helium in Table I. Both codes predict net currents at the beam radius (1.5 cm) that are substantially larger than net currents measured outside the beam. As shown in Fig. 1, an IPROP simulation (with fast electrons) predicts net currents outside the beam at the dB/dt monitor location which agree with experiment. In this simulation, fast electrons carry a significant fraction of the return current at the beam edge. An IPROP simulation without fast electrons does not agree with the experiment. Measurements of ion energies after transport show energy losses that are consistent with beam slowing in an induced electric field due to an effective net current within the beam channel that is larger than the net current measured outside the beam. These results imply that fast electrons and nonlocal ionization play an important role in this pressure regime.

Electron densities predicted by both codes are consistent with the measured densities for helium as indicated in Table I. The

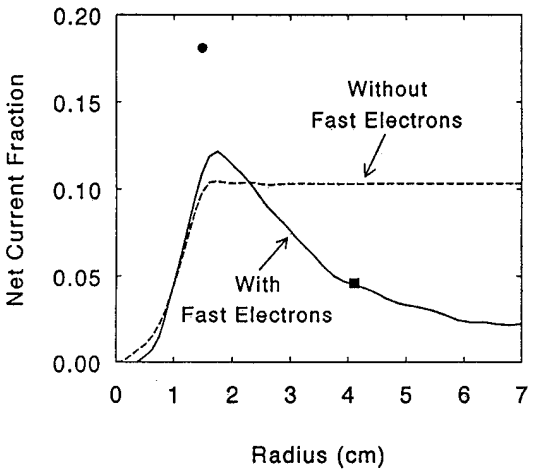


Fig. 1. Net current fraction enclosed within a given radius. Solid (dashed) curve is from IPROP simulation with (without) fast electrons. Square point is experimental measurement and circular point is from DYNAPROP simulation.

magnitude of the density is consistent with ion impact ionization being the predominant electron-production mechanism. At higher LMF-level currents, electron avalanche is expected to be the dominant mechanism.

Results from these and future experiments will be used to benchmark IPROP in order to extrapolate to LMF transport parameters. For BTSF, current neutralization must be evaluated both in the ballistic-transport regions and in the solenoidal-lens region. Net-current fractions of $\leq 0.1\%$ are required. Larger net currents will act as a distributed lens which must be taken into account. For SPT, net currents of $\geq 2\%$ are required in the pinch region. Current neutralization must also be evaluated in the ballistic focusing region for ZDT, WGT and SPT in order to determine the location of the beam focus.

III. LMF Transport Efficiency

The light-ion LMF approach uses a multimodular system with applied-B extraction diodes as ion sources. The number of modules N is expected to be between 10 and 30. Beams are extracted from these diodes and transported to the target. The transport efficiency η_t is defined as the ratio of the ion energy produced in all N diodes to the total ion energy which hits the target. η_t has been calculated as a function of various parameters so that LMF point designs can be developed for BTSF, ZDT, and WGT. Results for SPT should be similar to ZDT results.

Focus sweeping due to a voltage ramp for time-of-flight (TOF) bunching has recently been considered.[11] This voltage ramp will decrease η_t. Because BTSF is nearly achromatic[3,11], the focus sweep effect reduces η_t the least for this scheme. Results for all three transport schemes are shown in Figs. 2-4 as a function of the diode radius R and the bunching factor α. The parameter Δ is the distance between the anode and the foil which separates the diode vacuum region from the gas-filled transport region. For BTSF, Δ is varied to achromatically match the diode lens with the solenoidal lens. For the cases shown in Figs. 2-4, the beam microdivergence is 5 mrad, the focal length F is 150 cm, the total ion energy at the diode sources E_s is 20 MJ, the number of modules N is 20, the target radius is 1 cm, and the beam pulse duration at the target is 15 ns. Here, F refers to the solenoidal lens focusing length for BTSF, and the ballistic focusing distance between the diode and the channel entrance for ZDT, WGT, and SPT. The achromatic matching

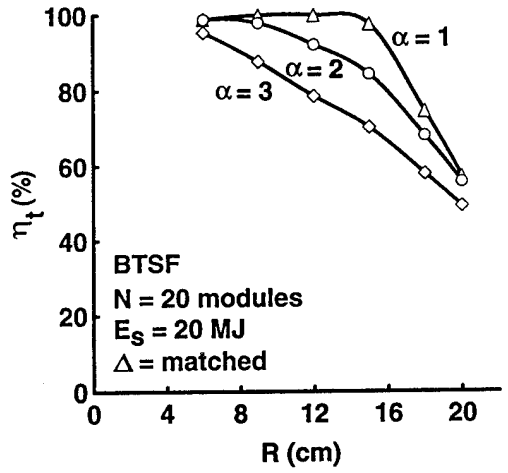


Fig. 2. Transport efficiency as a function of diode radius for a BTSF system.

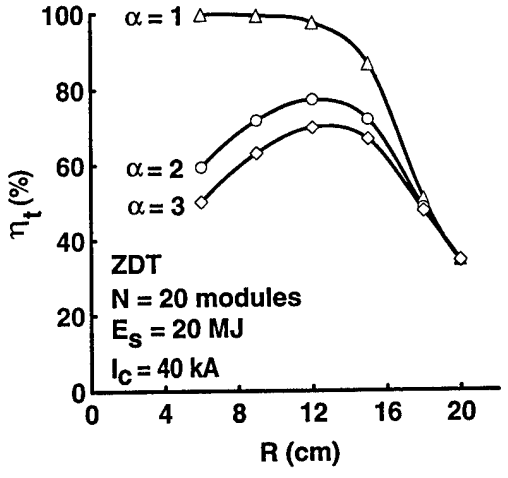


Fig. 3. Transport efficiency as a function of diode radius for a ZDT system.

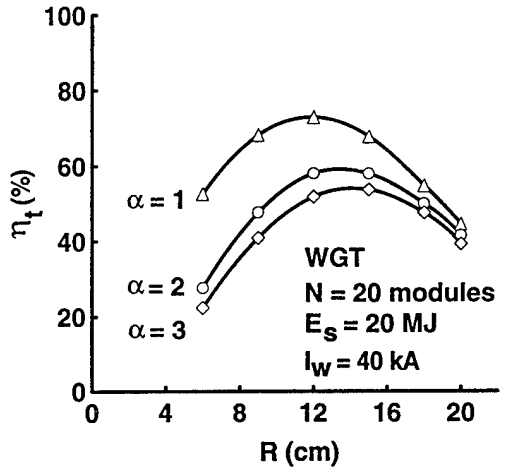


Fig. 4. Transport efficiency as a function of diode radius for a WGT system.

condition has been applied in the case of BTSF, while the channel current I_c and the wire current I_w are set equal to 40 kA for ZDT and WGT. These results also assume a square profile for the beam microdivergence and that the ion current from the diode scales as the square of the diode voltage.

Results indicate that reasonably high transport efficiency (> 50%) can be obtained for all three systems for bunching factors as large as $\alpha = 3$ with $R \leq 15$ cm. In particular, the point design for LMF using the baseline BTSF system with R = 15 cm and $\alpha = 2$ is calculated to have $\eta_t = 84\%$. At the same values of R and α, the ZDT system has $\eta_t = 72\%$ and the WGT system has $\eta_t = 60\%$.

The results assume that the system is tuned to obtain optimum power efficiency on target at midpulse. This maximizes η_t for a given set of system parameters. However, target considerations suggest that optimum power efficiency should occur near peak power (i.e., at the end of the pulse for a TOF ramped voltage pulse). It has been found[12] that tuning the system for optimum power efficiency at the end of the pulse can significantly reduce η_t. A compromise is obtained by tuning the system to optimize power efficiency three-quarters of the way through the pulse. In this case, η_t is only slightly reduced and the power efficiency at the end of the pulse is on the order of 95% for all three transport schemes.

IV. Summary

Beam-induced gas ionization experiments for evaluating beam transport schemes for LMF have begun. Future experiments on Gamble II will use an applied-B extraction ion diode. Presently, an exploding metal foil anode plasma source (EMFAPS) is being developed for this diode. Gas ionization induced by the annular ion beam from this diode will be studied both in field-free space and in the transverse magnetic field of a solenoidal lens. In addition, consideration of beam energy losses during transport, thresholds for beam-driven instabilities and background plasma magnetohydrodynamics will be combined with transport efficiency calculations to define an operational window for each LMF transport scheme.

V. References

* Work supported by the U.S. Department of Energy through Sandia National Laboratories.

+ National Research Council Research Associate at the Naval Research Laboratory.

1. J.J. Ramirez, *et al.*, Fusion Tech. **15**, 350 (1989).
2. D. Mosher, *et al.*, Proc. of the 8th Inter. Conf. on High-Power Particle Beams, (Novosibirsk, USSR, July 1990), p. 26.
3. C.L. Olson, Proc. of the 1988 Linear Accel. Conf., (Newport News, VA, Oct. 1988), p. 34.
4. P.F. Ottinger, *et al.*, J. Appl. Phys. **72**, 395 (1992).
5. P.F. Ottinger, *et al.*, J. Appl. Phys. **70**, 5292 (1991).
6. J.J. Watrous, *et al.*, J. Appl. Phys. **69**, 639 (1991).
7. R.F. Hubbard, *et al.*, Part. Accel. **37-38**, 161 (1992).
8. F.C. Young, *et al.*, Phys. Plasmas **1**, 1700 (1994).
9. R.F. Hubbard, *et al.*, NRL Memorandum Report No. 7112, 1992.
10. D.R. Welch, C.L. Olson and T.W.L. Sanford, Phys. Plasmas **1**, 764 (1994).
11. P.F. Ottinger, D.V. Rose, C.L. Olson, J. Appl. Phys. **75**, 4402 (1994).
12. D.V. Rose, P.F. Ottinger and C.L. Olson, to be published.

Development of a Plasma Lens as a Fine Focusing Lens for Heavy-Ion Beams

M. Stetter, J. Christiansen, C. Kumpf, U. Neuner, S. Stöwe, R. Tkotz

Physikalisches Institut, Abt. I, Universität Erlangen-Nürnberg, 91058 Erlangen, Germany

A. Tauschwitz, D.H.H. Hoffmann, P. Spiller

GSI 64220 Darmstadt and MPQ 8046 Garching, Germany

Abstract

Within the framework of the "High Energy Density in Matter" program, a plasma lens has been designed to focus a heavy-ion beam onto a 200 μm diameter spot (FWHM). This value is desired to get the necessary energy density on the target to create a plasma by means of a heavy-ion beam. It is determined by the parameters of the SIS-accelerator at GSI-Darmstadt. The calculated discharge current in an ideal plasma lens has to be between 300 and 400 kA for an emittance limited spot, dependent on initial beam radius and distance of the spot from lens exit. A flexible system has been built in order to investigate the various discharge mechanisms and their influence on the focusing properties at these high currents. Design considerations, the first beam tests and investigations of the plasma development at plasma lens currents up to 200 kA are discussed.

Introduction

Focusing high energy particles by conventional quadrupole multiplets is subject to fundamental limitations [1]. The main reason is that the focusing effect in such devices is second order, *i.e.* there is always one focusing and one defocusing plane. Therefore multiplets are necessary, leading to a rather long system length. On the contrary, the field configuration of a "wire lens", characterized by an axially symmetric and radially linear rising magnetic field, represents a perfect ideal lens. This field configuration is produced by a homogeneous axial current density in a plasma. The beam particles traverse this plasma which has densities between 10^{-6} and 10^{-10} g/cm^3. Scattering is negligible at these densities.

For an ideal lens the spot diameter of a beam with a given emittance scales inversely with the focusing angle α. A spot diameter of 200 μm (FWHM) is desired to get the energy density on the target necessary to create a plasma by means of a heavy-ion beam with the

given beam parameters of the SIS-accelerator at GSI-Darmstadt. Therefore α is fixed and the initial beam diameter at the lens entrance and the distance of the spot from the lens exit determine the current and length of the plasma column. Calculations for different target distances and initial beam diameters yield currents between 300 and 400 kA for a beam with 6 Tm rigidity at a particle energy of about 300 MeV/amu.

The main task of this experiment is the creation of a homogeneous current density distribution in the gas discharge during the focusing phase in order to get no lens aberration. One possibility to create a plasma cylinder with variable diameter and high discharge current is the dynamic Z-pinch [2]. The selected approach is the "wall stabilized discharge" where the contraction of the current-carrying sheath is inhibited and no bulk plasma motion occurs. This system is very simple and has shown very good focusing properties with currents up to 30 kA [3].

System design

We designed a flexible system to facilitate a wide range of geometrical and electrical discharge parameters. The plasma lens pulse generator is composed of up to six exchangeable capacitor banks, each with a capacity of 13.3 μF. These units are connected to the plasma lens by flexible low-inductance HV pulse cables, enabling an easy in-place adjustment of the plasma lens. The parameters are: capacitance, 13 - 80 μF; charging voltage, 5 - 20 kV; discharge current, 10 - 400 kA; current halfwave, 6 - 9 μs. The whole lens is surrounded by the target chamber, enabling vacuum in the chamber while low-pressure gas in the lens system is contained by 100 to 300 μm thick titanium windows.

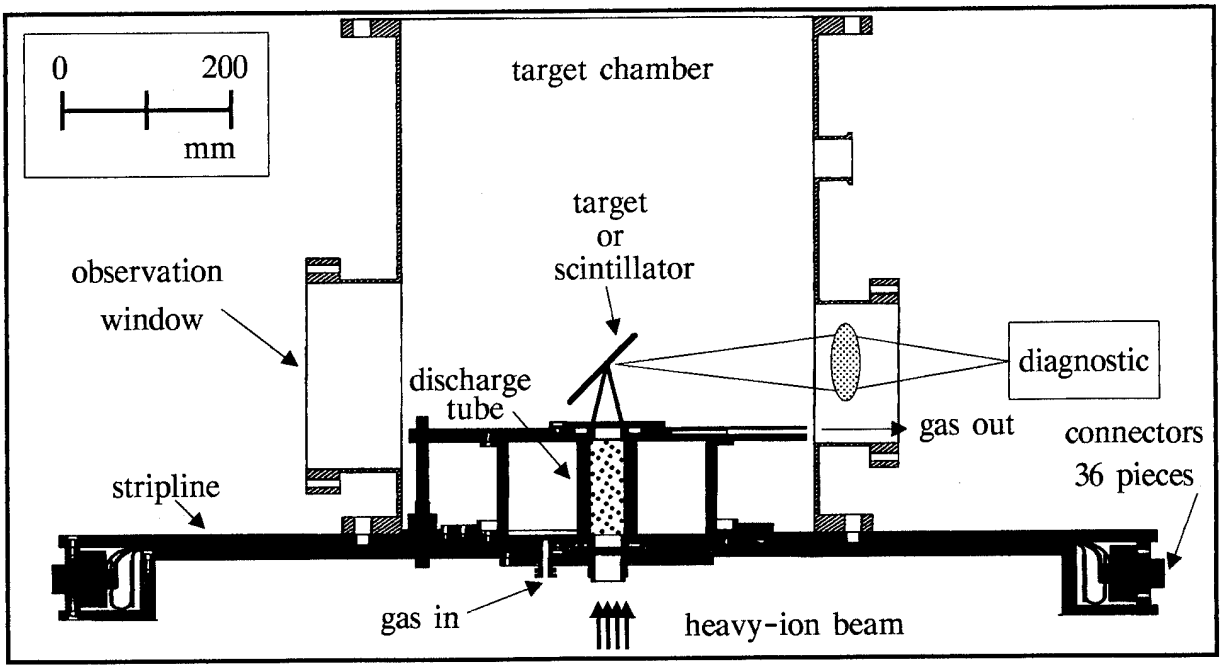


Fig. 1: schematic drawing of the plasma lens with the target chamber

Experiments

After completion of the plasma lens and the first capacitor bank the system was tested at the GSI UNILAC accelerator with a beam rigidity of 1.6 Tm, emittance of 5 π mm mrad and discharge currents up to 90 kA. For this parameter set no aberrations of the plasma lens have been observed, *i.e.* no deviation from the homogeneous current density distribution occured. The measured spot diameter of 350 μm (FWHM) agrees well with the 330 μm of the calculated emittance-limited focus [4].

In addition laboratory experiments with optical and spectroscopical measurements of the plasma are carried out to get scaling laws for the plasma behaviour of a wall stabilized discharge at these high currents. Unfortunately these experiments are limited because with currents exceeding 100 kA the quarz tubes are destroyed by the discharge. For the beam experiments we used alumina tubes.

The plasma development is similar for all investigated currents between 45 and 90 kA. The homegeneous ignition over the discharge volume is followed by a contracting shock wave. The time to reach the axis is about 1 μs, nearly independent of the discharge current. This shock wave is probably produced by the heating and desorbtion of adsorbates on the insulator tube. After a short expansion of the shock produced dense plasma on the axis, a second contraction phase is visible. The velocity is increasing with increasing current. This is the pinching of the current layer due to the magnetic fields. The pinch is expanding again and during current maximum a homogeneous plasma cylinder is visible. With these results it is possible to adjust the tube diameter and the gas pressure such that the diameter of the plasma is slightly greater than the incoming beam diameter.

This encouraging first tests were followed by two beam experiments at the GSI SIS/ESR facility, with 6 Tm beam rigidity and plasma currents up to 200 kA, in November 1993 and June 1994. The task was to verify the good focusing properties. The ion beam was the probe to determine the evolution of magnetic field distribution at these current levels.

The time-dependent development of the focus on plastic and quarz scintillators was detected by short time photography. The principle arrangement of a plasma lens and the diagnostic is described in [5]. The spacial resolution was 60 μm in vertical and 160 μm in horizontal direction. The diameter of the incoming beam was 14 mm and the diameter of the plasma column during best focusing was between 14 and 16 mm depending on the peak current and the gas pressure.

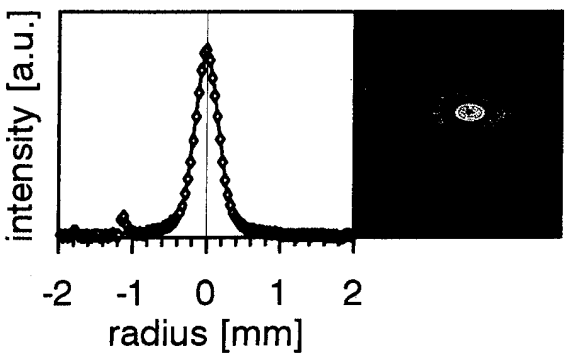


Fig. 2: Focus on the scintillator and vertical spot profile

Figure 2 shows the focused beam and the vertical beam profile at a target distance of 59 mm from the end of the plasma column. The diameter of the spot for this parameter range is 400 μm. The minimum spot diameter was 390 μm at a

target distance of 53 mm.

The measurement of the beam emittance is very difficult and the accuracy is only ±50%. Therefore we tried to determine the beam emittance by measuring the spot size at different target distances. As long as the focus is only emittance-limited one should find a linear dependence of the spot diameter as a function of the focal length. It is well known that the beam has about a factor of two higher emittance in the horizontal than in the vertical plane. The focus diameter as a function of focal length is shown in figure 3.

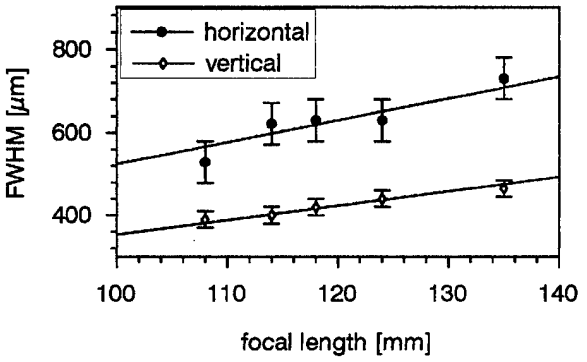


Fig. 3: focus diameter as a function of focal length for the horizontal and vertical beam profile

These results yield to 13±1 π mm mrad horizontal and 8.5±0.5 π mm mrad vertical emittance (FWHM). The reproducibility of focus diameter and focus position for several shots was 100% within the error of measurement.

Conclusion

The accuracy and reproducibility of wall stabilized plasma lenses at currents up to 200 kA have been demonstrated. Lens aberrations have not been detected. The next step is to increase the current to 300 kA by increasing the charging voltage of the capacitor banks. In laboratory the feasibility of the alumina discharge tubes and the thin titanium windows to withstand these higer currents has to be shown. We hope to reach the designed currents in autumn 1994. The lens with increased focusing power will be tested again at the SIS-beam. This optimized plasma lens should reach spot diameters very close to 200 μm if the emittance of the SIS-beam is within the designed values.

[1] E. Boggasch, B. Heimrich, D.H.H. Hoffmann, Nucl. Instr. and Meth. A336, 438 (1993)

[2] R. Kowalewicz, M. Scampamorte, S. Maury, S. Milner, H. Riege, J. Christiansen, K. Frank, U. Neuner, M. Stetter, R. Tkotz: *Proceedings of the III EPAC, Berlin,* 1992, p. 1539

[3] E. Boggasch, A. Tauschwitz, H. Wahl, K.G. Dietrich, D.H.H. Hoffmann, W. Laux, M. Stetter, R. Tkotz: *Appl. Phys. Lett.* 60, 2475 (1992)

[4] M. Stetter, J. Christiansen, U. Neuner, S. Stöwe, R. Tkotz, T. Wagner, E. Boggasch, A. Tauschwitz, D.H.H. Hoffmann, P. Spiller, Il Nuovo Cimento, 106A, N. 11, 1725 (1993)

[5] A. Tauschwitz, E. Boggasch, D.H.H. Hoffmann, M. De Magistris, U. Neuner, M. Stetter, R. Tkotz, T. Wagner, W. Seelig, H. Wetzler, Il Nuovo Cimento, 106A, N. 11, 1733 (1993)

This project has been funded by the Federal Minister of Research and Technology (BMFT) under the contract number 06 ER 462.

RESONANT AND CHAOTIC PHENOMENA IN A PERIODICALLY FOCUSED INTENSE CHARGED-PARTICLE BEAM

Chiping Chen
Plasma Fusion Center
Massachusetts Institute of Technology
Cambridge, Massachusetts 02139

Ronald C. Davidson and Qian Qian
Plasma Physics Laboratory
Princeton University
Princeton, New Jersey 08543

Robert A. Jameson
Accelerator Operations & Technology Division
Los Alamos National Laboratory
Los Alamos, New Mexico 87545

The exploration of the characteristics of periodically focused intense charged particle beams is one of the main thrusts in beam physics research and is critical to many advanced accelerator applications such as heavy ion fusion. In this paper, we discuss several novel effects induced by the self-electric and self-magnetic fields of an intense beam in a periodic focusing channel consisting of either a periodic solenoidal field or an alternating-gradient quadrupole magnetic field. It is shown that the self fields induce rich nonlinear resonances and chaotic behavior in the envelope oscillations of mismatched beams. A parametric instability threshold is derived analytically for halo formation in a mismatched space-charge-dominated beam and is found to be in good agreement with two-dimensional particle-in-cell simulations. For envelope-matched beams with nonuniform density profiles, single-particle orbits are also found to exhibit nonlinear resonances and chaotic behavior in high-current regimes, suggesting a microscopic mechanism for emittance growth. The implications of these findings are discussed regarding the design of high-current accelerators and high-current transport systems.

1. Introduction

The need for a better understanding of the physics of periodically focused intense charged-particle beams has intensified because it is critical to advanced accelerator applications such as heavy ion fusion, nuclear waste treatment, and coherent radiation generation. Since the late 1950's, several aspects of intense charged-particle beam transport in a periodic focusing channel have been investigated, including (i) the exploration of the equilibrium[1] and stability properties[2] of intense beams, (ii) the introduction of the concepts of root-mean-squared (rms) emittance and rms beam matching,[3,4] (iii) the derivation of rms beam envelope equations,[3,4]

(iv) the study of current intensity limits,[5] and (v) the exploration of emittance growth[6–8] and beam halo formation.[9] Despite these efforts, a fundamental understanding of the physics of periodically focused intense charged-particle beams is still being developed, particularly in the regime where the beam is not well matched into the focusing channel.

In this paper, we discuss two new phenomena in periodically focused intense charged-particle beams, namely, beam self-field-induced nonlinear resonances and chaotic behavior both in the envelope oscillations[10,11] of mismatched beams and in the transverse dynamics[12] of the particles in envelope-matched beams with nonuniform density profiles. We also show that there exists a mismatch threshold beyond which a parametric instability occurs, leading to halo formation.

2. Nonlinear Resonances and Chaotic Behavior in the Beam Envelope Oscillations

The envelope oscillations of an intense charged-particle beam propagating through the periodic solenoidal focusing field $\vec{B}(r,s)$ with the Kapchinskij-Vladimirskij (KV) distribution, are described by[10,11]

$$\frac{d^2 r_b}{ds^2} + \kappa_z(s) r_b - \frac{K}{r_b} - \frac{\epsilon^2}{r_b^3} = 0 \ . \tag{1}$$

In Eq. (1), r_b is the beam radius and $s = z = \beta_b ct$ is the axial coordinate, where $\beta_b c$ is the average axial velocity of the beam particles, and c is the speed of light *in vacuuo*. The periodic function $\kappa_z(s) = \kappa_z(s+S) = q^2 B_z^2(s)/4\gamma_b^2\beta_b^2 m^2 c^4$ characterizes the strength of the focusing field, where $B_z(s)$ is the magnetic field on the z-axis, S is the fundamental periodicity length of the focusing field, q and m are the particle charge and rest mass, respectively, and $\gamma_b = (1-\beta_b^2)^{-1/2}$ is the relativistic mass factor of the beam particles. The periodic step-function profile shown in Fig. 1 is assumed for $\kappa_z(s)$, and the vacuum phase advance over one axial period of such a focusing field is given approximately by $\sigma_0 = [S\int_0^S \kappa_z(s)ds]^{1/2} = [\eta S^2 \kappa_z(0)]^{1/2}$. The normalized beam perveance

$$K = \frac{2q^2 N_b}{\gamma_b^3 \beta_b^2 mc^2} \tag{2}$$

is a measure of the beam self-field[13] intensity, where N_b is the number of particles per unit axial length of the beam. The rms emittance ϵ is assumed to be constant.

For $d\kappa_z/ds \neq 0$ and $K \neq 0$, Eq. (1) describes a Hamiltonian system with one and one-half degrees of freedom and is *nonintegrable*. The Poincaré mapping technique,[14] which tracks an ensemble of phase-space trajectories as they intersect the phase plane (r_b, r_b') at successive axial positions $s = 0, 1, 2, \cdots$, is used to find the condition for beam matching into the focusing channel, and to explore the nonlinear resonances and chaotic behavior in the envelope oscillations of mismatched beams. Here, the 'prime' denotes the derivative with respect to s.

Figure 2 shows the Poincaré surface-of-section plots for a beam propagating through a periodic solenoidal field with step-function lattice (Fig. 1) in terms of the *dimensionless* parameters and variables defined by

$$\frac{s}{S} \to s \ , \quad \frac{r_b}{\sqrt{\epsilon S}} \to r_b \ , \quad S^2\kappa_z \to \kappa_z \ , \quad \frac{SK}{\epsilon} \to K \ . \tag{3}$$

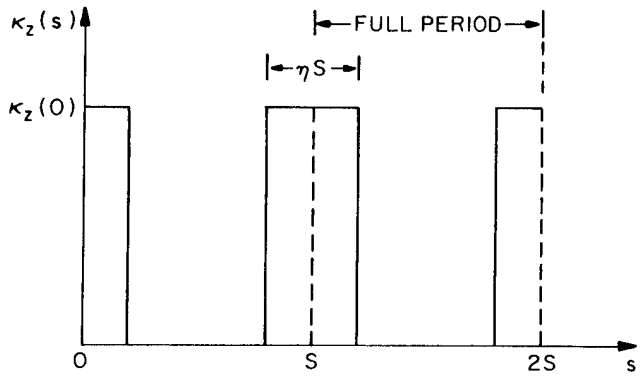


Figure 1: Periodic step-function lattice $\kappa_z(s)$ representing a periodically interrupted or alternating solenoidal focusing field.

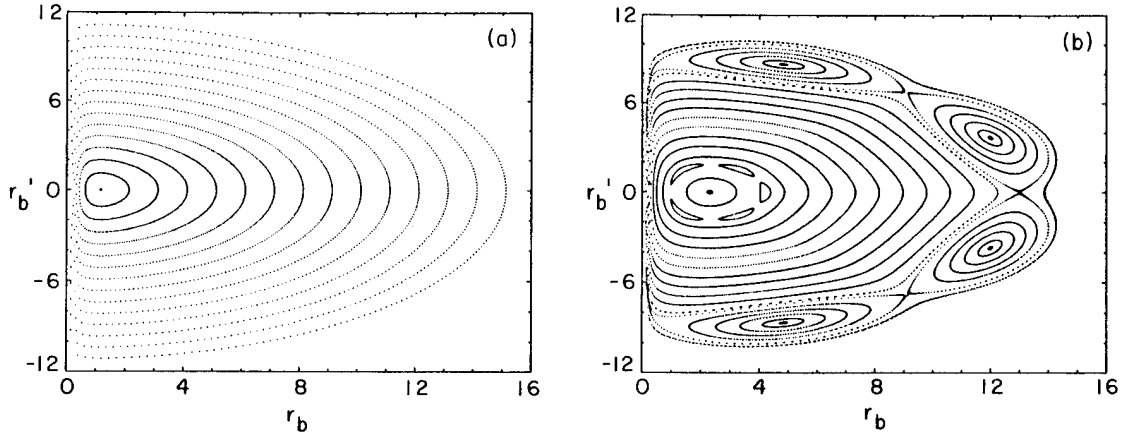


Figure 2: Poincaré surface-of-section plot for the envelope oscillations of tenuous and intense beams. The choice of system parameters corresponds to: (a) $K = 0$, $\eta = 1/6$, $\kappa_z(0) = 3.79$ ($\sigma_0 = 45.5°$), and (b) $K = 3$, $\eta = 1/6$, and $\kappa_z(0) = 3.79$ ($\sigma_0 = 45.5°$).

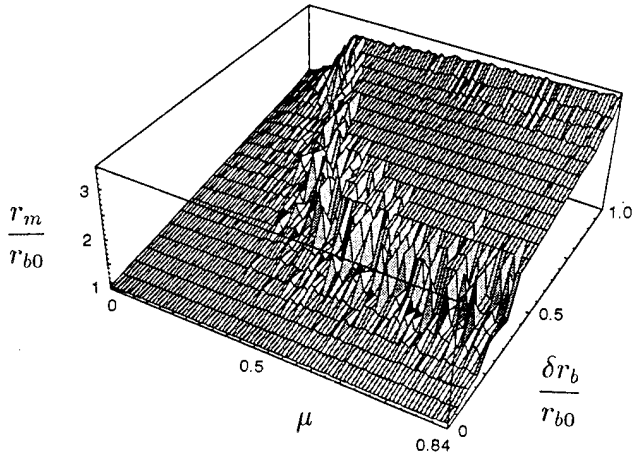


Figure 3: Relative maximum radius r_m/r_{b0} achieved by the beam particles as a two-dimensional function of the relative mismatch amplitude $\delta r_b/r_{b0}$ and the space-charge parameter $\mu = 1 - (\sigma/\sigma_0)^2$, obtained from particle-in-cell simulations. Here, r_{b0} is the radius of the corresponding matched beam.

Figure 2(a) corresponds to a *tenuous* ($K \to 0$) beam. The fixed point corresponds to a matched (equilibrium) beam with $r_b(s) = r_b(s + S)$ and is surrounded by an infinite number of invariant tori (contours), fourteen of which are shown in Fig. 2(a). Each of the tori describes a mismatched (nonequilibrium) beam whose envelope exhibits (slow) stable betatron oscillations about the (fast-oscillating) envelope of the matched beam. It should be emphasized that because Eq. (1) is integrable in the limit of a tenuous beam, there is no finite-size resonance, as illustrated in Fig. 2(a).

For a direct comparison with Fig. 2(a), the corresponding Poincaré surface-of-section plot is shown in Fig. 2(b) for an *intense* beam with normalized self-field perveance $K = 3$. It is evident that the rich phase-space structure in Fig. 2(b) is strikingly different from the simple phase-space structure in Fig. 2(a). In particular, there coexist fourth-order resonances (i.e., period-four orbits) and fifth-order resonances (i.e., period-five orbits) in the phase space shown in Fig. 2(b).

A (nonlinear) resonance condition is derived. Chaotic beam envelope oscillations are found for $\sigma_0 > 90°$ and sufficiently large K. The resonant and chaotic phenomena in the envelope oscillations are related to various instabilities found by Hofmann,[2] *et al.* for periodically focused high-current ion beams with the KV distribution. Detailed reports on these results are in Refs. 10 and 11.

3. Parametric Instability Threshold for Halo Formation in Mismatched Beams

For a matched KV beam, it is well known that the particle orbits are regular and stable. The preceding section indicates that for $\sigma_0 < 90°$, the envelope oscillations of a mismatched beam are mostly regular regardless of the mismatch amplitude, despite such rich nonlinear resonances shown in Fig. 2(b). Because perfectly matching a beam into a focusing channel is difficult in most practical applications, we examine here the effects of mismatch on the transverse dynamics of the particles in a mismatched beam. It is shown below that when the mismatch amplitude exceeds a certain threshold, a parametric instability occurs, causing some particles to migrate out from the interior (core) of the beam to form a halo with a maximum radius which can be several times larger than that of the core.

For present purposes, we ignore the effects of nonlinear resonances in the envelope oscillations and make the smooth-beam (mean-field) approximation

$$\kappa_z(s) \approx k_0^2 \equiv \frac{1}{S}\int_0^S \kappa_z(s)ds = \frac{\sigma_0^2}{S^2} \ . \tag{4}$$

Assuming that the beam (core) density is uniform, the transverse motion of an individual test particle is described by[15]

$$\frac{d^2r}{ds^2} + k_0^2 r - \frac{\epsilon_t^2}{r^3} = \begin{cases} K/r & \text{for } r > r_b(s) \ , \\ Kr/r_b^2(s) & \text{for } 0 \le r < r_b(s) \ . \end{cases} \tag{5}$$

In Eq. (5), $\epsilon_t = P_\theta/\gamma_b m\beta_b c = \text{const}$, where P_θ is the canonical angular momentum of the test particle. From Eqs. (1) and (4), the radius of a slightly mismatched beam can be expressed as

$$r_b(s) = r_{b0} + \delta r_b \cos(ks + \phi) \ , \tag{6}$$

where δr_b and ϕ are the amplitude and initial phase of the envelope oscillations induced by the mismatch, respectively. The radius of the corresponding matched beam is defined by

$$r_{b0} = \left\{ \left[\left(\frac{K}{2k_0^2} \right)^2 + \frac{\epsilon^2}{k_0^2} \right]^{1/2} + \frac{K}{2k_0^2} \right\}^{1/2} , \tag{7}$$

and the wavenumber (frequency) of the envelope oscillations is defined by

$$k = \left(2k_0^2 + \frac{2\epsilon^2}{r_{b0}^4} \right)^{1/2} = \frac{1}{S}(2\sigma_0^2 + 2\sigma^2)^{1/2} , \tag{8}$$

where $\sigma/S = \epsilon/r_{b0}^2$ is the phase advance per unit axial length for the matched beam.

For a particle outside the beam [i.e., $r > r_b(s)$], the total energy is conserved and there exists a maximum radial excursion which can be derived from Eq. (5). However, as soon as the particle enters the beam interior the total energy is no longer conserved due to the time-dependent (parametric) driving term, $Kr/r_b^2(s)$, in Eq. (5). Indeed, it can be shown analytically[16] that for a space-charge-dominated beam (i.e., $\sigma/\sigma_0 \to 0$), solutions to Eq. (5) become unstable for $r < r_b(s)$ whenever the mismatch amplitude δr_b exceeds the following threshold:

$$\left(\frac{\delta r_b}{r_{b0}} \right)_{\rm cr} \cong 0.42 , \tag{9}$$

where r_{b0} is defined in Eq. (7). Beyond this threshold some of the beam particles resonantly gain energy to form a halo.

The threshold condition in Eq. (9) is found in good agreement with the results from two-dimensional particle-in-cell simulations performed for beam propagation through a uniform linear focusing channel. To estimate the threshold value, the maximum radius achieved by the beam particles is recorded after the beam has propagated more than 50 periods of the (mismatched) envelope oscillations. The simulations are performed over a wide range of K and δr_b. The results are shown in Fig. 3, where the maximum radius achieved by the beam particles is plotted as a two-dimensional function of the relative mismatch amplitude $\delta r_b/r_{b0}$ and the space-charge parameter $\mu = 1 - (\sigma/\sigma_0)^2$. The onset of a plateau in Fig. 3 defines the parametric instability threshold which, in the space-charge-dominated limit (i.e., $\mu \to 1$), is given robustly by $\delta r_b/r_{b0} \cong 0.4$, in agreement with Eq. (9). The threshold increases as μ decreases, as expected.

4. Chaotic Behavior in Nonuniform Beams

To gain some insight about the *microscopic* mechanism(s) for the growth of emittance in a nonuniform-density beam and the associated density homogenization process, we analyze the dynamics of individual particles in beams with nonuniform density profiles. The analysis[12] is carried out in an alternating-gradient quadrupole magnetic field configuration for envelope-matched beams with nonuniform density profiles. It is shown, with the Lie group method, that the particle orbits become chaotic whenever the density across the beam is nonuniform *and* sufficiently high. Because the occurrence of chaotic particle orbits is associated with increasing the *coarse-grained* area or volume of the phase space occupied by the beam, it certainly contributes to emittance growth.

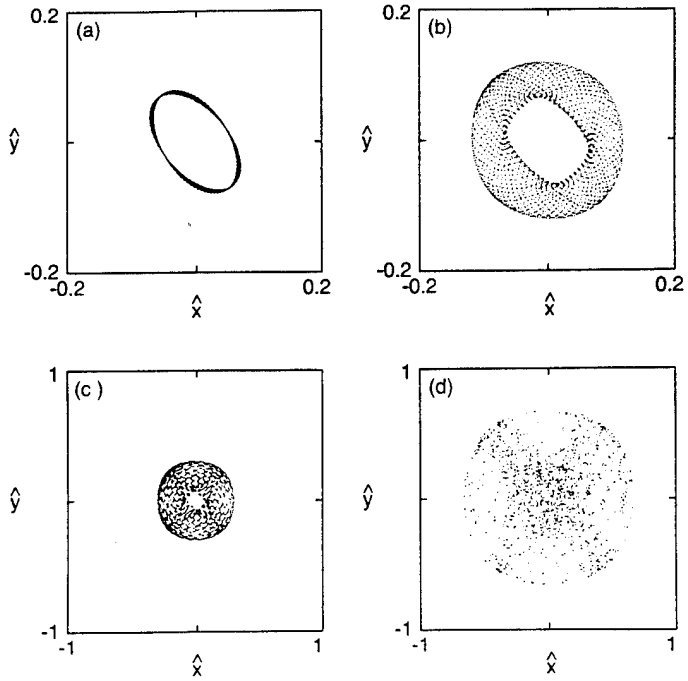


Figure 4: Poincaré surface-of-section plot projected onto the phase plane $(\hat{x}, \hat{y})$ for a test particle in a sinusoidal lattice with $\hat{\kappa}_{q0} = 0.1$ and $\hat{S} = S/r_b = 10$. The values of the beam perveance are (a) $K = 0.001$, (b) $K = 0.004$, (c) $K = 0.006$, and (d) $K = 0.007$.

The onset of chaotic particle orbits is demonstrated numerically[12] for a beam with a parabolic density profile and constant radius r_b corresponding to the average envelope of a well-matched beam propagating through the alternating-gradient quadrupole magnetic field. The paraxial equations of motion are

$$\frac{d^2\hat{x}}{d\hat{s}^2} + [\hat{\kappa}_q(s) - 2K]\hat{x} + K(\hat{x}^2 + \hat{y}^2)\hat{x} = 0 \ , \tag{10}$$

$$\frac{d^2\hat{y}}{d\hat{s}^2} + [-\hat{\kappa}_q(s) - 2K]\hat{y} + K(\hat{x}^2 + \hat{y}^2)\hat{y} = 0 \ , \tag{11}$$

where the quantities are normalized according to

$$\hat{x} = \frac{x}{r_b} \ , \quad \hat{y} = \frac{y}{r_b} \ , \quad \hat{s} = \frac{s}{r_b} \ , \quad \hat{S} = \frac{S}{r_b} \ , \quad \hat{\kappa}_q = r_b^2 \kappa_q \ , \tag{12}$$

and $\hat{\kappa}_q(\hat{s}) = \hat{\kappa}_{q0} \sin(2\pi\hat{s}/\hat{S})$.

The motion described by Eqs. (10) and (11) occurs in a five-dimensional phase space, which has a higher dimensionality than the three-dimensional phase space described by Eq. (1). Thus, the corresponding Poincaré map is a map defined on a four-dimensional hypersurface in the five-dimensional phase space $(\hat{x}, \hat{y}, \hat{x}', \hat{y}', \hat{s})$, where the "prime" denotes the axial derivative. In the numerical analysis, the projection of the Poincaré map is generated. Such projections onto the phase plane $(\hat{x}, \hat{y})$ are shown in Fig. 4 for cases (a) $K = 0.001$, (b) $K = 0.004$, (c) $K = 0.006$, and (d) $K = 0.007$. The choice of system parameters in Fig. 4 corresponds to $\hat{\kappa}_{q0} = 0.1$ and $\hat{S} = S/r_b = 10$. For the sinusoidal lattice, the critical

perveance for beam focusing is given by $K_c = \hat{S}^2\hat{\kappa}_{q0}^2/8\pi^2 = 0.0127$, and the vacuum phase advance is $\sigma_0 = \hat{S}\hat{K}_c^{1/2} = 65°$. For relatively tenuous beams, the orbits are quasiperiodic (regular) as illustrated in Figs. 4(a), 4(b), and 4(c). However, as the beam perveance is increased to $K = 0.007 < K_c$, the particle motion becomes completely chaotic as shown in Fig. 4(d).

5. Conclusions

We have studied the characteristics of intense charged-particle beam propagation through a periodic, linear focusing channel consisting of a periodic solenoidal or alternating-gradient quadrupole magnetic field. It was shown that the beam self fields induce a rich variety of nonlinear resonances and chaotic behavior in the envelope oscillations of a mismatched beam propagating through a periodic solenoidal magnetic field. Similar results were obtained for intense beam propagation through an alternating-gradient quadrupole magnetic field. The predicted nonlinear resonances and chaotic behavior are expected to be observable in beam transport experiments in which there is a mismatch between the beam and the periodic focusing field.

A parametric instability threshold was derived analytically for halo formation in mismatched intense beams in the smooth-beam (mean-field) approximation, and was found in good agreement with two-dimensional particle-in-cell simulations. We believe that the parametric instability threshold, which imposes a limit on acceptable mismatch, will serve as an important criterion in the design of high-current accelerators and high-current transport systems for low-beam-loss operation.

Also shown was the onset of chaos in the transverse dynamics of the particles in an envelope-matched intense beam with a nonuniform density profile propagating through an alternating-gradient quadrupole magnetic field. Based on the onset of chaotic particle orbits, a microscopic mechanism was suggested for the growth of emittance in nonuniform density beams. Further investigations are required in order to quantify anomalous transport induced by the chaotic particle orbits.

6. Acknowledgment

This work was supported in part by the U.S. Department of Energy and in part by the U.S. Office of Naval Research.

7. References

1. I.M. Kapchinskij and V.V. Vladimirskij, Proc. Int. Conf. on High Energy Accelerators, CERN, Geneva (1959), p. 274.
2. I. Hofmann, L.J. Laslett, L. Smith, and I. Haber, Part. Accel. **13**, 145 (1983).
3. P.M. Lapostolle, IEEE Trans. Nucl. Sci. **NS-18**, 1101 (1971).
4. F.J. Sacherer, IEEE Trans. Nucl. Sci. **NS-18**, 1105 (1971).
5. M. Reiser, Part. Accel. **8**, 167 (1978).
6. T.P. Wangler, K.R. Crandall, R.S. Mills, and M. Reiser, IEEE Trans. Nucl. Sci. **NS-32**, 2196 (1985).

7. O.A. Anderson, Part. Accel. **21**, 197 (1987).
8. M. Reiser, C.R. Chang, D. Kehne, K. Low, T. Shea, H. Rudd, and I. Haber, Phys. Rev. Lett. **61**, 2933 (1988); I. Haber, D. Kehne, M. Reiser, and H. Rudd, Phys. Rev. **A44**, 5194 (1991).
9. R.A. Jameson, Proc. 1993 Part. Accel. Conf. (1993), p. 3926.
10. C. Chen and R.C. Davidson, Phys. Rev. Lett. **72**, 2195 (1994).
11. C. Chen and R.C. Davidson, Phys. Rev. **E49**, 5679 (1994).
12. Q. Qian, R.C. Davidson, and C. Chen, Phys. Plasmas **1**, 1328 (1994).
13. R.C. Davidson, *Physics of Nonneutral Plasmas* (Addison-Wesley, Reading, MA, 1990).
14. A.J. Lichtenberg and M.A. Lieberman, *Regular and Chaotic Dynamics*, 2nd ed. (Springer-Verlag, New York, 1992).
15. R.L. Gluckstein, "Analytical model for halo formation in high current ion linacs," preprint (1994), and references therein.
16. C. Chen and R.A. Jameson, "Parametric instability threshold for halo formation in mismatched intense charged-particle beams," manuscript in preparation (1994).

HIGH-CURRENT ELECTRON BEAM TRANSPORT AND ACCELERATION IN LIA-30

V.S. Bossamykin, V.P. Veresov, A.I. Gerasimov, V.S. Gordeev,
V.P. Gritsina, A.V. Grishin, S.A. Gornostay-Pol'skii,
V.Ya. Averchenkov, S.A. Lazarev, O.N. Syutin,
A.D. Tarasov, A.S. Fedotkin

All-Russia Scientific Research Institute of Experimental Physics (VNIIEF),
Arzamas-16, Nizhni Novgorod Region, 607200 RF

Abstract

LIA-30, being 25 meters long, has the following parameters: electron energy ≤ 40 MeV, current 100 kA, pulse duration 30 ns. An annular electron beam is created in and transported along the vacuum channel by a longitudinal guiding magnetic field of 0.5 T. In the course of the experiment many parameters were being varied, namely: cathode diameter (10-25 cm), diode geometry, injection energy (2.5-7 MeV), amplitude (50-170 kA), pulse form and duration of the injected current. The temporal program of the accelerating module switchings was changed as well. The peculiarities of high-current beam propagation in the extended accelerator channel of LIA-30 are considered.

Introduction

Over several years scientists of VNIIEF have been developing high-current electron linear induction accelerators (LIA) with inductors on the base of lines with distributed parameters. The first accelerator of such a type with the inductors on radial lines LIA-10 (14 MeV, 40 kA, 20 ns) was originated in 1977 [1]. At present an improved accelerator LIA-10M (25 MeV, 50 kA, 25 ns) has been started up with the inductors on stepped transmission lines [2]. The most powerful accelerator is LIA-30 (40 MeV, 100 kA, 30 ns), brought into operation in 1989 [3]. While creating such facilities many complicated problems are to be solved, including mode optimization of high - current electron beam acceleration in the extended accelerating channel.

Accelerating System Description

The accelerating system of LIA-30 consists of 4 injecting and 32 accelerating modules. Each module consists of four identical inductors on radial lines with water insulation and a common accelerating tube. On the output of the inductors, being switched under a given temporal program, voltage pulses, having an alternative polarity, are formed. To accelerate, the first voltage pulse is used with an amplitude not exceeding 0.47 MV at pulse duration 30 ns (FWHM) in the idle mode. In the accelerating tubes magnetic solenoids are placed, one per every two inductors. The solenoids are covered with thin-walled metal shields and serve as cylinder drift tubes.

Formation, acceleration and transport of the intense annular electron beam take place in the vacuum ($1.3 \cdot 10^{-2}$ Pa) channel, being 25 m long in longitudinal magnetic guide field of 0.5 T. The vacuum cavity diameters of the injecting and accelerating modules are correspondingly equal to 1320 mm and 670 mm. One

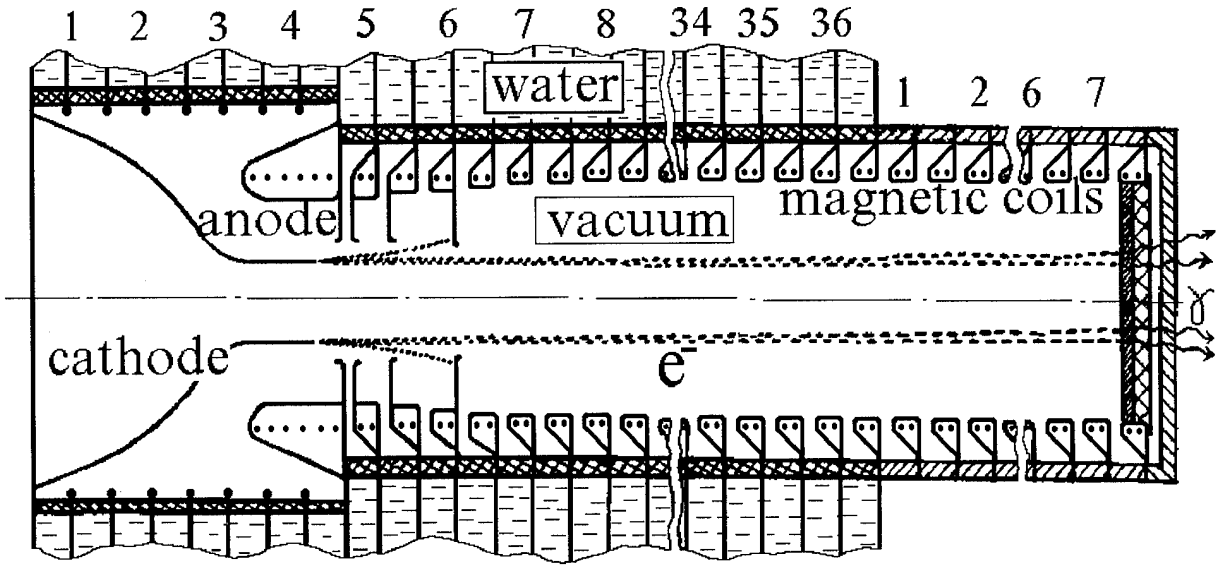


Fig. 1. A simplified diagram of LIA-30 accelerating channel.

of configurations tested is shown in fig. 1. The voltages of four injecting modules are summed on the diode. The immersed foilless diode is formed by a cylinder surface of the cathode and an anode diaphragm. An internal drift tube diameter is gradually increased from 390 mm in the 5-th module to 430 mm in the 7-th module and further remains constant. The electron beam increases its energy while passing 64 accelerating gaps and is further transported in an output device up to a target at the distance 3.5 m.

Peculiarities of Electron Beam Acceleration in LIA-30

If somewhat simplified the beam acceleration can be represented as follows. With strong enough external magnetic guide field annular electron beam motion is defined by a longitudinal component of pulsed electric field E_z. One can distinguish between two components of this field. The first one averaged over the axis of the vacuum channel is mostly defined by characteristics of the accelerating voltage pulse formation system: $E_{z1}(t) \approx E(t) - I_b(t) \cdot Z$, where $E(t)$ - averaged over an axis value of electric field, generated by the inductors in the idle mode; $I_b(t) \cdot Z$ - decelerating voltage, induced by a return beam current $I_b(t)$ on the inductors output gaps with impedance Z per unit length.

The second component deals with self-fields of the beam and is defined by the vacuum channel geometry and current pulse parameters: $E_{z2} \approx - [(\partial q/\partial z)/C + L \cdot \partial I/\partial t]$, where q - beam charge per unit length , L - inductance of the volume between the beam and the water insulation of the inductors per unit length, C - electric capacity between the beam and the drift tubes per unit length. The first item describes particle pushing away in the axis direction under the action of the electron beam space charge forces, and the second one describes an induction acceleration or deceleration under the effect of self-electric field. The expression for E_{z2} can be represented in the following form $E_{z2} \approx - [\partial q/\partial z + (\partial I/\partial t)/V^2]/C$, where the value $V=(L \cdot C)^{-0.5}$ may be considered as an effective velocity of electromagnetic wave propagation in the vacuum channel when the beam is substituted by the metal cylinder electrode of the same diameter. It should be pointed out that due to the existence of the

drift tubes in the accelerating channel this velocity is always less than the velocity of light c. If the LIA-30 the beam diameter would be equal, for example, to 150 mm, than $L \approx 2.9 \cdot 10^{-7}$ Hn/m, $C \approx 5.3 \cdot 10^{-11}$ F/m and $V \approx 0.85 \cdot c$.

For a further analysis we restrict our attention to the case, when all the particles have the same constant velocity V_b and $E_{z2} \approx - [1-(V/V_b)^2] \cdot L \cdot (\partial I/\partial t)$. Three transport modes can be realised. At the beam velocity $V_b=V$ self-fields of the beam must not effect significantly particle longitudinal motion. In the case $V_b<V$ at the leading edge, where $\partial I/\partial t>0$, under the effect of the self-fields an addition particle acceleration takes place due to predominance of Coulomb's forces over those of induction deceleration. Correspondingly, trailing edge deceleration is noted. In accelerators of LIA-30 type an electron velocity just at the injector output is close to the velocity of light and over the whole accelerating channel length, at least for the most of particles, the condition $V_b<V$ is realized. In this case in the absence of an external accelerating field electron deceleration must occur at the leading edge, while at the trailing edge acceleration is to occur. Assuming $V_b \approx c$, I=100 kA and front duration 5 ns regarding to the parameters, mentioned above, one can find $E_{z2} \approx 1.6$ MV/m, comparable with the averaged along the axis electric field amplitude under operation of the accelerating modules in the idle mode ($\leq$ 3 MV/m). The real processes are more complicated, but numerical simulation results confirm the regularities, mentioned.

Thus the peculiarity of high-current electron beam acceleration in LIA-30 is an important role of a longitudinal component of the self-electric field, that combined with a big length of transport may lead to a considerable deformation of the current pulse and decrease of transport efficiency.

Experimental Results

In fig. 2(a) the oscillogram is illustrated of a voltage pulse in the accelerating gap under the accelerating module operation in the idle mode (1), as well as the oscillogram of a voltage pulse (2), induced by the beam with current ~ 80 kA (3) on the accelerating gap of a module, uncharged. With the current increase velocity ~ $6 \cdot 10^{12}$ A/s the decelerating voltage at the leading edge achieves ~1/3 of an output voltage amplitude. In fig. 2(b) as an example the oscillogram is shown of the total voltage pulse at the accelerating gap (4) for the beam current ~ 120 kA (5) at the increase velocity ~ $8 \cdot 10^{12}$ A/s. The effect of the electron beam self-fields leading to deceleration of the initial pulse region and acceleration at the trailing edge is expressed explicitly. The total voltage pulse form depends on variation in time of module switching-on and the moment of the beam arrival to the accelerating gap. The absence of considerable deceleration at the leading edge can be ensured at the expense of inductors initiated earlier and/or decrease of injected current increase velocity. Experimental optimization of the accelerator operation modes is a mutual agreement of the injected pulse parameters and temporal program of modules initiation.

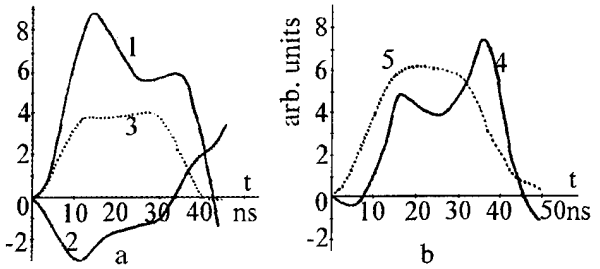


Fig. 2. Voltage (1,2,4) and current (3,5) pulses .

During experiments various injection modes were tested. Along with four injecting modules up to four accelerating modules formed the injector at the expense of a corresponding expending of the cathode electrode. Meanwhile a diameter of the cathode edge varied from 100 to 250 mm, injection energy differed from 2.5 to 7 MeV at

current 50-170 kA. An amplitude and current increase velocity, being obtained under a fixed diode geometry, varied at the expense of single injector module turning-off, as well as the temporal program choice of modules initiation. With a current value considerably exceeding 100 kA one couldn't manage to ensure with stability high-efficiency electron acceleration. During propagation of the beam over the accelerator the current pulse deformation is observed with sharpening of the leading edge, that leads to the thickness increase of annular beam and considerable losses of an accelerated charge. With beam current increase the problems also appear related with reproducibility of output parameters of the accelerator due to acceleration sensitivity towards possible deviations from the synchronization program, as well as to possible failure in operation of separate inductors.

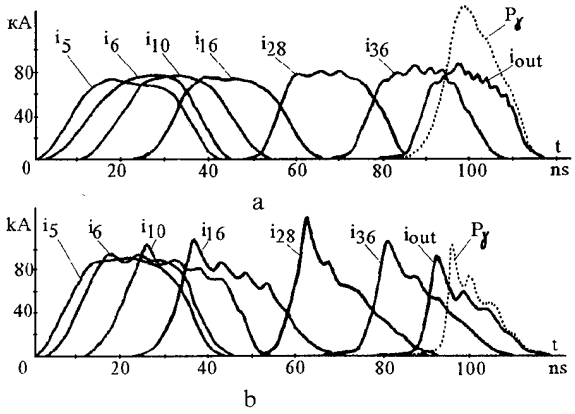


Fig. 3. Current pulses, registered in different accelerating modules (i5....i36), and bremsstrahlung pulse Pγ for different injection modes.

With currents ≤ 100 kA the acceleration is more stable. As an example a set of current pulse oscillograms is shown in fig. 3(a), registered in various accelerating modules in a one shot at the current ~80 kA and injected current increase velocity ~$6 \cdot 10^{12}$ A/s. To obtain high output bremsstrahlung one is to accept some deformation of the current pulse shape. In this operation mode electron beam acceleration is accompanied with current pulse duration reduction from 28 to 23 ns at charge transport efficiency ~0.9. Bremsstrahlung dose at 1 m distance from a target constitutes $6 \cdot 10^3$ rad (TLD) at power $4 \cdot 10^{11}$ rad/s. At the expense of current increase velocity rise and program varying of modules switching-on one can purposely obtain bremsstrahlung pulses with a sharp enough front (~ 3 ns) due to going over to the mode of the beam transport with deceleration at the leading edge, as it is illustrated in fig. 3(b). In this case the dose is reduced to $2.5 \cdot 10^3$ rad at power $3 \cdot 10^{11}$ rad/s.

Conclusion

The presence of cavities between the drift tubes and the water insulation of the inductors in the facility LIA-30 lead to additional deceleration at the leading edge of the electron beam being accelerated. Compensation of this effect is ensured by a prior (relative to the electron beam arrival time) switching-on of accelerating modules under restriction of the amplitude and the injected current increase velocity. By present a stable beam transport has been mastered with currents up to 100 kA at the current increase velocity up to $6 \cdot 10^{12}$ A/s.

References

[1] A.I. Pavlovskii, V.S. Bossamykin, V.A. Savchenko et.al. Powerful Electron Accelerator LIU-10 // Docl. Akad. Nauk SSSR, Vol. 250, No 5, pp. 1118-1122, 1980.

[2] V.S. Bossamykin, V.S. Gordeev, A.I. Pavlovskii et al. Linear Induction Accelerator LIA-10M// presented at the 9th IEEE Pulsed Power Conference, Albuquerque, NM, June 21-23, 1993

[3] A.I. Pavlovskii, V.S. Bossamykin, A.I. Gerasimov et al. Linear Accelerator with Radial Lines - LIA-30// Proc. 9th Intern. Conf. on High-Power Particle Beams.- Washington, DC, 1992. -vol. 1.- pp.273-283.

High Current Beam Propagation Studies at the Naval Research Laboratory

R.A. Meger, D.P. Murphy, M.C. Myers, D.J. Weidman,[a]
R.F. Fernsler, R.F. Hubbard, S. Slinker

Plasma Physics Division, Naval Research Laboratory,
Washington, DC 20375-5346

Experiments have been performed on the production, conditioning, and propagation of high current electron beams using NRL's SuperIBEX generator.[1] The objective of these experiments has been to produce high current density electron beams that are able to propagate multiple betatron wavelengths without suffering disruptive hose growth. The key to producing a hose-stable high current beam is to condition the beam by damping radial perturbations and tailoring the emittance profile to prevent growth of the instability. Results from recent experiments on beam production, conditioning, and propagation will be presented.

For the last 10 years the Naval Research Laboratory has been investigating the propagation of charged particle beams (CPBs) in the atmosphere for a variety of directed energy applications. Recently NRL has focused on developing techniques to stabilize the resistive hose instability which has been the primary hurdle to stable propagation in the atmosphere.[1,2]

The resistive hose instability results from the interaction of beam generated plasma currents with the beam current itself. The instability grows exponentially at a given location in the beam frame out of any noise or perturbations which match the local betatron oscillation frequency, $\omega\beta$, which is the natural oscillation frequency of beam electrons in the in the beam's electric and magnetic self fields. This resonant frequency can be different at different locations within the beam pulse. The characteristic of the instability is for the amplitude of oscillations to grow at a given location in the beam frame at the resonant frequency. Depending on the spread of oscillation frequencies contained by the beam at a given location in the beam pulse the entire beam can be excited to perform coherent hose motion or only a particular component can grow which feeds the local beam temperature. Once the instability is triggered it will grow at that location in the beam frame as the beam propagates as well as coupling to the beam slices behind the initiation point. The growth rates are fast enough that once initiated the hose amplitude can fully disrupt the beam in a few betatron periods, $2\pi/\omega\beta$. The instability can also grow and quench, feeding energy into beam emittance and leading to a rapid expansion of the beam cross section.

Efforts to control the growth of the hose instability center on minimizing the perturbations that initiate the instability and on limiting its growth rate by smearing out the spectrum of betatron oscillation frequencies at a given position in the beam.[3] This requires controlling the beam parameters, including current, voltage, and emittance, on the beam time scale, as well as damping any coherent oscillations which appear on the beam. In the NRL experiments this is done by first producing a beam with as little radial motion as possible and then passing this beam through a series of conditioning cells. A passive Ion Focused Regime (IFR) cell is used to tailor the

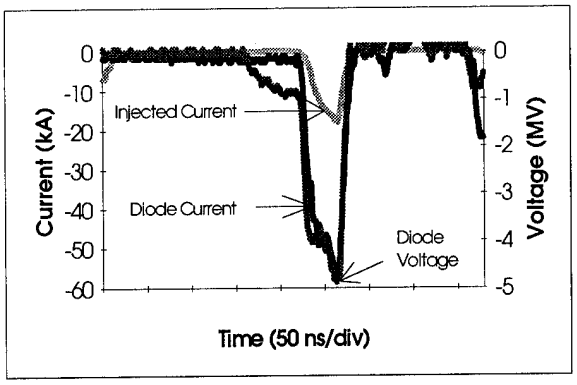


Figure 1. Diode voltage and current and injected beam current.

beam emittance profile. This is followed by a wire cell where current is driven by an external bank through a thin wire on the beam axis to phase mix coherent radial motion of the beam. Results from experiments at the various stages of beam conditioning will be discussed.

Experiments were performed on the SuperIBEX generator (5 MeV, 100 kA, 40 ns pulse).[1] Figure 1 shows the voltage, diode current, and injected beam current wave forms generated by the accelerator. An aperture is used to lower the injected beam current to the 15-20 kA regime as well as to select only the low emittance portion of the beam pulse. Figure 2 shows streak photographs taken 10 cm downstream of the anode foil from two different diode configurations. The unstable beam (a) comes from a 6 mm stainless steel cathode and a 52 mm aperture. The beam undergoes large amplitude radial motion on a 5 nanosecond time scale. The source of this radial motion is unknown. Without conditioning hose motion will disrupt this beam in a short propagation distance. The stable beam (b) was produced by the same cathode and a 12 mm diameter aperture. The small aperture appeared to give the most consistent beam with minimal radial motion. A large number of different diode configurations were investigated with (b) producing the most stable and consistent beams.

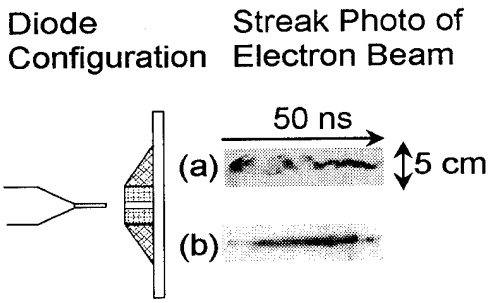


Figure 2. Diode configuration and streaks of beam downstream of aperture.

Just downstream of the injection aperture is the IFR radius tailoring cell shown in figure 3. Considerable theoretical work has been done on IFR cell conditioning.[4] This 20-cm diameter, 85-cm long cell uses a low density gas fill (5-20 mTorr argon) to provide a time-dependent radial electric field within the beam profile. Beam ionization of the background gas increases the space charge neutralization over the 40 ns long beam pulse. Initially, before the background gas is ionized, the radial electric and magnetic forces balance to within $1/\gamma^2$ where γ is the relativistic factor. This allows the beam radius to expand due to its own perpendicular temperature. As the space charge is neutralized, the magnetic forces start to pinch the beam. When the space charge neutralization fraction reaches $1/\gamma^2$ the electric and magnetic forces cancel. Further ionization allows the magnetic force to

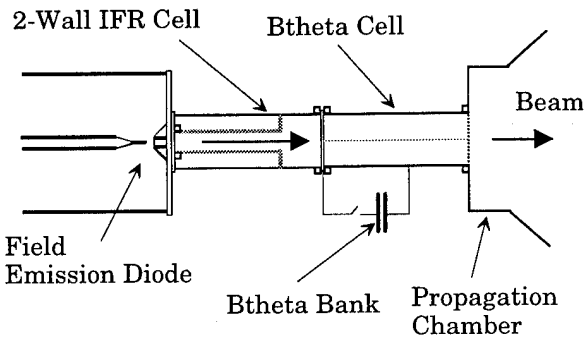


Figure 3. SuperIBEX beam conditioning system.

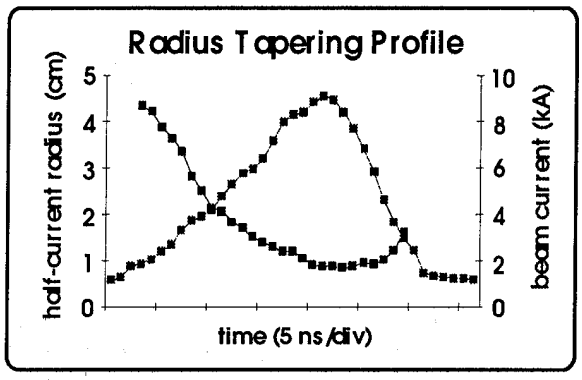


Figure 4. Radius and beam current for conditioned beam.

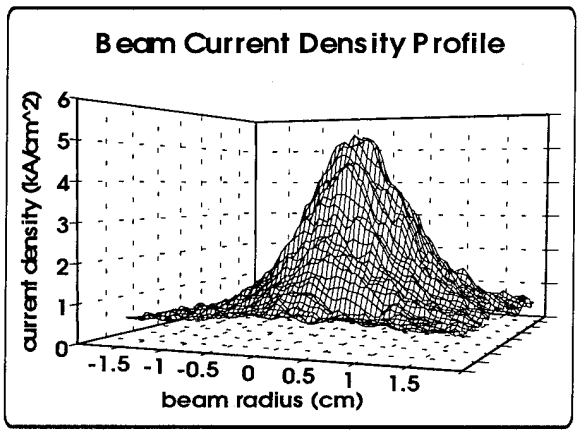


Figure 5. Beam current density from Cherenkov foil light near peak current.

dominate and the beam pinches to a smaller radius. Thus the IFR cell allows one to adjust the radial profile on the beam time scale. The latest version of the radius conditioning cell utilizes an inner wall made of 18 micron thick aluminum foil which extends from the injection point 65 cm downstream where a similar radial foil terminates the tube. This tube provides wall stabilization and centering for the beam as it traverses the IFR cell. The large diameter region at the downstream end allows the portion of the beam that escapes through the thin wall to rejoin the beam. Figure 4 shows the beam current and its half-current radius profile as measured by a segmented faraday cup.[5] The beam shows 10 kA peak current with a radius tailoring ratio of nearly 5:1 over the beam current profile. Time dependent centroid measurements show the beam to exit this IFR cell with a maximum of 2 mm radial motion from the beam axis. Figure 5 shows the beam current density as a function of space at a time near peak current taken from Cherenkov light captured by a framing camera. The 5 kA/cm^2 beam current density for a radius tailored beam is approximately the desired current density for applications. This radius tailoring must be converted into an emittance tailoring in order to stabilize the hose growth. This is done either by passing the beam through a thick scattering foil, which converts radius to emittance, or by providing some other means to convert radius to temperature. A scattering foil adds temperature to the beam resulting in a broader (lower current density) beam profile.

The final stage of the conditioning process utilizes a wire or B_θ cell shown schematically in figure 3. Image forces from an axial wire in a vacuum transport cell cancel to within $1/\gamma^2$. If a pinch current is driven along the wire a radial pinch force is imposed on the beam. Such a pinch force is highly anharmonic, pulling the beam electrons near the wire much harder than those further out. Thus coherent motion of the beam is smeared out by the anharmonic pinch force. The radius tailoring present upon injection will also be converted into perpendicular temperature (emittance) in the cell. The optimum wire current is set by matching the beam emittance in the cell introduced by the wire current to that for a beam equilibrium in the air downstream of the cell. This turns out to be approximately half of the beam effective current (beam current minus plasma current in the air) or in the 2-3 kA regime for a 10 kA SuperIBEX beam. In the experiments performed on SuperIBEX it is difficult to measure effect of the B_θ cell since the motion is damped to sub-mm levels. The best diagnostic is the stability of the beam as it

propagates. Preliminary results using a vacuum B_θ cell have shown an improvement in stable propagation range. Beams without macroscopic hose motion for up to 4 meters of propagation length have been observed. This represents stable propagation for nearly 15 betatron wavelengths in full density air. Detailed measurements on the effect of the vacuum B_θ cell are in progress.

Macroscopic stabilization of the hose instability is obvious from open shutter pictures of beams in the 5-m long, 2-m diameter propagation chamber. Unstable beams hose around and strike the chamber walls within 1 meter of entering the chamber. As stability is improved through beam conditioning, the beam straightens, often showing a multi-meter long curved trajectory which deviates from the injection axis by tens of centimeters over the 5-m propagation range. Further improvement in the beam conditioning results in a straight beam propagation. This does not, however, mean that the hose has been fully stabilized. Measurements of the beam expansion as a function of propagation distance show that the beam is expanding faster than would be expected from only gas scattering (Nordsieck expansion). Figure 6 shows the beam radius from an open shutter camera picture of a stabilized beam. The image was digitized and an Abel-inverted

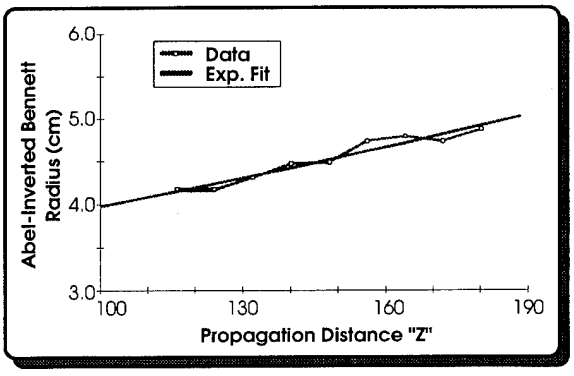


Figure 6. Beam radius derived from an Abel inversion of open shutter photo.

Bennett radius computed. Under most circumstances the observed expansion is faster than expected from analytic calculations using the beam parameters. One also finds that the higher the current density injected into the air, the more difficult it is to stabilize the beam and the faster the beam expands. A detailed measurement of the beam expansion is underway using multiple Cherenkov foil diagnostics to yield time resolved expansion data for the beam. This has required a significant effort to time correlate the electromagnetic and optical diagnostics. Preliminary data from these measurements agree with the open shutter measurements.

In summary a concerted effort to understand and stabilize the resistive hose instability for high current relativistic beams has been undertaken. Initial perturbations on the beam introduced by the diode have been minimized. A new IFR cell configuration which produces a 5 kA/cm^2 beam has been developed. A B_θ cell has been introduced to damp out residual radial motion. 10 kA beams have been stably propagated in full and partial pressure air backgrounds for up to 5 meters. The more subtle growth in beam cross-section due to the hose instability is being measured.

The authors would like to thank Dr. J. A. Antoniades and Dr. M. Lampe for numerous contributions to the research and to G. Littlejohn, A. Noll, and J. Picciotta for technical assistance in performing the work. This work was supported by the Office of Naval Research.

[a]Institute for Plasma Research, UMd, College Park, MD 20742-3511

[1]R.A. Meger, et al, Proceedings of the 9th Inter. Conf. on High-Power Particle Beams (Washington, DC, May, 1992), p. 99.
[2]E.P. Lee, Phys. Fluids **21**, 1327 (1978).
[3]R.F. Fernsler, et al, these proceedings.
[4]R.F. Hubbard, et al, J. Appl. Phys. **73**, 4181 (1993).
[5]T.A. Peyser, et al, Rev. Sci. Instrum. **62**, 2895 (1991).

NEW RESULTS OF THE FULL SCALE RIBBON BEAM EXPERIMENTS ON U-2 DEVICE

A.V.Arzhannikov, V.B.Bobylev, V.S.Nikolaev,
S.L.Sinitsky and A.V.Tarasov

Budker Institute of Nuclear Physics, 630090 Novosibirsk, Russia

ABSTRACT

The paper presents the experimental results on generating and transforming the ribbon (3.5x130cm) beam with the electron energy 1MeV, beam current up to 70kA and pulse duration 8 μs. 70% efficiency of the energy transfer from a capacitor storage to 0.4MJ ribbon beam has been obtained. The similar efficiency has been also achieved for the transformation of the ribbon beam to a compressed circular one at the optimal conditions. Measurements have shown an angular spread of the compressed beam is less than 10^0.

1. INTRODUCTION

Obtaining 1MJ electron beams with the current density and angular spread suitable for plasma heating experiments and for microwave generation becomes really solved problem if we turn our attention to the electron beams with a ribbon cross section. Motivated by this possibility experimental investigations on the ribbon beam generation, transport and transformation are carried out at U-2 device [1-2]. 200kJ energy content of the transformed and compressed beam with local parameters suitable for plasma heating in the GOL-3 solenoidal trap has been achieved on the U-2 accelerator [3]. Higher energy content of such beam could not be obtained in that experiment because of charge neutralization of the transformed beam was not sufficient. Another problem of the experiment was that the compressed beam had a cross section shape differing from a circle. To solve these two problems the last U-2 experiments has been devoted to.

2. OPERATION OF THE U-2 DEVICE

The U-2 device is operated by the following way [3]. One megavolt pulse is applied to a fibrous graphite cathode with 4.5x140cm emission surface. Electrons emitted by the cathode, are accelerated in a magnetically insulated diode and pass through the anode slit into a slit vacuum channel with a guiding magnetic field and inner dimensions 6x145 cm. This electron beam has the cross section 3.5x130 cm. After passing through 1m slit channel the ribbon beam enters into transforming unit intended for conversion of the ribbon cross section to the circle . At the finishing of such kind of the transformation the beam cross section is compressed in 10-20 times by a special magnetic system where the strength of the magnetic field increases from 4kG up to 40kG.

At these experiments in the comparison with the previous one [3] we have used a gas puffing in the vacuum chamber where the beam compression occurs. Besides that we have changed the profile of the emission surface of the cathode and added a special correction coils to the transforming unit for achieving an axially symmetric shape of the compressed beam cross section.

3. EXPERIMENTAL RESULTS

Beam transforming at gas puffing. At the beginning of the experiments on transforming and compressing the electron beam, an

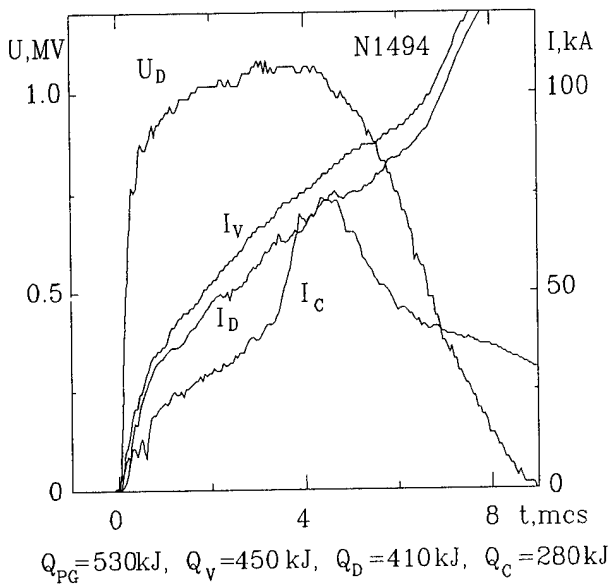


Fig.1. Set of signals characterizing the generation and transformation of the ribbon electron beam. U_d - diode voltage, I_v - current flowing from the pulse generator to the diode chamber, I_d - diode current, I_c - current of the compressed beam.

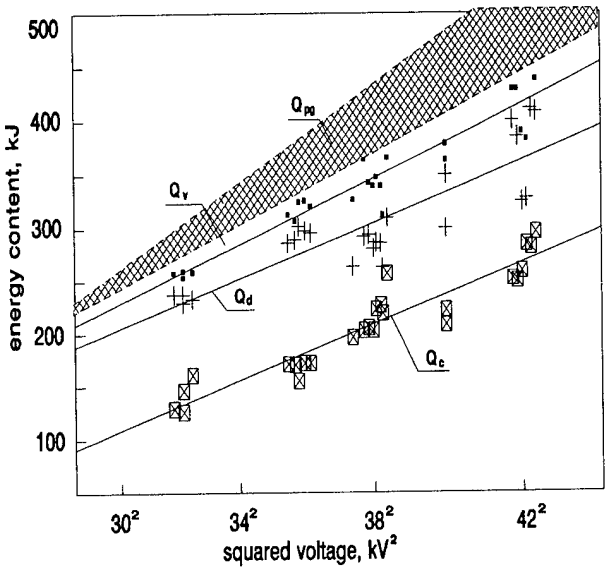


Fig.2. Total energy in the pulse passing through the various parts of the U-2 accelerator. Q_{pg} - energy in the capacitor storage, Q_v - energy transferred from the capacitor storage to the diode chamber, Q_d - energy of the ribbon beam in the diode, Q_c - energy of the circular compressed beam.

ionization of a residual gas by the beam electrons was used for its space charge neutralizing. The efficiency of the energy transfer from a capacitor storage to the compressed beam was obtained about 38% only because of the neutralization of the beam space charge was not enough. On this reason the next experiments have been done at a stationary gas puffing into the region where the beam compression is realized. This gas puffing should retain a low (about 5×10^{-5} Torr) pressure in the accelerator diode gap. According to this limitation we have possibility to increase the gas pressure in the compression system up to 2×10^{-4} Torr, not more. In this case the efficiency of the energy transfer from the capacitor storage to the compressed beam has been increased only up to 45% [3] but not so essentially as we hope.

The further increase of the efficiency could be expected at the additional increase of the gas pressure in the compression chamber by using a pulse gas puffing. Fig.1 demonstrates a set of signals registered in one of the typical shots with the pulse gas puffing at the optimal conditions. These conditions are: the pressure of the air in the puffing system is ~5atm, the time delay of the beam generation after the gas puff switching is close to 1.2ms. The gas pressure in the beam compress chamber has the values 10^{-3} Torr in this case and it is sufficient to realize the beam charge neutralization from the beginning of the beam pulse. The energy content of the compressed beam has reached 280kJ in this shot and it is 54% of the energy stored in a high voltage generator. At the increase of the time delay from 1.2 ms up to 1.5 ms we have observed the decrease of the energy of the compressed beam in the experiments that is connected with the breakdown of the accelerator diode gap in time shorter than 5μs. This breakdown has been caused by the increase of the gas pressure in the diode gap. If the time delay is decreased down to 1 ms the gas pressure in the region of the beam compression becomes insufficient for the space

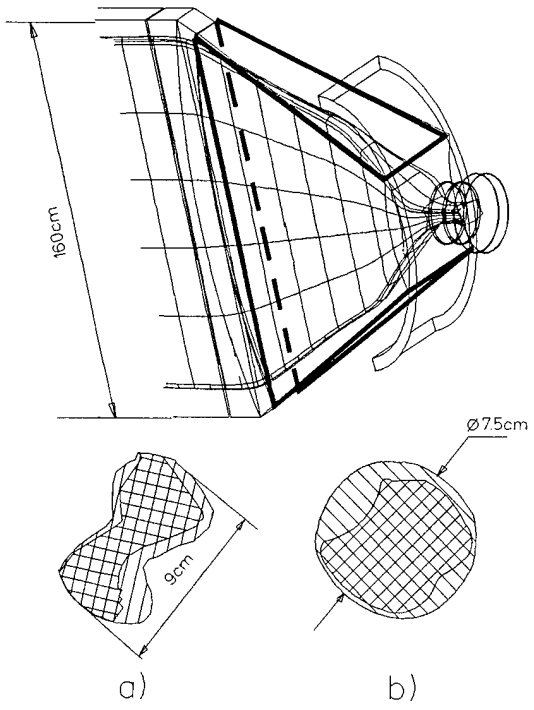


Fig.3. Schematic of the correction coils and the beam cross section shape: a) without correction, b) with correction.

charge neutralization of the beam during the first two microseconds. The using for the pulse puffing the gases with a low atomic weight, for example hydrogen, is turned out unacceptable because of the breakdown of the diode in a few microseconds in this case.

To analyze the efficiency of the U-2 accelerator operation the total energy passing through the various parts of this machine during the beam pulse is compared in the Fig.2. The total energy as a function of a squared voltage on capacitor banks of the storage is shown there. The shaded region is the energy in the storage, points - energy transferred from the storage to the vacuum chamber, crosses - energy of the electron beam in the accelerator diode and squares - energy of the beam after its compression. The straight lines in Fig.2 have been drawn on the experimental data according to the least squares method. From the Fig.2 one can conclude that in a wide range of the capacitor voltage the efficiency of the energy transfer from the capacitor storage to the ribbon electron beam in the diode is about of 70% and from the storage to the compressed circular beam - 50%.

70% efficiency of the transformation of the beam cross section from the ribbon shape to the circle is a result of losses of both tips of the ribbon cross section on a graphite limiter during the transformation. To prevent these losses and to obtain the beam with the circular cross section we use additional correction coils which have been added to the transformer unit. Geometry of the correction coils and views of the cross section shape of the compressed beam are shown in Fig.3. The correction coils are drown by the bold lines, cross shadowed region refers to the beam current density higher than 1kA/cm^2. The left picture (a) shows the case when the correction coils have been switched off and the right one (b) - these coils have been switched on. Looking at the pictures one can conclude that using these additional coils allows us to obtain a really circular shape of the compressed beam.

Angular spread measurements. To measure the angular spread of the electron beam after the transformation and compression the collector-calorimeter at the exit of the compression system has been replaced by a detector of the angular spread [4]. Besides that an additional magnetic system has been constructed for creation of a homogeneous magnetic field in the region close to the detector axis. Almost the whole electron beam is absorbed by a graphite plate at the exit of the compression system and only 8mm diameter cylindrical flow of the electrons passes through a hole in the plate. This cylindrical flow is expanded at its motion in the decreasing magnetic field which has the value 6kG at its homogeneous part in the angular spread detector. This detector looks like the graphite tube with the inner diameter 6mm. This tube is cut into four rings insulated each from other. The lengths of the rings are 1cm, 1cm, 2cm and 2 cm. During the flow passing through these rings some portions of the flow electrons are absorbed by the inner wall of the rings. The rest of the electron flow goes out from the tube and comes to a graphite

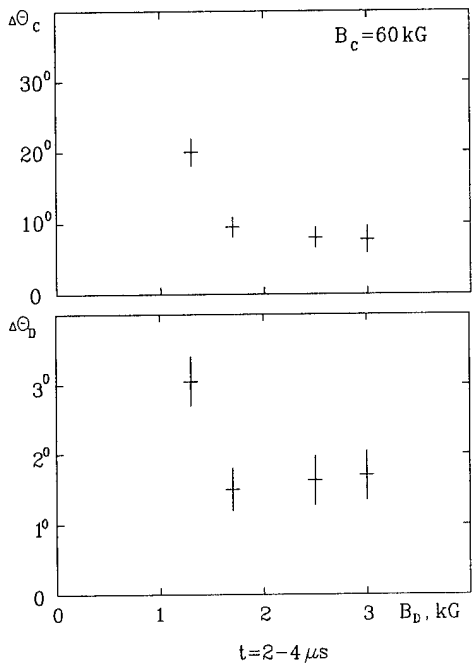


Fig.4. Angular spread of the E-beam at the accelerator diode $\Delta\Theta_D$ and at the compression system $\Delta\Theta_C$ as a function of the magnetic field B_D in the diode gap.

collector closing the tube exit. For obtaining the angular spread of the beam electrons the currents of the electrons absorbed by the rings have to be compared with the results of computer calculations. As a result of this comparison we have determined the angular spread of the beam electrons. The dependence of the beam angular spread on the strength of the magnetic field in the accelerator diode is shown in the Fig.3 for the two region of the electron trajectory: lower picture - at the anode of the accelerator diode, upper one - at the exit of the beam compression system. One can conclude from the Fig.4 that the angular spread of the compressed beam become less than 10^0 at the exceeding of the diode magnetic field the value about of 1.5kG. According to these results the experiment on the plasma heating in the solenoid by the electron beam shall be carried out at the magnetic field in the diode higher than this value. In addition a local current density of the compressed beam has been measured in the experiment. The current density has a value about 1 kA/cm^2 and it is close to the average current density of the beam calculated by the division of the beam current on the beam cross section.

4. CONCLUSION

So, 0.4 MJ energy content of the ribbon electron beam has been achieved at our investigations. It has been experimentally demonstrated that about 70% of the energy of this beam is transferred to the circular beam with the current density 1-1.5 kA/cm^2 and the angular spread less than 10^0 in the magnetic field 40-60kG.

5. ACKNOWLEDGMENTS

The authors thank Prof. D.D.Ryutov and Dr. V.S. Koidan for helpful discussions, the engineers A.D. Khilchenko, V.V. Konyukhov, A.G. Makarov and M.A.Agafonov for assistance at the U-2 device operating.

6. REFERENCES

1. A.V.Arzhannikov, A.V.Burdakov, V.V.Chikunov et al.,"GOL-3 Programme", *Proc. 8-th Intern. Conf. on High-Power Particle Beams*, Vol.I, p.14, Novosibirsk, USSR, 1990.
2. A.V.Arzhannikov, V.S. Nikolaev, S.L. Sinitsky et al., "FEL Driven by High Current Ribbon REB and Operated with Two Dimensional Feedback", *Technical Digest 14-th Intern. Free Electron Laser Conf.*, p.214, Kobe, Japan, 1992.
3. A.V.Arzhannikov, V.B. Bobylev, V.S. Nikolaev et al., "Ribbon REB Research on 0.7MJ Generator U-2", *Proc. 9-th Intern. Conf on High-Power Particle Beams,* Vol.II, p.1117, Washington, DC, USA, 1992.
4. A.V. Arzhannikov, V.S. Koidan, S.V. Loginov, "Measurement of the angular spread of the magnetized electron beam by its passing through the microholes", *Pribory tekchnika experimenta*, v.4, p.36, 1983.

Intense Electron-Beam Transport in the Ion-Focused Regime Through the Collision-Dominated Regime*

T. W. L. Sanford and J. W. Poukey
Sandia National Laboratories
Albuquerque, NM 87185-1193

D. R. Welch
Mission Research Corporation
Albuquerque, NM 87106

R. C. Mock
Ktech Corporation
Albuquerque, NM 87110

Abstract

This paper reviews the transport of the 19-MeV, 700-kA, 25-ns Hermes-III electron beam in long gas cells filled with N_2 gas spanning six decades in pressure from 10^{-3} to ~10^3 Torr. We show through measurements and theoretical analyses that the beam has two windows of stable transport: a low-pressure window (between ~1 and ~100 mTorr) that is dominated by propagation in the semi-collisionless IFR (ion-focused regime), and a high-pressure window (between ~1 and ~ 100 Torr) that is dominated by propagation in the resistive CDR (collision-dominated regime). In the CDR, 79±1.5% of the beam energy is transported over 11 m at 20 Torr. In the IFR, we show that intense radiation fields with controllable rise times and pulse widths can be generated on axis at a bremsstrahlung target. In summary, the measurements and analyses presented here provide a quantitative description of the Hermes-III beam transport over six decades in pressure.

Measurements and analyses[1,2,3] show that the 13-TW Hermes-III[4] electron beam has two windows of stable transport in long drift cells filled with N_2 gas terminated by a bremsstrahlung producing target: a low-pressure window (between ~1 and ~100 mTorr) that is dominated by propagation in the ion-focused regime (IFR)[5] and a high-pressure window (between ~1 and ~100 Torr) that is dominated by propagation in the resistive collision-dominated regime (CDR). In the transition region between the two windows, beam plasma-electron instabilities significantly disrupt propagation.

Propagation in both regimes (the IFR at early time and the CDR at later time) is observed from ~5 to ~100 mTorr, which produces two distinct bremsstrahlung pulses from the single injected beam pulse. As the pressure increases, two-stream instabilities terminate IFR propagation and the associated bremsstrahlung pulse earlier and earlier in time. Above 5 mTorr, this instability is sufficiently quenched by gas collisions that CDR propagation in the beam body can occur, leading to a second bremsstrahlung pulse.

Above 200 mTorr, the gas breaks down too rapidly for a significant IFR pulse to form, and for higher pressures only a single pulse in the CDR is propagated. Between ~200 mTorr and ~1 Torr the hollowing instability and lack of magnetic confinement limit CDR propagation. Only for pressures above ~1 Torr is stability achieved in the CDR. Above ~100 Torr, however, the resistive hose instability degrades propagation. Within this high pressure window, maximum energy transport occurs at ~20 Torr. The optimum results from a combination of two effects: (1) improved beam confinement from the magnetic pinching force generated by the residual net current (sum of beam and plasma return current) as the pressure is increased, and (2) reduced energy loss from the inductive

*This research was supported by the U. S. Department of Energy under contract DE-AC04-94AL85000.

fields and inelastic collisions as the pressure is decreased.

The experimental arrangement is similar to that described in Ref. 1 (Fig. 1). Current shunts IA1, IA2,..., IA5 in the anode and IC1 in the cathode monitor the current flow. The voltage across the diode at IA1 is obtained from parapotential flow theory using the measured total current from IA1 and boundary current from IC1. The net current flowing 20 cm upstream of the target at the end of the drift cell is obtained from IA4 and IA5. For the data presented here, the peak voltage and current at IA1 are measured to be 19.0±0.5 MV and 655±14 kA, respectively. The full-width half-maximum (FWHM) of the voltage pulse is 33.5±1.4 ns (25 ns FWHM power pulse). The uncertainties, as those elsewhere in the paper, refer to RMS shot-to-shot variation.

The compound-lens diode[6] is used to inject the Hermes-III annular electron beam at near paraxial angles and at 12-20 cm radii into the gas cell. This diode, shown in Fig. 1b, allows separate control of beam radius (by varying AK gap) and injection angle (by varying lens current I_E).

At the drift cell exit are placed a variety of diagnostics, including a calorimeter (Fig. 1c), a thermoluminescent dosimeter (TLD) array (Fig. 1d), and Compton diodes (CDs) (Fig. 1e). A microwave detector (MW) is placed near IA4 to detect plasma electron oscillations such as from a two-stream instability. TLDs are mounted every 25 cm along the top and bottom exterior to the 11-m drift cell. These measure localized beam loss and, thus, are sensitive to the presence of betatron oscillations, resistive hose and hollowing instabilities, and give some measure of θ-asymmetry.

The basic result of experiment, theory, and modeling with the 2D MAGIC[7] and 3D PIC code IPROP[8] is shown in Fig. 2. At low N_2 pressure (1-100 mTorr), the beam propagates with up to 30% efficiency in the IFR mode, where plasma electrons are blown out and the beam is focused by the residual ions. The plasma itself is produced from the initially neutral gas by impact ionization and ion avalanche. Late in the pulse, the charge neutralization fraction reaches unity and the plasma electrons are no longer ejected, leading

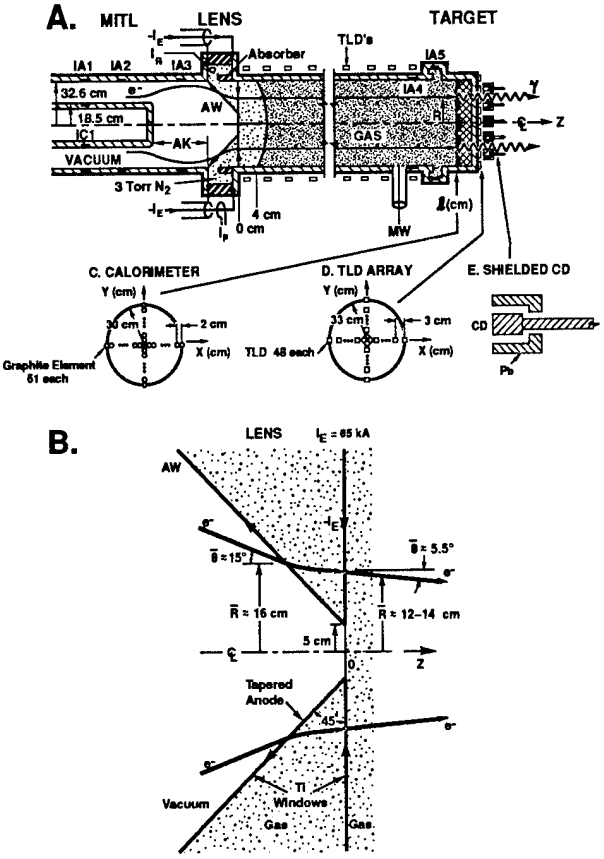


Fig. 1 (a) Schematic of experimental arrangement showing placement of the magnetically insulated transmission line (MITL), the compound-lens diode (LENS), the drift cell of length ℓ, and the bremsstrahlung target. (b) Detail of the compound-lens diode showing flow of the external current I_E and the average beam trajectory when the AK gap equals 20 cm. (c) Detail of upstream surface of the graphite calorimeter. (d) Detail of the TLD array showing TLD placement. (e) Detail of a shielded Compton diode.

to growth of the two-stream instability, which disrupts propagation. At intermediate pressure (p ≈ 0.1-1.0 Torr in Fig. 2), charge neutralization occurs rapidly, but current neutralization is weak due to magnetic field depression of the axial conductivity. The resulting strong magnetic fields pinch the beam, and a hollowing instability is excited sending much of the beam to the outer wall. Above a few Torr, the current neutralization is adequate to restrain the hollowing

instability. For these pressures, the beam propagates in the CDR, with a maximum efficiency of 79±1.5% at 20 Torr. At pressures above ~100 Torr, the hose instability sets in and quenches propagation.

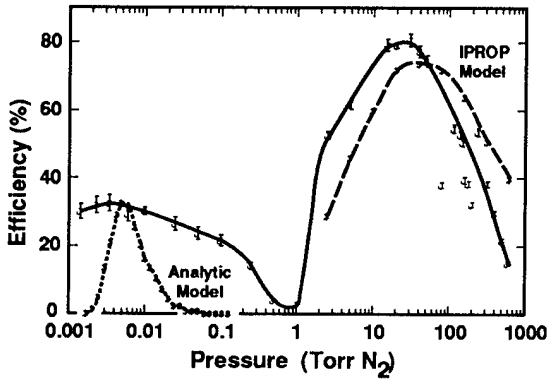


Fig. 2 Energy transport efficiency measured in the calorimeter [Fig. 1(c)] as a function of drift cell pressure, for ℓ = 11 m. Also shown is the two-dimensional IPROP model of Ref. 1 run with θ-symmetry for the CDR and the simple analytic model of Ref. 2 for the IFR.

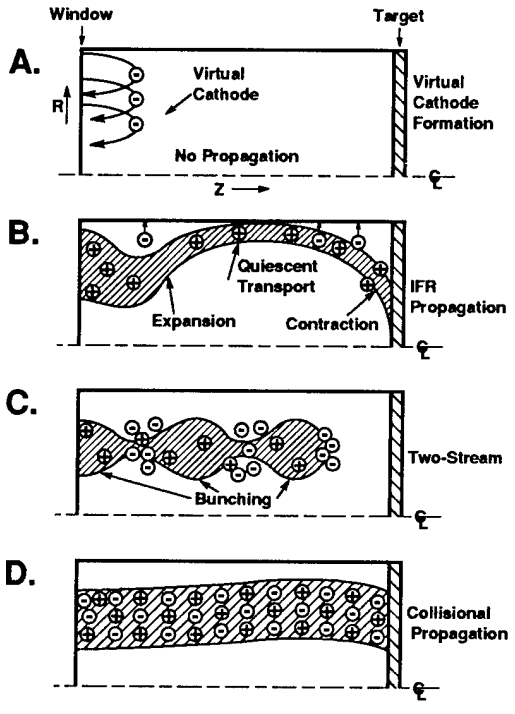


Fig. 3 Four temporal phases of beam propagation in the drift cell at low pressure: (a) virtual cathode formation, (b) IFR propagation, (c) two-stream instability formation, and (d) CDR propagation.

The qualitative physics at low to moderate pressures (or at early time and higher pressure) are summarized in Fig. 3. We can think of the four phases (virtual cathode, IFR, two-stream, and collisional propagation) as representing time development, increasing pressure, or increasing charge neutralization (up to unity in phases c and d). This picture is in agreement with the measurements in Fig. 2 and is also supported by the measurements of the TLDs mounted along the 11-m drift cell, the CD measurements, and the MW measurements.

Several other results of interest, seen in both code/analyses and measurement, are: (1) the radial beam profile at the target (Fig. 4) is strongly peaked on axis in the IFR (the foil-pinch effect when space-charge neutralization is incomplete), which leads to an intense on-axis radiation pulse, but relatively flat in the CDR; (2) over the range 5 to 50 mTorr the rise time and width of the associated radiation pulse in the IFR can be controlled by adjusting the pressure;[9] (3) a double radiation pulse is dramatically seen at ~ 0.1 Torr—the IFR pulse arrives first and the CDR pulse later (Fig. 5); and (4) current neutralization is maximum near 1.0 Torr as shown in Fig. 6.

In summary, we have measured, calculated, and understood the propagation of very high current electron beams over the wide pressure variation 10^{-3} to 10^{3} Torr.

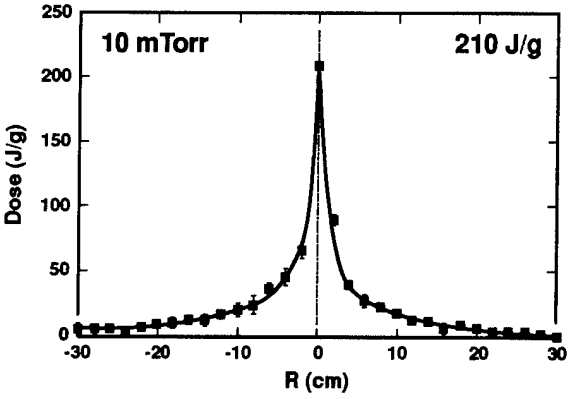


Fig. 4 Radial surface dose measured with the graphite calorimeter, corresponding to propagation shown in Fig. 3B, for a pressure of 10 mTorr and for ℓ = 11 m.

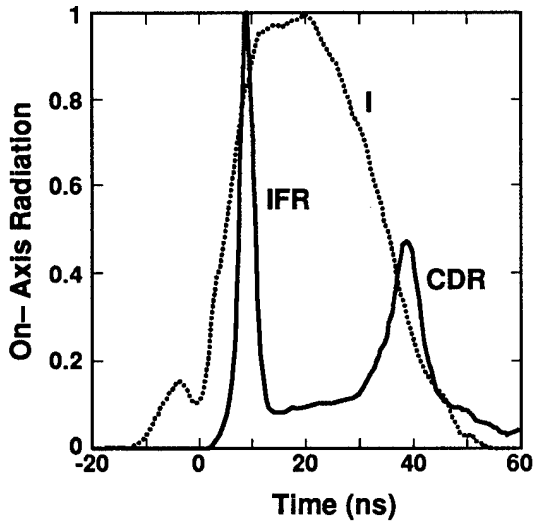


Fig. 5 Relative comparison of the on-axis radiation pulse measured at the target [corresponding to propagation shown in Fig. 3B (IFR) and Fig. 3D (CDR)] with the current pulse I measured upstream of injection (translated in time to the target) for a pressure of 100 mTorr and for ℓ = 11 m.

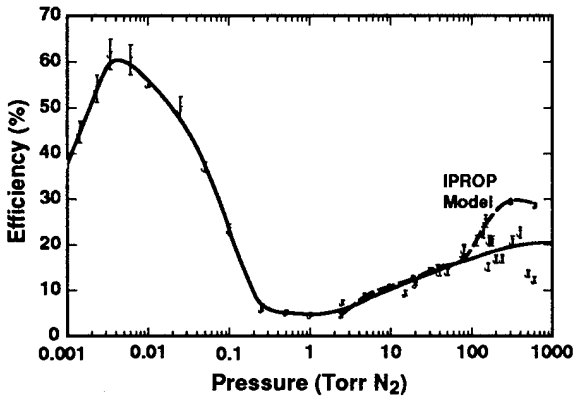


Fig. 6 The peak net current measured at the target as a percentage of the peak injected current versus the drift cell pressure. Also shown is the 2D IPROP model prediction for the collisional regime. Here ℓ = 11 m.

Acknowledgment

We thank J. J. Ramirez, J. E. Maenchen, J. E. Powell, and W. Beezhold for vigorous programmatic support; D. L. Hanson and J. E. Maenchen for reviewing and L. O. Peterson for typing this paper.

References

1. T. W. L. Sanford, D. R. Welch, and R. C. Mock, *Phys. Fluids* **B5**, 4144 (1993).

2. T. W. L. Sanford, D. R. Welch, and R. C. Mock, *Phys. Plasmas* **1**, 404 (1994).

3. D. R. Welch, C. L. Olson, and T. W. L. Sanford, *Phys. Plasmas* **1**, 764 (1994).

4. J. J. Ramirez, et al., *BEAMS '88, Proceedings of the 7th International Conference on High-Power Particle Beams*, Karlsruhe, Germany, July 4-8, 1988, ed. W. Bauer and W. Schmidt (Kernforschungszentrum Karlsruhe Gmbh, Karlsruhe, Germany, 1988), p. 148.

5. H. L. Buchanan, *Phys. Fluids* **30**, 221 (1987).

6. T. W. L. Sanford, J. W. Poukey, J. A. Halbleib, and R. C. Mock, *J. Appl. Phys.* **73**, 8607 (1993).

7. B. Goplen, et al., Mission Research Corp., Report No. MRC/WDC-R-068, Alexandria, VA (Sept. 1983).

8. B. B. Godfrey and D. R. Welch, *12th Conference on Numerical Simulations of Plasma*, San Francisco, CA (1987).

9. T. W. L. Sanford, D. R. Welch, and R. C. Mock, Sandia National Laboratories Report, SAND92-2618 (Sept. 1993).

QUASICONTINUOUS MODEL FOR ELECTRON FLOW IN MAGNETICALLY INSULATED MULTIGAP INDUCTIVE ACCELERATOR

D.D.Ryutov

Budker Institute of Nuclear Physics, Novosibirsk, 630090, Russia

R.N.Sudan

Laboratory of Plasma Studies, Cornell University, Ithaca, NY 14853, USA

ABSTRACT

This paper contains an analytical solution of the problem of electron flow in an inductive voltage adder operated in the positive polarity mode for the case when the number of stages is large, and the voltage distribution along the potential electrode (cathode) can be approximated as a smooth function. The stationary electron flow under such conditions has a laminar character. We present a simple analytic expression for the critical current in the anode conductor below which magnetic insulation collapses. We predict that, even if the anode current exceeds this critical value, there exists always some leakage to the anode. We present an analytic expression for the leakage current and for the energy of the electrons hitting the anode. A brief discussion of the possible role of instabilities and of an axial magnetic field is presented.

In recent years, experimental studies [1], numerical simulations [2,3,4] and theoretical models for a multigap inductive voltage adder [3,4,5] have been performed to predict its operation in the positive polarity mode for powering magnetically insulated ion diodes. It has been found from numerical studies [3,4] that the electron flow has a turbulent component due to vortices caused by excess electron emission from the sharp edges of the accelerating gaps. This feature can be incorporated into a new model [5] which is adequate for treating a finite number of gaps say, $N \lesssim 10$. In the present communication, we present an analytical theory of this system applicable to situations where the number of stages N is large and the sharp edges of the gaps are eliminated. The latter restriction will eliminate vortices and the electron flow can be treated as laminar.

The basic idea of our approach consists in the substitution of the step-wise axial dependence of the voltage at the outer (sectioned) electrode (cathode) by a smooth continuous distribution of voltage. A schematic of the system is shown on Fig.1. The negative external voltage $U(z)$ is assumed to be distributed in a smooth fashion along the outer electrode (cathode), being zero at the left end and reaching some negative value $-U_{max}$ at the right end. The inner electrode (anode) has zero potential. The radii of the inner and outer electrodes are a and b, respectively. We assume that the cathode surface can produce an unlimited emission and impose the condition that a normal component of the electric field on the cathode is zero. For the smooth axial distribution of the potential, and zero normal electric field, the electrons have a smooth start at the cathode and their

motion has a laminar character; i.e., without intersections of the electron trajectories with different starting points. The electron motion coincides, to high accuracy, with the $\mathbf{E} \times \mathbf{B}$ drift, the gyration energy being small in the parameter 1/N. This observation, which is similar to that used in theory of planar diodes [6], allows the formulation of a relatively simple set of equations. When expressed in terms of the axial current $I(r,z)$ within the radius r, and electrostatic potential $\phi(r,z)$, these equations read:

$$I\frac{\partial I}{\partial r} = \frac{r^2c^2}{4}\frac{\partial \phi}{\partial r}\left[\frac{1}{r}\frac{\partial}{\partial r}\left(r\frac{\partial \phi}{\partial r}\right) + \frac{\partial^2 \phi}{\partial z^2}\right], \tag{1}$$

$$\frac{r^2c^2}{4I^2}\left[\left(\frac{\partial \phi}{\partial r}\right)^2 + \left(\frac{\partial \phi}{\partial z}\right)^2\right] = 1 - \frac{1}{[1+e(\phi - U^*)/mc^2]^2}, \tag{2}$$

The meaning of U^* is the following: Any observation point A (Fig.1) is connected by the electron trajectory with some point A* in which the electrons passing through A have been emitted from the surface; we call A* a "conjugate point" to the point A; U^* is the cathode potential at the point conjugate to the point (r,z) . In other words, $e(\phi - U^*)$ is just the electron kinetic energy at the observation point. The boundary conditions for the set (1)-(2) are: $\phi/_{r=a} = 0$, $\phi/_{r=b} = U(z)$ and $\partial\phi/\partial r/_{r=b} = 0$. It is convenient also to introduce the total current within the radius $r = b$: $I(b,z) \equiv I_C(z)$ (the subscript "C" shows that this is a current I taken at the cathode surface).

Non-locality of the problem in z-direction, caused by the presence of U^* in Eq. (2), makes the set of equations (1)-(2) rather non-trivial. However, it turns out that in the case of most practical interest (small ratio $(b-a)/L$; small leakage) it can be, somewhat miraculously, solved analytically.

For a smooth potential distribution $U(z)$ the radial derivatives in the set of equations (1)-(2) are dominant over the axial derivatives, with the small parameter being $(b-a)^2/L^2$. Neglecting the sub-dominant terms, we reduce the set (1)-(2) to two ODE in radial variable r, with z entering these equations only as a parameter:

$$II' = r\phi'(r\phi')', \tag{3}$$

$$\frac{r^2}{I^2}\phi'^2 = 1 - [1 + \phi - U^*]^{-2}. \tag{4}$$

In these equations and in what follows below, we measure the potential in the units of mc^2/e (500 kV) and the current in the units of $mc^3/2e$ (8.5 kA). The primes denote the radial derivatives. These equations have two integrals:

$$r^2\phi'^2 = I^2 - I_C^2, \tag{5}$$

$$\phi - U^* = \frac{I}{I_C} - 1. \tag{6}$$

As both U and I_C are decreasing functions of z, one can express one of them in terms of another and obtain a single-valued relationship

$$U = U(I_C). \tag{7}$$

A concrete dependence (7) is to be determined as a result of the solution of the problem.

As is clear from Fig.1, the current I entering Eqs. (5) and (6) is just the cathode current I_C^* at the conjugate point. For a known dependence (7), Eq. (6), if written in the form

$$\phi - U(I_C^*) = \frac{I_C^*}{I_C} - 1, \tag{8}$$

allows, in principle, to find the dependence $I_C^*(\phi)$ for a given cross-section z=const. This consideration is a key element in the solution of the problem. Just through this relationship the coupling between phenomena taking place in different cross-sections occurs.

With the dependence $I_C^*(\phi)$ known, and with the understanding that I entering Eq.(5) is also I_C^*, one can integrate Eq.(5) to find the radial dependence of ϕ in a given cross-section:

$$ln\frac{r}{a} = -\int_0^{\phi} \frac{d\psi}{\sqrt{I_C^*(\psi) - I_C^2}}. \tag{9}$$

Now, the problem is to find the dependence (7). To do that, we write the relationship (9) for the cathode surface and switch to the integration over I_C^*, by using the relationship following from (8):

$$d\psi/dI_C^* = dU/dI_C^* + 1/I_C. \tag{10}$$

This leads to the following integral equation of the Abel type:

$$ln\frac{b}{a} = \int_{I_{C1}^*}^{I_C} \frac{(dU/dI_C^* + 1/I_C)dI_C^*}{\sqrt{I_C^{*2} - I_C^2}}, \tag{11}$$

where I_{C1}^* is a solution of Eqn. (8) with $\phi = 0$ (i.e., for the point conjugate to the point on the anode surface):

$$-U(I_{C1}^*) = \frac{I_{C1}^*}{I_C} - 1. \tag{12}$$

At large enough anode current I_A (see below), the electron leakage to the central rod is small, and the current in the central rod can be considered as constant. The current I_{C1}^* is just an anode current at the given cross-section. Clearly, at small leakage I_{C1}^* is just constant and equal to I_A (incidentally, the case of small leaks is most interesting from the experimental viewpoint). In such a case, one can replace the lower integration limit in

the Eq.(11) by a constant equal to I_A. Then this equation gets immediately solved by a standard technique of the Abel transform and gives the following result:

$$U(I_C) = -\frac{2}{\pi}\left[\sqrt{I_A^2 - I_C^2}ln\frac{b}{a} + \int_{I_C/I_A}^{1} \frac{dx}{\sqrt{x^2 - (I_C/I_A)^2}} ln\left(\frac{1}{x} + \sqrt{\frac{1}{x^2} - 1}\right)\right]. \qquad (13)$$

If the ratio b/a is not very close to unity, then, at $I_A \gg 1$, the last integral in (13) can be neglected, and we obtain a remarkably simple solution:

$$I_C = \sqrt{I_A^2 - \frac{\pi^2 U^2}{4ln^2(b/a)}}. \qquad (14)$$

We present it in the inverted form i.e., I_C vs U, because in practice it is the voltage distribution that is known. [Note that (13) with the second term on the RHS neglected can be expressed as $U = Z\sqrt{I_A^2 - I_C^2}$ where Z the so-called flow impedance is twice the vacuum impedance of the transmission line].

In actual inductive accelerators the gap varies with z. In this case, let $\xi \equiv b/a$ be monotonically dependent on z and we consider ξ to be a function of I_C. Then instead of Eqn. (13) we obtain

$$U(I_C) = -\frac{1}{\pi}\int_{I_C}^{I_A} \frac{d(I_C^{*2})ln\xi(I_C)}{\sqrt{I_C^{*2} - I_C^2}}. \qquad (13')$$

For ξ constant we obtain the earlier result (13). In order to allow axial variation let us consider

$$\xi = \xi_0 \exp[\alpha(I_A^2 - I_C^2)], \qquad (13'')$$

with α a parameter that determines by what amount the cross-section varies from left to right. Thus with $\alpha = ln(2)/I_A^2$, ξ can vary by a factor of 2. Integration of (13') yields

$$U(I_C) = -\frac{2}{\pi}\left[(ln\xi_0)\sqrt{I_A^2 - I_C^2} + \frac{4\alpha}{3}(I_A^2 - I_C^2)^{3/2}\right]. \qquad (13''')$$

The dependence of ξ on U is obtained from (13'') and (13'''). For different expression (13'') one can conceivably obtain all the required $\xi(U)$.

It is clear from Eqn. (14) that at a given maximum voltage U_{max} at the end of the line, there exists a minimum value of the anode current at which the laminar solution exists over the whole length of the device. This critical current is

$$I_{Acrit} = \frac{\pi U_{max}}{2ln(b/a)}. \qquad (15)$$

By noting that the current I_e carried by the electron flow in a certain cross-section of the device is just $I_A - I_C$, we obtain for I_e:

$$I_e = I_A - \sqrt{I_A^2 - \frac{\pi^2 U^2}{4ln^2(b/a)}}. \qquad (16)$$

Now we find a (small) electron leakage I_{leak} to the anode occurring from the left end of the device to the observation point. Clearly, $I_{leak} = I_A - I^*_{C1}$. From the expression (12), under the assumption that $I_{leak} \leq I_A$, one readily obtains:

$$\frac{I_{leak}}{I_A} = \frac{\pi^2}{8I_A ln^2(b/a)}\left(\left[1 - \frac{\pi^2 U^2}{4I_A^2 ln^2(b/a)}\right]^{-1/2} - 1\right). \tag{17}$$

One sees that the leak becomes substantial only at the currents less than the critical value; in such a case a collapse of the magnetic insulation occurs at the intermediate point of the device. However, even at $I_A > I_{Acrit}$ some leakage is present despite the fact that the solution is laminar.

Of some interest is the energy at which electrons hit the anode. It is equal to $-U(I^*_{1C})$ and can be found from the equation (12). Under the assumption of a small leakage, it is:

$$-U(I^*_{1C}) = \left[1 - \frac{\pi^2 U^2}{4I_A^2 ln^2(b/a)}\right]^{-1/2} - 1. \tag{18}$$

Again, only at a current close to the critical one, this energy can become comparable to the maximum applied voltage. In order for relationships (16) - (18) to be valid over the whole length of the accelerator, I_A should exceed I_{Acrit}.

The electron velocity which is directed almost exactly along the z-axis, is zero at the cathode surface and reaches a maximum corresponding to the energy (18) near the anode. This means that there is a shear in the electron flow which can serve as a drive for instability. However, one should note that the source of the free energy associated with this flow is relatively weak (as the drift energies are small as compared to the applied voltage) unless the current is very close to the critical value.

Axial magnetic field B_z has generally a negative effect on the performance of the adder as it allows electron leakage along the cathode surface. The maximum admissible level of B_z turns out to be quite small. It can be evaluated from the consideration that the z-component of the electron velocity gained from the axial electric field in the course of the electron drift from cathode to anode should be small as compared to the drift velocity. This leads to the following constraint on B_z:

$$\frac{B_z}{B_\varphi} < \frac{\rho_L^2}{(b-a)^2}, \tag{19}$$

where ρ_L is the electron Larmor radius in the magnetic field of the axial current, for the energy corresponding to the applied voltage.

Work supported by Sandia National Laboratories Contract No. 63-4881

1. D.L. Hanson, et al., "Operation of a High Impedance Applied-B Extraction Ion Diode on the SABRE Positive Polarity Linear Induction Accelerator", Proc. BEAMS '92, Ed. D. Mosher and G. Cooperstein, Naval Research laboratory, Washington, DC, v.II, p. 781.

2. S.E. Rosenthal, "Characterization of Electron Flow in Negative and Positive Polarity Linear Induction Accelerators", IEEE Trans. on Plasma Sc. **19**, 822 (1991).

3. B.W.Church and R.N.Sudan, Electron Flow in Positive-Polarity Multigap Inductive Accelerators, Proc. BEAMS '92, Ed. D. Mosher and G. Cooperstein, Naval Research laboratory, Washington, DC, v.III, p.1795.

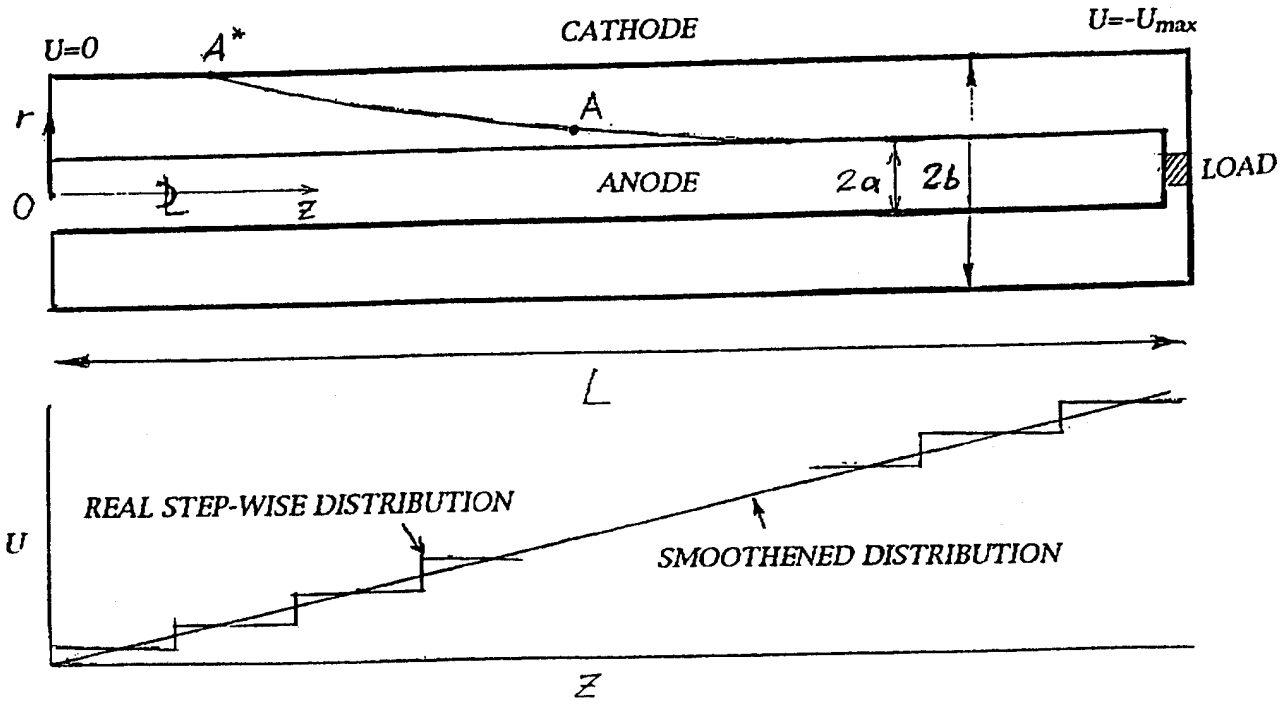
4. B.W. Church, "Two-dimensional Electron Dynamics in Magnetically Insulated Systems", Ph.D. Thesis, Cornell University (1994).

5. B.W. Church and R.N. Sudan, (in preparation) 1994.

6. B.N.Breizman, D.D.Ryutov, Soviet Physics - Doklady, v.20, p.857 (1976).

FIGURE 1

GEOMETRY OF THE PROBLEM



Acceleration and Compression of Compact Toroid Plasmas

G.F. Kiuttu, J.H. Degnan, R.E. Peterkin, E.L. Ruden, F.M. Lehr, C.A. Outten, C.D. Holmberg, G.P. Baca, D.E. Bell, G. Bird[a], Y.G. Chen, A.L. Chesley, S.K. Coffey[a], M.E. Dearborn, M.R. Douglas, J.L. Eddleman[b], S.E. Englert, T.J. Englert, A.Ya. Faenov[c], M. Frese[d], D. Gale[e], J.D. Graham[e], J.H. Hammer[b], C.W. Hartman[b], J. Havranek, T.W. Hussey, G. Marklin, H.S. McLean[b], A.W. Molvik[b], B.W. Mullins, S.A. Pikuz[f], D.W. Price, N.F. Roderick[g], S.W. Seiler[a], U. Shumlak, P.J. Turchi[h], and J. Watrous[d]
High Energy Plasma Division, Phillips Laboratory, Kirtland AFB, New Mexico

Abstract

For several years, Phillips Laboratory has been investigating, experimentally and computationally, magnetized plasma structures known as Compact Toroids (CTs). These plasmas, first proposed for laboratory acceleration by Hartman and Hammer at Lawrence Livermore National Laboratory, are axially symmetric, donut-shaped configurations with embedded toroidal and poloidal magnetic fields, which relax naturally to a minimum-free-energy state between concentric electrodes. As a result, they are stable to resistive and MHD perturbations. Once created, and under suitable conditions, they may be accelerated and compressed by magnetic forces in a coaxial gun configuration. In our laboratory, these forces are provided by the discharge of our Shiva Star 9.4 MJ fast capacitor bank, with currents in excess of 2 MA. In this paper we present recent results obtained in converging electrode accelerators at the 1 MJ stored energy level. Other parameters associated with the experiments are 10 μs acceleration time scale, 50 cm initial major radius, 10 cm initial minor radius, 1 m gun length, 1 mg CT mass, and various gaseous loads. In previous PL experiments, CTs were accelerated intact over meter lengths in straight (nonconverging) coaxial electrodes at average accelerations in excess of 10 billion gravities to speeds of roughly 50 cm/μs. Using 0-D and 2-D models, converging electrode geometries were designed and tested over the last year. Experimental results include compression in radius and thickness of factor 9 each, and speeds greater than 40 cm/μs.

---

[a] Physical Sciences, Inc., Alexandria, VA

[b] Lawrence Livermore National Laboratory, Livermore, CA

[c] NPO VNIIFTRI, Mendeleevo, Russia

[d] NumerEx, Inc., Albuquerque, NM

[e] Maxwell Laboratories, Inc., Albuquerque, NM

[f] Lebedev Physical Institute, Moscow, Russia

[g] Univ. of New Mexico, Albuquerque, NM

[h] Ohio State Univ., Columbus, OH

INTRODUCTION

Phillips Laboratory (PL) has been interested in accelerating plasmas to high kinetic energy for more than 20 years, and has investigated during this period of time coaxial and rail plasma guns [1], dense plasma foci, hollow Z-pinches [2], and, most recently, compact toroids [3]. There are many applications for such devices, but a primary use is the generation of intense x-rays. Implicit in all our high-energy acceleration schemes is the Shiva Star fast capacitor bank - a 9.4 MJ, 120 kV, pulsed power facility with currents up to several 10s of MA, and with rise time as short as 3 μs, depending on load inductance.

During the 1970s and early 1980s, we studied hollow cylindrical plasma implosions, as envisioned by Turchi and Baker [4]. In this scheme, power amplification for plasma heating was achieved by converting stored electrical energy first into kinetic energy of a radially imploding thin plasma shell. To first order, the plasma thermalization/radiation time was simply the plasma shell thickness divided by the terminal velocity. Zero-dimensional and one-dimensional codes showed high speeds and thin radial density profiles with consequently short thermalization times. However, experimentally, such short predicted thermalization times were never realized, as indicated by radiation pulse widths. And, although the scheme was very efficient in terms of overall x-ray conversion efficiency, the bulk of the radiation was in sub-kilovolt photons, and not as short in wavelength as was desired. Of course, the culprit was the ubiquitous Raleigh-Taylor instability which plagues electromagnetic plasma acceleration schemes. As we began to get a handle on the instability from both 2-D MHD simulations and theory performed by Roderick, Hussey, and others [5], we came to the conclusion that for hollow Z-pinch implosion schemes, the 10-cm radius, several microsecond time scales initially envisioned would result in unacceptable instability growth in the r-z plane.

Around 1980, C. Hartman and J. Hammer at Livermore began proposing the use of magnetized toroidal plasma acceleration loads [6]. The advantage of such configurations was stability to ideal and resistive MHD modes under modest acceleration. They, along with Eddleman and other colleagues, succeeded in beginning an experimental effort called RACE by the mid-1980s and developed theoretical and computational models. In the basic scheme, a magnetized low-β plasma donut (compact toroid) is accelerated to high velocity in a coaxial accelerator. Simple theory showed that as long as the pushing, or piston, magnetic field does not exceed the internal plasma magnetic field, the assembly can indeed be accelerated without gross distortion over relatively long time scales and distances. Of course, the big attraction of such a scheme is considerably simpler and cheaper pulsed power drivers compared to inherently unstable plasma configurations. Hartman proposed, as early as 1984, the use of the Shiva (2 MJ) capacitor bank facility at the Air Force Weapons Laboratory, to drive such loads [7].

Roughly coincident with the beginning of RACE experiments at LLNL, K. Hackett at PL realized the potential of compact toroids, and began our current MARAUDER - Magnetized Rings to Achieve Ultrahigh Directed Energy and Radiation - program. By the time CT formation experiments began near the end of the decade, Shiva had been upgraded to Shiva Star with six arms, and nearly 10 MJ of stored energy. Project leadership was assumed by J. Degnan, who developed the experiment from initial studies at the 100 kJ level to low-energy acceleration in straight coaxial geometry and preliminary acceleration and compression at the 1 MJ stored energy level [3]. The purpose of this paper is to review more recent CT acceleration and compression work at the 1 MJ stored accelerator energy level.

As a result of this work, we have confirmed our belief that compact toroids have

tremendous potential for high-directed-energy applications, and we have not yet encountered serious technical limitations to further development. Thus, we are optimistic about achieving CT plasma velocities of 100 cm/μs and densities of 10^{18} ions/cm^3. And, we are reasonably confident that these parameters can be achieved with the existing Shiva Star direct-drive capacitor bank.

The compact toroid has linked toroidal and poloidal magnetic flux sustained by internal poloidal and toroidal currents. When bounded by inner and outer coaxial conductors, theory, simulation, and experiment all show that such configurations relax toward a minimum free energy state characterized, in the low-β limit, by the internally force-free condition

$$\mu_0 \boldsymbol{j} = \nabla \times \boldsymbol{B} = \alpha \boldsymbol{B}, \qquad (1)$$

where α is a geometry-dependent eigenvalue.

Radially across the minor cross-section the toroidal field is typically unipolar, peaked near the center, and falls to near zero at the electrode boundaries, while the poloidal field component is bipolar, has a null near center, and is near peak value at the electrodes. In our experiments, the characteristic time for evolution of the CT to this equilibrium configuration after creation is on the order of 10 μs to 20 μs.

Once formed, the assembly can be accelerated and compressed in a traditional coaxial plasma gun. The equation of motion for the centroid of a compact toroid with internal magnetic fields in converging electrodes can be written simply

$$M \frac{d^2 S}{dt^2} = \frac{\partial}{\partial S}\left(\frac{1}{2} L I^2 - U_{CT}\right) \qquad (2)$$

where M is the CT mass, **S** is the CT trajectory coordinate, L is the driver circuit inductance behind the CT, and U_{CT}, the internal CT energy, is usually dominated by magnetic field energy. The first term on the right is the magnetic piston force, while the second term is the magnetic compression back force. Thus, for a given current history, assumed magnetic field distributions, and electrode geometry, one can calculate the accelerated CT trajectory. This equation is applicable to the point-model representation of the CT, and is the basis for 0-D, or so-called "slug" models. Further refinement can be obtained with a second Lagrange equation for the length of the toroid. This second equation has been incorporated into our SUPRSLUG dynamics code [8], as suggested by Yakubov and colleagues at VNIIEF [9].

EXPERIMENTAL RESULTS

The goals of the last year's experiments have been to evaluate compression of CTs by a factor of three in major radius with subsequent acceleration at stored energy levels of 0.3 to 1.1 MJ, and evaluate higher compressions in a "self-similar" bicone accelerator with factor nine reduction in both major and minor radii at a stored energy of approximately 1 MJ. The first of these goals was accomplished with the hardware shown in Figure 1, while the latter was accomplished with the 9X self-similar hardware shown in Figure 2.

Referring to the figures, one can see several radial diagnostic ports and radial apertures along the electrodes for magnetic pickup loops along both inner and outer electrodes. These probes are encased in quartz tubes and are inserted into the inter-electrode gap to monitor all three components of the CT and piston fields. They are the primary means of examining CT field structure, and tracking the CT trajectory. Since the electrodes float to high voltage during the discharges, we use analog fiber optic data links to feed the signals to the data recording equipment. B_θ traces are typically used to examine driver current continuity through the accelerator. The B_z

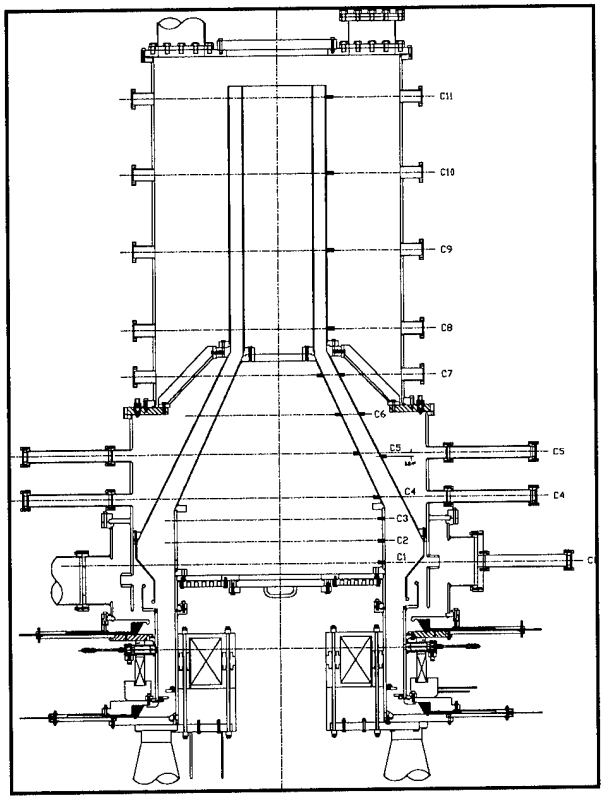


Figure 1 3X, non-self-similar electrode hardware

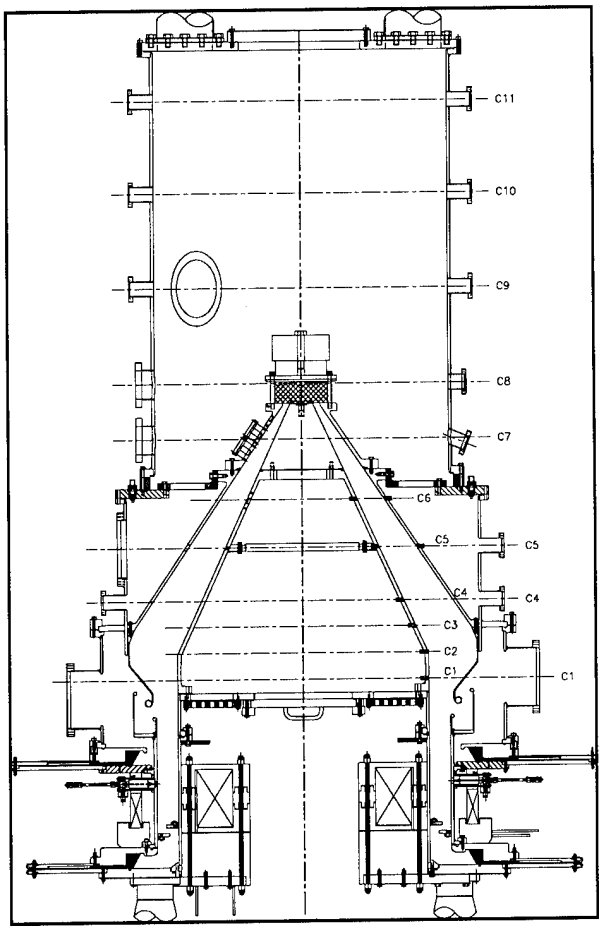


Figure 2 9X, self-similar electrode hardware

traces are a direct indication of the poloidal field structure of the CT as it passes each probe. To obtain the trajectory, the times of peak B_z are plotted versus axial probe location. Other diagnostics used to study CT behavior in the accelerator include interferometry and visible spectroscopy.

With the 3X radial compression electrodes, and the Shiva Star bank configured for 1/3 operation (12 of 36 modules, or 440 μf), we performed compression and acceleration experiments with nitrogen, neon, and argon gases at stored accelerator energies of 350 kJ, 800 kJ and 1100 kJ (charge voltages of 40 kV, 60 kV, and 70 kV, respectively), and formation-to-acceleration delays of 10 μs and 15 μs. For all experiments the injected mass was set at 1.6 mg, and the external radial bias field (used to form the CT poloidal field) was not varied.

Figure 3 shows an axial trajectory comparison for the three gases at the 1.1 MJ, 15 μs delay parameters. Note that in this, and the following, figure time is the vertical axis and axial position the horizontal axis. The data for each species are from a single shot, and multiple data points at an axial position represent different azimuthal measurement points. All three species achieve relatively constant speeds of approximately 30 cm/μs in the straight coax section of the accelerator. The highest absolute velocities were typically seen near the end of the compression cones rather than in the straight section, and reached nearly 50 cm/μs. The absence of further acceleration is believed to be due to nonadiabatic effects at the transition between the two sections of the accelerator. Both unfiltered vacuum x-ray diodes and simulations showed a burst of radiation at the time of arrival of the CT at the transition,

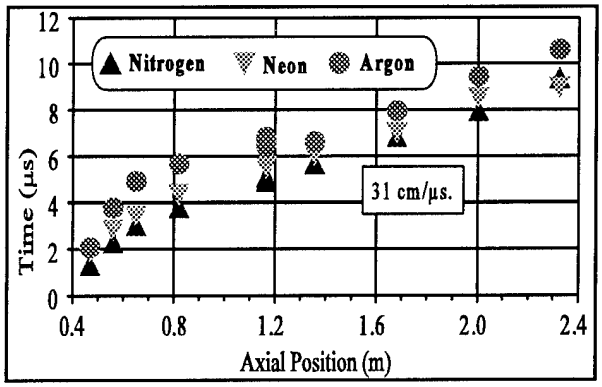


Figure 3 Gas trajectory comparison (3X electrodes, 1.1 MJ)

although the magnetic field structure appeared not to suffer any permanent change. Additional drag may have been introduced by radiation-driven gas desorption along the walls.

In Figure 4, we show a comparison of trajectories at different acceleration energies and delays for nitrogen CTs. Here, one can see an increase in characteristic speeds as the accelerator charge voltage (energy) is increased

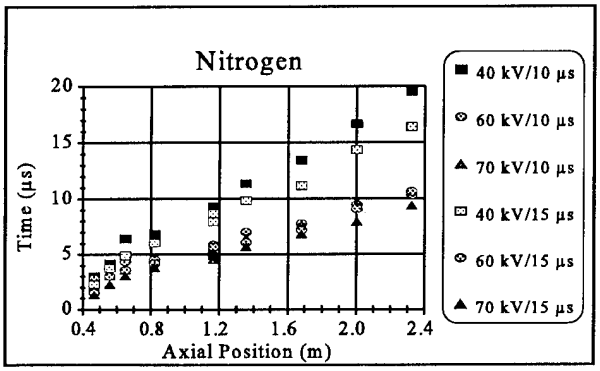


Figure 4 Voltage/delay comparison (N_2, 3X electrodes)

from 40 kV to 60 kV, but not significant further increase at the highest voltage setting. One can also discern an increase in velocity associated with the increase in acceleration discharge delay.

After completing these experiments, we restored full 36-module operation of Shiva Star and began to study higher compressions of neon CTs with the 9X self-similar electrodes. These electrodes were designed to experimentally test both higher compression ratios and the concept of self-similar compression; that is, longitudinal, as well as radial and azimuthal compression, which should occur for adiabatic compression. The radial and azimuthal components of the compression are set by the electrode polar gap angle and mean pitch angle (approximately 10 degrees and 30 degrees, respectively for the hardware of Figure 2). The longitudinal compression is measured by tracking the extent of the poloidal field along the trajectory. This length is characterized by the FWHM in time of the B_z signal times the CT velocity (given by the slope of the trajectory).

Figure 5 shows a typical trajectory plot from B_z signals for a 600 kilojoule accelerator shot. The error bars on the plot are just the temporal FWHM of each trace for length calculations. Figure 6 is the axial velocity component plotted against time for the data of

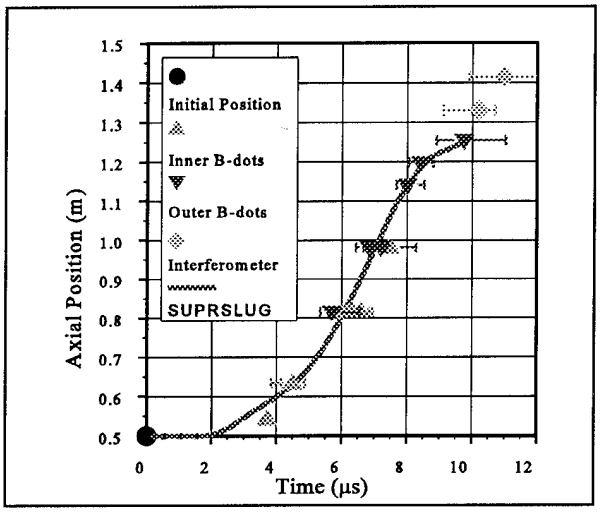


Figure 5 CT trajectory (Ne, 9X electrodes, 600 kJ)

Figure 5, and Figure 7 is a plot of the CT axial length for the data.

Several features are evident in these figures. First, for these electrodes and at this

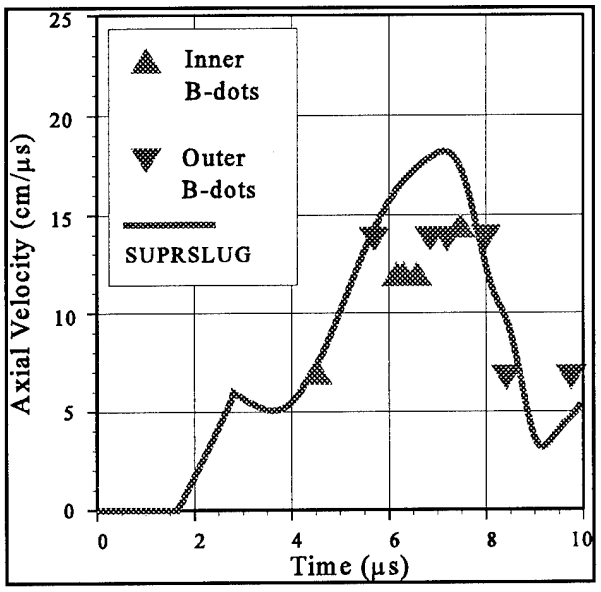


Figure 6 CT velocity (Ne, 9X electrodes, 600 kJ)

acceleration energy, the CT accelerates through the first 50 centimeters (first factor of three in radius) to a speed in excess of 15 cm/μs. Second, between 100 cm and 125 cm the CT undergoes a deceleration. The degree of deceleration is relatively reproducible, although selected shots have shown average axial speeds through the second factor of three in radial compression of 15 cm/μs. Third, there are longitudinal oscillations, in the CT length. These oscillations are induced by overdriving the CT early in the acceleration pulse. Still, there is net longitudinal compression, resulting in overall volume compressoin ratios inexcess of 100. For comparison, we show in Figures 5 - 7, results from SUPRSLUG calculations for a 1 mg CT. One can see that there is quantitative agreement with trajectory and qualitative agreement with length oscillations. For this geometry, simulations indicate that the CT behavior is relatively sensitive to parameters. In fact small, differences in initial CT magnetic energy or flux decay rates can change the exit velocity from greater than 10 cm/μs to 0 (compression force dominates the piston force at the end of the accelerator, resulting in bouncing), or blow-by of the piston field!

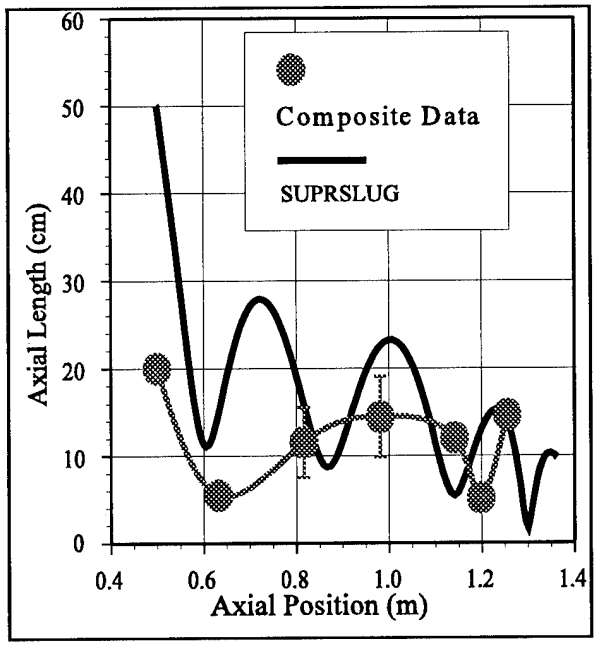


Figure 7 CT length (Ne, 9X electrodes, 600 kJ)

Figure 8 shows a plot of peak poloidal fields at the electrode walls as a function of axial distance through the accelerator for the shot corresponding to Figures 5 - 7. Note that

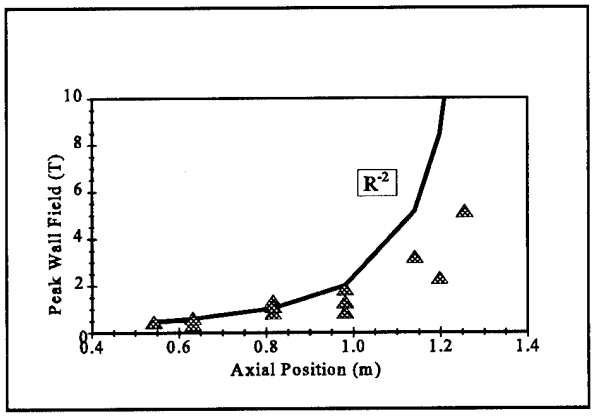


Figure 8 Poloidal flux comparison (Ne, 9X electrodes, 600 kJ)

if poloidal flux were conserved, the field would compress as R^{-2}, the inverse square of the major radius for the self-similar case. The departure from $1/R^2$ behavior as the CT moves down the accelerator suggests flux decay. If we assume that the axial component of the poloidal field varies approximately as $\sin(\pi x/g)$ radially with

respect to the magnetic centroid, where g is the local electrode radial gap, then we can estimate the poloidal flux from the peaks of the B_z signals. Such an estimate is shown in Figure 9.

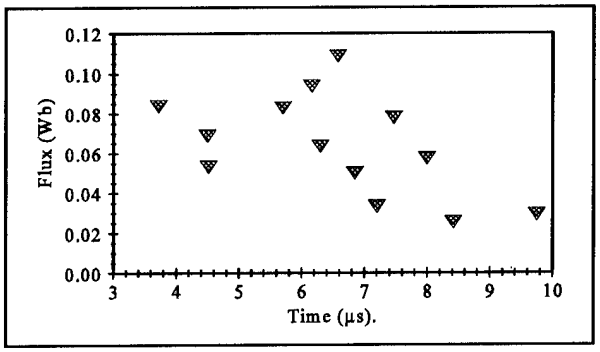


Figure 9 Poloidal flux decay (estimated from peak wall field)

Although there is considerable scatter (probably due to multiple azimuthal measurement points and radial "sloshing" of the mass centroid), we generally infer a poloidal flux decay of approximately 30% to 50% from the time of accelerator discharge through the time of arrival at the furthest downstream magnetic probe, at 126 cm.

LASNEX calculations for neon CTs stagnating against a perfect solid wall were performed, which showed a rather dramatic rise in K shell radiation output as the prestagnation velocity rose above 20 centimeters per microsecond. We therefore decided to place a steel target at the projected bi-cone apex, as shown in Figure 2, and field some radiation diagnostics (filtered vacuum x-ray diodes, filtered x-ray pinhole cameras, and curved crystal spectrographs). These diagnostics have consistently yielded evidence of x-ray production, but there has been considerable variation in both spectral content and yield. This is not unexpected, considering that we are just approaching the threshold for significant x-ray production. As expected, the highest yield for kilovolt photons (the helium-like neon resonance line is at 900 eV), corresponded to the shot with the highest inferred average velocity at the end of the accelerator. Two independent filtered XRDs on that particular shot gave an interpreted isotropic yield for the He-like Ne resonance line in excess of 10 kJ. For comparison, the CT terminal kinetic energy was estimated to be on the order of 40 kJ. Imaging convex-curved mica crystal spectrographs (designed and fabricated by our Russian colleagues) often show on the order of 1 kJ of neon K shell radiation. Both spectrograph and pinhole camera records indicate a relatively diffuse source with somewhat higher intensity near the exit of the accelerator, rather than at the target. There are usually higher-energy x-rays from the target (presumably iron K_α), as well, but the total energy associated with this emission is very small (< 1 J). Diagnostic measurements to better characterize the x-ray production are currently in progress.

CONCLUSION

CT experiments at the 1 MJ stored accelerator energy level have been conducted over the past year with approximately 1 mg mass compact toroids in two different compression geometries. Results from these experiments indicate that CTs can be accelerated with converging electrodes, and that at least two-dimensional compressions can be achieved. With exit velocities of order 10 cm/μs, neon CTs have produced K-shell x-ray yields of at least 1 kJ and as high as 10 kJ.

Ongoing studies include more detailed measurements of CT dynamics in the 9X self-similar accelerator. In particular, our He-Ne laser interferometer has been upgraded to two beams, and repositioned at the end of the accelerator to measure plasma exit velocity and density, the critical parameters for stagnation radiation production. We have also recently incorporated tantalum-capped flush-mount B-dot probes, courtesy of LLNL, in the high-compression region of the accelerator, since

quartz-encased probes do not survive there. Future electrodes have been designed with a "gentle bend" transition to a reduced pitch angle (Figure 10).

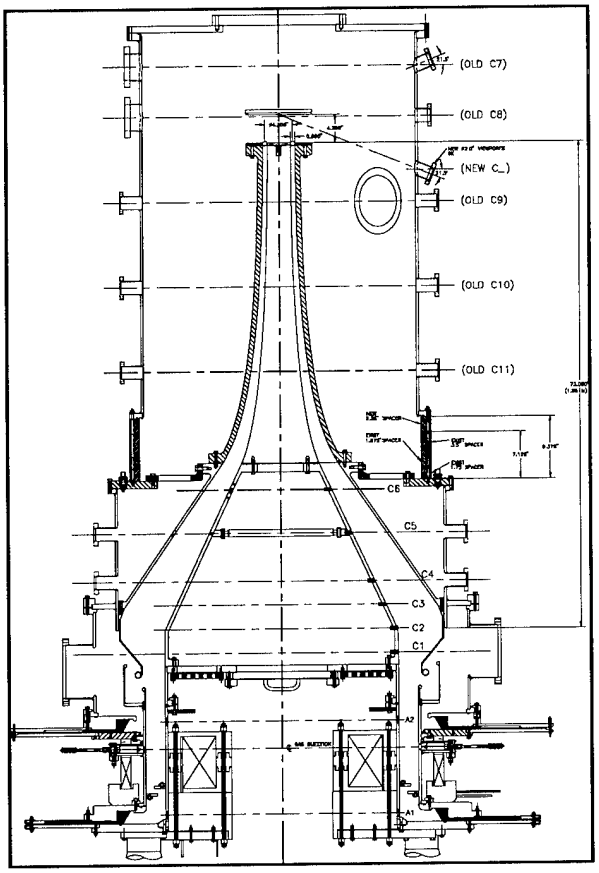


Figure 10 2-meter, 10X electrode hardware

The gentle bend was designed to overcome the problems associated with the nonadiabatic transition in the previous 2-meter accelerator. Calculations indicate that the added length of the new design will allow considerably better extraction of energy from the Shiva Star driver, with correspondingly higher terminal velocities. Experiments with this hardware are scheduled to begin in October 1994.

ACKNOWLEDGMENTS

We thank W. Sommars, K. Golby, W. Kaiser, T. Trujillo, and M. Clifton for assistance with experimental operations, and K. Hackett, J. Rowley, L. Wright, B. Baker, B. Godfrey, D. Beason, and the many individuals who have substantially contributed, directly or indirectly, to this effort over the years.

References

[1] G.F. Kiuttu and M.C. Clark, "Behavior of a high-density plasma in a rail gun accelerator," *Bull. Am. Phys. Soc.* vol. 22, p. 1099, 1977.

[2] W.L. Baker, M.C. Clark, J.H. Degnan, G.F. Kiuttu, C.R. McClenahan, and R.E. Reinovsky, "Electromagnetic-implosion generation of pulsed high-energy-density plasma," *J. Appl. Phys.* vol. 49, no. 9, p. 4694, 1978.

[3] J.H. Degnan, R.E. Peterkin Jr., G.P. Baca, J.D. Beason, D.E. Bell, G.Bird, S.K. Coffey, M.E. Dearborn, D. Dietz, M.R. Douglas, S.E. Englert, T.J. Englert, D. Gale, J.D. Graham, K.E. Hackett, J.H. Holmes, T.W. Hussey, G.F. Kiuttu, F.M. Lehr, G.J. Marklin, B.W. Mullins, D.W. Price, N.F. Roderick, E.L. Ruden, M. Scott, S.W. Seiler, W. Sommars, C.R. Sovinec, and P.J. Turchi, "Compact toroid formation, compression, and acceleration.", *Phys. Fluids B*, vol. 5 no. 8, p. 2938, August 1993, and references therein.

[4] P.J. Turchi and W.L. Baker, *J. Appl. Phys.*, vol. 44, 4936, 1973.

[5] T.W. Hussey, N.F. Roderick, and D.A. Kloc, "Scaling of MHD instabilities in imploding plasma liners.", *J. Appl. Phys.*, vol. 51, no. 1452, 1980.

[6] C.W. Hartman and J.H. Hammer, *Phys. Rev. Lett.*, vol. 48, p. 929, 1982.

[7] C.W. Hartman, J.H. Hammer, and J.L. Eddleman, "A linear pinch driven by a moving compact torus," in *Proceedings of the First Conference on Dense Z-Pinches for Fusion,*

Naval Research Laboratory, Washington DC, p. 79, 1984.

[8] G. F. Kiuttu, "SUPRSLUG: An enhanced 0-D dynamics code for modelling compact toroid acceleration and compression," to be published.

[9] V.B. Yakubov, VNIIEF, Sarova, Russia, private communication.

PLASMA RADIATION SOURCE IMPLOSION LIMITS DUE TO AZIMUTHAL ASYMMETRIES

David Mosher
Pulsed Power Physics Branch, Plasma Physics Division, Naval Research Laboratory
4555 Overlook Ave., S.W., Washington DC, 20375-5346

Abstract

Self-consistent compression limits produced by azimuthal asymmetries in the current return geometry, and in the distribution of current and mass in the PRS are determined with the simplest model able to produce such effects. It is shown that modest asymmetries can limit compression to the values observed in experiments.

Low-dimensional models of annular plasma radiation source (PRS) implosions usually predict radial compression ratios to be much larger than observed in experiments[1] unless artificial steps (specifying the final radius, enhancing transport coefficients[2], etc.) are taken to limit compression. The effects of multi-dimensional instabilities have been considered in this regard,[3-5] but compression limits associated with the nonlinear growth of initial azimuthal asymmetries in the load have not. Here, self-consistent compression limits produced by azimuthal asymmetries in the current return geometry, and in the distribution of current and mass in the PRS are determined. It is shown that modest asymmetries of these types can limit compression to the range of values observed in experiments.

The employed model is the simplest that can produce such effects, and can be applied to quite general load geometries and time-dependences. The PRS is modeled by N parallel wires distributed in the xy plane, the number representing either an actual multiple-wire-array load, or when large, a thin, annular load. Though the distribution of mass and current among the wires is arbitrary in the model, they are distributed here according to

$$m_k = m(1+\varepsilon_m sin\theta_k)/N$$
$$I_{k,1}(t) = I(t)(1+\varepsilon_i sin\theta_k)/N \qquad (1)$$

where m and $I(t)$ are the total line mass and axial (z-direction) current. The index k specifies the initial angular coordinate of each wire $\theta_k = 2\pi k/N$ on the mounting radius R. The fixed positions $\mathbf{r}_{k,2}$ of the N_w current return rods on radius R_w are similarly determined and each rod carries current $I_{k,2} = -I(t)/N_w$. At each time step during implosion of the wire ensemble, the magnetic field at a given wire location $\mathbf{r}_K(t)$ is determined by summing the contributions from all other N - 1 wires and the N_w return-current rods using

$$\mathbf{B}(\mathbf{r}_K) = 0.2\sum_{j=1}^{2}\sum_{k=1}^{N_j}\frac{I_{k,j}\mathbf{e}_z \times (\mathbf{r}_K - \mathbf{r}_{k,j})}{\left|\mathbf{r}_K - \mathbf{r}_{k,j}\right|^2} , \qquad (2)$$

where $N_1 = N$, $N_2 = N_w$, $k \neq K$ for $j = 1$, $r_{k,1}(t)$ is the instantaneous position of the k^{th} wire, the current is in amperes and other quantities are in emcgs units. The position of each wire is then advanced using

$$\frac{d^2\mathbf{r}_K}{dt^2} = \frac{0.1 I_{K,1}\mathbf{e}_z \times \mathbf{B}(\mathbf{r}_K)}{m_K} . \qquad (3)$$

The procedure is iterated past the time at which the wire ensemble achieves maximum compression. Maximum compression is defined by the minimum value of the wire ensemble's rms radius $< r >$ about the center of mass

$$m < r >^2 (t) = \sum_{K=1}^{N} m_K (r_K - r_c)^2 \quad , \qquad (4)$$

where the center of mass $\mathbf{r}_c$ is fixed by the initial mass distribution.

Consideration is limited to a sinusoidal current wave form defined by the maximum value I_0 at the quarter-period time t = T. Specific examples are presented for I_0 = 3 MA, T = 100 ns, m = 200 μg/cm, and R = 1 cm. For these values, peak compression occurs just after current maximum at about 105 ns. Equations (2) and (3) demonstrate that the solutions are invariant in the normalized variables r/R and t/T provided that the quantity $I_0^2T^2/mR^2$ remains constant, so that results can be applied to other generator and load parameters having implosions close to the time of current maximum.

Figure 1 summarizes the results of calculations using the above parameters for an annular mass asymmetry specified by ε_m = 0.1, ε_i = 0, and a uniform current return (achieved by choosing eight current-return rods on R_w = 100 cm). Shown are the variation of < r > with time and the spatial distribution of 300 wires at peak compression. The interesting folded pattern observed arises because maximum compression is achieved when some wires are moving inward while others are moving outward. The equations show that Fig. 1 applies if the value of $I_{K,1}^2/m_K$ is preserved, so that for small asymmetries, a history and distribution similar to that for ε_m will occur for $\varepsilon_i = \varepsilon_m/2$.

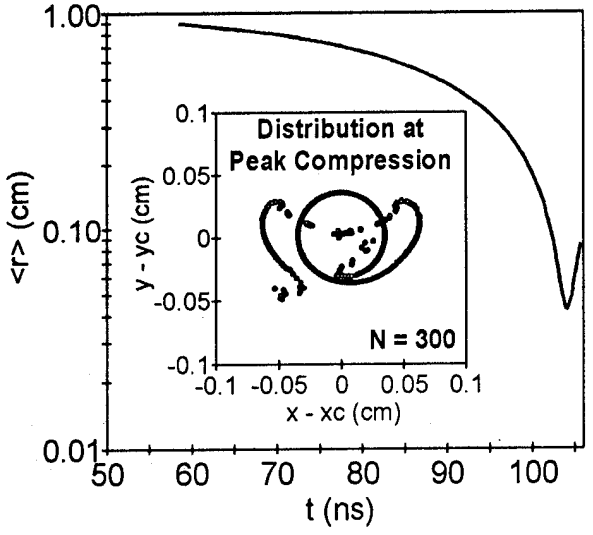


Figure 1 Implosion history and distribution at peak compression for a ±10% asymmetry in annular mass.

Figure 2 shows the equivalent results for a uniform-mass and -current annulus in the magnetic field of 8 current-return rods at R_w = 1.5 cm. The radial magnetic field of this configuration leads to a $\mathbf{j}_z \times \mathbf{B}_r$ force producing angular momentum that limits compression, while the azimuthal variation in $\mathbf{j}_z \times \mathbf{B}_\theta$ leads to a θ-dependent radial velocity so that an 8-fold symmetry is reflected in the spatial distribution.

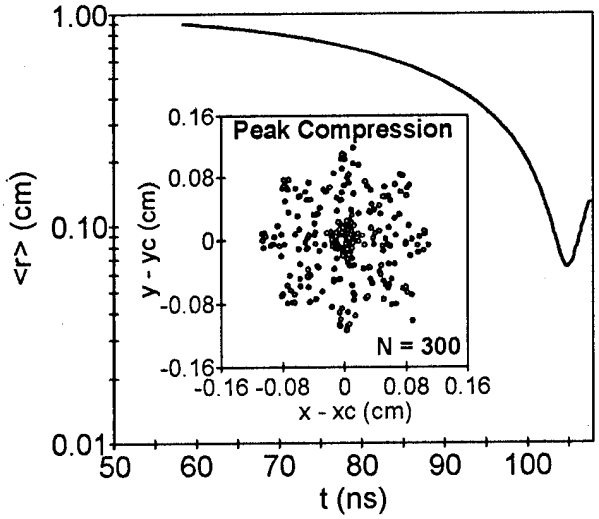


Figure 2 Implosion history and distribution at peak compression for a uniform mass and current annulus in the field of 8 return-current rods with R_w = 1.5 cm.

It is instructive to compare the growth of angular momentum for the two asymmetry types of Figs. 1 and 2. Though the mean angular momentum for the ensemble is always zero since there is no net torque, it is locally non zero with an ensemble-averaged rms value given by $<P_\theta>$. Figure 3 shows the growth in $<P_\theta>$ for: Fig. 2, a mass asymmetry defined by ε_m = 0.16, and a current asymmetry defined by

ε_i = -0.075. All three have radial compression histories nearly identical to that in Fig. 2. As expected, the angular-momentum histories are nearly identical for the mass and current asymmetries, growing as the asymmetry becomes more pronounced with radial compression. Angular momentum growth due to the return-current asymmetry peaks when the radius is about 1/2 of the initial value. Later, the driving asymmetry is reduced as the ensemble implodes to small radius where the magnetic field approaches a pure B_θ and angular momentum is conserved.

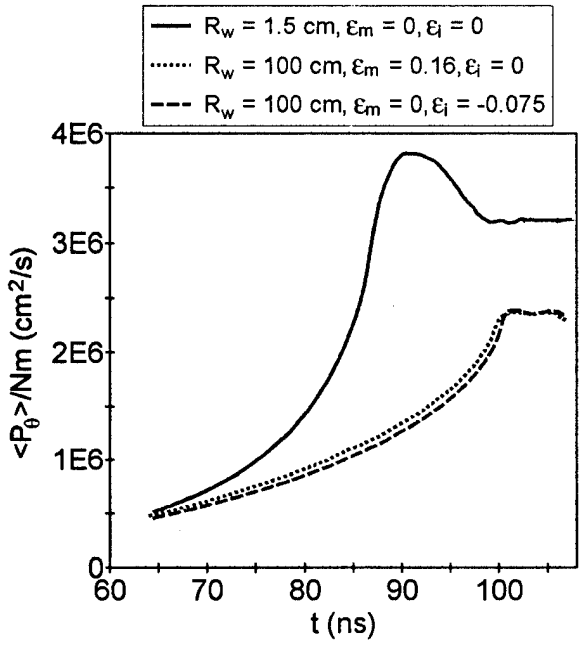


Figure 3 RMS angular momentum histories for three types of asymmetries with similar radial implosions.

Figure 4 summarizes the limits to radial compression imposed by load-mass and load-current asymmetries with a uniform return, and with the additional asymmetry of 8 current return rods at a radius of 1.5R. In the absence of the current-return asymmetry, the figure shows a nearly-linear dependence of minimum radius with asymmetry amplitude, and for small amplitudes, the expected equivalence of $\varepsilon_m/2$ and ε_i. With the added current-return asymmetry, the minimum radius asymptotes to the limit of Fig. 2. Although experimental load asymmetries have not been measured, reasonable 10's-of-percent levels lead to the experimentally-observed 10:1 compression range.

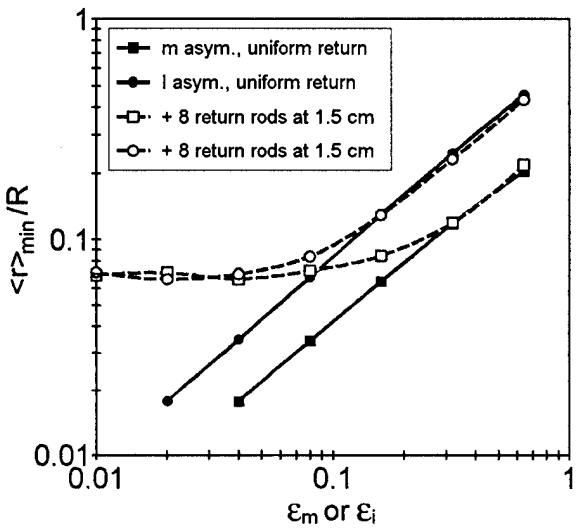


Figure 4 Variation of minimum compression radius with load-asymmetry amplitude for uniform return and a current-return asymmetry of 8 rods on 1.5R.

Compression limits due to the current return are summarized in Fig. 5 as functions of return-rod radius and return-rod number. The figure indicates that common current-return geometries, 6 or 8 rods mounted at about 1.5R, have azimuthal asymmetries that also limit the compression ratio to about 10:1. The figure also suggests how compression limits due to this asymmetry can be reduced. For experiments where wide-angle access to the radiation source is not critical, the number of rods can be increased to reduce the asymmetry amplitude at the plasma annulus. Also, the gap between the annulus and the return rods can be increased. Though this change leads to increased load inductance and may reduce peak load current, a net gain in x-ray performance may still result from improved symmetry. Increased gaps have the added benefit of reducing possible load-current losses to the return rods, which result in degraded PRS x-ray yield and poor reproducibility.

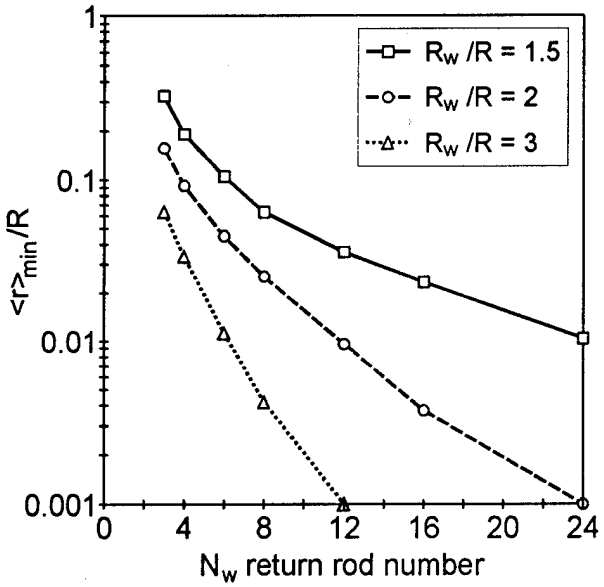


Figure 5 Variation of minimum compression radius with return-rod radius and return-rod number for uniform-mass and -current loads.

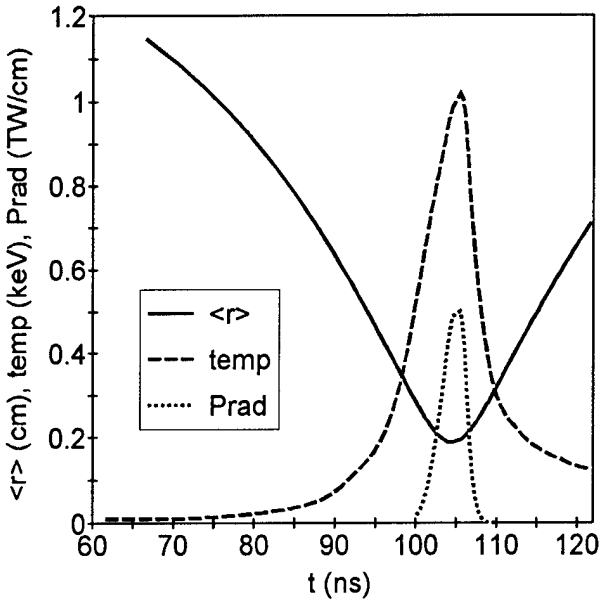


Figure 6 Rms radius, plasma temperature, and K-line radiation pulse for an argon implosion with $\varepsilon_m = 0.4$.

Radiation characteristics of an asymmetric PRS can be crudely approximated using a 2-level model for the K-lines[6]. For an ion mass m_i, the ion density is assumed to be given by $m/\pi<r>^2 m_i$. A radial mass-flow velocity is calculated from

$$mV_r = \sum m_K \mathbf{e}_r \cdot \mathbf{v}_K \qquad (5)$$

so that the kinetic energy associated with mass flow is $K_r = mV_r^2/2$. The "thermal" portion of the kinetic energy K_{th} is determined by subtracting K_r from the total ensemble kinetic energy. The plasma temperature is then determined by equating K_{th} to the internal energy using an appropriate equation of state[6]. Results of this calculation are shown in Fig. 6 for the case of an argon gas-puff with R = 1.4 cm, m = 100 μg/cm, ε_m = 0.4, and a uniform return. The combination of stagnation-thermalization and the density variation around peak compression leads to a radiation pulse duration of about 5-ns fwhm, consistent with measurements where radiation-pulse broadening due to axial asymmetries has been removed.[7]

In summary, self-consistent compression limits produced by azimuthal asymmetries in the current return geometry, and in the distribution of current and mass in the PRS have been determined using a simple model. It was shown that modest asymmetries limit compression and radiation pulse durations to the values observed in experiments, and that simple changes in the return-current configuration may lead to improved PRS performance.

[1] C. Deeney, et al., J. Appl. Phys. **72**, 1297 (1992).

[2] J.W. Thornhill, K.G. Whitney, C. Deeney, and P.D. LePell, Phys. Plasmas **1**, 321 (1994).

[3] F.S. Felber and N. Rostoker, Phys. Fluids **24**, 1049(1981).

[4] V.V. Vikhrev, V.V. Ivanov, and G.A. Rozanova, Fiz. Plazmy **15**, 77(1989) [Sov. J. Plasma Phys. **15**, 44(1989)].

[5] D. Mosher and D. Colombant, Phys. Rev. Lett. **68**, 2600(1992).

[6] D. Mosher, J. Giuliani, Jr., N. Qi, and M. Krishnan, Bull. Am. Phys. Soc. **38**, 2013(1993).

[7] D. Mosher, J.R. Boller, S.J. Stephanakis, F.C. Young, and C.M Dozier, J. Rad. Effects, Res. & Eng., 1994, in publication. Also, R.B. Spielman, informal communication.

TWO-DIMENSIONAL NUMERICAL SIMULATION OF IMPLODING PLASMA LINERS

A.D.Zoubov, G.A.Adamkevich, and I.V.Glazyrin
Federal Nuclear Center - Research Institute of Technical Physics
P.O.Box 245, 456770, Chelyabinsk Region, Snezhinsk, RUSSIA

Abstract

A computation analysis is performed to investigate 2D effects in imploding plasma liners. Some mechanisms degrade radiation output in the systems: the development of Rayleigh-Taylor (RT) type instabilities, "zippering" effect and instability of magnetized electrons current sheet. For the compressed double gas-puffs external axial magnetic field stabilizes short wavelength R-T instability. All these effects are studied numerically. The calculations were carried out using 2D three-temperature code TIGR-M. To predict liner shapes from supersonic gas puff injection, driven by time-dependent power pulse some calculations have been made. Dynamics of plasma in three-temperature MHD with Hall term is discussed.

Introduction

It is well known that simple Z-pinches (compressed plasma column) are subject to sausage and hydromagnetic RT type modes [1]. These instabilities represent the main obstacles for using the pulse plasmas because they can destroy the symmetry of the imploding shell, thus degrade radiation production. To date, a number of research groups have studied the instability development. Since the early papers on Z-pinch development it is known that sausage modes of instability can be suppressed by axial magnetic field [2]. But the classical pinch instability sausage modes grow slower than the hydromagnetic RT instability when the shell radius is large compared to the wavelength [3]. The theoretical analysis by A.B.Bud'ko et.al. [4] shows that a relatively weak axial magnetic field present in the beginning of implosion produces a "window of stability", i.e., a domain in the space of the parameters of the plasma motion for which the RT instability modes are completely suppressed. Experimental investigations at High-Current Electronics Institute (Tomsk) have also demonstrated that the largest degree of radial compression and suppression of instabilities can be achieved with the use of axial magnetic field [5]. In this paper we continue to investigate the dynamics of argon double gas-puff [6]. The focus of this study is on the dynamic evolution of disturbances caused by instabilities at the plasma-magnetic field interface and on treatment of suppression effect in detail rather than the determination of an optimal design configuration.

Numerical model

The numerical calculations were carried out using an extended version of 2D Euler-Lagrange MHD code TIGR-M [6],[7]. The model modified to include three-temperature approximation (electron, ion and foton temperatures) and Hall term in equation for mag-

netic field evolution.

The equation for magnetic field with Hall term used in the model is in the form

$$\frac{\partial \mathbf{H}}{\partial t} = \nabla \times (\mathbf{u} \times \mathbf{H} - \chi \nabla \times \mathbf{H}) -$$

$$- \frac{1}{e} \nabla \times \frac{\mathbf{j} \times \mathbf{H}}{n_e} - \frac{kc}{en_e} \nabla n_e \times \nabla T_e, \quad (1)$$

where $\mathbf{H}$ is magnetic field, $\mathbf{u}$ is velocity, $\mathbf{j}$ is electrical current density, p_e is pressure of electrical component, n_e is electron number density, e - electron charge magnitude, $\chi = c^2/4\pi\sigma$, σ - coefficient of electrical conduction. Here it is ignored the thermoelectric force.

Role of Hall term increases in the regimes of implosion when density, temperature, etc., vary in space. Fast magnetic field penetration into plasmas due to Hall term was studied in paper [8]. The magnetic field evolution, when govered by the electron dynamics, has been studied extensively in book [9].

A number of calculations were carried out using previosly imposed axial magnetic field. TIGR-M confines oneself for the particular case of configuration with two components of velocity and two components of magnetic field lying in the same plane as velocity vector does. Thus TIGR-M code does not calculate at the same time radial, axial and azimuthal (third) components of magnetic field. Hence a model for azimuthal component is required.

Because of the high magnitude of plasma conductivity the field penetration into the body of plasma is small. Therefore we assume the magnetic pressure can be calculated by term $H^2/8\ \pi$ applying to the upper bound of plasma. The comparison between the calculations with the assumption and correct field calculation has been made. It shows one's assumption is the possible way to take into account axial magnetic field.

Actual experimental current vs. time values provide the boundary condition for magnetic field at the outer boundary shell.

To investigate the gas arrival from supersonic Laval nozzle a number of calculations have been carried out. The design of the nozzle was chosen close to experimental one using at Tomsk [5]. The power driving the gas arrival (it increases to the maximum amplitude during t_0=50 μs) has been taken into account, after t_0 obtained density profile of gas was frozen and numerical grid remapping. In the next step this profile was used as a starting point for calculation of liner implosion.

Instability growth rate with and without axial magnetic field

RT instability could be severe enough to disrupt gas-puff during acceleration of plasma. This instability and its nonlinear saturation have been studied mainly in connection with the relevant experiments [3], [10], [11], [12]. Theoretical analysis [13] gives the rate of instability $\gamma \sim \sqrt{k}$, where k is the wave number of the perturbation.

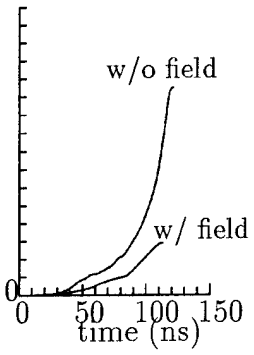


Figure 1. Growth rate vs. time

To investigate the development of disturbances a series of MHD calculations were performed with different wavelengths and different initial perturbations.

The liner configuration has been chosen to be modeled is representative of experiments being conducted at Tomsk [5]. The current driving the plasma dynamics has a form of sine wave with an amplitude of 1 MA and a quarter of period of 100 ns. All simulations were performed for argon double gas-puff with parameters: mass loading

of 40 μg/cm, density equal in outer and inner shells, radius of inner core of 0.5 cm, average radius of outer shell of 1.35 cm and thickness of 0.1 cm. The initial temperature of plasma was taken to be equal 3 eV initially. The density of the background plasma between shells was set for numerical convenience and was taken ten times less than in shell's one.

It has been proposed the method to estimate the instability growth in numerical simulations. We consider the local growth rate ω_n determined by equation

$$\Delta r_n = \Delta r_{n-1} \cdot e^{\omega_n \Delta t_n}, \qquad (2)$$

where $\Delta r_n = r_{max}(t_n) - r_m(t_n)$, r_{max} - radius of "bubble", $r_m = r(Z_0/2)$ - middle radius of the perturbation, $Z_0 = 1/2 \cdot k$.

Figure 1 shows growth rate vs. time for k=2. Because the sinusoidal current the rate coefficient increases quickly after 40 ns. The value of axial magnetic field was 50 kGs. Comparison of the curves shows that external axial magnetic field effectively suppresses instability. Calculations show that region between central core and outer shell acts just as the bumper. The perturbation of outer shell is transmitted through the compressed axial magnetic field existing in the intershells region with significantly small amplitude. This scheme will led to more uniform implosion results.

Results of implosion in 3T approximation

To provide a more realistic simulation of double gas-puff implosion a series of calculation was conducted for gas injection from the nozzle. Figure 2 shows corresponding gas density profiles at the initiation.

These initial profile allows more coupling of physical processes so as the hot spot formation.

It has been found in three-temperature simulation that ion component heats in hot spot due to shock wave propagation and then the plasma liner expands. On the other hand at the same time electrons are cooling due to

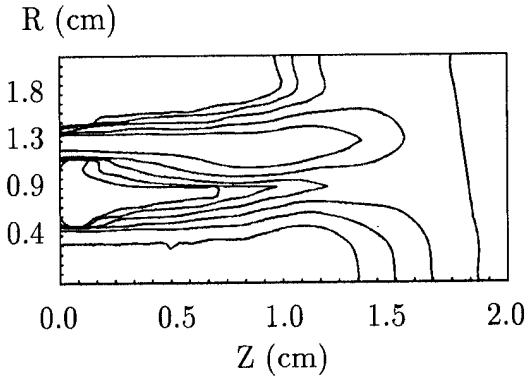


Figure 2. Initial density distribution. Max density = 10^{-5} g/cm^3. 6 contours correspond 2 decades

radiation output. In addition, thin shell carrying current in the body of plasma becames unstable due to magnetized electrons current sheet.

All these effects led to instabilities development and the "zippering" time (difference in time of implosions near cathode and near anode) was in the range of 15 ns. Figure 3 gives the density distribution at the time near the maximum compression.

Changes in mass profile, gas injection angle (for example, inwardly titled gas puff nozzle) can be used to achive greater implosion uniformity.

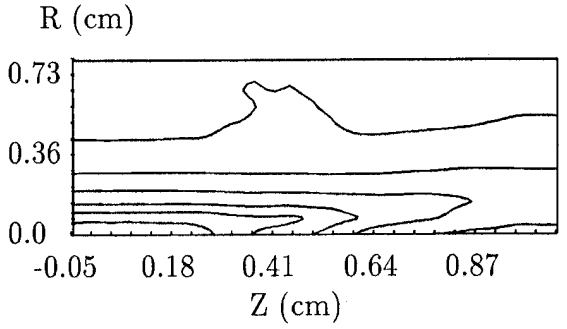


Figure 3. Density profiles at stagnation. Max density = $1.5 \cdot 10^{-3}$ g/cm^3. 6 contours correspond 1 decades

Conclusions

The model has been designed for calculations of entire implosion processes from gas injection to stagnation. First simulations of hot spot formation show that several nonlinear mechanisms determine one's dynamics. The investigation of the nonlinear phenomena of hot spot formation is presently underway. For correct study of the plasma dynamics with Hall MHD it is necessary to develop two-fluid model. For the plasma opening switch the same effects are investigated in paper [14].

In the case of Hall term addition the magnetic field penetrate quickly into the plasma. Anomalous effects associated with microinstabilities development can also led to fast penetration of magnetic field [15]. Hence the above-mentioned model for azimuthal component of the field ceases to be true and addition of the compenent calculation in TIGR-M code is needed.

There are thermoelectric term and and terms of viscous stress tensor which is not take into account in our calculations. The terms are included into 2D MHD code reported in paper [16].

Acknowledgments

The authors would like to thank A.A. Kondrat'ev for stimulating discussions, A.N. Shushlebin for his work on three-temperature approximation of TIGR-M developing, I.A. Litvinenko, I.V. Pavlov, V.V. Fedorov, V.I. Rot'ko for their assistence in numerical simulation.

References

[1] E.G.Harris, Phys.Fluids **5**(9), 1057(1962).

[2] G.Bateman, *MHD Instabilities* (MIT Press, Cambridge, MA, 1978).

[3] N.F.Roderick, and T.W.Hussey, in *Dense Z-pinches*, ed. by N.R.Pereira, J.Davis, and N.Rostoker (AIP Conference Proceedings **195**, New York, 1989), p.157.

[4] A.B.Bud'ko, M.A.Liberman, A.L.Velikovich, and F.S.Felber, Phys.Fluids B **2**(6), 1159(1990).

[5] S.A.Sorokin, S.A.Chaikovsky, in *Dense Z-pinches*, ed. by M.Haines and A.Knight (AIP Conference Proceedings **299**, New York, 1994), p.83.

[6] A.D.Zoubov, G.A.Adamkevich, I.V.Glazyrin, and A.A.Kondrat'ev, in *Dense Z-pinches*, ed. by M.Haines and A.Knight (AIP Conference Proceedings **299**, New York, 1994), p.180.

[7] A.Yu.Bisyarin, V.M.Gribov, A.D.Zoubov, etc, VANT, Ser.: Metodiki i Programmy Chisl. Resheniya Zadach Matem. Fisiki, **3**(17), 34(1984) (In Russian).

[8] A.Fruchtman and Y.Maron, Phys.Fluids B **3**, 1546(1991).

[9] A.S.Kingsep, K.V.Chukbar, and V.V. Yan'kov. in *Review of Plasma Physics*, ed. by B.Kadomtsev (Consultant Bureau, New York, 1990), Vol.16, p.243.

[10] T.W.Hussey, M.K.Matzen, and N.F.Roderick, J.Appl.Phys., **59**, 2677(1986).

[11] F.L.Cochran and J.Davis, Phys. Fluids B **2**(6), 1238(1990).

[12] P.Sheehey and I.R.Lindemuth, in *Dense Z-pinches*, ed. by M.Haines and A.Knight (AIP Conference Proceedings **299**, New York, 1994), p.157.

[13] M.Kruskal, M.Schwarzschild, Proc. Roy. Soc. **A223**, 348(1954).

[14] B.V.Oliver, L.I.Rudakov, R.J.Mason, and P.L.Auer, Phys. Fluids B **4**(2), 294(1992).

[15] I.V.Glazyrin, N.G. Karlykhanov, M.S. Timakova, and A.D.Zoubov, these proceedings.

[16] K.Jach, M.Mroczkowski, and W.Stepniewski, Polish J. Tech. Phys. **32**(1), 125(1991).

INTERMEDIATE DENCITY Z-PINCHES COMPRESSION DINAMICS INVESTIGATION.

Gordeev E.M., Dan'ko S.A., Kalinin Yu.G., Kopchikov A.V., Korolev B.D., Kuksov P.V., Smirnova E.A., Shashkov A.Yu., Yan'kov V.V.

Russian Scientific center "I.V. Kurchatov Institute"
123182, Moscow, Russia.

ABSTRACT.

Plasma neck development dynamics investigation was carried out on Module A5-1 installation, operated in a low-Ohm output impedance (0.04 Ohm, I_{max}=1.3 MA, τ=100 ns) regime. The plasma was created as result of an electrical breakdown of the cylindrical agar-agar fibers with 2-3 mm in diameter and 0.1-0.01 g/cm^3 density. Plasma point with 100 mkm size was formed at the moment near the current peak in a region where the neck with < 1 mm in diameter was done beforehand. The dense hot plasma temperature and density were T_e > 1 keV, n_e> 10^{22} cm^{-3} accordingly and the life time of the plasma point did not surpass 5 ns. In some experiments the formation of the hot plasma points were observed as a result of breakdown along the dielectric fiber or successive compressions.

1. INTRODUCTION.

The development of nanosecond pulse power generators technic with currents up to 10 MA opens new possibilities for thermonuclear investigations of Z-pinches. The high current rise > 10^{13} A/s at a load, obtained on these installations, allow to consider dense Z-pinches with the small radius < 1 mm and the initial density~ g/cm^3. The approach of thermonuclear ignition realization in a dense Z-pinch neck was proposed in /1/. The proposal is based on the maximum amplification of preliminary made perturbation as a result of neck instability with m = 0 mode. The small diameter of pinch may be obtained due to a well known phenomenon of self-focusing when the plasma streams along the pinch axis /2,3/. As the ignition is possible only in the small size neck then for obtaining of high energy output it is necessary that the detonation wave outgoing from the neck will be propagated on the essential mass of the pinch. The estimates carried out in /1/, show that the typical size of the neck, necessary for an ignition, is 1 mkm and the plasma temperature should be about 10 keV. Such size may be obtained as a result of small fiber cylinder compession made of the condensed D - T mixture with the density of 0.2 g/cm^3 and the initial diameter of 1 cm at 10 MA current.

The goal of our work was the experimental investigation of the neck development in a plasma, obtained as a result of an electrical breakdown of the cylindrical fibers of polimer porous materials having the intermediate density of 0.1-0.01 g/cm^3 with the preliminary made neck. Using such targets allows partially to model the condensed hydrogen at smaller current and, besides, to match the time of maximum compression with the rise time of a current for obtaining effective transfer of energy into the load.

Z-pinches usually are starting either by a breakdown of a rare gas /4/, solid metal /5/ or dielectrical wipes /6,7/. The region of intermediate densities was almost not investigation, except experiments carried out on Angara 5-1 /8/ end Module A5-1 /9/. One must point out on the investigations which are close by their final goal to the discribed one and which are based on the idea of a radiation collapse of pinches but which differ by compression mechanizm and the initial parameters of the pinch /10-13/.

2. EXPERIMENTAL ARRANGEMENT.

Experiments on a neck development were carried out on the Module A5-1 machine. The installation operated in a regime of a low-Ohm output impedance (0,04 Ohm). For obtaining the megaampere current level a lowering wave pulse transformer with the transformation coefficient of 6 was used. Energy transportation from the transformer to a load was realized by using a vacuum 3-D concentrator based on magnetically insulated transmission lines (MITL). Parallel connected MITL's were combined in the target unit where a load was mounted (Fig 1).

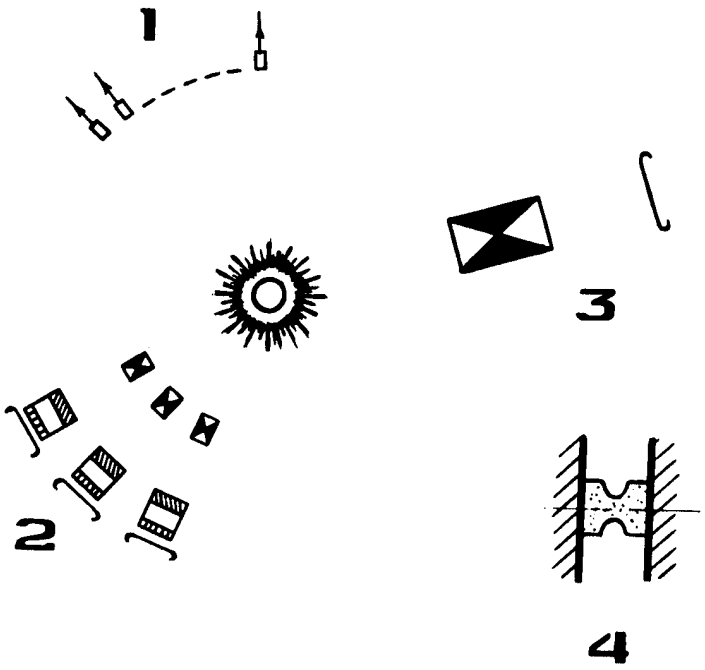


Fig 1. Experimental layout
1- X-ray semiconductor detectors, 2- X-ray framing cameras, 3- time integrated multihole obscure - chambers, 4- load.

For the observation angle increase of the discharge gap and the decrease of the target unit inductance a load was inserted on the axis of two metal cones with their tops looking opposite to each other. Total inductance of concentrator is 6 nH. Maximum value of the load current was 2 MA for 100 ns time. Neck radius and initial density of the fiber were choosed

from matching condition of the current rise time and the neck development time. For typical condition of our experiment (I=1 MA, τ=100 ns) the matching occurs for the initial neck diameter of 0.5-1 mm and the fiber densities of 10^{-2}-10^{-1} g/cm^3. Cylindrical fibers of 2.3-3.0 mm in diameter are made from porous polymers (agar-agar or PVC). Fiber density can be varied within the range of 10^{-3}-10^{-1} g/cm^3, fiber length was equal to 3 mm gap. The semiconductor array of detectors with 1 ns time resolution were used for plasma parameters dynamics measurements of emission in the energy region of 0.6-10 keV. For obtaining of information about the spectral composition of the emission the detectors were supplied with filters based on carbon , aluminium, chlorine, titan, manganese, copper materials. Usual quantitv of measuring channels was equal to 5-10. Simultaneously with x-ray pulses current and the pinch dI/dT were registered by means of magnetic probe, inserted to the cathode at the distance of 20 mm from the discharge gap axis and voltage V at the input of the target unit. Pinch structure was defined by using the time integrated pictures and frame photography. The time integrated X-ray photography of a discharge in the energy range of $h\nu$>200 eV with 1:2 magnification was observed with a multihole obscure chambers (4 hole with different diameters), supplied by filters. For frame photography three X-ray framing cameras were used with 3 ns exposure time. The four images with 1:2 magnification were formed with a multihole obscure-chamber located at the input of framing camers. In case of time resolution photography the obscure-chambers were supplied with the same filters as for time- integrated one.

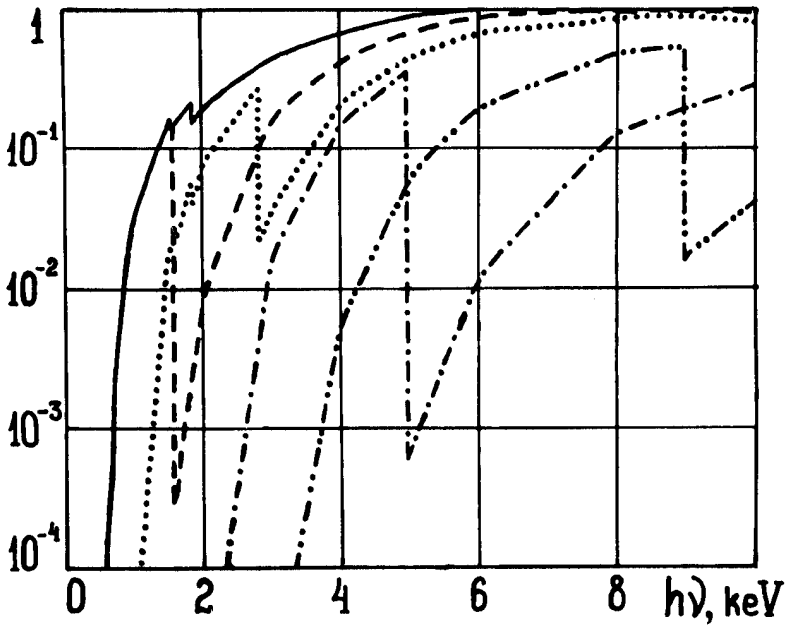


Fig 2. Spectral sensitiveness of semiconductor detectors with filteres: mylar 5 mkm (____); aluminium 5 mkm (---); PVC 30 mkm (...); titan 22 mkm (-·-); copper 15 mkm (-··-).

3. EXPERIMENTAL RESULTS.

From analysis of frame camera pictures made in soft X-ray emission range ($h\nu > 0.2$ keV), it follows that when the high voltage is applied to the electrodes of the discharge gap a breakdown of agar-agar fiber occurs. At 20 ns moment from the beginning of the pinch current the luminous shell of 0.2-0.3 mm thickness is formed (Fig 3). Under the electrodynamic force action the plasma implosion occurs with the average radial velosity 10^7 cm/s /9/. As a result of plasma compression on the pinch current rise time the single bright spot is formed (for initial density 10^{-2} g/cm^3) with minimum size < 100 mkm determined by the space resolution of X-ray framing cameras (70 mkm). The bright spot image with clear edges obtained in the rigion of $h\nu > 1$ keV is shown in the third frame of Fig 3. Behind more soft filter the

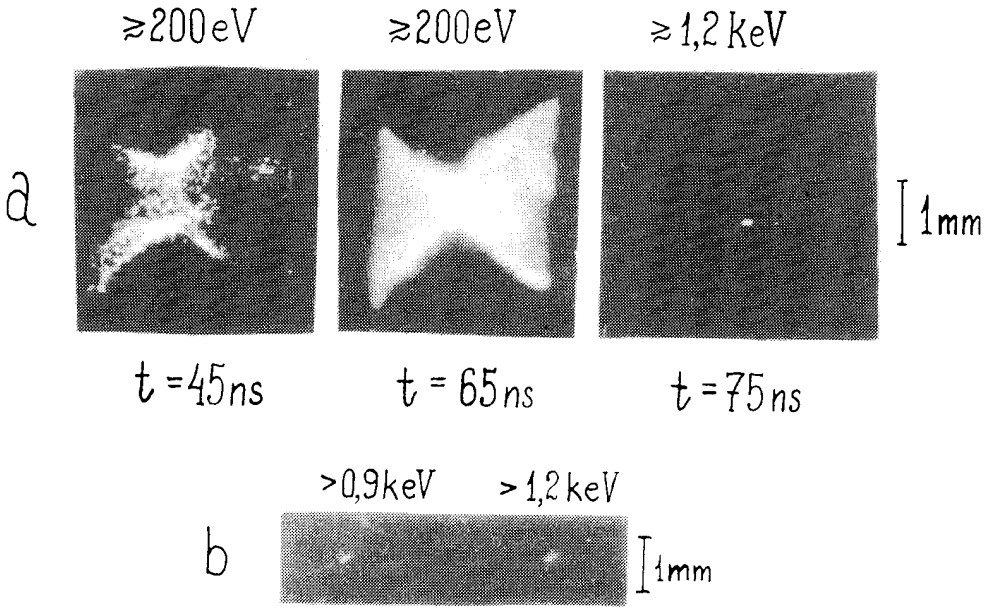


Fig 3. a) X-ray framing photography of agar - agar fiber (3 nsec exposure). b) the time integrated pictures

image has washed out edges and larger characteristic size. In case of the single bright spot formation usually the compact compression is observed in the neck region. The X-ray radiation is arisen at the current rise time with the jitter time of about ± 20 ns. Semiconductor detectors with filters registered X-ray pulses with FWHM of 5 ns (Fig 4). Note, that in some X-ray pulses have multipeak shape of each spike being the order of 5 ns wide. Moreover, sometimes detectors registered repeated pulses resolved in time (usually after the current maximum) (Fig 5). Evedently the repeated pulses were caused by the second compression.

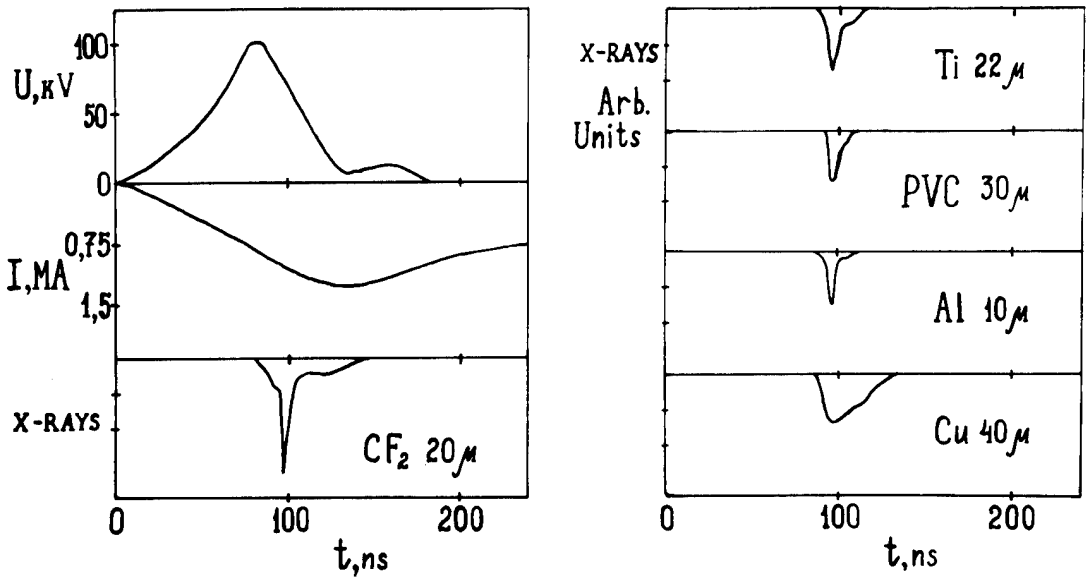


Fig 4. Voltage and current oscillograms and semiconductor detector signals showing the time - dependent X-ray emission through different filters.

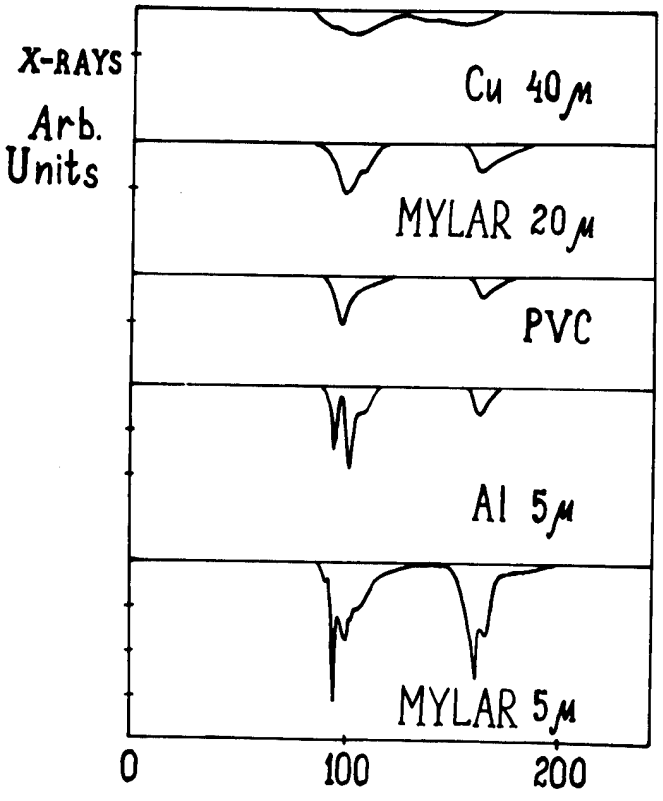


Fig 5. Oscillograms of X-ray pulses, showing the appearance of repeated emission.

The appearance of the soft X-ray emission is accompanied by high frequency oscillations on dI/dt curve which, perharps, are connected with unstable character of the neck development. The unstable plasma dynamic phase is marked by both the appearance of several X-ray peaks and the formation of some bright spots, being registrated by obscure - chambers (Fig 6). These effects are similar to those, which were discovered in the experiments with the metal wires /5/. In some shots a formation of tube structure is seen, which then splits into few bright spots. In this case the current is carried into the corona of rare plasma being in discharge periphery /15/, and then as a result of instability process the bright spots are formed. Plasma density at the distance of > 1 mm from the laser probing, equals to 10^{18} cm^{-3} /9/.

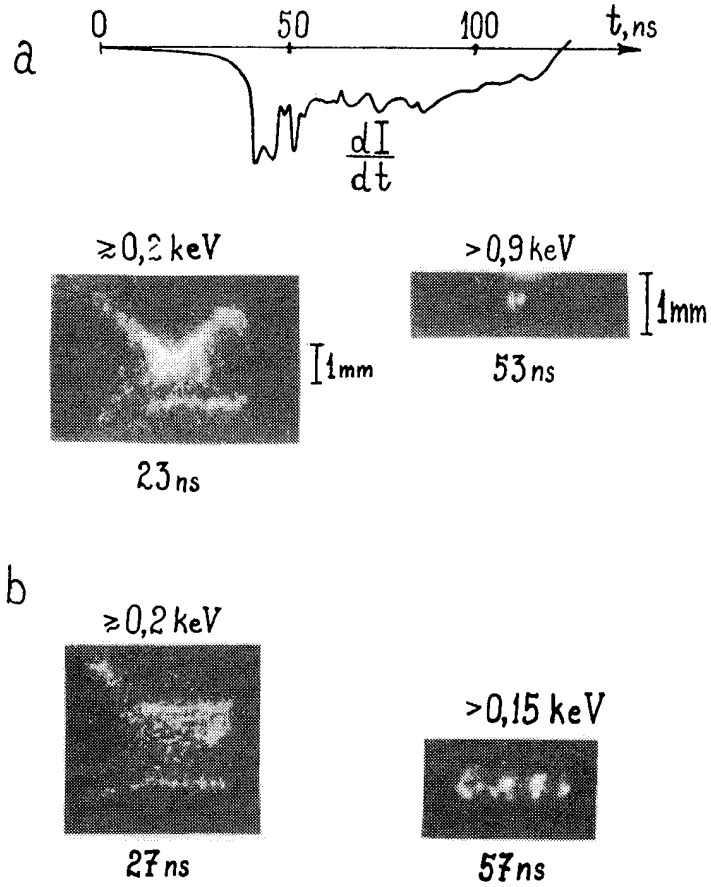


Fig 6. Oscillograms of current derivative (a), integrated x-ray pinhole photography of bright spot and framing pictures, showing the appearance of several bright spots.

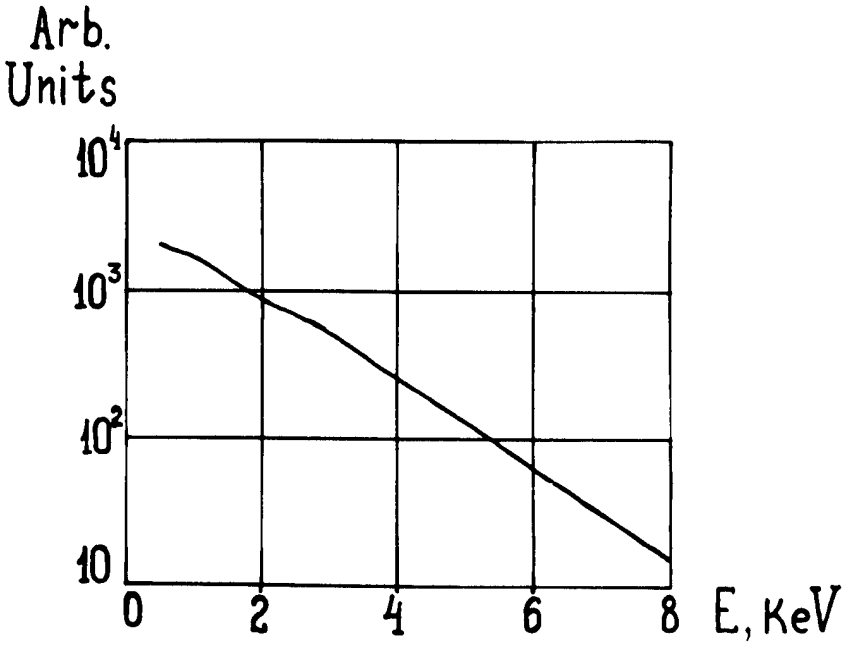


Fig 7. Energy spectrum of the radiation from the fiber plasma.

Spectral composition of plasma radiation in the energy region of $h\nu > 0.9$ keV (i.e. in the region where line of C,N and O_2 are absent) was defined by method of spectra reconstruction from pulses of X-ray detectors. For an apriori of spectrum was used the plasma emission spectrum of the given chemical composition, calculated on collision - emission model /16/. Instant radiation spectra is given in Fig 7 for the moment, corresponding to the maximum intensity of X-ray pulses.

The electron temperature, defined from bremsstrahlung and recombination spectra is 0.8 - 1.5 keV. The radiation power with photon energy $h\nu > 1$ keV achieves $(0.5 - 1)10^8$ W, the total energy radiated per pulse equal to several jouls. It is to be noted that the repeated pulses are the source of significantly lowerenergetic photons ($h\nu < 100$ eV). Calculated plasma density in frame of collisional radiational model is $n_e = 10^{22} cm^{-3}$ for hot region size of 80 mkm. These parameters are in accordance with Bennett relation for 1 MA current.

CONCLUSION.

The experiments showed rather deep development of the neck in a plasma formed as a result of the electrical discharge of dielectrical fibers with pleminary made neck when megaampere current is flowing. Further experiments will be directed to the investigation of the possibility for obtaining the extreme parameters of a hot plasma with the size < 1 mm.

Authors express their gratitude to Nedoseev S.L. and Medovchikov C.F. for help in the experiments.

REFERENCES.

1. V.V. Yan'kov, a) Preprint IAE - 4218/7, M. p.8, (1985). b) Phyz. Plasmy (Sov. J.), 17, 521, (1991).
2. A.C. Kolb, Rev. Mod. Phys. 32, 74., (1960).
3. V.V. Vikrev, S.I. Braginskii, In book: Plasma Theory Problems. Ed M.A. Leontovich. M. Atomizdat 10, 251, (1980).
4. N.V. Fillipov, Fiz. Plazmy. 9, 25, (1983).
5. L.E. Aranchuk et al, Fiz. Plasmy (Sov. J) 12, 1324, (1983).
6. I.D. Sethian et al, Proc. of the Int. School of Plasma Physics, Varenna, p.511, (1990).
7. Scudder et al, in ref /6/,p.519.
8. S.L. Nedoseev, in ref /6/,p.44.
9. S.A. Dan'ko et al, 6th Int Conf. on Megagauss Magnetic Field Generation and Related Topics, Albuerque (USA), p.44, (1992).
10. S.I. Braginskii, Zh Eksp. Teor Fiz. 33, 645, (1957).
11. R.S. Pease, Proc. Rev. Soc., B.70, 11 (1957).
12. V.V. Vikrev, Plasma Zh Eksp. Teor. Fiz. 27, 104, (1978).
13. M.G. Haines, in ref /6/, p.277.
14. S.L. Bogolyubskii et al, Proc of the 6th Int Conf on High Power Particle Beams, Kobe. p.451, (1986).
15. P.V. Sasorov, Sov. P'is'ma Phys. 12, 1324, (1986).
16. S.A. Dan'ko, O.N. Yartceva, Preprint IAE - 45/617, M.

K_α SPECTRAL DIAGNOSTICS FOR Mg AND Al PLASMAS IRRADIATED BY INTENSE Li BEAMS

J. J. MacFarlane and P. Wang
Fusion Technology Institute
University of Wisconsin
1500 Johnson Drive
Madison, WI 53706

J. E. Bailey, T. A. Mehlhorn, and R. J. Dukart
Sandia National Laboratories
P. O. Box 5800
Albuquerque, NM 87185

Abstract

K_α spectroscopy can be a valuable diagnostic method for determining plasma conditions in ion beam-heated targets. In intense light ion beam experiments, K_α emission lines can be observed as $2p$ electrons drop down to fill $1s$ vacancies created by beam-impact ionization. In this paper, we present results from collisional-radiative equilibrium (CRE) calculations for Al and Mg target tracer layers being irradiated by an intense Li beam. Presently, 9 MeV Li beams with power densities of 1-2 TW/cm^2 can be generated in Particle Beam Fusion Accelerator-II (PBFA-II) experiments at Sandia National Laboratories. It is shown that both emission and absorption K_α spectra show good sensitivity to temperature and density for the range of plasma conditions typically achieved in present PBFA-II experiments.

I. Introduction

K_α satellite spectroscopy has been shown to be a valuable technique in determining plasma conditions in high energy density plasma experiments [1-7]. K_α lines result from electronic $2p \leftrightarrow 1s$ transitions. Thus, in intense light ion beam experiments emission lines can be produced as $2p$ electrons drop down to fill $1s$ vacancies created by the ion beam. K_α absorption lines can be seen in the presence of an x-ray backlighter when the target ions have at least one vacancy in the $2p$ subshell. Bailey et al. [2] reported the first spectroscopic measurements of K_α x-ray satellites in an intense proton beam experiment. K_α emission spectra have also recently been measured in intense Li-beam experiments on PBFA-II [8].

The purpose of this paper is to show how K_α satellite spectroscopy can be used to diagnose conditions in target plasmas heated by intense Li beams. To do this, we have performed a series of collisional-radiative equilibrium (CRE) calculations to generate K_α emission and absorption spectra for Mg and

Al plasmas. In previous light ion beam experiments, only K_α satellite emission spectra from single-component tracers (i.e., Al) have been used for diagnosing plasma conditions [2,5,8-10]. However, it is expected that multicomponent tracers will be utilized in upcoming experiments to provide additional information for constraining the plasma temperature and density. This paper presents our initial results for Mg/Al tracers.

II. Theoretical Models

Next, we briefly describe the major features of our CRE and atomic physics models. Additional details can be found elsewhere [5,9-11]. Atomic level populations are determined by solving multilevel statistical equilibrium equations self-consistently with the radiation field and ion beam properties. Our atomic models for intermediate-Z tracer elements (here, Mg and Al) typically consist of $\sim 10^3$ energy levels distributed over all ionization stages. Roughly 60% of these are autoionization states with K-shell vacancies. Atomic structure and radiative data are computed using a configuration interaction (CI) model with Hartree-Fock wavefunctions. Ion beam-impact ionization is included in the statistical equilibrium equations, including multiple ionization transitions (i.e., the simultaneous ejection of a K-shell and one or more L-shell electrons). Ion-impact ionization cross sections are computed using a plane-wave Born approximation model with corrections for Coulomb-deflection, binding energy, and relativistic effects. Multiple ionization cross sections are then obtained using an independent event binomial distribution model [11]. Auger rates and fluorescence yields are calculated for each autoionizing level using a LS coupling formalism with Hartree-Fock wavefunctions. Calculated emission and absorption spectra include contributions from bound-bound, bound-free, and free-free transitions. In the calculations described below, radiation is transported using an escape probability model. Resonant self-absorption effects are included in computing both the photoexcitation rates and the emergent spectra. Line profiles include the effects of natural, Doppler, Auger, and Stark broadening.

III. Results

A series of calculations were performed independetly for thin, planar Mg and Al tracers of uniform temperature and density. Temperatures were varied between 30 and 50 eV. In all cases the tracer density was $n = 10^{-3}$ n_{solid} and the thickness was 200 μm, which corresponds to a 2000 Å foil which has expanded by a factor of 10^3. The ion beam was assumed to be composed of Li^{+3} with an energy of 9 MeV per ion. All calculated spectra include instrumental broadening, where a resolution of $\lambda/\Delta\lambda = 1500$ was assumed.

Calculated emission and absorption spectra for K_α satellite spectral region of Mg are shown in Fig. 1. The absorption spectra (shown in lower panels) probe the lower state populations of the K_α bound-bound transitions, and therefore provide a direct measure of the ionization distribution. For instance, B-like and Be-like Mg are the dominant ionization stages at $T = 40$ eV, while Li-like and Be-like Mg are prevalent at $T = 50$ eV. K_α satellite emission spectra (upper panels) reflect the populations of the upper levels of the K_α transitions (i.e., the autoionizing levels), which are populated by ion beam-impact ionization. Because of this, lines from one to two ionization stages higher are seen in emission. For example, the He_α line ($1s2p\,^1P \rightarrow 1s^2\,^1S$) and Li-like satellites are strongest in emission at $T = 40$ eV.

Additional information about plasma conditions can be obtained by performing experiments with multi-component tracers.

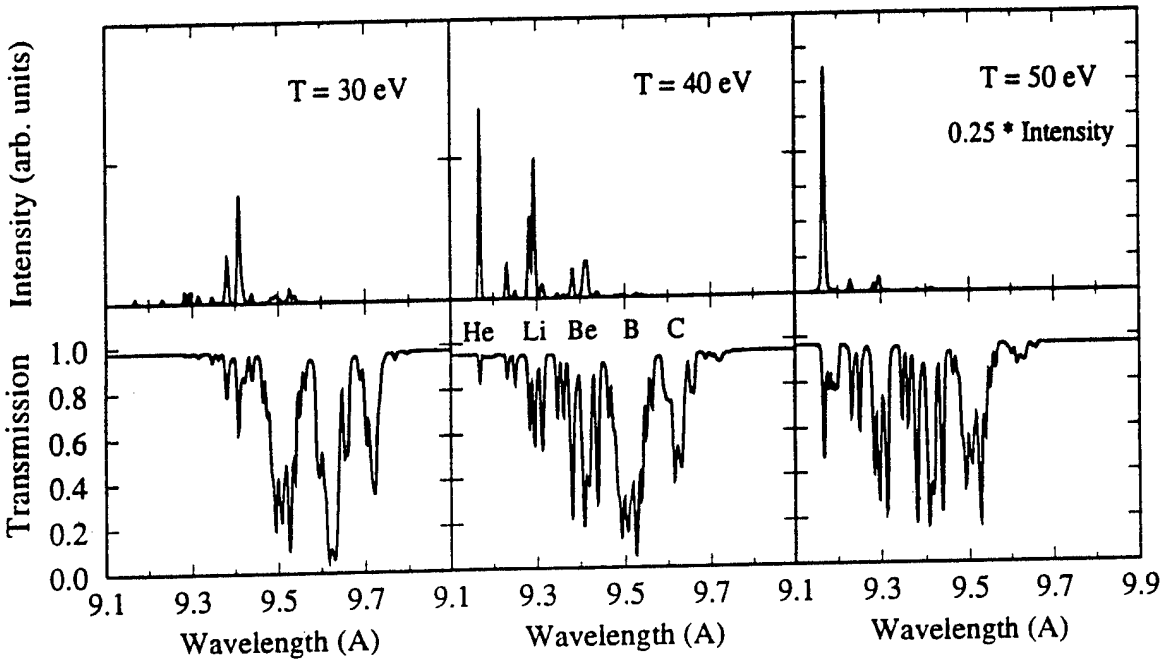


Fig. 1. Calculated Mg K_α emission (top) and absorption (bottom) spectra at $T = 30, 40$, and 50 eV. In each case, $n = 10^{-3}\, n_{\text{solid}}$ and $L = 200\,\mu$m. The satellite ionization stages are shown with the $T = 40$ eV absorption spectrum. Note the larger scale in the $T = 50$ eV emission plot due to the strong He_α line at 9.168 Å.

Figure 2 shows the K_α emission spectrum calculated for Al at $T = 40$ eV, along with the K_β absorption spectrum (involving $1s \rightarrow 3p$ transitions) for Mg at $T = 50$ eV. Here, we examine whether K_α emission from one of the tracers can be absorbed by the other. Note that in several instances the K_β lines of Mg are capable of absorbing K_α line emission from Al. In particular the Mg He_β line at $\lambda = 7.850$ Å lies directly between the two strongest Li-like Al K_α emission features. Also it is seen that Li-like Mg K_β satellites between 8.0 and 8.1 Å can absorb line radiation from the B-like Al K_α satellites. The overlap of part of the Al K_α spectrum with the Mg K_β satellites, however, need not necessarily lead to significant problems in analyzing the spectra. This is because the K_α satellite emission from the highest ionization stages (He-, Li-, and perhaps Be-like) will most likely be utilized to determine the peak temperatures obtained in light ion beam experiments, in which case only the Mg He_β line is capable of producing significant absorption.

Our results therefore indicate that K_α satellite emission spectra obtained from two-component Mg/Al tracers should provide enough information to accurately determine target plasma temperatures in the 30 eV to 50 eV range. New data from Mg/Al tracers will be obtained in upcoming PBFA-II Li beam experiments. Similar data will be obtained from NaF tracers in proton beam experiments at the Karlsruhe Light Ion Facility (KALIF) in Germany [12]. We also expect to utilize line intensity ratios from the He-, Li-, and Be-like K_α satellites to determine plasma temperatures

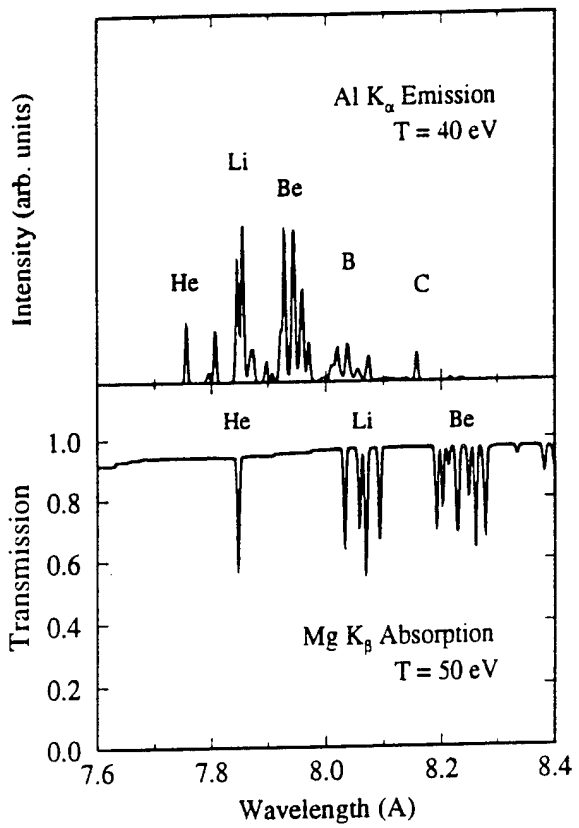


Fig. 2. Calculated Al K_α satellite emission spectrum at $T = 40$ eV and Mg K_β absorption spectrum at $T = 50$ eV. In each case, $n = 10^{-3}\, n_{\text{solid}}$ and $L = 200\,\mu$m. Note that at several wavelengths Al K_α emission lines can potentially be absorbed by Mg K_β lines.

and densities. This work will be described in detail elsewhere [13].

References

1. Nardi, E. and Zinamon, Z., 1981, *J. Appl. Phys.* **52**, 7075.

2. Bailey, J., Carlson, A. L., Chandler, G., Derzon, M. S., Dukart, R. J., Hammel, B. A., Johnson, D. J., Lockner, T. R., Maenchen, J., McGuire, E. J., Mehlhorn, T. A., Nelson, W. E., Ruggles, L. E., Stygar, W. A. and Wenger, D. F., 1990, *Lasers and Particle Beams* **8**, 555.

3. Perry, et al., 1991, *Phys. Rev. Lett.* **67**, 3784.

4. Chenais-Popovics, C., Fievet, C., Geindre, J. P., Gauthier, J. C., Luc-Koenig, E., Wyart, J. F., Pepin, H. and Chaker, M., 1989, *Phys. Rev. A* **40**, 3194.

5. MacFarlane, J. J., Wang, P., Bailey, J., Mehlhorn, T. A., Dukart, R. J. and Mancini, R. F., 1993, *Phys. Rev. E* **47**, 2748.

6. Abdallah, J., Clark, R. E. H., and Peek, J. M., 1991, *Phys. Rev. A* **44**, 4072.

7. Foster, et al., 1991, *Phys. Rev. Lett.* **67**, 3255.

8. Bailey, J. E. et al., 1993, presented at the 6th International Workshop on Atomic Physics for Ion Driven Fusion, Santa Fe, NM.

9. Wang, P., MacFarlane, J. J. and Moses, G. A., 1993a, *Phys. Rev. E* **48**, 3934.

10. MacFarlane, J. J., Wang, P., Bailey, J. E., Mehlhorn, T. A., and Dukart, R. J., 1994, *Lasers and Particle Beams*, in press.

11. Wang, P., MacFarlane, J. J., and Moses, G. A., 1994, *Lasers and Particle Beams*, in press.

12. Goel, B., Ludmirsky, A., Baumung, K., Bluhm, H., Buth, L., Höbel, W., Meisel, G., Rusch, G., Stolz, O., MacFarlane, J. J., and Wang, P., 1994, these proceedings.

13. MacFarlane, J. J., Wang, P., Bailey, J. E., Mehlhorn, T. A., and Dukart, R. J., 1994, in preparation.

NUMERICAL SIMULATION FOR A PRACTICAL LARGE-SIZE PELLET IMPLOSION

Shigeo Kawata and Tetsuya Saitoh
Nagaoka University of Technology
Nagaoka 940-21, Japan

Abstract

In this paper we introduce and discuss a concept of a large-size-pellet inertial confinement fusion(ICF) in which a fuel pellet contains the deuterium-tritium fuel of about one gram. In the large-size-pellet ICF the fuel compression ratio is about 100 times of the solid density in order to realize $\rho R > 3 g/cm^2$. Because of the low compression ratio, the constraints required for the fuel compression are relaxed compared with those for the high-compression implosion scheme of a small pellet. This concept of the large-size-pellet implosion may present an alternative way to the ICF. In this paper we present the one-dimensional numerical analyses for the large-size-pellet implosion in the impact ICF. The simulation results show that an enough fusion energy output may be obtained in the large-size-pellet ICF.

In the inertial confinement fusion (ICF) a small reactor pellet is compressed to about 1000 times of the solid density in order to extract the fusion energy in a short time with the high reaction rate, and to save the input driver energy. The requirement for the uniformity of the small pellet compression is quite severe.[1] It is well known that the nonuniformity should be suppressed less than a few %. An alternative scheme is a low-compression one, which is presented and discussed in this paper. In the low-compression scheme a fuel should contain a larger DT mass compared with that in a high-compression pellet in order to attain $\rho R > 3 g/cm^2$; For example, about one gram of the DT fuel may be required. Because of the low compression ratio and the large size of the pellet, the low-compression scheme relaxes the uniformity requirement and that for the driver energy focusing. However this scheme has a disadvantage of the larger input driver energy, which should be larger than several ten MJ for the 1-gram DT fuel pellet.

LARGE-SIZE PELLET ICF

One of the main objectives in the large-size-pellet ICF is to reduce the fuel compression ratio. In the large-size-pellet ICF a fuel radius is about 1cm depending on a pellet structure and on the total fuel mass being contained in the capsule. Because of the low compression, the uniformity requirement can be relaxed.

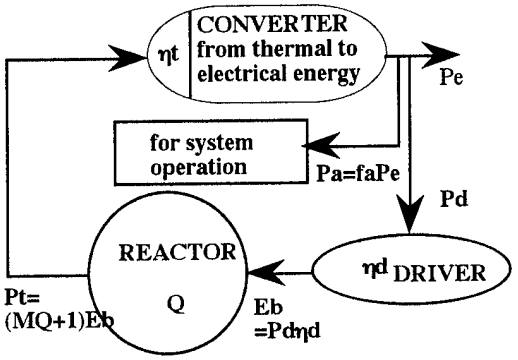


Fig.1 Energy balance

First an energy balance is described by $P_a+P_d+P_e=\eta_t P_t$ (see Fig.1). Here P_t is the output thermal energy which is presented by $(MQ+1)E_b$. Here M is the multiplication factor at the blanket, $Q=R_fG$, R_r the repetition rate, G the pellet gain, η_t the conversion efficiency from the thermal to the electric energy, P_e the net electric output energy, P_d the energy supplied to a driver machine and $P_a=f_aP_e$ the energy required to drive the reactor system. Then we obtain the expression for Q: $Q = [1+(1+f_a)P_e/P_d] /(\eta_t M\eta_d) - 1/M$

The input energy being required to compress and heat the fuel is estimated by the sum of the heating energy $W_h=38.3M_{DTh}T_i$ *J* and the energy (pressure work) to compress the fuel. In this calculation electrons are assumed to be in the perfect-degenerate gas state. Here M_{DTh} is a part of the fuel (M_{DT} *mg*) heated up to T_i *eV* by the input energy and its radius is assumed to be 3 times of the radius at which a produced α particle stops. The pressure work is $W_P=114(\kappa^{2/3}-1)M_{DT}J$, where κ is the compression ratio. In our calculation $\rho R= 3g/cm^2$, the implosion efficiency 5%, η_d=20%, M=1.1, f_a=0.1, R_r=1 and η_t=45%. Finally we obtain the relation between the compression ratio and the beam input energy, as shown in Fig.2. The numerical values beside the line denote the total DT mass. For the large pellet containg about 1 *gram* of the DT, the required compression ratio is rather low and is less than 100. This figure shows that the large-pellet ICF may be another candidate in ICF, although the input energy is large.

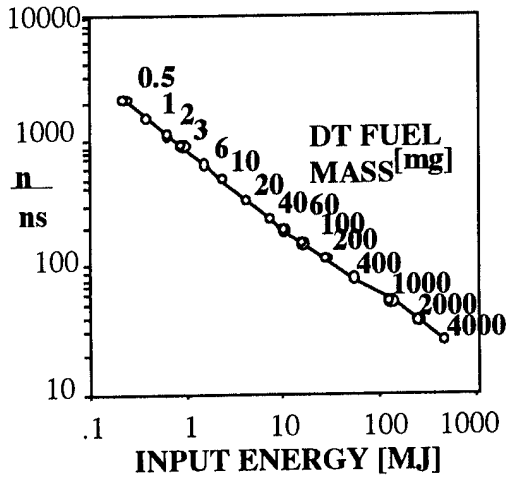


Fig.2 Density compression ratio versus the input energy

The uniformity requirement can be

estimated as follows: First the nonuniformity of the implosion speed δv_{imp} is estimated. From approximated relations of $R_0=v_{imp}t_f$ and $\delta R=\delta v_{imp}t_f$, $\delta v_{imp}/v_{imp}= \delta R/R_0= (\delta R/R)(R/R_0)= (\delta R/R)\kappa^{-1/3}$. Here R_0 is the initial radius, R the final radius of the pellet and κ the volume compression ratio. On the other hand ρR is proportional to R^{-2} and $\delta(\rho R)/(\rho R)_0= (1+\delta R/R)^{-2}$. Then $\delta R/R=[\delta(\rho R)/(\rho R)_0]^{-1/2}-1$. Combining these relations, we obtain $\Delta = \delta v_{imp}/v_{imp} = [\{\delta(\rho R)/(\rho R)_0\}^{-1/2} - 1] /\kappa^{1/3}$. From this result $\Delta_{low\text{-}\rho}/\Delta_{high\text{-}\rho} = (\kappa_{high\text{-}\rho}/\kappa_{low\text{-}\rho})^{1/3}$ for the fixed allowable $\delta(\rho R)/(\rho R)_0$. Here $\Delta_{high\text{-}\rho}$ shows the nonuniformity in the conventional high- compression scheme and $\Delta_{low\text{-}\rho}$ presents one in the large-pellet ICF. For the high-compression scheme the volume compression ratio $\kappa_{high\text{-}\rho}$ is about 10000 and for the large-pellet ICF $\kappa_{low\text{-}\rho}$ may be a few hundreds to 500 in our pellet employed in this paper. Therefore the factor of $\Delta_{low\text{-}\rho}/\Delta_{high\text{-}\rho}$ is about 2.7~4: Consequently the tolerable nonuniformity in the large-size-pellet ICF may be about 5~8%.

PELLET SIMULATION

In this study we treat the fuel pellet and the projectile as fluids so that their motions are described by the hydrodynamic equations. The basic equations are equations of continuity, motion and energy. In order to simulate the large-size pellet we employed the three-temperaturemodel[2]. We include the DT reaction and the fuel depletion by the reactions. In our model we consider the α particle heating and disregard the neutron heating. We use the diffusion equation for the α particle transportation. We also use the SESAMI library as an equation of state. Figure 3 shows a fuel pellet structure employed in this study. A DT gas is located at the pellet center. The mixture of DT(95%) and Pb(5%) covers the main DT fuel as an ablator and a pusher. The projectile is made of the solid Pb and accelerated to about 100 *km/s*.

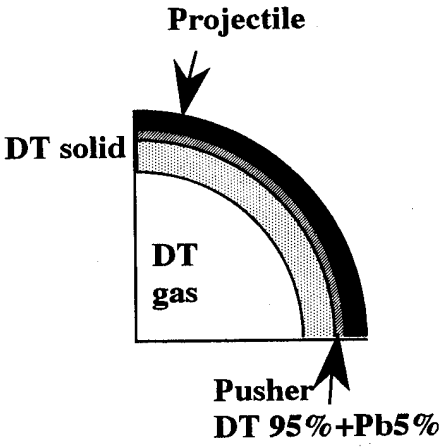


Fig.3 Pellet structure and the projectile

Table 1 shows the parameter values employed in the simulation and a part of the results obtained. In order to make the first shock wave weak we employed a shaped density projectile as follows: $\rho=\rho_{pusher} + (\rho_{Pb}-\rho_{pusher})[(r-r_{in})/(r_c-r_{in})]^2$ for $r_{in} < r < r_c$ $(=(r_{in}+r_{out})/2)$ and $\rho=\rho_{Pb}$ (=the solid Pb density) for the other outer part of projectile. Here r_{in} and r_{out} are the radii of the inner and outer surfaces of the projectile, respectively. By a strong shock wave launched by the projectile collision, first the inner DT gas reacts slightly but at this time the main solid DT is not yet ignited. After the further

compression, the solid DT is heated up and then burned. The maximum ρR is $7.25 g/cm^2$. The peak DT number density is 434 times of the solid density. The fusion energy output is 64.7GJ and the pellet gain is 407. This result shows that the large-size-pellet scheme may be another candidate in ICF.

Table 1. Parameter values employed and Results

DT gas radius	5.00 [mm]
DT gas density/DT solid density	1/10000
DT solid layer thickness	2.43 [mm]
Total DT fuel mass	0.25 [g]
Pusher thickness	0.500 [mm]
Pb projectile thickness	2.47 [mm]
Pb projectile speed	120 [km/s]
Input energy	159 [MJ]
Max. DT ion temperature	12.0 [keV]
Maximum ρ R	7.25 [g/cm^2]
Max. compression ratio of DT	434
Fusion energy output	64.7 [GJ]
Pellet gain	407

By using the shaped projectile the initial shock wave becomes weak compared with that by using an unshaped one. Consequently the reflected shock is also weak and the implosion in this case is more stable. In this case the deceleration phase by the reflected shock becomes rather stable against the Rayleigh-Taylor(R-T) instability: $\gamma\tau$ during the deceleration phase by the reflected shock is about 1.2, although $\gamma\tau$ during the stagnation phase is about 3.7. These estimation results present that the large-size pellet may survive the R-T instability.

CONCLUSIONS

In this paper we presented the concept of the large-pellet ICF, and discussed about it based on the one-dimensional hydrodynamic computer simulations and the simple estimations. The results of this work demonstrate that the large-pellet ICF scheme may supply the enough fusion energy output. The results of the researches also show that the large pellet may be robust against the nonuniformity compared with the small pellet.

The disadvantages of the scheme are as follows: 1) The input energy is large, that is, more than 100 MJ in our simulation. The solution for this problem may rely on the future development of the energy driver. 2) The second problem is in a reactor design. Probably the large-pellet ICF scheme required a large rector vessel[3] and the technological extensions of the reactor design. We believe that the large-pellet ICF is an alternative way to the future energy source.

REFERENCES

1. S.Kawata and K.Niu, Jpn. J. Appl. Phys., **53**, 3416(1984).

2. N.A.Tahir, K.A.Long and E.W. LAING, J. Appl. Phys., **60**, 898(1986).

3. A.Szoke and R.W.Moir, **UCRL-101429**, (1990).

SPECTROSCOPIC INVESTIGATIONS OF THE PLASMA BEHAVIOR IN A PLASMA OPENING SWITCH EXPERIMENT

M. Sarfaty, R. Arad, A. Weingarten, Ya.E. Krasik,
R. Shpitalnik, Y. Maron, and A. Fruchtman

Department of Particle Physics
Weizmann Institute of Science
Rehovot 76100, Israel

ABSTRACT

Spectroscopic diagnostics were used to study the electron density, the electron kinetic energy, and the particle velocities in a coaxial positive-polarity Plasma-Opening-Switch (POS). A gaseous plasma source, mounted inside the inner POS high-voltage electrode, injects the plasma radially outward into the inter-electrode region. A laser evaporation technique was employed to locally seed the plasma with various species to allow for measurements with high spatial, temporal and spectral resolutions. The electron density was determined from the ionization times of a few species. The electron energy was studied using measurements of absolute line intensities and time dependent collisional-radiative calculations. The velocity distributions of various ions were obtained from emission-line Doppler broadenings and shifts. The ion motion was found to start early over most of the plasma. Together with the relatively low ion velocities and the nearly linear velocity dependence on the ion charge-to-mass ratio, this leads to the conclusion that the magnetic field penetrates the plasma early in the pulse. The ion velocity dependence on the axial location and the local electron density were used to infer the time dependent axial distribution of the magnetic field in the plasma, which indicates the formation of a relatively high current density at the load-side edge of the plasma.

I. INTRODUCTION

Investigating the behavior of plasmas carrying high short-duration currents is of major importance for improving the understanding of fundamental plasma physics phenomena, such as magnetic field penetration into plasmas and plasma flow under magnetic and electric fields. Such phenomena are believed to be dominating the operation of Plasma Opening Switches (POS) used to switch high currents into various loads in times of 10^{-8}-10^{-7} s,

In previous studies, information on the magnetic field evolution in the POS plasma was obtained by the use of magnetic loops inserted into the plasma[1,2]. In spite of the variety of studies performed, it appears that the time dependent magnetic field distribution, the plasma flow, and the electron heating are still not well understood. Systematic experimental investigations are still highly required to examine the various underlying theories[3-6], and to suggest ways to improve the POS operation.

Here, we report developing measurements which we believe are required for understanding the plasma behaviour rather than on improving the performance of our switch. We present the use of nonintrusive techniques to determine the plasma electron density and the velocity distributions of ions during the 180-ns-long current pulse. A lower bound was obtained for the electron energy which enabled us to determine the electron density from the ionization times of various species seeded into the plasma.

We developed a method, using laser evaporation, to locally seed the plasma with various elements, which allowed for measurements that are local in r, z, and θ. This also enabled us to select elements with line emissions that are useful for the various measurements. Our spectroscopic system allows for a high spectral resolution to discriminate against impurity lines, commonly abundant in pulsed-power experiments, and to observe relatively small Doppler broadenings and shifts. A gaseous plasma source mounted inside the inner high-voltage electrode of the coaxial POS injects the plasma radially outwards into the interelectrode gap. The electron density and temperature of the source plasma as well as the particle velocity distributions prior to the pulse were determined.

The spatially resolved ion velocities in the plasma showed that the ion motion starts over most of the plasma within the first 40 ns of the pulse, indicating fast magnetic field penetration into the plasma. This conclusion is supported by the relatively low ion velocities and their monotonic dependence on the charge-to-mass ratio. Together with the locally determined electron density, the axial ion velocities were used to obtain the forces on the ions, and thus enabled us to suggest a time-dependent magnetic field distribution in the plasma. The axial ion velocities at the load-side edge of the plasma are found to be significantly higher than in the rest of the plasma, implying a relatively high current density at this edge of the plasma.

II. THE EXPERIMENTAL ARRANGEMENT AND DIAGNOSTICS

IIA. The Plasma Opening Switch

In our experiments we use a coaxial configuration (r_a = 2.5 cm, r_c = 5 cm) with an upstream inductance L=120 nH as shown in Fig. 1. The positive high-voltage pulse is delivered by an LC-water-line generator (4.1 kJ, 300 kV, 1Ω) to the inner electrode supplying a peak current of 135$\pm$10 kA with a quarter period of 90 ns. The POS load is a shorted coaxial line with an inductance of 25 nH. Two calibrated Rogowski coils and two sets of four $\dot{B}$ loops azimuthally separated by 90^o are used to measure the upstream and downstream currents and the current azimuthal symmetry.

The plasma source is installed inside the inner POS electrode and injects the plasma radially outward through a 75% transparent stripped cylindrical anode into the interelectrode region. The downstream current of our POS could be changed in the experiments by varying the time between the gas discharge and the high-current generator pulse. Typical waveforms of the upstream current I_u, the downstream current I_d, and the current

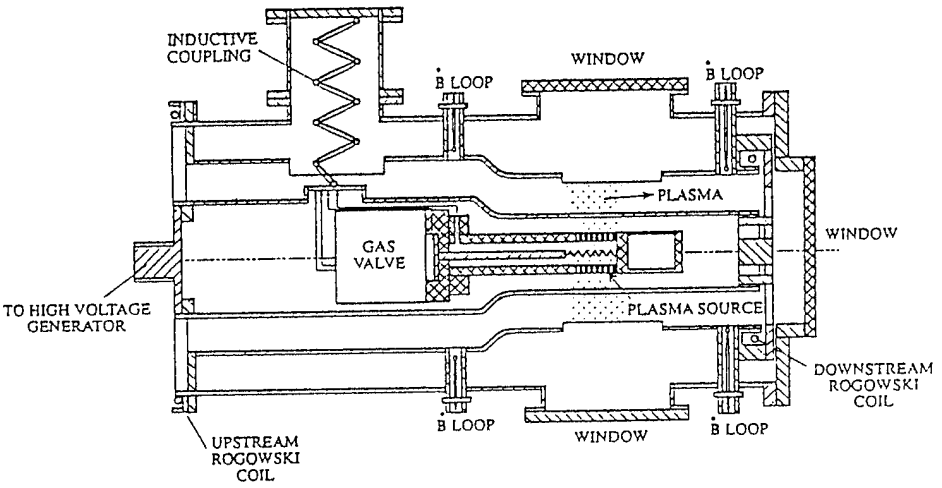


Fig. 1. Schematic illustration of the coaxial Plasma Opening Switch (POS) configuration. The plasma source is mounted inside the inner cylindrical high-voltage electrode, connected to the LC-water-line pulse generator. The power for the gas valve and the plasma source is inductively coupled to the inner electrode. The upstream and downstream currents are measured by Rogowski coils and by two sets of $\dot{B}$ loops, placed upstream and downstream the POS. The voltage at the output of the waterline was measured by a capacitive voltage-divider (not shown in the Figure) placed near the water-vacuum interface. The POS chamber has one axial window (in the load side) and four transverse windows for optical accesses.

$I_{pos} = I_u - I_d$ through the plasma are given in Fig. 2(a). The voltage across the switch given by $V_{pos} = V_{wl} - L_u \frac{dI_u}{dt} \simeq L_d \frac{dI_d}{dt}$, where V_{wl} is the waterline output voltage and L_u and L_d are the upstream and downstream vacuum inductances, respectively, together with the POS impedance defined by $Z_{pos} = \frac{V_{pos}}{I_{pos}}$ are shown in Fig. 2(b). The downstream current rises to nearly a plateau at $\simeq$100 ns indicating a drop in the plasma resistance. In this paper, we mainly discuss measurements for the period until this time. A detailed description of the electrical measurements performed[7] will be described in a subsequent publication.

II.B. The Diagnostic Systems

The POS chamber has optical windows that allow for axial and radial spectroscopic observations. The spectroscopic system shown in Fig. 3 includes a 1-meter spectrometer equipped with a 2400 grooves/mm grating giving a spectral resolution $\simeq$0.06Å. The mirrors M1 and M3 are used to scan in different experiments the POS anode-cathode gap radially and axially. The light at the spectrometer exit window is imaged using a cylindrical lens onto a rectangular fibre-bundle array which allows for further dispersion of the light. The fibre-bundle array transmits the light to 10 photomultiplier-tubes followed by a

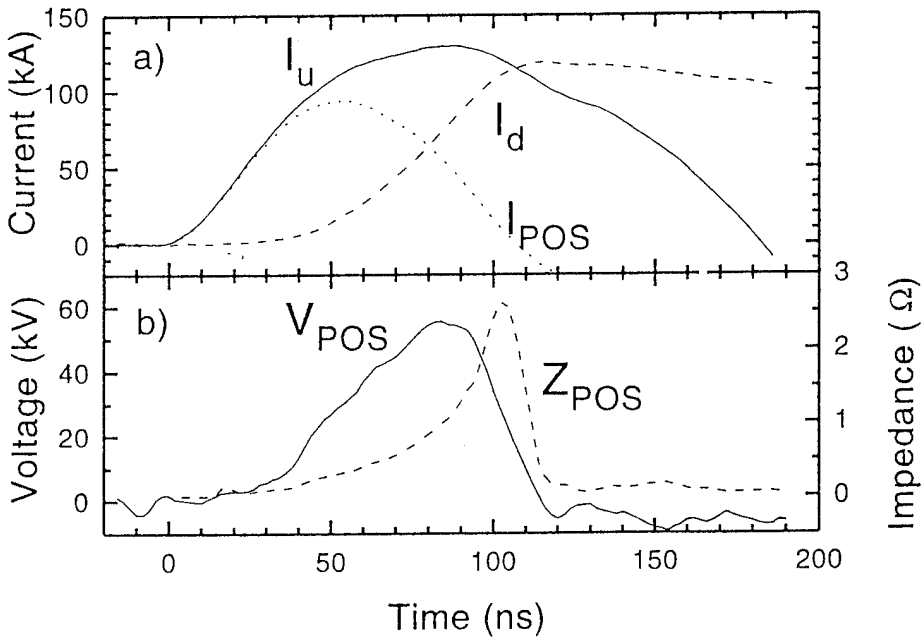


Fig. 2. (a) Waveforms of the upstream current I_u, downstream current I_d, and $I_{pos} = I_u - I_d$. (b) The anode-cathode voltage in the plasma region, V_{pos}, and the plasma impedance, Z_{pos}, as defined in the text.

multichannel digitizer, giving the time dependent line spectral profile in a single discharge with a temporal resolution of 4 ns. The fused-silica optics, the spectrometer, and the photomultiplier-tubes allow for sensitivity in the region 2000-7500Å. Absolute calibration of the spectroscopic system over the entire spectral range was performed.

Another feature of our diagnostics is the use of a pulsed laser (Nd:Yag, 20 ns, 50 mJ per pulse at $\lambda \simeq 1.06$ μm) to evaporate into the POS interelectrode gap material initially deposited on the anode strips. This allows for seeding the plasma with ions and neutral particles desired for the various measurements. The laser pulse is applied $\simeq 1$ μs prior to the high current pulse producing a conical column of seeded material between the POS electrodes with a diameter that increases from $\simeq 0.2$ cm near the anode to $\simeq 1$ cm in the middle of the POS gap. The axial location z of the seeded column was varied in the experiments by moving the spot of the laser beam on the anode strip. Observation of light emission from the seeded particles enabled us to obtain measurements that are local in r, z, and θ. The spatial resolution in the z direction is determined by the seeded-column diameter and that in the r and θ directions, $\simeq 0.05$ cm and $\simeq 0.5$ cm, respectively, by the imaging optics.

IIC. The Plasma Source

The plasma gun developed[7] is based on producing plasma in 144 gas-filled capillaries placed in the walls of a hollow cylindrical tube. For the measurements reported here, CH_4 was used for the plasma source, producing plasma composed of protons, carbon ions, and

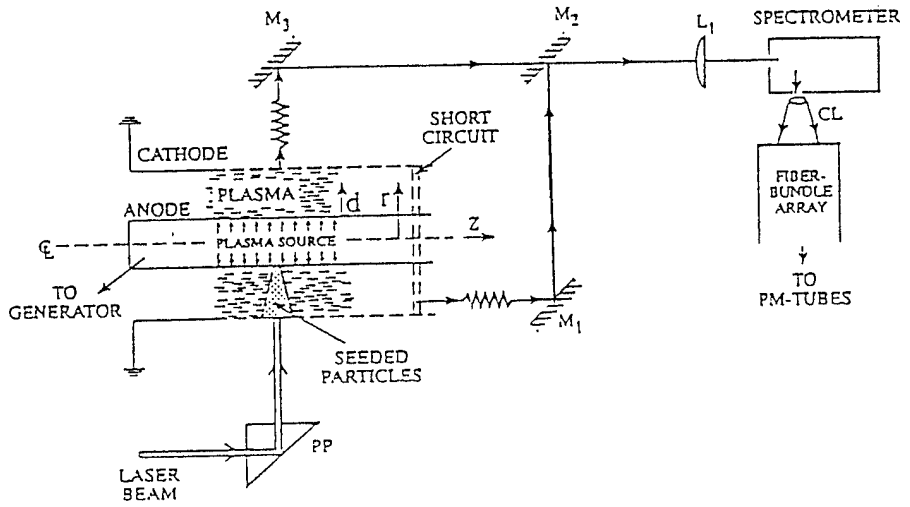


Fig. 3. The diagnostic systems used for the experiments. Light from the plasma is collected axially (through the short-circuit load of the POS) or radially, and is directed into a spectrometer by the use of the mirrors M_1, M_2, and M_3 and the lens L_1. The light at the exit-window is further optically dispersed using the cylindrical lenses CL and is projected onto a rectangular optical-fibre array. The signal transmitted through each fibre is measured by a photomultiplier-tube (PM). The laser beam used to evaporate material from the anode surface is directed onto the anode via the prism PP that is used to vary, in different experiments, the axial location of the laser beam spot on the anode. The dotted area shows the column of the seeded particles. Here, r is the radial location and d is the distance from the anode surface.

neutral hydrogen and carbon.

The electron density and temperature prior to the current pulse were determined from single-probe measurements, microwave cut-off technique, and observations of H_α and H_β spectral profiles. The hydrogen line profiles were analyzed self-consistently to give the electron density and the hydrogen velocity distribution. The electron density thus obtained decreases from $1.3\pm0.2\times10^{14}\ cm^{-3}$ 0.5 cm from the anode to $\simeq 6\pm2\times10^{13}\ cm^{-3}$ near the cathode surface. The axial plasma length was $\simeq$ 4 cm at a radial distance $d \simeq 1$ cm from the anode and the electron density and temperature were uniform within $\pm15\%$ over this region. The uniformity in the azymuthal dimension was within $\pm15\%$. The reproducibility of these parameters was found to be $\pm20\%$. The plasma radial flow velocity was $(1.5\pm0.5)\times10^6$ cm/s and the electron temperature was found to be near 2 eV.

III. MEASUREMENTS AND DATA ANALYSIS

IIIA. Electron kinetic energy

Bounds on the electron energy were obtained by observing line intensities from various

species and transitions. In Fig. 4 we present the population of the 2p ($^3P^0$) level of LiII (lying at $\simeq$61 eV) obtained from the absolute intensity of the 5485-Å line in experiments in which lithium was seeded in the plasma. In this figure $z = 0$ and $d = 0.7$ cm, where z is the axial position relative to the axial plasma center with positive z being towards the load, and d is the radial distance from the anode surface (see Fig. 3). It is seen that the line intensity starts rising at $t \simeq$20 ns and reaches nearly a plateau at $t \simeq$60 ns. Using our collisional-radiative model for lithium and an upper limit for the LiII density ($5 \times 10^{13}\, cm^{-3}$) we obtained a lower bound of at least a few tens of electronvolts for the mean electron energy ε_e shortly after the application of the current pulse. We then used estimates of the classical collision rate and concluded that most of the electrons will attain energies ≥ 5 eV within a few nanoseconds.

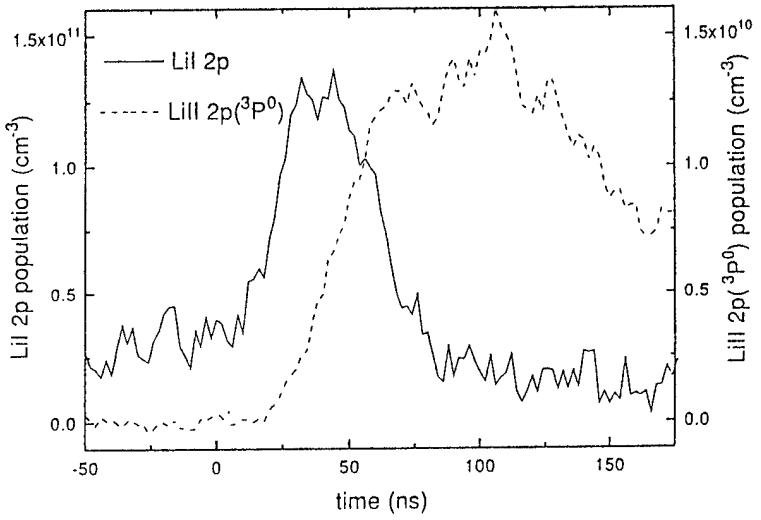


Fig. 4. The time-dependent population densities of the LiI 2p level and the LiII 2p ($^3P^0$) level, obtained from axial observations of the LiI 6708-Å (2p-2s) and the LiII 5485-Å ($2p(^3P^0)$ - $2s(^3S)$) intensities, respectively, for $z = 0$ and $d = 0.7$ cm. Here, lithium was seeded into the plasma and the laser beam was directed to the anode surface at $z = 0$, see Fig. 3.

We also observed the BaIII 3368-Å ($6p[5/2]_3$- $6s[3/2]_2$) line, with an upper level that lies at $\simeq$22 eV. The time-dependence of the absolute line intensity is consistent with the results of LiII.

The axial dependence of the line intensities of LiII and BaIII, obtained in the seeding experiments, showed a propagation from the generator side of the plasma to the load side. The line intensities started rising at t$\simeq$ 20 ns at the generator side ($z = -1.8$ cm) and at t $\simeq$ 50 ns at the load side ($z = +1.4$ cm) for $d = 0.2$ to 1.2 cm from the anode.

IIIB. Electron density

The use of Stark broadening in determining the electron density in pulsed power systems is limited because of the effects of the presence of collective electric fields on the line profiles[8]. Evidences for such collective fields were also found in our POS experiment. Therefore, we determined the electron density during the high-current pulse from the ionization times of various species locally seeded into the plasma. For these measurements, the ionization times must be insensitive to the mean electron kinetic energy ε_e. Therefore, for those measurements we selected particles with low ionization energy, such as LiI, BaI, BaII, MgI, and CaI, since their ionization rates saturate when ε_e for most of the electrons in the POS plasma rises to a few electronvolts. As shown in Sec. IIIA, ε_e rises during the pulse to a value which is sufficient to saturate these ionization rates. An example of the LiI 2p population during the pulse obtained from the intensity of the LiI 6708-$\mathring{A}$ (2p-2s) line observed axially (in the z-direction), is shown in Fig. 4. In this figure $z = 0$ and d =0.7 cm. It is seen that the line intensity rises, presumably due to a rise in the mean electron energy, and then decays due to ionization (the decay could not result from a drop in the electron or ion densities since line intensities of species that ionize negligibly during the pulse, such as MgII and BaIII, do not decrease at the relevant times). For LiI, for example, we used an ionization rate of 3×10^{-7} cm^{3}s^{-1}, which is obtained from collisional-radiative calculations for electron energies above 5 eV. Using the ionization times of various species we have determined the electron density to be $(1.3 \pm 0.5) \times 10^{14}$ cm^{-3}, for d =0.7 cm from the anode surface, and for $z = -1.8$ to 1.4 cm. Due to the temporal and spatial dependencies of the line intensities the electron density is determined for t =30-70 ns at the generator side and for t =60-100 ns at the load side. The uncertainty in n_e mainly results from the irreproducibility in the line-intensity time dependence.

IIIC. Particle Velocities

The particle velocity distributions were obtained from the Doppler dominated spectral profiles of various emission lines. The plasma seeding technique was employed to measure local velocities of singly charged magnesium ions, seeded in the plasma. It was verified and confirmed that MgI ionization into MgII could not affect the MgII velocity.

The axial velocity of MgII was determined for ten different axial locations of the seeded-MgII column. In Fig. 5(a) we present an example of a velocity distribution obtained from the 2796-Å (3p-3s) line spectral profile for $z = -0.2$ cm. Fig. 5(b) shows the velocity distribution seen at the load-side edge of the plasma, $z = +1.4$ cm, also for $d = 0.7$ cm. Here, the velocity distribution shows relatively high velocities, together with velocities similar to those seen for z up to 1.0 cm. The velocity distribution given in Fig. 5(b) was satisfactorily fitted by two Gaussian curves that describe the two ion velocity components. The emission intensities of the slow and fast component showed that ions at the load-side edge of the plasma in a region $\simeq$0.5 cm wide in the z-direction, can be assumed to move

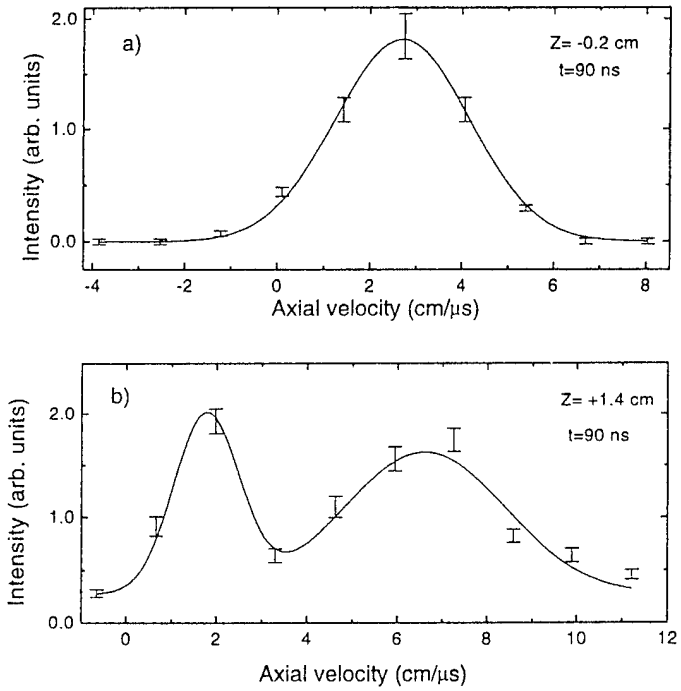


Fig. 5. (a) An example of the MgII velocity distribution obtained from the spectral profile of the MgII 2796-Å ($3p(^2P^0)$ - $3s(^2S)$) line observed axially in the magnesium-seeded experiments for $t = 90$ ns, $z = -0.2$ cm, and $d = 0.7$ cm. The line is a Gaussian fit to the data. (b) The MgII velocity distribution obtained from the MgII 2796-Å line spectral profile observed axially for $t = 90$ ns, $z = +1.4$ cm, and $d = 0.7$ cm. Low-velocity and high-velocity components are seen. The line is a fit of two Gaussian curves to the data.

with the higher velocity. Hence, about 13% of the plasma ions in the 4-cm-long plasma acquire the high velocities. The shifts of the spectral profiles were used to obtain the directed velocities towards the load shown in Fig. 6 for four axial locations at $d = 0.7$ cm. It is seen that at the generator-side edge of the plasma ($z = -1.8$ cm), the directed velocity remains low, while in the axial center $z = -0.2$ cm it rises to $\simeq 2\times10^6$ cm/s at $\simeq$100 ns. At the load side edge of the plasma, $z = +1.4$ cm, the fast velocity component shows a peak values that is $\simeq 3$ times higher than that of the slow component which is not shown in Fig. 6. Note that the ion motion for all axial locations starts within the first 40 ns of the pulse. The MgII velocities were also measured for $d = 0.2$ and 1.7 cm showing phenomena similar to those found for $d = 0.7$ cm.

Similar temporal behavior was observed for other ions. The measured velocities of LiII, MgII, CaII, and BaII ions were found to scale inversely proportional to their mass within $\pm$ 25% .

Axially integrated velocities were determined for the various charge states of carbon.

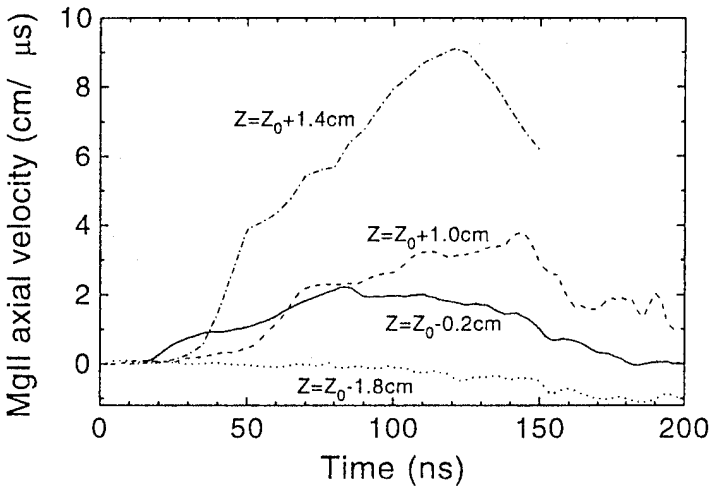


Fig. 6. The time-dependent mean axial MgII velocities obtained from the Doppler shifts of the MgII 2796-Å line for $d = 0.7$ cm. Given are results for the axial locations: $z = z_0 - 1.8$ (close to the generator-side edge of the plasma), $z_0 - 0.2, z_0 + 1.0$, and $z_0 + 1.4$ cm, where z_0 is the axial center of the POS. For the axial position $z = z_0 + 1.4$ cm (the load side edge of the plasma) only the fast velocity component is shown. The velocity of the slow component is similar to the one shown for $z = z_0 + 1.0$ cm.

The measured carbon velocities at t$\simeq$ 100 ns at $d = 0.5$ cm from the anode were 1.5, 3.0, and 4.5 cm/μs for CII, CIII, and CIV, respectively. Radial ion velocities were observed using radial lines of sight at various axial locations. The velocities obtained in this manner are integrated along the radial dimension of the plasma. For all carbon ions the measured radial velocities towards the cathode were comparable to the axial velocities towards the load.

IV. DISCUSSION

The measured ion velocities allow us to study the distribution of the magnetic field in the plasma. If the magnetic field does not penetrate the plasma, the magnetic field pressure is expected to push the plasma at its boundary with a velocity $\simeq V_A$, where $V_A \simeq \frac{B}{\sqrt{4\pi\rho}}$, B is the magnetic field at the vacuum, and ρ is the plasma mass density. The pushing velocity would be within a factor of 2 of this velocity, depending on the pushing mechanism (specular reflection, snow-plow or a shock wave). The plasma in our experiment is of an electron density $n_e \simeq 1.3\times10^{14}$ cm^{-3} and is composed of protons and carbon ions. Its mass density is estimated to be $\rho \cong 7.5 \times 10^{-10}g\cdot cm^{-3}$. Thus, for $B \simeq 8.7$ kG (using $I_u = 130$ kA and $r = 3$ cm corresponding to $d = 0.5$ cm), the maximum velocity V_A is $\simeq 9 \times 10^7$ cm/s, which reduces to an average velocity $V_A \simeq 4.5 \times 10^7$cm/s taking into account the finite rise time of the magnetic field. As described in Sec IIIC, the measured ion velocities are much lower. This discrepancy between the ion velocities expected for no magnetic field

penetration and the measured ion velocities, implies magnetic field penetration into the plasma, which causes a larger part of the plasma to be pushed thus enabling each ion to gain less momentum.

The assumption of magnetic field penetration is supported by further evidences. The measured velocities are charge-dependent, higher for higher charge-states, indicating field penetration. The mass-dependence observed (see Sec. IIIC), showing lower velocities for the heavier ions, is also consistent with this picture. Magnetic field penetration is expected to result in a linear dependence of ion velocities on the charge-to-mass ratio. However, ionization and charge exchange processes affect this velocity dependence. Nevertheless, the observed monotonic dependence is highly supportive of magnetic field penetration.

The field penetration is also supported by the local ion-velocity measurements. It is shown in Fig. 6 that ions in the entire axial plasma length start to be accelerated as early as t=40 ns. This enables us to conclude that accelerating electric fields, formed by the magnetic pressure, are present across the plasma already at this early time.

We now turn to a quantitative estimate of the magnetic field distribution in the plasma which we obtain from the measured ion velocities by assuming that the ions are accelerated by the Hall electric field. If a current flows through a region in the plasma, the mean axial velocity of ions of mass M and charge Ze in this region satisfies [5)]

$$\frac{dV_z}{dt} = \frac{Z}{M}\frac{1}{8\pi\delta n_e}(B_1^2 - B_2^2)\ . \tag{1}$$

Here, B_1 and B_2 are the intensities of the magnetic field at the axial boundaries of the region, δ is the width of the region, and n_e is the (assumed uniform) electron density. It is assumed that the ions are uniformly distributed in the region. Eq.(1) is obtained from an axial integration of the ion equation of motion over the region, in which the plasma pressure is assumed to be much smaller than the magnetic field pressure.

The measured velocities are inconsistent with a uniform magnetic field distribution across the axial length of the plasma. We therefore, used the axial velocities at different axial positions and Eq. (1) to calculate the magnetic field distribution at various times for d = 0.7 cm. At each time $t = 40, 60, 80$, and 100 ns, the magnetic field distribution is calculated as follows. The plasma is divided axially into intervals whose centers are at $z = -1.8, -1.4, -0.2, +0.2, +1.0$ and $+1.4$ cm. The acceleration at each interval is estimated from the axial velocities observed at each z, such as those given in Fig. 6. Assuming a density $n_e \cong 1.3 \times 10^{14}$ cm^{-3}, as given in Sec. IIIB, we calculate the change in B^2 across each interval. Then, starting from the generator side, where the magnetic field B_u is obtained from the upstream current, we calculate B across the plasma. Fig. 7 describes the approximate magnetic field distribution in the plasma, as it evolves in time. The figure shows fast magnetic field penetration into the plasma and a formation of a relatively high current density at the load-side edge of the plasma.

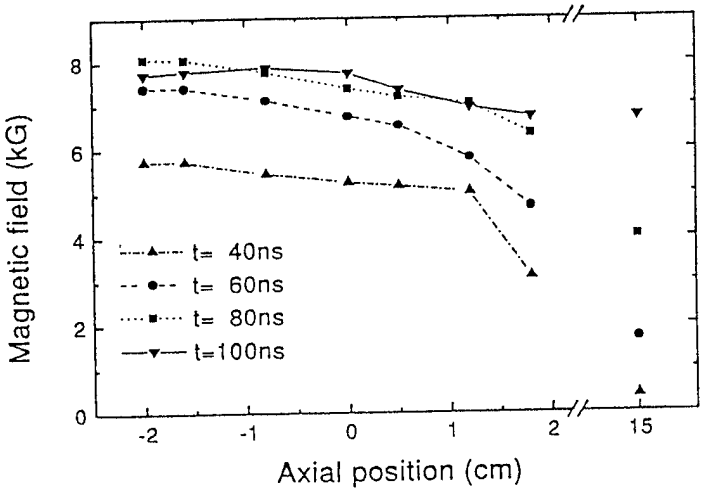


Fig. 7. Axial magnetic field distributions for several times at $r = 3.2$ cm (i.e., $d = 0.7$ cm from the anode surface) obtained from the axial time-dependent local MgII velocities such as those given in Fig. 6. In the calculation, we used an electron density 1.3×10^{14} cm^{-3}, as given in Sec. IIIB. The data points are connected by straight lines. The points at $z = 15$ cm give the magnetic field obtained from the downstream current measured by the Rogowski coil near the shorted load.

As shown in Fig. 7, the calculated magnetic field at the load side of the plasma is larger than B_d, the magnetic field at the load that is obtained from the downstream current. The difference in these values of the magnetic field may result from electron flow in the vacuum section between the plasma and the load or from current through a plasma present in this section.

The data here analyzed were obtained for $d = 0.7$ cm. As said in Sec. IIIC, similar results were obtained for $d = 0.2$ and 1.7 cm. Thus, we believe the magnetic field distribution here given reflects the distributions in the region between 0.2 and 1.7 cm from the anode.

Our measurements thus lead to the conclusion that fast magnetic field penetration into the plasma occurs. They also indicate that a high current density is formed in the load side of the plasma early in the pulse.

V. SUMMARY

In this study we presented local measurements of the electron density, electron kinetic energy, and velocity distributions for ions in a coaxial Plasma Opening Switch. The early start of the ion motion, the relatively low ion velocities, and the nearly linear dependence of the ion velocity on the charge-to-mass ratio suggests magnetic field penetration into the plasma within the first 40 ns of the pulse. Assuming that the ions are accelerated by the Hall electric field, we used the local ion velocity measurements to infer the magnetic field

distribution in the plasma. The high ion velocities at the load-side edge of the plasma imply the presence of a relatively high current density at this location.

The generality of the observed phenomena should be examined by varying the plasma parameters, the POS load, and the POS polarity. More detailed measurements of the ion motion in various radial and axial positions in the plasma and with a higher spatial resolution are required. Local Zeeman-splitting measurements of the magnetic field, similar to those described in Ref. 9, are currently underway. These measurements may help to improve the understanding of the magnetic field energy dissipation.

ACKNOWLEDGMENTS

The authors are grateful to A. Fisher for helpful discussions. Thanks are due to S. Shkolnikov and Yu. Ralchenko for considerable help in the data analysis and to P. Meiri, Y. Macabi, M. Sidi, and D. Liram for their skilled technical assistance. This work was supported by the ONR, USA, grant No. N00014-91-J-4104 and by the Israeli Academy of Science.

References

1. C.W. Mendel, Jr. and S.A. Goldstein, J. Appl. Phys. **48**, 1004 (1977).
2. P. Ottinger, S.A. Goldstein, and R.A. Meger, J. Appl. Phys. **56**, 774 (1984).
3. B.V. Weber, J.R. Boller, R.J. Commisso, J. Appl. Phys. **45**, 1043 (1984).
4. K.V . Chukbar and V.V. Yan'kov, Sov. Phys. Tech. Phys. **33**, 1293 (1988); Ya.L. Kalda and A.S. Kingsep, Sov. J. Plasma Phys. **15**, 508 (1989); A.V. Gordeev, A.V. Grechikha, A.V. Gulin, and D.M. Drozdova, Sov. J. Plasma Phys. **17**, 381 (1991).
5. A. Fruchtman, Phys. Fluids **B3**, 1980 (1991); A. Fruchtman and K. Gomberoff, Phys. Fluids **B4**, 117 (1992); K. Gomberoff and A. Fruchtman, Phys. Fluids **B5**, 2841 (1993).
6. A. Fruchtman and L.I. Rudakov, Phys. Rev. Lett. **69**, 2070 (1992); Bull. Am. Phys. Soc. **38**, 1993 (1993).
7. M. Sarfaty, Ph.D. Thesis, Feinberg Graduate School, Weizmann Institute of Science, Israel (1993); M. Sarfaty, R. Arad, Ya.E. Krasik, Y. Maron, B. Pereiaslovets, S. Shkolnikov, R. Shpitalnik and A. Weingarten, in Abstracts 1993 International Conference on Plasma Science, Vancouver, Canada, 1993, (IEEE Service Center, 1993), p.113.
8. H.J. Kunze and H.R. Griem, Phys. Rev. Lett. **21**, 1048 (1968); G.V. Sholin and E.A. Oks, Sov. Phys. Dokl. **18**, 254 (1973).
9. Y. Maron, E. Sarid, E. Nahshoni, and O. Zahavi, Phys. Rev. **A39**, 5856 (1989).

SELF-COLLIDING BEAMS AS AN ALTERNATIVE FUSION SYSTEM

Norman Rostoker and Michl Binderbauer
Department of Physics, University of California, Irvine, CA 92717-4575

Abstract

Recent experiments with TFTR, D-III-D and JET involve the injection and trapping of low density beams of high energy large orbit ions. These experiments proved that large orbit non-adiabatic ions slow down and diffuse classically in the presence of anomalous fluctuations and transport of the majority particles which were adiabatic. Accordingly, we consider fusion reactors based on classical confinement of fuel ions and fusion products. The analysis begins with equilibrium solutions of the Vlasov-Maxwell equations[1] and proceeds through considerations of stability, classical transport, ignition, beam extraction and direct conversion.

Introduction

Magnetic confinement systems in plasma physics involve particles where the orbit radius and orbit period are small compared to the characteristic scales of length and time. In particle accelerators they are of the same order. There is a considerable difference between the physics of adiabatic and non-adiabatic particles; for example, strong focusing is non-existent for adiabatic particles and even weak focusing is quite different. It is an experimental fact that the non-adiabatic particles are much better confined than the adiabatic particles of plasmas. High energy non-adiabatic particles have been studied and employed in fusion plasmas as a minority particle for heating and because the reaction products must be considered. Fusion plasmas where non-adiabatic ions are the majority particle have been studied many years ago - *DCX* and *OGRA* (1958-1968)[2] and *MIGMA*[3] (1975-1985). From 1988-1992 experiments were carried out with high energy large orbit ions in Tokamaks (*TFTR*, D-III-D and *JET*).[4] These experiments proved that large orbit ions slow down and diffuse classically in the presence of anomalous fluctuations and transport of the majority plasma particles which were adiabatic. The possibility of classical confinement for a dense plasma of non-adiabatic ions is suggested by these experiments.[1] We consider high beta self-consistent FRC-equilibria described by the Vlasov/Maxwell equations. Classical calculations of slowing down and diffusion are made with test particle models for a D-He^3 plasma. In a steady state or long pulse reactor, the electron temperature is determined by the balance between electron heating by ions and electron cooling by Bremstrahlung. The D-He^3 fuel is maintained in density by injecting D and He^3 neutrals at low energy (100 keV). The energy and momentum are maintained by interaction with the fusion products, 14.7 MeV protons and 3.67 MeV He^4.

Equilibrium Distributions of a D-He^3 Plasma

We consider distribution functions of the form

$$f_j(\vec{x},\vec{v}) = \left(\frac{m_j}{2\pi T_j}\right)^{\frac{3}{2}} n_j(r,z)\exp\left\{-\frac{m_j}{2T_j}\left[(v_x+\omega_j y)^2+(v_y-\omega_j x)^2\right]\right\} \tag{1}$$

where ω_j and T_j are the same for all ions, but for electrons $\omega_e < \omega_j$ and $T_e \neq T_j$. The equilibrium solution of the Vlasov-Maxwell equations is obtained by solving simultaneously

$$n_j = n_{oj}\exp\left[\frac{m_j(\omega_j r)^2}{2T_j} - \frac{e_j\Phi}{T_j} + \frac{e_j A_\theta \omega_j r}{cT_j}\right] \tag{2}$$

$$\nabla \times \vec{B} = \frac{4\pi}{c} \sum n_j e_j r \omega_j \hat{\theta} \tag{3}$$

$$\sum n_j e_j \cong 0 \tag{4}$$

$\Phi(r,z)$ and $A_\theta(r,z)$ are potentials. The electric and magnetic fields are $\vec{E} = -\nabla\Phi$ and $\vec{B} = \nabla \times A_\theta \hat{\theta}$. Eq. (4) is the condition for quasi-neutrality. If n_j, Φ, A_θ depend only on r and there is only one type of ion, these equations can be solved[1] analytically. They have been solved numerically[1,5] when there is more than one ion species, or n_j etc. depend on r and z.

For a D-He^3 plasma we assume the peak density is $n_o = 10^{14}$ cm^{-3} for ions, the peak is located at $r_o \cong 30$ cm, $T_i = 100$ keV, $T_e = 50$ keV, $\frac{1}{2} m_i (\omega_i r_o)^2 = 800$ keV (D), 1200 keV (He^3). One dimensional solutions are plotted in Fig. 1. - density distributions, magnetic field and electric field. The boundary is located where $\Phi(R) = -\int_0^R E_r dr = 0$ and the separatrix is where $\Psi(R_s) = \int_0^{R_s} B_z(r) r dr = 0$. The density at the separatrix is $n(R_s) \cong 2.6 \times 10^{-4} n_o$ and at the wall $n(R) \cong 5.3 \times 10^{-5} n_o$ so that scattering of fuel ions outside the separatrix is negligible.

Stability Considerations

Large orbit ions average fluctuations so that transport is produced only by fluctuations of wavelength larger than the gyro-radius. This has been observed with two dimensional models and computer simulation[6]. It explains the results with non-adiabatic ions in tokamaks[4]. For the plasmas under consideration where essentially all ions are non-adiabatic, micro-instabilities would not be important. Long wavelength stability is required but it should be noted that there would be no magnetohydrodynamic instabilities such as Alfvèn waves since MHD does not apply. From the extensive research in FRC's[7] (field reversed configurations) we know of two long wavelength instabilities - the rotational kink mode that has been eliminated with quadrupole windings and the tilt mode that is stabilized by finite gyroradius. It is possible that both modes will be stabilized by energetic particles. There has been an idealized[8] model calculation of stability for a field reversed system with betatron orbits for all ions. The model involves an infinitely long annular layer of zero thickness. The techniques of this paper are being applied to the ring and the high beta Migma.

Classical Scattering

The test particle method to evaluate slowing down and diffusion is based on the Fokker-Planck equation where one particle is singled out and the remainder of the particles have Maxwell Distributions.

$$\frac{\partial f_i}{\partial t} = -\frac{\partial}{\partial \vec{v}} \cdot f_i \langle \Delta \vec{v} \rangle_i + \frac{1}{2} \frac{\partial}{\partial \vec{v}} \cdot \frac{\partial}{\partial \vec{v}} \cdot f_i \langle \Delta \vec{v} \Delta \vec{v} \rangle_i \tag{5}$$

$$\langle \Delta \vec{v} \rangle_i = \langle \Delta v_\parallel \rangle_i (\vec{v}/v) \tag{6}$$

$$\langle \Delta \vec{v} \Delta \vec{v} \rangle_i = \langle \Delta v_\parallel^2 \rangle_i (\vec{v}\vec{v}/v^2) + \langle \Delta v_\perp^2 \rangle_i [1 - (\vec{v}\vec{v}/v^2)] \tag{7}$$

$$\langle \Delta v_\parallel \rangle_i = \frac{4\pi (Z_i e^2)^2}{m_i} \ln \Lambda \sum_j n_j Z_j^2 \left(\frac{1}{m_j} + \frac{1}{m_i} \right) \frac{\partial}{\partial v} \left(\frac{1}{v} \mathrm{erf} \frac{v}{\sqrt{2}\, v_j} \right) \tag{8}$$

$$\langle \Delta v_\perp^2 \rangle_i = \frac{4\pi (Z_i e^2)^2}{m_i^2 v} \ln \Lambda \sum_j n_j Z_j^2 \left[\mathrm{erf} \frac{v}{\sqrt{2}\, v_j} + \frac{\partial}{\partial v} \left(\frac{v_j^2}{v} \mathrm{erf} \frac{v}{\sqrt{2}\, v_j} \right) \right] \tag{9}$$

$m_j v_j^2 \doteq T_j$, $\ln \Lambda \cong 20$, the test-particle is denoted by i and the summation is over all types of field particles. It is convenient to separate the contributions from each type of field particle. For example, the time for scattering through a large angle of particle i of energy W_i by electrons is

$$\tau_{ie} = \frac{W_i}{(\partial W_\perp / \partial t)_{ie}} \qquad \text{where} \quad \left(\frac{\partial W_\perp}{\partial t} \right)_{ie} = m_i \langle \Delta v_\perp^2 \rangle_{ie}$$

and $\langle \Delta v_\perp^2 \rangle_{ie}$ means the term in the sum in Eq. (9) due to electrons is the only term retained. The slowing down is determined by

$$\frac{\partial v_\parallel}{\partial t} = \langle \Delta v_\parallel(v) \rangle_i \qquad \text{where } v_\parallel = \int \frac{\vec{v}' \cdot \vec{v}}{v} f_i(\vec{v}', t) d\vec{v}' \tag{10}$$

and the contributions of various field particles can be separated in the sum given by Eq. (8). The inequalities usually satisfied are $v_e > v > v_i$ where v is the velocity of an ion test particle. For electron test particles we assume $v \sim v_e$. The time for an electron to be scattered by an ion through a large angle is

$$\tau_{ei} \cong \frac{\sqrt{m} T_e^{\frac{3}{2}}}{\pi e^4 \ln \Lambda} \frac{1}{n_e \langle Z^2 \rangle} = .45 \times 10^{-3} \text{ sec} \tag{11}$$

where $\langle Z^2 \rangle = \sum n_i Z_i^2 / n_e = \frac{5}{3}$. The electron-electron scattering time τ_{ee} is of the same order of magnitude. The ion-ion scattering time is $\tau_{ii} \sim (m_i/m)^{1/2} \tau_{ee}$, where m_i is the ion mass. τ_{ii}, τ_{ee} are the times to establish a Maxwell distribution. These times are much shorter than any of the other scattering times to be considered. Therefore, the distributions must be close to Maxwellian at all times. This justifies the choice of equilibrium distributions. For Maxwell distributions the ion-ion scattering and electron-electron scattering terms of Eq. (5) vanish. The remaining scattering terms describe interactions between ions and electrons which have different temperatures and mean velocities. The ion-electron scattering time is

$$\tau_{ie} = \frac{3\sqrt{\pi}}{2} \frac{m_i}{m} \frac{W_i}{T_e} \frac{\langle Z^2 \rangle}{Z_i^2} \tau_{ei} = 108 \text{ sec (D); } 61 \text{ sec (He}^3\text{)} \tag{12}$$

In a time τ_{ie} the amplitude of Betatron oscillations will increase by

$$\frac{V}{\Omega_i} = \frac{V A_i}{10^7 Z_i \langle B_z \rangle} \cong 5.8 \text{ cm (D); } 4.35 \text{ cm (He}^3\text{)} \tag{13}$$

$V = .88 \times 10^9$ cm/sec is the average velocity of D or He^3. A_i and Z_i are the mass and atomic numbers of the ions. $\langle B_z \rangle \cong 30$ kG is an estimate of the average magnetic field when scattering takes place. Thus τ_{ie} is an estimate of the diffusion time.

Sustained Operation of a Self-Collider/FRC Reactor

In order to form the equilibrium plasma of a self-collider, it would probably be necessary to use pulsed high current neutralized ion beams.[1] However, as nuclear reactions take place and the density of fuel ions decays, the fuel ions could be replaced by a low current sustainer beam. The sustainer beam should be a beam of neutralized atoms such as is presently employed for heating tokamaks, for which there is well developed technology. It should be injected tangential to the annular distribution of plasma near the null field radius of the FRC. A convenient energy for injection would be 100 keV. The plasma would ionize the beam of neutrals after which the 100 keV ions would be decelerated by electrons and accelerated by the fuel ions. We assume a D-He^3 plasma with the properties previously described in Fig. 1. Eq. (10) is appropriate to calculate the slowing down by electrons, i.e.:

$$\left.\frac{dW_i}{dt}\right]_d = -\frac{4\pi}{3}\sqrt{\frac{2}{\pi}} n_e Z_i^2 e^4 \frac{\sqrt{m}}{m_i} \ln \Lambda \frac{W_i}{T_e^{\frac{3}{2}}} = -\frac{W_i}{\tau_{si}} \tag{14}$$

where $W_i = \frac{1}{2} m_i v^2 = 100$ keV initially and $v_e \gg v$, the injection velocity. To evaluate the acceleration of the injected ions by the fuel ions, consider the frame of reference in which the fuel ions are stationary. In this frame $v' = v_o - v$ where $v_o = .88 \times 10^9$ cm/sec and $W_i' = \frac{1}{2} m_i (v_o - v)^2 = 450$

keV (D); 760 keV (He^3).
From Eqs. (8) and (10) $dv'/dt = -dv/dt$ is determined.

$$\left.\frac{dW_i}{dt}\right]_a = m_i v \frac{dv}{dt} = -\frac{2\pi (Z_i e)^2}{m_i} \ln\Lambda \sum_j n_j Z_j^2 \left(\frac{1}{m_j} + \frac{1}{m_i}\right) \frac{v}{2v_j^2} F\left(\frac{v_o - v}{\sqrt{2}\, v_j}\right) \tag{15}$$

$$F(x) = \frac{d}{dx}\left(\frac{1}{x}\mathrm{erf}x\right) \cong -\frac{4}{3}\frac{x}{\sqrt{\pi}} \quad \text{for } x \ll 1$$
$$\cong -\frac{1}{x^2} \quad \text{for } x \gg 1$$

For the injection energy of 100 keV, the second inequality is applicable in which case

$$\left|\frac{(dW_i/dt)_a}{(dW_i/dt)_d}\right| = \frac{3\sqrt{\pi}}{4} \frac{T_e^{\frac{3}{2}}}{\sqrt{W_i W_i'}} \sqrt{\frac{m_i}{m}} \sum_j \frac{n_j Z_j^2 [1 + (m_i/m_j)]}{n_e} = 18\ (\mathrm{D});\ \ 12\ (\mathrm{He}^3)\ . \tag{16}$$

The acceleration due to the fuel ions dominates over the deceleration due to electrons initially and until $W_i \to 800$ keV (D) ; 1200 keV (He^3). When $v = v_o$, then $dW_i/dt = 0$. When $v \to v_o$, the first asymptotic approximation for $F(x)$ is applicable in which case

$$\frac{(dW/dt)_a}{(dW/dt)_d} = \sqrt{\frac{W_i'}{W_i}} \left(\frac{T_e}{T_j}\right)^{\frac{3}{2}} \frac{1}{n_e} \sum_j n_j Z_j^2 \left(1 + \frac{m_j}{m_i}\right) \sqrt{\frac{m_j}{m_i}} \tag{17}$$

The electron drag and the acceleration due to fuel ions become equal when $W_i'/W_i = 10^{-4}$, or the velocity v reaches to within 1% of v_o. The time scale for slowing down by electrons is

$$\Delta t_{ie} = \frac{W_i}{(dW_i/dt)_d} = 2.31\ \mathrm{sec}\ (\mathrm{D});\ \ .87\ \mathrm{sec}\ (\mathrm{He}^3) \tag{18}$$

and the time scale for acceleration by fuel ions is therefore shorter by about a factor of 10.

The electrons colliding with the fuel ions will be accelerated in the direction of the ions. In equilibrium described by Equs. (1)–(4) the average angular velocity of electrons is $\omega_e < \omega$. The effect of collisions can be treated with fluid equations linearized about the equilibrium.

$$\frac{\partial}{\partial t}\delta v_r + \delta v_\theta (\Omega_e - 2\omega_e) = \frac{e}{m}\frac{\partial}{\partial r}\delta\Phi - \frac{T_e}{m}\frac{\partial}{\partial r}\frac{\delta n}{n} \tag{19}$$

$$\frac{\partial}{\partial t}\delta v_\theta - \delta v_r \Omega_e = \frac{r(\omega_e - \omega)}{\tau_{ei}} \tag{20}$$

$\Omega_e = eB_z/mc \gg \omega_e$; ω is the angular velocity of ions. The perturbed quantities are of the same order as the collision term. δv_r, δv_θ are the mean velocity components that develop because of collisions. Since electrons move along field lines much faster than they can drift across field lines and the electron "Maxwellization" time τ_{ee} is of the same order as τ_{ei}, the perturbed electron density $\delta n = ne\delta\Phi/T_e$ is established much faster than Ω_e or T_e can change. Therefore the right hand side of Eq. (19) vanishes. δv_θ, δv_r oscillate with the cyclotron frequency and the average values are zero. Electrons are not accelerated by collisions with ions because they do not cross field lines except by drifting and the guiding center drift from the electric field is cancelled by the diamagnetic drift due to the pressure gradient.

The fuel ions are decelerated by the electrons and accelerated by the fusion products: 14.7 MeV protons and 3.67 MeV He^4. The protons are presumably emitted isotropically in a frame

of reference where the fuel particles are at rest. Since $v_p \gg v_o$, the fuel particle velocity, the protons are emitted approximately isotropically. However, diamagnetic effects in an FRC alter this substantially as illustrated in Fig. 2. Particle orbits with $v_\theta < 0$ (the direction of diamagnetic current) are curved towards the null circle and execute Betatron orbits. Particles with $v_\theta > 0$ curve away from the null circle. Particles that initially have a modest value of v_r produce a substantial current if $v_\theta < 0$ and very little current if $v_\theta > 0$. The fusion products (3,4) transfer momentum to the fuel ions and accelerate them. Fuel ions (1,2) transfer momentum to electrons and are decelerated. For a steady state

$$\frac{dn_j}{dt} = n_1 n_2 \langle \sigma v \rangle_F - \frac{n_j}{\tau_j} = 0 \qquad ; j = 3,4 \tag{21}$$

(n_j, T_j), $j = 3,4$ are density and lifetime of the fusion products. $\langle \sigma v \rangle_F$ is the fusion reactivity which is 2×10^{-16} cm^3/sec for D-He^3 at 100 keV. The density of fusion products is substantially reduced because of their large energy. Although they are created in the fuel region, they have a much larger gyro-radius as illustrated in Fig. 3. The ratio of acceleration to deceleration of the fuel ions is

$$\frac{\sum_{3,4}[N_j m_j/\tau_{sj}]\langle v_\theta \rangle_j}{\sum_{j=1,2} N_j m_j v_o/2\tau_{sj}} \cong 1 \tag{22}$$

$$\begin{aligned} N_j &= n_j 2\pi r_o \Delta r \quad \text{for } j = (1,2);\ r_o = 30 \text{ cm},\ \Delta r \cong 5 \text{ cm} \\ &= n_j A_j \\ &= 2\pi r_o \Delta r n_1 n_2 \langle \sigma v \rangle_F \tau_j \quad \text{for } j = (3,4) \end{aligned}$$

A_j is the area occupied by the fusion products. τ_{sj} is a slowing down time of the fusion products by the fuel ions. τ_j is the lifetime of the fusion products which is assumed to be the time for a large angle scattering. $\langle v_\theta \rangle_j$ is the mean angular velocity of the fusion products relative to the fuel ions. The present estimate involves many averages; the result is of order unity.

Energy Balance

The fusion power generated is

$$P_F = 2\pi r_o \Delta r n_1 n_2 \langle \sigma v \rangle \varepsilon_f = 5540 \text{ watts/cm}$$

$\varepsilon_f = 18.4$ MeV is the energy release for each reaction. The injected ions for fuel replacement involve a power

$$P_I = 4\pi r_o \Delta r n_1 n_2 \langle \sigma v \rangle \epsilon_I = 60 \text{ watts/cm}$$

assuming the injected energy is 100 keV. The injected current is

$$I = \sum_j Z_j e \frac{dN_j}{dt} = .6 \text{ milliamps/cm} .$$

The power required to accelerate the injected ions from 100 keV to .8 MeV D and 1.2 MeV He^3 is

$$P_A = 9 \times 60 = 540 \text{ watts/cm} .$$

Electrons are heated by the fusion products according to Eq. (14). The electron temperature is not assumed in the present calculation. The power density is

$$\sum_{j=3,4} n_j \frac{dW_j}{dt} \cong 8 \times 10^6 T_e^{-3/2} \text{ watts/cm}^3 .$$

In a high Beta plasma the Bremstrahlung dominates over synchrotron radiation. The power density is

$$1.5 \times 10^{-32} n_e^2 \langle Z \rangle \sqrt{T_e} = .22 \times 10^{-2} \sqrt{T_e} \text{ watts/cm}^3$$

$n_e = 3n_o$ $n_o = 10^{14}$ cm$^{-3} = n_1 = n_2$, $\langle Z \rangle = \sum n_i Z_i^2 / \sum n_i Z_i = 5/3$. Equating the electron heating to the Bremstrahlung results in $T_e = 60$ keV which is close to that previously assumed. The Bremstrahlung power loss from the fuel region dominates so that

$$P_B = .22 \times 10^{-2} \sqrt{T_e} 2\pi r_o \Delta r = 509 \text{ watts/cm} .$$

The power available for direct conversion is

$$P = 5540 - 2 \times 60 - 540 - 509 = 4370 \text{ watts/cm} .$$

It is assumed that the sustainer beams are produced with 50% efficiency.

The above calculations are estimates for a model that provides a semi-quantitative description of an elongated FRC. The intent is to illustrate the physical processes involved in steady state operation. A quantitative study will require at least a two dimensional model and computer simulations.

Acknowledgement

This work was supported in part by a grant from the Plasma Physics Research Institute of the Lawrence Livermore National Laboratory.

References

1. N. Rostoker, F. Wessel, H. Rahman, B.C. Maglich, B. Spivey and A. Fisher, *Phys. Rev. Lett.* **70**, 1818 (1993).

2. S. Glasstone and R.H. Lovberg, *Controlled Thermonuclear Reactions*, D. Van Nostrand Co., New York (1960), Chapter 9.

3. D. Al-Salameh et al., *Phys. Rev. Lett.* **54**, 796 (1985); B.C. Maglich, *Nucl. Instrum. Methods Phys. Res., Sect. A* **271**, 13 (1988).

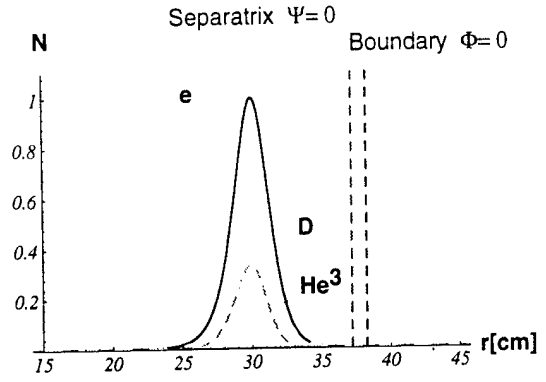
4. W. Heidbrink, J. Kim, and R.J. Groebner, *Nucl. Fusion* **28**, 2097 (1988); W. Heidbrink, *Phys. Fluids B* **2**, 4 (1990); W. Heidbrink et al., *Phys. Fluids B* **3**, 3167 (1991); S.J. Zweben et al., *Nucl. Fusion* **31**, 2219 (1991).

5. N. Rostoker and H. Rahman, "Large Orbit Confinement for Aneutronic Systems," *Nonlinear and Relativistic Effects in Plasmas*, Ed. V. Stefan, Am. Inst. of Phys., New York, p. 116 (1992).

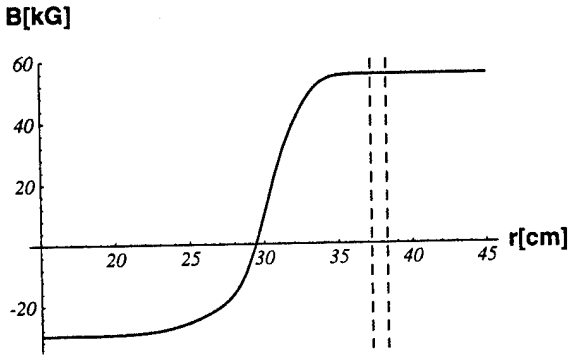
6. H. Naitou, T. Kamimura, and J. Dawson, *J. Phys. Soc. Jpn.* **46**, 258 (1979).

7. M. Tuszewski, *Nucl. Fusion* **28**, 2033 (1988).

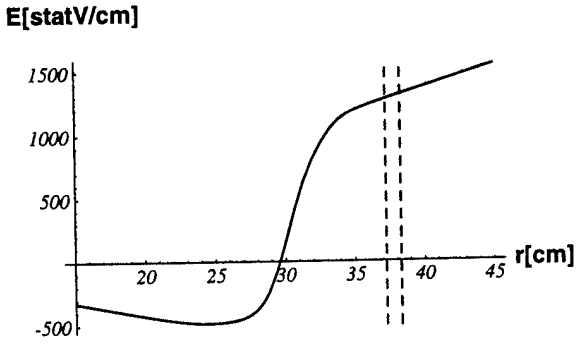
8. H.V. Wong, H.L. Berk, R.V. Lovelace, and N. Rostoker, *Phys. Fluids B* **3**, 2973 (1991).



a.) Density profiles of electrons, D-ions and He^3-ions.



b.) Magnetic field in kG.



c.) Electric field in statvolt/cm.

Fig. 1. One Dimensional Model of a D-He^3 Field Reversed Configuration.

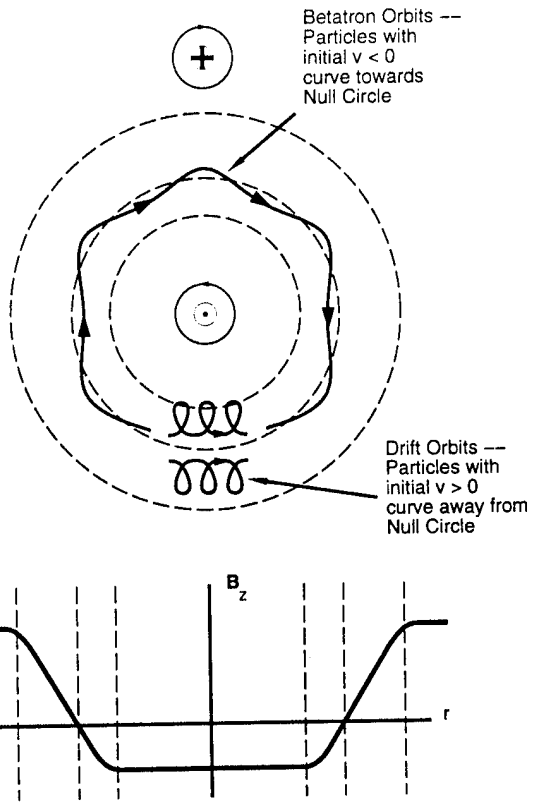


Fig. 2. Typical Particle Orbits (for $v_\theta < 0$ and $v_\theta > 0$) and Magnetic Field Configuration.

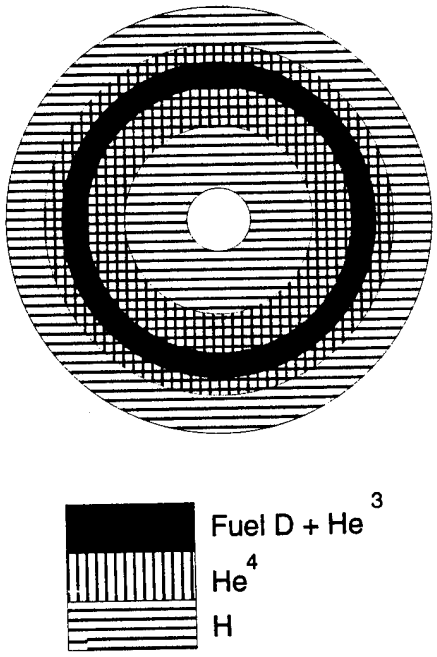


Fig. 3. Distribution of Fusion Fuel and Reaction Products.

USE OF PULSED E-BEAMS FOR THE INITIATION OF SPECTRAL LUMINESCENCE IN SOLIDS

Gennady A.Mesyats, Vladimir V.Osipov, Sergey G.Mikhaylov & Vladimir I.Solomonov

Institute of Electrophysics Russian Academy of Science

34 Komsomolskaya Street 620219 Ekaterinburg, Russia

Abstract

The work is devoted to the pulsed cathodoluminescence (PCL) of solids that occurs upon irradiating them latter by high-current pulsed e-beams. The parameters of e-beams that cause no irreversible disintegration in the material under investigation are given. The conclusion has been made that PCL can be used in a spectral-emission analysis of solids being single-piece structures, thereby offering a new field of application for electron beams.

The properties of a solid are determined by its chemical composition, structure, and the presence of defects. Theoretically, they can be determined with the use of a spectral-emission analysis, since any actual body contains impurity ions. In a nonmetallic body, these ions form own structure of energy levels in the forbidden energy band. This structure bears not only the properties of the impurity ion but also all individual properties of the lattice and the presence of defects. This shows up in the spectra of the luminescence appearing during optical transitions between these levels. However, no spectral-emission analysis of solids being single-piece systems has been developed up to now, because the excitation of luminescence in such systems by conventional methods is ineffective.

The pulsed cathodoluminescence we discovered [1-2], that appears in solids upon irradiation of them by high current pulsed e-beams, is best suited for solving the above-mentioned problem. We present here experimentally obtained spectral and amplitude PCL characteristics and measurements of the electron beam parameters that bound above and below the region where no defects are formed in specimens under investigation; at the same time, this analysis can be carried out under the simplest environmental conditions, i.e., in the air at room temperature.

The experiments were performed on a setup whose schematic diagram is shown

in thus figure. The electron beam produced by a pulsed accelerator (1) was extracted in the air onto a mineral specimen (2) placed in a metallic chamber (3). The luminescence light flux from the specimen was focused onto the input slit of a diffraction polychromator (4). The luminescence spectrum of width 300 nm was measured with the use of a multichannel (512 elements) photoreceiver (5) adapted to a computer (6). A spectral range from 350 to 900 nm was analyzed. Two types of accelerator were used. The first one was a compact electron accelerator of the RADAN type producing e-beam of pulse duration 2 ns and electron energy (E) smoothly controllable within a range from 100 to 200 keV. The electron current density at the specimen was varied from 700 to 50 A/cm^2 by using calibrated metallic grids. The second electron accelerator used was a device of the SINUS type and produced e-beams of pulse duration 12 ns, electron energy 300 keV, and current density 10 A/cm^2 . Both accelerators were repetitive systems. More then two thousand specimens including natural minerals of 61 species, industrial crystals, glasses and ceramics were tested.

All specimens luminesced upon irradiation by an e-beam. The luminescence centres were in main the ions of transitional d-chemical elements such as chromium, manganese, iron, cobalt, and titanium and the ions of rare earth elements such as dysprosium, samarium, etc. It has been found that the wavelength of the spectral bands and lines for the same impurity ion in specimens of difference mineral species are substantially district from each other. The wavelength of the PCL for the same ion has been found to depend, more weakly but regularly, on the presence of defects in the lattice around this ion. The PCL spectrum for the same specimen is highly stable. An the same time, the spectra for various specimens of the same mineral species always contain lines and bands characteristic of this mineral species and extra bands that are characteristic of the given specimen.

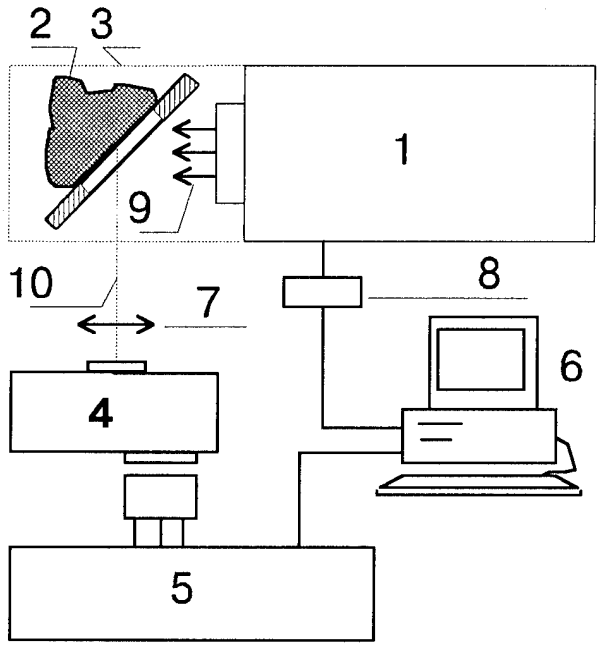


Fig.

7 - lens, 8 - instance block, 9 - e-beam, 10 - luminescence flux.

The PCL intensity increases to a rough linear low with growth of the e-beam peek power (P = j x E) when its pulse duration is constant. But the peek power rise can produce a destruction of inner or/and external structure of specimens.

The electron beam action on a mineral may cause the formation of two main types of defects: radiation-induced defects and heat-induced defects. The first ones appear as a result of the displacement of

mineral ions or knocking of them out of the lattice sites. This process is characterized by some threshold electron energies. These defects show up as a change in the specimen color. The second type defects appear as a result of the overheating of the irradiated zone of a specimen and the irreversible structural rearrangement of this zone. This processes threshold in its nature by the electron beam energy introduced in the specimen.

The oxygen is the lightest chemical element into most dielectric minerals. Because it determines practically threshold energy of generation of radiation-induced defects. We observed these defects in quartz specimens with 300 keV electron energy. But we did not observe them with electron energy less than 180 keV both in quartz and in other oxide minerals. Even it takes place for oxide minerals that they contain in them composition more light chemical elements as oxygen. For example the emerald contains beryllium but we did not observe these defects into its with the 200 keV electron energy. The electron energy threshold decreases for monoxide minerals with the lightest chemical elements. For example it is 110-120 keV for diamond.

We did not observe the overheating defects into nobody specimens in our experimental conditions. We made this observation both visual by an optical microscope and instrumentally by the control of the same PCL characteristics. The last is very sensitive to the modification of the crystal structure. We obtained that a sharp change of the PCL intensity and spectra was appearing during this processes. So we investigated the PCL of asbestos specimens which was heating during 10 minutes under different temperature. And we observed the sharp jump of its intensity near the phase conversion thermal points.

We obtained by measure of the PCL kinetics that its spectra was having both short-life (decay time (τ) is a few μs) and long-life (τ is a few ms and more) bands. While the spectra of traditional luminescence of solids has only long-life bands, and its intensity is to 3-4 orders less than its value of the PCL.

It gives us a possibility to use a CCD-detector for spectra registration. The detector is a device which integrates the photo signal during the storage time. Such a way, we may record both all PCL spectra and only short- or long-life spectral bands by simple change of CCD-detector storage time. All spectra may be used for precise investigation of solids including the research of their crystal, defective and energy levels structures. The more simple long-life bands spectra may be used for determination of mineral species, quality, orelocation of a specimen of unknown stone.

Thereby the information and quality of the PCL spectra are enough for realization of nondestructive spectral-emission analysis of solids. Now the PCL may be to use for quickly precision identification of gems and in other fields: mineralogy; geology; mining industry; production of glasses, semiconductors, optical crystals, ceramics; criminology and science.

1. G.A.Mesyats, S.G.Mikhaylov, V.V.Osipov, V.I.Solomonov. Pisma v JTPh, (Russia), V.18, No 3, P.87-90, 1992.
2. S.G.Mikhaylov, V.V.Osipov, V.I.Solomonov. JTPh, (Russia), V.63, No 2, P.52-64, 1993.

FREON DESTRUCTION IN ATMOSPHERE BY RELATIVISTIC ELECTRON BEAM

Vladimir Kulbeda, Nikolai Popov, Pavel Sopin, and Gennadii Sorokin

Moscow Radiotechnical Institute, RAS
Warshavskoe highway 132
113519 Moscow, Russia

Abstract

*The use of relativistic electron beam (REB) to initiate freon destruction in the dissociative electron attachment reactions at the height less than that of the ozone layer (10 - 15 km) is proposed. The REB advantages are the lower electron temperature of the beam excited plasma (what results in higher reaction rate), the high efficiency of ionization energy cost (up to 50%), and also the high efficiency of modern accelerators. The recent experimental results support the supposition of high efficiency, which at pressure of 760 Torr and CFC mixing ratio of 25-650 ppm may be of 40-100 eV/molecule. The REB power needed for cleaning the atmosphere volume of 100*100*10 km should be of order of 1 - 10 MW, considering the reaction energy cost of order of 100 eV/mol and the mean CFC concentration recovery time of order of 3 months, may be taken as acceptable. The proposed variant REB atmosphere excitation may be part of broader program of active atmosphere experiments.*

Due to the ozone layer depletion, the problem of catalytic fluorocarbon molecule destruction is now of great interest. We propose the use of relativistic electron beam (REB) to initiate freon destruction in the dissociative electron attachment reactions at the height less than that of the ozone layer (10 - 15 km). In that case the products of decomposition of CFC molecules form clusters, attach to aerosols and drop out with rains.

One of the most efficient freon decomposition mechanism is the electron dissociative attachment to CFC molecules, for example:

$$e + CFCl_3 \rightarrow CFCl_2 + Cl^-$$
$$k \sim 5*10^{-8}\ cm^3/s \qquad (1)$$

One should note that the reaction rate drops which increasing temperature. Also, there is a possibility of chain reaction development, if the electron detachment from the reaction products may be guaranteed. The reaction (1) may become the chain one if the electron would be detached from the Cl^- ion or from its derivatives $Cl^-(H_2O)_n$. It is known that this detachment may take place in reactions with excited oxygen atoms $O(^3D)$ or ground level hydrogen atoms [3].

$$Cl^- + H \rightarrow HCl + e$$
$$k \sim 10^{-9}\ cm^3/s$$

In beam plasma the hydrogen atoms are produced effectively in the water dissociation reactions and the $O(^3D)$ atoms are produced in predissociation of highly excited oxygen molecules.

The REB freon decomposition reaction should be compared with UHF discharge decomposition. But recent experiments show that in the last case for freon concentration less then 10^{-3}% the energy cost exceeds 1000 eV/mol. The REB advantages are the lower electron temperature of the beam excited plasma (what results in higher reaction rate), the high efficiency of ionization energy cost (up to 50%, e.g. [1]), and also the high ef-

ficiency of modern accelerators. One also should note that at small CFC molecule concentration the degradation electron energy spectrum in the beam excited plasma is not significantly deformed, what make possible extrapolation of experimental results, obtained in laboratory conditions corresponding to low atmosphere. The recent experimental results [2] support the supposition of high efficiency, which at pressure of 760 Torr and CFC mixing ratio of 25-650 ppm may be of 40-100 eV/molecule.

When analysing the atmosphere excitation by REB, besides the CFC molecules destruction and the direct ozone molecules formation, one should take into account nitrogen oxides formation. The relation of the NO synthesis efficiency and that of the CFC decomposition is of the order of 1.5 - 3. But the nitrogen oxides concentration exceeding that of freons by more than one order of magnitude, the additional NO_x concentrations are of no importance up to the 90% decomposition CFCs. One should note that in analysing the ozone synthesis dynamics at altitudes $h \geq 15$ km the vibrational excitation of ozone molecules must be taken into account. As shown in ref.[4], reactions with vibrationally excited ozone molecules result in additional decomposition of O_3 molecules. Such mechanism of generation of oxygen atom should be taken into account when analysing REB efficiency at high altitudes.

The estimated value of REB power needed for cleaning the atmosphere volume of 100*100*10 km should be of order of 1 - 10 MW, considering the reaction energy cost of ~ 100 eV/mol and the mean CFC concentration recovery time of order of 3 months, may be taken as acceptable.

The proposed variant of using REB for atmosphere excitation may be part of a broader program of active atmosphere experiments.

References

1. G.E.Norman, P.I.Sopin, and G.A.Sorokin. Mat. model. (in Russian), 1989, **1** (2) 13.

2. L.Bromberg et al. Phys. Lett. 1993, **A173** 293.

3. N.Aleksandrov et al. Pis'ma v ZhTF (in Russian), 1992, **18** (23) 73.

4. N.Popov. Proc. 12th Europ. Sect. Conf. Atom. Molec. Physics Ionized Gases (ed. L.Tsendin). St.Peterburg, 1992, P.93.

PULSED ELECTRON BEAMS FOR THE IRRADIATION OF FLUE GASES

G.A.Mesyats and Yu.N.Novoselov

Institute of Electrophysics
Ural Division Russian Academy of Sciences
34, Komsomolskaya st., Ekaterinburg 620219, Russia

Abstract

We discuss the advantages that the use of pulsed electron beams provides in cleaning flue gases from sulphur oxides. By contrast with continuous accelerators, using pulsed electron accelerators for gas cleaning purposes permits a substantial increase in beam current density. This results in higher formation of negative oxygen ions in an ionized flue gas. Significantly, it becomes possible to realize a chain SO_2 oxidation mechanism owing to which an electron can participate in the SO_2 oxidation process five or ten times. The optimal current density ranges between 10^{-3} and 10^{-2} A/cm^2, values at which the energy expended to remove an SO_2 molecule is, as a minimum, approximately 1 eV/mol. There are limitations on the beam current pulse duration, which is less than 10 μs. With these pulse lengths the advantages of the chain SO_2 oxidation mechanism are used more efficiently.

The modern development of industrial society creates serious problems to the safe existence of the biosphere, including man. Cleaning air from toxic exhausts becomes therefore one the challenges. The global problem of air cleaning can be solved in a number of ways. We restrict our attention to one of the possible methods. This is based on using pulsed electron beams as applied to the problem of cleaning flue gases power plants from sulphur oxides.

Currently several flue gas cleaning technologies are available, which employ different chemical processes involving the participation of SO_2 molecules. The most promising of such technologies are, in our view, those that employ electron accelerators. These technologies consist of irradiating a gas stream with electron beams, whereby the flue gases are ionized and reactions occur in them, where SO_2 are oxidized to H_2SO_4. Adding ammonia to the ionized gas leads to formation of the ammonium salts $(NH_4)_2SO_4$, which are well-known fertilizers [1,2]. In the event of using continuous electron beams whose current density does not exceed 10^{-6} to 10^{-5} A/cm^2, the processes of oxidation of SO_2 occur with the participation of free radicals (OH, O, HO_2 and other). The role of the electron beam here boils down to building up free radicals.

However, extensive uses of the electron-beam cleaning method are hampered by high expenditures of en-

ergy for implementing it. For power plants, these expenditures may be as high as 5 to 7% of the installed capacity. High expenditures come from the considerable amount of energy needed to remove one toxic molecule. Numerous investigations have shown that the value of expenditure of energy ε for the removal of one SO_2 molecule ranges between 8 and 15 eV/mol.

In our view, the reason for this is the nonoptimal organization of plasma chemical processes in the flue gas. The processes of removing toxic molecules here do not involve the participation of high-reactivity charged and excited particles. This is the case because the concentration of such particles produced by continuous electron beams is low. The increase in the degree of ionization of large flue gases volumes is due to the electron beam current density rising to values that are basically unattainable in continuous accelerators.

We have suggested using pulsed electron beams for flue gas cleaning [3,4]. Irradiation of flue gases by pulsed electron beams of increased density will permit realizing a charged and excited particle concentration that is optimum for the removal of specific toxic impurities. In what follows we present the most important results of these experiments.

The experiments were performed with accelerators with the electron energy of 200 to 300 keV. We made use of plasma-cathode accelerators in which pulse duration and beam current could be readily controlled by varying the parameters of cathode-producing plasma. The accelerators parameters and composition of gas mixture are shown below.

1.Accelerator with a broad plasma cathode

Electron energy	200 keV
Current density	10^{-4}-10^{-1}A/cm^2
Pulse duration	5 - 25 μs
Electron beam cross-section	10 x 100 cm^2
Gas volume irradiated	10 *l*

2.Accelerator with a radially divergent beam

Electron energy	300 - 200 keV
Current density	10^{-5} - 10^{-3} A/cm^2
Pulse duration	30 - 120 μs
Electron beam cross-section	1.5 m^2
Gas volume irradiated	170 *l*

3.Gas mixture
[N_2] - is the main content of the gas mixture
[O_2] - 5, 10, 15%
[SO_2] - 0.05, 0.1, 0.5, 1.0%
[H_2O] - 0.5, 5, 10%

The main objective of the experiments was to ascertain the energy losses e expended to remove an SO_2 molecule dependence on the beam current density j and beam pulse duration τ.

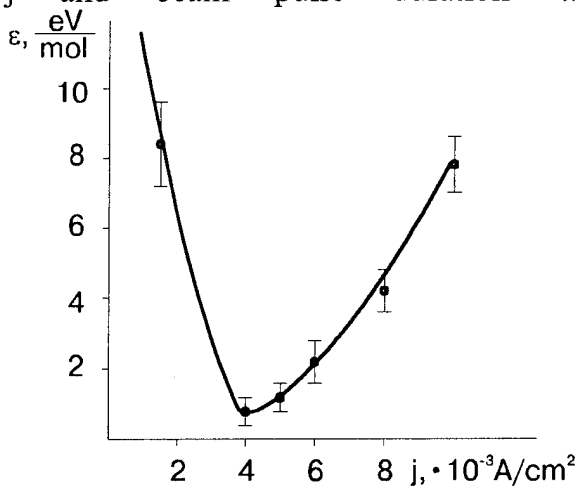


Fig 1. Energy losses ε dependence on electron beam current density j.

The experiments confirmed our assumption regarding to the existence of an optimal beam current density (fig.1). It is seen that quantity ε varies substantially as the current density is varied. The minimal ε was 0.7 eV/mol at an optimal current density of $4x10^{-3}$ A/cm^2. A strong influence on the value of ε is exerted by the variation in the moisture content of the gas mixture. At an optimal current density an increase in the percentage of water from 0.1 to 5% leads to the ε decreasing from 2.2 to 0.7 eV/mol (fig.2).

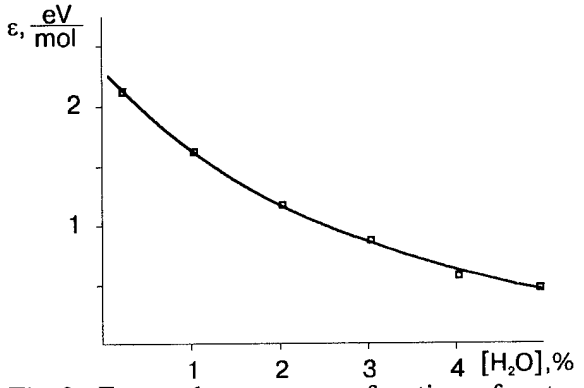


Fig 2. Energy losses ε as a function of water

The energy losses ε are determined not only by the density of the beam current but also by the duration of its pulse. Experimental results are presented in fig.3. As it can be seen, increasing the duration τ over 10 μs results in an increase in ε.

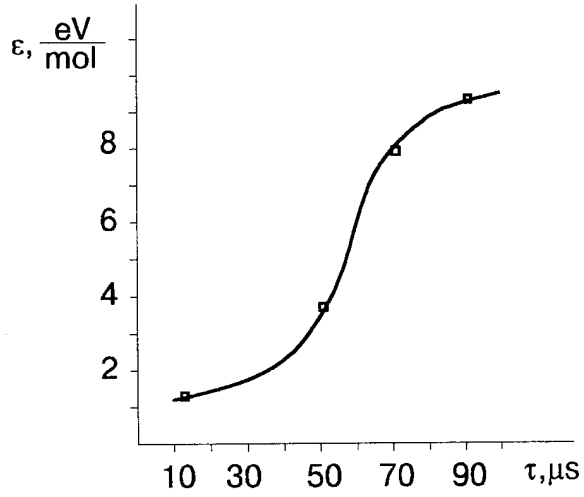


Fig 3. ε dependence on beam pulse duration τ.

Our results can be explained by invoking the chain mechanism of oxidation of SO_2 in an ionized flue gas. An electron beam of increased density injected into a flue gas generates not only free radicals but also a considerable number of charged and excited particles. In air negative ions of oxygen are produced which can initiate chain oxidation reactions of SO_2. In simplified form the mechanism of removing SO_2 can be represented as:

$$e \xrightarrow{O_2} O_2^- \xrightarrow{O_2^*} O_3^- \xrightarrow{SO_2} SO_3^- \xrightarrow{H_2O} H_2SO_4 + e$$

The electron that has become free in the latter reaction can enter into attachment reaction with oxygen again, thereby closing the chain of plasma chemical reactions.

As the beam current density and, accordingly, the concentration of negative ions are increased, the chain mechanism comes into play. With the beam current density being optimum, the chain has probably maximum length, and the beam electrons are used most efficiently. An increase in beam current density and, accordingly, in high-energy electron concentration leads to the O_2^- ions being destroyed by an electron impact. And when the current density is high, part of the electrons recombine with positive ions N_2^+ without entering into chain reactions. As a consequence, the energy losses ε increases.

An increase in the density of water vapour in the flue gas promotes the formation of sulphuric acid in the latter reaction of chain, and in this case the value of ε decreases.

The one of chain break reactions is ion-to-ion recombination between negative oxygen ions O_2^- and positive nitrogen ions N_2^+. This reaction is parasitic and leads to a decrease in the concentration of negative oxygen ions.

The characteristic time of it under the conditions of our experiments is 10 μs. This means that at a greater pulse duration the exponential increase of rate of ion-to-ion recombination dramatically decreases the concentration of negative ions. As this occurs, the efficiency of the chain mechanism drops.

Thus our results provide evidence that using pulsed electron beams to clean flue gases from sulphur oxides shows promise of success and permits one to choose optimal accelerator parameters. Efficient removal of sulphur oxides calls for effecting a chain reaction. This necessitates the use of pulsed repetitive accelerators with a pulse duration of several microseconds and with an optimal current density. The electron energy and the pulse repetition rate in every particular case depend on the volumetric consumption of the flue gases and on the flue duct dimensions.

This work has been supported by DNA, contract DNA 001-93-C-0018.

References.

[1] J.M.Leonardt, 1984, Rad.Phys. Chem., 24(1),p.167-177

[2] N.Frank, S.Hirano, K.Kawamura, 1988, Rad.Phys.Chem., 31(1-3), p.57-82.

[3] D.L.Kuznetsov, G.A.Mesyats, Yu.N.Novoselov, 1992, IX Int. Symp., High Current Electronics. Russia,p.356-357.

[4] A.V.Ignat'ev,D.L.Kuznetsov, G.A.Mesyats, Yu.N.Novoselov, 1993, Proc. XXI Int. Conf. on Phenomena in Ionized Gases, Bochum, Germany,PartII, p.124-125.

HYDRODYNAMIC BEAM-TARGET INTERACTION EXPERIMENTS ON THE KARLSRUHE LIGHT ION FACILITY KALIF

K. Baumung, H.J. Bluhm, P. Hoppé, H.U. Karow, D. Rusch, O. Stoltz, J. Singer
G.I. Kanel*, A.V. Utkin*, and S.V. Razorenov*

Kernforschungszentrum Karlsruhe, D-76021 Karlsruhe, Germany;
* Permanent address: High Energy Density Research Center,
Russian Academy of Sciences, Moscow 127412, Russia

Abstract

We have investigated the beam-target interaction by studying the hydrodynamic response of 10- to 100-μm-thick targets. Laser-Doppler-velocimetry is used to measure the mass flow velocity at the rear target surface. Applying the hydrodynamic relations used in shock wave physics and the Hugoniot EOS of the target material power density, ablation pressure, and the proton range can be determined as a function of time. We have extended the velocimeter to provide 1-dim-spatial resolution along a measuring line of several millimeters length. For the first time, the ablative acceleration and the ablation pressure history could be measured as a function of the distance to the ion diode axis. From the radially resolved hydrodynamic target response we expect complementary information on beam properties and the beam-target interaction process.

I. Introduction

The **KA**rlsruhe **L**ight **I**on **F**acility (KALIF) [1] is a 1.7 MV, 600 kA, 50 ns FWHM pulsed power accelerator. The experiments described below were performed using a self-magnetically insulated extractor-type proton diode. This so-called B_Θ-diode [2] provides a peak power density of ~0.2 TW/cm^2 in a ~8-mm-diameter focal spot. We have investigated the beam-target interaction by studying the hydrodynamic response of 10- to 100-μm-thick targets exposed to the ion beam. Laser-Doppler-velocimeters of the ORVIS [3] type and, recently, a modified line-VISAR [4] are used to measure the mass flow velocity at the rear target surface. From the velocity profiles, properties of the ion beam, the beam-target interaction process, and material properties of the target like the dynamic tensile strength at strain rates >10^7s^{-1} and under nanosecond load durations [5] can be deduced. An analytical model based on an acoustic approximation was established [6, 7] allowing to explain details of the pressure response early into the KALIF pulse by the time dependence of the beam front power density and the ion range.

II. Measuring principle

In the experiments described below, the primary measuring quantity is the so-called mass or particle velocity u_p of the target surface opposite to the ablation plasma. This velocity is connected with the density ρ and the pressure p by the hydrodynamic relations used in shock-wave physics. For our case with a pressure wave propagating into an undisturbed material of density ρ_0 and zero pressure these relations are:

$$u_s \rho_0 = \rho_1 (u_s - u_p) \qquad (1)$$

$$p_1 = \rho_0 u_s u_p \qquad (2)$$

$$H(p, u_p, \rho) = 0 \qquad (3)$$

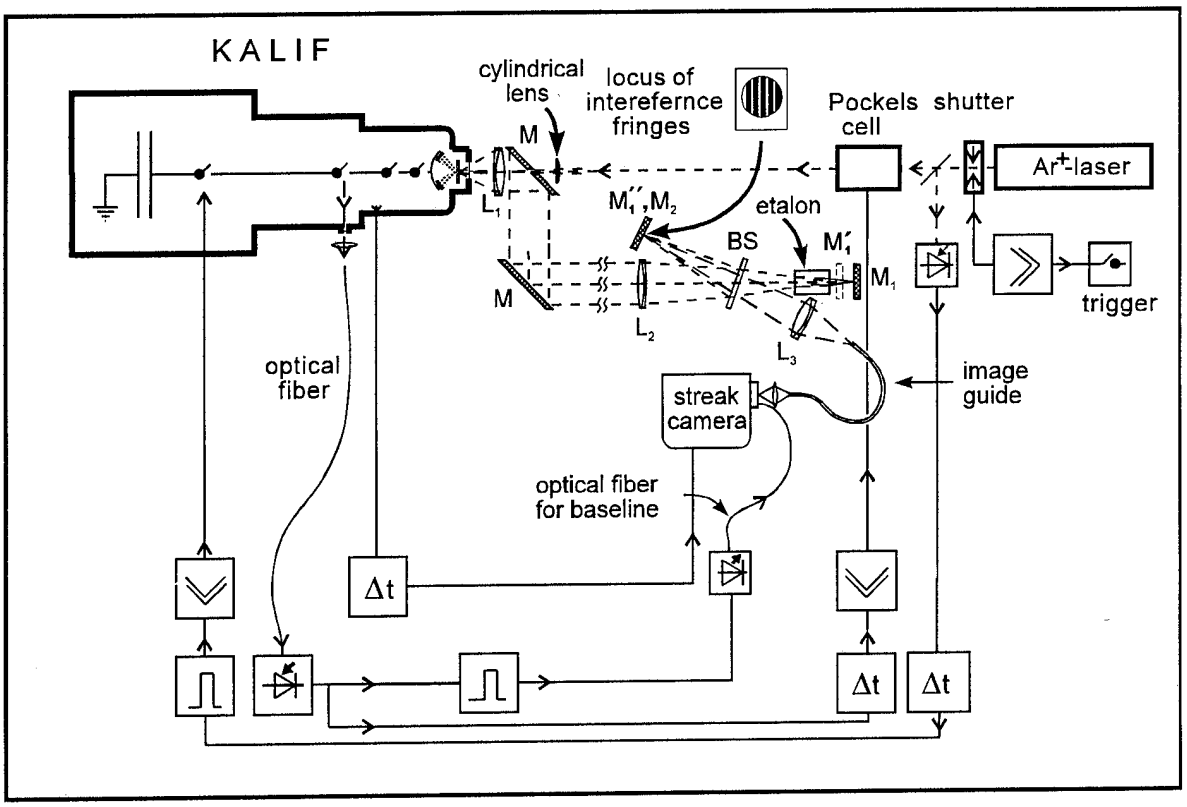


Fig. 1: Schematic diagram of the experimental setup including the novel line VISAR

Equation (1) describes the mass conservation, u_s being the pressure dependent sound velocity and ρ_1 the density of the compressed material. Equation (2) describes the momentum conservation and H is the Hugoniot equation of state relating the hydrodynamic quantities. With the Hugoniot EOS of the target material known, the measurement of one of the quantities - in our case u_p - is sufficient to determine the others.

III. Experimental setup

In the ORVIS velocimeter laser light is focused to a 100-µm-diameter measuring spot and spatial resolution is not considered. We have performed dynamic tensile strength measurements on metal single crystals at very high strain rates [5]. The short pressure pulses needed for these experiments are generated either by direct material ablation by the KALIF beam (~30 ns FWHM) or by impact of 30- to 50-µm-thick foils (3-15 ns FWHM) which are ablatively accelerated to velocities of several km/s. For the evaluation one-dimensional geometry and plane waves are assumed in the 100- to 500-µm-thick samples. In order to check the flatness of the pressure profile and the ablative acceleration, but also in order to investigate the spatial behaviour of the beam as a function of time we have set up a modified line VISAR (see Fig. 1) allowing to illuminate a line of up to 5 mm length and to measure the velocity history along this line. To obtain a sharp picture of the target surface its image has to be focused onto the slit of the streak camera. On the other hand, in order to obtain interference fringes of good contrast, the locus of the fringes has to be imaged onto the camera slit, too. The interference fringes are localized in the air wedge which is formed by mirror M_1 and the image M_2", in the beam splitter BS, of mirror M_2 [8]. To improve the luminosity two lenses L_1 and L_2 are used to image the target onto mirrors M_1 and M_2 of the interferometer. A macro lens L_3 is used to image both, the intermediate picture of the target and the interference fringes onto the input of a 5-mm-diameter image guide connected to an IMACON 675 streak camera. The camera is equipped with an intensified CCD-array and a PC-based image processing system. We expect the spatially resolved

measurements to be a complementary tool for beam and beam-target interaction diagnostics.

IV. Results

IV.1. Ablative acceleration

The energy deposited by the ion beam within a ~20-μm-thick layer leads to a pressure buildup which is unloaded into one direction by material ablation and into the other direction by transmitting a pressure wave into the adjacent cold material. This pressure wave is connected with a mass flow away from the ablation zone. The reverberation of pressure waves from the ablation zone to the rear surface and decompression waves running in the opposite direction successively increase this mass velocity: the non-ablated part of the target is "ablatively accelerated".

Fig. 2 shows, for the first time, the spatially resolved velocity history of a 33-μm-thick aluminum foil which was ablatively accelerated by the B_Θ-diode. The initial jump to ~2 km/s (which is due to a time-of-flight compression or "bunching" of the beam front on its 14 cm trajectory between the anode and the target) is fastest in the central region where the velocity seems to stagnate until the arrival of a second pressure wave at ~4 ns. Two millimeters out of the beam axis, the velocity increase continues smoothly. This result confirms, that, within a central area of ~1 mm diameter, the assumption of plane waves which is a basic requirement for the spall strength measurements is fulfilled for both, direct drive and impact experiments using ablatively accelerated flyer plates. From the spatially resolved measurements also follows that the power maximum coincides within a couple of tenths of a millimeter with the diode axis. This is somewhat surprising in view of the relatively simple diode design with its fairly inhomogeneous flash-board ion source.

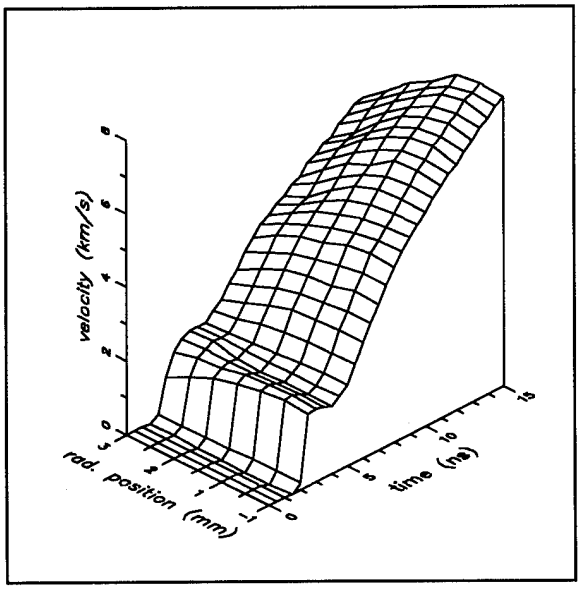


Fig. 2: Spatially resolved ablative acceleration of a 33-μm-thick Al foil.

In direct drive acceleration experiments we have launched homogeneous target foils of ~10 to 25 μm residual thickness to velocities beyond 13 km/s. The potential of multilayer targets is being investigated by code simulation and experimentally, with the goal to reach hypervelocities. Simulations suggest that, using an optimized triple layer target consisting of a thin high-Z tamper, a low-Z ablator, and the actual flyer, hypervelocities exceeding 20 km/s could be obtained. This would open the possibility to investigate, by impact experiments, the state of matter in the 100- to 1000-GPa-range. Applications range from EOS and phase transition measurements up to micrometeorite simulations.

IV.2. Ablation pressure measurements

The quantitative and time-resolved measurement of the ablation pressure is the first step in determining the thermodynamical state of the dense plasma created by the interaction of the ion beam with condensed matter. With the B_Θ-diode providing a peak power density of ~0.2 TW/cm^2 we measured peak amplitudes ~25 GPa (cf. Fig. 3). According to hydrocode simulations such pressures should be achievable by power densities of <0.1 TW/cm^2. The inconsistency is under investigation

Fig. 3 shows the evolution in time of the ablation pressure as a function of the radial distance from the KALIF axis. With the B_Θ-diode, the bunching of the beam front results in an initial jump of the power density which leads to a fast pressure increase.

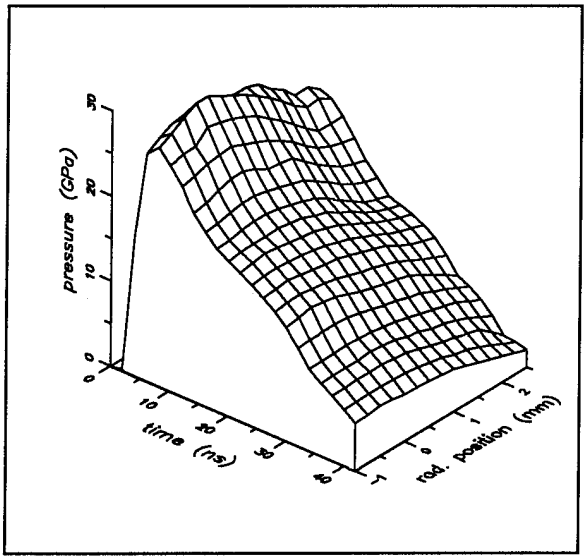


Fig. 3: Spatially resolved ablation pressure history .

Although the power density increases further into the KALIF pulse, the increase rate is not sufficient to maintain the pressure. Like in Fig. 2 with the ablative acceleration the pressure drops by a few percent only in a 1-mm-diameter area around the axis.

Conclusions

Our experiments on KALIF have demonstrated that a comparatively simple method like the investigation of the hydrodynamic response of planar targets by sub-nanosecond resolution velocimetry is a useful tool for high-power ion beam and beam-target interaction diagnostics. For the first time the spatial dependence of the ablative acceleration and the ablation pressure could be measured as a function of time. This opens up new diagnostic possibilities for the examination of beam properties (focus dynamics, filamentation) and the formation of hydrodynamic instabilities. The potential of KALIF as a generator of intense pressure pulses for matter and materials research has been verified in various experiments. With optimized triple layer targets under development hypervelocities exceeding 20 km/s are expected This would open the possibility to investigate, by impact experiments, the state of matter in the 100- to 1000-GPa-range.

Acknowledgment

The authors appreciate the continuos interest and support of their joint work by G. Kessler, director of the Institut für Neutronenphysik und Reaktortechnik, KfK Karlsruhe, and V.E. Fortov, director of the High Energy Density Research Center, Moscow, of the Russian Academy of Sciences. This work was supported by the German Ministry for Research and Technology and The NATO Science Programme.

References

[1] H. Bluhm, K. Böhnel, L. Buth, P. Hoppé, H. U. Karow, A. Klumpp, D. Rusch, T. Scherer, U. Schülken, and J. Singer: Experiments on KfK's light ion ac accelerator KALIF, *Dig. Tech. Papers, 5th IEEE Pulsed Power Conf.*, Arlington, VA, June 10-12, 1985, pp. 114-117.

[2] W. Schimassek, W. Bauer, and O. Stoltz, *Rev. Sci. Instum.*, **62**, 168 (1991).

[3] D.D. Bloomquist, S.A. Sheffield, *J. Appl. Phys.*, **54**(4), 1717 (1983).

[4] W. F. Hemsing et al. : VISAR: Line-imaging interferometer, *Ultrahigh- and High-Speed Photography, Videography, Photonics, and Velocimetry,* L. L. Shaw et al. (ed.), Proc... SPIE 1346, pp. 133-140 (1990).

[5] G.I. Kanel, S.V. Razorenov, A.V. Utkin, V.E. Fortov, K. Baumung, H.U. Karow, D.Rusch, and V. Licht: Spall Strength of Molybdenum Single Crystals, *J. Appl. Phys.* **74**(12), 7162 (1993).

[6] G. I. Kanel, A.V. Utkin, K. Baumung, H. U. Karow, D. Rusch, and V. Licht: Dynamics of the high-power ion beam-target interaction, *this conference*.

[7] K. Baumung, H.U. Karow, D. Rusch, H.J. Bluhm, P. Hoppé, G.I. Kanel, A.V. Utkin, and V. Licht, High-Power Proton Beam-Matter Interaction Diagnostics by Analysis of the Hydrodynamic Response of Solid Targets, to be published in *J. Appl. Phys.* **75**(11), June 1st (1994).

[8] M. Born and E. Wolf, Principles of Optics, 6th ed. (Pergamon Press, Oxford, 1980), p.301.

Ion Beam Surface Treatment: A New Capability For Surface Enhancement

R. W. Stinnett, D. C. McIntyre, R. G. Buchheit, E. L. Neau
Sandia National Laboratories
Albuquerque, NM 87185-5800

John B. Greenly, and Michael O. Thompson
Cornell University
Ithaca, NY 14853

G. P. Johnston, University of New Mexico
Albuquerque, NM 87131

D. J. Rej, Los Alamos National Laboratory
Los Alamos, NM 87545

Abstract

The emerging capability to produce high average power (5-350 kW) pulsed ion beams at 0.2-2 MeV energies is enabling us to develop a new, commercial-scale thermal surface treatment technology called Ion Beam Surface Treatment (IBEST). This new technique uses high energy, pulsed (≤250 ns) ion beams to directly deposit energy in the top 2-20 micrometers of the surface of any material. The depth of treatment is controllable by varying the ion energy and species. Deposition of the energy with short pulses in a thin surface layer allows melting of the layer with relatively small energies and allows rapid cooling of the melted layer by thermal diffusion into the underlying substrate. Typical cooling rates of this process (10^9-10^{10} K/sec) cause rapid resolidification, resulting in the production of non-equilibrium microstructures (nano-crystalline and metastable phases) that have significantly improved corrosion, wear, and hardness properties.

We have conducted IBEST feasibility experiments with results confirming surface hardening, nanocrystaline grain formation, metal surface polishing, controlled melt of ceramic surfaces, and surface cleaning using puilsed ion beams.

Introduction

Recent advances in high average power, pulsed ion beam systems are enabling a new technology to achieve rapid melt and resolidification of surfaces. Researchers at Sandia National Laboratories and Cornell University have developed the capability to produce 5-350 kW average power pulsed ion beams at 0.2-2 MeV energies using a repetitively pulsed (up to 120 Hz) concept designed for long component lifetimes. This new capability is enabling us to develop a commercial-scale thermal surface treatment technology called Ion Beam Surface Treatment (IBEST). This new technique uses high energy, pulsed (typically ≤100 ns) ion beams to directly deposit energy in the top 2-20 micrometers of the surface of any material. The depth of treatment is controllable by varying the ion energy and species. Deposition of the energy in a thin surface layer (Figure 1) allows melting or vaporization of the layer with relatively small energies (1-10 J/cm^2 for metal surfaces) and allows rapid cooling of the

melted layer by thermal diffusion into the underlying substrate. Solidification of metals at the cooling rates typical of this process (10^9-10^{10} K/sec) results in the production of non-equilibrium microstructures (nano-crystalline and metastable phases) in the surface layer. Experiments with both laser and ion beams[1-8] have shown that surfaces produced by this rapid thermal quenching have significantly improved corrosion, wear, and hardness properties.

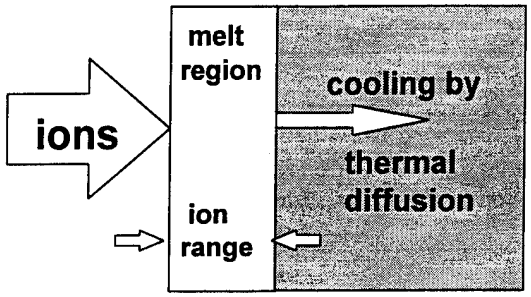


Figure 1. Ion BEam Surface Treatment (IBEST) uses a pulsed, high energy (0.2-2 MeV) ion beam to deposit energy over the classical ion range, typically 2-20 microns, in a surface, raising its temperature to melt. Thermal diffusion rapidly (10^9-10^{10} K/sec) cools the surface, leading to the formation of amorphous layers and the production of non-equilibrium microstructures by rapid quenching.

Ion Beam Surface Treatment (IBEST) is a thermal process that does not significantly change the atomic composition of the sample. The ion pulse rapidly heats a thin surface layer to melt using typically only $3x10^{13}$ ions per pulse. Over the ion range the implanted ion concentration is less than 10^{-3} atomic percent. The short pulse length allows the heated depth to be confined to approximately the ion range by limiting the effect of thermal diffusion. Thermal diffusion lengths in 60 ns are 1 and 4 microns in stainless steel and aluminum respectively, less than the proton range in the materials at typical IBEST ion energies of 0.4-1 MeV. The use of a new Magnetically-confined Anode Plasma (MAP) ion beam system[11-14] described later allows any gas ion to be used to deposit energy in materials. Protons, having the largest range in materials, can provide relatively deep treatment ranging from 5-15 microns in aluminum for energies of 0.5 to 1 MeV respectively.

The effects of Ion Beam Surface Treatment are similar to surface treatment using pulsed lasers but IBEST technology provides unique capabilities that allow it to avoid many problems intrinsic to pulsed laser technology including poor energy coupling to metals, inefficient in-depth treatment, edge effects, and high cost. IBEST technology provides intrinsic in-depth energy deposition, large energy per pulse, low capital cost of hardware, and relatively high (15%) wall-plug-to-surface electrical efficiency. Some of the advantages of IBEST over lasers are illustrated by Figure 2.

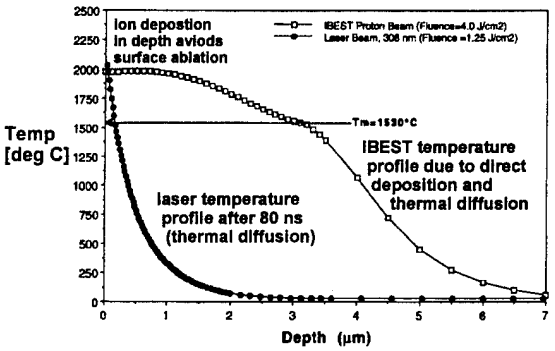


Figure 2. Pulsed ion beams deposit their energy efficiently in-depth, avoiding surface ablation while allowing relatively deep melting versus pulsed lasers. Parameters for RHEPP-I and carbon steel were used for this calculation.

The energy coupling of ion beams to a material is independent of the surface preparation and only weakly dependent on the actual material. The availability of a clean, single species ion source opens up

new areas for metal studies, especially in the rapid solidification behavior of alloys. Thermal quench rates and solidification velocities can be controlled by varying the beam energy and the ion species.

The typical area treated by a single IBEST pulse ranges from 100-1000 cm^2 depending on the application. This capability and our new repetitive pulse technology are key elements enabling high volume commercial applications.

Results Of Initial Experiments

IBEST experiments have been performed on several facilities including Sandia's Repetitive High Energy Pulsed Power (RHEPP) facility, Cornell University's LION accelerator, and LANL's Anaconda accelerator. These experiments are supported by an integrated team of researchers in pulsed power, beam physics, and materials science from Sandia National Laboratories, Cornell University, Los Alamos National Laboratories, and the UNM/LANL/SNL Advanced Materials Laboratory. Single pulse and burst-mode tests at 1/3 Hz have been used to produce initial treated samples while hardware for full scale repetitive operation is being optimized. Results from initial analysis confirm surface hardening, amorphous layer and nanocrystalline grain size formation, metal surface polishing, controlled melt of ceramic surfaces, surface cleaning of hydrocarbon layers from 304 stainless steel, oxide layer removal, and corrosion resistance.

These initial experiments clearly demonstrate the ability of Ion Beam Surface Treatment to significantly modify the properties of materials. The ion source for all of these initial experiments was a "flashover" source which produces a mixed species ion beam. Other experiments[15] at Cornell University using this ion source have indicated that these beams are made up of approximately half H^+ ions and half heavier ions, predominantly C^+ and C^{++}. Future experiments will be done using the new, single species, Magnetically-confined Anode Plasma ion source described later in this article. The following sections describe our initial experiments in more detail.

Treatment O-1 tool steel

These samples were treated using Cornell University's LION accelerator (1 MeV, 4Ω, 40ns FWHM). The ion energy during the FWHM of the power pulse varied from approximately 0.5-1 MeV. The ion energy delivered to the surface was approximately 10 (+/- 30%) J/cm^2 as measured by biased and apertured ion collectors and the load voltage monitor. The samples were located approximately 25 cm from the beam system. Treatment was done at a vacuum level of approximately $2x10^{-4}$ torr.

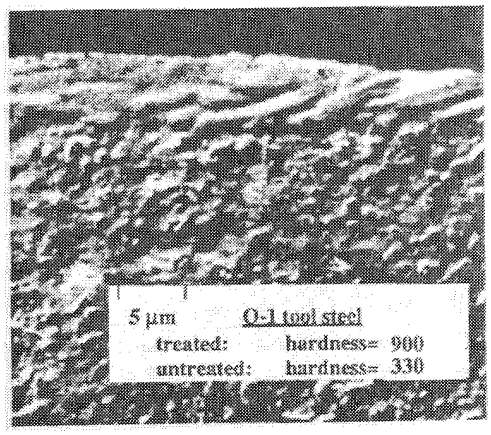


Figure 3. This cross sectional view of an O-1 tool steel sample shows the effects of rapid surface melting and cooling by a 50 ns, 10 J/cm^2, 0.5-1 MeV mixed proton/carbon beam.

Cross-sections of IBEST-treated O-1 tool steel samples were examined[18] using an optical microscope as well as cross-sectional and plan view Transmission Electron Microscopy (TEM). An optical micrograph of the cross-section of an IBEST-treated

sample is shown in Figure 3. The near-surface several microns of the sample were featureless. In contrast, the underlying untreated tool steel material had an equilibrium structure composed of α-Fe (bcc-iron) and large iron carbides. The results of the optical metallography evaluation suggested that the iron carbides in the treated region had been largely redissolved into the bcc-iron matrix. The TEM examination of the IBEST-treated O-1 tool steel sample revealed that the near surface region of the sample was composed of microcrystalline grains approximately 20 nm in diameter. Hardness testing on the O-1 tool steel samples was performed using a Shimadzu microindentation hardness tester. Knoop indentations were made using a 25 gr load on the knoop tip yielding a Knoop hardness (H_k) of $H_k = 900$ for the treated surface and $H_k = 330$ for the untreated surface of O-1 tool steel.

Both the optical metallography and TEM results indicate that carbon was dissolved into the Fe matrix during the pulsed beam treatment. The kinetics of the iron carbide dissolution process during heating, melting, and resolidification were apparently more rapid than the kinetics required for carbide reprecipitation during cooling. The presence of FeO in the treated layer suggests that oxide was incorporated into the layer from the oxidized, untreated surface when melting occurred during treatment. Oxygen may also have been incorporated during melting from the background gasses in the treatment chamber.

Polishing of Ti-6Al-4V

In other experiments we treated Ti-6Al-4V on the Anaconda accelerator (400kV peak voltage, 40 kA total current, 500 ns pulse duration) at a treatment level of 7 J/cm^2 (+/- 30%) at 250-400 keV using a 400 ns ion pulse. The surfaces were treated using 4 pulses separated by at least 5 minutes between pulses. The untreated and treated surfaces are shown in Figure 4. The surface roughness of the untreated, machined surface was approxmately 5 microns. IBEST treatment resulted in a reduction of roughness to 0.1 micron. The energy deposited in the top 3-4 microns of the near surface region in these experiments was more than sufficient to raise the temperature to the melting point and was likely large enough to cause some ablation of the surface. The time the surface was above the melting point can be roughly estimated from the energy deposition profile and the calculated thermal diffusion properties of the material to be 250-500 ns.

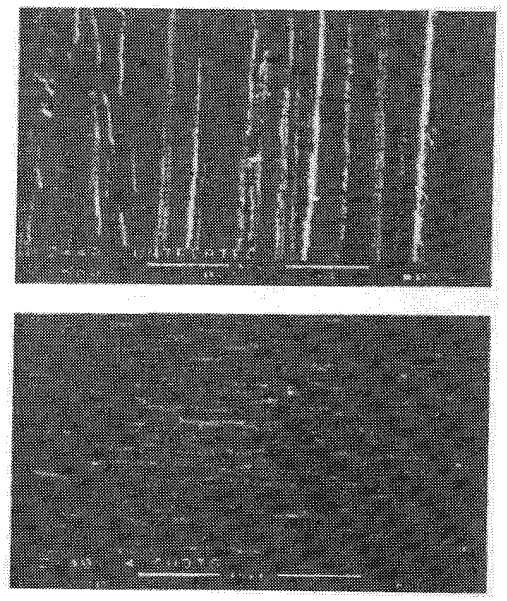


Figure 4. IBEST treatment of a Ti-6Al-4V machined surface (top) treated with 4, 400 ns, 7 J/cm^2 mixed proton and carbon beam pulses demonstrates significant surface smoothing to a 0.1 micron scale roughness.

Corrosion resistance

Initial corrosion resistance studies have been performed on the RHEPP facility at Sandia National Laboratories. In this work,

samples were treated using a 700 keV, 60 ns, mixed proton-carbon beam at 2-3 J/cm^2. Corrosion resistance of the treated aluminum alloy surfaces has been assessed by electrochemical testing and by salt spray exposure testing. Treated alloys tested thus far include 2024-T3 (Al-4.4Cu-1.5Mg-0.6Mn), 6061-T6 (Al-1.0Mg-0.6Si), and 7075-T6 (Al-5.6Zn-2.5Mg-1.6Cu). Electrochemical tests used include anodic polarization and electrochemical impedance spectroscopy (EIS) conducted in an areated aqueous 0.5M NaCl solution. Exposure testing has been conducted at controlled temperatures in a saturated salt fog environment per ASTM B117. Anodic polarization of 2024-T3 has shown that passive current densities are reduced and pitting potentials are shifted to more positive potentials indicating improved resistance to localized corrosion. Figure 5 illustrates these results.

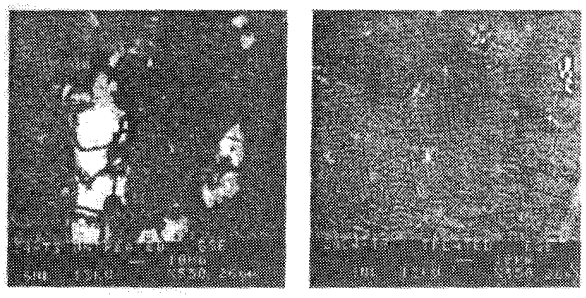


Figure 5. A 168 hour salt fog test (ASTM B117) of untreated and treated samples of Aluminum 2024-T3 shows resistance to pitting due to IBEST treatment.

Controlled melt and resolidification of an alumina surface

On the LION accelerator at Cornell University we treated a polished Al_2O_3 sample with a single pulse at a level of 10-20 J/cm^2 to demonstrate controlled melt and resolidification. The result is shown in Figure 6. This technique shows promise for surface porosity reduction but also shows some microcracking on a 0.1 micron scale.

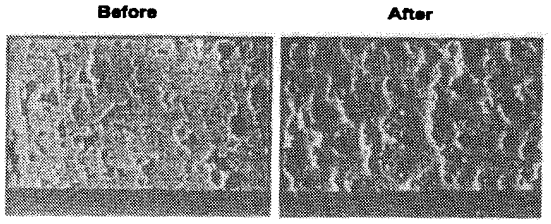


Figure 6. This alumina sample was treated using a single pulse, 0.6-1 MeVmixed proton and carbon beam at 10 J/cm^2. The result shows controlled melt and resolidification of the ceramic surface without serious problems although some 0.1 micron scale cracking was observed. The width shown is 100 microns.

Enabling Technologies For IBEST

Until recently pulsed ion beams have not been considered a viable technology for routine materials processing applications because of their inability to deliver the multi-kilowatt average powers with long component lifetimes needed for commercial processing applications. During the past few years there has been significant progress in two complementary technologies that now enable the design of 5-500 kW average power, >10^8 shot lifetime ion beam surface treatment systems for materials processing.

The first of these advances is the development of a compact, low impedance, electrically efficient, repetitively pulsed, magnetically switched pulsed power system capable of 10^9 pulse component lifetimes. This prototype system (Figure 7), the Repetitive High Energy Pulsed Power (RHEPP) facility[10] (0.8 MV matched voltage, 35Ω, 60 ns FWHM pulse duration, 120 Hz repetition frequency), began operation this year at Sandia National Laboratories. This new facility, the first of its kind in the world, is designed to operate continuously at 120 Hz, delivering 150 kW

average power. This system has demonstrated operation at 50% electrical efficiency from the wall plug to energy delivered to a matched load. RHEPP is also designed to allow operation at reduced pulse rates or in single pulse mode if desired. Its capability to efficiently produce high average power, high voltage electrical pulses using a compact design is a breakthrough for the commercial application of pulsed power.

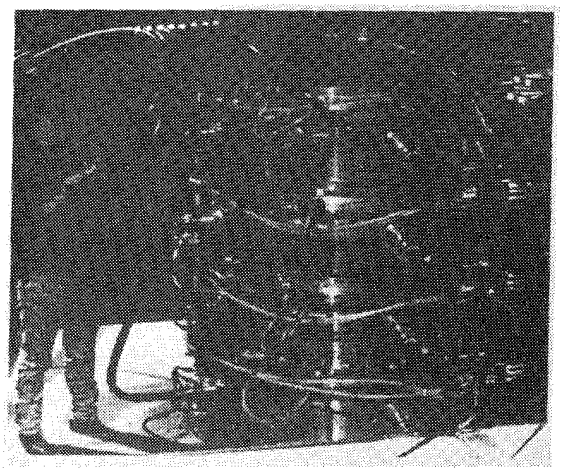


Figure 7. The RHEPP accelerator is designed to operate at 120 Hz, delivering an average power of 150 kW in 0.8 MV, 60 ns pulses.

The second advance is an ion beam system that is capable of operating repetitively and efficiently to transform the pulsed power of RHEPP into an ion beam. An ion beam system capable of operating at repetitive pulse rates of 100 Hz in 10 pulse burst mode (active cooling was not part of the design) was demonstrated[13] at the Cornell University Laboratory of Plasma Studies. An improved version of this system is now being fielded on the RHEPP facility at Sandia for operation in burst mode. This system, the Magnetically-confined Anode Plasma (MAP) ion source, shown in Figure 8, is based on the concept of drawing ions from a single species plasma anode rather than the solid, flashover anode used in standard single pulse ion beam systems. The plasma can be formed from any gas ion.

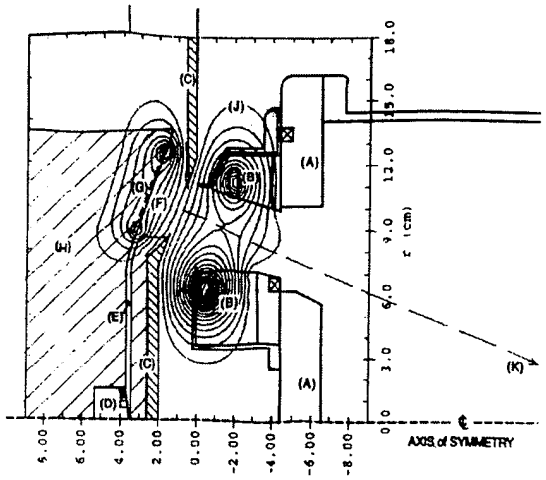


Figure 8. MAP Ion Diode for RHEPP. The cathode assembly (A) with slow magnetic field coils (B); the anode electrodes/magnetic flux shapers (C); the fast gas valve (D); the gas nozzle (E); the gas breakdown and plasma formation region (F); the fast-driving magnetic field coil (G) in the insulation support structure (H), the magnetic flux of the slow and fast coils, as they are at the time of the RHEPP accelerating pulse (J); the ion beam propagation direction to the material target (K).

In experiments conducted to date on RHEPP-I, we have used the MAP diode to produce active anode plasmas using hydrogen, helium, nitrogen, and air. These results and the optimum operating parameter ranges we determined are consistent with those used in earlier experiments at Cornell University[13].

The MAP ion beam system produces an annular beam which is brought to a broad focus symmetric about the axis shown in the figure. In the cathode (ground potential) electrode assembly (A), slow (100 μs risetime) magnetic field coils (B) produce magnetic flux which provides the magnetic insulation of the accelerating gap between the cathode and the anode (high voltage) electrode assembly (C) connected to the output of the RHEPP generator. The ion source that supplies ions to the accelerating

gap is contained within the anode assembly. The MAP source operates in the following way: a fast gas valve (D) on the axis of the anode assembly produces a rapid (200 μs) gas puff which is delivered through a supersonic nozzle (E) to produce a highly localized volume of gas (F) directly in front of the surface of a fast-driving coil (G) located in an insulating support structure (H). After preionization by a 1 μs induced electric field, the fast coil is energized, inducing a loop voltage of 20 kV on the gas volume, driving a breakdown to full ionization, and moving the resulting plasma toward the flux-excluding anode field-shaping electrodes (C) in about 1.5 μs, to form a thin magnetically-confined plasma layer. The RHEPP pulse is then applied to the anode assembly, accelerating ions from this plasma layer to form the ion beam. The magnetic flux surfaces (J) at the time of beam extraction are shown. The beam propagates in vacuum to a broad focal area at the target plane at the right of the figure, where material samples (K) are placed for treatment.

Conclusions

We have demonstrated that Ion Beam Surface Treatment (IBEST) can significantly alter the microstructures of the near surface region of materials and thus the material properties. The effects of IBEST include hardening, corrosion resistance, polishing and cleaning.

The developing repetitive pulsed power and beam technology on which IBEST is based is a new capability that can provide new capabilities for cost-effective surface treatment for a variety of applications.

References

1. E. M. Breinan, B. H. Kear, L. E. Greenwald, and C. M. Banas, "Laser Glazing, a New Process for Production and Control of Rapidly Chilled Metallurgical Microstructures," Lasers in Modern Industry, (Dearborn, Michigan 1979), 147-166.

2. H.-W. Bergmann, B. L. Mordike, "Laser and Electron-Beam Melted Amorphous Layers,"J. Mat. Sci., (1981), 863-869.

3. R. Fastow, "Pulsed Ion Beam Surface Modification of Materials", Ph.D. thesis, Cornell University, 1985.

4. R. Rastow, Y. Maron, and J. Mayer, "Pulsed ion beam melting of silicon", (Phys. Reb. B, 31,893 (1985)

5. G. E. Remnev, and V. A. Shulov, "Practical Applications of High-Power Ion Beams," 9th International Conference on High-Power Particle Beams, Washington, D.C., 5/25-29, 1992.

6. S. A. Chistjakov, A. M. Gagarin, R. G. Koishibaev, Yu Yu Rjuchkov, V. A. Kuzminikh, V. M. Milutin, V. A. Pirogov, V. A. Perov, A. D. Pogrebnjak, S. V. Plotnik, G. E. Remnev, Yu G. Rusin, and V. P. Janovskii, "Ion Mixing of Near Surface Layers in Au-Cu, Cu-Mo Systems Irradiated by HPIB," Physics Letters, Vol. 131, No. 1, 8/1, 1988, 73-77.

7. V. L. Kutuzov, M. Yu. Ovsyannikov, I. G. Romanov, A. D. Pogrebnk, and G. E. Remnev, "Mechanical and Frictional Properties of Tool Steels Exposed to HPIB Irradiation," Mechanical and Frictional Properties of Tool Steels, 11/8, 1988, 361-364.

8. Y. Shimotori, M. Yokoyama, H. Isobe, S. Harada, K. Masugata, K. Yatsui, JAP **63**, 968 (1988).

9. TRIM-90.05, J. Ziegler and J. Biersack

10. H. C. Harjes, K. J. Penn, K. W. Reed, C. R. McClenahan, G. E. Laderach, R. W. Wavrik, J. L. Adcock, M. E. Butler, G. A. Mann, G. E. Pena, G. J. Weber, D. VanDeValde, L. E. Martinez, D. Muirhead, P. D. Kiekel, D. L.

PLASMA AND ION BEAM PROCESSING AT LOS ALAMOS

D.J. Rej, H.A. Davis, I. Henins, W.A. Reass, J.T. Scheuer,
J.A. Tobin, M. Tuszewski, W.J. Waganaar, B.P. Wood
Physics Division, Los Alamos National Laboratory, Los Alamos, NM 87545

G. P. Johnston,* M. Nastasi, R.E. Muenchausen, K.C. Walter, D.B. Williams**
Materials Science & Technology Division, Los Alamos National Laboratory, Los Alamos, NM 87545

R.J. Faehl
Applied Theoretical Division, Los Alamos National Laboratory, Los Alamos NM 87545

J.R. Conrad. N. Horswell, K. Sridharan,
Nuclear Engineering Dept., Univ. Wisconsin, Madison WI 53706

D.R. Tallant, R.L. Simpson
Sandia National Laboratory, Albuquerque, NM 87185

M.O. Thompson
Materials Science and Engineering Dept., Cornell Univ., Ithaca, NY 14853

Abstract

Efforts are underway at Los Alamos National Laboratory to utilize plasma and intense ion beam science and technology for the processing of advanced materials. A major theme involves surface modification of materials, e.g., etching, deposition, alloying, and implantation. In this paper, we concentrate on two programs, plasma source ion implantation and high-intensity pulsed ion beam deposition.

INTRODUCTION: Over the past 25 years, plasma technologies have found increased use in a wide variety of industrial processes.[1] Manufacturing applications include reactive ion etching and cleaning, ion implantation, thin film deposition, polymerization, bulk chemical processing, and spray coatings. Efforts are underway at Los Alamos National Laboratory (LANL) to utilize plasmas and beams for the processing of advanced materials. These activities are outgrowths of U.S. Department of Energy defense and energy research programs. A major theme of our effort is the surface modification of materials. Magnetized coaxial plasma guns, originally developed for magnetic fusion and space propulsion programs, are being used for polymer and metal etching.[2] Novel rf sources are under development for semiconductor implantation and film growth.[3] Cleaning and decontamination[4] processes are being studied on a large scale.

In this paper, we briefly review two LANL programs involving high-energy ion currents: plasma source ion implantation (PSII) and high-intensity pulsed ion beam deposition (HIPIBD). Further details about these two projects can be found in the cited references.

PLASMA SOURCE ION IMPLANTATION (PSII): PSII (Fig. 1) is an innovative technique[5] to generate high dose implants into complicated shapes in a simple, efficient, and cost-effective manner. A negative high-voltage pulse is applied to a workpiece which is immersed in a plasma. Ions are accelerated by the electrical potential and are implanted into the surface of the workpiece. PSII offers several improvements over conventional techniques. Particle accelerators are eliminated. PSII is a non-line-of-sight process enabling conformal implantation, *i.e.*, ions are accelerated from all directions simultaneously into all exposed surfaces of the workpiece. Consequently, cumbersome workpiece manipulation fixtures and beam rastering are unnecessary. Efficiencies are high since the perpendicular trajectories into the workpiece eliminate the need for masking. Implant times are short since high-current, pulsed-power supplies compatible with this process can provide two orders of magnitude higher average currents than conventional accelerators. Since large areas can be implanted concurrently, ion current densities to the workpiece can be kept low to avoid overheating problems sometimes encountered in beam-line implants. PSII processing cost of approximately $\$0.01/cm^2$ have been projected.[6]

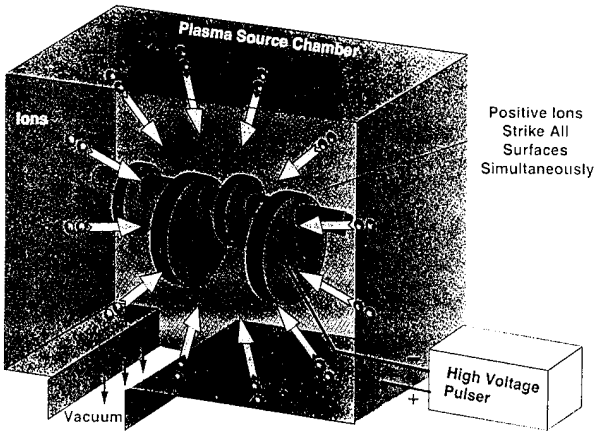


Fig. 1 Plasma Source Ion Implantation (PSII)

In collaboration with the General Motors Corp. and the U. of Wisconsin, the PSII process is being investigated on a large scale.[7] The LANL PSII facility[8,9] can accommodate large, heavy parts in a 4.6-m-long, 1.5-m-i.d. chamber. Argon, nitrogen, methane, acetylene, ethane, or oxygen plasmas have been produced by a $\leq$ 1 kW capacitively-coupled 13.56-Mhz rf discharge. Experiments are conducted in relatively low density ($n = 10^{14}$-10^{15} m^{-3}) plasmas produced in background fills of 0.3 mtorr or less. Ions are accelerated by a high-voltage pulser capable of producing 125-kV, 60-A pulses with a 4% duty cycle.[10] Similar hardware have achieved operating lifetimes of 70,000 hours in particle accelerator and radar installations.

First tests were performed at 50 kV with nitrogen implants into M2 tool steel.[11] Both coupons and manufactured components, with surface areas of 4 m^2, were processed. Implanted doses D_i between 1 and $1.5\times10^{17}cm^{-2}$ were estimated from the total time-integrated modulator current and workpiece area, correcting for the secondary electron emission. Since the plasma consisted of unknown proportions of N_2^+ and N^+, the actual implanted nitrogen dose was between 1 and $2D_i$. Nitrogen contents were determined by resonant non-Rutherford back scattering of 8.9 MeV He ions to be $(1.0\pm0.1)\times10^{17}cm^{-2}$. In addition, oxygen was detected in both the implanted (with dose $1.1\times10^{17}cm^{-2}$) and unimplanted (with dose $0.6\times10^{17}cm^{-2}$) samples.

Surface mechanical properties were evaluated with a Knoop microhardness tester at loads ranging from 2 to 10 grams. A modest ($\sim$ 20%) improvement in microhardness was observed.[11] The improvement became more apparent at low loads since the indentation depth approached the implanted layer thickness. However, even at the lowest load employed, the indentation depth was large enough to include substrate effects; thus, the improvement in hardness in the near surface regions was underestimated. Large scatter in hardness data were observed at low loads because of inherently large uncertainties associated with the measurement of smaller indents, the second phase carbide distribution in the steel, and the surface roughness. The principal hardening mechanism is speculated to be due to nitride formation with iron and the alloying elements present in the steel.

Secondary electron emission is an important issue in PSII. As each ion is implanted, electrons are liberated from the workpiece and are rapidly accelerated through the sheath potential. In most experiments to date, the energetic secondaries stream along collisionless trajectories until they strike and are stopped by grounded objects such as the processing chamber walls. For many metallurgic applications, the secondary electron emission coefficient γ is large,[12] typically ranging between 5 and 20. Consequently, uncontrolled loss of secondaries can significantly reduce system efficiency, while the bremsstrahlung x-rays produced by energetic electron bombardment of the chamber walls poses a potential safety hazard. Methods to suppress secondary losses, such as magnetic insulation[13] or negative ion implants with positive applied voltages, have been proposed.

PSII implants are conformal as long as the plasma sheath dimensions remain small compared to the workpiece feature sizes. For certain applications, this condition may not be easily attained because of hardware limitations described below. During the quasi-steady, space-charge limited current phase, the plasma acts as a resistive load to the high-voltage pulsed power supply. This load impedance Z_p for an expanding planar sheath is obtained by combining the Child-Langmuir equation with Ohm's law,

$$Z_p = [9/4\varepsilon_o]\,[M/2e]^{1/2}\,\{s^2/[A(\gamma+1)V^{1/2}]\} \quad ,$$

where M is the ion mass, A is the workpiece area, V is the magnitude of the applied voltage, and s is the plasma sheath dimension which for planar geometries is given by[14]

$$s(t) = [2\varepsilon_o V/en]^{1/2}\,[(2/3)\omega_{pi}t + 1]^{1/3} \quad .$$

Present-day high-voltage switching technology can drive load impedances of approximately 100 Ω or more.[10,15] For a specified voltage and workpiece

area, this limit corresponds to a minimum sheath dimension (or plasma density). For A = 5 m^2, γ = 7, Z_p = 100 Ω, and V = -100 kV, relatively large sheaths, s $\geq$ 0.1 m, are mandatory for an N_2^+ plasma and planar geometry.

Implant conformality and dose uniformity into practical geometries were estimated with multi-dimensional particle-in-cell computations of plasma electron and ion dynamics, and Monte Carlo simulations of ion transport in solids.[11] Simulations were performed for a 100-kV N_2^+ implant into an elongated workpiece geometry corresponding to the Pierce punch that was PSII treated and reported in Ref. 5. At early times (t < 0.3 μs), the cylindrical shape of the punch was still roughly retained. After about 2 μs, the expanded sheath became spherical and any shape information about the punch was "washed out." Ions were always accelerated toward the part, in the direction normal to the sheath.[11]

III. PULSED ION BEAM DEPOSITION: The congruent evaporative deposition of polycrystalline and amorphous thin films (illustrated in Fig. 2) appears especially well suited for intense ion beams. When the ion beam strikes a target, substantial amounts of target material may be evaporated and ionized. For example, an energy fluence of 1 kJ/cm^2 deposited over a 5 μm ion range will heat the target surface about 5×10^5 K or approximately 40 eV per atom. The ablated plasma may then be condensed at phenomenal rates onto an adjacent substrate as a film.[16-19]

Experiments were performed on the Los Alamos Anaconda HIPIB generator.[20] The magnetically-insulated diode was configured in an extraction geometry shown in Fig. 2. The ions were formed by the flashover of a conical annulus of Lucite attached to the anode electrode. The field was generated by pulsed electromagnets (configured on the cathode side) and flux-excluding metal components located in the vacuum chamber. The diode was connected directly to the Marx generator and operated to produce 300-keV, 30-kA, 0.4-μs-pulsewidth beam of H, C, and O ions.[21]

Diamond-like carbon (DLC) films were prepared by ablation of graphite targets. The ion beam removed approximately 10 mg of graphite per pulse, based on weight measurements before and after 20 pulses. This is in approximate agreement with the $\sim$ 7 mg/pulse calculated by a simple thermal model based on one-dimensional heat conduction with mass removal by vaporization. The time evolution of the ablated plume is shown by the framing photographs in Figs. 3 and 4. Time is referenced to the firing of the Marx generator. For clarity, the substrate assembly has been temporarily removed while taking these photographs. Illumination of the target is evident at time t = 200 ns, which corresponds to the arrival of the intense ion beam. A plume begins to emerge at t = 600 ns, which is approximately near the end of the beam pulse. The plume is highly directed with a diameter of 150 mm corresponding to the beam spot size as viewed by the camera. The plume expands at approximately 2.0×10^4 m/s, which corresponds to a carbon atom or ion directed energy of 24 eV. A broader, slower moving plume emerges later at t $\approx$ 4 μsec.

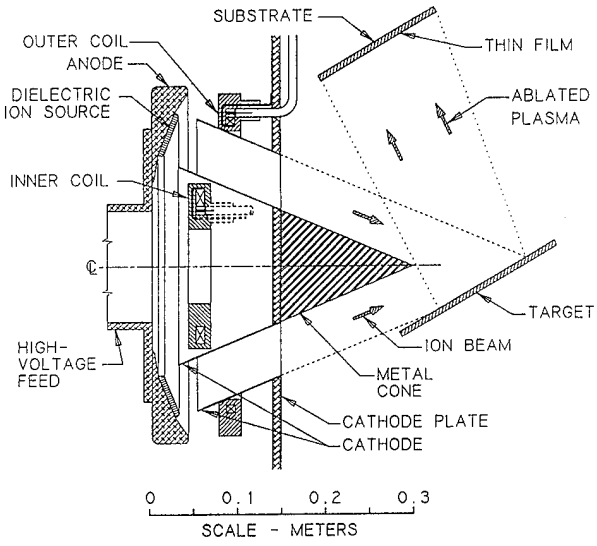


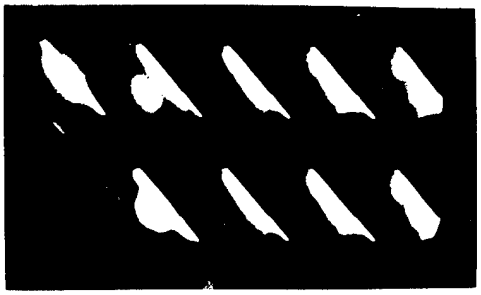
Fig. 2 Ion diode configuration used in HIPIBD

Most of the deposited films were uniform, light brown, translucent, and nonporous with some particles in the micron size range. Film deposition rates were 25$\pm$5 nm/pulse onto substrates that were 150 mm from and normal to the target. This rate dropped to about 12 nm/pulse at 40° off normal and less than 2 nm/pulse at 80°. For a 225 mm target-to-substrate separation, 15$\pm$3 nm/pulse was deposited normal to the target. Fast thin-film calorimetry at the substrate position,[22] revealed instantaneous deposition rates greater than 1 mm/sec. The electrical resistivity varied from 1 to 1000 Ω-cm, increasing with larger target-to-substrate separations. Raman Spectra indicated that most of the films were DLC with significant amounts of sp^3-bonded C, detected by parallel electron energy loss spectroscopy.[23]

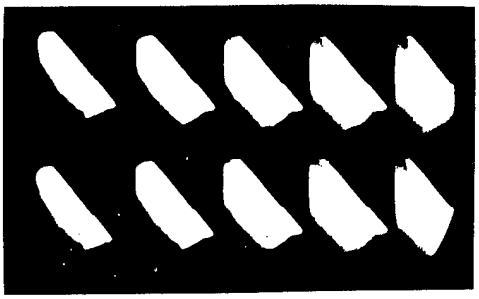


0.2 0.6 1.0 1.4 1.8 2.2 2.6
time = 0 0.4 0.8 1.2 1.6 2.0 2.4 μs

Fig. 3 Framing photographs of graphite ablation



1 3 5 7 9
time = 0 2 4 6 8 μs



9 11 13 15 17
time = 8 10 12 14 16 μs

Fig. 4 Framing photographs of graphite ablation

ACKNOWLEDGMENTS: This research is supported by the U.S. Dept. of Energy through Laboratory Directed Research and Development and through the Defense Programs Technology Transfer Initiatives.

Permanent addresses:

* U. New Mexico, Albuquerque, NM, 87131
** Lehigh Univ., Bethlehem, PA, 18015

REFERENCES:

[1] *Handbook of Plasma Processing Technology,* edited by S. M. Rossnagel, J. J. Cuomo, W. D. Westwood (Noyes Publications, Park Ridge, NJ, 1990).

[2] J. T. Scheuer *et al.*, Proc. 30th Joint Propulsion Conf., JPC-94-3234 (IAAA, in press).

[3] M. Tuszewski *et al.*, J. Vac. Sci. Tech. **B12**, 973 (1994).

[4] J. C. Martz *et al.*, J. Nucl.Mat **182,** 277 (1991).

[5] J. R. Conrad *et al.*, J. Applied Physics **62**, 4591 (1987).

[6] D. J. Rej and R. B. Alexander, J. Vac. Sci. Tech. (in press).

[7] D. J. Rej, J. R. Conrad, J. V. Mantese, Materials Technology **8**, 89 (1993).

[8] B. P. Wood *et al., Mat. Res. Soc.* Symp. Series **Vol. 279** (MRS, Pittsburgh, PA, 1993), p.345.

[9] B. P. Wood *et al.*, J. Vac. Sci. Tech **B12**, 870 (1994).

[10] W. A. Reass *et al.*, J. Vac. Sci. Tech **B12**, 854 (1994).

[11] D. J. Rej *et al., Mat. Res. Soc.* Symp. Series **Vol. 316** (MRS, Pittsburgh, PA, 1994), p.593.

[12] M. Shamim *et al.*, J. Appl. Phys. **70,** 4756 (1991).

[13] D. J. Rej *et al.*, J. Vac. Sci. Tech **B12**, 861 (1994).

[14] J. T. Scheuer *et al.*, J. Appl. Phys. **67**, 1241 (1990).

[15] D. M. Goebel, J. Vac. Sci. Tech **B12**, 838 (1994); D. Deb *et al.*, J. Vac. Sci. Tech **B12**, 828 (1994).

[16] Y. Shimotori *et.al.*, J. Appl. Phys. **63**, 968 (1988).

[17] O. I. Goncharov *et al.*, in *Proc. 8th Intern. Conf. on High-Power Particle Beams*, B.N. Breizman, B.A. Knyazev Editors (World Scientific Publishing Co., Teaneck, NJ, 1991), Vol. **II**, p. 1243.

[18] D. J. Rej *et al.*, in *Proc. 9th Intern. Conf. on High-Power Particle Beams*, edited by D. Mosher and G. Cooperstein (Naval Research Laboratory, Washington, 1993) Vol **I**, p 88.

[19] D. Hinshelwood *et al.*, these proceedings.

[20] D. J. Rej *et al.*, Rev. Sci. Instr. **64**, 2753 (1993).

[21] H. A. Davis *et al.*, these proceedings.

[22] M. O. Thompson, private communication (to be published).

[23] G. P. Johnston *et al.*, J. Appl. Phys (in press).

Intense Ion Beam Characterization and Thermal Modeling for Beam Materials Processing

H. A. Davis, D. J. Rej, and W. J. Waganaar
Los Alamos National Laboratory
Los Alamos, New Mexico 87545 USA

G. P. Johnston
University of New Mexico,
Albuquerque, New Mexico 87131 USA

C. L. Ruiz and F. A. Schmidlapp
Sandia National Laboratories
Albuquerque, New Mexico 87185 USA

Abstract

We have developed an intense ion beam to investigate materials processing applications. Initial experiments have focused on thin film formation by depositing beam-ablated target material on substrates. Measurements of beam properties governing target ablation are presented here. Techniques include Thomson parabola particle spectroscopy to measure the ion beam atomic composition and the energy spectrum of each beam component, and thermal imaging to measure the beam incident energy density. Measurements are used as input to a computer model of the beam-target interaction. Comparison of computational results with target ablation and target energy absorption are found to be in good agreement.

We have developed an intense ion beam (V=350-500 keV, I=30 kA, 0.4 μs) to investigate materials processing applications.[1] The beam is formed in a B_r magnetically insulated diode with a Lucite surface flashover anode in either ballistically focused (see figure 1) or unfocused geometry. The anode-to-cathode gap spacing is 2 cm for the unfocused beam and 3 cm for the focused beam with an applied transverse magnetic field in the diode of 1.5-2 times B_{crit}. The annular anode, with 450 cm^2 surface area, has a mean diameter of 24 cm. The beam is transported away from the diode through two thin grounded, concentric cylinders (for the unfocused beam) or conical sections (for the focused beam) which form the cathode. The full convergence angle of the focused beam is 45^0 and the focus is 35 cm from the anode.

Potential material processing applications include glazing and joining, alloying and mixing, cleaning and polishing, nanophase powder synthesis, and thin-film deposition.[2,3,4] Initial experiments have emphasized thin-film formation by depositing beam ablated target material on substrates. We have deposited films with complex stoichiometry such as $YBa_2Cu_3O_{7-x}$[5] and formed diamond-like-carbon films.[6] These beams must deposit significant energy per unit volume in the target to vaporize and ionize solid material. Measurements and analysis of beam properties governing target ablation are presented here.

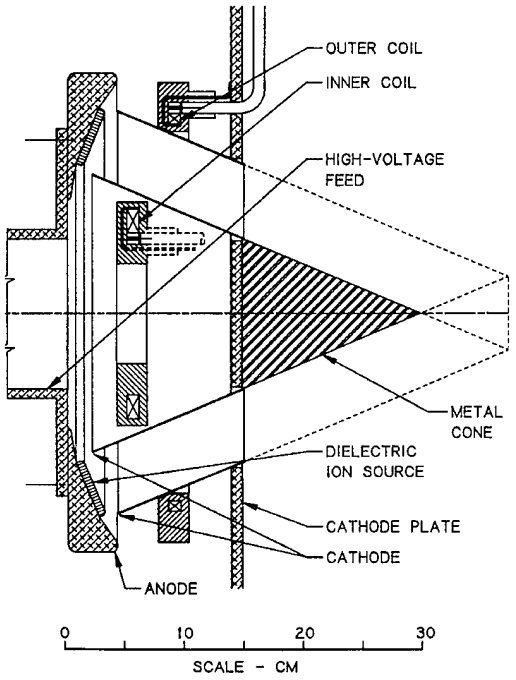


Figure 1. The focused diode.

The energy deposited per unit volume in solid targets is largely determined by the beam energy deposition depth profile and the incident beam energy density. Calculations show the time dependence of these quantities is relatively unimportant for our time scale and beam fluence. To infer the deposition profile, we have used a Thomson parabola particle spectrometer to measure the ion beam atomic composition and the energy spectrum of each beam component. The energy deposition profile in the target is calculated with the TRIM ion transport code using this data as input. The beam incident energy density has been measured using thermal imaging of a beam target.[7] These measurements are used as input to a computer model of the beam-target interaction treating energy input from the beam, latent heat of ablation, and thermal transport. Results of the calculations are described here.

In the Thomson parabola measurements, a small portion of the beam is collimated by a pair of pinholes with the front pinhole having 0.18-mm diameter and the rear having 0.08-mm diameter. The resulting beamlet is passed through deflection plates having parallel electric and magnetic fields transverse to the beamlet direction. The deflected beam components trace out parabolas in the plane perpendicular to their paths -- one for each value of charge-to-mass ratio in the beam. Unambiguous identification of the beam species follows from these measurements and knowledge of the anode atomic composition. The particle positions are recorded on CR-39 plastic which is etched in a NaOH bath to make the tracks visible. Counting and analysis of the track positions yields the beam composition and energy spectra for each species. The energy spectra are determined from the relative number of tracks at different positions along either the magnetic or electric field axes. Data from up to six shots are taken on one CR-39 detector to average shot-to-shot variations.

For the unfocused diode, the beam is composed of a mix of H^+, C^+, C^{++}, O^+, and O^{++}, the elements of the anode material. Traces of H_2^+ (1% or less) and C^{+++} (a few per cent) are also observed. The ratio of the oxygen components to the carbon components is about 0.8. The ratio of the heavy ions to H^+ varies from shot-to-shot averaging about one in agreement with mass absorption measurements made with thin Mylar films. The general shape of the spectra, minimum and maximum particle energies, and peak of the distributions are in good agreement with the voltage and ion-beam current time histories.

Particle spectra for the focused beam are shown in the figures 2 and 3. Data for track scans along both the magnetic and electric axes are shown in each figure. The H^+ spectrum is broad as expected from the voltage and current waveforms with particle energies ranging from 140 to 350 keV. The peak energy is in agreement with the peak diode voltage, and the maximum in the spectrum at about 190 keV corresponds to the diode voltage at maximum ion beam current. The carbon spectrum consisting of the combined C^+ and C^{++} components

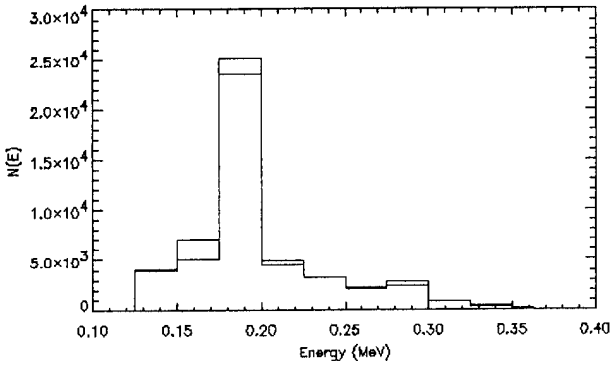


Figure 2. Hydrogen spectrum for focused beam.

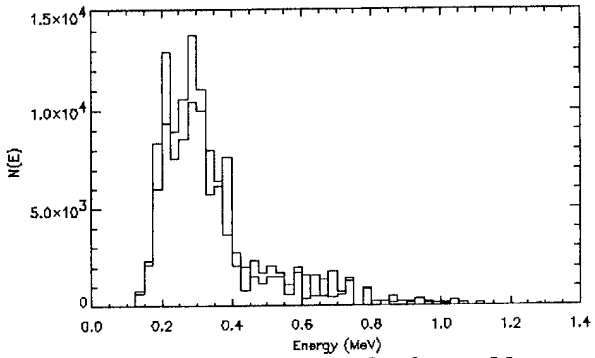


Figure 3. Carbon spectrum for focused beam.

has a minimum energy also at 140 keV and a maximum energy of approximately twice the peak diode voltage, as expected for the doubly charged component. The spectrum has a broad peak from 200 to 400 keV. The composite oxygen spectrum, not shown, is the same as the carbon spectrum within experimental uncertainty. The beam number fractions are 20% H, 42% C, and 38% O with about 12% of the total energy in the hydrogen component. The hydrogen content relative to the heavier species is lower here than for the unfocused beam. The reason is not known. One possibility is that the portion of the beam passing through the focus, measured here, may contain a higher fraction of the heavier stiffer species than the surrounding halo. We intend to test this hypothesis in the future.

Beam energy-density measurements are made using thermal imaging as described in reference 6. If target ablation is negligible, the incident beam energy-density profile can be related to the temperature rise in a target intercepting the beam. At the beam focus target ablation is significant so that the absorbed energy is less than the incident beam energy. Thus the target temperature rise provides an underestimate of the beam energy density. To avoid this problem (see figure 4), we have placed a 3.75-cm-dia circular titanium aperture at the beam focus allowing the most intense portion of the beam to be transmitted. The transmitted portion of the beam expands beyond the aperture where it strikes a second target located where ablation known to be negligible (The onset of ablation has been measured with a technique using wire screen filters to attenuate the beam, and calculated with the code described below.). The target is imaged with an infrared camera to obtain a temperature change profile. The area integral of the profile is used to infer the total beam energy passing through the aperture. The mean energy density at the beam focus is obtained by dividing by the aperture area. The beam energy density at the focus is 30 ± 15 J/cm^2. Currently the total beam energy is derived from a manual integration of the temperature change profile. To automate the process and improve the accuracy of the integration technique, we have developed the capability to read uncolorized video temperature data into a computer for integration and image analysis.

The beam-target interaction is modeled with a one-dimensional heat-transport code with energy input from the beam and latent heat of ablation included as an energy sink. The equation solved numerically is

$$\rho c_p(T)\frac{\partial T(x,t)}{\partial t} = \frac{\partial\left(K(T)\dfrac{\partial T(x,t)}{\partial x}\right)}{\partial x} + S(x,t),$$

where T, x, and t are the temperature, spatial coordinate, and time respectively. $S(x,t)$ contains the beam heating and latent heat of ablation, and $\rho, c_p,$ and K are the density, specific heat, and thermal conductivity. The one-dimensional approximation is justified since beam penetration

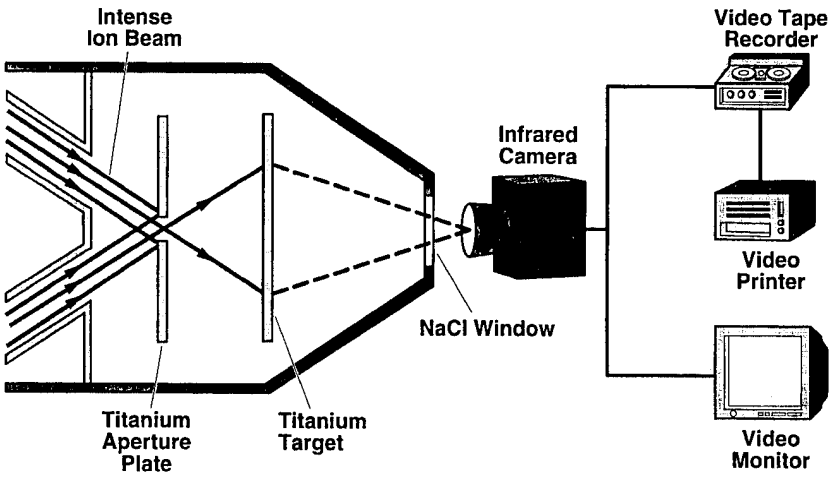


Figure 4. Energy density measurement.

and heat transport lengths are negligible compared to characteristic lateral scale lengths. The model uses temperature dependent thermal conductivity and heat capacity, and assumes constant density. Hydrodynamic motion of the target blowoff is ignored since time-resolved photographs of the target blowoff show that the plume does not move out of the beam path during the pulse. Also, we ignore radiation since estimates indicate it is probably not important for the beam fluence levels currently achieved. A single phase change from solid to vapor is assumed. For graphite this is exact. For other materials the latent heat of fusion and vaporization are combined into a single latent heat of ablation. The ablation temperature is taken to be the boiling point of the target material. Typically the latent heat of vaporization is much larger than the latent heat of fusion so this is a good approximation. For example, the ratio is 4% for titanium.

First calculations used time dependent diode voltage and beam current measurements to model the beam energy input. Here, energy deposition in the target is a function of position and time. The mix of beam species was taken from the spectrometer measurements. This approach has the disadvantage of not properly accounting for multiply ionized species that are accelerated to energies above the diode voltage, since the ratio of the different charge states in the diode region is not known. More recently, we have used the measured particle spectra to model energy input to the target. Since this is a time integrated measurement, we assume the spectrum is a constant function of time over the beam pulse. This approach properly accounts for multiply ionized species. Calculations show that the constant spectra assumption is a good approximation. Ablation is modeled by assuming that all the material in a computational cell is ablated when the material in that cell has reached the ablation temperature, and the beam has supplied the latent heat of ablation. For the focused beam the particles strike the target at non-normal incidence reducing their penetration depth in the target. This, however, is compensated for by an increase in the beam cross-sectional area at the target so that the net energy deposited per unit mass is to first order unchanged from that of normal incidence. Because the deposition depth is shorter, the scale length for thermal transport is reduced. However, the effects of thermal transport are weak so that calculations for normal incidence can probably be used safely. We intend to investigate this issue in more detail later. In the remaining we analysis we assume normal incidence.

For the unfocused beam a 50/50 mix of

carbon and hydrogen ions was used in the calculations as an approximation to the measured spectrum, which also includes oxygen. When the calculated ablated mass is plotted as a function of beam energy density, there are two jumps in the ablated mass. The first occurs when the beam energy density is just above the threshold for ablation. Here, the ablated mass jumps from zero to a value corresponding to ablation of a penetration depth for the shorter-range, carbon ions. When the beam energy density is approximately five times the ablation threshold (close to the ratio of the hydrogen ion penetration depth to carbon penetration depth) mass corresponding to a hydrogen-range-thick layer is ablated. This behavior was observed for both graphite and titanium targets. The ablation threshold for graphite was approximately 12 J/cm^2 and for titanium it was about 5 J/cm^2.

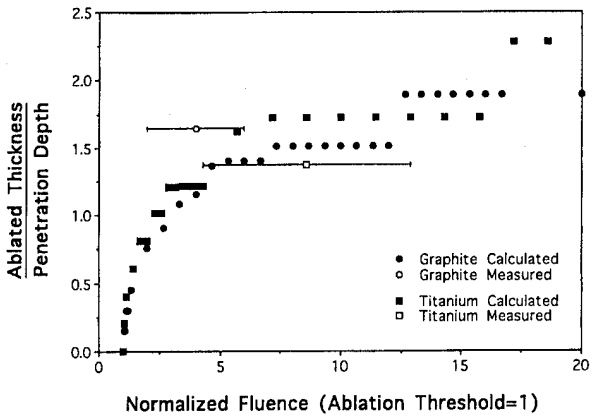


Figure 5. Ablated mass density as a function of beam energy density.

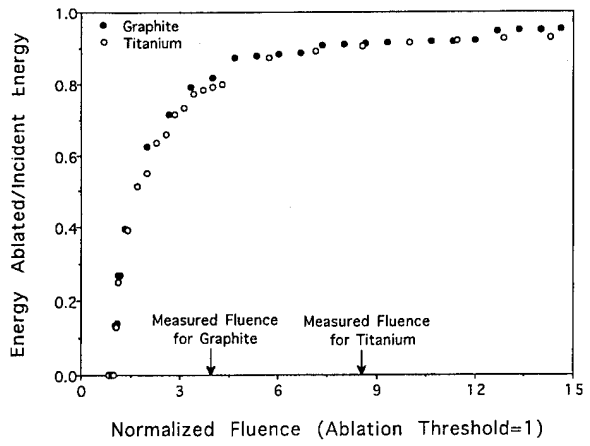


Figure 6. Energy in the ablated mass as a function of normalized beam energy density.

Figure 5 shows the calculated ablated mass per unit area for the focused beam as a function of beam energy density. The ablated mass is normalized to the mass in a penetration-depth thickness (an average over ion species is used for the penetration depth). The energy density is normalized to the ablation threshold energy density with a value of one corresponding to the onset of ablation. Normalized parameters were used to overlay data for different materials. The measured ion beam spectrum for the focused beam was used for these calculations. Calculated points for both graphite and titanium are shown along with measured values. Both sets of points overlay well when plotted with normalized parameters. The ablation threshold for graphite is 7.5 J/cm^2 and 3.5 J/cm^2 for titanium. These are lower than for the unfocused beam because of the larger fraction of carbon and oxygen ions which have shorter penetration depths than hydrogen. Again above a few times the ablation threshold, the ablated mass density changes slowly with beam energy density and has a value roughly corresponding to the mass

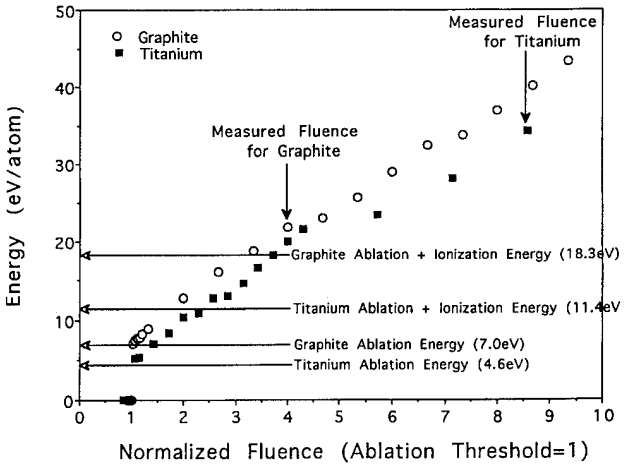


Figure 7. Energy deposited per atom as a function of normalized fluence for titanium and graphite.

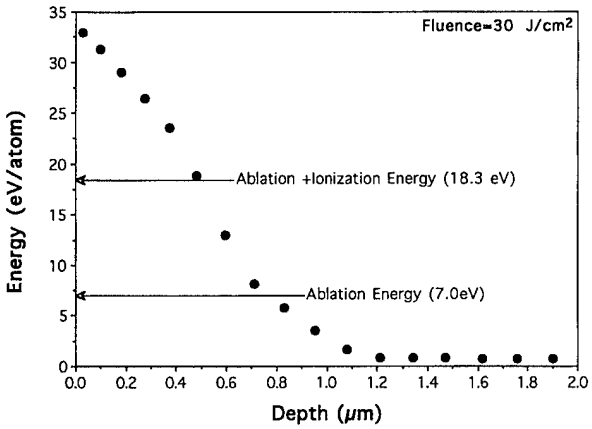


Figure 8. Energy per atom versus depth for graphite.

density in an average penetration-depth thick layer. Agreement between the calculations and measured values is good within experimental uncertainty. For graphite the mass ablated was 0.2 mg/cm^2 and for titanium it was 0.3 mg/cm^2 over approximately 50 cm^2.

Figure 6 shows the calculated energy density deposited in the ablated material normalized to the incident energy density in the beam. Data for graphite and titanium plotted against normalized energy density are shown. The measured beam fluence corresponding to each material is indicated. The points again overlay for both materials with ablation efficiencies of around 70 to 90 % for beam fluences above a few times the ablation threshold indicating good coupling to the target blowoff at these beam fluences.

Figure 7 shows the calculated energy per ablated atom deposited as a function of normalized beam fluence for both graphite and titanium. Again the points overlay reasonably well for the two materials. The ablation energies and ionization energies are shown for both materials. The average energy for graphite at the measured beam fluence is about 22 eV, and it is about 35 eV for titanium. These are both well above the energy needed to ablate and ionize plume material indicating that much of the blowoff should be ionized.

Figure 8 shows the calculated energy absorbed by each atom as a function of distance from the target surface for graphite. The peak total energy at the surface is about 33 eV corresponding to about 15 eV of kinetic energy for the most energetic ions in the plume. This is in approximate agreement with time-resolved photographic measurements and time-of-flight measurements from time-resolved substrate sensors. The photographs show that the peak kinetic energy is in the range of 6 to 24 eV. The substrate sensors indicate about 24 eV. The calculations indicate that most of the material in the plume is ionized.

*Work supported by U.S. DOE under contract W-7405-ENG-36.

[1]D.J. Rej, R.R. Bartsch, H.A. Davis, R.J. Faehl, J.B. Greenly, and W.J. Waganaar, Rev. Sci, Instrum. **64,** 2753 (1993).
[2]R.W. Stinnett, et. al. (these proceedings).
[3]D.R. Hinshelwood, et. al. (these proceedings).
[4]D.J. Rej, et. al. (theses proceedings).
[5]D.C. Gautier, et. al., *in Beam-Solid Interactions: Fundamentals and Applications*, edited by M. Nastasi, et. al., Mat. Res. Symp. Proc., Vol. 279 (1993) p. 657.
[6] G.P. Johnston, et. al., JAP (in Press).
[7]Harold A. Davis, R. Richard Bartsch, and Donald J. Rej (these proceedings).

UTILIZATION OF HIGH POWER ION BEAMS AND HIGH CURRENT ELECTRON BEAMS FOR MODIFICATION OF METALLINE MATERIALS.

Alexander D.Pogrebnjak
Department of Ion Plasma Deposition
Sumy Institute of Surface Modification
Sumy Research Center, P.O.Box 163
244030 Sumy, Ukraine

Abstract

The brief review of results on the application of high power ion beams (HPIB) and high current electron beams (HCEB) for the modification of metalline materials and mixing of refractory films deposited to the metalline substrate is presented. The main factors of HPIB and HCEB treatment affecting the structure phase transitions, defect formation in the surface and inside the substrate are: the fast quenching from liquid and solid states, the formation of elastic, plastic and shock waves, the formation of stress gradients and the mass transfer during liquid and solid phases. The examples of HPIB application for modification and mixing in hermetically sealed ferreed contacts resulting in improving the electro-erosion resistance and resistance; and of HCEB application for hardening, wear decreasing, increasing the corrosion resistance and decreasing the brittle damaging ability are demonstrated.

At the end of the 70th and the beginning of the 80th, the pulsed treatment of semiconducting materials (annealing of implanted layers, formation of silicides etc.) using, first, high current electron beams and then high power ion beams has got a strong impulse. Further it became clear that the beams of nano- and microsecond duration could not be applied in semiconductor technology because of the formation of defects and macro damages. So the necessity to find the new application spheres for the beams of the mean power got arisen. High current electron beams and high power ion beams started to be applied to modify metal and alloy, ceramics and polymer surfaces which was realized both through mixing the surface thin films in liquid phase and through thermal treatment.

One should note also the essential progress in the development of HCEB and HPIB accelerator sources for the purposes of surface modification both in laboratory conditions and to treat small series of tools in industry [1,2].

Over the period of 15 years the application of the above mentioned beams has been developing abruptly, irregularly.

This brief review presents investigation results on mixing the metalline coverings of hermetically sealed ferreed contacts using HPIB irradiation. Usually to provide the low and stable resistance and the resistance to electric erosion of the gas filled hermetically sealed ferreed contacts of the mean and low power, the halvanic coverings on the basis of gold (Au/Co, Au/Ni and Au/Ni/Rh alloys) are used. Because of the uncontrolled deviations in concentration of doping material in comparison with the optimum value, these contacts may feature the low resistance to cold welding, to arc separation. In addition, an increase in the resistance of the contacts in the switching circuit is possible due to the formation of low conductivity films at contact zones which is the result of high concentration of carbon containing impurities in the coverings. We used the contacts of the MKA-2701 type with double layered covering of Ni ~ 2μm , and Au ~ 0.5μm . HPIB irradiation was performed within the following regime: E_{mean} = (0.2 to 0.5) MeV, pulse duration of 80 to 100ns, j = (20 to 100) A/cm², the beam composition was 50%C, 50%H.

To investigate mixing process occuring in the contacts, the RBS and AES methods were used.

Figure 1 a,b,c shows the element profiles for the contacts in initial and irradiated states which were obtained by the AES technique. One can see that Au got mixed with Ni after irradiation.

The resource tests of the contacts were per formed in the following parameters of the circuit commutation: $U_k = 60$ V, $I_k = 0.08$ A. The tests demonstrated that the minimum resource of operation increased by a factor of 4-5 in comparison with the initial non-irradiated contacts covered by the electrochemical alloy Au/Ni.

The tests performed within the micropower switching regime when $U_k = 2x10^{-2}$V, $I_k = 10^{-2}$ A, demonstrated that the resistance of the contacts was stable during the total term of their operation and did not exceed 0.05 Ohm. All the electrical parameters of the hermetical contacts satisfy the requirements of technical conditions and the output of such tools corresponds to the standard level.

In other works [4] we applied the HCEB for mixing thin films of a metal deposited to the massive matrix. For this purpose the Ta/Fe and Mo/Fe systems were used. These systems are characterized by different heat and physical as well as thermal and dynamical characteristics. For example, the melting temperature of Ta is 3270K, and that of Fe is 1813K. The Fe boiling temperature is only 3145K which is a bit lower than the melting temperature of Ta. The electron source described in [5] has been studied.

Figure 2 demonstrates the calculated time dependences of the interphase boundary position (a melt-a solid) for the system Ta/Fe (a) and Mo/Fe (b). In this case the film thickness is 100 nm and the HCEB energy flow values vary. One can see that when the energy flow is increasing from 2.3 to 5.2 J/cm^2, the thickness of the melted iron layer and the time of its existence are increasing also from 2.7 to 7.8μm and from 2 to 10 μs, respectively (for the case of the Ta film). In the case of the pure iron these characteristics changed as from 0.7 to 2.5 μm and from 0.5 to 3 μs, respectively. Calculations showed that when the energy flow is increasing, the maximum cooling rate in a surface is decreasing from 10^9 to 10^8K/s, and the velocity of the crystallization front is decreasing from 2 to 1 m/s

In the case of pure iron irradiation, thewse charactewristics were 10^{10} to 10^9K/s and 5 to 2 m/s, respectively.

Figure 3 demonstrates the RBS energy spectra before (curve 1) and after HCEB irradiation (curves 2 to5) for α-Fe samples.

The RBS results (Fig.3, curves 1 to 5) evidence that the HCEB irradiation mixes the Ta and Fe components in the system: the Ta film-the Fe substrate, irrespective of the value of energy flow including w = 2.3 J/cm^2 which is the value when the Ta film is not to be melted according to calculations (Figure 2b). This is evidenced, first, by the absence of a plateau in Ta peaks (curves 2 to 5) of irradiated samples which speaks about the absence of the pure Ta film in the α-Fe surface after HCEB irradiation. The steps seen in Fig3 (curves 4,5) indicate the possible formation of the layer with the constant composition (thickness of to 100 nm) in the case of high energy flows (4.2 and 5.2 J/cm^2); the relative element content of the layer can be determined with the help of AES data . A decrease in the Ta peak intensity with increasing energy flow intensity (Fig.3, curves 2 to 5) evidences that the mixing of Ta-Fe components is accompanied by the partial depletion of the initial Ta mass. The depletion of Ta in the process of irradiation of the Ta/Fe system results from the evaporation and sputtering of some fraction of the Ta film by the over heated vapours of the α -Fe substrate.

Figure 4 demonstrates the RBS energy spectra obtained for the system: the thin Mo film (of 150nm thickness)- the α -Fe substrate in the initial state (1) and after HCEB irradiation within various regimes (2-4). The spectrum of the initial sample (1) shows two parts: the peak with the plateau corresponding to Mo and the continuous spectrum corresponding to the α-Fe substrate. As the result of HCEB irradiation with the energy flow of 2.3 J/cm^2 the components of the system Mo/Fe

got mixed, see Fig.2. This is indicated both by a decrease in the Mo peak and by the absence of the plateau in this peak (this speaks of the absence of the pure Mo film in the surface). When the energy flow increases to 3.3 J/cm^2, deeper mixing of the Mo film with the iron matrix occurs, see Fig.4, curve 3. The evaluation of the stoichiometry of this layer yields the following composition: $Fe_{80}Mo_{20}$ (Fe_4Mo). Within the depths of 100 to 150 nm the molybdenum concentration sharply decreases. When the energy flow increases to 4.5 J/cm^2, the essential mass depletion of the initial film due to the sputtering occurs.

So, one needs the energies of 3.3 J/cm^2 for the effective mixing of the Mo/Fe system, in this case the compound Fe_4Mo which is absent in the equilibrium diagram of states is formed. Measurements of the microhardness of the mixed layer (Ta with Fe) demonstrated its significant increase in comparison with the case of the usual Fe quenching. Simultaneously the resistance of the surface to the brittle damaging increased. Also I should like to note the essential increase of corrosion resistance to acidic media. In conclusion, the results presented in this review demonstrate that the HCEB and HPIB of the average power may be successfully applied for improving the service characteristics of tools made of metalline materials.

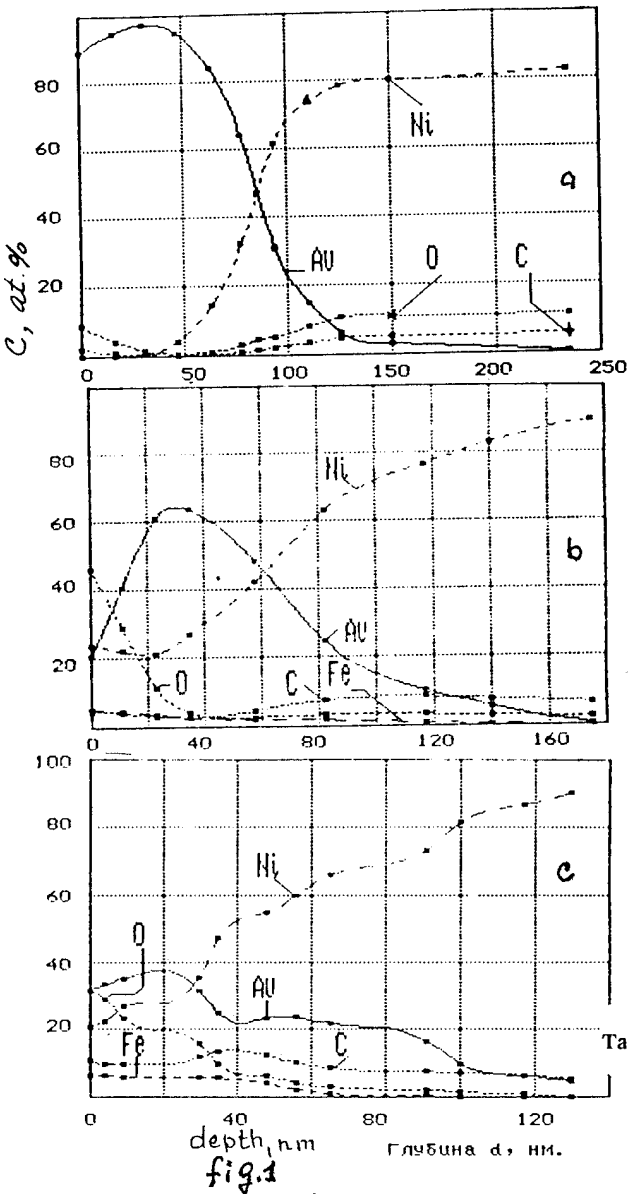


fig.1

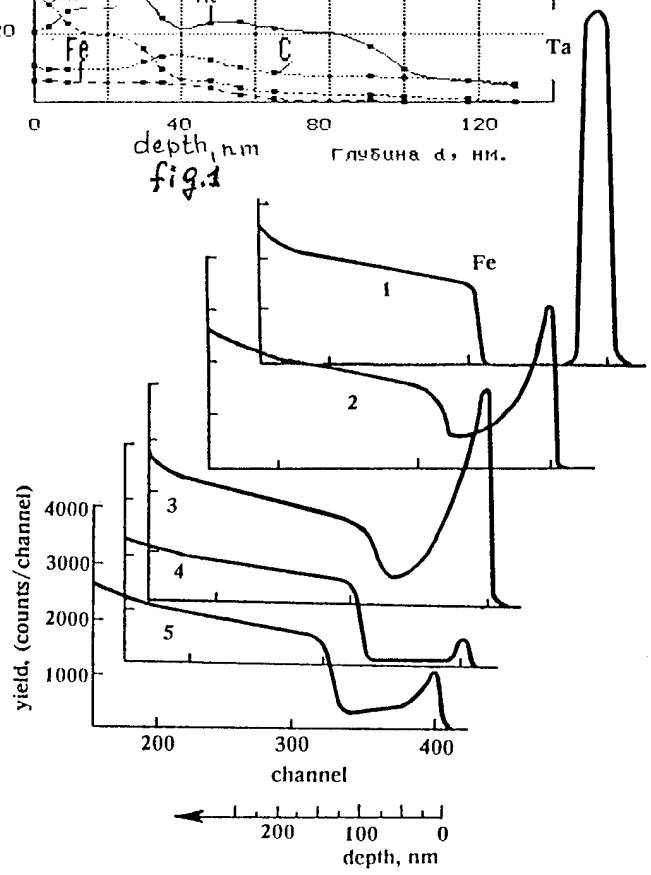


fig. 3

References

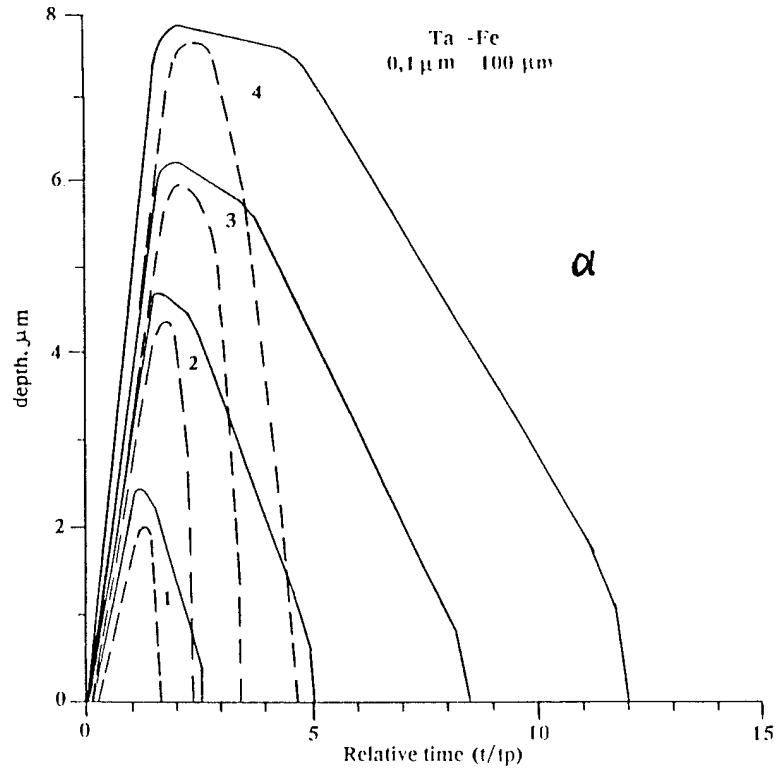
[1] A.D.Pogrebnjak. Phys.Stat.Sol. a 1990, 117, p.17-51.

[2] A.D.Pogrebnjak, D.I.Proskurovsky. Phys.Stat.Sol. 1994 will be published.

[3] A.B.Markov, D.I.Proskurovsky, V.P.Rotstein.Preprint TNTs SO RAN, N17, 1993, 63p.

[4] Yu.F.Ivanov, A.B.Markov, D.S.Nazarov, G.E.Ozur, A.D.Pogrebnjak, D.I.Proskurovsky, V.P.Rotstein.Preprint. TNTs SO RAN N18, 20p.

[5] G.E.Ozur, D.I.Proskurovsky. Pisma v Journal Tekhn.Phys.. 1988, 14, 413.


Ta -Fe
0,1 µm 100 µm
a
depth, µm
Relative time (t/tp)
0
2
4
6
8
0
5
10
15
1
2
3
4

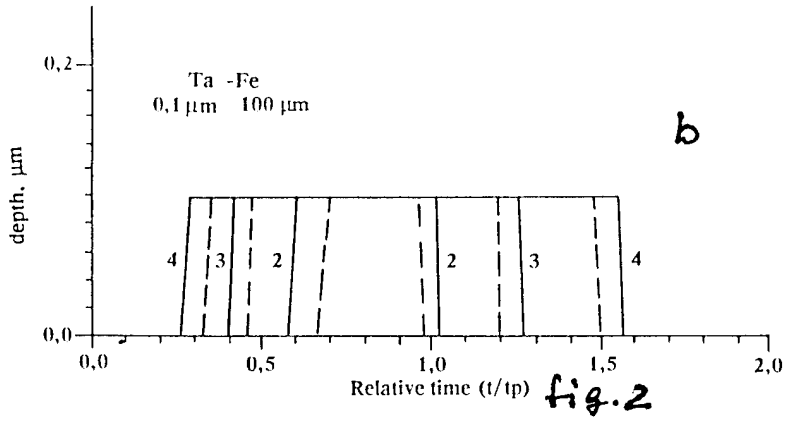

Ta -Fe
0,1 µm 100 µm
b
depth, µm
Relative time (t/tp)
0,0
0,2
0,5
1,0
1,5
2,0
4
3
2
2
3
4

fig.2

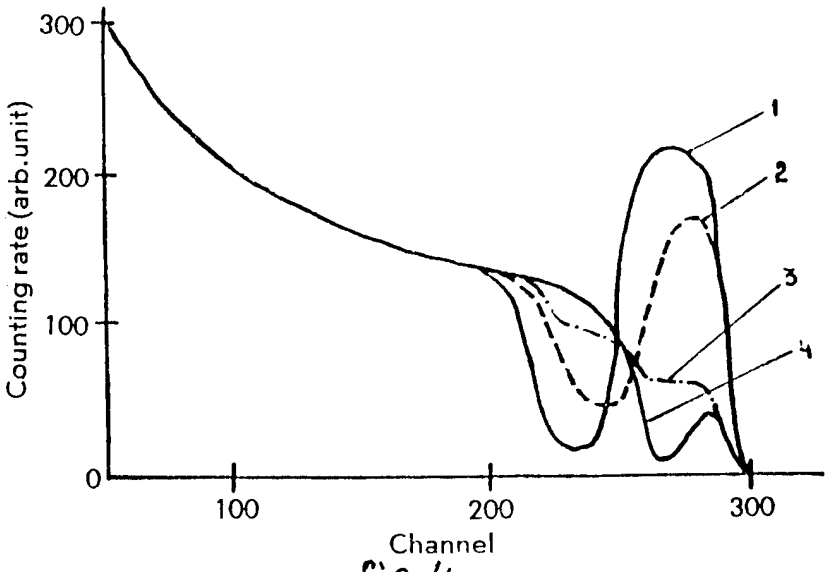

Counting rate (arb.unit)
Channel
0
100
200
300
1
2
3
4

fig.4

DYNAMICS OF THE HIGH-POWER ION BEAM INTERACTION WITH TARGETS

A.V.Utkin, G.I.Kanel
(Institute of Chemical Physics, Russia Academy of Sciences),

K.Baumung, H.U.Karow, D.Rusch,
(Kernforschungszentrum Karlsruhe),

V. Licht (University of Karlsruhe, Karlsruhe, Germany)

Response of plane targets to the high-power proton beam has been investigated using time-resolved laser Doppler velocimetry with sub-nanosecond temporal resolution. Results of measurements are free-surface velocity profiles of metal foils accelerated by the ablative pressure. An acoustic model was established for a semi-quantitative interpretation of the phenomena observed. The evolution in time of the ablation zone has been deduced from performed experiments. Responses of single and double foil targets have been compared to clear up a thermoconductivity contribution into the ablation process.

INTRODUCTION

Intense ion beams represent a powerful tool for the investigation of material behavior under extreme conditions. A basic requirement in this context is the knowledge of the beam-target interaction mechanisms. The methods of shock wave physics can be useful here not only to diagnose a response of matter heated by a high-power beam but also for the analysis of beam parameters. Such experiments were performed at the Karlsruhe Light Ion Facility "KALIF" [1].

EXPERIMENTAL TECHNIQUE

KALIF is a 1.8 MV, 600 kA, 50 ns FWHM pulsed power accelerator delivering up to 40 kJ proton beam energy at a peak power density of 1TW/cm^2 in a diameter focus of 8 mm.

We used the "B_θ-diode" [2] as an ion source which provides a proton beam with a power density of ~0.2 TW/cm^2. Targets were Al foils 10 to 100 μm thick which were placed in the focal plane of the diode.

Monitoring of wave processes in target was realized with ORVIS [3]. Velocity histories of the target rear free surface and the interface between the target and LiF or PMMA plate were recorded. The maximum time resolution of the velocity measurements is equal to 200 ps. The fringe constant of the ORVIS can be varied from 180 m/s to >10 km/s. The accuracy of the velocity measurements in performed experiments is estimated to be 5 to 50 m/s.

HYDRODYNAMICS OF THE ION BEAM INTERACTION WITH SOLID TARGETS

Figure 1 shows initial parts of typical free surface velocity histories of aluminum targets 33 μm thick. These shots were some different in the shape of KALIF voltage pulses. As can be seen the acceleration of target is not monotonous. The measured profiles often show a characteristic spike (shot 3329) or plateau (shot 3334). Several steps can be discerned which are related to reflections of the compression wave inside the target between the rear free surface and the boundary to the ablation plasma.

To understand the different structure of the first jump an analysis of wave process related with fast bulk energy deposition was performed using an acoustic approach. The simplified situation is following.Energy deposi-

tion takes place in a layer of thickness δ at the surface of a semi-infinite target. In the initial phase, the energy deposition occurs with constant volume, and, due to heating, the pressure P increases as $\Gamma E/V$, where Γ is the Gruneisen parameter, V and E are specific volume and energy. With the beginning of the process, unloading waves C_+ and C_- start from the free surface of the energy deposition zone and from its boundary to the undisturbed material (Fig.2). The circulation of these waves defines the shape of the compression pulse which is induced into the target by ion beam.

In acoustic approach the distributions of particle velocity u in the energy deposition zone, satisfying to the boundary conditions (P=0 at h=0, and $P=\rho_0 c_0 u$ at $h=\delta$, where ρ_0 is the density, c_0 is the sound velocity) is found by Laplace method [4]. For $h=\delta$ the particle velocity is:

$$u(t,\delta)=\Gamma_0\Big[E(t)\theta(t)-2E(t-\tau)\theta(t-\tau)+ +E(t-2\tau)\theta(t-2\tau)\Big]/2c_0, \qquad (1)$$

$\tau=\delta/c_0$ is the period of a wave circulation, and $\theta(x)$ is the Haviside unit function.

Let us consider the influence of deposition power $W(t)=dE(t)/dt$ on the particle velocity at $h=\delta$ for dependence of power vs time as:

$$W(t)=W_0+W_1 t.$$

1. $W_1=0$: the power is constant. In this case the velocity profile shows a triangular shape (Fig.2, curve 1), u increases as $\Gamma_0 W_0 t/2c_0$ up to the moment $t=\tau$. The front of unloading wave from irradiated surface reaches the zone boundary at this moment; after that the velocity decreases to zero for $t\geq 2\tau$.

2. $W_0=0$: the power rises from zero linearly in time. In this case the velocity increases monotonously to its maximal value $u_s=\Gamma_0 W_0 \tau^2/2c_0$ when $t=2\tau$, after that it remains constant (Fig.2, curve 2).

3. $W_0>0$ and $W_1>0$. For the general case we obtain velocity profiles as shown in Fig.2 by curve 3. The velocity increases monotonously up to the

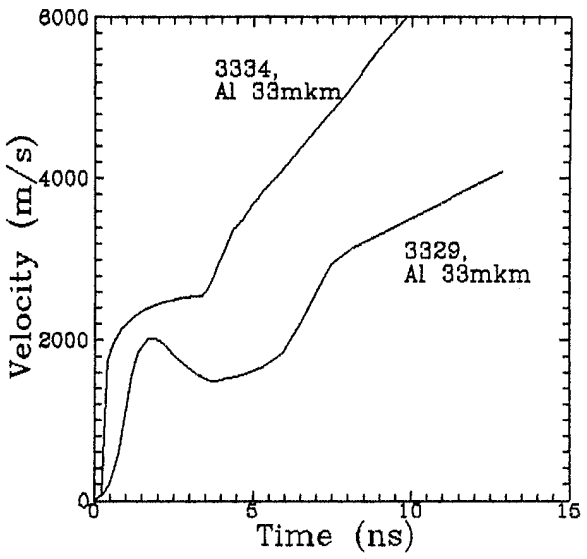


Figure 1. Free surface velocity of aluminum targets for different parameters of ion beam.

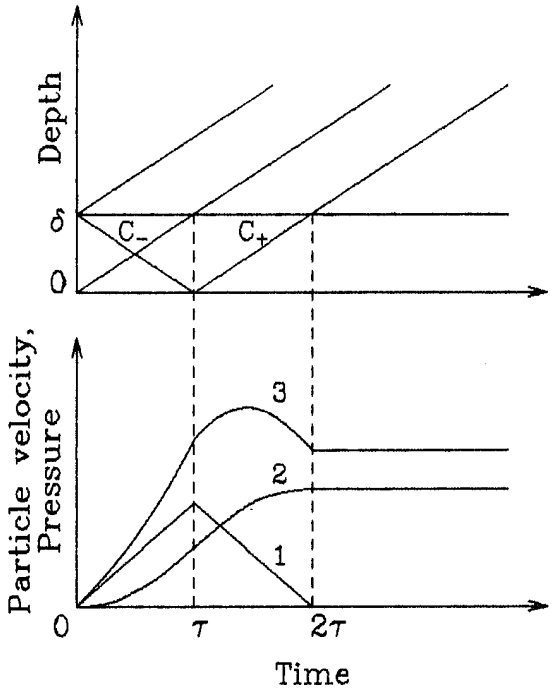


Figure 2. The time-distance diagram and particle velocity profiles of the bulk energy deposition process.

arrival of the unloading wave. The further evolution depends on the relation between W_0 and W_1. If $W_1\tau \le W_0$ the velocity reaches a maximum value at $t=\tau$, decreases during $\tau < t < 2\tau$ and then remains constant and equals to u_s. Otherwise, the velocity reaches a maximum value at $t=2\tau - W_0/W_1$.

So, in all cases, for times $t>2\tau$, the velocity depends on the increase of the energy deposition rate W_1 only.

APPLICATION OF THE ACOUSTIC ANALYSIS TO THE EXPERIMENTAL DATA

Coming back to Figure 1, one can see the velocity profile for shot 3329 has the spike and resembles case 3 in Fig.2, whereas the shot 3334 is similar to the case 2 where $W_0=0$. From the times τ of these two shots - ~1.6 ns for shot 3329 and ~0.5ns for shot 3334- one deduces initial ion energies of 0.7 MeV and 0.3 MeV. These values are in good agreement with the energies calculated from the measured diode voltage.

The values of free surface velocity after the first increase can be used to estimate the power density $I=\rho_0 \delta \cdot W$ [TW/cm^2]. For shot 3329, we find a jump of the power due to the bunching of I_0~0.01 TW/cm^2 and an increase rate of I_1~0.001 TW/(cm^{2}ns). For shot 3334 the jump of power density is zero. The increase rate I_1~ 0.02 TW/(cm^{2}ns)

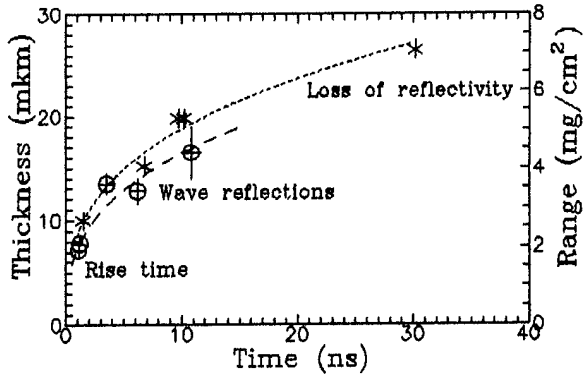


Figure 3. The dependence of the ions range vs time. Dashed lines are the results of approximation.

is significantly higher than in the shot 3329 and results in a stabilization of the velocity at higher level.

Figure 3 shows the energy deposition depth as a function of time. The dependence was found from results of experimental series with parameters of electrical pulse in KALIF similar to shot 3329. An estimation of the initial range of the ions was made on the basis of rise time measurements for thinnest (11 μm) foils according to acoustic analysis presented above. The analysis of the pressure pulse reverberations in the residual part of the targets yields the range values at later times.

The total recording time for thin foils is limited by loss of intensity of the reflected laser light.This may be caused by vaporization of a target when the ion range exceeds the foil thickness,or when a heat wave reaches the rear surface, or by hydrodynamics instabilities. The duration of light reflection was longer in experiments using a solid window. In this case reflectivity should disappear due to material evaporation, and measuring the time of loss reflectivity for foils of different thicknesses yields the evolution in time of the ablation zone. Results of such estimations are presented in Fig.3 also.

To investigate the role of thermal conductivity from the ablation zone into the adjacent cold matter, experiments with two foils separated by a gap were performed. The 100-μm-wide gap is to hydrodynamically and thermally separate the second foil during the KALIF pulse. As can be seen in Fig.4,the power transmitted by a 22.5 μm thick filter is negligible. This confirms that the evaporation zone markedly expands beyond the proton range within a 5 μm.

THE STATE OF THE FLYER

Figure 5 shows the velocity history of the interfaces after impact of a 75-μm-thick Al flyer on a thick PMMA plate, and of the impact of a 50-μm-thick flyer on a LiF plate. The

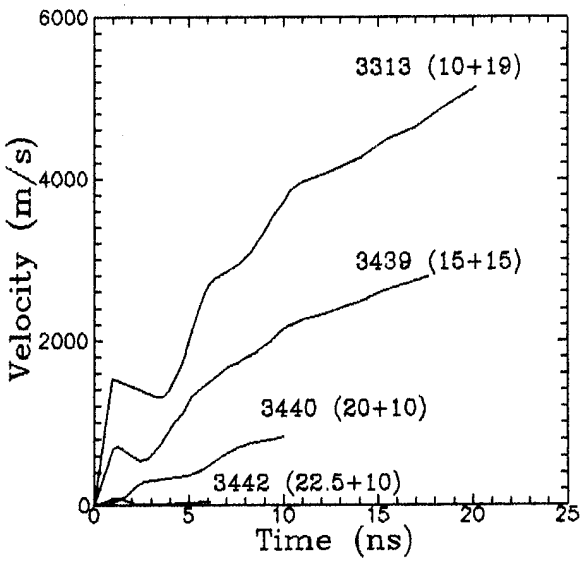


Figure 4. Free surface velocity of Al targets in experiments with filters.The thicknesses of filters and targets are indicated.

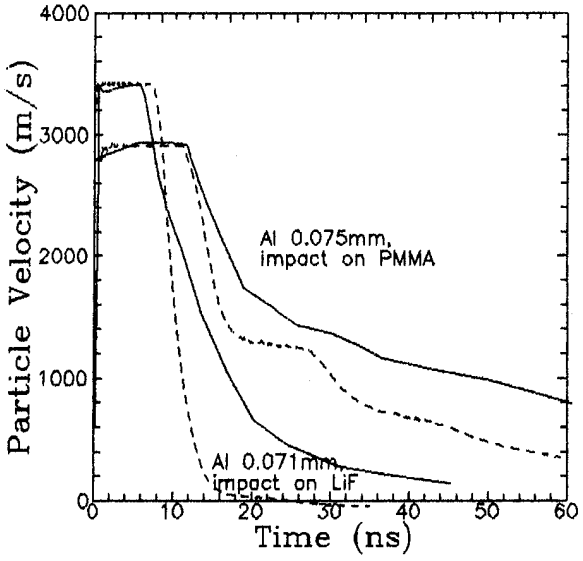


Figure 5. The interface velocity history after impact of foils.

time interval between the beginning of the foil movement and impact was 38 ns and 50 ns,respectively.For comparison, interface velocity profiles obtained by computer simulation are presented in this figure by dashed lines. The simulation has been done using a range of 22.5 μm. Calculated duration of the velocity plateau coincide with measured value in the shot with PMMA. But in the shot with LiF the calculated value is smaller than measured one.That is due to the propagation of the melting boundary. The effect was not observed in the shot with PMMA because the time before impact was equal to the time of needed for reaching the maximum of ion energy and beam power, and the position of the melting layer was still defined by the beam parameters.

CONCLUSION

The results of the investigation demonstrate the time-resolved measurements is a useful tool for analysis of the beam-target interaction.Registrations of the ablative acceleration of thin plates, and of the state of the launched flyers give information about the matter behavior under the high pressure and temperature.

ACKNOWLEDGEMENT

The authors appreciate the continuos interest and support of their joint work by G.Kessler, director of the Institut for Neutronenphysik und Reaktortechnik,KfK Karlsruhe,and V.E. Fortov, director of the High Energy Density Research Center, Moscow, of the Russian Academy of Sciences.

This work was performed with the support of the German Ministry for Research and Technology and The NATO Science Programmme.

REFERENCES

[1] W.Bauer,H.Baumung,H.J.Bluhm, H.U. Karow. Diagnostische Verfahren zur Untersuchung intensiver Ionenstrahlen und der Strahl -Target-Wechselwirkungen. KfK-Nachrichten, 1992, 24, S.19.

[2] W.Schimassek. Erzeugung und Fokussierung eines intensiven gepulsten Protonen- Strahles mit einer selbstmagnetisch B_θ- isolierten Ionendiode. Dissertation, KfK 455, 4, 1989.

[3] D.D.Bloomquist, S.A.Sheffield. J. Appl. Phys, v.54, p.1717, (1983).

[4] K.Baumung,H.U.Karow,D.Rusch,H.J. Bluhm,P.Hoppe,G.I.Kanel,A.V.Utkin, and V.Licht. High-Power Proton Beam-Matter Interaction Diagnostics by Analysis of the Hydrodynamic Response of Solid Targets. To be published in J.Appl.Phys., June 1 st (1994).

E-BEAM HEATED PLASMA AS A TOOL FOR ITER DISRUPTION SIMULATIONS

V.T.Astrelin, A.V.Burdakov, V.V.Filippov, V.S.Koidan, S.V.Lebedev, K.I.Mekler, P.I.Melnikov, V.V.Postupaev, A.F.Rovenskikh, M.A.Shcheglov, K.V.Tsigutkin, S.G.Voropaev

Budker Institute of Nuclear Physics, 630090 Novosibirsk, Russia

H.Wuerz

Kernforschungszentrum Karlsruhe, Postfach 3640, D-76021 Karlsruhe, Germany

Abstract

The high-power hot plasma stream of E-beam heated plasma in the GOL-3 facility is used for exploratory plasma stream-target interaction experiments under conditions rather typical for the thermal quench phase of ITER tokamak plasma disruptions. The recent experimental results are presented.

1.Introduction. One of the key problem in tokamak fusion technology is the damage of the ITER tokamak divertor plates by the hot plasma during disruption events. In this case the energy densities of about 10 MJ/m^2 are estimated to be dumped to the divertor [1]. Such high heat loads result in instantaneous evaporation of the divertor plate material and it could limit the lifetime of the divertor. In existing tokamaks ITER typical heat loads are not achievable. Therefore the divertor material behavior has to be studied in facilities which allow a simulation of the ITER disruption conditions. As the electrons have a much longer range in the substance, than the ions of comparable energies, that the adequate energy spectrum of the plasma particles (mainly electrons) is important point for the simulation experiments.

The GOL-3 facility [2,3] by some of it's parameters is interested in application to simulate such experiments. Thus it was used for exploratory hot plasma stream-target experiments [4-6]. This paper presents our recent results.

2. Device and diagnostics. GOL-3 facility is a 7m open trap with magnetic field up to 6 T in homogeneous part. The hot plasma is prepared by the injection of high-power relativistic electron beam (0.8 MeV, 50 kA, 5 μs) into a neutral gas or preformed plasma. This hot plasma escapes through the ends of the facility. The hot plasma stream consists of the two components: bulk plasma electrons ($n_e \sim 10^{15}$ cm^{-3}) with T_e up to 1 keV and "suprathermal" electrons ($n_s \sim 3*10^{13} cm^{-3}$) with characteristic energy of 10-20 keV. The specific energy of the hot plasma stream can be up to 3 MJ/m^2 and the E-beam energy density in these condition is about 30 MJ/m^2.

GOL-3 device has a specially designed test chamber situated at the end opposite to the beam injection point (Fig.1). A magnetic field (2-12 T) can be in the test zone. The facility allows to study the samples of up to 6 cm diameter. The tilt of the samples to the magnetic field can vary from 0 to 90 degrees. Various substances (but mainly graphite) were exposed to a plasma stream.

The test chamber is supplied with a set of diagnostics specially designed for the studies of the plasma-target interaction.

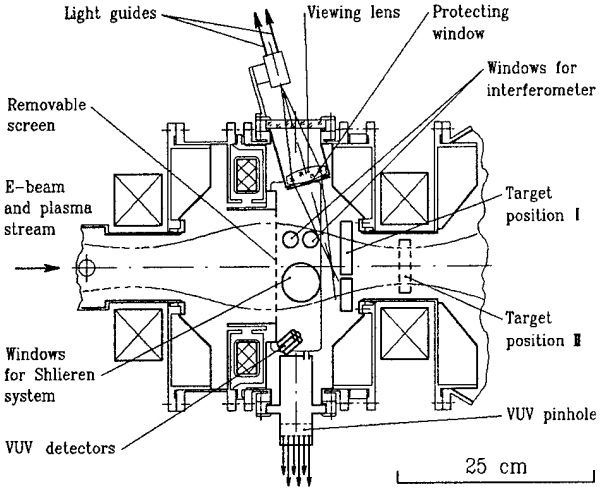


Fig.1. Test chamber

and it propagates both along and across magnetic field with the velocity ~10^6 cm/c. The cloud of evaporated substance

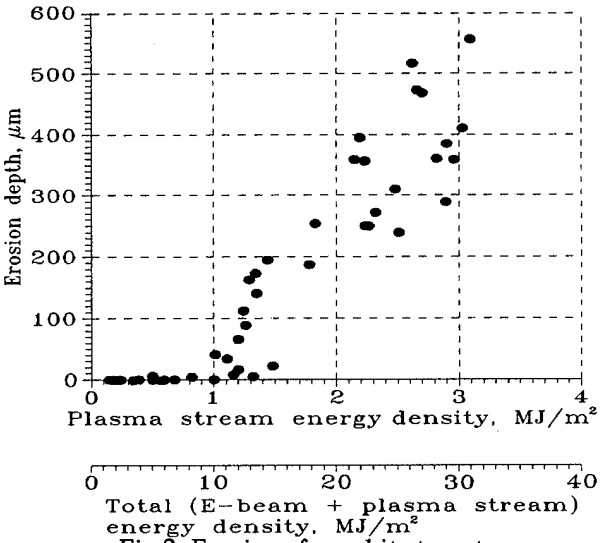


Fig.2. Erosion of graphite target

The facility is equipped also with the instrumentation needed for the studies of the surface damage: microbalancing, optical microscopy, microprofilometry, scanning electron microscopy.

3. Experimental results. The experimental results have shown that there are two different modes of interaction between the plasma stream of the GOL-3 device with solid target (graphite). A slight erosion of graphite of a few microns depth occurs in the first mode of interaction. In this mode the plasma energy is mainly absorbed in a thin layer of the target surface and E-beam specific energy less than 10 MJ/m^2. In front of the target surface the cloud of the evaporated substance is formed. In this case, on the boundary of a cloud faced to the irradiating flow a plasma corona is created with a temperature of 1-2 eV, density ~10^{17} cm^{-3} and an expansion velocity along the magnetic field of 2*10^6 cm/s. The main part of the evaporated substance has a temperature of 0.3-0.5 eV shields to a large extent the surface against the energy of incident plasma flow. These our results are quite close to those of experiments on irradiation of materials by flows from plasma guns [7,8].

With an excess of certain threshold of energy density of plasma stream on a surface (~1 MJ/m^2) the processes of interaction between the GOL-3 plasma flow and target surface change. The erosion depth starts to grow with an increase in energy density in plasma stream and it can reach ~500 micrometers per pulse at an energy density of 3 MJ/m^2 (Fig.2) for the fine-grain graphite MPG-6. In the mode of large erosion the substantial fraction of the vapor cloud is observed in the form of dust. The similar phenomena were observed on experiments with electron and laser beams [9-11]. In the paper [6] we came to the conclusion on the explosive character of graphite destruction during the volumetric energy release of fast electrons in the target substance. In order to understand the reasons and mechanism

of a large erosion the more detail analysis of the processes of the fast electrons interaction with target was made.

Using different diagnostics as: the Thomson scattering of ruby laser; a multifoil analyzer of the fast plasma electrons; the magnetic analyzer of electron energy spectrum for relativistic beam, the distribution function over electron energies was found out for electrons reaching the target (Fig.3). Knowing the electron spectrum in a flow incident to the solid target in various regimes of the GOL-3 device enables one to calculate the distribution of energy release by the depth of graphite target which are then compared with the results of erosion measurements.

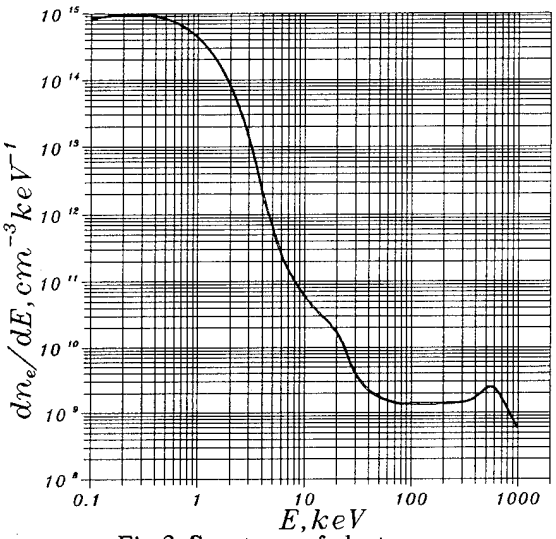


Fig.3. Spectrum of electrons

The distribution of the absorbed (over the target depth - x) energy of fast electrons was found out by:

$$\frac{dQ}{dx}(x) = \int_0^{E_{max}} \frac{dQ}{dE}(E)\, K(x,E)\, dE,$$

where $\frac{dQ}{dE}(E)$ is a time integrated distribution of the total energy of electrons incident to the target, $K(x,E)$ is distribution of energy release in a graphite target of monoenergetic electrons which was calculated by Monte-Karlo method with EMSH code [12].

The calculations have been performed for the energy release distribution over the target depth for characteristic regimes of the GOL-3 device. Fig.4 shows the calculated energy release over the depth of fine grain graphite MPG-6 for the shots with different energy content in a plasma flow (with electron energy of up to 30 keV): 0.8,1.4, 2.5 and 3 MJ/m^2. Note that the total energy content in the flow irradiated the target taking into account the whole electron energy spectrum up to 1 MeV is higher by the order of magnitude being respectively: 8, 14, 25 and 30 MJ/m^2. The comparison of this cal-

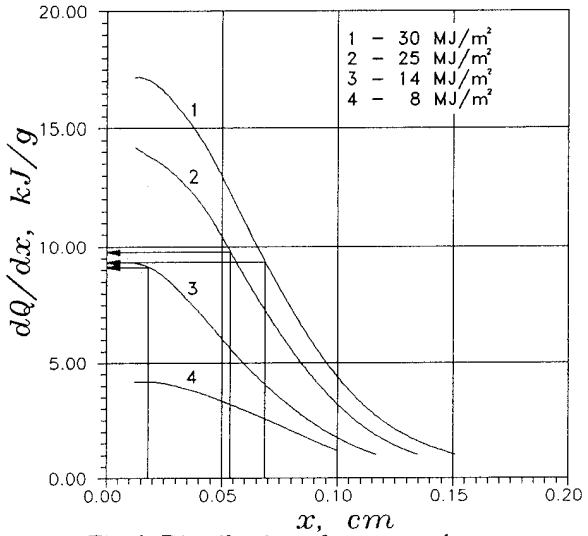


Fig.4. Distribution of energy release

culation with the graphite erosion observed in reality in these shots gives the graphite destruction threshold which turns to be in 8-10 kJ/g. This value is much less then that given in literature for the vaporization enthalpy (see, for example, [13]). This means that in case of our experiments the graphite destruction is of explosive character and it probably occurs as a result of a few factors:

material cracking (assumingly along the grain edges) because of fast heat tensions, vaporization inside the material and its "explosion" under action of vapor pressure; in this case, the scattering of a material occurs in the form of large fragments (clusters) of graphite.

The obtained results enable one to have somewhat new outlook on the possible consequences of hot plasma interaction with divertor plate of ITER tokamak in the regime of disruption. According to technological design of ITER the temperature of a plasma reaching the divertor plate in the disruption regime is 10-20 keV. At these temperatures the main electron energy will be released in a quite thin surface layer. However, the role of high energy part of electron distribution function (especially taking into account the contribution of runaway

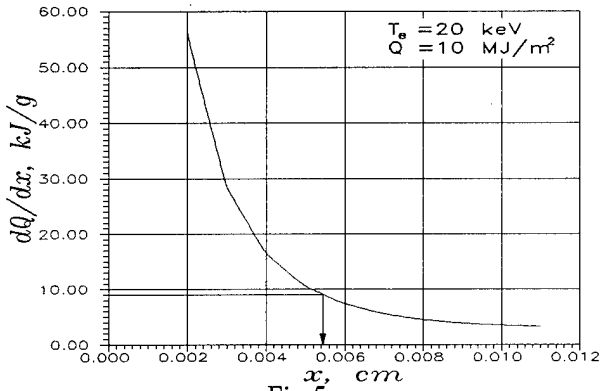


Fig.5.

electrons and the preliminary heating of divertor) might turn to be quite substantial. In fact, because of that the threshold of material destruction is lower then the evaporation energy, even the small contribution of 50-100 keV electrons can be sufficient for the graphite explosion and for the appearance of large erosion. For illustration of this statement Fig.5 shows the calculation of the energy release distribution over the depth for the Maxwellian flow of electrons with temperature of 20 keV and energy density of 10 MJ/m^2. For such parameters, the destruction threshold is achieved at the depth of 50 micrometers. Therefore, the graphite erosion may reach the value of order of tens microns. Note that electrons responsible for the explosive erosion are not shielded by vapor cloud. Thus, at the interaction of hot plasma with a surface the explosive erosion can be tens-hundred times larger than that obtained under conditions of the surface shielding by the cloud of evaporated substance at the same density of an incident energy.

4. Conclusion. E-beam heated plasma is a usefull tool for tokamak disruption simulations.

REFERENCES

1. T. Kuroda et al. ITER Plasma Facing Comp., ITER Document. Series N.30, IAEA, Vienna, 1991
2. A.V. Arzhannikov et al., Proc. 8-th Int. Conf. on High Power Particle Beams, Vol.1, p.14, Novosibirsk (1990)
3. A.V. Arzhannikov et al., Proc. 9-th Int. Conf. on High Power Particle Beams, Vol.1, p.127 (1992)
4. A.V. Burdakov et. al., 20th EPS Conference on Controlled Fusion and Plasma Physics, Lisboa, v. 17c, part II (1993)
5. A.V. Burdakov et al., Proc. XXI Int. Conf. on Phenomena in Ionized Gases, Vol.2, p.177 (1993)
6. A.V. Burdakov et. al., 6th Intern. Conf. Fusion Reactor Materials, Stresa, Italy, (1993), Abstracts, p. 63, to be published in Journal of Nuclear Materials.
7. N.I. Arkhipov et. al., Fusion Technology, (1992), pp. 171-175.
8. T.A. Burtseva et. al., Journal of Nuclear Materials, 191-194 (1992), pp. 309-314.
9. A.I. Melker, I.L. Tokmakov, Fizika i khimija obrabotki materialov, 5 (1977), pp. 62-67, (in Russian).
10. J. Linke et. al., Fusion Technology, (1990), pp. 428-432.
11. J.G. Van der Laan and H.T. Klippel, Journal of Nuclear Materials, 179-181 (1991), pp. 184-188.
12. V.A. Tayursky, Preprint BINP N.89-16, Novosibirsk, 1989 (in Russian)
13. J.G. Van der Laan et. al., Journal of Nuclear Materials, 196-198 (1992), pp. 612-617.

Evaluation of Temperature and Pressure of Ablation Plasma in an Intense, Pulsed, Ion-Beam Evaporation

Xiangdong Kang, Katsumi Masugata and Kiyoshi Yatsui
Laboratory of Beam Technology & Department of Electrical Engineering
Nagaoka University of Technology, Nagaoka, Niigata 940-21, Japan

Abstract

An ablation plasma in an intense, pulsed, ion-beam evaporation has been evaluated from the measurement of ion-flux density by a biased-ion collector. The target mass loss is detected by the measurement of the weight of the target in the comparison before and after the shot. An one-dimensional hydrodynamic model is introduced by assuming a high-power, light-ion beam-driven expansion and the following adiabatic expansion into vacuum. Using this model, it is possible to deduce the temperature and the pressure from the data of the ion flux and the mass loss of the target, respectively. This method can also be applicable to other intense pulsed energy sources such as lasers or electron beams.

I. Introduction

Recently, an intense, pulsed, light-ion beam (LIB) has been successfully applied for materials science. Particularly, various thin films have been effectively prepared by intense pulsed ion-beam evaporation technique (IBE).[1-8] The deposition characteristics of the IBE have been found to be different from other methods such as vacuum deposition or sputtering. Principally, the IBE is similar to a pulsed-laser evaporation, but the mechanism of the energy deposition is different. Since, only the surface layer of the target, which corresponds to the stopping range of the LIB, is effectively heated by the IBE, the mass of the evaporated material per unit area (M) is considered to be constant in time. To study the behavior of the ablation plasma in the IBE, we have successfully introduced a one-dimensional model to deduce the temperature (T_0) or the pressure using the experimental data on the ion flux or the mass loss of the target.[5-8]

The purpose of this paper is to investigate the basic characteristics of the ablation plasma produced by the IBE. The ablation plasma has been observed from the measurement of ion-flux density by a biased-ion collector. The target mass loss is detected by the measurement of the weight of the target in the comparison before and after the shot. From the model, the analytic solutions are derived to deduce the temperature and pressure by using the data of the ion flux and the mass loss of target determined experimentally, respectively.

II. Experiment

Figure 1 shows the cross-sectional view of the experimental setup. An intense, pulsed, charged-particle beam generator "ETIGO-II",[1] which consists of a Marx generator, a pulse-forming line and an ion diode, was used in the experiments. The LIB, which mainly consists of protons, is extracted from the geometrically focused, magnetically insulated diode with a flashboard anode of polyethylene. The target of Ti, inclined 45° with respect to the beam axis, was located at z = 140 mm downstream from the anode. The ion flux of the ablation plasma was measured by a biased-ion collector (BIC)[9] with the potential of - 20 V. The distance between the BIC and the surface of target is x = 3.7 cm.

The patterns of LIB-damage on target (Ti) and evaporation-particle deposition on glass substrate have been measured, where the substrate was placed at the same position as that of the BIC, resulting in the diameter of ~ 3.5 cm and ~ 4 cm, respectively. Since these

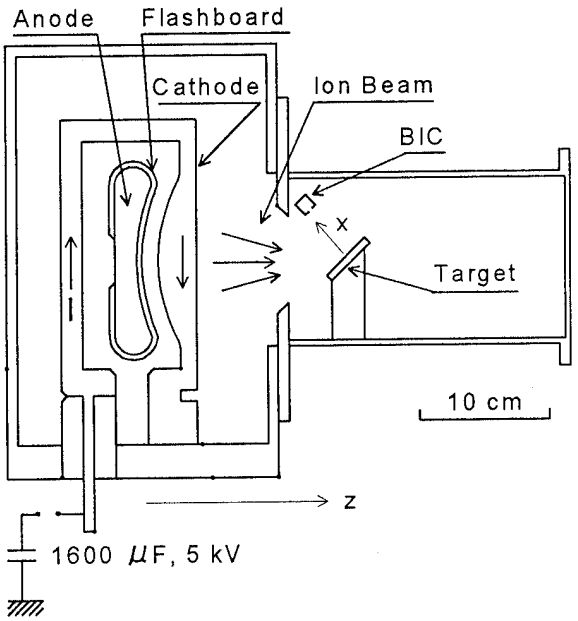


Fig. 1 Cross-sectional view of experimental setup for IBE.

two patterns are approximately the same size, the IBE process seems to be considered to be one-dimensional. The target mass loss has been measured by the comparison of the weights of the target before and after the shots. The mass of the evaporated material per unit area (M) was estimated to be ~ 1.4 mg/cm^2 for the LIB power density of ~ 1 GW/cm^2 with the pulse width of $\tau \sim 70$ ns.

III. Analytic Solution for IBE

To study the basic characteristics of the ablation plasma for the IBE process, an one-dimensional hydrodynamic model was proposed.[5] In this model, we separate the process of the IBE into two stages. The first stage (a) is the high-power LIB-driven expansion. It includes the interaction of the LIB with the target, resulting in the evaporation of the surface, and the interaction of the evaporated material with the incident LIB. Thus, a high-density plasma is produced, and subsequently expansion takes place. In this stage, since the surface layer determined by the range of LIB is heated quickly, the time derivative of the mass of the evaporated material per unit area is assumed to be zero, namely M = constant. For the second stage (b) after the termination of the LIB, an adiabatic expansion of the plasma into vacuum takes place, which leads to the deposition of thin films on the substrate.

By using this model, we have obtained the analytic solution[5] for the IBE as

$$v = \frac{x}{t}, \tag{1a}$$

$$T = T_0 \frac{1+f_0}{1+f}\left[\frac{\tau}{t}\right]^{\gamma-1}\left(\frac{(1+\alpha)(3+\alpha)}{2(\gamma-1)}+\frac{(3+\alpha)^2}{4}\right)^{-\frac{\gamma-1}{2}}, \tag{1b}$$

$$\rho = \frac{\frac{M}{t}\sqrt{\frac{m}{kT_0(1+f_0)}}}{\sqrt{\frac{\pi}{2}\left(\frac{2}{\gamma-1}+\frac{3+\alpha}{1+\alpha}\right)}}\exp\left[-\frac{\frac{1}{2}m\left(\frac{x}{t}\right)^2}{kT_0(1+f_0)\left(\frac{2}{\gamma-1}+\frac{3+\alpha}{1+\alpha}\right)}\right], \tag{1c}$$

where T_0 is the temperature (T), f_0 the average ionization (f) at $t = \tau$ and $x = 0$, α is the constant, and γ, m, t, ρ, v, k, and x are the specific heat constant, the particle mass, the time, the mass density, the velocity, the Boltzmann constant, and the distance from the target, respectively. Assuming the data of ion flux, which diagnosed by BIC placed at the position of x = 3.7 cm, as $J_{BIC} \propto \rho v$, we can obtain J_{BIC} as

$$J_{BIC} = \frac{Q_0}{t^2}\exp\left\{-\frac{\frac{1}{2}m(\frac{x}{t})^2}{[\frac{2}{\gamma-1}+\frac{3+\alpha}{1+\alpha}]kT_0(1+f_0)}\right\}, \tag{2}$$

where Q_0 is the constant. The temperature T_0 can be obtained by

$$kT_0 = \frac{\frac{1}{2}m(\frac{x}{t_{max}})^2}{[\frac{2}{\gamma-1}+\frac{3+\alpha}{1+\alpha}](1+f_0)}, \tag{3}$$

where t_{max} represents the time at which the BIC signal attains the peak. In eq. (3), $\alpha > 0$ and $\alpha < 0$ corresponds to the cases that the LIB power rises and falls in time, respectively. In the estimate of T_0, constant energy deposition rate

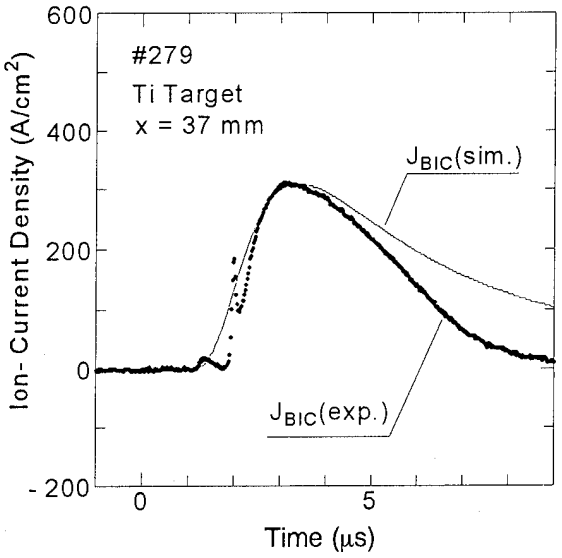


Fig. 2 BIC data of the experiment (dots) compared with the simulation (solid line) for Ti target at LIB power density of ~ 1 GW/cm^2.

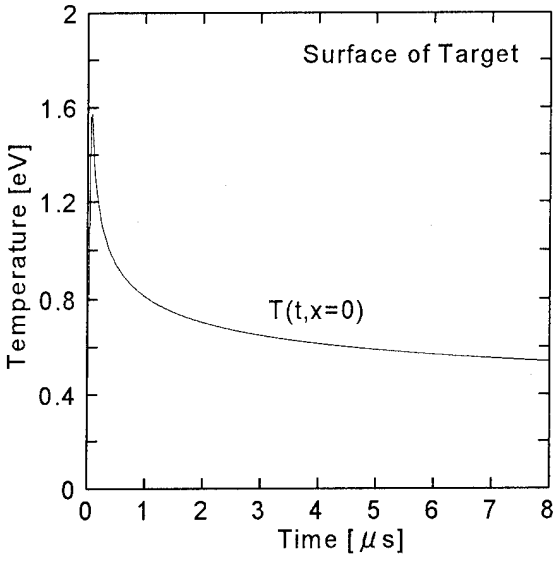


Fig. 3 Calculated curve of temperature $T(t, x)$ as a function of time (t) at $x = 0$.

($\alpha = 0$) is assumed in the stage (a).[5] For the excited or ionized monoatomic species, we put $\gamma = 1.2 \sim 1.3$.[10] By use of Saha equation, we have also estimated the average ionization (f_0) for Ti.[5]

Furthermore, at the position of the substrate, $x = 3$ cm, the dynamic pressure, $p_d = \frac{1}{2}\rho v^2$, and the static pressure, $p = (\gamma - 1)\rho e$, can be given by

$$p_d = \frac{Mx^2}{\sqrt{2\pi}t^3 u_0}\exp\left\{-\frac{(x/t)^2}{2u_0^2}\right\}, \qquad (4)$$

and

$$p = \frac{2M(\gamma-1)(\frac{\sigma_0}{u_0 t})^\gamma u_0^2}{\sqrt{2\pi}\left\{2+\frac{(\gamma-1)(3+\alpha)}{1+\alpha}\right\}\sigma_0}\exp\left\{-\frac{(x/t)^2}{2u_0^2}\right\}, \qquad (5)$$

where, the specific energy:

$$e = \frac{kT(1+f)}{m(\gamma-1)}$$

was used, and u_0 and σ_0 were given by

$$u_0 = \frac{3.7[\mathrm{cm}]}{\sqrt{2}t_{\max}},$$

and

$$\sigma_0 = \frac{2u_0\tau}{(3+\alpha)\sqrt{1+\frac{2(1+\alpha)}{(3+\alpha)(\gamma-1)}}},$$

respectively.

IV. Results and Discussion

Figure 2 shows the time evolution of the BIC data. From Fig. 2 and eq. (3), we estimate $T_0 \sim$ 1.6 eV. The corresponding theoretical curve of J_{BIC} which is calculated by eq. (2) was also plotted in Fig. 2 by solid line. From this estimation and our model, we can calculate the variation of the temperature as a function of the time on the surface of the target (x=0) as shown in Fig. 3. Initially, the plasma is in the stage (a) of the LIB-driven expansion. The temperature increases quickly from 0 eV to its peak of 1.6 eV in 70 ns. After the LIB terminates, the plasma is in the stage (b) of the adiabatic expansion. The thermal energy of the plasma is converted into kinetic energy, and the plasma cools rapidly to its half peak of ~ 0.8 eV within 1 μsec. Later, the plasma temperature starts to decrease slowly, which means the conversion of the thermal energy

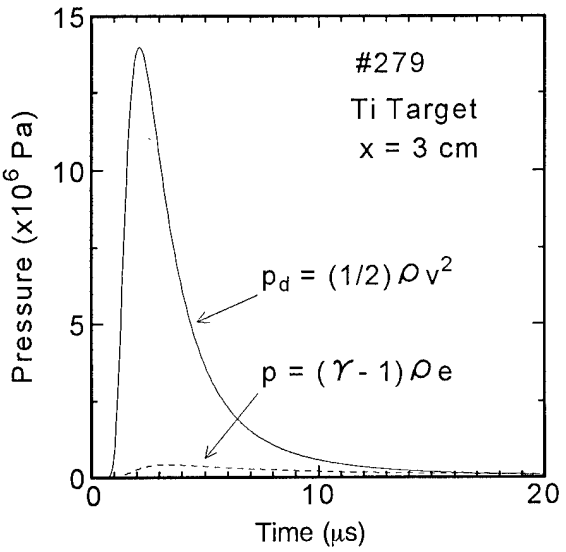


Fig. 4 Calculated curves of dynamic (p_d) and static (p) pressures as a function of time at x = 3 cm for Ti target at LIB power density of ~ 1 GW/cm^2.

into the kinetic energy is slow in the low plasma density.

From the mass-loss data of $M \sim 1.4$ mg/cm^2 and BIC data of Fig. 2 ($u_0 \sim 0.8$ cm/μs), the dynamic pressure of the ablation plasma estimated by eq. (3), $p_d = \frac{1}{2}\rho v^2$, at $x \sim 3$ cm is plotted in Fig. 4 by a solid line. We see p_d (peak) ~ 1.4 $\times 10^7$ Pa and its pulse width is ~ 2.4 μs.

Furthermore, using eqs. (4) and (5), the static pressure (p) at $x \sim 3$ cm is also plotted in Fig. 4 by a dashed line. We see p is much smaller than p_d in the IBE. In other words, the kinetic energy of the ablation plasma is much larger than the thermal energy.

V. Summary

The characteristics of the ablation plasma produced by the IBE has been studied experimentally and theoretically by the measurement of the ion flux and the target mass loss. Using the analytic solution derived from one-dimensional hydrodynamic model, the temperature of T_0 is deduced to be 1.6 eV on the surface of the Ti target, the dynamic pressure of the ablation plasma $p_d \sim 1.4 \times 10^7$ Pa and the pulse width of ~ 2.4 μs (at $x \sim 3$ cm) at the LIB power density of ~ 1 GW/cm^2 and τ (pulse width) ~ 70 ns. The present method will be sufficiently applicable to the ablation plasma such as produced by intense lasers or electron beams.

REFERENCES

1. K. Yatsui, A. Tokuchi, H. Tanaka, H. Ishizuka, A. Kawai, E. Sai, K. Masugata, M. Ito and M. Matsui: *Laser and Particle Beams* **3** (1985) 119.
2. Y. Shimotori, M. Yokoyama, S. Harada, H. Isobe, K. Masugata and K. Yatsui: *J. Appl. Phys.* **63** (1988) 968.
3. Y. Shimotori, M. Yokoyama, S. Harada, K. Masugata and K. Yatsui: *Jpn. J. Appl. Phys.* **28** (1989) 468.
4. K. Yatsui: *Laser and Particle Beams* **7** (1989) 733.
5. X. Kang, K. Masugata and K. Yatsui: *Jpn. J. Appl. Phys.* **33**, 1155 (1994).
6. K. Yatsui, X. Kang, T. Sonegawa, T. Matsuoka, K. Masugata, Y. Shimotori, T. Satoh, S. Furuuchi, Y. Ohuchi, T. Takeshita and H. Yamamoto: *Phys. Plasmas* **1**, 1370 (1994).
7. X. Kang, K. Masugata and K. Yatsui: "Characteristics of Ablation Plasma in Intense, Pulsed, Ion-Beam Evaporation", *Trans. IEE Japan* **114**, #9 (1993) (in Japanese) (in press).
8. X. Kang, K. Masugata, and K. Yatsui, "Ablation Plasma Temperature Produced by Intense, Pulsed, Ion-Beam Evaporation", *Jpn. J. Appl. Phys.* **33** (1994) (in press).
9. C. Eichenberger, S. Humphries, Jr. and J. Maenchen: *J. Appl. Phys.* **48** (1977) 1447.
10. Ya. B. Zeldovich and Yu. P. Raiser: "*Physics of Shock Wave and High Temperature Hydrodynamic Phenomena*" (Academic Press, 1968), Vol. II, p. 573.

The Use of 2-D Distributed Feedback for Synchronization of Radiation in FEL's driven by Intense Sheet and Tubular Relativistic Electron Beams

N.S.Ginzburg, N.Yu.Peskov, A.S.Sergeev

Institute of Applied Physics, Russian Academy of Sciences, 46 Ulyanov Street, 603600 Nizhny Novgorod, Russia.

Abstract

It is proved that there is the possibility to use 2-D distributed feedback to ensure powerful spatial-coherent microwave emission of sheet and tubular relativistic electron beam with transverse size exceeding wavelength by the factor $10^2 - 10^3$.

Introduction

For generation of superpower microwave radiation it is perspective to drive FEL's by intense sheet and tubular (hollow) relativistic electron beams with particle energy 1-2MV, total current up to 100kA and power up to 100GW. However, the typical transverse size of such beams runs up to 10^2cm [1,2]. As a result, the main problem is to provide spatial coherence of emission from different parts of electron beams. For solving this problem in [3,4] the use of two-dimensional distributed feedback, which may be realized in a planar and coaxial 2-D Bragg resonator, proposed. The additional transverse electromagnetic energy fluxes arising in these resonators should synchronize radiation of electron beams with the transverse size essentially exceeding the wavelength.

FEL with Planar 2-D Bragg Resonator and Sheet Electron Beam

Let us consider the planar 2-D Bragg resonator (Fig.1a) formed by two metal plates with width l_x, length l_z and distance between them a_0, which are corrugated as $a = a_1\left(\cos\left(\bar{h}x - \bar{h}z\right) + \cos\left(\bar{h}x + \bar{h}z\right)\right)$, where $\bar{h} = \sqrt{2}\pi/d$, d is corrugation period, a_1 is corrugation depth. Assuming $\bar{h}a_1 << 1$ we will seek the field in the resonator in the form of four coupled waves: $\mathcal{A}_\pm$ propagating in the $\pm z$ and $\mathcal{B}_\pm$ propagating in the $\pm x$ directions:

$$\vec{E} = \mathrm{Re}\left[\vec{y}_0\left(\mathcal{A}_+(x,z,t)e^{-i\bar{h}z} + \mathcal{A}_-(x,z,t)e^{i\bar{h}z} + \right.\right.$$

$$\left.\left. + \mathcal{B}_+(x,z,t)e^{-i\bar{h}x} + \mathcal{B}_-(x,z,t)e^{i\bar{h}x}\right)e^{i\omega t}\right], \quad (1)$$

where $\omega = \bar{h}c$ is Bragg frequency.

We investigate here excitation of the 2-D Bragg resonator by a sheet relativistic electron beam. Suppose that electrons oscillate either in the undulator field (ubitron) or in the uniform axial magnetic field (cyclotron autoresonance maser). In assumption that only the $\mathcal{A}_+$ wave is synchronous to the electrons moving in the $+z$ direction and the rest partial waves do not interact with the beam, the oscillations build-up can be described by the following system of equations:

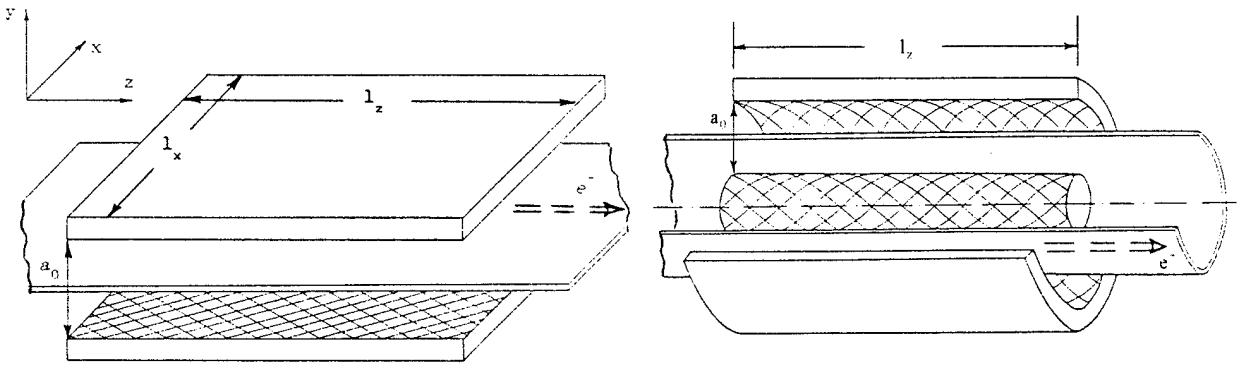


Fig.1 *The general scheme of FEL-generator with two-dimension Bragg resonator driven by sheet (a) or tubular (b) electron beam (the drift velocity of electrons directed along z coordinate)*

$$\left(\frac{\partial}{\partial Z}+\beta_{gr}^{-1}\frac{\partial}{\partial\tau}\right)\mathcal{A}_+ + \sigma\mathcal{A}_+ + i\alpha(\mathcal{B}_+ + \mathcal{B}_-) = \frac{1}{\pi}\int_0^{2\pi} e^{-i\theta}d\theta_0$$

$$\left(-\frac{\partial}{\partial Z}+\beta_{gr}^{-1}\frac{\partial}{\partial\tau}\right)\mathcal{A}_- - \sigma\mathcal{A}_- + i\alpha(\mathcal{B}_+ + \mathcal{B}_-) = 0$$

$$\left(\pm\frac{\partial}{\partial X}+\beta_{gr}^{-1}\frac{\partial}{\partial\tau}\right)\mathcal{B}_\pm \pm \sigma\mathcal{B}_\pm + i\alpha(\mathcal{A}_+ + \mathcal{A}_-) = 0 \qquad (2)$$

$$\left(\frac{\partial}{\partial Z}+\beta_{ll}^{-1}\frac{\partial}{\partial\tau}\right)^2\theta = \mathrm{Re}\left(\mathcal{A}_+ e^{i\theta}\right)$$

Boundary conditions for Eqs.(2) take the form

$$\mathcal{A}_+(X,-L_z/2)=0\,,\quad \mathcal{A}_-(X,+L_z/2)=0\,,$$
$$\mathcal{B}_+(-L_x/2,Z)=0\,,\quad \mathcal{B}_-(+L_x/2,Z)=0\,,$$
$$\theta|_{Z=-L_z/2}=\theta_0\in[0,2\pi)\,, \qquad (3)$$
$$\left(\frac{\partial}{\partial Z}+\beta_{ll}^{-1}\frac{\partial}{\partial\tau}\right)\theta\Big|_{Z=-L_z/2}=-\Delta\,.$$

Here

$$Z=\bar{h}zC\,,\quad X=\bar{h}xC\,,\quad \tau=\omega tC\,,\quad v_{gr}=\beta_{gr}c$$

$$C=\left(\frac{eI_0\lambda^2\kappa^2\mu}{8\pi\gamma_0 mc^3 a_0}\right)^{1/3}$$ is gain parameter,

α is wave coupling coefficient, θ is electron phase relative to synchronous wave, Δ is initial mismatch of synchronism, κ is parameter proportional to the oscillatory particles velocity, μ is bunching parameter, I_0 is electron current, $L_{x,z}=h\bar{l}_{x,z}C$, σ is ohmic losses (these losses are important for FEL with coaxial Bragg resonator, so in this section we suppose $\sigma=0$).

Dependencies of efficiency on time at the region of parameters, where the establishment of the stationary regime of generation takes place, are presented in Fig.2. At the stationary regime spatial structures of partial waves $\mathcal{A}_\pm$ and $\mathcal{B}_\pm$ are close to the structures of corresponding waves for the most high-Q mode of "cold" resonator (compare Fig.3 and Fig.3 in Ref.[4]). The frequency of this mode, as well as the oscillations frequency, coincides with the Bragg one. It is important to note that transverse distribution of the amplitude of synchronous wave $\mathcal{A}_+$ does not depend on transverse coordinate x that provides equal energy extraction for all parts of the electron beam.

From Eqs.(2) it can be shown that at stationary conditions $(\partial/\partial\tau=0)$, when the fundamental mode is excited, distribution of waves along longitudinal coordinate, as well as efficiency, does not change when conditions $\alpha^2 L_x = const$ and $L_z = const$ are satisfied. Such a scaling gives us the possibility to increase the width of the interaction space

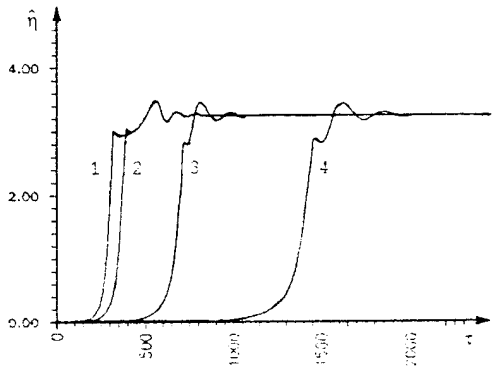


Fig.2 *Build up stationary regime of oscillations. Dependencies of normalized efficiency on time:* $L_z = 4$, $\Delta = -1{,}82$, $\alpha^2 L_x = 1{,}25$: 1 $L_x = 0{,}8$; 2 $L_x = 3{,}2$; 3 $L_x = 12{,}8$; 4 $L_x = 28{,}8$.

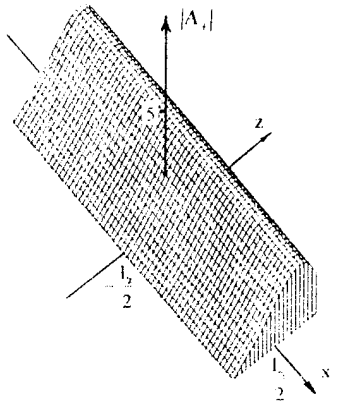


Fig.3 *Spatial distribution of partial wave amplitude* $\mathcal{A}_+$ *in the stationary regime of oscillations:* $L_z = 4$, $\Delta = -1{,}82$, $L_x = 12{,}8$, $\alpha = 0{,}32$.

simultaneously decreasing coupling parameter (for example, decreasing corrugation depth). Computer simulation of nonstationary equations (2) confirms this conclusion. If $L_z \le 5$ the synchronization regime is stable at least up to $L_x \le 30$ However, the transitional time increases with increasing system's width (see Fig.2).

Using the theory carried out we have designed the FEL with wavelength 4mm and output power up to 20GW driven by relativistic electron beam with transverse size 140cm , electron current 1kA/cm , particles energy 1MeV and pulse duration 10^{-6}s (accelerator **U-2** , *INP RAS, Novosibirsk* [1]).

FEL with Coaxial 2-D Bragg Resonator and Tubular Electron Beam

Scheme of the FEL with tubular electron beam and coaxial 2-D Bragg resonator is presented in Fig.1b. For this scheme double-periodic corrugation of the walls couples the $\mathcal{A}_\pm$ waves propagating in $\pm z$ direction and the $\mathcal{B}_\pm$ waves propagating in the azimuthal $\pm\varphi$ direction. Let us assume that the resonator radius R exceeds essentially the distance between the plates and the wavelength ($R >> \lambda, a_0$). Under these conditions, neglecting low curvature of the plates, we can describe excitation of this resonator by tubular electron beam with the help of Eqs.(2), where $X = R\varphi$ is coordinate along the perimeter of the resonator. Boundary conditions (3) in the longitudinal direction for waves $\mathcal{A}_\pm$ and for electrons don't change, while in the transverse direction the conditions of cyclicity are valid:

$$\mathcal{A}_\pm(-L_x/2, Z) = \mathcal{A}_\pm(+L_x/2, Z) ,$$
$$\mathcal{B}_\pm(-L_x/2, Z) = \mathcal{B}_\pm(+L_x/2, Z) , \qquad (4)$$

where $L_x = 2\pi RC$ is normalized perimeter of the resonator. According to relations (4) it is possible to expend solutions of Eqs.(2) in Furies series and considered every term as a mode with azimuthal index m.

An important specific feature of coaxial 2-D Bragg resonator is exitation of a non-disappeared azimuthal-symmetric eigenmode (i.e. a mode with the infinite quality factor), if we don't take into account ohmic or diffraction losses for the partial waves $\mathcal{B}_\pm$. At the same approximation, azimuthal nonsymetric eigen-modes ($m \neq 0$) have finite losses (finite quality). Therefore, under excitation of such a resonator by electron beam selective discrimination azimuthal nonsymetric modes arise. However, establishment of stationary generation regime the losses ($\sigma \neq 0$) for partial waves $\mathcal{B}_\pm$ have principal importance.

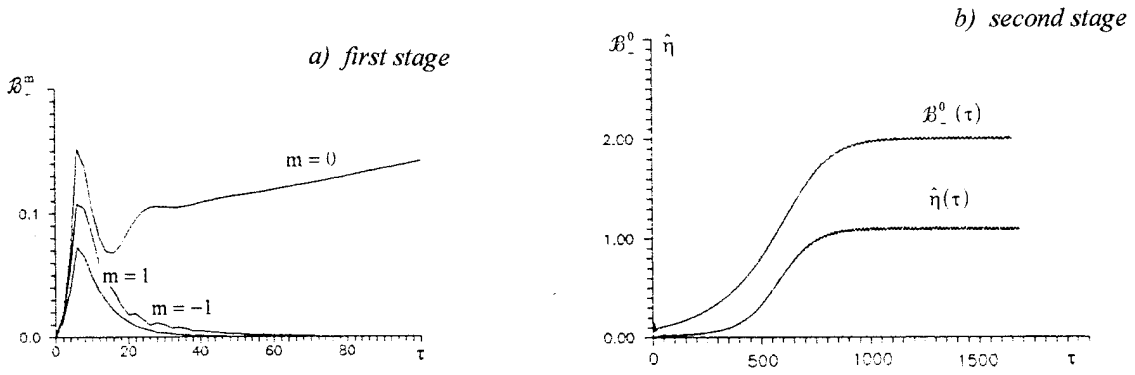


Fig.4 *Normalized efficiency and amplitudes of azimuthal harmonics in spectrum of partial wave* $\mathcal{B}_+$ *vs time:* $L_z = 6{,}8$, $\Delta = -0{,}65$, $L_x = 12{,}8$, $\alpha = 0{,}1$, $\sigma = 0{,}1$

Transient process may be divided into two stages. At the first, relatively short stage, during several passes of partial waves over resonator azimuthal symmetric distributions of waves amplitudes are formed. At the next stage, lasting for a longer time than the first one, storage of electromagnetic energy in resonator occurs. At the end of this stage the stationary single-frequency generation regime establishes. This conclusion is illustrated by Fig.4 that represents the time-dependencies of different azimuthal harmonics in spectrum $\mathcal{B}_\pm$ in the cross-section $Z = L_z$.

At time $t = 0$ we take the wave $\mathcal{A}_+$ as initial perturbation, in the spectrum of which amplitudes of different harmonics with number $m \in \{-1, 0, 1\}$ are equal. At first, transformation of the wave $\mathcal{A}_+$ into the waves $\mathcal{B}_\pm$ takes place and the amplitude of all harmonics in spectrum of $\mathcal{B}_\pm$ growth. But then, amplitudes of all harmonics except $m = 0$ fall practically to zero. As is clear from comparing Fig.4a and Fig.4b, the main part of the transitional process occupies the second stage (stage of energy storage) when distribution of waves amplitudes is azimuthal symmetric and equal energy extraction from different parts of electron beam take place. Due to this reason, total transitional time only to a small degree depends on the perimeter of the system L_x . Characteristics of stationary regime of generation do not depend on full perimeter too.

Note that the establishment of stationary regime we observe in the computer simulation at least to the value of normalized perimeter $L_x = 30$ what corresponds to $R/\lambda \approx 10^2$ under gain parameter $C = 10^{-2}$. This confirms the possibility of using large size tubular electron beams for generation of powerful spatial-coherent radiation.

References

1. Arzhannikov A.V., Nikolaev V.S., Sinitsky S.L. e.a. // J. of Appl. Phys., vol.72, no.4, pp.1657-1659, 1992.
2. A.N.Bastrikov, S.P.Bugaev, I.N.Kiselev e.a. // Zh. Tekh. Fiz., vol.58, no.3, pp.483-488, 1988.
3. Ginzburg N.S., Peskov N.Yu., Sergeev A.S. // Pis'ma v Zh. Tekh. Fiz., vol.18, no.9, pp.23-28, 1992 (Sov. Tech. Phys. Lett., vol.18, no.5, pp.285-287, 1992).
4. Ginzburg N.S., Peskov N.Yu., Sergeev A.S. // Optics Commun., vol.96, no.4-6, pp.254-258, 1993.

INCREASING USEFUL FEL UNDULATOR APERTURE, BEAM CURRENT AND POWER OF AN ELECTRON BEAM PROPAGATING IN A LONGITUDINAL MAGNETIC FIELD

V.A. Papadichev
Lebedev Physical Institute, 53 Leninsky Prospect,
117924 Moscow, Russia

Abstract

Transverse inhomogeneity of undulator magnetic field prevents using large diameter electron beams for FEL because of longitudinal velocity spread. A method of beam conditioning was proposed by A.M. Sessler et al. [1]. The method is rather complex and expensive, so it is most suitable for large FEL facilities to obtain unique ultrashort-wavelength radiation. When an electron beam is transported in a longitudinal magnetic field, a simpler method of beam conditioning becomes possible. One can equalize $\beta_{\parallel}$ *across the beam by imparting supplementary cyclotron velocities to inner electrons with a profile* $\Delta v[1 - (r/r_0)^2]$, *where* r *and* r_0 *are current radial coordinate and beam outer radius, respectively. Related devices to achieve* $\beta_{\parallel} = const.$ *are described and discussed as well as the influence of beam space charge.*

1. Introduction

The transverse inhomogeneity of the undulator magnetic field and betatron oscillations of electrons moving off-axis cause the electrons to acquire additional transverse velocities, leading to the spread in longitudinal velocity $v_z = v_{\parallel}$ in the beam. This prevents the outer particles of the beam from taking part in the amplification of the electromagnetic wave along the entire FEL length because being a bit slower than the resonant, synchronous particles (supposed to be paraxial here), they soon fall out of phase with the amplified wave. Accelerating the off-axis particles so that they acquire additional axial velocity one can have beam electrons moving through the undulator with the same longitudinal velocity. This method was proposed recently by A.M. Sessler and coworkers [1]. A special 10 - 50 m long focusing lattice consisting of 10 - 50 periods and having accelerating cavities operating in the TM_{210} mode are to be employed. This complex system is most suitable for large FEL facilities to obtain unique ultrashort-wavelength radiation.

On the other hand, many FEL experiments are conducted with high-current electron beams at low and medium electron energies (0.5 - 15 MeV). Such beams are usually transported in a longitudinal magnetic field to prevent beam blow-up due to space-charge forces. Undulator field inhomogeneity prevents using large-diameter beams and fully exploiting the high-power possibilities of pulsed accelerators. The wide-spread last years' tendency of using microundulators makes the problem more acute since the useful aperture of the undulator becomes too small without beam conditioning. Of course, one could employ the above method, but there is the simpler one for the beam propagating in a magnetic field, which is more appropriate for the modest size of accelerators used. In this case, as it will be shown below, the electrons do not experience betatron oscillations and subjected only to a slight azimuthal drift and undulator orbital motion modified by the longitudinal magnetic field. Cyclotron gyration as a free motion is also possible in addition to those induced orbital and drift motions. So it is possible to equalize $\beta_{\parallel}$ across the beam, i.e., to compensate mainly for the increase of the transverse orbital velocity with the radius, by imparting supplementary cyclotron velocities to inner electrons with a radial profile $\Delta v_c[1 - \alpha r^2/r_0^2]$.

The effect of the azimuthal drift velocity on the longitudinal velocity of electrons can be taken into account, but is usually negligible in the majority of FEL experiments, as will be shown in Sect. 2. A method of excitating the required profile of cyclotron gyration velocities and appropriate devices for it are described in Sect. 3. Comparison of two methods of electron beam conditioning for FEL use is made in the concluding Sect. 4.

2. Electron motion in an undulator with longitudinal magnetic field

The equation of the transverse electron motion for the simple model of a round cylindrical beam in the helical undulator, using the method of [2], can be written as:

$$d^2\eta/dz^2 - ik_c^2 d\eta/dz + k_{bs}^2 v_{\|}\eta = - i(e/(m_o c^2\gamma\beta_{\|}))(B_x + iB_y) . \quad (1)$$

where $\eta = x + iy$, $i = (-1)^{1/2}$, $v_z = v_{\|} = \text{const}$, $k_c = \omega / v_{\|}$ is the cyclotron-motion wave number, $\omega = (eB_{\|})/(m_o c\gamma)$ cyclotron frequency in longitudinal magnetic field $B_{\|}$; B_x and B_y undulator field components, $k_{bs} = (k_\beta^2 - k_s^2)^{1/2}$ is the betatron wave number accounting for space-charge forces $e(E_r - \beta_{\|}H_\theta)$ when $B_{\|} = 0$, $k_\beta = k_o K/(\gamma 2^{1/2})$ is the betatron wave number without space-charge influence when $B_{\|} = 0$, $K = \beta_\perp\gamma$, $k_s = (2I_b/I_o)^{1/2}/(\gamma^{1/2}\beta_{\|}\gamma_{\|}r_o)$ is the space-charge wave number accounting for electrical and magnetic fields $e(E_r - \beta_{\|}H_\theta)$ of the homogeneous cylindrical beam, I_b the beam current, $I_o = m_o c^3/e \approx 17$ kA, r_o beam outer radius, and $\gamma_{\|} = (1 - \beta_{\|}^2)^{-1/2}$, γ - the electron energy in rest mass units $m_o c^2$, $\beta_{\|} = v_{\|}/c$ electron longitudinal velocity in units of the velocity of light.

The equation (1) is a linear second-order differential equation with constant coefficients and the presence of the right-hand member. To determine the undulator orbit of zero approximation, we suppose here the undulator field with the period l_o and wave number $k_o = 2\pi/l_o$ to be $B_x + iB_y = B_\perp [\cos(k_o z) + i \sin(k_o z)]$ with no dependence on the transverse coordinates because this dependence was taken into account in the first order by adding $k_{bs}^2 v_{\|}\eta$.

The forced (orbital) oscillations are

$$\eta_1 = Ce^{ik_o z} \quad (2)$$

with C determined after substituting (2) into (1)

$$C = -i(eB_\perp/(m_o c^2\gamma\beta_{\|}))/(k_{bs}^2 + k_c k_o - k_o^2) . \quad (3)$$

The general solution is

$$\eta = Ae^{ik_1 z} + Be^{ik_2 z} + Ce^{ik_o z} \quad (4)$$

where $k_{1,2} = k_c/2 \pm ((k_c/2)^2 + k_{bs}^2)^{1/2}$ (5)

are wave numbers of modified cyclotron gyration and azimuthal drift caused by the undulator focusing and beam space-charge forces. Since usually $k_{bs} << k_c$, one has

$$k_1 \approx k_c \text{ and } k_2 \approx - k_{bs}^2/k_c . \quad (6)$$

A and B depend on initial coordinates and velocities. If $x = y = v_x = v_y = 0$ at $z = 0$, then

$$A = C(k_o - k_2)/(k_2 - k_1) ; \quad B = C(k_o - k_1)/(k_1 - k_2) \quad (7)$$

Thus, electrons experience three types of motion: 1) undulator orbital motion $\eta_1 = Ce^{ik_o z}$, 2) cyclotron gyration $Ae^{ik_1 z}$ with slightly increased cyclotron frequency $\Delta\omega/\omega = k_{bs}^2/k_c^2$ and 3) low-frequency circular drift $Be^{ik_2 z}$ with $k_d = k_2 \approx k_{bs}^2/k_c$. Exciting cyclotron gyration with the necessary radial profile, one can compensate for the increase of orbital velocity with radius and make $\beta_{\|}(x,y) = \text{const}$. The electron trajectory is in this case a linear superposition of three gyrations: orbital, cyclotron and "betatron".

The potential drop in a cylindrical beam of radius r_o, electron density n and total current I_b can be obtained by integrating the electric field $E_r = 2\pi ner$,

$$\Delta V_b = \pi ne(r^2 - r_o^2) \text{ or } \Delta\gamma/\gamma = \pi ne^2(r^2 - r_o^2)/(m_o c^2 \gamma) = (I_b/(I_o \gamma \beta_{||})(r^2/r_o^2 - 1) \quad (8)$$

3. Cyclotron gyration excitation

The required profile of cyclotron velocity taking into account the potential drop is:

$$\beta_c^2(r) = (\beta_{\perp o}^2 k_o^2 r_o^2 + \beta_{d,max}^2 - 2I_b/(I_o \gamma^3 \beta_{||}))(1 - r^2/r_o^2) \quad (9)$$

Several devices are suitable for that purpose. First, it should be noted that electrons have cyclotron gyration with the amplitude proportional to the value of undulator magnetic field on the radius of injection if undulator field starts abruptly (nonadiabatic injection). It is necessary therefore to subtract the same transverse velocity equal to that of the outer electron from all electrons to obtain the required v_c profile (Fig. 1). Some small mismatch due to undulator stray field or space-charge effects can be corrected by other means (device # 2).

The second device could be used when the undulator has an adiabatic entry, i.e., with slowly rising field, and injecting the beam into it results in negligible beam cyclotron velocities after passing the entry. One can employ in this case a combination of two short sections ($l \leq l_o/2$) of a helical undulator and dipole magnets consisting of two windings, which can occupy the same axial positions as the undulator sections.

It is possible to calculate the transverse velocities acquired by the electrons after passing a section of the undulator or homogeneous dipole magnetic field [2]. If $V(0) = 0$ at $z = 0$, then the transverse velocity $V = v_x + iv_y$

$$V = -(ie/(m_o c\gamma)) e^{ikz} \int_o^z (B_x + iB_y) e^{ikz} dz \quad (10)$$

and one obtains for the transverse velocity V_h in the helical undulator, beginning at $z = 0$,

$$V_h = V_o[1 + 2\pi^2(r/l_o)^2] (e^{ik_o z} - e^{ik_c z}) \quad (11)$$

where $V_o = (k_o \beta_{\perp o}) / (k_o - k_c)$. The transverse velocity V_1 acquired by the electron after passing the homogeneous field $B_x = B_1$ from z_1 to z_2 is:

$$V_1 = (eB_1/(m_o c k_c)) e^{ik_c z} (e^{ik_c z_2} - e^{ik_o z_1}) \quad (12)$$

4. Conclusion

A new simple method of electron beam conditioning for FEL, i. e., securing $\langle \beta_{||}^2(x,y,z) \rangle^{1/2} = \text{const.}$, is proposed for the case when the beam propagates in a longitudinal magnetic field. It consists of exciting cyclotron velocities in the beam with a radial profile that compensates for $\beta_{||}$ decrease of outer electrons in the beam due to undulator field inhomogeneity. The method could be employed for increasing the useful beam currents an order of magnitude.

The proposed scheme of electron beam conditioning appears simpler and cheaper than that published earlier by A.M. Sessler et al. [1], though it requires using an axial magnetic field. The required devices may be no longer than several tens of centimeters and some centimeters in diameter. If axial magnetic field is used for transporting the electron beam, it can be used for beam conditioning with no substantial extra expenditures. For example, if the project of [1] had an electron beam propagating in an axial magnetic field and used cyclotron gyration excitation, it would be necessary to have $\Delta\beta_c / \beta_{\perp o} = 2.10^{-4}$ or $\Delta\beta_c = 4.10^{-6}$ instead of accelerating outer electrons of the beam to $\Delta\gamma m_o c^2 = 3.6$ MeV at $\gamma m_o c^2 = 54$ MeV.

Acknowledgements

The author would like to thank O.A. Smith, M.A. Mashkov and L.S. Kitaiskaya for their assistance in preparation of the paper.

References

[1] A.M. Sessler, D. H. Whittum and L.-

H. Yu, Phys.Rev. Lett. 68 (1992) 309.
[2] V.A. Papadichev, Proc. 12th Int. FEL Conf., Paris, France (1990), Nucl. Instr. and Meth. A304 (1991) 749.

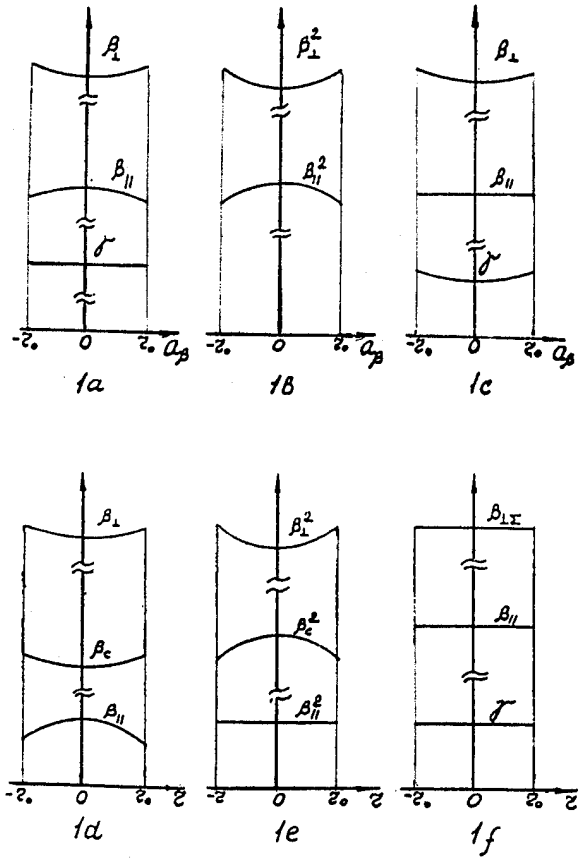


Fig.1. Comparison of two methods of beam conditioning: transverse $\beta_\perp$ and longitudinal $\beta_\parallel$ normalized velocities and electron energy γ (in units m_0c^2) dependences on betatron oscillation amplitude (1a, 1b and 1c for $B_\parallel = 0$);

1a,1b - velocity and energy profiles before conditioning, 1c - after conditioning (it is necessary to accelerate outer electrons of the beam to achieve $\beta_\parallel$ = const. if $B_\parallel = 0$).

1d, 1e and 1f - $\beta_\perp$, $\beta_\parallel$ and γ dependences on radius r for $B_\parallel \neq 0$: 1d - before conditioning with orbital and cyclotron velocities uncorrelated; 1e and 1f - after conditioning, resulting in $\beta_\parallel$ = const.

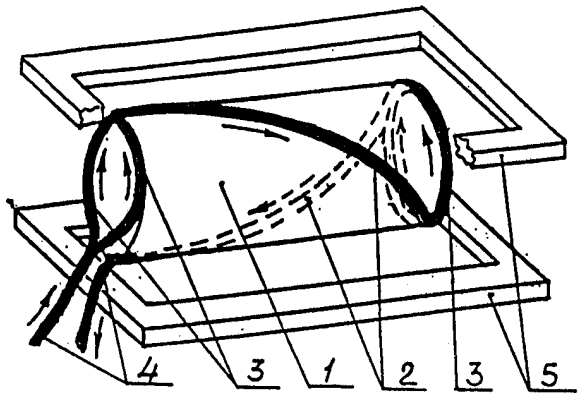


Fig.2. Schematic drawing of one section of the conditioner: 1 - half-period-long helical undulator section, 2 - undulator winding, 3 - connecting wires, 4 - power feed, 5 - dipole magnetic field windings.

The NIKE Electron Beam-Pumped KrF Amplifiers

J.D. Sethian, C.J. Pawley, S.P. Obenschain, K.A. Gerber,
and V. Serlin
Plasma Physics Division, Naval Research Laboratory,
Washington, DC 20375

T. Lehecka
Science Applications International Corporation, McLean, VA 22102

M.W. McGeoch
PLEX Corporation, Brookline, MA 02146

Abstract

The NIKE laser at the Naval Research Laboratory is an angularly multiplexed KrF laser system designed to study the physics of direct drive laser fusion. NIKE will produce 3 kJ of 248 nm light in a 4 nsec pulse. The two final amplifiers are both electron beam pumped systems. The smaller of the two amplifiers, which has a 20 cm x 20 cm aperture, is fully integrated into NIKE. Faraday Cups, pressure jump diagnostics, and dosimetry media have verified that the energy deposition and pumping uniformity meet the NIKE requirements. Using the observed deposition, we have employed our own models to accurately predict the observed gain of the input laser pulse. The larger amplifier has a 60 cm x 60 cm aperture and is pumped by two independent electron beam generators, with each side capable of producing a 670 kV, 500 kA, 290 nsec flat top electron beam. The electron beam from one side has deposited between 30 and 45 kJ into the gas. Our calculations show that the combined deposition from both sides should be sufficient to produce the required 5 kJ laser output, with 3 kJ reaching the target. Faraday Cup measurements show the current injected into the cell across the 200 cm x 60 cm cathode to vary by less than 10%. In both amplifiers the transmission efficiency from cathode to laser cell is around 50%.

Nike is a large angularly multiplexed Krypton-Fluoride (KrF) laser under development at the Naval Research Laboratory. It is designed to explore the technical and physics issues of direct drive laser fusion[1]. When completed, Nike will deliver, onto a planar target, 3 kJ of 248 nm light in a 4 nsec pulse with intensities exceeding 2 x 10^{14} W/cm^2. Spatially and temporally incoherent light[2] will be used to reduce the ablation pressure nonuniformities to less than 2% in the target focal plane. The Nike laser consists of a commercial oscillator/amplifier front end, an array of gas discharge amplifiers, two electron beam pumped amplifiers (one with a 20 cm x 20 cm aperture, the other with a 60 cm × 60 cm aperture) and the optics required to relay, encode, and decode the beam.

To achieve a high power beam, Nike uses angular multiplexing[3]. Because KrF is not a good storage medium (the decay time from the excited state is only a few nsec), the

energy must be extracted continually during the pumping (i.e. e-beam) pulse. This limits the extracted laser power to the rate at which energy can be deposited into the amplifier. In practice, conventional electron beam systems require pump times of a few hundred nsec, which is much longer than the ICF requirement of only four nsec. Angular multiplexing allows these timescales to be matched: In Nike, the front end creates a single pulse that is the desired 4 nsec long. This pulse is divided, amplified and then divided and amplified again to obtain a train of 4 nsec long pulses. This train is broken up so that each pulse passes sequentially through the amplifiers, but at a slightly different angle from the previous one. This allows the amplifiers to effectively drive one seemingly continuous pulse. After amplification, the individual pulses are delayed and steered the appropriate amount so that they all arrive simultaneously on target, thus creating a single, 4 nsec long, high power pulse. Both of the two final amplifiers are double sided e-beam systems, in which the beams are guided into their respective laser cells with magnetic fields.

The smaller 20 cm amplifier is driven by a single 18 kJ Marx. The Marx charges two coaxial lines, which each drive a 300 kV, 75 kA, 180 nsec diode. The 20 cm is shown in Figure 1.

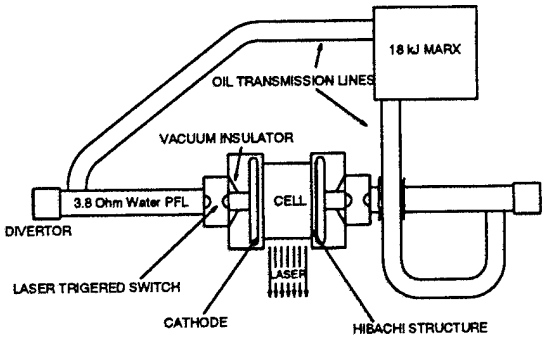


Figure 1: The Nike 20 cm amplifier

Using an array of Faraday cups, pressure jump transducers, and dosimetry media, we have verified that the electron beam deposits sufficient energy to meet the Nike gain requirements, and is sufficiently homogeneous to meet the Nike uniformity requirements. One of the salient features of the 20 cm amplifier is the efficient electron beam transmission through the diode/laser cell window support structure. Our measurements show the transmission efficiency is almost 50%, where the efficiency is defined as the total energy deposited into the cell divided by the total electron beam energy transmitted through the cathode stalk. This is an uncharacteristically high figure for a device of this size. Using the observed energy deposition, we have employed our own models to accurately predict the observed gain of the input laser pulse. This is shown graphically in Figure 2, which plots the experimentally determined and theoretically predicted laser output energy as function of the laser input and the electron beam pump power. The agreement between the two is quite good.

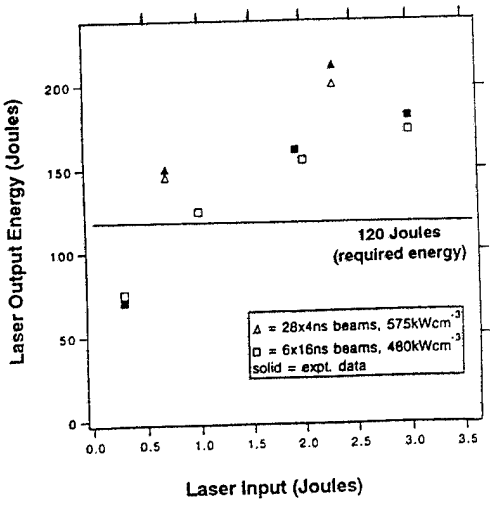


Figure 2. The laser energy output from the 20 cm amplifier. The open data points are code predictions, the solid are data. The solid line is the amplifier design goal of 120 Joules laser output.

The injected electron beam current density is very uniform. Figure 3 shows two overlaid traces; one of the beam current in the cell as measured with a 2.3 cm diameter Faraday cup, the other of the current through the cathode shank. The agreement between the two is excellent. This result is obtained at several other Faraday cup positions across the electron beam aperture, suggesting that the electron beam does have a uniform current density.

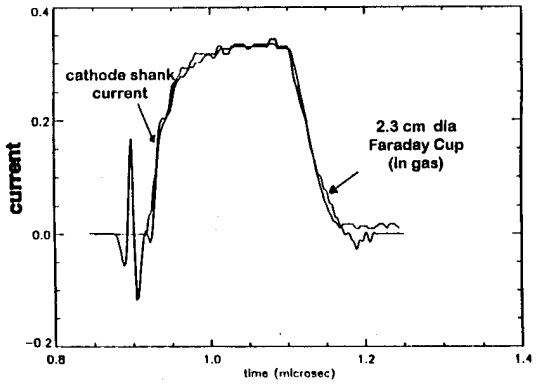


Figure 3: Beam current in the gas overlaid with the cathode shank current.

The pulsed power for the 20 cm amplifier has proven to be quite reliable and reproducible; it has fired over 300 times without a failure, and the diode current traces can be overlaid on a day to day basis. The 20 cm amplifier is fully operational and has been integrated into the laser.

The larger 60 cm amplifier is pumped by two independent electron beam generators.[4] Each side is capable of producing a 500 kA, 670 kV electron beam, but the diode power and impedance can be varied by up to 20% as required by the laser kinetics or electron beam transport. The entire 60 cm amplifier has been assembled, and the electron beam/pulsed power tests completed. The 60 cm amplifier is shown in Figure 4.

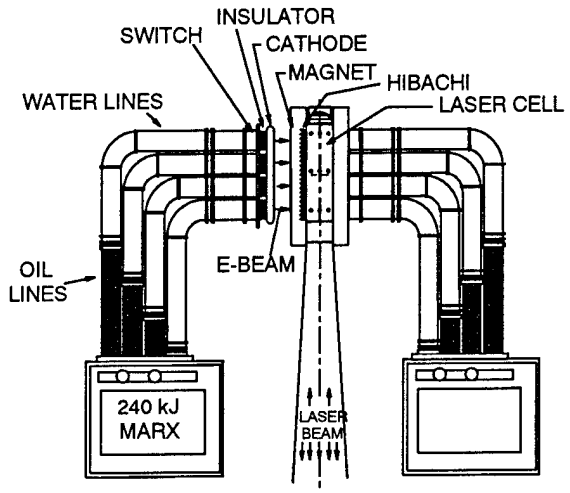


Figure 4: The Nike 60 cm amplifier

In order to achieve 5000 Joules in laser energy, the electron beams must deposit 40 kJ (each side) into the gas. In Figure 5, this energy deposition has been achieved at normal operating voltages (50 kV Marx charge). The data was obtained with Baratron and Piezo gauges that sense the pressure rise in the cell, and corroborated with electrical measurements comparing the current in the cathode to that in the cell. In all cases, a 10% correction factor has been applied to allow for radiation loss.

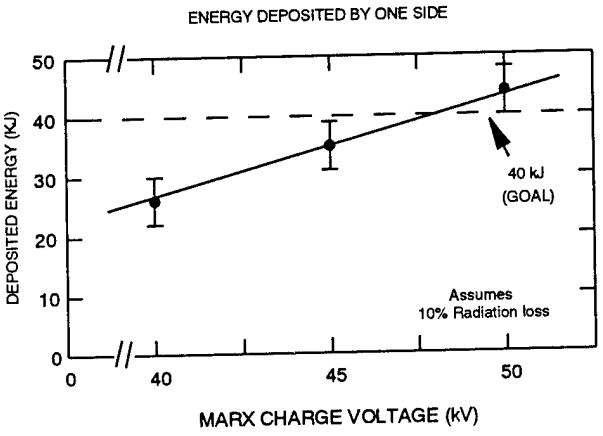


Figure 5; Energy deposited into the gas meets the 40 kJ per side requirements of Nike.

Figure 6 shows measurements with a Faraday cup array of the injected beam current in the cell across the 200 cm × 60 cm electron beam aperture. The current varies by less than 10% throughout the 240 nsec portion of the current pulse that will be used to amplify the laser beam. These measurements also show that the beam transmission efficiency from cathode to laser cell, is, as in the 20 cm amplifier, in the range of 50%. The beam is macroscopically stable over the range of guide fields between 2-4 kG.

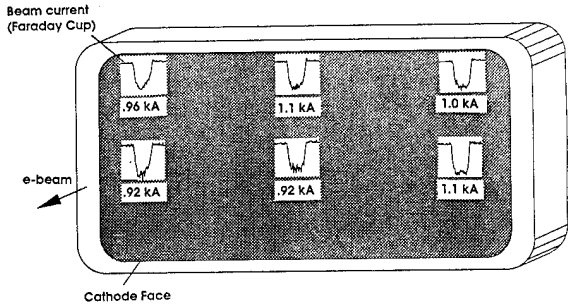


Figure 6, Electron beam current, measured with an array of Faraday cups.

The 60 cm amplifier has completed its e-beam tests and is now being converted into an amplifier. It is anticipated that the system will be complete by late summer of 1994.

The authors would like to acknowledge the contributions of W.D. Webster of East Coast Engineering; O.C. Barr of Pharos Technical Enterprises; A. Mangassarian of SAIC; I. D. Smith, P.A. Corcoran and R.G. Altes of Pulsed Sciences, Inc; and R.L. Morse, J. Sawyer, D. W. Williams and J. Peterson of Commonwealth Technologies, Inc.

This work is sponsored by the US Department Of Energy.

1. S.E. Bodner et al. "Nike KrF Laser Development for Direct Drive Laser Fusion" in Fourteenth International Conference on Plasma Physics and Controlled Nuclear Fusion Research, Wurzburg, Germany, 30 Sept.- 7 Oct., 1992. IAEA-CN-56, IAEA, Vienna, 1993.

2. R.H. Lehmberg and J. Goldhar, "Use of Incoherence to Produce Smooth and Controllable Irradiation Profiles with KrF Lasers," *Fusion Technology* **11**, 532 (1987).

3. R.P. Sandoval, "Angular Multiplexing as a Technique for Short Pulse Amplification in a High Gain Xenon Amplifier," *J. Appl. Phys.*, **49**, 5745 (1978).

4. J.D. Sethian, S. P. Obenschain, C. J. Pawley, I.D. Smith, P.A. Corcoran, R.A. Altes, and M.W. McGeoch, Proceedings of The Eight IEEE Pulsed Power Conference, Albuquerque, NM, (June, 1994).

TO THE ELECTRODYNAMICS OF THE HYBRID PLASMA-WAVEGUIDE STRUCTURES (THEORY AND EXPERIMENT)

Antonov A.N., Berezin A.K., Bliokh Yu.P., Degtar Yu.A., Fainberg Ya.B., Egorov A.M., Kovpik O.F., Kornilov E.A., Lodygin A.V., Lubarsky M.G., Markov P.I., Mitin L.A., Miroshnichenko V.I., Onishchenko I.N., Sotnikov G.V., Svichensky V.G.
National Science Center
"Kharkov Institute of Physics and Technology"
310108 Kharkov, Ukraine
The whole investigation is headed by Fainberg Ya.B.

Abstract

The plasma filled slow-wave structures (hybrid structures) have been considered and their advantages for the generation of electromagnetic radiation and for particles acceleration have been shown in comparison with vacuum structures. Dispersion characteristics, field topography and microwave power flux distribution in a chain of inductively connected cavities with plasma filled beam channel have been investigated. The generation and amplification regimes were considered. The gain, start current, thresholds of bifurcation and efficiency were estimated. The electrodynamic characteristics have been experimentally investigated for the slow-wave structures of a ring-meander type and a chain of cylindrical cavities with plasma filling. The generators were created on this base in S-band with an efficiency about 50% and high output power of 40 kW in continuous operation and 100 kW in pulse of 4 ms duration. It has been elaborated and created the power beam-plasma generator of stochastic oscillations in decimeter range using helix-plasma systems. The efficiency was 38% and output power reached 70 kW in pulse of 400 μs duration.

Introduction

Prediction of the beam-plasma instability [1,2], discovery of the beam-plasma discharge [3–5] and the investigation of the plasma waveguide electrodynamics [6] laid the base of the new branch of the plasma physics — the plasma electronics. Numerous theoretical and experimental investigations, carried out in the KIPT in this field, brought to the elaboration of the new kind of HF-devices of the regular and stochastic oscillations, so called beam-plasma generators and amplifiers (BPG). The physical principles of their creation were firstly formulated in 1965. Later they were partly published in our works [7–9] and in other authors articles [9–11].

The theory was devoted to investigations of the hybrid structures electrodynamics and stochastization mechanisms and spectrum evolution in such strong nonlinear and nonequilibrium systems as BPG's are.

Experiments were performed with relativistic beams in quite plasma waveguides [12,13], and in corrugated waveguides, filled with plasma [14,15] showing the impressive efficiency enhancement. KIPT experiments are firstly represented here on the hybrid structures excitation by the nonrelativistic beams. The essential advanced elaboration and technological perfection of amplifiers were made in VEI [16]. Some experiments with BPG were fulfilled in MRTI [17].

The main advantages of the beam-plasma devices using the plasma-filled slow wave structures (hybrid structures) are:
— the possibility of power increase by rising of the vacuum limiting current due to the compensation of the beam charge;
— the volume character of the excited wave leading to the considerable increasing of the growing rate and connected with it efficiency enhancement in comparison with the vacuum case;
— tuning of the excited frequency by changing the plasma density;
— the possibility to realize the interaction in a large volume and, hence, to obtain high power output;
— the increasing of the energy change between the beam and excited wave and efficiency enhancement due to self consistent nonlinear plasma parameters evolution properly changing the electrodynamic characteristics of the structure;
— a great number of the eigen modes under plasma filling allows to vary and to enrich obtained spectra keeping the possibility of their governing.

Theory

Some conventional slow-wave structures — helix, chain of coupled cavities, corrugated waveguide, sequence of rings and coaxial grating — were investigated under plasma filling for different wavelength ranges and frequency bands. The main feature of these devices is firstly the essential change of dispersion properties and field topography due to plasma filling. Secondly, there is a possibility of parametric coupling of the plasma waves with E-type electromagnetic mode of the vacuum structure due to the partial filling and structure periodicity.

The illustration can be done with the chain of inductively coupled cavities with plasma filled transit channel. Dispersion equation (DE) for this hybrid structure was obtained by the method of partial regions [18] and the theory of the slit antenna [19] and is given in [20]. In Fig.1 DE is represented in dependence of frequency ω for all other parameters fixed and plasma density $x_p = \omega_p L/\pi c = 0.5$

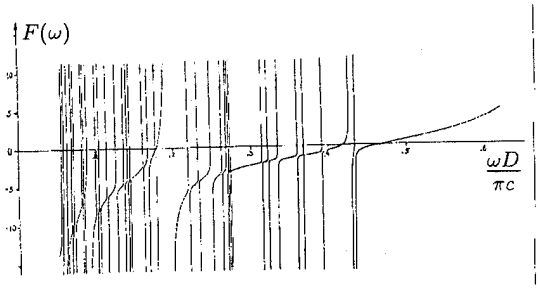


Fig. 1.

(ω_p is plasma frequency, L is structure period). It is seen the appearance of the great number space harmonics of the radial modes of the low frequency plasma wave ($\omega < \omega_p$). It is not simple to trace the line with small incline corresponding to changed vacuum electromagnetic wave. The displacement of the cross point (i.e. the wave frequency ω) depends on the plasma density and can be used for tuning. Radial topography of the longitudinal field $E_z(r)$ is shown in Fig.2 for $x_p = 0$ — (1), 0.5 — (2), 1.5 — (3). Volume property of the wave is evident for high plasma density.

The solving of the DE with the beam gives the expression for the growing rate that is inversely proportional to the derivative $q \sim \partial D/\partial\omega$ at the root point $\omega = \omega_0$ and is proportional to the geometric factor $G \sim$

$\int_0^a E_z(r)^2 r\,dr$ (a is the channel radius). It means that in spite of numerous resonant modes the only mode with minimum derivative excites by the beam but not the dense spectrum. Besides, the growing rate is increasing with plasma density rise, because E_z becomes volumetric and, hence, G grows. The efficiency dependence on the plasma density is determined by two competitive factors. On the one hand the maximum field amplitude is conditioned by the beam trapping and is proportional to the squared growing rate. It means that $E_{z\,max}$ is larger for denser plasma. On the other hand the HF-power flux through the cavity region is determined by the field value at the clearance between drift tubes. Comparatively to the value on the axis it is less for denser plasma. Consequently efficiency has a maximum value for the optimum plasma density, conditioned by $\omega_p \approx \omega_0$ as numerical calculations shows.

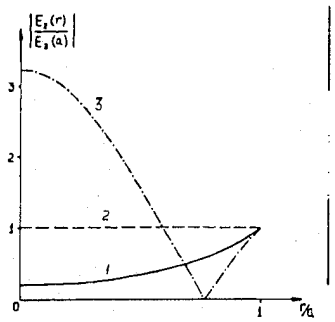


Fig. 2.

By applicating the method of functional map [21] the thresholds of stochastic generation are obtained. The stochastization mechanism is the alternating turbulence as in conventional vacuum devices. However because of sufficiently larger growing rate in the hybrid structures the thresholds are lower. Besides, the presence of a great number of radial modes and their space harmonics and also low frequency plasma motion (ion sound, density modulation etc.) leads in the nonlinear regime to more homogeneous spectra of the stochastic automodulation comparatively to the vacuum case.

Experimental results of centimeter generation

Experimental realization of the generation in centimeter range has been carried out with slow-wave structure of CCP with plasma filled channel and is represented in Fig.3. Electron

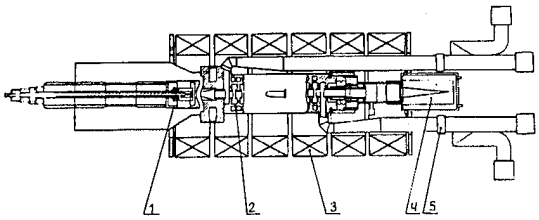


Fig. 3.

gun (1), providing beam current 10 A at voltage 40 keV, matched with compact high efficient ion-getter pump maintaining pressure 10^{-6} Torr; slow wave structure composed of copper cavities with slits and drift tubes (2) was placed in a solenoid producing magnet field 3 kG (3); cooled collector (4), was capable to dissipate the power up to 260 kW; the power output was carried out by the waveguide 74 × 36 mm through the cooled wideband window made from sapphire (5) the plasma of density $5\cdot10^{10}-10^{12}$ cm^{-3} was produced as a result of beam-plasma discharge in the transit channel under gas tap. The standing wave coefficient was $1.5 \div 2.0$ in the frequency band $2.4 - 5$ GHz. The electron gun has the protection from ion bombardment. Start current was 100 mA and the threshold of stochastization was 1.0 A in a good agreement with calculations. With current increasing the generated frequency band overlapped the whole passband of the structure. The efficiency reached 40% for the optimum conditions in continuous operation. Varying phase velocity by the structure geometry electronic efficiency was obtained 50% and output power 40 kW. For the pulse operation during 4 ms the power was 100 kW.

Frequency spectrum is wide and homogeneous in the band of about a half of octave (see Fig.4). The experimental corroboration of the existence of the plasma filling optimum in the theory is demonstrated in Fig.5. Here the dependence of output power on gas pressure is represented.

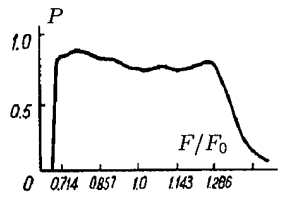


Fig. 4.

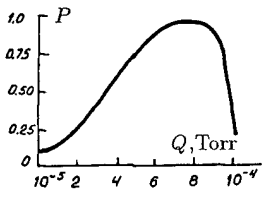


Fig. 5.

Experimental results of decimeter generation

In decimeter range of wavelength the BPG of stochastic oscillations has been elaborated and created using of plasma-helix structure with a single or modified contra-wound helix circuits that are operating in quasi continuous or continuous regimes. The generator (Fig.6) is consist of the following units: 1 —

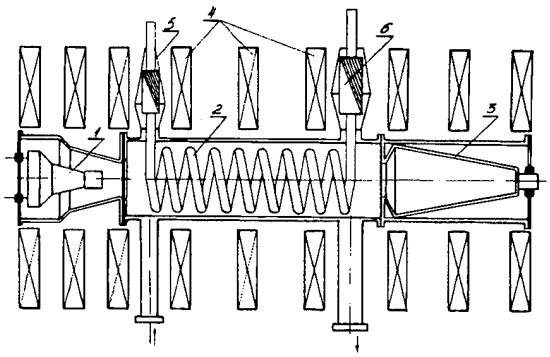


Fig. 6.

electron gun, 2 — helix structure, matched with beam-plasma interaction region, 3 — collector, 4 — solenoid, 5 — UHF-load, 6 — UHF power register. The beam current is 13 A, beam energy — 15 keV, magnetic field strength — 1100 G, plasma density — $6 \cdot 10^{10}$ cm^{-3}. The total generated power was 80 kW with efficiency 40%.

References

[1] A.I.Akhiezer, Ya.B.Fainberg, Dokl. Ac. Scie. USSR **69**, 555 (1949).

[2] D.Bohm, E.Gross, Phys. Rev. **75**, 595 (1949).

[3] A.K.Berezin, Ya.B.Fainberg et al., Atomnaja Energija **11**, 493 (1961).

[4] I.F.Kharchenko, E.A.Kornilov, Ya.B.Fainberg et al., J. Tech. Phys. **31**, 761 (1961).

[5] W.D.Getti, L.D.Smullin, J. Appl. Physics **34**, 3421 (1963).

[6] Ya.B.Fainberg, M.F.Gorbatenko, J. Tech. Phys. **29**, 549 (1959).

[7] Ya.B.Fainberg et al., Dokl. Ac. Scie. Ukr.SSR Seria A, No11, 56 (1990).

[8] A.K.Berezin et al., Preprint KPTI 91-52, Kharkov, 31p. (1991).

[9] E.A.Kornilov et al., IV Simp. on High Current Electronics, June 21–30, 1992, Russia, p.132.

[10] G.I.Batskikh et al., Beams-90, July 2–5, 1990, Novosibirsk, USSR, **2**, p.1173.

[11] V.I.Perevodchikov et al., Beams-92, May 1992, Washington, USA.

[12] Ya.B.Fainberg et al., Preprint KPTI 72–07, Kharkov, 32p. (1972).

[13] M.V.Kyzelev et al., JETP **63**, 1358 (1982).

[14] Yu.V.Tkach et al., Physika plasmy **5**, 5 (1979).

[15] Y.Carmel et al. Phys. Rev. Lett. **62**, 20 (1989);2 Int. Workshop "Strong Microwaves in Plasmas", Nizhny Novgorod Russia, August 15–22, 1993, S-34.

[16] M.A.Zavjaliv et al., ibid, S-40.

[17] K.G.Gureev et al., ibid, S-15.

[18] A.D.Grigoryev, V.B.Yankevich, book "Resonators and resonator slow wave UHF systems". M. 1984.

[19] M.L.Levin, J.Tech.Phys. **21**, 787 (1961).

[20] Ya.B.Fainberg et al., IX Semimar on UHF electronics and radiophysics. Saratov 1993, p.66.

[21] Yu.P.Bliokh et al., Izvestiya Vuzov Ser. Appl. Nonlinear Dynamics **1**, 34 (1993).

EXPERIMENTAL STUDIES OF HIGH-POWER HARMONIC GYROKLYSTRONS

W. Lawson, J. P. Calame, J. Cheng, M. K. E. Flaherty, V. L. Granatstein, B. Hogan, V. Irwin, P. E. Latham, H. W. Matthews, G. S. Nusinovich, and M. Reiser

Institute for Plasma Research and Electrical Engineering Department
University of Maryland, College Park, MD 20742 USA

Abstract

At the University of Maryland, we have developed several gyroklystron configurations, the characteristics of which are approaching the predicted requirements for the next generation linear collider. These studies have revolved around a test bed capable of producing a 450 kV, 160-260 A, 1 μs beam immersed in a 5.5 kG (nominal) axial magnetic field with an average ratio of electron perpendicular to parallel velocities near one. We present results for a series of second-harmonic two-cavity tubes that culminated in a peak power of 32 MW at 19.7 GHz with an efficiency of 28% and a large-signal gain of 27 dB. The experience gained from these tubes has been incorporated into the design of a 17.136 GHz, 100 MW, coaxial, second-harmonic, two-cavity gyroklystron. We conclude the paper by detailing the design of the new test bed, the single-anode magnetron injection gun, and the microwave circuit.

At the University of Maryland, we have been exploring the suitability of gyroklystrons as drivers for the next generation of linear colliders. Our work has culminated in peak powers near 30 MW in 1 μs pulses near both 10 GHz and 20 GHz with fundamental mode [1] and second harmonic [2] interactions, respectively. The beam voltage has hovered near 450 kV and beam powers have always been about 100 MW. Large-signal gains have been in the 27 dB - 40 dB range. These results represent a significant increase beyond the previous state-of-the-art for similar gyroklystrons, but are still below the currently anticipated power level requirements. We have formulated plans to modify the current system to enable us to exceed the 100 MW level for output power. The details of the 30 MW second-harmonic experiments and a discussion of the designs for the 100 MW system are the presented in the sections below.

The 30 MW system

A 1 μs, 460 kV, 400 A line-type modulator is used to energize a thermionic double anode magnetron injection gun. The gun produces a current up to 260 A; the rest of the current is shunted through a resistive divider which provides the voltage to the intermediate anode. This divider is not properly compensated due to excessive stray capacitance which ultimately leads to a time variation in velocity ratio across the pulse. The drive power is supplied by a 100 kW, 9.7 - 10 GHz magnetron. An arrangement of eight water-cooled coils powered by four independent supplies allows for considerable flexibility in producing variations in the axial field profile.

Seven different second-harmonic tubes were tested. Most of the variations were related to the output cavity but some were related to the drift region and the input cavity. The layout of the third tube is depicted in Fig. 1. The input cavity resonates at 9.87 GHz in the TE_{011} mode, has a coupling slot on the radial wall, and uses a thin lossy ceramic ring to reduce the quality factor. The drift regions before the input cavity and between the two cavities are heavily lined with lossy dielectrics. The first three tubes had resonant traps in the main drift tube to isolate the input cavity from any TE_{01} signal at 19.7 GHz that might come back from the output cavity. This proved to be unnecessary, so they were removed from the remainder of the tubes because they had a deleterious effect on tube stability at lower frequencies.

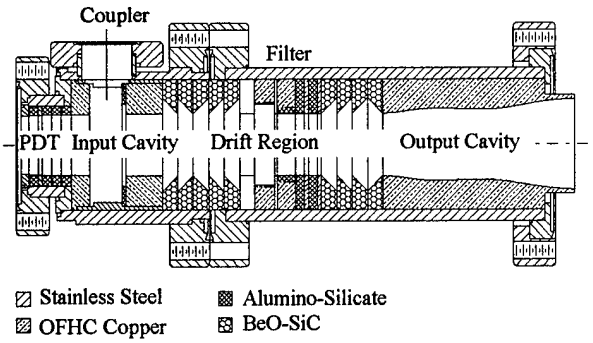


Figure 1. The third second-harmonic tube.

The output cavities were designed with radii that precluded amplification at the drive frequency in the TE_{011} mode. All but the fifth tube utilized adiabatic radial wall transitions to minimize mode conversion from the TE_{02} to the TE_{01} mode. The fifth tube had sharp transitions and operated with a mixed mode output that was strongly dependent on the beam parameters. It had a step in the output cavity radius in an attempt to minimize power flow back to the input cavity. The final two tubes started with the geometry of the fourth tube and added an inner conductor that was loaded with lossy dielectrics, spanned the input cavity and the two drift regions, and was supported in the drift region by tungsten pins. The input cavity length was adjusted to recover the proper resonant frequency.

The progress in producing amplified power is illustrated in Fig. 2, where we plot the time dependence of the microwave output pulses for the maximum operating points for the first 4 tubes. The first tube had an exceedingly long output cavity and produced no measurable amplification because of stability problems. The dominant mode was a TE_{01} mode at 10.9 GHz. The second tube's output cavity was significantly shorter and was able to produce about 12 MW. The third tube had a

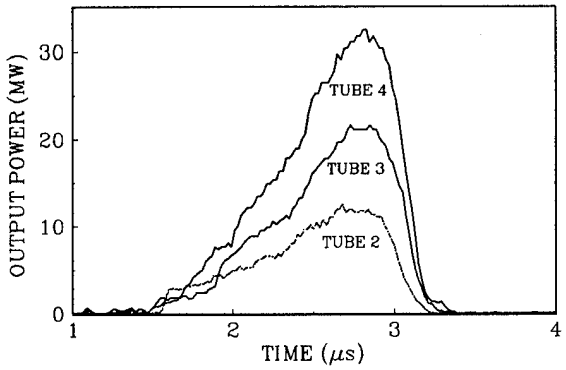


Figure 2. The evolution of output power.

slightly different resonant trap and a somewhat shorter output cavity as well. It's maximum power was 21 MW. The fourth tube was identical to the third except that the resonant trap was replaced by tapered BeO-SiC ceramics. This tube produced 32 MW at 19.7 GHz with 28% efficiency and 27 dB Gain. The beam parameters at the optimal point included a voltage of 457 kV and a current of 244 A. The magnetic field had a slight uptaper.

The mixed mode tube and the two coaxial tubes had some advantages in terms of stability, but produced lower peak output powers. The mixed mode tube produced a maximum of 20 MW with an efficiency of 23%. The second coaxial tube had a maximum output of 28

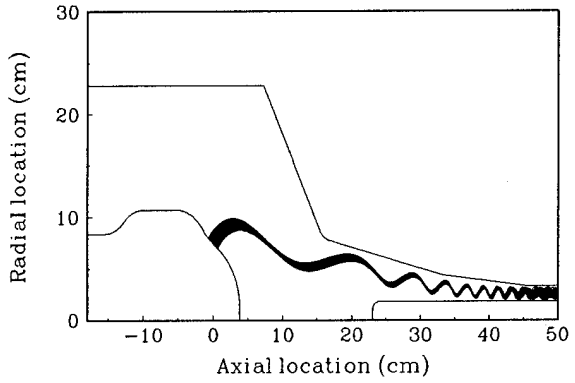


Figure 3. The magnetron injection gun layout.

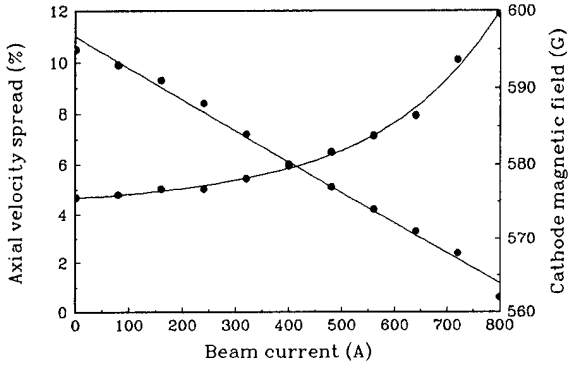


Figure 4. Axial velocity spread as a function of current.

MW, but could only reproducibly generate 21 MW with an efficiency of 21%. Beam scrape-off limited the accessible range of magnetic fields and pin erosion cut the experiments short. Subsequent theoretical analysis predicted this failure and indicated that other materials should survive the beam densities associated with our experiment.

The 100 MW System

To scale the current system to an output power level of 100+ MW, we have chosen to boost the beam power mainly by increasing the current while keeping the current density at about the same level. We will also decrease the operating frequency to six times the current SLAC frequency to allow a little more flexibility with our magnet system. By doubling the number of pulse-forming networks (from 4 to 8), we will increase the current capability of our modulator to 800 A. With minor adjustments, we will increase the modulator's voltage capability from 460 kV to 500 kV. The existing magnets and supplies will be used on the new system, with the single exception that the gun coil will require twice as much current due to a decreased magnetic compression ratio. Most of the vacuum hardware will be utilized on the new system. The magnetron drive, the electron gun, all of the output waveguide, and most of the microwave diagnostics will have to be replaced. Much of the new hardware has already been procured or designed.

We have designed a single-anode magnetron injection gun which will allow us to fully exploit the upgraded modulator. This gun has a sufficiently large emitter strip radius to keep the current density levels at the same value as our current gun. Fig. 3 depicts the electrode layout and the simulated beam trajectory. In Fig. 4, we plot the dependence of velocity spread on beam current; we maintain a constant velocity ratio of 1.5 by adjusting the cathode magnetic field. A wide range of currents are accessible with spreads well below 6 % to 400 A and below 10% to 720 A. This gun is currently under construction at Varian Associates in Palo Alto.

A rough schematic of the tube is shown in Fig. 5. The required input cavity has a quality factor of about 50. Drive power will be coupled through two slots in the radial wall separated by 180°. The cavity will be realized by a dip in the inner conductor radius to 1.1 cm that extends about 2.29 cm.

The drift tubes will be heavily attenuated with two layers of lossy dielectrics on the outer conductor, and one layer on the inner conductor. The ceramics will be either non-porous BeO-SiC or carbonized alumino-silicate. The final arrangement of ceramics will depend on cold-test results for fundamental mode attenuation. The inner and outer radial dimensions are 1.83 cm and 3.33 cm, respec-

tively. This represents a beam clearance of about 1.1 mm. The length of the drift tube is 9 cm. The inner conductor will be supported by CVD diamond pins.

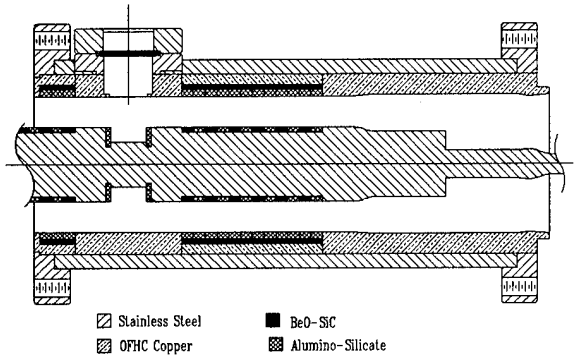


Figure 5. The coaxial second-harmonic circuit.

Two output cavities are being considered at this time. The first is a simple cavity that is realized by increasing the outer radius to 3.651 cm over a 3 cm transition length. All radial wall transitions are smooth to minimize mode conversion. The main cavity length is 0.64 cm. Axial energy extraction is accomplished with an output lip that has a 0.1 cm flat section after a 1 cm transition length and has an outer radial dimension of 3.58 cm. The Q of the cavity is 529 and the predicted ratio of power traveling into the drift tube compared to the power flow into the output waveguide of -24 dB.

The expected efficiency is nearly 35% at the simulated electron beam axial velocity spread of 6%. Start oscillation simulations indicate that the cavity is marginally stable.

The second configuration we are considering is a complex TE_{02}/TE_{03} cavity (depicted in Fig. 5). The overall physical length is 10.6 cm. All transitions are smooth except for the TE_{02}/TE_{03} interface. The Q of the cavity is 295 and the predicted ratio of power traveling into the drift tube compared to the power flow into the output waveguide of -36.5 dB. The output mode should be over 96% TE_{03}. While this cavity is inherently more stable than the preceding one, to date we have only achieved simulated efficiencies of 20%. Mode competition with third harmonic operation seems to be the limiting factor, and we are exploring ways to improve this efficiency further.

Summary

We have produced over 32 MW of power at 19.7 GHz with 28% efficiency and 27 dB gain via a two-cavity second-harmonic gyroklystron. We are in the process of tripling the current capability of our microwave test bed and have designs of a second-harmonic coaxial tube that should be 35% efficient. The combined result of these two efforts is that we expect to produce at relevant frequencies the power levels that are anticipated to be required of future linear colliders.

References

[1] S. Tantawi, et al. IEEE Trans. Plasma Sci., vol. 20, p. 205 (1992).
[2] H. W. Matthews et al., IEEE Trans. Plasma Sci. (in press).

THE LONG-PULSE, HIGH-CURRENT RELATIVISTIC KLYSTRON AT 500 MW AND BEYOND

M.V. Fazio, W.B. Haynes, B.E. Carlsten, R. M. Stringfield
Los Alamos National Laboratory
MS H851, Los Alamos, NM 87545, USA

Abstract

This paper describes the development of an L-band annular beam, high-current relativistic klystron for producing a peak power of 1 GW at a pulse length of 1 μs. The tube consists of three cavities: the input cavity driven by a 300 kW magnetron, an idler cavity, and an output cavity. The tube has produced 475 MW and an energy per pulse of 160 J. The microwave output pulse terminates prematurely, before the peak power in the electron beam pulse is reached. The pulse shortening is believed to be caused by too high a voltage across the gap of the output cavity. The result is electron reflection in the output gap leading to beam disruption and high voltage breakdown across the gap. Current experimental results are presented with an emphasis on the design of output cavities for coupling microwave power from high current, very low impedance modulated electron beams.

I. Relativistic Klystron Description

The RKA configuration is shown schematically in Fig. 1. The electron beam is formed from a 6.2-cm-diam. annular explosive field-emission cathode made of stainless steel. The beam is guided and slightly compressed by a converging 0.5 T axial magnetic field to a nominal 5.9 cm diameter beam with a 5 mm thickness. The RKA drift pipe diameter is 7.3 cm. The typical beam voltage is 620 kV with the current increasing from 3 to 6 kA during the pulse. The beam has a microperveance of about 11. The increasing current is caused by the drop in electron gun impedance during the pulse due to plasma closure of the anode-cathode gap. The input and idler cavities are of the quarter-wave coaxial geometry type. The input cavity is coupled through an iris into reduced-height WR-650 waveguide that tapers to full height and connects to a 500 kW L-band magnetron. The idler cavity has an annular tuning ring which gives flexibility in inductively tuning the cavity over a range of about 100 MHz.

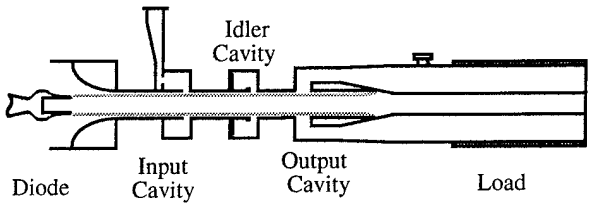


Fig. 1: Schematic diagram of the RKA

The output cavity is a noseless pillbox design with annular coupling irises near the outer diameter that couple the microwave power into a low impedance coaxial transmission line. A tapered impedance transformer transitions to standard 50 Ω, 6-in-diameter coaxial line dimensions. In this 50 Ω section of line is a calibrated, high directivity, in-house-designed bi-directional coupler for accurate measurement of the microwave power traveling in the TEM mode. The directivity of the coupler is 20 dB. The 50 Ω coaxial transmission line is terminated with a matched (VSWR = 1.2) coaxial dummy load built into the end of the coaxial transmission line. The entire structure, including the load, is under vacuum. This was done in order to avoid having to simultaneously develop a high power window

This work was supported and funded jointly by the DoD Office of Munitions and the DOE Defense Programs through the joint DoD/DOE Munitions Technology Development Program, the Army Research Laboratory, and the Air Force Phillips Laboratory.

capable of reliably transmitting 1 GW of power. The tube has been operated at vacuum levels from 5E-5 to 7E-7 Torr. A more complete description of the RKA and the experimental work can be found elsewhere [1].

The output cavity must be designed to produce an electric field across its gap of sufficient magnitude and phase that the electron bunches are significantly slowed, thereby giving up kinetic energy to the microwave field in the cavity. The output cavity must be made resonant, and the output cavity gap shunt impedance must be matched to the beam impedance to provide the gap voltage that extracts most of the available kinetic energy. If the output cavity gap voltage is too high, two things can happen. Beam electrons can be reflected back upstream causing disruption of tube operation, and rf breakdown can occur in the output cavity. Too low a gap voltage produces very little slowing of the electron bunches resulting in very poor conversion efficiency of electron kinetic energy to microwaves. If the output cavity is not resonant, most of the power will be lost in higher order modes. Our high-current RKA has a nominal harmonic current (I_1) impedance of around 200 Ω. In a microwave cavity, where R_S is the shunt impedance and Q is the loaded Q, the quantity R_S/Q depends only on the geometry [2]. In a TM_{010}-type cavity the value R_S/Q is around 50, and there is little one can do to alter the geometry. If one desires to match the cavity impedance to the beam impedance of 200 Ω, this implies a Q of about 4.

II. Experimental Results

The beam modulation section of the RKA consists of the input cavity and one idler cavity. This section of the tube is performing as designed, and is providing a modulated electron beam with a harmonic current $I_1 = 0.65\ I_0$ where I_1 is the fundamental harmonic at 1.3 GHz and I_0 is the dc beam current. The modulated beam current lasts for the duration of the pulsed power pulse when the output cavity is not on the tube. When the output cavity is in place the electron reflection at the output gap causes the beam modulation to be prematurely disrupted. The performance of the input cavity is detailed in reference [1] and will not be repeated here.

A. Idler Cavity

The role of the idler cavity is to substantially increase the beam modulation that is initiated by the input cavity. The idler cavity is placed at the position downstream of the input cavity where the beam modulation reaches its highest value, which is where I_1/I_0 is about 10%. The idler cavity can be inductively tuned over about 100 MHz, from 1300-1400 MHz. Measurements were made of beam harmonic current modulation (I_1) as the rf input power was varied and as the idler cavity tuning was changed. The harmonic current increases, as predicted, as the idler cavity tuning moves toward the 1.30 GHz rf drive frequency for a given amount of input drive. We could not adjust the idler cavity frequency any closer than 1325 MHz because the peak surface field at the idler cavity gap exceeded the level for rf breakdown.

Beam modulation data were taken for different idler tuning frequencies and input cavity drive powers to find the best combination for maximum beam modulation. This data showing beam modulation (I_1/I_0), at the location of the output cavity gap, as a function of input drive power, is plotted in Fig. 2. The data showing the beam modulation as a function of idler cavity tuning is somewhat incomplete because we installed the output cavity as soon as it was available.

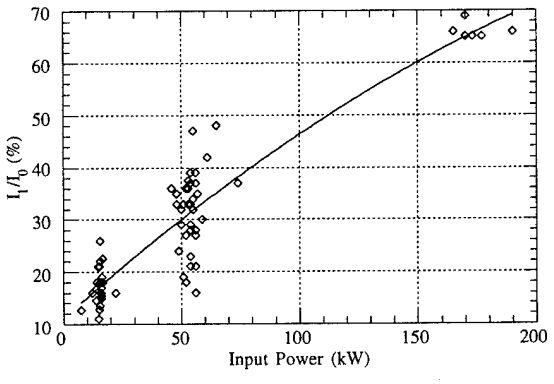


Fig. 2: Beam modulation (%) after the idler cavity as a function of input drive power.

From PIC code simulations, the amount of modulated current out of the idler cavity for maximum output was determined to be 65-75% [3]. The amount of extractable beam power is usually given as $P = (V \times I_1) / 2$. For this case with a voltage of 620 kV and a harmonic current of 3.3 kA, about 1 GW of power is in the fundamental harmonic. Because of the effect of the space charge potential depression [3], the output cavity can only extract about 70% of this power, and should produce 700 MW of rf output power or 700 J per pulse.

B. Output Cavity

The original output cavity downstream endwall (the wall containing the coupling irises) was modified, based on cold tests, to have a loaded Q of ~10. The much lower loaded Q resulted in much lower electric fields across the cavity gap thereby reducing the rf breakdown problem. This change created a better match between the modulated beam impedance and the cavity shunt impedance for better conversion efficiency from beam power to microwave power.

So far, the highest energy obtained with the modified output cavity, in a single pulse, has been 160 J. Data are shown in Fig. 3 where rf output power, beam voltage, and beam current are all overlaid on the same time scale. The peak power is 375 MW. Note that the rf power goes away before the beam voltage reaches its maximum value. This will be discussed later. Other shots have recorded higher peak powers (475 MW), although at a slightly lower energy per pulse (140 J).

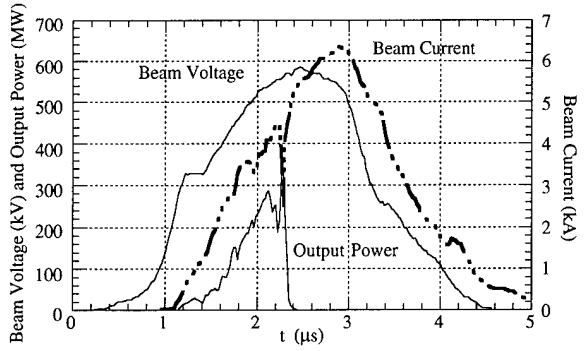


Fig. 3: Output power, beam voltage and current for shot 1308.

The signals from the two B-dot loops located 90 degrees apart on the upstream wall of the output cavity are shown in Fig. 4. They track together indicating that the output cavity is operating in the proper mode. The B-dot signals are plotted in Fig. 4 in terms of the output cavity gap voltage they represent. The actual voltage across the 2.76 cm output gap at 375 MW reaches 370 kV producing an average electric field of about 134 kV/cm. From the HFSS simulation [4], the magnitude of the peak gap voltage, across the geometrical cavity gap, was found to be as high as 538 kV with a peak surface electric field of 225 kV/cm when 500 MW was being coupled into the output coax. This gap voltage is high enough to turn electrons around in the beam. Therefore, it was obvious that the modified output cavity would never be able to reach the desired output power level of 1 GW.

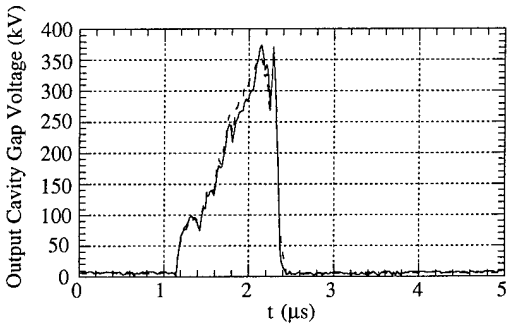


Fig. 4: Output cavity gap voltage for shot 1308.

At this point it was not yet certain why the rf pulse was terminating prematurely. The most reasonable explanation at the time was that the output cavity was producing fields high enough to reflect electrons back up the beam-line and/or start some oscillation phenomenon such as a virtual cathode. Fig. 5 shows traces representing magnetron forward and reflected power, the B-dot loop signal in the idler cavity, and the B-dot signal in the input cavity.

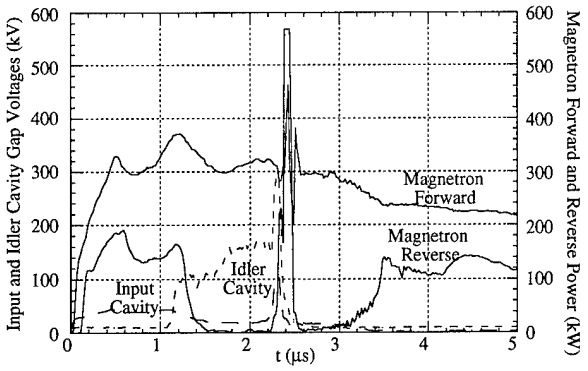


Fig. 5: Input and idler cavity gap voltages and magnetron power for shot 1308.

All of these signals have a spike at the time the rf output power goes away. These signals are bandpass filtered with a bandwidth of several hundred MHz around 1.3 GHz, so the spike appears to be the result of an rf modulation on the beam (space charge wave) traveling back up the beam toward the cathode. The interpretation of the observation is complicated by the fact that the output gap appears to be breaking down at this time as well.

C. New Output Cavity Design

A completely new output cavity with a lower loaded Q has been designed using HFSS. The new output cavity has a lower output gap voltage, thereby reducing the chance for electron reflection across the gap. For an output power of 500 MW, the geometrical gap voltage is calculated to be 365 kV, and the peak surface field is 246 kV/cm. The peak surface field has not increased substantially over the value in the modified original cavity, but the gap voltage has been drastically decreased. The peak surface field is what causes the rf breakdown, while electron reflection is determined by the line integral of the electric field along the electron trajectory across the region of the output gap. The lower gap voltage should allow the new cavity to consistently extract 0.5 to 1 GW for the microsecond-long beam pulse. The output cavity section is coupled to the low impedance coaxial line though 4 irises defined by 4 posts. The output coax then tapers to the standard 6-in-diam., 50Ω line dimensions. This cavity has a resonant frequency of 1300 MHz and a loaded Q of about 4.1 according to HFSS. To date, the latest version of the cavity has only produced approximately 120 MW average for 500 ns. The exact cause of the pulse termination has not yet been identified.

III. Summary

Peak powers approaching 500 MW at 1.3 GHz have been produced in pulses of 1 μs nominal baseline-to-baseline duration. The half power pulse width is 0.5 μs. These pulses contain an energy of about 160 J. Rf output begins on the rising portion of the current pulse and terminates just before the highest part of the pulsed voltage curve is reached.

Theory and modeling work has elucidated some important aspects of the space charge dominated physics of the RKA that have been supported by the experimental results. We now have a qualitative understanding of the various tube parameters and their impact on RKA design. These parameters include voltage, current, beam diameter, beam drift pipe diameter, and output cavity shunt impedance. Three dimensional cavity modeling has proven to be critical for designing the very low Q output cavity needed for converting the low impedance modulated electron beam to microwaves. The thrust will be to increase the output power to 1 GW and to widen the pulse to 1 μs.

References

[1] M.V. Fazio, W.B. Haynes, B.E. Carlsten, and R.M. Stringfield, "A 500 MW, One Microsecond Pulse Length, High Current Relativistic Klystron," submitted to the *5th Special Issue on High Power Microwave Generation of the IEEE Trans. on Plasma Sci.,* October 1994.

[2] E.L. Ginzton, *Microwave Measurement*s, McGraw-Hill Book Co., 1957, p. 435.

[3] B.E. Carlsten, R. J. Faehl, M.V. Fazio, W.B. Haynes, and R.M. Stringfield, "Intense Space-Charge Beam Physics Relevant to Relativistic Klystron Amplifiers," submitted to the *5th Special Issue on High Power Microwave Generation of the IEEE Trans. on Plasma Sci.,* October 1994.

[4] High Frequency Structures Simulator code marketed by Hewlett Packard.

RELATIVISTIC MAGNETRONS AND KLYSTRONS AT LONG PULSE DURATIONS

James Benford, Jerrold S. Levine, S. K. Lam,
Bruce D. Harteneck, David Price and Michael J. Willey
Physics International Co.
2700 Merced Street
San Leandro, CA 94577

Abstract

Extending the pulse duration of high power, relativistic microwave sources beyond ≈100 ns is a great challenge because of pulse shortening mechanisms such as gap closure and RF breakdown. We are exploring the long pulse operation of both relativistic magnetrons and relativistic klystron amplifiers. Together they represent the major classes of HPM sources: crossed field devices and linear beam tubes. We are improving the quality of the surface conditions by a variety of techniques, operating at low (~10^{-7}Torr) vacuum and reducing the electric fields in the interaction region where possible. Thus far we have produced high power magnetron pulses with durations of 400 ns and conducted a beam propagation experiment on the RKA which shows stable operation for the entire duration of the electrical pulse.

INTRODUCTION

Future applications of high power microwaves will require high average powers, sometimes only for short bursts. The average power of a microwave device is

$$\bar{P} = \hat{P}\, f\, t = \hat{P}\, (DF)$$

where $\bar{P}$ is the average power, $\hat{P}$ is the peak power, f is the repetition rate, t is the pulse duration and (DF) is the duty factor. High peak powers have been produced in many sources.[1] Typically powers of 1 - 10 GW have been achieved up to ~ 35 GHz.

Thus the technical challenge is two-fold: to increase the repetition rate and to extend the pulse duration. This means we must sustain high electric fields on a repetitive basis and over longer durations while avoiding RF breakdown and gap closure. Physics International has been investigating extending the repetition rate and the pulse duration of both relativistic magnetrons and relativistic klystron amplifiers in order to achieve higher average powers. Together they represent the major classes of HPM sources: crossed-field devices and linear beam tubes.

In recent years we have operated several types of relativistic magnetrons and relativistic klystrons at repetition rates up to 250 Hz and found stable operation at peak powers up to 1 GW.[2] In this regime, operation is not limited by gas buildup between pulses, by electrode erosion or by microwhisker depletion. Thus far we found that high peak powers are not limited by rf breakdown so that even higher peak powers are probably achievable at such repetition rates, producing an average power, of perhaps 100 kW at 1000 pps.

Pulse durations > 100 ns and approaching 1 μs are widely pursued for all high power sources. A number of experimental disciplines are necessary for long pulse operation. It is clearly desirable to maximize the anode-cathode spacing, and it is essential to align and center components so that the axis of the magnetic field, the cathode and the wall are coincident. Vacuum cleanliness is essential for reaching long pulse durations.

To achieve longer pulse durations we use two pulsed power sources, one 17 Ω and one 50 Ω, each at 500 kV, with FWHM of 500 ns and a base to base duration of 800 ns.

We've been able to eliminate most pulse-shortening mechanisms from consideration by experimental design and others have been found not to be important, especially in the magnetron.

RELATIVISTIC MAGNETRONS

As is observed in all high power devices, the pulses from our magnetrons are shorter than the electrical pulse when the duration is > 100 ns. The variety of mechanisms suggested for this ubiquitous phenomena in the magnetron are:

- Cathode Plasma Motion - outward radial expansion changing the rf boundary and altering the resonance should eventually produce impedance collapse.
- Anode Plasma Motion - azimuthal spreading occludes resonators but first changes vane shape and alters the resonance. Inward expansion can also cause impedance collapse.
- Plasma Streaming - plasma generated upstream flows into the diode and disrupts the beam's interaction with the vanes.
- RF Breakdown - critical rf field exceeded, causing local electron emission and multipactoring.
- Iris Sparking - critical rf field exceeded at the iris between the resonator and the extraction waveguide.
- Diode Voltage Variation - deviation from flat top alters the resonance.
- Impedance Mismatch - generator of too low impedance feeds mechanism that terminates microwave output.

Recently we have used two types of rising sun resonators to study long pulse effects in the L- band. One has six resonators, as have all of our previous magnetrons, and the second magnetron has ten resonators. This allows larger gap spacing, lower RF energy density and redistributes the electromagnetic energy so that most of the energy is in the larger resonators. For both devices we used two waveguides to extract from the magnetron.

On the basis of our observations, we find the plasma streaming, rf breakdown, iris sparking and diode voltage variation mechanisms are ruled out or very unlikely. The remaining contenders are plasma motion and impedance mismatch between the electrical driver and the magnetron.

Figure 1 shows the microwave pulse duration for the ten vane magnetron. Here the anode-cathode gap is 1.6–2.8 cm, the electrical characteristics are 200–500 kV, 3–12 kA, 100–500 ns. The pulse duration is as long as 400 ns. Generally longer pulses can be obtained by using higher impedance pulsed power. Note that in this magnetron, the conversion efficiency varies from 10 to 20%, a good efficiency for operation of relativistic magnetrons.

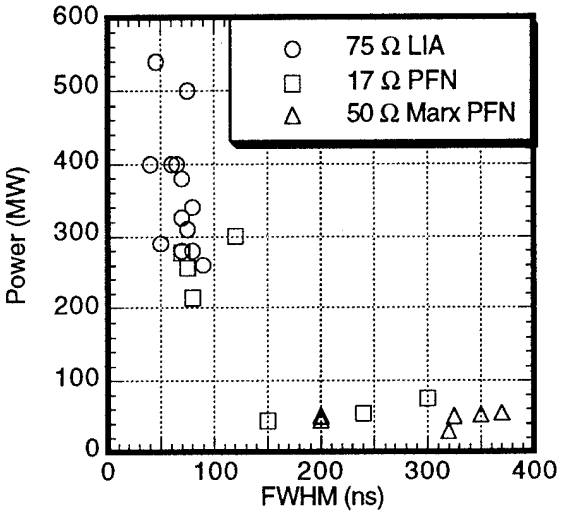


Figure 1. Power from a ten vane magnetron as a function of pulse width and impedance of pulsed power driver.

In contrast, Figure 2 shows power as a function of the pulse duration for a collection of data from experiments at PI in which the impedance of the electrical driver was typically a factor of three less than that of the magnetron. The typical efficiencies for Figure 2 are ~ 5–10%.

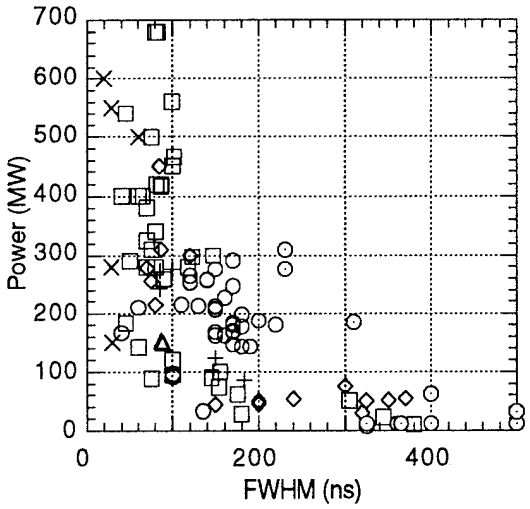


Figure 2. Power as a function of pulse width from experiments on several six and ten vane magnetrons.

The voltage-current characteristic of the ten vane magnetron shows it to be a constant voltage device, with the operating voltage controlled by the magnetic field. Hence, when driven by a high impedance source, low current and thus low power pulses result. However, when driven by a low impedance source, it may draw more current than is optimal. The result is lower efficiency and shorter pulses. Perhaps this is because the electrodes receive higher current densities, and/or because the plasma density in the interaction space becomes too large.

Observations of a relativistic magnetron by Gleizer *et. al.*[3] at Tomsk show high closure velocity when microwaves are present and low velocity when there are few or no microwaves. Our results are consistent with a mechanism in which the intense microwave fields cause rapid cross-field diffusion of cathode (or anode) plasma. This is observed as a rapid impedance drop. The plasma motion alters the resonance condition of the magnetron and, as the enhanced cross-field motion continues, the microwaves terminate. Then cross-field diffusion slows as does the impedance fall rate. Recent gyrotron experiments at Strathclyde are consistent with this scenario.[4]

Evidence for this mechanism is shown in Figure 3. Here we show the normalized rate of impedance collapse, (1/Z) dZ/dt, as a function of the microwave pulse width. Clearly, slower impedance collapse corresponds to increasing pulse width. The closure velocity implied is ~10cm/ μs at 100ns and ~1cm/ μs at 300ns. The physical signature of the microwave enhanced closure model is that closure velocity and impedance fall correlate with increased microwave power or electric field in the resonator. Figure 4 shows impedance fall rate does increase with field in the resonator. The critical level appears to be fields above ~200 kV/cm.

Therefore our conclusion is that two pulse shortening mechanisms survive experimental scrutiny: rapid plasma motion, perhaps caused by the microwave fields themselves, and current effects caused by impedance mismatch.

RELATIVISTIC KLYSTRON

Our development efforts with the relativistic klystron amplifier[5] have concentrated on repetitive operation. (We found there was no degradation of the pulse due to repetitive operation at 200 pps for a 200 shot burst of 250 MW pulses.[6]) Only recently have we begun a program that will lead to a long pulse RKA.

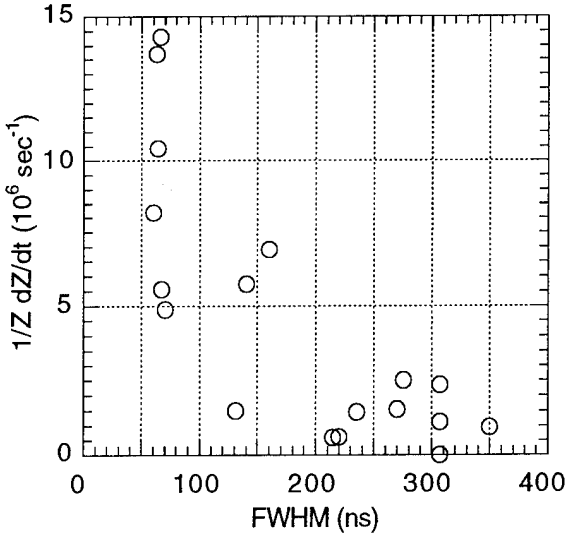


Figure 3. Rate of impedance drop as a function of pulse width for the ten vane magnetron.

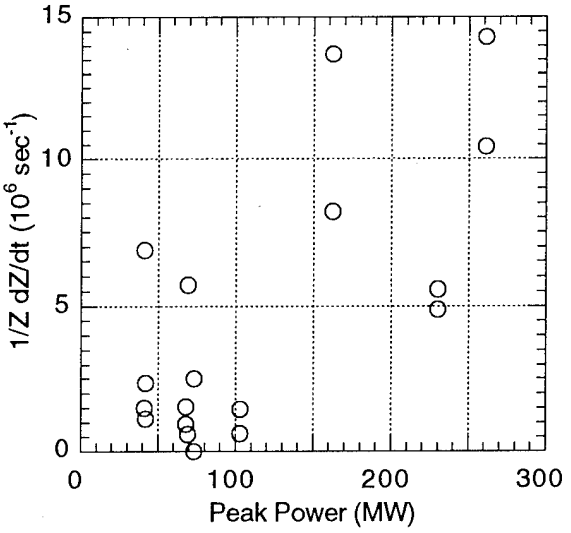


Figure 4. Rate of impedance drop as a function of peak power in the ten vane magnetron.

As the initial phase in the long pulse RKA experiment, we conducted a diode/beam transport test. This was to define a cathode tip shape and diode gap that would produce the required beam parameters (5 kA at 500 kV) without impedance collapse and to determine if instabilities would preclude transport of the electron beam. Witness plates verified that the annular beam shape was preserved. Two Rogowski coils were used to measure the

current: the Upstream monitor to measure the current on the cathode shank and the Transmitted monitor to measure the beam current after it had propagated 40 cm in the drift tube. Typical data are shown below in Figure 5. Although it appears that the cathode shank begins to emit after a few hundred ns, the transmitted current trace is quite flat. Since CAMEL-X/LP has a much lower impedance than the load (even including the cathode shank loss current), the voltage variation during the pulse is small. The beam should therefore be perfectly suitable for the RKA.

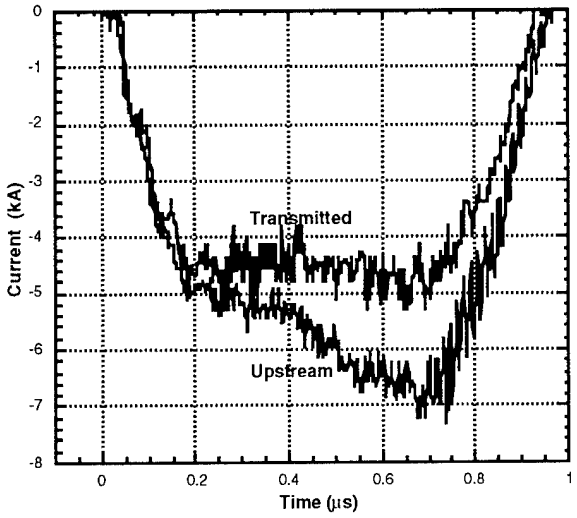


Figure 5. Voltage and current measurements from the diode/beam transport experiment on CAMEL-X/LP (500 kV, 17 Ω, 500 ns FWHM).

CONCLUSIONS

In the magnetron, pulse shortening is due to at least two mechanisms. The electrical interaction when the magnetron is driven by too much current produces shortened pulses and causes reduced efficiency. There is also an impedance drop simultaneous with the microwave pulse which occurs for high RF electric fields. We attribute this to a microwave enhanced closure mechanism. If this effect is a general phenomena, it has implications for many other microwave devices. Only devices that prevent high electric fields from entering the diode can avoid pulse shortening. So gyrotrons and CARMs as well as all O-type Cerenkov devices and some free electron lasers will be vulnerable. Pulse shortening has been observed in these sources. The only device fundamentally immune to the effect is the klystron, which connects the bunching cavities and the diode with drift spaces cut off to the microwaves. Perhaps the other devices could be modified to prevent pulse shortening by inserting cut off sections after the diode.

At this point in our experiments, we have seen that an electron beam suitable for an RKA can be created and transported for a pulse duration of 500 ns. RF production for that pulse length awaits further experimentation.

ACKNOWLEDGMENT

The work reported here has been sponsored by the US Army, BMDO/IS&T, and the Defense Nuclear Agency. The RKA bunching section was supplied by M. Friedman and V. Serlin of the Naval Research Laboratory.

REFERENCES

1 J. Benford and J. Swegle, *High Power Microwaves*, Artech House, Norwood, MA, 1992.

2 J. Benford, N. J. Cooksey, J. S. Levine and R. R. Smith, "Techniques for High Power Microwave Sources at High Average Power," *IEEE Trans. Plasma Sci.*, **21**, 388 (1993).

3 I. Z. Gleizer, A. N. Didenko, A. S. Sulakshin, G. P. Fomenko and V. I. Tsvetkov, "Limitation on the Duration of the Microwave Emission in a High-Current Magnetron," *Sov. Tech. Phys. Lett.*, **6**, 19 (1980).

4 K. Ronald, S. N. Spark, A. D. R. Phelps, W. He and H. Yin, "Plasma Diagnostic Observations on Pulsed, Cold Cathode, Gyrotrons," EUROEM'94, FRA-03-02, Bordeaux, France (1994).

5 M. Friedman, J. Krall, Y. Y. Lau and V. Serlin, "Externally modulated intense relativistic electron beams," *J. Appl. Phys.*, **64**, 3353 (1988).

6 J. S. Levine, B. D. Harteneck, S. K. Lam, C. W. Parks, "High-current relativistic klystron research at Physics International," *Intense Microwave Pulses II*, Howard E. Brandt, Ed., Proc. SPIE 2154, 19 (1994).

Modelling Magnetically Insulated Transmission line Systems Using Flow Impedance

C. W. Mendel, Jr. and S. E. Rosenthal
Sandia National Laboratories, Albuquerque, NM 87185

Abstract

Many pulsed power systems are large and complex. As a result, simulations of these systems can be difficult, expensive, and unwieldy. This paper describes a model that accurately describes most systems, and can be run in a few minutes on a modern personal computer. The model assumes that the system can be approximated by coaxial magnetically insulated transmission lines whose impedance varies with position along the line. The effects of distributed electron charge and current are included. The transmission lines are described in terms of Telegrapher equations derived for this more complex situation. There are two equations in the magnetic and electric voltages, and a third involving the electron charge and current. The voltages are related to the line charge and current by flow impedance. The model describes all fields at the surface of the electrodes, and therefore the currents and charges on those electrodes. The model can be used for design and for data analysis. It will be compared to two-dimensional, time-dependent particle-in-cell (PIC) simulations.

Static Problem: First consider the static 1-D problem. We have a coaxial line with azimuthal symmetry. It has distributed charge and current, as shown in Fig. 1. We have chosen positive polarity, but the change to negative polarity is trivial. It is convenient to transform to variable R

$$R=\frac{1}{2\pi}\sqrt{\frac{\mu_o}{\epsilon_o}}\ln\left(\frac{r_o}{r}\right)$$

where $r_o>0$ is arbitrary. The line impedance is just $Z_v=R_a-R_c$. Also, instead of $B_\phi(R)$ and $E_r(R)$, we use the current I(R) and charge Q(R)

$$B_\phi(R)=\frac{\mu_o I(R)}{2\pi r}$$

$$E_r(R)=\frac{Q(R)}{2\pi\epsilon_o r} \quad .$$

The magnetic and electric voltages are

$$cA(R)=c\int_r^{r_c} B_\phi dr=\int_{R_c}^{R} I(R)\,dR$$

$$V(R)=\int_r^{r_c} E_r dr=c\int_{R_c}^{R} Q(R)\,dR$$

and $A_a=A(R_a)$, $V_a=V(R_a)$.

We define two flow impedances: electric Z_f, and magnetic Z_m, by

$$V_a=Z_f cQ_a+(Z_v-Z_f)\,cQ_c$$

$$cA_a=Z_m I_a+(Z_v-Z_m)\,I_c \quad .$$

Figures 2 show electric potential profiles for two situations. In Fig. 2a the electric field at the cathode, and therefore the cathode charge Q_c, are zero. In Fig. 2b the field is reversed at the cathode, as often happens after wave reflection from a load. Notice that the

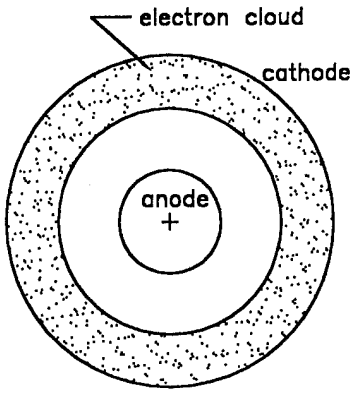


Figure 1 Cross section of a coaxial MITL in positive polarity.

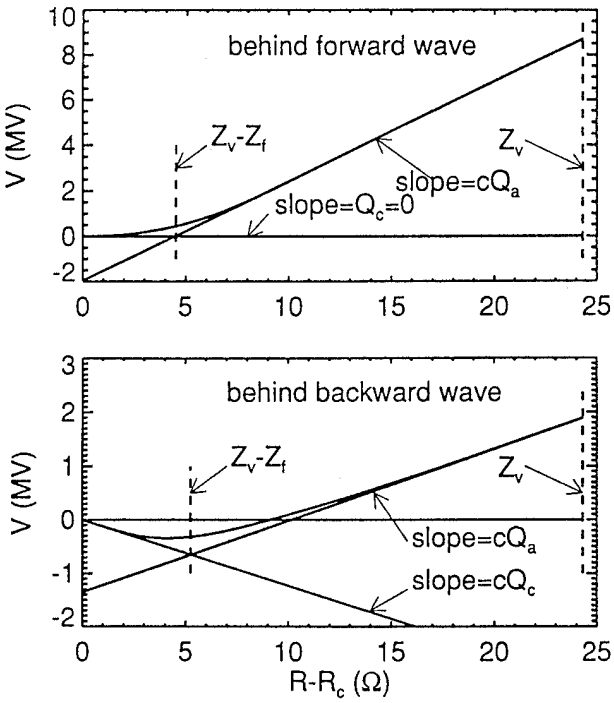


Figure 2 Electric potential profiles taken from simulations. The first (upper) is behind a forward wave, and the second (lower) is behind a backward wave.

electron layer could be replaced by the same charge in a thin layer at R-R_c=Z_v-Z_f, and V_a, Q_a, and Q_c would be the same. A similar situation occurs for Z_m and the current layer. It is usually accurate to approximate Z_m=Z_f, and we shall do so here.

Since the electron current and charge densities are

$$j_z = \frac{1}{2\pi r}\frac{dI}{dr}$$

$$\rho = \frac{1}{2\pi r}\frac{dQ}{dr}$$

the net radial electro-magnetic force T_r is

$$T_r = -j_z B_\phi + \rho E_r$$

$$= \frac{-\mu_o}{(2\pi r)^2}\frac{d}{dr}\left(\frac{I^2 - c^2Q^2}{2}\right) .$$

But electrons are so light that $T_r \doteq 0$. Thus I_a^2-$c^2Q_a^2$=I_c^2-$c^2Q_c^2$.

Dynamic problem: Now consider the dynamic 2-D problem. We want a system of Telegrapher equations that will correctly calculate an ensemble of test problems. The test problems could be experimental, but we will use PIC simulations since sufficient experimental data are not available. What experimental data are available agree with PIC simulation. The test we will use is that the model correctly calculate the step conditions across forward wave fronts and for wave fronts reflected from loads shown in Fig. 3.

We now transform the azimuthal component of Faraday's law and the radial component of Ampere's law. We assume azimuthal symmetry. Q(R,z,t) and I(R,z,t) have the same definition as above, but they are no longer simply the enclosed electron

charge and current. In addition define S and J by

$$E_z(r,z,t)=\frac{S(R,z,t)}{2\pi\epsilon_o r}$$

$$j_r(r,z,t)=\frac{J(R,z,t)}{2\pi r} \quad .$$

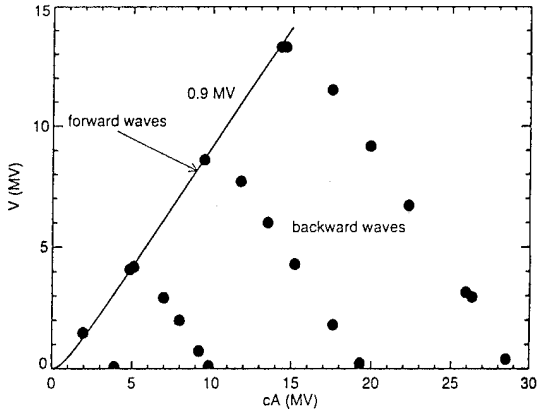


Figure 3 Voltage plotted versus magnetic voltage behind forward and reflected waves in a MITL for an ensemble of simulations.

Maxwell's equations then become

$$\frac{\partial I}{\partial t}+c^2\frac{\partial Q}{\partial z}$$

$$+\frac{c^2}{2\pi}\sqrt{\frac{\mu_o}{\epsilon_o}}\frac{\partial}{\partial R}\left(\frac{S}{r(R)}\right)=0$$

$$\frac{\partial Q}{\partial t}+\frac{\partial I}{\partial z}+J=0 \quad .$$

The definitions of A and V do not change, but they are no longer simply the scalar potential and axial component of vector potential. Integrating Maxwell's equations from cathode to anode we get two Telegrapher's equations

$$\frac{\partial A}{\partial t}+\frac{\partial V}{\partial z}=0$$

$$\frac{\partial V}{\partial t}+c^2\frac{\partial A}{\partial z}-I_a\frac{dR_a}{dz}+I_c\frac{dR_c}{dz}$$

$$+c\int_{R_c}^{R_a}JdR=0$$

Because we have three conductors (anode, cathode, and electron cloud) we need a third Telegrapher's equation. We get it by taking the difference between the second Maxwell's equation at the anode and cathode. Defining $I_e=I_a-I_c$, $Q_e=Q_a-Q_c$

$$\frac{\partial Q_e}{\partial t}+\frac{\partial I_e}{\partial z}+J(R_a)-J(R_c)=0$$

We solve problems in three variables, A,V,Q_e. I_e can be written in terms of these using the definitions of $Z_v(z)$, $Z_f(z)$, and the pressure balance between anode and cathode

$$I_e=I_e(A_a,V_a,Q_e)=\frac{cA_a}{2Z_f-Z_v}$$

$$\mp\left[\frac{c^2A_a^2}{(2Z_f-Z_v)^2}-\frac{2V_acQ_e}{2Z_f-Z_v}+c^2Q_e^2\right]^{1/2}$$

where the sign is opposite that of A.

Given a function $J(R,A_a,V_a,Q_e)$ we can get a solution, and the get the currents and charges from the flow impedances and I_e. We have derived a function J that gives the jump conditions of Fig. 3.

Some comparisons to PIC simulations are shown below.

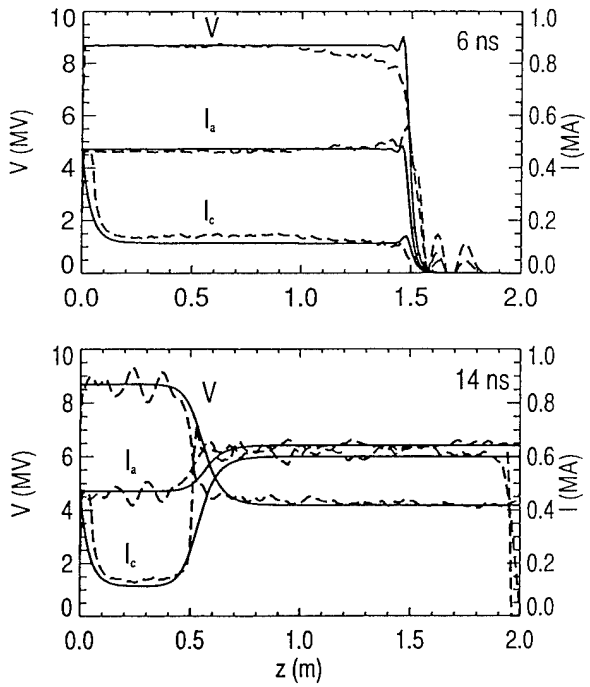


Figure 4 Model (solid) and simulation (dashed) calculations of the electric voltage, and the anode and cathode currents for a step voltage in a 24.3 Ω, 2.0 m long MITL. Times are 6.0 ns (upper) and 14 ns (lower).

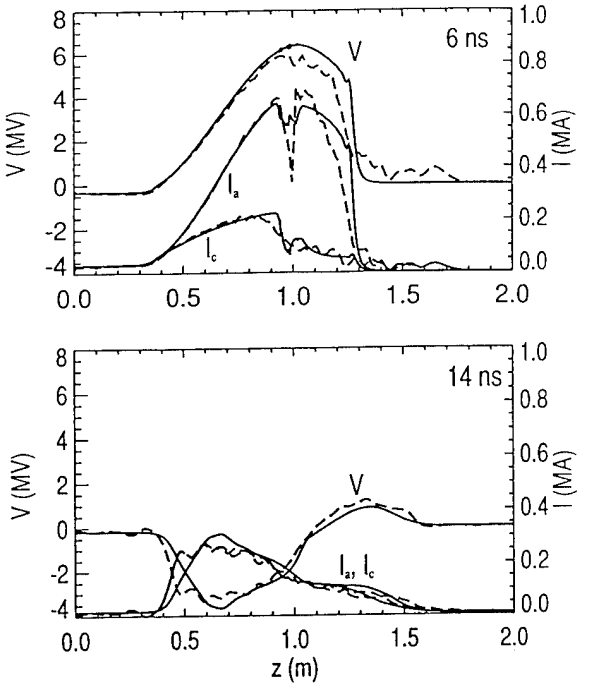


Figure 5 Model (solid) and simulation (dashed) calculations for a 5.0 ns wide (at the base) pulse travelling down a MITL that begins at 11.9 Ω and changes abruptly to 24.3 Ω at the middle of the 2.0 m long line. Times are 6.0 and 14.0 ns.

Conclusion

We have developed a set of Telegrapher equations that describe power flow in magnetically insulated transmission lines. These equations are derived in a rigorous way. There is one function, $J(R,A_a,V_a,Q_e)$, that is determined by fitting data from an ensemble of PIC simulations, and that does not vary between problems. In addition the flow impedance must be determined from analysis, simulation, or experiment, any of which should be accurate. In the modelling presented here the flow impedance is independent of time, but this is not required.

This model can be used to study large, complicated pulsed power systems on a small computer, in less time and at a small fraction of the cost of a PIC simulation. It can also study larger problems than are practical for PIC simulations.

This work supported under US Department of Energy contract DE-AC04-94AL85000.

Conduction phase to opening phase transition in the plasma opening switch

J.M. Grossmann, S.B. Swanekamp*, R.J. Commisso, P.J. Goodrich#, D.D. Hinshelwood#, J.D. Huba, P.F. Ottinger, and B.V. Weber

Plasma Physics Division, Naval Research Laboratory, Washington, DC 20375
* Science Applications International Corporation, McLean VA 22102
# JAYCOR, Inc., Vienna, VA 22182

Abstract

The transition between the conduction phase and opening phase of a long-conduction-time plasma opening switch (POS) is examined with the aid of numerical simulations. Evidence of three physical mechanisms is observed: magnetic pressure, magnetic field transport, and gap erosion resulting from ion acceleration out of electrostatic potential hills. Gap erosion occurs in the radial middle of the POS where the quantity B^2/n is at its largest.

I. Introduction

An integral part of inductive energy storage systems is the plasma opening switch (POS), which bridges the anode-cathode gap of a section of transmission line as the storage inductor charges with current.[1] During the conduction phase, the POS conducts all of the generator current, allowing none to pass to the load. During the POS opening phase, an increasing fraction of generator current is delivered to the load. Several physical mechanisms control the conduction and opening phases of POS operation. These include magnetic pressure, magnetic field transport, and electrostatic gap formation. Magnetic pressure deforms and displaces the plasma by J×B forces.[2, 3] Magnetic field transport mechanisms allow magnetic field (current) to penetrate into the plasma rather than being shielded out of the plasma. These mechanisms include the Hall effect (EMH),[4, 5, 6] electron inertia,[7] and resistive diffusion.[8] Electrostatic gap formation has been described in earlier numerical investigations of short-conduction-time POS, where a potential hill is observed to form near the cathode on the generator side of the plasma fill.[9] Large electrostatic forces accelerate ions out of the potential hill region and the potential hill migrates along the cathode toward the load, leaving a magnetically insulated gap in its wake. When the potential hill reaches the load side of the plasma fill, current begins to flow to the load.

Two of the most important unresolved issues in POS research are how the POS transitions between the conduction and opening phases and how gaps form in the plasma. This paper will describe PIC simulations of this transition in the context of long-conduction-time POS operation. The simulations exhibit all three of the mechanisms mentioned above. Electrostatic gap opening is observed for the first time to occur away from the cathode and in the radial middle of the plasma.

II. Simulation set-up

Since the simulations described here focus on the transition between the conduction and opening phases of POS operation, a density profile similar to the one found at the end of the conduction phase in fluid simulations of the POS is used as an initial condition to the PIC simulations. Experimentally, the POS opens and the conduction phase ends roughly when the current reaches the load end of the POS.[10] Fluid code simulations yield a generic picture of the conduction phase of long-conduction-time POS in which J×B forces deform and displace the plasma both radially and axially.[3, 11, 12] When the current reaches the load end, the density profile is shaped like a saddle with a radial density minimum in the middle of the POS fill region and density rising toward the electrodes. Similar density distributions are used here as initial distributions in PIC simulations of the transition to

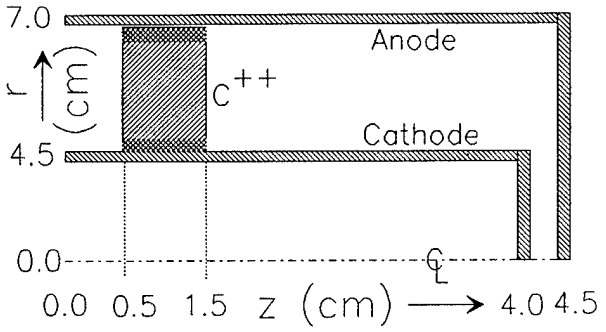


Fig. 1. Schematic of simulation region.

opening. The geometric configuration of the simulations is shown in Fig. 1. The left side of the simulation region is connected to a capacitor-inductor circuit designed to mimic a typical generator. The capacitor is assumed to be almost completely discharged so that the circuit is preloaded with current and the POS plasma carries 1.2 MA from the beginning of the simulation. A short section of transmission line connects the POS to a diode load on the right. The diode impedance is nominally 4 Ω, but drops to about 1 Ω late in time when a significant amount of electron flow enters the diode region. The diode impedance is set by introducing a resistive material in the diode gap with a prescribed resistivity.

The axial length of the initial plasma fill is 1 cm and the axial density profile is taken to be uniform. Several initial radial density profiles were investigated, all of which had the same electron density at the cathode, but different minimum densities in the middle of the plasma and/or a choice of whether the density rose again toward the anode or remained uniform. While most of the plasma ions consist of doubly ionized carbon, immobile ions are placed in regions of radial width 2 mm from both electrode surfaces. The gap formation process in the radial middle of the plasma is independent of the use of immobile ions near the electrodes. However, when carbon ions are used near the electrodes at densities accessible to simulations, gaps can form at the electrodes that are nearly as large as the gap in the radial middle of the plasma (depending on the relative magnitudes of the electrode vs. intra-electrode plasma densities). Long-conduction-time POS experiments strongly suggests gap formation in the radial middle of the plasma,[3] not near the electrodes. It is assumed that this is due to the presence of large plasma densities near the electrodes. The use of immobile ions reduces the size of gaps near the electrode surfaces and brings them closer to those expected in experiment and may be interpreted as a computationally convenient means of modeling high density electrode plasmas.

III. Simulation Results

The results reported here are for the specific case where the density at the cathode ($r = 4.5$ cm) is 10^{15} cm^{-3}, then drops smoothly to 2×10^{14} cm^{-3} at $r = 5.5$ cm, and then remains uniform to the anode radius of $r = 7.0$ cm. Results obtained for the same density profile for $r \leq 6.0$ cm, but thereafter rising to 10^{15} cm^{-3} toward the anode, are similar to those in which the density remains uniform all the way to the anode. Other results for which the density minimum is 10^{14} cm^{-3} rather than 2×10^{14} cm^{-3} are similar except that larger gaps form in the lower density plasma and the time during which the POS remains in the conduction phase is shorter.

Early in simulation, the plasma is accelerated axially toward the load by the J×B force. Magnetic field also begins to penetrate the plasma and a current channel front migrates axially through the plasma. In the region, $5.5 \text{ cm} \leq r \leq 7.0$ cm (where the plasma was initially radially uniform), the magnetic front travels with the penetration speed, $v_H = cB/(4\pi ne r) \approx 2$ mm/nsec, associated with the Hall effect due to cylindrical curvature.[5] In the region near the cathode, $4.5 \text{ cm} \leq r \leq 5.5$ cm (where the initial plasma density gradients are negative), a current channel front is also observed to penetrate axially into the high density plasma. The rate of penetration is slightly slower than in the region $5.5 \text{ cm} \leq r \leq 7.0$ cm. This magnetic penetration near the cathode cannot be explained by the Hall effect since the combination of cylindrical curvature and density gradient effects[4] are in a direction to expel magnetic field rather than allow penetration. The magnetic field penetration may be associated either with electron vorticity[13, 6] or electron inertia effects.[7] Electron vortices are observed near the cathode in these

particular simulations and are a recurring feature of POS simulations in general.

At about the point that the current channel reaches the load edge of the plasma, potential hills begin to form in the region 5.5 cm ≤ r ≤ 5.8 cm and propagate axially through the plasma. Large electrostatic electric fields in the potential hills accelerate ions out of the potential hills. This process of ion acceleration has the effect of eroding a radial gap in the plasma. The gap extends through the axial length of the plasma and has a radial width of about 3 mm. The term gap is used here to mean a region largely evacuated of plasma in which a large fraction of electrons are magnetically insulated. After the gap forms, electron flow is observed downstream (toward the load) of the POS region. The electron current flow runs axially in the POS region, but turns radially toward the anode in the region downstream of the POS.

Some of the effects described above can be seen in the next two figures. In Fig. 2, the electron density just before and after gap formation is shown. The minimum density in these iso-density

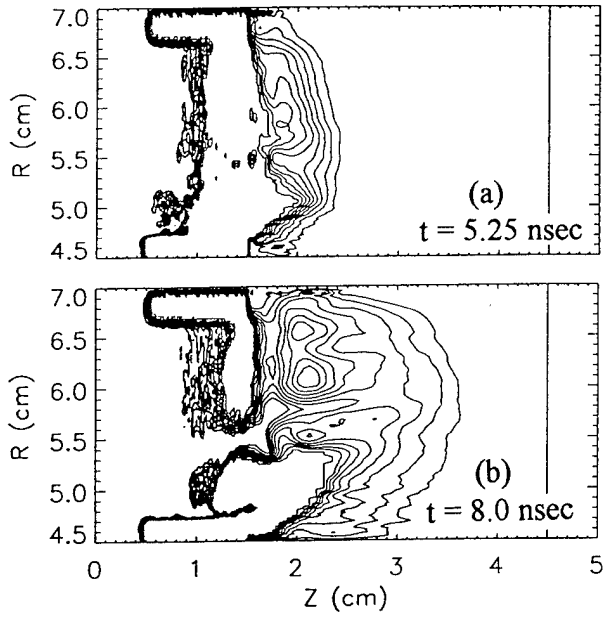


Fig. 2. Iso-density contours in the POS plasma

contours is chosen to be 10^{13} cm^{-3} and the maximum density is 10^{14} cm^{-3}. Higher and lower densities exist, but are not shown for clarity. The interval between contour lines is 10^{13} cm^{-3}. Initially, the plasma occupies the region 0.5 cm ≤ z ≤ 1.5 cm. In Fig. 2a, the left boundary of the plasma has been displaced axially by J×B forces. The right boundary shows a low density cloud of plasma flung downstream of the initial fill region in a bow-shaped cloud. The appearance of small density depressions inside the plasma in the region near r = 5.5 cm shows the density thinning effect of potential hills that have formed in that region. In Fig 2b, a gap has fully eroded in the plasma, and the cloud of low density plasma has been further accelerated into the downstream transmission line.

Contours of the current streamlines ($2\pi rB/\mu_0$) are shown in Fig. 3 just before and after gap formation. The maximum contour is 1.2 MA

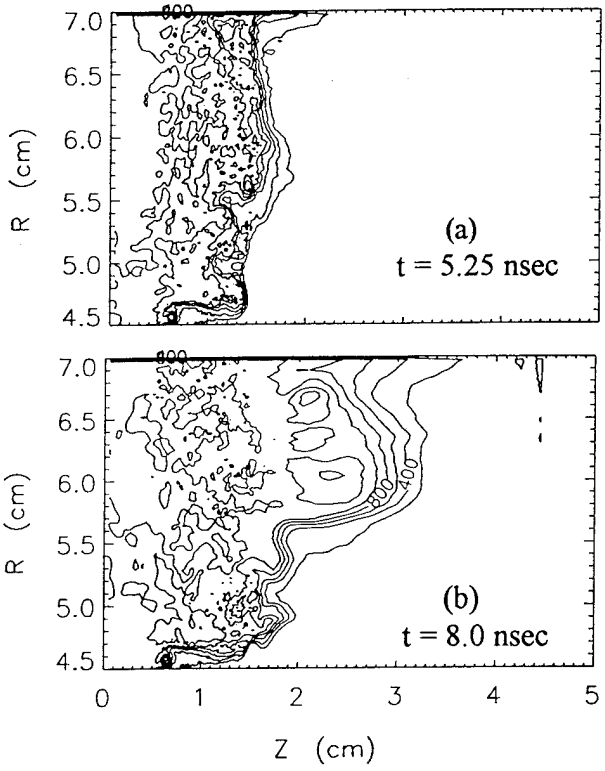


Fig. 3. Current streamlines

and the minimum is 200 kA with an interval between contours of 200 kA. In Fig. 3a, a narrow current channel is seen to have penetrated to the load edge of the plasma. The current has penetrated axially throughout the plasma except in parts of the immobile ion region near the cathode. In Fig. 3b, the current in regions on the cathode

side of the gap (Fig. 2b) is seen to flow in the high density POS plasma, while the current on the anode side of the gap flows in the low density plasma cloud axially downstream of the original POS fill region.

The electron flow downstream of the POS immediately after POS opening is not magnetically insulated away from the anode because the downstream region is filled with a cloud of ions that have been flung downstream of the POS during the conduction phase. These ions tend to be dragged axially toward the load and radially toward the cathode by the electric fields associated with electron E×B drift. As the ion cloud is removed in this manner from the downstream transmission line, the electron flow becomes increasingly insulated from the anode and flows into the load.

IV. Summary

The transition between the conduction phase and the opening phase has been examined with 2-D PIC simulations. A current channel is observed to migrate axially through the initial plasma fill region while the POS is still in its conduction phase. The plasma is displaced by J×B forces at the same time that magnetic transport effects allow current channel penetration. When the channel reaches the load end of the initial plasma fill, gap formation is observed. For the densities used here, gap sizes are roughly consistent with Hawk experiments.[10] These preliminary results show good agreement with previous simulations[14] of gap formation near the cathode where gap sizes and potential hill magnitudes scaled as d (cm) $\approx 10^9$ B/n_e and φ (MV) $\approx 5 \times 10^4$ B^2/n_e, with B(Gauss) and $n_e(cm^{-3})$ is the electron density . These scaling results predict gap sizes d $\approx$ 2.7 mm and potential hills of magnitude $\varphi \approx 700$ kV, in agreement with the present simulations. Gap formation in these and previous simulations occurs before the POS plasma has any information about the load. The radial position of the gap coincides with the location of largest B^2/n_e. This is where potential hill magnitudes are largest and where magnetic pressure forces are expected to produce the most axial plasma displacement.

Many issues remain to be resolved. Understanding the physical mechanism(s) that define the transition between the conduction phase and the electrostatic gap formation phase, as well as the gap formation process itself, could lead to experimental techniques to increase the gap size. More work is also needed on the interactive coupling of the POS and load and on understanding the mechanism that allows magnetic field transport in the region near the cathode where the density decreases with radius.

V. Acknowledgments

Simulations were performed with the MAGIC[15] code supported through the AFOSR's sponsored MAGIC Users Group. This work is supported by DNA.

VI. References

[1] See Special Issue on Fast Opening Vacuum Switches, IEEE Trans. Plasma Sci. **PS-15**, 629 (1987).
[2] W. Rix, D. Parks, J. Shannon, J. Thomson, E. Waisman, IEEE Trans. Plasma Sci. **PS-19**, 400 (1991).
[3] D.D. Hinshelwood, B.V. Weber, J.M. Grossmann, R.J. Commisso, Phys. Rev. Lett. **68**, 3567 (1992).
[4] A.S. Kinsep, Yu.V. Mokhov, K.V. Chukbar, Sov. J. Plasma Phys. **10**, 495 (1985).
[5] A. Fruchtman, Phys. Fluids B **3**, 1908 (1991).
[6] R.J. Mason, P.L. Auer, R.N. Sudan, B.V. Oliver, C.E. Seyler, J.B. Greenly, Phys. Fluids B **5**, 1115 (1993).
[7] B.V. Oliver, L.I. Rudakov, R.J. Mason, P.L.Auer, Phys. Fluids B **4**, 294 (1992).
[8] R.M. Kulsrud, P.F. Ottinger, J.M. Grossmann, Phys. Fluids **31**, 1741 (1988).
[9] J.M. Grossmann, P.F. Ottinger, R.J. Mason, J. Appl. Phys. **66**, 2307 (1989).
[10] R.J. Commisso, P.J. Goodrich, J.M. Grossmann, D.D. Hinshelwood, P.F. Ottinger, B.V. Weber, Phys. Fluids B **4**, 2368 (1992).
[11] J.D. Huba, J.M. Grossmann, P.F. Ottinger, to be published in Phys. of Plasmas (1994).
[12] J.J. Watrous, M.H. Frese, private communication.
[13] A. Fruchtman, K. Gomberoff, Phys. Fluids B **5**, 2371 (1993).
[14] J.M. Grossmann, S.B. Swanekamp, P.F. Ottinger, R.J. Commisso, D.D. Hinshelwood, B.V. Weber, submitted to Phys. of Plasmas (1994).
[15] B. Goplen, L. Ludeking, D. Smithe, G. Warren, MAGIC Users Manual, Mission Research Tech. Report No. MRC/WDC-R-282.

MAGNETODYNAMICS OF MULTICOMPONENT PLASMA

L. Rudakov
RRC Kurchatov Institute 123182 Moscow, Russia

Abstract

Magnetic field penetration and plasma components dynamics under magnetic pressure has been studied. Plasma ions with highest Z/M are moving ahead centrum of mass and down the frozenin magnetic field together with electrons. The problems of nonlinear magnetic field diffusion in plasma and the magnetic field redistribution in a thin shell, accelerated by magnetic pressure are solved.

I. INTRODUCTION

Due to the progress in pulse power techniques the experimental studies of Z-pinches compressed by current up to 10 MA are running actively[1,2]. Such pinches plasma in density range 10^{17} - 10^{19} cm^{-3} is formed as a result of ionization of gas jet inside cathode - anode gap. Plasma usually consists of ions with different Z/M. It can happen due to mixture of different gases or because of corona equilibrium, where two or three consequent Z are most representative. Another subject of broader investigations is POS plasma with a density 10^{14} - 10^{16} cm^{-3}, which is a mixture of ionized hydrogen and carbon [3,4].

The typical time duration for POS is $t_0 = 10^{-7}$s. For the magnetic field around 10^4 G the next inequality take place:

$$\omega B_p > 1/t_0 > \omega_{Bc} \qquad (1)$$

where ω_{Bp}, ω_{Bc} are cyclotron frequencies for proton and single ionized carbon. The next inequality take place for the scale of the problem:

$$Vc/\omega_{Bc} > \delta > V_p/\omega_{Bp} \qquad (2)$$

if we estimate proton and ion velocities as a Alfven velocities.

At these conditions it is very important to take into account the effects which specify the multicomponent plasma behavior. Such effects have been studied for semiconductor plasma, for slightly ionized plasma and for high current Z-pinches[5-7]. General set of equations for multicomponent plasma can be found in ref., [8] for slightly ionized plasma in ref., [6] and for Z-pinches in ref., [9].

II. THE EQUATIONS FOR POS PLASMA

For an easier understanding of physics, we consider the next two simple models. The first one is applied to POS plasma. We will consider plasma consisting of two kinds of ions: protons and single ionized carbon atoms. Because of big difference in ions masses the C+ movement corresponds to those of centrum of mass and can be described by equation:

$$n_c M_c \frac{dV}{dt} = -\frac{\partial}{\partial z}\frac{B^2}{8\pi} \qquad (3)$$

n_c, M_c - density and mass of C^+. We will consider the half-space problem, $z > 0$. Magnetic field will be one component, $\vec{B} = 0, B, 0)$. In equation of proton motion we neglect the internal term and Lorentz force because of

inequality (1). But we take into account the friction between protons and C^+ due to collisions with a frequency $\nu_p\left(T_p, n_c\right) \rangle\rangle \omega_{Bp}$.

$$e\vec{E} - \nu_p\left(\vec{V}_p - \vec{V}\right) = 0 \quad . \tag{4}$$

The equations for electrons and for electric and magnetic fields are:

$$\left(\vec{E} + \frac{1}{c}\vec{V}_e \times \vec{B}\right) = \frac{\vec{j}}{\sigma} \quad , \tag{5}$$

$$-\frac{1}{c}\frac{\partial \vec{B}}{\partial t} = \nabla \times \vec{E} \quad , \tag{6}$$

$$\Delta \times \vec{B} = \frac{4\pi e}{c}\left(n_c \vec{V}_p + n_c \vec{V}_c - n_e \vec{V}_e\right) \quad . \tag{7}$$

In quasineutral plasma with magnetized electrons nonmagnetized ions are drifting under Hall electric field. In the set of equations (4), (5), (7) we can exclude E and V_e:

$$\nu_p\left(V_{p-V_c}\right)_z = -\frac{1}{8\pi M_p n_e}\frac{\partial B^2}{\partial z}, n_e = Z_c n_c + n_p \tag{8}$$

$$\frac{\partial B}{\partial t} + \frac{\partial}{\partial z} V_{zc} B = \frac{c^2}{4\pi\sigma}\frac{\partial^2 B}{\partial z^2} - \frac{\partial}{\partial z}\frac{n_p}{n_e} V_{zp} B =$$

$$= \frac{c^2}{4\pi\sigma}\frac{\partial^2 B}{\partial z^2} + \frac{\partial}{\partial z}\frac{n_p}{n_e^2}\frac{B}{8\pi M_p \nu_p}\frac{\partial B^2}{\partial z} \tag{9}$$

The protons are moving away from the plasma border under the force $-\frac{1}{8\pi}\frac{\partial B^2}{\partial z}$, that is why we have to use the equation for proton density

$$\frac{\partial n_p}{\partial t} + \frac{\partial}{\partial z} V_{zc} n_p = -\frac{\partial}{\partial z} n_p \left(V_p - V_c\right)_z + \frac{N - n_p}{\tau_i} =$$

$$= \frac{\partial}{\partial z}\frac{n_p}{n_e}\frac{1}{8\pi M_p \nu_p}\frac{\partial B^2}{\partial z} + \frac{N - n_p}{\tau_i} \tag{10}$$

The last term qualitatively describes the tendency of n_p to equilibrium stat N. In part 4 we will demonstrate the importance of this phenomena.

The Hall electric field does the work on the drifting protons according to eqs. (4) and (8).

$$\frac{d\varepsilon}{dt} = \left(V_p - V_c\right) e n_p E_z = \frac{n_p}{M_p \nu_p}\left(\frac{\nabla B^2}{8\pi n_e}\right)^2 = \frac{j^2}{\sigma_{eff}} \tag{11}$$

$$\sigma_{eff} = \frac{M_p c^2}{B^2}\frac{n_e^2}{n_p}\nu_p \quad , \tag{12}$$

ε- internal energy of plasma. So, we have got an equation describing ions heating in form of usual Joule heating.

III. EQUATIONS FOR MULTI-COMPONENT PLASMA OF Z-PINCHES

Multi-ionized plasma is typical for fast Z-pinches. For description of such plasma the model where two ionization stat $Z_1 = Z_1(t)$ and $Z_2 = Z_1 + 1$ for atoms with mass M are used.

Centrum mass velocity is described by Eq.:

$$M\left(n_1 + n_2\right)\frac{dV_r}{dt} = -\frac{\partial}{\partial r}\left(\frac{B^2}{8\pi} + p\right) \quad , \tag{13}$$

$$V_r = \frac{(n_1 V_1 + n_2 V_2)_r}{n_1 + n_2} \quad .$$

In approximation $v_1 \rangle\rangle \frac{ZeB}{Mc}, \frac{1}{t_o}$ the relative movement of ions is described by eq.:

$$m(v_1 + v_2)(V_2 - V_1)_r = e(Z_2 - Z_1)E_r =$$

$$-\frac{Z_2 - Z_1}{8\pi n_e}\frac{\partial}{\partial r}B^2, n_e = Z_1 n_1 + Z_2 n2 \quad . \qquad (14)$$

Instead of (9) we get if $\partial B / \partial r \rangle\rangle B / r$:

$$\frac{\partial B}{\partial t} + \frac{\partial}{\partial r}V_r B = \frac{c^2}{4\pi\sigma}\frac{\partial^2 B}{\partial r^2} -$$

$$-\frac{\partial}{\partial r}\frac{n_1 n_2}{n_1 + n_2}\frac{(V_2 - V_1)_r B}{n_e} =$$

$$= \frac{c^2}{4\pi\sigma}\frac{\partial^2 B}{\partial r^2} + \frac{\partial}{\partial r}\frac{n_1 n_2}{n_1 + n_2}\frac{(Z_2 - Z_1)B^2}{4\pi M(v_1 + v_2)n_e^2}\frac{\partial B}{\partial r} \quad . \qquad (15)$$

In general case the equation for B in multicomponent Z-pinches plasma can be found in ref.[9]. Instead of eq. (10) we get:

$$\frac{\partial}{\partial t}(n_1 + n_2) + \frac{\partial}{\partial r}(n_1 + n_2)V_r = 0 \quad , \qquad (16)$$

$$\frac{\partial n_2}{\partial t} + \frac{\partial}{\partial r}n_2 V_r = -\frac{\partial}{\partial r}\frac{n_1 n_2}{n_1 + n_2}(V_2 - V_1)_r +$$

$$+\frac{n_1 - n_2}{\tau_i} =$$

$$= \frac{\partial}{\partial r}\frac{n_1 n_2}{n_1 + n_2}\frac{(Z_2 - Z_1)}{8\pi M n_e (v_1 + v_2)}\frac{\partial B^2}{\partial r} + \frac{n_1 - n_2}{\tau_i} \qquad (17)$$

The second terms in the right part of eqs. (9) and (15) look like nonlinear diffusion terms. It describes the magnetic field flow with electrons followed the drifting ions with highest Z/M in Hall electric field. This effect was studied for semiconductor plasma and is know n as magnetoresistance[5]. For switching - the penetration of magnetic field and current through plasma slab[6].

It should be mentioned that Hall field works as a separator of light ions. It draws away the protons form plasma boundary which moves with velocity of centrum of mass. Due to this effect proton density and diffusion coefficient in eq. (9) are strongly decreasing. The diffusion still high enough only because of appearance of new protons. This important phenomena has not been taken into account in ref.[9].

IV. MAGNETIC FIELD PENETRATION IN PLASMA INDUCED BY PARTICLES SEPARATION UPON MASS

We will use the set of eqs. (3), (9), and (10) describing the POS plasma. We neglect carbon ions motion because of big difference between mass of proton and C+. We suppose for simplicity $n_p \langle\langle n_e$ and v_p = const. For this case the equation for B and n_p will be:

$$\frac{\partial B}{\partial t} = \frac{c^2}{4\pi\sigma}\frac{\partial^2 B}{\partial z^2} + \frac{\partial}{\partial z}\frac{n_p}{n_e^2 v_p 8\pi M_p}\frac{\partial B^2}{\partial z}, \qquad (18)$$

$$\frac{\partial n_p}{\partial t} = \frac{\partial}{\partial z}\frac{n_p}{n_e}\frac{1}{8\pi M_p v_p}\frac{\partial B^2}{\partial z} + \frac{N - n_p}{\tau_i} \quad . \qquad (19)$$

As $n_p / n_e \langle\langle 1$ we neglect $\frac{\partial n_p}{\partial t}$ in eq. (19), but we keep $\frac{\partial B}{\partial t}$ in eq. (18). Then the eq. (19) can be integrated

$$\frac{n_p}{n_e}\frac{1}{8\pi M_p v_p}\frac{\partial B^2}{\partial z} = e^{-\frac{z}{\lambda_0}}\int_0^z \frac{N}{\tau_i} e^{\frac{z}{\lambda_0}} dz, \lambda_0 =$$

$$= -\frac{\partial B^2}{\partial z}\frac{\tau_i}{8\pi M_p v_p n_e} \quad . \qquad (20)$$

Near the boundary, $z\langle\langle\lambda_0$, eq. (18) can be written as:

$$\frac{\partial B}{\partial t} + \frac{\partial}{\partial z} zB\frac{N}{n_e\tau_i} = \frac{c^2}{4\pi\sigma}\frac{\partial^2 B}{\partial z^2} \quad , \qquad (21)$$

and for $z\rangle\rangle\lambda_0$ as:

$$\frac{\partial B}{\partial t} = \frac{\partial}{\partial z}\frac{N}{n_e^2 v_p 8\pi M_p}\frac{\partial B^2}{\partial z} \quad . \qquad (22)$$

Such equation for B field diffusion was studied in ref.[6].

We have neglected the regular diffusion induced by electron-ion collision ν_{ei} in eq. (22) because it is very small for typical cases $\left(V_{ei}V_p\langle\langle\omega_{Be}\omega_{Bp}\right)$. But it must be taken into account near the plasma boundary. Protons are pushed away from boundary by Hall electric field. The magnetic flux in plasma q_B is controlled by regular diffusion and is described by equation

$$q_B = -\frac{c^2}{4\pi\sigma}\frac{\partial B}{\partial z} + zB\frac{N}{n_e\tau_i} = \frac{cB_0}{\left(2\pi\sigma\tau_i\right)^{\frac{1}{2}}} \quad . \qquad (23)$$

This flux supports nonlinear diffusion described by eq. (22) at the big distance. This process looks like a magnetic wave propagation:

$$B = \left(\frac{12\pi M_p v_p n_e^2}{N} q_B\right)^{\frac{1}{3}} \left(z_0(t) - z\right)^{\frac{1}{3}} \quad . \qquad (24)$$

Wave velocity can be found from the relation for $z_0\rangle\rangle z_1$ (see Figure 1).

$$q_B = \frac{d}{dt}\int_{z_1}^{z_0} B dz = \left(q_B\frac{12\pi M_p v_p n_e^2}{N}\right)^{\frac{1}{3}} z_0^{\frac{1}{3}}\frac{dz_0}{dt} \quad . \qquad (25)$$

So:

$$\frac{dz_0}{dt} \sim t^{-\frac{1}{4}} \quad , \qquad (26)$$

or:

$$\frac{z_0}{B_0 t / \left(4\pi n_p M_p\right)^{\frac{1}{2}}} = \frac{1}{\left(v_p t\right)^{\frac{1}{4}}}\left(\frac{v_p}{\omega_{Bp}}\right)^{\frac{1}{2}}\frac{1}{\left(\nu_{ei}\tau_i\right)^{\frac{1}{4}}} \quad . \qquad (27)$$

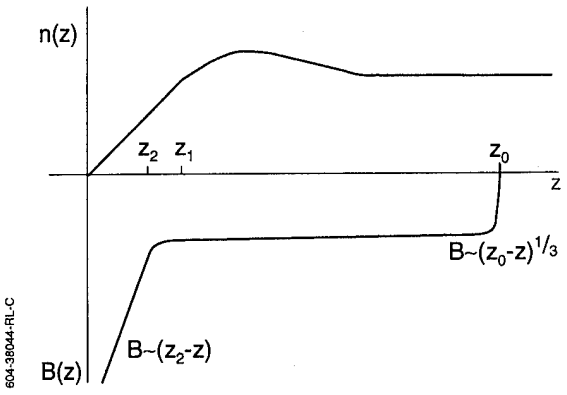


Figure 1

In previous calculations we supposed $v_p = const$. It is easy to consider the ions heating in accordance with eqs.. (11), (12). In nonlinear magnetic wave (24) the change of internal energy $\nabla\varepsilon$ is equal:

$$\nabla\varepsilon = \frac{q_B B}{16\pi}\frac{1}{dz_0/dt} \quad . \qquad (28)$$

If the temperature of C^+ and protons is the same, but electrons get a small part of energy, then we have:

$$\frac{3}{2}(n_c+n_p)T_i=\frac{B_1B}{16\pi},q_B=B_1\frac{dz_0}{dt} \quad . \qquad (29)$$

For this case $T_i \sim B, v_p \sim B^{-\frac{3}{2}}$. Then instead of eqs. (24), (26) we have:

$$B\sim(z_0(t)-z)^{\frac{2}{9}},\frac{dz_0}{dt}\sim t^{-\frac{2}{11}} \quad . \qquad (30)$$

On Figure 1, the dependence of and $n(z,t)$ on coordinate z is shown. The field amplitude B_0 for case $z_0 \rangle\rangle z_1, v_p = const$ can be estimated from eqs. (23), (24), (27).

$$\frac{B_1}{B_0}=\left(\frac{\nu_{ei}}{\omega_{Be}}\right)^{\frac{1}{2}}\left(\frac{M}{m}\right)^{\frac{1}{8}}\left(\frac{t}{\tau_i}\right)^{\frac{1}{4}} \quad . \qquad (31)$$

V. THIN SHELL ACCELERATION BY MAGNETIC PRESSURE

Now we will consider the dynamics of thin shell under the magnetic pressure. In accordance with ref.[2] we describe the density distribution in the shell moving with acceleration g by equation:

$$nMg=\frac{\partial B^2}{\partial r},n=n_1+n_2 \quad . \qquad (32)$$

We suppose that the equilibrium $n_1 = n_2$ take place for two ionization states, $T_e = T_i = const$, $n_e T \langle\langle B^2/8\pi$. The last inequality is fulfilled for dense, high radiative plasmas. For this case eqs. (15), (16) can be rewritten as $(Z_2 - Z_1 = 1)$:

$$\frac{\partial b}{\partial t}+\frac{\partial}{\partial r}vb=\frac{\partial^2 b}{\partial r^2}+\beta^2\frac{\partial}{\partial r}n_0^2\frac{b^2}{n^2}\frac{\partial b}{\partial r} \quad , \qquad (33)$$

$$b=\frac{B}{B_0},\beta=\frac{eB_0}{cMv_i(n_o)}\left(\frac{M}{2m}\right)^{\frac{1}{4}},4\pi n_0 Mg\delta_0=B_0^2.$$

Here and below in this section r and t are normalized: $r \to r/\delta_0, t \to tc^2/4\pi\sigma\delta_0^2, B_0$ - magnetic field amplitude on plasma boundary for $t > 0$. $v \langle\langle gt$ - plasma velocity inside shell.

$$\frac{\partial n}{\partial t}+\frac{\partial}{\partial r}nv=0 \quad . \qquad (34)$$

In eqs. (32), (33), (34) we can use b as variable instead of r and search a solution for $\varphi(b,t) = \partial b/\partial r$. Excluding n and v

$$4\pi nMg=b\varphi,v=\frac{\partial b/\partial t}{\varphi} \quad ,$$

we can get the next equation for φ (see ref.[2])

$$-\frac{\partial\varphi^2}{\partial t}=(\varphi^2-B^2)\frac{\partial\varphi^2}{\partial b^2} \quad . \qquad (35)$$

Its general solution is

$$\varphi^2=F\left[(\varphi^2-B^2)t-b^2\right] \quad , \qquad (36)$$

F - arbitrary function. As examples we consider two particular solutions. The first is:

$$\varphi=\frac{db}{dr}=\left(\frac{b^2}{t}+\beta^2\right)^{\frac{1}{2}} \quad . \qquad (37)$$

For $b > \beta t^{\frac{1}{2}}$ eq. (37) corresponds to exponential solution

$$b\sim\exp\left(\frac{R-gt-r}{\delta_s}\right),\delta_s=\left(\frac{c^2t}{4\pi\sigma}\right)^{\frac{1}{2}} \quad . \qquad (38)$$

But for $\beta^2 t > 1$ magnetic field and density drop to zero on the inner side of shell as $(r+\delta-R+gt)$, but current density still constant.

$$\delta = \delta_0 v_i(n_0)\frac{Mc}{eB_0}\left(\frac{2m}{M}\right)^{\frac{1}{4}}, 4\pi M n_0 \delta_0 g = B_0^2 \ . \quad (39)$$

The other particular solution is (see Fig. 2)

$$\varphi^2 = \frac{C}{b^2+\beta^2 t-\varphi^2 t} \ . \quad (40)$$

$$\text{If } \frac{1}{\beta^2} > t > \frac{1}{\beta^4}, \beta^2 > 1 \ . \quad (41)$$

For

$$B \sim n \sim (r+\delta-R+gt)/\delta(t), \delta \sim t^{-\frac{1}{2}}. \quad (42)$$

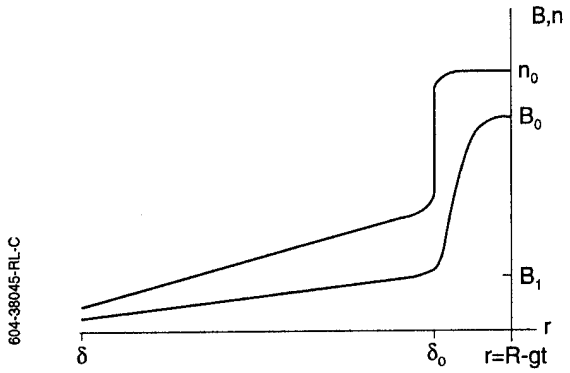


Figure 2

As it was discussed in ref.[2], the solutions like (37), (40) with $\varphi \neq 0$ on the inner side of shell are changing drastically if we take into account a small plasma pressure. Plasma and magnetic pressure accelerate low dense plasma from inner surface and destroy the shell.

We have considered only two solutions of eq. (35),k but we suppose that the remarks made in ref.[9] about existence of indestructible one-dimensional solution like (38) with $\delta_S = \beta\left(\frac{c^2 t}{4\pi\sigma}\right)^{\frac{1}{2}}$ is questionable.

VI. CONCLUSION

Magnetic field penetration in multicomponent plasma is strongly different from usual field diffusion due to electrons friction. Because of separation of particles with high Z/M under Hall electric field - they move together with part of electrons brining the frozenin magnetic field into plasma. This effect does not change strongly the magnetic flux coming in plasma, because the flux is controlled by usual diffusion near the boundary. But there is redistribution of the entering magnetic flux on the largest scale , than usual skin depth:

$$z_0 / \left(\frac{c^2 t}{4\pi\sigma}\right)^{\frac{1}{2}} = \left(\frac{\omega_{Be}}{\nu_{ei}}\right)^{\frac{1}{2}}\left(\frac{\nu_i t}{\nu_{ei}\tau_i}\right)^{\frac{1}{4}}$$

This effect can have influence on quality of POS working parameters and on the quality of plasma shell acceleration by magnetic pressure. When magnetic field comes to inner side of the shell the separation of particles with highest Z/M begins. Such a plasma with frozenin magnetic field will be accelerated to axis, and the efficiency of plasma shell acceleration will decrease.

VII. ACKNOWLEDGMENT

Author thanks his colleagues from Kurchatov Institute K. Chukbar, A. Gordeev, A. Kingsep and A. Fruchtman from Weizmann Institute for helpful discussions. He is very grateful for hospitality to the Weizmann Institute of Science, Israel, where due to discussion of theoretical problems and new experimental data of

Y. Maron's group the preliminary ideas were realized in this paper.

REFERENCES

1 See, for example, Dense Z-pinches (AIP Conference Proceedings No. 195, N. Pereira, J. Davis, N. Rostoker, eds., Amer. Inst. Phys., NY 1989)

2 Ibid L. Rudakov. Magnetically Accelerated Plasma Stability, p. 290

3 D. Hinshelwood, B. Weber, J. Grossman, R. Commisso. Phys. Rev. Lett., 1992, 68, p 3567

4 M. Sarfaty, Y. Maron, Ya. Krasik, A. Weingarten, R. Arad, R. Shpitalnik, A. Fruchtman. Spectroscopic Investigations of the Plasma Behavior in a Plasma Opening Switch Experiment.. Submitted to BEAMS '94 Conference, June 20-24 1994, San Diego, CA USA

5 V. Vladimirov, V. Gorshkov, Ju. Javlinsky, JETP, 1975, 65, p. 750

6 F. Felber, R. Hunter, N. Pereira, T. Tajima, Appl. Phys. Lett. 1982, 41 (8), p. 705

7 G. Barak, N. Rostoker, Appl. Phys. Lett. 1982, 41, p.918

8 S. Braginsky in Review of Plasma Physics, ed. by M. Leontovich (Consulting Bureau, NY 1969) vol. 1, p.205

9 A. Gordeev, Fizika Plasmy, 1987, 13, p.1235

CIRCUIT CHARACTERIZATION OF MAGNETICALLY INSULATED ELECTRON FLOW

Donald E. Parks, Paul Steen
S-Cubed, Division of Maxwell Laboratories, Inc.
3398 Carmel Moutain Road
San Diego, CA 92121-1095

Abstract

We consider a switch characteristic corresponding to magnetically insulated electron flow in a gap between an effective cathode and anode. The current voltage relationship in a circuit containing parallel switch and load elements remains that of the switch independent of the load for load impedance which is not too small. This concept to which the analytic model investigated in this paper conforms is confirmed by two-dimensional PIC calculations for electron flow in a magnetically insulted gap leading into a vacuum feed terminated by a resistive load.

1. Introduction

The physical mechanisms underlying the operation of long conduction time (~1 μs) plasma opening switches have been the object of intensive research over the last decade. Although the physics of conduction in the POS is not completely understood, recent experiments point to the importance of Hall fields as well as ordinary magnetohydrodynamic (MHD) forces (resulting in a snowplow of the plasma) in the low voltage, conduction phase of the switch. The physical mechanisms that operate during current switchout to produce voltage in the switch remain less well understood, certainly quantitatively, than those that control conduction. Notwithstanding this, it is likely that plasma erosion, MHD forces, or both are involved in the opening process.

Commisso et al, have described the POS in terms of switch limited operation and load limited operation. [1] An open circuited load is an example of the former case, and the circuit I-V characteristic is that of the switch. Waisman [2] has suggested that even for finite (but not too small) load impedance and for a switch characteristic corresponding to magnetically insulated electron flow, the circuit characteristic remains that of the switch, independent of the load. This property for magnetically insulated flow will be clarified below. That the circuit properties are determined completely by the switch for sufficiently high load impedance carries with it the implication that for discharge of an inductively stored energy into a parallel switch-load combination in which the load impedance begins at a finite value, the time evolution of switch voltage remains independent of the load for some time. This notion to which the model set forth in this paper conforms is confirmed by PIC calculations for electron flow in a narrow gap opening into a vacuum feed terminated by a resistive load.

2. The Opening Gap

The physics of the opening phase of the switch is believed to involve the formation of a sheath, or gap of size D(t) which varies with time, across which the flow of electrons is inhibited by the magnetic field. Figure 1 illustrates the basic elements of the model and helps to establish notation.

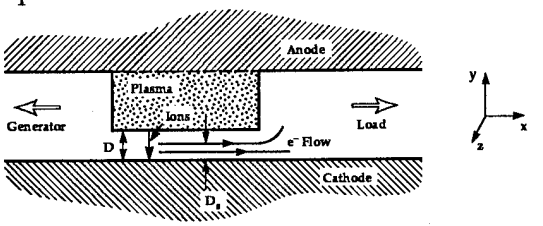


Figure 1. The Opening Model. The opening model for the switch is a one-dimensional model, assuming Brillouin electron flow parallel to the cathode and space charge limited ion flow from plasma to chathode. The gap D forms through ion erosion of the switch plasma. The height of the sheath above the cathode is D_S.

For the geometry of Figure 1, Creedon [3] derived the following relation between gap voltage V, sheath voltage V_s and anode magnetic field for Brillouin flow of electrons in the gap D,

$$\frac{eB_aD}{mc^2}=\gamma_s\left[\ell n\left[\gamma_s+\left(\gamma_s^2-1\right)^{1/2}\right]+\frac{\gamma_0-\gamma_s}{\left(\gamma_s^2-1\right)^{1/2}}\right] \quad (1)$$

where $\gamma = 1 + eV/mc^2$.

The cathode boundary field B_c for these solutions is given by $B_c = B_a/\gamma_s$, a result which holds for the flow patterns other than Brillouin flow. The value of γ_s does not follow a priori from Creedon's analysis. Wang and DiCapua [4] have proposed that γ_s follows from a minimum total energy principle, electromagnetic energy plus electron kinetic energy, and have examined the consequences of this principle for one-dimensional systems. One consequence of their analysis is that over a wide range of voltages there is little quantitative difference between the value of γ_s determined from the minimum energy principle and the value determined by requiring that the current be a minimum with respect to γ_s.

The minimum current condition yields the following relation between the diode and sheath values of γ_0

$$\gamma_0=\gamma_m+\left(\gamma_m^2-1\right)^{3/2}\ell n\left[\gamma_m+\left(\gamma_m^2-1\right)^{1/2}\right] \quad (2)$$

where γ_m is the value of γ_s at the current minimum. Together with eq. (1), this result constitutes a unique diode current-voltage (I-V) characteristic. In the following, we will apply Creedon's I-V characteristic to the opening phase of the plasma opening switch.

3. Analysis of a Simple Circuit

We now consider the behavior of a circuit containing a hypothetical switch element with a current voltage relationship characterized by equations (1) and (2). We suppose that the switch element is part of the circuit represented in Figure 2 and is driven by a constant current generator. At t = 0, we impose the initial condition that the switch carries the entire current I_0, while the current I_L in the load vanishes. For t > 0, current is switching into the load.

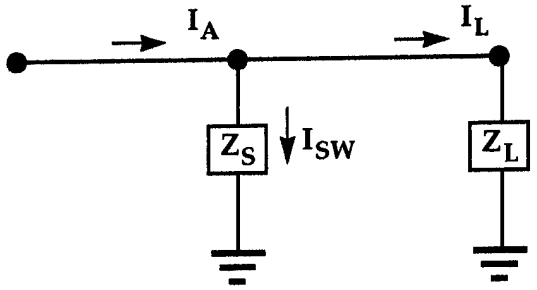


Figure 2.Circuit model with switch element charcterized by eqs. 1 and 2.

We assume that until the load current is large enough to equal the cathode current required for magnetically insulated flow, the switch operates at the current minimum, and that otherwise the value of γ_s is determined by the load current. Specifically

$$\gamma_s = \min(\gamma_m, I_A/I_L). \quad (3)$$

We shall refer to switch or load limited phases, respectively, according as γ_s is given by γ_m or I_A/I_L. In the initial phase of opening (ignoring a brief Child-Langmuir bipolar erosion phase), while $I_L \ll I_A$, the circuit is switch limited.

4. Comparison with PIC Calculations

Calculations were performed with the FRED particle-in-cell code to evaluate the accuracy of the analytic treatment of the electrons in the switch gap, to test the assumption that for small load currents the switch voltage is load independent, and to determine the fate of the electrons as they drift out of the gap. The geometry used for the calculations is shown in Figure 3.

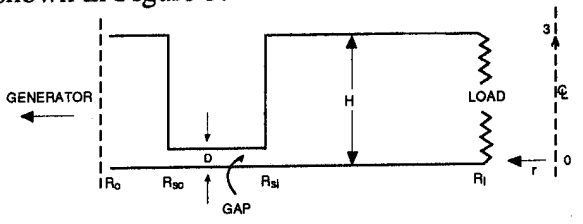
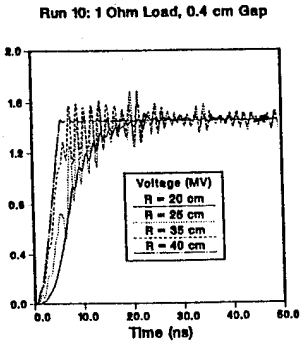


Figure 3. Geometry for PIC calculations.

The axisymmetric geometry corresponds to the top one-half of ACE-4,[5] the bottom half given by reflection of the figure in the plane z = 0. Relevant dimensions are H = 5 cm, R_i = 20 cm, R_0 = 50 cm, R_{si} = 40 cm and R_{s0} = 45 cm. The switch gap D is fixed at 0.4 cm. The tangential electric field vanishes in all boundaries except at r = R_i and r = R_0. The entire cathode surface is capable of space charge limited emission of electrons.

At the input boundary at R = R_0, the current increases on a linear ramp for 5 ns at which time it becomes constant at 4.3 MA. The load is a fixed resistor extending from cathode to anode, and for the calculations that follow is given values of 15.3 Ω, 1 Ω, 1/3 Ω and zero ohms, the first corresponding closely to open circuit conditions, the latter to more nearly matched load conditions and to an inductively short-circuited load, respectively. The inductance of the system between R_0 and R_i is about 8 nH, giving L/R times (in vacuum) ranging from about 0.5 ns at 15.3 Ω to about 25 ns at R = 1/3 Ω. We attempt to run the calculations until the system reaches a steady, or quasi-steady state corresponding to the asymptotic input current of 4.3 MA.

Figure 4 shows the voltage waveforms at various radial positions for the three values of resistance. In the 15.3 Ω and 1 Ω cases corresponding to switch limited operation the voltage achieves a steady value, apart from small oscillations consistent with a switch impedance of about 1/3 Ω. In both cases the characteristic time to achieve "steady state" voltage after allowing for the current rise time of 5 ns is consistent with the L/R time.



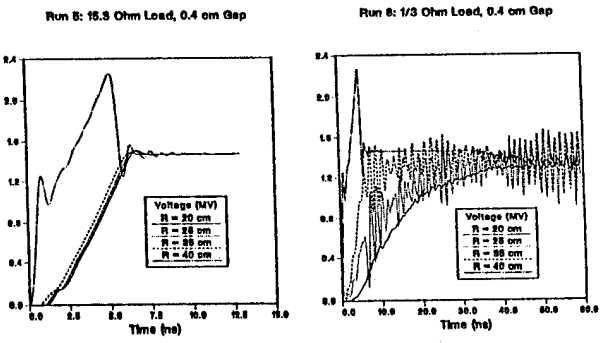


Figure 4. Voltage histories at various points in the diode for three values of load resistance.

The value of switch voltage, 1.4-1.5 MV, and impedance, 1/3 Ω, determined from the PIC results compare favorably with the results calculated from the model, Figure 5.

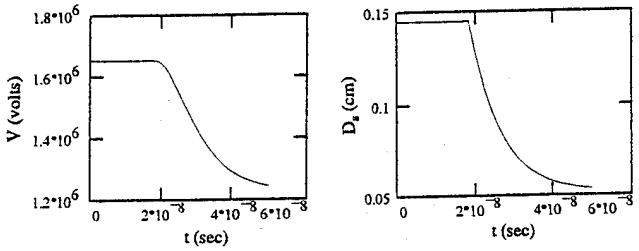


Figure 5. Gap voltage and sheath height for R_L =1/3 Ω

The corresponding analytic result for the case of a 1 Ω and 15.3 Ω loads are precisely the same, namely, V = 1.66 MV, for t < 50 ns, based on the criterion of eq. (3) whereby the value of γ_s still is that corresponding to minimum current.

The largest perceptible differences between the 15.3 Ω and 1 Ω cases occur in the feed on the load side of the 0.4 cm gap. The salient features are the development of a potential minimum, the electron repelling electric field at the cathode, the apparent tendency toward formation of a diamagnetic current loop shielding the interior of the region from the magnetic field of the surface currents, and the closure of current paths at the cathode surface just on the upstream (generator) side of the load.[6] This closure evidently corresponds to the return of

launched electrons to the load. Similar results are reported by Grossman and Swankamp. [7]

The patterns observed for the case of a 1 Ω load are even more pronounced for the 1/3 Ω load, a case which illustrates a departure at $t \approx 20$ ns from the apparent switch limited behavior for 15.3 Ω and 1 Ω loads. The potential hill and the diamagnetic current loop appear more fully developed for this case.[6]

The results of the calculations for an inductive short circuit load, Figures 6 and 7, provide the most striking example of dynamic switch limited operation. As with a resistive termination, a voltage plateau of 1.4 MV develops in the interval between about 7 ns and 20 ns, followed by a voltage collapse ending in a steady oscillation of voltage about a small value. The occurrence of this transition at about 20 ns is analogous to the one observed in the 1/3 Ω case at about 35 ns, but which is absent during the computational time interval of the 15.3 Ω and 1 Ω cases.

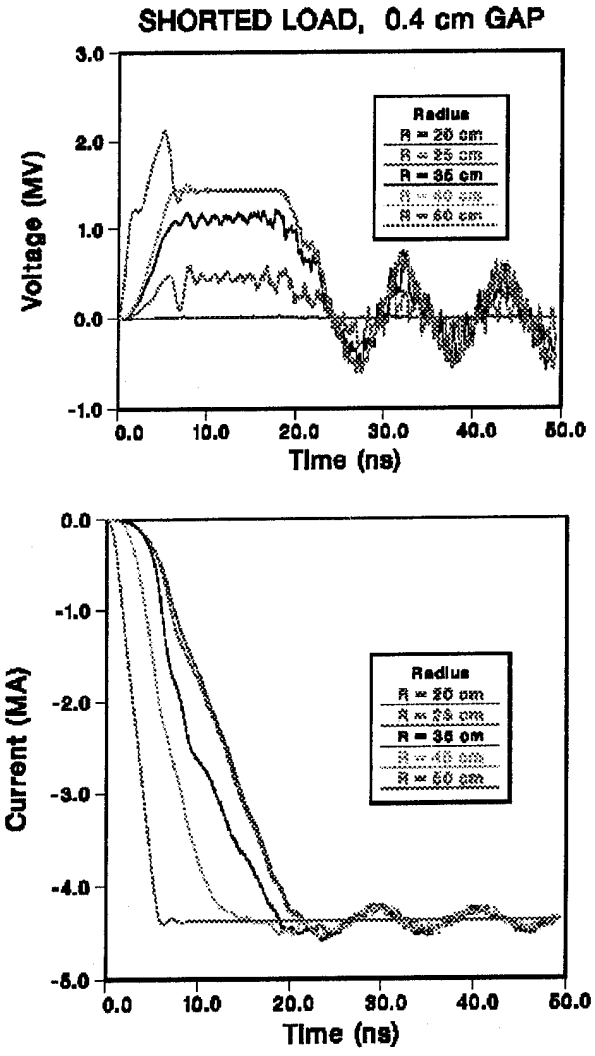


Figure 6. FRED 2-D PIC simulation of ACE-4 radial geometry swtich design.

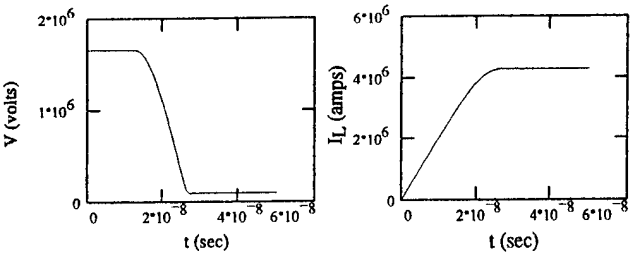


Figure 7. Voltage and load current for short circuit (RL=0.01Ω).

REFERENCES

1. Commisso, R.J., P.J. Goodrich, J.M. Grossman, D.D. Hinshelwood, P.F. Ottinger, and B.V. Weber, "Character-ization of a Microsecond-Conduction-Time Plasma Opening Switch," Phys. Fluids B4 (71), p. 2368, 1992.
2. Waisman, E., et al., Above Ground Test (AGT) Evaluation Support Program, S-Cubed Quarterly Report, SSS-DPR-90-11948, Nov. 1990.
3. Creedon, J.M., "Magnetic Cutoff in High Current Diodes," J. Appl. Phys. 48 (3), p. 1070, 1977.
4. Wang, M.Y., M.S. DiCapua, "Operating Point of Long Magnetically Insulated Vacuum Transmission Lines," J. Appl. Phys. 51 (11), p. 5610, 1980.
5. Thompson, J., P. Coleman, C. Gilbert, D. Husovsky, A.R. Miller, J. Rauch, W. Rix, K. Robertson and E. Waisman, Proceedings of the 10th International Conference on High Power Particle Beams, San Diego, CA, June 20-24, 1994.
6. Parks, D. P. Steen, R. Ingermanson, and E. Waisman, "A Plasma Opening Switch Model with Launched Electrons and Magnetically Enhanced Ion Erosion," S-Cubed Topical Report, SSS-DTR-94-14769, September 1994.
7. Grossman, J. and S. Swanekamp, these proceedings.

CHORDAL LINE-INTEGRALS AND THE 2-D SNOWPLOW MODEL OF THE MICROSECOND PLASMA OPENING SWITCH

Randall Ingermanson, Don Parks, Eduardo Waisman
S-Cubed, Division of Maxwell Laboratories, Inc.
3398 Carmel Mountain Road
San Diego, CA 92121-1095

Dave Hinshelwood, Bruce Weber
Naval Research Laboratory, Code 6773
4555 Overlook Avenue, SW
Washington, D.C. 20375

Abstract

In recent years, it has become clear that MHD processes dominate the conduction phase of microsecond plasma opening switches such as HAWK and ACE-4. A useful tool for analyzing this phase is the 2-D snowplow model. The model provides an efficient way to predict the thinning of density line-integrals observed in experiments.

Two main questions remain to be addressed: 1) What is the thickness of the snowplow front? 2) Does the snowplow model accurately predict the position of the snowplow front as a function of time? Both of these issues can be resolved by a careful analysis of the chordal density line-integrals measured on HAWK.

Here we extend the model to include a finite snowplow thickness, and we refine the computer code to compute chordal line-integrals. By comparing the results to measurements made on HAWK, we estimate the thickness and position of the snowplow front as functions of time.

I. Introduction

Until recently, the conduction phase of the microsecond plasma opening switch was poorly understood. When interferometric measurements of the plasma density in HAWK were published in 1991, it became clear that the dominant conduction mechanism is controlled by MHD processes. Weber, et. al., [1,2] showed that a simple 1-D snowplow model explained the conduction times over a broad range.

Soon afterward, it was shown [3] that a 2-D snowplow model could give quantitative predictions of the detailed behavior of the measured density line-integrals. In order to construct a practical computer code incorporating this model, it was necessary to solve certain technical problems: how to impose boundary conditions and how to implement adaptive mesh refinement along the snowplow front.

Initially, only axial density line-integral measurements were available. More recently, chordal line-integral data has been taken, and this allows a more refined analysis of the experiments. In particular, two new questions can be studied:

1) What is the thickness of the snowplow front?
2) Does the snowplow model accurately predict the position of the snowplow front as a function of time?

Both of these issues can be resolved by a careful analysis of the chordal density line-integrals measured on

HAWK. In this paper, we extend the 2-D snowplow model to include a finite snowplow thickness, and we refine the computer code to compute chordal line-integrals. By comparing the results to measurements made on HAWK, we estimate the thickness and position of the snowplow front as functions of time.

2. HAWK Geometry

In the HAWK experiments studied here, the geometry is shown in Figures 1 and 2.

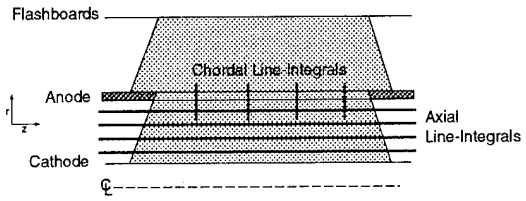


Figure 1.

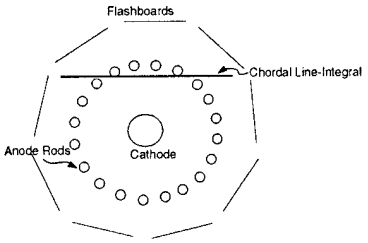


Figure 2.

The anode rods are at a radius of 7 cm, the cathode radius is 2.5 cm. The switch is 8 cm long. The plasma is generated by flashboards, and its density is assumed constant in the Z direction. The radial density distribution is measured by taking axial line-integrals of the electron density by interferometry and dividing by the switch length. Axial line-integrals are taken at radii of 3, 3.5, 4, 5.5, and 6.5 cm. Chordal line-integrals are taken at positions 1, 3, 5, and 7 cm down the switch. The chordal line of sight has an outer radius of 8.1 cm, and an inner radius of 5.1 cm. Both axial and chordal line-integrals are taken without pulsed power, and then with pulsed power.

The axial line-integrals allow us to extrapolate a density distribution in the region $r_c<r<r_a$. If we compute the expected chordal line-integral without pulsed power, we find a large discrepancy with the measured chordal line-integral. This, we attribute to plasma between the anode rods.

We assume that with pulsed power, there will again be a contribution from this plasma, which we can approximate by the discrepancy measured without pulsed power.

3. 2-D Snowplow Model

The 2-D snowplow model [4,5,3] is a cartoon of the plasma dynamics. It makes the following simplifying assumptions: 1) Perfect cylindrical symmetry, 2) Current flows only on the surface of the plasma, 3) Magnetic pressure acts normal to the plasma surface 4) Mass is scooped up inelastically and accumulates in a thin front with zero pressure.

We can then use the measured current to compute the magnetic field, and the measured axial line-integrals (without pulsed power) to compute the density of the interior plasma (with pulsed power).

The model then reduces to a coupled set of mass and momentum equations, which can be discretized on a 1-D curve representing the snowplow front. No energy equation is solved, because the process is assumed inelastic. Because the model is so simple, a microsecond conduction time POS can be simulated on a low-end workstation in less than a minute.

The boundary conditions of the model are non-trivial, as noted in [4]. The first reasonable suggestion for boundary conditions was made in [3], and we use the same technique here.

The model assumes a front of zero thickness, leading to an infinite density at the surface (and therefore, possible singularities in computing the line-integrals). In reality, one expects the front to be smeared out by some unknown form-function. We will show that an exponential function

with characteristic length λ roughly matches the data, where λ is of order 1 cm.

4. The Current Sheath Follows a Snowplow Trajectory

The concept of the "trajectory" of a 2-D snowplow front is poorly defined. In this section, we adopt the following strategy: 1) Tentatively define the trajectory using the positions of the chords and the measured times of the peaks in chordal line-integrals, 2) Find the meaning of these peak times in the context of the snowplow model, and assign a meaning to "trajectory" within the model, 3) Compute the theoretical trajectory and fit it to the measured one.

The measured chordal line-integrals with pulsed power are plotted in Figure 3.

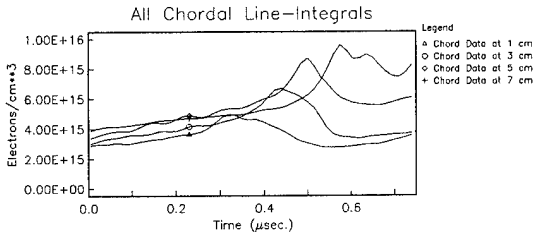


Figure 3.

From these plots, we extract the peak times corresponding in some sense to the arrival at the points Zi = {1, 3, 5, 7} cm. The resulting "experimental trajectory" is plotted in Figure 4.

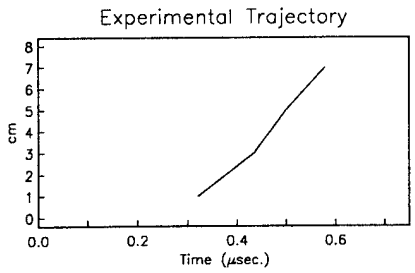


Figure 4.

Now what does the peak in the chordal line-integral really mean? For the real physical device, we have no way of saying for sure; but in the snowplow model, we can. Consider the computed chordal line-integral at Z = 5 cm, shown in Figure 5. The peak time is 503 nsec.

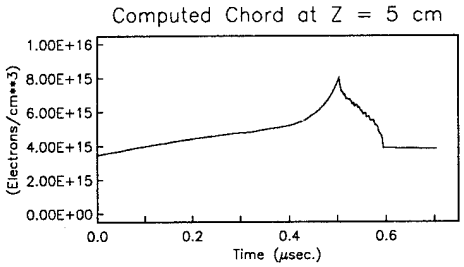


Figure 5.

Figure 6 shows that at 503 nsec, the computed position of the snowplow front is just contacting the line-of-sight of the chordal line-integral, at the minimum radius R_{min} = 5.1 cm. We therefore define the "trajectory" of the snowplow model as the Z position of that point on the snowplow front at R = R_{min}.

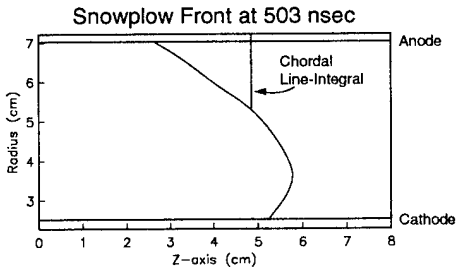


Figure 6.

Figure 7 shows a fit of the theoretical trajectory to the measured trajectory. The fitting parameters are as follows. The plasma has an initial spread, both upstream and downstream, of Δz = 1.65 cm; the plasma continues to spread outward with velocity v_z = 3.0e6 cm/sec; the ratio of atomic mass to ionization is A/Z = 8.0.

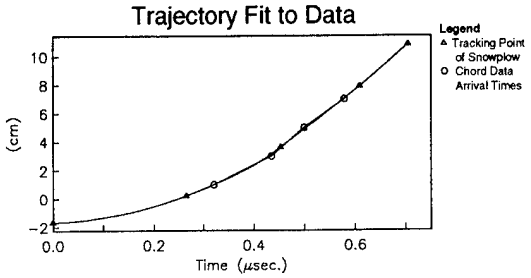


Figure 7.

5. Measurement of the Snowplow Thickness

As shown in the previous section, the peak time of the chordal line-integral corresponds to the arrival of the snowplow front at the chord's Z position. Prior to this arrival time, the chordal line-integral can be regarded as the sum of the undisturbed plasma and the plowed plasma. Since the line-integral of the undisturbed plasma was also measured, we can subtract the two curves and obtain an estimate of the line-integral of the snowplowed material alone.

This estimate is the difference of two experimental curves. Using the results of the snowplow model, we can correct for the time-dependent effects due to mass accretion. And knowing the trajectory of the front, we can relate position to time. The result is a rough estimate of the (line-integrated) spatial density distribution, which we normalize to a peak value of 1, since the interpretation of the amplitude is unclear. Figure 8 shows the results obtained at the four chordal positions. These curves roughly approximate the form-function we mentioned in Section 3. As time progresses, the front thickness increases from a few mm to a couple of cm.

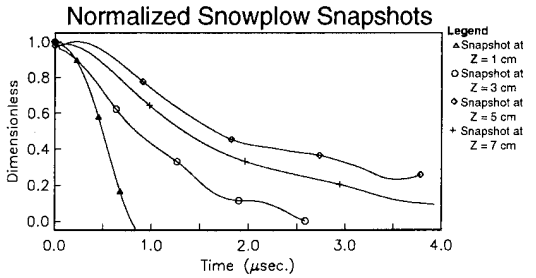


Figure 8.

6. Chordal Line-Integrals

In Figure 9, we show a comparison between a computed and a measured chordal line-integral, at Z=5 cm. The difference in amplitude of the peaks is probably due to increased ionization in the snowplow front, an effect not yet accounted for by our model. Note that the tail that begins at 600 nsec is *entirely* due to the residual plasma between the anode rods, as discussed in Section 2.

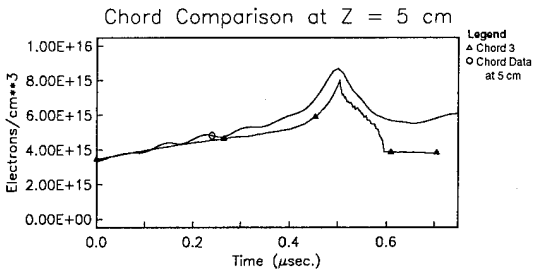


Figure 9.

7. Conclusions

The current sheath within the POS follows a snowplow trajectory with reasonable parameters. The snowplow front has a thickness of order 1 cm. The 2-D snowplow model provides a fast and reasonably accurate method of studying the time-evolution of the POS conduction phase.

References

1 Weber, B.V., J.R. Boller, R.J. Commisso, P.J. Goodrich, J.M. Grossmann, D.D. Hinshelwood, and P.F. Ottinger, "Conduction Limits and Scaling of Microsecond-Conduction-Time Plasma Opening Switches," APS Plasma Physics Annual Meeting, 1991.

2 Hinshelwood, D.D., R.J. Commisso, P.J. Goodrich, J.M. Grossmann, J.C. Kellogg, and B.V. Weber, "Density Measurements of Microsecond-Conduction-Time POS Plasmas," BEAMS '92.

3 Ingermanson, R.S., D.E. Parks, E.R. Salberta, and E. Waisman, "Two-Dimensional Studies of Current Conduction in Plasma Opening Switches," BEAMS 92.

4 Hussey, T.W., M.K. Matzen, and N.G. Roderick, "Large-Scale-Length Non-Uniformities in Gas Puff Implosions," J. Appl. Phys. **59** (8), 1986.

5 Salberta, E., D. Parks, and E. Waisman, "General Solution for Asymmetric Snowplow in Z-Pinch-Like Geometry," Phys. Fluids B4 (10) 3440, Oct. 1992.

HIGH POWER PLASMA OPENING SWITCH OPERATION ON HAWK

P.J. Goodrich*, R.J. Commisso, J.M. Grossmann, D.D. Hinshelwood*,
R.A. Riley**, S.B. Swanekamp***, and B.V. Weber
Pulsed Power Physics Branch, Plasma Physics Division
Naval Research Laboratory, Washington DC 20375

Abstract

The Hawk pulsed power generator is used in plasma opening switch (POS) experiments in the 1-μs conduction time regime to study long conduction time switch physics. Cathode and anode geometries, especially in the switch region, can have a major impact on switch performance. There is a tradeoff between higher voltage and lower conducted current as the radius of the cathode center conductor is decreased. Tapering the cathode over the switch length has produced the best performance to date: 0.7 TW at 0.75 μs conduction times with flashboard plasma sources and 1.6 MV has been generated at 1 μs conduction times with cable gun sources. There is a limit on the minimum radial gap in the switch and downstream region below which voltage and current transfer are reduced. Switch performance deteriorates as the anode outer conductor just downstream of the switch, but at the same radius as the switch rods, is extended toward the load. As observed in past experiments, POS performance is independent of the plasma source used (flashboards, cable guns, or gas guns) in a given switch/load configuration. A helical center conductor in the switch region, which increases the total insulating magnetic field by a factor of 2.3, resulted in dramatically degraded switch opening for conduction times greater than 0.35 μs.

Introduction

The Hawk generator is a 600 nH, 1-μF Marx bank that stores 225 kJ with an erected voltage of 640 kV at 80-kV charge to deliver up to 720 kA in 1.2 μs to a plasma opening switch (POS). Previous experiments[1] with flashboard plasma sources have identified hydrodynamic plasma distortion as the dominant mechanism that controls much of the POS operation. Maximum load power is determined by an effective gap for magnetic insulation in the POS. Empirically, this gap is limited to about 3 mm in size in Hawk. Above a critical load impedance--the switch limited regime--current is lost between the switch and the load, typically nearer the load, with the voltage remaining constant; at lower impedance--the load limited regime--the voltage decreases in proportion to the load impedance. Maximum load power is obtained at this critical impedance.

In general, increasing the cathode magnetic field--by conducting more current or decreasing the cathode radius--allows the fixed gap POS to remain insulated at a higher voltage (V~B). However, for a given plasma density, the switch opens earlier for smaller radius cathodes (larger magnetic fields, a consequence of MHD-limited conduction[2,3]). In this manner, up to 2 MV at 0.6 μs conduction, with ~0.6 TW load power at 7 Ω critical impedance, was generated with a 2.5 cm diameter cathode.[4] Using the same plasma delay, the voltage was

850 kV but at 0.9 μs conduction, with 0.4 TW load power at 1.7 Ω impedance, with a 10 cm diameter cathode.[4]

In this paper, recent Hawk experiments with further modifications to the POS electrode geometry--tapered cathodes, changing the anode downstream of the switch, and a helical center conductor--are discussed. Three plasma sources are used: flashboards (FB), cable guns (CG), and gas guns (H_2, He, and Ar).

Tapered Cathodes

Tapering the cathode center conductor in the switch region optimizes the tradeoff between a higher voltage but a lower conducted current for a given plasma delay as the switch radius is reduced. A larger radius on the generator side allows longer conduction while the smaller radius on the load side, which is probably near the plasma center-of-mass location at opening, generates higher POS voltage.

Figure 1 shows a 10 cm to 5 cm diam cathode taper through the 8 cm length switch. The cathode tip shown here is flared to ~9.5 cm diam, one technique used to reduce the load impedance at peak power. Figure 2 is a plot of peak switch voltage as a function of load impedance at peak power on shots with a 10 to

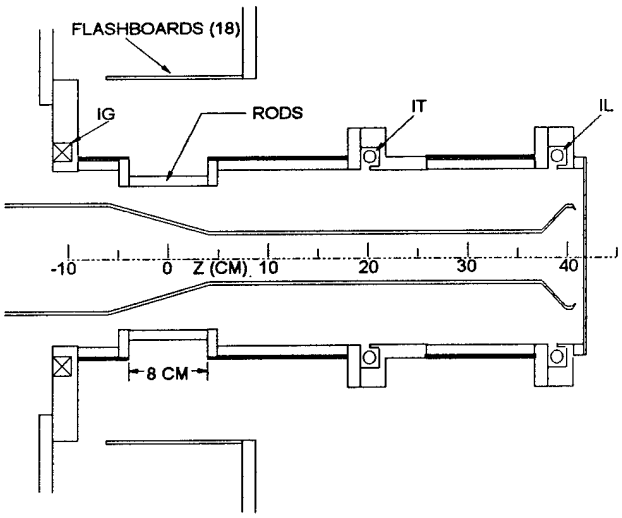


Figure 1. Hawk POS configuration with a 10 to 5 cm diam cathode taper in the switch region.

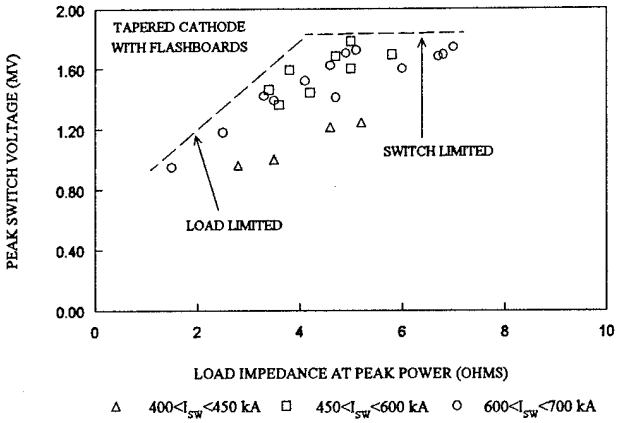


Figure 2. The switch operational regimes depend on the load impedance. Cathode is a 10 to 2.5 cm diam taper.

2.5 cm diam cathode taper and flashboard plasma sources. The operational regime depends on the load impedance. In switch-limited operation, above about 4 Ω, the voltage is 1.7 MV on the longest conduction shots.

The highest load power to date has been produced in this taper geometry operating near the critical impedance. Figure 3 is a 0.75 μs conduction time shot where 0.7 TW was produced and 55 kJ delivered to the load--20% energy efficiency--at a 3.5 Ω load impedance. Above this impedance, in switch-limited operation, the load current is lower. For example, load power is about 0.5 TW at 5 Ω load impedance.

In typical switch-limited operation, this current loss occurs closer to the load than the switch (figure 4). Subsequent experiments with

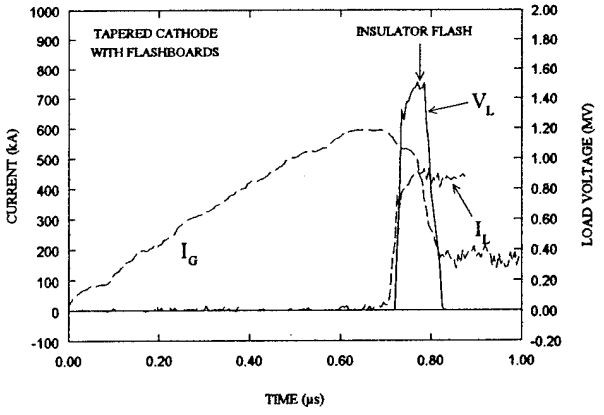


Figure 3. Tapered cathodes have produced the highest power , 0.7 TW at 3.5 Ω critical load impedance.

cathode current monitors at the load (and a resistive wire voltmeter near the load) suggest the load current, at least at peak power, is primarily cathode current. This is consistent with PIC code simulations of Hawk.[5] Current which is lost upstream of the load, but near the load, is probably vacuum electron flow.

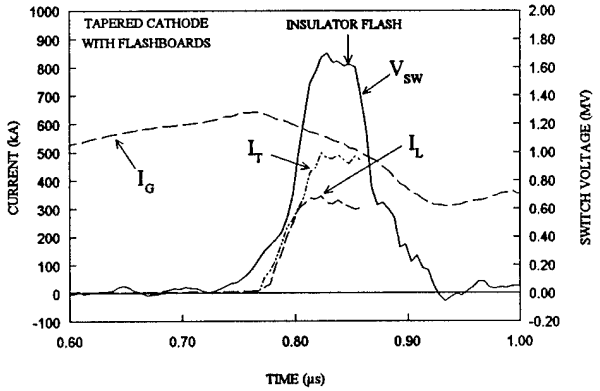


Figure 4. Current losses typically occur near the load in switch-limited operation.

Figure 5 shows peak switch voltage versus conduction time for shots using a 10 to 2.5 cm diam taper, 10 cm diam, and 2.5 cm diam cathodes with flashboard, cable gun, and gas gun plasma sources. Tapered cathodes produce higher voltage than straight cathodes especially at longer conduction times (> 0.8 μs). Conduction times above 0.75 μs were not pursued with the faster plasma velocity flashboards since sufficient switch plasma reaches the load on longer plasma delay shots and results in load-limited operation.

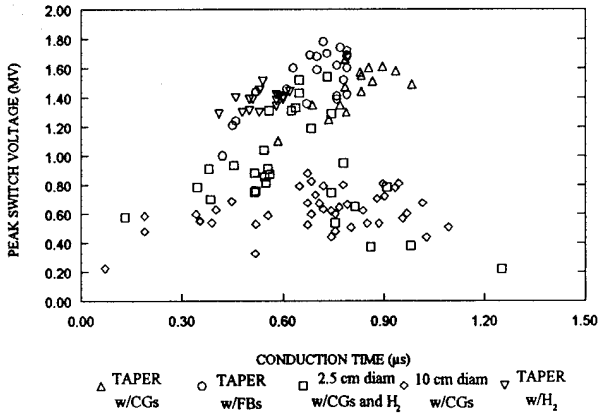


Figure 5. Tapered cathodes produce higher voltage than straight cathodes at longer conduction times.

This plot shows that switch performance is independent of the plasma source (flashboards, cable guns, or gas guns) in a given geometry, i.e. switch/load configuration, consistent with previous results[4]. As is also typical, the smaller radius cathodes (2.5 cm diam) generally generate higher voltage than the larger cathodes (10 cm diam) at a given conduction time. In figure 6, "flow impedance", defined here as V_{SW}/I_G, is plotted as a function of conduction time for the data in figure 5. This is a lower limit on the flow impedance because the downstream cathode current is not included here. The tapered cathodes are associated with higher flow impedance and maintain this flow impedance at longer conduction times (~3 Ω at 1 μs).

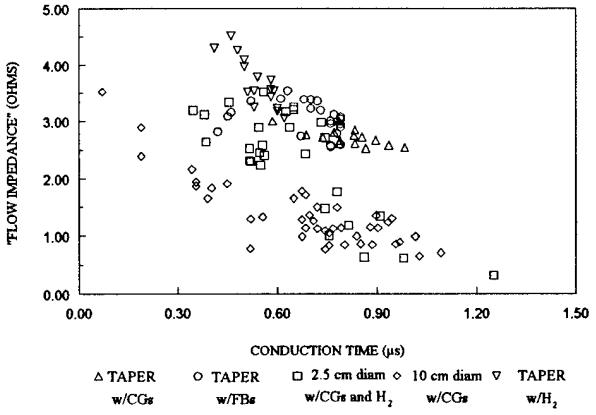


Figure 6. Tapered cathodes are associated with higher flow impedance than straight cathodes and maintain this flow impedance at longer conduction times.

Anode Modifications

Changes to the anode outer conductor can also effect switch opening. One modification was to add an extension to the anode just downstream of the switch at the same radius as the switch rods, providing a radial gap of 2 cm in this region with the straight 10 cm diam cathode. The usual configuration is to expand out to a 4 cm gap immediately downstream of the switch rods (see figure 1).

Switch performance--switch voltage and load current--deteriorated with the extension, as shown in figure 7. This figure shows data from three shots with a 6 cm, 2 cm, and no extension and the same 0.95 μs conduction time. There is clear evidence that electrons are lost at this anode switch extension. Simulations show that the vacuum electrons flow primarily near the anode as the switch opens,[5] so current loss at this reduced radius location is not unreasonable.

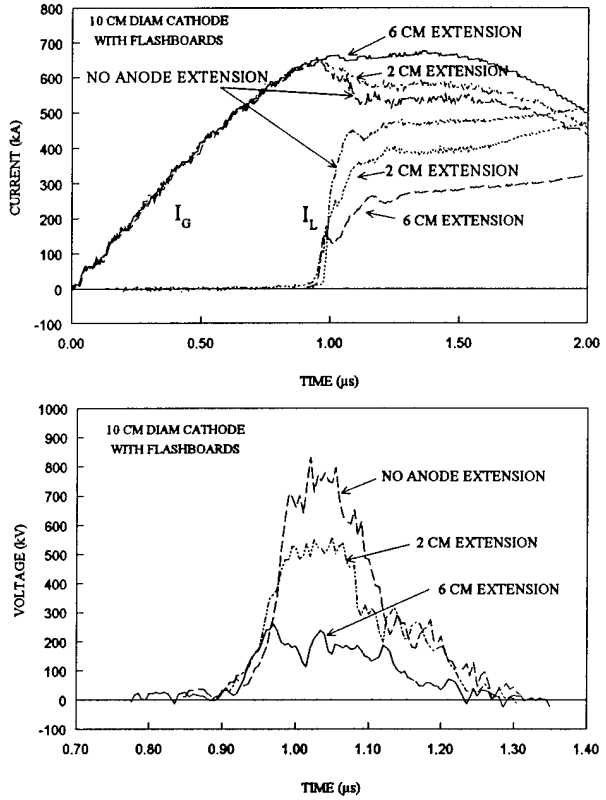


Figure 7. An extension added to the anode just downstream of the switch, but at the same radius as the switch, degrades switch opening.

Helical Center Conductor

A helical center conductor with a pitch of four and a 10 cm diam was tested in the switch region. The helix increases the total insulating magnetic field in the switch by a factor of 2.3. Conduction time for a given plasma delay was the same as the solid 10 cm diam cathode, suggesting that the additional B_z field does not contribute to hydro forces limiting conduction. However, switch opening was very poor, with both short circuit and diode loads, for conduction times greater than 0.35 μs. For conduction times less than 0.35 μs with short circuit loads, results with the helical center conductor were similar to results with the solid 10 cm diam cathode.

Summary

These experiments illustrate the importance of the electrode geometry on switch conduction and opening. Tapering the cathode over the switch length optimizes the tradeoff between a higher voltage but lower conducted current as the cathode radius is decreased. In this manner, 0.7 TW load power was produced at 0.75 μs conduction as well as 1.6 MV generated at 1 μs conduction. There is a limit on the minimum radial gap between electrodes in the switch region and also downstream of the switch below which voltage and current transfer efficiency are reduced. A helical center conductor in the switch region resulted in dramatically degraded switch opening for conduction times over 0.35 μs.

* JAYCOR, Vienna, VA
** NRC Research Associate
*** SAIC, McLean, VA

---

[1]D.D. Hinshelwood, et al., Phys. Rev. Lett., **68**, 3567 (1992).
[2]R.J. Commisso, et al., Phys. Fluids B **4**, 2368 (1992).
[3]B.V. Weber, et al., IEEE Trans. Plasma Sci., **19**, 757 (1991).
[4]P.J. Goodrich, et al., in *Proc. 9th Int. Conf. on High Power Particle Beams*, 609 (1992).
[5]S.B. Swanekamp, et al., these *Proceedings.*

SIMULATIONS OF VACUUM ELECTRON FLOW IN INDUCTIVE-ENERGY-STORE PULSED-POWER SYSTEMS

S.B. SWANEKAMP[a], J.M. GROSSMANN, R.J. COMMISSO,
P.J. GOODRICH[b], P.F. OTTINGER, and B.V. WEBER
Plasma Physics Division,
Naval Research Laboratory, Washington, D.C. 20375-5346

The current understanding of the opening process of a long-conduction-time (>300 ns) plasma opening switch (POS) involves the formation of a fairly small (2-4 mm) vacuum gap. As the switch opens, electrons which are magnetically insulated in the switch gap flow into the downstream magnetically insulated transmission line (MITL). Since the vacuum electron flow can be a large fraction of the net current, it is important to understand the nature of this flow. In this paper the vacuum electron flow into an MITL as the POS opens is studied with the particle-in-cell method. Simulation results are presented for both the Decade Proto-type Module-1 (DPM1) at Physics International and the HAWK inductive energy store accelerator at NRL. The simulations show vacuum electron flow primarily near the anode as the POS opens. The HAWK simulations suggest that a low density plasma (~10^{12} cm^{-3}) can significantly alter the electron flow in the MITL.

I. Introduction

In the closed state, the POS must conduct megampere currents for times approaching 1 μs.[1] During this time electrical energy is converted into magnetic energy and stored in the primary storage inductor. To achieve high output powers, the POS must open on a time scale short compared the conduction time and deliver the stored magnetic energy to a particle-beam-diode or imploding-plasma load.

Considerable advances have been made in understanding the conduction and opening phases of the μs-conduction-time POS.[2] However, much less is understood about the power flow out of the POS as the switch opens into the magnetically insulated transmission line (MITL) that connects the POS and load. This paper presents results of particle-in-cell (PIC) computer simulations of the vacuum electron flow in the MITL as the POS opens. These simulations are performed for two experimental geometries: the Decade Prototype Module 1 (DPM1) at Physics International, and the HAWK inductive energy store accelerator at the Naval Research Laboratory.

II. Power-Flow Simulations for DPM1

In the DPM1 experiment a Marx charges a *0.75* μF water capacitor (C_{TC}) to an initial voltage of *700 kV*. During the conduction phase, the capacitor discharges through the POS as current and magnetic energy build up in the *250 nH* primary storage inductor (L_S). The quarter cycle of the $L_S C_{TC}$ discharge is *680 ns* and the peak current is approximately *1.2 MA*.

A schematic of the DPM1 POS and MITL geometry is shown in Fig. 1. Plasma is introduced into the POS prior to the main pulse by a set of *8* cable guns spaced around the azimuth of a coaxial transmission line.[3] The location of plasma in the switch region is controlled by two masks which limit the axial extent of the plasma introduced into the MITL. Plasma from the cable guns

cable guns flows into the POS through a *2.5-cm* opening between the masks. The load consisted of a *60-120 cm* (*2-4 ft*) long MITL with a vacuum impedance of *80* Ω and a cathode radius of *4.5 cm* terminated by an electron beam diode.

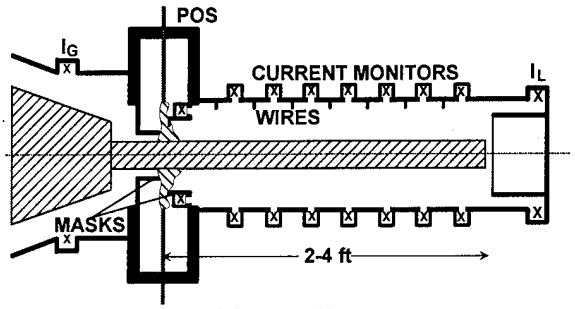


Fig. 1 Schematic of the DPM1 experiment.

Diagnostics include a voltage and current monitor upstream of the POS and an array of current monitors downstream of the POS. Another diagnostic used in these experiments consisted of a series of wires that protruded *2.5 cm* through the anode of the MITL. The first of these wires protruded from the downstream mask with additional wires placed *15 cm* apart and half-way between the anode current monitors as indicated in Fig. 1. The damage patterns on these wires were used to detect the presence of high energy electrons near the anode in the MITL.

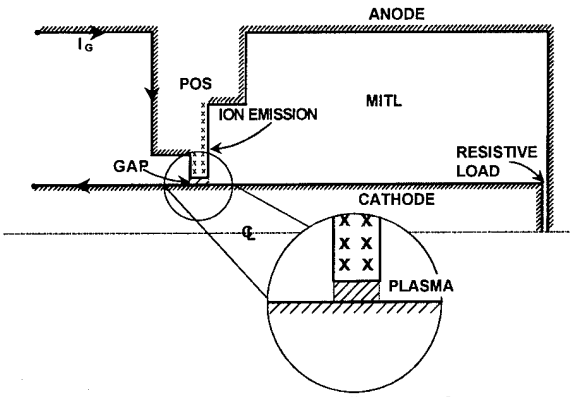


Fig. 2 Model for DPM1 power-flow simulations.

A schematic of the POS, MITL and load models used in the DPM1 simulations is shown in Fig. 2. The model assumes that the plasma distortion and redistribution that takes place during the conduction phase has already occurred and that the POS plasma carries the full generator current (1.2 MA) at *t=0*. The POS model assumes that a *2.5-cm* long, *0.35-cm* switch gap exists between the anode and cathode. The switch gap is initially bridged with plasma which provides a very conductive path for the generator current at t=0.

The ions in the plasma prefill were taken to be 10^6 times more massive than the proton mass with an initial velocity sufficient to clear the switch gap in *30 ns*. As the prefill ions clear the gap, magnetic energy flows past the switch and into the downstream MITL.

The portion of the anode that would be high density plasma in the experiment is modeled as a conducting boundary and treated as a space-charge-limited C^{++} ion emitter. The entire cathode surface in the MITL is modeled as a space-charge-limited source of electrons and the electron beam diode is modeled as a resistive load. In Ref. 4 it is shown that the voltage and current measurements are in good agreement with those predicted by simulation.

The emitted electrons and C^{++} ions at *t=30 ns* are shown in Figs. 3a and 3b. Figure 3a shows a significant fraction of the electron flow launched into the MITL is concentrated near the anode where the electrons $\boldsymbol{E}\times\boldsymbol{B}$ drift parallel to the anode conductor. As the electrons approach the vertical anode plate the electron orbits bend 90° and continue to $\boldsymbol{E}\times\boldsymbol{B}$ drift toward the load region. From the ion positions shown in Fig. 3b, we see that an ion space charge cloud evolves off of the anode emission surfaces. This positive space charge is neutralized by electron flow from the POS region forming a tenuous ($n\sim10^{12}$ cm^{-3}) quasi-neutral plasma that drifts axially toward the load at approximately 0.3 cm/ns. This plasma can affect MITL losses by

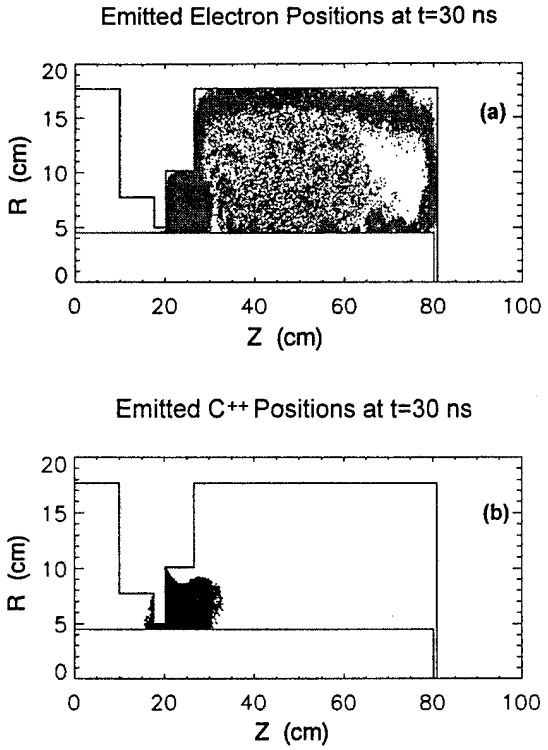


Fig. 3 Emitted electron (a) and C^{++} (b) positions in the down-stream MITL at t=30 ns.

providing a conductive path between the anode and cathode.

When the series combination of the load impedance and the effective impedance of the MITL inductance [$Z_{eff}=(LdI_L/dt)/I_L \sim L/t$] is large compared to the POS flow impedance, the POS operates in the switch-limited regime.[2] In this regime, the switch behaves as the load and the POS voltage is limited by the size of the switch gap. In the switch-limited regime a significant amount of electron current is lost in the POS. As a result of these losses, many electrons are not insulated at the load end of the POS gap. Those electrons that do flow into the MITL have been accelerated to nearly the full POS potential. If electrons then $\boldsymbol{E}\times\boldsymbol{B}$ drift along equi-potential lines as they enter the downstream MITL, electron flow from the POS would be concentrated near the anode as seen in the simulations.

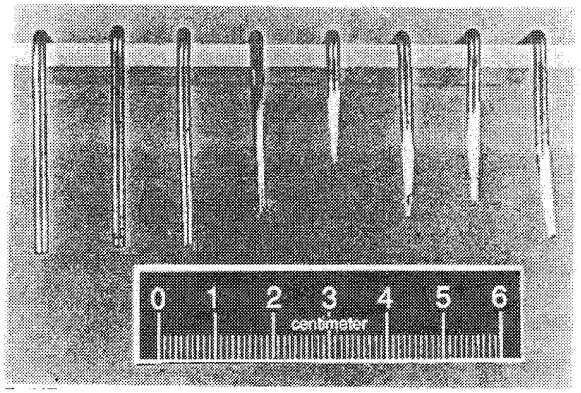


Fig. 4 Damage produced on the wires protruding from the anode.

Damage on the wires[5] protruding from the anode is shown in Fig. 4. Notice that the first few wires are relatively undamaged. This may be the result of plasma in the MITL which can shield the wires from the high energy electrons. The remaining wires show a large amount of damage indicating the presence of high energy electrons near the anode. This agrees qualitatively with the electron flow pattern observed in the simulations.

III. Power-Flow Simulations for HAWK

A schematic of the HAWK power-flow experiment is shown in Fig. 5. The diagnostics that are of interest for comparison with simulations are the anode (I_A) and the cathode (I_K) currents nearest the load. The diode voltage and plasma density were also measured. Simulations and experiments have been performed with both plasma-filled and vacuum electron-beam-diode loads. However, since the comparison between experiment and simulation are similar for both PFD and vacuum diode loads, we will only show results from the PFD load. The simulation model for HAWK was very similar to that used for the DPM1 simulations except the geometry was changed to more closely match HAWK.

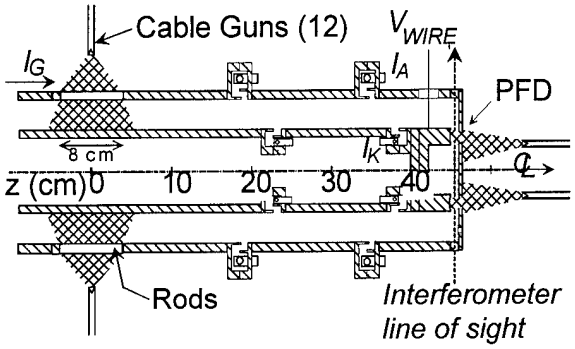


Fig. 5 HAWK power flow experiment.

Figure 6 shows anode and cathode current measurements near the load along with the load voltage and PFD density during a shot. The current measurements show that, over most of the voltage pulse, more than 100 kA of the total current is in the form of vacuum electron flow.

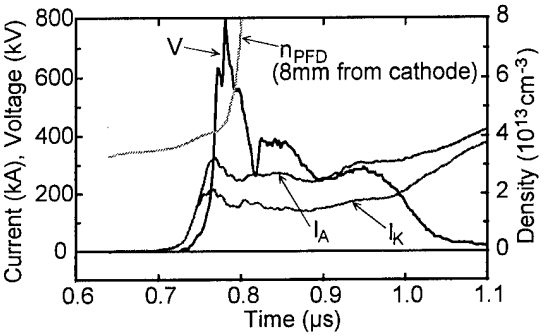


Fig. 6 Power-flow data on HAWK with a PFD load.

Anode and cathode currents just downstream of the POS and near the load predicted from the simulations are shown in Fig. 7. At the load, HAWK simulations show very little vacuum electron flow. This is in sharp contrast to the large measured vacuum flow seen in Fig. 6. The predicted anode and cathode currents just downstream of the POS shows a significant amount of vacuum electron flow and is similar to the measured anode and cathode currents near the load. The vacuum electron flow near the POS predicted in the simulations is the result of the low density plasma that expands into the MITL as the POS opens (Fig. 3b). In regions of the MITL where there is no plasma in the MITL very little vacuum flow is observed in the simulations

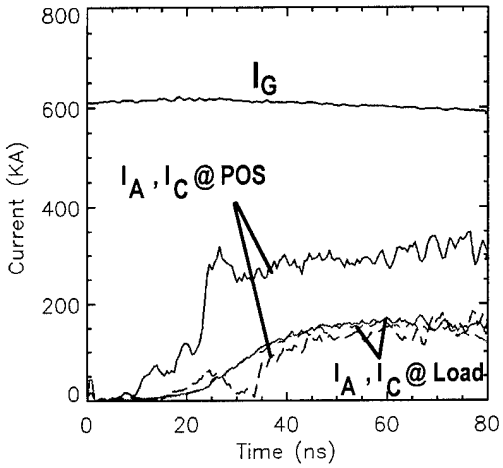


Fig. 7 Anode and cathode currents just downstream of the POS and just upstream of the load.

for these parameters. Therefore, the measured vacuum flow could be caused by tenuous plasma (~10^{12} cm^{-3}) in the MITL. Future plans for power-flow on HAWK include more detailed measurements of the plasma distribution in the MITL and additional simulations to better understand the nature of the electron flow between a POS and load.

Acknowledgments

The authors would like to thank Dr. John Goyer for his participation throughout the course of this work. Simulations performed with the MAGIC[6] code through the AFOSR's sponsored Magic Users Group. This work was supported by DNA.

[a]SAIC, McLean, VA 22102.
[b]JAYCOR, Vienna, VA 22182.

---

[1]See guest editorial and articles in special issue on fast opening vacuum switches, PS-15, 629 (1987).
[2]R. J. Commisso, P. J. Goodrich, J. M. Grossmann, D. D. Hinshelwood, P. F. Ottinger, and B.V. Weber, Phys. Fluids B **4**, 2368 (1992).
[3]J.R. Goyer, D. Kortbawi, F.K. Childers, and P.S. Sincerny, J. Appl. Phys. **74**, 4236 (1993).
[4]S.B. Swanekamp, J.M. Grossmann, P.F. Ottinger, R.J. Commisso, and J.R. Goyer, to be published in the Sept. 1, 1994 issue of J. Appl. Phys.
[5]Wire damage photograph provided by J. Goyer.
[6]B. Goplen, L. Ludeking, D. Smithe, and G. Warren, MAGIC User's Manual, Mission Research Tech. Report No. MRC/WDC-R-282.

EXPERIMENTAL RESEARCH OF ELECTRON MAGNETO-HYDRODYNAMICS EFFECTS IN MICROSECOND POS

G.S.Belenki, G.I.Dolgachev, Yu.G.Kalinin,
M.S.Nitishinski, A.G.Ushakov, L.P.Zakatov

RRC Kurchatov Institute, 123182, Moscow, Russia

ABSTRACT

The paper presents new data aimed at understanding and characterizing of microsecond Plasma Opening Switch (POS) plasma. In planar geometry both optical and probe experiments were carried out in two regimes. Erosion regime with sharp current interruption is characterized by current penetration with a velocity 10^8 cm/s through plasma having its impedance at several Ohms from current beginning. Ion probes show substantial ion current along all POS cathode area. In another regime with higher plasma concentration there is no sharp switching, plasma has high conductivity and current penetrates into plasma an order as slow. Electron-image frames show instabilities at the last stage of rising current that could be important illustration when considering Electron magneto HydroDynamic (EHD) effects.

The experiments were carried out at modified TAINA[1] facility with the parameters as follows: Marx pulse voltage generator was used as primary energy source with output voltage 600 kV, 28 kJ stored energy, total current 80 kA rising within 1.6 μs.

Experiments were made in two regimes with "low" and "high" concentration. These notions are conventional because the plasma concentration was not measured at the practice. The energy fitted at one plasma gun spark gap was 2 and 10 J correspondingly. Unlike the coaxial geometry usual for the experiment the planar geometry (**Fig.1**) was chosen to provide a simple optical registration from two sides and to make optical results easily interpreted.

Plasma guns placed 2 cm below the cathode included 8 sequential flashboards combined at 8 parallel sections fed from pulsed source. POS itself was used as a load - no inductive load was placed downstream the POS.

Open planar electron-image converter (EIC) with open micro-channel plate at the input was used for plasma photography in soft x-rays. Frames were taken through the pinhole camera having 0.3 mm pinhole with 80 ns exposition. Some of the frames were obtained using EIC sensitive in optical range.

A diagnostic of ion flows included a set of ion collectors placed into the crossed magnetic field (**Fig.1**).

Reesearching microsecond POS in a coaxial geometry a local decrease of the light inside POS volume was found while drive current rising.[2-3] These results were obtained for both continuous light and separate optical lines. It was shown that this decrease is not connected with plasma burning down (a temporal behavior of Hydrogen and Helium lines was analyzed)

but with a value of <*nl*>. D.Hinshelwood[4] carried out experiments on direct concentration measurement where the effect of the local <*nl*> decrease was also found.

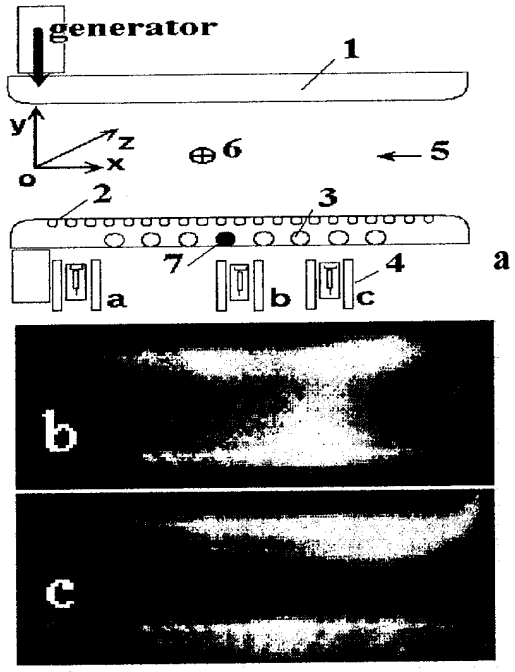


Fig.1 A-POS scheme, 1-anode, 2-cathode, 3-plasma guns, 4-ion probe, 5-6- directions of viewing, 7-plasma gun displacement when "high" concentration; B,C -POS EIC frames in a visible light at 0.7 and 1.6 μs after current beginning; exposure - 100 ns.

The experiments with "low" concentration total drive current is differed dramatically from that of the "short-circuit" regime. When drive current reaches 0.1 of its amplitude at a stage of energy storing in the inductiveness the POS impedance reaches several Ohms and then it sharply increases several times when the drive current reaches 40% of the amplitude (**Fig.2**).

Fig.3 illustrates ion currents on POS cathode registered by ion probes placed as it is shown at **Fig.1-a**.

Evidently plasma erosion, we understand ion leaving from plasma under term "erosion", begins 100 ns after. This is evidence of high magnetic field penetration velocity into the plasma (more than 10^8 cm/s). The ion density is 20 A/cm^2, i.e. ions transfer 50% of the total current through POS.

Fig. 1-b,c illustrates a visible light luminescence where the main part of the light is concentrated in the area of maximum ion flow. The plasma luminescence in ultra-violet spectral area was not detected due to low sensitivity of the Micro-Channel Plate.

In experiments with high concentration no substantial changes of POS resistance were observed and the drive current goes closely to that of short-circuit (**Fig.2**). Ion currents to the cathode were not detected upper than 1 A/cm^2.

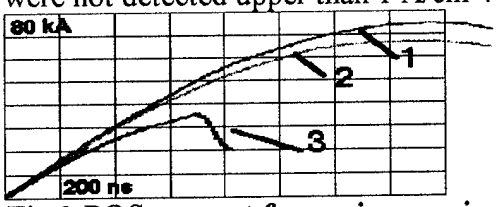


Fig.2 POS current for various regimes: 1- short-circuit regime, 2- "high concentration regime, 3-"low" concentration regime

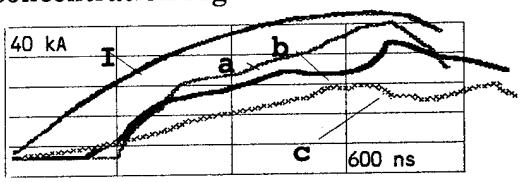


Fig.3 Ion currents on the probes placed in various places under the POS cathode from "a" to "c" according to Fig. 1. I -drive current through POS

At the same time the plasma luminescence increases sharply in the ultra-violet light. **Fig.4** gives a consequential row of pictures taken by electron-optic image camera for different moments after the current beginning. These pictures were taken from the "load" (far from generator) side (in direction 5 **Fig.1-a**)and others

(**Fig. 5**)- from "side"-view of POS (direction **Fig.1-a**).

The luminescence begins from the generator side (**Fig. 5-a,b,c**) and goes along POS toward the "load side" with 10^7 cm/s. The frames of luminescence in crossed direction (**Fig. 4-a,b,c**) show that plasma is raked up to the center of POS. Formation of multi-layer structure of the light as well as its assimetry at the last stage apparently are the results of an instability formation.

This light and concentration dynamics allow to suppose the connection with some effects predicted within the frames of electron-magneto-hydrodynamic theory (EHD)[5-9].

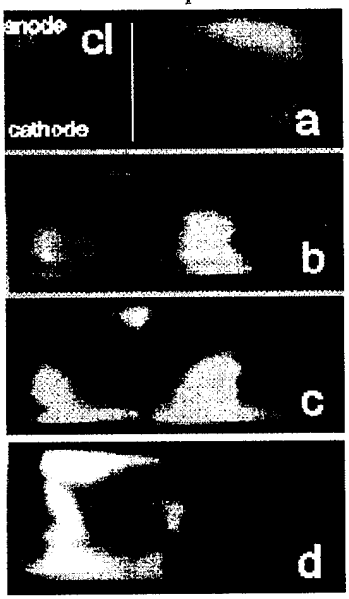


Fig.4 Pictures of POS gap taken by EIC with a micro-channel plate at the output in ultra-violet light at different moments after the current beginning from the "load" view (5) at Fig. 1-a.. Exposition - 80 ns. From "a" to "d" moments are: 0.2, 0.7, 1.0, 1.3 μs correspondingly. Current reaches its maximum at 1.6 μs. The first frame was taken with enhanced sensitivity of MCP unless the light from plasma is invisible. POS gap is 8 cm. A length from *CL* to electrode edge (frame border) is 12 cm.

If one connects light penetration velocity at 1/2 of POS length (10^7 cm/s), with a convection of current flow on a concentration gradient[5], $V = \frac{Hc}{8\pi e}\frac{\partial}{\partial y}(\frac{1}{n})$, (H - magnetic field near POS) then he could obtain the plasma concentration near anode as $n \approx 10^{14}$ cm^{-3}. Current and field could penetrate as a "shock wave". After the penetration of the magnetic field a "current layer" may be created where ions are accelerated toward the cathode in a Hall electric field[6]. The layer penetrates with $\approx 10^7$ cm/s that corresponds to the velocity ($v = \frac{H}{(4\pi nm)^{1/2}}((\omega_e t)^2 z\frac{\omega_p}{c}\frac{M}{m})^{-1/5}$)[6].

A dark cone which "removes" the light toward the electrodes could be connected with low plasma concentration behind the front of the shock wave in the current layer. The density gradient toward the anode is not a condition of current wave

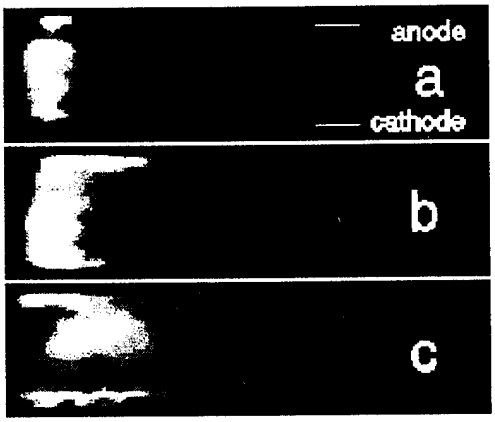


Fig.5 Pictures of POS taken from the "side" view (as direction (6) at Fig.1) at 0.7, 1.0, 1.3 μs after current beginning from "a" to "c" correspondingly. Interelectrode gap is 8 cm. Total length - 30 cm.

movement. But in this case the corresponding velocity

($u = v_{Ae}(\frac{c}{6w_{pe}x})^{1/3}(\frac{m}{M})^{1/3}$)[6] is lesser ($v \approx 10^5$ cm/s), than observed one.

The phots discussed could be applied to illustrate simulations of POS electron concentration dynamics and B-field penetration[7] which have included EHD-effects.

It is worth to outline the peculiarities of near-electrode plasma dynamics. A dark thin layer near the cathode (**FIG. 5-c**) could be connected with a double layer "growing" from "left-down" corner of the POS as a result of Buneman instability[8]. Interpreting a thickness (0.6 cm) as a gap of the double layer $\approx c/\omega_{pe}$ one can obtain a concentration near the cathode $\approx 10^{12}$ cm^{-3}

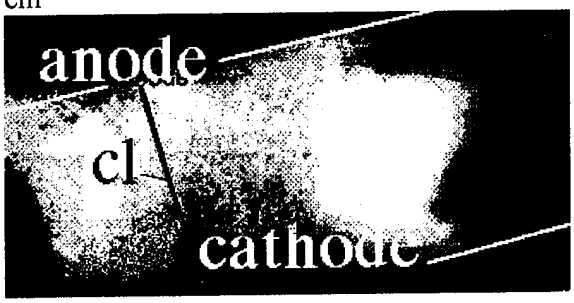


Fig. 6 A picture of the interelectrode gap of POS at 0.9 μs after the current beginning with a maximum sensitivity of the MCP was taken from the "load" view as at Fig.6. The position of electrodes and central line are analogous to those at Fig.4.

An interesting detail is a thin non-luminescent layer near the anode (**FIG.6**) obtained with enhanced sensitivity of MCP that could be interpreted in the frames of EHD as a result of such a precise effect as anomalous fast penetration of current with a velocity of $v_A/2$ and thickness c/w_p, pointed out in.[9]

ACKNOWLEDGMENTS

The authors are grateful to Prof. A.S.Kingsep and Prof. L.I.Rudakov for useful discussions on POS physics.

This work was supported by The Russian Foundation of Fundamental Sciences (RFFI) (Res. Grant N 94-02-03059-a) and the Institute of Radiation Ecology Technologies, Russia.

REFERENCES

1.Yu.P.Golovanov et al. Sov. VANT, Series Thermonuc. Fusion, vol.2, p. 40, 1988.

2.Yu.P.Golovanov et al. Sov. J. Plasma Phys., vol. 14, p. 519, 1988.

3.G.I.Dolgachev et al. Sov. J. Plasma Phys. vol. 17, p. 679, 1991.

4.D.D.Hinshelwood et al. Phys. Rev. Lett., vol. 68, p.3567, 1992.

5.A.S.Kingsep et al. Sov. J. Plasma Phys., vol. 10, p. 495, 1984.

6. L. I. Rudakov Sov. J. Plasma Phys. vol. 19, p.835, 1993.

7. R.J.Mason et al. Proc. of IX Int. Conf. on High Power Particle Beams BEAMS'92, Washington DC, May 25-29, 1992, vol.1, p. 547. H.A.Davis et al. ibid., p. 615.

8. A.S.Kingsep , A.A.Sevastianov Sov. J. Plasma Phys. 17, p. 685, 1991.

9. A.V.Gordeev et al. Sov. J. Plasma Phys. vol. 17, 1991.

Experiments with Gas Puff Plasma Guns on GIT-4 Generator

P.S.Ananjin, V.B.Karpov
Institute of Nuclear Physics, Tomsk;
A.A.Sinebryukhov,V.A.Sinebryukhov
Institute of Electrophysics, Ekaterinburg;
V.A.Kokshenev, B.M.Koval'chuk, F.I.Fursov, V.P.Yakovlev
Institute of High Current Electronics, Tomsk.

Presented are the results of upgraded Plasma Opening Switch study with new plasma source: Gas Puff Plasma Guns. Gas Puff Plasma Gun is a coaxial plasma accelerator with radial gas injection into gun gap. This gun produces fast, low divergence flow of pure plasma. To create the plasma we use in experiment different gases from hydrogen to krypton. The best switch characteristics were reached with hydrogen plasma. Switch voltage made up to 2 MV at POS current over 1 MA. The measurements of ion beam parameters were made using track detectors, Thompson parabola spectrometer and nuclear activation technique.

Introduction

In the experiments with Plasma Opening Switches (POS) of megaampere current range either cable plasma guns or flashboard plasma source are conventionally used [1]. As it is shown elsewhere, such sources generate plasma consisting of approximately 50% hydrogen ions and 50% carbon ions in charge state of 1—3. In order to investigate POS behavior and switching features as functions of plasma composition, the experiment with Gas Puff Plasma Guns (GPPG) was carried out.

Similar experiments have been carried out earlier on DOUBLE accelerator [2] with POS current amplitude up to 250 kA. The goal of this research is the upgrade of those experiments to megaampere current level.

Experimental Setup and Diagnostics

Presented experiments were carried out on GIT-4 generator at 480 kV of pulsed voltage of negative polarity. Taking into account pulser parameters, a coaxial POS electrode geometry was chosen with outer electrode diameter of 300 mm and inner electrode diameter of 102 mm. A coaxial vacuum line with length of 1.4 m and corresponding lumped inductance 330 nH served for a load. The generator inductance upstream the POS location was about 240 nH.

The POS hardware design allows to install up to eight plasma guns simultaneously. Each GPPG is a coaxial plasma accelerator with fast gas valve injecting gas radially into

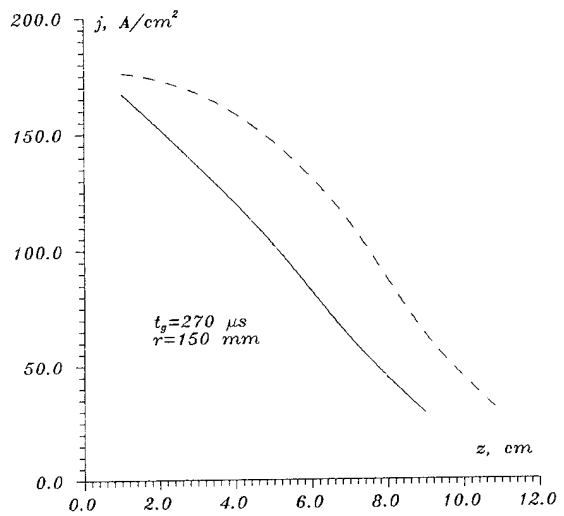


Fig. 1a. Plasma ion current density distribution across the plasma flow. Solid line - gun current 68 kA, dashed - 155 kA.

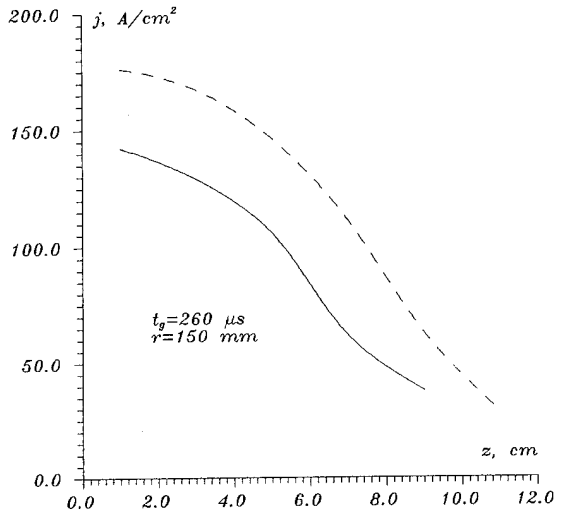


Fig. 1b. Plasma ion current density distribution across the plasma flow. Solid line - positive polarity of central electrode, dashed - negative polarity.

gun interelectrode gap. Pulsed gas valve, placed at potential gun electrode, is energized through insulating coil from capacitor bank of 100 μF, with period of the discharge of 30 μs. In order to increase the plasma flow intensity comparing with obtained in [2], the voltage pulse is applied to inner electrode of the gun. Feeding bank capacity is increased to 5 μF instead of 3 μF in previous experiment.

Plasma flow characterization was made for modified GPPG with hydrogen gas fill. The ion current density along plasma flow crossection in 150 mm away from the gun outlet is shown in Fig. 1 a,b. As followed from these measurements, such a gun forms high velocity plasma flow with divergence 15—20° and ion saturation current at cathode location of 150 A/cm^2.

For switch parameters measurement the self-integrated current monitors placed both upstream and downstream the POS were used. The active voltage divider measured voltage pulse at interface location. The ion beam diagnostics installed inside POS cathode included track detectors and graphite targets for nuclear activation under high energy proton beam deposition in the reaction $^{12}C(p,\gamma)^{13}N(\beta^+)$. Thompson parabola spectrometer was used to measure ion beam composition and energy.

Experimental Results

Switching characteristics. Most experimental runs were dedicated to POS study with hydrogen plasma fill. The detailed ion beam measurements also were carried out for hydrogen plasma. In this experiment, the existence of optimum gap between gun outlet and POS cathode was established as well as in the experiments with cable plasma guns. The optimum gap for most effective switch performance was found to be 150 mm. The increase gun number from 4 to 8 keeping the same capacitor bank parameters (the current in the circuit of each plasma gun decreased from 90 to 65 kA) weakly changes POS characteristics. This is probably due to similar plasma flow parameters in the switch interelectrode gap.

Twofold increase of the inner electrode di-

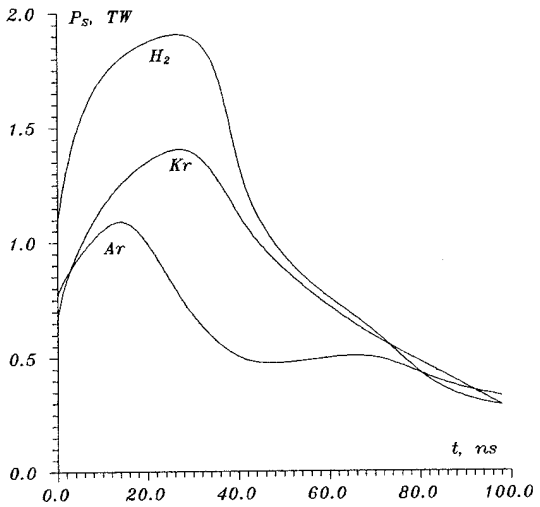


Fig. 2. Switch power vs time for various gases.

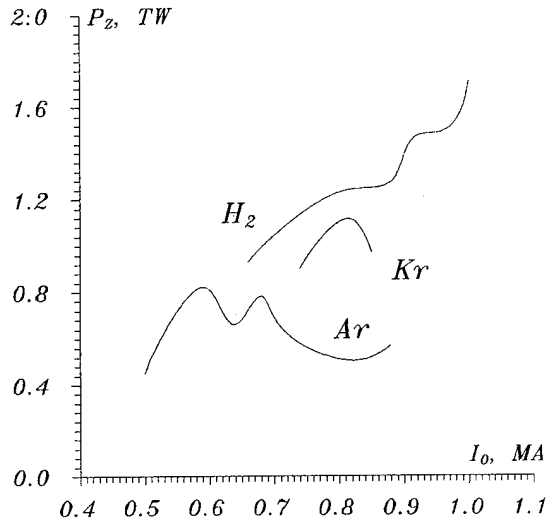


Fig. 3. Switch power vs switch current for various gases.

ameter in the switch region resulted in 1.3 times POS current rise at the same plasma fill time delay. The switch impedance was 3 times lower in this experimental run.

The change of gas in the GPPG from hydrogen to Ar and Kr led to switch characteristics deterioration (Fig.2). Moreover, we could not reach the POS current amplitude as high as in hydrogen experiments. The time delay between guns triggering and accelerator pulse was equal for hydrogen 5-7μs, for argon 6-9 μs and for krypton 8.5-10.5 μs. The delay increase over given values don't results in POS current rise, the switching characteristics become worse. The switch power versus stored current is given in Fig.3. Noteworthy, that such a dependence for hydrogen plasma is different from curves corresponding to Ar and Kr plasma fill, which have a maximum. The power of switch for hydrogen plasma increases monotonously within whole range of POS current.

Basing on upstream current monitor and insulator voltage, the vacuum inductance upstream the POS was calculated as following:
$L_v(t) = (1/I_g) \int U_a dt$
During the first half of the conduction time this inductance remains a constant and is equal to calculated inductance of a coaxial line (240 nH). Nevertheless, 100—300 ns prior the opening the inductance starts to increase and reaches the considerable value just at opening moment (see Table 1.).

Table 1. Vacuum inductance increasing during conduction phase.

Gas	H_2	Ar	Kr
ΔL, nH	60—80	35—55	30—50
I_0	0.7—1	0.6—0.85	0.7—0.85

Track measurements. The traces at the track detectors, placed inside the cathode with holes of 2 and 4 mm in diameter, showed that ion beam is shifted from the holes downstream. The upstream side of the trace is shifted at 0—10 mm, the downstream side is shifted at 30—40 mm. This trace shift can be explained with two reasons: a) the bending of the trajectories of low energy ions due to magnetic force; b) the ion beam has large divergence due to uncomplete charge neutralization.

The Thompson spectrometer, placed 40 cm downstream from plasma injection location, showed that ion beam consists mostly from

hydrogen ions with energy 500—1300 keV. The switch voltage in these shots reached 1500 kV. The absence of carbon ions observed was probably due to long distance from spectrometer to plasma source.

Activation measurements. The activation measurements showed the sharp proton current maximum observed 35—45 cm downstream from plasma guns location. The corresponding plot is given in Fig. 4. The total number of protons with energy over 600 keV was found to be in limits $(1.4 - 2.2)10^{17}$ particles per pulse. The part of proton current in the total switch current accounted using activation data was equal to 0.45—0.65.

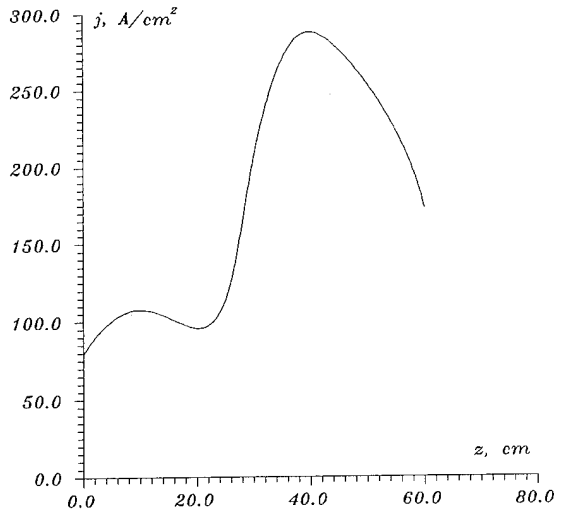


Fig. 4. Proton current density along POS length.

Analysis of Experimental Data

The best switching properties were obtained for hydrogen plasma. The POS current reached 1 MA during $1\mu s$ conduction time, POS voltage made up 1.8—2 MV, switch impedance reached 3—4 Ohm at POS voltage maximum.

It should be noted, that GPPG were not powerful enough for GIT–4 accelerator: switch current did not exceed 1 MA at GPPG capacitor bank energy of 9 kJ compared to 5 kJ of bank energy if cable guns are used allowing to conduct higher POS current (1.3 MA during $1.5\mu s$). This is a possible reason for monotonous power increase with switch current at hydrogen plasma.

The increase of vacuum inductance can be explained as either current channel displacement in direction of a load or voltage drop in the switch having different from Idl/dt reasons. Noteworthy, that the switch behavior depends on gas type used in the gun: the additional inductivity decreases with increase atomic number monotonously, but switch power is minimal for Ar and slightly rises for Kr.

The number of high energy protons, obtained from nuclear activation, reached 2.10^{17} particles. This number corresponds to 70% of pull energy deposited in POS during switching process. Taking into account, that these protons are accelerated in near cathode vacuum gap of switch as in the magnetically insulated coaxial ion diode, we can evaluate the effective switch gap. For $N_p = 2.10^{17}$, $l_{switch} = 60cm$ and $n_i = (2 - 3)10^{14}$, the gap value is approximately equal to 3—4 mm.

Comparing obtained results with ones described elsewhere [2] we can conclude, that the upgrade of switch current to 1 MA instead of 200 kA requires 1.5 orders of plasma mass increase in the switch region. The best switching characteristics as well as in [2] were obtained for pure hydrogen plasma.

References.

1. S.P.Bugaev, A.M.Volkov, B.M.Koval'chuk et al. IEEE Trans. on Plasma Sci., V.18, no.1, P.115 (1990).
2. P.S.Ananjin, V.B.Karpov, Ya.E.Krasik et al. Ibid, V.20, no.5, P.537 (1992).

FIRST EXPERIMENTAL OBSERVATION OF SWITCHING THE MICROSECOND ELECTRON BEAM BY RECONNECTION OF THE MAGNETIC FIELD LINES

A.V.Arzhannikov, S.L.Sinitsky and A.V.Tarasov
Budker Institute of Nuclear Physics, Novosibirsk,630090
Russia

Abstract

The paper presents the experimental results on fast (~10μs) switching of the microsecond ribbon (1x12cm) REB by reconnection of the guiding magnetic field lines. Conditions for switching the electron beam from one channel to another has been found. High efficiency of the beam transport through the switching unit has been obtained.

1. INTRODUCTION

Microsecond ribbon electron beams have a good perspective for heating plasma in a long solenoidal trap and for generation of a powerful microwave radiation in the millimeter wavelength band [1,2]. For increasing the total energy of these beams up to 1MJ the idea to switch into one vacuum channel a few electron beams generated consequently in similar diodes was proposed in [3,4]. This switching should be realized by quick reconnection of the guiding magnetic field lines. Such replacing of the magnetic field fluxes may be also used for defense of the diodes from a flow of a high temperature plasma, outgoing from the trap.

2. EXPERIMENTAL SETUP

In order to test a possibility of the fast switching of two similar beams into one vacuum channel we have used the way in which the beam electrons pass through the channels in the opposite direction. It means that in our experiments the electron beam is generated in one diode but then this beam is consequently switched into one of two identical vacuum channels by reconnection of the guiding magnetic field lines in a special unit. A schematic of the experiments is shown in Fig.1. The electron beam is generated in the

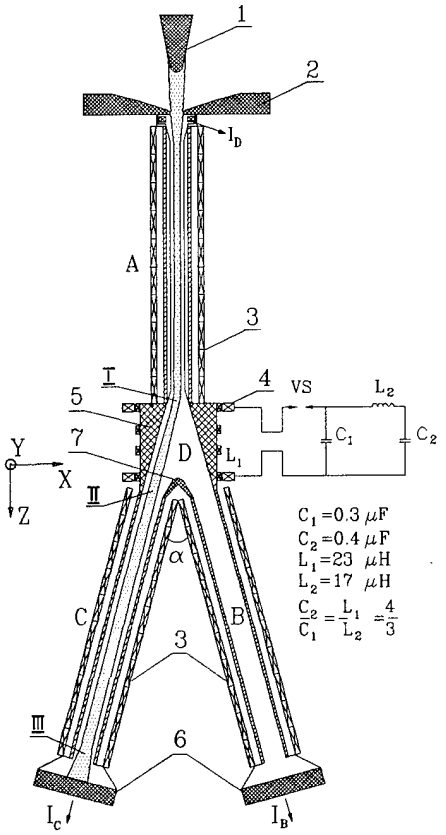


Fig.1. Schematic of the experiment.
1 - cathode, 2 - slit anode, 3 - magnetic coils, creating the guiding magnetic field, 4 - coils, creating the switching magnetic field, 5 - switching unit, 6 - collectors of the beam electrons, 7 - graphite limiter.

magnetically insulated ribbon diode and then it passes through a slit vacuum channel A with the length 50cm and the inner cross section 1.8x24cm. After passing the channel A the beam enters into a switching unit D which is connected with two identical vacuum channels B and C. These channels are similar to channel A, only their inner cross section has another value 3.8x24cm. The angle α between the axises of these two channels is equal to 30^0. There are graphite collectors absorbing the beam electrons at the exit of the two channels and the beam current is measured by using these collectors. The magnetic coils (3) wound on the walls of the channels A,B,C and the switching unit D create the guiding magnetic field up to 10kG. Besides that special magnetic coils (4) provide quickly varied magnetic field in the region D. This field has a perpendicular direction to both the guiding magnetic field lines and the larger dimension of the beam cross section. For the fast penetration of the perpendicular switching magnetic field into the vacuum channel of the unit D its walls have been made of dielectric material and an inner surface of the walls has been covered by low conducting material - graphite textile. Simultaneous measurements of the electric current in the coils (4) I_S and the switching magnetic field in the unit D have shown that the forms of these signals are similar and the amplitude of the field coincides with the quantity which is obtained by the computer calculations on the measured current I_S.

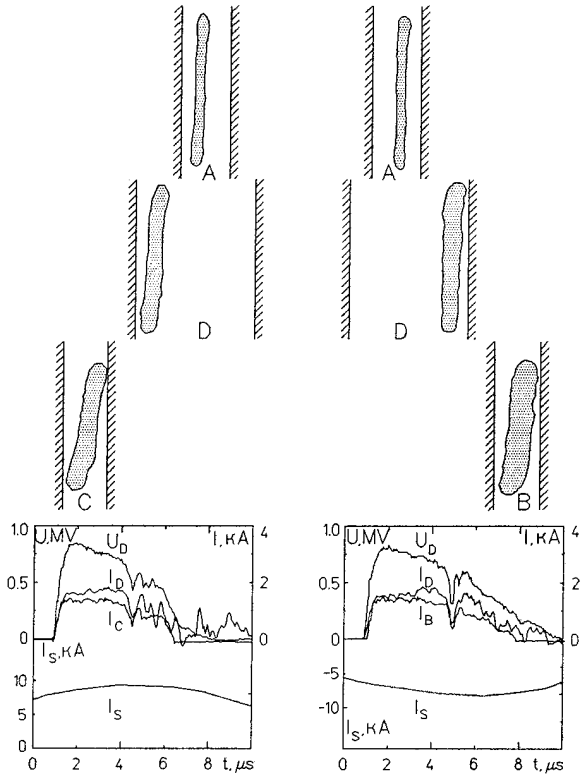


Fig.2. The cross section shape of the beam at the places pointed I,II,III in the Fig.1 and the sets of oscillograms characterizing the beam passing into the channel C (left) and the channel B (right).

3. EXPERIMENTAL RESULTS

In the first series of the experiments the optimal values of the switching and the guiding magnetic fields as well as the optimal time delay between the beginning of the magnetic field lines reconnection and the beam generation have been chosen. The diode voltage - U_D, the beam current at the entrance of the channel A - I_D, the current of the beam at the exit of the channels C and B - I_C and I_B respectively, have been measured in the experiments. Besides that we have registered the current I_S in the coils (4) which determines the value and direction of the switching magnetic field in the unit D. The shape of the beam cross section in various parts of the beam way has been registered by its imprints on the plastic films with 50μm thickness. In the Fig.2 the results of two consecutive shots at the optimal value of the switching current I_S in the coils (4) are presented. These two shots have the same value of the current I_S but the opposite directions of it during the beam pulse. In this figure one can see the cross section shapes of the beam detected in these two shots at three places along the beam passing through the chamber. These three places are pointed in the Fig.1 by the numbers I,II,III. The upper pair of imprints refers to the place I in the channel A, the middle one - to the place II at the exit of the switching unit and finally the lower one - to the place III at the exit of the channel C (left) and the

channel B (right). It is seen from this figure that if the beam is generated in the time interval with the positive switching current I_S the beam moves through the switching unit D into the channel C. At the negative current I_S the beam moves into the channel B. It should be noted that the beam cross section becomes wider and slightly rotates inside the switching unit D. It takes place because of only one wall of the unit D is close to the beam border. The same phenomena occurs at the beam passing through the channels B and C where conducting walls are far from the beam border. It was shown in [4,5] that for the stable equilibrium transport of the ribbon electron beam in a slit vacuum channel the beam thickness should fill 2/3 of the gap between its walls. If this condition is not satisfied the beam cross section may be deformed during the beam transport.

To conclude this part of experiment description we state that after passing through three plastic films the beam has the current at the exit of the channels B and C which is close to the current at the entrance of the channel A. It means that the losses of the electrons during the beam transport through the channels are small and the beam switching by the reconnection of the magnetic field lines has been realized with high efficiency.

Another important problem to complicate the realization of the beam switching, is generating plasma in the switching unit during the beam passing there. If the plasma conductivity is enough for keeping the magnetic field during 10 μs, the reconnection of the magnetic field lines becomes impossible there and the switching of the next beam should not be possible too. On this reason we have made another series of experiments in which the process of the switching of the magnetic field is realized during the beam pulse and some part of the beam electrons falls down to the graphite limiter (7) (see the Fig.1). The result of these experiments are demonstrated by the oscillograms in the Fig.3. The upper set of oscillograms corresponds to the case when the beam generation occurs during the switching of the magnetic field from the channel B to the channel C. The middle one refers to the case when the current I_S is practically constant during the beam pulse. And finally the lower set corresponds to the case when in the beginning the beam moves into the channel C and then according to the behavior of the guiding magnetic field flux it is switched to the channel B. In all these cases shown in Fig. 3, the beam current I_C at the exit of the channel C is close to the diode current I_D if the switching current I_S in the coils (4) has the optimal value but then I_C quickly decreases as soon as the current I_S deviates from the optimal value. If the beam is generated during the time when the current I_S is negative we have the same character of the oscillograms for the current in the channel B.

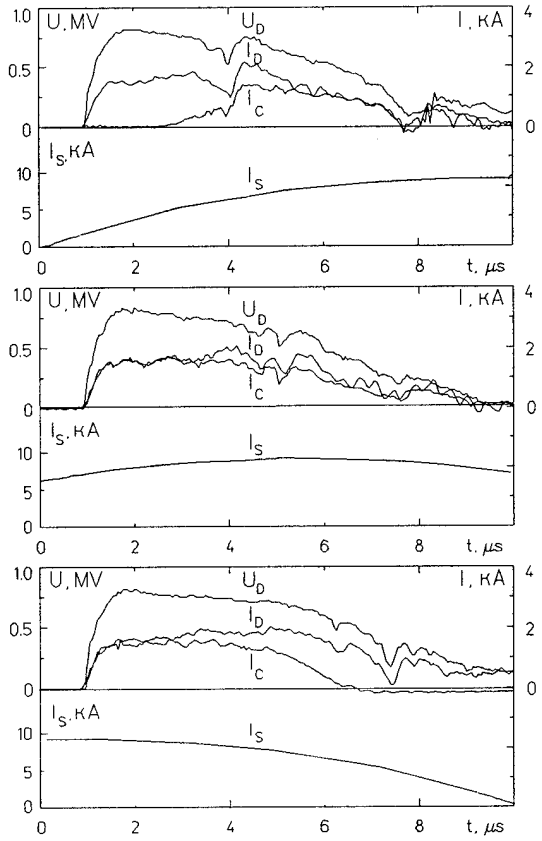


Fig.3. Sets of oscillograms describing the process of the beam switching according to the variation of the current I_S in the coils (4).

So, the plasma appeared in the switching unit at the beam passing through it, does not prevent the reconnection of the guiding magnetic field lines.

4. CONCLUSION

As a result of the performed experiments one can state that the switching of the high current beam in the time of 10μs by reconnection of the guiding magnetic field lines has been realized for the case of its ribbon cross section. If we take into account that 0.4MJ energy content of the single ribbon beam has been obtained now [6], then this process opens the perspective to achieve 1MJ level in the beam- plasma experiments.

5. ACKNOWLEDGEMENTS

The authors wish to thank Dr. V.S.Nikolaev, R.P.Zotkin for design of the experimental setup and M.A.Agafonov, A.V.Kutovenko for assistance at the experiments.

6. REFERENCES

1. A.V.Arzhannikov, A.V.Burdakov, V.V.Chikunov et al. *Proc. of the 9-th Intern. Conf on High-Power Particle Beams, Washington, 1992, p. 127.*
2. A.V.Arzhannikov, S.L.Sinitsky and M.V.Yushkov. *12-th Intern. Free Electron Laser Conf., Program and Abstracts, Paris, 1990, p.105.*
3. S.G.Voropaev, B.A.Knyazev, V.S.Koidan et al. *Dokladi 3 All-Union Conf. on Engin. Problems of Thermonuclear Reactors, Leningrad, 1984, Moscow, 1984, v.1, p.298 (in Russian).*
4. A.V.Arzhannikov, V.T.Astrelin and S.L.Sinitsky. *Proc. of the XVIII Intern. Conf. on Phenomena in Ionized Gases, Swansea, 1987, contr. papers., p. 206.*
5. A.V.Arzhannikov, V.T.Astrelin, V.A.Kapitonov et al. *Proc. of the 8-th Intern. Conf. on High-Power Particle Beams, Novosibirsk, 1990, v. 1, p. 256.*
6. A.V.Arzhannikov, V.B.Bobylev, V.S.Nikolaev et al. *Proc. of the XVI Intern. Symposium on Discharges and Electrical Insulation in Vacuum, Moscow, 1994, p. 392.*

SWITCHING CHARACTERISTICS OF ALUMINUM FOILS USED IN SMALL INDUCTIVELY ENERGY STORAGE SYSTEM

M. Sato, T. Nakamura and S. Nobuhara
Department of Electrical Engineering,
Himeji Institute of Technology,
2167 Shosha, Himeji, Hyogo 671-22, Japan

Abstract

Vaporization of fine wires in water has a good performance as the opening switch, and is able to be utilized easily. On the other hand, it is expected that the exploding foils have also a good performance but there is a few report as opening switches. So we constructed a small pulsed power generator, and investigated switching characteristics of aluminum foils.

The condenser of 50 kV, 3.2 μF was used at the charged voltage of 20 kV. With copper wires, the peak voltage and the pulse width were 85 kV and 800 ns, respectively. When 8 μm thick aluminum foils were used, the peak voltages were not changed, but its pulse width became long. Moreover the power consumed in the switch increased 50 %. This fact suggests that the larger power is able to be transferred to a load.

1. Introduction

Vaporization of fine wires in water, which is well known as the name of the exploding wire[1], have a good performance as the opening switch, and is able to be utilized easily. On the other hand, the exploding foil were widely investigated as the fuse, and have also a good performance[2]. However there is a few report of experimental results as opening switches[3]. So we constructed a small pulsed power generator, and investigated the switching characteristics of aluminum foils used as the opening switch.

The constructed small pulsed power generator is similar to the "ASO-I" at Kumamoto University[4]. The generator is a coaxial type, and consists of an inductively storage, a switching and a diode section. The condenser of 50 kV, 3.2 μF are placed, and was used at the charged voltage of 20 kV. In the experiments, the diode section was kept as the open circuit and was used to measure the voltages across the switching section. In the case of the copper fine wires, the peak voltage and the pulse width were 85 kV and 800 ns, respectively. When 8 μm thick aluminum foils were used as the opening switch, the peak voltages were not changed in contrast to the case of the copper wires, but its pulse width became long. Moreover the power consumed in the switch section increased 50 % in contrast to the case of the copper wires. This fact suggests that the larger power is able to be transferred to a load.

2. Experimental Setup

Figures 1 (a) and (b) show the schematic drawing of the small pulsed power generator and its equivalent circuit, respectively. The constructed generator is

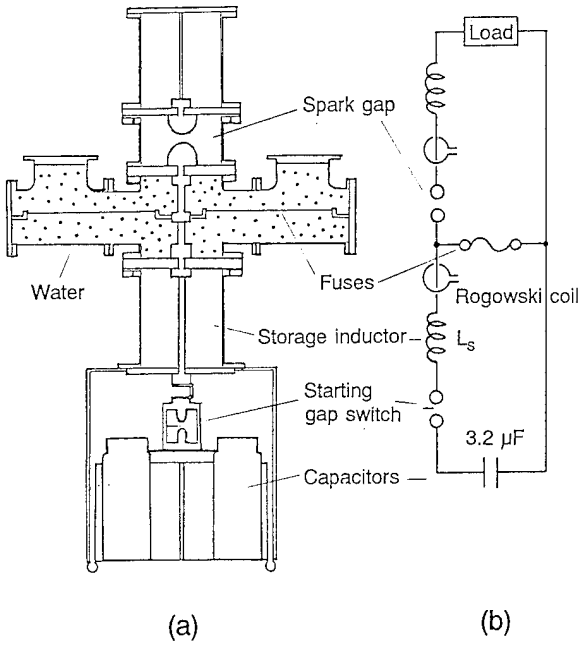


Fig. 1 Schematic drawing of the generator (a) and its equivalent circuit (b).

approximately 2 m high, 1 m wide, and consists of an inductively storage, a switching and a diode section. These sections were mainly made of stainless steel pipes of which diameters were about 10 inches. In the inductively storage section, the eight condensers of 50 kV, 0.4 μF are placed, and were used at the charged voltage of 20 kV. When the condensers are charged and discharges through a gap switch, a current flows into the inductively storage section. This part is coaxial type, but a small coil is inserted as a center conductor in order to increase an inductance. The measured inductance of the coil was 3.0 μH, and a total inductance was 3.5 μH.

A vessel located in the switching section has four ports, and T-shaped pipes were attached to each port. In each T-shaped pipe, some copper fine wires or an aluminum foil were set as the fuse. After setting of the fuse, water is filled in the vessel and the T-shaped pipes. In the case of the copper wire, its diameter ranged from 0.1 to 0.3 mm. The lengths of the wires were varied from 5 to 25 cm. The 8 μm thick aluminum foils were used as the fuse. The length and the width of them were 15 cm and 13 mm, respectively. In the diode section, a self triggered gap switch was shorted, and a resistive voltage divider was located instead of a diode to measure the voltages across the switching section. The voltage divider has the main resistance of 1 kΩ, and this value was sufficiently high compared to the impedance of the fuse. A Rogowski coil is placed between the inductively storage and the switching section in order to measure the current flowing into the fuse.

3. Experimental Results

Figures 2 (a) and (b) show the typical wave-forms of the voltage and the current, and time history of an impedance, respectively. In this shot, the four copper wires were set in the switching section. The diameter and the length of them were 0.1

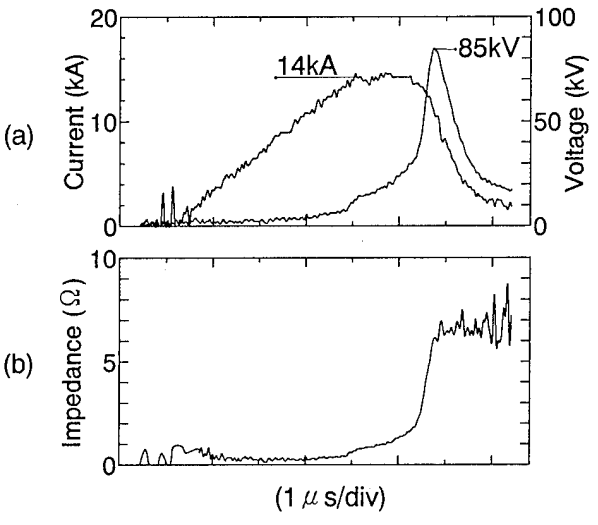


Fig. 2 Typical wave-forms of the voltage and the current (a), and time history of the impedance (b).

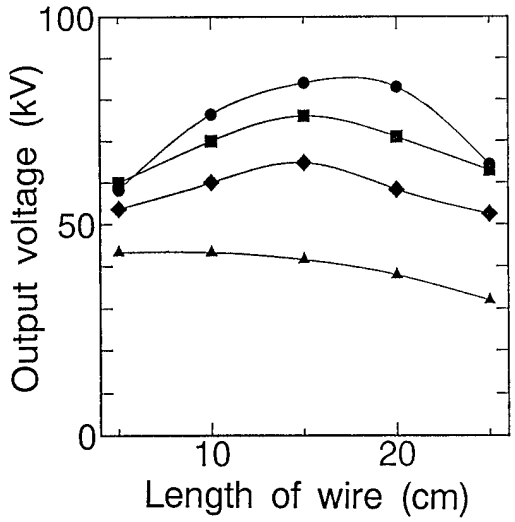


Fig. 3 Dependence of output voltage on the length of the wire. Numbers of wires; ●:4, ■:3, ◆:2, ▲:1.

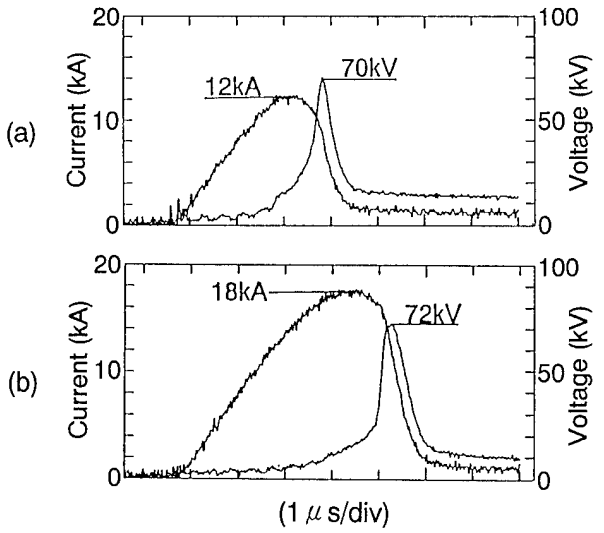


Fig. 4 Wave-forms of the voltages and the currents obtained with the copper wires (a) and the aluminum foil (b).

mm and 15 cm, respectively. In Fig. 2 (a), the current increases linearly in an initial phase. After the current reaches at the maximum value of 14 kA, it decreases with a steep slope. The voltage increases sharply around the maximum value of the current, and its peak value is 85 kV. The pulse width of the voltage is 800 ns in FWHM. The impedance was calculated by the values of the voltage and the current at the same time, and displayed as time history in Fig. 2 (b). Initially the impedance is significantly low value, but rapidly shifts to the high value of 6.5 Ω due to exploding of the wires.

Dependence of output voltages (peak values) on the length of the wire ia shown in Fig. 3. In this figure, each line corresponds to the data obtained with the copper wires of different numbers. This figure shows that higher voltages are obtained at the length of 15 cm, and also shows that the large number of the wire makes the output voltage high. These results are popular characteristics in the exploding wires[4].

The wave-forms of the voltage and the current obtained with the copper wires and the aluminum foil are shown in Figs. 4 (a) and (b), respectively. Although the shots having similar peak voltages were selected, the maximum values of the currents are quite different. That is, those obtained with the aluminum foil and the copper wires are 18 and 12 kA, respectively. Moreover the pulse width becomes longer in the case of the aluminum foil. In Fig. 4 (a), the two copper wires were used, and the diameters and the lengths of the wires were 0.1 mm and 15 cm, respectively.

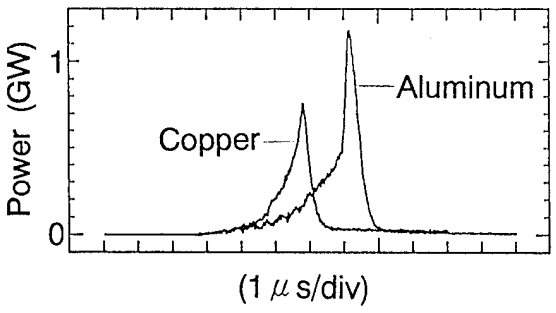


Fig. 5 Time history of the powers.

Figure 5 shows the powers calculated by the values of the voltages and the currents shown in Fig. 4. The peak values obtained with the aluminum foil and the copper wires are 1.2 and 0.75 GW, respectively. These values show that 50 % larger power is consumed in the aluminum foil used as the fuse. This fact suggests that the larger power is able to be transferred to a load (diode).

It is considered that the switching characteristics of the aluminum foil is better than that of the copper wire. However it has some problems. For example, the used aluminum foils were so thin that setting of the aluminum foils was difficult. In other word, the aluminum foil was easily shredded during setting. Since the current was small in our generator, reproducibility was so poor. Therefore dependence as shown in Fig. 3 was not obtained in the case of the aluminum foil.

4. Summary

We constructed a small pulsed power generator, and investigated the switching characteristics of the aluminum foils. The major results are followings:

1. With the copper wires, the peak voltage and the pulse width were 85 kV and 800 ns, respectively.
2. With the aluminum foil, the peak voltage was not changed in contrast to the case of the copper wires, but its pulse width became long.
3. The power consumed in the aluminum foil increased 50 % in contrast to that with the copper wire.

It is considered that the switching characteristics of the aluminum foil is better than that of the copper wire. However the aluminum foil has the problems in the case of the small pulse power generator; the poor reproducibility and the difficulty in setting.

References

1)For example:
F. D. Bennett and G. D. Kahl:
Exploding Wires, Vol.4 (1968) 1.

2) T. L. Berger: IEEE Trans. Plasma Sci. PS-8 (1980) 213.

3) D. Conte, R.D. Ford, W. H. Lupton and I. M. Vitkovitsky: Proc. IEEE Int. Pulsed Power Conf., (1979) 276.

4) H. Akiyama, K. Fujita, T. Majima, N. Shimomura and S. Maeda:
Proc. 6th IEEE Int. Pulsed Power Conf., (1987) 627.

HIGH POWER ELECTRON GENERATORS BASED ON CHARGING OF A PULSE-FORMING LINE BY MEANS OF ELECTRICALLY EXPLODED WIRES

B. A. Kablambaev, A. V. Luchinsky, V. M. Makhrin,
N. A. Ratakhin, V. S. Sedoi, and V. P. Sergeenko
High Current Electronics Institute, Tomsk, Russia

Most of the currently operating high-power megampere generators have been developed in one of two circuit designs. In the former case, the generator consists of a high-operating-voltage (HV) microsecond Marx generator (U > 1.5 - 2 MV), several cascades of water pulse-forming lines (FL), a transmission line, and a vacuum diode. In the latter case, these are a rather low-operating-voltage (LV) microsecond Marx (U < 1 MV), an inductive energy store, a POS, and a proper diode. Each of these circuit designs has certain deficiencies. In the former case, these are the well-known operating difficulties with the HV Marx (more stringent requirements the insulation and the bulky element base), and the presence of bulky microsecond FLs with their provision systems, that increase the installation size. In the latter case, these are a rather low switch resistance at the stage of current switching into a load, hence, a slightly increased output voltage and, particularly, power. At the same time, there exist well-known low-current high-power HV e-beam generators, which are built in the circuit design including a LV (~ 1 MV) microsecond Marx, an inductive energy store, an exploding wire (EW) switch, and a vacuum diode. In such generators, the above mentioned problems are solved by increasing the initial voltage four to six times. But these circuits have a low energy efficiency (< 30 %) related to the EW operation into a resistive load (diode). However, it can be supposed that a capacitive load, because of its specific impedance, may have a higher energy efficiency for the same maximum voltages. Thereby, we consider the operation of the high-power high-current generator (HPHCG) with the circuit design "LV Marx - inductive storage - EW switch - fast FL - transmission line - diode". Here the main problem is the efficiency of energy transfer from the Marx to the HV-FL. Some relevant information is in Refs. 1 and 2.

In our opinion, the creation of HPHCGs in this hybrid circuit design is justified for the following conditions: the voltage across the FL capacitance is 3.5-6 times higher than the initial (erected) Marx voltage, the factor of energy transfer from the Marx to the FL capacitance is 0.4-0.5, and the time for charging of the FL capacitance is 300-350 ns. In this case, we may believe that (as compared to the extensively used circuit design "HV Marx - μs-FL, etc.") the somewhat lower

energy efficiency for this hybrid circuit is fully compensated by the lower costs of the Marx and service system.

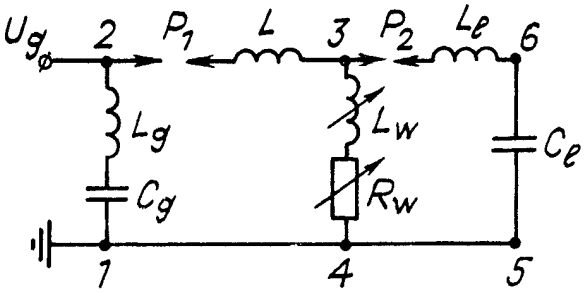


Fig. 1.

Let us consider some limitations on the main circuit parameters (Fig. 1). First, from the law of conservation of energy (LCE), we have a trivial equation: $(U/U_g)^2 = \eta_e(C_g/C_l)$, where η_e is the energy efficiency. Second, the time needed for the current to increase to its maximum in the circuit 1-2-3-4 (Fig. 1) is ten times longer than the charging time of the capacitor C_l after the breakdown of the spark gap P_2. Note that even for an ideal current switch, we have:

$$R_w\big|_{t < t_l} = 0, \quad R_w\big|_{t \geq t_l} = \infty,$$

$$\eta_e = \frac{L_g + L}{L_g + L + L_w} \frac{L_g + L}{L_g + L + L_l}.$$

That is, L_w and L_l should be markedly less than $L + L_g$ to obtain the required value of η_e. The last two equations conflict to one another and limit the choice of the value of $L + L_g$. Now, let us consider the requirements for the resistance R_s. The maximum energy stored in the inductance $L + L_g$ is calculated from the LCE for the circuit 1-2-3-4 and is given by:

$$\frac{(L_g + L)I_m^2}{2} = \frac{C_g U_g^2}{2} \frac{L_g + L}{L_g + L + L_w} \times \left\{ \frac{1 - 2\int_0^{t^*_m} \alpha I^{*2} dt^*}{1 + \alpha_m^2} \right\} \approx \frac{C_g U_g^2}{2} \frac{L_g + L}{L_g + L + L_l} \times \frac{1}{1 + \alpha_m^2 + 2\int_0^{t^*_m} \alpha(t) dt^*}. \quad (1)$$

Here $I^* = \frac{I\rho}{U_g}$, $\rho = \sqrt{\frac{L_g + L + L_w}{C_g}}$, $t^* = \frac{t}{\sqrt{(L_g + L + L_w)C_g}}$, $\alpha(t) = R_w(t)/\rho$, $\alpha_m = \alpha(t^*_m)$.

The last equality is valid, if a rises sharply nearby the current maximum, which is usually the case. From Eq. (1) it follows that the parameter α should be appreciably less than unity to obtain the required values of η_e. The main requirements for R at the stage of current switching into a load can readily be understood based on a simplified circuit (Fig. 2). For the maximum energy in the load, from the LCE it follows that

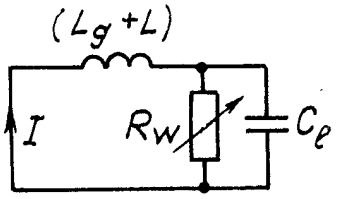


Fig. 2.

$$\frac{C_g U_g^2}{2} = \frac{(L_g + L)}{2} I_m^2 \times$$

$$\frac{1 - 2\int_0^{t'_m} \beta(t') U^{*2}(t') \, dt'}{1 + \beta_m^2}, \qquad (2)$$

where $t' = \frac{t}{\sqrt{(L_g + L)C_g}}$, $U^* = \frac{U}{I_m\sqrt{(L_g + L)/C_g}} = \frac{U}{I_m \rho}$, $\beta_m = \beta(t'_m)$.

From Eq. (2) it follows that for efficient energy transfer, β_m, should be much less than unity ($\beta_m << 1$). Also, it can be seen why the capacitive load matches well with the switch. For matching, the integral in Eq. (2) should be much less than unity, if $\beta_0 >> 1$ at the initial time. This is quite possible, since the integrand consists of the product of the abruptly falling β and the abruptly rising function U^*.

An analysis of Eqs. (1)-(2) also shows that to fulfill the mentioned requirements, it is necessary that the resistance R, within the time between the maximum current in the primary circuit and the maximum voltage across the capacitive load, increase no less than 50 times. Further optimization of the parameters is possible using the code [3] that considers the the variation resistance in depending on the input energy (or the time). Optimization is also possible by experiment on a low-energy installation. Both of this ways have been used. The results of the experiment are presented in Ref. 4. The computation has shown that to optimize the circuit parameters, including the EW switch, values η_e = 0.4 - 0.5 are quite allowable. A similar result has been obtained in an experiment with the energy ~1 kJ. (At a later time, we intend to use an installation with the stored energy ≥100 kJ, to verify the predictions and experimental results for this energy level).

The main parameters were as follows: C_g = 1.53 μF, U_g = 0.44 MV, L_g = 0.29 μH, L = 1.5 μH, L_w = 0.5 μH, L_l = 0.2 μH, and C_l = 40 nF. This was a preliminary experiment aimed at verification of the predictions rather than at optimizing η_e. It has been found that the agreement was good; the water FL was charged to U = $3.5U_g$ with η_e = 0.3-0.35 in a time t = 0.3-0.4 μs. We hope that an optimization of the circuit by the main parameters will allow η_e = 0.4-0.45 to be achieved for the given stored energy and that a compact subterawatt generator will be realized.

References

1. L. Liebing. Pulsed charging of capacitors by means of exploding wires. Z. Angew. Phys., Bd. 26, H 5, P. 345 (1969).

2. Yu. A. Kotov, N. G. Kolganov, and V. S. Sedoi. Forming of high-voltage pulses by means of explosion of wires. In: *Powerful nanosecond sources of accelerated electrons* [in Russian]. Nauka, Novosibirsk (1974).

3. V. A. Burtsev, N. V. Kalinin, and A. V. Luchinsky. *Electrical explosion of wires and its use in electrophysical*

installations [in Russian]. Energoatomizdat, Moscow (1990).
4. A. F. Korostelev, V. S. Sedoi, and A. V. Luchinsky. High-efficiency pulsed charging of capacitors by exploding wires. This Conf.

HIGH-EFFICIENCY PULSED CHARGING OF CAPACITORS BY EXPLODING WIRES

A.F. Korostelev, V.S. Sedoi, and A.V. Luchinsky
High Current Electronics Institute,
4 Akademichesky Ave., Tomsk, Russia

Abstract

Pulsed charging of a capacitor from an LC circuit by means of exploding wires (EW) has been investigated experimentally using a method of physical simulation. The efficiency of energy transfer is shown to be a maximum under the matched condition, when the specific action of the electrically exploded wire is equivalent to the potential action of the circuit. By the time of switching-on the capacitor, the specific energy introduced into the wire must be equal to the sublimation energy. Under this and other specifying conditions, the energy stored in the circuit inductance is $0.56W_0$ *at the maximum current. Simultaneous with variation of the circuit and load parameters, the EW parameters were varied with conservation of the similitude. As a result the overvoltages* $K = 4 \div 6.7$ *have been achieved with the transferred energy* $0.5W_0$.

The energy conversion in an *LC* circuit with an electrically exploded wire (EW) occurs in two stages peculiar to an *L* store. First, the energy with losses for the EW heating, is stored in the circuit inductance; the EW absorbs energy and fuses and then, in the liquid state, it heats up to the onset of fast expansion of the material. This is the heating stage (the EW resistance depends on the energy introduced into the wire) and, at the same time, the stage of the inductive energy storage, the current in the inductance rapidly rises. At the second stage, the EW resistance depends mostly on the density of the expanding metal, it increases by several orders of magnitude for a short time (the proper explosion stage), and the inductive energy is released with power amplification in the wire whose resistance is rapidly rising.

This is natural that an exploded wire must be chosen such that, on the one hand, its resistance at the heating stage limit the inductance current as slightly as possible and, on the other hand, the energy introduced into the EW until the onset of the second stage be sufficient for EW sublimation and transition into nonconducting state. When taking up an energy, the EW reduces the current. Hence, an optimal combination of the wire and circuit parameters must exist that should be found.

It is known [1, 2] that at the heating stage the wire resistivity ρ is a function of the introduced energy density w and that the specific action

$$h_{ex} = \int_0^w dw/\rho = \int_0^{t_{ex}} j^2 dt, \qquad (1)$$

where j is the current density and t is the time, h_{ex} is an integrated characteristic of the electrophysical properties of a given metal. Compared to the introduced energy density, the specific action h_{ex} depends on the rate of energy introduction not so strongly. For the copper wires we can take $h_{ex} = 2 \times 10^5$ A^2s/mm^4. Also, there exists a potential action of a circuit, $H_0 = i_0^2(LC)^{0.5}/2$, where i_0 is the shorting current. The ratio $h_{ex}S^2/H_0 = H_{ex}/H_0 = h_{ex}/h_0$ defines the main dimensionless characteristics of an LC circuit with an EW [3, 4]:
the maximum circuit current

$$y_m = i_m/i_0 = 0.75(H_{ex}/H_0)^{0.25}, \quad H_{ex}/H_0 \leq \pi;$$

the energy density introduced into the wire during the first current pulse (specific energy per unit volume calculated for initial volume Sl; here S is the cross section area and l is the EW length):

$$w_{ex}/w_0 = (H_{ex}/H_0)^{0.5}; \quad H_{ex}/H_0 \leq 1,$$
$$w_0 = CU_0^2/(2Sl) = W_0/Sl; \qquad (2)$$

the current at the onset of explosion:

$$y_i = 0.56(i_i/i_0)(H_{ex}/H_0)^{0.25}, \quad H_{ex}/H_0 \leq 1. \qquad (3)$$

From relationships (1)-(3) it can be seen that the matched explosion regime, where $H_{ex}/H_0 = 1$ is of certain interest such that the whole introduced energy is released in the wire (if the circuit resistance is negligibly small). In this case, by the onset of the second stage, the primary energy store has been completely discharged and the energy $y^2W_0 = 0.56W_0$ is stored at the maximum current and $y_i^2W_0 = 0.32W_0$ at the onset of explosion. This energy can be transferred into the external circuit of a load if a large enough energy density $w_i = W_i/Sl$ has been introduced into the wire until the instant the load is switched on, and the wire of length l is able to withstands the appearing voltage.

The critical wire length l_{cr} (the least length securing an explosion with a current pause) can be taken as a starting one [5]. For copper wires, the condition for the occurrence of a current pause beginning [6] is described by the criterional expression

$$l_{cr}/Sz = 1.85 \times 10^3 [10^{-6} h_0 (LC)^{0.5}/d]^{0.36} \qquad (4)$$

where d is the diameter of wires and z is the characteristic circuit impedance.

According to Refs. 7 and 8, the resistance of the EW and the overvoltage appearing at the proper explosion stage peak when the specific energy introduced in the EW during the first current pulse equals the sublimation energy w_s of the metal. For $w < w_s$, the rate of variation of the material density is small, and for $w > w_s$, ionization processes are effective. Therefore, the energy $w = w_s$ can be

sufficient for the EW to go into a non-conducting state. Then, from Eq. (2), in view of Eq. (4) and w_s = 47.5 J/mm^3 for copper, we can find a relationship ensuring $w = w_s$:

$$(LC)^{0.5}/d = 43(h_{ex}/h_0)^{0.39},\ \mu s/mm. \quad (5)$$

As a result, the initial conditions are easily determined:

from h_{ex}/h_0: the cross section of the wire $S = (W_0/zh_{ex})^{0.5}$ mm^2;
from relationship (5): $d = (LC)^{0.45}/43$ mm;
the number of wires $n = 4S/\pi d^2$;
from (4): $l_{cr} = 10^9 4Sz$ mm. (6)

The expected efficiency of energy transfer for the load connected at the beginning of the proper explosion state will be $\eta = \eta_i = 0.32$. An increase in η up to $\eta_m = 0.56$ can be achieved by earlier connection of the load (at a higher inductance current) and by use of a switch of a shorter length to retain the energy introduced into the EW at the same level.

The method described requires experimental verification and search for maximum values of the energy transfer efficiency and the electric field.

The operation of the *LC* circuit with EW onto a capacitive load has been studied on a test bench which allowed a variation the wire (n, d, and l) and circuit (C, L, and U_0) parameters according to Eqs. (6) with retention of similarity. The water insulated capacitor with plane-parallel electrodes was used as a load. The diagnostics included oscilloscope recording of the total current, switch current, switch voltage, and load voltage by means of two resistive shunts and two voltage dividers. In the experiment, the values η = 0.53 and y = 0.73 have been actually obtained, which are close to the maximum values obtained a priori: η = 0.56 and y = 0.75. The overvoltage factor is related in a natural fashion to the capacitance ratio:

$$K = y(C/C_l)^{0.5}. \quad (7)$$

As a result, the overvoltages K = 4 - 6.7 have been achieved with high energy transfer efficiency.

The investigation has shown that the above discussed way of rising the efficiency of energy transfer has lead to reasonable results. It is important that the experiment was performed using the physical simulation methods. This circumstance permits one to extend the range of applicability of the experimental data obtained to the similarity bounds. The combination of the wire and electric circuit parameters is such that

$$(U_0/U_l)y(C/C_l)^{0.5}(2\overline{R}/z) = 1 \quad (8)$$

where $\overline{R} = \overline{\rho}l/S$, $\overline{\rho} = w_s/h_{ex}$ (the integrated average EW resistivity) and $y = 0.73(h_{ex}/h_0)^{0.25}$.

Three similarity criteria describe the exploding wire and circuit parameters:

$$\Pi_1 = h_{ex}/h_0,\ \Pi_2 = \overline{R}/z,\ \Pi_3 = C/C_l.$$

The first two criteria Π_1 and Π_2 refer to the heating stage or the stage during which an inductive is stored energy. At the second stage, the inductive energy is transferred to the load, the wire

explodes, and the criterion Π_3 becomes effective. For optimal conditions, we have

$$h_{ex}/h_0 = 1, \quad 2\overline{R}/z = 1,$$
$$0.73\,(U_0/U_1)\,(C/C_1)^{0.5} = 1,$$

and then the combination of dimensionless values, Eq. (8), transforms to Eq. (7).

In conclusion, it should be said about feasible uses of the results obtained. First, a feasibility of use of the inductive-capacitive stores is extended, when the energy transfer to a load is achieved by means of an intermediate capacitor [9]. The efficiency of such circuit can be higher. Second, the results are usable for deciding of circuit parameters at cascade switches in which a current switches to a following cascade [10] and the first cascade operation conditions are similar to above considered. Third and forth, these results may be used in small pulsed voltage generators development for testing circuits of an equipment with a large own capacity; these may be too used to generate power radio pulses [11].

References

1. R. Rudenberg, *Transients in Electric Power Systems*. Inostr. Liter., Moscow (1955) (in Russian).
2. G. W. Anderson and F. W. Neilson, In *Exploding Wires*, vol. 1. Plenum Press, New York (1959) pp. 97-103.
3. Yu. A. Kotov, O. M. Samatov, V. S. Sedoi, et al., In *Fields and Pulsed Power Systems*: Proc. MG-5 Conf. - Novosibirsk, 1989. - New York, 1990, pp. 497-502.
4. Yu. A. Kotov, V. S. Sedoi, and L. I. Chemezova. Preprint No. 41, 1986, High Current Electronics Inst., Tomsk.
5. E. C. Cnare and F. W. Neilson, In *Exploding Wires*, vol. 1. Plenum Press, New York (1959) pp. 93-96.
6. E. I. Azarkevich, Yu. A. Kotov, and V. S. Sedoi, Zh. Tekh. Fiz. **45**, 175-177 (1975).
7. V. S. Sedoi, Zh. Tekh. Fiz. **46**, 1707-1710 (1976).
8. A. B. Andrezen, V. A. Burtsev, and V. M. Vodovozov, Zh. Tekh. Fiz. **50**, 2283-2294 (1980).
9. B. A. Kablambaev, A. V. Luchinsky, V. I. Makhrin, N. A. Ratakhin, V. S. Sedoi, and V. P. Sergeenko. This conf.
10. H. Akiyama, K. Fuita, and S. Maeda. Laser and Particle Beams, **5**, 487-593 (1987).
11. V. M. Kulgavchuk, Pribory i tekhn. eksper., No 1, 132-137 (1965).

SIMULATION OF FLASHOVER GENERATED BY STRONG TEM-WAVE IN MITL WITH INNER COAXIAL DIELECTRIC INSERT

Eugene Galstjan
Moscow Radiotechnical Institute
Warshawskoe Shosse 132
Moscow 113519, Russia

Abstract

Extremely sharp rise time of high-power relativistic electron beam was achieved by using of the long dielectric insert build into the cathode line of the magnetically insulated transmission line (MITL)[1]. Presented paper is devoted to a theoretical treatment of this process.

Efficiency of the sharp front formation grows owing to its dependence on the speed of the flashover front propagation. So, an estimation of this dependence is a step of great importance in solution of the problem. To do this, the problem of TEM - wave diffraction on the coaxial line and dielectric insert conjunction has been solved rigorously. It allows the electric field to be found at any time moment and at any point of dielectric. The flashover front speed has been estimated on physical grounds which can be derived from experimental data for the early phase of dielectric surface flashover in vacuum.

It has been known that a quite sharp electron beam rise time (up to 4 ns) may be achieved by using of the electromagnetic shock wave formation phenomenon taking place in long enough (~ 10 m) magnetically insulated transmission lines (MITL)[2]. To reduce the MITL length and to achieve an extremely sharp wave front (less 1 ns) it has been suggested to build into the cathode line a sufficiently long dielectric insert. Efficiency of the shock wave formation has been assumed to grow owing to a dependence of its front velocity on the speed of the flashover front propagation. To test this hypothesis, experimental investigations were made[1]. The results of the investigations call for a theoretical support. The problem as a whole is very complicated and required an in-depth analysis. In the initial stage of solution I would like to restrict my consideration to the breakdown time delay. For this reason, the main objective of this paper is an estimation of the speed of the flashover front propagation.

It would be of interest to mention briefly the mechanism of surface breakdown. When a high-voltage stress is applied to the insulator, the insulator surface acquires a positive charge by electron multiplication through a secondary emission process. Due to the electron bombardment of the insulator surface, neutral and ionized atoms, and molecules are released from the insulator surface by electron-stimulated desorption (ESD). A fraction of the desorbed neutrals are ionized by electron collisions and complete breakdown soon follows. In order to obtain

expressions for the electron fluxes that are responsible for the desorption and ionization of adsorbed gases, the electric field on the insulator surface must first be determined.

Electric Field

To ease the problem, let us consider the structure consisting of the conjunction of a coaxial line and a round waveguide with inner dielectric rod. The axis Z is directed along the axis of the structure. TEM-wave runs to the boundary (Z=0) and reflects from it without transformation into high modes, because there is no propagating high mode in the frequency region of the problem in hole structure. At the same time we have to take into account all non propagated high modes for keeping the accuracy of the fields estimation.

The total field in the region of $z<0$ we present as the sum of the incident field $E_{\mathrm{R}}^{(0)}(r,z,t)$ and the excited one $E_{\mathrm{R}}(r,z,t)$. In the region of $z>0$ the total field coincides with the excited one. Other components of the electromagnetic field can be obtained from the Maxwell equations. The metal walls of the structure are considered to be perfectly conducting. The excited field must satisfy the wave equation, the boundary condition, the condition of radiation at the infinity, the initial condition, the condition of the finite energy per unit of length in the whole structure. By using the Fourier transformation we reduce the problem to the problem of diffraction of the monochromatic TEM-wave on the considered structure. This problem has been solved by using the generalized matching method (GMM), based on factorization method in the Jones formulation[3]. The precision of the GMM and the relative simplicity in obtaining numerical results has dictated the choice of this method for the solution of the problem of diffraction.

Let us now pass over the intermediate calculations and proceed directly to the final expressions for electric field in the round waveguide represented in simple form

$$E_{\mathrm{R}}(r,z,t)=\frac{V_0}{b\ln b/a}\sum R_n(r,t)\exp(-\alpha_n z/b)$$

where a is inner radius, b is outer one, V_0 is the maximum value of voltage, R_n,α_n are sophisticated functions derived from the solution of the problem. Expression for E_{Z} may be written in a similar manner. The numerical values of these functions in the needed points had been computing in the process of the field calculations.

So, the first step of the solution has culminated in the creation of the program for the components of the electric field calculation as the base for the future simulation. On the other hand, the expressions for the electric fields provides a way of estimating the flashover behavior.

Flashover

An extended high voltage flashover model (HVF), so called "gaseous model", was sug-gested and theoretically estimated by Avdien-ko[4]. More recent works - theoretical analysis[5] and the use of novel high-speed diagnostics in experimental investigations[6] - essentially amp-lified HVF theory. In particular, the existence of dielectric surface charging and a saturation of the current amplification mechanism in early phase of flashover, the major role of desorbed gases from the insulator surface and following gaseous discharge near the surface were pointed out there.

The problem under consideration differs essentially from those listed above in that the excited electric fields on the

dielectric surface are extremely non uniform, much like a corona discharge.

Early in the process, all the electrons striking the insulator surface are emitted from the triple junction, for the secondary emitted electrons leave the surface under action of the field E_R before a surface positive charge has compensated this field. Denote the time delay required for this by τ_1. Apparently, this primary charging is held roughly uniform along the dielectric rod, because of the necessary amount of the electrons leaving the surface is proportional to the electric field E_R, but the higher is the electric field, the higher is the current of the background electrons. The current density necessary for the transverse field "neutralization" in 1 ns is

$$J[\mathrm{A/cm^2}] \sim 0.2 E_R[\mathrm{kV/cm}],$$

and it is easy to be attained. Further charging of the dielectric surface leads to appearance of the field pressing the electrons to the surface.

An electron emitted from the surface with an energy A_0 =4 eV reaches a height Δr

$$\Delta r < A_0 / eE_R,$$

and the range of trajectory is

$$\Delta z = 4 A_0 E_Z / eE_R^2,$$

where $\Delta r, \Delta z$ in cm, A_0 in eV, E_R, E_Z in V/cm are the components of the total field. The dimensions of trajectory are very small compared to the radius of the curvature of the surface and therefor it can be considered as a plane and the fields to be local uniform. In this

case we may write down an simple equation for the number of the secondary electrons emitted from the unit area n (in $1/cm^2$)

$$dn/dt = n/\tau_C$$

and a characteristic time of the surface charging is

$$\tau_C = A_0 / E_R(\sigma - 1)V_R.$$

Where σ is an average secondary emission rate and $V_R \sim 4*10^7 A_0^{1/2} = 8 \bullet 10^7$ cm/s is the average transverse velocity. It should be noted that the numerical value of τ_C is less 1 ns if the transverse electric field is above 10 V/cm.

When the surface charge density becomes sufficiently high, many of the secondary electrons emitted from the insulator surface will be attracted back onto the surface. The trajectory range of the electrons will decrease as the surface charge density increase. The energy at impact will therefor decrease. It will do so until the impact energy is equal to A_1 - the lower of the two energies at which the rate of secondary emission $\delta = 1$. In this case we have to take into account not only the above process, but also the space charge of the layer of the secondary electrons. Corresponding equation shows the existence a limit value both for the thickness of the layer, and for the number of the emitted electrons. The average thickness of the layer of the secondary electrons is about $10^{-4} - 10^{-3}$ cm and the limit value of the electron density in the layer is

$$\rho_\varepsilon \sim 4*10^{12} E_R^2 / (A_1 - A_0),\ 1/\mathrm{cm^3}.$$

Now the density of the current perpendicular to the surface can be obtained as

$$J_R = e\rho_e V_R,$$

and we may turn to definition of the density of the desorbed gases. The desorbed gases from material like Plexiglass (polymethyl methacry-late) contain a higher percentage of hydrogen and water vapor particularly in the case of an unbaked vacuum systems. In order to find the density of desorbed gas, the velocity V_0 at which a desorbed neutral leaves the dielectric surface must be known.

However, only a few data are available on the value of V_0. The average velocity of the gas molecules may be assumed of the order of the sound speed $V_0 \sim 10^5$ cm/s. The density of the desorbed molecules n_D can be estimated from the value of V_0 and the gas desorption rate

$$n_D = K_D J_R / eV_0, \ 1/\text{cm}^3.$$

As is shown in the paper[5] a desorption probability in the range K_D =4-8 molecules/el. seems to be a reasonable value. The desorbed gas density in the region of the high field E_R, E_Z~ 100 - 300 kV/cm amounts up to $n_D \sim 10^{18}$.

It is sufficiently proper density[4] that the breakdown to be getting the start.

So the density of the desorbed gas is distributed sufficiently non uniform along the dielectric rod. Under action of the electric field E_Z the secondary electrons move from the region of the high density to the region of the low density with the mean speed

$$V_Z = 8*10^7 (A - A_0)^{1/2}.$$

In the range of the electron energy

$$A_1 < A < A_2,$$

where the rate of the secondary electron emission is more than the unity $\delta > 1$, the speed

values fall in the range

$$2.5 \cdot 10^8 < V_Z < 1.5 \cdot 10^9 .$$

This current changes the equilibrium state and will cause the energy of electrons and consequently the rate of the secondary emission to increase, resulting in the enhancement of the desorbed gas density. The velocity of the flashover front may be roughly estimated as

$$V_F \sim eE_Z / m\nu_m = 10^{25} E_Z / n_D \sim 2 \bullet 10^9 \text{ cm/s},$$

where ν_m (in 1/s) is the collision frequency of hydrogen. The value of this velocity available from the experiments[1] $V_F \sim 10^9$ cm/s is in good agreement with the above one.

Summary

The simple theoretical estimation in the framework of the gaseous model gives the good agreement with the experiment. This clearly demonstrates the validity of the underlying physical model.

References

[1] L.N.Kazanskiy and E.A.Galstjan. Ibid., P1-31.

[2] M.S. Di Capua and D.G.Pellinen. J. Appl. Phys., vol. 50(5), p. 3713, 1979.

[3] B.Noble. Methods based on the Wiener-Hopf technique. Perg.Press., NY., 1958.

[4] A. A. Avdienko and M. D. Malev. *Zhurnal Technicheskoi Fiziki*, vol. 47(8), p. 1697, 1977; vol. 49(5), p. 987, 1979 (in Russian).

[5] A. S. Pillai and R. Hackam. J. Appl. Phys., vol. 53(4), p. 2983, 1992.

[6] F. Hegeler *et al.* IEEE Trans. on PS, vol. 21(2), p. 223, 1993.

Outgassing and Plasma Development in the Early Phase of Dielectric Surface Flashover in Vacuum

G. Masten,*) T. Müller, F. Hegeler, H. Krompholz, L.L. Hatfield, and M. Kristiansen
Departments of Electrical Engineering and Physics, Texas Tech University, Lubbock, TX 79409-3102

Abstract

Surface flashover along dielectric interfaces is the limiting factor in high voltage systems and in particle accelerator technology. The processes leading to flashover are far from being fully understood. With a high sensitivity laser beam deflection method, gradients of gas and plasma densities above the surface are measured, and correlated to high resolution current, x-ray, and luminosity signals, with a temporal resolution of better than 6 ns. Experimental results show a preflashover phase with linearly rising current accompanied by x-ray emission during which no plasma is observed, followed by an exponential current rise associated with the build-up of a plasma channel several micrometers above the surface. Estimates of the electron drift velocity and the current density in the plasma channel point to gaseous ionization processes responsible for the plasma build-up. The results are consistent with the saturated secondary electron emission avalanche model, with electron induced outgassing as the main process causing surface flashover.

I. INTRODUCTION

Surface flashover is a limiting factor in the performance of many accelerator systems and components. It occurs usually at electric field amplitudes much lower than those for bulk breakdown, vacuum breakdown, or gas breakdown. The physical mechanisms involved in flashover are far from being clear, and a variety of different models have been proposed. These models can be broadly categorized as based on "above-surface" [1-4] or "below-surface" [5-8] processes. The standard model [1,2] hypothesizes electron emission from field enhancement sites at the cathode into vacuum, a secondary electron avalanche along the dielectric (which is quickly saturated by surface charge processes), and electron induced gas desorption. The final breakdown occurs in the desorbed gas layer above the surface, according to this model.

Previous experimental results in our test apparatus demonstrate an initial phase of flashover with a duration of 10 to 20 ns, in which the current rises linearly to an amplitude of several amperes, followed in a second phase by an exponential current rise with an *e*-folding time constant on the order of one nanosecond. The first phase is accompanied by soft x-ray emission that ceases at the transition to the second phase. The role of free electrons during this first phase is indicated by the suppression of current, visible luminosity, and x-ray production in the presence of an insulating magnetic field [9].

This work describes the experimental detection of above-surface charge carrier amplification processes utilizing a laser beam deflection sensor [10,11], in conjunction with previously developed fast electrical and luminosity diagnostics.

II. EXPERIMENTAL SETUP

The test apparatus [9,12] has a coaxial geometry that provides for fast electrical diag-

*) Present affiliation: New Mexico Engineering Research Institute, on contract to the Phillips Laboratory, VTP Space Power Laboratory, Kirtland AFB, New Mexico 87117.

nostics with current [9,13] and voltage sensors having subnanosecond resolution. High voltage is supplied to the test sample with a cable discharge, either in self breakdown mode or triggered with an additional spark gap switch. The laser deflection sensor (see Fig. 1) detects gradients in the refractive index above the dielectric surface, time correlated with other signals of interest. It utilizes a focused 10 mW HeNe laser beam (spatial resolution at the sample site 20 μm) incident on a bi-cell solid state photodetector (Silicon Detector Corporation model SD 113-24-21-021) to provide a signal with angular sensitivity ranging from 0.0074 mV/μrad to 1.5 mV/μrad and a rise-time ranging from 0.9 ns to 10 ns, dependent on the amplifier used. To accommodate the divergence of the focused laser beam, cylindrical samples with a diameter of 1.9 cm and a gap width of 4 to 5 mm have been used. To localize the arc channel on the sample circumference, the electrodes were coated with an epoxy, except for a 1.5 mm strip on the face of the electrodes. A Hamamatsu C979 streak camera was used to gather information on luminosity, with a spatial resolution of 25 μm perpendicular to the surface, and 120 μm parallel to the surface.

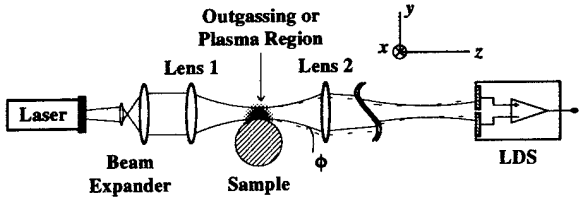


Fig. 1. Measurement geometry of the laser deflection sensor. Beam diameter has been greatly exaggerated for clarity.

III. EXPERIMENTAL RESULTS

Laser deflection sensor measurements were taken in the middle of the test gap for Pyrex, alumina, and Lexan samples at beam center heights of 5 μm, 25 μm, 75 μm, and 175 μm. Typical examples for the acquired waveforms are depicted in Fig. 2. Near the sample surface, the signals begin with the second phase exponential current rise, usually with a downward deflection. Far away from the surface, deflection signals may begin a few nanoseconds after the start of the exponential current rise, with a deflection away from the surface. At intermediate height, bipolar signals are seen. Analysis of the laser deflection measurements is complicated by the unpredictable location of the incipient flashover channel with respect to the laser beam, and there are rather large statistical variations in these waveforms. Approximately three quarters of the signals obtained for alumina and Lexan follow the rough categorization suggested by the waveforms in Fig. 2 for each height. For Pyrex, larger variations are observed.

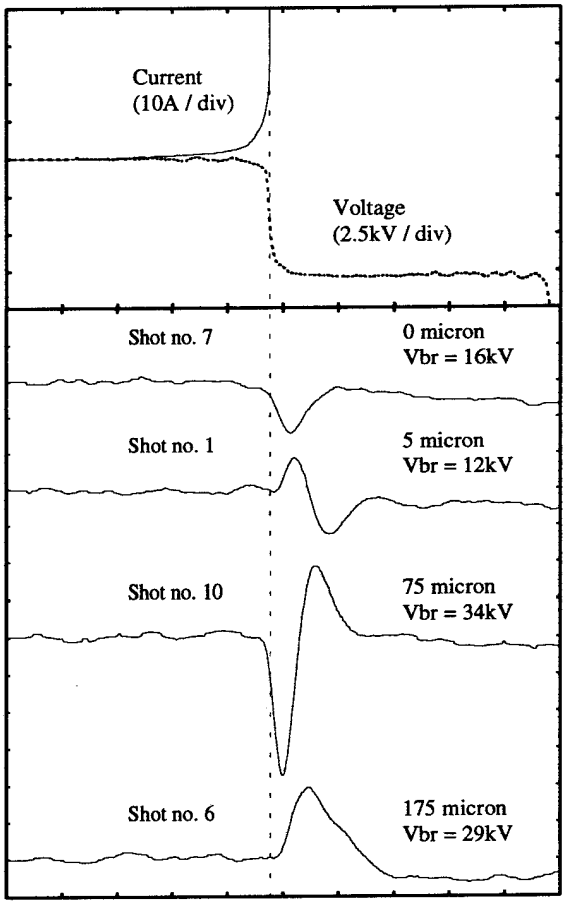


Fig. 2. Example of laser beam deflection signals near the center of the gap at various heights above an alumina sample. Electrode gap is 4 mm. The dotted vertical line indicates the point at which the current begins an exponential rise to its full discharge amplitude. Deflection signals are 5 mV/div at a sensitivity of 180 V/rad. Assuming that the entire beam is deflected, this corresponds to a beam deflection of 28 μrad/div.

Streak camera pictures with the slit parallel to the surface show light emission

starting simultaneously with the onset of the exponential current rise, occurring simultaneously within two nanoseconds over the entire gap width. Fig. 3 shows an example for a streak camera picture with the slit perpendicular to the surface, with the peak intensity approximately 30 μm above the surface, and an FWHM size of 50 μm, which corresponds to two pixels of the Hamamatsu temporal analyzer, that was used. This light emission lasts two nanoseconds (FWHM) and starts at the beginning of the exponential current rise.

IV. DISCUSSION

The laser beam deflection angle ϕ is related to the gradient of the refractive index η, in the small-angle approximation (c.f. Fig. 1 for the coordinates used) by

$$\phi = \frac{1}{\eta}\int \frac{\partial \eta}{\partial y} \cdot dz$$

which can be re-written in terms of the particle number density n, as

$$\phi \cong \int K \cdot \frac{\partial n}{\partial y} \cdot dz$$

where $K = d\eta/dn$ is the specific refractivity. The refractivity of neutrals is positive, and the refractivity of a plasma, primarily due to electrons, is negative. Therefore, the probe beam is expected to deflect away from the densest region of a plasma and toward the densest region of neutral gas, as depicted in Fig. 4. The direction of the deflection at different points in the gap, as well as the rapid change of the signals vs. time, imply that plasma is the primary cause for the deflection. Direct detection of neutral gas has not yet been achieved. For detectable gas densities on the order of 10^{17} cm^{-3}, the ionization frequency for our experimental conditions (E/n > 10^{13} Vcm^2) is on the order of several 10^9 s^{-1}, so that the "lifetime" of neutrals is one order of magnitude smaller than our temporal resolution. Different plasma channel profiles and diameters (from 6 μm to 30 μm) have been used to estimate the electron number density, resulting in the relation

$$\frac{n(t)}{10^{22}\,cm^{-3}} = 0.5\frac{\phi(t)}{rad}$$

which is correct within a factor of two. This relation is valid only for times within 2 - 3 ns of the arc channel ignition, i.e for the beginning of the signals in Fig. 2.

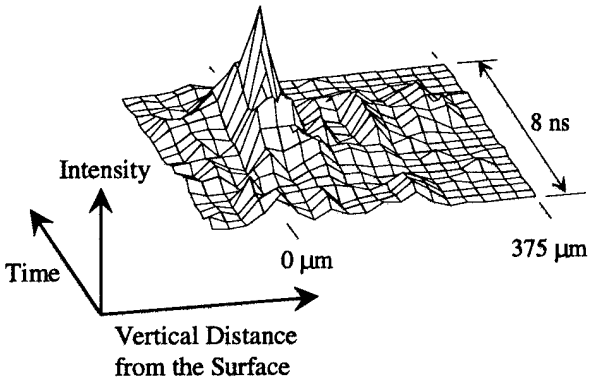


Fig. 3. 3-D representation of a streak camera picture with the slit perpendicular to the surface. The picture was taken close to the anode. The peak occurs approximately 50 μm above the surface, with a duration of 5.4 ns at its base. The full-width-half-maximum dimensions are 50 μm and 2.0 ns.

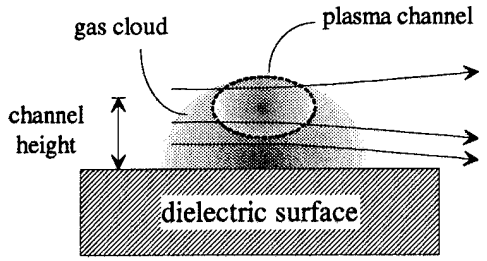


Fig. 4. Conceptualized drawing of possible neutral gas and plasma density profiles, and expected beam deflection directions, at the transition from pre-flashover processes to full breakdown.

The initial electron density generation rate is then on the order of several 10^{25} cm^{-3}s^{-1}. Bipolar signals are interpreted to indicate a shift of the plasma channel with respect to the probe beam within 10 - 20 ns of the arc channel ignition, confirming that the channel diameter is comparable to the probe beam diameter of 20 μm. Additional deflection data have been taken for Pyrex only, showing that the incipient arc channel is attached to the dielectric surface at the cathode, but at a

distance of several 10 μm away from the dielectric surface at the anode.

Streak camera measurements confirm the deflection data, i.e. a channel with a diameter of 25 to 50 μm is observed near the insulator surface during formation of the discharge. The temporal behavior of the light emission corresponds to the power dissipation in the test gap, given by the product of voltage and current. Prior to breakdown, the emission is most intense near the cathode.

V. CONCLUSION

With a high sensitivity laser beam deflection sensor, and with previously developed electrical and passive optical diagnostics methods, the following phenomena are observed during initiation of surface flashover: A first phase is characterized by a linearly increasing current, where free electrons play a major role in the charge transport. A second phase starts with the transition of the linear current increase to an exponential current increase. This phase is associated with the formation of a plasma channel above the surface, presumably due to collisional ionization of electron induced desorbed gas atoms. The results are seen as an experimental confirmation of the "standard model" for dielectric surface flashover.

ACKNOWLEDGMENT

This work was supported by BMDO/T/IS through DNA/RAST. G. Masten and F. Hegeler were sponsored in part by a grant from IEEE-DEIS. T. Müller was sponsored by the Deutsche Forschungsgemeinschaft.

REFERENCES

[1] V. H. Boersch, H. Hamisch, and W. Ehrlich, "Oberflächenentladungen über Isolatoren im Vakuum," Zeitschrift für angewandte Physik. vol. 15, no. 6, pp. 518-525, 1963 (in German).

[2] R. A. Anderson and J. P. Brainard, "Mechanism of pulsed surface flashover involving electron-stimulated desorption," J. Appl. Phys. vol. 51, pp. 1414-1421, March 1980.

[3] S. P. Bugaev, A. M. Iskoldskii, and G. A. Mesyats, "Investigation of the pulsed breakdown mechanism at the surface of a dielectric in vacuum. I. Uniform Field," Soviet Physics – Technical Physics, vol. 12, no. 10, pp. 1358-1362, April 1968.

[4] J. D. Cross, "High speed photography of surface flashover in vacuum," IEEE Trans. Electrical Insulation, vol. EI-13, pp. 145-148, June 1978.

[5] J. P. Vigouroux, C. Le Gressus, and J. P. Duraud, "Electrical Surface Breakdown: Secondary Electron Emission and Electron Spectroscopy of Insulators," Scanning Electron Microscopy II, pp. 513-520, 1985.

[6] N. C. Jaitly and T. S. Sudarshan, "DC Surface Flashover Mechanism Along Solids in Vacuum Based on a Collision-Ionization Model," J. Appl. Phys., vol. 64, no. 7, pp. 3411-3418, October 1988.

[7] C. LeGressus *et al.*, "Flashover in wide bandgap high purity insulators: Methodology and mechanisms," J. Appl. Phys., vol. 69, no. 7, pp. 6325-6333, May 1991.

[8] R. G. Bommakanti and T. S. Sudarshan, "Time resolved prebreakdown X-Ray emission from polycrystalline alumina-bridged vacuum gaps for impulse stresses," J. Appl. Phys., vol. 71, pp. 2181-2188, March 1992.

[9] F. Hegeler, G. Masten, H. Krompholz, and L. L. Hatfield, "Current, Luminosity, and X-Ray Emission in the Early Phase of Dielectric Surface Flashover in Vacuum," IEEE Trans. on Plasma Science, Vol. 21, No. 2, April 1993, pp. 223-227.

[10] E. W. Gray, "Vacuum surface flashover: A high pressure phenomenon," J. Appl. Phys., vol. 58, no. 1, pp. 132-141, July 1985.

[11] C. L. Enloe, R. M. Gilgenbach, and J. S. Meachum, "Fast, Sensitive Laser Deflection System Suitable for Transient Plasma Analysis," Rev. Sci. Instrum., vol. 58, no. 9, pp. 1597-1600, September 1987.

[12] G. Masten, T. Mueller, F. Hegeler, H. Krompolz, and L. L. Hatfield, "Real-Time Detection of Outgassing and Plasma Buildup During the Early Phase of Dielectric Surface Flashover," 9th IEEE International Pulsed Power Conf., Albuquerque, NM, June 21-23, 1993.

[13] H. Krompholz, J. Doggett, K. Schoenbach, J. Gahl, C. Harjes, G. Schaefer, and M. Kristiansen, "Nanosecond Current Probe for High-Voltage Experiments," Rev. Sci. Instrum.,vol. 55, no. 1, pp. 127-128, January 1984.

CONTROL OF A LARGE VACUUM WAVE PRECURSOR ON THE SABRE VOLTAGE ADDER MITL AND EXTRACTION ION DIODE *

M.E. Cuneo, D.L. Hanson, J.W. Poukey, P.R. Menge,
M.E. Savage, J.R. Smith[a], and M.A. Bernard[b]
Sandia National Laboratories
P.O. Box 5800, Albuquerque, NM, 87185-1186

Abstract

SABRE is a ten-cavity magnetically insulated voltage adder (6 MV, 300 kA) used to study ion beam production in high voltage extraction applied-B ion diodes. Observations indicate that the machine power initially propagates in a large-amplitude vacuum wave prior to electron emission. This vacuum wave "precursor" has an important impact on the turn-on and impedance history of ion diodes. Typical precursor characteristics are shown using transmission line, diode, and beam current and voltage data and are compared to TWOQUICK PIC-code simulations. Two techniques are under investigation to control the precursor and its effects on diode performance. A plasma opening switch (POS) has been used to erode the precursor. Field enhancing inserts are also planned to decrease the macroscopic fields required for electron emission from the cathode. This will limit the distance over which vacuum and insulated waves separate due to propagation at different velocities. Experimental data from the POS technique and TWOQUICK simulations of the insert technique are presented and discussed.

Introduction

SABRE is a ten-cavity magnetically insulated voltage adder operated in positive polarity (6 MV, 300 kA) [1] to study ion beam production in high voltage extraction applied-B ion diodes [2,3]. Observations indicate that power propagates along the coaxial output transmission line as a large vacuum wave prior to electron emission [1]. The vacuum wave is identified as the region where transmission line anode and cathode currents are equal indicating no electron emission. After the electron emission threshold is reached locally, power propagates in a magnetically insulated wave. The faster vacuum wave "precursor" ($\beta=v/c=1$) and slower magnetically insulated wave ($\beta\leq 0.8$) separate as they propagate to the diode over the 9.7 m machine length. In the worst case this can result in two separate pulses at the extraction diode.

The precursor initiates diode plasma formation and dominates the first 20-30 ns of the impedance history since the precursor voltage is large enough to cause electron emission from both the cathode feed and cathode tips [2]. The elimination of this precursor is considered a prerequisite for the development of active ion sources. Precursor elimination is also desired to stop premature formation of electrode plasmas to impede gap closure, and to delay neutral production leading to charge exchange production of fast neutrals. Precursor elimination may give a higher rate of rise of the beam power. Application of this magnetically insulated inductive adder technology to ion beam fusion will require elimination of the precursor, since the proposed systems have very long magnetically insulated transmission line (MITL) delivery systems resulting in two electrical pulses at the diode.

*This research was supported by the U. S. Dept. of Energy under contract no. DE-AC04-94AL85000.
[a]Titan/Advanced Innovative Technologies, [b]K-Tech

Precursor Characteristics

Fig. 1 shows that the precursor dominates the first 20-25 ns of the diode voltage and current. Fig. 1 gives the diode voltage VDIODE, a composite of the inductively-corrected MITL voltage from a magnetic spectrometer and diode voltage from a range-filtered Faraday cup array, upstream MITL cathode current IMCAT from shunts, diode cathode current IDCAT from B-dots, and ion beam currents IIBDOT and IIFCUP from B-dots and scaled Faraday cups respectively. The precursor drives a low enhancement (≈ Child-Langmuir) ion beam at the diode because the sheath electrons are overinsulated during the precursor (Vcrit/V ≈ 2.5) and the high vacuum wave impedance (about 100 Ω in Fig. 1) restricts diamagnetic sheath compression [4]. The line labeled VCL in Fig. 1 represents a Child-Langmuir (CL) scaling of IIFCUP to voltage, agreeing well with the measured precursor voltage. We also observe that the precursor current depends on diode impedance which is a function of diode geometry, ion species, and magnetic field profile and strength.

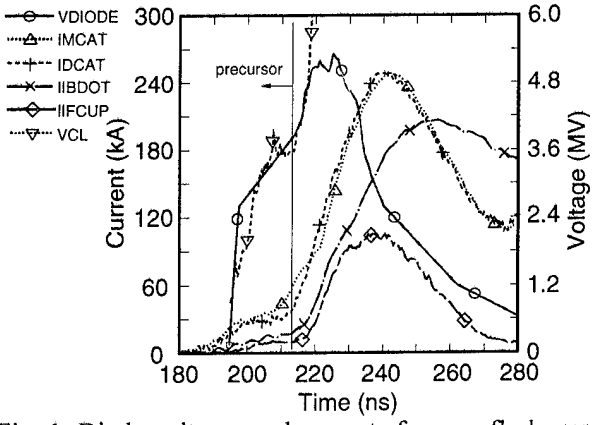


Fig. 1. Diode voltages and currents for wax flashover with precursor (extended cathode tip diode [3]).

The SABRE inductive adder consists of two sets of five cavities, each cavity charged to a nominal 850 kV. Each set of five cavities is charged through a single electrically triggered gas switch. Firing of the downstream set is delayed to compensate for wave transit time between the two cavity sets. Different output voltage waveshapes are observed depending on this delay interval.

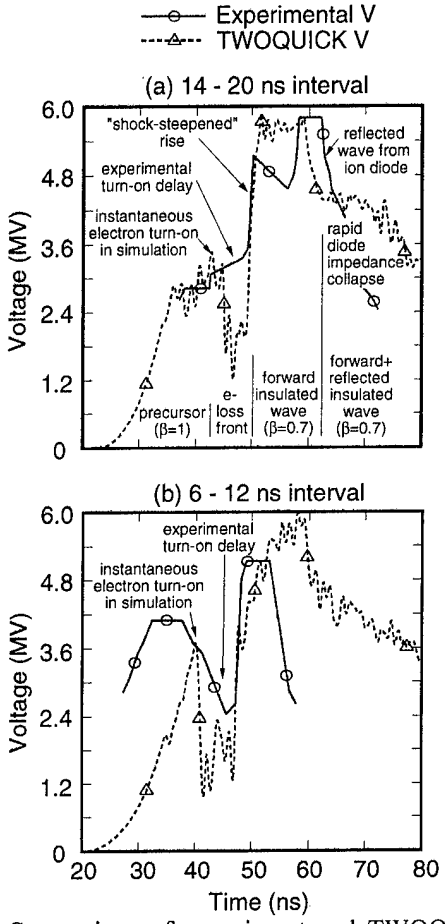


Fig. 2. Comparison of experiment and TWOQUICK simulations for different switching intervals.

Fig. 2 compares time-resolved MITL voltages measured 1 m from the diode with TWOQUICK PIC-code simulations [5] for two different switching intervals. The MITL electron emission threshold electric field was 300 kV/cm for these simulations. The data is obtained using a magnetic spectrometer to measure the energy and arrival times of protons accelerated across the MITL gap, with a correction for the particle transit time. Fig. 2a compares data and simulation with a 14 ns switching interval. The data features are typical of switching intervals in the 14-20 ns range. Fig. 2b compares data with an interval of 8 ns to a simulation for a 0 ns interval. The data features are typical of intervals of 6-12

ns. Significant features of the data and simulation are labeled on the figure. We make the following observations:

(1) Switch intervals of 14-20 ns optimally add the insulated waves from the two sets of cavities for wave velocities of β=0.6 to 0.8. The result is a precursor blended into the insulated pulse (Fig. 2a). Switch intervals of 6-12 ns add the vacuum waves from the two sets, giving a lower amplitude insulated pulse and a well separated precursor of larger amplitude (Fig. 2b). MITL, diode, and ion beam currents and Faraday cups also show these waveshape differences

(2) The separation of precursor and insulated wave is larger than can be accounted for strictly on the basis of propagation times. Erosion of the electron loss front, and shock steepening of the insulated wavefront as the velocity increases with wave voltage both contribute to the larger separation.

(3) The simulations show a greater separation between precursor and insulated wave in contrast to experiments. Electron turn-on in the idealized simulation is instantaneous once the threshold is exceeded. A 5-10 ns sheath development period can account for the smoother transition between the measured precursor and insulated wave.

(4) The simulations do not show as clear a difference for various switching intervals in separation and amplitude of precursor and insulated wave as do the experiment, although shorter intervals do give a larger separation. Differences can be explained by use of a simulation cavity input voltage that is about 15-20 ns too wide and by the instantaneous sheath turn-on in the simulation.

(5) The simulations show that the peak precursor voltage varies with threshold field. The measured amplitude of the precursor is consistent with threshold fields of 200-300 kV/cm.

The precursor is a prominent aspect of the SABRE data in amplitude and timing for several reasons:

(1) The MITL gaps and therefore impedances ($\approx$ 9 cm and 40 Ω at output) are large and hence the electric field threshold for electron emission (200 to 300 kV/cm) is not reached until 40-60% of the maximum voltage is present. The emission voltage is related to the emission threshold field by:

$$V_{emission} = E_{threshold} r_c \ln(r_c/r_a),$$

where r_c and r_a are the radii of the cathode and anode. The peak amplitude of the precursor in Fig. 2 agrees with this analytical estimate. The scaling of this formula with r_c implies that positive polarity operation will have a larger precursor in comparison with negative polarity.

(2) The rapidly falling forward wave and diode impedance further reduces the ratio of insulated pulse voltage to precursor voltage.

(3) SABRE is long (9.7 m) allowing ample distance for precursor and insulated wave to separate and the voltage of the insulated wave gives a slower propagation velocity compared to β=1. Note that positive polarity lowers the voltage compared to negative polarity [1], slowing the insulated wave by comparison.

(4) Wave addition effects from different gas switch timings, erosion of the electron loss front and shock steepening of the insulated wavefront all contribute to a larger separation of precursor and insulated wave.

Precursor Elimination

Two techniques are under investigation to control the precursor and its effects on ion diode operation. A plasma opening switch (POS) located 20 cm upstream of the diode has been used to erode the precursor by filling the MITL gap with plasma. Field enhancing inserts are planned for the transmission line cathode to decrease the macroscopic fields required for electron emission. These inserts will be located in the 4.2-m long coaxial extension transmission line downstream of the voltage adder region.

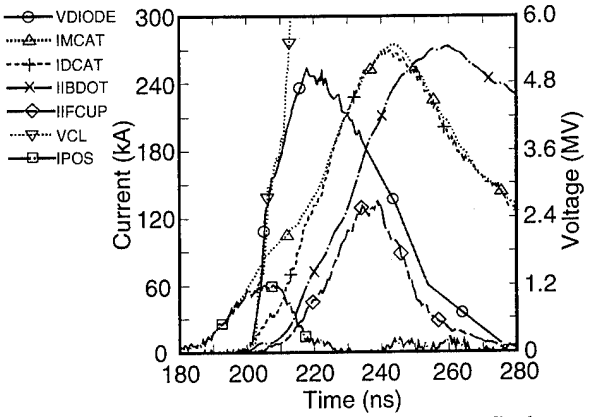


Fig. 3. Diode voltages and currents for wax flashover with optimal POS precursor erosion (extended cathode tip diode [3]).

Fig. 3 shows diode voltage and currents for a wax flashover source with optimal precursor erosion ($\approx$ 1.3 mCoul) by POS. The waveforms in Fig. 3 can be compared directly to those in Fig. 1 with a full precursor. The additional signal IPOS is the POS current, the

difference between IMCAT and IDCAT. A detailed comparison between Fig. 1 and Fig. 3 shows:

(1) Elimination of the precursor allows the ion current to quickly exceed the CL level (10 ns vs. 25 ns).
(2) The increase of peak cathode current from 240 to 270 kA and peak ion beam current from 94 to 131 kA is due to undermatching of the POS/diode system to the MITL [1].
(3) The peak ion power is essentially the same (≈ 0.5 TW) but the voltage at peak ion power is decreased from 4.6 to 3.8 MV.

We also note that the POS appears to be able to simultaneously provide the necessary charge (A-s) for erosion of the precursor while also providing an appropriate range of timing and action (A^2-sec) for ohmically vaporizing a metal film as an active plasma source, with the film thickness as the adjustable parameter.

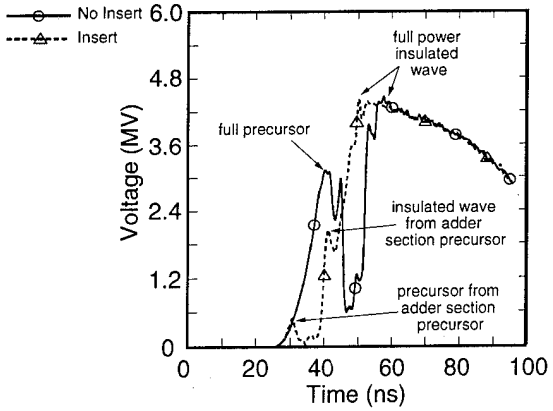


Fig. 4. Comparison of TWOQUICK diode voltage with and without cathode inserts in extension MITL.

Fig. 4 shows TWOQUICK simulated diode voltage behavior where a 300 kV/cm emission threshold in the entire machine (No Insert) is compared with the case of 300 kV/cm in the adder and 30 kV/cm cathode insert in the extension MITL (Insert). Note that the insert starts formation of the insulated wave earlier in the forward wave and limits the distance over which the vacuum and insulated waves can separate by propagation at different velocities. There is still a small vacuum wave of about 500 kV launched before electron sheath turn-on in the extension MITL. This could be eliminated with a either a low-level POS or a dielectric flashover insert on the anode if it appears to adversely affect diode performance.

Other precursor mitigation/elimination techniques are also possible. Increasing the cavity voltage on SABRE to 1 MV would result in a faster insulated wave and a less prominent precursor at the diode. SABRE could be made into a vacuum wave adder with no electron flow if the threshold for electron emission could be increased by about a factor of two to 400-600 kV/cm by surface coating or treatment of the MITL cathode.

Summary

A high impedance vacuum wave precursor has been observed on the SABRE MITL, diode, and beam current and voltage data. Its presence and characteristics are well understood. The TWOQUICK simulations show that the data are qualitatively consistent with a 200-300 kV/cm turn-on threshold and a 5-10 ns development period of the electron sheath. The precursor drives a 20-30 ns long Child-Langmuir level ion beam at the diode. A low-level POS effectively erodes the precursor. TWOQUICK simulations show the promise of field enhancing inserts for precursor modification. This concept will be tested in future experiments.

The authors acknowledge useful discussions with Ian Smith and Cliff Mendel and excellent experimental support from G. Ziska and the SABRE operations team.

References

[1] M.E. Cuneo, et al., "Observation of Reflected Waves ...," 9th Inter. IEEE Pulsed Power Conf., 1993.
[2] D.L. Hanson, et al., Proc. BEAMS92, NTIS PB92-206068, Vol. II, p. 781.
[3] D.L. Hanson, et al., "Improved Field Geometries for SABRE ...," these proceedings.
[4] M.E. Cuneo, et al., "Operation of Passive ...," 20th IEEE Inter. Conf. on Plasma Science, 1993.
[5] J.W. Poukey, et al., "Recent TWOQUICK Particle Simulations...," these proceedings.

ACCELERATING VOLTAGE INCREASE IN HIGH-POWER ACCELERATOR

L.N.Kazanskiy, I.L.Korenev, A.A.Oreshin
Moscow Radio Technical Institute
132, Varshavskoye shosse
Moscow, 113519, Russia

Abstract

At the MRTI power high-current accelerator ZET accelerating voltage has been increased up to 3 MV relatively to initial value of 1.5 - 2.0 MV. The design modifications made were minimized. The high-voltage oil transmission line connecting the Marx generator with magneto insulated diode is used now as a forming line commutated by sharpening SF_6-discharger. The main problem was to charge the 50-Ohm line rapidly up to 4.0 - 4.5 MV keeping the Marx generator voltage at less than 2.5 MV. The rapid charge was realized due to careful choice both inductance between the Marx generator and the forming line and auxiliary resistor loading Marx generator. The relativistic electron beam (2.5 - 3.0 MeV, 20 -30 kA, 90 ns pulse and 15 ns front duration) was produced in result. The physical experiments with the beam were carried out.

Introduction

The high-current electron accelerator ZET was constructed to obtain the microsecond beam pulses at operating voltage of 1.5 - 2.0 MV. The similar device was described in paper [1]. The best data of accelerated beam - 2.3 MeV, 50 kA, 1500 ns - were achieved in a number of pulses. A number of improvements have been carried out during last years: the beam front duration reduced down to 10 ns and the two-channel configuration was realized [2].

The accelerator is in use for researches in field of power relativistic microwave engineering mainly. The radiation pulses of power level of 1.5 - 2.0 GW in X-band with duration of 50 - 60 ns were obtained at the relativistic electron beam (REB) parameters of energy from 1.5 MeV to 2.0 MeV and current from 10 kA to 15 kA.

Recently the work has been performed to increase the accelerating voltage of one channel up to 3.0 - 3.5 MV at the beam current of 15 - 20 kA. These parameters of REB allow making investigations of the further increasing of the microwave radiation power. In addition, the possibility will appear for production of REB of usual characteristics at the lowered charge voltage in Marx generator and, thereby, for extension of the life time of the Marx generator capacitors.

Modification of accelerator.

The 50 Ohm coaxial oil transmission line connects the Marx generator with the magneto insulated electron diode. The line length is 9 m, diameters of electrodes are of 35 cm and 120 cm. The sharpening SF_6-discharger described in paper [2] is included at the line output.

Maximum duration of the microwave radiation pulse is defined by physical phenomena of the microwave generation. It is less than 50 - 60 ns for our device and, thereby, the REB pulse duration of 100 ns

would be sufficient. So the possible decision is using the transmission line as a pulse forming line (PFL - 90 ns, 50 Ohm) commutated by the sharpening SF_6-discharger. To obtain the accelerating voltage in the mentioned above electron diode U_d up to 3.0 - 3.5 MV it is sufficient to charge the line up to voltage U_L = 4.0 - 4.5 MV. This is a result of well known equation:

$$U_d = U_L Z_d/(Z_L + Z_d)$$

wherein Z_d= 150- 200 Ohm is the diode impedance, Z_L = 50 Ohm - the PFL impedance. The mismatch of line and diode does not influence on generation of the microwave radiation which is finished during the first wave of the accelerating voltage pulse: $t = 2\sqrt{\varepsilon}l/c$ = 90 ns, l = 9 m - the line length, ε = 2.2 is the oil permitivity, c- velocity of light. The important problem was keeping the voltage at the output of Marx generator and along its column less than 2.5 - 2.6 MV. This value is the limit voltage for high voltage breakdown. Another problem was keeping the duration of the PFL charge less than 400 - 500 ns (according to the operation conditions of SF_6-discharger). To achieve these goals the careful search of the electrical circuit elements accompanied by a great deal of computational researches was made.

Electrical circuit and simulations

To charge PFL up to voltage exceeding the output voltage of Marx generator the load resistor R_1 was included before the charge inductance L_1 connecting Marx generator and PFL. The electrical circuit diagram is shown in fig.1a. We succeed in obtaining of the necessary difference between PFL and Marx generator voltages which are more than 1.5 MV for the charge time mentioned above only due to resistor R_1.

The optimum values of R_1 and L_1 for maximum ratio U_L/U_d during the minimum possible time of the PFL charging were found by numerical simulation of the voltages and currents on time for circuit shown in fig.1b. For calculation PFL was simulated by series of identical elementary LC-circuits. The number of LC-circuits n = 10 turned out sufficient for careful simulation. The optimum values R_1 = 190 - 200 Ohm and L_1 = 18 - 24μH were found. In particular R_1 = 200 Ohm and L_1 = 22μH were chosen. The curves calculated for the Marx generator voltage U_M, PFL voltage U_L and U_I - voltage of the charge inductance - are shown in fig.2. The ratio U_L/U_d equals to 1.55 for the charge time of 450 ns. The observed oscillograms coincide with calculated curves of voltages with accuracy of 5% .

Experiments and operation.

The load resistor R_1 is made from the polyethylene pipe (diameter 11 cm, length 90 cm) filled with the water solution of $CuSO_4$. Butt-ends of the pipe are of stainless steel. The shock energy capacity of resistor is 0.5 MJ at heating $15^0C/pulse$. The charge inductance (16 spires, diameter 16.5 cm, length 26 cm) is made from steel rod (diameter 0.8 cm), that was thermally treated and galvanically covered with copper.

The tests were conducted at the PFL voltage up to 4.3 MV (Z_L = 170 Ohm, series connected damping resistor R_d = 20 Ohm). The electron beam current of 18 kA with the particle energy of 3.1 MeV was obtained (the hollow beam diameter equals to 3.8 cm , focusing longitudinal magnetic field is of 2.3 T). The typical oscillograms are shown in fig.3. The increasing of diode impedance will allow to raise the particle energy up to 3.5 MeV.

Our microwave generators (2 MeV, 10 -12 kA) operate at the Marx generator voltage (voltage of the cascade charging) equals to 50 - 55 kV instead of voltage equals to 70 - 75 kV, which was necessary before. During 350 - 400 ns the charging of PFL was made up

to voltage less than maximum one to facilitate the SF_6 -discharger operation.

In many experiments on the shock-wave generation and on sharpening of the electron beam front in the magnetically insulated transmission lines (MITL) the charge voltage of PFL was from 3.5 MV to 4.0 MV. The input voltage of MITL about 1.5 MV was obtained, when the MITL impedance was about 35 Ohm and damping resistor was of 20 Ohm siriesly included.

The accelerator has been operating successfully, as descried above, during 18 months. About two thousands pulses was produced in total.

Conclusion

Now the design of the new large-scale high current accelerators is not expediently in any country. Probably, it is a good idea to modify existing and operating devices keeping in mind their surplus energy capacity. The work described in this report is the example of such modification.

References

1..N.Bystrinov, S.P.Bugaev, M.I.Vorobyushko et. al. The high current electron accelerator GAMMA. Prib. Tech. Exper. (Russian), 1983, n 2, p.p.36-41.

2. G.I.Batskikh, L.N.Kazanskiy, A.A.Oreshin. Super power accelerator for microwave electronics. The 9-th International Conference on High-Power Particle Beams. Washington, 1992, v.1, p.p.449-454.

3. E.B.Abubakirov, V.I.Belashov, N.I.Zaitsev et.al. High power single-mode Cherenkov generator. The 8-th International Conference on High-Power Particle Beams. Novosibirsk, 1990, v.2, p.p. 1155-1160.

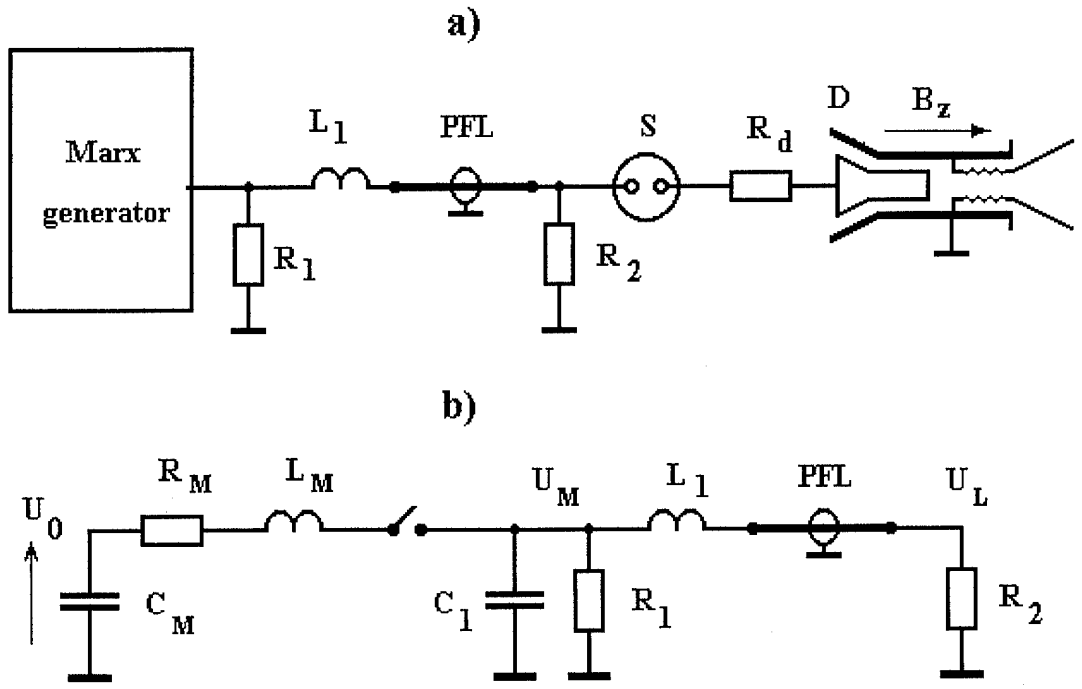


Fig.1. The electrical circuit diagram of accelerator (a) and equivalent circuit diagram of the pulse forming line charging (b). C_M= 80 nF, R_M= 100 Ohm, L_M = 8 μH - parameters of the Marx generator discharge circuit, C_1 = 0.6 nF - capacity of the Marx generator output electrode, PFL - pulse forming line (50 Ohm, 2.5 nF, 9 meters, 90 ns), R_2 = 3000Ohm, R_d = 20 Ohm, U_0 - the shock voltage of Marx generator.

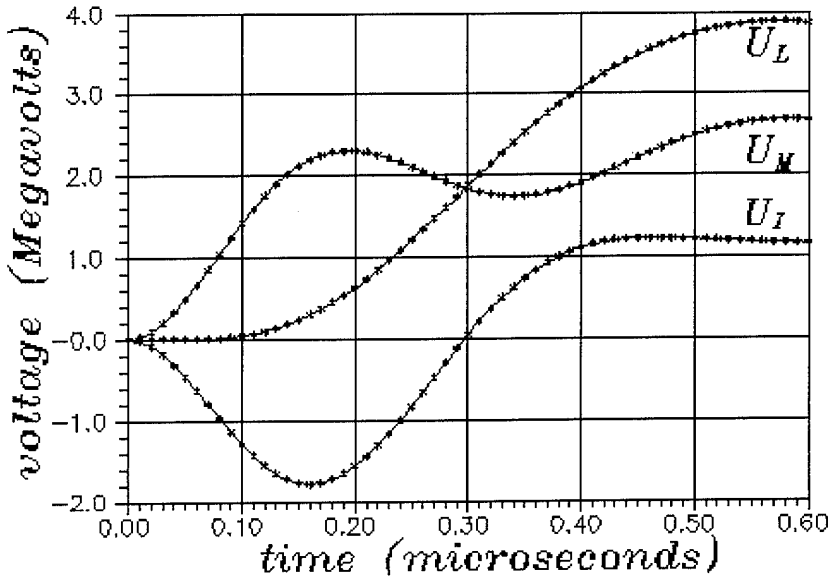


Fig.2. Calculated voltages of Marx generator U_M , pulse forming line U_L and charging inductance $U_I = U_L - U_M$ via time.

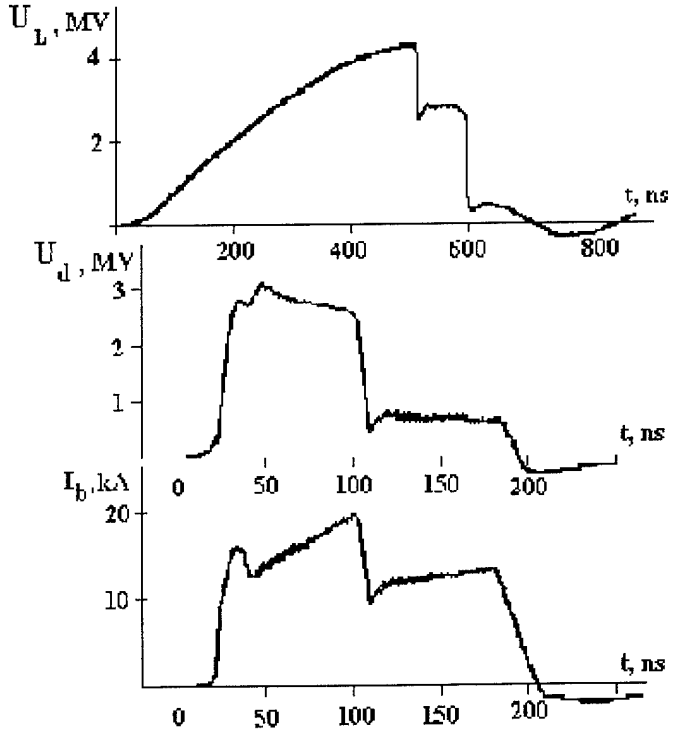


Fig.3. Oscillograms of voltages of pulse forming line U_L, diode U_d and beam current I_b. The charging voltage of Marx generator equals to 65 kV, magnetic field in diode - 2.1 T.

PBFA-II Modification for High-Power High-Convergence Implosion Experiments*

M. G. Mazarakis, D. L. Smith, L. Bennett, J. W. Poukey,
R. E. Olson, T. R. Lockner, and J. J. Ramirez
Sandia National Laboratories
Albuquerque, NM 87185-1193

Abstract

A linear inductive voltage adder design for PBFA II is presented that could permit high convergence radiatively-driven implosion experiments with two ring-shaped two-stage extraction diodes. The design incorporates two linear inductive voltage adder modules with ferromagnetically-loaded cavities, one for the upper half and another for the lower half of PBFA II, and can be positioned vertically or horizontally in a head-to-head linear configuration with the diodes at the center. The design provides a total of ~ 20-MV and 100-TW electrical power delivered to the diodes. If diode, ion, and transport efficiencies are taken into account, the design is capable of depositing 55 TW to a 6-mm diameter target, which corresponds to a specific peak power density of 50 TW/cm^2.

Introduction

Figure 1 is a drawing of the PBFA-II[1] accelerator's present configuration. The entire device is contained in two concentric tanks. The outer is the oil tank which includes thirty-six 370-kJ Marx generators as its prime power source. The inner tank is filled with deionized water and contains the pulse compression and transmission network which provide the pulse power to the vacuum insulator. The vacuum insulator contains the voltage adder, plasma opening switches, and ion diode.

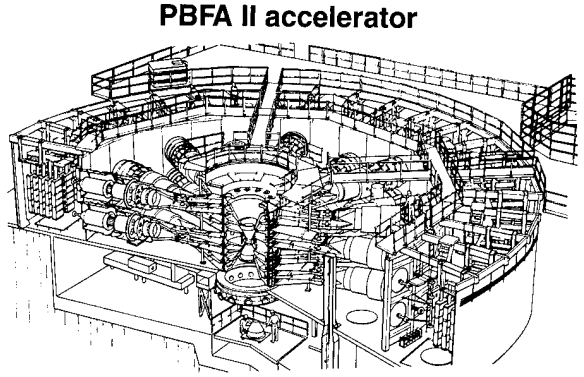


Fig. 1 PBFA II accelerator, present configuration

Each of the 36 Marxes pulse charges a cylindrical intermediate storage capacitor which is connected to three successive coaxial pulse forming lines through a laser triggered gas switch. The cascading pulse forming lines are switched to each other with self-breaking water switches (Fig. 2), compressing the pulse to ~ 50 ns FWHM (full width half maximum) at 2.2 ohms.

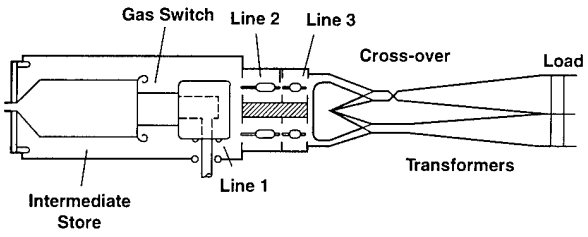


Fig. 2 PBFA II pulse forming line

This enclosed coaxial geometry is then opened to a triplate (Fig. 2). One side of the triplate is convoluted (the upper one in Fig. 2) to invert the electric field before being connected to two of the ten vacuum boundary levels. The spacing of the strip lines is gradually increased between the convolute and the vacuum tube to increase the voltage by 2.8. We believe this region is responsible for

*This research was supported by the U. S. Department of Energy under contract DE-AC04-94AL85000.

most of the observed energy losses since much of the unrecoupable energy is stored in water outside the open triplate lines. This is well documented in Ref. 2.

There are in total 72 radially converging strip transmission lines. Groups of nine are connected in parallel across each level, driving each stage with 1.1 ohms for a total impedance of half of the insulating stack of 4.4 ohms. The upper and lower halves of the stack are connected in parallel, yielding a total impedance of the water section up to the vacuum interface of 2.2 ohms. There is a significant impedance mismatch at the vacuum interface, from 1.1 ohms at each level in the water to 20 ohms for each conical voltage adder. This mismatch induces reflections which further increases the energy loss. The final energy loss is from electrons emitted in the four voltage adding gaps (feeds) which find their way to the ion diode. The cathode electrode of each feed emits electrons which are magnetically trapped and drift in the direction of power flow as sheath current. The sheath electrons are injected into the common radial gap of the voltage adder and most are eventually lost to the anode. Most of these losses in the vacuum section could have been alleviated if the plasma opening switches (POS) were being used. Without POS the large impedance of the voltage adder necessary for their efficient operation becomes a liability.

Proposed Modifications

The modifications proposed in this paper are intended to replace all the lossy sections mentioned above using a fully enclosed coaxial pulsed power system. The system would also replace the present radial focusing diode with two two-stage extraction ring shaped diodes. The two-ring illumination of a hohlraum target constitutes a substantial improvement in illumination symmetry over a radial focusing (barrel) diode. The design incorporates two linear inductive voltage adder modules with ferromagnetically-loaded cavities, one for the upper half and another for the lower half of PBFA II. Each of the 36 coaxial 2.2-ohm transmission lines is split into four 8.8-ohm lines which drive an oil-filled symmetrization manifold surrounding each inductively isolated cavity (Fig 3). There is one manifold for each set of four cavities. As building blocks for the voltage adders, we are utilizing 3-MV cavities similar to those we have designed for the LMF accelerator.[3] Assuming fully charged Marxes to 95 kV, SCREAMER[4] calculations predict each cavity will supply a 3.2-MV, 50-ns FWHM voltage pulse to the accelerating gap. We have analyzed two design options: one with eight cavities per module (Fig. 3), fed by nine 8.8-ohm transmission lines, and a second one with 12 cavities per module (Fig. 4) fed by six 8.8-ohm lines. The second design is more efficient and provides a total of ~ 20-MeV kinetic energy to the lithium ions with 100-TW electrical power delivered to the diodes (Fig. 5). Taking diode, ion, and transport efficiencies into account, this system is capable of depositing 55 TW onto a 6-mm diameter target, which corresponds to a specific peak power density of 50 TW/cm^2. This modification eliminates PBFA's open convolute voltage transformers and extends the closed coaxial configuration from the pulse forming lines all the way to the ion diodes.

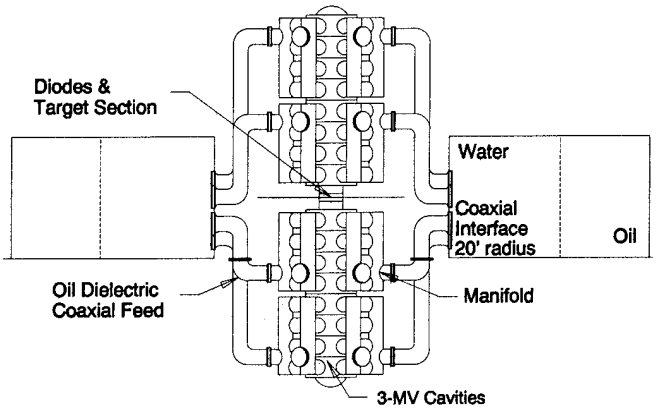


Fig. 3 PBFA-II proposed inductive voltage adder modification (Option A)

Each inductive module has two voltage adders to drive each stage of the two-stage extraction diode. The voltage of the first stage and the current of both stages are dictated by the target requirements and diode design. The optimum voltage for the first stage is ~ 10 MV. In option A the first and second stage

voltage adders are identical and provide 9.2-MV, 2.5-MA to the diode (Fig. 4). In option B the first stage voltage is 8.7 MV and the second stage 12 MV. The usable current, e.g., the boundary current, is again 2.5 MA.

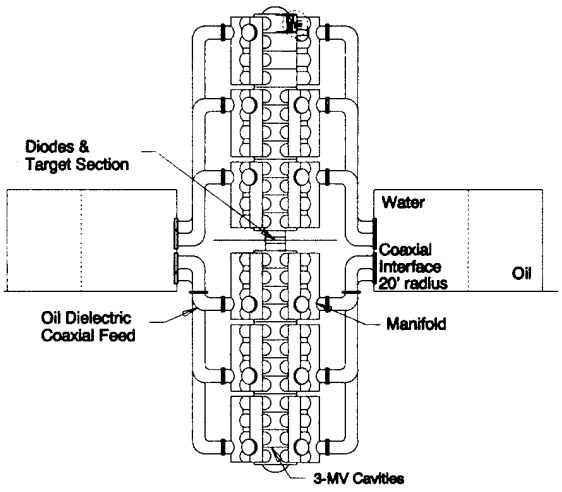


Fig. 4 PBFA-II proposed inductive voltage adder modification (Option B)

Accelerating Module Design

The voltage adders were designed utilizing Creedon's[5] parapotential flow and Cliff Mendel's[6] pressure balance theories. Both formalisms agree in predicting the minimum and boundary currents for negative polarity voltage adders. The electron flow in a positive polarity adder is more complex, and there is not yet an analytical theory describing the flow to provide mathematical MITL design expressions. Experiments on the HERMES III[7] and SABRE[8] accelerators along with numerical simulations have demonstrated that a positive polarity voltage adder will operate at lower impedance than negative. The design options presented here are not as yet validated with numerical simulations. Most HERMES III simulations in negative and positive polarity[9] suggest that a 10-15% power loss should be anticipated going from undermatching in negative to positive polarity. This is reflected in the diode parameters of Fig. 5.

The voltage addition and transmission to the diode uses a triaxial MITL similar to the LMF[3] design. Actually the peak power delivered to the diode by each of the PBFA-II modules (~ 50 TW) would be equal to the power delivered by one LMF module B (~ 50 TW). Hence, a modified PBFA II could be utilized as a test bed for the LMF accelerator.

The accelerating module of option A has eight cavities grouped into two sets of four—one set for each stage. The modules of option B have 12 cavities: five for the first stage and seven for the second. Both options utilize 3-MV cavities. A triaxial adder system is designed for each module (Fig. 5) to provide the two separate voltage pulses to the diode. The voltage addition occurs in two magnetic insulated transmission lines (MITLs) nested one inside the other. The center hollow cylinder (anode) of the second MITL also serves as the outer cathode electrode for the extension of the first voltage adder MITL.

The number of cavities per voltage adder is such to provide a final operating MITL impedance larger than the impedance of the ion diode. Undermatching the diode load reduces the sheath electron current in the MITL and provides for more efficient pulse power coupling. The power coupling efficiency for this design depends on the final voltage of each adder, typically 65% to 75%.

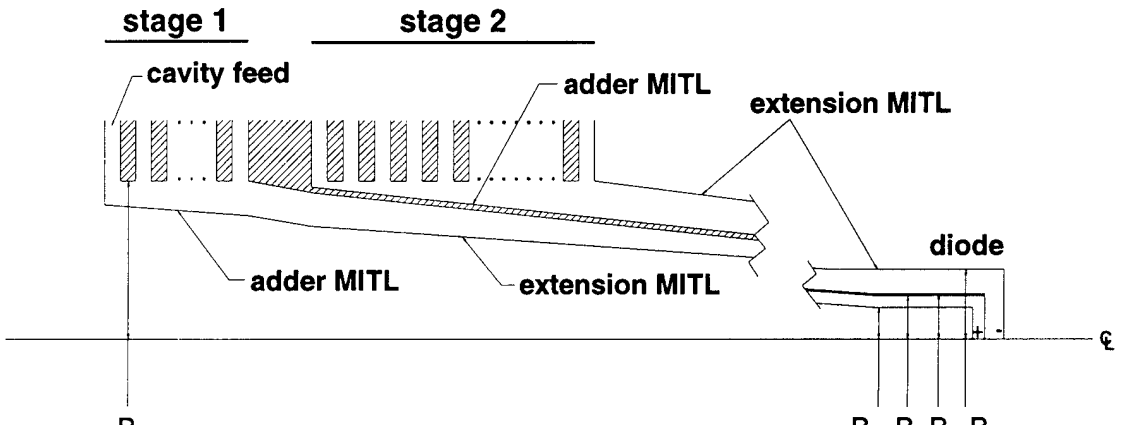
Conclusion

The proposed design is a potential modification of PBFA II to provide increased power and improved symmetry. It eliminates the open convolute voltage transformers of the old design and extends the coaxial configuration from the pulse-forming lines to the inductive cavities.

The original PBFA-II design relied on plasma opening switches (POS) to provide power and voltage gain to 100 TW and 30 MV in a single-stage radial focusing diode. Present PBFA-II typical operation provides 20 TW at 10 MV (at 3/4 energy). The new conceptual design presented here does not utilize POS and aims at driving two 2-stage extraction diodes each with 9-MV first stage and 9- to 12-MV second stage with a total electrical power of 90-100 TW.

References

1. B. N. Turman, et al., "PBFA II, A 100-TW Pulsed Power Driver for the Inertial Confinement Fusion Program," *Proc. 5th IEEE Pulsed Power Conference*, Arlington, VA, June 10-12, 1985, pp. 155-161, IEEE #85CH2121-2.
2. T. H. Martin, et al., "PBFA II, The Pulsed Power Characterization Phase," *Proc. 6th IEEE Pulsed Power Conference*, Arlington, VA, June 29-July 1, 1987, pp. 225-232, IEEE #87CH2522-1.
3. M. G. Mazarakis, et al., "The Light Ion Pulsed Power Induction Accelerator for the Laboratory Microfusion Facility (LMF)," *Proc. 1993 IEEE Particle Accelerator Conference*, Washington, DC, May 17-20, 1993, pp. 667-669, IEEE #93CH3279-7.
4. M. L. Kiefer, et al., "SCREAMER, A Pulsed Power Design Tool User's Guide," June 26, 1991, Sandia National Laboratories, Albuquerque, NM.
5. J. H. Creedon, "Magnetic Cutoff in High-Current Diodes," *J. Appl. Phys.* **48**, No. 3, 1070 (1977).
6. C. W. Mendel, Jr., et al., "A Simple Theory of Magnetic Insulation from Basic Physical Considerations," *Laser and Particle Beams* **1**, Part 3, 311 (1983).
7. J. J. Ramirez, et al. "HERMES-III—A 16-TW, Short Pulse Gamma Ray Simulator," *Proc. 7th Int'l. Conference on High Power Particle Beams*, Karlsruhe, Germany, July 4-8, 1988, pp. 148-157.
8. J. Corley, et al., "SABRE, A 10-MV Linear Induction Accelerator," *Proc. 8th IEEE Pulsed Power Conference*, San Diego, CA, June 16-19, 1991, pp. 920-923, IEEE #91CH3052-8.
9. J. W. Poukey, private communication, August 19, 1993.



Two design options for the PBFA II module (R_5 = 76 cm)

Design Option	# Cavities Stage 1	# Cavities Stage 2	# Cavities Total	R_1 cm	R_2 cm	R_3 cm	R_4 cm	V_1 MV	V_2 MV	I_{diode} MA	P TW
A	4	4	8	20	21.6	22	23.8	9.2	9.2	2.5	46
B	5	7	12	20	23.1	23.5	28.6	8.7	12	2.5	52

Fig. 5 Design of the PBFA-II proposed voltage adder module.

POWER ELECTRON BEAM FRONT SHORTENING IN MITL WITH INNER COAXIAL DIELECTRIC INSERT

Lev Kazanskiy, Eugene Galstjan
Moscow Radiotechnical Institute
Warshawskoe Shosse 132
Moscow 113519, Russia

Abstract

The starting point for this investigation is a suggestion that it is possible to get the clearly defining shock electromagnetic wave in quite short modified magnetically insulated transmission line (MITL). The line modification resides in the inner coaxial dielectric insert. One may consider the insert as a distributed matched sharpening spark gap. Dielectric insert has been put up at the input of the two meters long coaxial MITL.

The parameters of high voltage pulse supplying at line input are as follows: 1.5 MV, 20 - 30 kA, 90 ns, front duration - 30 ns. The current pulse with front duration less than 1 ns has been observed at the line output. The output current has ranged up to about 10 - 12 kA. The input/output current difference is attributable to transverse plasma motion and the stable current leakage generation. In short circuit regime plasma has connect the line in about 100 ns.

By now the technology of the high-power high-current relativistic electron beams with microsecond duration has developed. The same technology is used in high-power electric pulses generation, for instance, in the investigations of the liners. However at present the high-power beams of the sub nanosecond duration are necessary for some problems of the applied physics. The maximum power parameters achieved by means of the usual technology are limited by value 100 -300 MW[1]. For this reason a search for new ways of the high-power REB generation is the topical problem. It is obvious that this problem may be reduced to the generation of the pulses with sub nanosecond front duration, so there are a lot of methods to shorten the pulse duration up to the front duration. For instance by using the parts of the short-circuited transmission lines[1,2].

In view of the fact that the vacuum insulator of the diode of the high-power accelerator is the element with the minimum electric strength and the minimum transmitted flow of the electromagnetic energy, the final front shortening has to take place in the vacuum part of the high-voltage diode. In our opinion, MITL is the best place to sharpen the high-voltage pulse, for MITL capacity to trasmitt the considerably flows of the electromagnetic energy[3].

The phenomenon of the front sharpening takes place in MITL, because the velocity of the electron flow in MITL depends on the voltage. However the finite time of electron emission and the weak nonliniarity lead to the limitations of this process. The best front duration achieved in MITL is 4 ns[3]. The strong nonlinear element is efficient at increasing the shock electromagnetic wave generation effi-ciency. A dielectric rod

inserted in the inner electrode of the MITL may considered as the element of this sort. The velocity of the electromagnetic wave and consequently the electron flow is defined by the speed of the flashover front along the dielectric surface. The flashover front takes the dielectric surface to the conducting state and allows the electro-magnetic wave to propagate. It should be noted that the speed of the flashover front may be sufficiently high due to high values of the electric fields in the front region, but this speed can not be relativistic one, for the influence of the ions. In our opinion the region of the MITL with the inner dielectric insert is close to the ideal for the electromagnetic shock wave generation, for the very steep flashover characteristics. In terms of electrical engine-ering the dielectric insert may be considered as a long sparking-gap.

Experimental Apparatus

To display the effect the preliminary experiments were provided without a special modification at the first channel of the accelerator ZET that generates a 3.5-MeV, 15-kA, 90-ns electron beam for the study of the high-power MW generators[4,5]. Initially ZET was designed and mounted to be a long pulse accelerator (2.5 MeV, 30 kA, 500 ns), and more recently was modified for the generation the electron beam with the nanosecond front. The 50-Ω PFL, charging by Marx generator up to ~ 4 MV, was used for the diode feed. The damping resistor (~ 20 Ω) was connected in series with the diode, PFL and the SF_6 - filled spark-gap. With the MITL impedance ~ 35 Ω, the parameters of the pulse at the MITL input were as follows: 1.2 MV, 30 kA, 90 ns (the front duration τ_F~15 ns). The system with the used diagnostic (two return current shunts and the C-divider) are shown in Fig.1. We had the possibility to change both the length of the dielectric rod in the range from zero to 50 cm and the dimension of the final gap.

The structure has the grave practical disadvantage that the solenoid was rigidly fixed at the outer electrode. On the one hand, it gave the possibility to provide the experiments in the presence of the magnetic field in the range from 0.2 to 1.0 T, on the other hand it did not allow us to vary the locations of the diagnostic. In addition, the outer electrode has the cone conjunctions owing to the part of the current passes by the shunt CS2 and the collector forms a resonator with the inherent frequency about 1 GHz.

Experimental Results

Initially was investigated the structure without the dielectric insert. Its characteristics coincided with the theoretically predicted. The minimum current of the magnetic insulation established in the line and the prepulse was exhibited at its output end. The current measured with the shunt CS1 was nearly twice as large as that for the shunt CS2. In the short-circuit regime both of the currents have the same value.

In the experiments with the dielectric insert, the length of the dielectric rod was equal to 25 cm, 37 cm, and 50 cm sequentially. Each of the dielectric rods was investigated with the different dimensions of the final gap: 0 cm (short-circuit regime), 7 cm and 13 cm. With the gap dimensions of 7 cm and 13 cm and the input voltage of 1.2 - 1.5 MV the obtained results are as follows. The input current with front duration of 15 ns was about 30 - 35 kA, the output one - 15 - 20 kA and the front duration of the output current was estimated as less than 0.5 ns. It should be noted that the output current was sufficiently modu-lated may be due to the above mentioned "resonator" in the collector. At least the simu-lation of excitation of the resonance cavity by the pulse with the front

duration of 0.5 ns or less shown the good agreement with the experi-mental data.

In the used range of the input voltage the time delay depended on the voltage value only weakly. Changing the lengh of the dielectric rod from 50 cm to 25 cm leaded to the reduction of the time delay from $\tau_d \sim 60$ ns to $\tau_d \sim 40$ ns. In addition, an essentially fast plasma motion was found, especially, in the short-circuit regime. The transverse gap con-nected up in 100 - 120 ns, that is the plasma velocity was about of $3 \cdot 10^7$ cm/s.

To gain a better understanding of the flashover phenomenon the above experiments was repeated in the presence of the external magnetic field B_Z aligned with the axis of the structure. With $B_Z < 0.25$ T the output signals did not change practically, though the time delay reduced, otherwise ($B_Z > 0.25$ T) the reduction of the input current and the steep rise of the output current. In doing so, the front of the output current retained its duration of 1 ns. The measured time delay at $B_Z=0$ for different length of Plexiglass rod is given in Fig.3a. The variations in the time delay for different values of the magnetic field is shown in Fig.3b.

Conclusions

The assumption that it is possible to shorten the front of high-power REB up to sub nanosecond value was borne out by the experiments. 1.5-MeV, 15-kA, 90-ns, 20-GW electron beam with the front duration of 0.5 ns was generated by using MITL with the inner dielectric insert. Undoubtedly, further study of this phenomenon is appropriate.

References See Ibid. P1-23.

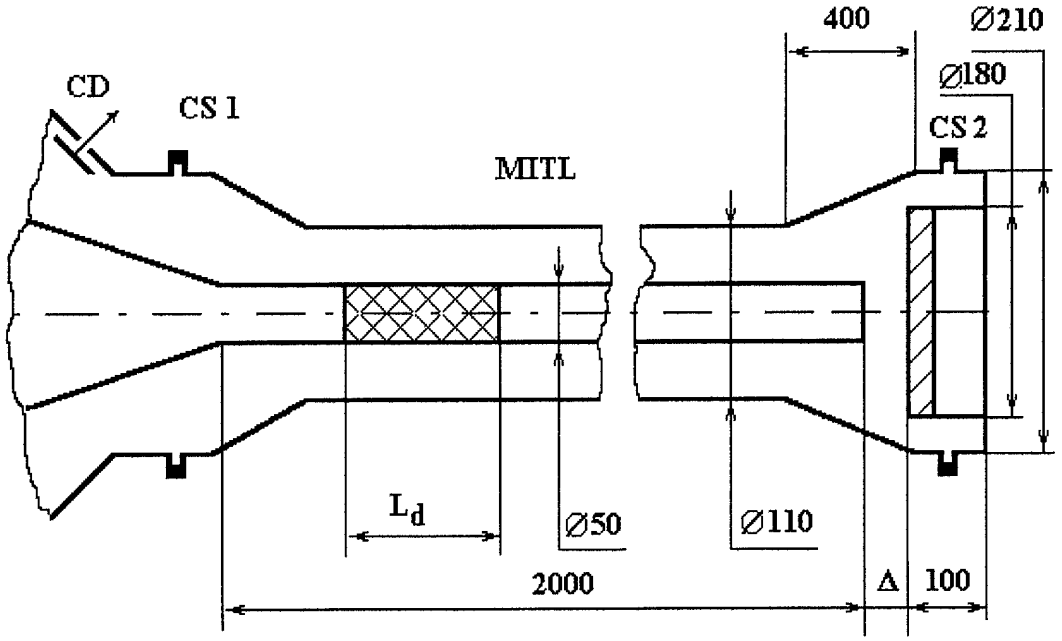
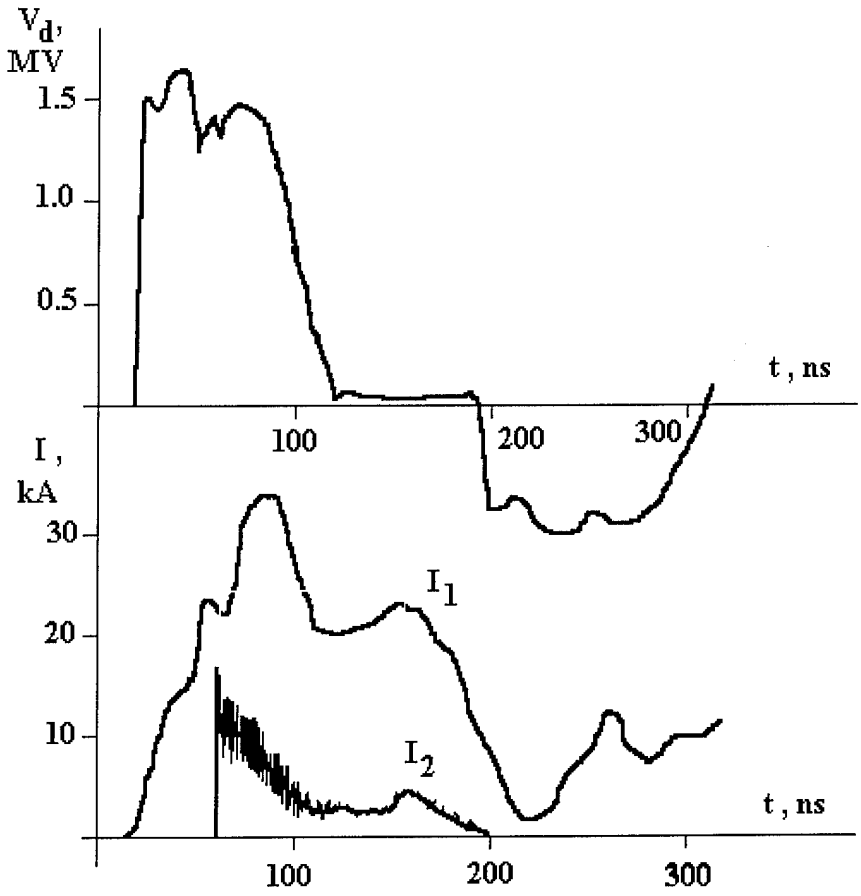
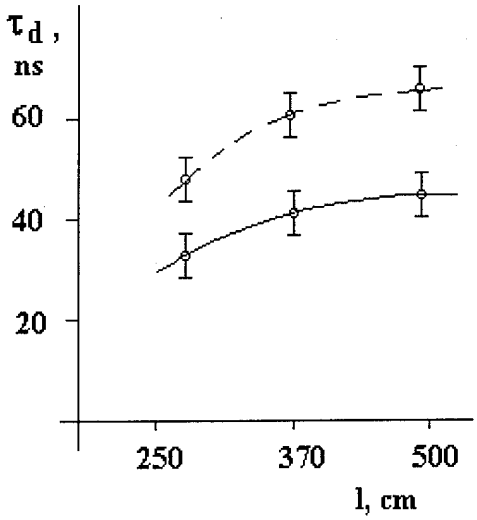
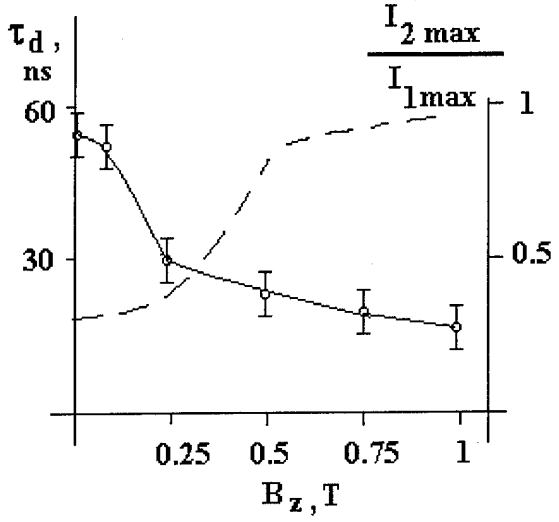


Fig. 1. Schematic of the experimental set up.


V_d, MV
1.5
1.0
0.5
t , ns
100
200
300
I , kA
30
20
10
I_1
I_2
t , ns
100
200
300


τ_d , ns
60
40
20
250
370
500
l, cm


τ_d , ns
60
30
$\frac{I_{2\,max}}{I_{1max}}$
1
0.5
0.25
0.5
0.75
1
B_z , T

MRTI ACTIVITY IN THE FIELD OF ACCELERATORS 1946-1992

Batskikh G.I.,Seleznev V.D.
Moscow Radiotechnical Institute
Russian Academy of Sciences
Warshavskoe shosse 132, 113519 Moscow,
Russia

Abstract

From 1946 through 1992 the Moscow Radiotechnical Institute of Russian Academy of Sciences (MRTI) participated in the development of accelerators: Phasotron, various Proton Synchrotrons, Accelerating and Storage Complex (UNK), Linear Proton Accelerators, Meson Physics Facility Accelerator, Linear Electron Accelerators and the Industrial High Voltage Accelerator. The parameters of these accelerators are described in the paper.

The first accelerator built with MRTI involvement was 680 MeV phasotron in Dubna Joint Institute for Nuclear Research (JINR). Phasotron was started-up in 1949 and is still in operation being the world's largest machine of the type. MRTI specialists developed RF accelerating system with mechanical frequency variator. The rotor of the device rotated in vacuum at a frequency of 50 turns per second.

Phasotron Parameters

1.Energy of accelerated particles, MeV	680
2.Mean accelerated current, μA	0,3
3.Peak magnetic field, T	1,7
4.Magnetic field decay (dn/n), %	3-5
5.Diameter of magnet poles, m	6
6.Accelerating voltage, kV	15-20
7.Acceleration frequency, MHz	14-27
8.Weight of magnet, t	7000

Then a series of proton synchrotrons followed: on the energy of 10 GeV in 1957 for JINR, on 7 GeV in 1962 for the Institute for Theoretical and Experimental Physics (ITEP,Moscow), on 1 GeV in 1965 for MRTI and on 76 GeV in 1967 for the Institute for High Energy Physics (IHEP, Protvino). The specialists of MRTI for JINR and ITEP accelerators created RF accelerating systems and control systems, the latest incorporated hard focusing and beam feedback systems. For the MRTI and IHEP accelerators the automated control system and accelerating system with the beam feedback were developed. The first one was completely built in MRTI and represented a type of accelerators controlled by computer.

The Accelerating and Storage Complex (UNK) is under construction in IHEP, Protvino. The beam diagnostic system, Complex automated control systems and accelerating system for superconducting ring are being deviced by MRTI experts.

3 TeV Accelerating and Storage Complex (UNK) Parameters

1. Energy of accelerated particles, TeV		3
2. Accelerated beam intensity, p/pulse		$6 \cdot 10^{14}$
3. Diameter of equilibrium orbit, m		6615
4. Peak induction on the orbit, T		5
5. Focusing system		FODO
6. Number of magnet blocks:	dipoles	2194
	quadrupoles	496
7. Peak accelerating voltage, MV		7
8. Acceleration frequency, MHz		200
9. Acceleration cycle, s		40

Proton Synchrotrons Parameters

№	Main Data	Synchrophasotron	7 GeV	76 GeV	1GeV
1	Energy of accelerated particles, GeV	10	7	76	1
2	Injection energy, MeV	9	24,6	100	1
3	Accelerated beam intensity, p/pulse	10^{12}	10^{12}	10^{12}	10^{10}
4	Diameter of equilibrium orbit, m	56	80	236,3	11,92
5	Peak induction on the orbit, T	1,5	0,8475	1,2	1
6	Field gradient index, (n)	0,65	460 Focusing system-FODO Number of magnet blocks-112	440 Focusing system-FODO Number of magnet blocks-120	190 Focusing system-FODO Number of magnet blocks-100
7	Energy increase per turn, keV	2,2	4,35	200	2
8	Acceleration frequency variation, MHz	0,18...1,45	0,67...8,31	2,6...6,1	1,25...25
9	Acceleration cycle, s	3,3	1,55	4	0,5
10	Number of cycles per minute	5	10	8	30
11	Weight of magnet, t	36000	2500		16

The linear proton accelerators I-2 and I-100 were built as injectors for proton synchrotrons with the energy of 7 GeV for ITEP and 76 GeV for IHEP, respectively. The accelerator of the meson facility is being started up at the Institute for Nuclear Research (INR,Troitsk). It is designed for simultaneous acceleration of protons and negative hydrogen ions. The design of accelerator was completed in 1976 but due to funding shortage commissioning dragged out. At present the injector, accelerator with drift tubes (100 MeV) and the initial part of accelerator with disc-and-washer (60 MeV) have been started up.

Linear Proton Accelerators Parameters

№	Main Data	I-2	I-100	MEGAN	
				initial part	basic part
1	Energy, MeV	24,6	100	100	600
2	Peak pulse current, mA	230	100	50	50
3	Current pulse duration, μs	300	60	100	100
4	Energy spread, %	0,8	2	$\pm$0,6	$\pm$0,4
5	Type of accelerating system	Drift tubes	Drift tubes	Drift tubes	Washers and diaphragms
6	Resonator operation frequency, MHz	148,5	148,5	198,2	991
7	Peak RF power, MW	1...2	5	13,3	78,3
8	Mean power, kW	2	3,15	450	950
9	Pulse repetition rate, Hz	0,5...2	1	100	100
10	Resonators Q-factor	50000	50000	64000...50000	20000...31200
11	Equilibrium phase,grad	37	37	26...60	33
12	Energy increase,MeV/m	1,3	1,25	1,5	2,1
13	Shunt impedance, MΩ/m	40	40	60...40	26...42,7
14	Lenght, m	18,4	80	70	350
15	Diameter of resonators, m	1,9	1,324...1,087	105...89	about 40
16	Number of resonators	2	3	5	27
17	Reduced effective emittance, cm • mrad			0,6	1,5

Linear electron accelerators have been put into operation as follows: in 1976 at the Kurchatov Institute of Atomic Energy (Moscow) with the energy of 60 MeV for investigations in the field of neutron and solid-state physics; in 1985 at the All-Union Research Institute of Experimental Physics (Arzamas) with the energy of 50 MeV for application problems; in 1985 at the All-Union Research Institute of Pulsed Technology (Moscow) with the energy of 10 MeV, picosecond pulses for spectrometry. Linear electron accelerators have been also designed for application in medicine, for medical equipment sterilization and gammer inspection systems at customs.

Industrial high voltage accelerator (energy -250...600 keV continuous current of electrons - up to 100 mA) is consisted of two blocks (high voltage rectifie and accelerator itself) connected by high voltage cable. Accelerator is mounted inside the tank (dia. 60 cm, 80 cm high) filled up with SF_6 gas. The installation is designed for chemical radiation technology. Scanning system provides for irradiation of up to 1,5 wide surfaces by a beam extracted through a foil into the atmosphere.

Linear Electron Accelerators Parameters

№	Main Data	Used in	research	works	In	applied	works
1	Energy , MeV	60	50	10	4	9	8
2	Energy spread, %	5	20	15	10	10	10
3	Pulse current, A	3...1	10	15...100	0,3	1	0,8
4	Pulse repetition rate, Hz	50...900	2400	up to 200	300	200	200
5	Pulse duration	10 ns...6μs	10 ns	10 ns&40 ps	4μs	6μs	6μs
6	Energy increase, MeV/m	9	7	7	12	7	7
7	Operating frequency, MHz	1818	1818	2450	2797	1818	1818
8	Peak RF power, MW	120	40	7	2,5	15	15
9	Mean RF power, kW	108	100	5	3	18	12
10	Length, m	18	8	1,5	0,33	1,5	1,5

STATUS OF AIRIX

J.LAUNSPACH, P.ANTHOUARD, J.BARDY, C.BONNAFOND, P.DELSART, A.DEVIN, P.EYHARTS, P.EYL, J.LABROUCHE, J.DE MASCUREAU, E.MERLE, G.PLOYART, A.ROQUES, P.LETAILLANDIER, M.THEVENOT, D.VILLATE, L.VOISIN

Commissariat à l'Energie Atomique
Centre d'Etudes Scientifiques et Techniques d'Aquitaine
BP N°2 - 33114 LE BARP - FRANCE

Abstract

The AIRIX Induction Accelerator is currently being developed at CESTA for Flash-Radiography applications.It is similar to the apparatus designed at Los Alamos for the DARHT project. It consists in an injector built by PSI and a series of accelerating cells provided for increasing the electron energy up to 20 MeV. The injector, a classical pulsed power electron generator (4MeV - 3.5kA - 60 ns) described elsewhere in this conference, is now in operation. Before completing the accelerator, first experiments are being carried on at CESTA in order to achieve the PIVAIR milestone.It consists in gradually building, settling and coupling to the injector, 16 induction cells to upgrade the beam energy from 4 MeV to 8 MeV. This PIVAIR step has been designed in order to check the different technologies developed for the accelerating cells, study the problems of beam transport and focusing, and hence anticipate the whole accelerator performances with the help of numerical simulations.

I - INTRODUCTION

The main goal of the AIRIX facility is the production of high quality powerful radiographic flashes. The high dose and short pulse width specifications require high peak current. On that purpose, the advantage of induction accelerator is its ability to accelerate at modest energy a high current with a beam quality required to obtain a small focal spot.

PIVAIR milestone is designed as a validation of AIRIX up to 8 MeV, and consists of a 4 MeV injector, 4 assemblies of 4-250 kV induction cells and a final focus solenoid. (Fig. 1)

II - INJECTOR

The PIVAIR injector is the same type as the one used at Los Alamos on the ITS facility for the DARHT program. It comprises a 4 MV pulsed generator designed by PSI [1] and a diode designed by LANL [2].

A more complete description of this injector and the first results are given in a companion paper (LANL - CESTA) elsewhere in this conference. [3]

A comparison of the designed performances and measured results are given on table 1.

	Specifications	Measured
Diode Voltage	> 4 MV	4029 kV ±4 kV
Voltage flatness	<±1%	<±1%
Pulse width	>60 ns (flat top)	±1% in 60.5 ns
Beam current	> 3.5 kA	3.6 kA
Voltage reproductibility	± 1 %	0.077 % (1σ)
jitter	< 1.5 ns	0.66 ns
Shot rate	1 per minute	

Table 1

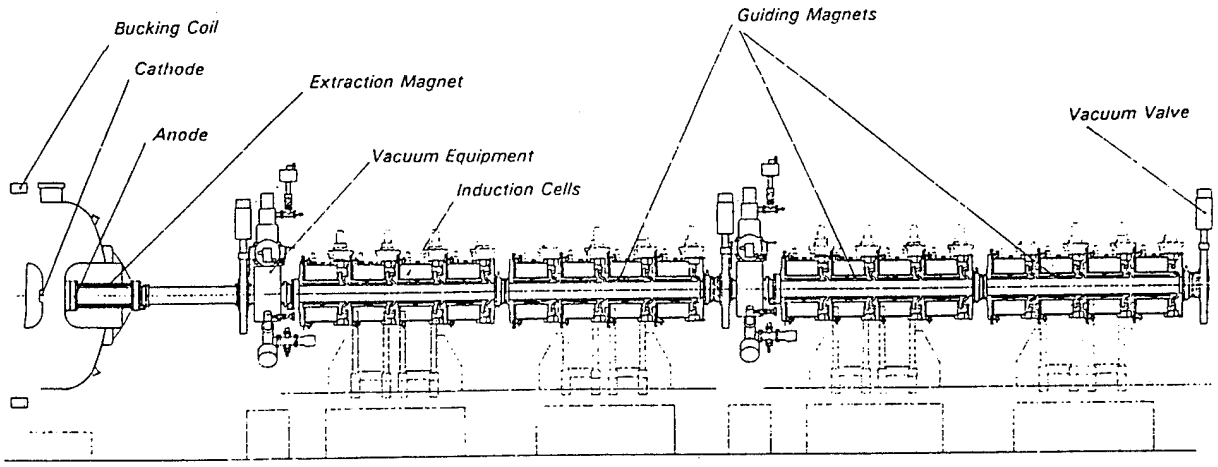


figure 1 PIVAIR Accelerator

Complementary studies are carried through at CESTA in order to improve reliability and perfomance of the machine.

III - INDUCTION CELLS

The injector will be connected with a first block of 4 induction cells in order to start the PIVAIR experiment.

Different prototype induction cells suited for the AIRIX accelerator have been studied, designed and fabricated.

For the PIVAIR accelerator, three prototype cell configurations will be tested

Each configuration comprises 11 TDK PE11B ferrite cores (250 mm I.D. , 500 mm O.D. and 25.4 mm thick) housed in a non magnetic steel body, a 4-layer bifilar-wound solenoïd magnet with iron homogenizer rings and two printed circuit dipole trim coils. The accelerating gap is 19 mm width and the cell length is 444 mm.

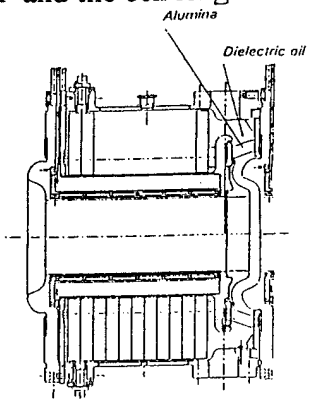


Figure 2-a . 1st configuration

- In the first configuration, oil is used as dielectric surrounding the ferrite and an alumina brazed on the cell provides vacuum insulation between beam pipe and oil.
- To minimize BBU effects, accelerating cells are designed for a low transverse impedance which is a fonction of gap geometry and dielectric constant of materials. In the second configuration, a REXOLITE insulator is used and the shape gap was modified.

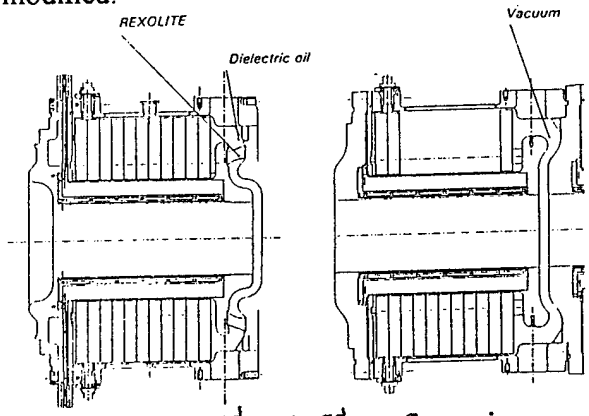


Figure 2-b. 2nd and 3rd configurations

- Because of the low repetition rate, oil is not needed. A ferrite under vacuum geometry without insulator has been studied and disigned. This third configuration is under fabrication and will be tested in a few months.

The three configurations are shown in the figure 2.

The FLUX -2D electrostatic code was extensively used in order to optimize gap

geometry. We limited the electric field to 200 kV/cm on the electrodes that form the accelerating gap.

To calculate the transverse impedance of the cell, we used the 2D electromagnetic simulation code PALAS. Fig. 3 shows the calculated transverse impedances for the three configurations.

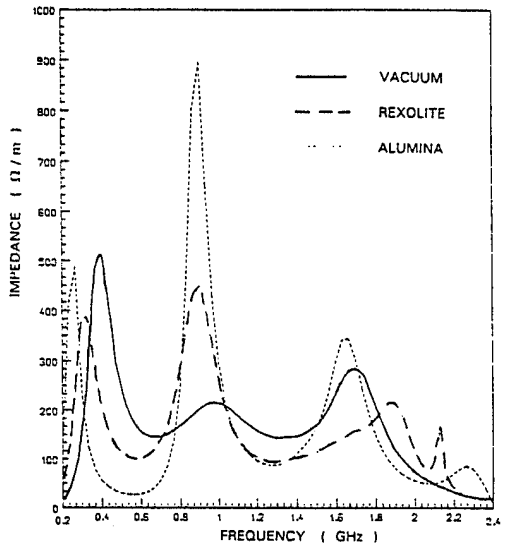


Figure 3. Calculated impedances of the three configurations

IV - PULSED POWER GENERATORS

The AIRIX high voltage pulse generator which is currently being developed at CESTA has been designed to drive two induction cells. It consists of six parts :

- a water filled blumlein,
- a coaxial structure spark-gap,
- a Blumlein Charging Unit,
- a spark-gap triggering unit,
- a high voltage supply unit
- a control and main triggering unit.

The blumlein is pulse-charged by the Blumlein Charging Unit up to 300kV in 5μs and is switched by an electrically triggered spark-gap.

The blumlein charging unit is built using a double primary 1:11 step-up transformer. Each primary is connected in line with a 1.2μF capacitor and an EEV CX1722F thyratron. When the blumlein charge is completed the coaxial spark-gap is switched by the spark-gap triggering unit which consists of a 1:5 step-up transformer, a 60nF primary capacitor, a 600pF secondary capacitor, an EEV CX1725X thyratron and a ferrite magnetic switch.

The output voltage of the spark-gap triggering unit is equal to -150kV. The rate of rise of this signal is greater than 5kV/ns and the triggering unit jitter is equal to 750ps (1σ).

Each blumlein provides a nominal -250kV flat top voltage pulse of 80ns (measured at 97% of peak voltage) which is adjustable in the range of -100kV to -300kV.

Fig 4 shows experimental results of high voltage pulse generator loaded by two cells

The typical jitter of the complet pulse generator is less than 1.9ns (1σ) for any consecutive 50 shots with a 0.05Hz P.R.F.

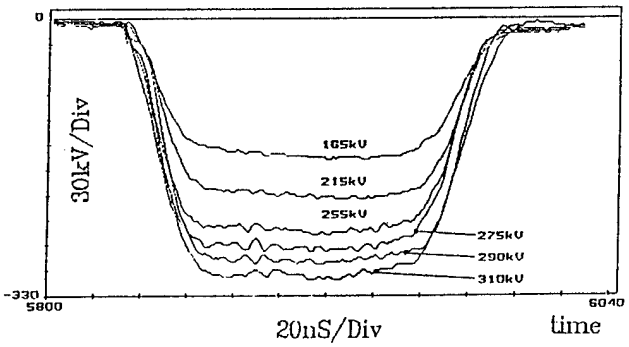


Figure 4 .Output pulse of Blumlein loaded by two cells

The high voltage supply unit and the control and main triggering unit are ancillary circuits which respectively deliver the high voltage energy required to charge the primary capacitors and provide the control and the synchronization of the different parts of this pulsed power system.

V - BEAM TRANSPORT

PIVAIR is designed to study beam transport and focusing problems.

A series of experiments was carried to measure beam currrent, beam diameter and profile at the exit of the injector as a fonction of the extraction magnet strength.

The injector has been modeled with the Particle-In-Cell code M2V . In the simulations,the cathode diameter was 7.5 cm, the AK gap was 17.5 cm and the diode voltage was 4 MV. The current emitted was fixed to 3.5 kA.

An example of the diode simulation is shown in fig.5.

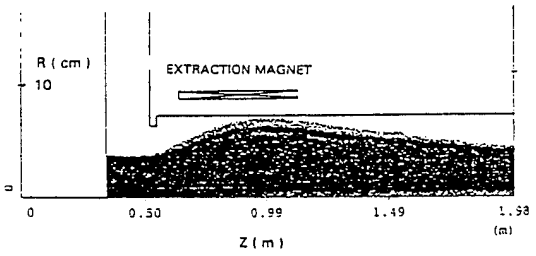


Figure 5 . Diode simulation

PIC simulations are impractical for long distances. For beam transport simulations into the whole PIVAIR accelerator, we can use a simple envelope code based on the envelope equation of LEE and COOPER [4], or we can use a modified version of TRACE - 3D [5].

These two codes can not model the AK region, so, the initial conditions for these two codes are obtained from a M2V simulation at 20 cm from the cathode surface. In the envelope code, the radius to be input is the rms radius from M2V and we adjust slope to obtain M2V data at downstream locations.

Now, we can simulate the electron beam transport into the 16 solenoids with the envelope code. The magnet strength is adjusted to an almost constant radius.

The result is shown in Fig. 6 and we can see a good match into the solenoids for 200 A in the extraction solenoid.We have assumed a normalized emittance of 1400 π.mm.mrad.

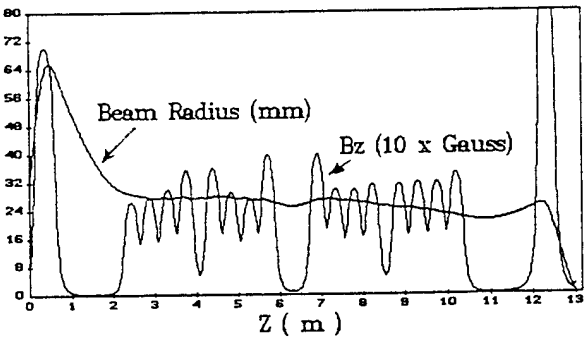


Figure 6 .Beam radius and axial magnetic field profile

We plan to insert between the injector and accelerator an rf cavity which will induce a tranverse oscillation on the beam and to measure the growth of this oscillation through the accelerator to estimate BBU effects and to compare with results of our BBU code.

REFERENCES

1 - Pulse Science Inc 600 Mc Cormick Street CA 94577.
2.- T.P.Hughes, R.L.Carlson, D.C.Moir, J. Appl. Phys. **68**, 2562 (1990)
3 - J. Launspach and alii, this conference
4.- E. P. Lee and R.K.Cooper, Part. Accel. 7, 83 (1976)
5 - K. R. Crandall LA-5332 (1973)

First Operation of New Inductive Accelerating Module at JAERI

H. Ishizuka
Fukuoka Institute of Technology, Wajiro, Higasiku, Fukuoka, 811-02 Japan

S. Musyoki, M. Shiho, K. Sakamoto, H. Maeda
Japan Atomic Energy Research Institute, Naka Fusion Research Establishment
Naka-machi, Ibaraki 311-01 Japan

Y. Watanabe
Nissei Sangyo Co.Ltd, 1-24-14 Nishi-shinnbashi, Minato-ku, Tokyo 105 Japan

A. Tokuchi
Nichicon Co. Ltd, 2-3-1 Yagura, Kusatu, Shiga, 525 Japan

Y. Yamashita
Hitachi Ltd. Kokubucho, Hitachi, Ibaraki,316 Japan

S.Nakajima
Hitachi Metals Ltd. 5200 Mikajiri, Kumagaya, Saitama 360 Japan

and

S. Kawasaki
Saitama University, Faculty of Science, 255 Shimo-ohkubo, Urawa 338 Japan.

Abstract

A new electron induction acceleration unit is completed and operated at JAERI. Several new technologies are involved therein: (1)New Fe-based nanocryostal-line soft magnetic material "Finemet" is used in foil. Its higher saturation flux density and lower power loss than the other Fe based amorphous alloys improves the performance. (2) The waveform of the accelerating voltage can be kept constant within ±1 % during the pulse, and moreover the ramp of the pulse can be varied in the range of +/- 200 kV/130ns. (3) The accelerating units are divided into two parts: One is for the beam generation and the other for the post acceleration. The latter is fabricated so that the driving circuit be separated from the acceleration column. A final beam of 2.5 MeV (variable for 1.3-2.5 MeV), 3 kA and 160 ns flat top is expected.The results of a cold test of the system combined with the power supply and acceleration cell are given.

Recent demand for a high power and tunable source of mm/cm microwave is distinguished especially in the field of the researches of CTR (for plasma heating) and high energy particle accelerators (such as Linear Collider). At JAERI, We have studied a Raman FEL with a mildly relativistic intense electron beam propagating in a focusing wiggler, in an amplifier regime in the frequency range of 30-45 GHz, mainly aiming ECRH heating of a Tokamak plasma as the research target [1, 2].

For the experiment, an electron beam of 800-900 keV and 2 kA was generated during 160 ns using 4 inductive acceleration units of 250 kV each, with a magnetic compression technique, drived by a power supply of 30 kV primary voltage and a series of pulse forming lines including magnetic switches [3]. The device is being upgraded recently, to get a final particle energy of 2-2.5 MeV and an intensity of 3-5 kA with a pulse length of 130-160ns. It is developed for more detailed researches of Raman FEL as the performance with a tapered wiggler, on which we have investigated so far numerically [4], and that with a micro-emitter of an extremely low emittance [5]. The other application field including the researches of high power beam electronics (CARM, relativistic klystron,

peniotron, channeling radiation), intense beam-plasma interaction and even the study of basic physics involved in acceleration of intense ion beam, which is a fundamental factor of the concept of particle inertial fusion should be also fairly interesting.

The new device has incorporqated some typical features. Firstly, the ramp of the acceleration voltage can be varied within the range of +/-200 kV/160ns, making the impedance of a section of PFN variable to control and study the londitudinal beam dynamics. It could meet either a high current cathode of surface explosive type, the impedance of which intrincically evolves rapidly during the pulse. Secondly the accelerator has two independent modules, being connected in series. One (for beam generation) is assembled as the usual inductive acceleration structure [6], while the other (for post-acceleration) is equipped with an acceleration column providing with multiple intermediate graded electrodes, so that the beam is accelerated adiabatically. The column is separated from and surrounded by the induction core and driving circuit, to reduce electric noise caused by the current flowing in the vacuum vessel. The acceleration pulse is feeded from the circuit to the electrodes through connection structures (Fig. 1). Details of the device and the results of the preliminary test of the power supply were reported elswhere [7,8]. The accelerator is completed recently and this paper describes the results of a cold test for the assembly including the power supply and acceleration cells with a dummy load. The performance of the circuit and its relevance to the economics of an induction accelerating device in a future energy plant [9] are discussed.

The schematic of the PFL complex is given in Fig.2. For designing the accelerator, the circuit operation was numerically analysed using an EPM computer program, to expect various modes of the output wave form as shown in Fig.3 [8], which now can be compared with the test result measured for the normal mode (flat pulse) given in Fig.4. The performance of the injector module shows a nearly satisfactory operation, where the pulse has a flat top over 160 ns within ±2.9 % at a level of the pulse height of 1MV. The post-acceleration module gives a similar pulse up to the pulse height of 700 kV, which is kept flat up during 130ns. The B-H characteristics of the magnetic cores of the modules, being measured at the experiment show that they were not saturated and kept the magnetic properties presented by tne manufacturer, up to the conditions stated above at least. We expect a total acceleration of 2-2.2 MV as prescribed.

The choice of the magentic core was one of the most crucial problems from a technical point of view. It consists of wound foils of an alloy of Fe-based nanocrystalline soft magnetic material (commercially called "Finemet"), manufactured by Hitachi Metals. The magnetic characteristics of the core presented are listed in Table I, which are measured for a rather small model of the core to be the basis of the original design of the acceleration system. It is customary that a magnetic core of wound foils shows frequently a scale effect: a larger size model does not necessarily have the same properties with in a small model, due to an increase of magnetic stress. The saturation level, permeability and magnetic loss of the induction core are supposed to be crucial element for the concept of Heavy Ion Fusion [9], as an energy plant.

These properties measured at this experiment is compared with a survey made before on this point [8], where it was concluded that an alloy "Metglass" similar to to "Finemet" might be the best choice at that time [5]. The core with our new material demonstrated now that it could be much better than the material assumed before.

The generation of an electron beam and experiments using it will be late this year after the completion of x-ray shielding room.

As the conclusion, so far as the cold test of the power supply and the acceleration cell is concerned, the results are close to satisfaction up to the level of acceleration field we tested. An accleration pulse of 1-1.2MV with a duration of 160 ns and an impedance of 300 ohms can be applied to the beam generation module and 0.7-0.8 MV to the post-acceleration cell. The voltage ramp can be controlled at least by +/-200 kV/160ns. The new acceleration cell shows a much smaller stray capacity to the earth potential and less electic noise level due to the separated structure. It can produce faster rise of the pulse. The effect on the beam post-acceleration will be investigated in near future. The properties of the core we used reveal promising for the economic point of view of beam generation/acceleration.

References

[1]S. Allen et al.,Phys. Rev. Lett. 72 1348 (1994).

[2]M.A.Allen et al., Phys. Rev. Lett 63 2472 (1987); A.M.Sessler and S.S.Yu, ibid. 58 2439 (1987).

[3]S.Humphries, Jr., Principles of Charged Particle Acceleration, John Wiley, N.Y. 1986, p263.

[4]S.Kawasaki et al., Nucle. Inst. and Meth. in Phys. Res. A341 316 (1994).

[5]H.Ishizuka et al., Proc. of 1993 Particle Accelerator Conf., IEEE, p1566 (1993)

[6] [3]p283

[7] [5]p676

[8]M.Shiho et al., Nucle. Inst. and Meth. in Phys. Res. A341 412 (1994)

[9]D.Keefe, AIP Conf. Proc.152, Heavy Ion Fusion, Washington D.C. 1986, p63

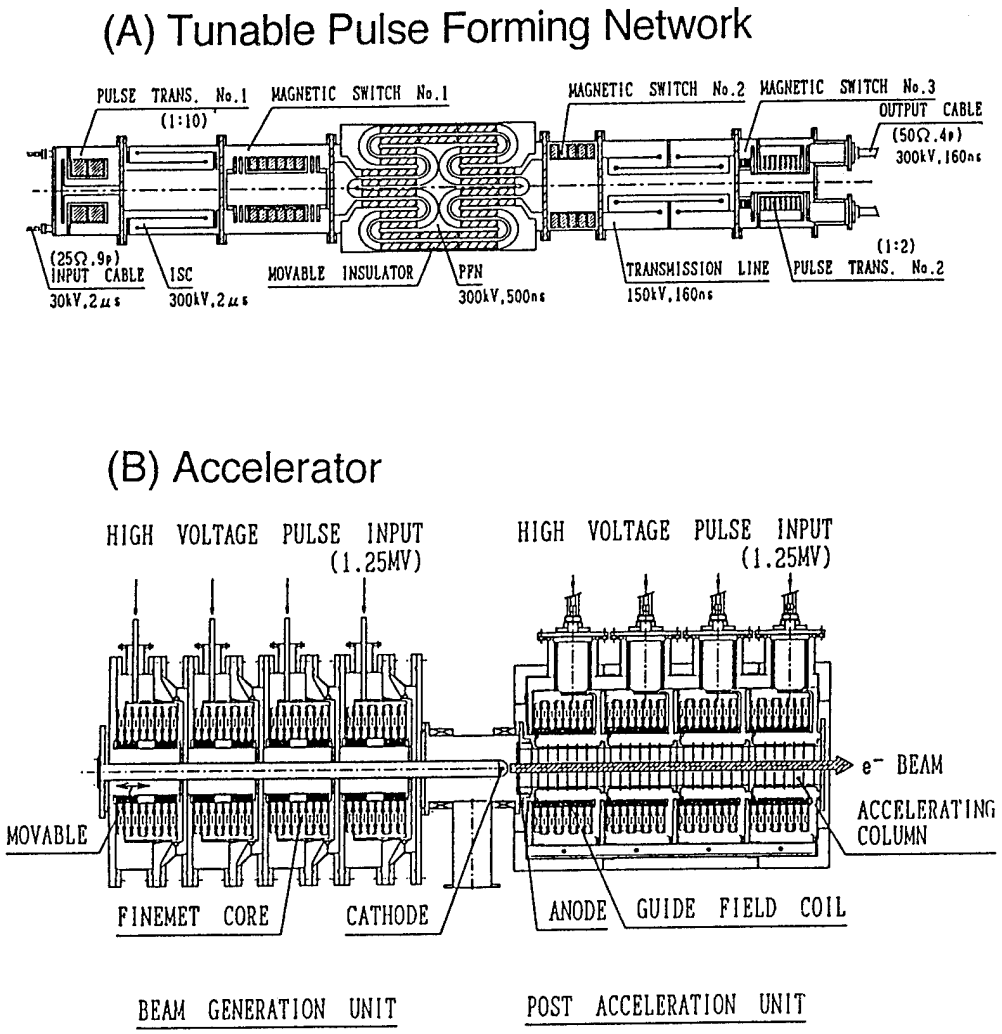
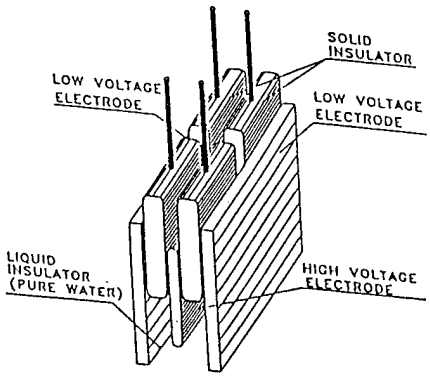


Fig. 1 Schematic view of the induction linac.



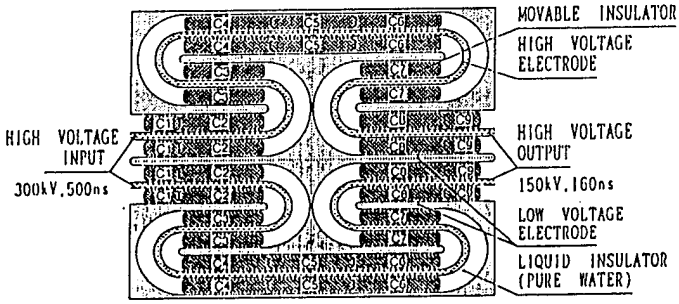
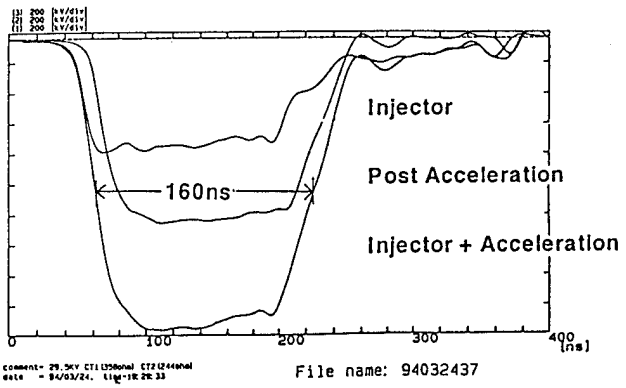


Fig. 2 Schematic view of the PFL complex.

A) Normal Operation



B) Ramp UP Operation

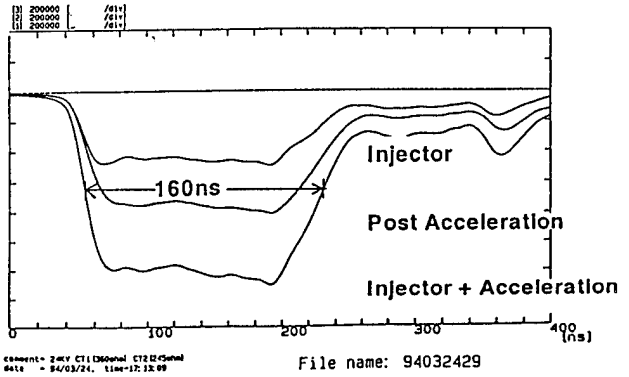


Fig. 4 Experimental wave forms

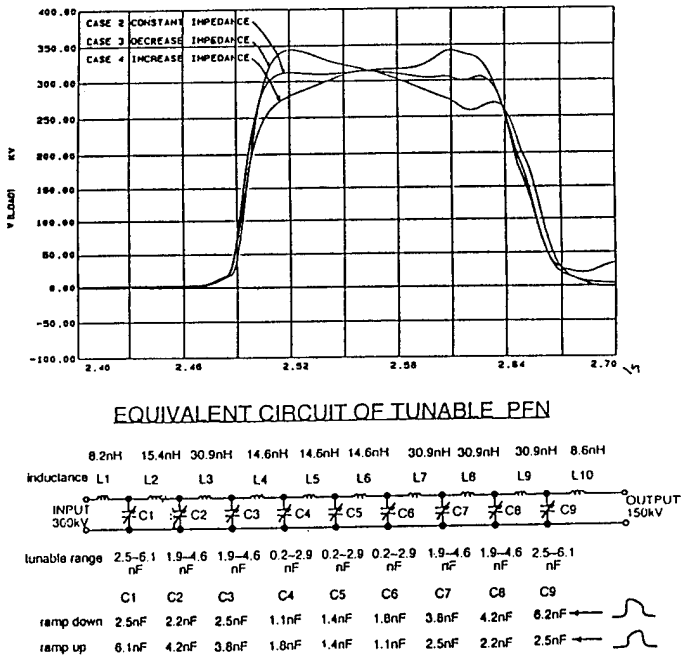


Fig. 3 Simulated wave forms.

FINEMET CORE PARAMETERS

1)	Core Dimension, Dout x Din x H (mm)	580x320x25.4
2)	Effective cross section, Ae(mm^2) a)	2278 (3302x0.69)
3)	Mean magnetic path length, le(mm) b)	1413
4)	Effective core volume, Ve(mm^3) c)	3219351
5)	Packing Factor, K	0.69
6)	Saturation induction, Bs(T)	1.35
7)	Remanence ratio, Br/Bs	0.90
8)	Coercive force, Hc (A/m)	1.3
9)	Magnetostriction, $\lambda s(\times 10^{-6})$	+2.3
10)	Curie temperature, Tc(°C)	570
11)	Effective induction swing, $K_{\Delta}Bm(T)$	1.76

a) $Ae = \frac{(Dout - Din)\cdot H\cdot K}{2}$ b) $le = \frac{\pi(Dout - Din)}{ln(Dout / Din)}$ c) $Ve = \frac{(Dout^2 - Din^2)\cdot\pi\cdot k}{4}$

Tab. 1 FINEMET core parameters.

Multipole Field Calculations for DARHT*

Thomas P. Hughes, Robert E. Clark
Mission Research Corporation
1720 Randolph Road SE, Albuquerque, NM 87106

Paul W. Allison, David C. Moir
Los Alamos National Laboratory
Los Alamos, NM 87545

Abstract

We calculate the beam-induced multipole fields in (a) an induction accelerating cell with two drive rods and (b) a diagnostic section of beam pipe with 4 port holes. For (a), the primary induced field is a quadrupole, while for (b), it is an octopole. The electromagnetic field solver BTEC *was used to compute the field strengths in each case. Corrective measures are discussed.*

Introduction and Summary

The DARHT accelerating cell is connected to the pulsed power by two radial drive rods. During the flat-top of the accelerating pulse, these rods conduct a total current equal to the sum of the beam current and leakage current. We have used a 3-D electromagnetic field solver to compute the non-axisymmetric fields produced in the beam-pipe when the leakage current is zero. (The results can be scaled to include the leakage current.) We find that, out to a radius of about 3 cm, the dominant field is a quadrupole with $\int(\partial B_y/\partial x)\,dz \approx$ 2.3 gauss, which is in line with analytic estimates. When the effect of ferrite is included, the quadrupole strength increases to 3 gauss. The quadrupole field can be corrected with a static magnetic quadrupole to the extent that the current in the drive rods is constant during the main part of the beam pulse.

*Work performed under the auspices of the U.S. Department of Energy.

To allow insertion of diagnostic targets into the beam line, a section of beam pipe with 4 ports was designed. We used the 3-D field solver to calculate the beam-induced fields in this structure. The main induced field is an octopole. We find that, at a radius of 6 cm, the magnitude of the force it produces is comparable to the net monopole self-field force of a 3 MV beam, i.e., it is a significant effect if the beam radius is large.

Quadrupole Calculation

A sketch of the accelerating cell is shown in Fig. 1a. The two drive rods which feed the pulsed power to the cell are 180 degrees apart. We used the 3-D gridded field solver BTEC (Ref. 1) to model the problem. BTEC allows problems like this to be set up reasonably easily by hewing objects such as cylinders and planes out of a 3-D mesh.

A section of the grid is shown in Fig. 1b. In this geometry, the ferrite region was represented by a perfect conduc-

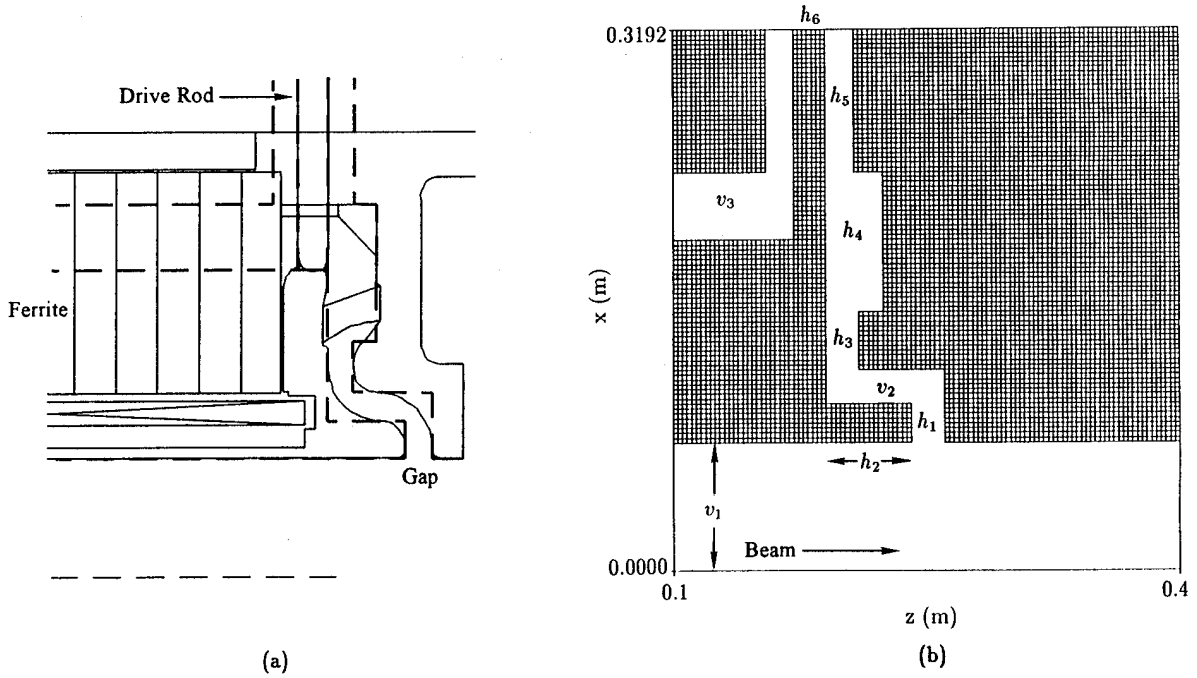


Figure 1. Simplified gap geometry, outlined by dashed line, used in initial BTEC calculations is shown in (a). Frame (b) shows a section of the BTEC grid. Vertical dimensions (cm) are: $v_1 = 7.4$, $v_2 = 2$, $v_3 = 4.0$. Horizontal dimensions (cm) are $h_1 = 2$, $h_2 = 5.14$, $h_3 = 2$, $h_4 = 3.43$, $h_5 = 1.7$, $h_6 = 2$. Cell size is $\Delta x = 0.2850$ cm $= \Delta y$, $\Delta z = 0.2857$ cm.

tor. Wave-transmitting boundary conditions were applied at the left and right boundaries. The grid resolution was $\Delta z = 0.2857$ cm, $\Delta x = 0.285$ cm $= \Delta y$.

During the flat-top of the beam current pulse the drive rods conduct a current equal to the sum of the beam current and the leakage current. Cell measurements indicate that the leakage current has an approximately constant value of about 500 A. This means that each drive rod carries a current of about $(3000 + 500)/2$ A. In the following, we do not include the leakage current, but the results can be simply scaled to take it into account.

We drive a current along the axis of the beam pipe in Fig. 1b, and slowly ramp it in time to the nominal DARHT current of 3 kA. A current equal to the beam current flows in the drive rods. We calculate instantaneous integrals of the transverse Lorentz force along the beam pipe, viz.,

$$W(t) = e \int (\mathbf{E}_\perp - v_z \hat{z} \times \mathbf{B}_\perp)\, dz \quad (1)$$

where e is the electronic charge. The integral is taken over a 25 cm length centered on the gap. To isolate the weak non-axisymmetric fields from the strong axisymmetric self-fields of the beam, we use a current traveling at the velocity of light to excite the structure, and use $v_z = c$ in Eq. 1. In this situation, $W(t)$ is zero in a straight pipe, because the electric and magnetic forces cancel exactly. We compute $W(t)$ at a number of points along the x- and y-axes. (The drive-rods are along the x-axis.). The values are plotted versus radius in Fig. 2. Out to a radius of about 3 cm, the curves have a constant slope, indicating a quadrupole field component, as expected. The magni-

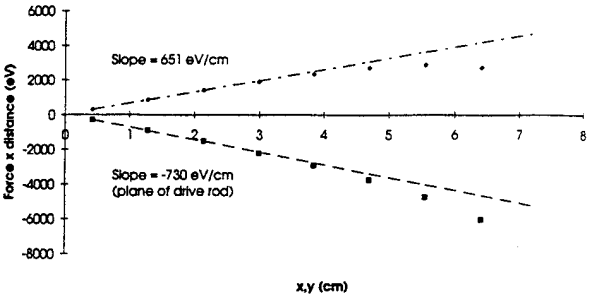


Figure 2. Radial variation of integrated transverse force vs. radius along x-axis (plane of drive-rods) and y-axis. The dashed lines are straight-line fits to the first three points. (Run L12).

tudes of the two slopes, obtained by fitting a straight line to the first three points on each curve, differ by about 10% indicating some numerical error. The focusing strength of the quadrupole is given by the quantity $\int(\partial B_y/\partial x)dz \approx 2.3$ gauss, where we have used the average of the two slopes.

A second set of calculations used a modified geometry where the ferrite was modeled as a region with a given μ, rather than as a perfect conductor. To get a base measurement, we first ran with $\mu = 1$ (i.e., the permeability of free space). This gave a quadrupole strength of 2.4 gauss, which is slightly higher than the 2.3 gauss obtained for the geometry in Fig. 1. We then ran with $\mu = 250$, the approximate low-frequency, low-signal value measured at LLNL (Ref. 2). This increased the quadrupole strength to 2.96 gauss, presumably due to magnetic field enhancement by the ferrite in the region of the drive rods.

A simple analytic estimate of the quadrupole strength is obtained by considering a geometry consisting of a beam pipe, a radial line and two rods shorting the gap. In the limit of small pipe radius, $a/g \ll 1$, where a is the beam-pipe radius and g is the gap width, the quadrupole strength due to current in the rods is easily estimated from the Biot-Savart expression for a wire, giving

$$\int\left(\frac{\partial B_y}{\partial x}\right)dz = \frac{Z_0 I_1\ (\mathrm{A})}{300}\frac{g\ (\mathrm{cm})}{\pi D^2\ (\mathrm{cm})}\ \mathrm{g} \quad (2)$$

where I_1 is the current carried by each rod, D is the radial position of the rods, and $Z_0 = 377\ \Omega$. For the DARHT cell parameters ($I_1 = 3000/2$ A, $g = 1.9$ cm, $D = 23.3$ cm) this gives 2.1 gauss (vs. 2.3 gauss from BTEC for the geometry in Fig. 1b). Gluckstern and Cooper (Ref. 3) carried out an analytic calculation for this geometry for the opposite (small-gap) limit, which is more appropriate to the DARHT cell, and also considerably more complicated to treat. For DARHT parameters, their expression gives a value of 3 gauss.

To the extent that the sum of the leakage and beam currents is constant in time, the quadrupole force is also constant, and so can be corrected using a compensating static magnetic field.

Octopole Calculation

A sketch of the 4-port structure is shown in Fig. 3. Four symmetrically placed

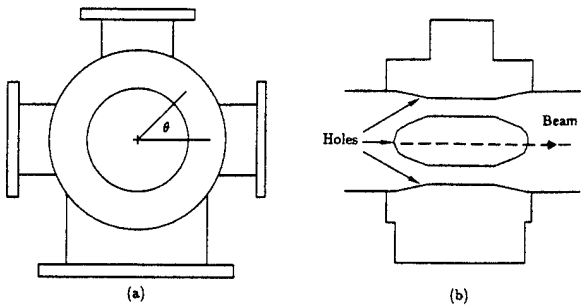


Figure 3. Sketch of 4-hole section of beam pipe looking (a) down the beam-line, and (b) transverse to the beam-line.

3" by 8" holes are cut in a section of beam pipe. One of the four pipes providing access to the holes has a larger diameter than the other three. We neglect this in the calculation, making all four pipes identical. We model the problem using dimensions as close to those of the actual device as allowed by the finite grid size. A cross-section of the grid through the beam axis is shown in Fig. 4. The axial length of the region modeled is 37.5 cm.

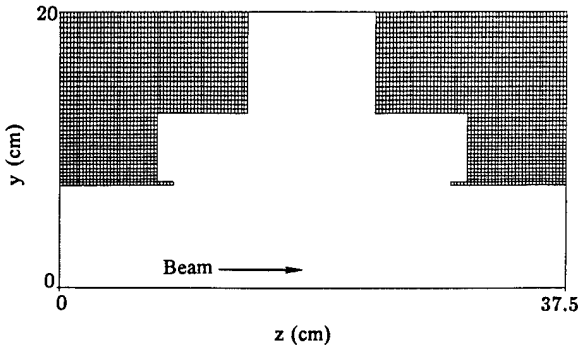


Figure 4. Section of the 3-D BTEC grid used to compute induced electric and magnetic fields (cf. Fig. 3b).

As with the quadrupole calculation, we drive a current along the axis of the beam pipe and slowly ramp it in time to a value of 3 kA. We compute $W(t)$ at a number of points along $\theta = 0$ and $\theta = 45°$ (see Fig. 3). The values are plotted versus radius in Fig. 5. We see that the numerical values are fitted reasonably well by the function $W_{\rm oct}(r) = 120r^3$ (cm) eV. For comparison, the (analytically derived) integrated monopole force due to the self-fields of a 3 kA beam on a particle with energy γ over the 37.5 cm length of the simulation region is $W_{\rm mono}(r) = 6.76 \times 10^6/\gamma^2 r$ (cm) eV. Equating $W_{\rm oct}$ and $W_{\rm mono}$, we find that for a 3 MV beam, the monopole and peak octopole forces are equal at a radius of about 5.9 cm. We verified this by redoing the calculation of $W(t)$ for a current travelling with $v_z = 0.989c$ (3 MV). The results show the predicted cancellation occurs along $\theta = 45°$ near $r = 6$ cm. This comparison illustrates that the magnitude of the octopole field is non-negligible for large beam radii. The effect of the holes can be reduced by (a) reducing their size, (b) applying a compensating magnetic octopole or (c) ensuring that the beam has a small $\lesssim$2 cm) radius in this region.

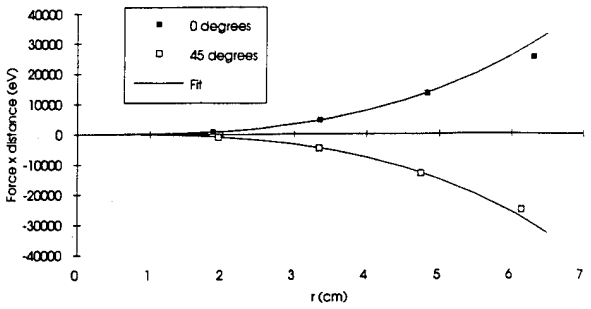


Figure 5. Radial variation of integrated transverse force vs. r for $\theta = 0$, 45°, overplotted by the function 120 r^3.

REFERENCES

1. BTEC is maintained by Bob Clark at Mission Research Corporation.
2. J. DeFord, private communication.
3. R. L. Gluckstern and R. K. Cooper, AT-7 Memo, August 4, 1993.

DEVICE EMIR - M GENERATOR OF IMPULSE ELECTRON BEAMS, BREMSSTRAHLUNG AND ELECTROMAGNETIC FIELDS.

V.S.Diyankov, B.N.Lavrent'ev, R.N.Munasypov,
I.V.Prosolenko, V.A.Filatov.
Federal Nuclear Center - Russian Scientific
Research Institute of Technical Physics
P.O.Box 245, 454070, Snezhinsk, RUSSIA

Abstract

*Impulse high voltage electron beam accelerator EMIR - M consists of a capacitive energy storage in the form of Marx generator with 24 parallel modules, an intermediate inductive storage, an electrically exploding wire current interrupter (EEWCI), and diode type accelerator tube. Marx generator open - circuit voltage is up to 1.52 MV. The generator has 0.58 MJ store energy when the capacitance is 505 nF. Its proper inductance is 1450 nH. The characteristic impedance of the generator - interrupter circuit is 2.5 Ohm. The EEWCI provides obtaining an accelerating voltage up to 5 MV and diode current 50...100 kA with the current pulse width 50...200 ns. The device is used in the following modes of operation: (1) Extraction of electron beam out of diode with an energy density up to 300 J/cm^2 and pulse width 100 ns; (2) Bremsstrahlung generation with an effective gamma foton energy approximately 1 MeV. Maximum dose rate near anode is 2 * 10^{12} Rad/s; (3) Generation of electromagnetic field in the radiation zone by another generator. An electric field up to 400 kV/m and magnetic field up to 1.2 kA/m are attainable with pulse rise time 40 ns and full width at half - maximum of 1μs. The electromagnetic field may be generated simultaneously with the radiation impulse, time shifted relative to one or separately.*

Device EMIR - M represents an assemblage of two impulse high - voltage facilities. The first one is an electron accelerator, consisting of Marx generator, an inductive storage, an electrically exploding wire current interrupter, a switch and accelerator tube. The second facility is an impulse high - voltage generator with a system for an electromagnetic field creation.

Both facilities are packaged in such a way that the gamma radiation impulse or impulse electron flow and the impulse electromagnetic field may be created in a test volume simultaneously or separately.

Besides Marx generator design and its division into two independent blocks allow to generate two sequence radiation impulses with a controlled time interval with the same accelerator tube.

The device EMIR - M common view is shown in Fig. 1.

Bipolar charged Marx generator consists of 24 independent modules grouped into 2 independent blocks with 12 modules in

each one. The outputs of modules in each block are connected with collector. Each collector is connected with an exploding wire assembly (EWA) with own inductive conductor.

The characteritiscs of 24(12) - module Marx generator and the device are following: charge voltage - 30...85 kV; output capacitance - 0.5(0.25) μF; the proper inductance - 1.45 μH; the total inductance of the circuit with electrically exploding wires (EEW) - 3.15(5.65) μH; EWA inductance - 0.9 μH; the total inductance of the switch and accelerator tube - 1.57μH. The module block tank dimensions are 5.8 * 3.7 * 3.8 m^3. The Marx generator module dimensions are 0.97 * 0.6 * 2.94 m^3. The module consists of 19 sections. The 100 kV 0.4 μF capacitor is mounted in each section. Each module has channels for charging, triggering, current measurement, spark gap tube filling and blow - down with a dry pressed air.

Module sections are switched with three - electrode dry compressed air spark gaps triggering due to resistive (or capacitive) connections with preceding section.

The first (start) module spark gap is a field distortion one. It is triggered due to potential drop out of its intermediate electrode.

All module spark gaps are placed in a common polyethylene tube in 250 mm from each other. Spark gaps "see" each other that provides their mutual ultraviolet radiation.

The inductive storage is a frameless coil made from steel tube 30 mm diameter. The coil diameter is 0.3 m, the length is 1.5 m. The number of the coil turns may be changed.

The EWA is a technological assembly provided the installation of copper wires, their explosion and the explosion products removal. The EWA represents the system of hermetically closing polyethylene tubes 130 mm inner diameter and 4 m length, in which the EEW holders are placed. Before the device work this tubes are filled with air pressed up to 4 at.

The EEW set for operation modes is formed with approximately 100 copper wires 0.1 mm diameter and 4...6.5 m length.

The EWA is placed in a cylindrical tank, which is located between the Marx generator tanks. The EWA tank is 4.7 m high and 3.2 m diameter. All the tanks are connected with the branch pipes 1.4 m diameter. The inductive storage coils, connected the Marx generator collectors with EWA, are placed is this branch pipes.

The accelerator tube switch is an usual two - electrode self - breaking transformer oil spark gap. The first electrode is a plate (accelerator tube flange). The second electrode is a potential one and is made as a ring edge 225 mm diameter. It may have also an another form.

The accelerator tube (diode) design is similar to the multitude of the such type arrangements. The basic diode element is a vacuum insulator, which represent the set of sequential insulating and gradient rings. Insulating rings are made with caprolon; gradient rings are aluminium. There are 19 insulating rings 100 mm thickness or 46 rings 40 mm thickness. Gradient rings are made figured to provide the screening of the vacuum surface of the insulator. The insulator inner diameter is 1080 mm, the length is 2 m.

The diode electrodes represent a coaxial 700 mm length, in which inner and outer electrode's diameters are 100 mm and 500 mm, respectively.

According to operational mode the end of diode's outer electrode of this coaxial is completed with tantalum target for bremsstrahlung generation or titanium foil "window" for electron beam extraction.

Electromagnetic field generator consists of an usual Marx generator, output arrangement with a pulse - forming capacitor and a field creation system (FCS). Marx

generator has four bipolar charged sections constructed with 0.1 μF capacitors. The spark gaps between sections are three - electrode field distortion triggering type. Marx generator and output arrangement are placed in a transformer oil filled tank, which dimensions are $1.15 * 0.7 * 0.7$ m^3.

Output arrangement consists of three - electrode sharpening gas spark gap and pulse - forming capacitor. This arrangement is designed for sharpening the leading edge of the voltage impulse. Pulse - forming capacitor is constructed with a set of ceramic capacitors with an equivalent capacitance 1175 pF.

All Marx generator spark gaps are filled with a dry pressed air.

FCS presents two plane - parallel electrodes loaded to resister 100 ... 150 Ohm. FCS is placed relatively accelerator tube in such a way that gamma photon flow direction near axis is parallel to electric field vector.

The dimentions of the FCS potential electrode are $1.68 * 1.19$ m^2 "Grounded" electrode of FCS has some greater dimensions and the form, which follows the contour of the test box profile, but it hasn't galvanic connection with this box. The spacing between the electrodes of FCS may be 0.5...1.5 m.

The generator works in aperiodic R - L - C discharge mode.

The characteristics of this facility are following: output Marx generator capacitance is 25 nF, charge voltage is 20...70 kV, discharge circuit inductance is 1.2 μH, FCS voltage is 60...210 kV, the electric and magnetic field strengthes are 60...210 kV/m and 180...630 A/m, respectively, when the spacing between the FCS electrodes is 1 m.

To measure electric and magnetic fields the probes and their calibration equipment are developed.

When joint radiation and electromagnetic actions are performed on the test objects the time interval between this actions may be controlled in wide limits beginnig from coincidence of the leading edges of the impulses.

Some results of the experimental research of the device are given in Fig 2...4. .

The device is provided the joint or separate action of the impulse gamma radiation and the electromagnetic field on the test objects. The dose rate is up to 10^{12} Rad/s with ~ 50 ns radiation impulse duration and 1 MeV average gamma foton energy. The accelerator tube voltage is up to 5 MV and electron beam current is up to 100 kA. The electric and magnetic field strengthes are controlled in the limits of 40...400 kV/m and 120...1200 A/m, respectively.

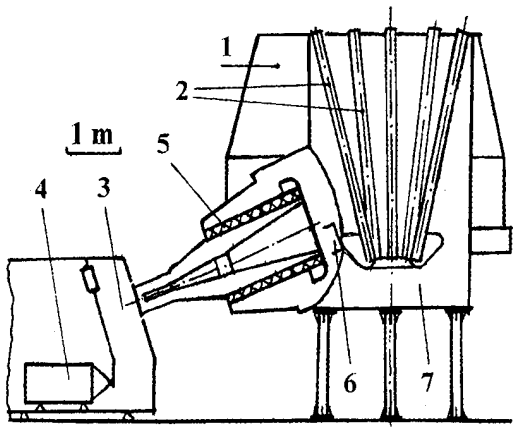


Fig. 1. Device common view: 1 - Marx generator tank; 2 - EEW channels; 3 - test zone; 4 - electromagnetic field generator; 5 - diode insulator; 6 - diode switch; 7 - EWA tank.

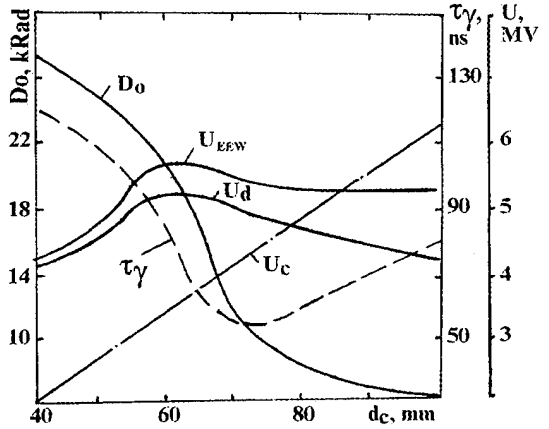


Fig. 3. Influence of the diode switch gap on some accelerator characteristic: U_{EEW}, U_C, U_d - EEW voltage, diode connection voltage and diode voltage, respectively;
D_0 - radiation dose near diode target center; τ_γ - radiation impulse duration.
Experimental conditions; 12 - module Marx generator with 1.5 MV output voltage and 290 kJ energy store; EEW: number - 75, diameter - 0.08 mm, length - 6.4 m; diode gap - 70 mm; steel target 5.6 mm thickness.

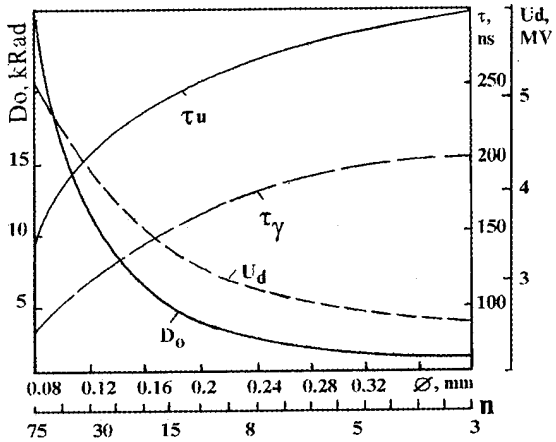


Fig. 2. Influence of the EEW diameter (or their number n) on accelerator characteristics. D_0 - radiation dose near diode target center, U_d - diode voltage, τ_u, τ_γ - the durations of the diode voltage impulse and radiation impulse,
n - EEW number.
Experimental conditions: 12 - module Marx generator with 1.5 MV output voltage and 290 kJ energy store; 6.4 m EEW length; steel target 5.6 mm thickness.

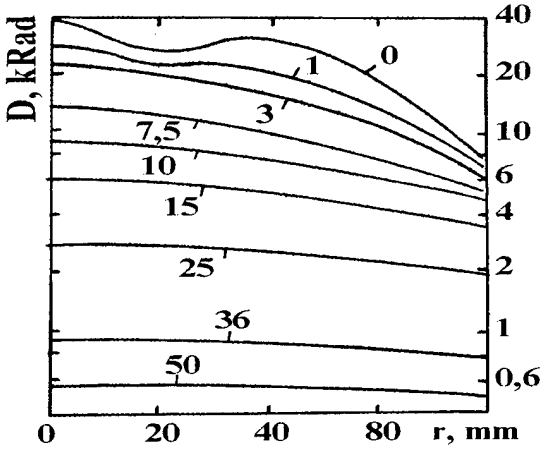


Fig. 4. Radiation dose distribution at the different distances (sm) from target.
r - distance from diode axis.
Experimental conditions: 24 - module Marx generator with 1.5 MV output voltage and 580 kJ energy store; EEW: number - 120, diameter - 0.09 mm, length - 6 m; diode switch gap - 60 mm, diode gap - 100 mm; tantalum target 2 mm thickness.

EXPERIMENTAL STUDY OF A HIGH-POWER ELECTRON BEAM GENERATOR "PIRIT-120"

A.I. Pavlovskii, N.F. Popkov, A.S. Pikar', V.I. Kargin, E.A. Ryaslov.

All-Russia scientific research institute of experimental physics (VNIIEF), Arzamas-16, Nizhni Novgorod region, 607200, RUSSIA.

INTRODUCTION

To sharpen an electromagnetic pulse using plasma erosion opening switches (PEOS) is the most easy and reliable method, which does not require a "fast operating" capacitor bank [1]. In this method the energy stored in a "slow operating" capacitor bank is converted into a magnetic inductance energy, which is switched on before a load. When a circuit of an inductive storage breaks, a short electromagnetic pulse is generated which is delivered into a load.

PEOS operating is based on the property of a nigh-current discharge in a plasma to increase resistance sharply, when current reaches a critical current [2]. Because of the fact that power increase is followed by significant voltage increase, the generators based on PEOS have found wide application in acceleration engineering aiming to receive electron beams and generation of X-ray bremsstrahlung pulses.

The work presents the results of studies on the "PIRIT-120" pulse generator. The parameters of the generator are: V=1 MV, I=250 kA, W=120 kJ.

DESCRIPTION OF THE FACILITY.

Fig.1 shows structural design of "PIRIT-120". Three Marx generators served as initial energy storage connected in parallel. The total capacity of the generators is 0.96 μF, inductance is 0.25 μH. The stored energy with 100 kV of the charging voltage is 120 kJ. A transmission line included 3 KVI-500 cables, its total inductance is 0.25 μH. The inductance of a transmission line up to PEOS is 0.72 μH. Time for discharge current in line is 6 μs, an amplitude of a discharge current is 400 kA. The output of Marx generator is connected to a collector of a double inductive storage using high-voltage KVI-500 cable Fig.2. The vacuum portion of a storage is separated from a collector by a polyethylene insulator 3 with a diameter of 450 mm. Six plasma guns 4 of a surface-erosion type are located at the distance of 1200 mm from an insulator. A vacuum line is a coaxial one, it consists of a number of sections 5, connected by adapting rings 6, where inductive current probes 7 are located. The external coaxial diameter is 214 mm, internal one is 80 mm. At the end of the line a target 8 and a voltage divider are located. To prevent the insulator lighting by PEOS plasma and to protect it from target evaporation products it is closed by a dielectric disk 10 and a set of metal washers 11.

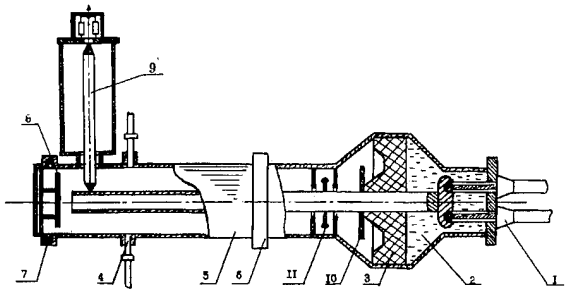


Fig.1. Structural design of "PIRIT-120".

The facility operates the following way. After Marx generator and GIT generator, which powers plasma guns, have been charged, GIT discharges are triggered and plasma is injected into a gap of an inductive storage. In a delay time T, which is necessary to fill a gap with plasma and

create the necessary density, the Marx generator operators, the inductive storage contour is closed via PEOS, when the critical current is reached, the sharp increase of plasma resistance takes place and the energy is transferred into a load.

CALCULATION RESULTS

To define efficiency of energy transfer from a power source to a load we conducted a numerical analysis of Marx generator operation into an inductive storage via PEOS. PEOS operation is based upon the double layer formation in a plasma, filling interelectrode gap, erosion of this plasma and magnetic insulation of an electron beam. PEOS operation may be divided into several steps.

1. Filling of inductive storage interelectrode gap with plasma. Plasma density $n \approx \left(10^{12} \div 10^{13}\right) cm^{-3}$ and injection velocity $V_p \approx \left(10^6 \div 10^7\right) cm/s$ are defined by conditions of its generation and acceleration.

2. Formation of a cathode double layer DL as a potential jump, when pulse voltage is applied. Plasma density close to a cathode, necessary for double layer formation is defined from the ratio [3].

$$I_i \approx \left(\frac{m_e}{m_i}\right)^{\frac{1}{2}} \cdot \left(\frac{Z}{A}\right)^{\frac{1}{2}} \cdot I_e > n_p e V_p Z \cdot \pi DL,$$

where L - is a plasma layer length, D - is a cathode diameter, V_p - is plasma velocity in a radial direction.

3. DL increase under plasma dispersal. In doing so the current in a chain increases and a flux of ions coming from a plasma into a gap is not sufficient to support a bipolar flux on the plasma interface. The corresponding to the moment saturation current of an ion component looks like:

$$j_p = e n_p V_p Z.$$

An additional ion flux is formed as a result of plasma decay, which leads to increase of effective PEOS resistance and the voltage across the DL, correspondingly.

4. With further current increase intensification of dispersal effected by a magnetic field takes place. Electron trajectories bend. When electron flux through DL increases critical current value [4] $I_{кр} = I_A \cdot \beta \cdot \gamma \cdot g$ for magnetic shielding, inductive storage circuit starts to break.

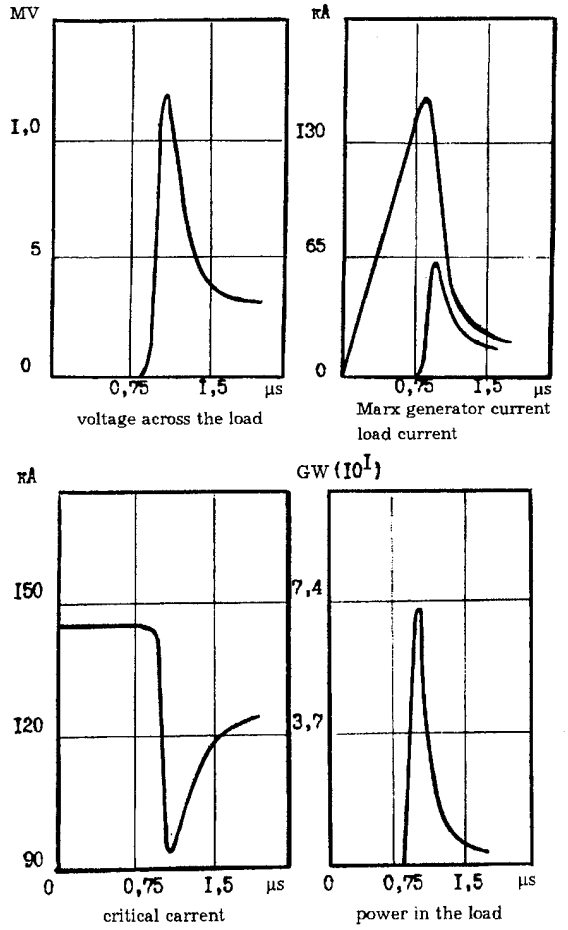
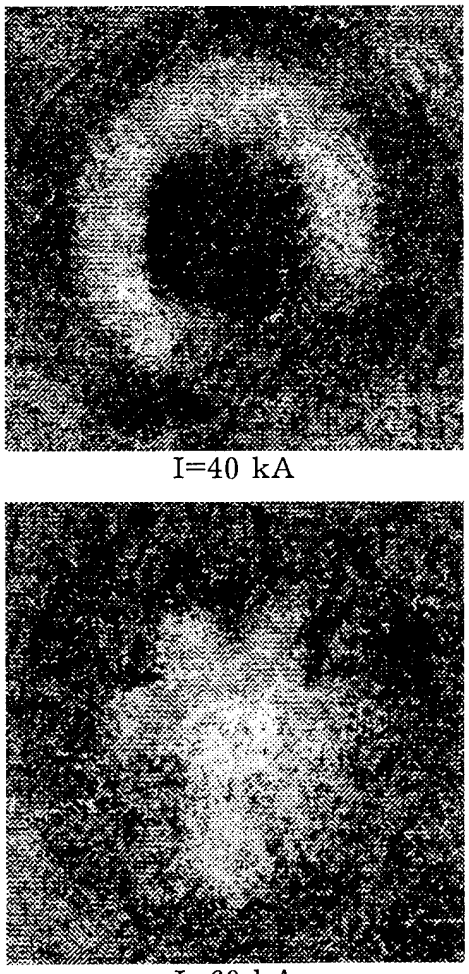


Fig. 2. Calculation results for vacuum diode.

5. After an electron flux is magnetically locked, ion current still flows, because to lock an ion flux the field by $(m_i/m_e)^{1/2}$ fold greater is required. But ion current density is so little that DL expansion continues and leads to a complete break of an inductive storage circuit.

To make a numerical calculation of "PIRIT-120" operation we used code, based upon the above given model [5]. The results of this calculation for vacuum diode are given in Fig. 2.



I=40 kA

I=60 kA

Fig.3. Pin-hole images of the electron beam.

THE RESULTS OF THE EXPERIMENTS.

In the first experiments we used a vacuum diode as a load. The distance from a PEOS to diode is 900 mm, a cathode diameter is 40 mm, the length of a cathode-anode gap changes from 5 to 30 mm. Voltage on a diode measured by a resistive voltage divider is 1.4 MV. The maximum beam current with which its structure formed by hollow cathode, has been retained, does not exceed 50 kA. With further current increase the pin-hole images right after the anode show the areas of the most intensive radiation, but there is no precisely expressed structure (Fig.3).

In order to measure X-ray radiation thermoluminescent dosimeters (TLD) were used. They were located at the distance of 50 mm from a tantalum target with the thickness of 100 mcm. The maximum X-ray dose reached 3 krad per pulse. X-ray pulse duration recorded by p-i-n diodes is 100 ns.

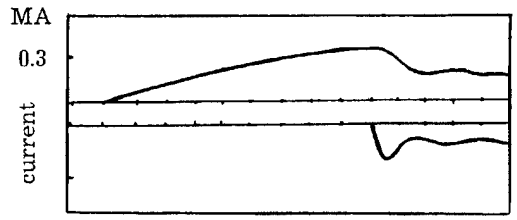
Erosion track, left on the central electrode of an inductive storage, when plasma is shifted, effected by the force $\vec{F} = 1/c \cdot [\vec{j} \times \vec{B}]$, had the length of 700 mm. This value well agrees with the calculated value, when PEOS critical current is 300 kA and the magnetic field on the surface of an electrode is 12 kOe.

$$I_{кр} = n_p e V_p \cdot (m_i/m_e)^{1/2} \cdot \pi DL$$

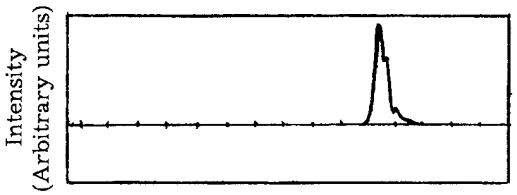
The value [m/m] for single ionized hydrogen atom is -100. Plasma density and its velocity were defined in preliminary experiments:

$n_p \approx 10^{12}\,cm^{-3}$, $V_p \approx 6 \cdot 10^6$ cm/s.

Then $L_{calc} = 600 \div 700$ mm.



1. - current line;
2. - current load.



Signal from p-i-n-diode X-ray detector.
Marks - 100 nsec.

Fig. 4.

In the following experiments one portion of an inductive storage was disassembled and a distance from the PEOS to a load was reduced to

450 mm. During the time required to power the inductive storage (1.4 μs) plasma reached the load, filled interelectrode gap and plasma diode was formed.

Table I.

Gap (K-A), mm	8	8	27	27
U_{PEOS}, kV	60	60	80	80
Time delay, μs	4.5	6.0	6.0	9.5
Storage current, kA	225	290	310	310
Load current, kA	205	220	255	200
Moment of current transfer, μs	1.1	1.3	1.7	2.25
Radiation energy, J	90	270	55	-

In this case diode current has been increasing and reached the value 50-60% of storage current (Fig.4). The presence of hard X-ray bremsstrahlung confirms that there is an electron beam in plasma. Cathode diameter change did not practically effect the diode current. At the same time the change of the gap length between a cathode and anode leads to current and X-ray yield. Table 1 gives the results of the experiments for two values of the cathode-anode gap with various delay times and voltages of PEOS powering.

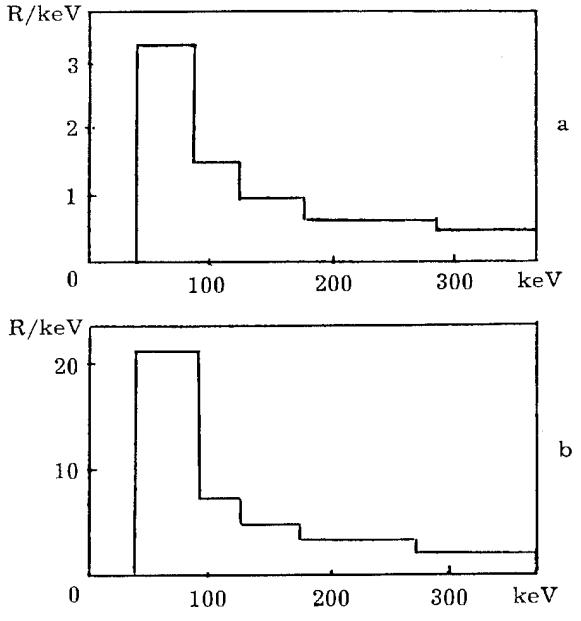


Fig. 5. Spectral X-ray distribution with various time-delays:

a - τ_3=4.5 μs, V_{PEOS}=60 kV;

b - τ_3=6 μs, V_{PEOS}=60 kV.

In all pulses, when time delay or PEOS powering voltage increases the moment of current transfer into a load is shifted to the area of larger times. When $t_3 \approx 9.5$ μs and $V_{PEOS} \approx 80$ kV the current transfer moment comes far beyond maximum of the storage current. It is associated with plasma density increase and hence PEOS critical current. As storage current does not increase any more the moment of transfer comes only when plasma disperses. In doing so X-ray rate drops sharply. The maximum X-ray rate, measured using TLD at the distance of 50 mm from a target, reached 2.5 krad.

To define spectral X-ray composition we used TLD spectrometer, comprising seven detectors based on aluminum phosphate glass with copper filters of various thickness. Detectors were located in an aluminum casing of a spectrometer at the radius of 45 mm. The task was solved by choosing a spectrum and comparing an absorption line, obtained on the basis of this spectrum, with the experimental curve. Fig. 5 gives spectral X-ray distributions with various time delays. Energy estimation in the range from 50 to 500 keV is 90 J for τ_3=4.5 μs and 270 J for τ_3=6 μs. The average quantum energy in the radiation spectrum of a plasma diode is from 70 to 100 keV.

REFERENCES

1. App. Phys. Left, 1983, v. 42, p. 943.
2. J. App. Phys., 1984, v. 56, p. 774.
3. A.I. Pavlovskii et al. Optimization Study for Characteristics of Pulsed Energy Sources with Plasma Switch, Sixth international conference on megagauss magnetic field generation and related topics. November 8-11, 1992, Albuquerque, New Mexico (USA), Book of abstracts, p. 207.
4. J. App. Phys., 1977, v. 48, p. 1970.
5. Shafranov V.D., sb. "Voprosy teorii plasmy", vyp. 2, M.: Atomizdat, 1963, pp. 92-131.

EXPERIMENTAL STUDIES OF ELECTRON BEAM EXPLOSIVE HIGH-POWER GENERATORS

A.I. Pavlovskii, N.F. Popkov, A.S. Pikar', E.A. Ryaslov, V.I. Kargin

All-Russia Scientific research institute of experimental physics (VNIIEF), Arzamas-16, Nizhni Novgorod region, 607200, Russia

INTRODUCTION

Megajoule pulse accelerators of charged particle beams, powered by capacitor banks, Angara-5, Hermes III and others have a weight of several hundred tons and the cost of their construction is hundreds million of dollars. Application of new, more energy-consuming energy sources, particularly, magnetocumulative generators (MCG) and explosive current opening switches enables to decrease dimensions, weight and cost of accelerators significantly.

The first results of experiments to power pulse iron-free betatron by a magnetocumulative generator were published in work [1].

Early 80-s were marked by beginning the work on creation of small megajoule accelerators with direct drive [2]. This paper is devoted to some interesting works made in the scope of this program.

In the process of we considered various circuits for powering the inductive accelerators, accelerators with a shaping line and direct driven accelerators with an inductive storage, using an MCG. The obvious advantage of a system with an inductive storage is the possibility to create facilities with the energy density up to 10^8 J/m^3. When current contour breaks and the energy commutates, high-volt high-power pulse is generated for the short time (~1 μs) This pulse is used to receive the beams of charged particles.

DESCRIPTION OF AN ACCELERATOR DESIGN

In all accelerator designs, considered in the paper, turned MC generator is used. The generator has a profiled current contour with a width of 160 mm, enabling to reach current pulses of 10 to 15 MA with the voltage of several tens kilovolts. To coordinate diode impedance with such a law-resistance energy source we used iron-free increasing transformer and a high-resistance helical opening switch with an explosive plasma or electric explosive opening component.

Fig.1 shows equivalent electrotechnical design of an explosive electron beam accelerator, related to a primary circuit.

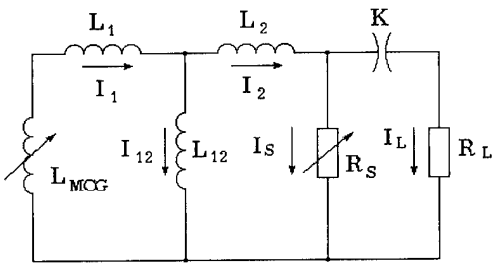
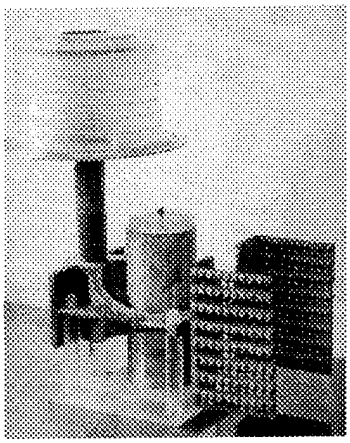
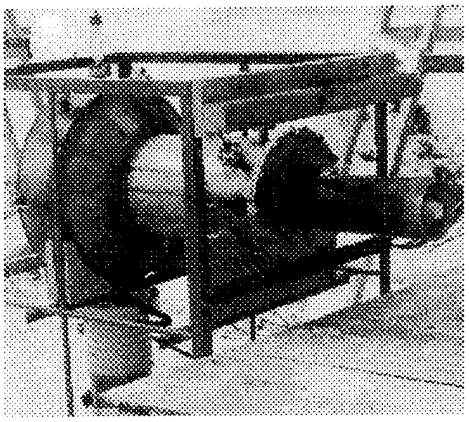


Fig.1. Equivalent electrotechnical design of an explosive accelerator, related to a primary circuit.

a



b



c

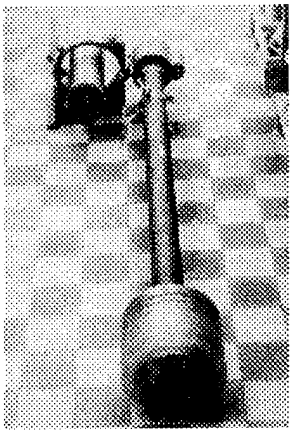


Fig.2. External sight of high-current electron beam accelerators, powered by MC generators:
a) L474-1 accelerator with an explosive plasma opening switch powered by a single-turned MC-generator (without an external current conductor); b) L475 accelerator with an explosive plasma opening switch powered by a three-turned MC-generator; c) L476 accelerator with an electric explosive foil opening switch.

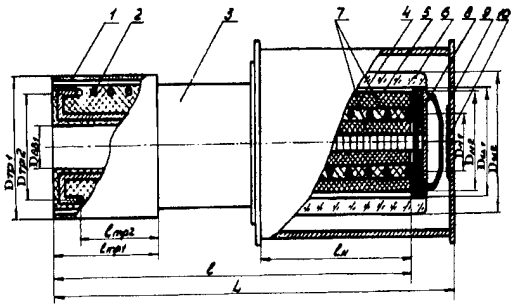


Fig.3. Structural design of L474-1 accelerator.
1 - the primary turn of a transformer; 2 - the secondary turn of a transformer; 3 - an external current conductor; 4 - a helix of an inductive storage; 5 - a plasma channel; 6 - the insulator of an accelerating tube; 7 - HE charge; 8 - a cathode; 9 - an anode; 10 - a target.

MC-generator is powered by a capacitor bank with 1.2-1.7 MA current. During the generator operation of 30 μs the current increases up to 10-15 MA. When the current contour is breaked by the switch R_s the voltage pulse is generated and the energy is transferred from the storage into the load R_L. Fig. 2 shows the external sight of the designs of three high-current electron beam accelerators, powered by MC generators.

Fig.3. shows structural design of L474-1 accelerator. A secondary winding of the transformer represents a helix made of a copper tube with an 40 mm external diameter and 2 mm wall thickness. Number of turns is 8.

The reverse current conductor of a secondary winding is a copper tube with a cut. A secondary winding of the transformer is connected to store inductance of an explosive helical opening switch. The explosive current opening switch represents

a cylinder of plexiglass with the length of 185 mm. The internal diameter of a cylinder is 210 mm, an external diameter is 270 mm. The internal surface has trapezoidal depressions at the length of 140 mm. The external surface of an opening switch serves as an insulator of an accelerating tube where a high-voltage electrode (cathode) is fixed.

A hollow cathode has an external diameter of 186 mm, an internal one of 90 mm, a surface, which faces an anode is 6°. A solid-state discharge opening switch of 2 mm thickness is located between an opening switch and a cathode. In addition to a solid state discharger a system has a mechanical closing switch, connecting discharge electrodes to an explosive opening switch, when it operates. Vacuum gap in a diode is 28 mm.

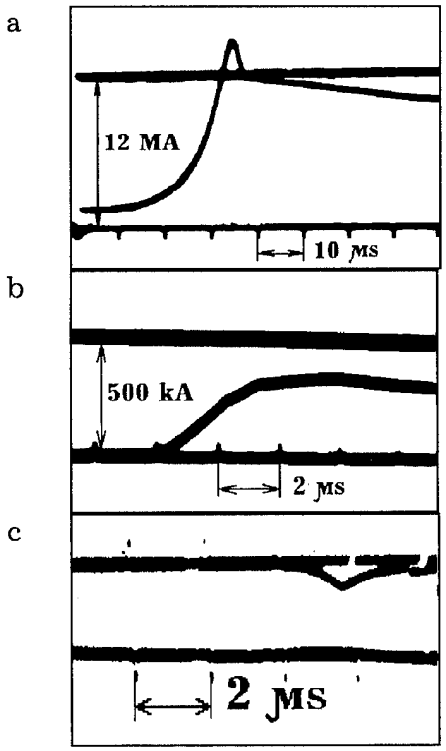


Fig. 4. Oscillograms of an experiment with L474-1 accelerator.
a) MC-generator current; b) diode current; c) X-ray radiation pulse.

EXPERIMENTAL RESULTS

Fig. 4 and Fig. 5 give typical oscillograms, received in experiments. The current of a MC-generator (L474-1) increases up to 15 MA and then during the time break of ~1 μs it decreases up to 12 MA. In doing so a beam of electrons with an amplitude of 200 kA is generated on a diode. The instant of X-ray pulse appearance correlates well with a diode current pulse.

For comparison all experimental results are tabulated.

	L474-1	L474-2	L475	L476
Number of turns	1	2	3	1
Inductance, nH	230	480	650	230
Transformation coefficient	8	7	5	18
Storage inductance, nH	770	770	1500	4200
MCG current, MA	15	12	10	10
Storage current, MA	0.9	1.1	0.8	0.36
Opening switch length, m	0.2	0.2	0.5	1
Storage energy, kJ	250	450	550	220
Voltage on an opening switch, MV	0.25	1.2	1.5	0.8
Diode current, kA	200	250	140	150
Pulse duration, μs	2	0.5	1.0	1.5
Beam energy, kJ	30	120	200	50

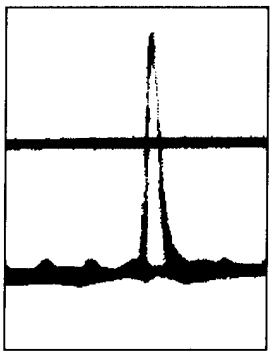


Fig. 5. Current derivative oscillogram of storage (L474-2) is 10^{12} A/s.
Time marks are 2 μs.

CONCLUSION

Analysis data, presented in a paper, shows that electron beam generators, powered by magnetic cumulative generators are better then those described in publications by compactness, transportability and specific energy characteristics.

The authors conducted experimental investigations of various arrangements and basic functional systems, they also made their optimization according to output parameters. All this confirms that it is very promising to create accelerators with electron energy of ~10^7 eV and beam current >10^6 A with energy supply of an inductive storage being several tens of megajoules.

The developed technology may be successfully used for creation relatively inexpensive machines with several tens megajoule energy store to power electron and ion diodes, plasma toroids, Z-pinches, etc.

REFERENCES

1. A.I. Pavlovskii, G.D. Kuleshev, R.Z. Ludayev, et al. Impul'snyj beszheleznyj betatron s pitaniem ot magnitokumulyativnogo generatora. Atomnaya energiya, 1976, t. 41, vyp. 2, s. 142-144.

2. A.I. Pavlovskii, N.F. Popkov, V.I. Kargin, A.S. Pikar', E.A. Ryaslov Magnetic Cumulation Generator As a Power Source to Accelerate Intense Electron Fluxes. - Megagauss Fields and Pulsed Power Systems, 1990, pp. 449-452.

ELECTRON ACCELERATOR WITH INDUCTIVE STORAGE FOR VIRCATOR LOAD

E.V.Chernikh,A.N.Didenko,K.V.Gorbachev,V.E.Fortov,
A.B.Ivanov,E.V.Nesterov,S.A.Roschupkin,V.P.Shumilin,
V.A.Stroganov,V.P.Tarakanov
High Energy Density Res.Centre
Russian Academy of Sciences
IVTAN,Izhorskaja,13/19,Moscow,127412,Russia
e-mail: karat@tarak.msk.su

Abstract

The vircator with the inductive storage scheme is studied. The experiment as well as numerical simulations indicate the strong influence of the power supply scheme on the vircator generation efficiency. The results 3-D numerical modelling of the vircator are presented.

Introduction

In recent years has been a strong interest in taking advantages of the inductive energy storages for powerful microwave pulses generation [1,2,3]. The use of the inductive storage permits to simplify essentially the design and to reduce the dimensions of the device. However, for the realization of these advantages it is necessary to use any effective interrupter of a current, as far as the oscillators of powerful microwave pulses, as a rule, represent systems with high current relativistic electron beams. One of the such current interrupters, which was well built up for itself in practice, is the electroexploding opening switch.

To preserve main advantage of an inductive storage, the primary source of energy should be adequate under specific power characteristics. For such a source one can use the magnetic flux compressor, which can transform the high explosive chemical energy in the electromagnetic energy effectively enough. However, such a generator is one-time energy source. That is why, for the research of the matching problems of the microwave oscillator with the inductive storage it is expediently to use the magnetic flux compressor simulator - pulse current generator.

Concerning to the oscillator of powerful pulses microwave radiation, the most acceptable in the considered scheme, on our sight, is the vircator [4]. The main advantage of this type of an oscillators is the absence of an external magnetic field.

The first attempts to realize in practice the considered above scheme (pulse current generator or magnetic flux compressor - inductance - electroexploding opening switch - sharpening gas switch - vircator)[3] came to the next problems: it has appeared that the process of microwave oscillation in the vircator differs considerably from that in conventional schemes, when as the sources of a voltage, the high current accelerators with forming lines are used [4]. This is because of

the time-delay between the beginnings of the oscillations and current and voltage pulses on the diode. The generation begins, as a rule, in a phase when the current and voltage decreasing. The efficiency in this case is rather low.

Experimental results

The research of the matching problems of the vircator with inductive storage were carried out on the installation which was described in [5].

The electrical circuit of the installation is shown on Fig. 1. The capacitance of the pulse current generator ($C = 3.2\mu F$) was charged up to the voltage U = 50-70 kV. The controlled gas switch S1 was filled in with a dry nitrogen (1-10 atm). The starting pulse on the switch control electrode was feeded from the pulse transformer. As the electroexploding opening switch (EOS) a set of the parallel copper wires with 50 mkm diameter was used. The switch was operated at the atmospheric pressure.

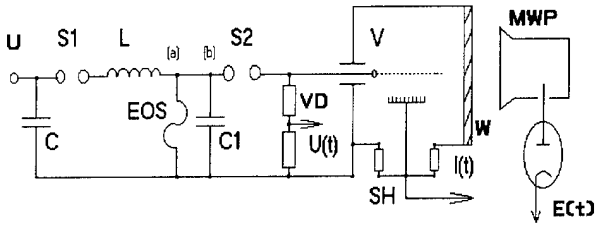


Fig. 1

After the switch S1 is closed, the current in a circuit of the EOS begins to flow, so the energy stores in the inductance (L=4.6 mkHn). At highest current the EOS is opened (wires are exploded) and, after the operation of the sharpening gas switch S2, the high voltage pulse is formed on the vircator (V) diod gap. As a result of the explosive emission, the high current electron beam is formed, which, when passing through the anode grid (transparent ability of the grid about 0.7) is forming the virtual cathode. The fluctuations of the virtual cathode and electrons vibrations between real and virtual cathodes can bring to the powerful microwave oscillations. This radiation is removed from the chamber through the organic glass window (W) to the open space.

The main electrophysical parameters (currents and voltages) in various parts of the installation as well as microwave radiation characteristics were measured. As far as we are interested in the vircator oscillation regime, in a set of electrophysical parameters we shall note only the diode voltage (U(t)) and current (I(t)). The U(t) value was measured by a high-voltage two-step divider (VD). The high-voltage shoulder of VD was executed as bifillar conductor, been made on the nichromium wires. The beam current was measured by the cathode shunt (SH). The signals from gauges were transmited through the delay cable line to the fast oscilloscope (6 LOR-04 M), been located in the screened room.

The parameters of the microwave radiation: the waveform of the electrical field ($E(t)$), total energy and frequency were recordered. As the waveform probe (MWP), the high-frequency tube diode was used, the signal from which was recordered on oscilloscope 6 LOR-04 M too. The total microwave energy was measured by the calorimeter [6] and the microwave frequency was determined with the help of the acoustic delay-line [7].

As it was shown [5], the faster forward pulse front does not cause the reduction of a delay-time of the oscillations, but brings to the increasing of the power. Thus, in the inductive storage scheme, it is possible to generate the current and voltage pulses on the vircator diode with the peak values and front-times being close to that, received with the help of conventional forming lines. However, the level of the radiation power in this case is much lower. For the explanation of this fact it is possible to assume the

existence in a vircator two modes of oscillations, which can be characterized by various electrons beam bunching degrees, hence, the efficiency of oscillations can be different. The mode with an effective oscillations can be received only in the situation when in a system (vircator plus a source of a high-voltage pulse) some certain conditions are realized. One can assume that these conditions are linked with the realization of some instability in the system.

For the illustration of this idea, let us consider the next simple model. In the RLC-circuit with variable load resistance $R(t)$, the apperiodic instability is possible if $dR/dt < -1/C$. This means that the instability is developed only in the case, when the load resistance decreases in time enough quickly. The electronic diode in some approximation represents nearly such a situation, i.e. on the forward front of the pulse, the conditions for the development of an instability in a system can be satisfied. The inductive storage scheme can be described as the parallel connection of the monotonous time decreasing resistance of a diode and the EOS resistance, increasing monotoneously in time. The total resistance of the load, growing in the initial phase, then starts to drop. The negative time derivative of the resistance dR/dt will be less then in the case of the diode and the instability can not be realized, decreasing the efficiency of generation. The correction of the situation is possible by using the sharpening capacitance (C1 on Fig. 1. It is constructive capacitance between an internal screen and the chamber of the installation. C1 = 1.2 nF in our case). To increase the efficiency of the sharpening capacitance it is possible when the additional switch between points (a) and (b) Fig. 1 exists.In this case the generation time delay was a little decreased, but the efficiency was increased essentially [5].

KARAT simulation

The process of electromagnetic radiation was simulated numerically by the fully electromagnetic PIC code **KARAT** [8]. At first let us consider the results of the 2.5-D axisymmetric simulation. On Fig.2 the cross section $(z - r)$ of a device with the beam particles and the phase plane $(Pz - z)$ are shown.

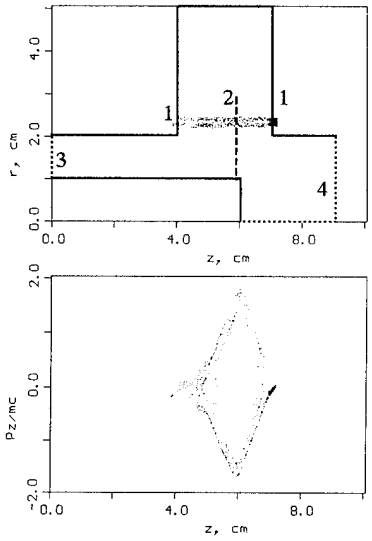


Fig.2

The voltage between the cathode (marked in 1) and anode foil (2) was generated by launching through the left coax (3) of the TEM wave from two different sources. In the first case this coax was as the load for the LC-circuit with inductance $L = 1.\mu Hn$ and capacitance $C = 5.pF$. At the initial time this capacitance was charged to $.5MV$. Then a discharge through the inductance and the coax with beam load on the right hand began. In the second case on left hand of coax the voltage source was defined. The time averaged voltage evolutions coincide nearly in both cases. The main distinguish is the different reflection conditions for microwave on left hole. As the result, the electric field amplitude of the generated mode increases two times.

Also the 3-D simulation of the vircator by code **KARAT** [8] was performed. On Fig.3 the cross sections $(x-z)$,$(y-z)$ $(y-x)$ of a device with the beam particles and the phase plane $(Px-x)$ are shown. (Big points correspond to the mesh boundary points. The region marked in 3 at right hand correspondes to the region with finite conductivity.)

The shape and sizes of the simulation region correspond to the experimental installation. The generation of the electromagnetic radiation on the frequency $3.-4.GHz$ (the experimental results are $3.-3.2GHz$) is seen.

Acknowledgments

The authors would like to thank to Ermolenko A.V. and Zajtsev B.D. for the help in the frequency measurements, Kamenskiy V.A. and Zherlitsin A.G. for the help, fruitful discussions.

The work supported by the Russian Fund of Fundamental Res.(93-02-14604).

References

[1] Brodskij A.Ya., Vdovin V.A., et.al., Dokl.Acad.Nauk USSR, v.314, No.4, 846-849, 1990.

[2] Azarkevich E.I., Didenko A.N., et.al., Dokl.Acad.Nauk USSR, v.319, No.2, 352-355, 1991.

[3] Azarkevich E.I., Didenko A.N., et.al.,- Microwave pulses from chemical energy of high explosive. Preprint, Chernogolovka, 1992.

[4] Didenko A.N., Zherlitsin A.G., et.al., Pis'ma v J.Tech. Phys., v.3, No.24, 1510-1513, 1983 (Russian).

[5] Chernikh E.V., Didenko A.N., et.al.,- Euro Electromagnetics, Bordeaux, France, May 30 - June 4, 1994. (to be published).

[6] Shkvarunets A.G., Rukhadze A.A., Strelkov P.S. - Broad band relativistic plasma microwave oscillator. 4th Interstates Symposium on Plasma Electronic. 8-10 September 1993, Kharkov. Plasma Phys. (Russian, to be published).

[7] Guljaev Yu.V., Ermolenko A.V., et.al., Dokl.Acad.Nauk USSR, v.305, No.6, 1372-1374, 1989.

[8] Tarakanov V.P., *User's Manual for Code* **KARAT**, BRA,Inc., V.A.,USA,(1992).

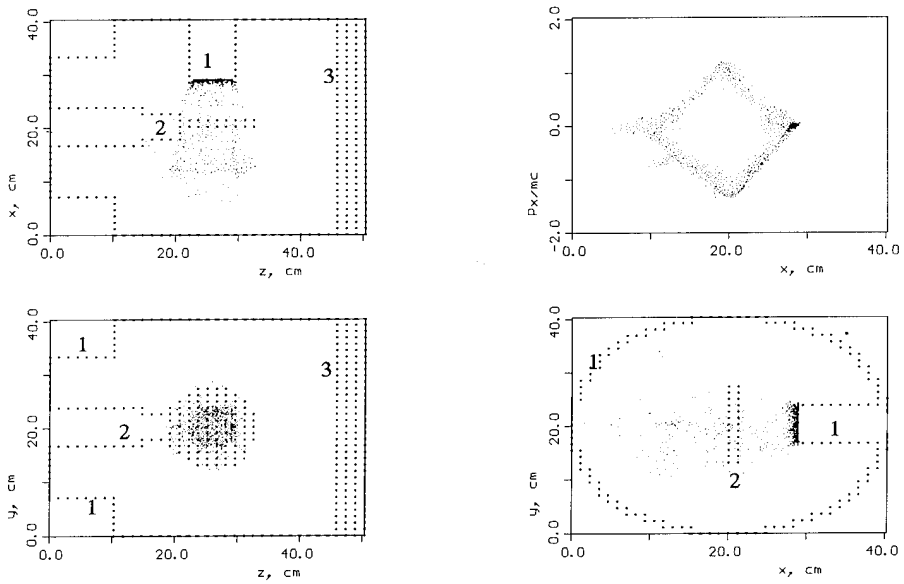


Fig.3

ACCELERATION OF INTENSE ION BEAM BY Z-PINCH

H. U. RAHMAN, P. NEY

IGPP University of California, Riverside

F. J. WESSEL N. ROSTOKER AND V. M. BYSTRITSKII

Department of Physics University of California, Irvine

The Z-pinch is considered for acceleration of an intense ion beam. The imploding Z-pinch traps an applied axial magnetic field and conserves trapped magnetic flux. The axial magnetic field increases due to compression of the outer pinch and attains values up to 10's of Megagauss with field risetimes of, $dB_z/dt > 5$ MG/ns, and with orders of magnitude shorter rise time than the Z-pinch current. For ion beam acceleration, low energy ions are initially injected and trapped inside this rising magnetic field. Due to the conservation of canonical-angular momentum the ions are accelerated to a final azimuthal energy which can be a hundred to a thousand times greater than their initial energy ($E_{\theta final} \geq 10$'s of MeV/amu). Such a beam of high energy ions could have many applications, including the production of intense X-ray radiation, radio-nuclides, fusion, etc.

INTRODUCTION

Annular Z-pinches are known to compress the trapped magnetic flux to very high field intensities at an extremely fast time scale. A schematic of the magnetic flux compression by Z-pinch is illustrated in Figure 1. In this scheme an annular Z-pinch plasma implodes onto an axial B_z-magnetic field compressing it to multi-Megagauss fields with at least an order of magnitude shorter rise time than the Z-current. The rise time of the compressed axial magnetic field is a few ns. Key features of such flux-compression Z-pinches have been studied on a small-scale pulsed-power source at UC-Irvine[1-3] and on higher power machines in the USSR[4] and at Sandia National Laboratories.[5] The measured axial fields were 1.6 MG (UCI), 2.5 MG (USSR) and 40 MG (Sandia). The axial magnetic field compressed on such a short time scale and of high intensity can be effectively used to accelerate intense ion beams up several 100 MeV. Figure 2 illustrates schematically the injection, trapping and acceleration of such an intense ion beams. An axial magnetic field is injected into the pinch discharge region and shaped near the cathode electrode producing a mirror configuration. An oppositely directed magnetic field is applied inside the ion source so that a magnetic-cusp exists between the two pulsed-power systems. The cusp magnetic field configuration is necessary for the injection and trapping of the ion beam by the axial magnetic field trapped inside the Z-pinch plasma shell. After the magnetic fields are established the ion-beam accelerator is energized, injecting ions through the magnetic cusp. The axial velocity of the ion beam is reduced as it passes through the cusp, converting axial energy into rotational. After exiting the cusp the ions pass into the axial-magnetic field and are trapped inside the Z-pinch plasma shell. The rotating-ion beam encounters a mirror-magnetic field (at the upstream cathode electrode) where it conserves canonical-angular momentum and reflects. At a prescribed moment, when the length of pinch is filled by the ion beam, the pinch generator is energized so that the liner begins to accelerate and implode radially inward.

In the process of implosion the ion beam azimuthal velocity increases and the diameter of the ring decreases, due to field compression, reducing the ion loss-cone angle. The ions in the beam will also be accelerated by the induced electric field in the θ-direction by the rapid change of magnetic field.

In high-energy ion-beam sources the

ions are observed to emerge charge and current neutralized. Sudan[13] has considered this problem for the case of a compressed neutralized ion ring. The presence of neutralizing electrons are crucial for the injection and trapping of the ion beam in the axial magnetic field that is compressed by the hollow Z-pinch plasma. Once the beam is trapped, electrons provide only a neutralizing background without affecting the dynamics in any significant way. From the conservation of angular momentum, simple scaling laws can provide estimates of azimuthal velocity $U_\phi = U_0(r_0/r)$, ion beam energy $\epsilon = \frac{1}{2}Nm_iU_\phi^2 = \epsilon_0(r_0/r)^2$, and ion current $I_i = I_{i0}(r_0/r)$ where r_0 is the initial radius and r is the final radius of the ring. Assuming a compression ratio $(r_0/r)^2 = 1000$, and the length of the compressed beam $L = 4$ cm, the total energy of the beam would increase from W_{i0} = 23 kJ to W_{if} =23 MJ after ring compression. This requires a magnetic field of order, $B_{zf} = 55$MG.

Dynamic Model

The simplest dynamic model assumes a thin-shell implosion of an annular Z-pinch with an entrained magnetic field and a trapped ion beam. The dynamic equation of motion for the outer liner is written as

$$\frac{d^2R_1}{dt^2} = -\frac{I_p^2}{100M_1R_1^2} - \frac{R_1}{4M_1}[B_0^2 - B_z^2 - < B_{zs} >^2 (\frac{R_2^2}{R_1^2 - R_2^2})], \quad (1)$$

where R_1 is the liner radius, I_p is the pinch current, M_1 is the mass per unit length of the liner and B_0 is the initially applied axial magnetic field. The compressed magnetic field is $B_z = B_0(R_0/R_1)^2$, the self magnetic field due to the ion beam is $< B_{zs} > \approx cL(I_i + I_e)/\pi R_2^2$, where $L = 4\pi^2R_2^2/lc^2$ is the inductance per unit length for the ion shell, $I_i = ZNev_{i\phi}$ is the ion current, $I_e = -ZNev_{e\phi}$ is the electron current, N is the number of ions per unit length and R_2 is the radius of the ion beam shell. The pinch current $I_p = I_{max}\sin^2(\pi t/2t_{1/4})$ is assumed again.

The azimuthal momentum balance and radial force balance for a nonrelativistic ion shell are given by

$$\frac{dv_{i\phi}}{dt} + \frac{v_{i\phi}}{R_2}\frac{dR_2}{dt} = -\frac{Ze}{m_icR_2}\frac{d}{dt}(R_2A_{i\phi})$$

$$= -\frac{Ze}{m_ic2\pi R_2}\frac{d}{dt}[\pi R_2^2B_z + cL(I_i + I_e)], \quad (2)$$

$$\frac{d^2R_2}{dt^2} - \frac{v_{i\phi}^2}{R_2} = \frac{Ze}{m_i}\{E_r + \frac{1}{c} < v_{i\phi}(B_z + B_{zs}) >\}. \quad (3)$$

The electrons have a small gyroradius and will simply drift according to

$$\mathbf{E} + c^{-1} < \mathbf{v}_e \times (\mathbf{B} + \mathbf{B}_s >= 0. \quad (4)$$

The electrons drift radially inward with the beam and the ϕ and r components of the electron equation furnish

$$E_r + c^{-1} < v_{e\phi}(B_z + B_{zs}) >= 0, \quad (5)$$

$$E_\phi + \frac{1}{c}\frac{dR_2}{dt} < (B_z + B_{zs}) >= 0, \quad (6)$$

Equation (6) states that the azimuthal electric field in the frame moving radially inwards with the ion shell vanishes which ensures that the flux linked by the ion shell remains constant, i.e.,

$$\pi R_2^2B_z + L(I_i + I_e) = \Phi_0 = \pi R_{2i}B_{zi} + L_0I_0. \quad (7)$$

where R_{2i} and B_{zi} are the initial values, and the electron current is taken to vanish in the initial state. From equations (2) and (7) we obtain

$$v_{i\phi} = v_0(\frac{R_{2i}}{R_2}), \quad (8)$$

$$I_i = I_0(\frac{R_{2i}}{R_2}), \quad (9)$$

Substituting equation (5) in equation (3) and taking the averages, the radial equation of motion for the ion shell can be written as

$$\frac{d^2R_2}{dt^2} - \frac{v_{i\phi}^2}{R_2} = \frac{L(I_i+I_e)^2}{2\pi R_2^2 m_2} + \frac{B_z}{m_2 c}(I_i+I_e), \quad (10)$$

where $m_2 = Nm_i$ is the mass per unit length of the ion shell. Equations (1), (8), (9) and (10) completely defines the problem of the beam compression by a Z-pinch.

These equations are numerically solved for the parameters of two point designs: $M_1 = 30\mu$gm/cm, $I_z = 1.5$ MA, $B_z = 50$ kG, $t_{1/4} = 150$ ns, $R_1 = 2$ cm, $L_{pinch} = 1$ cm, initial ion energy, $E_{i0} = 100$ keV (i.e., 90 % of the injection energy), number of injected ions, $N_i = 10^{14} cm^{-1}$, using protons, and for $M_1 = 38\mu$gm/cm, $I_z = 10$ MA, $B_z = 50$ kG, $t_{1/4} = 50$ ns, $R_1 = 4$ cm, $L_{pinch} = 1$ cm, $E_{i0} = 50$ keV, $N_i = 10^{13} cm^{-1}$, using protons again. These optimized initial conditions insure that the ion trajectories are initially contained within the liner and that the implosion occurs at maximum current.

For the 1.5 MA case, Figures 3a-h display the results for the outer-column radius, ion-shell radius, their respective velocities and the ion energy as a function of time. The outer Z-pinch liner reaches a final radial velocity of, $V_{lf} = 0.03$ cm/ns and radius, $R_{1f} = 4$ mm (Figures 3a,b). The ion shell achieves slightly smaller values of radial velocity and final diameter (Figures 3c,d). As shown the final azimuthal velocity of the ions approaches, $V_{\phi f} = 2.0$ cm/ns, for an equivalent energy of, $E_{if} = 2.3$ MeV/nucleon (Figures 3e,f). About 30% of the liner-kinetic energy is converted into ion-azimuthal energy. The remaining energy is stored in the compressed-magnetic field.

Figures 4a-h display the results computed for the 10 MA case, in which the outer Z-pinch liner reaches a final-radial velocity of, $V_{lf} = 0.4$ cm/ns and final radius of, $R_{1f} = 1$ mm (Figures 4a,b) and similarly for the ion ring (Figures 4c,d). As shown in Figs. 4e,f the final-azimuthal velocity of the ions approaches $V_{\phi f} = 15$ cm/ns for an energy of 150 MeV/nucleon. The efficiency of energy conversion from the liner into ion azimuthal energy is 50 %.

Stability Issues

During the acceleration of the outer Z-pinch the Rayleigh Taylor instability grows like, $\xi = \xi_0 \exp(\gamma t)$, where $\gamma = \sqrt{kg}$, k is the wave number of the perturbation, $g = B_z^2/8\pi m$, m is the mass/unit area of the Z-pinch. Since the distance over which the outer Z-pinch accelerates is $s \simeq 0.5gt^2$ we obtain, $\xi \simeq \xi_0 \exp\sqrt{2sk}$. This instability can be controlled by minimizing the initial perturbation ξ_0 and the distance s over which the outer Z-pinch accelerates. Since the outer Z-pinch in this geometry traps an axial magnetic field and compresses it to an extremely high value, the B_z and B_θ components of the magnetic field combine to produce a magnetic shear near the outer surface of the Z-pinch. The sheared magnetic field should stabilize the outer surface of the Z-pinch. The inner surface should become unstable when it is decelerated by the trapped B_z field. However, in this case the deceleration takes place over a very short distance of the order of, $a_0 = 200$ μm. Therefore, this instability will not grow to a level where it can disrupt the plasma shell and deteriorate the implosion. Our earlier experiments of flux compression has shown a stable implosion in similar geometries.

There is an additional stabilizing effect due to increasing the mass of the Z-pinch as it "snowplows" during acceleration. Since the wavenumber is related to the radial-mass gradient (i.e., proportional to the inverse of the liner-shell thickness), thicker shells are predicted to be more stable. Moreover, since the plasma becomes highly collisional at final stagnation betatron oscillations of the ring will not occur and the ring should be stable.

Conclusion

In this paper we proposed and calculated an effective method of accelerating intense ion beams from the initial energies of few ten's of keV to final energies of 100's of MeV/amu. Acceleration of the ion beam is obtained by a rapidly rising magnetic field during the compression of the magnetic flux by a fast annular Z-pinch imploding plasma. Another advantage of this method is that the

beam current also amplifies due to the ring compression. The energy of the ions goes as R_0^2/R^2 whereas the current goes as R_0/R. Such intense ion beams can be used for inertial confinement fusion (ICF)[9], manufacturing of the nuclear isotopes for medical applications, intense nonthermal X-ray sources and basic physics research. Preliminary investigations show that the implosion of such a configuration may not be subjected to the severely disruptive instabilities that are commonly observed in standard Z-pinches. The complete calculations of instabilities and the multi-dimensional numerical modelling is the next objective.

Acknowledgments. This research wa supported by the Department of Energy, Office of Fusion Energy.

References

1. H. U. Rahman, P. Ney, F. J. Wessel, A. Fisher and N. Rostoker, Proc. 2nd Int. Conf. on High Density Pinches, Laguna Beach, April 26-29 (1989), AIP Conf. Proc., p. 351.
2. F. J. Wessel, F. S. Felber, N. C. Wild, H. U. Rahman, E. Ruden and A. Fisher, Appl. Phys. Lett. **48**, 1119(1986).
3. F. J. Wessel, N. C. Wild, A.Fisher, H. U. Rahman, A. Ron and F. S. Felber, Rev. Sci. Instrum. **57**, 2247(1986).
4. F. S. Felber, F. J. Wessel, N. C. Wild, H. U. Rahman, A. Fisher, C. M. Fowler, M. A. Liberman, A. L. Velikovich, J. Appl. Phys., **64**, 3831-3845(1988).
5. N. A. Ratakhin, S. A. Sorokin, S. A. Chaikovsky, Proc. Seventh Int. Conf. on High Power Particle Beams,Vol. II, 1204, (1988), and S. A. Sorokin and S. A. Chaikovsky, AIP Conf. Proc. (1989), N. R. Pereria, J. Davis, and N. Rostoker, Editors, p. 345.
6. F. S. Felber, M. M. Malley, F. J. Wessel, M. K. Matzen, M. A. Palmer, R. B. Spielman, M. A. Liberman and A. L. Velikovich, Phys. Fluids, **31**, 2053, (1988).
7. R. N. Sudan and E. Ott, Phys. Rev. Lett. **33**, 355(1974).
8. J. Bailey, Y. Ettinger, A. Fisher, and N. Rostoker, Appl. Phys. Lett. **40**, 460(1982); J. Appl. Phys. **60**, 1939(1986).
9. R. N. Sudan, Laser and Particle Beams, **11**, 415(1993).

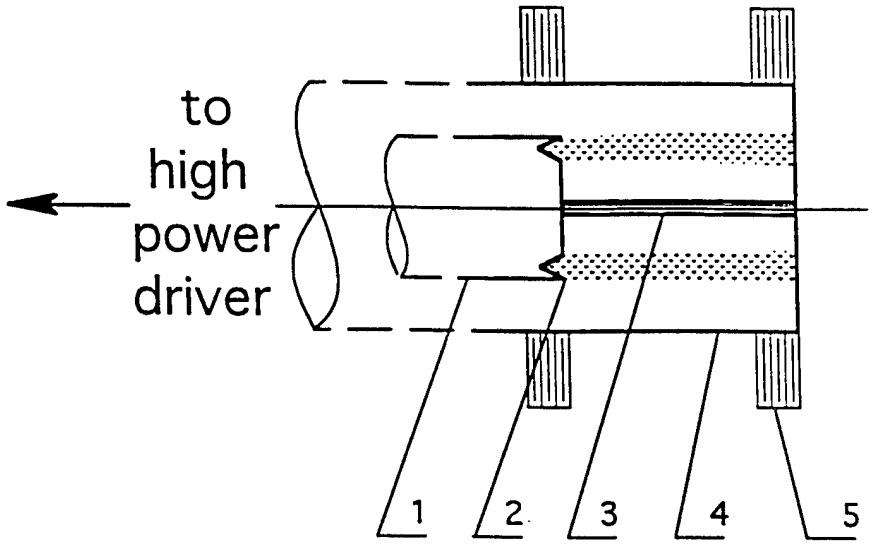


Figure 1. Schematic configuration of the Z-θ pinch: 1) cathode electrode (injector/ nozzle/ support), 2) imploding-outer liner (gas- puff/plasma jet/or foil), 3) co-axial target (cryogenic, deuterium-tritium fiber), 4) anode electrode (return-current conductor), 5) Helmholtz magnetic-field coil.

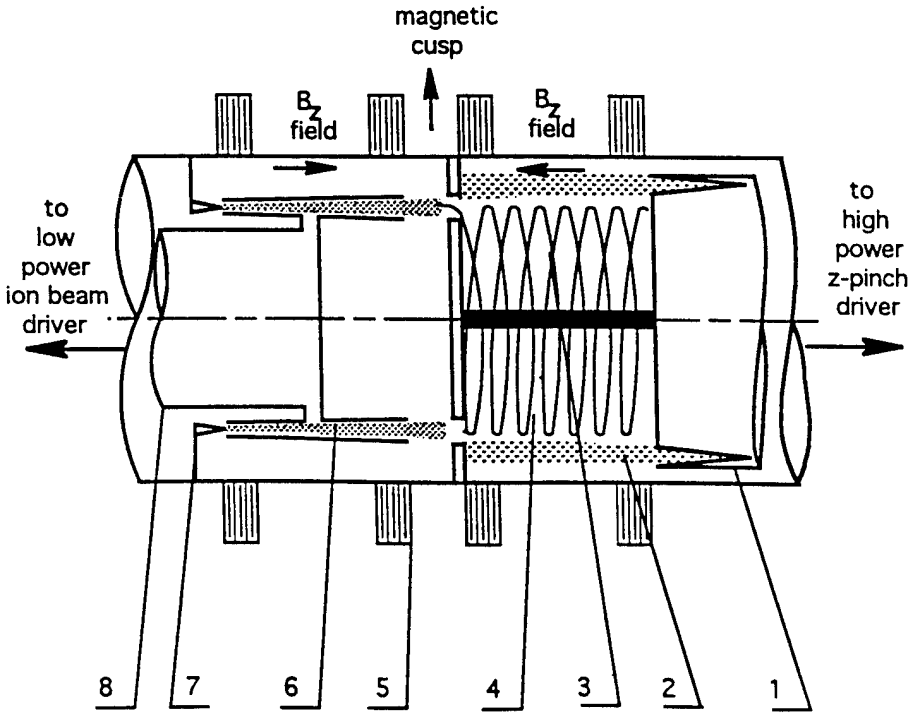


Figure 2. Schematic illustration of the staged pinch for ion acceleration: 1) Z-pinch electrodes (injector/ nozzle/ support), 2) imploding-liner (gas-puff/plasma jet/or foil), 3) coaxial target, 4) trapped ions, 5) Helmholtz magnetic field coil, 6) ion beam, 7) cathod, 8) anode.

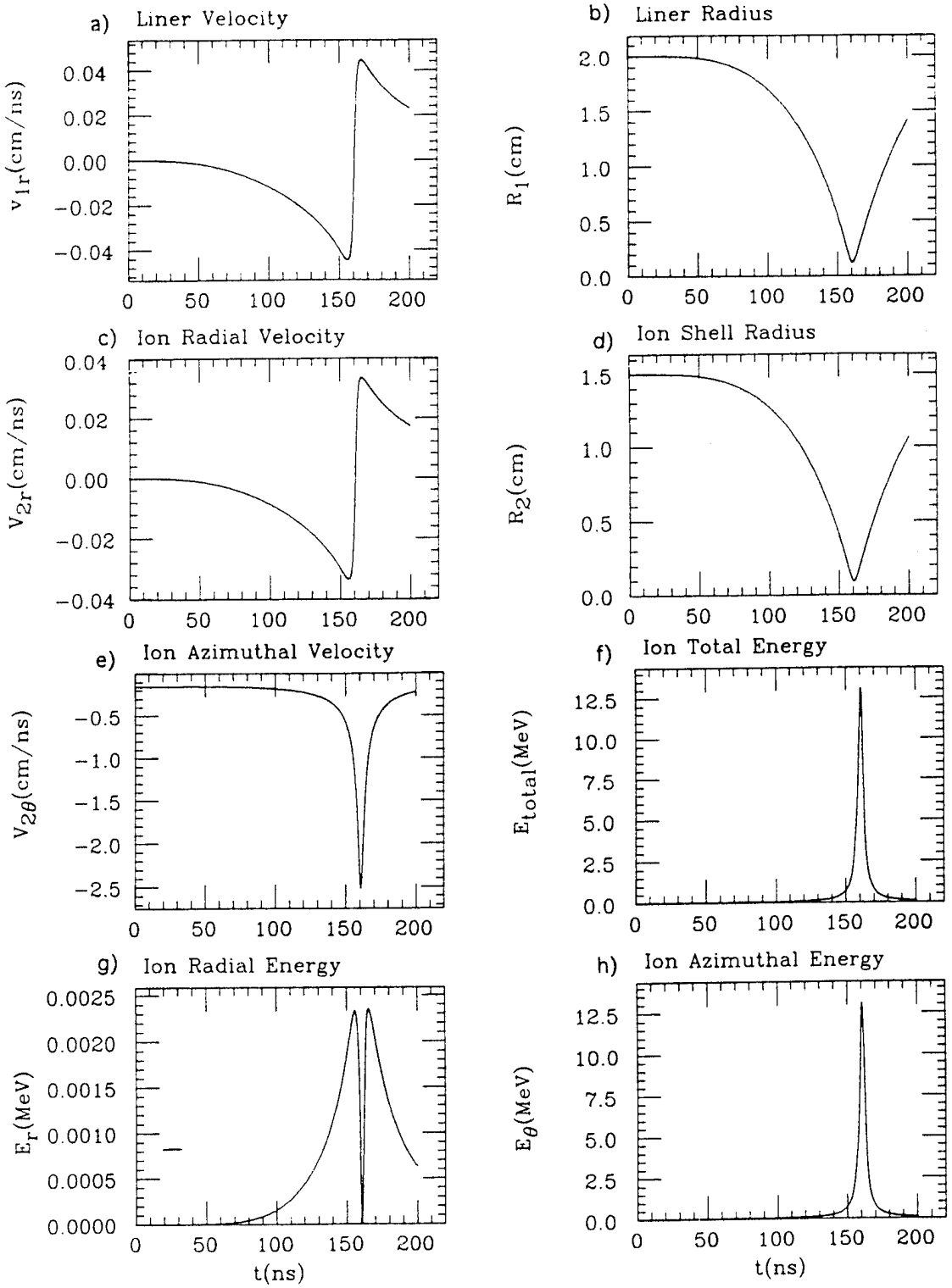


Figure 3. Implosion dynamics for the SRX fielded on the UCIrvine Z-pinch: a) outer liner velocity, b) outer liner radius, c) ion radial velocity, d) ion shell radius, e) ion azimuthal velocity, f) ion total energy, g) ion radial energy, h) ioin azimuthal energy. Initial conditions: I_z = 1.5 MA, B_z = 2.2 T, R_1 = 2 cm, R_2 = 1.5 cm, M_1 = 0.06 x10^{-3} gm/cm, N_i = 10^{15} cm^{-1}, E_{io} = 113 keV, He^{+2}.

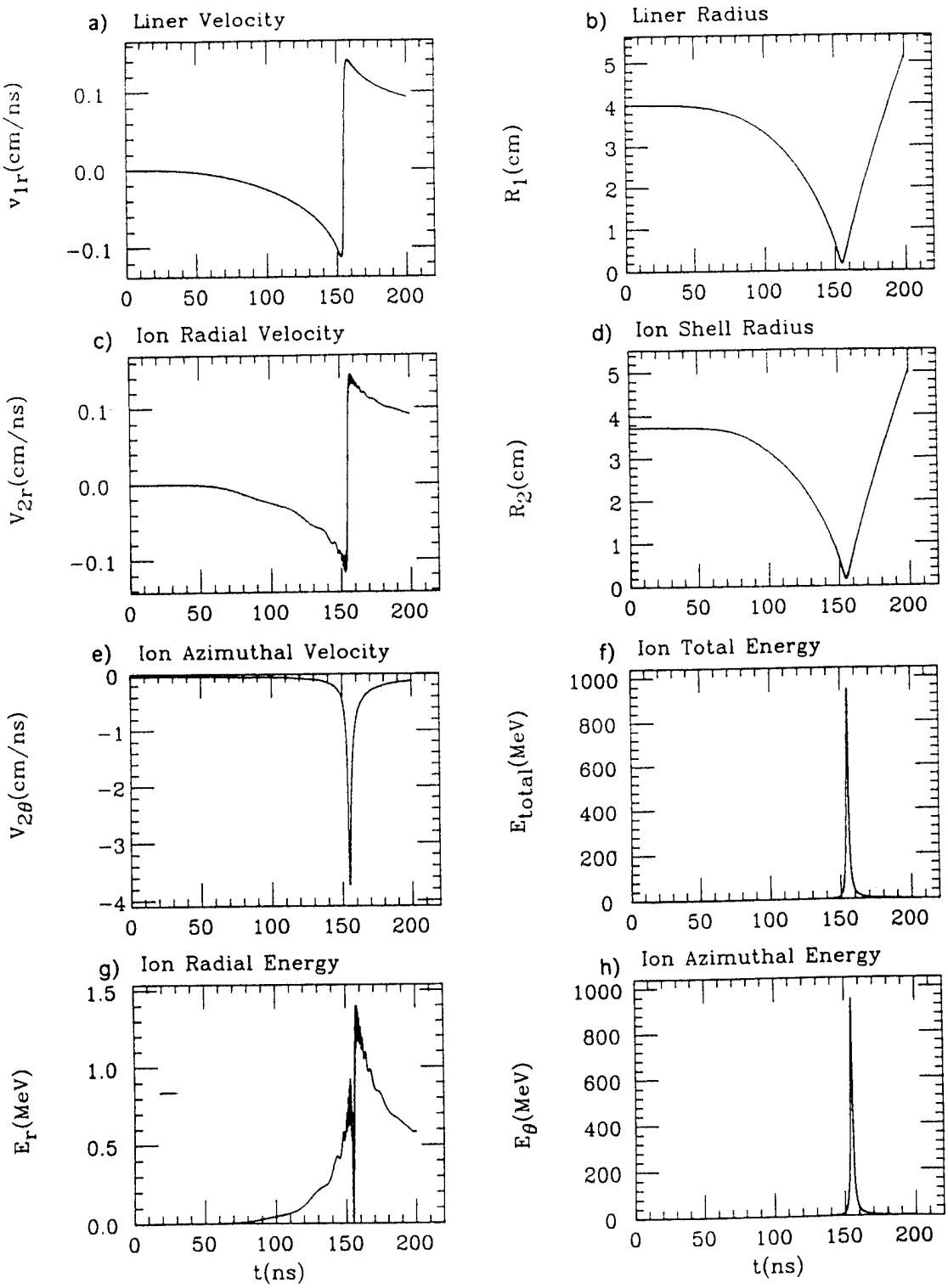


Figure 4. Implosion dynamics for the SRX fielded on the Jupiter Z-pinch: a) outer liner velocity, b) outer liner radius, c) ion radial velocity, d) ion shell radius, e) ion azimuthal velocity, f) ion total energy, g) ion radial energy, h) ion azimuthal energy. Initial conditions: I_Z = 60 MA, B_Z = 5.5 T, R_1 = 4 cm, R_2 = 3.8 cm, M_1 = 22 x10^{-3} gm/cm, N_i = 4 x10^{16} cm^{-1}, E_{io} = 880 keV, Xe^{+8}.

Recent TWOQUICK Particle Simulations of One- and Two- Stage Transmission Lines and Diodes on PBFA and SABRE*

J. W. Poukey, M. E. Cuneo, and T. R. Lockner
Sandia National Laboratories
P. O. Box 5800
Albuquerque, NM 87185-1186

Abstract

This paper presents recent particle simulation studies of the pulsed-power machines PBFA and SABRE. The code used is the 2-D electromagnetic TWOQUICK. For SABRE we emphasize the single-stage case and compare with experiment. Here the voltage adder, magnetically-insulated-transmission-line (MITL), and proton applied-B extraction diode are all included in the fully time-dependent simulations. Results include vacuum wave precursor effects vs. cathode turn-on threshold, and the sheath-retrapping benefits of diode undermatching. For PBFA we emphasize the 2-stage case and compare with experiments using lithium ions. Here we include the transmission lines and MITLs feeding the 2-stage barrel diode. Results show that good operation is critically dependent on careful B-field shaping in the feeds and diode.

In this paper we discuss recent particle simulation studies done for the ICF program at Sandia using the 2-D PIC electromagnetic code TWOQUICK.[1] In support of recent experiments, we make "realistic" models of the Sandia pulsed-power device PBFA[2] and SABRE,[3] including voltage adders, MITL feeds, turn-on thresholds, and careful approximations to the applied magnetic fields as separately calculated by R. S. Coats using the ATHETA code.[4]

For PBFA we emphasize the 2-stage system,[5,6] with a lithium ion barrel diode. Each stage of this diode is fed by a transmission line with the final section matched in impedance to the PIC region, where electron losses are explicitly calculated. Output analyzed includes voltages, currents, and B fields vs. time at positions of interest, together with the usual electron and ion flow maps. Preliminary comparison with specific early PBFA 2-stage shots looks reasonable. It appears that the shape of the B-lines in the diode and feeds is critical to obtaining efficient operation.

Figure 1 shows the configuration and electrons in a typical simulation in cylindrical geometry, assuming no θ-variation. An artificially short input voltage waveform (10 ns rise to 4.5 MV, 10 ns flat, 10 ns fall) is fed into each stage on the rhs of Fig. 1 using a transmission line model to simulate the feeds and stack region of PBFA. The pulse enters the PIC simulation region at z = 28 cm. Stage 1, between anode A and "midplane" M, emits electrons from M and lithium ions Li^+ from A in $0 < z < 3$ cm, as seen in Fig. 2. The Li^+ pass through foil F_1 where they may be stripped to Li^{+3} (not included in this run), then through foil F_2 into a gas cell (vacuum cell in this run). Stage 2, between M and cathode K, further accelerates the ions with (in principle) little increase in divergence.

Figures 1 and 2 illustrate the operation and some of the problems encountered with this type of setup and applied B. Although stage 1 is fairly good (about 10% current loss), stage 2 shows larger loss (360 kA) and somewhat reduced voltage. Also, examination of ion phase space plots shows that at this high current level (740 kA max), the ions near F_1

are slowed and a few are reversed in radial velocity (partial virtual anode VA). Also, some are lost to the wall due to space-charge spreading.

Figures 3 and 4 show a recent simulation with an improved B (applied), provided by R. Coats.[4] Note also the "curved" anode, to help flatten B in gap 2. The electron map in Fig. 3 shows only a very small loss in both stages. The large I_i = 1.1 MA peak in Fig. 4 does not form a VA; there is no reversal of radial velocity and negligible wall loss. As seen in Fig. 4, the diode voltage on stage 2 is slightly larger than in stage 1, a good result (input voltage = 5 MV per stage with pulse shape and transmission line feed model as before).

For positive-polarity SABRE, we model the voltage adder, MITL extension, and applied B proton extraction diode. Generally, we show good comparisons with some measurements, some discrepancy with others. We also compare well with the flow-impedance model of C. Mendel.[7] Voltage precursor effects dominate both MITL operation and diode impedance history. (See paper by M. Cuneo et al.,[8] this conference.) Undermatching the diode impedance to the self-limited line operating impedance can be optimized with the simulations to yield maximum diode power. Using realistic input voltage waves into the adder gaps, the system is followed for about 100 ns. Beside the usual output, cathode electric field plots are of particular interest, particularly after the main pulse has reflected from the diode load. Parameter variations include emission thresholds, radial gaps, and diode V_{crit}. The pressure $r^2(E^2 - c^2B^2)$ is found to be independent of radius r, as predicted by Mendel.[7]

The setup for a typical TWOQUICK run of SABRE is shown in Fig. 5. Into each of the 10 feeds we input the experimental voltage waveform of 0.75 MV (max). Figure 5 shows the (saturated) electron flow at 48 ns. At 48 ns, the forward magnetically insulated voltage wave (indicated by electron front) has not reached the load (rhs), but by 72 ns the reflected wave is causing some retrapping of the electrons. The load here is an applied-B proton diode, barely visible in Fig. 5 but shown in detail in Fig. 6. Note that this is an extraction diode, unlike the barrel diode used in PBFA. For the case of Figs. 5 and 6, we obtain a diode voltage peak of 4.3 MV and I_i of 0.2 MA, as seen by the time plots in Fig. 7. Unfortunately, we also obtain a large vacuum wave "precursor" pulse. One of our main goals is to understand and eliminate this undesirable precursor.[8]

Table I shows some parameter studies. Cases 45, 56, 48, 74, and 67 show that the precursor amplitude is roughly proportional to E_{thr}, the threshold field for emission turn-on at the cathode. We have found that the precursor can be nearly eliminated by lowering E_{thr} in the MITL (last 4m in Fig. 5) to 30 kV/cm. Basically, early sheath production causes the insulation wave to be a larger fraction of the forward wave. This suggests one way of eliminating the precursor in SABRE, namely field-enhancing inserts on the cathode. (The other way is to add a plasma opening switch near the load to erode the precursor.) For details, see ref. 8. Some other conclusions can be drawn from Table I and other parameter studies done over the past year with TWOQUICK: (1) the diode can be calculated independently of the feeds and MITL, to a fair approximation, for proper input;[9] (2) coupling from line to diode is somewhat sensitive to design of the electrodes and applied B in the diode; (3) protons emitted in the MITL can be used as a voltage diagnostic; (4) the diode impedance must be undermatched by the proper amount (roughly a factor 2 below the vacuum Z_0)[3] for good ion efficiency; (5) jitter in the input feed pulses of up to ± 10 ns is not a problem; (6) the present radial gaps in SABRE are not optimal - better voltage and less loss can be obtained with gaps based on the pressure-balance model of Mendel and

Rosenthal;[10] and (7) a 5-10 ns cathode turn-on period "fills in" the gap between vacuum and insulated wave (Fig. 7) in qualitative agreement with experiment.[3]

Table I. SABRE runs with TWOQUICK. All these cases had a proton-diode load with the experimental B (applied) of shot 589 (provided by R. Coats). Input V = 0.75 MV/ feed peak. AK gap in diode is 9 mm. r_A = radial gaps in feed region, pb = pressure balance design [ref. 10], V_p = precursor amplitude. Table shows peak V and I. "d" = diode, "i" = ion.

Run	V_c^{MV}	r_A	$E_{thr}^{kV/cm}$	I_d^{MA}	V_d^{MV}	I_i^{MA}	V_p^{MV}
45	7	exp	10	.23	4.4	.22	0
48	7	exp	200	.22	4.4	.22	2
50,55	10	exp	200	.21	5.1	.21	2
51,59	7	exp	300	.23	4.5	.22	3
52	5	exp	200	.26	3.3	.25	2
56	7	exp	100	.24	4.2	.23	1
60	0	exp	300	.32	1.8	.03	1/2
65	7	pb	300	.22	4.8	.21	3 1/2
67	7	exp	400	.25	4.0	.24	4
72	7	exp	300	.25	4.1	.24	4
74	7	exp	300	.24	4.3	.22	3

We have also used TWOQUICK to attempt the design of a possible 2-stage system for SABRE, using the existing hardware to the extent possible. The load is now a 2-stage extraction diode. We have been only partly successful. Without discussing details here, the essential problem is the design of a B-field (with or without midplane coils) which allows good line-to-diode coupling, substantial enhancement of I_i, and simultaneously prevents large losses in the feeds of both stages. Although there are other possible setups to be tried, our main-line approach has been essentially the addition of a "midplane" to Fig. 5 and 6. Generally, the resulting electron losses along the B-lines in the feeds near the diode have been prohibitive.

References

*This research was supported by Martin Marietta/U.S. Dept. of Energy under contract DE-AC04-94AL85000.

1. D. B. Seidel and T. D. Pointon, to be published.
2. N. A. Krall and S. E. Rosenthal, J. Appl. Phys. 70, 2542 (1991).
3. M. E. Cuneo et al., "Observation of Reflected Waves on the SABRE Positive Polarity Inductive Adder MITL," Proc. IEEE 1993 Pulsed Power Conf., Albuquerque, NM, 1993.
4. R. S. Coats, J. P. Quintenz, and D. B. Seidel, ATHETA User's Guide, Sandia Labs Memo, Aug. 1993.
5. T. R. Lockner, S. A. Slutz, J. W. Poukey, and W. Stygar, "Theoretical and Experimental Studies of the 2-Stage Ion Diode," Proc. IEEE 1993 Pulsed Power Conf., Albuquerque, NM, 1993.
6. S. A. Slutz and M. P. Desjarlais, J. Appl. Phys. 67, 6705 (1990).
7. C. Mendel et al., J. Appl. Phys. 71, 3731 (1992); Proc. Beams 92, Vol. I, p. 449 (1992).
8. M. Cuneo et al., "Control of a Large Vacuum Wave Precursor on SABRE,"this conference.
9. S. E. Rosenthal, IEEE Trans. Plas. Sci. 19, 822 (1991).
10. C. W. Mendel, Jr., D. B. Seidel, and S. E. Rosenthal, Laser and Part. Beams 1, 311 (1983).

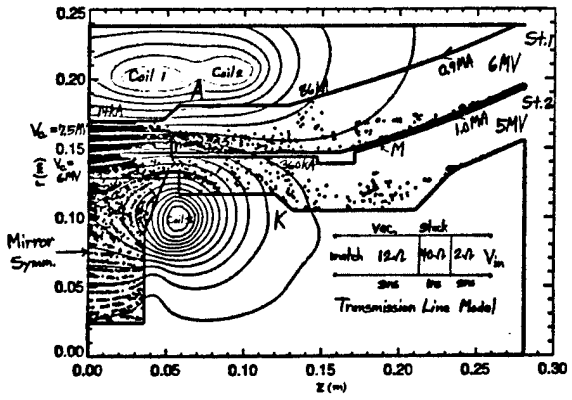


Fig. 1 PBFA 2-stage simulation at t = 30 ns using TWOQUICK. Electrons and B-lines (applied) are shown. Input voltage wave enters from rhs; it is calculated from a transmission line model representing feed lines and insulator stack and matched to the PIC region in each stage. A = anode, M = midplane separating stages, K = cathode. The B field is generated by three coilsets. The lhs boundary is mirror symmetry, i.e., only half the system is simulated. The foils F are taken to be perfect conductors which are transparent to all particles. Result of this run is 5.7 MV (stage 1), 4.0 MV (stage 2), with ion current = 740 kA (max).

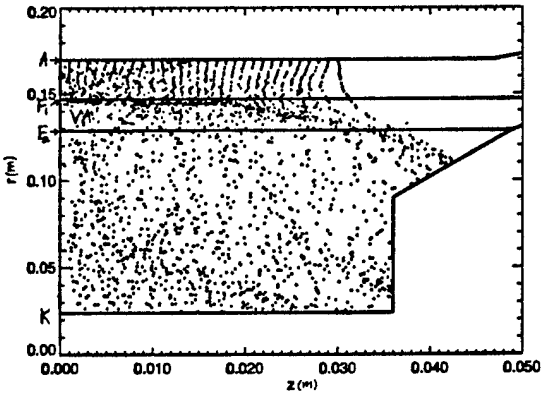


Fig. 2 Li^+ ions for case of Fig. 1. No stripping in foils. Note expansion of ion beam in z and partial VA.

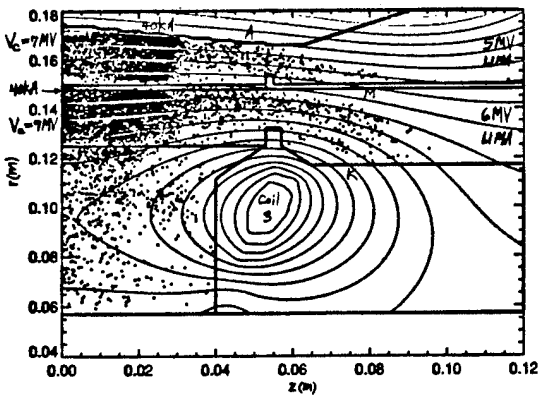


Fig. 3 A recent PBFA simulation with improved B-field design. The electrons at 27 ns and applied-B are shown. Both stages have acceptably small electron losses. Note curved anode and flatter B in stage 2.

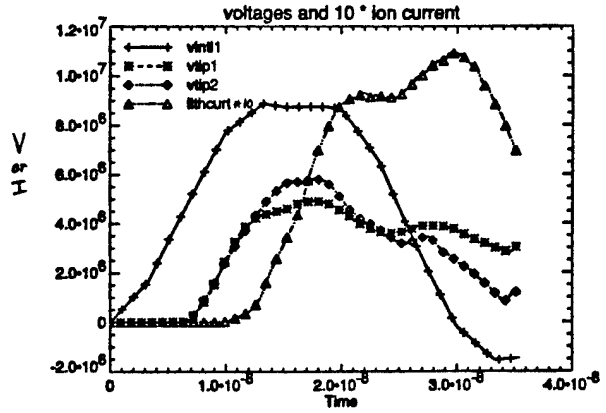


Fig. 4 Voltages at transmission line input (vint/1) and on diodes for both stages (Vtip) and ion current vs. time (lithcurt) for "improved" case in Fig. 3. $I_i(t)$ is multiplied by 10.

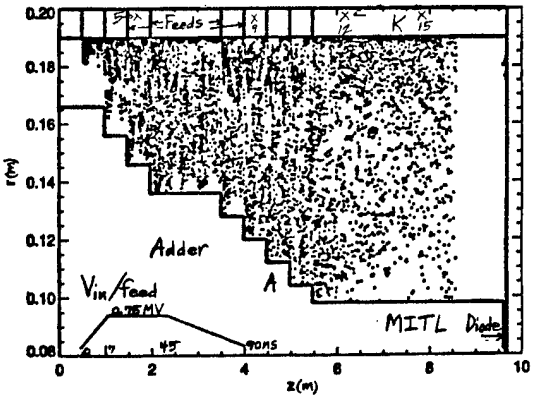


Fig. 5 SABRE single stage run with TWOQUICK. Electron map is shown at 48 ns. Input voltage = 750 kV per feed. "Probes" shows position of some of the B dots in the experiment. The diode load can barely be seen on the rhs.

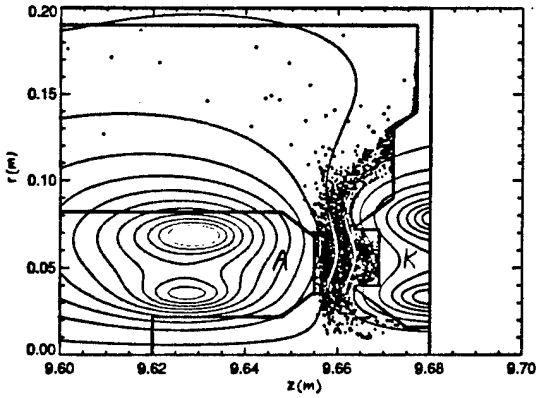


Fig. 6 SABRE extraction diode at 72 ns for case of Fig. 5 (run 74, Table I). Shown are electrons and B-lines (V_C = 7 MV).

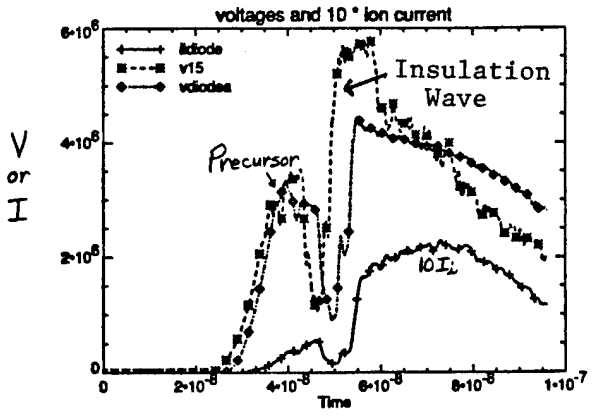


Fig. 7 Time dependence of V(probe 15), V(diode), and ion current for SABRE run 74. Note precursor.

Extraction Ion Diode Studies for Optimized Performance: Divergence, Ion Species, and Parasitic Load*

J. B. Greenly, R. K. Appartaim, J. C. Olson and L. Brissette
Laboratory of Plasma Studies, Cornell University

Recent advances worldwide in pulsed ion beam generation with magnetically-insulated ion diodes in annular extraction geometry have brought several issues to the forefront in the search for optimal performance from these diodes. Beam divergence, ion species composition, and diode impedance and power coupling behavior are all issues of central concern in obtaining the best possible beams from these sources. The LION pulser(1.2 MV, 4 Ω, 40 ns) at Cornell University has been used to investigate several aspects of these issues. The basic experimental approach is to vary diode operating parameters, and to diagnose the resulting changes in diode performance. The LION diode is shown in Fig. 1. Diagnostics include beam current density(magnetically-insulated Faraday cups), ion species-resolved beam divergence(Rutherford-scattering shadowboxes), ion species and energy composition (Thomson parabola spectrometer, Rutherford-scattering magnetic spectrometer), diode voltage and current diagnostics(rogowskii and B-dot current monitors, inductive divider and electron-launching voltage monitors), electron loss detection(collimated bremsstrahlung detectors and in-anode collectors), and in-gap light emission(visible light streak photography and emission spectroscopy).

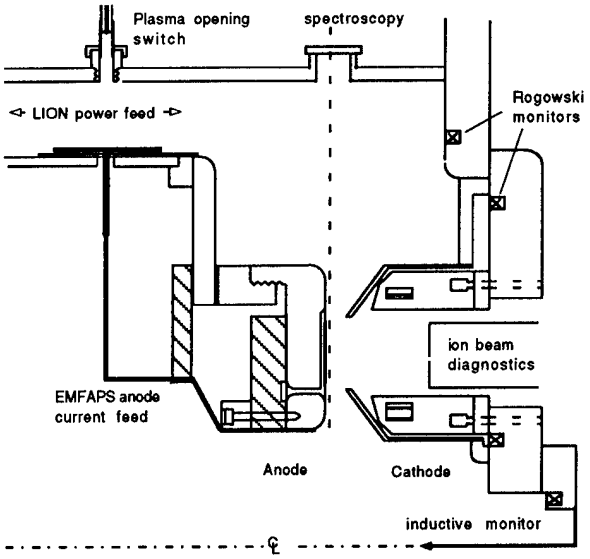


Figure 1: LION applied-B extraction ion diode

Of the basic diode operating parameters, the strength of magnetic insulation has the strongest effect on performance. Beam divergence and power coupling are always at their best with strong insulation, that is, with $V/V_{crit} < 0.4$, where V is diode voltage and V_{crit} is the critical voltage for loss of magnetic insulation. Other diode conditions, such as use of an electron limiter on the anode, or differing ion source conditions, also have clear effects. Lowest divergence of 22 ± 3 mrad HWHM(pinhole shadowbox) for protons is obtained at an enhancement(ion current density J over the Child-Langmuir value J_{cl}) < 10. This can be achieved either with a limiter or with an active anode at low V/V_{crit}. Protons are always observed to have higher divergence than heavier species (mostly carbon) in mixed beams. The lowest divergence observed has been 15 ± 2 mrad, for the heavier species in mixed beams from passive anodes at low enhancement, measured by the imaging of the anode groove structure in the Rutherford-scattering magnetic spectrometer.

Recently, an investigation has been made into the effects of ablation and hole closure on aperture-based diagnostics. It is clear that small apertures are substantially altered, even early in the pulse, by ablated material, and that typical apertures of 0.5 mm diameter introduce

energy loss, charge-changing, angular scattering and even total cutoff of some ion species in these beams of >1 MV, >1 kA/cm^2. Hole closure is affecting all of our diagnostics with submillimeter pinholes. Vaporizing stainless steel requires an energy input of approximately 10 kJ/g. Early in the LION pulse the non-protonic component of the beam is well-described as 1 MeV carbon ions at up to 1 kA/cm^2. This is sufficient to vaporize a carbon range of stainless steel(about 0.8 μm) in 5-10 ns. If, for instance, half of this material moves into the hole, then carbon ions will be scattered by >60 mrad and protons by >8 mrad, while the effective diameter of the hole may also change. Thus the pinhole shadowbox divergence measurements, which are not corrected for these effects, are not quantitatively reliable, although we believe that the comparisons among different operating regimes are qualitatively reliable. Efforts continue to develop a local microdivergence diagnostic that avoids this problem.

Two types of Faraday cup ion current diagnostics are used on LION. Originally, small aperture(0.5 mm dia.), electrically biased and magnetically-insulated cups were located in the insulating field, about 1 cm from the anode. In a series of similar shots we sequentially increased the aperture size of a Faraday cup from 0.5 mm to 5 mm, and observed the duration of the current pulse seen by the cup to increase with aperture size up to at least 3 mm. The increase in signal duration is consistent with a hole closure velocity of 0.7 cm/μs due to ablated material. To avoid closure effects, we have constructed new, large aperture(5 mm) magnetically-insulated Faraday cups. The cup current is measured by a small, low-inductance resistor(0.1 Ω) to prevent self biasing. Large aperture cups are located in the insulating field at 3.5 cm from the anode, and 21 cm downstream from the anode in a permanent magnet field. The downstream Faraday cups allow us, to some extent, to examine the various species present in the beam by time of flight separation.

We are also employing a time resolved Thomson parabola spectrometer to study the ion beam. Time resolution is achieved with a circuit that applies a steady voltage to the plates in the spectrometer, then shuts off the voltage quickly($\approx$2 ns) when the circuit is triggered. By combining timing information on the shutoff with time of flight information derived from the diode voltage, we can determine, for ions arriving at the shutoff time, the charge states in the spectrometer and the charge states in the accelerating gap. We can also detect energy loss *én route* to the detector. Targets from the time resolved Thomson parabola show that ions have lost energy and changed charge *én route* to the detector, probably due to closure of the primary aperture.

A major recent focus of Lion experiments is the so-called "parasitic" load. Fig. 2(b) illustrates the parasitic load as originally identified: a deficit in ion beam current as measured by standard Faraday cups during the latter part of the pulse. It is now clear that this deficit is due to the hole closure effects described above. No such deficit is seen with the large-aperture cups. However, the degree of the deficit with small-aperture cups is strongly affected by the diode operating conditions. The LION diode uses either passive epoxy-filled grooved anodes, or active EMFAPS(evaporating metal foil anode plasma source) anodes. With low V/V_{crit} and optimized EMFAPS anodes driven in such a way as to give minimum possible time between plasma initiation and diode voltage, there is essentially no deficit, while with EMFAPS driven so as to produce copious plasma before the diode voltage is applied, a very severe deficit can be produced. With passive anodes and $V/V_{crit} < 0.5$, this deficit is nearly absent with 6.5 mm gap(Fig 2(a)), but is large with 5.5 mm gap as shown in Fig. 2(b). Although it is true that larger deficits always occur in regimes with higher ion currents, we believe that the deficit is not mainly due to worse Faraday cup hole-closure with higher currents. We find instead, that there is an important difference in beam composition between these two cases, and we now define the "parasitic load" by this difference. Our working definition of the "parasitic load" is a change in beam composition toward high charge states of heavy ion species. When

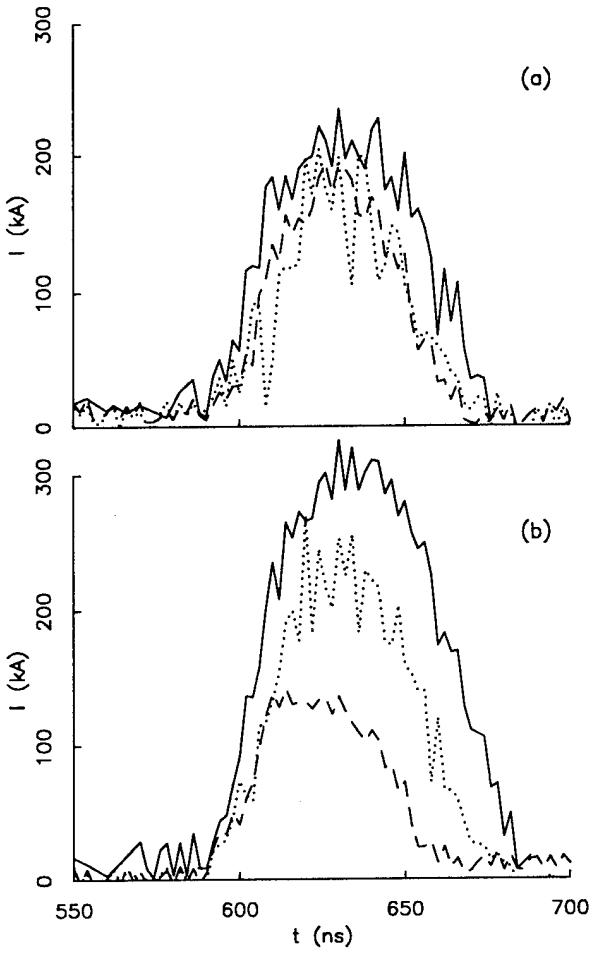


Figure 2: Currents in the (a) non-parasitic load case and (b) parasitic load case. Solid curve is the diode current, dotted and dashed curves are the current inferred from large and small aperture cups respectively.

this change occurs, the small-aperture Faraday cup closure prevents these species from entering, and the current "disappears". When this change is absent, the substantial proton fraction of the beam can penetrate the cup throughout the pulse. There is no evidence as yet for any substantial fraction of ions with far less than the full gap energy. Our evidence for this change is as follows.

On parasitic load shots, the time resolved Thomson diagnostic shows a notable absence of carbon accelerated as singly ionized in the diode. The downstream Faraday cups likewise end at an early time, consistent with the arrival of higher charged, faster moving ions like C^{3+} and C^{4+}. On non-parasitic load shots, signals from the downstream cups last well into the arrival times of C^{2+} and C^{1+}, and the Thomson parabola detects ions accelerated as C^{1+}. There are downstream cups at three radial positions(2, 4.5, and 7 cm); the radial distribution is more uniform in the parasitic load case, also consistent with larger deflection of higher ion charge states. The Rutherford-scattering magnetic spectrometer shows that the proton fraction in the beam is essentially zero below 500 kV(late in the drooping voltage pulse) in the parasitic load case, while in the non-parasitic load case proton current persists to the end of the pulse. In both cases heavier ions persist to the end.

Spectroscopic diagnostics in the diode gap are being used to investigate the mechanism of the parasitic load. The diode plasma emission in the visible region has been observed using a 1 m, $f/10.4$ monochromator and photomultiplier viewing along a line of sight parallel to the anode. Using emission lines identified in time-integrated photographs of the plasma spectrum, the temporal behaviour of neutral and ionic species has been studied. The most important results are as follows.

Successive ionization stages of carbon are seen to appear at successively later times during the voltage pulse(Fig. 3). CIV appears at the time of the parasitic load. The relative suppression of low charge states in parasitic load regime is shown by the OII 4414.9Å line in Fig. 4.

A comparison of typical continuum radiation for parasitic and non-parasitic load shots is shown in Fig. 5. A higher continuum level is seen during the power pulse in the non-parasitic load case. At the pulse end, the intensity becomes higher in the parasitic load case.

By moving the line of sight into the gap in 1 mm increments, the spatial distribution of the plasma has been investigated. The plasma appears to be confined to a region <1.5 mm from the solid anode in both parasitic and non-parasitic regimes.

The most salient feature of the spectroscopic data from passive anodes is the sudden strong

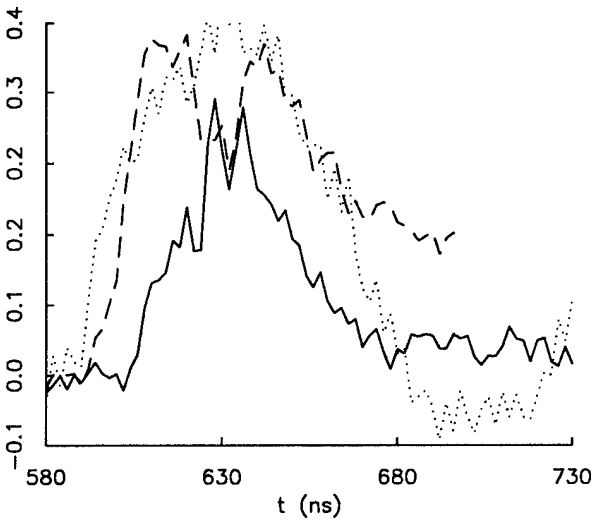


Figure 3: CII 4267Å(dashed) and CIV 5801.5Å(solid) emission, diode current (dotted)

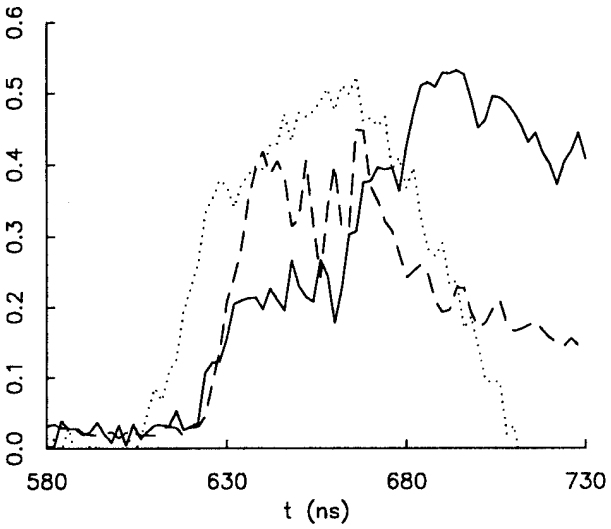


Figure 4: OII 4414.9Å line emission in the parasitic(solid) and non-parasitic(dashed) cases, diode current(dotted)

increase in intensity of emission lines from higher charge states of carbon(eg, CIV) characteristic of the parasitic load. These species appear to be produced in the anode plasma, which remains within about 1 mm of the anode surface, rather than out in the gap, and thus appear to indicate a sudden strong increase in ionization of the anode plasma at this time. Conversely, low charge states like OII are reduced in the parasitic case early in the power pulse, also consistent with increased ionization,

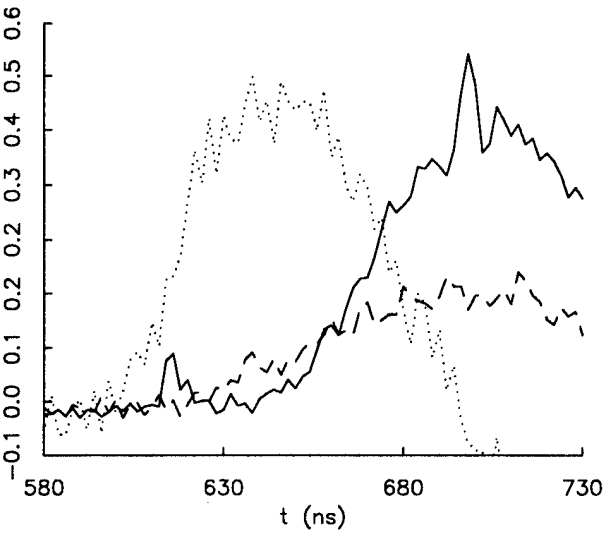


Figure 5: Continuum emission in the parasitic(solid) and non-parasitic(dashed) cases, diode current(dotted)

and appear strongly only at the pulse end, when recombination should occur. The continuum radiation, which should be produced by recombination, is lower during the power pulse in the parasitic case, consistent with stronger anode plasma ionization. We believe the primary candidate for the source of this energy input to the anode plasma is current driven in the plasma, which is larger with the higher ion current density and higher enhancement and electron diamagnetism in the parasitic load regime. A PIN diode bremsstrahlung diagnostic has not revealed any enhanced electron loss in the parasitic load case. Electron loss to the anode plasma surface rises with the ion current, peaks strongly during the maximum rate of rise of ion current, and falls to a low level after peak ion power.

In conclusion, optimal power coupling, divergence, and proton fraction in LION experiments all occur with enhancements below about ten and current densities below about 1.5 kA/cm^2. The mechanisms that degrade performance, while their details remain uncertain, are always associated with diode conditions beyond these limits.

*Supported by Sandia National Laboratories.

Impedance Characteristics of Multistage Ion Diodes

Michael Desjarlais
Sandia National Laboratories
P. O. Box 5800
Albuquerque, NM 87185-1186

Abstract

We further develop a theory of multistage diodes that includes the possibility of emission of ions in the final stage. The exact solutions are extremely cumbersome and are not practical for most applications. We have developed approximate solutions that are very accurate, require no integrations, and may be rapidly calculated using a simple iterative scheme. These solutions for the total current as a function of voltage are used in time-dependent modeling of a two-stage diode.

Introduction

Multistage ion diodes offer the possibility of independent control of voltage and current, improved divergence, and higher beam energy. If the beam current density being injected into a given stage is sufficiently large, the emitted current in the latter stage can be shut off through the formation of a virtual anode. These conditions allow the maximum transfer of power into the desired injected beam. However, these conditions can be difficult to achieve and depend on the electron distribution in the latter stage. Under some conditions, ions will be emitted in secondary stages. This emission diverts available power away from the injected beam and can significantly reduce the release of stored inductive energy during the latter half of the injected beam pulse.

In this paper we develop a theory of the impedance characteristics of multistage diodes that includes the possibility of emission of ions in the final stage. This provides us with a total current (injected plus emitted) characteristic for the latter stage. Solutions are obtained for two different electron distributions: a very thin electron sheath referred to as the superinsulated model, and a constant electron density between the virtual cathode and the anode referred to as the saturated model. The exact equations that are solved to obtain the emitted current in the final stage are exceedingly cumbersome for practical application, requiring root-solves over one or more imbedded integrations. We present here an approximate representation of these equations that is very accurate and which can be rapidly solved using a simple iterative scheme requiring no integrations. The solutions are suitable for time-dependent calculations; an example is shown.

This paper builds directly on previous work in Refs. 1 and 2. Because of the limited space here and the complexity of the material, we will refer frequently to those papers. The notation, geometry, and coordinate system used here are the same as in the earlier work. (See Ref. 2.)

Superinsulated electron sheath

In order to develop the total current characteristic for the latter stage of a two stage system, we would like to solve for the extracted ion beam consistent with a known injected beam, the diode voltage, and the diode parameters. We start the analysis for the approximate solutions from Poisson's equation in Eq. (4) of Ref. 2.

$$\frac{d^2\phi}{dx^2} = k_e^2(x) - \left(\frac{j_b}{\sqrt{w+v-\phi}} + \frac{j_x}{\sqrt{v-\phi}} \right). \quad (1)$$

Note that here the normalized injected beam j_b and the normalized extracted beam j_x are kept explicitly. The first integration of Poisson's equation over the dynamic gap g yields

$$g = \frac{1}{2}\int_0^v d\phi \left[j_b \left(\sqrt{w+v-\phi} - \sqrt{w} \right) + j_x \sqrt{v-\phi} \right]^{-\frac{1}{2}}. \quad (2)$$

Defining

$$\tilde{j} = j_b + \frac{j_x \sqrt{v-\phi}}{\sqrt{w+v-\phi} - \sqrt{w}} \quad , \quad (3)$$

treating it as a constant, and taking it out of the integrand, leads to

$$\begin{aligned} g\sqrt{4\tilde{j}} &= \int_0^v d\phi \left(\sqrt{w+v-\phi} - \sqrt{w} \right)^{-1/2} \\ &= v^{3/4} \Lambda_{si}(0) \end{aligned} \quad , \quad (4)$$

where

$$\Lambda_{si}(0) = \frac{4}{3}\left(\sqrt{1+\frac{w}{v}} + 2\sqrt{\frac{w}{v}} \right) \sqrt{\sqrt{1+\frac{w}{v}} - \sqrt{\frac{w}{v}}} \, . \quad (5)$$

Solving for $\tilde{j}$,

$$\tilde{j} = \left(\frac{\Lambda_{si}(0)}{2} \right)^2 \frac{v^{3/2}}{g^2} \, . \quad (6)$$

Using Eq.(3) as a guide, we look for solutions of the form $j_x = f(v, w)\left(\tilde{j} - j_b \right)$ that preserve the exact solution in the limits $w \to \infty$, $j_b = 0$, and $w = 0$. These conditions are met by

$$j_x = \frac{16}{9\Lambda_{si}^2(0)} \left(\tilde{j} - j_b \right), \quad (7)$$

for $\tilde{j} > j_b$. The dynamic gap g is given by (see Refs. 1 and 2.)

$$\frac{g}{d} = \frac{d - x_x}{d - (x_x / F_{si})} \, , \quad (8)$$

where $F_{si} \approx \sqrt{1 - (v/v_1(\Gamma))^2}$. Γ is the ratio j_x/j_b. For $v_1(\Gamma)$ we introduce another approximation

$$v_1(\Gamma) \approx v_1(0) + \left(\frac{\Gamma}{\Gamma + \alpha_{si}\sqrt{v_c/w}} \right)^{1/2} (v_* - v_1(0)) \, , \quad (9)$$

where $\alpha_{si} = 0.42$ and $v_* = 0.75 v_c$. The quantity $v_1(0)$ is from Eq. (11) of Ref. 1 and is given by

$$\frac{v_1(0)}{v_c} = \frac{3}{4} + \frac{3w}{2v_c} - \left[\left(\frac{3w}{2v_c} \right)^2 + \frac{3w}{4v_c} \right]^{1/2} . \quad (10)$$

The solution is now reduced to a simple iteration of Eqs. (9) (starting with $\Gamma = 0$) and (7) (using (6) for $\tilde{j}$ and (8) for g). The result from (7) gives a new Γ for (9). In practice the iterations converge more smoothly if 25% of the new guess for Γ is combined with 75% of the old guess for Γ. The results of an example calculation for four different injected beam currents (the $V = 0$ intercept) are shown in Fig. 1. There is very good agreement between the exact and approximate solutions.

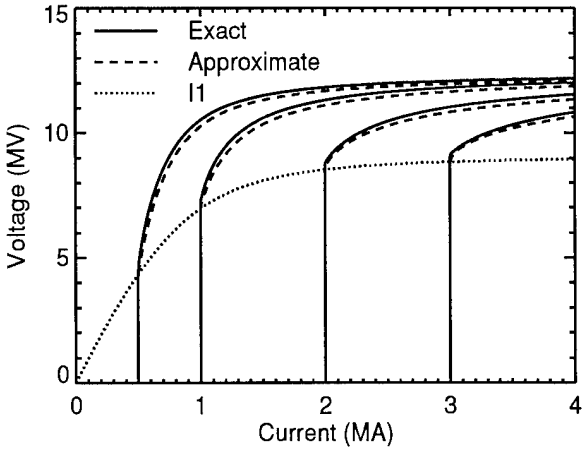


Fig. 1 Total current-voltage characteristics for the case of a superinsulated electron sheath with a V_{crit} of 16 MV, injected beam of Li^{+3} (Li^{+1} accelerated to 12 MV in the first stage), a diode gap of 1.6 cm, an anode area of 800 cm^2, and a 1:2 charge-to-mass ratio (Z/A) for the emitted beam in the second stage.

The current I_1 is also shown; for an injected beam current less than I_1, there is emitted beam in addition to the injected beam. For each injected current the additional current above that value is the emitted current.

Saturated electron sheath

Following an analogous path for the saturated case

$$j_x = \frac{\pi^2}{\Lambda_{sat}^2(0)}\left(\tilde{j} - j_b\right), \tag{11}$$

where

$$\tilde{j} = \left(\frac{\Lambda_{sat}(0)}{2}\right)^2 \frac{v^{3/2}}{g^2}, \tag{12}$$

and $\Lambda_{sat}(0)$ is defined by the $\Gamma = 0$ limit of Eq. (17) of Ref. 2. The integral for $\Lambda_{sat}(0)$ can be done explicitly and is given by $\Lambda_{sat}(0) = \pi/P_0^{3/2}$, with $P_0 = \sqrt{1 + w/v} - \sqrt{w/v}$. The relation for the dynamic gap g is given by

$$\frac{g}{d} = \frac{d - x_x}{d - (x_x/F_{sat})}, \tag{13}$$

where (see Ref. 2)

$$F_{sat} \approx \left[1 - (v/v_1(\Gamma))^2\right]^{3/5}. \tag{14}$$

We use the same form of the approximation for $v_1(\Gamma)$ as in the superinsulated case:

$$v_1(\Gamma) \approx v_1(0) + \left(\frac{\Gamma}{\Gamma + \alpha_{sat}\sqrt{v_c/w}}\right)^{1/2} (v_* - v_1(0)), \tag{15}$$

with $\alpha_{sat} = 0.28$ and $v_* = 0.60 v_c$. In this section $v_1(0)$, $v_1(\Gamma)$, and v_* refer to the appropriate quantities for the saturated case. $v_1(0)$ is found by setting β and Γ to zero in Eq. (19) of Ref. 2 and solving for $v \equiv v_1(0)$. The integral can be done explicitly, yielding an implicit relation for $v_1(0)$:

$$\frac{v_c}{v_1(0)} = \frac{3}{2}\frac{\sqrt{2S}}{\sqrt{P_{10}}} - \left[\frac{S}{P_{10}} - \frac{3}{4P_{10}^2}\right] \log \frac{\sqrt{2S} - \sqrt{P_{10}}}{\sqrt{2S} + \sqrt{P_{10}}}, \tag{16}$$

where $P_{10} = \sqrt{1 - w/v_1(0)} - \sqrt{w/v_1(0)}$ and $S = \sqrt{1 - w/v_1(0)}$. This relation for $v_1(0)$ converges rapidly from the starting guess

$$v_1(0)_{sat} = \frac{0.8 v_1(0)_{si}}{1 + 5.7\,(w/v_c)}. \tag{17}$$

In Eq. (17) the labels 'sat' and 'si' for saturated and superinsulated are included explicitly to avoid confusion. $v_1(0)_{si}$ is given by Eq. (10). The solution is then an iteration of Eqs. (15) and (11) in the same manner as the superinsulated case. The results of a sample calculation for four different injected beam currents (the $V = 0$ intercepts) are shown in Fig. 2.

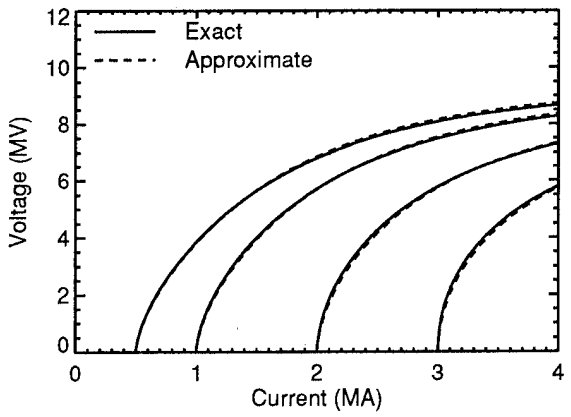


Fig. 2 Total current-voltage characteristics for the saturated electron sheath and the parameters of Fig. 1.

The agreement between the exact and approximate solutions is excellent. Note the absence of I_1 in this plot. Unlike the superinsulated case, $I_1(V)$ for the saturated case is non-zero for $V = 0$ and is given in *mks* units by

$$I_1(0) = 2\pi^2 \varepsilon_0 \sqrt{\frac{2q}{M}} \frac{W^{3/2}}{d^2} A, \tag{18}$$

where qW is the injected beam energy and A is

the anode area. For these parameters the intercept is off the scale at just above 4 MA.

It is clear from comparing Fig. 2 to Fig. 1 that the saturated electron distribution leads to considerably more beam emission in the second stage than the superinsulated distribution. This means a much lower operating voltage for a given accelerator load line. For high injected beam energies, the emitted beam current is almost independent of the injected current. This is because at higher input energy, the injected beam density is flatter across the gap and it is readily neutralized by the saturated electron distribution. This leaves the diode relatively unaffected by the injected beam and emission occurs as if the injected beam is not present.

A second example for the saturated case is shown in Fig. 3 with the same parameters as Figs. 1 and 2 except that the voltage of the first stage is reduced to 3 MV. Now the current I_1 is low enough to effect the emission of second stage beam in the voltage and current range shown. However, except at low voltages and relatively high injected currents, there is still considerable beam emission.

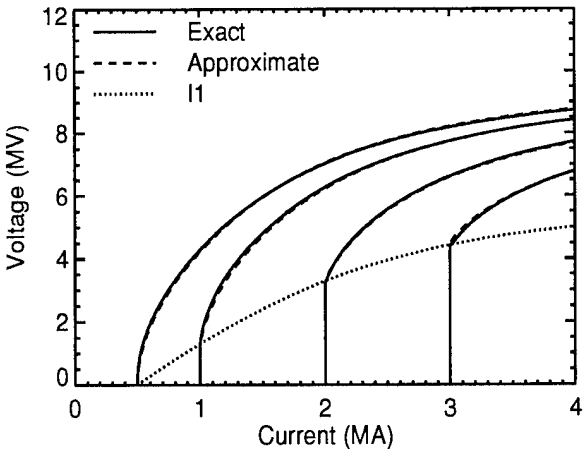


Fig. 3 Total current-voltage characteristics for the saturated case with the parameters of Figs. 1 and 2 except that the first stage voltage is reduced to 3 MV.

Time-dependent modeling

The approximate solutions have been incorporated into the SCREAMER[3] accelerator modeling code. The results of a calculation modeling a two-stage diode on the PBFA II accelerator are shown in Fig. 4. The injected beam is Li^{+1} at about 5 MV. The emitted beam has a 1:2 charge-to-mass ratio (Z/A), suggestive of a flashover source. It is assumed, somewhat pessimistically, that the second stage has full area emission and the electron sheath is saturated. The second stage has an effective open circuit voltage of about 10 MV. The total anode feed current is IAFEED, the total of injected plus emitted current is IION, the injected current is IBEAM, the emitted beam is IX, and the second stage voltage is VDIODE.

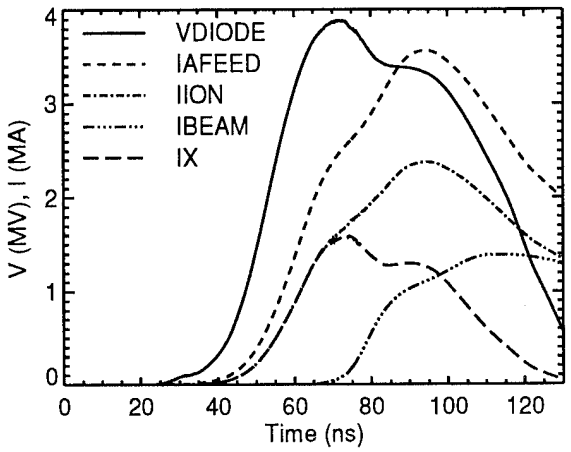


Fig. 4 Results of a time-dependent SCREAMER calculation using the approximate solution for the saturated case.

This work was funded by the U. S. Department of Energy under Contract DE-AC04-94-AL85000.

References

[1] S. A. Slutz and M. P. Desjarlais, J. Appl. Phys. **67**, 6705 (1990).

[2] S. A. Slutz, Phys. Fluids B **5**, 209 (1993).

[3] M. L. Kiefer and M. M. Widner, in *Proceedings of the 5th IEEE Pulsed Power Conference*, Arlington, VA, 1985, p. 685.

PROPERTIES OF MULTI-STAGE MAGNETICALLY INSULATED ION DIODE : EXPERIMENTAL RESULTS AND SCALING FOR LIGHT ION FUSION SYSTEM

S.Miyamoto, K.Yasuike, N.Shirai, G.Takahashi, N.Shoumoto, K.Yamamoto, K.Imasaki*, K.Horioka†, T.Aoki†, S.Kawata‡ C.Yamanaka* and S.Nakai

Institute of Laser Engineering, Osaka University, Suita, Osaka, Japan
*Institute for Laser Technology, Osaka, Japan
†Tokyo Institute of Technology, Nagatuta, Midoriku, Yokohama, Japan
‡Nagaoka University of Technology, Nagaoka, Niigata, Japan

Abstract

Multi-stage, extraction geometry magnetically insulated ion diode will be the sources of intense bright ion beams for light ion inertial fusion drivers. Two-stage diodes with carbon beam are studied on Reiden-SHVS (2MV + 2MV, 100ns) induction adder accelerator. The experimental results show that the divergence of carbon beamwere improved with ion current density $J_i \approx J_{10}$ where J_{10} is an equivalent space charge limit current of ion beam injected diode. Modules of fusion driver were designed applying the experimental results of divergence improving and chrage storipping feature of multi-stage applied-B ion diode.

Light-ion-beam drivers based on the pulsed power technology are a favorable driver for energy application due to its high efficiency to generate and low cost to construct. For inertial fusion energy by light ion beam, (a) development of high power, efficient, and (b) understanding of the ion diode physics and reduction of beam divergence are required. We have studied magnetically insulated ion accelerator and demonstrated an improvement of ion beam divergence with a two-stage diode [1].

Parameters which describe behavior of multi-stage magnetically insulated ion diode are a diode voltage V/V_{crit}, and an ion current density J_i/J_{cl} or J_i/J_{10} where $V_{crit} \approx cB_{app}d$ is a critical insulation voltage, B_{app} and d are an applied magnetic field and a diode gap, J_{cl} is a space charge limiting current and J_{10} [2] is an equivalent space charge limited current for post-acceleration stage. The improvement factor of beam divergence by post acceleration is determined by the ratio of final acceleration energy of ion and injected ion energy. Previous experiments with proton beam shows that the beam divergence is improved from 52+-18 mrad to 27+-6 mrad for the first and the second stage voltage of 0.6MV and 1.2MV, respectively.[3]

Figure 1(a) shows a setup of two stage ion diode. Two annular extraction type, magnetically insulAted ion diodes were set at the central part of Reiden-SHVS induction adder accelerator which has positive and negatuve outputs of maximam voltage of 2MV and current of 40kA each during 100ns. Ion sources are carbon plasma injection from the rear side of an aluminum anode with three injection slit. Beam consists of carbon ions and more than 30% of protons. Divergence of ion beam at first and second stage diode were measured by small tree-channel scatter-shadow-boxes (SB) as shown in Fig.1(b). To estimate a beam divergence from a results of this small-flight-SB, we have to make fitting with a calculated distribution of ions in the shadow-box. Ion distributions in the shadow box are measured by CR-39 track ditector.

Typical wave forms of voltage, current, impedance and transmitted ion current density are shown in Fig.2. Two different cases of diode parameter are shown, gaps of the second diode (AK_2) were 8.3 mm (a,b) and 33.3 mm (c,d). The conditions of the first stage diode were same. The larger AK_2 case correspond to a case of high injection current density compared with the critical current densities of the second stage diode. Due to the plasma injection as a

ion source, the impedance of the first stage is low value at the beginning of the pulse. In contrast, the impedance of the second stage diode is very high at beginning, and is decreasing with increasing the injection current from the first stage. The impedance increasing again at the end of the pulse due to the decreasing the injection current, which indicates an impedance controll of ion diode by injection current. This is an important adovantage of the beam-injected diode to use as the fusion driver.

Example of measured track density distributions in radial direction are shown in Fig.3. (a) and (b) are results of the first and the second stage for small current injection into the second-stage diode. Three different distributions correspond to the different track diameter, 1 to 2μm, 2 to 3μm, and larger than 3μm. The calibration of track diameter on CR-39 indicates that the tracks larger than 3μm in diameter are due to the carbon beam for 4-hours etching in 70°C, 6.25N:Naoh. Fitting of track distribution indicates that the carbon beam divergence of 40 mrad in first diode was improved to 30 mrad. This improvement roughly agrees with a prediction by voltage ratio $\approx \sqrt{(1+(V_2/V_1))}$.

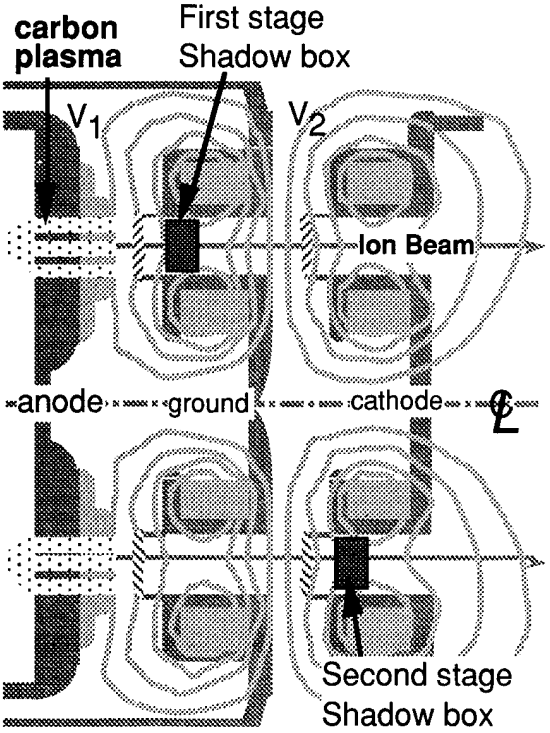


Fig.1(a)Setting of two-stage diode and Shadow-boxes.

Figure 4 shows a carbon beam distribution in SB for low (a) and high (b) current injection compared with the equivalent space-charge limited current J_{10}. The ratios were (a) 0.8 and (b) 4.5. Then, in case (b), the beam divergence at the second diode is expected to get worse due to the electron sheath instability. The results show (a) improvement and (b) no improvement of beam divergence.

Modules of fusion driver were designed using the divergence improving factor of 2 with low ion current injection ($J_i/J_{10}\approx 1$) and charge stripping feature of multi-stage applied-B ion diode. The design parameters are shown in Table I. Lithium beam driver of 30MeV, 740TW on fusion target was achieved with 60 modules of a first stage of 6MV, 2.2TW and a second stage of 8MeV, 8.8TW. The beam divergence angle of 14mrad at the first stage will be improved and to 7mrad.

[1] S.Miyamoto, K.Yasuike, K.Imasaki, C.Yamanaka and S.Nalkai Proceedings of 9th International Conf. on High-Power Particle Beams, Washington, DC, May 25-29, PB-27 (1992).
[2] S.A.Slutz and M.P.Desjarlais, J.Appl.Phys., vol.67, no.11, pp.6705-6717(1990).
[3] S.Miyamoto, K.Yasuike, N.Shirai, K.Imasaki, C.Yamanaka and S.Nakai, IEEE Trans. on Plasma Science, vol.PS-21, no.5 (1993).

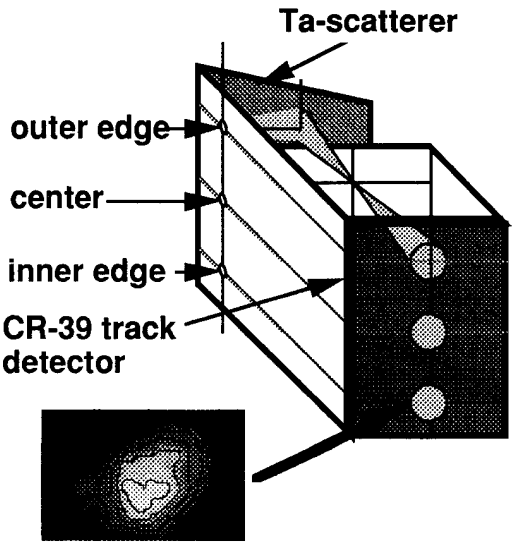


Fig.1(b) Small, scattering shadow-box.

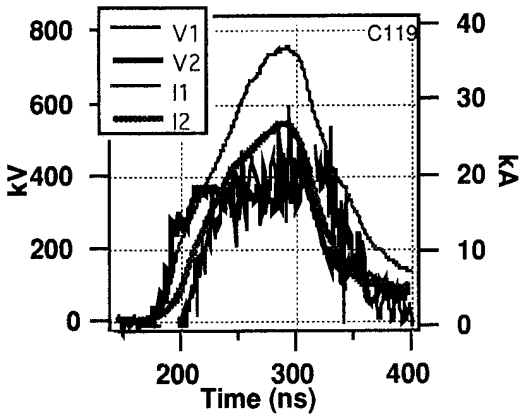


Fig.2(a)

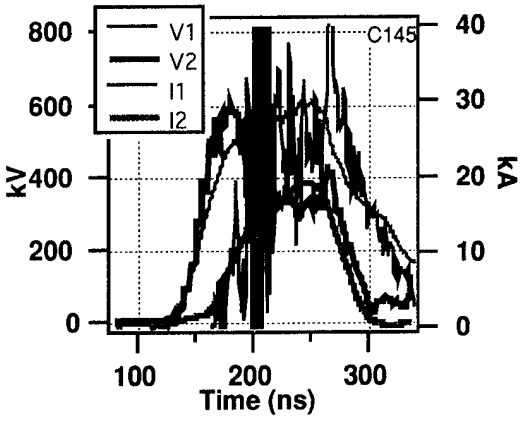


Fig.2(c)

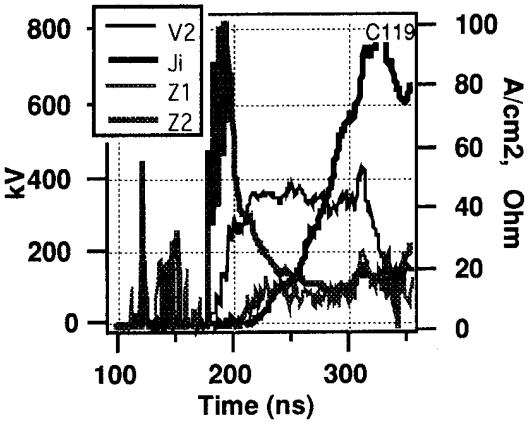


Fig.2(b)

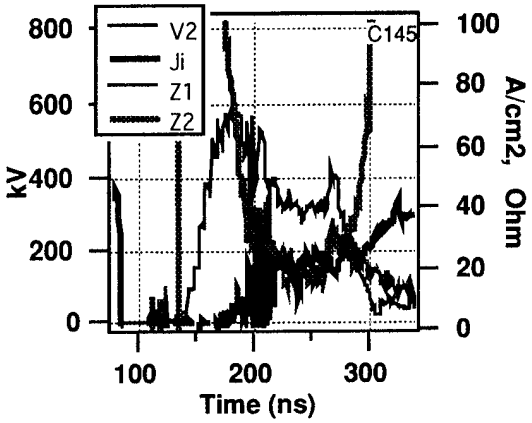
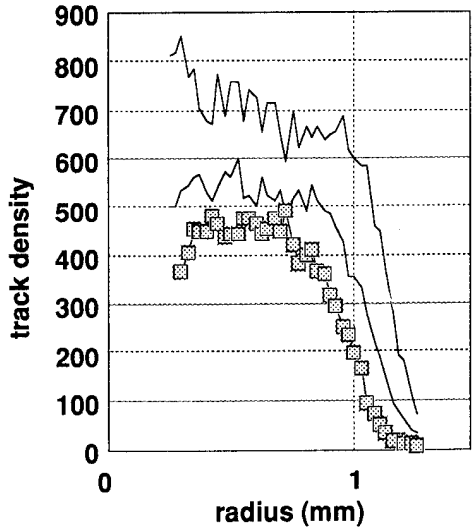
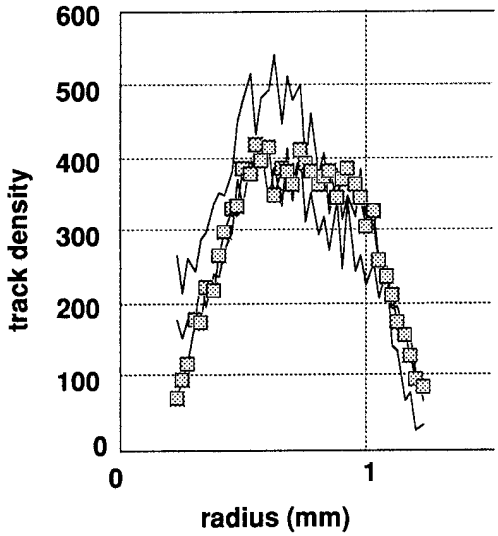


Fig.2(d)

Fig.2 Typical waveforms of voltage , current, impedance and transmitted ion current density.



(a) Beam center, AK2=9.3, first stage
1-2 μm, 2-3μm, >3 μm = carbon



(b) Beam center, AK2=9.3, second stage
1-2 μm, 2-3μm, >3 μm = carbon

Fig.3 Measured track density distributions in radial direction. (a) and (b) are results of the first and the second stage for small current injection into the second-stage diode. Three different liness correspond to track diameter, 1 - 2μm, 2 - 3μm, and > 3μm.

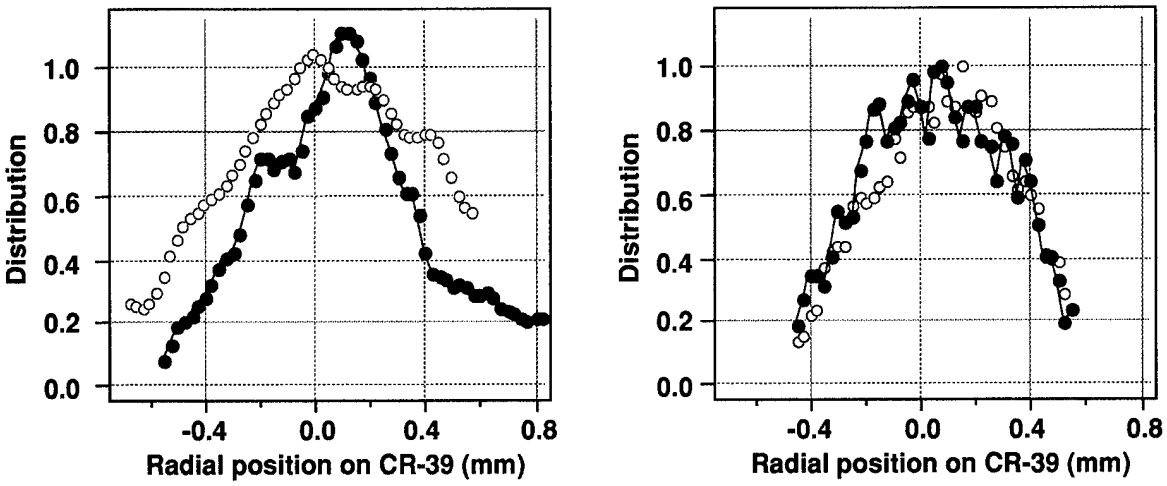


Fig.4 Carbon beam distribution in SB for low (a) and high (b) current injection compared with the equivalent space-charge limited current J_{10}.

Table I The design parameters of lithium beam driver of 30MeV, 740TW.

Lithium beam		30 MeV	Stripping
Atomic mass number		7	60 beams
Parameters		**1st stage**	**2nd stage**
Diode voltage	V	6 MV	8 MV
Critical voltage ratio	Vc/V	3	1.5
Insulation B field	Bapp	7 T	7 T
Critical insulation voltage	Vc	18 MV	12 MV
Diode gap	d	0.88 cm	0.60 cm
Ion charge state	Z	1	3
Space charge limit current	J(C-L)	389 A/cm2	2274 A/cm2
Equivalent space charge limit	J(10)	-	6304 A/cm2
Critical current for 2nd diode	J(20)	-	9632 A/cm2
Enhancement	J(i)/J(10)	5	0.93
Ion current density	J(i)	1946 A/cm2	5837 A/cm2

Reactor driver parameters		
Total beam power (@ target)	P	739 TW
Total beam energy (@ target)	E	8 MJ
Pulse width (@ target)	t	10.83 ns
Beam intensity (@ target)	I	120 TW/cm^2
Beam number	N	60
Bunching ratio	Bf	2
Transport efficiency	Teff	0.7
Target radius	r	0.7 cm
Target area	St	6.16 cm2
Total beam power (@ diode)	Pt	528 TW
Total beam energy (@ diode)	Et	11.43 MJ
Beam intensity (@ diode)	Pd	0.058 TW/cm2
Beam power (1-beam)	Pb	8.8 TW
Beam cross section (1-beam)	Sb	151 cm2
Beam divergence angle	$\Delta\theta$	7 mrad
Beam brightness	B	1191 TW/cm2rad2
Focusing length	F	1.000 m
Beam solid angle (total beam)	$\Delta\Omega/4\pi$	0.072
Outer diode radius	Ro	12 cm
Inner diode radius	Ri	9.8 cm

CHARACTERIZATION OF A HIGH-RESOLUTION FRAMING-CAMERA DIAGNOSTIC FOR SABRE ION BEAM MEASUREMENTS

J.R. Smith[a], T.W.L. Sanford, M.E. Cuneo,
D.L. Hanson, M. A. Bernard[b], and R.C. Mock[b]
Sandia National Laboratories
P.O. Box 5800
Albuquerque, NM 87185

Abstract

This paper presents characteristics of a high-resolution framing-camera system that has been developed for diagnosis of the SABRE ion beam. The measured temporal and spatial resolution are 6.5 ns and ~ 1 mm respectively. Preliminary measurements of the SABRE ion beam taken immediately downstream of the diode are presented.

Introduction

Ion beam transport from diode to target is a key element in the Inertial Confinement Fusion program at Sandia National Laboratories. Ion transport issues include beam uniformity and filamentation. Time-resolved measurements with high spatial resolution are required for both concerns. In order to address these issues, a framing-camera system has been developed for beam transport experiments on the SABRE accelerator.

SABRE is a ten-stage linear induction adder operated in positive polarity (6 MeV, 300 kA, 50 ns). It produces an intense, annular, ion beam, by using an applied-B extraction diode [1]. For the work discussed here a scintillator is used as an ion beam target. It converts energetic ions into visible light, which is recorded with a high-resolution framing-camera system. In this paper the camera system is described, and measurements of the temporal and spatial resolution are presented. Results of preliminary tests on the SABRE accelerator are also given.

Camera System

The main system components are shown in Fig. 1. They are: a framing-camera with telescope attachment, a high-voltage pulser, a MicroVAX computer with video monitor, a video printer, and a text printer.

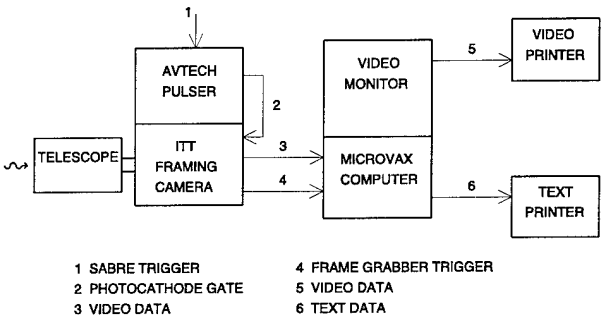


Figure 1. Framing camera system components.

The framing camera (ITT # 14758 [2]) contains an image intensifier and a charge injection device (CID) as shown in Fig. 2. The image intensifier consists of the following elements: fiber optic input window, type S20 photocathode [3], microchannel plate (MCP), type P20 phosphor convertor [3], and a fiber optic output window. The S20 photocathode converts incoming photons to electrons.

*This work supported by the U. S. Department of Energy under contract no. DE-AC04-94AL85000.
[a]Titan/Advanced Innovative Technologies, [b]K-tech Corporation.

The MCP amplifies these electrons (gain is externally adjustable), and the P20 phosphor converts the amplified electron signal back to photons. A tapered fiber optic bundle couples the image intensifier to the CID, which converts and stores the incoming light as electrical charge. The camera is shielded from the SABRE radiation environment with a steel box, and uses an uninterruptable power supply for electrical isolation.

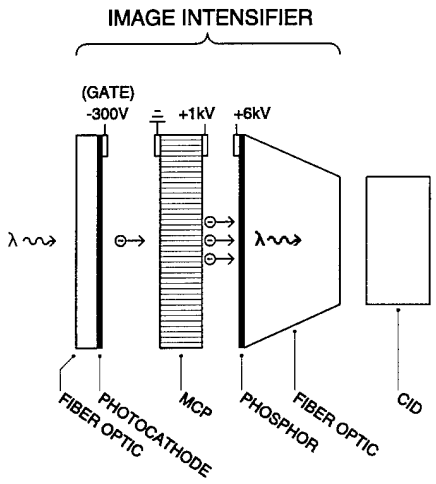


Figure 2. ITT framing camera elements.

An Avtech pulser [4] provides a bias pulse (300 V), which gates the camera's photocathode (Fig 2.) and thus serves as an electronic shutter. It has an adjustable pulse width from 4 ns to 6 ms for setting the frame exposure time. The pulser has an 80-ns internal delay, and is triggered from the SABRE trigger network.

The MicroVAX computer contains a frame-grabber board which "reads" the CID, and enables image storage on a hard-disk. The resulting image is a 512 x 512 pixel array with 8-bit (0-255) gray-scale resolution. The video monitor displays the image immediately after a shot.

Temporal Resolution

Calibration of frame exposure time is important for accurate diagnosis of ion beam dynamics. Frame exposure time was measured using a pulsed infrared laser (2 ns, 820 nm). A series of laser images were recorded where the interval between the start of the laser pulse and photocathode gate was varied in 1-ns increments. Analysis of these images yields the exposure time corresponding to a specific photocathode gate width. Three different series were recorded with gate widths of 4, 11, and 18 ns (FWHM).

Results are given in Fig. 3 for the 4-ns gate width. The intensity of an image was defined by the camera pixel that records the beam apex. Each data point shown is the average of four intensity measurements, where the error bars are the standard deviation about the mean. The exposure time is 6.5 ns (full width at tenth maximum), when corrected for the 2-ns laser pulse width.

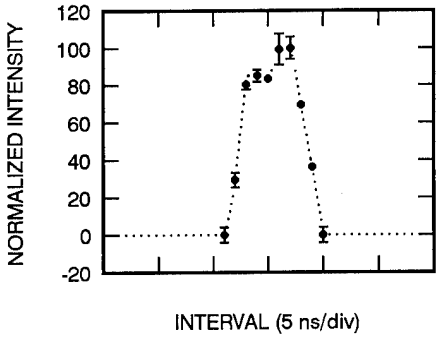


Figure 3. Measurement of frame exposure time. Photocathode gate width = 4 ns.

Exposure time vs gate width for all 3 series is given in Fig. 4. A calibration curve from the ITT manual, also shown in Fig. 4, agrees well with the measured values, and provides confidence in the accuracy of our calibration. Note that exposure time approximately equals gate width, except for small exposure times where exposure time is greater than gate width. This difference is because the minimum exposure time is limited by inherent photocathode delay. The minimum exposure time of 6.5 ns (4-ns gate width) is acceptable for temporal resolution of the 50-ns SABRE ion beam.

material. The stainless steel mask, shown in Fig. 8a, intercepts a 65° ion-beam sector, and has 4 oblong windows (channels). It is range thick to all ions. Behind each window is a foil of different thickness. The foils serve two functions: they block diode light from camera view, and they act as ion range filters to discriminate ion species and energy. The final layer is a 1 mm sheet of Bicron 418 scintillator (1.4 ns decay time).

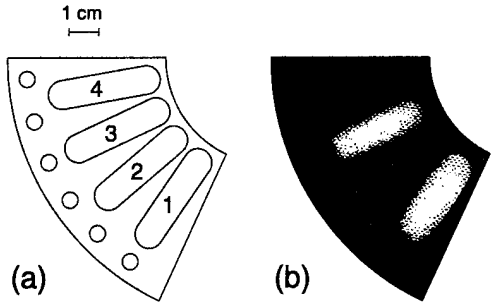


Figure 8. (a) Scintillator mask. (b) Results for SABRE shot #1063.

Only ions with range greater than the foil thickness penetrate and deposit energy in the scintillator, thereby emitting light. Lower voltage ions are completely stopped in the foil. Alternatively, ion stopping may be described in terms of cutoff energy, where only ions with energy greater than the cutoff energy penetrate through a foil. Foil thickness and cutoff energy for SABRE shot #1063 (proton and carbon ions) are given in the table below.

Channel	Foil Thickness	Ion Cutoff Energy	
1	2.5 μm Ta	H 0.3 MeV	C 2.6 MeV
2	35 μm Ta	H 3.4 MeV	C $> 4\ V_{diode}$
3	12.5 μm Al + 9.5 μm mylar	H 1.2 MeV	C $> 4\ V_{diode}$
4	100 μm Ta	H $> 4\ V_{diode}$	C $> 4\ V_{diode}$

Note that for a cutoff energy greater than V_{diode} for protons, or 4 V_{diode} for carbon ions (assuming C^{4+} is the highest charge state), no ions reach the scintillator. Shot #1063 data is shown in Fig. 8b, and is discussed below. Channel (1) recorded light indicating the presence of H and/or C ions with energies greater than the cutoff values given above. The foil in channels (2), (3), and (4) blocked all carbon ions, so their analysis is restricted to protons. Channel (2) recorded no light, indicating no protons above 3.4 MeV, and channel (3) observed light, signifying protons above 1.2 MeV. The peak (average) diode voltage for shot # 1063 was 4.2 MeV (2.5 MeV). It is likely channel (2) recorded no ions exceeding 3.4 MeV because of a substantial drop in number density at the high end of the energy spectrum. Channel (4) is filtered to block both H and C ions, and is intended to measure scintillator response to diode bremsstrahlung radiation. No light was recorded for this channel, indicating bremsstrahlung-induced scintillation is below background. Frame exposure time for this shot was longer than the ion pulse width.

Summary

A high resolution framing camera system has been fielded on SABRE. Its temporal resolution is 6.5 ns, and spatial resolution is $\sim$ 1 mm. Importantly, the initial tests show that the amplitude of scintillator light produced by the SABRE ion beam exceeds the observation threshold level. Moreover, unwanted scintillator light due to bremsstrahlung is minimal and therefore does not obscure the ion-produced scintillator signal. Future plans include time-resolved measurements of ion beam uniformity, with energy and species cuts for both passive and active ion sources.

The authors acknowledge key contributions to this work by J.E. Maenchen, E.L. Neau, C.L. Olson, I.R. Shokair, and K.W. Struve.

References

[1] D. L. Hanson et. al., Improved Field Geometries for SABRE . . ., paper P1-59 of this conference.

[2] International Telephone & Telegraph, Electro-Optical Products Division, 3700 East Pontiac St, Fort Wayne, IN 46801.

[3] R. W. Wayant and M. N. Ediger, editors, *Electro-optics Handbook*, McGraw-Hill, New York, pp. 18.2-18.10 (1994).

[4] Avtech Electrosystems Ltd., Ogdensburg, NY.

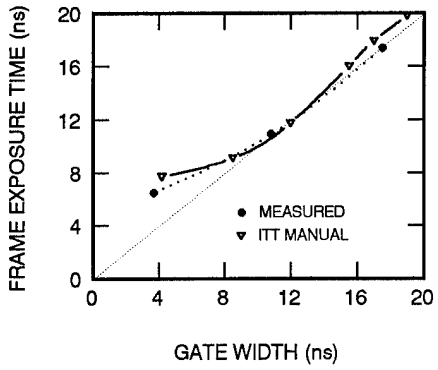


Figure 4. Frame exposure time vs gate width.

Spatial Resolution

In order to detect ion-beam features such as filamentation, high spatial resolution is necessary. High-gain framing cameras are susceptible to electromagnetic pulse radiation and x-radiation. To minimize radiation-induced problems, the ITT camera was located outside of the SABRE cell as shown in Fig. 7. To simultaneously obtain high spatial resolution and large stand-off distance, the scintillator is imaged using a Celestron telescope mounted to the camera. Spatial resolution for the camera system was measured using the resolution chart shown in Fig. 5. Four tests were performed using two different Celestron telescopes (4" diam, 8" diam) at two object distances (14 m, 28 m).

The accompanying plot in Fig. 5 is a horizontal scan of the chart image using the 8" telescope with a 14 m object distance. Limiting resolution is determined from the scan and is defined as the maximum number of line-pairs/mm (lp/mm)

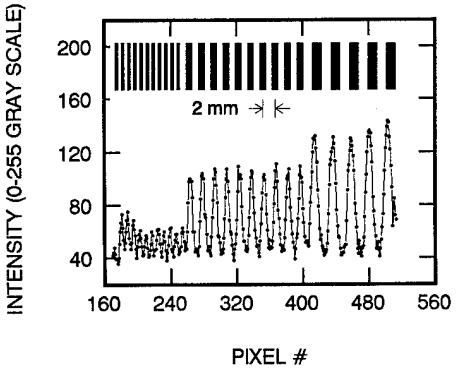


Figure 5. Scan: 8" telescope, 14-m object distance.

that can be discerned (i.e. intensity difference of alternating black and white lines exceeds background level).

Limiting resolution of all four scans are summarized in Fig. 6. The present setup on SABRE uses the 8" telescope with a 24 m object distance (Fig. 7). For this case, Fig. 6 indicates the limiting resolution was 0.6 lp/mm. Dimensions of the order of 1 mm may be observed with this resolution, which is sufficient for the ion-beam attributes of interest.

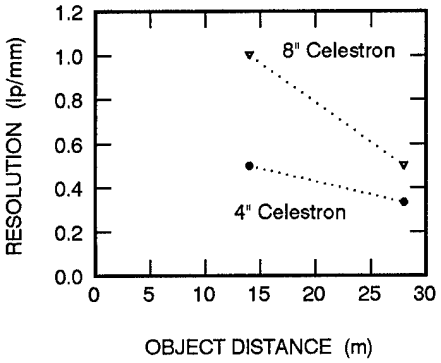


Figure 6. Spatial resolution vs object distance.

SABRE Measurements

The setup for imaging the SABRE beam is shown in Fig. 7. The scintillator, placed 6-cm downstream of the diode (in vacuum), emits light in the visible spectrum via ion collisions. Two front-surface turning mirrors are used to direct this light to the camera.

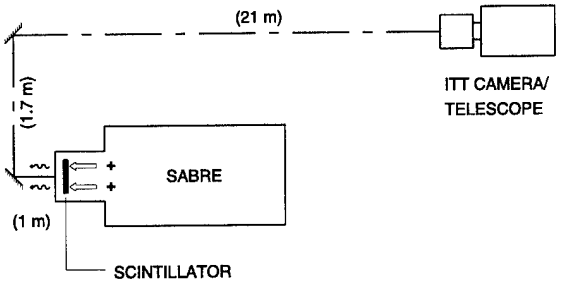


Figure 7. Setup for ion beam imaging on SABRE.

The scintillator package consists of three layers. In the order encountered by the ion beam, they are: a stainless steel mask, a metal (or metal and plastic) foil, and a scintillator

VUV SPECTROSCOPIC OBSERVATIONS ON THE SABRE APPLIED-B ION DIODE

A. B. Filuk, T. J. Nash, D. D. Noack

Sandia National Laboratories, P.O. Box 5800, Albuquerque NM, 87185-1187

Abstract

We are using VUV spectroscopy to study the ion source region on the SABRE applied-B extraction ion diode. The VUV diagnostic views the anode-cathode gap perpendicular to the ion acceleration direction, and images a region 0-1 mm from the anode onto the entrance slit of a 1 m normal-incidence spectrometer. Time resolution is obtained by gating multiple striplines of a CuI- or MgF_2-coated micro-channel plate intensifier. We report on results with a passive proton/carbon ion source. Lines of carbon and oxygen are observed over 900-1600 Å. The optical depths of most of the lines are less than or of order 1. Unfolding the Doppler broadening of the ion lines in the source plasma, we calculate the contribution of the source to the accelerated C IV ion micro-divergence as 4 mrad at peak power. Collisional-radiative modeling of oxygen line intensities provides the source plasma average electron density of $7x10^{16}$ cm^{-3} and temperature of 10 eV. Measurements are planned with a lithium ion source and with VUV absorption spectroscopy.

BACKGROUND

High-power applied-B ion diodes are being studied at Sandia as drivers for light-ion ICF [1]. Spectroscopy has been used successfully on ion diodes as a non-perturbing probe of conditions in the ion source anode plasma and in the anode-cathode (AK) gap [2] [3]. The readily-accessible visible part of the spectrum can yield a wealth of information from spectral line shapes [3], but unfolding competing line broadening effects can be difficult, and for some ions such as Li^+ the strongest lines are in the vacuum-ultraviolet (VUV). Optics, detectors, and calibration sources make the VUV a challenging part of the spectrum to work in. We are doing what are to our knowledge the first detailed spectroscopic measurements of diode physics in the VUV. The goals of this work are to obtain the ion beam divergence at the source (loosely referred to as the source 'temperature') from Doppler broadening of ion emission lines, and to study mechanisms for beam divergence growth in both the anode plasma and in the acceleration and drift regions. This work reports on observations of a flashover ion source anode plasma.

VUV DIAGNOSTIC ON SABRE

VUV observations are made on the extraction ion diode on SABRE [4]. The device generates an ion beam of about 5 MV peak voltage, 100 kA peak ion current, and 25 ns full-width-half-maximum (FWHM) duration. A passive wax flashover ion source generates an anode plasma from which proton/carbon mixed ion beams are produced.

The VUV diagnostic on SABRE has been described in earlier work [5]. Figure 1 shows schematically the components and the line-of-sight relative to the SABRE AK gap. The vacuum line-of-sight elliptical mirror focuses light from the AK gap into a 1 m normal-incidence spectrograph. The 7 striplines of the CuI-coated micro-channel plate (MCP) in the exit plane are gated with 3 ns time resolution at intervals of 8 ns, to provide the spectrum at 7 time frames. The MCP frame signals are converted to visible photons via a phosphor, and a fiber-optic faceplate couples the light to film.

The ~1 mm wide line-of-sight at the anode is inclined about 1° toward the anode face to view emission from even a very thin anode plasma and to reduce possible optical depth effects. Alignment is done by reverse-propagating a visible laser

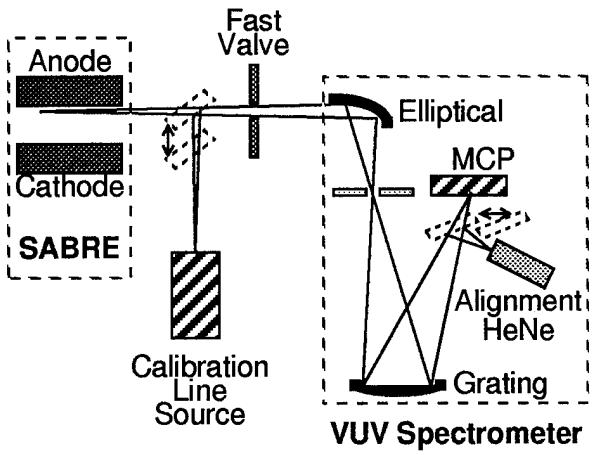


Fig. 1. Schematic of VUV diagnostic relative to the SABRE AK gap.

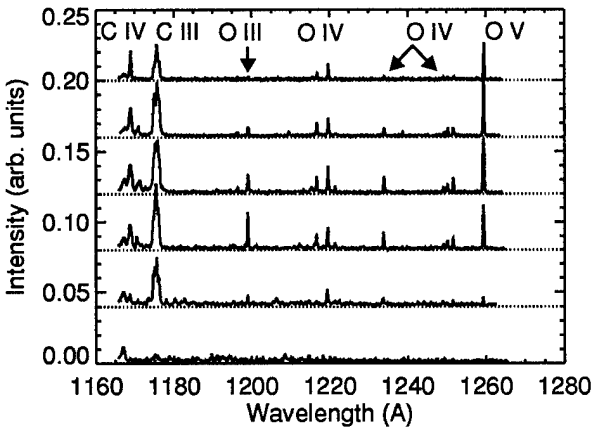


Fig. 2. Lineouts of spectra at 8 ns intervals. Spectra are offset for clarity.

through the VUV system to the anode face. The observations reported here viewed the 900-1600 Å portion of the spectrum with a 2400 l/mm grating. An Ar calibration source is used to characterize the instrument function. The films are digitized and analyzed on a computer.

GENERAL OBSERVATIONS

VUV spectral lines of predominantly C and O ions are first observed during the rise in the main ion beam current, after the peak brems-induced noise signal and about 15-20 ns after the start of measurable ion current in the precursor pulse [6]. The appearance of C and O lines in the anode plasma appears to be correlated with the onset of a significant fraction of higher-charge, non-protonic ions in the beam as seen by filtered Faraday cups. On every shot the C and O lines were seen at or before this rise in higher-charge non-protonic ions in the beam at the anode. The Ly_α line of H was occasionally seen at the detection threshold, later in the pulse when all line intensities were greatest.

As shown in Figure 2, the line emission is mainly from C and O ions. Lines of C II-IV and O III-VI were seen. The C lines are generally more intense and wider than the O lines, which are dominated by the instrument width. The lower-charge-state ion lines were much brighter earlier than later relative to lines of the higher charge states, reflecting the non-equilibrium level populations.

Estimates for the absolute sensitivity of the VUV instrument require that the emission seen originates in a dense ($\sim 10^{15}$-10^{18} cm^{-3}) plasma rather than in the low-density ($\sim 10^{12}$ cm^{-3}) AK gap region. Indeed, no emission was detected when the line-of-sight was more than 2 mm off of the anode face. Spectral lines of C III and O IV,V were observed when viewing near the cathode tip. Comparable intensities were seen including and excluding the tip from the field of view, so the lines are unlikely to be an artifact of anode plasma light scattering off the tip into our instrument. Our conclusion is that a cathode plasma extends a few mm into the AK gap from the cathode tip.

WIDTHS & DOPPLER TEMPERATURES

One of our main objectives is to measure the Doppler broadening of ions to obtain the beam divergence at the ion source. The lower-energy, well-populated levels of VUV transitions are less susceptible to Stark broadening and Zeeman splitting than those in the visible. For anticipated anode plasma magnetic fields less than 2 T on SABRE, the Zeeman splitting would increase the linewidths by less than 0.1%. The Stark broadening of the lines is also small because of the low-lying upper levels; for example C IV 1548,1551 Å has a Stark-broadening FWHM of 0.006 Å at an electron density $n_e=1\times10^{17}$ cm^{-3} and temperature $T_e=5$ eV [7].

In our case the two effects that compete with Doppler broadening are the instrument width

and opacity broadening. The instrument function is well-characterized as a Gaussian of 0.29(1) Å FWHM. The O lines have measured widths of about 0.3-0.4 Å, making them instrument-width dominated even when viewed in second-order to reduce the $\Delta\lambda/\lambda$. When opacity effects were not dominating, the instrument width was subtracted in quadrature from the measured width to obtain an upper bound for the Doppler broadening. The "Doppler temperature" T_D (in energy units) is defined from the unfolded Doppler FWHM $\Delta\lambda$ and ion mass M as

$$T_D = \frac{Mc^2}{4\alpha}\left(\frac{\Delta\lambda}{\lambda}\right)^2$$

where $\alpha = 2\ln 2$.

Opacity broadening of lines is of particular concern in the VUV because the most intense lines are resonance or near-resonance lines [8]. Viewing pairs of lines from nearly-degenerate J=3/2 and J=1/2 upper levels, such as C IV 2s-2p 1548, 1551 Å or O VI 2s-2p 1032, 1038 Å, provides a check on opacity effects. In an optically thin plasma where these two upper levels are in LTE, the line intensities should be in the ratio of the level multiplicities, 2:1. As the optical depth approaches 1 this ratio is reduced and the more intense line becomes wider. Figure 3 shows lineouts of the C IV line pair at 8 ns intervals for a single shot. The earliest lineout (t_3) shows the 1548 Å

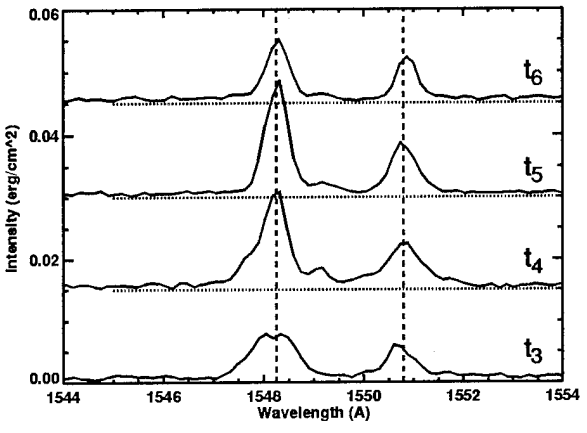


Fig. 3. Lineouts of the C IV 1548,1551 Å pair showing opacity effects early in time. Lineouts have been offset for clarity.

profile is strongly broadened and even partially self-reversed near line-center. Later in time, however, the line intensities and widths are consistent with small optical depth. On some shots it appears that the C IV line pair optical depth remained significant throughout the pulse. A similar phenomenon was seen for the O VI line pair.

In general then, unless one has a clear indication of small optical depth as at the later times of Figure 3, the instrument-unfolded line widths cannot be assumed free of opacity broadening. On the other hand, it was observed that line widths where opacity effects were clearly present but not dominant were comparable to or slightly larger than widths where opacity effects were small. Further, non-resonance lines such as O IV 625.9 Å had widths comparable to those of the O IV resonance lines. Our conclusion is that in general the optical depths in our lines are less than or of order 1, and can modestly increase the line widths.

Figure 4 shows the unfolded C IV T_D for the times in Figure 3, along with an arbitrarily-scaled Faraday cup current for timing reference.

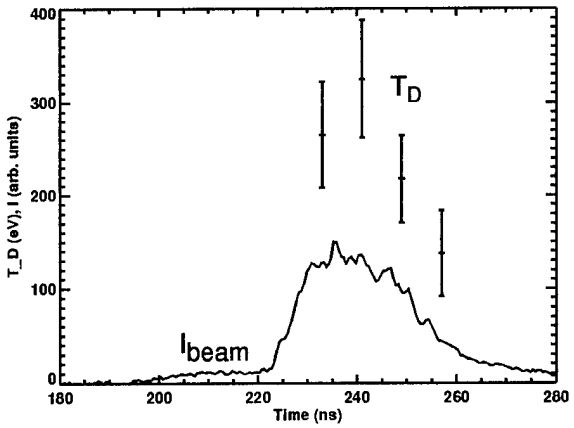


Fig. 4. Unfolded Doppler temperatures at times of Figure 3, along with relative ion beam current from Faraday cups.

Note that the T_D value for the earliest time, obtained from the width of the longer-wavelength peak at t_3 in Figure 3, is only an upper bound due to possible opacity broadening. Ions with large transverse temperatures have been seen using flashover ion sources on other applied-B diodes [9], but the mechanisms responsible are not yet well understood. With the diode voltage of 4 MV at peak power (230 ns in Figure 4), the T_D of

270 eV gives a divergence of 4 mrad for these ions.

Unfolding the C III 977 Å line widths on a different shot gave T_D values of 350-500 eV, but the significance of opacity broadening for this resonance line could not be determined so this range is an upper limit. The C II 1010 Å line seen was an unresolved triplet so the width could not be extracted.

INTENSITIES & CR MODELING

The O III-V lines provide line intensity ratios suitable for extracting plasma properties. A collisional-radiative (CR) code is used because the electron density is too low for LTE and too high for coronal treatments. Flashover plasmas have been characterized on other ion diodes with CR modeling [10]. The model uses fixed given values of n_e and T_e, and a source of O I whose supply rate increases linearly with time to account for continuous injection of anode material [10]. Since only relative level populations are used, the CR results are independent of the source rate and only depend on time and the average n_e and T_e. The calculation assumes a simple uniform region of optically-thin emission. The intensities of the lines will not be significantly different for optical depths of 1 or less [10].

The second-order lines of O III 600 Å, O III 610 Å, O IV 617 Å, and O V 630 Å were used to calculate three intensity ratios of O III/IV and O IV/V. These lines were chosen because of their charge states, strengths, and nearby wavelengths such that the instrument response could be assumed constant and all intensities acquired on a single shot. The frame-to-frame response does not enter into the line ratios, but with an earlier MgF_2-coated MCP it was observed to be approximately constant. Figure 5 shows the intensities of these lines from Figure 2, along with the beam current history.

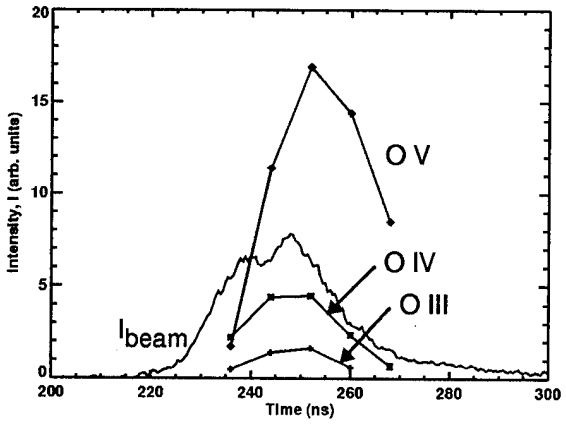


Fig. 5. Relative intensities of O III-V lines and relative ion beam current from Faraday cups.

The O line ratios fit a CR-modeled average n_e and T_e of 7×10^{16} cm^{-3} and 10 eV for most of the pulse duration. The fit was sensitive to 50% changes in n_e and 30% changes in T_e. The calculated and observed ratios are only weakly dependent on time after an initial phase. An unresolved issue is whether the O emission comes from the same plasma region as the C emission.

FUTURE WORK

Our plans are to use this diagnostic to determine lithium beam divergence at the source on upcoming lithium ion source experiments. With increased signal-to-noise we also plan to do absorption experiments using a continuum VUV light source, viewing absorption from the AK gap and the extraction region to study mechanisms for divergence growth.

The authors acknowledge helpful comments from J. Bailey and M. Cuneo. Thanks to Y. Maron for discussions and CR calculations, and to the SABRE experimental team. Funding for this work has been provided by the U. S. Department of Energy under Contract DE-AC04-94-AL85000.

[1] J.P. VanDevender and D.L. Cook, *Science* **232**, 831 (1986)

[2] R. Pal and D. Hammer, *Phys. Rev. Lett.* **50**, 732 (1983). Y. Maron et al, *Phys. Rev. Lett.* **57**, 699 (1986), and *J. Appl. Phys.* **61**, 4781 (1987).

[3] J.E. Bailey et al, submitted to *Phys. Rev. Lett.*

[4] M.E. Cuneo et al, "Observations of Reflected Waves...", 9th IEEE Pulsed Power Conference, 1993.

[5] T. Nash et al, *Rev. Sci. Instr.* **64**, 2493 (1993).

[6] M.E. Cuneo et al, "Control of a Large Vacuum Wave Precursor...", these proceedings.

[7] M.S. Dimitrijevic and N. Konjevic, *J. Quant. Spect. Rad. Transfer* **24**, 451 (1980).

[8] H.R. Griem, *Plasma Spectroscopy* (Academic, 1964), Ch 7.

[9] Y. Maron et al, *Phys. Rev. A* **39** 5842 (1989).

[10] Y. Maron et al, *Phys. Rev. A* **40**, 3240 (1989), and **41**, 1074 (1990).

Improved Field Geometries for SABRE Extraction Ion Diode Operation with Passive Ion Sources*

D. L. Hanson, M. E. Cuneo, S. E. Rosenthal, R. S. Coats, P. R. Menge,
J. E. Maenchen, J. R. Smith[a], and M. A. Bernard[b]
Sandia National Laboratories
Albuquerque, NM, 87185-1193

Abstract

The SABRE Facility at Sandia National Laboratories is an integrated testbed for the study of high voltage ion beam production and transport in extraction geometry for inertial confinement fusion. Our major emphasis is on the development of active ion sources, but several techniques are under investigation to improve diode performance with passive hydrocarbon and LiF ion sources. The operation of passive sources is particularly sensitive to details of the magnetic and electric field geometries and can provide insight into divergence and parasitic load mechanisms which also affect high voltage diode performance with active sources. We demonstrate that an outer cathode tip extension can eliminate cathode feed electron participation in source turn-on and virtual cathode evolution. Experimental data and TWOQUICK PIC code simulations indicate that instability-induced cross-field diffusion of cathode tip electrons at small radius plays a dominant role in diode operation with a passive source. An improved diode geometry is presented with reduced feed electrode participation and better electron confinement at the anode emission area for lithium sources.

SABRE consists of a ten-cavity positive polarity linear induction voltage adder (6 MV, 300 kA) coupled through a long magnetically insulated transmission line to an applied-B extraction ion diode. The long term goal of research with this testbed is to develop a high impedance, high power extraction geometry light ion driver module for inertial confinement fusion. Although our main emphasis is on the development of active ion sources with improved divergence and impedance characteristics for beam transport and focusing studies, experiments are also underway to improve diode operation with passive ion sources. These sources provide a simple way to generate ions to test accelerator performance, accelerator-to-diode coupling, and ion beam diagnostics. They allow us to study electric and magnetic field geometries, sources of divergence, divergence reduction techniques, and parasitic load mechanisms which affect high voltage diode performance with active sources.

Passive sources produce ions either through an electron-assisted desorption and flashover process or through field emission mechanisms. The operation of passive sources is therefore particularly sensitive to the details of the magnetic and electric field profiles and the electrode geometry in the diode region. A previous study [1] of the SABRE diode with a wax flashover ion source showed that electron emission from the cathode feed region near the short cathode tips played a dominant role in the formation and evolution of the A-K gap electron sheath. The cathode electric field generated by both the main voltage pulse and the large vacuum wave precursor present on SABRE [2] can exceed the threshold for electron emission and launch

* This research was supported by the U. S. Dept. of Energy under contract no. DE-AC04-94AL85000.
[a] Titan/Advanced Innovative Technologies, [b] Ktech Corp.

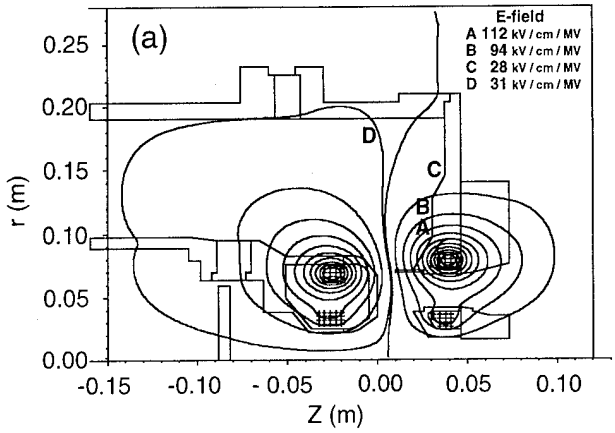
electrons into the A-K gap close to the anode surface. Such feed electrons appear to have a positive effect by producing more rapid ion beam enhancement. But the complex electron sheath structure which results, consisting of two initially distinct groups of electrons which undergo diamagnetic compression and cross-field diffusion, complicates understanding and optimization of diode performance with a passive source.

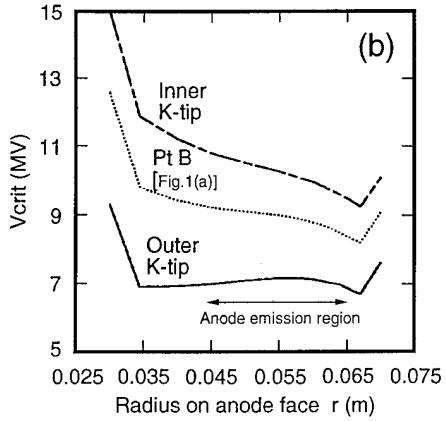
To study the effects of reduced feed electron participation in electron sheath formation, experiments and simulations have been performed with an extended cathode tip geometry, shown in Fig. 1(a). Normalized electric field values (kV/cm/MV) at the cathode electrode boundary (without electron emission) are also shown in Fig. 1(a). With >2 MV applied to the diode A-K gap, electric fields in the region near the outer cathode tip (points A and B in Fig. 1(a)) exceed the electron emission threshold of 200-300 kV/cm. However, electrons emitted from the extended cathode tip will shield this region, reducing the effective fields, and emitted electrons following the flux surfaces will be intercepted by the cathode tip and should not contribute to the electron sheath.

Diode operation in this geometry has been investigated for two distinct classes of magnetic field profile. Each profile has the magnetic field separatrix positioned near midgap to provide the anode flux required for future lithium beam focusing experiments. The anode is insulated from each point on the cathode by a (B_r, B_z) external magnetic field to a voltage V_{crit}. For diode voltages $V < V_{crit}$, electrons emitted from the cathode that conserve canonical momentum and energy are insulated from the anode. For the **Uniform Insulation** (UI) field profile shown in Fig. 1(a), V_{crit} with respect to the extended outer cathode tip is essentially flat across the anode emission area (Fig. 1(b)). Other parts of the cathode boundary where electron emission is possible are more strongly insulated than the outer cathode tip and do not contribute significantly to the electron sheath. (See for example cathode region B in Fig. 1(a) whose V_{crit} is shown in Fig. 1(b).) If no other effects were operating here, such a field profile should result in roughly uniform ion emission as a function of radius. However, experimental observations with witness plates and Faraday cup arrays for the UI field profile show ion emission heavily weighted toward the inner anode radius (Fig. 1(c)), particularly after peak ion power.

Production of a radially uniform ion beam requires a substantial adjustment of the field profile away from the UI profile. The field profile required to produce uniform radial ion beam enhancement at peak ion power is a sensitive function of both the average insulating field V_{crit} and the diode voltage waveform, and must be tuned to produce optimum uniformity for a given set of operating parameters. Anode V_{crit} profiles and the radial distribution of ion current density for such a **Uniform Emission** (UE) field profile are presented in Fig. 2. Experiments with the UE field profile show that the diode runs at higher impedance and lower efficiency than a similar configuration without an extended cathode tip [1], indirect evidence for a change in the electron sheath charge distribution resulting from the elimination of feed electrons. The effect of eliminating feed electrons can also be seen in the behavior of the vacuum wave precursor [2]. Without feed electrons and with limited instability growth to raise electron charge density near the anode, the diode runs at higher early impedance. During the precursor, the enhancement of ion current density over the Child-Langmuir density is twice as large in the geometry with feed electrons [1] as in the geometry with the extended outer cathode tip.

TWOQUICK [3] PIC code simulations also indicate the elimination of feed electrons in this new geometry. Most electrons emitted from the feed region are intercepted by the





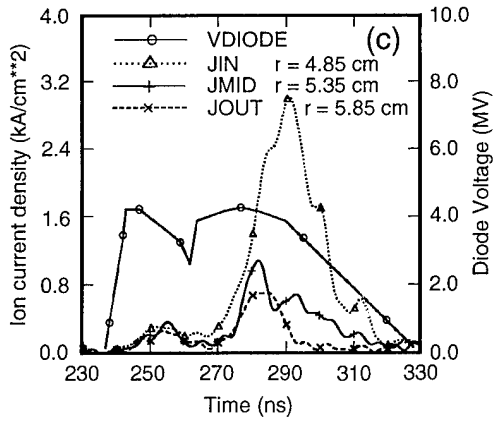
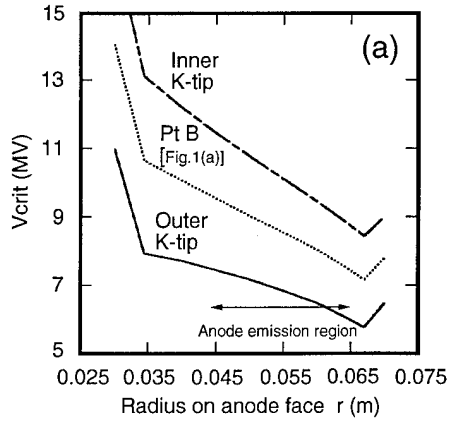


Figure 1. (a) Uniform insulation (UI) magnetic field profile for SABRE shot 996 with E-field values at selected boundary points; (b) insulating magnetic field V_{crit} between selected cathode locations and the anode face; (c) diode voltage VDIODE from a filtered Faraday cup array, and average ion current densities at the midpoint (JMID) of the anode emission area, and at the inner (JIN), and outer (JOUT) radii indicated, for SABRE shot 996.

outer cathode tip. Charge density in the A-K gap from feed electrons is lower by more than a factor of 200 compared to the cathode tip electron component. The TWOQUICK simulations do not yet reproduce the detailed radial distribution of ion current density observed in the experiment. They do however suggest that instability-induced cross-field diffusion [4] of sheath electrons from the cathode tip plays a dominant role in diode operation, and will need to be taken into account when designing appropriate field profiles for optimum extractor performance



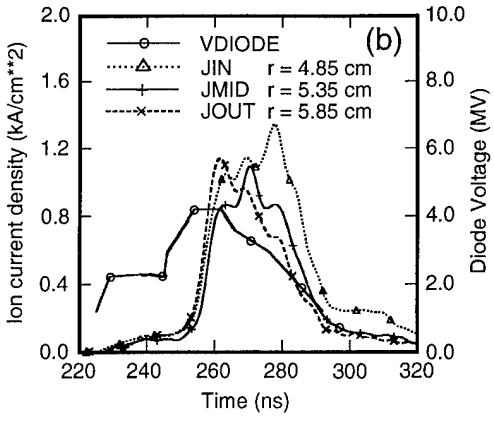


Figure 2. (a) Insulating magnetic field V_{crit} between selected cathode locations and the anode face for the uniform emission (UE) magnetic field profile of SABRE shot 1020; (b) diode voltage VDIODE from a filtered Faraday cup array, and average ion current densities at the midpoint (JMID) of the anode emission area, and at the inner (JIN), and outer (JOUT) radii indicated, for SABRE shot 1020.

with marginally-insulated sources. Diode efficiencies from experiments and from simulations with an instability model to drive cross-field diffusion are lower than from simulations without diffusion. Without fluctuations, the sheath resides on magnetic field lines that are energetically accessible at the given time in the pulse. By instability-induced cross-field transport, however, electrons can reach previously inaccessible magnetic field lines closer to the anode. If these lines are angled toward the anode at the inside radius (as in the UI profile), greater electron density will occur near the inside radius of the anode than would be expected from magnetic insulation conditions alone. Owing to this effect of the instabilities, a uniform ion current density, which corresponds to a radially uniform electron density over the anode face, requires a nonuniform V_{crit} magnetic field profile (the UE profile). TWOQUICK simulations show in Fig. 3 how nonuniform the radial electron density profile at the anode would be in the absence of instabilities, while the same magnetic field profile yields a reasonably uniform distribution when instabilities are modelled.

The extended cathode tip geometry discussed above eliminates feed electron participation in diode operation. However, the field profiles available with this electrode geometry limit efficient diode operation with either flashover or field emission sources. Fig. 4 shows an improved diode geometry under development for use with both passive and active sources. The feed cathode is recessed to completely eliminate feed electrons and the radial placement of the anode field coils is modified to provide a wider range of field geometries, including field profiles with better electron confinement at the anode area for lithium sources.

In summary, SABRE experiments and numerical simulations show that feed electrons and instability-induced cross-field diffusion of virtual cathode electrons can play a major role in the operation of high voltage extraction ion diodes. Careful design of electric and magnetic field geometries is essential for optimum diode performance with passive ion sources.

References

[1] D. L. Hanson et al., Proc. BEAMS 92, NTIS PB92-206068, Vol. II, p. 781.

[2] M. E. Cuneo et al., "Control of a Large Vacuum Wave Precursor...," these proceedings.

[3] TWOQUICK is a relativistic, electromagnetic, 2 1/2-dimensional PIC code developed at Sandia National Laboratories as part of the QUICKSILVER suite of 2- and 3-D PIC codes; see J. P. Quintenz et al., Laser and Particle Beams, to be published.

[4] M. P. Desjarlais et al., Phys. Rev. Lett. **67**, 3094 (1991); M. P. Desjarlais and T. D. Pointon, Proc. BEAMS 92, NTIS PB92-206068, Vol. II, p. 775.

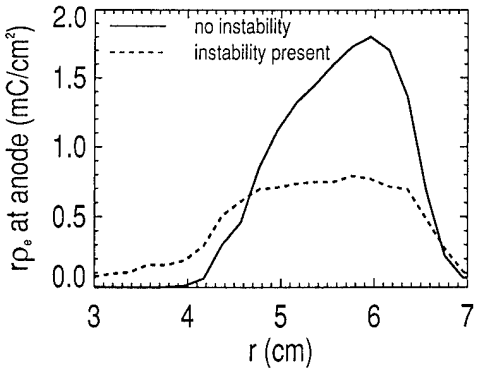


Figure 3. Radial electron density profile at the anode with and without instabilities from TWOQUICK electromagnetic PIC code simulations.

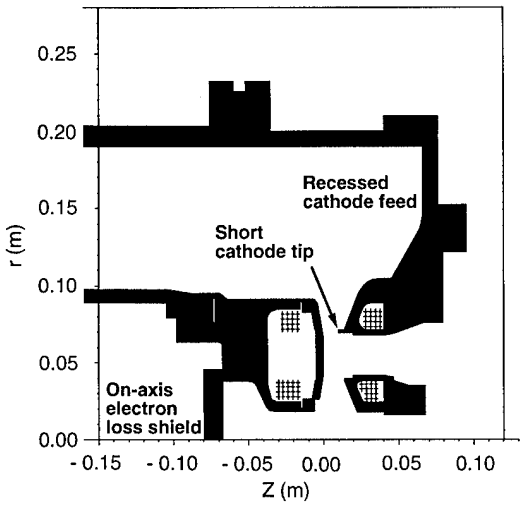


Figure 4. Improved extraction diode geometry.

LEVIS Ion Source and Beam Characterization on PBFA-II*

T.J. Renk, G.C. Tisone, R.G. Adams, J.E. Bailey, A.B. Filuk,
D.J. Johnson, and T.D. Pointon
Sandia National Laboratories, Albuquerque, NM 87185

Abstract

We report on the continuing development of the LEVIS (Laser Evaporation Ion Source) lithium active ion source for the 15-cm radial focussing ion diode on PBFA-II. We found previously that DC-heating of the anode surface to 150°C maximum for 5 hours resulted in a pure lithium beam. This paper discusses the characterization of LEVIS source uniformity by Faraday cup arrays and multiple lines of sight for visible light spectroscopy. These diagnostics give some evidence of nonuniformity in both A-K gap electric fields and ion current density. Despite this, however, the measured focal spot size appears smaller than with a passive LiF source operated in the same magnetic field topology. Experiments using a curved anode for vertical beam focussing show reduced ion beam turn-on delay by 5 ns by altering the magnetic field topology as well as anode curvature. Another 3-5 ns reduction was achieved by switching from a passive LiF to the active LEVIS source.

Introduction

The Laser Evaporated Ion Source (LEVIS) has been developed as a lithium ion source for the 15-cm radial focussing ion diode on the PBFA-II accelerator at Sandia National Laboratories. LEVIS is an active source, i. e. it makes use of a two-stage laser irradiation of the anode surface to produce a plasma prior to the diode power pulse, from which ions can be accelerated. A Nd:YAG pulse (1.06 μm, 8 ns, ~ 0.2 J/cm^2) produces a thin vapor layer (~1 mm, 10^{16} cm^{-3}) by evaporation of lithium from a thin-film alloy. The vapor layer is then ionized by a dye laser (670.8 nm, 1 μs, ~ 50 mJ/cm^2) tuned to the first resonant transition of lithium. We have reported previously[1] on the preparation of the thin-film LiAg used as the lithium-bearing source, on the optimization of the laser fluence levels, the uniformity of the laser energy deposition, and the development of a DC-heating technique for cleaning the LiAg surface prior to a machine shot. Time- and space-resolved spectroscopic observations in the anode-cathode (A-K) gap of the LEVIS source[2] verified the existence of a preformed plasma with LEVIS, and the absence of this plasma when a passive LiF ion source[3] was fielded on PBFA-II instead of LEVIS. These observations also showed large reductions in relative impurity line intensities in the A-K gap (factor 3-5 for carbon lines, factor 40 for hydrogen) after 3 hours of DC-heating to a maximum 125 degrees C, implying that impurity concentrations in the anode plasma were greatly reduced. The resulting ion beam was almost entirely free of proton and carbon contaminants, measured at the beam focus. Spectroscopic meaurements also indicated control of the anode plasma thickness by varying the timing of the vaporization laser firing relative to the power pulse. Thus we have previously shown the validity of the LEVIS concept as a source for a pure Li beam on PBFA-II.

This discussion concentrates on the behavior of the ion beam produced by the LEVIS source, in particular as compared with the beam produced by the LiF source, which has been optimized by extensive testing on PBFA-II. One result produced by both sources is that the beam focal spot size on target is

*This research was supported by the U. S. Department of Energy under contract DE-AC04-94AL85000.

consistent with a 20-35 mrad divergence, despite the fact that the source divergence has been estimated from spectroscopic observations at considerably less. LEVIS source divergence has been estimated at 4-9 mR, about half the15 mR LiF source divergence. There are several possible causes of the increase in spot size: electromagnetic instabilities in the A-K gap; and nonuniformities in the anode source plasma. Theoretical studies[4] have predicted a correlation between nonuniform ion emission and beam divergence. The effect is maximized when the length scale of nonuniformities is comparable to the A-K gap. It was a goal of the measurements detailed here to assess the importance of these contributions to LEVIS focal spot size.

In addition, almost all prior LEVIS shots used a flat anode geometry in the vertical dimension, which aids in clarifying the spectroscopic observations, but limits the power density on target. We fielded a curved focussing anode to both raise signal levels on diagnostics located at the beam focus, and to better compare LEVIS performance directly with a LiF source operated with the same diode parameters (insulation field topology, etc.).

Configuration

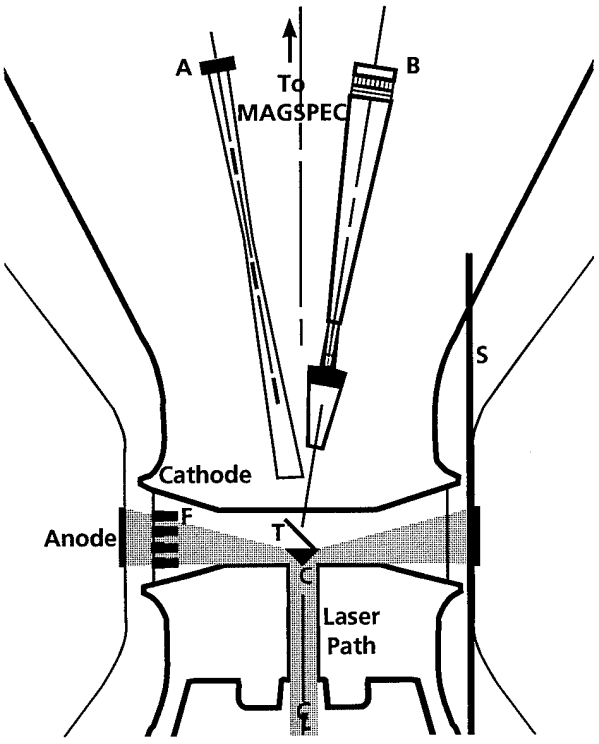


Figure 1

Figure 1 shows an overview of the diode region, the spectroscopy line-of-sight (S), and the various beam diagnostics discussed below. At each of two locations 180 degrees apart in azimuth, there were between 4 and 7 individual lines-of-sight (LoS) for spectroscopic observations on any given shot, each with a 2 mm resolution. Light from the two LEVIS lasers arrives from below, reflects off the laser distribution cone (C), and illuminates a 6-cm anode height coated with LiAg, creating a plasma from which the ion beam is drawn. The resultant beam propagates radially inward through a 1.5 μ mylar foil towards a gold scattering target (T) on axis. Scattered ions are measured by an array of diagnostics. A Magnetic Spectrometer (MAGSPEC) is located 1.1 meter above the target along the axis of symmetry. The MAGSPEC utilizes both 3 linear arrays of PIN diodes and CR-39 nuclear track-counting material to form a time- and energy-resolved image of the beam focus. Ions are also scattered slightly off axis towards a single frame camera (A), with another piece of CR-39 behind a 7.5 MeV Li range filter, giving a time-integrated focal image, from which total ion energy on axis can be estimated. The Ion Movie Camera (B), a 2-D array of PINs also located slightly off-axis, generates a time-resolved image of the beam focus.

A small fraction of the ion beam is collected by an array of Faraday cups (F) located at the radius of the mylar foil. A total of 12 cups were fielded in groups of 4 located 90 degrees apart. Several cups per shot were filtered with 36 μ Al, which transmitted only protons, thus allowing qualitative measurement of hydrogen impurities in the Li beam. Though it appears in the drawing that the Faraday cups interfered with the laser beams, through the use of reflecting mirrors this interference was kept to a minimum.

Results

Several different configurations were studied, and their results discussed here: flat anodes using both LEVIS and passive LiF ion sources, a focussing anode shot with each type of source, and a flat anode shot in which the LiF source was subject to the same DC heating cycle as the LEVIS source. The heated LiF shot differed only slightly in behavior from unheated LiF results.

The LEVIS source exhibited more azimuthal

variation in Faraday cup magnitude than the LiF source. Typical variations in cup magnitudes for LiF were ± 20 to 30%, with as much as 15 ns temporal variation in attainment of peak magnitude. This variation increased slightly on the heated LiF shot. The variation on LEVIS shots ranged from ± 15% to as much as factors of 5 variation in peak magnitude. The LEVIS shots also exhibited little temporal variation in the signal peak. These combined observations suggest large local variations in current density being drawn from the LEVIS source. There was little correlation, however, between this Faraday cup variation and the size of the resulting beam focus, as will be discussed below.

The Faraday cups filtered to accept only protons generally followed the same behavior for either source, i.e. minimal amplitude before peak beam power, followed by increasing proton contamination.

Spectroscopic measurements of the electric field in the two LoS locations indicated the presence of large field asymmetries as a function of time, for both LEVIS and LiF sources. Fig. 2 shows average electric field for the two azimuthal locations at two different times in the diode power pulse. The 58 ns plot roughly corresponds to the time of peak beam power. Based on these and other observations, the degree of asymmetry is seen to increase and decrease several times during the power pulse.

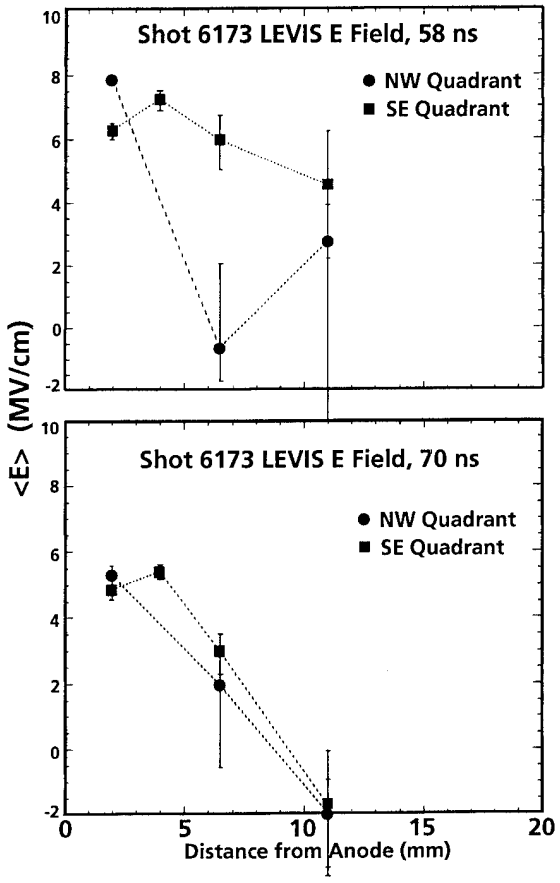


Figure 2

Both ion sources thus appear to suffer both electric field fluctuations of significant magnitude, and azimuthal variations in Faraday cup signals, with more temporal variation in the signals with the LiF source, and more peak magnitude variations with LEVIS.

The focal spot behavior is estimated from the time-dependent Ion Movie Camera image, and the time-integrated Single Frame Camera and Magnetic Spectrometer CR-39. It is difficult to estimate spot behavior with the Ion Movie Camera for flat anodes, due to small signal levels. The other diagnostics have consistently yielded a spot size FWHM of between 8 and 9 mm for a half-dozen LEVIS shots taken with a flat anode, with energies delivered to the center comparable with LiF shots with similar geometry (~ 75 kJ). The LiF shots taken in flat geometry in this test series yielded large (13 mm) spot sizes, with energy delivery comparable to the flat LEVIS shots. This is a larger spot size than the 10 mm that is typically attained with LiF shots in flat geometry. But even using the smaller 10 mm figure, the flat LEVIS focal spot size is consistently smaller than for an LiF source operated with the same diode parameters. This smaller LEVIS spot size occurs despite the more nonuniform beam behavior as indicated by the Faraday cup waveforms.

One shot each was taken with the LEVIS and LiF sources in the same focussing geometry. Use of a curved anode results in a different magnetic field topology in the A-K gap, and may help to explain the difference in operating behavior with both sources, relative to their flat counterparts. In both cases, the "turn-on" time of the diode, i.e. the time when significant signal appears on the Faraday cups, was earlier than with flat anodes. In flat geometry the turn-on time was similar for both sources, but with a curved anode, the LEVIS source turned on a full 10 ns earlier, while for LiF the figure was 5-7 ns earlier. Because of the focussing geometry, the signal levels on the Ion Movie Camera increased for

both sources, enabling time-dependent focal images for both cases. These data are portrayed in the form of plots of maximum signal level, and are shown in Figs. 3 and 4 for a LEVIS shot (6173) and LiF (6176), respectively. The x-axis indicates position within a row of PIN diodes imaging the horizontal axis of the beam focus. The y-axis shows the maximum signal level at each PIN location at times ranging from 0 to 27.5 ns into the ion beam pulse. Except for the ion source, these were otherwise identical shots. In Fig. 4, the data have been time-shifted 4 ns to align the two power pulses. In Fig. 3, analysis of

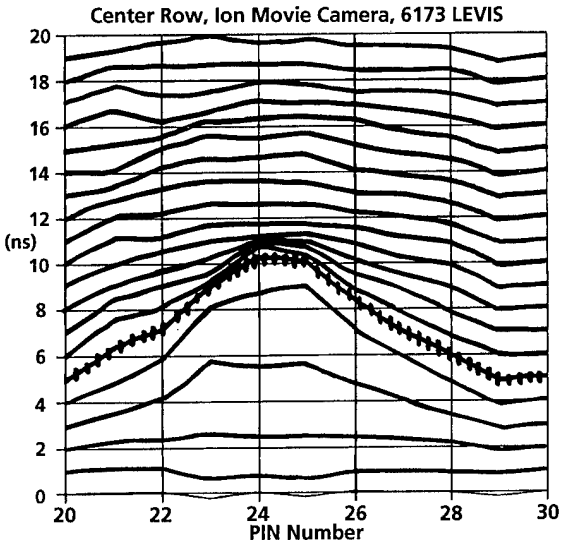


Figure 3

the plots show that the LEVIS beam attained an 8mm FWHM at about 4 ns into the beam pulse. This corresponds to a total beam divergence of 27 mR. The vertical-hatched contour at 5 ns indicates the time of approximately the maximum signal level attained during the pulse. By 8 ns, the focus has increased to 9-10 mm, and the intensity level has decreased significantly. In Fig. 4, by contrast, a 10 mm FWHM is attained at a similar 4 ns (the FWHM of the vertical-hatched contour), but the number of significant level contours exceeds the LEVIS shot. This indicates a beam of inferior focus but of longer duration with the LiF source. The energy delivered to the center was larger on the LiF shot, 80 kJ compared to about 40 kJ for the focussing LEVIS shot. Some of this may be explained by the larger Faraday cup signals on Shot 6176 (LiF), but the Ion Movie Camera clearly indicates that the beam focus disappears earlier with the LEVIS source.

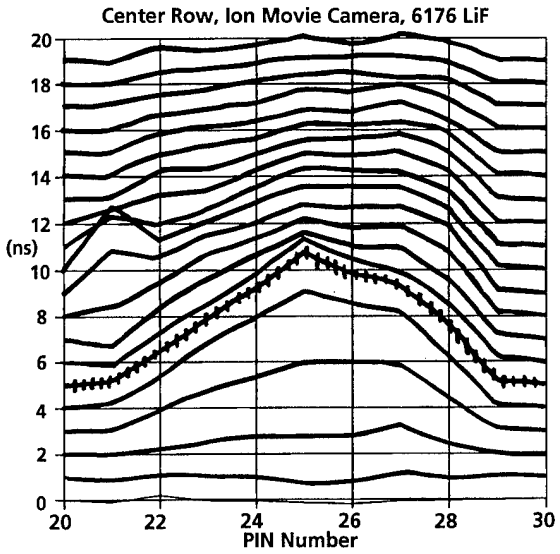


Figure 4

To gain further insight into the beam behavior with the two ion sources, the diode was modeled with the 3-D, fully electromagnetic QUICKSILVER[5] particle-in-cell (PIC) code. The diode geometry was accurately modeled, but the vacuum transmission lines above and below the diode were not. The LEVIS source was assumed to be a Child-Langmuir emission surface, while the LiF anode was modeled as a source of field-emitted ions with a threshold emission voltage of 9 MV.

A characteristic signatures of the PBFA-II ion diode seen in previous QUICKSILVER simulations was the presence of two electromagnetic instabilities. Early in time, a high frequency diocotron mode does not significantly affect ion orbits. This is followed by a transition to a lower frequency 'Ion Mode' when the beam current density reaches an enhancement between 6 and 10 over the two-species Child-Langmuir value, greatly increasing beam divergence. Since space-charge-limited sources operate at higher enhancement earlier in time, they make this transition earlier and more abruptly. The simulation of the curved anode LEVIS shot showed an earlier transition from the diocotron to the Ion Mode than with LiF, and the resulting beam divergence degradation similarly worsened. Beam divergence increased in the Ion Mode to 40 mR with the LiF source, and 70 mR with LEVIS. This latter figure is large enough to completely diffuse the beam focus, which is consistent with the Ion Movie Camera data from the LEVIS shot.

Another simulation of the curved LEVIS shot was performed with a 15% increase in the insulating magnetic field. In this simulation, the onset of the Ion Mode was delayed by 5 ns, and the beam divergence in the Ion Mode phase was reduced to a maximum of 50 mR. Thus, one approach to improvement of LEVIS focal behavior suggested by QUICKSILVER is diode operation with higher magnetic field, which has been seen to improve overall beam quality in experiments with other diodes.

It must be pointed out that in terms of power on target and energy delivered to the center, the LiF shot 6176 exceeded LEVIS 6173 by factors of two (80 to 40 kJ, 0.4 to 0.2 TW/cm^2). Other shots with the LiF source on PBFA-II have yielded power densities exceeding 1 TW/cm^2. However, the LiF source and geometry have been optimized over many shots, and we report here the result of only one focussing LEVIS experiment. A LEVIS optimization path would be different from that taken with LiF to capitalize on LEVIS advantages. For instance, the magnetic spectrometer on the focussing LEVIS shot clearly indicates ions emitted well before the diode voltage peaked, in contrast to the LiF source. This led to ion velocity (and beam power) bunching, which cannot occur where the beam voltage is monotonically decreasing during ion emission. This observed velocity bunching is a design requirement for future higher power ion driven inertial confinement fusion concepts.

Summary

A number of beam experiments were undertaken on PBFA-II in which both the LEVIS and LiF ion sources were operated. With each source, both flat and focussing anodes were fielded. The goal of these experiments was to investigate the possible contribution of anode plasma nonuniformities and electromagnetic instabilities to the increase in beam divergence from the 4-9 mR inferred at the anode surface, to the 20-30 mR seen at the target.

Measurements from a multiple Faraday cup array indicated considerable azimuthal variation in peak magnitude in the case of the LEVIS source, more than with a passive LiF source. Both sources exhibited considerable azimuthal variation in electric field in the A-K gap. Despite the Faraday cup behavior, the LEVIS source in flat geometry consistently produced smaller focal spot sizes than for a LiF source operated in similar geometry.

When the anode was switched from flat to curved, both sources "turned on" significantly sooner, 5-7 ns in the case of the LiF source, and 10 ns with the LEVIS source. On the one LEVIS shot using a curved anode, ion emission began well before the diode voltage peaked, leading to beam power bunching not seen with the LiF source. It should be pointed out that, because of the general delay in ion current iniation experienced in all Applied B diodes, a reduction in this delay of only 5 ns could potentially lead to a significant increase in beam power. The beam diagnostics showed that the LEVIS focussing beam focal spot size was smaller than for an otherwise identical shot taken with a LiF source, but the beam dwell time on target was reduced, leading to decreased peak beam power and energy deposited as compared to LiF. QUICKSILVER simulations of both sources indicate that a possible explanation for this behavior is that the LEVIS-generated beam is more susceptible to the Ion Mode instability. QUICKSILVER also suggests that a way to improve the LEVIS divergence is to operate the diode with a higher insulating magnetic field.

References

1. G.C. Tisone, T.J. Renk, D.J. Johnson, R.A. Gerber, and R.G. Adams, *Proceedings of the 9th Int'l Conf. on High-Power Particle Beams (Beams '92)*, Washington, DC, D. Mosher and G. Cooperstein, Eds., p. 800.
2. A.B. Filuk, J.E. Bailey, K.W. Bieg, A.L. Carlson, T. J. Renk, and G.C. Tisone, *Proceedings of the 9th Int'l Conf. on High-Power Particle Beams (Beams '92)*, Washington, DC, D. Mosher and G. Cooperstein, Eds., p. 794.
3. R.W. Stinnett, T.A. Green, D.J. Johnson, T.R. Lockner, T.A. Mehlhorn, J.E. Bailey, A. Filuk, and L.P. Mix, *Proceedings of the 9th Int'l Conf. on High-Power Particle Beams (Beams '92)*, Washington, DC, D. Mosher and G. Cooperstein, Eds., p. 788.
4. S.A. Slutz, Phys. Fluids B **4**, 2645 (1992).
5. D.B. Seidel, M.L. Kiefer, R.S. Coats, T.D. Pointon, J.P. Quintenz, and W.A. Johnson, in *Computational Physics*, A. Tenner, Ed., World Scientific, Singapore, 1991, p. 475.

Energy Resolved Measurement of the Characteristics of B_r Ion Diode

Katsumi Masugata, Etsuji Chisiro, Akira Matsuyama, Hiroaki Nakajima, and Kiyoshi Yatsui

Laboratory of Beam Technology, Nagaoka University of Technology, Nagaoka, Niigata 940-21, Japan

Abstract

The characteristics of B_r-magnetically insulated ion diode has been studied by new types of ion energy spectrometers. Dependence of the characteristics of the diode has been evaluated on the geometry of insulating magnetic field. Turn-on characteristics have been found to be improved when insulating magnetic flux ($2\pi rdB_r$) increases with radius. Two dimensional, energy-resolved divergence angle of proton, carbon, oxygen, and negative ions have been evaluated independently. The divergence angle has been found to have weak dependence on energy or ion species, though ion trajectories strongly depend on them. Fine structure on the order of 1 mrad is observed in the measurement of energy-resolved injection angle distribution of the ion beam. This seems to be due to the non-uniformity of the anode plasma.

1. Introduction

An intense pulsed light ion beam (LIB) is one the hopeful candidate of the energy driver of inertial confinement fusion (ICF). To apply LIB to ICF, it is most important to develop highly bright ion diode. For the purpose, we are studying the characteristics of B_r-type magnetically insulated ion diode (B_r-MID).

In this paper, we describe the characteristics of B_r-MID evaluated by using a newly developed energy spectrometers. Turn-on characteristics, energy-resolved 2-dimensional (2D) divergence angle, energy-resolved injection angle distribution are described in detail.

2. Experimental Set-up

Figure 1 shows the cross-sectional view of B_r-MID. The diode is constructed of an aluminum anode, a pair of stainless cathode, and a pair of insulating magnetic field coil. The anode has a dimension of outer radius = 55 mm, inner radius = 25 mm, and has a active surface from r = 30 to 50 mm where epoxy filled grooves of depth and width =1 mm are made as the ion source. As a cathode, a pair of cylinder (inner and outer cathode) is faced to the anode at gap length d = 5 mm. For the production of insulating magnetic field, pair of multi-turn coil is placed in the inside and outside of the cathode. The current of each coils can be independently controlled to control the field distribution.

In the experiment, diode is powered by a pulse power system "ETIGO-II" [1]. By using a vacuum pre-pulse in the vacuum chamber, the pre-pulse voltage is reduced to be less than 1/3 of the pre-pulse observed in the diode voltage (V_d) [2].

Figure 2 shows the distribution of insulating B_r field and magnetic flux ($\Phi_r = 2\pi rdB_r$). Two types of distribution (type 1 and type 2) are used to evaluate the effect. In type 1, Φ_r is constant and in type 2, Φ_r increases with r.

For the measurement of the dependence of 2D divergence on energy and/or species, it is necessary to obtain the energy and/or mass resolved beam profile in φ_θ-φ_r space where φ_θ and φ_r are the injection angle of the beam in θ and r direction. For the purpose, multi-pinhole type Thomson-parabola spectrometer [3] (MTPS) has been developed.

The schematic of MTPS is shown in Fig 3. The MTPS is constructed of a 1st pinhole, electric- and magnetic-deflector, multi-pinhole plate and detector. The ion beam of each injection angles are selected by a 1st pinhole and a multi-pinhole plate. As a magnetic deflector permanent magnet is used to make the spectrometer compactness. The electric deflector is operated in 2 mode. In case of time integrated measurement, DC voltage is applied to

insulating magnetic flux increases with radius.

2D, Energy resolved divergence of proton, C^+, O^+, and O^- have been evaluated independently. The divergence angle have a weak dependence on energy or ion species, though ion trajectories strongly depend on them. Fine structure on the order of 1 mrad is observed in the measurement of energy-resolved injection angle distribution.

REFERENCES

[1] A. Tokuchi et al: Proc. 2nd Int'l Symp. on ICF Res. by High-Power Particle Beams, Nagaoka, ed. by K. Yatsui, 430 (1986).

[2] H. Sugimura et al: Proc. BEAMS 92, II, 847 (1992).

[3] K. Masugata et al: Proc. BEAMS 92, II, 853 (1992).

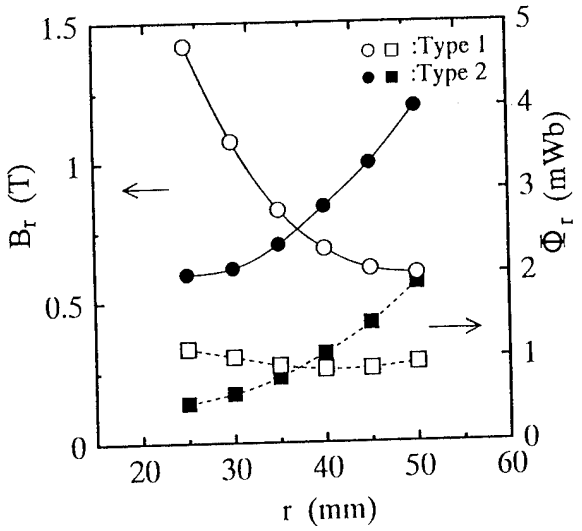


Fig.2 Distribution of insulating Br field and magnetic flux(Φ_r) for type1 and type2.

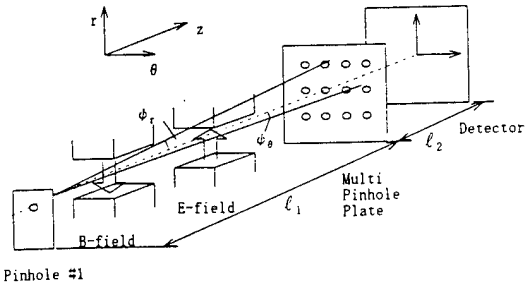


Fig.3 Schematic of MTPS.

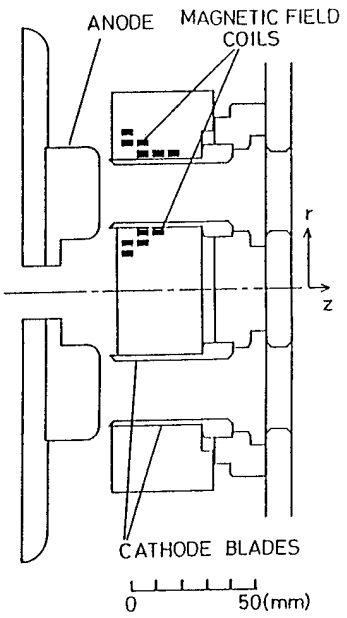


Fig.1 Cross-sectional view of Br-MID.

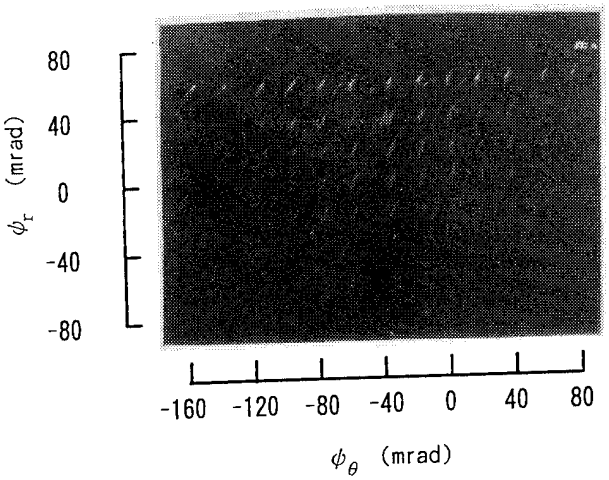


Fig.4 Typical trace obtained on CR-39 in the time integrated mode of MTPS.

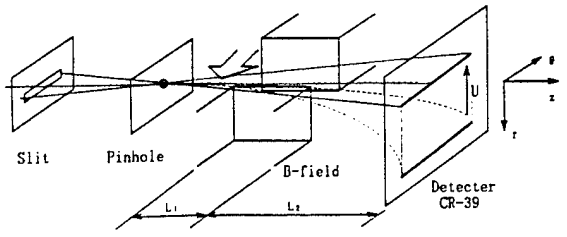


Fig.5 Schematic of Slit-MS.

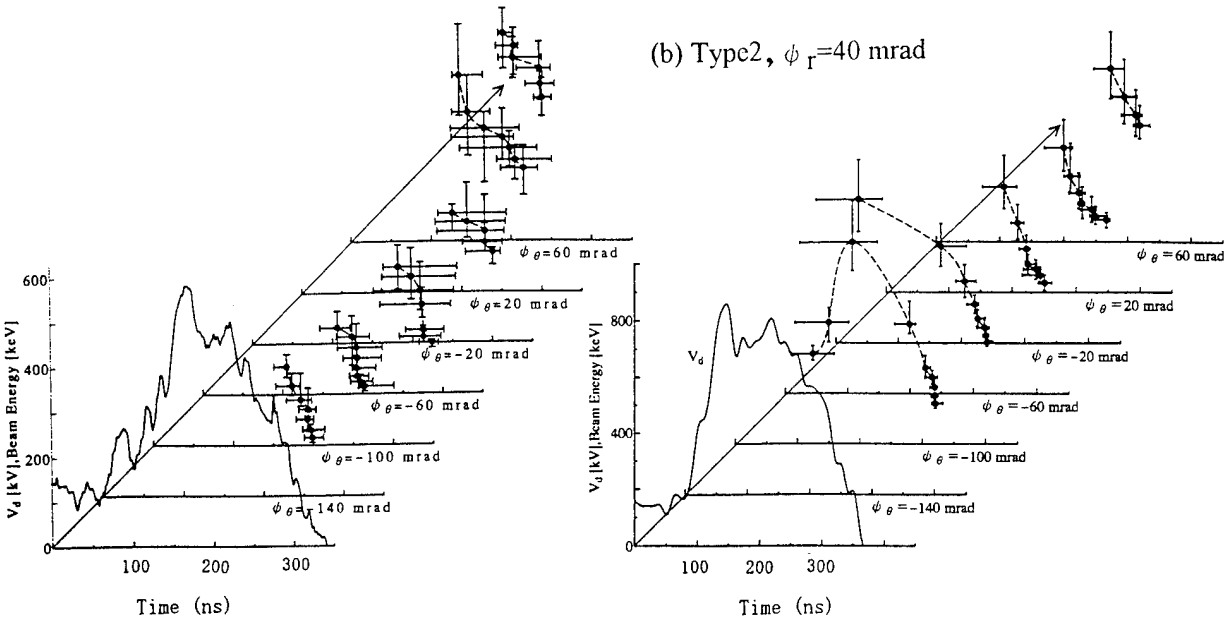


Fig.6 Time-energy diagram of proton observed on (a) Type1 and (b) Type2 diode.

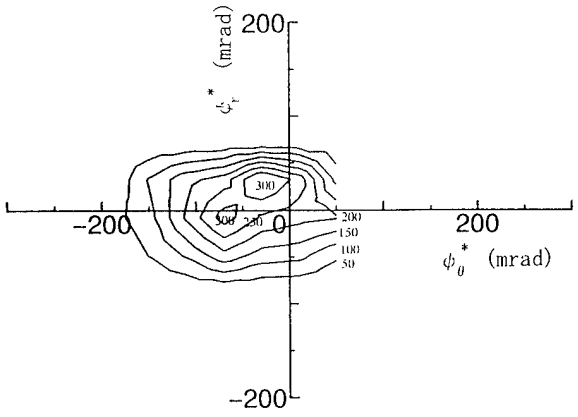
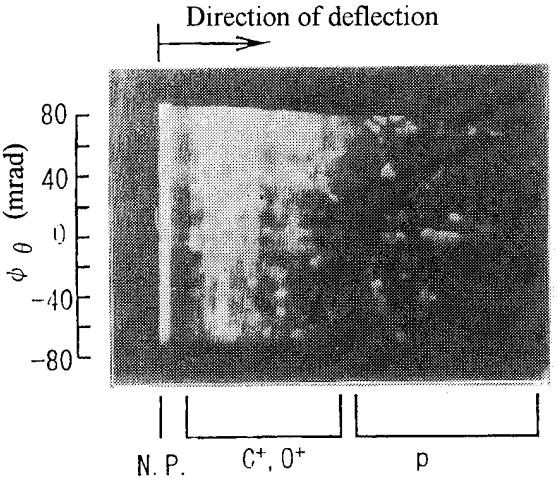


Fig.7 Track density distribution of C^+(300keV) in ϕ_r^*-ϕ_θ^* space.



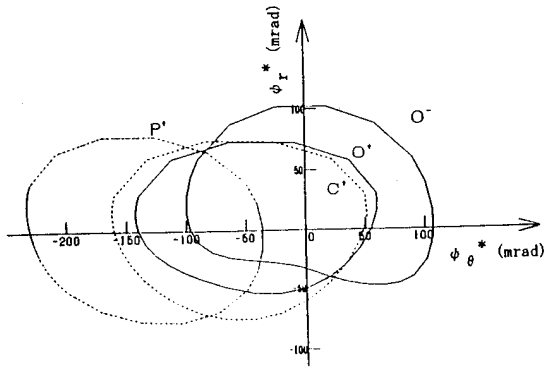


Fig.8 Outline of the profile of each ions of energy =300keV.

the defector, where slanted pulse is applied for the time resolved measurement.

Figure 4 shows typical trace obtained on CR-39 in the time integrated mode. As seen from Fig. 4, parabolic traces are independently produced, each of which correspond to the set of φ_θ and φ_r.

MTPS is useful since it can be used to obtain a profile of LIB in 2D space of φ_θ-φ_r, however, the data obtained is intermittent. To obtain a continuous profile in 1D space of φ_θ or φ_r, magnetic spectrometer with beam injection slit (slit-MS) is used. The schematic is shown in Fig. 5. In slit-MS, LIB is injected into a magnetic deflector through a slit and pinhole. As the ion beam with 1D information of injection angle is energy analyzed by the deflector and recorded on CR-39. Eventually, the ion density profile is recorded on 2D space of energy and φ.

2. Experimental Result

a) Turn-on Characteristics

To evaluate the turn-on characteristics for 2 types of insulating magnetic field geometry, MTPS is operated in the time resolution mode. The evaluation is done for each traces corresponding to the sets of injection angles (φ_θ, φ_r). Time of flight collection are made for each data and plotted on time-energy diagram.

Figure 6 shows the time-energy diagram of proton for several set of φ_θ, φ_r. V_d is also shown for comparison. For type 1, beam is observed after the peak of V_d. In contrast to the case, for type 2, in some set of φ_θ, φ_r, proton beam is observed in the rise time of V_d. The anode is inspected after the shots, whole surface is damaged in type 2, whereas only the inside of the surface in type 1.

Form the data obtained, we conclude that, in the case of type 2, electrons irradiate the whole surface of anode in the rise time of V_d. By the irradiation, the production of abode plasma is promoted. On the contrary, in the case of type 1, insulation of electron is good and turn on is delayed.

b) 2D Divergence Angle

Dependence of divergence angles on ion energy or ion species has been evaluated for the diode of type 2. In this experiment, MTPS is used in the time integrated mode. The track density for each ion is evaluated for each trace of the set of (φ_θ, φ_r). The injection angle (φ_θ, φ_r) is carefully collected to obtain a real injection angle (φ_r^*,φ_θ^*).

Figure 7 shows the track density distribution of C^+(300 keV) in φ_r^*-φ_θ^* space. From the FWHM of the distribution, we evaluate the divergence angle in r direction (ϕ_r) to be ≈50 mrad. Table 1 shows the list of divergence angles evaluated by the method, from the figure, we see that divergence angle has a weak dependence on the ion species or magnetic field distribution.

Figure 8 shows the outline of the envelope of the profile. As seen form the figure, 2D shape of the divergence are almost same, but the positions are shifted for each species. This seems to be due to the difference of the deflection in the insulating magnetic field.

Table 1 Divergence angle

	ϕ_θ (mrad)			ϕ_r (mrad)		
ions (keV)	p (300)	C^+ (300)	O^+ (300)	p (300)	C^+ (300)	O^+ (300)
Type 1	60	74	70	51	44	51
Type 2	69	60	64	43	50	52

c) Averaged Beam Composition

Ion beam compositions have been evaluated for each injection angle by using MTPS. This data is averaged over the injection angle. The results are shown in table 2. As seen from the table we see that 60 % of the beam is proton in average.

Table 2 Averaged beam composition

	Ions(keV)	p (300)	C^+(300)	O^+(300)	O^-(300)
Number density (%)	Type 1	58	23	15	4
	Type 2	67	24	6	3

d) Continuous Profile on Injection Angle (φ)

By using slit-MS, a continuous profile of the beam on φ is observed. Figure 9 shows the example obtained on the diode of type 2. From the figure, we see that the beam is intermittent and has a fine structure in a 2D space of φ and energy. The scale length of the structure is in the order of 1 mrad. If this structure is due to the non uniformity of the anode plasma, corresponding scale length of the non-uniformity is in the order of 0.1 mm.

3. Conclusion

The characteristics of B_r-magnetically insulated ion diode has been studied by new types of ion energy spectrometers. A turn-on time and ion-beam current have been found to be improved when

EXTRACTION, APPLIED-B ION DIODE WITH EXTERNALLY-DRIVEN, ACTIVE ANODE PLASMA SOURCE

J. M. Neri, D. D. Hinshelwood,* J. R. Boller, R. Fisher,* J. Greenly,***
W. A. Noonan,** P. F. Ottinger, S. J. Stephanakis, and F. C. Young
Pulsed Power Physics Branch, Plasma Physics Division
Naval Research Laboratory, Washington, DC 20375-5346

Abstract

We report the first use of an external current source to drive an exploding foil anode plasma source. The source is fielded in an extraction, applied-B ion diode furnished by Sandia National Laboratories (SNL). An ion beam is produced with parameters approaching those required for ion beam transport research in support of the DOE ICF program. The time-resolved ion beam current density is measured using Rutherford scattering and a novel Faraday cup developed at Cornell University.

We are developing an extraction, applied-B ion diode, on the Gamble II generator at NRL, for ion-beam-transport research in support of the SNL ion-beam ICF effort. An ion beam with a voltage above 1 MV and a proton current above 200 kA is required. At present we are using diode hardware from the SNL SABRE generator. Development of this diode on Gamble II is a challenge because of the relatively low (~1 MV) voltage, high (~300 kA) ion current, and small (~60 cm^2) anode area involved. These result in required enhancement factors 2-3 times greater than those in similar experiments on LION[1] at Cornell, SABRE[2] at SNL, and KALIF[3] at KfK, Karlsruhe. The need for stable, low-impedance diode operation with early turn-on (to avoid insulator flashover) necessitates the use of an active anode plasma source. We are using a version of the Exploding Metallic Foil Anode Plasma Source (EMFAPS). First developed at Cornell,[1] this technology has been advanced significantly by work at KfK.[4,5] This source comprises a thin metallic foil deposited on an insulating anode substrate. A plasma opening switch is used to divert the leading edge of the generator current through the foil, rapidly heating the foil and releasing desorbed gases. Subsequent breakdown of this gas layer results in a uniform, largely protonic plasma conformal to the anode surface.

The relatively large jitter of the Gamble II Marx and intermediate water switch precludes reproducible current diversion with a plasma switch. Instead, we report here on the first use of an EMFAPS driven by an external pulser, triggered in our case by the water-swtich output. A four-stage L-C inversion pulser is used to drive 30-40 kA through the foil with a 10-90 risetime of 20 ns. An array of 30, RG-223 cables connects the pulser to the foil though the Gamble II transit-time isolator. The total jitter, arising from the pulser and the Gamble II oil output switch, is about 15 ns, which is seen to be acceptable.

The EMFAPS anode and experimental arrangement used in bench tests are shown in Fig. 1a. The anode comprises an epoxy substrate cast between a stainless outer ring and a thin brass inner ring. First, copper current contacts are sputter-deposited over the epoxy-metal joints. Then, 400 to 1200-Å aluminum films are sputter-deposited over the entire anode face. These films are characterized by a thin-film monitor during deposition and by electrical resistance measurements afterwards. Typical film resistance is about four times the bulk value.

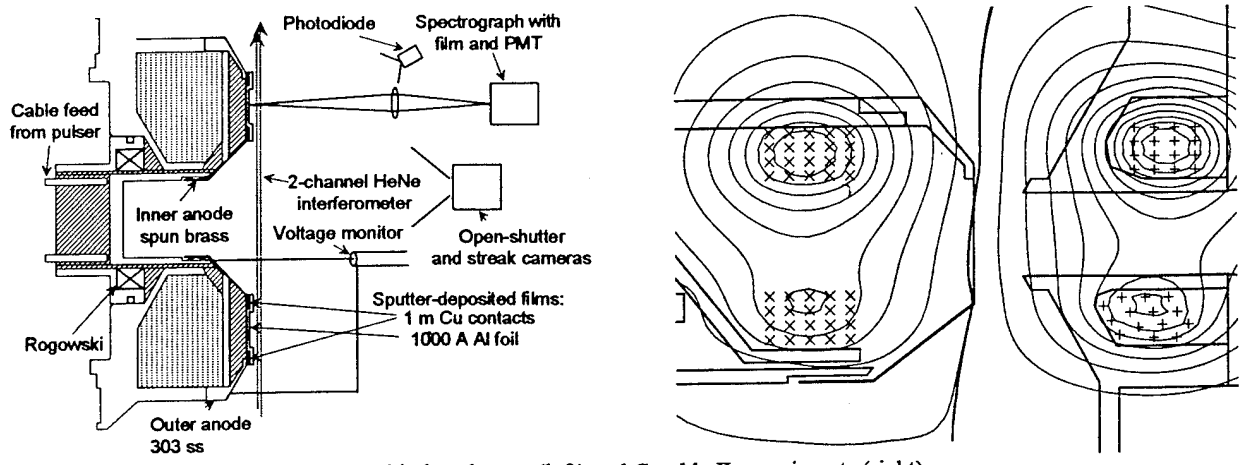


Fig. 1: The EMFAPS arrangement used in bench tests (left) and Gamble II experiments (right).

The foil voltage is measured by a probe with connections on the front side to eliminate inductive pickup. Electrical data from a 1200-Å foil are shown in Fig. 2a. The foil resistance breaks down after an energy input of about 1.5 J. Both this value, and the foil resistance, are consistent with breakdown occurring at melt. This is the expected behavior of an EMFAPS, since melting results in strong gas desorption.

Other diagnostics used to study the EMFAPS operation are shown in Fig. 1a. Open-shutter photographs show some arcing at the foil contacts that varies shot-to-shot, although streak photography indicates that these arcs tend to occur after the times of interest. A HeNe interferometer with heterodyne phase detection is used to measure the electron density. The observed density is seen to be localized to within 1.5 mm of the cathode surface during the times of interest. Typical data are shown in Fig. 2b. The negative phase shift late in time indicates a large neutral component that may also be affecting the phase shift earlier in time. Two-color interferometry is planned for the future to allow resolution of both components.

The diode arrangement on Gamble II, along with a typical, calculated field geometry, is shown in Fig. 1b. This calculation, which includes the effects of magnetic field diffusion through the anode and cathode structures, is performed using the code ATHETA.[6] We have recently measured rA_θ directly, and found a discrepancy with the code predictions. The cathode coil flux into the diode gap is about 20% greater than predicted, which has

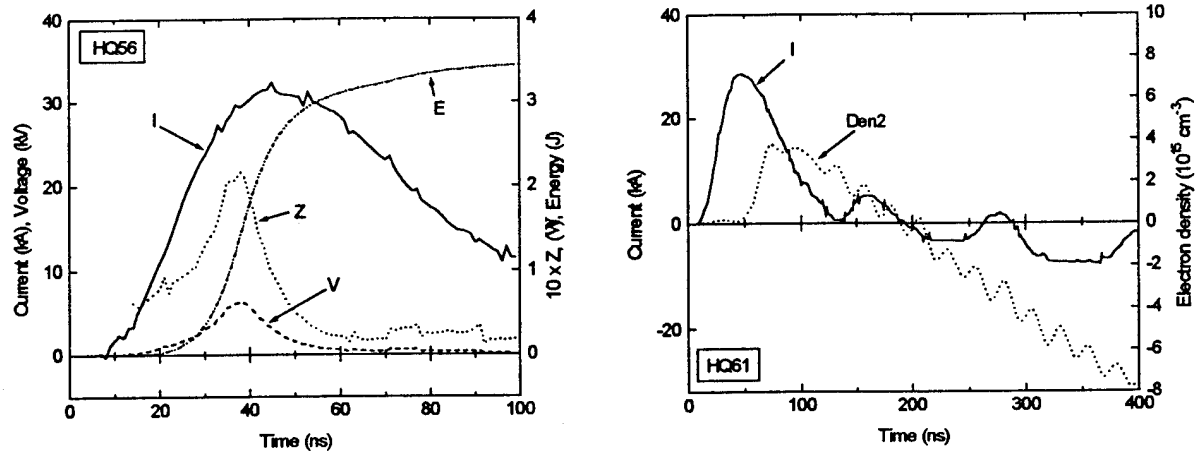


Fig. 2: Electrical (left) and electron density (right) data from EMFAPS bench experiments.

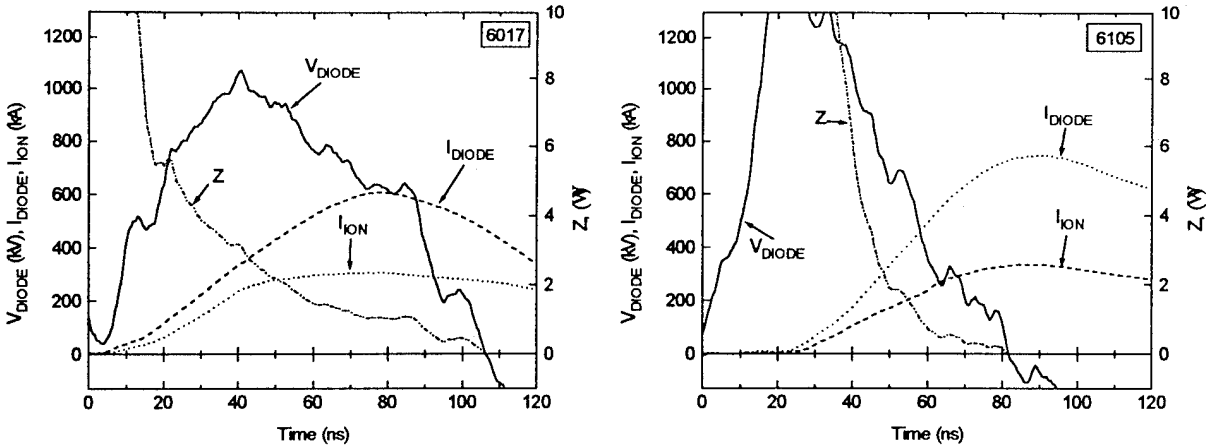


Figure 3: Electrical waveforms obtained with (left) and without (right) driving the EMFAPS on Gamble II shots.

the effect of pushing the separatrix back into the anode. We are studying this discrepancy further.

The ion beam is transported through 1-Torr air, which is separated from the diode vacuum by a 1.8-μ polycarbonate foil located behind the cathode tips.

Diode electrical data from our best shot to date is shown in Fig. 3a. This shot had the calculated field geometry shown in Fig. 1b, with the above caveat. The ion current begins early with reasonable efficiency. Later in time, the electron loss increases, loading down the generator and limiting the ion beam energy to 15 kJ. The effect of the EMFAPS is seen by comparing these data to those in Fig. 3b, from a similar shot taken without driving the foil current. Here the ion current begins much later although the diode actually shorts out earlier. The lower early-time impedance obtained with the EMFAPS will allow the diode to be operated at higher power in the future without insulator flashover.

Shots have been taken with different magnetic field configurations, pulser delays, foil thicknesses and foil resistivities. The anodes used on some shots had a 75-μ thick copper insert cast into the epoxy at a distance of 2 mm behind the anode surface. This insert is designed to conserve flux during the shot timescale, preventing the expanding, diamagnetic electron cloud from pushing flux into the anode during the shot.

The pulser delay has been the most important parameter to date. In general, increasing the delay (up to at least 80 ns) hastens the diode current onset without affecting the time of impedance collapse. The need for such a long delay, and the large neutral component to the anode plasma mentioned previously, indicate that the pulser may not be driving the foil hard enough.

Little or no effect of foil thickness or resistivity, or the use of an anode insert, is seen. Changes in the field configuration on the order of 10 percent have shown little effect. Future experiments using a more optimum field configuration (i.e., Fig 1b) may show more sensitivity of diode performance to these variables.

The ion beam is diagnosed using shadowbox techniques and Rutherford scattering. The shadowbox data show a microdivergence on the order of 20 mrad, and some angular momentum. The latter is expected because of the separatrix location inside the anode that existed on these shots. The 90-degree Rutherford scattering yield from a thick aluminum target is compared in Fig. 4a with the signal predicted based on the ion current and voltage waveforms, the assumed total beam area, and the scattering geometry. The prediction has an uncertainty

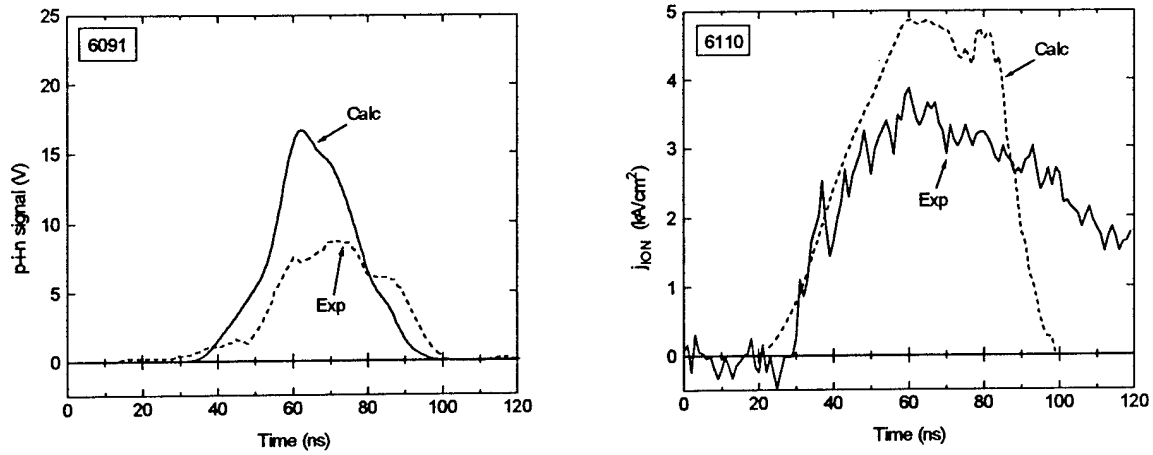


Figure 4: Observed and calculated signals from Rutherford scattering (left) and a large-aperture Faraday cup (right).

of about 20 percent. The signals are similar in shape although the observed signal is lower than predicted. In general, reasonable shape agreement is observed, including signals from shots where the detector was located far enough away to resolve differences in the ion voltage. Averaged over 9 shots, the integral of the observed signal is 65 percent of the integral of the predicted signal. This is evidence of a non-protonic component of the ion beam, since the p-i-n had a foil filter that would stop any heavier ions.

A large-aperture Faraday cup[7] was used to diagnose the ion beam on one shot. This cup is unbiased and was located 1.5 cm behind the cathode foil, where the diode magnetic field provides good insulation of secondaries and co-moving electrons. The cup is terminated with a 0.05-Ω shunt to reduce the voltage produced. Calculated and observed signals are compared in Fig. 4b. The tail on the observed signal is not understood at present. The observed signal is about 70 percent of the predicted value, a value consistent with the Rutherford scattering data.

In order to obtain ion beam parameters adequate for transport experiments, the diode impedance late in time must be increased without sacrificing the early ion current onset. We plan to accomplish this by increasing the diode gap while driving the foil with more current. A Marx-waterline pulser, capable of driving over 50 kA through the foil, has been constructed and will be used in future experiments. The aluminum anode foil will be replaced by hydrogen-loaded titanium in effort to boost the proton component of the beam.[4,5] The use of a more optimum field geometry is also expected to improve the diode performance.

In conclusion, we have demonstrated operation of an EMFAPS driven by an external current source in an extraction applied-B diode. Future improvements to the diode are expected to produce an ion beam with parameters suitable for transport research.

It is a pleasure to acknowledge helpful discussions with Mike Cuneo and Kerry Lampa of SNL and Hans Bluhm and Peter Hoppe of KfK. This work was supported by the US DOE through Sandia National Laboratories.

* JAYCOR, Vienna, VA
** NRC Research Associate
*** Cornell University

1. G. D. Rondeau, Ph.D. thesis, Cornell Univ., NY (1989).
2. M. Cuneo, et al, Proc. 1993 Pulsed Power Conf., p. 423.
3. H. Bluhm, et al, Proc. IEEE, 80, 995 (1992).
4. H. Bluhm, et al, Proc. Beams 90, p. 927 (1990).
5. H. J. Bluhm, et al, IEEE Trans. Pl. Sci., 21, 560 (1993).
6. J. P. Quintenz and D. B. Seidel, Sandia internal rep. SAND84-1336 (1985).
7. J. Olson, Cornell University, personal communication.

A TECHNOLOGICAL ION SOURCE WITH HOLLOW CATHODE IN MAGNETIC FIELD

Gavrilov N.V., Mizgulin V.N., Nikulin S.P., Ponomarev A.V.
Institute of Electrophysics
Ural Division of the Russian Academy of Sciences
620219, Ekaterinburg, Russia

Abstract

An ion beam source based on a hollow-cathode, glow discharge in a magnetic field capable of producing gas and carbon ion broad beams with a cross-sectional area of up to 200 cm^2 has been developed. The source comes in two modifications, the first one generating continuous beams of low-energy ions with a current of up to 150 mA is used for ion - assisted deposition of coatings. The other one generating ion beams in a pulse - repetitive mode with a current of up to 1 A, ion energy of up to 40 keV, pulse duration of 1 - 2 ms and a pulse - repetition rate of 3 - 50 Hz is used for ion implantation in metals and polymers. The source features a straightforward design and power supply, high reliability and long lifetime, this being due to the use of cold-cathode discharge needing no initiating system.

Introduction. The lifetime of ion sources using thermoionic cathodes is substantially restricted in industrial installations because of a rather poor vacuum and reactive gas media. It is one of the reasons for slowed-down introduction of highly efficient ion technologies in industry [1]. This stimulates interest in designing of ion sources based on cold - cathode discharges. However, the hindered ignition of cold - cathode discharges under low gas pressures complicates the source design and power supply circuit.

It is known, that values of igniting and operating voltages for discharges in magnetic fields differ insignificantly [2]. For this reason, the use of such discharges for plasma generation in ion sources may be of interest. But the use of a strong magnetic field increases the discharge voltage and gives rise to sharp spatial nonuniformity of discharge plasma and to the emergence of different kinds of plasma instabilities, impairing the emission properties of plasma. Conditions for ensuring stable and uniform plasma generation in large volumes under low gas pressures in magnetic fields need to be known preliminary for using such a glow discharge for high - power ion beam generation.

Experiment. The ion source electrode system (Fig. 1) contains a rod anode 1 and a cylindrical hollow cathode 2 with ends at cathode potential. The magnetic field was created by solenoid 3. The ions were extracted by accelerating electrode 4. The advantages of two well-known types of low-pressure discharges with oscillating electrons (hollow-cathode discharge and discharge in magnetic field) are implemented in this electrode system. The escape of γ-electrons, which are accelerated by the cathode potential drop and which make main contribution to gas ionization, is hindered both as a result of the small value of anode - to - cathode surface ratio and influence of magnetic field. This ensures the stable operation of the high - current glow discharge under the lowest gas pressures in comparison with

other known gas - discharge systems [2,3]. For example, stable ignition and operation of pulse discharge in the millisecond range of pulse durations with currents of up to

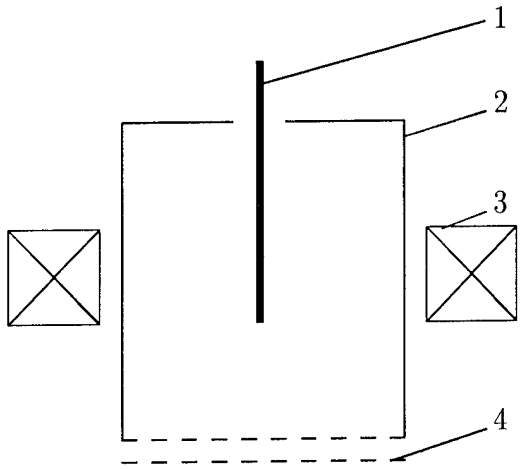


Fig. 1. Electrode system.

10 A in an electrode system with a hollow cathode having a length and a diameter of 150 mm are ensured at argon pressure **p** as low as 0.01 Pa. The discharge voltage was a function of gas species and pressure, magnetic field induction, pulse repetition rate and was equal to 500 - 900 V. Nitrogen, argon and carbon - containing gases have been used as feed gases. The effects of magnetic induction **B** and electrode dimensions on the value and space distribution of ion current extracted from gas - discharge plasma have been investigated. Ions have been extracted through the round holes 5 mm in diameter, arranged in chess-board order at one of the cathode ends.

Measurements of ion emission and ion beam current density have been carried out by means of a movable collector, placed in the plane of the emitter electrode or at a distance of 20 cm from it. In the latter case ions were accelerated by means of multiaperture optics. Measurements have shown that the extracted ion current I_b slightly decreases with increasing **B**. For example, I_b was decreased from 0.5 A to 0.45 A when **B** was increased from 0.4 mT to 1 mT at argon pressure 0.06 Pa. Moreover, an abrupt rise of the noise component of I_b takes place under the influence of strong magnetic fields. The possibility of decrease of **B** has been limited due to the violation of discharge maintenance condition. The efficiency of ion extraction, determined as $\alpha = I_b / I_d$, where I_d is the discharge current, reached the value ~ 0.07 with the lowest possible values of **B**, which is approximately equal to the ratio of emission hole total area to the cathode surface area. This result is an indirect evidence of plasma concentration uniformity at the cathode cavity, this being confirmed by direct measurements of radial distributions of ion emission current density **j(r)** (Fig. 2, curve 1). The variation of **j** with respect to the average value of current density within the beam cross section area 100 mm across in diameter was not in excess of 0.08. Beam current density distribution (Fig. 2, curve 2) differed from the previous plot because of angular divergence of single beamlets.

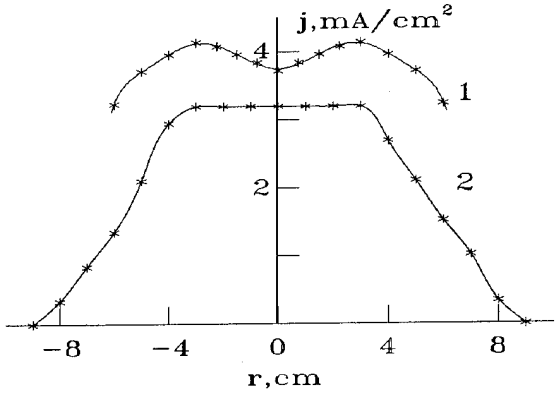


Fig. 2. Distributions of ion emission (1) and beam (2) current density.

Reduction of anode diameter and increase of its length lead to the growth of I_b; the optimal value of cathode length **l** has been found to be approximately equal to the cathode diameter **d**. For big values **l** the

extraction efficiency decreased, and for low values of l it increased insignificantly, but the discharge operation was hindered and the gas efficiency of the source has been deteriorated. The use of a hollow cathode in the shape of a truncated cone made it possible to increase α up to 0.12. But in this case the discharge voltage and minimal value of **B** increased. Accordingly, the noise component of **j** increased, too. It should be mentioned, that the growth of $\mathbf{I}_d$ led to a decrease of α. A possible explanation of this fact may be the redistribution of gas density at the cathode cavity due to intensive carry - over of ions from the central region to the walls of discharge chamber.

Applications. As a result of investigations two ion source modifications having identical electrode system, but different operating modes and purposes, have been designed. The first one, operating in a continuous mode with a discharge current of up to 2 A, generates low - energy ion beams intended for ion - assisted deposition of coatings. Two - electrode ion optics is used to form 2 - 3 -keV ion beams. To provide secondary electrons cut - off the accelerating electrode is kept at negative potential - 1 kV relative to the grounded vacuum chamber. Feed gas is bled into the gas - discharge system, the pressure in the vacuum chamber hereat being about 0.02 - 0.2 Pa. The source produces beams of nitrogen, argon, oxygen and other gas ions with a beam current up to 150 mA and beam cross - section 200 cm^2. When the source is used for ion - assisted deposition of coatings, its stable simultaneous operation with vacuum arc vaporizer is ensured and a high quality of adhesion of coating to glass, ceramics and metals is achieved.

The other source modification has been designed for pulse - repetitive ion implantation of metals. To generate ion beams with currents of up to 1 A and ion energies of up to 40 keV, a three-electrode multiaperture optics is used. The pulse duration is 1 - 2 ms and pulse repetition rate is 3 - 50 Hz. Beams of N_2, Ar and carbon - containing gas ions have been obtained. Mass-charge analysis carried out with the help of a 180° magnet spectrometer has shown that contamination by ions of electrode material in the beam is less than 1%.

The effect of ion implantation on the surface structure and properties of stainless steel "12X18H10T" (0.12% C, 18% Cr, 10% Ni) has been investigated experimentally. As a rule, low - temperature ion implantation is used to preserve the bulk properties of steel and to modify these ones in subsurface layers. To increase the depth of the modified layer the material is annealed after implantation or the implantation is carried out at high temperature, which is maintained by an auxiliary heater[4]. In this work the use of a powerful high current density ion source made it possible to combine ion implantation and simultaneous heating of the specimen by ion beams to high temperatures of up to 1000 °C without additional heaters.

Disk - shaped specimens of stainless steel measuring 18 x 1.4 mm had an initial roughness $\mathbf{R}_a = 0.2$ μm. Microhardness $\mathbf{H}_v$ was measured with an indentor loads of 50 to 200 g. Ions of C_3H_8, N_2, NH_3, Ar and O_2 gases were used to irradiate the specimens.

Investigations have shown, that carbon ions have had the biggest effect on the $\mathbf{H}_v$ values for stainless steel. The value of $\mathbf{H}_v$ increases with the dose growth, the temperature dependence of $\mathbf{H}_v$ having a maximum at 750 °C (Fig. 3). The maximum value of $\mathbf{H}_v = 15$ GPa was achieved after treatment by 30 keV - ion beam with a dose equal to $2 \cdot 10^{18} cm^{-2}$, the initial value of $\mathbf{H}_v$ being 2 GPa. A 1.5 - fold increase of $\mathbf{H}_v$ has been obtained by using a nitrogen ion beam. Implantation of argon and oxygen ions has an insignificant effect on $\mathbf{H}_v$.

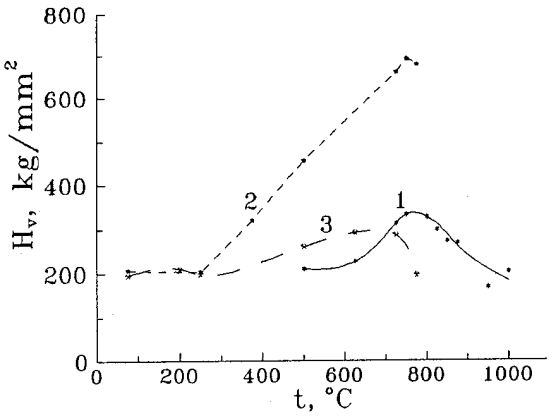


Fig. 3. The temperature dependence of microhardness.
1 - C^+, D = $1.5 \cdot 10^{17}$ cm^{-2},
2 - C^+, D = $5 \cdot 10^{17}$ cm^{-2},
3 - N^+, D = $5 \cdot 10^{17}$ cm^{-2}.

The investigation of depth concentration profile of implanted ions have shown that the thickness of the doped layer is a function of irradiation modes and might exceed substantially the range of ions. For example, the thickness of the doped layer exceeded 3 μm under conditions of high - temperature (500°C) and high - dose ($5 \cdot 10^{17}$cm^{-2}) implantation, this regime having been realized by using a 30 keV carbon ion beam with pulse current of 1 A and pulse repetition rate of 50 Hz. Carbon depth concentration profiles were determined by nuclear reaction method using 0.9 MeV deuterium beam generated by Van de-Graaf accelerator (Fig. 4).

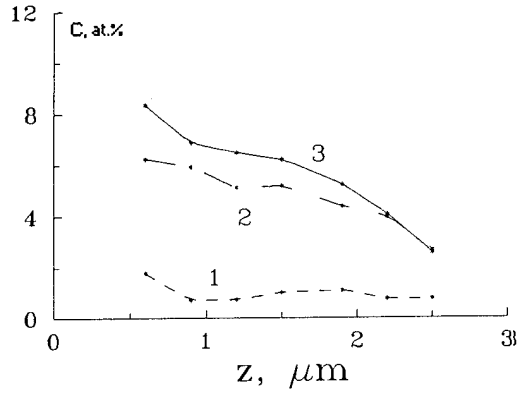


Fig. 4. Carbon depth concentration profiles. Temperature of specimens: 1 - 250 °C, 2 - 380 °C, 3 - 500 °C for 10, 25, 50 Hz accordingly.

X - ray measurements of implanted specimens have shown, that their mechanical properties change as a result of structural and phase transformations in the surface layers. For example, implantation of carbon ions at the temperature of 250 - 500°C leads to a change of lattice parameters of austenitic f.c.c. structure from 3.59 Å to 3.69 Å. When the temperature of specimens was raised to 650 - 800°C a partial $\gamma \rightarrow \alpha$ transition took place with the formation of a martensite phase. It should be noted, that the martensite phase is formed only if the heating of specimens is effected by ion beam power. An additional heater was used to maintain the high specimen temperature when pulse repetition rate being lowered from 50 to 5 Hz, or if ions with low energy (5 keV) were employed. In this case a b.c.c. structure was formed as a result of $\gamma \rightarrow \alpha$ transition, but $\mathbf{H}_v$ increased only by 20 - 30%.

REFERENCES

1. H.R. Kaufman, J. Vac. Sci. Technol. **21**, 725 (1982).

2. E.M. Oks, A.A. Chagin, Zh. Tekh. Fiz. **58**, 1191 (1988),(in Russian).

3. A.S. Metel, Zh. Tekh. Fiz. **54**, 241 (1984),(in Russian).

4. D.L. Williamson, R. Wei, P.J. Wilbur, Nucl. Instr. Meth. **B 56/57**, 625 (1991).

FOCUSING POWERFUL BEAMS OF NEGATIVE IONS AND NEUTRALS

A. G. Mozgovoy and V. A. Papadichev
P. N. Lebedev Physical Institute
Leninsky Prosp. 53, Moscow 117924, Russia

Abstract

A scheme of obtaining powerful focused beams of neutral atoms after stripping negative ion beams is presented. A focusing diode with magnetic insulation was constructed after successful experiments in the generation of powerful beams of H^-, C^-, F^-, and Pb^- in coaxial geometry. The cathode and anode are in the form of partial, concentric, spherical surfaces, i.e., the diode is intended for so-called ballistic focusing of beams on a target at the center of spherical surfaces. Magnetic insulation is provided by a coil placed on the high-voltage cathode. Cathode plasma was created in the diode by a new method, namely, by bombarding the cathode surface with positive ions. For this purpose, preliminary plasma was created behind the anode in which holes had been drilled. Experiments were performed on ERG accelerator at 600 - 800 kV (11 ohms, 200 ns) using a mylar detector and calorimeter.

1. Introduction.

Perhaps the most difficult problem to be solved in studying light-ion inertial confinement fusion is focusing the superhigh-power positive ion beam on a target of subcentimeter diameter [1,2]. The main obstacle is very high ion space-charge density in the beam, which prevents transporting an unneutralized beam for distances greater than the anode-cathode gap of the ion diode, i.e., several millimeters. Space-charge compensation by plasma electrons or electrons moving together with ions alleviates the problem, but does not solve it completely: instabilities, oscillations, space-charge fluctuations occur in the system, followed by ion scattering and an increase in ion beam emittance. Thus it is very difficult (or impossible) to reach the required beam power and energy deposition densities on the target [3,4].

One of the alternative ways to overcome arising difficulties with positive-ion beam transporting and focusing is the use of negative ions [3]. It is possible now to obtain current densities of negative ions up to several hundred amperes per square centimeter at the diode output [3]. Several species of negative ions were obtained and accelerated: from hydrogen, carbon, fluorine to iodine and lead. As is well known, negative ions can be easily stripped on a plasma charge-exchange target or by laser light without substantially deteriorating the beam emittance. So a scheme of ballistic focusing can be adopted: negative ions from a spherical diode are directed radially (except for magnetic deflection in the diode) for

some small distance after passing the anode. This distance that negative ions travel as charged particles in the magnetic field of opposite sign and larger magnitude than that of a magnetically insulated diode is required for the overall momentum to be zero so as to sharply focus the beam on the target. Thus, the neutrals after negative-ion stripping move radially and are not subjected to instabilities, scattering or deflections in magnetic and electrical fields.

As with positive ions, it is possible to use a single spherical diode (having ion emitting surface as part of the sphere) with axial magnetic flux shaped barrel-like by the metallic anode and cathode, or to employ many modules producing ion beam from a small part of a sphere and with each having its own magnetic field for insulation (B_r). The schemes of both diode types are shown in Fig.1 and Fig.2.

Experiments were performed using coaxial [5] and quasicoaxial [6,7] diodes with magnetic insulation. They showed that it is possible to obtain up to 200 A/cm^2 of H^- and 10-20 A/cm^2 of C^-.No obstacles are foreseen to increasing these values by an order of magnitude. Various methods of cathode plasma formation were tried: surface discharge on a dielectric initiated by a natural or externally applied prepulse [8,9] or laser beam [10], all of which give nearly the same current density of H^-. Recent studies at the Lebedev Physical Institute with coaxial diodes showed that initiating cathode plasma by positive ion bombardment extracted from a specially prepared anode plasma and accelerated by diode voltage allows to obtain various species of negative ions accelerated in the diode: H^-, C^-, F^-, I^-, Pb^- [11]. Thus, one can obtain the required type of ion by proper multilayer target design.

2. Experimental studies.

The latest experiments at Lebedev Institute were conducted with B_r diodes of two types: plane and spherical (focusing). Cathode plasma was formed by positive ion bombardment of dielectric. By proper choice of anode plasma density, anode cathode gap and insulating magnetic field amplitude,we were able to sustain a quasistationary regime with flat-top pulses of diode voltage and current. Stationary plasma in the diode is essential to ensure stability of emitting surface of plasma with low noise level, uniform beam current density and low angular divergence. The main difficulty in these experiments (not yet completely overcome) was the nonuniformity of radial current flow on the cathode surface. Such nonuniformity results in spotty emission of negative ions and reduces the total current of negative ions. As shown in [8], electron current density in cathode plasma must be greater than a threshold value of 3-4 kA/cm^2 (or 25 kA/cm^2 in skin-layer) to produce negative ions continuously because they are destroyed in collisions. It is necessary to take special measures to produce homogeneous diode current flow and ion current density (see Conclusion). The spotty emission can also be responsible for instability growth and beam divergence.

Our experiments were performed on ERG accelerator (V=660 kV, Z=11 Ohms, pulse duration = 200 ns). The basic diagram is shown in Fig.1. Flat coil (1) for creating magnetic insulation is at high potential on the cathode. Various constructions of the coil were tested. The coil was fed via a decoupling inductance. To avoid undesirable voltage breakdown and gas release, one terminal of the coil was always connected to the cathode and to the other a short-circuiting spark gap (2) was connected so that the potential of the entire coil would

be the same as that of the cathode during the pulse. The coil surface facing the anode served as the cathode and was covered with a layer of polyethylene (3).

A copper or stainless-steel plate with holes drilled in them for the passage of ions (50% transparency) served as the anode (4).

Plasma was injected behind the anode from two sources to obtain more symmetry. It served as a source of positive ions, which after acceleration in the diode bombarded the cathode, thereby creating cathode plasma. By varying the plasma density from the sources and the delay time between the plasma gun pulse and the accelerator pulse, we were able to select favorable conditions for breakdown of cathode polyethylene and quasistationary regime of diode operation. By changing the plasma volume and density behind the anode, one can also, in principle, achieve the required conditions for complete stripping of extracted negative ions.

For diagnostics, mylar film (6) was used to register ions and a calorimeter to measure total beam energy. Gas release after a pulse was measured to monitor cathode breakdown and diode operation.

We showed in earlier experiments, that to generate negative ions it was necessary to create a layer of dense, low-temperature plasma with sharp boundaries on the surface of the cathode. The required plasma was obtained by positive-ion bombardment of polyethylene on the cathode simultaneously with diode electron current flow along the cathode plasma from the outer region to the central where the anode-cathode gap is less. The resulting magnetic field had B_r and B_z components from the coil and a B component from diode current, which caused an azimuthal and radial drift of plasma and electrons. Different cathodes were used to obtain a focused or a parallel beam. The main difficulty in these experiments was obtaining

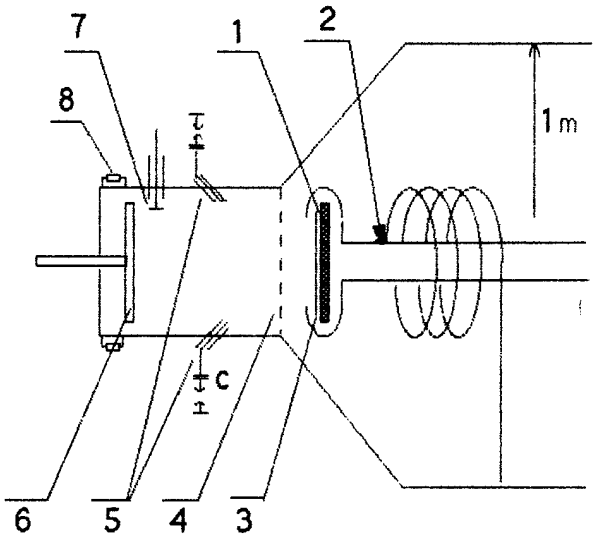


Fig. 1

1. Flat coil; 2. Short-circuiting spark gap; 3. Polyethylene layer;4. Anode; 5.Plasma gun; 6. Mylar film; 7. Calorimeter; 8. Shunt H^-

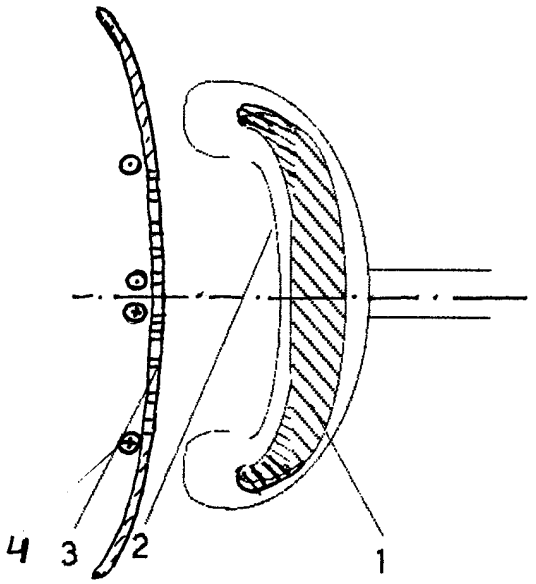


Fig. 2

Spherical geometry diode.
1. Cathode coil; 2. Polyethylene layer;
3. Anode; 4. Anode coils.

an accelerator current flow on the surface of polyethylene because it covered the coil that was at cathode potential and part of the overall current could miss the polyethylene. Traces on the polyethylene surface also indicate that the flow is local and non-symmetrical, which is evidently, in the first place, related to non-uniformity of the plasma behind the anode after cathode bombardment. In our experiments, we only found H^- ions of up to 5 A/cm^2, but we have not yet measured the density of energy at the focus of the focusing diode.

A diode with plasma anode was also tested. Such a configuration is similar to plasma erosion opening switches (PEOS). Here, current density of up to 20 A/cm^2 from an area of more than 700 cm^2 was registered. The external magnetic field (B_z) decreases this density by about 5 times. About one-half of the transmitted flux consists of ions. An interposed 2-micron film reduces the signal from the calorimeter by 50%.

Conclusion.

The best solution for producing uniform H^- is to excite I_θ current, but this requires a fast magnetic flux network not yet fully developed at the Lebedev Institute.

It appears that there is no specific problem making the situation worse for negative ions than for positive ions. In particular, angular divergence of the beam depends primarily on plasma behaviour, and plasma instabilities should be very much like in the similar magnetic field configuration of a spherical diode geometry either for negative or positive ion production. Current densities of 0.2 - 0.6 kA/cm^2 seem to be sufficient to obtain total currents of 1 - 5 MA of light negative ions. The main experimental problems of obtaining uniform plasma emission is equally important for producing both high-power positive and negative ion beams.

Acknowledgement

The authors would like to thank V. S. Voronin and A. V. Mayne for their assistance.

References

[1] T.Mehlhorn et al. Proc. of 9th Int. Conf. on High-Power Particle Beams, Washington,D.C., USA, 1992, p. 31

[2] H.Bluhm et al. Proc. of 9th Int. Conf. on High-Power Particle Beams, Washington,D.C., USA, 1992, p. 51

[3] V.Papadichev, Laser and Particle Beams (1991), vol.9, no.1, pp.167-189

[4] A.Agafonov et al. Pisma v. J.Techn. Fis.(USSR) 7, 1258

[5] A.Kolomensky et al. Proc. 6th Int. Conf. on High-Power Particle Beams, Kobe, Japan, p. 208

[6] A.Fisher, et al. Proc. 6th Int. Conf. on High-Power Particle Beams, Kobe, Japan, p. 116

[7] S.Moustaizis et al. Proc. 6th Int. Conf. on High-Power Particle Beams, Kobe, Japan, p. 119

[8] V.Papadichev et al 7th Int. Conf. on High-Power Particle Beams, Karlshruhe, FRG, p. 479

[9] A.G. Mozgovoy and V.A. Papadichev. Proc. of 9th Int. Conf. on High-Power Particle Beams, Washington,D.C., USA, 1992, p. 824.

[10] V.Papadichev et al 7th Int. Conf. on High-Power Particle Peams, Karlshruhe, FRG, p. 715.

[11] A.G. Mozgovoy and V.A. Papadichev. Proc. of 9th Int. Conf. on High-Power Particle Beams, Washington,D.C., USA, 1992, p. 818.

Negative Ions from Magnetically Insulated Diodes†

R. Prohaska, E. Garate, A. Fisher* and N. Rostoker,
Physics Department,
University of California, Irvine

Abstract

In previous work[1] using a 1 MV, 50 ns, 7 Ω pulseline we have measured ~35 A/cm^2 H$^-$ current density from a cylindrical diode with a polyethylene-titanium hydride cathode. Recently we have modified the system to permit radial diagnostics and the extraction of beams through four access ports. A 125 kV, 1 μs external bipolar prepulse can be used prior to the main pulse. The insulation field can be up to ~3 Tesla and the diagnostics include Faraday cups and CR-39 track recording plastic. Cathodes constructed of different density polyethylene and polyethylene-titanium hydride composites are under study. With the new configuration we have observed 100 A/cm^2 H$^-$ using the polyethylene-titanium hydride cathode. In an effort to generate longer pulse duration ion beams the diode is now driven by a 650 kV, 1 μs, Marx generator. We have designed and done preliminary tests on a beam forming diode which uses fiber emitters to assist surface flashover and stabilize impedance.

† Work supported by ONR/SDIO.

* Permanent address: Naval Research Laboratory.

Introduction

The production of H$^-$ requires a supply of hydrogen in some form, a supply of electrons and ample opportunity for them to interact (collide) but once the interaction has occurred the negative ions formed must be free to escape the interaction region without further collisions. These requirements make it difficult to produce significant quantities of H$^-$ in any sort of steady-state thermal equilibrium. Typical dc sources of H$^-$ are limited to current densities on the order of ~100 mA/cm^2 for areas larger than a few cm^2.

A plasma created by flashing over a dielectric provides free electrons and neutral atoms (or molecules, which can participate in dissociative attachment). If a density gradient exists at the surface, a reasonable fraction of the H$^-$ present can be extracted provided the gradient is not much longer than the mean free path. H$^-$ production was demonstrated in a magnetically insulated diode[2] in 1976.

In early experiments, current densities of H$^-$ ions for various diode designs[3-5] at UCI have been a few A/cm^2. In the past several years we have studied diodes similar to the coaxial design of the Lebedev Physical Institute, Moscow, Russia, where current densities of up to 200 A/cm^2 have been reported[6] using nuclear activation of a carbon target. A crucial difference between the early UCI diodes and those developed at the Lebedev Institute was the design of the magnetic insulation. Early UCI designs used conductive backing on the ion source and tight magnetic insulation similar to that used for positive ion diodes in an effort to create directed beams with high efficiency. Both features limited the surface current density within the cathode plasma.

In the Lebedev devices electron flow along the magnetic field was restrained only by space charge at the end of the cathode. The ion source was a solid piece of insulating material (polyethylene) ensuring that all axial electron current flowed in the surface plasma. The discharge formed where the electrons cross the dielectric provided the surface plasma from which negative ions were then extracted radially across the magnetic field.

Experimental Setup

In recent experiments at UCI employing the coaxial diode (Figure 1) current densities of up to 100 A/cm^2 from a passive polyethylene cathode loaded with TiH_2 have been measured using a pinhole camera and CR-39 track recording plastic. These experiments were done on the machine Apex, a 1 MV, 50 ns, 7 Ω pulseline with a natural negative prepulse of ~100 kV with 400 ns duration. We have also modified the pulseline to include an external LC circuit which can generate a bipolar, 125 kV, 1 μs duration prepulse (similar prepulse characteristic as in the Lebedev Institute experiments cited above).

Ion diagnostics consisted of Faraday cups and CR-39 track recording plastic. Faraday cups were placed in the diode insulation field, biased positive to recover secondary electrons and equipped with 2 μm mylar stripping foils to convert the negative ions to positive for easy discrimination from leakage electrons. CR-39 loses its sensitivity if placed in vacuum for prolonged periods[7]. A 2 μm mylar window was supported on a perforated metal screen to form a vacuum-air

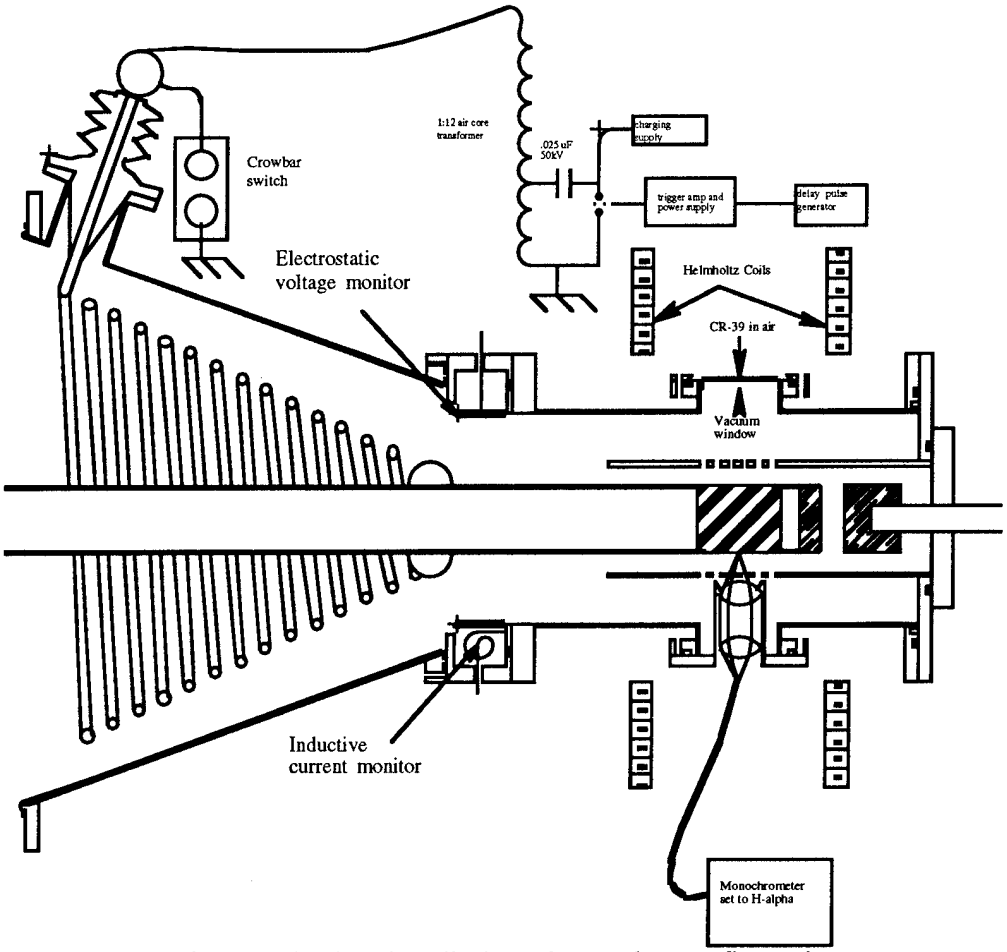


Figure 1. Schematic showing diode and prepulse configuration.

interface, allowing the CR-39 to remain in air at all times. A brief exposure to Am^{241} alpha particles furnished reference tracks and development was in 6N NaOH at 70° C until the alpha tracks were satisfactorily etched.

A pinhole was placed within the vacuum chamber, usually on the anode. Pinholes were made in metal (usually tantalum) foil using an electrolytically etched tungsten pin. Sizes ranged from 25 to about 70 μm, determined by microscope after fabrication. The combination of a pinhole and the CR-39 constituted a simple camera, forming a time-integrated image of the ion-emitting area of the cathode. It also reduced the total number of ions reaching the vacuum-air window and CR-39, resulting in longer window life (tens of shots) and a countable number of tracks on the film.

Knowing the number of tracks on the film and the size of the pinhole the ion current density at the pinhole is easily calculated. Given the size of the CR-39 image and the object and image distances one can make an estimate of the beam divergence, from which an estimate of the current density at the cathode can be made. In the event of a good shot tracks usually overlap near the center of the image resulting in an undercount; hence this measurement tends to be conservative.

An electrostatic voltage monitor in close proximity to the cathode furnished voltage information, while B-dot probes provided a measure of current both at the cathode shank and farther downstream in the region of the collector.

Insulation fields were provided by either simple solenoids or Helmholtz coils. Fields over 3 Tesla could be achieved with solenoids, while the Helmholtz coils were limited to slightly over 1 Tesla for mechanical reasons. A 1000 μ F capacitor bank was used, resulting in risetimes of 1 to 3 ms. The vacuum chamber and metallic parts of the diode were made of stainless steel to ensure prompt, uniform field penetration.

Overall length of the cathode was typically 3 cm, with diameter ranging from 1 to 2 cm depending on the experiment. The cathode shank was always approximately the same diameter as the cathode. Cathodes loaded with TiH_2 were turned from solid low density polyethylene rod stock. Dovetail grooves about the circumference retained TiH_2 using sodium silicate (water glass) as a binder. Axial gaps of 1 to 2 cm were used to achieve a satisfactory total current and voltage.

We have recently begun work on a diode capable of forming a unidirectional beam (Figure 2). A symmetric design using a magnetic cusp for insulation is shown, with fiber emitters mounted both at the inner and

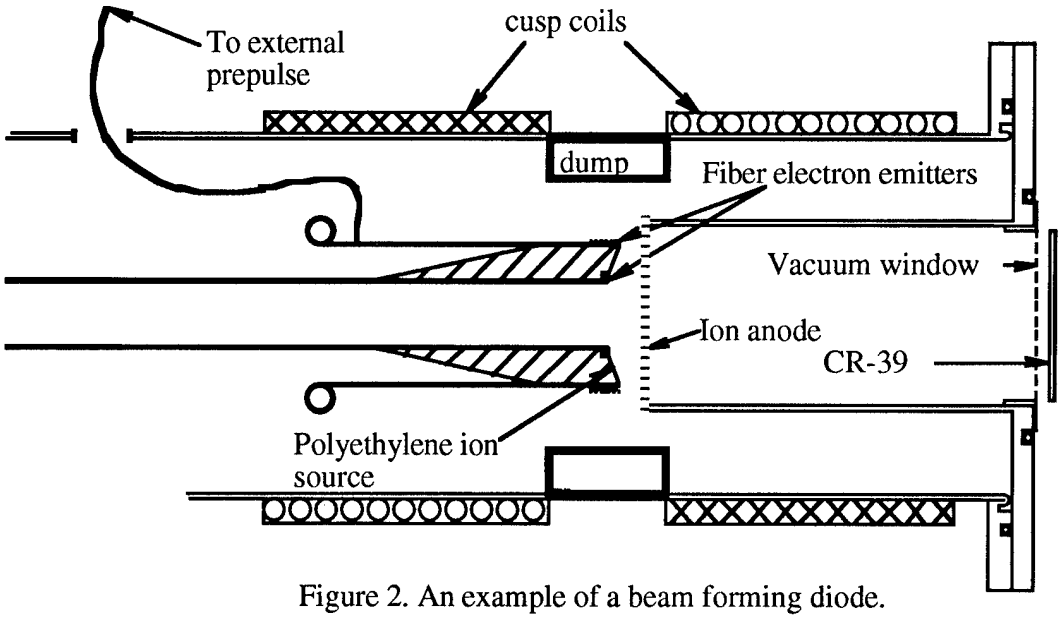


Figure 2. An example of a beam forming diode.

outer periphery of the ion-emitting surface. The fibers at the inner periphery are intended to provide uniform breakdown on the cathodsurface, while those at the outer periphery provide a well-behaved load into which the plasma current can flow radially to ground along the cusp field while negative ions are extracted axially.

Conclusions

The highest current density of H^- observed to date is 100 A/cm^2 from a polyethylene-titanium hydride composite cathode mounted in a cylindrical diode. A negative prepulse of ~100kV with 400 ns duration was present. A diode capable of forming a directed beam has been designed and preliminary test of its voltage holding ability are complete.

References

1 E. Garate, et al. Proceedings of the 6th Int'n'l Symposium on Production and Neutralization of Negative Ions and Beams, James Alesi, Ed. AIP Press, Upton, NY 1992 pp 422-429

2 A. Fisher and N. Rostoker, Bull. Am. Phys. Soc., 21, 1097, (1976).

3 A. Fisher, H. Lindenbaum, N. Rostoker, C. E. Wiswall, S. L. Cartier and J. C. Leader, in Microwave and Particle Beam Sources and Directed Energy Concepts, Howard E. Brandt, Ed., Proc. SPIE 873, 190, 1988.

4 A. Fisher, H. Lindenbaum, N. Rostoker, S. L. Cartier and C. E. Wiswall, in Microwave and Particle Beam Sources and Directed Energy Concepts, Howard E. Brandt, Ed., Proc. SPIE 1061, 439, 1989.

5 R. Prohaska, A. Fisher and N. Rostoker, in Microwave and Particle Beam Sources and Directed Energy Concepts, Howard E. Brandt, Ed., Proc. SPIE 1407, 598, 1991.

6 Papadichev V.A., Pikuz S.A., Shelkovenko T. A., Review Of Scientific Instruments, 1990 Jan, V61 N1:439-441.

7 R. Prohaska, E. Garate, V. Papadichev, A. Fisher and N. Rostoker, Vacuum Desensitization of CR-39 Track Recording Plastic submitted to Review of Scientific Instruments

PULSED ION BEAMS EXTRACTED FROM VACUUM ARC ION SOURCE WITH DOUBLE ACCELERATOR GAP

Kazuhiko HORIOKA, Jun HASEGAWA and Mitsuo NAKAJIMA
Department of Energy Sciences, Tokyo Institute of Technology
Nagatsuta 4259, Midori-ku Yokohama, Japan 227

ABSTRACT

We propose a new vacuum arc ion source with double diode structure. The well defined ion flux of the first (pre-acceleration) gap controls the dynamics of the second (main) gap. The main gap operates space charge or source limited mode depending on the current level of the injected ions. An insulator spark source is used to trigger a metal vapor vacuum arc discharge driven by a 20-element LC pulse forming network (PFN: 5Ω-100μs). The vacuum arc discharge typically produces plasma flux of 10^2mA/cm^2 level at 10cm from the anode surface. An electrostatic grid is used to separate ions from plasma electrons. A high voltage LC-PFL of 10μs pulse length directly drive the second grid and the cathode to negative high potential. In the first gap, the voltage divided from the main voltage pulse accelerates ions to appropriate energy for stable formation of the ion emitting surface in the second (main) extraction gap.

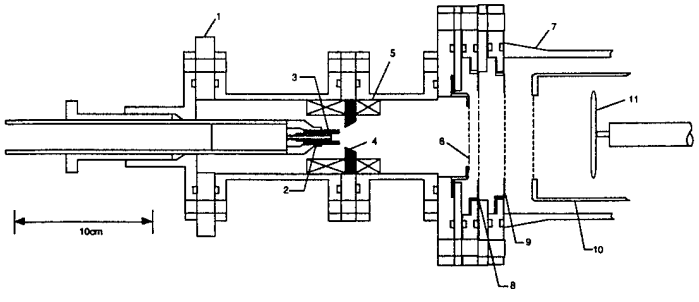
INTRODUCTION

Although the vacuum arc ion source can produce almost all kind of metallic ions by changing the cathode material, it has intrinsically time-varying properties.[1] The plasma flux fluctuates in short time scale and it has not overall reproducibility also in long time scale.

In order to suppress spiky short fluctuation, a grid controlled extraction method was proposed.[2,3,4] The high frequency oscillation of vacuum discharge plasma source is suppressed by the space charge effect in the gap. However, this operational mode creates potential hump (Virtual Anode) which defines the ion emitting surface in the gap. The peak value of the potential hump and its position are determined by the drift velocity and the flux level of the source plasma. Then, it is supposed that a low frequency fluctuation of ion emitting surface still remains due to the virtual anode oscillation. In order to investigate the effects of the virtual anode oscillation and also to improve the beam quality, we propose a vacuum arc ion source operated with the double diode structure.

PRINCIPLE OF DOUBLE GAP ACCELERATOR

Fig.1 shows the schematic diagram of the vacuum arc ion source. The basic components are the copies of conventional grid controlled vacuum arc ion sources.[2,3,4] The basic concept of the double gap accelerator is schematically shown in Fig.2. In the beam acceleration region, there are two grids(G1,G2). Their electric potentials(ϕ) and the intervals of these grids(G1-G2-C) can be easily adjusted to an appropriate operational mode. The formation process of virtual anode in the second (main) gap(G2-C) is controlled by the applied voltage and space charge limited current in the first (pre-acceleration) gap(G1-G2). The well controlled ion flux from the first gap defines stable ion emission surface in the second gap. So the main roles of the first grid are the stabilization of high frequency oscillation and the injection of well controlled ion beam flux to the main acceleration gap.



1. INSULATOR 2. TRIGGER ELECTORODE 3. ARC CATHODE 4. ARC ANODE 5. MAGNET
6. PLASMA GRID 7. GLASS VACUUM CHAMBER 8. EXTRACTION (FIRST) ANODE 9. EXTRACTION (SECOND) ANODE
10. EXTRACTION CATHODE 11. LARGE AREA COLLECTOR

Fig.1 Schematic of the Vacuum Arc Ion Source with Double Gap

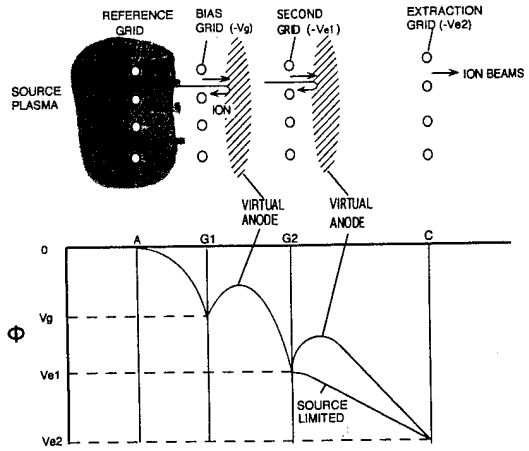


Fig.2 Principle of Grid-Controlled Double Gap

EXPERIMENTAL SET-UP

The experimental apparatus for the measurement of ion plasma flux is shown in Fig.1. A Krytron pulser is coupled to an insulator spark source through a ferrite transformer. The insulator spark source triggers a metal vapor (Cu) vacuum arc driven by a 20-element LC pulse forming network(PFN(1)). It has an impedance of 5Ω and provides flat top current of 100μs pulse length to a matched load. As shown in Fig.3, typically, the arc source is operated at 300A current level. The vacuum arc discharge produces plasma flux level of 10^2mA/cm^2, at 10cm from the anode surface.

The electrostatic bias grid is used to separate ions from plasma electrons. The acceleration (main) voltage pulse is applied on the two acceleration gaps by a 10-element LC-PFL(PFL(2)) of 10μs pulse length. All of the cathode components are inductively isolated by a pulse transformer. The applied voltages on the first and the second gap are controlled by a voltage divider, which also works as a matching load resistor for the PFN(2). In the first gap, the voltage divided from the main pulse accelerates ions of space charge limited current density. So, the intrinsic short time source fluctuation of vacuum discharge is stabilized at the first gap. The well behaved almost constant current ions are injected into the second (main) extraction gap with appropriate energy and current density for stable formation of virtual anode.

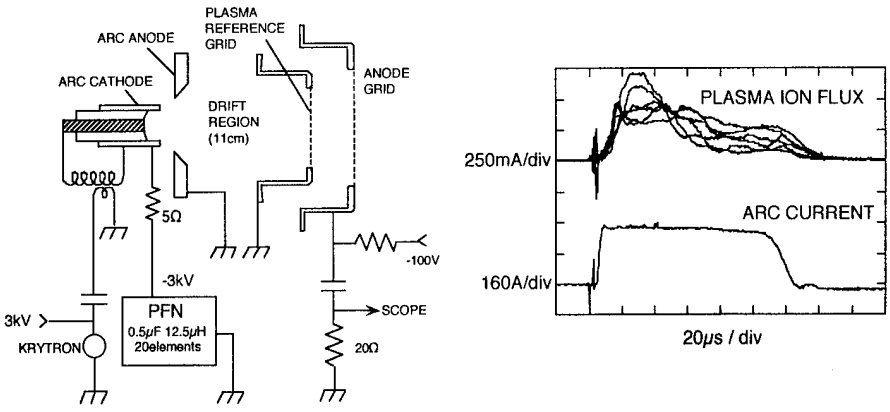


Fig.3 Electric Circuit and Typical Waveforms of Arc Current and Ion Flux

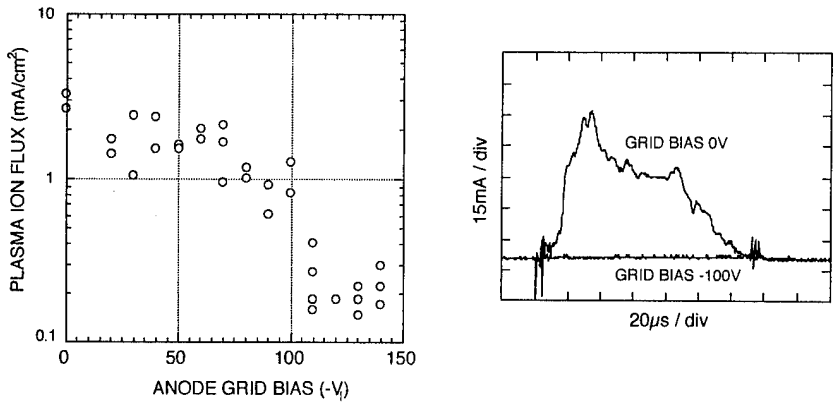


Fig.4 Measured Plasma Ion Flux vs Grid Bias Voltage (Vg)

EXPERIMENTAL RESULTS

For the basic characterization, the ion source was operated with single gap mode. Fig.3 shows six-shot overlay of the typical waveforms of plasma ion flux from the vacuum arc ion source. As has been reported in the past experiments, an initial overshoot was observed in the plasma flux signal. The average reproducibility of plasma flux was not good. The plasma flux and the current of the extracted ion beams were measured with a Faraday cup, which had auxiliary electrodes to avoid the effect of secondary electron. Fig.4 shows the measured plasma flux versus the bias grid voltage. It says that when we increase the negative bias voltage of the first grid(G1), the plasma flux is suppressed less than one-tenth.

Extracted ion beams are measured with the Faraday cap as a function of acceleration voltage. Typical waveforms of the ion beam current is shown in Fig.5. In the beam extraction experiment, the gap size was 2cm and the grid bias voltage was -100V. The ion beam current and the plasma ion flux to the bias grid was measured simultaneously. The correlation between them is shown in Fig.6. The plasma ion flux was monitored at the bias grid(Fig.3) and the beam current was measured with the Faraday cup. As shown in the figure, when the extraction high voltage(-10kV) was applied on the gap, plasma flux signal was eroded almost the same quantity. The close correlation between these signal verifies the reflective motion of plasma ions; ie, virtual anode formation in the gap, around the grid mesh.

Extracted ion current was measured as a function of acceleration voltage(Ve). The results were plotted in Fig.7. It can be seen that the measured current level was ten to hundred times

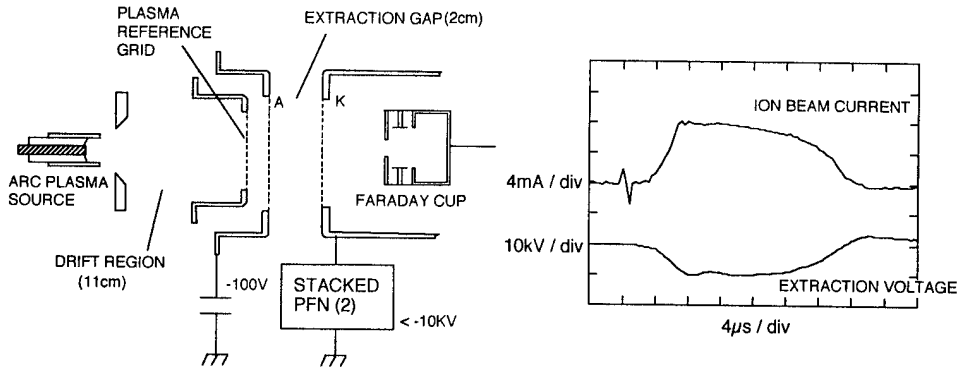


Fig.5 Typical Signal of Extraction Voltage and Ion Beam Current

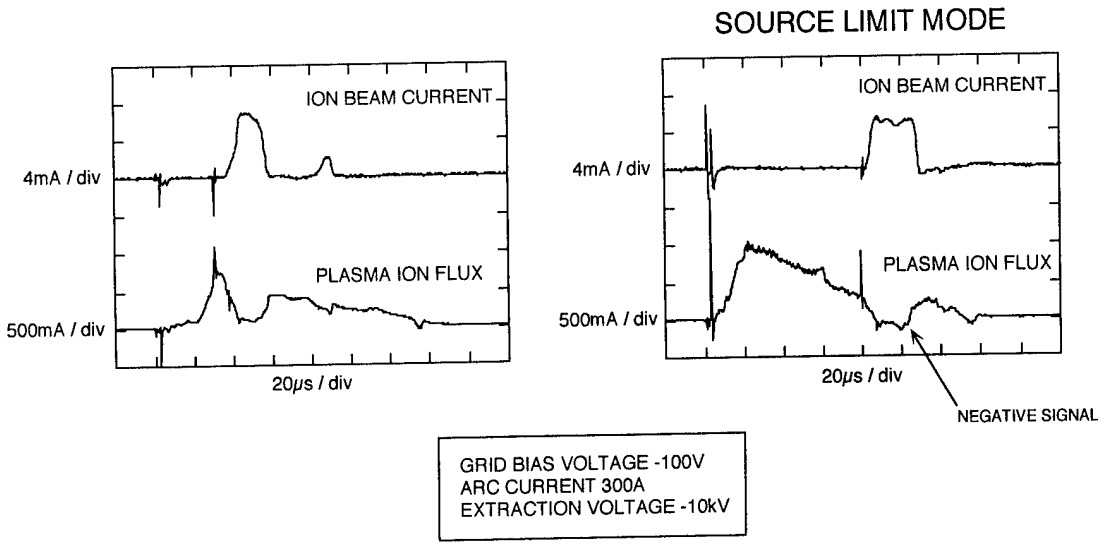


Fig.6 Correlation between Ion Beam Current and Plasma Ion Flux

of Child-Langmuir Law, especially at low voltage level. In order to clarify the cause of these ion enhancement, we have to make measurements of the ion current scaling and also the quantitative estimation of the virtual anode dynamics including the electron flow in the gap. We are also making measurements on the energy spectrum, species, charge state distribution, optical quality and emittance of the extracted beams.

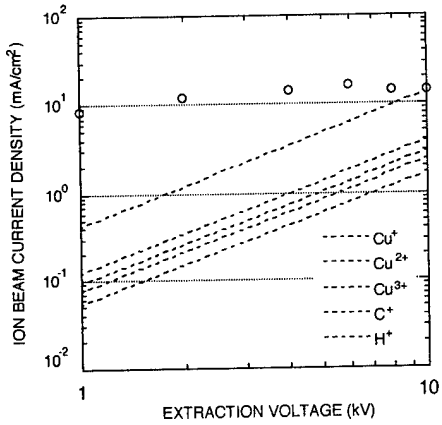


Fig.7 Extracted Ion Current vs Ve

CONCLUSIONS

In order to stabilize ion emitting surface of the grid controlled vacuum discharge ion source, we have proposed double gap acceleration structure. For the first step of the investigation, the basic characterization of the vacuum arc ion source was performed. We have confirmed the virtual anode formation in the acceleration gap from the simultaneous measurements of extracted ion beams and the flux to the bias grid mesh. A large ion current enhancement was observed at low extraction voltage region.

In the next phase of investigation, our primary attention will be placed on the dynamics of the virtual anode. In order to investigate it, a double gap acceleration system is now under development.

REFERENCES

1 I.G.Brown, B.Feinberg and J.E.Galvin, J. Appl. Phys., 63(10), pp.4889-4898 (1988)
2 S.Humphries,Jr., C.Burkhart, S.Coffrey, G.Cooper, L.K.Len, M.Savage, and D.M.Woodall; J. Appl. Phys., 59(6), pp.1790-1798 (1986)
3 H.L.Rutkowski, R.M.Johnson, W.G.Greenway, M.A.Gross, D.W.Hewett and S.Humphries,Jr; Rev. Sci. Instrum. 61(1), pp.553-555 (1990)
4 S.Humphries,Jr.. and H.Rutkowski; J. Appl. Phys., 67(7), pp.3223-3232 (1990)

"CATALYTIC RESONANCE IONIZATION" - A NOVEL UNIVERSAL TECHNIQUE FOR THE FORMATION OF A TWO-COMPONENT ANODE-PLASMA

B.A.Knyazev[a], P.I.Melnikov[a], H.Bluhm
Kernforschungszenrtum Karlsruhe,
Institut für Neutronenphysik und Reaktortechnik,
D-76021 Karlsruhe, PO Box 3640, Germany
[a]*Permanent address:* Novosibirsk State University,
630090 Novosibirsk, Russia

Abstract

In this paper we describe a technique to produce planar and volumetric ion sources of nearly every element. This technique is based on a generalization of the LIBORS-process (Laser Ionization Based On Resonant Saturation) which because of its similarity to chemical catalytic reactions has been called CATRION (CATalytic Resonance IONization). A vapor containing the desired atomic species is doped with a suitable element possessing resonance transitions that can be pumped to saturation with a laser. By superelastic collisions with the excited atoms and by stimulated bremsstrahlung absorption seed electrons are heated and multiplied. It is the heated electron component which then by collisional processes also ionizes the desired atomic species. This technique will work efficient if both the atom and the ion of the dopant posses resonant transitions that can be pumped by the same laser. Instead of using tunable dye lasers we propose to apply gas lasers which are more robust and appropriate for repetitive long term operation. We present a large number of coincidences between gas laser wavelength and resonant transitions in suitable atoms.

The production of spatially localized plasma layers in contact with surfaces in a vacuum environment is often required in pulsed-power technology. Such plasmas consisting of specific elements are needed for the formation of plasma anodes in high-power accelerators for inertial fusion or industrial applications. In both cases the plasma must be sufficiently uniform and dense.

We propose a novel technique for the production of multicomponent plasmas with high repetition rates and supposedly high efficiencies. This technique also allows to adapt the system to form a plasma with arbitrary elemental composition. Our technique is based on a generalization of the well-known LIBORS-process (Laser Ionization Based On Resonant Saturation) which because of its similarity to chemical catalytic reactions has been called CATRION (CATalytic Resonance IONization).

In both techniques a layer of a gas/vapor with specific elemental composition and sufficiently high density has to be created near a

surface in the first stage of the process. It can be produced by means of any suitable technique, e.g. a pulsed injection of gas through special apertures in the surface or a pulsed heating of a surface by an electric current or by laser radiation. The heating leads to emission of a dissolved gas and/or to evaporation of material from the surface. In any case, a transient gaseous layer (further to be referred as "gas") is formed.

In the second stage the gas is exposed to intense laser radiation which provides a saturated population of the resonant atomic level. By superelastic collisions with these excited atoms and by stimulated bremsstrahlung absorption, seed electrons are heated and multiplied. It is the heated electron component which then by collisional LIBORS-processes also ionizes the gas [1,2]. The configuration of the CATRION plasma source is schematically shown in Fig.1.

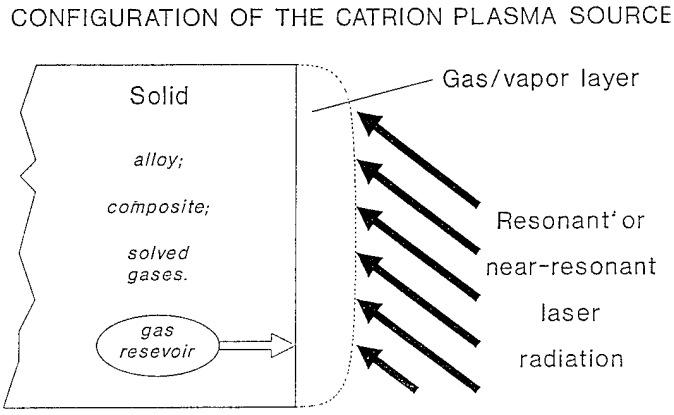


Fig.1. Anode plasma formation by means of a resonant laser radiation in the LIBORS and the CATRION techniques.

The LIBORS-technique has been applied successfully to the formation of a lithium-plasma anode in the PBFA-II diode [3] with the help of the resonant radiation from a dye laser. In principle, any element can be ionized by the LIBORS technique, but to ionize other elements a set of new dye-lasers with wavelengths corresponding to a resonance transition in the level system of these elements should be applied. Unfortunately, flashlamp-pumped dye-lasers are characterized by low efficiency and by low operational life. Their wavelengths do not cover the UV spectral range, whereas resonance transitions of many elements are just occuring in that range. These disadvantages can be overcome by use of the CATRION technique if the application allows the admixture of a specific element in the plasma.

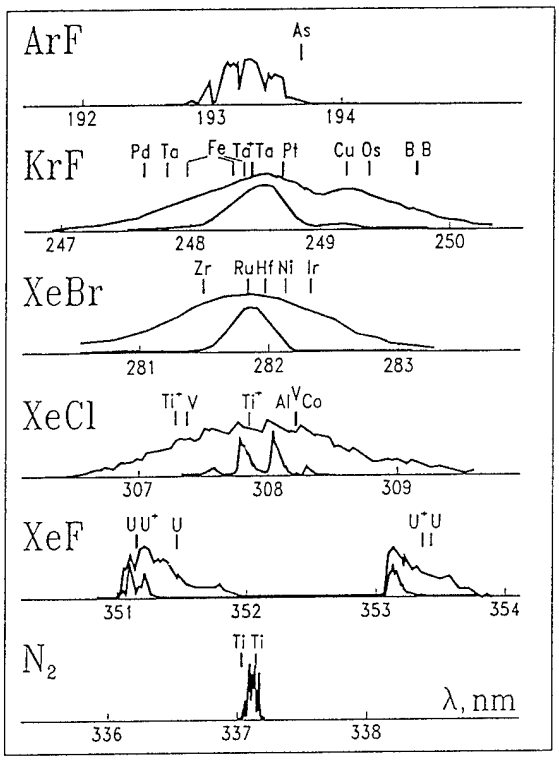


Fig.2. The lasing spectra of a certain robast gas lasers and the nearby resonance spectral lines of several elements.

To ionize a gas by means of this technique one has to add to the gas a certain amount of atoms with resonance transitions coinciding with the lasing wavelength of any robust pulsed laser. We have identified seventeen elements of the periodic table, whose resonance transitions overlap with or are closed

to the lasing spectra of eximer lasers. Fig.2 demonstrates the shapes of lasing spectra of the most effective eximer lasers (as well as of nitrogen laser) and the resonance transitions of the above mentioned elements. The upper curves are the fluorescence spectra of corresponding laser transitions. The lasing spectra can be tuned, in principle, inside these ranges by the use of selective laser cavities.

This special element, which we will call further a "catalyst", absorbs the intense laser radiation in the saturation regime and provides a high non-equilibrium population of the upper level of the "catalyst"-atom. Because of the high density in the layer and the saturation of the transition, the probability for electron and photon-electron collisions with the excited atom exceeds the probability of radiative transitions and quenching collisions. As a result, the temperatute of the seed electrons in the layer sharply grows and the electrons finally ionize all components of the gas.

It should be pointed out, however, that the rate of ionization of *excited* catalyst atoms is higher then of other *non-excited* components of the gas mixture. This can lead to only patrial ionization of the atoms of interest to us. This difficulty can be overcome if a catalyst ion have the resonance transition at the same wavelength. We have found two "catalysts" (Ta and U) for which both the atom and the single-charged ion have resonance transitions at the same wavelength. This allows to continously pump laser energy into the layer even after complete ionization of the "catalyst"-atoms has occured.

To estimate the laser intensity required to achieve saturation we have derived the balance equation for the population of a resonance level under steady-state conditions. Let A_{21} and A_{2k} are the Einstein coefficients for the resonance and for the cascade transitions respectively and j_ω is the spectral power density of the laser radiation. The cross-sections for the stimulated transitions σ_{12} and σ_{21} are equal to

$$\sigma_{21}(\omega) = \frac{\lambda^2}{4} a_{21}(\omega) A_{21},$$

$$\sigma_{12} = \frac{g_2}{g_1}\sigma_{21}, \quad \int a_{21}(\omega)d\omega = 1.$$

By definition, the saturation parameter is equal to unity, when the rates of spontaneous and stimulated transitions from the upper level (the terms in the square brackets of eq. (1)) are equal. If the laser line is sufficiently broad as compared to the atomic line-width, the saturated radiation intensity j_ω^S is given by the following relation:

$$j_\omega^S = \frac{4}{\lambda^2}\left(1 + \frac{\sum_k A_{2k}}{A_{21}}\right).$$

Let us design the expression in the brackets by ξ. In the case of a two-level system $\xi = 1$, and $j_\omega^S = 4/\lambda_{21}^2\ [cm^{-2}]$. Multiplying j_ω^S by the photon energy $\hbar\omega_{21}$ and transforming from frequency to wavelength, we obtain for J_λ^S:

$$J_\lambda^S = \frac{1.4 \cdot 10^{14}\xi}{\lambda^5[nm]}\left(\frac{kW}{cm^2 nm}\right).$$

The quantity J_λ^S/ξ depends only on the laser wavelength and is presented for several gas lasers in Table I. If cascade transitions from the resonance level are possible these intensity values can be much higher.

Table I. Laser wavelength (nm) and saturated intensity (kW/cm^2nm)

laser	ArF	KrF	XeBr	XeCl	N_2	XeF
λ	193	248	282	308	337	351
J_λ^S/ξ	530	150	80	50	33	27

It should be noted that, on the one hand, the specific value of saturation must be sufficiently low, to produce the most effective absorption of the laser light in the vapor cloud,

and on the other hand, it should be sufficiently high to provide an adequate rate of energy transfer to the electrons. To reach a saturation parameter close to unity and to deposit the laser radiation with high efficiency, the lasing spectrum and the atomic absorption line must overlap at least partially.

From Fig. 1 one can see that for certain atoms the overlapping is not too good, and very high laser intensities may be required to saturate these transitions. However, one important point to remember is that the absorption line can be significantly broadened in the intense resonant light field [4] or due to collisions among gas particles ("pressure broadening"). Overlapping may also be improved by tuning of the laser spectra with a selective resonator within the spectral ranges shown in Fig. 1. An ultimate solution to the problem of optimizing both the vapor density and the radiation intensity is beyond the scope of this work and needs experimental investigations.

Finally, we can list the advantages of the technique of Catalytic Resonance Ionization(see. Fig.3):

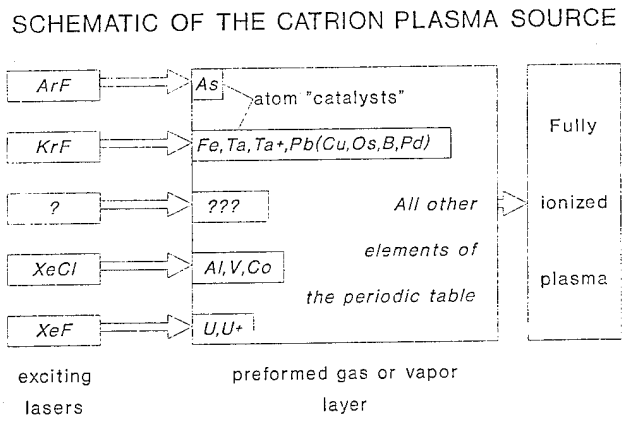


Fig.3. Schematic of the CATRION plasma source.

(i) For the ionization of gaseous layers which can consist of very different chemical elements including the "catalyst", one needs a single non-tunable pulsed laser only. To prepare the system for the formation of a plasma with other elemental composition only the initial gas mixture must be changed. In this case, the only necessary restriction is to include in the new gas composition the same "catalyst". If it is more convenient, a new laser and a corresponding "catalyst" can be used. A sufficiently large number of "catalysts" simplifies the problem of fabrication of suitable surfaces and allows to obtain very complex gas mixtures.

(ii) When a short-wavelength laser is applied for the irradiation a copious amount of seed electrons will naturally occur. They will be produced automatically by means of photoionization of excited atoms. This cannot be obtained with the longer wavelength dye lasers.

(iii) The coincidence of wavelengths of resonance transitions in both the atom and the ion, identified for at least two "catalysists" gives us the possibility to pump laser energy into the gas even after complete ionization of the "catalyst" atoms. This possibility does not exist in the usual LIBORS process.

(iv) For the case of a multicomponent plasma there is in addition the possibility to vary the densities of the components independently. This allows to change the absorption coefficient of resonance radiation and to control the rate and the volumetric characteristics of the gas ionization.

References

1. R.M.Measures, P.G.Cardinal, Phys. Rev. A, 23, 804 (1981).
2. V.A.Kas'yanov, A.N.Starostin, Plasma Chemistry, issue 16. Moscow: Energoatomizdat, 1990 (in Russian).
3. G.C.Tisone, T.J. Renk, D.J.Johnson, R.A.Gerber, R.G.Adams, Proc. BEAMS-92, V.2, 800, 1992.
4. A.Maitland, M.H.Dunn, Laser Physics, North-Holland, 1969.

Results of the Reacceleration Experiment: Experimental Study of the Relativistic Klystron Two-Beam Accelerator Concept*

Glen Westenskow and Tim Houck
Lawrence Livermore National Laboratory
P.O. Box 808
Livermore, CA 94550

Abstract

We recently demonstrated the reacceleration of a bunched beam through an induction accelerator cell in support of the two-beam accelerator concept. We present the results of this experiment including amplitude and phase measurements of the extracted microwave power at 11.424 GHz. We also describe progress in achieving a two-beam accelerator microwave source design that is efficient and cost effective for linear collider applications.

Relativistic klystrons are being developed as an rf power source for high gradient accelerators applications that include compact accelerators, large linear electron-positron colliders, and FEL sources. In a relativistic klystron two-beam accelerator[1] (RK-TBA), the drive beam passes through a large number of rf output structures. High conversion efficiency of electron beam energy to rf energy can be achieved in the relativistic klystron by using reacceleration of the bunched drive beam.

The Reacceleration Experiment was designed to study the RK-TBA concept. Figure 1 is a photograph of the beamline and Figure 2 is a schematic of the experiment. A 5-MeV, 1-kA induction beam is modulated by a transverse deflection technique (Chopper) to generate several hundred amperes at 11.4 GHz. The extraction section is comprised of three traveling-wave output structures and two induction cells located between the outputs. The output structures operate at 11.424 GHz in the TM_{01} mode with a $2\pi/3$ phase advance per cell and phase temperature sensitivity of about 0.1 °/°C. Additional parameters are listed in Table 1. The induction cells used for reacceleration of the modulated current are each pulsed at 250 kV. The design of the modulator and the experiment has been described in detail elsewhere.[2,3] Here, we report on the results.

Figure 3 shows the maximum power achieved, with no pulse shortening, from each output. The "flat top portion" of the pulse lasts about 25 ns. This time is the length of the current pulse minus both the transient time of the drive cavity in the modulator and the fill time of the output structures. Linear collider applications place severe constraints on amplitude and phase variation. The anticipated requirements are for phase to be within ±1°, and for amplitude to be within ±1% over the power pulse.

Table 1. Parameters for the output structures.

Design Parameter	#1	#2	#3
# of Cavities (Undamped)	4	5	6
# of Cavities (Damped)	2	2	0
Aperture (mm)	13	14	14
Fill Time (ns)	1.35	1.22	1.05
Group Velocity	0.13 c	0.167 c	0.167 c

Output power was limited by the vacuum pressure and hydrocarbon contaminants in the vacuum system. The induction cells use neoprene o-ring seals and insulating oil. These cells represent the major source of the contaminants. The operating pressure was in the mid 10^{-7} torr range at the vacion pumps in the output waveguide. The highest rf output power levels obtained were about 20% greater than those shown in Figure 3. However, these higher power pulses exhibited pulse shortening. Table 2 lists power levels and maximum sustainable surface electric fields. Figure 4 shows a combined, coincident power pulse for the three outputs.

*The work was performed under the auspices of the U.S. Department of Energy by Lawrence Livermore National Laboratory under contract W-7405-ENG-48.

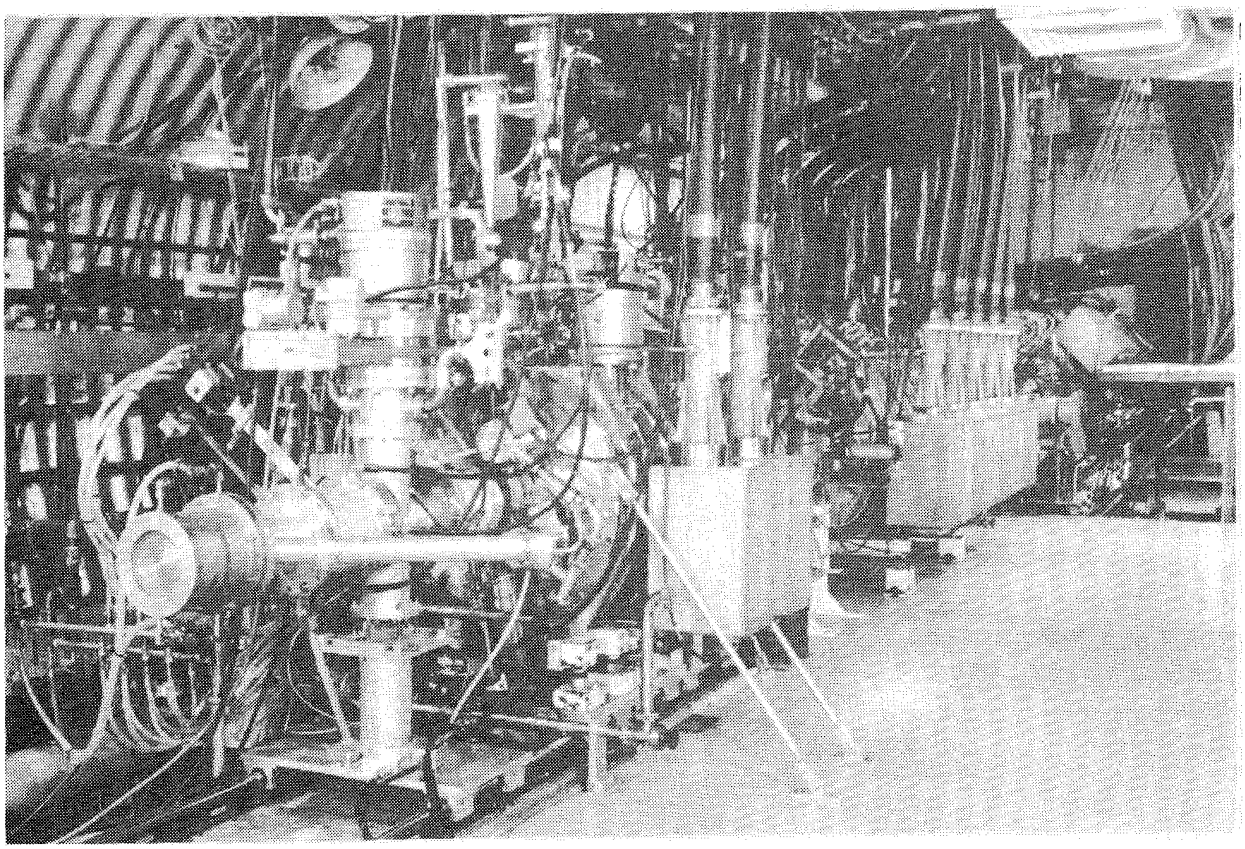


Figure 1. Photograph of the Reacceleration Experiment Beamline. The injector is located in the background to the left of the raised platform. The large cylindrical cables extending from the ceiling deliver the pulsed power to the induction cells of the injector/accelerator. The rectangular boxes attached to the cables contain compensation resistors and bus bars. The induction cells used for reaccelerating the beam are located just left of center in the photograph.

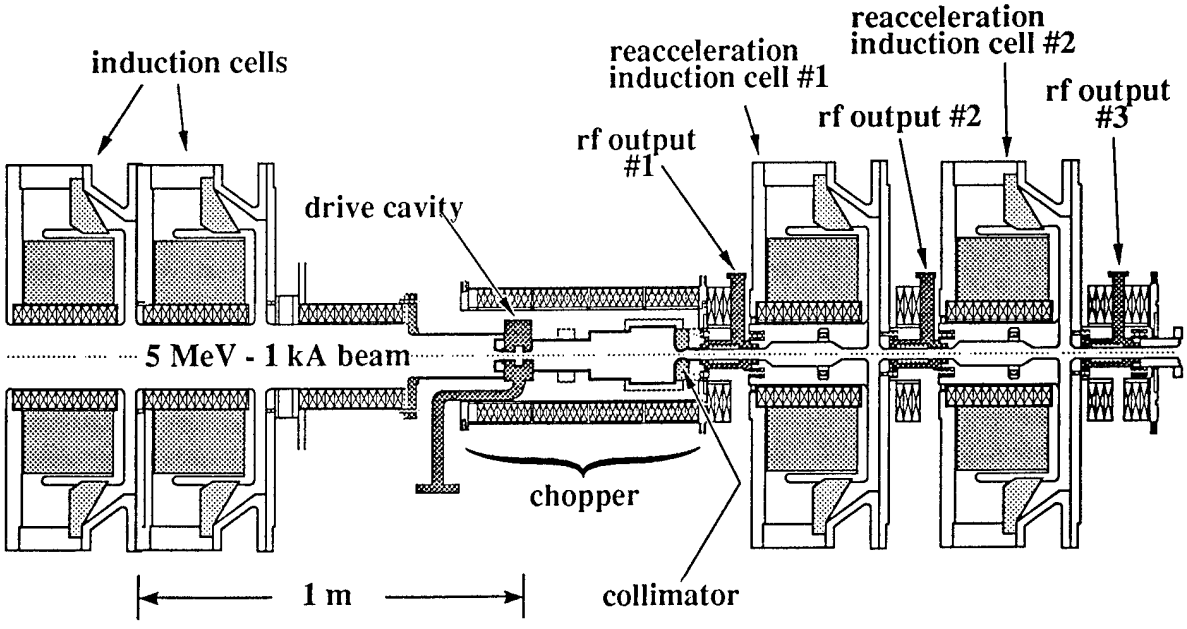


Figure 2. Schematic of the Reacceleration Experiment.

Table 2. Maximum rf output powers achieved for each structure.

Output	"Flat top" Power (MW)	Surface E-Field (MV/m)	Peak Power (MW)
TWS#1	64.5±4%	60	86
TWS#2	88.5±3%	75	101
TWS#3	50.0±3%	60	59

Figure 5 shows the phase of the power from the first output structure with respect to the modulator reference. The phase is measured by mixing the output power pulse of the first structure with the frequency doubled modulator drive pulse in a double balanced four-diode ring mixer. The variation shown in Figure 5 is primarily due to beam loading of the drive cavity in the modulator. The contribution due to energy (velocity) variation of the beam is negligible for two reasons: the short drift distance from the point the beam is modulated to the output structure and the high beam energy.

Figure 6 shows the phase of the power from the third output structure with respect to the first. The phase variation can be explained by the beam energy variation during the pulse. For this case, the energy variation is about ±2.5% and the phase variation is ±3°, in agreement with the standard equation

$$\Delta\varphi = -\frac{L\omega}{c}\left\{(\gamma - 1)(\gamma + 1)^3\right\}^{-1/2}\frac{\Delta V}{V},$$

where L=0.95 cm is the distance between the two outputs, V ≈ 4.6 MeV is the beam energy, and the modulation frequency is 11.424 GHz.

Current transport below 500 amperes was not an issue in the experiment. Figure 7 shows a comparison of current entering the modulator and exiting the last output structure without modulator drive. The two curves agree to within the uncertainty of the diagnostics indicating no measurable current was lost. Measurements taken at two intermediate positions also confirm full current transport.

Beam breakup was observed for dc current levels above 550 amperes and with a beam energy of 4.6 MeV. A typical current pulse exhibiting BBU is contrasted with a full width pulse in Figure 8. The 550 amperes is a substantially greater dc current than when the beam is modulated (≈ 380 amperes) and agrees

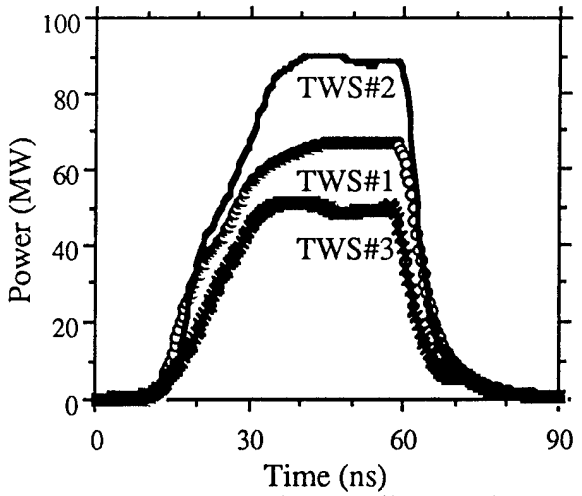


Figure 3. Maximum "flat top" power levels.

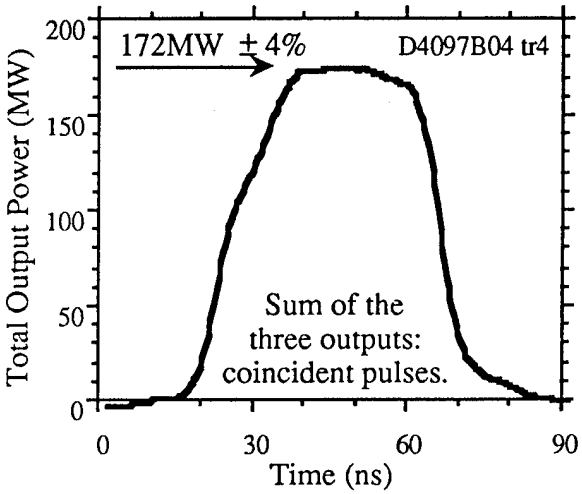


Figure 4. Maximum combined power level.

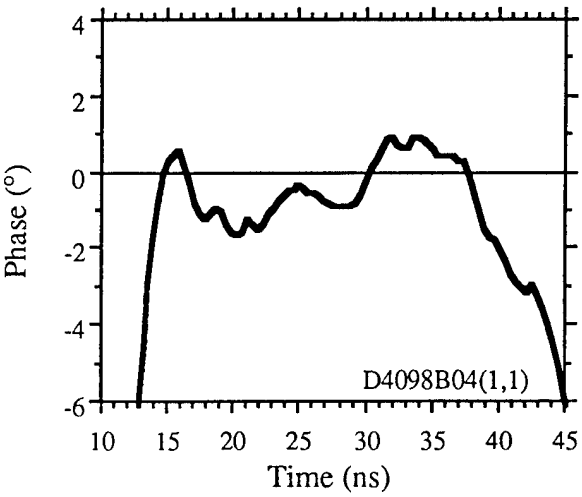


Figure 5. Phase of the first output with respect to the modulation reference.

with computer simulation. Beam break-up due to the excitation of higher order modes in the

acceleration gaps and the output struc-tures is a serious issue for long RK's. The OMICE Code,[4] formerly called the BBU Code, was developed at LLNL to study transverse instabilities in RK's and has been benchmarked against our experiments.

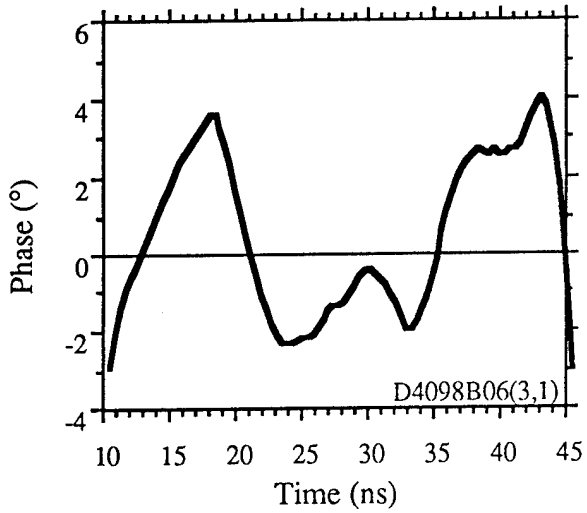


Figure 6. Phase of the third output with respect to the first output.

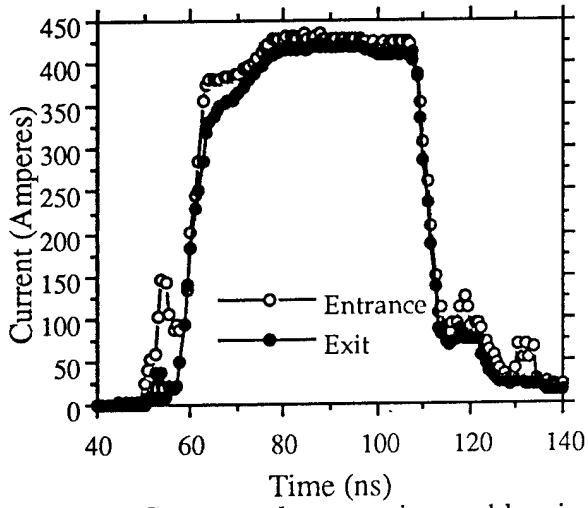


Figure 7. Current pulses entering and leaving the experiment show low losses.

Our experience gained from the RK experiments has enabled us to design an efficient and cost effective RK-TBA microwave source. The modulator for this design is similar to that used in the Reacceleration Experiment. The transverse modulation technique is phase stable and compact. Its efficiency is enhanced by partially modulating the beam with the chopper and then further compressing the phase space with idler cavities. Also, the transverse modulation is performed at an intermediate energy. The beam is accelerated to full energy during the compression stage. The induction modules are constructed of metglass with each core driven at 20 kV for 200 ns of "flat top." Five cores are sleeved to produced 100 kV across an accelerating gap. This technique eliminates the need for an external high voltage step-up transformer. We intend to conduct experiments to study issues related to this new design.

Acknowledgments

We thank J. Haimson and B. Mecklenburg for the design and construction of the modulator and output structures used in the experiment; A. Meyers and S. Petz provided technical support for the experiment. S.S. Yu led the design effort for the proposed RK-TBA Power Source. A.M. Sessler furnished theoretical support and program guidance.

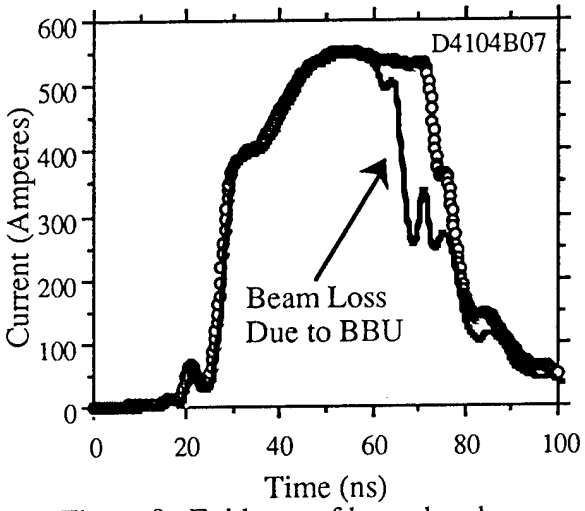


Figure 8. Evidence of beam breakup.

References

[1] A.M. Sessler and S.S. Yu, "Relativistic Klystron Version of the Two-Beam Accelerator," Phys. Rev. Letts., 58, 2439 (1987).

[2] J. Haimson and B. Mecklenburg, "Design and Construction of a Chopper Driven 11.4 GHz Traveling Wave rf Generator," Proc. of the 1989 IEEE Particle Accel. Conf., pp. 243-245, 1989.

[3] G.M. Fiorentini, et al., "Design of a Reacceleration Experiment Using the Choppertron," SPIE Symposium on Intense Microwave Pulses I, Vol. 1629-71,1992.

[4] T. Houck, et al., BBU Code Development for High-Power Microwave Generators," Proc. 16th Int'l LINAC Conf., pp. 495-497, 1992.

HIGH POWER LIGHT ION BEAMS AT AEA TECHNOLOGY, CULHAM

Elizabeth Surrey
AEA Technology
Physics Technology Department
Culham, Abingdon, Oxon, UK

Abstract

High power particle beams have been under development at AEA Technology, Culham for over 20 years. Initially directed towards the requirements of the fusion programmes at JET and Culham, the applications now include defence and industrial fields. The work described here concentrates on the production of negative ions for fusion and defence.

Fusion

The use of neutral particle beams to heat the plasma in a magnetically confined fusion device has been accepted since the 1960's. The energy per nucleon is set by the plasma ion temperature and the range of injected neutral particles. For JET, this value was 80keV/nucleon, with a pulse length of ~10s. The final design for the JET injectors required eight beam sources per injector, each delivering either 60A of hydrogen at 80keV (80% H^+) or 30A of deuterium at 160keV for up to 20s. This constituted a source and accelerator with area and energy approximately four times that of any previous European system.

For the ion source the major technology problems were providing uniform plasma density across the 180 x 450mm^2 extraction area and raising the proton yield to 80%. Adapting work by Ehlers[1] it was realised that by providing a long range magnetic field, the "filter", across the source, the volume where ionisation occurs could be controlled. This observation accounted for the previously unexplained high proton yield of the DITE II source built at Culham[2,3]. This weak field arrangement of DITE II was accommodated into the prototype JET source and the final PINI (positive ion neutral injector) design gave a proton yield in excess of 80% at 2kA/m^2 [4].

The demands of future fusion devices for neutral beams of energies up to 500keV precludes the use of positive ions due to the drop in charge exchange cross section at energies above 80keV per nucleon. The neutralisation of negative ions however is almost independent of energy at 60% for a simple gas neutraliser. To provide a negative ion beam equivalent to the positive JET beam requires a current density of 320A/m^2 uniformly distributed over an area of 296cm^2. The high efficiency of neutralisation for negative ions is due to the low attachment energy (0.75eV) of the electron and this, whilst beneficial for neutralisation, also means that negative ions are difficult to produce. In addition, electrons are also extracted from the plasma and these must be removed from the beam without impairing the beam optics.

The negative ion programme at Culham, has concentrated on the volume production of negative hydrogen and deuterium ions through dissociative attachment to vibrationally excited molecules. The source for negative ion production was essentially unchanged from the PINI but the magnetic filter field plays a different role. In the hot dense driver region primary electrons, in addition to producing ionisation, also produce vibrationally excited molecules which cross the filter into the extraction

region. The plasma in this region is composed of positive ions and cool electrons which have diffused across the filter by collisions. Typically, the electron temperature in the extraction region is 1eV, for which the dissociative attachment rate is maximised. Thus the filter provides the necessary environment for negative ion formation in the extraction region.

The exact role of the filter field was (and still is) a major field of study at Culham. The filter field can be configured in two ways: a dipole across the source parallel to the extraction grid, or "supercusp" a field running axially in the source from its perimeter at the extraction grid to the centre of its back plate. Both orientations were investigated and optimum current densities were similar at 250A/m^2 D^- but the dipole filter introduced a non-uniformity in the plasma through j x B drift. For the multiaperture systems envisaged for fusion applications this was not acceptable. Subsequent optimisation of the position and strength of the supercusp field resulted in a peak D^- current density of 420A/m^2.

The fractional density of negative ions rarely exceeds 0.5 of the total negative charge, the remainder being electrons. Un-suppressed, the extracted electron to negative ion current ratio is typically 60 for hydrogen and 100 for deuterium. These co-extracted electrons are usually removed from the beam after the first acceleration gap by means of a static magnetic field transverse to the beam axis. To minimise the power load of the electron current Culham developed several devices employing magnetic and electric fields[5]. These suppression systems have reduced the current ratio to 0.5 for hydrogen and 2 for deuterium.

As part of a wider European programme for negative ion development, construction began at Culham of a prototype neutral beam injector for NET/ITER called DRAGON. The basic specification is for 200keV, 4A beam of D^- ions.

Historically current densities of D^- have always been lower than for H^-, typically by a factor of 2.5 to 3. To achieve the required densities for DRAGON, stripping losses in the accelerator needed to be minimise requiring the source to operate at a lower pressure than the PINI, which reduces the efficiency of the source. This can be compensated by increasing the magnetic confinement at the source walls. For the DRAGON source of dimensions 80 x 55 x 22cm^3 rigidity against implosion required a wall thickness of 8mm which would reduce the confinement cusp field strengths[9]. The problem was eliminated by placing the source entirely in vacuum, which allowed the thickness of the source walls to be reduced to 2.5mm

The extraction area of the source consisted of 228 holes each of 13mm diameter arranged in clusters of four in six columns. The total area is 377.3cm^2 and allowing for stripping losses required a current density of 176A/m^2 distributed uniformly over this area. Such a large area precluded the use of a dipole magnetic filter due to the reasons described above. The source was configured with the supercusp filter field.

Initial experiments were conducted in hydrogen to characterise the injector without the problems of neutron production and to obtain a database for comparison with other systems. The maximum current was 1.5A H^- for a 2 second 36kW discharge and 2.4A for a 1 second 39 kW discharge. In deuterium the best performance achieved was 0.5A D^- from a 25kW discharge. Both currents were recorded for beam energies of 100keV.

The system is now installed at CEA Caderache, France where it forms part of the MANTIS experiment.

A second use for neutral beams in fusion is as a diagnostic device for the detection of impurity species. Under construction at present are two neutralised proton beamlines

for plasma diagnostics on the UKAEA Fusion experiment COMPASS and for the National Institute for Fusion Science at Nagoya. These are based on those designed and constructed for TEXT[9] at University of Austin, Texas and PBX at Princeton. The modular design of these beamlines using standardised components makes them readily adaptable to a wide range of applications. The ion sources provide in excess of 200mA/cm^2 H^+ which give up to 100mA/cm^2 H^0 at beam focus on the TEXT device. The accelerator is a tetrode configuration, slightly modified from the JET design. Beam divergencies of ~0.6° have been recorded at 40keV with the total current determined by the number of apertures. The NIFS beamline will provide 6A H^+ at 50keV in 200ms pulses producing 800A/m^2 in a 6.3cm diameter beam at the target plane; the COMPASS beam line will provide 1A D^0 at 60keV within a 56mm diameter beam.

Defence

Since 1987 Culham has been developing cw H^-/D^- high brightness injectors for applications in the SDI programme. In this context both beam current and emittance set operational requirements for the system performance; size and weight are additional constraints. For this application the negative ion sources developed under the fusion programme were too large to be accommodated on the platform. In addition, the emittance constraint precluded the use of multiaperture systems so that the necessary beam current must be achieved from a single aperture. The source dimensions were reduced from 55 x 31 x 21cm^3 to 19.5 x 14 x 10cm^3 and beams were extracted from single apertures of up to 24mm diameter. Reducing the physical size of the source has certain consequences for its performance. In a small cuboid source it is difficult to arrange a supercusp filter in which the filament cathodes are fully shielded by the magnetic field. This can result in primary electrons leaking into the extraction region, raising the electron temperature and so reducing the negative ion yield. Unfortunately the dipole filter, whilst simple to arrange can lead to plasma non-uniformity at the beam extraction aperture, which in turn can result in emittance growth in the beam[6]. (The same is also true of the electron suppression field). For fusion applications the beam emittance was not a severe constraint; in the SDI programme beam brightness was a key issue.

Through a combination of increased understanding of the physical process in a volume ion source and better design, the performance of the source was improved almost two fold to give 44mA H^- and 18mA D^- current corresponding to a current density of 219A/m^2 and 90 A/m^2 in a 20kW discharge[8]. This represented a 100% increase in arc efficiency compared to the large negative ion source.

There is a well documented[7] catalytic effect on negative ion yield if cesium is added to the source. The process(es) by which this is achieved in unclear ; it could be due to both surface and volume effects. Adding cesium to the source plasma provided 86mA of H^- and 40mA D^- currents.

Transporting these currents in a well collimated, unaberrated beam requires careful design of the accelerator optics. A triode system was used, with the intermediate grid shaped to allow for beam expansion without interception. The design was based upon simulation by the code IONTRAK, developed at Culham, which resulted in 30% higher transmissions at larger beam currents. Modifications to the geometry of the structure surrounding the extraction aperture were also made which resulted in significant changes in the beam emittance. Firstly, the strong dependency of emittance on extraction voltage (potential difference across the first accelerating gap) was removed, secondly the spherical aberrations present in the outer edges of the emittance diagram disappeared and thirdly, the absolute value of emittance was reduced.

For a 52mA H^- beam a normalised rms emittance of 0.2πmm mrad was recorded. There was some evidence that beam brightness fell with increasing beam current which could be due either to emittance growth related to the plasma density at the extraction plane or to growth induced by the accelerator.

Conclusion

Over a 20 year period, AEA Technology at Culham have developed plasma sources capable of delivering cw or true dc high current beams. Together with the capability to provide the ions, the technology required to transport the beam in the early stages of acceleration and to deliver beams of energies up to 1MeV has been assessed. For some applications, beam quality is as important as beam current and the process contributing to emittance and aberration have been investigated closely. The figure of 86mA H^- remains the highest cw H^- current extracted from a single aperture and was achieved by applying comprehension of the plasma physics to the design of the negative ion volume source.

References

1. Ehlers KW & Leung KN Rev Sci Instrum 52 1452 1982.

2. Hemsworth RS et al Proc Joint Verenna - Grenoble Int. Symp. on Heating in Toroidal Plasmas, Grenoble France 1978.

3. Hemsworth RS et al 9th Europ. Conf. Cont. Fus. & Plasma Phys. 1979.

4. Deschamps an et al Proc 15th Symp. Fusion Tech., Utrecht, 588, 1988.

5. L. M. Lea et al Rev Sci Inotrum, 61, 409 (1990).

6. A.J.T. Holmes & E. Surrey Rev Sci Instrum., 62, 1173 (1991)

7. Y. Okumura et al Proc V Int Symp on the Production and Neutralisation of Negative Ions and Beams, Brookhaven 1989 AIP Conf Proc 210 169 (1990).

8. R. McAdams, et al "Final Report on Advanced cw Ion Source and RFQ Studies" AEA-CLM-InTec-1405 (1993).

9. J.R. Coupland et al, IEEE 12th Symp. Fusion Engineering, Monterey, 285 (1987).

OBTAINING NEGATIVE-ION BEAMS OF MICROSECOND DURATION IN A MAGNETICALLY-INSULATED DIODE

V.A. Papadichev
Lebedev Physical Institute
Leninsky Prospect 53
117924 Moscow, Russia

V.N. Pashentsev
Moscow State Engineering Physics Institute (Technical University)
Kashirskoe av. 31
115409 Moscow, Russia

Abstract

A magnetically-insulated diode and diagnostics of a negative-ion beam are described. Plane and cylindrical cathode forms were tested. Experimental spatial and angular characteristics of a ion beam are presented. Microsecond negative-ion beam current density was investigated by means of a Faraday cup.

Introduction

Negative hydrogen-ion beams with a current of 7 kA, 200 A/cm^2 density, 600 - 800 keV particle energy and up to 200 ns pulse duration have been obtained in magnetically insulated high-current diodes [1-4]. Our experimental investigations are aimed at obtaining negative-ion beams of microsecond duration. Other distinguishing features are the absence of a prepulse before the high-voltage pulse, lower particle energy (not more than 300 keV) and the use of a diode with plane-geometry magnetic insulation, which is more suitable for extracting a negative-ion beam than a coaxial diode.

Experimental Setup and Diagnostics

A diagram of the experimental setup is shown in Fig. 1. The anode of the diode has a 11x6 cm^2 cross-section and is 25-cm long. The upper and lower parts are of cylindrical form. The cylindrical cathode is displaced 15 mm upwardly from the anode axis. It consists of a 12-mm-diameter, 40-mm-long, perforated polyethylene tube drawn over an 8-mm-diameter copper rod. The 6 - 8-kG insulating magnetic field is created by means of two coils. To extract the negative-ion beam from the diode, a grid of 3-mm-diameter holes was drilled in the anode (28% transparency) between the coils. The size of the window was 3x9 cm^2. The axial electron current of the

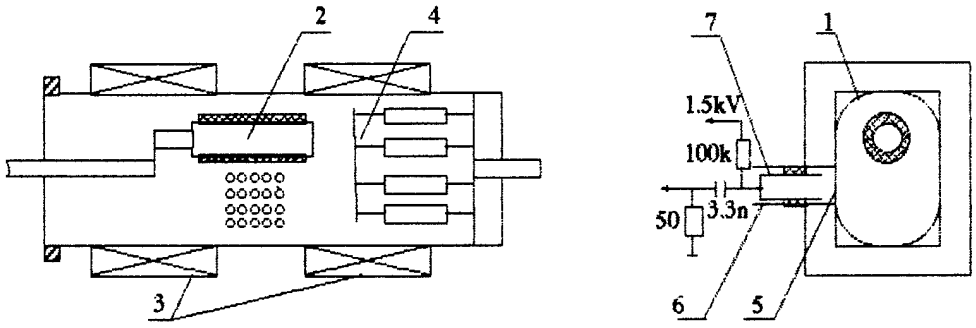


Fig.1. Scheme of Experimental Setup: (1) anode, (2) cathode, (3) magnet coils, (4) axial electron beam collector, (5) Faraday cup collimator, (6) housing, (7) negative-ion beam collector.

diode was measured by a shunt at the butt collector. The form of the cathode plasma and its transverse dimensions were determined from the impression of the electron current on the collector witness plate since, due to the skin effect, current flows along the plasma surface, and plasma, in expanding due to instability, penetrates into magnetic field. Electron current along magnetic field lines transfers plasma cross-section image at the cathode to the butt collector with minor distortions, but gives, of cource, the integrated in time picture.

The following diagnostics were used in measuring the parameters of negative-ion beams. Beam impressions were recorded by means of metal-coated mylar film and track detectors [5]. To measure the spatial and angular characteristics of the beam, a 7 slit collimator and a CR-39 track detector placed at a 30^0-angle to the anode were used. The mass composition of the beam was measured by means of track detectors (CR-39 and lavsan) having different registering thresholds for ion masses. Lavsan film does not register negative ions lighter than boron, while a CR-39 detector registers accelerated ions of all chemical elements. Current densities of ion beams were not measured by means of track detectors because after chemical development in NaOH tracks for densities greater than 10^6-10^7 particles/cm^2 merge. To measure current densities of negative-ion beams, a biased Faraday cup was used [Fig.1]. It consisted of a collimator with a 1.1-mm-diameter aperture, 12-mm-diameter housing and stainless-steel collector in the form of a 36-mm-long hollow cylinder having a 6-mm and 8-mm inner and outer diameter, respectively. The distance between the collimator and collector along the axis is 5-10 mm. Positive bias serves to return secondary electrons knocked out of the collector by the ion impact. In order for the bias potential to remain positive during the beam current pulse, the charge of the condenser is made several times greater than the charge of the negative ions entering the Faraday cup. An experiment was done to measure the possible electron leakage current from the diode. To eliminate possible admixture of negative ions to the electron beam in this case, the entry aperture of the Faraday cup was covered with a 15-μ lavsan film. The film prevented passage of negative ions since the path length of ions in it was less than the film thickness. Experiments indicated that leakage electrons that could freely pass through the film were not registered by the Faraday cup. Collector plasma that forms in the Faraday cup under action of the beam and diode anode plasma also do not affect the Faraday cup readings. This was verified by withdrawing the Faraday cup collector by 15-20 mm from the collimator. The position of the negative-ion signals did not change thereby (the plasma signal should be delayed by 1-2 μs in this case). Usually diode plasma shorted the Faraday cup collector to the housing 4-5 μs after the end of the voltage pulse.

Experimental Result

Initial experiments in obtaining the negative-ion beams involved finding cathode forms for which the operation of magnetically-insulated diodes is stable with the duration of the high-voltage pulse in the microsecond range. Plane and cylindrical forms with dielectric coating were tried. When using plane cathodes, a polyethylene plate perforated with 2-mm-diameter holes (5-mm apart in both directions) was placed over a 5.5x5 cm^2 stainless-steel plate or in a gap of the metal cathode. The pulse duration was less than 1μs, which means early diode shorting by plasma occurred through the magnetic field. In subsequent experiments, we used a cylindrical cathode placed along the center of the anode or the cathode was displaced 15-mm upward from the anode axis. The magnetically-insulated diode was stable in operation and the voltage pulse duration was 1.2-1.4 μs. A metal-coated mylar film was used to register the displaced beam generated below or above the cathode, depending on the direction of the magnetic field. For detailed study of the beam profile, we used a slit collimator and a CR-39 track detector placed at a 30^0 angle to the anode. The spatial and angular

characteristics of the beam are shown in Fig.2. The trajectories of ions obtained externally to the anode are extended linearly into the diode. In view of the large ion masses, the trajectory curvature is small and the straight lines within the diode are close to ion trajectories, in any case near the anode. It can be seen from Fig.2 that the beam consist of two groups of ions: group 1 moving radially and group two a displaced beam. The generation of a displaced beam is due to drift of cathode plasma in the crossed electric and magnetic diode fields, since in changing the direction of the magnetic fields the ion beam accelerated to the opposite anode wall. The beam center is displaced 10-mm downward from the anode axis. The ion beam has a cross-section of 2x3 cm^2 and an angular divergence of ±0.2 rad. Angular spread of the negative-ion beam is due to inhomogeneous cathode plasma, two-component beam content and cylindrical cathode form. Experiments indicated that the beam contains hydrogen and carbon negative-ions. One slit was left in the collimator at the center of displaced beam. A CR-39 track detecter was placed at 60° to the anode in order to obtain greater separation of the trajectories of ions with different masses in the diode magnetic field. To obtain impressions of C-ion trajectories, lavsan film was used instead of CR-39 detector. From comparison of beam impressions on two track detectors, the trajectory of H^- ions was found on a CR-39 detector. The displacement of H^- ions relative to C-ions corresponded to the direction of the diode magnetic field.

To determine the time dependence of negative-ion beam intensity, the Faraday cup was first placed at the center of the displaced beam and then the radial one. Diode voltage

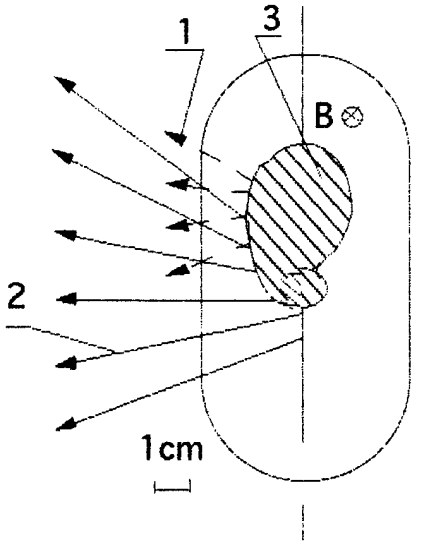


Fig.2. Spatial and angular characteristics of an negative-ion beam: (1) radial beam ions, (2) displaced beam ions, (3) cathode plasma form as seen from the impression of axial electron current on the butt collector.

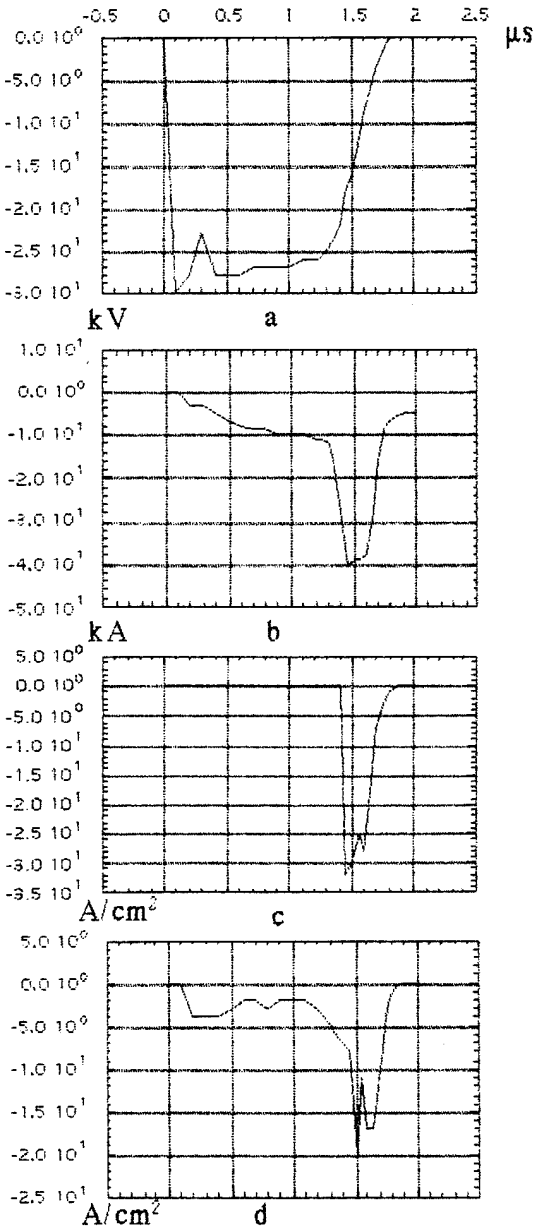


Fig.3. Pulses: (a) diode voltage; (b) axial electron current; current densities of (c) negative-ion displaced beam and (d) negative-ion radial beam.

pulses, axial electron current, and current density of negative-ion displaced and radial beam are shown in Fig.3. It can be seen that the displaced beam is generated on the trailing edge of the voltage pulse. Its current density behind the anode is 30-40 A/cm^2, current pulse duration 0.2-0.3 μs and maximum ion energy 140-160 keV. The radial beam had a current density of up to 1 A/cm^2 over the flat top of the voltage pulse. At the end of the ion current pulse, a signal from the edge of the displaced beam was observed.

Conclusion

It was established in the course of experimental investigation of negative-ion beam intensity that the radial beam current density was almost an order of magnitude less than the calculated current density limited by space charge (j = 8.1 A/cm^2, U = 280 kV, anode-cathode gap d = 1 cm, H^-). The effective gap d between the cathode plasma and anode was determine from the impression made by the axial electron beam on the butt collector. Evidently, the radial beam current density is limited by the low emissive power of the cathode plasma due to the low concentration of negative ions on its boundary. This can be explained by the absence of the prepulse and rather low axial current during the most part of the pulse except its end.

The displaced beam current density is an order of magnitude greater than the calculated current density limited by space charge (j = 3.2 A/cm^2, U = 150 kV, d=1 cm). The effective gap between cathode plasma and anode is probably less than 1 cm and the negative-ion density is high due to the large axial current flowing along the cathode plasma [3]. As distinct from the radial beam, the displaced beam is generated on the trailing edge of the voltage pulse when diode axial current increases sharply. The effective gap in the diode may be about 3-4 mm if one assumes cathode plasma expansion through the magnetic field to the anode and partial field penetration in the plasma. In this case, the impression of the axial electron beam on the butt collector will be less than the transverse dimension of the cathode plasma and the real gap will be smaller. The head-on flow of positive ions from the anode plasma approximately doubles the current density of negative ions. Ionization of a layer of adsorbed hydrocarbon atoms and molecules on the anode may be due to bombardment by negative ions of the beam and by ultraviolet radiation of cathode plasma. Large angular divergence in the displaced beam is mainly due to cylindrical form of the cathode. Cathode plasma is formed first on the cathode parts facing the anode where the electric field is the largest and then drifts around the cathode expanding towards the anode. Thus, the most favorable conditions for negative-ion generation in plasma are created in this marginal part of plasma and ion current density is peaked at the end of the voltage pulse

Acknowledgements

The authors thank M.A. Mashkov and O.A. Smith for their help in preparing the paper.

References

1. Agafonov A.V., Kolomensky A.A., Lebedev A.N. et al., JETP, 1983, V. 84 N. 6, p. 2040.

2. Mikhalev P.S., Papadichev V.A., Pashentsev V.N. et al., Proc. 3d Europ. Workshop on Prod. and Appl. of Light Negative Ions, Amersfoort, Netherlands, 1988, p. 231.

3. Papadichev V.A., Laser and Particle Beams, 1991,V. 9, N.1, p. 167.

4. Mozgovoy A.G. and Papadichev V.A., Proc. 9th Int. Conf. on High-Power Particle Beams, Washington, D.C., USA, 1992, p. 818.

5. Lindenbaum H., Fisher A. and Rostoker H., Proc. 7th Int. Conf. on High-Power Particle Beams, Karlsruhe, FRG, 1988, p. 677.

INVESTIGATION OF BEAM ACCELERATION AND EXTRACTION ON A STELLATRON

Y. Song, A. Fisher, and N. Rostoker

Department of Physics
University of California, Irvine, California 92717

ABSTRACT

The stellatron accelerator of the University of California at Irvine (UCI) [Phys. Fluids B2, 3149 (1990)] was modified to accommodate beam extraction. The magnetic field coils were reconstructed to adapt an extraction port. A fiberglass-graphite-epoxy chamber replaced the glass chamber that cracked frequently during the previous experiment. Improvement in the magnetic field configuration has significantly reduced the current loss during acceleration. A 1.1 kA, 12 MeV electron beam was generated by initially forming a 1.2 kA beam with plasma start-up. The beam radius was 5~7 mm. Beam extraction was performed with two auxiliary pulsed current coils and up to 15% of the beam was extracted from the chamber. The extraction process was analyzed by computational orbit simulations.

I. INTRODUCTION

The stellatron[1] is constructed from a conventional betatron[2] by adding a toroidal magnetic field and a rotational quadrupole magnetic field also called helical field. The beam current in a conventional betatron is limited by the space charge during injection. The toroidal field serves to focus the beam against the space charge and increase the beam current[3,4], and the helical field is used to improve the beam stability[5-8]. Experimental results have shown that such a field configuration can significantly extend the current carrying capability of a conventional betatron. Electron beams with current of 1 kA, energies of 10 MeV and 20 MeV have been generated on the accelerators in the University of California at Irvine (UCI)[9] and in the Naval Research Laboratory (NRL)[10], respectively.

The magnetic field configuration of the stellatron is shown in Fig.1. Although the toroidal and helical fields increase the beam current in a conventional betatron significantly, the presence of these strong magnetic fields makes beam extraction far more difficult, as the electron orbits become more complex and the electrons are reluctant to cross the field lines. Standard methods used to extract beams from a conventional betatron[11-15] are not directly applicable to the stellatron because of the differences in their field configuration and beam dynamics[8].

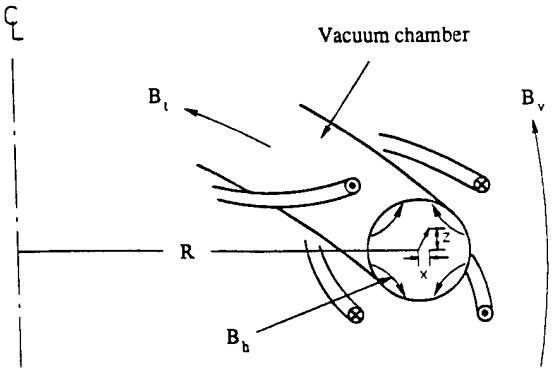


Fig.1. Magnetic field configuration in a stellatron.

II. EXPERIMENTAL TECHNIQUES

Beam generation and acceleration had been successfully demonstrated on the previous UCI stellatron[9]. However, there were two major problems which made the former system unsuitable for beam extraction. 1) the structure of the old toroidal field coils could not be modified to accommodate an extraction channel, 2) the old glass-made vacuum chamber was too

fragile to adapt an extraction port and the wall of the chamber cracked frequently during the experiment. Therefore, the stellatron was redesigned. The schematic diagrams of the present system are shown in Fig.2, and the major experimental parameters are shown in Table I.

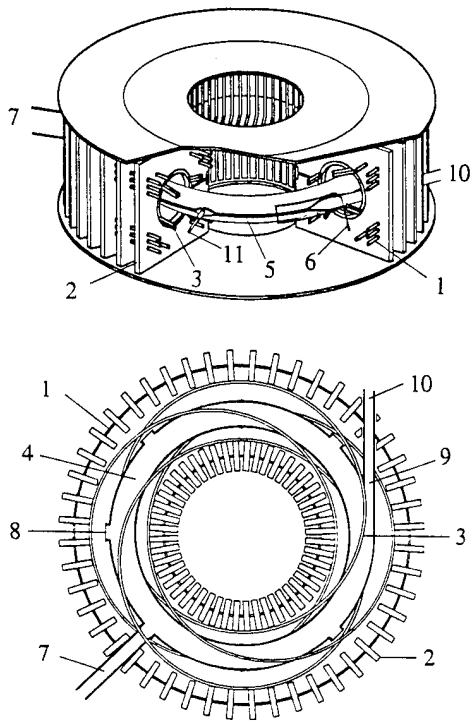


Fig.2. Schematic diagrams of the UCI stellatron: 1. betatron field loops, 2. toroidal field coils, 3. helical windings, 4. vacuum chamber, 5. spiller coils, 6. kicker coil, 7. pumping port, 8. injection ports, 9. extraction port, 10. drift tube, 11. plasma injector.

The Fiberglass-Graphite-Epoxy (FGE) had been used before, however, its performance was much worse than that of the glass chamber mainly because its inner wall outgassed too much under particle bombardment[16]. Despite this, the mechanical strength of the FGE chamber make it more suitable for beam extraction. Therefore it was chosen to be used in the present experiment, in the belief that its drawback could be remedied by improving the magnetic configuration so that during the acceleration most of the beam electrons would be well trapped in the magnetic field and kept from hitting the chamber wall.

Table I. Major Experimental Parameters

Vacuum Chamber	
Major radius R	41 cm
Minor radius r_0	4.5 cm
Background Pressure	~10^{-6} Torr
Betatron Field B_b	
Peak Field B_{b0}	up to 1.2 kG
Field index n	0~1.2 (inside the torus)
Rise time τ_b	40~46 μs (0 to peak)
Toroidal Field B_t	
Peak Field B_{t0}	up to 16 kG
Field ripple	<0.5% (inside the torus)
Rise time τ_t	~75 μs (0 to peak)
Helical Field B_h	
Field period	2
Wire minor radius r_h	9.5 cm
Peak current I_{h0}	up to 35 kA
Rise time τ_h	~80 μs (0 to peak)
Spiller Field B_s	
Peak current I_{s0}	up to 5 kA
Rise time τ_s	~0.8 μs (0 to peak)
Kicker Filed B_k	
Peak current I_{k0}	up to 15 kA
Rise time τ_k	~1 μs (0 to peak)

The toroidal field, originally provided by 36 multi-turn coils, is now provided by 48 single-turn coils. Each new coil is a 1/2" thick square aluminum plate with a circular opening of 20 cm in diameter. Because of their simple shape, the new coils can be manufactured and supported more accurately than the old ones, leading to less field error and better symmetry. More importantly, the new coil structure can easily accommodate an extraction channel by modification of several coils, hollowing out the portion intersected by the channel. The betatron field was generated by 16 loops which extend around the major diameter of the accelerator passing through holes in the toroidal field coils. The present betatron coil

structure is better than the previous design[9] in several respects: 1) it offers more freedoms to program the betatron field distribution and to optimize the accelerator's performance; 2) its total inductance is lower and therefore the rise time of the betatron field is shorter, reducing the acceleration time by a factor of 2 compared with the older design; 3) it is about 30% more energy efficient because of the more compact betatron field distribution. The helical field is generated by four continuously twisted wires carrying current in alternate directions. The helical wires are supported by G-10 fiberglass epoxy rings inlaid into the toroidal coils.

The electron beam in the chamber is formed by plasma start-up[9]: plasma is injected into the chamber and confined in the rising toroidal and helical fields, a runaway current is induced when applying the betatron field. Plasma is produced by a plasma gun made of a 1/4" diameter rigid coaxial cable. Beam extraction is performed by using two auxiliary pulsed current coils called the spiller coil and kicker coil, respectively. The spiller coil consists of two loops wound on the inner and outer equators of the chamber, as shown in Fig.3. Inside the chamber, the magnetic field generated by the spiller coil is opposite to that of the betatron field, causing the beam orbit to expand radially. The kicker coil is a 6 cm×25 cm rectangular one-turn loop. It generates a localized magnetic field near the extraction port, guiding the beam electrons out of the chamber.

III. EXPERIMENTAL RESULTS

After plasma was injected into the chamber, it was confined in the rising toroidal and helical fields. A runaway current was induced when the betatron field was applied. The measurement showed that a beam appeared almost immediately following the start of the betatron field. The beam current increased rapidly and reached a peak in the first few microseconds as the electrons gained velocity and became relativistic. The amplitude of the initial peak current depended on both the amount of the plasma injected and the strengths of the toroidal, helical and betatron fields. Because the outgassing from the inner surface of the FGE chamber was much worse than the glass chamber under electron bombardment, it had to confine most runaway electrons in the magnetic field and keep them away from the chamber wall. In the present experiment, the upper limits of the betatron field and the toroidal field were 1.2 kG and 16 kG, respectively. The initial beam current formed after the injection was up to 1.5 kA.

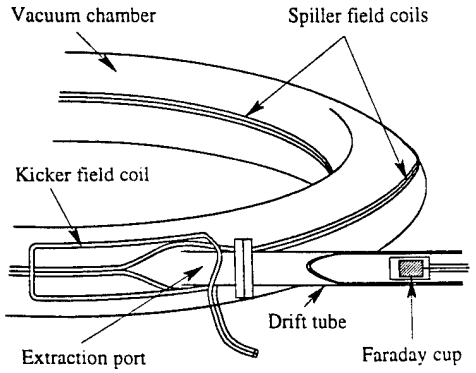
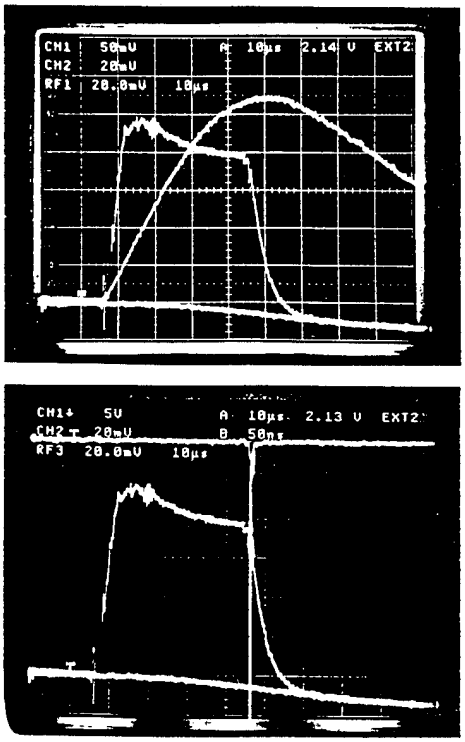


Fig.3. Schematic diagram of the beam extraction .

After reaching its peak, the beam current decreased as acceleration went on. In the previous experiment, two types of current losses had been found during acceleration[9]: early current disruption, followed by the gradual current decay. On the previous stellatron, more than 50% of the beam current was lost during the acceleration. Although the initial beam current in the glass chamber could be over 4 kA, the maximum beam current dropped to less than 1 kA when the peak electron energy exceeded 10 MeV[16]; the current losses were much worse when the FGE chamber was used[9]. Both of these current losses were also observed in the present experiment, However, they have been reduced significantly after programming the betatron field distribution and optimizing the time delays between B_b, B_t and B_h. A beam of 1.1 kA

and 12 MeV was achieved by initially forming a 1.2 kA beam, the current loss during the acceler-ation was about 10%. The early current disru-ption became more pronounced as the initial beam current was increased, because the ranges of the operation parameters became narrower as the betatron and toroidal fields approached their upper limits. A typical current wave form is shown in Fig.4, along with the wave forms of the betatron field and the X-ray yield during the beam extraction.



(a)

(b)

Fig.4. Typical wave forms of beam current, betatron field, and X-ray yield. (a) The beam current (the square trace, ~260 A/div.) was cut off by the spiller and kicker fields at the peak of the betatron field (the sinuous trace, 0.2 kG/div.) where the beam energy is ~12 MeV. (b) X-ray yield (upper trace) burst at the beam cut-off.

Beam extraction was performed by using the spiller field and the kicker field at the end of acceleration. When only the spiller field was applied, the beam orbit expanded outwards due to the sudden reduction of the betatron field and eventually hit the wall of the chamber. X-ray yield distribution indicated that the centroid of the beam took a helical orbit in the chamber. The abrupt beam current cut-off was not observed when only the kicker field was applied, even with I_{k0} up to 15 kA. This showed that in the stellatron the beam orbit was quite stable against local disturbances. When the spiller and kicker fields were both applied, most beam electrons would hit the chamber near the kicker coil if I_{k0}>5 kA. According to the spot size on the picture taken at where the beam struck the chamber, the beam radius was about 5~7 mm. By properly positioning the kicker coil near the extraction port up to 15% of the beam electrons were extracted into the port. The remaining electrons hit the wall of the chamber near the extraction port. In order to pass through the magnetic field coils around the chamber, the extracted electrons had to propagate about 20 cm in a drift tube attached behind the extraction port. Most of the electrons hit the wall of the drift tube during their first 6 cm of propagation. The distance of propagation has been increased to about 12 cm after installing a copper tube inside the drift tube. The copper tube has a 1.5 mm slot along its axis and was used to shield the external magnetic field components transverse to the drift tube.

IV. COMPUTATIONAL ANALYSIS OF EXTRACTION

A computer code which integrates the single-particle equations of motion has been utilized to study the orbit characteristics of an electron during the extraction from the stellatron. The total magnetic field used by the code is the superposition of the betatron field, the helical field, the toroidal field, and the fields produced by the spiller coil and the kicker coil. The typical experimental parameters are used in the computer program.

The orbit calculation shows that in the stellatron the electron orbit is usually a non-closed helix. The presence of the toroidal field and helical field make the extraction from the

stellatron much more involved than from a conventional betatron. For example, one way of extracting a beam from a conventional betatron is by locally reducing the betatron field. However, the calculation indicates that this method is not applicable in the stellatron.

The calculation confirmed that by applying a localized transverse magnetic field, such as the kicker field, one could guide the beam into an extraction port. However, τ_k should not be too long compared with $\Im$, the gyro period of the electron around the major axis of the chamber, otherwise the extraction possibility would be low. Besides, if only the kicker field were used for extraction, I_{k0} would have to be quite large because the major magnetic fields, i. e., B_b, B_t and B_h, were very strong during extraction. The calculation showed that for typical experimental parameters: B_{b0} =1 kG, B_{t0}=10 kG, and I_{h0}=7 kA and assuming $\tau_k=\Im\approx 9$ ns, efficient extraction required $I_{h0}\geq 30$ kA. However, if a spiller field with I_{s0}=0.45 kA and τ_s=150 ns was used to pre-expand the electron orbit before the kicker field was initiated, I_{h0} could be reduced to ~8 kA. Fig.5 shows the projections of the caiculated electron orbit on (a) the minor cross section and (b) the major cross sections of the chamber when both the spiller and kicker field are used for extraction. The calculation also shows that I_{h0} can be reduced further by properly locating the kicker coil relative to the helical winding. In the optimum case, I_{h0} can be reduced to about 3.5 kA from 8 kA.

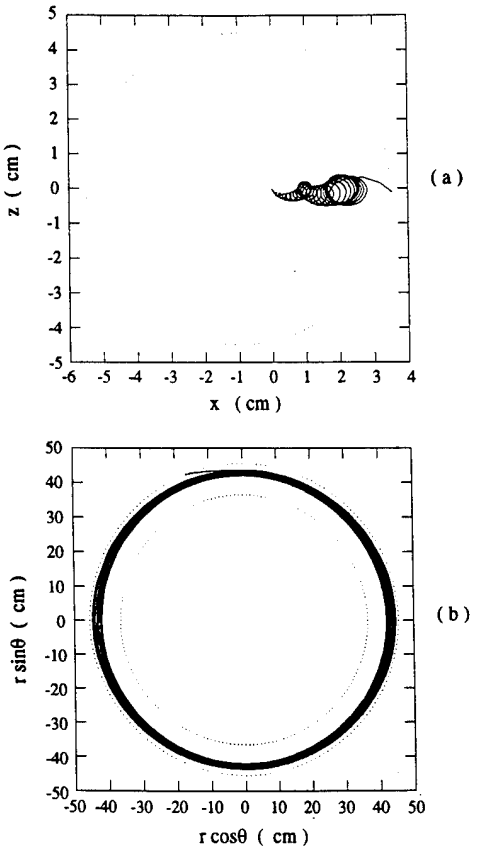


Fig.5. Projections of a calculated electron orbit when both B_k and B_s are applied. B_k started at the peak of B_s.

V. CONCLUSIONS AND DISCUSSIONS

The UCI stellatron has been modified for beam extraction. This is done by reconstructing the magnetic field coils and using a FGE vacuum chamber with an extraction port. A drift tube, connected behind the extraction port, allows the electrons to pass through the the coil structure. On the present system, the magnetic configuration is more compact and energy efficient, both the beam current and energy have exceeded the previous results. A 1.1 kA, 12 MeV beam was observed and the current loss during the acceleration was about 10%, while it was over 50% in the previous stellatron when obtaining a 1 kA, 10 MeV beam[9,16]. This indicated that the beam orbit was more stable in the present magnetic field configuration. The beam radius was measured as 5~7 mm. Beam extraction was performed by a spiller coil and a kicker coil. Up to 15% of the beam electrons was extracted into the extraction port. The low extraction efficiency is mainly due to the long rise time of the kicker field ($\tau_k \approx 1$ μs), as shown by the orbit calculation. Another problem was how to guide the extracted electrons through the magnetic coils

in the form of a beam. The electrons loss during their propagation in the drift tube is probably caused by 1) the magnetic field components transverse to the axis of the drift tube and 2) the expansion of the beam in the absence of focusing fields. It was found that the transverse components of the magnetic field inside the drift tube, except at the entrance, could be significantly reduced by inserting a copper tube inside the drift tube; the copper tube was slotted along its axis to allow penetration of the magnetic field component parallel to its axis. By doing this the propagation distance of the beam inside the drift tube has been increased to 12 cm from about 6 cm. The second cause may be remedied by using a pulsed current solenoid to generate an axial magnetic field inside the drift tube.

The computational simulation has shown that the combination of a spiller and a kicker can be used for beam extraction from the stellatron. Although the simulation is for a single electron orbit, it may well describe the orbital characteristics of the beam electrons because the beam's self-field effects are usually not significant compared with the effects of the external magnetic fields. The calculation indicated that τ_s should be comparable with or shorter than $\mathfrak{I}$, otherwise the extraction efficiency would be low. In the present stellatron this means that $\tau_k \leq 9$ ns. The calculation also indicated that I_{h0} required for extraction could be minimized by adding the spiller field and by properly positioning the kicker coil relative to the helical winding. For typical parameters used in the experiment, the calculation indicated that $I_{k0} \geq 3.5$ kA. In practice the required I_{h0} might be somewhat higher if the shield effect of the chamber wall to the kicker field was taken into account. In generating such a short rise time and high current pulse in the kicker coil, the main problem is how to avoid electric breakdown between this coil and other magnetic field coils.

ACKNOWLEDGMENTS

The authors are indebted to Hiroshi Ishizuka for his contributions to the previous stellatron experiment and to the design of the present system. We also thank Karl Yee for his participation in the early stage of this work and Robert Prohaska for his technical assistance.

This work was supported by the Office of Naval Research.

REFERENCES

[1] C. W. Roberson, A. Mondelli, and D. Chernin, *Phys. Rev. Lett.* **50**, 507 (1983)
[2] D. W. Kerst, *Nature* **157**, 90 (1940)
[3] N. Rostoker, *Particle Accelerators* 5, 93 (1973)
[4] P. Sprangle and C. A. Kapetanakos, *J. Appl. Phys.* **49**, 1 (1978)
[5] G. Barak and N. Rostoker, *Phys. Fluids* **26**, 856 (1983)
[6] H. Ishizuka, G. Lindley, B. Mendelbaum, A. Fisher, and N. Rostoker, *Phys. Rev. Lett.* **53**, 266 (1984)
[7] G. A. Roberts and N. Rostoker, *Phys. Fluids* **28**, 1968 (1985)
[8] C. W. Roberson, A. Mondelli, and D. Chernin, *Particle Accelerators* **17**, 79 (1985)
[9] H. Ishizuka, *Phys. Fluids* B **2**, 3149 (1990)
[10] C. A. Kapetanakos, L. K. Len, T. Smith, S. J. Marsh, D. Dialetis, P. Loschialpo, D. Dialetis, and J. Mathew, *Phys. Fluids* B **5**, 2295 (1993)
[11] L. S. Skaggs, G. M. Almy, D. W. Kerst, and L. H. Lanzl, *Phys. Rev.* **70**, 95 (1946)
[12] S. L. Fawcett and E. C. Crittenden Jr., *J. Appl. Phys.* **17**, 444 (1946)
[13] K. Gund and H. Reich, *Z. Physik* **126**, 383 (1949)
[14] J. D. Lawson, H. E. Walford, and J. H. Aram, *Nature* **166**, 234 (1950)
[15] R. S. Foote and Ben Petree, *Rev. Sci. Inst.* **25**, 694 (1954)
[16] H. Ishizuka, R. Prohaska, A. Fisher, and N. Rostoker, *Proceedings of the 7th International Conference on High-Power Particle Beams*, Karlsruhe, Germany, 1988, (Kernforschungszentrum, Karlsruhe, Germany 1988), Vol. II, p. 857

HIGH CURRENT GENERATION FROM FIELD EMISSION TIP CATHODES

Y. Song, E. Garate, and N. Rostoker

Department of Physics
University of California, Irvine, CA 92717

ABSTRACT

Electron beams with current up to 1.2 A and current density over 10^7 A/cm^2 have been generated from a pulsed, field emission tip cathode etched from commercial grade tungsten wire. Electron beams with current up to 0.8 A were also generated from a single molybdenum tip. The applied tip-anode voltage was up to 50 kV with pulse duration from 300 ns to 1.2 μs. Scanning electron micrographs indicate that tip radii varied between 100 nm to 1 μm. The background pressure in the system was below 3×10^{-9} Torr. Depending on the brightness, these types of electron beams could be suitable for channeling radiation X-ray lasers and might considerably decrease the operating wavelength of free-electron lasers at moderate beam energies.

I. INTRODUCTION

This work was initiated by the study of channeling radiation X-ray lasers. The idea of channeling radiation X-ray lasers is based on a relativistic electron beam propagating through axial or planar crystal channels and populating transverse bound states[1]. Transitions between these discrete states yield narrow width, strongly forward peaked and tunable X-ray radiation[2]. The channel radiation gain is mainly determined by the properties of the electron beam. It has been shown[3] theoretically that stimulated emission can occur for channeled electrons if the current density is $j\sim10^6$ A/cm^2, the total current $I>5$ mA, the electron energy $E>5$ MeV, and the perpendicular energy is <10 eV so that electrons remain in a channel. For the X-ray laser application considered, the best electron source is the field emission tip employed in the scanning electron microscope (SEM)[4], which typically has high current density ($\geq10^6$ A/cm^2) and very small perpendicular energy (<1 eV). The only problem is that the beam currents in typical SEMs are too low (~10 nA) for such application.

Previous work[5] suggests that high brightness, high current density electron beams can be generated from pulsed field emission tip cathodes. The mechanism of field emission can be understood as follows: When a strong electric field is applied on a metal cathode, free electrons "tunnel" through the metal's surface potential barrier when the latter is thinned by the applied field. In order to achieve field emission, the applied field has to be $>10^7$ V/cm. This is realized by using tip cathodes with very small radius. According to Fowler and Nordheim[6], the current density, j, of field emitted electrons is given by

$$j = a(F^2/\phi)\exp[-b\phi^{3/2}f(y)/F] \qquad (1)$$

where j is in A/cm^2, ϕ is the work function of the metal in eV, F is the applied field in V/cm; a and b are approximately constants with $a=1.54\times10^{-6}$ and $b=6.83\times10^7$, and $f(y)$ is Nordheim's elliptic function of the variable $y = 3.79\times10^{-4}F^{1/2}/\phi$. For a smooth tip

$$F = V/kr \qquad (2)$$

where V is the applied voltage on the tip, r is the tip radius, and the geometrical factor $k\approx5$

near the tip apex and increases with increasing polar angle.

A field emission electron source typically has very high current density. For example, applying a 10 kV voltage on a tungsten tip with radius 250 nm and work function $\phi = 4.5$ eV yields $j \approx 10^8$ A/cm^2 according to the above equation. Another important feature of the field emission electron beam is its very small transverse energy spread, normally between 0.2~0.5 eV[4]. Therefore the electron emission from a tip cathode is characterized by a high current density and very small beam emittance. For a tip of a given radius, a higher current density and hence larger total current can be achieved by applying a higher voltage. However, initiation of a vacuum arc and subsequent tip destruction will take place at very large current densities, about 10^8~10^9 A/cm^2 for microsecond pulse emission[7]. Larger total currents can be obtained by blunting the tip and applying higher voltages without initiating a vacuum arc. Higher current densities will be possible for shorter duration pulses since heating of the tip during emission depends on the pulse length.

II. EXPERIMENTAL SET-UP

The system set-up is shown in Fig.1. The vacuum chamber was constructed from standard Del Seal vacuum fittings (flange o.d.: 2-3/4", tube o.d.: 1-1/2"). The tip cathode was installed into the chamber via a ceramic feed-through which insulated the cathode from the grounded anode and the rest of the vacuum chamber. The anode was made of a piece of metal screen. The tip-anode distance could be varied from 1.5 mm to 5 mm. Two kinds of screens were used: one was copper (50 μm wire thickness, 45% transparency) and the other was tungsten (25 μm wire thickness, 90% transparency). The purpose of this was to compare the secondary particle emissions from different screens hit by the electrons emitted from the tip. An emission monitor was located about 25 mm behind the anode screen. The monitor was made of conductive glass coated with electronic phosphor. It could be used both as a charge collector to measure the emission current and as a phosphor screen to monitor the emission pattern.

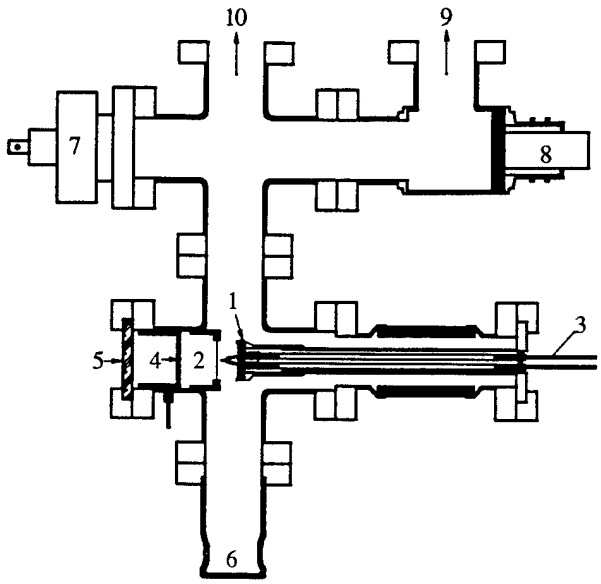


Fig. 1. System set-up: 1. cathode assembly, 2. anode screen, 3. heating wire, 4. emission monitor, 5, 6. view windows, 7. vacuum gauge, 8. gate valve, 9. to cryo pump, 10. to ion pump.

Commercial grade tungsten and molybdenum wires were used as tip materials. The tips were fabricated by using techniques similar to those outlined by Dyke *et al*[8]. A piece of 0.125 mm diam. tungsten or molybdenum wire was spot-welded onto a V-shaped tungsten filament. The tip was etched by immersing it in a NaOH solution and by applying ac voltage between the tip and a remote electrode in the solution. The sharpness of the tip depended on the amplitude of the applied voltage and the concentration of the solution. SEM measurements showed that the tip radius varied from less than one hundred nanometers to a few micro-meters. A typical etched tip is shown in Fig.2. The filament was mounted on the cathode shank and installed into the vacuum

chamber through a feed through. After installation, the tip was heated before operation. This was to smooth the tip surface and achieve a desired tip radius. During heating the tip temperature was monitored by an optical pyrometer. The pre-heating procedure was usually done in vacuum below 10^{-7} Torr.



Fig. 2. A SEM graph of a typical etched tungsten tip. Scale size is shown in the lower right hand corner.

The working background pressure inside the vacuum chamber was below 3×10^{-9} Torr which was the minimum measurable pressure of the vacuum gauge. The evacuation of the chamber consists of two steps. First, the chamber was baked to ~200°C and evacuated to 10^{-6}~10^{-7} Torr by a cryo pump. Second, the chamber was isolated from the cryo pump by closing a gate valve, and an ion pump was used for final evacuation. No further baking was performed during the second step.

Voltage was applied to the tip cathode from a pule forming line, consisting of one roll of RG-8 coaxial cable and a 1:4 step up transformer. Depending on the cable's length, the pulse duration was varied between 300 ns to 1.2 μs. Voltage up to 50 kV could be applied to the cathode. The voltage was measured using a Tektronix high voltage probe and monitored by a digital storage oscilloscope.

III. RESULTS AND DISCUSSION

Electron emission currents up to 1.24 A were achieved using tungsten tip cathodes. According to the tip radius measured by SEM, the current density near tip surface was calculated to be over 10^7 A/cm^2. Emission currents up to 0.82 A were observed from the molybdenum tip cathodes. The voltage and current traces of a typical tungsten tip are shown in Fig.3. The Fowler-Nordheim plots of tungsten tip #17 and molybdenum tip #7 are shown in Fig.4. Typical emission patterns of molybdenum tip #5 are shown in Fig.5.

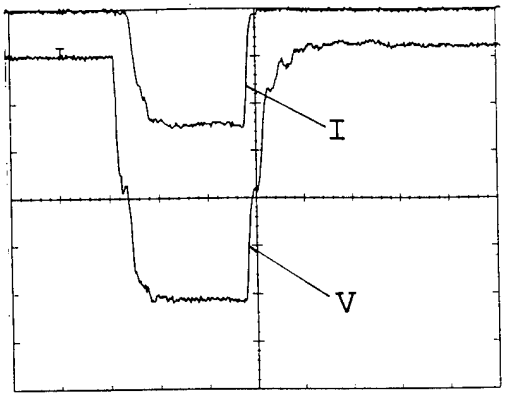


Fig. 3. Voltage and current traces of a tungsten tip. V: 8.7 kV/div., I: 0.27 A/div., time scale: 500 ns/div.

According to the sizes of the emission patterns on the phosphor screen, the emission half angle was 12~30° for tungsten tips and 14~30° for molybdenum tips. Cold field emission was used during the experiment. However, when emission current was high (~1 A), it was found that "flashing" the tip could reduce the chance of vacuum arc and sustain the tip longer and also reduce the fluctuation of emission current. Here flashing means heating the tip briefly without applying voltage. It could desorb the layer of contaminants on the tip which cause emission irregularies and smooth the surface of pitting caused by ion bombardment during emission. The temperature of flashing is fairly critical. Too hot would dull the tip while too cool could not desorb the contaminants. Usually, higher heating

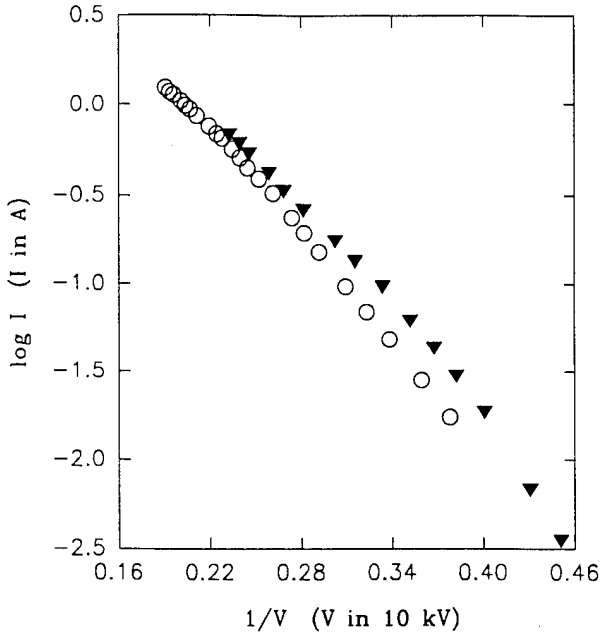
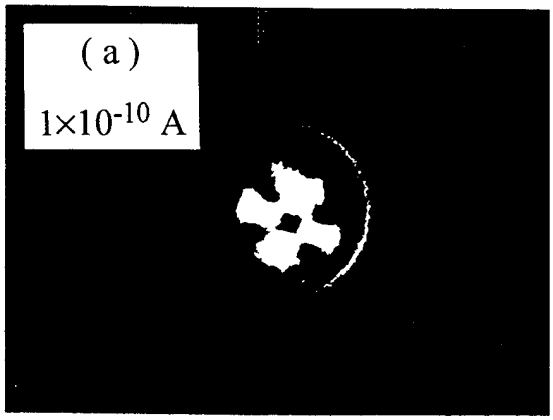
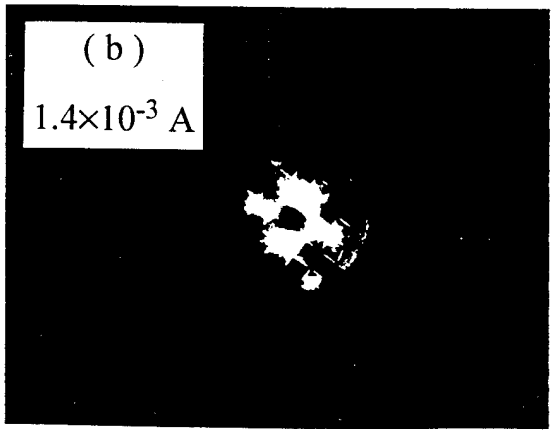
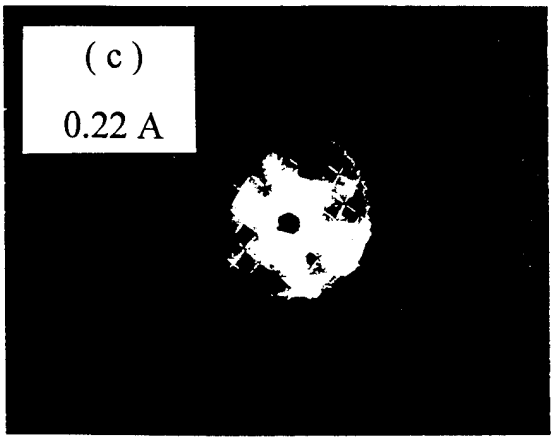


Fig. 4. The Fowler-Nordheim plots for tungsten tip #17 (circles) and molybdenum tip #7 (triangles).







Figs. 5a-5c. Typical emission patterns of molybdenum tip #5 at different currents.

temperature can be used for a tip with larger radius. Fig. 4. shows that for both the tungsten and molybdenum tips *log I* has a linear relationship with V^{-1} except at high voltages where the slopes decrease. According to the explanations of Dyke *et al*[5], this is mainly the effect of space charge. On the tip surface, the work function varies from point to point on different crystal planes. As the tip voltage increases, the current density in areas of lower work function is high enough, say $j>10^7$ A/cm^2, that space-charge effect becomes evident. This retards further current density increase in these areas, while current density continues to increase with increasing voltage at the areas of low emission. At even higher voltage the field emission would initiate a vacuum arc that damaged the tip. Another cause for the slower growth of emission current at high voltage was that the tip became duller after being run for a period of time at high emission currents. However, a check conducted during the experiment indicated that this effect was less significant than the space charge effects. The emission current of a tip was first measured at a low voltage, then the voltage was increased high enough so that the slowdown of emission became apparent. Then the voltage was decreased gradually to the initial value and the

emission current was re-measured. It was found that the current decrease due to the tip dulling was usually less than fifteen percent. It was also found that the space charge effect became insignificant when the current density near the tip surface was lower than 3×10^6 A/cm^2. For a tip of 1 μm radius, the total emission current at such current density is about 100 mA.

Usually a tip was damaged by a vacuum arc that was initiated when the applied voltage was raised to such a limit that the emission current density was too high (>10^8 A/cm^2). In one test, a tungsten tip emitter survived several hundreds of shots with the fluctuation of emission current from shot to shot of less than 10%. The tip was finally destroyed by raising the voltage less than 5%. It is likely that the tip can last much longer if the voltage is kept 5~10% below its critical value.

The maximum emission currents in the experiment were mainly limited by the dimension and configuration of the system, electrostatic breakdowns between the cathode feed through and ground prevented applying higher tip-anode voltages. Given our experience, it is likely that higher emission currents can be achieved by doing the following: 1) using a better tip material, e. g., single crystal wire for which the low work function crystal planes yield high current density at relatively low voltage; 2) using a tip cathode with larger radius, however this would require a higher tip-anode voltage; 3) shorter pulse duration for the tip-anode voltage, this would reduce the resistive heating of the tip during emission that initiates the vacuum arc[9].

Besides channeling radiation X-ray lasers, high current density and high brightness electron beams have many other useful applications, including free electron lasers, Cherenkov radiation, parametric X-ray generation and high brightness X-ray production using Compton scattering. Cathode tips mounted in an rf cavity could also produce high brightness short pulse (ps) electron bunches. The beam emittance of a field emission source is[4]

$$\varepsilon = r\theta \tag{3}$$

where θ is the average divergence angle and r is the apparent size of the beam source[10]

$$r \sim R(V_\perp / V)^{1/2} \tag{4}$$

with R the true geometric tip radius, $V_\perp$ the spread in transverse energy of emitted electrons and V the applied voltage. Typically $V_\perp$ is very small for dc field emission electron sources (0.2~0.5 eV)[4]. Whether it increases significantly for pulsed field emission sources operating at high currents (>100 mA) needs to be determined. However, according to the calculation of T. E. Everhart[11], the emitted electrons gain $V_\perp$ in a short distance very close to the emitter surface (<1 μm). Since emission current density depends on the field strength at the emitter surface, it is likely that even for pulsed high current emission $V_\perp$ will not increase significantly as long as the current density is not too high. As an example is the estimation of the emittance of tungsten tip #17 ($R \approx 1$ μm) operated at V=32 kV and emission current $I \approx 100$ mA. $\varepsilon < 1\times10^{-3}$ π mm·mrad assuming that $V_\perp$=1 eV and θ=30°. Because the beam emittance of a field emission source is usually extremely small, direct measurement is very difficult.

It is believed that main problem of a field emission electron source is the unstable performance of the tip and its fragility at high current emission[12]. This experiment shows that it can be solved by keeping the emission current density from being too high, say $j<3\times10^6$ A/cm^2. If a much higher current density is needed, flashing the tip after each shot can reduce the fluctuation of emission current and prolong the tip lifetime significantly. It has been found that there are several benefits of operating the tip at relatively low current density: 1) the lifetime of the tip is long, 2) the effects of space charge

and tip dullness are negligible, and 3) the fluctuation of emission current and beam emittance are small. For a tip of 1 μm radius operated at $j \sim 3 \times 10^6$ A/cm^2, the total emission current $I \sim 100$ mA which is sufficiently large for channeling radiation. An even higher current may be obtained by using a tip of a larger radius and higher applied voltage.

ACKNOWLEDGMENTS

This work was supported by the Office of Naval Research. We are very grateful to Dr. Amnon Fisher for his many inspiring suggestions. We also thank Dr. O. Gornostaeva and E. Hallenberg for their help during the experiment.

REFERENCES

[1] V.V. Beloshitsky and M.A. Kumakhov, *Phys. Lett.* **A69**, 247 (1978)
[2] J.U. Anderson, E. Bonderup, and R.H. Pantell, *Ann. Rev. Nucl. Part. Sci.* **33**, 453 (1983)
[3] M. Strauss and N. Rostoker, *Phys. Rev.* **A40**, 7097 (1989)
[4] J. F. Hainfield, *Scanning Electron Micro-scopy* **1**, 591 (1977)
[5] W.P. Dyke and W.W. Dolan, *Advances in Electronics and Electron Physics* **8**, 89–185 (1956), Academic Press, NY.
[6] R.H. Fowler and L.W. Nordheim, *Proc. R. Soc. London Ser.* **A119**, 173 (1928)
[7] W.P. Dyke and J.K. Trolan, *Phys. Rev.* **89**, 799 (1953)
[8] W.P. Dyke, J.K. Trolan, W.W. Dolan, and G. Barnes, *J. Appl. Phys.* **24**, 570 (1953)
[9] W.W. Dolan, W.P. Dyke, and J.K. Trolan, *Phys. Rev.* **91**, 1054 (1953)
[10] J.C. Wiesner and T.E. Evertart, *J. Appl. Phys.* **44**, 2140 (1973)
[11] T.E. Everhart, *J. Appl. Phys.* **38**, 4944 (1967)
[12] C. Travier, *Particle Accelerators* **36**, 33 (1991)

HIGH CURRENT BEAM EMISSIONS FROM SPACECRAFT

Shu T. Lai
Phillips Laboratory
29 Randolph Road
Hanscom AFB, MA 01731

Abstract

During high current charged particle beam emissions from a spacecraft, the spacecraft potential floats relative to the ambient plasma. There are important questions about the upper limits of beam current emitted into the ambient plasma and of the spacecraft potential. The usually accepted view is that the beam current emitted reaches its upper limit when the spacecraft potential reaches the beam energy. In this view, any attempt to emit a current beyond the critical value would result in partial beam return while both the effective beam current emitted and the spacecraft potential would remain unaffected. Surprisingly, results from three recent beam experiments in space show that the spacecraft potential can exceed the beam energy when very high beam currents are emitted. These results show that the usual limits on the beam current emitted and the spacecraft potential achieved are incorrect. Study of space charge beam divergence shows that the usual limits can be exceeded.

INTRODUCTION

When an electron beam is emitted from a spacecraft, the spacecraft potential tends to float positively relative to the ambient plasma. As a result, the spacecraft attracts ambient electrons. At equilibrium, the potential is governed by current balance. When the beam current greatly exceeds the ambient plasma current, the former controls the potential.

There are important questions about the upper limits of beam current emitted into the ambient plasma and of the spacecraft potential. Until recently, it was commonly believed that a spacecraft cannot be supercharged, i.e., the spacecraft potential can not exceed the beam energy. In this view, any attempt to emit a current beyond the critical value would result in partial beam return while both the effective beam current emitted and the spacecraft potential would remain unaffected. Therefore, the beam current emitted would reach its upper limit (the classical limit) when the spacecraft potential reaches the beam energy.

Surprisingly, results from three recent electron beam experiments in space, conducted by Russian, Norwegian, and US teams, show that the spacecraft potential can exceed the beam energy when very high beam currents are emitted [1,2,3,4,5]. These results show that the usual limits on the beam current emitted and the spacecraft potential achieved are incorrect.

All of the observations are steady state events and therefore not attributable to plasma fluctuations. Although there are computer simulations of supercharging in plasma time scales [6,7,8], they are not directly applicable for explaining the steady state results observed.

We derive an improved beam envelope formula for modeling high current charged particle beam emission in steady state from an oppositely charged spacecraft. As the beam

propagates outwards through an attractive spacecraft potential sheath, the beam electrons slow down, thereby increasing the space charge density and beam divergence. The divergence gives angular momentum to the beam electrons, so some of them may not return to the spacecraft, even if the spacecraft is charged beyond the beam energy [Fig.1].

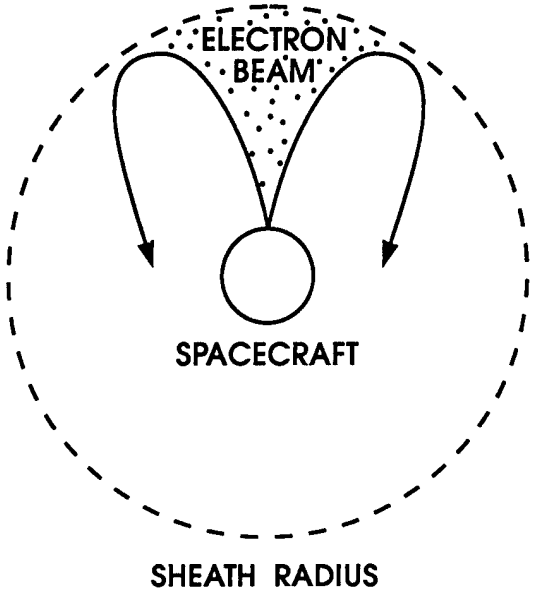


Figure 1. Beam divergence and beam return

The scope of this paper is to study this theoretical possibility at geosynchronous altitudes. We do not attempt to model the detailed conditions of the experiments. Spacecraft electric fields at geosynchronous altitudes are often dominant over the ambient magnetic fields.

CURRENT BALANCE

The current balance for a spacecraft emitting an electron beam is given by the Langmuir plasma probe model [9]:

$$I_e\left(1+\frac{e\phi}{kT}\right)^{\alpha}+I_i\exp\left(-\frac{e\phi}{kT}\right)=I_b+I_r \quad (1)$$

where I_e and $_i$ are the ambient electron and ion current at zero spacecraft potential ϕ, and I_b and I_r are the electron beam current and beam return current respectively, and e is the magnitude of an electron charge. The exponent α depends on the spacecraft geometry [10] and is unity for a spherical spacecraft.

Secondary electrons from the spacecraft surfaces have low energies (a few eV) and therefore cannot leave a positively charged spacecraft (kV). The ambient ion current, I_i, is typically two orders of magnitude smaller than I_e at geosynchronous altitudes as measured on the SCATHA satellite [11]. A positively charged spacecraft ($\phi>0$) would repel the ambient ions during electron beam emissions. Therefore, I_i ($\ll I_e$) is neglected in eq(1).

When a beam leaves a spacecraft with no beam return current, I_r, the spacecraft potential ϕ increases monotonically with the beam current, I_b (eq.1). However, when ϕ reaches a critical value ϕ_c, I_r becomes finite and, the net beam current I_{net} leaving the spacecraft is reduced accordingly.

$$I_{net}(\phi) = I_b - I_r(\phi)\,\Theta(\phi-\phi_c) \quad (2)$$

where $\Theta(x)$ is a step function ($\Theta=0$ for $x<0$, and 1 for $x\geq 0$).

In the usually accepted view, the critical value, $e\phi_c$, equals the beam energy E. When the beam current I_b reaches a critical value, I_c, the potential ϕ reaches ϕ_c. The energy conservation law governs: the attractive potential reaches the beam energy, the beam comes to a halt and returns. Any attempt to increase I_b beyond the critical current I_c does not affect the net current, I_{net} (= I_c), or the spacecraft potential ϕ (= ϕ_c).

Beam divergence is the key to understanding why the above view is fallable. When an electron beam comes out from its exit point, the beam is packed with space charge potential energy, so the beam expands as it propagates. This energy is in addition to that gained by the beam electrons accelerating across

the electrostatic grids before the beam comes out. For example, a 1 keV electron beam of 0.1 amp, 1 mm radius, has a beam expansion electric field of 960 V/cm, which means the total beam energy is above 1 keV.

BEAM DIVERGENCE

From Gauss, Biot-Savart, and Faraday laws, the equation of motion of an electron on the beam envelope is:

$$m\frac{d^2}{dt^2}r(x) = \frac{1}{4\pi\epsilon_o}\frac{2eI}{r(x)V(x)}\left(1-\frac{V^2}{c^2}\right) \quad (3)$$

where r(x) is the radius of the beam at distance x from the beam exit point (x=0), I the current, m the electron mass, and V the beam velocity. We denote r_o to be r(0) and integrate eq(3):

$$2r_o\left[\frac{\pi\epsilon_o}{eI}\right]^{1/2}\int_0^{[\ln(r/r_o)^{1/2}} dz\exp(z^2) =$$

$$= \int_0^x dx\frac{1}{m^{1/2}V^{3/2}(x)}\left(1-\frac{V^2(x)}{c^2}\right)^{1/2} \quad (4)$$

Since the beam is emitted from a spacecraft with an attractive potential ϕ_s floating with respect to that of the ambient plasma, the beam velocity V(x) depends on the spacecraft potential profile ϕ(x):

$$\frac{1}{2}mV^2(x) - e\phi(x) = \frac{1}{2}mV^2(0) - e\phi_s \quad (5)$$

where ϕ_s is the spacecraft potential. For simplicity, we assume a profile ϕ(x) of the Debye form [12]:

$$\phi(x) = \frac{\phi_s R}{x+R}\exp\left(-\frac{x}{\lambda}\right) \quad (6)$$

for a spherical spacecraft of radius R. ϕ_s is the spacecraft potential, and λ the plasma shielding distance of the potential profile.

If the beam is emitted into an ambient plasma, the space charge density of the expanding beam equals that of the ambient plasma at a distance x_a. Beyond x_a, the beam space charge density becomes negligible and the beam electron motion is governed by the spacecraft potential ϕ(x) only. Whether the beam electrons return to the spacecraft depends on their energy and angular momentum and the geometry of the spacecraft.

Eqs(4,5,6) can be solved numerically. Two examples are shown [Fig.2]. In the first example, beam energy = 1 keV, beam current 10 mA, and spacecraft radius 60 cm, and spacecraft potential ϕ_s = 1200 V. We have computed the sheath potential profile, electric field, charge density and electron velocity as a function of distance x along the beam. In the second example, ϕ_s = 0 V. The beam divergence is much larger with spacecraft charging (ϕ_s = 1200 V) than without spacecraft charging (ϕ_s = 0). This implies that the angular momentum gained by the beam electron is larger with charging.

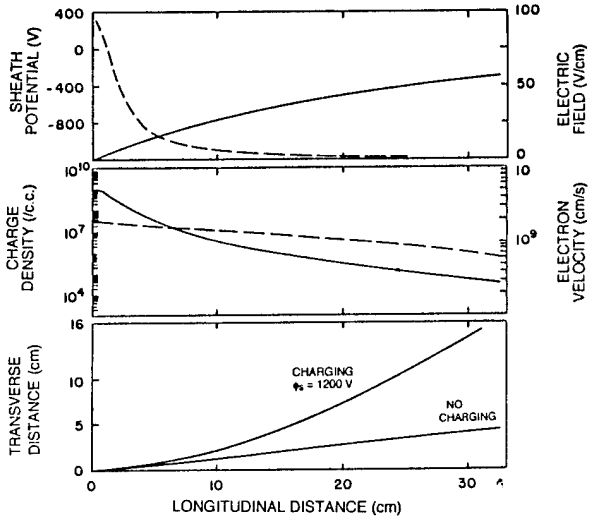


Figure 2. Beam divergence in an attractive sheath.

To demonstrate that the angular momentum gained may prevent the beam electron from returning to the spacecraft, we show the computed orbits of a case in which the beam energy = 1 keV, the spacecraft radius 10 cm, and the spacecraft potential 1.6 kV. The

beam divergence increases with the beam current. A critical current exists at about 19 mA, beyond which the beam envelope is open [Fig.3]. The beam electrons on the open envelope escape to space because of their high angular momentum.

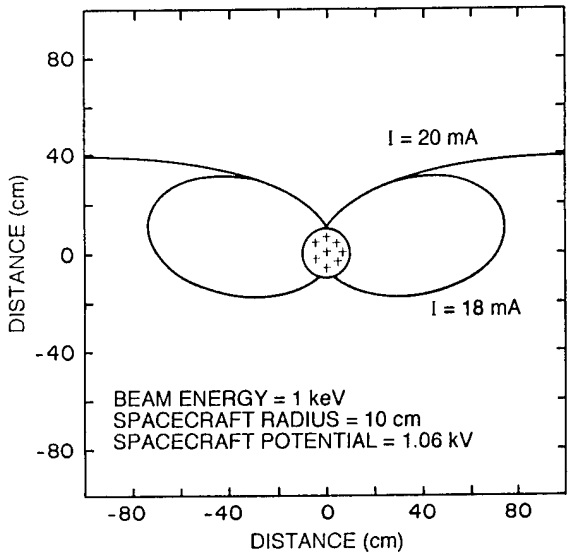


Figure 3. Envelopes of large current beams in an attractive sheath.

SUMMARY

The level of spacecraft charging increases with the beam current emitted. In the usual view, a spacecraft can be charged as high as the beam energy only, and, the beam current emitted into space reaches its upper limit when the charging limit is reached. Recent experiments have shown that both limits can be exceeded in steady state. These results have surprised the space researchers. We offer an explanation. The space charge divergence of the beam can impart angular momentum to the beam electrons. With high angular momentum, they may not return. We have shown computed results demonstrating such a theoretical possibility. Since some electrons do not return for currents above this threshold, the spacecraft potential must rise above the beam energy to attract more ambient electrons for current balance.

REFERENCES

[1] Kochmaryov, L.Y., S.B. Lyakhov, and A.D. Mayorov, *Plasma Phys.* (Russian), Vol.11, 622, 1985.

[2] Olsen, R.C., *J. Electronics*, Vol.20, 43-57, 1987.

[3] Managadze, G.G., V.M. Balebanov, A.A. Burchudladze, T.I. Gagua, N.A. Leonov, S.B. Lyakhov, A.A. Martinson, A.D. Mayorov, W.K. Riedler, M.F. Frederich, K.M. Torkar, A.N. Laliashvili, Z. Klos, and Z. Zbyszynski, *Planet. Space Sci.*, Vol.36, 399-410, 1988.

[4] Maehlum, B.N., Troim, J., N.C. Maynard, W.F. Denig, M. Frederich, and K.M. Torkar, *Geophys. Res. Lett.*, Vol.15, 725-728, 1988.

[5] Denig, W.F., N.C. Maynard, W.J. Burke and B.N. Maehlum, *J. Geophys. Res.*, Vol.96, 3601-3610, 1991.

[6] Singh, N. and K.S. Hwang, *Phys. Script.*, Vol.40, 295-301, 1989.

[7] Winglee, R. M. and P. L. Pritchett, *J. Geophys. Res.*, Vol.93, 5823-5844, 1988.

[8] Mandell, M.J. and I. Katz, in Proceedings of Spacecraft Charging Technology Conf., 464-485, R.C. Olsen, ed., Naval Postgrad. School, Monterey, CA, ADA-263477, 1991.

[9] Mott-Smith, H.M., and I. Langmuir, *Phys. Rev.*, Vol.28, 727-763, 1926.

[10] Lai, S.T., *J. Geophys. Res.*, Vol.99, 459 - 468, 1994.

[11] Reagan, J.B., R.W. Nightingale, E.E. Gaines, R.E. Myerott, and W.L. Imhoff, in Spacecraft Charging Technology, NASA2181/ AFGL-TR-81-0270, ADA114426, 1981.

[12] Whipple, E.C. Jr., J.M. Warnock and R.H. Winckler, *J. Geophys. Res.*, Vol.79, 179, 1974.

COMPACT HIGH-CURRENT RIBBON E-BEAM DIODE

V.G.Shpak, M.I.Yalandin, and S.A.Shunailov
Institute of Electrophysics,
Ural Division of the Russian Academy of Sciences,
34 Komsomolskaya St., Ekaterinburg, Russia, 620219

Abstract

Experimental investigations of a compact high-current accelerator injecting a 500×5 mm² ribbon electron beam (≈200 keV, ≈1 kA) are presented. The main peculiarity of this work is a short accelerating-voltage pulse width (about 4 ns). An experimental demonstration of the traveling-wave operation mode of a space-extensive vacuum diode is adduced.

Introduction

Some lab investigations and applications demand space-extensive (SE) e-beams. The successful test of a compact electron accelerator generating a ribbon e-beam 110x5 mm² in cross section [1] stimulated the designing of a vacuum diode with a more space-extensive electron beam. As the length of a ribbon e-beam diode is comparable with "electrical" pulse width and the accelerating voltage pulse is transmitted along the SE-diode as a TEM-wave, we supposed that such a vacuum diode must operate as a long transmitting line with distributed losses represented by the electron beam current. The above described operation mode of a vacuum diode can be characterized as a wave mode. Therefore, we call a SE vacuum diode energized by a short accelerating pulse a *Traveling Wave Diode* (TWD).

In contrast to a classical transmission line, the losses in a TWD are rather high and have a complex longitudinal-coordinate and time dependence. Thus a detailed analysis should take into account the input and output matching of the vacuum diode transmission line; the dynamics of cathode plasma formation and of the electron beam characteristics. Plasma formation represents a complex unsteady-state process typical for explosive emission and ferroelectric cathodes [2]. Besides, local cathode emission processes depend directly on high voltage pulse parameters. Analyzing such a model theoretically is a rather difficult problem. To prove the possibility of creating TWDs, we have carried out experimental investigations using a specially designed setup (Fig.1).

Experimental setup

The nanosecond high-voltage driver used was a commercial pulsed power RADAN 303B supply source [3]. This source generated 4-ns pulses with rise and fall times of 1 ns and represented a double forming line (DFL) with a 45-Ohm impedance and a 150-pF capacitance. The DFL charging voltage could be easily controled and varied from 10 to 200 kV. The vacuum diode had the configuration of a coaxial line. The central electrode about 600 mm long was connected to the driver's output and served as a cathode holder (Fig.2). The diode line had an impedance of 50 Ohm and a capacitance

of 70 pF. We used a metal-dielectric cathode (Fig.3) whose operation is based on firing a plasma in the metal-dielectric contact in a strong electric field. Such a cathode represents a row of metal points pressed to a plate of alumina ceramics. The in-service wear of these points does not change the diode's characteristics because of the constant presence of a metal-dielectric contact. The cathode length was 480 mm. A 60-μm aluminum-beryllium foil window was used as the anode. Parallel installation of the dielectric plates at both sides of the cathode permitted forming sharp beam borders on the foil window and thus reduced the electron losses on internal walls of the diode. This construction makes it possible to design the diode window as a narrow slot and use the body of the diode as the foil heat radiator. The cathode-anode separation and the accelerating-gap uniformity along the diode can be readily varied over a wide range. To measure the electron beam current in air, a special vacuum collector was designed. Beam energy was estimated by means of a calorimeter 150-mm long. Moving the calorimeter along the foil window permited monitoring beam energy homogeneity over the entire length of the window. The beam size was measured from traces on a dosimetry film placed at different distances from the anode foil.

Experimental results

The beam current provided the parallel shunting of the TWD, i.e., short-circuit-type mismatching of the DFL and TWD. Thus, the effective TWD impedance estimated was about 30 Ohm and the traveling-pulse amplitude did not exceed 0.8 of the DFL output voltage. Beam generation determined the further decrease in the amplitude of the traveling pulse as the latter passed along the TWD. This is the fundamental difference of the TWD from a "short diode" energized by the DFL [1]. With the TWD output end (exit) being open, traveling-pulse reflection and voltage doubling occurred.

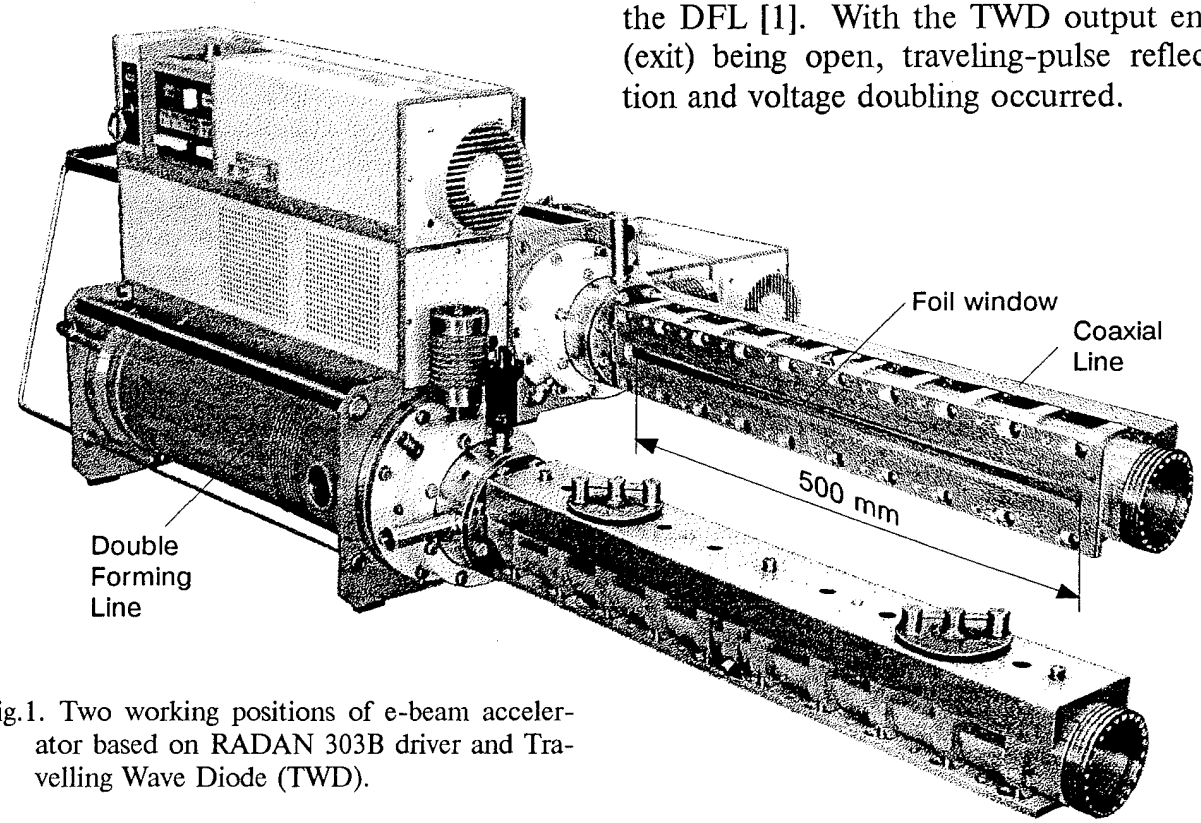


Fig.1. Two working positions of e-beam accelerator based on RADAN 303B driver and Travelling Wave Diode (TWD).

In first experiments the cathode-anode gap was uniform and had a maximum value of 16 mm (Fig.2,a). In that case the beam generation efficiency was low at the entrance into the vacuum line and the shunting of the line was insignificant. Under such conditions the transmission of a high-voltage pulse to the open end of the line was effected with small amplitude losses. So higher-energy electrons were injected in the vicinity of the line's open end. In this experiment a drastic heterogeneity of beam energy was observed in different places of the foil window. Nevertheless, a maximum specific beam energy, 0.35 J/pulse, was attained near the open end of the vacuum line (Fig.4, curve 1) in this mode of operation. When we evenly decreased the anode-cathode gap, this beam energy value deminished (Fig.4, curve 2). This fact can be explained by the enhancement of the beam-current shunting effect at the entrance into the vacuum line.

The mode with uniform beam energy distribution (Fig.4. curve 3) was achieved by using a nonuniform anode-cathode separation (Fig.2,b): 10 mm at the beginning of the diode and 16 mm at the end. In this case a large part of the beam current at the diode input had already been generated by the traveling voltage pulse. The reflected pulse determined the increase in voltage amplitude at the end of the line and also, with some delay, at the

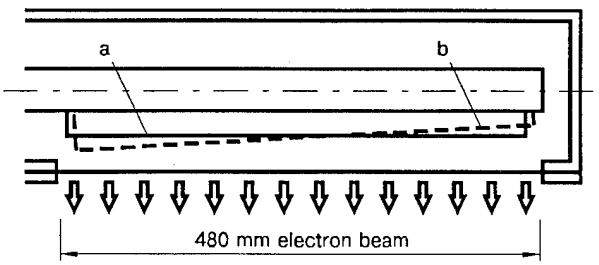


Fig. 2. Traveling Wave Diode configuration.

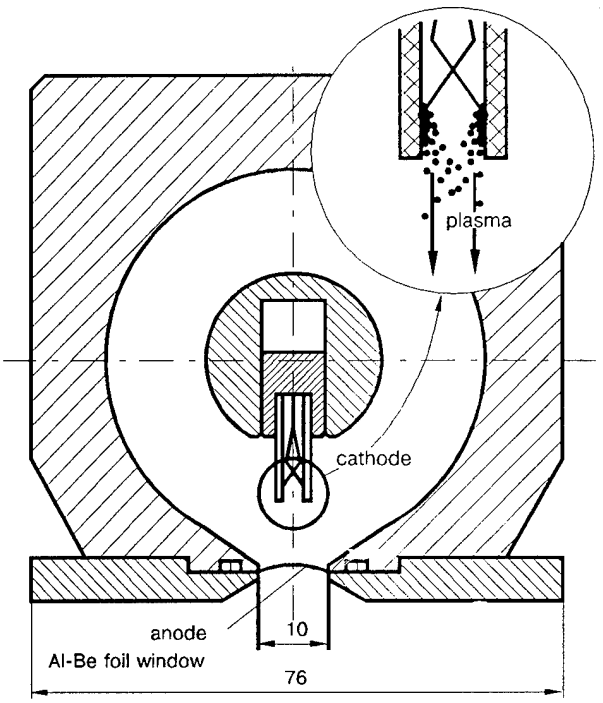


Fig. 3. Cross section of the transmitting line and the cathode unit.

beginning of it. Traces of current pulses (Fig.5,a,b) from the vacuum probe corroborated such an explanation. The current pulse at the entrance into the line (Fig.5,a) consists of two parts. One part is determined by the operation of the cathode when a traveling voltage pulse is passing. The other part, which is a peak, arises from the increase in voltage due to the reflected pulse. At the end of the line the cathode begins to operate at high voltage amplitudes. The current pulse width here is less than the driver's pulse width. It is normal if we take into ac-

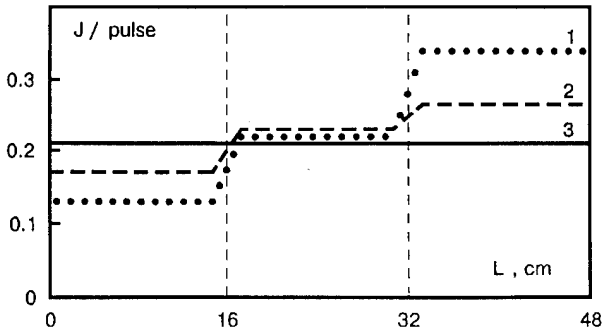


Fig. 4. Electron beam energy distribution along TWD axis.

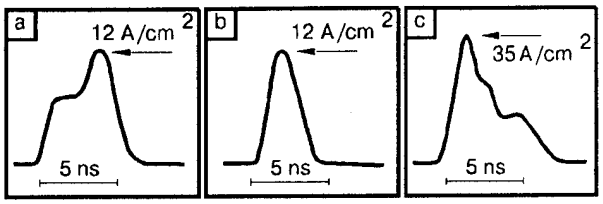


Fig.5. TWD current pulses measured by vacuum probe at different points (a,b). Current pulse of the "short" e-beam diode (c) [1].

count the finite rise and fall time of the accelerating pulse and also the rather high value of anode foil "cut-off" energy (about 110 keV for 60 μm aluminum-beryllium foil).

The current pulse traces (Fig.5,a;b) registered for the TWD differ from those obtained when operating with the "short" diode (Fig.5,c) [1,3]. Practically the entire short-diode cathode begins to operate at a voltage that can exceed the DFL charging voltage. In this case the electron energy and e-beam current have a maximum at the initial moment of time.

Special experiment has been devised to prove the principal influence of wave processes on TWD operation. An additional section with a 50-Ohm resistive load was installed at the end of the vacuum line, thereby permitting voltage pulse reflections to be removed. Here the e-beam energy value fell by more than a factor of 10 at the end of the TWD and by a factor of 4 at the TWD input in comparison with uniform energy distribution. Clearly, the traveling voltage pulse "operates" already at the beginning of the cathode, the voltage value being insufficient for the cathode to perform well at the end of the TWD.

Note some peculiarities which characterize our experiments. The experimental setup can operate continuously at a reprate of 10-25 pps. Short (up to 20 s) bursts at a 100 pps reprate were admissible. The electron beam was generated properly under a vacuum of 10^{-1}-10^{-2} Torr. The main parameters of the accelerator with the TWD are listed below:

AL-Be foil window thickness	60 μm
e-energy	200 keV
Peak e-beam current	1 kA
Current density on the foil	100 A/cm^2
Pulse width	3 ns
Beam cross-section	5x480 mm^2
Beam energy per pulse	0.7 J
PRF (prolonged mode)	10-25 pps
PRF (short burst, 20 s)	100 pps
Average beam power	7-70 W
Weight (RADAN 303B included)	34 kg

Conclusions

It has been shown experimentally that a compact RADAN 303B pulsed power 4-ns driver can be used to generate a 500-mm ribbon electron beam. The vacuum diode operation can be described by the wave processes that occur when a nanosecond accelerating voltage pulse is transmitted along the diode. Taking into account this wave character of accelerating pulse transfer, it is possible to ensure a uniform energy distribution of the ribbon electron beam extracted through the anode foil.

References.

[1]. V.G.Shpak, M.I.Yalandin, S.A.Shunailov, "Compact High-Current Ribbon e-beam Diode", in: *Proc. of XVI ISDEIV Int. Symp.*, Moscow-St.Pepersburg, 1994, pp.427-430.

[2]. G.A.Mesyats, "Physics of Electron Emission from Ferroelectric Cathodes", in: *Proc. of XVI ISDEIV Int. Symp.*, Moscow-St.Pepersburg, Russia, 1994, pp.419-422.

[3]. V.G.Shpak, M.I.Yalandin, S.A.Shunailov, "Compact high-current Accelerators Based on the RADAN SEF-303 Pulsed Power Source", *IEEE Proc. 9th Int.Pulsed Power Conf.*, Albuquerque, NM,1993.

FERROELECTRIC ELECTRON BEAM SOURCES

D. Flechtner, J. D. Ivers, G. S. Kerslick, J. A. Nation, and L. Schächter
Laboratory of Plasma Studies and School of Electrical Engineering
Cornell University, Ithaca, New York 14853

Abstract

Ferroelectric materials offer the possibility of compact electron sources, with modest requirements to initiate the emission process. We are studying such sources as possible injectors for microwave generation. The source consists of a polarized ferroelectric ceramic disk with silver electrodes coated on both faces. The front electrode consists of a periodic grid created by etching the silver to expose a line pattern of ceramic. This electrode functions as the cathode in a planar diode geometry with an accelerating gap adjustable from 0.1 to 5 cm. A rapid change in the polarization state of the ceramic is achieved by applying a 1-2 kV, 150 ns pulse between the electrodes of the ferroelectric. Early work used a coaxial cable to maintain an anode potential of up to 1 kV across the A-K gap. The emitted electron current was measured as a function of the gap spacing and the anode potential. The current varies linearly with the anode voltage, up to 1 kV, for gaps < 10 mm, and typically exceeds the Child-Langmuir current density by at least two orders of magnitude. Current densities in excess of 70 A/cm^2 have been measured. More recent work has used a 300 ns pulse forming network to apply a potential of up to 15 kV at the anode. Results of emittance and scaling measurements under these conditions are reported.

Ferroelectric materials offer the possibility of compact electron sources, with modest requirements to initiate the emission process. Recent experiments [1-3] have demonstrated that it is possible to extract high current density electron beams from ferroelectrics. The emitted beams may be useful in injectors for both low and high current accelerators and for microwave generation devices. Ferroelectric materials typically have a bound surface polarization charge density of $\geq$ 10 $\mu C/cm^2$. The electric field, arising from the remnant polarization charge of the polled ceramic, is of order of $\mathbf{P}/\epsilon_0 \sim 10^8$ V/cm, but is screened from the surroundings by free charge attracted to the surface of the ferroelectric. By using ferroelectrics with a gridded electrode electron emission occurs when the polarization state of the material is changed rapidly and the surface density of free charge, required to screen the polarization field from the region exterior to the ceramic, is changed. Switching the ferroelectric thus sets up a charge distribution in the gap that can allow a diode current to flow. In the absence of an applied voltage across the diode the emitted electrons reflex in the gap and, unless the gap is small, (comparable to the gridded structure periodicity) no net current flows. When a diode voltage is applied a fraction of the electrons cross the gap and a diode current is measured. The current flow and the cathode processes are closely connected and the description of the emission characteristics requires a coupling of the two regions [4]. In this paper we present experimental observations of the characteristics of a vacuum diode using a ferroelectric cathode.

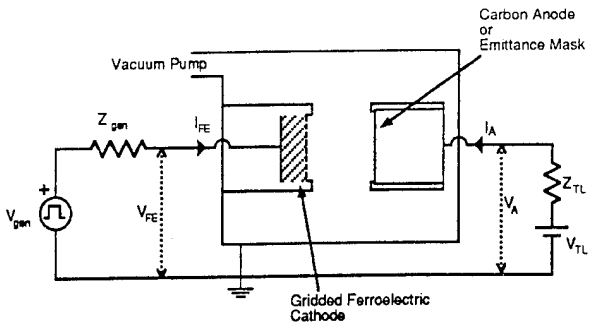


Fig. 1. Schematic showing the experimental arrangement of the ferroelectric cathode in a vacuum diode.

Fig. 1 shows a schematic diagram of the experimental arrangement. A 1 mm thick, 2.5 cm diameter ferroelectric LTZ-2 (Lead-Zirconium-Titanate) ceramic disk is mounted as the load on a 10 Ω transmission line. The line is switched by a krytron applying a 150 ns wide, $1-2$ kV pulse to the ferroelectric. The sample is oriented with the polarization vector pointing towards the diode gap. The ferroelectric is coated with thin silver electrodes on both surfaces. The front electrode serves as the cathode and consists of a periodic grid created by etching the silver in 200 μm wide strips to form a line pattern of exposed ceramic. The effective emission area is $\sim$ 1 cm^2. A graphite anode is used to form a planar diode geometry with an accelerating gap adjustable from 0.1 to 5.0 cm. For gaps $<$ 1.5 cm the anode is maintained at a positive potential with respect to the cathode by a charged transmission line. At larger gaps a 300 ns pulse forming network is used to apply a potential of up to 15 kV to the anode. The diode current (I_A) is measured as a function of gap spacing and anode potential (V_A). Recent measurements have also been made for pulsed anode operation with larger gaps ($\sim$ 5 cm), and anode voltages ($\sim$ 14 kV). The diode current is measured as a function of the delay time after the polarization switching pulse is applied. The emittance of the beam is measured by replacing the graphite anode by a mask, consisting of 150 μm wide slits, and scanning the beam image formed on electron recording film.

Fig. 2 shows traces of the voltage pulse applied to the ferroelectric (V_{FE}) and the current (I_{FE}) through the ferroelectric sample. Note that the current through the ferroelectric is of order 100 A and is always larger than the diode current. Both the current through and the voltage across the ferroelectric are independent of the diode operating conditions. However, the diode characteristics are strongly dependent on the state of the ferroelectric ceramic, and the diode current drops to zero if the ceramic is not pulsed.

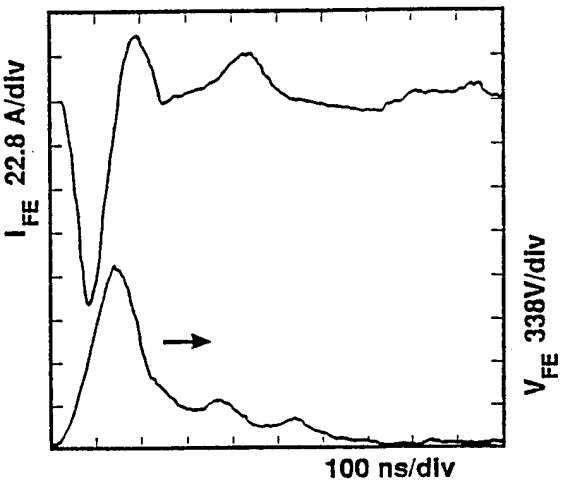


Fig. 2. Traces of the current (I_{FE}) through and the voltage cross the ferroelectric (V_{FE}). These traces are insensitive to the diode current and gap spacing. Note that the voltage pulse on the ferroelectric is 150 ns in duration.

Measurements of diode current for A-K gaps up to 1.0 cm indicate a linear scaling of current with gap voltage. For gap voltages of 300 V typical diode currents are $20 - 25$ A. Peak emission current densities of up to 70 A/cm^2 have been obtained experimentally.

For pulsed diode operation the anode potential was applied by a 300 ns, 20 Ω pulse forming line. Fig. 3 shows the applied diode voltage and diode current waveforms for a 5 cm gap and an applied potential of 14 kV. The delay of 1.2 μs refers to the time between the pulse applied to the ferroelectric and that applied to the anode. The emitted current pulse length is equal to that of the diode voltage pulse. Typical diode impedances in this configuration exceeds several hundred Ohms. The Child-Langmuir current density for these conditions is 155 mA/cm^2, compared to the 50 A/cm^2 measured.

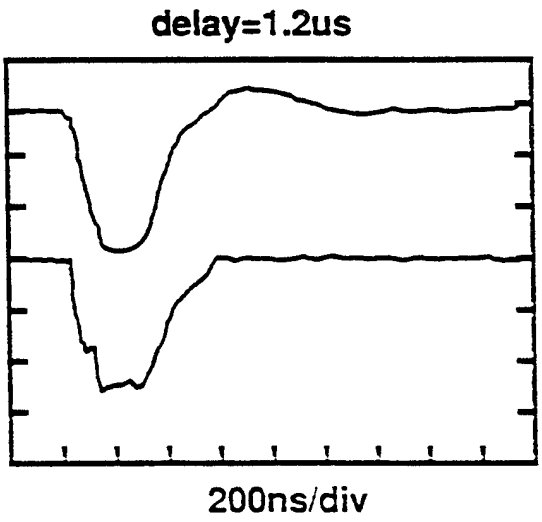


Fig. 3. Diode current (lower trace) measured for 5 cm gap with 14 kV anode voltage pulse (upper trace). The delay between V_{FE} and the applied anode pulse is 1.2 μs. Scales are 20 A/div for lower trace and 5.6 kV/div for upper trace, both at 200 ns/div.

The diode current has been measured for a range of delays up to 2.5 μs and the results are shown in Fig. 4. It should be noted that the measured diode current is independent of the polarity of the ferroelectric pulsing voltage (V_{FE}). These results, with a 5 cm diode gap, cannot be accounted for by diode plasma closure. But are consistent with a model [4] in which the gap impedance is controlled by the changing gap capacitance, which in turn is determined by the polarization state of the ferroelectric.

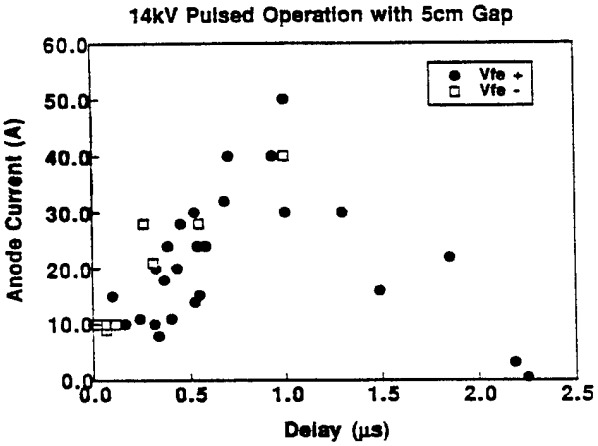


Fig. 4. Anode current as a function of the delay between V_{FE} and the applied anode pulse. Note current is independent of polarity of V_{FE}.

The emittance has been measured under pulsed conditions for 14 kV applied across the 5 cm gap. The emittance mask is a thick copper disk with 7 parallel 150 μm wide 1 cm long slits, with a 2 mm separation. The individual beamlets expand behind the plate at a rate set by the beam emittance and space charge effects. The expansion is recorded using radiochromic film, located 2 cm behind the mask. The film is subsequently scanned in a microdensitometer to obtain the expanded beamlet profiles shown in fig. 5. We fit the scanned

data to a Gaussian profile and from this determine the beam emittance and brightness. The normalized rms emittance, $\epsilon_{N_{rms}}$, is measured to be $12\pi\ mm - mrad$, for $I_A = 8.4\ A$, where

$$\epsilon_{rms} = (< x^2 >< x'^2 > - < xx' >^2)^{1/2}$$

and $\epsilon_{N_{rms}} = \beta\gamma\epsilon_{rms}$. We have calculated that the corrections for finite slit width and space charge effects should amount to no more than 5% of the measured value. The beam brightness is $B = 1.2\ 10^9 A/m^2\ rad^2$, where B is

$$B = \eta I_A/\pi^2 \epsilon_{N_{rms}} \epsilon_{N_{rms}}$$

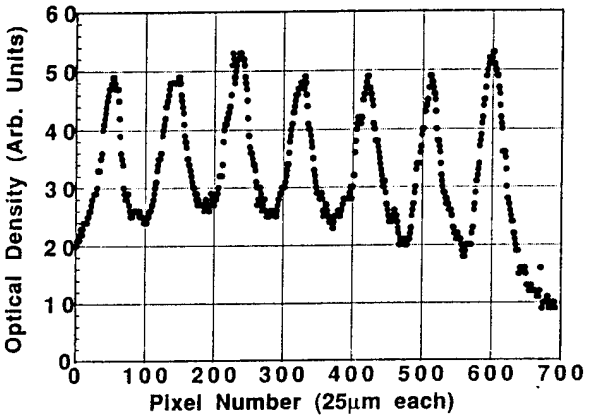


Fig. 5. Optical density profile of the 7 slit emittance mask recorded on radiochromic film and scanned with a microdensitometer.

We have shown experimentally that when a ferroelectric ceramic is used as the cathode of a vacuum diode we can extract current densities up to 70 A/cm^2. These levels can exceed, by up to two orders of magnitude, the Child-Langmuir limiting current. The dependence of the current on the voltage is approximately linear rather than $V^{3/2}$ and is limited, at present, by the impedance of the generator switching the ferroelectric disk. Observations demonstrate that the current flow does not result from a plasma fill of the diode as a result of the pulsing of the ferroelectric. The duration of the beam current can exceed that of the pulsing voltage on the ferroelectric (V_{FE}) and the current flow in the diode is controlled by changing the polarization of the ferroelectric. The normalized rms emittance of $12\pi\ mm - mrad$, with a beam current of 8.4 A is comparable to that from thermionic sources.

This work is supported by the US DOE.

References

[1] J. D. Ivers, L. Schächter, J. A. Nation, G. S. Kerslick and R. Advani, *J. App. Phys.*, **73**, 2667, (1993).

[2] H. Gundel, J. Handerek and H. Riege, *J Appl. Phys.*, **69**, 975 (1991).

[3] A. Sh. Airapetov, I. I. Ivanchik, A. N. Lebedev, I. V. Levshin and N. A. Tikhomirova, *Sov. Phys Dokl.*, **35**, 267 (1990).

[4] L. Schächter, J. D. Ivers, J. A. Nation and G. S. Kerslick, *J. App. Phys.*, **73**, 8097, (1993).

MODEL OF THE VACUUM DIODE WITH ADSORBATE ANODE OPERATION

V.Engelko**, C.Schultheiss*

*- Kernforschungszentrum Karlsruhe GmbH, Postfach 3640, D-76133 Karlsruhe, F.R.G.
**-Efremov Institute of Electrophisical Apparatus, 189631, St.Petersburg, Russia

Abstract

For experiments with divertor materials under ITER disruption conditions a proton beam with pulse duration longer than 10 - 20 μs and energy density attributed to the emitting surface of more than 20 mJ/cm^2 is needed. The most simple version of such a proton source is a vacuum diode, operating in a bipolar flow regime.The emitter of electrons is a plasma formed at the cathode due to an explosive emission. A plasma formed at the anode surface as a result of desorbtion and ionization of adsorbates by electrons is a source of ions. In order to understand the experimental results obtained in the test diode investigation and to predict real scale diode parameters model of the diode with adsorbate anode operation was developed. The results of calculations showed that such diode is able to produce ion beam with energy density attributed to the anode surface of more than 20 mJ/cm^2. The whole pulse duration of the ion beam can be large than 20 μs. But effective part of the pulse when power density exceeds needed level is around 10 μs. The model can be used also for analyzing of the vacuum breakdown effects in vacuum diodes operating in long pulse mode.

The aim of the paper is to analyze the possibility of using the vacuum diode with adsorbate anode for generation of the intense (1 kA) long pulse (more than 10 μs) proton beams for experiments with divertor materials under ITER disruption conditions. The experiments curried out with the test diode showed that there are two stages in the time dependence of the diode current. During the first stage the diode perveance increases up to 1.8-2 of the initial magnitude. The time interval needed for this increase up to the bipolar space charge limited value depends on the interelectrode gap, on the applied voltage, the vacuum conditions and material from which the anode working part is prepared. For example for graphite fabric anode this time is equal to 10 μs. The ion current appears at the beginning of the voltage pulse. During the greater part of the firs stage the magnitude of the ion current is rather small. Only at the end of this stage the ion current achieves the space charge limited level. At the beginning of the second stage the ion current increases slowly, but at the end of this stage it increases fastly. In order to understand the experimental results obtained in the small test diode and to predict the real scale diode parameters a model of the diode with adsorbate anode operation was developed. Two stages of the diode operation in bipolar mode are identified: 1)- with saturative ion flow; 2)- with space charge limited ion flow. During the first stage the ion current density increases up to the space charge limited value. At the end of this stage the electric field at the anode surface turns to zero. This is the condition for an anode plasma to appear. The time dependence of the ion current density at the second stage is determined by the anode plasma expansion and the time behavior of the applied voltage.

Diode operation with saturative ion flow. At both stages of the diode operation the ions are produced due to desorption and ionization of the adsorbates at the anode surface. The intensity of production of the ions is determined by the expression

$$\frac{dN_i}{dt} = \frac{j_e \sigma n_o v_o t}{e} \qquad (1)$$

where j_e -the electron current density, n_o - the density of the desorbed gas, σ - the cross-section of neutrals ionization, v_0 -velocity of neutrals, e - the electron charge.

At the first stage of the diode operation there is an electric field at the anode which removes ions from the anode surface immediately after their appearance. Therefore the ion current density j_i can be written as

$$j_i = e\frac{dN_i}{dt} = \frac{\sigma a}{e} j_e^2 t \qquad (2)$$

where a -is the amount of desorptions per electron. The appearance of the ions in the diode leads to an increase of the electron current density because of the increase of the electric field near the emissive surface of the cathode. This electron current density increase can be described by the following relation

$$j_e = f(\frac{j_i}{j_{ie}}) j_{eo} \qquad (3)$$

where j_{eo} is the electron current density without ions, $j_{ie} = 1.86 j_e \sqrt{m/M}$ is the space charge limited ion current density in bipolar mode of the diode operation, m and M are electron and ion masses. For analytical modeling f(x) can be approximated by the expression

$$f(x) = 1 + 0.86x^2 \qquad (4)$$

From (2)-(4) one can obtain for j_e

$$j_e = \left[1 + 0.86\left(\sigma a j_e^2 t / 1.86 e\sqrt{m/M}\right)^2\right] j_{eo} \qquad (5)$$

Thus, the electron and ion densities increase with time.In the time moment t_1 where the ion current density achieves the limit value $j_{ie}$the electric field at the anode turns into zero. This is the end of the first stage . The duration of the first stage can be determined from the equation

$$j_i(t_1) = \frac{\sigma a}{e}(1.86 j_{eo})^2 t_1 = 1.86 j_{eo}\sqrt{m/M} \qquad (6)$$

From (6) we obtain

$$t_1 = \frac{e}{1.86\sigma a}\sqrt{m/M} \qquad (7)$$

On the other hand t_1 can be determined from the treatment of the current and voltage oscillograms. Thus, it is possible to determine the magnitude of σa needed for the calculation of the ion beam parameters.

Diode operation with space charge limited ion flow. The dependence the ion and electron currents on time after formation of the anode plasma is determined by its expansion. As before the intensity of the ions generation at the anode is determined by the expression (1). For providing the bipolar ion current density the following intensity of the ions production is needed

$$\frac{dN_i}{dt} = \frac{j_e}{e}\sqrt{m/M} \qquad (8)$$

Therefore the intensity of the anode plasma generation is given according to

$$\frac{dN_{ap}}{dt} = \frac{j_e}{e}\left(\sigma n_o v_o t - \sqrt{m/M}\right) \qquad (9)$$

Taking into account the movement of the anode plasma boundary into the vacuum gap we can write for the anode plasma density

$$n_{ap} = \frac{\int_0^t j_e\left(\sigma n_o v_o t - \sqrt{m/M}\right)dt}{e\int_0^t v dt} \qquad (10)$$

or taking into account (7)

$$n_{ap} = \frac{1}{e}\sqrt{m/M}\,\frac{\int_0^t j_e\left(\frac{j_e t}{1.86 j_{eo} t_1} - 1\right)dt}{\int_0^t v dt} \qquad (11)$$

The plasma at the adsorbate anode is created with zero electric field at the anode surface. Therefore $j_{ap} = j_{CL}$ where j_{ap} is the ion current density provided by the anode plasma, j_{CL} is the Child-Langmuir current density

$$j_{ap} = 0.4 e n_{ap}\sqrt{kT_e/M} \qquad (12)$$

$$j_{CL} = \frac{1.86}{9\pi}\sqrt{2e/M}\,\frac{U^{3/2}}{\left(d - \int_0^t v dt\right)^2} \qquad (13)$$

k - is the Boltzmann constant, d is the interelectrode gap, U is the diode voltage, v is the anode plasma expansion velocity. Taking into account (11) the following relation for the electron and ion current densities at the

second stage of the diode peration are obtained

$$j_e = \frac{1.86\sqrt{2e/m}\,U^{3/2}}{9\pi\left(d - 0.4\sqrt{kT_e/M}\,\frac{\int_0^t j_e\left(\frac{j_e t}{1.86 j_{eo} t_1} - 1\right)dt}{j_e}\right)^2}$$

$$j_i = j_e\sqrt{m/M} \qquad (14), (15)$$

For taking into account the time dependence of the diode voltage the Kirchoff equations have to be applied.

Results of calculations. For calculating the ion beam parameters the magnitude of σa must be known. As this value depends on the real experimental conditions experimental data have to be used for its determination.

For obtaining σa only one oscillogramm of the diode voltage and current is needed. From this oscillogramm the dependence of the diode perveance on time can be calculated and from this dependence t_1 and σa can be determined. For a graphite fabric as an anode, with residual gas pressure $\propto 10^{-6} torr$ after heating and conditioning of the anode surface by some shots a value of $1.6\ 10^{-16} cm^2$ was obtained for σa.

In Fig.1 the calculated time dependence of the ion current is presented for the capacitive generator discharging through the diode. In Fig.2 the experimental oscillograms are given. The calculated and measured magnitudes of the duration of both stages of the diode operation and of the ion current at the end of the first stage are in good agreement. The ion current at the end of the pulse is less than calculated one. But if the vacuum chamber is filled with hydrogen of pressure (1-2) 10^{-4} torr for some minutes then the ion current at the end of the pulse increases up to the calculated value (60A).

In Fig.3 the calculated dependence of the duration t_1 of the first stage on the initial value of the electron current is shown. In Fig.4 the calculated curves of the dependence of the whole pulse duration on the diode voltage and experimental data are presented. In both cases there is agreement between calculated and measured magnitudes. Thus, one can conclude that the model developed is adequate for describing the real diode behavior and therefore can be used for calculations of the ion beam parameters in a real scale facility.

As main specific parameters of the ion diode the ion beam energy density W_a and the power density P_a are considered. For disruption simulation W_a and P_a must be at least 20 mJ/cm^2 and 1 kW/cm^2 accordingly. The results of calculations showed that the required W_a level can be obtained with a diode voltage exceeding 30 kV and with an electrode gap exceeding 3 cm. In the range of $d > 3$ cm W_a practically does not depend on d. It also does not depend on the high voltage generator capacity when it is large than 10^{-2}S μF with S - the area of the anode in cm^2. In Fig.5,6 the dependencies of W_a and P_a on the intensity of the ions generation at the anode surface (it is connected with t_1 through (7)) is shown. One can see that the whole pulse duration of the ion beam can be large than 20 μs (up to 50 μs). But the pulse duration for $P_a >$ 1 kW/cm^2 is only around 10 μs. A decrease of σa (intensity of ions production) by a factor of 2 leads to an increase of W_a by a factor of 1.4.

Thus, the results of calculations show that the ion diode with adsorbate anode is able to produce the ion current with needed for disruption simulation energy density but with pulse duration only around 10 μs. Note that the model developed can be used

for the analyzes of the vacuum breakdown effects in the vacuum diode operating in the long pulse mode.

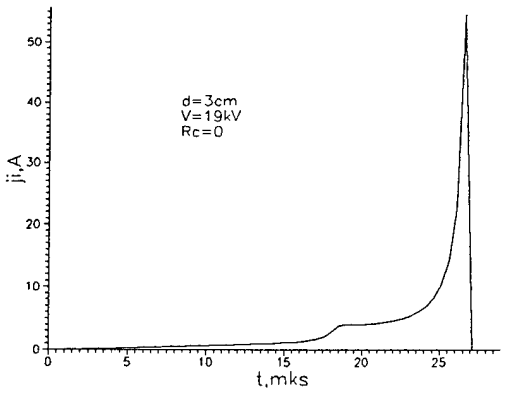


Fig.1 Calculated ion current dependence on time.

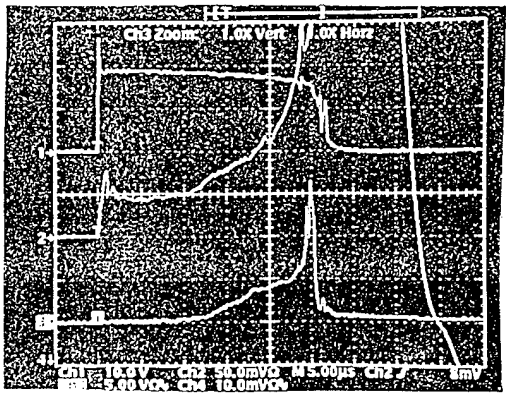


Fig.2 Oscillogramms of: 1-diode voltage (10 kV/div); 2- diode current (100A/div); 3- ion current (5A/div)

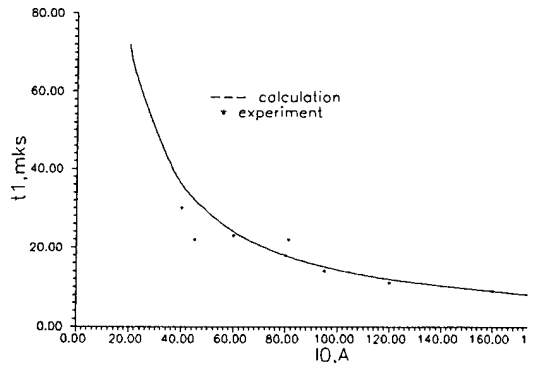


Fig.3 Dependence of t_i on the initial value of the electron current

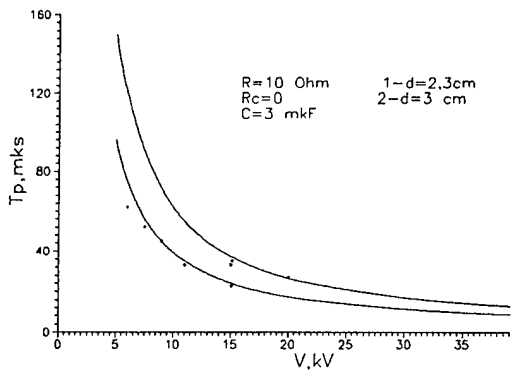
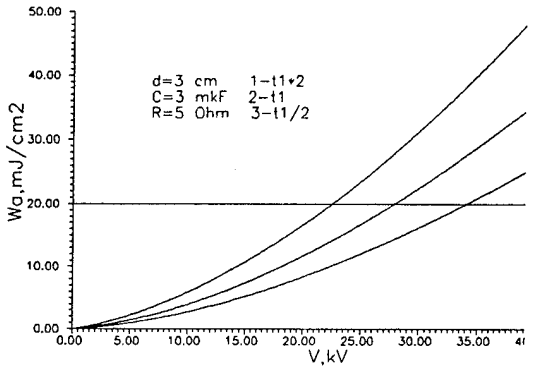


Fig.4 Dependence of pulse duration on diode voltage



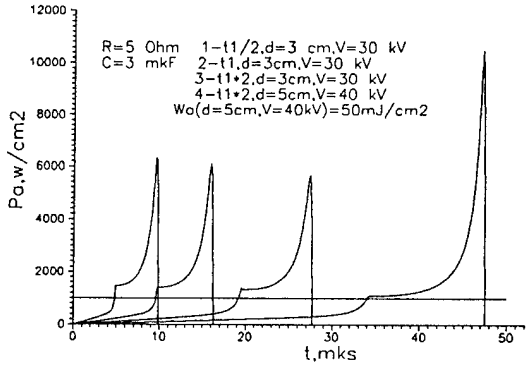


Fig. 6.7 Dependence of Wa and Pa on intencity of ions production

A LARGE-AREA X-RAY DIODE FOR THE SNOP ACCELERATOR

S.P. Bugaev, I.A. Buryak, A.V. Luchinsky, V.K. Petin, N.A. Ratakhin,
N.A. Smirnov, and V.F. Fedushchak
Institute of High Current Electronics
Russian Academy of Sciences, Siberian Division
4 Akademichesky Ave., Tomsk 634055, Russia

Abstract

An investigation of the possibility to form nanosecond electron beams has been performed on the SNOP-1 and SNOP-2 generators with the goal to create X-ray sources for testing objects of area 5 to 3000 cm^2. The experiments were carried out at voltages 0.4 to 1 MV, currents 200 to 600 A, and beam energies 10 to 20 kJ. Diodes with pinching, annular, and sheet beams were tested. It has been demonstrated that the accelerators can be smoothly tuned for irradiation of objects of area 5 to 3000 cm^2 with a rather good energy matching between the accelerator and the diode.

The present-day installations for radiation testing of objects within the spectrum $\hbar\nu$ = 20 to 100 keV that provide the highest doses and the largest irradiated areas are extremely intricate and too costly [1, 2].

In testing equipment parts, most frequent are objects of area 1 to 10^3 cm^2 which call for radiators, optimized in cost and efficiency, that would offer high enough uniformity of the radiation produced and the possibility of tuning by dose.

Superhard X-ray sources can be based on subcritical current diodes, pinch diodes, or diodes with annular beams stabilized by magnetic field of the forward and return current-carrying wires, as the case requires.

These options for the creation of superhard X-ray sources with varied energy density and irradiated area were investigated on the installations SNOP-1 ($V \le 650$ kV, $I \le 300$ kA, $\tau_{0.5} \approx 70$ ns) and SNOP-3 ($V \le 550$ kV, $I \le 850$ kA, $\tau_{0.5} \approx 65$ ns).

Diodes with a pinching electron beam would be appropriate for the production of high-energy-density radiation fluxes at small objects. In doing this, it has no sense to strive to realize a mode with the highest achievable at the anode current density ~ 10^8 A/cm^2. Since, owing to the need of protecting the object from electrons (using light and radiation-transparent material of thickness ~ 1 cm) and powerful impact actions, the object cannot be placed less than 1.5 to 2 cm from the converter, a radiation source with a characteristic size of ~ 1 cm is quite suitable to resolve this problem.

The optimum mode of diode operation is that with the electron current density and the energy density at the anode 100 to 200 kA/cm^2 and 3 to 7 kJ/cm^2,

respectively; the pulse duration therewith should be some tens of nanoseconds.

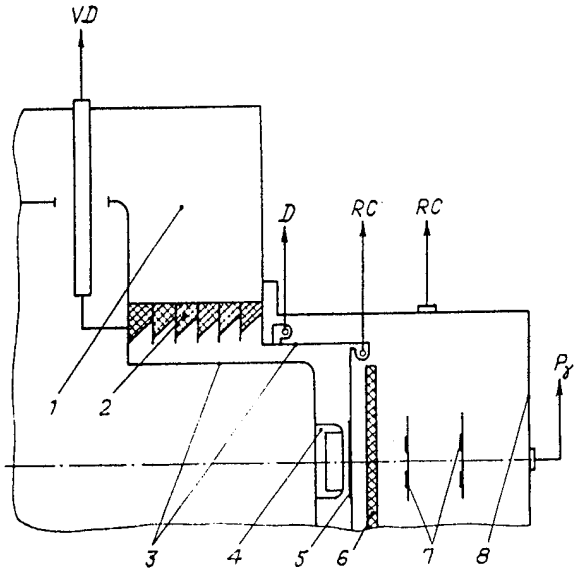


Fig. 1. Schematic of the output unit of the SNOP-1 installation. *1* - water transmission line, *2* - section insulator, *3* - current-carrying wires of a magnetically insulated water line, *4* - cathode, *5* - foil anode, *6* - absorber, *7* - TLD, *8* - photon radiation power gage, *9* - current pickup, *10* - d*I*/d*t* gage, *11* - voltage pickup.

The experiments with a pinch diode on the SNOP-1 installation (Fig. 1.) used stainless-steel cathodes with a sharp edge diameter of 30 to 100 mm. Used as an anode were copper and tantalum foils of thickness 10 to 140 μm. The A-K gap spacing, $d_{A\text{-}K}$, was 2 to 7 mm. The experiments were carried out with a diode voltage of 0.4 to 1 MV and an electron beam energy and power reaching 10 kJ and 0.18 TW, respectively. Typical waveforms of voltage V, diode current I, electron beam power P_e, and photon radiation power P_γ are given in Fig. 2. As a result, a reproducible matched mode of diode

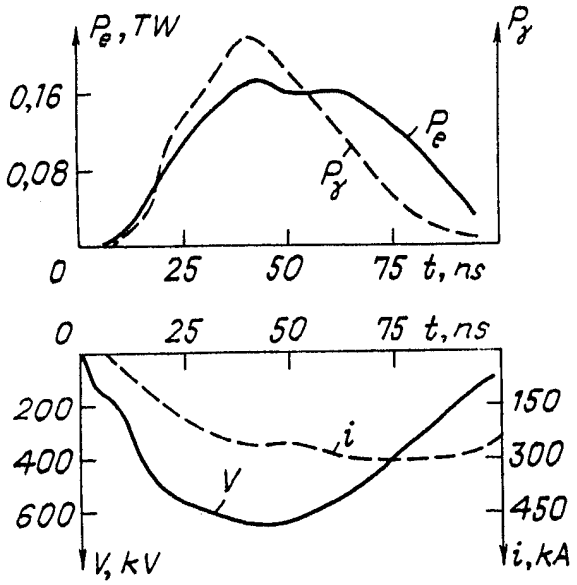


Fig. 2. Typical waveforms of voltage V, diode current I, electron beam power P_e, and photon radiation power P_γ.

operation with the current $I \leq 300$ kA, the voltage $V \leq 650$ kV, and the beam diameter at the anode ~ 1 cm was realized. This mode ensured a maximum radiation dose within a range of 20 to 100 keV. To optimize the radiation yield by the thickness of the foil target, a series of tests with an optimized pinch diode was carried out on the SNOP-1 installation. The experiment used a stainless-steel cathode with a sharp edge diameter of 50 mm and copper foil of thickness 20 to 140 μm as a target; the A-K gap spacing was 2.7 mm. Figure 3 shows the total radiation dose at a distance of 8 cm from a copper target as a function of the target thickness. The measurements were performed by LiF thermoluminescent dosemeters (TLDs) capable of indicating photons with $\hbar\nu > 10$ keV. Simultaneous measurements of the total radiation dose by IS-7-glass TLDs (capable of indicating photons with $\hbar\nu >$ 45 keV) have shown that the dose depends only slightly on the target thickness within the thickness range investigated. This

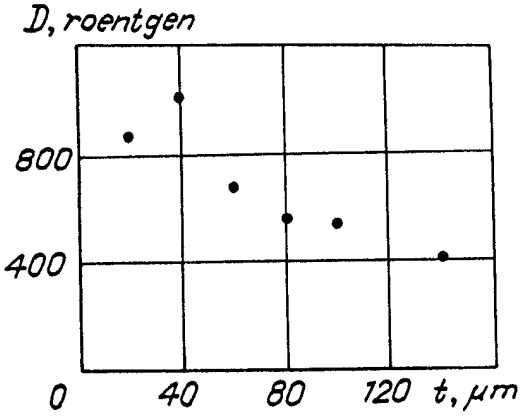


Fig. 3. Total radiation dose at a distance of 8 cm from a copper target as a function of the target thickness.

suggests that the run of the curve in Fig. 3 is due to the escape of photons with 10 keV < $\hbar\nu$ < 45 keV. Using a Ta foil target instead of a Cu foil target allowed a 1.7-2-fold increase in total radiation dose.

Analysis of the dose measurements for various distances from the target allows the conclusion that in the pinch diode experiments, the total dose D depends on the distance R from the target as $D \propto R^{-2}$ for $R > 3$ cm and D decreases by a factor of 3 to 3.4, as R is increased from 2 to 4 cm.

The radiation source based on the SNOP-1 pinch diode is capable of irradiating objects of area several square centimeters with the total radiation dose, measured by an IS-7-glass TLD, 10 to 12 krad and the radiation power 2×10^{11} rad/s.

The radiation source based on the SNOP-3 pinch diode ($V_d \sim 800$ kV, $I_e \sim 360$ kA, $w_e \sim 13$ kJ, $P_e \sim 0.3$ TW) allows irradiation of objects of area 10 to 20 cm^2 with the total radiation dose, measured by an IS-7-glass TLD, about 12 krad and the radiation power 3×10^{11} rad/s.

To irradiate large-area objects, a pinch-diode-based radiation source can be used. In this case, the current can be found from the formula [3]

$$I = 8.5\gamma^n \frac{r}{d_{A\text{-}K}} \ln(\gamma + \sqrt{\gamma^2 - 1});$$
$$n = 0.5 \div 1;$$

the beam diameter at the anode therewith is a factor of about less than the cathode radius r. By varying the distance from the radiation source to the object and r as a function of the object size and the required degree of uniformity of the radiation field, one may realize the needed radiation field parameters. However, the use of a pinch diode for irradiation of large-area objects (10^3 to 10^4 cm^2) would call for diodes with a disproportionately large cathode diameter (several meters) and would hardly ensure the needed uniformity and stability of the radiation field.

To investigate the feasibility of a source capable of irradiating large-area objects, an experiment was performed on the SNOP-1 accelerator where an annular electron beam ($V \sim 600$ kV, $I_e \sim 250$ kA, $w_e \sim 8$ kJ, average beam diameter ≈ 80 mm) was produced by the technique described in Ref. 1. The essence of this technique is that a voltage is applied to the cathode through current-carrying folds passed through holes in the anode plane, and the beam is stabilized by the magnetic fields of the currents in the return current-carrying wires inside and outside the annular beam.

To investigate the feasibility of a large-area radiation source producing a moderate radiation power uniformly distributed in area behind the target, an experiment was performed on the SNOP-3 installation with a plane electron diode carrying a nearly-critical current ($I_{cr} = 8.5\beta\gamma r/d_{A\text{-}K}$). The electron diode ($V_d \sim 670$ kV, $I_e \sim 600$ kA, $\tau_{0.5} \sim 50$ ns) is

formed by a plane duralumine cathode of diameter 650 mm with velvet pasted on it that covers the cathode surface completely or partially in the form of 30-mm concentric rings spaced 30 mm apart, and a plane anode with the electrode separation 14 to 18 mm. In this experiment, some "sweep-off" of the beam electrons was observed. This makes possible to realize a radiation source of area about 3000 cm^2 with the maximum-to-minimum dose ratio equal to 3:1. Thus, partial pinching of the beam in the diode with an annular cathode allows improved exposure in sources designed for irradiation of large-area objects.

References

1. K. Ware, N. Lotel, et al. Bremsstrahlung Source Development on Black Jack-5. Proc. 5th IEEE Pulsed Power Conf., Arlington, 1985, pp. 118-121.
2. Sandia National Laboratories Radiation Facilities. Broshure prepared by G. A. Zawadskas et al. July 1987, p. 29.
3. V. P. Smirnov, Production of intense electron beams. - Prib. Tekh. Eksper., No 2, pp. 7-31, 1977.

A TWO-BEAM VIRTUAL CATHODE DEVICE

William Peter and Ya. E. Krasik
Department of Physics
Weizmann Institute of Science
Rehovot, ISRAEL

Abstract

Two concepts using counterstreaming high-space-charge relativistic electron beams are described. In one concept, two counterstreaming electron beams are injected into a drift beam. Depending on their current and energy, either zero, one, or two virtual cathodes are formed. In some cases (when the current of each beam is half the space charge limit current I_L), the two beams take turns 'forming a virtual cathode. Applications to high-power microwave generation and collective ion acceleration are indicated.

We report on a continuing investigation of the application of counterstreaming relativistic electron beams to high-power microwave generation and collective ion acceleration. Of primary interests are (1) the possibility of controlling the motion of a virtual cathode for ion acceleration, (2) creating multiple and coherent virtual cathodes for the purpose of high-power microwave generation, and (3) investigating the dynamics of virtual cathodes.

To illustrate, consider a relativistic electron beam of radius r_b injected from the left-hand side into a uniform dirft tube of radius R. Let the current of this beam be I_1, and the normalized velocity be β. If I_1 is larger than the space-charge-limit current I_L described by $I_L = (\gamma^{2/3}-1)^{3/2}(mc^3/e)/[1+2\ ln\ (R/r_b)]$ a virtual cathode will form. This assumes the ends of the drift tube are sufficiently far apart to approximate an infinitely long drift tube. If L is the distance between the ends of the drift tube, this is equivalent to requiring the condition $L > 2.589(R/r_b)^{0.133}$[3].

Consider the beam in the same drift tube with $I_1 < I_L$, and now inject an oppositely-directed beam from the other side of the drift tube with a current I_2. If $I_1 + I_2 > I_L$, what will happen? *Will both beams form virtual cathodes even though the current in each individual beam is less than the space-charge-limited value?*

Our ideas are analyzed with the help of particle-in-cell simulations done with OOPIC [1, 2], an object-oriented, 2-1/2 dimensional, fully electromagnetic and relativistic particle-in-cell code. OOPIC has a suite of state-of-the-art visualization tools which are especially helpful in analyzing the the results of the simulation. Our preliminary

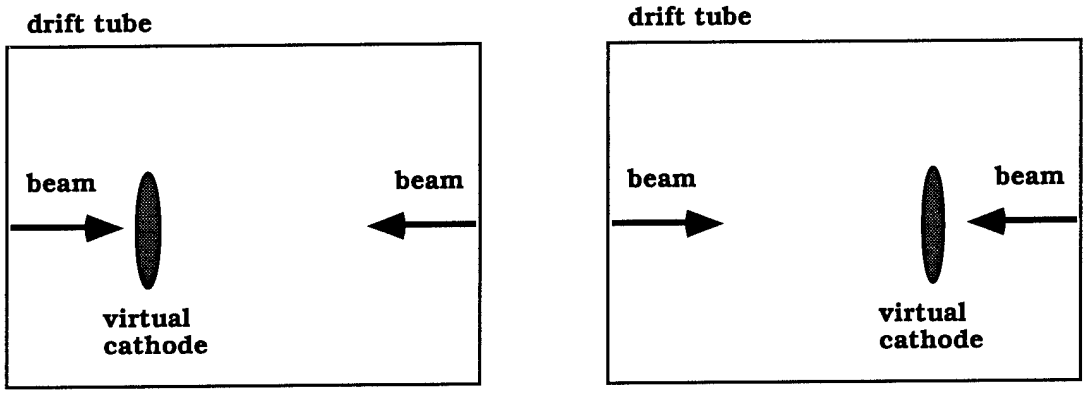


Fig. 2. Cartoon showing the "bouncing" virtual cathode phenomenon. Two counterstreaming beams with a current $I = (1/2)\ I_L$ are injected into a drift tube. There is no steady-state, but an oscillatory state in which (1) the beams both form two virtual cathodes, and (2) each beam takes turns forming a virtual cathode (shown above).

simulations suggest the following: In the case where the combined current of the two beams together (i.e., the sum of $I_1 + I_2$) is less than I_L no virtual cathode forms. In the case when each beam has a current greater than the limit current ($I_1 > I_L,\ I_2 > I_L$), two steady-state virtual cathodes form. In the intermediate case $I_L < I_1 + I_2 < 2I_L$ there is no steady state, but rather an oscillatory state where the beams alternately form a virtual cathode at the same time and "take turns" forming a virtual cathode. This state is currently being investigated since it may have an unusually good power efficiency.

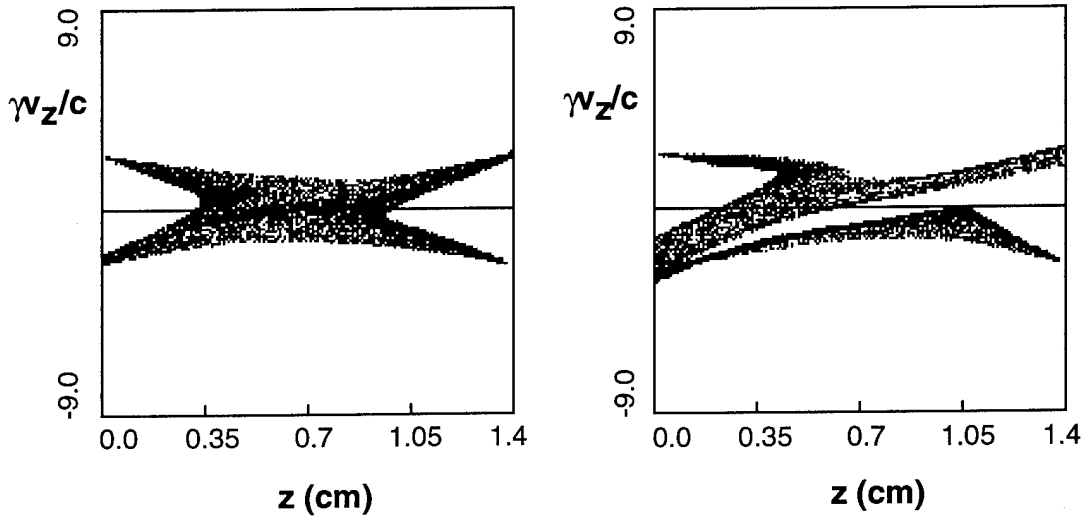


Fig. 3. Phase space plots (v_Z vs. z) from a 2-1/2 dimensional particle-in-cell simulation for two beams ($I_1 + I_2 > I_L$) at times t=0.9 ns (left) and t=4.5 ns (right). In the first figure, both beams form a virtual cathode. A little later (the second figure) the virtual cathode on the right-hand side "disassembles". The configuration oscillates (as discussed in the text).

Note that the $I_L < I_1 + I_2 < 2I_L$ case is somewhat similar to the experiment at the General Physics Institute in Moscow [4]. As shown in Fig. 4, this experimental configuration relies on only one injected electron beam ($I \sim 10$ kA) which is injected into a drift-tube discontinuity. There is a strong magnetic field of 25 kG, and the beam energy is typically 430 keV. The drift tube radii are adjusted so that the beam does not form a virtual cathode in the first tube, but forms a virtual cathode in the second tube. That is, if the limit current in the small-radius drift tube is I_{1L} and the limit current in the large-radius drift tube is I_{2L}, then the beam current satisfies $I_{2L} < I < I_{1L}$ and $I > (I_{1L} + I_{2L})/2$. When the beam reaches the large-radius tube it forms a virtual cathode. As the beam is reflected, additional space charge is now present in the drift tube such that a virtual cathode can now exist. In the work at the General Physics Institute, the space-charge barrier reflecting the particles starts to move toward the injection region, leaving a high-density, low-velocity plasma behind [5]. This high-density, low-velocity plasma exists because of the balance of momentum flux "pressures". It is a surprisingly stable configuration, and has been labeled by the Moscow group the "squeezed-beam" state [4,5].

Experiments using a drift-tube discontinuity have also been performed at U.C. Irvine [6,7]. In the Irvine experiments, the beam entering the large drift tube was observed to hit the drift tube wall in the vicinity of the discontinuity. This result is in agreement with our simulations. Note that the two-beam virtual cathode device described above may also allow a squeezed-beam state to form, in which case it would be more "experimentally friendly", since there would be no radial discontinuity to perturb the beam.

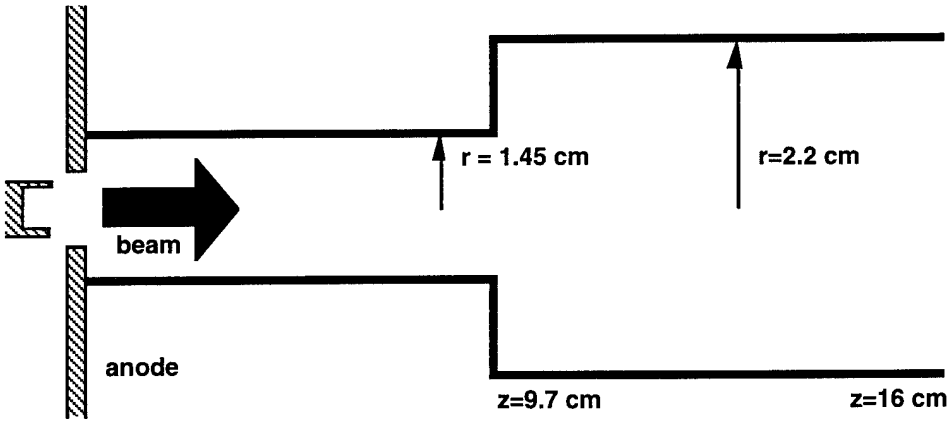


Fig. 4. Schematic drawing of the experiment at the General Physics Institute in Moscow (similar to an earlier experiment at UC Irvine). An annular REB is injected into a drift tube with a radial discontinuity.

References.

[1] OOPIC is a joint project of U.C. Berkeley, FM Technologies, George Mason University, Univ. of Tennessee at Knoxville, Knoxville College, and Berkeley Research Associates. It is funded by the U.S. Air Force Office of Scientific Research.

[2] J. P. Verboncoeur, A. B. Langdon, and C.K. Birdsall, Bull. Am. Phys. Soc.,

[3] R. B. Miller, Air Force Weapons Laboratory Technical Report AFWL-DYS-TN-75-113, 1975, and R. B. Miller and D.C. Straw, J. Appl. Phys. **47**, 1897 (1976).

[4] A. M. Ignatov and V. P. Tarakanov, Phys. Plasmas **1**, 741 (1994).

[5] A. V. Fedotov, private communication.

[6] F. Mako, Ph.D. dissertation, Univ. of California, Irvine, 1979 (unpublished).

[7] A. Fisher, private communication.

NUMERICAL STUDY OF RELATIVISTIC ELECTRON BEAM PUMPING BY VIRTUAL CATHODE

I.G. Yovchev
Dept. of Physics, High Institute of Chemical Technology
8, K. Ohridsky Blvd., Sofia 1156, Bulgaria

K.G. Kostov and N.A. Nikolov
Department of General Physics, Sofia University
5, J. Bourchier Blvd., Sofia 1126, Bulgaria

In this article a new method for electron beam pumping by means of virtual cathode is proposed. The electron beam is generated in a foilless diode, whose anode tube is connected directly to a wider output drift tube. The emitted by cold plasma emission from hollow cathode electrons propagate in an external homogeneous magnetic field. The virtual cathode is formed at the wide drift tube entrance. Computer simulations show an essential beam pumping behind the virtual cathode. The transmitted electron beam pitch-ratio α reaches value above 1 which is sufficient for development of the maser instability.

Among the most promising high-power microwave devices are those that use a virtual cathode. It is formed when an electron beam current injected into an evacuated drift tube exceeds the space-charge limiting current. Two basic geometries - foil and foilless diode could be used for virtual cathode operation. For low frequency operation, virtual cathode devices (vircators) use foil diode, whose anode is a high transparency mesh or a thin foil [1]. The foilless diode configuration in conjunction with an axial guide magnetic field is exploited at high frequency vircators [2].

Experiments [3,4] and computer simulations [3,5] report only transverse magnetic (TM) modes generation. Two sources of microwave emission exist in the axial vircator: virtual cathode oscillations and bunched reflected electrons. First of them excites E_z and E_r fields, while the second - E_z and $H\varphi$ fields (in cylindrical coordinates). Both pairs of fields couple into the TM_{on} waveguide modes [3]. However some previous experiments demonstrate an excitation of transverse electric (TE) modes by an axially extracted foilless diode vircator [6]. The absence of TM modes in these experiments leads us to conclusion that the above mentioned radiation mechanisms are not realized. Another microwave generation mechanism - maser instability could be reason for TE modes excitation. For its development however, a significant beam pumping is needed [7]. The pumping process'

characteristic quantity is the pitch-ratio $\alpha=v_\perp/v_z$ ($v_\perp$-electron transverse velocity component, v_z-electron longitudinal velocity component).

Computer simulations performed in [5] show that the high-density space charge cloud at the virtual cathode imparts transverse momentum to the reflected electrons. We suppose that the oscillating virtual cathode is also able to impart an additional transverse momentum to the transmitted electrons.

The beam current transmitted through the virtual cathode is approximately equal to the space-charge limiting current. Hence the electrons, propagating after virtual cathode region are subjected to strong space charge depression, which leads to an essential decrease of their longitudinal velocity v_z.

Both the transverse velocity increasing and axial velocity decreasing result in an essential beam pumping. The aim of this article is the numerical investigation of the electron beam pumping by virtual cathode.

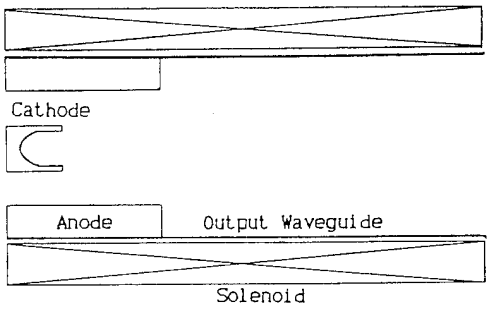


Fig.1 Schematic diagram of the foilless diode vircator

An outline of the modeled system is shown in Fig. 1. The numerically studied configuration is 36 mm diameter, 50 mm length anode tube foilless diode. The electrons are generated by cold plasma emission from a 15-mm-diameter hollow graphite cathode and they propagate into an external homogeneous magnetic field B_z= 4.5 kG. The formed hollow electron beam is injected into a wide output 56-mm-diameter drift tube. The diode voltage is 350 kV. Both the anode and drift tubes are grounded. The modeled system parameters are as close as possible to the real system parameters.

We use a relativistic, particle-in-cell, $2\frac{1}{2}$ dimensional computer code, developed in [8] to simulate the virtual cathode behavior and to calculate the beam pitch-ratio downstream the virtual cathode.

The diode current injected into the output drift tube is 1.8 kA. The virtual cathode forms at t = 1.420 ns and reflects some of the beam electrons back to the diode region. The mean value of the current propagating behind the virtual cathode region is approximately 1.35 kA. The potential minimum begins to oscillate in space and time (see Fig. 2). The period of the oscillations T is evaluated to about 108.7 ps, which corresponds to the oscillation frequency of 9.2 GHz.

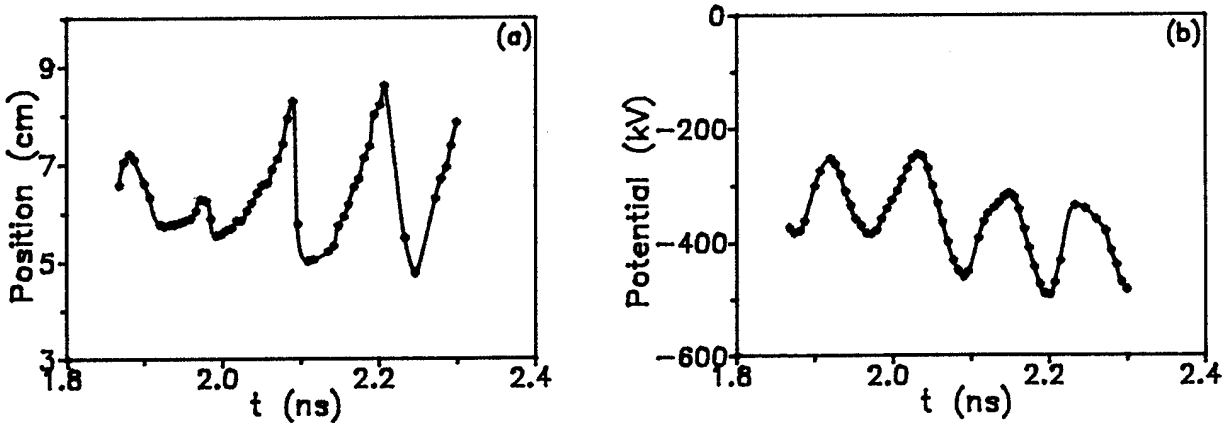


Fig. 2. The time histories of (a) the virtual cathode position and (b) the magnitude of the virtual cathode potential

In Fig. 3 the potential versus the axial coordinate z at r = 5.6 mm for moment of time t= 2.181 ns is shown.

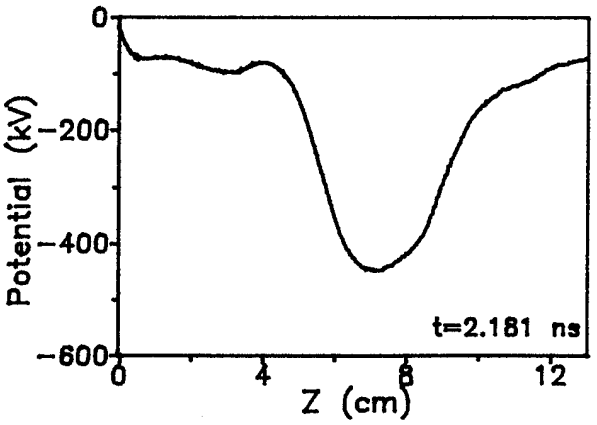


Fig. 3. Potential distribution in the vircator

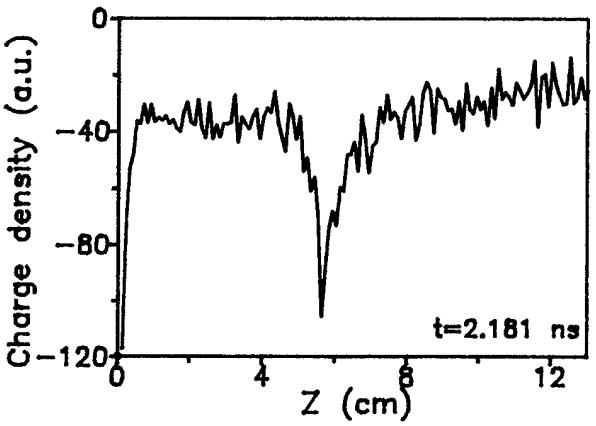


Fig. 4. Distribution of charge density in the vircator

Fig. 4 shows the charge density as a function of axial distance at the same moment of time, given in Fig. 3. Such potential and charge density dependencies are in agreement with previous computer simulations [9].

The values of α are averaged over the time interval from t=1.420 ns, when the virtual cathode is formed to t=2.280 ns. It is well seen from Fig. 5 that α reaches values over 1 behind the virtual cathode region. This is almost twice larger than the values of α in the anode tube. Before the virtual cathode formation the pitch-ratio does not exceed 0.3. So we can conclude that the virtual cathode for presented vircator parameters causes considerable beam pumping. In Fig. 5, the values of α for the virtual cathode region are not given because there the average electron longitudinal velocity v_z is small, which leads to the very large pitch-ratio α values.

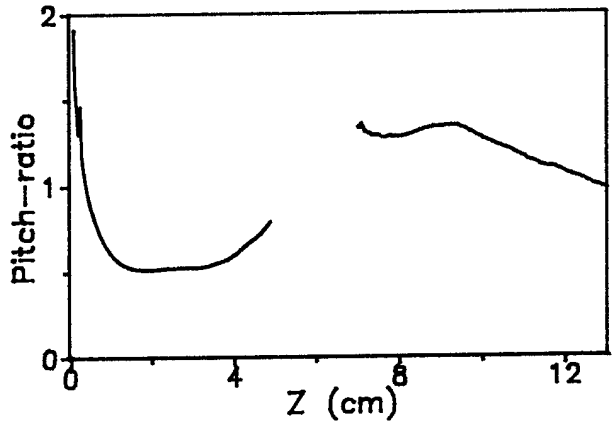


Fig. 5. Pitch-ratio as a function of axial coordinate

As a summary we have numerically investigated foilless diode virtual cathode oscillator. The injected electron beam current is a little above the space-charge limited current for the output drift tube and a virtual cathode is formed at the drift tube entrance. It oscillates in space and time with characteristic frequency of 9.2 GHz. With the presence of a moderate guide magnetic field of 4.5 kG the pitch-ratio α behind the virtual cathode reaches values over 1. These values are enough for maser instability development in particular for gyrotron operation.

Acknowledgments: This work was supported by Bulgarian Ministry of Science and Education under contract No F-75. The authors wish to thank Dr. Bernhard Schmidt for his financial support.

REFERENCES

[1] D. J. Sullivan, J. E. Walsh, and E. A. Coutsias, in High-Power Microwave Sources, edited by V. Granatstein and I. Alexeff (Artech House, Boston 1987), Chap. 13.

[2] D. J. Sullivan, IEEE Trans. Nucl. Sci., NS-30, 3426 (1983).

[3] R. D. Scarpetti and S. C. Burkhart, IEEE Trans. Plasma Sci., PS-13, 506 (1985).

[4] H. Sze, J. Benford, T. Young, D. Bromley and B. Harteneck, IEEE Trams. Plasma Sci., PS-13, 492 (1985).

[5] T. J. T. Kwan, Phys. Rev. Lett., 57, 1895 (1986).

[6] K. G. Kostov, N. A. Nikolov, and V. A. Spassov, Electronics Lett., 29, 1069 (1993).

[7] P. Sprangle and A. T. Drobot, IEEE Trans. MTT-25, 528 (1977).

[8] I. G. Yovchev, I. P. Spassovsky, N. A. Nikolov, K. G. Kostov, and V. A. Spassov, J. Appl. Phys., 74, 3052 (1993).

[9] T. L. Lin, W. T. Chen, W. C. Liu, Y. Hu, and M. W. Wu, J. Appl. Phys., 68, 2038 (1990).



